

1 DRAFT 0.8
2 July 22, 2011
3 CERN report
4 ECFA report
5 NuPECC report
6 LHeC-Note-2011-001 GEN
7



8 **A Large Hadron Electron Collider at CERN**

9 Report on the Physics and Design
10 Concepts for Machine and Detector

11 **LHeC Study Group**

12 THIS IS THE VERSION FOR REFEREEING, NOT FOR DISTRIBUTION



Abstract

14 The physics programme and the design are described of a new electron-hadron collider, the LHeC, in which
15 electrons of 60 to possibly 140 GeV collide with LHC protons of 7000 GeV. With an ep design luminosity
16 of about $10^{33} \text{ cm}^{-2}\text{s}^{-1}$, the Large Hadron Electron Collider exceeds the integrated luminosity collected at
17 HERA by two orders of magnitude and the kinematic range by a factor of twenty in the four-momentum
18 squared, Q^2 , and in the inverse Bjorken x . The physics programme is devoted to an exploration of the energy
19 frontier complementing the LHC and its discovery potential for physics beyond the Standard Model with
20 high precision DIS measurements which are projected to solve a variety of fundamental questions in strong
21 and electroweak interactions. The LHeC thus becomes the world's cleanest high resolution microscope,
22 designed to continue the path of deep inelastic lepton-hadron scattering into unknown areas of physics and
23 kinematics. This includes electron-ion (eA) scattering into a range extended by four orders of magnitude as
24 compared to previous lepton-nucleus experiments. The LHeC may be realised as a ring-ring or linac-ring
25 collider. For both options the optics and beam dynamics studies are presented, along with technical design
26 considerations on the interaction region, magnets, cryo, rf, civil engineering and further components. A
27 design study is also presented of a detector suitable to perform high precision DIS measurements in a wide
28 range of acceptance using state-of-the art detector technology, which is modular and of limited size enabling
29 its fast installation. The detector includes tagging devices for electron, photon, proton and neutron detection
30 near to the beampipe. The LHeC may be built and is designed to be operated while the LHC runs. It so
31 represents a major opportunity for particle physics to progress and for the LHC to be further exploited.

LHeC Study Group

33 C.Adolphsen¹, S.Alekhin^{2,3}, H.Aksakal⁴, P.Allport⁵, J.L.Albacete⁶, V.Andreev⁷, R.Appleby⁸, N.Armesto⁹,
 34 G.Azuelos¹⁰, M.Bai¹¹, D.Barber³, J.Bartels¹², J.Behr³, O.Behnke³, S.Belyaev⁴, I.BenZvi¹¹, N.Bernard¹³,
 35 S.Bertolucci⁴, S.Bettoni⁴, S.Biswal⁴⁷, J.Blumlein³, H.Boettcher³, H.Braun⁴⁸, S.Brodsky¹, A.Bogacz¹⁴,
 36 C.Bracco⁴, O.Brueening⁴, E.Bulyak⁴⁹, A.Bunyatian³, H.Burkhardt⁴, R.Calaga¹¹, E.Ciapala⁴, R.Ciftci¹⁵,
 37 A.K.Ciftci¹⁵, B.A.Cole¹⁶, J.C.Collins¹⁷, J.Dainton⁵, A.De.Roeck⁴, D.d'Enterria⁴, A.Dudarev⁴, A.Eide¹⁸,
 38 E.Eroglu¹⁹, K.J.Eskola²⁰, L.Favart²¹, M.Fitterer⁴, S.Forte²², P.Gambino²³, T.Gehrmann²⁴, C.Glasman²⁵,
 39 R.Godbole²⁶, B.Goddard⁴, T.Greenshaw⁵, A.Guffanti²⁷, C.Gwenlan²⁸, T.Han²⁹, Y.Hao¹¹, F.Haug⁴, W.Herr⁴,
 40 B.Holzer⁴, M.Ishitsuka³⁰, M.Jacquet³¹, B.Jeanneret⁴, J.M.Jimenez⁴, H.Jung³, J.M.Jowett⁴, D.Kayran¹¹,
 41 F.Kosac¹⁹, A.Kilic¹⁹, K.Kimura³⁰, M.Klein⁵, U.Klein⁵, T.Kluge¹², G.Kramer¹², M.Korostelev⁸, A.Kosmicki⁴,
 42 P.Kostka³, H.Kowalski³, D.Kuchler⁴, M.Kuze³⁰, T.Lappi²⁰, P.Laycock⁵, E.Levichev³², S.Levonian³, V.N.Litvinenko¹¹,
 43 A.Lombardi⁴, C.Marquet⁴, B.Mellado²⁹, KH.Mess⁴, S.Moch³, I.I.Morozov³², Y.Muttoni⁴, S.Myers⁴, P.R.Newman³³,
 44 T.Omori³⁴, J.Osborne⁴, Y.Papaphilippou⁴, E.Paoloni³⁵, C.Pascaud³¹, H.Paukkunen⁹, E.Perez⁴, T.Pieloni³⁶,
 45 E.Pilic¹⁹, A.Polini³⁷, V.Ptitsyn¹¹, Y.Pupkov³², V.Radescu³⁸, S.Raychaudhuri²⁶, L.Rinolfi⁴, R.Rohini²⁶,
 46 J.Rojo²², S.Russenschuck⁴, C.A.Salgado⁹, K.Sampai³⁰, E.Sauvan³⁹, U.Schneekloth³, T.Schoerner Sadenius³,
 47 D.Schulte⁴, N.Soumitra²³, H.Spiesberger⁴¹, A.M.Stasto¹⁷, M.Strikman¹⁷, M.Sullivan¹, B.Surrow⁴⁰, S.Sultansoy¹⁵,
 48 Y.P.Sun¹, W.Smith⁴², I.Tapan¹⁹, P.Taels⁴³, H.Ten.Kate⁴, J.Terron²⁵, H.Thiesen⁴, L.Thompson⁸, K.Tokushuku³⁴,
 49 R.Tomas.Garcia⁴, D.Tommasini⁴, D.Trbojevic¹¹, N.Tsoupas¹¹, J.Tuckmantel⁴, K.Tywoniuk⁴⁴, G.Unel⁴,
 50 J.Urakawa³⁴, P.VanMechelen⁴³, A.Variola⁶, R.Veness⁴, A.Vivoli⁴, P.Vobly³², R.Wallny⁴⁵, G.Watt⁴, G.Weiglein¹²,
 51 C.Weiss¹⁴, U.A.Wiedemann⁴, U.Wienands¹, F.Willeke¹¹, V.Yakimenko¹¹, A.F.Zarnecki⁴⁶, F.Zimmermann⁴,
 52 F.Zomer³¹

53 ¹ *SLAC, Stanford Linear Accelerator, USA*
 54 ² *Serpukhov Institute, Russia*
 55 ³ *DESY, Hamburg, Germany*
 56 ⁴ *CERN, Geneva, Switzerland*
 57 ⁵ *Liverpool, UK*
 58 ⁶ *IPhT Saclay, France*
 59 ⁷ *LPIMoscow, Russia*
 60 ⁸ *Cockcroft Institute, UK*
 61 ⁹ *University of Santiago de Compostela, Spain*
 62 ¹⁰ *Montreal University, Canada*
 63 ¹¹ *Brookhaven National Laboratory, BNL, USA*
 64 ¹² *Hamburg, Germany*
 65 ¹³ *University of California in Los Angeles, UCLA, USA*
 66 ¹⁴ *Jefferson Laboratory, USA*
 67 ¹⁵ *Ankara University, Turkey*
 68 ¹⁶ *Columbia University, USA*
 69 ¹⁷ *Pennsylvania State University, USA*
 70 ¹⁸ *NTNU, ??*
 71 ¹⁹ *Uludag University, Turkey*
 72 ²⁰ *Jyvaskyla University, Finland*
 73 ²¹ *IIHE Brussels, Belgium*
 74 ²² *INFN Milano, Italy*
 75 ²³ *INFN Torino, Italy*
 76 ²⁴ *Zurich, Switzerland*
 77 ²⁵ *Madrid, Spain*
 78 ²⁶ *Tata Institute, India*
 79 ²⁷ *Freiburg University, Germany*
 80 ²⁸ *Oxford University, UK*
 81 ²⁹ *Harvard University, USA*

82 30 *Tokyo Institute of Technology, Japan*
83 31 *Orsay, LAL, France*
84 32 *BINP, Russia*
85 33 *Birmingham, UK*
86 34 *KEK, Japan*
87 35 *Pisa, Italy*
88 36 *EPFL, Lausanne, Switzerland*
89 37 *Bologna, Italy*
90 38 *Heidelberg, Germany*
91 39 *Lyon, France*
92 40 *Massachusetts Institute of Technology, MIT, USA*
93 41 *University of Mainz, Germany*
94 42 *Madison, USA*
95 43 *Antwerpen, Belgium*
96 44 *Lund University, Sweden*
97 45 *ETHZ, Zurich, Switzerland*
98 46 *Warsaw, Poland*
99 47 *Orissa University, India*
100 48 *Paul Scherrer Institute, Switzerland*
101 49 *Charkov, Ukraine*

102

Preface

103

104 Preparations for new, big machines take time. The idea of an electron-proton collider in the LEP-LHC
105 tunnel was discussed already in 1984 [?], at the first LHC workshop at Lausanne. This was the time when
106 the first ever built ep collider, HERA, was approved by the German government, a machine of about 30 GeV
107 electron beam energy and nearly 1 TeV proton beam energy, a combination of a warm dipole electron ring
108 with a superconducting dipole proton ring, in a 6 km circumference tunnel. The machine started operation
109 8 years after its approval. It reached luminosities of $10^{31} \text{ cm}^{-2}\text{s}^{-1}$ in its first phase of operation which could
110 be enlarged by about a factor of 4 in the subsequent, upgraded configuration. HERA never attempted to
111 collide electrons with deuterons nor with ions, a sad premiere in the history of deep inelastic scattering.

112 The realisation of HERA had followed a number of attempts to realise ep interactions in collider mode,
113 mainly driven by the unforgettable Bjoern Wiik: Since the late 60's, he and colleagues had considered such
114 machines and proposed to probe proton's structure deeper with an ep collider at DORIS [?], later at PETRA
115 (PROPER) [?] and subsequently at the SPS at CERN (CHEEP) [?]. Further ep collider studies were made
116 for PEP [?], TRISTAN [?] and also the Tevatron (CHEER) [?].

117 In 1990 at a workshop at Aachen, the combination of LEP with the LHC was discussed, with studies [?, ?, ?]
118 on the luminosity, interaction region, a detector and the physics as it appeared before HERA. Following a
119 request of the CERN science policy committee (SPC), a brief study of the ring-ring ep collider in the LEP
120 tunnel was performed [?] with the estimated luminosity of about $10^{32} \text{ cm}^{-2}\text{s}^{-1}$.

121 At the end of the eighties it had been realised that there was a possible end of increasing the energy
122 of ep colliders in the ring-ring configuration, because of the synchrotron radiation losses of an electron ring
123 accelerator. The classic SLAC fixed target ep experiment already had used a 2 mile linac. For ep linac-ring
124 collider configurations, two design sketches were published, in 1988 [?] and in 1990 [?], which considered
125 electron beam energies of up to a few hundred GeV. As part of the TESLA linear collider proposal, an
126 option (THERA) was studied [?] to collide electrons of a few hundred GeV energy with protons, and also
127 ions, from HERA at DESY. Later, in 2003, the possibility was evaluated to combine LHC protons with CLIC
128 electrons [?]. It was yet realised, that the bunch structures of the LHC and CLIC were not compliant with
129 the need for high luminosities.

130 When in September 2007 the SPC asked again for whether one could realise an ep collider at CERN,
131 some of us had written a paper [?], in the year before, in which for the first time it had been shown in detail
132 that a luminosity of $10^{33} \text{ cm}^{-2}\text{s}^{-1}$ was achievable. This appeared possible in a ring-ring configuration and
133 based on the ultimate LHC beam, with $1.7 \cdot 10^{11}$ protons in bunches 25 ns apart. Due to the smallness of
134 the tune-shift, it was found to be feasible to simultaneously operate pp with the LHC and ep in the new
135 machine, which in 2005 was termed the LHeC [?]. Thus it appeared possible to realise an ep collider which
136 was complementary to the LHC, much like HERA was to the Tevatron, with an integrated luminosity of
137 $\text{O}(100) \text{ fb}^{-1}$, a factor of hundred more than HERA had collected over its lifetime of 15 years.

138 It was clear that with a centre of mass energy of about $\sqrt{s} \simeq 1.5 \text{ TeV}$ an exciting programme of energy
139 frontier deep inelastic scattering (DIS) measurements was in reach, comprising searches and analyses for
140 physics beyond the Standard Model, novel measurements in QCD and electroweak physics to unprecedented
141 precision, as well as DIS physics at so low Bjorken x , that all the known laws of parton and gluon interactions
142 were to be modified for avoiding the violation of unitarity. It had also been realised that the kinematic region,
143 in terms of four momentum transfer squared, Q^2 , and $1/x$, accessed in lepton-nuclear interactions could be

144 extended by 4 orders of magnitude using the ion beams of the LHC. A salient theme of the LHeC therefore
145 is the mapping of the gluon field, over six orders of magnitude in Bjorken x , in protons, neutrons and nuclei,
146 with unprecedented sensitivity.

147 In the fall 2007, (r)ECFA and CERN invited us to work out the LHeC concept to a degree, which would
148 allow to understand its physics programme, evaluate the accelerator options and their technical realisation
149 and to also design a detector, which would be affordable and capable of realising a high precision, large
150 acceptance experimental programme of deep inelastic scattering at the energy frontier. The electron beam
151 energy was set to be around 70 GeV, with due consideration of a much increased energy also. The wall plug
152 power which would be spent for the electron beam was limited to 100 MW.

153 For the installation of the LHC it had been decided to remove LEP from the tunnel and to also reuse the
154 injector chain. If one wants to realise an ep collider based on the LHC, a new electron machine has to be built.
155 The subsequent report details two solutions for the chosen default electron beam energy of $E_e = 60$ GeV.
156 One can either build and install a new ring, with modern magnet technology, on top of the LHC, using
157 a new 10 GeV injector. One can alternatively build a linac, i.e. two 10 GeV superconducting linacs in a
158 racetrack configuration, which by employing energy recovery techniques has the equivalent of about 1 GW
159 power available to also reach 10^{33} cm⁻²s⁻¹ luminosity. The linac would be of about the same length as the
160 one used for the discovery of quarks at SLAC [?, ?], the Q^2 , however, with which parton interactions were
161 studied at the LHeC exceeded that from 1969 by a factor of nearly 10^5 .

162 It was early on agreed that for the report a few years were to be devoted, also because none of the people
163 engaged had anything near to full time for this endeavour. There were three workshops held, in 2008-2010,
164 which annually assembled about a hundred experts on theory, experiment and accelerator to develop the
165 LHeC design concepts. The project was presented annually to ECFA and in 2008 to ICFA, see [?]. In view
166 of the unique electron-ion scattering programme of the LHeC, the design effort became also supported by
167 NuPECC, and the LHeC is now part of the NuPECC roadmap for European nuclear physics as released in
168 2010 [?]. Following an intermediate report to the Science Policy Committee of CERN, in July 2010, the SPC
169 considered the LHeC “an option for a future project at CERN”.

170 The LHeC by its nature is an upgrade of the LHC. It enriches the physics harvest related to the gigantic
171 investment in the LHC substantially. Whatever the outcome of the searches at the LHC for physics beyond
172 the Standard Model is, an ep collider operating at the energy frontier is guaranteed to deepen the under-
173 standing of TeV scale physics and thus will support the development of the theory of particles and their
174 interactions.

175 The LHeC needs the LHC proton and ion beams to be operational and so the design is made for syn-
176 chronous pp and ep operation, as well as AA and eA , including deuterons. Should the LHC be eventually
177 upgraded to even higher beam energy, beyond 7 TeV per beam [?], it would open an even higher energy reach
178 for ep also. There is a future for deep inelastic scattering at the energy frontier, beginning with the LS3
179 shutdown of the LHC, envisaged for 2022, likely leading into further decades. As Frank Wilczek put it, “one
180 of the joys of our subject is the continuing of our culture that bridges continents and generations” [?].

181 Our science is driven by curiosity, by theoretical expectations, sometimes too great, but also by experiment
182 and technology, and the authors of this study therefore hope that the LHeC may be given the chance to
183 contribute to the common efforts of our community for a deeper understanding of nature.

184
185 Max Klein (Chair of the LHeC Steering Committee)

Geneva, July NNth, 2011

186
187 The current, preliminary version of this report, as of July NNth, is handed to the referees appointed by the
188 CERN directorate. Following their reports, also considering further developments and necessary updates
189 of the current draft, the report will be handed to CERN, ECFA and NuPECC. It so is directed to become
190 part of the European deliberations about the future directions of particle physics, which must be seen in the
191 context of the LHC and its now outcoming results at half its design energy.

192 **Contents**

193

Part I

194

Introduction

Chapter 1

Lepton-Hadron Scattering

It is almost exactly 100 years since the birth of the scattering experiment as a means of revealing the structure of matter. Geiger and Marsden's experiment [?] and its interpretation by Rutherford [?] set the scene for a century of ever-deeper and more precise resolution of the constituents of the atom, the nucleus and the nucleon. Lepton-hadron scattering has played a crucial role in this exploration over the past 55 years. The finite radius of the proton of about 1 fm was first established through elastic electron-proton scattering experiments [?]. Later, through deep inelastic electron proton scattering at Stanford [?, ?], proton structure was understood in terms of quarks, still the smallest known constituents of matter. With the discovery of Bjorken scaling with Q^2 of the proton structure function $F_2(x, Q^2)$ for the originally accessed values around $x \simeq 0.2$ and its quark model interpretation in terms asymptotic freedom [?, ?], deep inelastic scattering (DIS) became a field of fundamental theoretical importance [?] to the understanding of the strong interaction. Precise measurements of the parton momentum distributions of the nucleon became a major testing ground for the selection and development of Quantum Chromodynamics (QCD) [?] as the appropriate theory of the strong interaction.

QCD is a Yang-Mills gauge theory, in which the interaction between confined quarks proceeds via coloured gluon exchange. With improved resolution, as provided by increased Q^2 , quarks can be resolved as quarks radiating gluons, whilst gluons may split into quark-antiquark pairs or, due to the non-abelian nature of the underlying gauge field theory, into pairs of gluons. The development of QCD calculations beyond leading order is one of the most remarkable recent achievements of particle physics theory and experiment. It leads to a consistent description of all perturbatively accessible hadron observables, including the logarithmic violations of the scaling of F_2 away from $x \sim 0.2$, as has recently been precisely measured over a wide kinematic range at HERA [?].

As discussed in detail in Section II, several fundamental properties of nature could be explored more deeply than hitherto through a continued programme of scattering electrons from protons and nuclei at a Large Hadron electron Collider (LHeC), as is proposed in sections III and IV. A few of the most pressing questions are outlined briefly below.

- The Standard Model of particle physics contains a remarkable, but unexplained, symmetry between quarks and leptons [?], with three generations, in each of which two quarks and two leptons are embedded. It was pointed out long ago [?] that it appears somewhat artificial that the basic building blocks of matter share the electromagnetic and the weak interactions but differ in their sensitivity to the strong interaction. Many theories which unify the quark and lepton sectors, such as models based on the E6 gauge group [?], R -parity violating supersymmetry and left-right symmetric extensions of the Standard Model [?], predict new resonant states with both lepton and baryon numbers, usually referred to as leptoquarks. Although some of the specific theories have not been supported by experiment, the search for leptoquarks has been a prime motivation for high energy scattering experiments. An LHeC, in combination with the existing LHC programme, can extend this search into a previously unexplored mass region, with the prospect of deciphering the leptoquark quantum numbers.

233
234
235
236
237
238
239
240

241
242
243
244
245

246
247
248
249
250
251
252
253
254

255
256
257
258
259
260

261
262

263
264

265
266
267

268
269
270

271
272
273
274

275
276
277
278
279

- The mass of baryons is almost entirely due to strong interaction field energy, generated through quark and gluon vacuum condensates in a manner which is not yet well understood. It may be accessible through a more detailed mapping of QCD dynamics, particularly in the low x region of proton structure, where gluon densities become very large and $g \rightarrow gg$ splittings dominate. The search for the Higgs boson, which explains the masses of the electroweak bosons, is currently the central focus of particle physics and is expected to be resolved within the next year by the ATLAS and CMS experiments. The question of hadronic mass deserves similar exploration, especially for glueball states, which may be produced in ep collisions.
- No analytic proof yet exists that QCD should exhibit the property of colour confinement, though it is reasonable to assume that it is a consequence of gluon dynamics, as reflected for example in popular hadronisation models [?] and Monte Carlo simulations on the lattice. Studying the behaviour of gluons under new extreme conditions and contrasting the conditions under which the proton stays intact with those in which it is destroyed may help to shed light on the precise mechanism at work.
- the strong coupling constant α_s decreases as energy scales increase, in contrast to the energy dependence of the weak coupling and the fine structure constant. It appears possible that the three constants approach a common value at energies of order 10^{15} GeV, such that the distinctions we make between the electromagnetic, weak and strong interactions are merely a consequence of the low energy scale at which we live. The possible grand unification of the known interactions has been one of the major goals of modern particle physics theory and experiment. Progress in this area requires that we know α_s , by far the most poorly constrained of the fundamental couplings, much more accurately than is currently the case. The LHeC promises a factor of ten reduction in the uncertainty on α_s based on a major renewal and extension of the experimental and the theoretical basis of DIS.
- After quarks were discovered, a distinction was soon made between valence and sea quarks [?]. However, it was not until the high energy colliding beam configuration of HERA became available that the rich partonic structure of the proton was fully realised. Despite the resulting fast development of our knowledge of the parton distribution functions (PDFs) in the proton, there are still many outstanding important questions concerning quark-gluon interactions in hadronic matter, which cannot be answered with currently available data.
 - Modern determinations of PDFs assume that sea quarks and anti-quarks have the same momentum distributions. Experimental constraints are required to test this assumption.
 - Similarly, the strange-quark density is often assumed to be a fixed fraction of the down-quark density, for which there is no experimental verification.
 - With no high energy DIS data available from deuteron scattering, the low x quark content of the neutron is unresolved. It is important to test the assumption of isospin symmetry, which relates for example the neutron down quark distribution to the proton up-quark distribution.
 - The gluon density is still not precisely determined, particularly at small and large x values. This has implications for example to our knowledge of the Higgs boson cross section at the LHC, since the dominant production mechanism is through gluon-gluon fusion.
 - At small x the gluon distributions can be described in terms of the solutions of the BFKL equation for the Pomeron wave function. The QCD Pomeron is a composite state of reggeized gluons. The investigation at the LHeC of the odderon and other Reggeons constructed from gluons will be important for our understanding of hadronic spectra.
 - With no data on the scattering of leptons from heavy ions with colliding beam kinematics, our knowledge of the modifications to nucleon parton densities when they are bound inside nuclei, rather than free, is restricted to high x values. This is reflected in a lack of detailed understanding of shadowing phenomena, particularly for the gluon density and a corresponding lack of knowledge of the initial state of heavy ion collisions at LHC energies.

- 280 – The emission of partons is assumed in PDF fits to be governed by the linear DGLAP evolution
281 equations, an approximation to a full solution to QCD in which parton cascades are ordered
282 in transverse momentum. There are good reasons to believe that the DGLAP approximation is
283 insufficient to describe the Q^2 evolution of low x partons, even within the x range to which the
284 LHC rapidity plateau corresponds. Inclusive DIS and jet data in an extended low x kinematic
285 regime are required to resolve this situation.
- 286 – The understanding of the role of heavy quarks in QCD is still at its infancy. Charm may exist in
287 an intrinsic state [?]. The b density, which plays an important role in the production mechanisms
288 for new particles in many LHC scenarios, is measured to only about 20 % accuracy and the role
289 of top quarks in DIS is completely unknown due to the limited energy and luminosity of HERA.
- 290 – While ordinary quark distributions correspond to an incoherent sum of squared amplitudes, a new
291 approach has been developed, which uses quark amplitudes and Generalised Parton Distributions
292 (GPDs) to understand proton structure in a new, three-dimensional way [?,?]. Our understanding
293 of GPDs is limited by the relative paucity of experimental data on exclusive DIS channels.
- 294 • The rapid rise of the proton gluon density as x decreases cannot continue indefinitely. At x values within
295 the reach of LHeC ep and eA scattering, a transition takes place from the currently known DIS regime
296 in which the proton behaves as a dilute system to a new low x domain in which parton densities saturate
297 and the proton approaches a 'black disk' limit [?]. This latter region represents a fundamentally new
298 regime of strong interaction dynamics, for which a rich phenomenology has developed, but where the
299 detailed mechanisms and the full consequences are not yet known. Experimental data at sufficiently
300 low x with scales which are large enough to allow a partonic interpretation are urgently required in
301 order to test the models and fully understand the behaviour of partons at high densities.

302 Despite its huge success in describing existing high energy data, the Standard Model is known to be
303 incomplete, not only due to the absence of an experimentally established mechanism for electroweak sym-
304 metry breaking. As the exploitation of the TeV energy regime and the high luminosities of the LHC era
305 develops further, a full understanding can only be obtained by challenging the existing theory through new
306 precision measurements, as broad in scope as possible, with initial states involving leptons as well as quarks
307 and gluons. Furthermore, many of the remaining open fundamental questions in our field are associated with
308 the strong interaction sector of the Standard Model, to which a future facility such as the LHeC provides
309 unique experimental sensitivity.

Chapter 2

Design Considerations

The following sections describe briefly which general considerations have determined the LHeC design as presented in this report. Major changes to the underlying assumptions would naturally require an appropriately changed variation of the design.

2.1 DIS and Particle Physics

Deep inelastic scattering experiments with charged leptons may be classified as low energy, medium and high energy experiments. The pioneering low energy DIS experiment, which discovered quarks, was performed at SLAC. Classic medium energy experiments were the BCDMS and the NMC experiments at CERN, while HERA, the first ep collider ever built, had pushed the DIS energy reach to the Fermi scale. This allowed the field of deep inelastic scattering to develop as part of the energy frontier particle physics, complementary to the Tevatron and LEP. In all three areas, the field of DIS is considering upgrade projects with the 12 GeV upgrade at Jlab, the medium energy colliders at Jlab and/or BNL, possibly fixed target further neutrino experiments and the LHeC.

The LHeC provides the only realistic possibility for an energy frontier ep programme in the coming probably three decades. Owing to the LHC, there is one opportunity to complement the TeV scale pp machine with a TeV energy ep collider, besides a pure lepton collider in this energy range. It took about 30 years for HERA, LEP and the Tevatron to be built, operated and analysed. The exploration of the tera energy scale is subject to similar time horizons.

2.2 Synchronous pp and ep operation

The intense, energetic hadron beams of the LHC provide the unique possibility to realise a luminous experimental programme of deep inelastic scattering at TeV energies. The LHeC is therefore by its nature an upgrade to the LHC, which gives it its site and in a way determines its dimensions too. The first design consideration builds on the assumption that the LHC still runs in pp mode when an electron beam becomes operational. This has several implications:

- The LHeC has to be built in the coming about 10 years.
- The design has to be adapted for synchronous pp and ep (and AA and eA) operation, as with magnets in the IR to steer three beams and with civil engineering and detector modularity requirements to be compliant with the LHC operation and upgrade programme.
- The synchronous operation of pp and ep allows to collect a high integrated luminosity and makes the most efficient use of both the proton beams and the electron beam installation too.

341 It can not realistically be assumed today, that the ep physics would commence only when the pp programme
 342 was finished: because of the finite LHC lifetime, which nowadays is estimated to be about 20 years.

343 The LHeC is thus thought and designed to accompany the proton and the ion physics programme of the
 344 LHC in its high luminosity phase, now assumed to begin in 2023.

345 2.3 Choice of Electron Beam Energy

346 The centre of mass energy squared of an ep collider is $s = 4E_e E_p$. It determines the maximum four-
 347 momentum transfer squared, Q^2 , between the electron and the proton because $Q^2 = sxy$, where x is the
 348 fraction of four momentum of the proton carried by the struck parton while y is the inelasticity of the
 349 scattering process which in the laboratory frame is the relative energy transfer, with $0 < x, y \leq 1$.

350 HERA has operated with a proton beam energy of $E_p = 0.92$ TeV and an electron (and positron) beam
 351 energy of $E_e = 27.5$ GeV. With Sokolov-Ternov build-up times of about half an hour, the electron beam
 352 became polarised and mean polarisations of up to 40% were achieved. HERA has not accelerated any
 353 hadron beam other than protons. The LHeC has to surpass these parameters significantly for a unique and
 354 exciting programme to be pursued.

355 The LHeC can use an up to 7 TeV energy proton beam. For this design study the electron beam energy
 356 is set to 60 GeV. This implies that the gain in s , or Q^2 at fixed (x, y) , as compared to HERA will be a
 357 factor of 16.6, or about 4 in \sqrt{s} . The real gain in range of Q^2 and x will even be larger as with the superior
 358 luminosity even the highest Q^2 values and x close to 1 become accessible. The kinematic range of the LHeC
 359 as compared to HERA at low x and at high Q^2 is illustrated in Fig. ??.

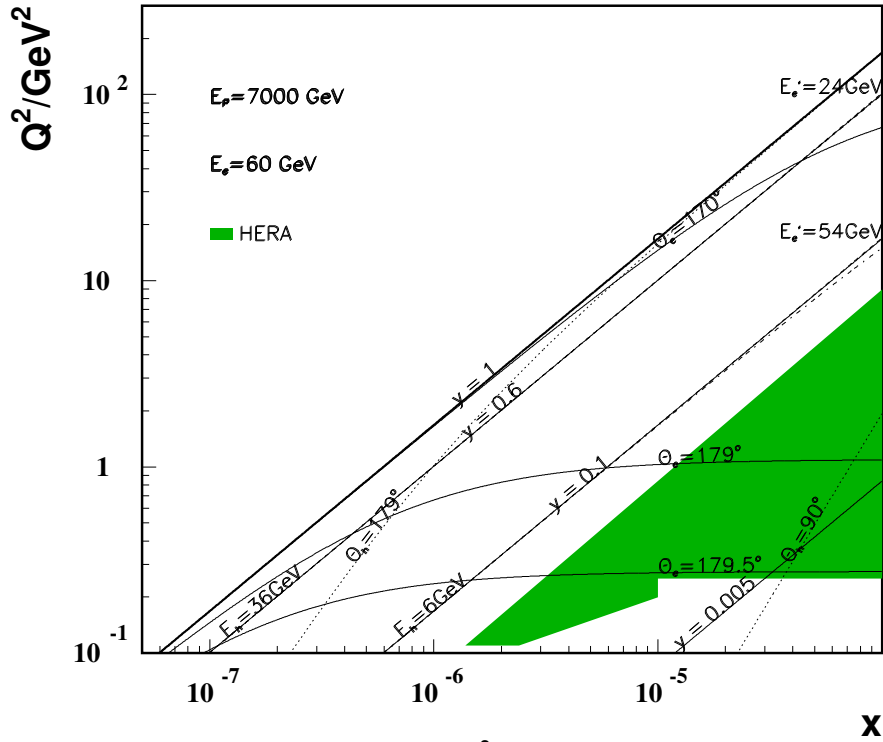
360 The choice of a default $E_e = 60$ GeV for this design report is dictated by physics and by practical
 361 considerations:

- 362 • New physics has been assumed to appear at the TeV energy scale. At the time of completion of this
 363 report, the LHC has excluded much of the sub-TeV physics beyond the Standard Model (SM) but
 364 leaves the possibility open of resonant lepton-parton states with masses of larger than about 500 GeV,
 365 for which the LHeC would be a particularly suitable machine with a range of up to $M \lesssim \sqrt{s}$.
- 366 • High precision QCD and electroweak physics require a maximum range in $\ln Q^2$ and highest Q^2 ,
 367 respectively. The unification of electromagnetic and weak forces takes place at $Q^2 \simeq M_Z^2$ which is much
 368 exceeded by the LHeC energies. Part of the electroweak physics requires lepton beam polarisation which
 369 as is shown below, for the ring, may reach values as at HERA at 60 GeV but much less at significantly
 370 larger E_e , and for the linac, may be around 90% for electrons at all E_e .
- 371 • The discovery of gluon saturation requires to measure at typical values of small $x \simeq 10^{-5}$ with $Q^2 \gg$
 372 M_p^2 , where M_p is the mass of the proton. The choice of energies ensures this discovery at the LHeC in
 373 the DIS region, both in ep and in eA .
- 374 • Energy losses by synchrotron radiation, $\propto E_e^4$, both in the ring and the return arcs for the linac, can be
 375 kept at reasonable levels, in terms of the power, P , needed to achieve high luminosity and the radius
 376 of the racetrack return arcs for the linac too.

377 It so appears that 60 GeV is an appropriate and affordable choice. It yet is well possible that the 60 GeV
 378 may not be the final value of the electron beam energy, especially if the LHC would find non-SM physics
 379 just above the now chosen energy range. The design therefore also considers a dedicated high energy beam
 380 of 140 GeV as an option, which yet has not been worked out to any comparable detail ¹.

¹Such a large E_e would also fit better to a future HE LHC, when about 16 TeV proton beam energy might become available in the yet much farther future, as that would keep the $e - p$ beam energy asymmetry tolerable.

LHeC - Low x Kinematics



LHeC - High Q^2 Kinematics

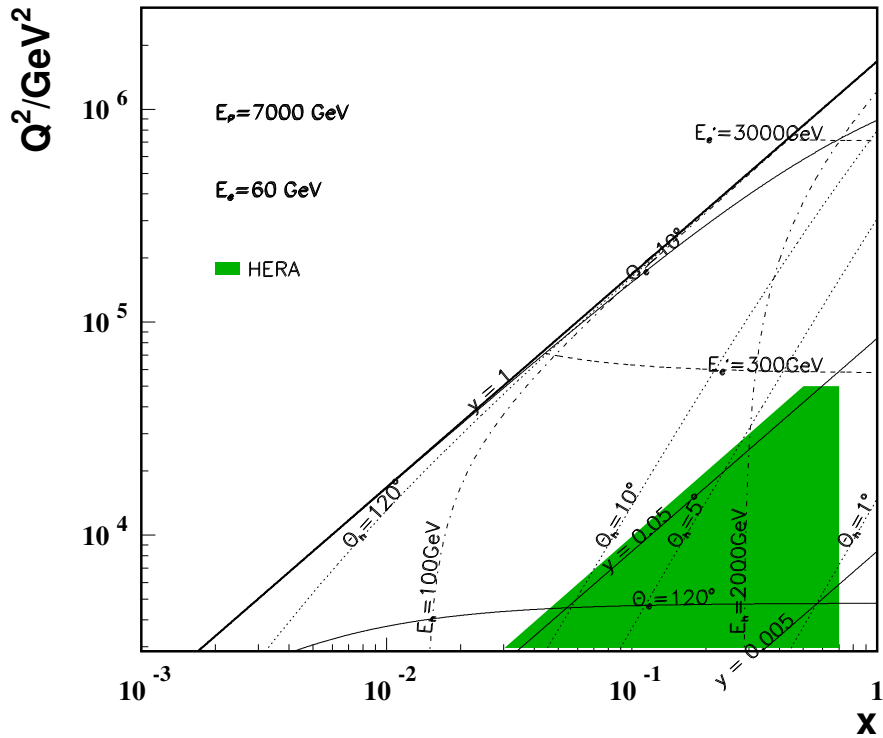


Figure 2.1: Kinematics of ep scattering at the LHeC at low x (top) and high Q^2 (bottom). Solid (dotted) curves correspond to constant polar angles θ_e (θ_h) of the scattered electron (hadronic final state). The polar angle is defined with respect to the proton beam direction. Dashed (dashed-dotted) curves correspond to constant energies E'_e (E_h) of the scattered electron (hadronic final state). The shaded area illustrates the region of kinematic coverage in neutral current scattering at HERA. The energy and angle isochrone lines are discussed in the detector design chapter in detail.

2.4 Detector Constraints

One easily recognises, in Fig. ??, that the asymmetry of the electron and proton beam energies poses severe constraints to the detector design: i) the “whole” low Q^2 and low x physics requires to measure the electron, of energy $E'_e \lesssim E_e$, scattered in backward direction between about 170° and 179° , and ii) the forward scattered final state, of energy comparable to E_p , needs to be reconstructed down to very small angles in order to cover the high x region in a range of not too extreme Q^2 .

The current detector design considers an option to have split data taking phases, like HERA I and II, with different interaction region configurations, a high acceptance phase, covering $1^\circ - 179^\circ$, at reduced luminosity and a high luminosity phase, of acceptance limited to $8^\circ - 172^\circ$. In the course of the study, however, an optics was found for the high acceptance configuration with only a factor of two reduced luminosity. It is likely, therefore, that the TDR will lead to a unification of these configurations and correspondingly weakened demands on the modularity of the inner detector region.

Synchronous ep and pp operation implies that at least one of the four IPs, currently occupied by experiments, will have to be free'd for an LHeC detector. It was decided to use for this report IP2 as an example site and to limit the study of bypasses, in the ring option, to IP1 and IP5. This does not imply that any decision was taken about which experiment one would favour to stop in ten years.

2.5 Two Electron Beam Options

It was shown a few years ago [?] that an electron beam in the LHC tunnel would allow to achieve an outstanding luminosity of about $10^{33} \text{ cm}^{-2}\text{s}^{-1}$ in ep interactions for both electrons and positrons. It is obvious, however, that while such a ring may be built without any major technical obstacle, installing it on top of the LHC magnet ring would be a non-trivial engineering task. For this reason it was decided to consider besides this “ring-ring (RR)” option also a “linac-ring (LR)” configuration, with a linear electron accelerator tangential to the LHC. For the comparison of RR and LR options, E_e was kept the same 60 GeV. The ring may extend to somewhat higher energies, while only a Linac would allow to exceed 100 GeV E_e largely.

This report presents all major components and considerations for both the RR and the LR configuration. A choice between the two configurations is envisaged soon after the appearance of the CDR. It is important to consider that the RR configuration delivers high electron and positron luminosity, with difficulties for high polarisation, while the LR configuration has a high potential for polarised electrons but difficulties to deliver an intense positron beam, yet offering also a photon beam option. A choice of one over the other option has primarily to be based on physics but as well technical, cost and further considerations, which is why considerable effort had been spent to develop both options to the required detail. No attempt is made in the report to favour one over the other configuration. In the period of this design study both options came into a very fruitful interaction and occasional competition which nicely boosted both designs.

2.6 Luminosity and Power

The relation of the luminosity, power and energy differs for the RR and the LR configurations. In the case of the ring accelerator, as for HERA, the luminosity for matched beams is determined by the number of protons per bunch (N_p), the normalised proton beam emittance (ϵ_p), the x, y coordinates of the proton beam beta function values at the interaction point ($\beta_{x,y}$) and the electron beam current (I_e) as

$$L = \frac{N_p \cdot \gamma}{4\pi\epsilon\epsilon_p} \cdot \frac{I_e}{\sqrt{\beta_{px}\beta_{py}}}, \quad (2.1)$$

420 with $\gamma = E_p/M_p$. The design luminosity assumes the so-called ultimate proton beam parameters for $E_p =$
 421 7 TeV with $1.7 \cdot 10^{11}$ protons per bunch and $\epsilon_p = 3.8 \mu\text{m}$. Eq. ?? then corresponds to

$$L = 8.2 \cdot 10^{32} \text{cm}^{-2} \text{s}^{-1} \cdot \frac{N_p 10^{11}}{1.7} \cdot \frac{m}{\sqrt{\beta_{px} \beta_{py}}} \cdot \frac{I_e}{50 \text{mA}}, \quad (2.2)$$

422 where the electron beam current is given by

$$I_e = 0.35 \text{mA} \cdot P[\text{MW}] \cdot \left(\frac{100}{E_e[\text{GeV}]}\right)^4 \quad (2.3)$$

423 Consequently one needs to minimize the β functions and gains linearly with P and like E_e^4 when decreasing
 424 the electron beam energy. With $\beta_{x(y)} = 1.8(0.5) \text{m}$, see the optics section, one obtains a typical value of
 425 $10^{33} \text{cm}^{-2} \text{s}^{-1}$ luminosity for $E_e = 60 \text{GeV}$ with 30 MW of beam power. The dependence of $L(E, P)$ is shown
 426 in Fig. ?? (top) for the RR configuration. While with the matching requirement for each E_e an evaluation
 427 would have to be done of the β functions, one yet recognises that the RR option has a great potential to
 428 indeed achieve very high luminosities, even exceeding $10^{33} \text{cm}^{-2} \text{s}^{-1}$ if E_e was a bit lowered and P somewhat
 429 enlarged.

430 For this design report on the LHeC a wall-plug power limit was set of 100 MW, about one fifth of what
 431 one is considering for CLIC, for example. With a 10 years running period at such a high luminosity and
 432 N_p probably enlarged, one can consider an integrated luminosity for the LHeC of $O(100) \text{fb}^{-1}$ a realistic
 433 perspective in simultaneous operation with the LHC. This is two orders of magnitude more than HERA
 434 delivered. That is necessary for exploiting the high Q^2 and large x boundaries. It means that the whole
 435 low Q^2 physics program, with the exception of rare processes as DVCS and subject to trigger acceptance
 436 considerations, may yet be pursued in a rather short period of time.

437 A linear electron beam colliding with a storage ring proton beam was considered quite some time ago [?].
 438 Its luminosity, for head-on collisions, can be obtained from the following relation [?], similar to Eq. ??

$$L = \frac{N_p \cdot \gamma}{4\pi\epsilon\epsilon_p} \cdot \frac{I_e}{\beta^*}, \quad (2.4)$$

439 which scales as

$$L = 8 \cdot 10^{31} \text{cm}^{-2} \text{s}^{-1} \cdot \frac{N_p 10^{11}}{1.7} \cdot \frac{0.2 \text{m}}{\beta^*} \cdot \frac{I_e}{1 \text{mA}}, \quad (2.5)$$

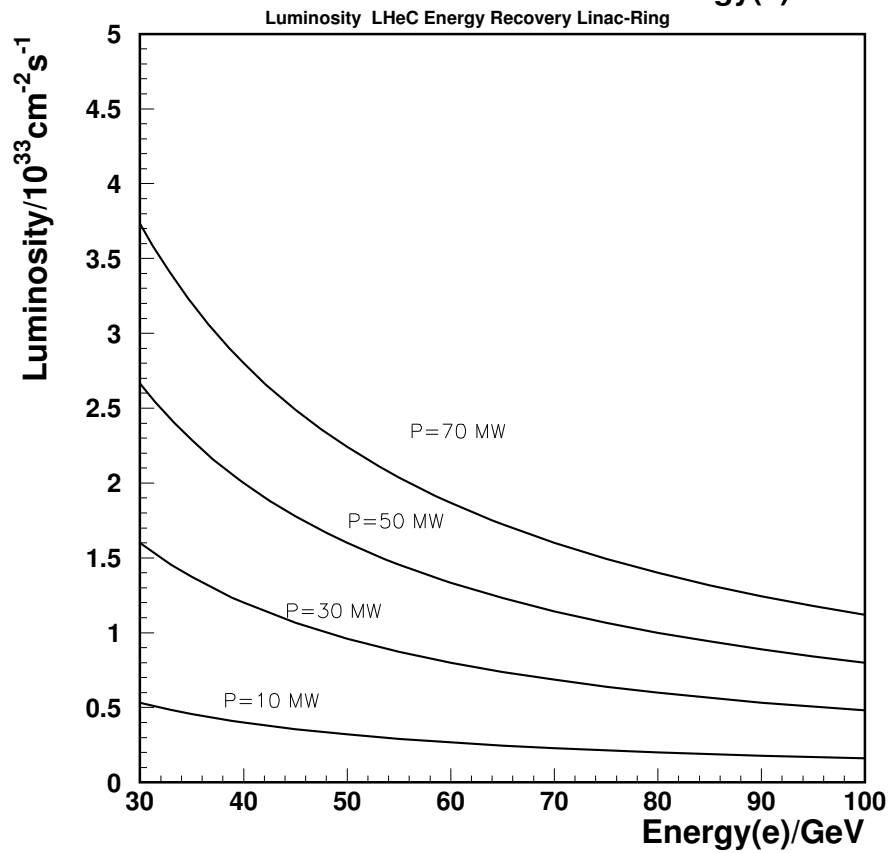
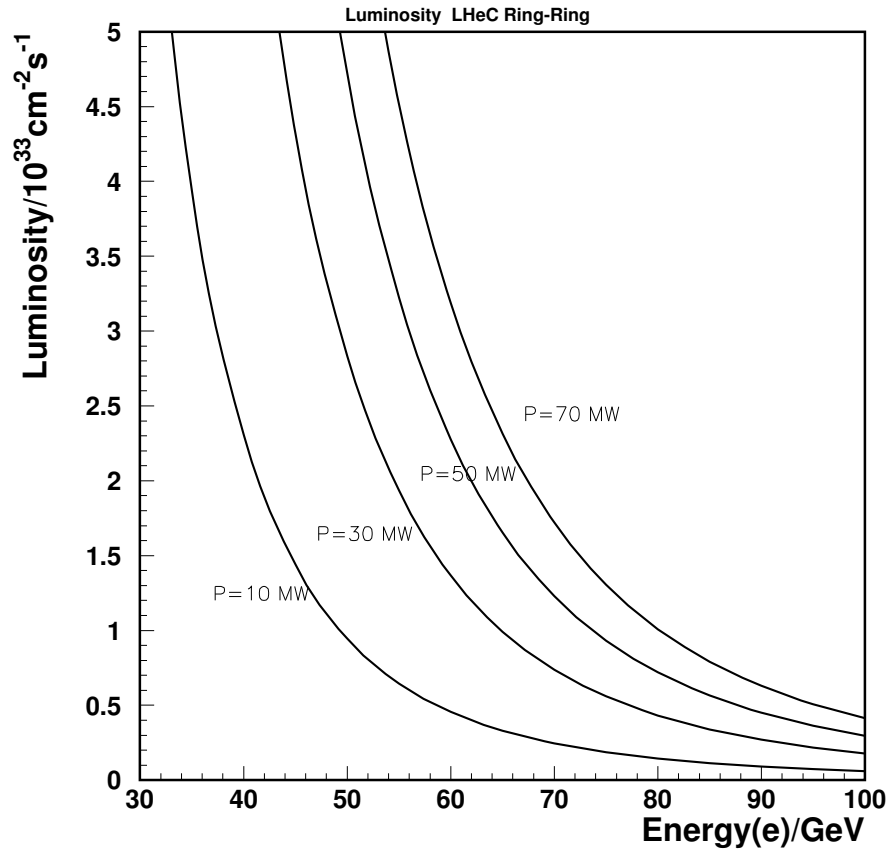
440 where the electron beam current is given by

$$I_e = \text{mA} \cdot \frac{P[\text{MW}]}{(1 - \eta)E_e[\text{GeV}]}. \quad (2.6)$$

441 Here η denotes the efficiency of the energy recovery process. It is easy to see that a pulsed linac without
 442 recovery is short by an order of magnitude in the luminosity to the RR configuration, even for an ambitious
 443 β^* value of 0.1 m, which is introduced in the LR section. With energy recovery, however, and an efficiency
 444 above 90% as is expected to be realistic for the LHeC case, one obtains luminosities of similar value as in
 445 the RR case, see Fig. ?. The energy recovery linac (ERL) operates the cavities in CW mode at moderate
 446 gradients of typically 20 MV/m.

447 The recovery of energy requires a racetrack geometry of the linac with return arcs, or possibly two linacs
 448 of opposite orientation as was originally considered [?]. This introduces synchrotron radiation losses as a
 449 parameter of concern to the LR configuration also. With the design here proposed, the arcs have a bending
 450 radius of 764 m, which leads to a LR accelerator of about 9 km length, which is one third of the LHC
 451 circumference, and requires a small compensation stage for the energy losses in the arcs.

452 A straight high energy, pulsed linac is also considered, which at $E_e = 140 \text{GeV}$, reaches a luminosity of
 453 about $5 \cdot 10^{31}$, the design value of the HERA upgrade phase. One can also contemplate about stages of ERL
 454 returns, which provide much higher luminosities in this case, as is briefly demonstrated in this report too.



16
 Figure 2.2: Estimated luminosity, in units of $10^{33} \text{ cm}^{-2} \text{ s}^{-1}$, for the RR configuration (top) and the LR energy recovery configuration (bottom), displayed as a function of the electron beam energy with the beam power as a parameter, see text.

⁴⁵⁵ Chapter 3

⁴⁵⁶ Executive Summary

⁴⁵⁷ The excutive summary will be added after the completion of the referee process.

458

Part II

459

Physics

Chapter 4

Precision QCD and Electroweak Physics

This chapter elucidates the LHeC physics prospects in the fields of high precision QCD tests and electroweak physics. The first section ?? discusses inclusive deep inelastic scattering and consists of three parts: cross sections and structure functions, the simulation of LHeC data and a special part on the longitudinal Structure Function \mathbf{F}_L . The second section ?? describes the determination of parton distributions using the simulated data. After introducing the QCD fit Ansatz, the prospects for determining various quark distributions are detailed, with a focus on valence, strange and top quarks. Then the sections ?? and ?? discuss the expected improvements in the determination of the gluon distribution and of the strong coupling constant, respectively. Section ?? concludes the discussion on parton distribution determinations from inclusive data with the prospects from electron-deuteron scattering. The next section ?? details the expected electroweak physics highlights at LHeC. The following two sections ?? and ?? explain the precision QCD tests that can be performed at LHeC with heavy flavours (charm and beauty) and with jets in the final state, respectively. The chapter concludes with section ?? on the prospects for measuring the total photoproduction cross sections.

4.1 Inclusive Deep Inelastic Scattering

4.1.1 Cross Sections and Structure Functions

The scattering amplitude for electron-proton scattering is a product of lepton and hadron currents times the propagator characteristic of the exchanged particle, a photon or Z_0 in neutral current scattering, a W^\pm in charged current scattering. The inclusive scattering cross section therefore is given by the product of two tensors,

$$\frac{d^2\sigma}{dx dQ^2} = \frac{2\pi\alpha^2}{Q^4 x} \sum_j \eta_j L_j^{\mu\nu} W_j^{\mu\nu}, \quad (4.1)$$

where j denotes the summation over γ , Z_0 exchange and their interference for NC, and $j = W^+$ or W^- for CC. The leptonic tensor $L_j^{\mu\nu}$ is related to the coupling of the electron with the exchanged boson and contains the electromagnetic or the weak couplings, such as the vector and axial-vector electron- Z_0 couplings, v_e and a_e , in the NC case. This leptonic part of the cross section can be calculated exactly in the standard electroweak $U_1 \times SU_2$ theory. The hadronic tensor, however, describing the interaction of the exchanged boson with the proton, can only be reduced to a sum of structure functions, $F_i(x, Q^2)$, but not be fully calculated. Conservation laws reduce the number of basic structure functions in unpolarised ep scattering to $i = 1 - 3$. In perturbative QCD the structure functions are related to parton distributions f *via* coefficient

489 functions C

$$[F_{1,3}, F_2] = \sum_i \int_0^1 [1, z] \frac{dz}{z} C_{1,2,3} \left(\frac{x}{z}, \frac{Q^2}{\mu_r^2}, \frac{\mu_f^2}{\mu_r^2}, \alpha_s(\mu_r^2) \right) \cdot f_i(z, \mu_f^2, \mu_r^2), \quad (4.2)$$

490 where i sums the quark q , anti-quark \bar{q} and gluon g contributions and $f_i(x)$ is the probability distribution of
 491 the parton of type i to carry a fraction x of the proton's longitudinal momentum. The coefficient functions
 492 are exactly calculable but depend on the factorisation and renormalisation scales μ_f and μ_r . The parton
 493 distributions are not calculable but have to be determined by experiment. Their Q^2 dependence obeys
 494 evolution equations. A general factorisation theorem, however, has proven the parton distributions to be
 495 universal, i.e. to be independent of the type of hard scattering process. This makes deep inelastic lepton-
 496 nucleon scattering a most fundamental process: the parton distributions in the proton are measured best
 497 with a lepton probe and may be used to predict hard scattering cross sections at, for example, the LHC. The
 498 parton distributions are derived from measurements of the structure functions in NC and CC scattering, as
 499 is discussed below.

500 4.1.2 Neutral Current

501 The neutral current deep inelastic ep scattering cross section, at tree level, is given by a sum of generalised
 502 structure functions according to

$$\frac{d^2\sigma_{NC}}{dx dQ^2} = \frac{2\pi\alpha^2 Y_+}{Q^4 x} \cdot \sigma_{r,NC} \quad (4.3)$$

$$\sigma_{r,NC} = \mathbf{F}_2 + \frac{Y_-}{Y_+} \mathbf{xF}_3 - \frac{y^2}{Y_-} \mathbf{FL}, \quad (4.4)$$

503 where the electromagnetic coupling constant α , the photon propagator and a helicity factor are absorbed in
 504 the definition of a reduced cross section σ_r , and $Y_{\pm} = 1 \pm (1-y)^2$. The functions \mathbf{F}_2 and \mathbf{xF}_3 depend on
 505 the lepton beam charge and polarisation (P) and on the electroweak parameters as [?]

$$\begin{aligned} \mathbf{F}_2^{\pm} &= F_2 + \kappa_Z (-v_e \mp P a_e) \cdot F_2^{\gamma Z} + \kappa_Z^2 (v_e^2 + a_e^2 \pm 2P v_e a_e) \cdot F_2^Z \\ \mathbf{xF}_3^{\pm} &= \kappa_Z (\pm a_e + P v_e) \cdot xF_3^{\gamma Z} + \kappa_Z^2 (\mp 2v_e a_e - P(v_e^2 + a_e^2)) \cdot xF_3^Z. \end{aligned} \quad (4.5)$$

506 In the on-mass shell \overline{MS} scheme the propagator function κ_Z is given by the weak boson masses (M_Z , M_W)

$$\kappa_Z(Q^2) = \frac{Q^2}{Q^2 + M_Z^2} \cdot \frac{1}{4 \sin^2 \Theta \cos^2 \Theta} \quad (4.6)$$

507 with the weak mixing angle $\sin^2 \Theta = 1 - M_W^2/M_Z^2$. In the hadronic tensor decomposition [?] the structure
 508 functions are well defined quantities. In the Quark Parton Model (QPM) the longitudinal structure function
 509 is zero [?] and the two other functions are given by the sums and differences of quark (q) and anti-quark (\bar{q})
 510 distributions as

$$\begin{aligned} (F_2, F_2^{\gamma Z}, F_2^Z) &= x \sum (e_q^2, 2e_q v_q, v_q^2 + a_q^2) (q + \bar{q}) \\ (xF_3^{\gamma Z}, xF_3^Z) &= 2x \sum (e_q a_q, v_q a_q) (q - \bar{q}), \end{aligned} \quad (4.7)$$

511 where the sum extends over all up and down type quarks and $e_q = e_u, e_d$ denotes the electric charge of up-
 512 or down-type quarks. The vector and axial-vector weak couplings of the fermions ($f = e, u, d$) to the Z_0
 513 boson in the standard electroweak model are given by

$$v_f = i_f - e_f 2 \sin^2 \Theta \quad a_f = i_f \quad (4.8)$$

514 where $e_f = -1, 2/3, -1/3$ and $i_f = I(f)_{3,L} = -1/2, 1/2, -1/2$ denotes the left-handed weak isospin charges,
 515 respectively. Thus the vector coupling of the electron, for example, is very small, $v_e = -1/2 + 2 \sin^2 \Theta \simeq 0$,
 516 since the weak mixing angle is roughly equal to $1/4$.

517 At low Q^2 and low y the reduced NC cross section, Eq. ??, to a very good approximation is given by
 518 $\sigma_r = F_2(x, Q^2)$. At $y > 0.5$, F_L makes a sizeable contribution to $\sigma_{r,NC}$. In the DGLAP approximation of
 519 perturbative QCD, to lowest order, the longitudinal structure function is given by [?]

$$F_L(x) = \frac{\alpha_s}{4\pi} x^2 \int_x^1 \frac{dz}{z^3} \cdot \left[\frac{16}{3} F_2(z) + 8 \sum e_q^2 \left(1 - \frac{x}{z}\right) z g(z) \right], \quad (4.9)$$

520 which at low x is dominated by the gluon contribution. A measurement of F_L requires a variation of the
 521 beam energy.

522 Two further structure functions can be accessed with cross section asymmetry measurements, in which
 523 the charge and/or the polarisation of the lepton beam are varied. A charge asymmetry measurement, with
 524 polarisation values P_{\pm} of the e^{\pm} beam, determines the following structure function combination

$$\sigma_{r,NC}^+(P_+) - \sigma_{r,NC}^-(P_-) = -\kappa_Z a_e (P_+ + P_-) \cdot F_2^{\gamma Z} + \frac{Y_-}{Y_+} \kappa_Z a_e \cdot [2x F_3^{\gamma Z} + (P_+ - P_-) \kappa_Z a_e x F_3^Z] \quad (4.10)$$

525 neglecting terms $\propto v_e$ which can be easily obtained from Eq. ???. If data are taken with opposite polarisation
 526 and charge, the asymmetry represents a measurement of the difference of quark and anti-quark distributions
 527 in NC, see Eq. ??. In contrast to what is often stated, the charge asymmetry is a parity conserving quantity
 528 $\propto a_e a_q$. Assuming symmetry between sea and antiquarks, it is a direct measure of the valence quarks,
 529 $x F_3^{\gamma Z} = 2u_v + d_v$ in ep . This function was measured for the first time in μ^{\pm} Carbon scattering by the
 530 BCDMS Collaboration [?] at large $x > 0.2$ and for Q^2 of about 50 GeV². With the LHeC, for the first time,
 531 high precision measurements of $x F_3$ in NC become possible as is demonstrated in Sect. ??. These will access
 532 the valence quarks at low $x \lesssim 0.001$ for the first time in direct measurements.

533 A genuine polarisation asymmetry measurement, keeping the beam charge fixed, according to eqs. ?? and
 534 ?? determines a similar combination of $F_2^{\gamma Z}$ and $x F_3^{\gamma Z}$

$$\frac{\sigma_{r,NC}^{\pm}(P_L) - \sigma_{r,NC}^{\pm}(P_R)}{P_L - P_R} = \kappa_Z [\mp a_e F_2^{\gamma Z} + \frac{Y_-}{Y_+} v_e x F_3^{\gamma Z}] \simeq \mp \kappa_Z a_e F_2^{\gamma Z} \quad (4.11)$$

535 neglecting again the term $\propto v_e$. The product $a_e F_2^{\gamma Z}$ is proportional to combinations $a_e v_q$ and thus a direct
 536 measure of parity violation at very small distances.

537 The structure function $F_2^{\gamma Z}$ accesses a new combination of quark distributions and is measurable for the
 538 first time, and with high precision, at the LHeC, see Fig. ??, in which the result is shown of its possible
 539 measurement. The remarkable precision on $F_2^{\gamma Z}$ illustrates the huge potential in precision and range which
 540 the LHeC brings. For the study of electroweak effects one clearly desires to have the maximum beam energy
 541 and polarisation available as the comparison of the two results for different beam conditions but the same
 542 luminosity in Fig. ?? shows.

543 The polarisation asymmetry also permits a high precision measurement of the weak mixing angle at
 544 different Q^2 values, below and to much higher values than M_Z^2 , at which $\sin^2 \Theta$ was precisely measured at
 545 LEP and the SLC, see Sect. ??.

546 4.1.3 Charged Current

547 The inclusive polarised charged current $e^{\pm}p$ scattering cross section can be written as

$$\frac{d^2 \sigma_{CC}^{\pm}}{dx dQ^2} = \frac{1 \pm P}{2} \cdot \frac{G_F^2}{2\pi x} \cdot \left[\frac{M_W^2}{M_W^2 + Q^2} \right]^2 Y_{\pm} \cdot \sigma_{r,CC}. \quad (4.12)$$

548 The reduced charged current cross section, analogous to the NC case Eq. ??, is a sum of structure function
 549 terms

$$\sigma_{r,CC}^{\pm} = W_2^{\pm} \mp \frac{Y_-}{Y_+} x W_3^{\pm} - \frac{y^2}{Y_+} W_L^{\pm}. \quad (4.13)$$

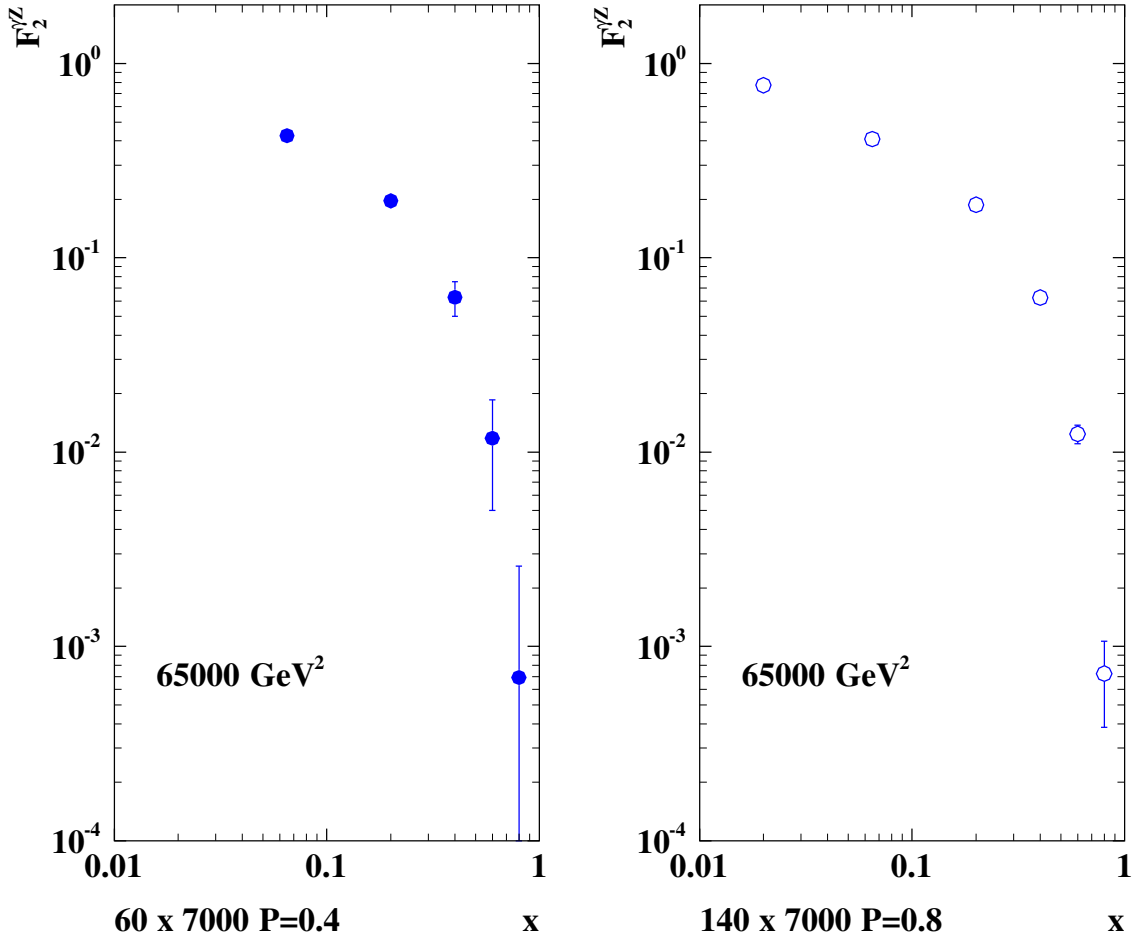


Figure 4.1: Simulation of the measurement of the γZ interference structure function $F_2^{\gamma Z}$, shown as a function of x for a typical high Q^2 value, for two LHeC configurations ($E_e = 60$ GeV and $P = \pm 0.4$, left) and ($E_e = 140$ GeV and $P = \pm 0.9$, right). The proton beam energy is 7 TeV and the luminosity assumed is 10 fb^{-1} per polarisation state. This function is a measure for parity violation and provides additional information on the quark distributions as it is proportional to $e_q v_q$ to be compared with e_q^2 in the lowest order function F_2 . Shown are statistical uncertainties only. The systematic uncertainty can be expected to be small as in the asymmetry many effects cancel and because at the LHeC such asymmetries are large, and the polarisation possibly controlled at the per mille level, as is discussed in the technical part of the CDR.

550 In the on-mass shell scheme, the Fermi constant G_F is defined, see for example [?], using the weak boson
 551 masses as

$$G_F = \frac{\pi\alpha}{\sqrt{2}M_W^2 \sin^2\theta(1 - \Delta r)} \quad (4.14)$$

552 with $\sin^2\theta = 1 - M_W^2/M_Z^2$ as above. The higher order correction term Δr can be approximated [?] as
 553 $\Delta r = 1 - \alpha/\alpha(M_Z) - 0.0094(m_t/173\text{GeV})^2/\tan^2\theta$, and thus introduces a dependence of the DIS cross
 554 section on the mass of the top quark. The choice of G above allows the CC cross section, Eq. ??, to be
 555 rewritten as

$$\frac{d^2\sigma_{CC}^\pm}{dx dQ^2} = \frac{1 \pm P}{2} \cdot \frac{2\pi\alpha^2 Y_+}{Q^4 x} \cdot \kappa_W^2 \cdot \sigma_{r,CC}, \quad (4.15)$$

556 with

$$\kappa_W(Q^2) = \frac{Q^2}{Q^2 + M_W^2} \cdot \frac{1}{4\sin^2\theta}, \quad (4.16)$$

557 which is convenient for the consideration of NC/CC cross section ratios.

558 In the QPM (where $W_L^\pm = 0$), the structure functions represent beam charge dependent sums and
 559 differences of quark and anti-quark distributions and are given by

$$W_2^+ = x(\bar{U} + D), \quad xW_3^+ = x(D - \bar{U}), \quad W_2^- = x(U + \bar{D}), \quad xW_3^- = x(U - \bar{D}). \quad (4.17)$$

560 Using these equations one finds

$$\sigma_{r,CC}^+ \sim x\bar{U} + (1-y)^2 xD, \quad (4.18)$$

$$\sigma_{r,CC}^- \sim xU + (1-y)^2 x\bar{D}. \quad (4.19)$$

561 Combined with Equation ??, which approximately reduces to

$$\begin{aligned} \sigma_{r,NC}^\pm &\simeq [c_u(U + \bar{U}) + c_d(D + \bar{D})] + \kappa_Z[d_u(U - \bar{U}) + d_d(D - \bar{D})] \\ c_{u,d} &= e_{u,d}^2 + \kappa_Z(-v_e \mp Pa_e)e_{u,d}v_{u,d} \quad d_{u,d} = \pm a_e a_{u,d} e_{u,d}, \end{aligned} \quad (4.20)$$

562 one finds that the NC and CC cross section measurements at the LHeC determine the complete set U, D, \bar{U}
 563 and \bar{D} , i.e. the sum of up-type, of down-type and of their anti-quark-type distributions. Below the b quark
 564 mass threshold, these are related to the individual quark distributions as follows

$$U = u + c \quad \bar{U} = \bar{u} + \bar{c} \quad D = d + s \quad \bar{D} = \bar{d} + \bar{s}. \quad (4.21)$$

565 Assuming symmetry between sea quarks and anti-quarks, the valence quark distributions result from

$$u_v = U - \bar{U} \quad d_v = D - \bar{D}. \quad (4.22)$$

566 4.1.4 Cross Section Simulation and Uncertainties

567 The LHeC extends the kinematic range as compared to HERA in the negative momentum transfer squared
 568 Q^2 from a maximum of about 0.03 to 1 TeV² and towards low x , e.g. for $Q^2 = 3\text{GeV}^2$, from about $4 \cdot 10^{-5}$ to
 569 $2 \cdot 10^{-6}$. The projected increase of integrated luminosity by a factor of 100 allows to also extend the kinematic
 570 range at large x , in charged currents, from practically about 0.4 to 0.8. Due to the enlarged electron beam
 571 energy E_e the range of high inelasticity $y \simeq 1 - E'_e/E_e$ should extend closer to 1. A reduced noise in the
 572 calorimeters may allow to reach lower values of y than at HERA, also because the hadronic y is determined
 573 as the sum over $E - p_z$ divided by twice the with the LHeC enhanced electron beam energy. While these
 574 extensions of kinematic coverage and improvements of statistical precision are impressive, an estimate of the
 575 impact of LHeC NC and CC cross section measurements on derived quantities such as structure functions
 576 and parton distributions requires to also estimate the expected systematic measurement accuracy as may be
 577 achieved with the detector described in Chapter ?? below. In the following the assumptions and simulation

578 results are presented for the NC and the CC cross sections, which are subsequently used in QCD fit and
 579 other analyses throughout this report.

580 The systematic uncertainties of the DIS cross sections have a number of sources, which at HERA have
 581 broadly been classified as uncorrelated and correlated across bin boundaries. For the NC case, the uncor-
 582 related sources, apart from data and Monte Carlo statistics, are a global efficiency uncertainty, due to for
 583 example tracking or electron identification errors, photoproduction background, calorimeter noise and ra-
 584 diative corrections. The correlated uncertainties result from imperfect energy scale and angle calibrations.
 585 In the classic kinematic reconstruction methods used here, and described in Sect. ?? one uses the scattered
 586 electron energy E'_e and polar angle θ_e complemented by the energy of the hadronic final state E_h ¹. The
 587 correlated errors are due to scale uncertainties of the electron energy E'_e and of the hadronic final state
 588 energy E_h . There are also systematic errors due to an uncertainty of the measurement of the electron polar
 angle θ_e . The assumptions used in the simulation of pseudodata are summarised in Table ??.

source of uncertainty	error on the source or cross section
scattered electron energy scale $\Delta E'_e/E'_e$	0.1 %
scattered electron polar angle	0.1 mrad
hadronic energy scale $\Delta E_h/E_h$	0.5 %
calorimeter noise (only $y < 0.01$)	1-3 %
radiative corrections	0.5%
photoproduction background (only $y > 0.5$)	1 %
global efficiency error	0.7 %

Table 4.1: Assumptions used in the simulation of the NC cross sections on the amount of uncertainties from various sources. These assumptions correspond to the typical or best of what was achieved in the H1 experiment. Note that in the cross section measurement the energy scale and angular uncertainties are relative to the Monte Carlo and not to be confused with resolution effects which determine the purity and stability of binned cross sections. The total cross section error due to these uncertainties, e.g. for $Q^2 = 100 \text{ GeV}^2$, is about 1.2, 0.7 and 2.0 % for $y = 0.84, 0.1, 0.004$.

589 In the absence of a detailed detector simulation at this stage, the systematic NC cross uncertainties due
 590 to E'_e , θ_e and E_h are calculated, following [?], from the derivatives of the NC cross section in the chosen bins
 591 taking into account the Jacobians where needed. The results have been compared, for the HERA kinematics,
 592 with the H1 MC simulation of systematic errors [?] and found to be in very good agreement for all three
 593 sources. The resulting error depends much on the kinematics. At low Q^2 , for example, the systematic cross
 594 section error due to the uncertainty of θ_e rises because of $\delta Q^2/Q^2 = \delta E'_e/E'_e \oplus \tan(\theta_e/2) \cdot \delta\theta_e$ while at high
 595 Q^2 it is negligible. Low Q^2 is the backward region, of large electron scattering angles with respect to the
 596 proton beam direction.
 597

598 A particular challenge is the measurement at large x because the cross section varies as $(1-x)^c$, with
 599 $c \simeq 3$, and thus the relative error is amplified $\propto 1/(1-x)$ as x approaches 1. At high x the hadronic final
 600 state is scattered into the forward detector region where the energy calibration becomes challenging. The
 601 calculated correlated NC cross section errors are illustrated in Figs. ?? and ?? for $Q^2 = 2$ and 20000 GeV^2 ,
 602 respectively. In the detector chapter these calculations have been taken to define approximate requirements
 603 on the scale calibrations in the different detector regions. An example for the resulting cross section

¹Basically one determines Q^2 best with the electron kinematics and determines x from $y = Q^2/sx$. At large y the inelasticity is essentially measured with the electron energy $y \simeq 1 - E'_e/E_e$. At low y one has $y = E_h \sin^2(\theta_h/2)/E_e$ with the hadronic final state energy E_h and angle θ_h which results in $\delta y/y \simeq \delta E_h/E_h$ to good approximation. There have been various refined methods proposed to determine the DIS kinematics, as the double angle method or the so-called sigma method. For the estimate of the cross section uncertainty behaviour as functions of Q^2 and x , however, the simplest method using Q_e^2, y_e at large y and Q_e^2, y_h at low y is transparent and accurate enough within better than a factor of two. In much of the phase space, moreover, it is rather the uncorrelated efficiency or further specific errors than the kinematic correlations, which dominate the cross section measurement accuracy.

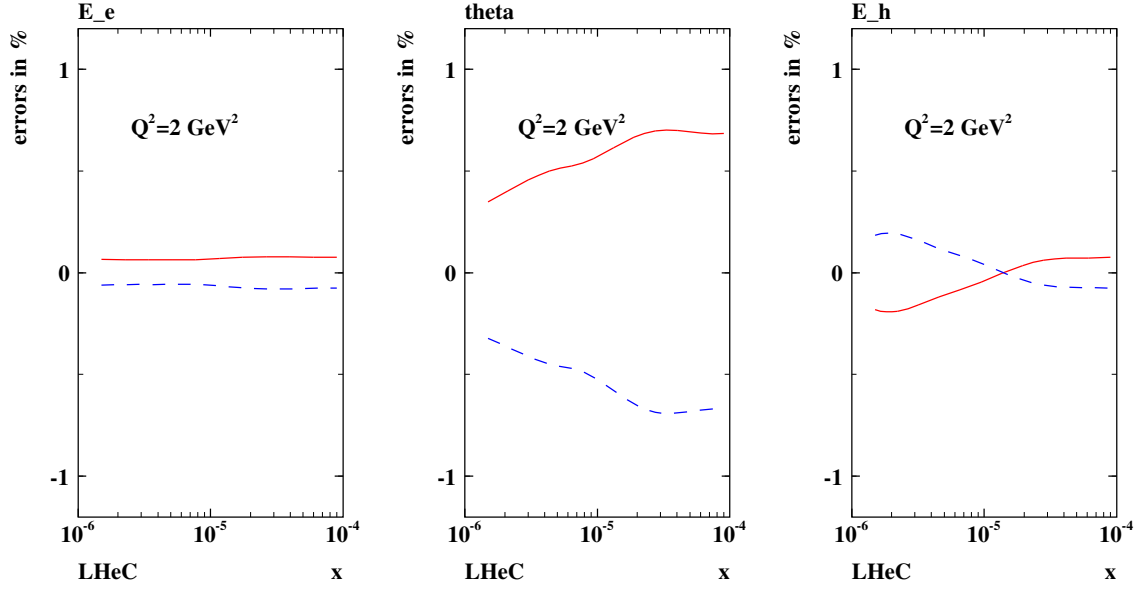


Figure 4.2: Neutral current cross section errors, calculated for $60 \times 7000 \text{ GeV}^2$, as result from scale uncertainties of the scattered electron energy $\delta E'_e/E'_e = 0.1\%$, of its polar angle $\delta\theta_e = 0.1 \text{ mrad}$ and the hadronic final state energy $\delta E_h/E_h = 0.5\%$, at low $Q^2 = 2 \text{ GeV}^2$ and correspondingly low x .

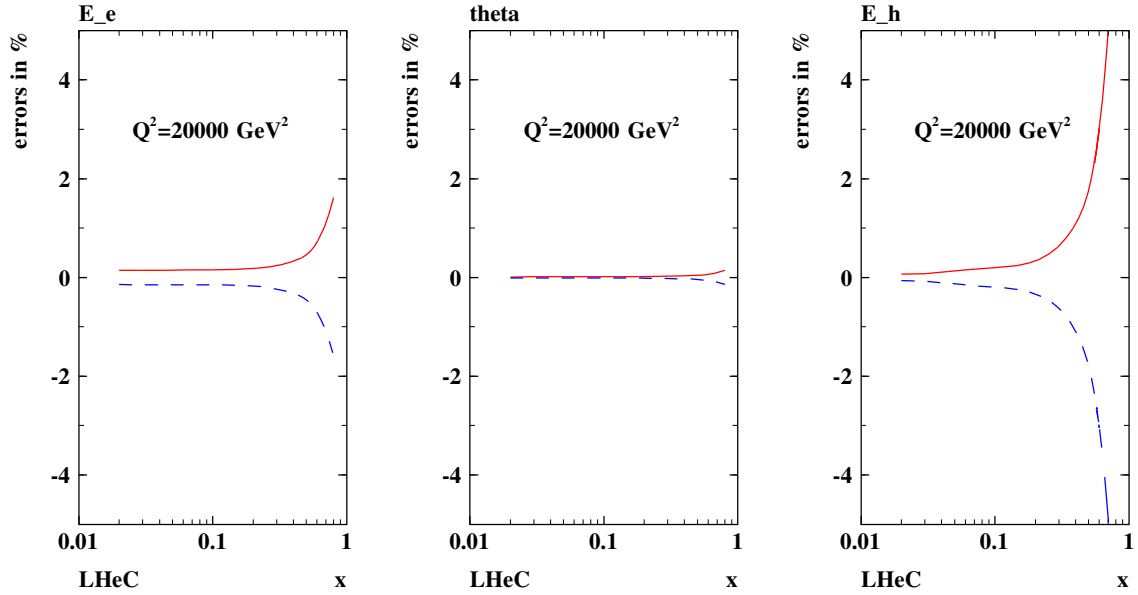


Figure 4.3: Neutral current cross section errors, calculated for $60 \times 7000 \text{ GeV}^2$ unpolarised e^-p scattering, as result from scale uncertainties of the scattered electron energy $\delta E'_e/E'_e = 0.1\%$, of its polar angle $\delta\theta_e = 0.1 \text{ mrad}$ and the hadronic final state energy $\delta E_h/E_h = 0.5\%$, at large $Q^2 = 20000 \text{ GeV}^2$ and correspondingly large x . Note that the characteristic behaviour of the relative uncertainty at large x , i.e. to diverge $\propto 1/(1-x)$, is independent of Q^2 , i.e. persistently observed at $Q^2 = 200000 \text{ GeV}^2$ for example too.

604 measurement is displayed in Fig. ??.

605 For the CC case, a similar simulation was done, albeit with less numeric effort. An illustration of the
 606 high precision and large range of the inclusive CC cross section measurements is presented in Fig. ??.

607 The systematic cross section error, based on the H1 experience, was set to 2% and for larger $x > 0.3$ a term
 608 was added to allow the error to rise linearly to 10% at $x = 0.9$. For both NC and CC cross sections
 609 the statistical error is given by the number of events but limited to 0.1% from below. With these error
 610 assumptions a number of data sets was simulated, both for NC and CC, which is summarised in Table ??.

611 The energies of these sets had been chosen prior to the final baseline energy choice. For the simulation of
 the F_L measurement, described below, a separate set of beam energies is considered.

Set	E_e/GeV	E_N/TeV	N	L^+/fb^{-1}	L^-/fb^{-1}	Pol
A	20	7	7	1	1	0
B	50	7	7	50	50	0.4
C	50	7	7	1	1	0.4
D	100	7	7	5	10	0.9
E	150	7	7	3	6	0.9
F	50	3.5	7	1	1	0
G	50	2.7	7	0.1	0.1	0.4
H	50	1	7	-	1	0

Table 4.2: Conditions for simulated NC and CC data sets for studies on the LHeC physics. Here, A defines a low electron beam energy option which is of interest to reach lowest Q^2 because Q_{min}^2 decreases $\propto E_e^{-2}$; B is the standard set, with a total luminosity split between different polarisation and charge states. C is a lower luminosity version which was considered in case there was a need for a dedicated low/large angle acceptance configuration, which according to more recent findings could be avoided since the luminosity in the restricted acceptance configuration is estimated, from the β functions obtained in the optics design, to be half of the luminosity in the full acceptance configuration; D is an intermediate energy linac-ring version, while E is the highest energy version considered, with the luminosities as given. It is likely that the assumptions for D and E on the positron luminosity are a bit optimistic. However, even with twenty times lower positron than electron luminosity one would have 0.5 fb^{-1} , i.e. the total HERA luminosity equivalent available in option D for example. F is the deuteron and G the lead option; finally H was simulated for a low proton beam energy configuration as is of interest to maximise the acceptance at large x .

612

613 4.1.5 Longitudinal Structure Function F_L

614 The inclusive, deep inelastic electron-proton scattering cross section at low Q^2 ,

$$\frac{d^2\sigma}{dx dQ^2} = \frac{2\pi\alpha^2 Y_+}{Q^4 x} [F_2(x, Q^2) - f(y) \cdot F_L(x, Q^2)], \quad (4.23)$$

615 is defined by two proton structure functions, F_2 and F_L with $y = Q^2/sx$, $Y_+ = 1 + (1-y)^2$ and $f(y) = y^2/Y_+$.
 616 The two functions reflect the transverse and the longitudinal polarisation state of the virtual photon probing
 617 the proton structure, i.e. $F_T = F_2 - F_L$ and F_L , respectively. The positivity of the transverse and longitudinal
 618 cross sections requires $0 \leq F_L \leq F_2$. Since for most of the kinematic range the y dependent factor $f(y)$ is
 619 very small, there follows that F_L causes in most of the kinematic range only a small correction to the reduced
 620 cross section, which is governed by F_2 , apart from the regio of maximum y . At small x , the inelasticity is
 621 given as $y \simeq 1 - E'_e/E_e$. Therefore, in order to extract F_L , DIS has to be measured extremely accurately
 622 at small scattered lepton energies, which is a question of how large E_e is, how to trigger and how to control
 623 the background from particle production at low energies. A variation of the beam energies is required to
 624 separate the two functions measured at the same x and Q^2 by variation of $y = Q^2/sx$.

LHeC

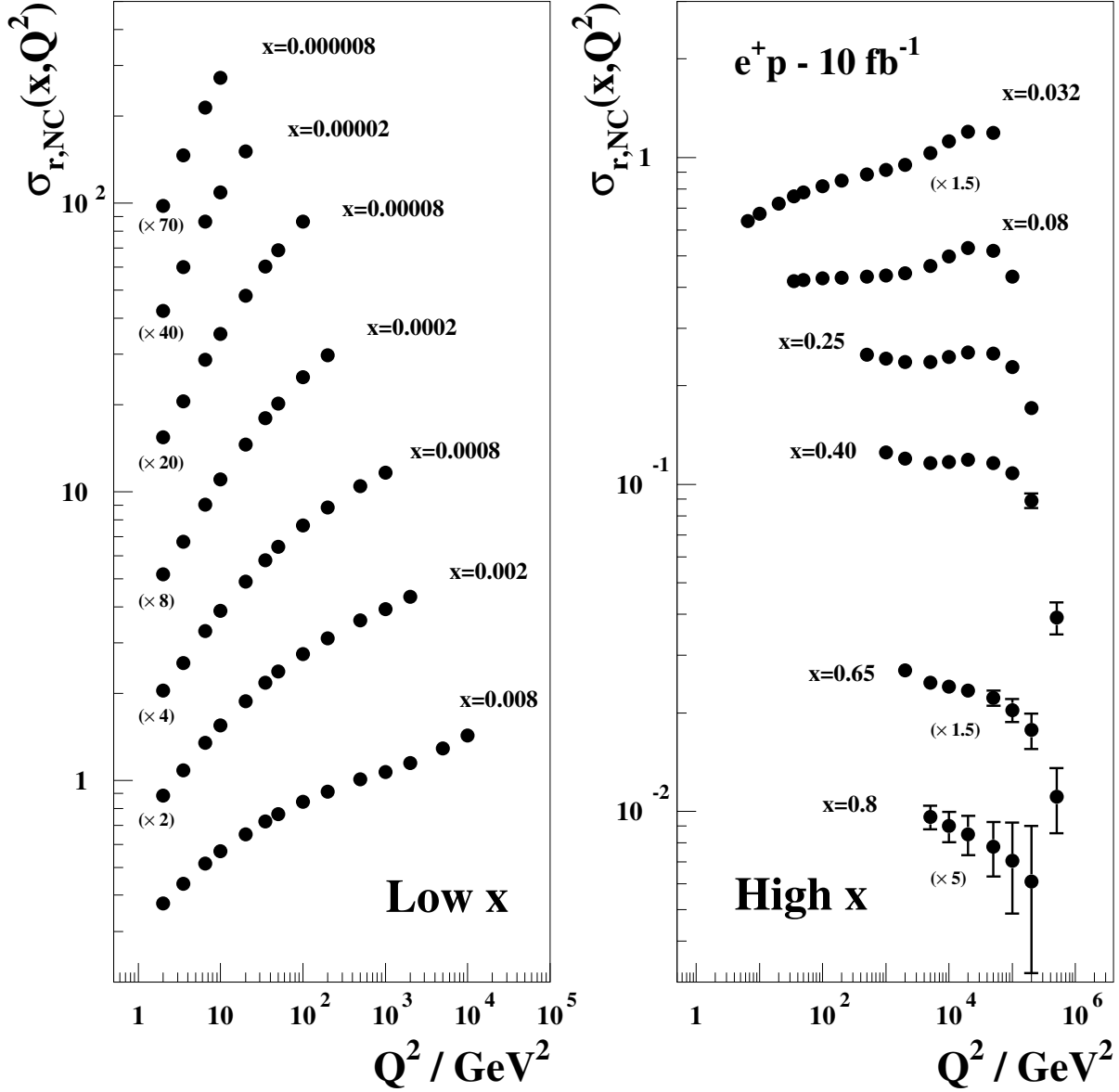


Figure 4.4: Simulated neutral current cross section measurement for an integrated luminosity of 10 fb^{-1} in unpolarised e^-p scattering at $E_e = 60$ and $E_p = 7000$ GeV. The reduced NC cross section is measured at unprecedented precision and range. Plotted is the total uncertainty which, where visible at high x and Q^2 , is dominated by the statistical error. Similar data sets are expected with different beam polarisations and charges, and in CC scattering, for $Q^2 \geq 100$ GeV 2 . The strong variations of σ_r with Q^2 , as at $x = 0.25$, are due to the effects of Z exchange as is discussed and illustrated subsequently. Departures from the strong rise of the reduced cross section, $\sigma_r \simeq F_2$, at very low x and Q^2 are expected to appear due to non-linear gluon-gluon interaction effects in the so-called saturation region.

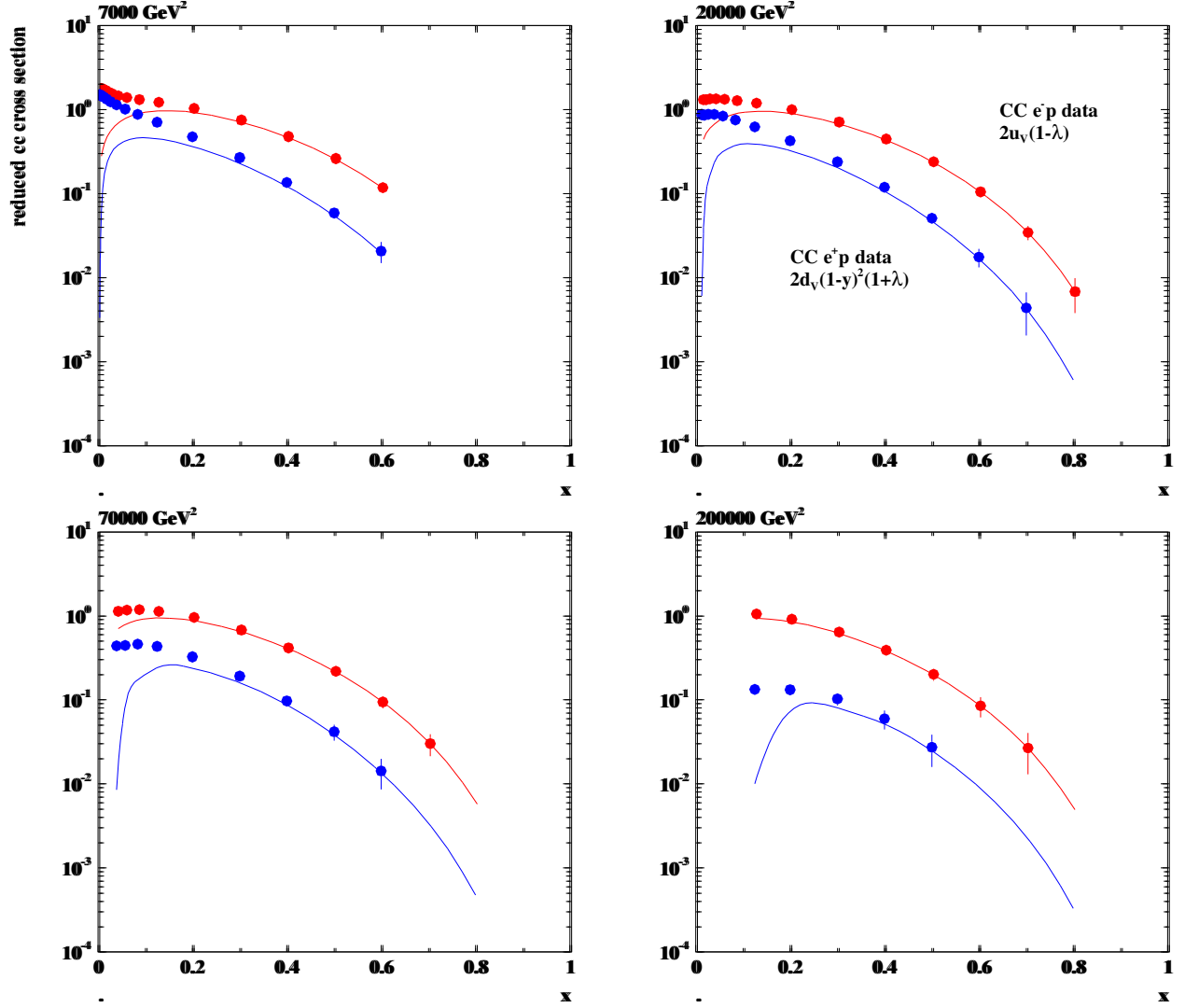


Figure 4.5: Reduced charged current cross sections with statistical uncertainties corresponding to 1 fb^{-1} electron (top data points, red) and positron (lower data points, blue) proton scattering at the LHeC, The curves are determined by the dominant valence quark distributions, u_v for e^-p and d_v for e^+p . In the simulation the lepton polarisation is taken to be zero. The valence-quark approximation of the reduced cross section is seen to hold at $x \geq 0.3$. A precise determination of the u/d ratio up to large x appears to be feasible at very high Q^2 .

625 A first measurement of F_L at low x at HERA has recently been performed by the ZEUS Collaboration [?]
626 and by the H1 Collaboration [?]. For the study of the gluon distribution at lowest x , the H1 data are crucial
627 as only H1 has measured F_L below Q^2 of about 10 GeV^2 owing to their backward detector constellation
628 upgraded in the nineties. The F_L measurement at HERA was performed towards the end of the accelerator
629 operation and could only extend over a period of three months with about 10 pb^{-1} of integrated luminosity
630 spent at two reduced proton beam energies, 450 and 565 GeV, besides the nominal 920 GeV. The H1 result is
631 consistent with pQCD predictions. The ratio $R = F_L/(F_2 - F_L)$ has been found to be independent of x and
632 Q^2 at 20% accuracy, i.e. $R = 0.26 \pm 0.05$ [?]. This interesting relation deserves a more precise investigation
633 and may break when the region of saturation is entered at lower x than HERA could access.

634 The LHeC will extend this initial measurement by using higher luminosities and dedicated detector
635 conditions into a much enlarged kinematic range. Since the LHeC is supposed to run synchronously with the
636 LHC, the simulation presented here has been made with reduced electron beam energies keeping the proton
637 beam energy untouched. The following set of energies and integrated luminosities: (60, 1), (30, 0.3), (20,
638 0.1) and (10, 0.05) (GeV, fb $^{-1}$). Note that the F_L measurement requires to also have data with the opposite
639 beam charge in order to be able to reliably subtract the non DIS background which at high y is substantial.
640 This has not been simulated here.

641 In the low x studies below a similar simulation was used for which the luminosity assumptions were
642 similar but a set of reduced proton beam energies was considered. The advantage of lowering E_p is that the
643 maximum y for all beam energy configurations can be high, e.g. 0.95 for $E_e = 60 \text{ GeV}$. When E_e is lowered
644 instead, one has to accept a lower y_{max} as below a few GeV of energy the background is too high for a
645 reliable measurement to be performed. The results of both F_L simulations, with reduced E_e or E_p , come
646 out to be very similar.

647 The result of the simulation study is shown in Fig. ?? . The technique applied is the conventional separa-
648 tion of F_2 and F_L by fitting a straight line to the various reduced cross section data points at fixed Q^2 and
649 x with $f(y)$ as the parameter and separating the uncorrelated from the correlated systematic uncertainties
650 which partially cancel in such an analysis. The expected accuracy on F_L is typically 4% at Q^2 of 3.5 GeV^2
651 or 7% at Q^2 of 25 GeV^2 at a number of points in x , with mainly similar contributions from the calculated
652 correlated and the assumed uncorrelated systematic uncertainties, and less due to statistics which yet starts
653 to become important for $Q^2 \geq 100 \text{ GeV}^2$. The LHeC thus will provide the first precision measurement of
654 $F_L(x, Q^2)$ ever, in a region where the behaviour of the gluon density ought to change significantly and new,
655 non-linear laws for parton evolution should emerge.

656 A related measurement of prime interest is the determination of F_L in diffraction, as is discussed below.
657 A pioneering measurement of F_L^D has been performed by H1 (-cite when published in July-).

658 4.2 Determination of Parton Distributions

659 Despite a series of deep inelastic scattering experiments with neutrinos, electrons and muons using stationary
660 targets and with HERA, despite the addition of some Drell Yan data, the knowledge of the quark distributions
661 in the proton is still limited. It often relies on pQCD analyses using various assumptions on the Bjorken
662 x dependence of the PDFs and their symmetries. The LHeC has the potential to put the PDF knowledge
663 on a qualitatively and quantitatively new and superior basis. This is due to the kinematic range, huge
664 luminosity, availability of polarised electron and positron beams, as of proton and deuteron beams, and to
665 the anticipated very high precision of the cross section measurements as has been discussed above.

666 The LHeC has the potential to provide crucial constraints and many determinations of parton distri-
667 butions completely or rather independently of the conventional QCD fitting techniques. For example, the
668 valence quarks can be measured up to high x , and all heavy quarks be determined from dedicated c and b
669 tagging analyses with unprecedented precision. Therefore, the then evolving QCD fits based on real LHeC
670 data will be set-up with a massively improved and better constrained input data base. Their eventual effect
671 is thus not easy to simulate now, it yet may be illustrated based on the currently used procedures.

672 The striking potential of the determination of the quark and gluon distributions will be discussed and
673 illustrated below. For the various PDFs, the current knowledge is illustrated with a series of plots based

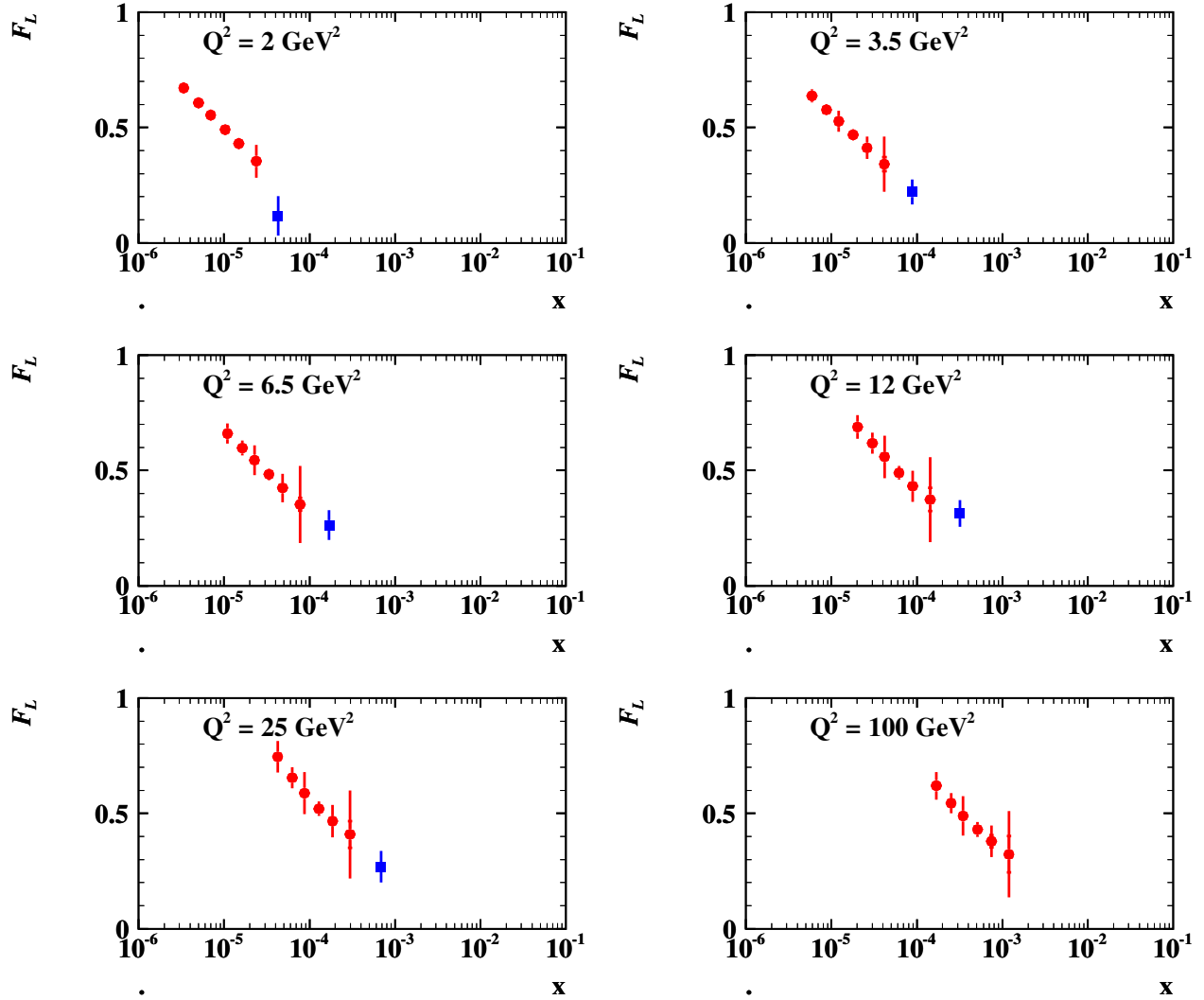


Figure 4.6: Simulated measurement of the longitudinal structure function $F_L(x, Q^2)$ at the LHeC (red closed circles) from a series of runs with reduced electron beam energy, see text. The inner error bars denote the statistical uncertainty, the outer error bars are the total errors with the additional uncorrelated and correlated systematic uncertainties added in quadrature. The blue squares denote the recently published result of the H1 Collaboration, plotting only the x averaged results as the more accurate ones, see [?]. The LHeC extends the measurement towards low x and high Q^2 (not fully illustrated here) with much improved precision.

674 on the world’s best PDF determinations available today. Simulations of essentially direct quark distribution
675 measurements, as for the charm quark, will be shown. Moreover, a consistent set of standard QCD fits has
676 been performed using the simulated LHeC and further data which is first described in what follows. This is
677 used to illustrate the effect the inclusive NC and CC data from the LHeC are expected to have on the PDF
678 uncertainties.

679 Currently extensive work is being performed to test and further constrain PDFs with Drell-Yan scattering
680 data from the LHC. This naturally focusses on the Z and W^\pm production and decay. While such tests are
681 undoubtedly of interest, they require an extremely high level of precision as at scales $Q^2 \simeq M_{W,Z}^2$ any
682 effect due to PDF differences at smaller scales is washed out by the overriding effect of quark-antiquark pair
683 production from gluon emission, below the valence quark region. The present QCD fit results also use a set
684 of simulated $W^+ - W^-$ asymmetry data of ultimate precision in order to be able to estimate the effect the
685 Drell-Yan data will have besides the LHeC in the determination of the PDF’s.

686 4.2.1 QCD Fit Ansatz

687 NLO QCD fits are performed in order to study the effect of the (simulated) LHeC data on the PDF knowledge.
688 Fits are done using the combined HERA data published and so available todate (HERA I), adding BCDMS
689 proton data as the most accurate fixed target structure function set of importance at high x , simulated
690 precision $W^+ - W^-$ asymmetry LHC data, using the LHeC data alone and in combination. In the fits, for the
691 central values of the LHeC data, the Standard Model expectation is used, smeared within the uncorrelated,
692 Gaussian distributed uncertainties and taking into account the correlated uncertainties as well.

693 The procedure used here is adopted from the HERA QCD fit analysis [?]. The QCD fit analysis to extract
694 the proton’s PDFs is performed imposing a $Q_{min}^2 = 3.5 \text{ GeV}^2$ to restrain to the region where perturbative
695 QCD can be assumed to be valid. The fits are extended to lowest x for systematic uncertainty studies, even
696 when at such low x values non-linear effects are expected to appear.

697 The fit procedure consists first in parametrising PDFs at a starting scale $Q_0^2 = 1.9 \text{ GeV}^2$, chosen to
698 be below the charm mass threshold. The parametrised PDFs are the valence distributions xu_v and xd_v ,
699 the gluon distribution xg , and the $x\bar{U}$ and $x\bar{D}$ distributions, where $x\bar{U} = x\bar{u}$, $x\bar{D} = x\bar{d} + x\bar{s}$. This ansatz
700 is natural to the extent that the NC and CC inclusive cross sections determine the sums of up and down
701 quark distributions, and their antiquark distributions, as the four independent sets of PDFs, which may be
702 transformed to the ones chosen if one assumes $u_v = U - \bar{U}$ and $d_v = D - \bar{D}$, i.e. the equality of anti- and
703 sea quark distributions of given flavour.

704 The following standard functional form is used to parameterise them

$$xf(x) = Ax^B(1-x)^C(1+Dx+Ex^2), \quad (4.24)$$

705 where the normalisation parameters (A_{uv}, A_{dv}, A_g) are constrained by quark counting and momentum sum
706 rules.

707 The parameters $B_{\bar{U}}$ and $B_{\bar{D}}$ are set equal, $B_{\bar{U}} = B_{\bar{D}}$, such that there is a single B parameter for
708 the sea distributions, an assumption the validity of which will be settled with the LHeC. The strange quark
709 distribution at the starting scale is assumed to be a constant fraction of \bar{D} , $x\bar{s} = f_s x\bar{D}$, chosen to be $f_s = 0.31$.
710 In addition, to ensure that $x\bar{u} \rightarrow x\bar{d}$ as $x \rightarrow 0$, $A_{\bar{U}} = A_{\bar{D}}(1 - f_s)$. The D and E are introduced one by
711 one until no further improvement in χ^2 is found. The best fit resulted in a total of 10 free parameters [?],
712 while fits with a tested set of 14 parameters lead to very similar results. As discussed above this will change
713 considerably when the LHeC data become available and more flexible parameterisations and methods can
714 be tested. This has been studied to some extent in the simulation for α_s presented below.

715 The PDFs are then evolved using DGLAP evolution equations [?] at NLO in the \overline{MS} scheme with the
716 renormalisation and factorisation scales set to Q^2 using standard sets of parameters as for $\alpha_s(M_Z)$. These,
717 as well as the exact treatment of the heavy quark thresholds, are of no significant influence for the estimates
718 of the PDF uncertainties to which the subsequent analysis is only directed. The experimental uncertainties
719 on the PDFs are determined using the $\Delta\chi^2 = 1$ criterion.

720 **4.2.2 Valence Quarks**

721 The knowledge of the valence quark distributions, both at large and at low Bjorken x , as derived in the
 722 current world data QCD fit analyses is amazingly limited, as is illustrated in Fig. ?? from a comparison of
 723 the leading determinations of PDF sets. This has to do, at high x , with the limited luminosity, challenging
 724 systematics rising $\propto 1/(1-x)$ and nuclear correction uncertainties, and, at low x , with the smallness of the
 valence quark distributions as compared to the sea quarks. The impressive improvement expected from the

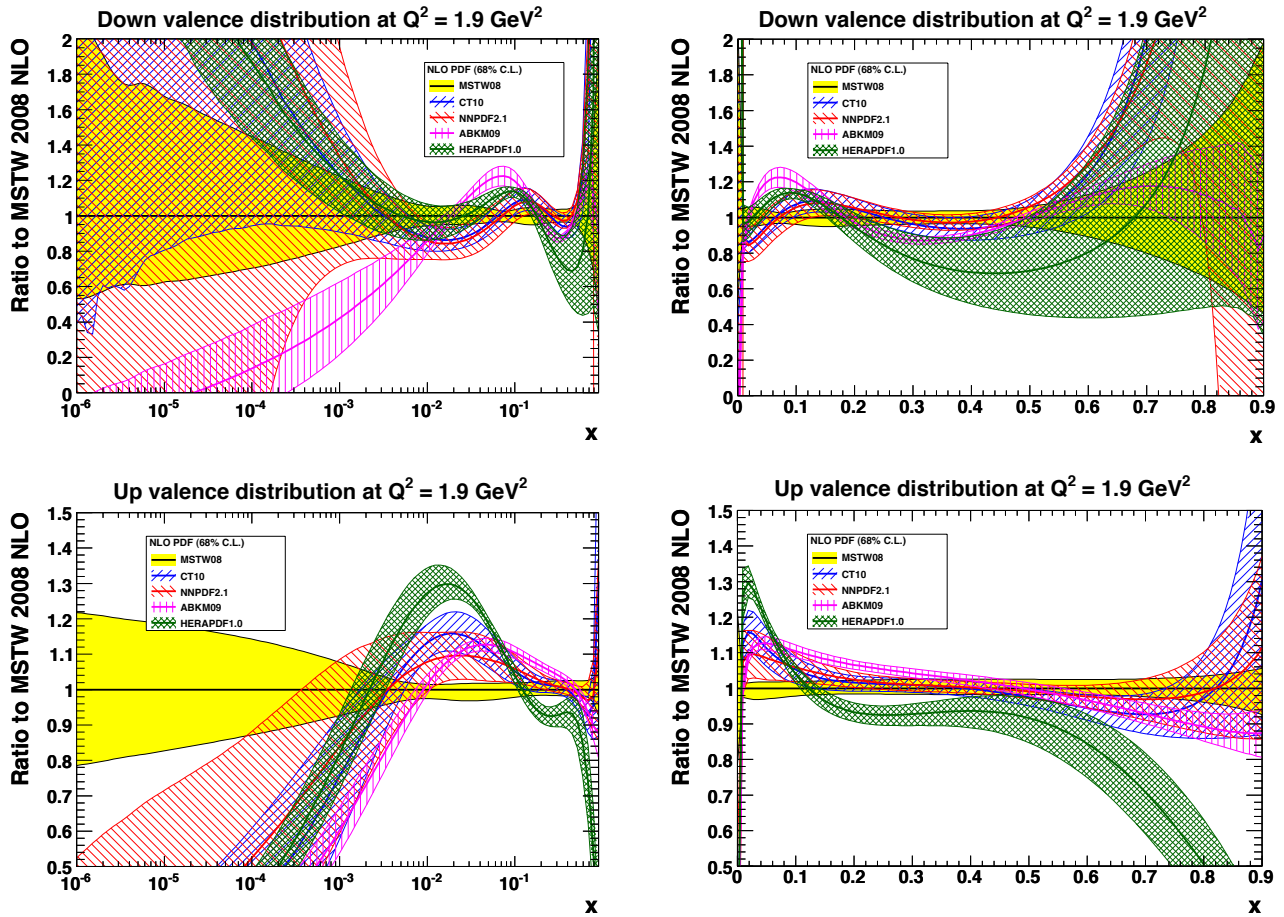


Figure 4.7: Ratios (to MSTW08) and uncertainty bands of valence quark distributions, at $Q^2 = 1.9 \text{ GeV}^2$, for most of the available recent PDF determinations. Top: up valence quark; down: down valence quark; left: logarithmic x , right: linear x .

725 LHeC is demonstrated in Fig. ?? . As can be seen, the uncertainty of the down valence quark distribution at,
 726 for example, $x = 0.7$ is reduced from a level of 50 – 100 % to about 5 %. The up valence quark distribution is
 727 better known than d_v , because it enters with a four-fold weight in F_2 , due to the electric quark charge ratio
 728 squared, a big improvement yet is also visible. These huge improvement effects at large x are a consequence
 729 of the high precision measurements of the NC and the CC inclusive cross sections, which at high x tend to
 730 $4u_v + d_v$ and u_v (d_v) for electron (positron) scattering, respectively. At HERA the luminosity and range
 731 had not been high enough to allow a similar measurement as will be possible for the first time with the
 732

733 LHeC. This is illustrated in Fig. ?? which compares recent results of the ZEUS Collaboration, on the CC cross section with the LHeC simulation.

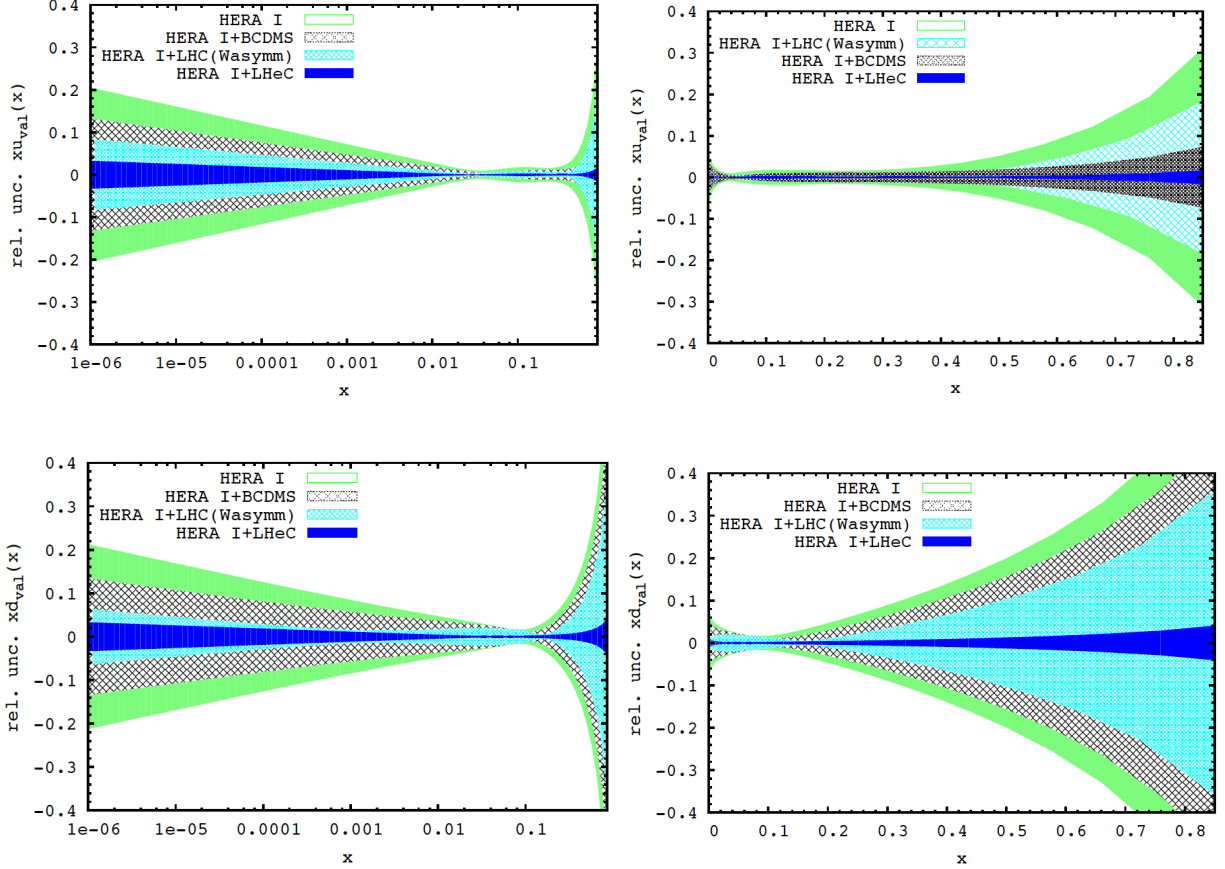


Figure 4.8: Uncertainty of valence quark distributions, at $Q^2 = 1.9 \text{ GeV}^2$, as resulting from an NLO QCD fit to HERA (I) alone (green, outer), HERA and BCDMS (crossed), HERA and LHC (light blue, crossed) and the LHeC added (blue, dark). Top: up valence quark; down: down valence quark; left: logarithmic x , right: linear x .

734

735 Access to valence quarks at low x can be obtained from the $e^\pm p$ cross section difference as introduced
736 above:

$$\sigma_{r,NC}^- - \sigma_{r,NC}^+ = 2 \frac{Y_-}{Y_+} (-a_e \cdot k x F_3^{\gamma Z} + 2v_e a_e \cdot k^2 x F_3^Z). \quad (4.25)$$

737

738 Since the electron vector coupling, v_e , is small and k not much exceeding 1, to a very good approximation the
739 cross section difference is equal to $-2kY_-a_e x F_3^{\gamma Z}/Y_+$. In leading order pQCD this “interference structure
function” can be written as

$$x F_3^{\gamma Z} = 2x [e_u a_u (U - \bar{U}) + e_d a_d (D - \bar{D})], \quad (4.26)$$

740

with $U = u + c$ and $D = d + s$ for four flavours. The $x F_3^{\gamma Z}$ structure function thus provides information

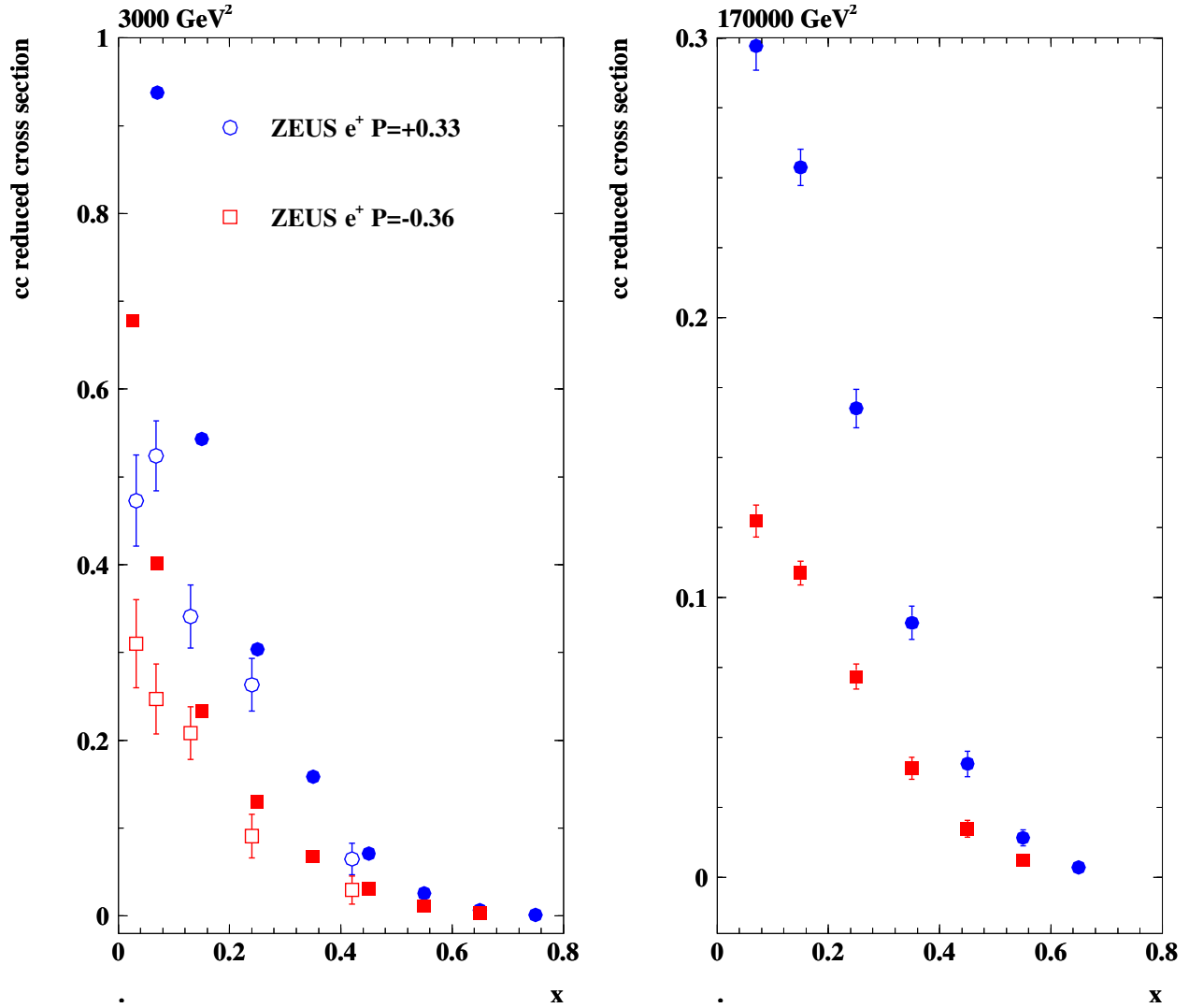


Figure 4.9: Reduced charged current e^+p scattering cross section versus Bjorken x for different polarisations $\pm P$ and values of Q^2 . Closed points: LHeC simulations for 10 fb^{-1} ; open points: ZEUS measurements based on the full HERA statistics of about 0.15 fb^{-1} per polarisation state. Note that the reduced CC cross section at fixed x and Q^2 contains an explicit dependence on the beam energy via the ratio of inelasticity dependent factors Y_-/Y_+ , which is at the origin of the simulated and measured cross section differences apparent at lower x .

741 about the light-quark axial vector couplings (a_u, a_d) and the sign of the electric quark charges (e_u, e_d).
 742 Equivalently one can write

$$xF_3^{\gamma Z} = 2x[e_u a_u(u_v + \Delta_u) + e_d a_d(d_v + \Delta_d)]. \quad (4.27)$$

743 In the naive parton model as in conventional perturbative QCD, it is assumed that the differences $\Delta_u =$
 744 $(u_{sea} - \bar{u} + c - \bar{c})$ and $\Delta_d = (d_{sea} - \bar{d} + s - \bar{s})$ are zero ². Inserting the SM charge and axial coupling values
 745 one finds

$$xF_3^{\gamma Z} = \frac{x}{3}(2u_v + d_v + \Delta) \quad (4.28)$$

746 with $\Delta = 2\Delta_u + \Delta_d$. Neglect of Δ leads to a sum rule [?], which in leading order is

$$\int_0^1 xF_3^{\gamma Z} \frac{dx}{x} = \frac{1}{3} \int_0^1 (2u_v + d_v) dx = \frac{5}{3}. \quad (4.29)$$

747 The $xF_3^{\gamma Z}$ structure function thus is determined by the valence quark distributions and predicted to be only
 748 very weakly depending on Q^2 . Fig. ?? shows a simulation of $xF_3^{\gamma Z}$ and its comparison with the so far most
 749 accurate measurement from HERA. With such a high precision interesting tests are possible of the relation
 750 of $xF_3^{\gamma Z}$ to xW_3 , which should only differ by the weak couplings involved in NC and CC.

751 4.2.3 Strange Quarks

752 The strange quark distribution $s(x, Q^2)$ has been very difficult to measure. In DIS some information is
 753 obtained from di-muon production in neutrino-nucleon scattering. Often s is linked to the behaviour of the
 754 sea quarks. Recently the HERMES Collaboration, from kaon multiplicities, derived an unusual behaviour
 755 of the strange quark density as compared to previous analyses [?]. Some hints for a difference between the
 756 s and \bar{s} distributions have been discussed. The existing information on the sum of the strange and anti-
 757 strange quark distributions is plotted in Fig. ?. Obviously there is no real understanding of the strange
 758 quark distribution in the proton available. This will change with the LHeC. Here s and \bar{s} may be very
 759 well measured as a function of x and Q^2 from the $W^+s \rightarrow c$ and $W^-\bar{s} \rightarrow \bar{c}$ processes, i.e. with charmed
 760 quark tagging in CC DIS using electron and positron beams, respectively. The precision for s which may
 761 be obtained is illustrated in Fig. ?. Accurate measurements may be obtained for the first time ever. The
 762 simulation of \bar{s} obviously leads to the same picture such that over a wide kinematic range possible differences
 763 between s and \bar{s} may be established.

764 4.2.4 Top Quarks

765 The top is the heaviest of the quarks. It decays before hadrons are formed. It has not been explored in
 766 DIS yet because the cross sections at HERA have been too small [?]. This is different at the LHeC where
 767 top in charged currents is produced with a cross section of order 5 pb as can easily be estimated from the
 768 LO calculation of Wb scattering. At the LHeC therefore, for the first time, one can study top quarks in
 769 deep inelastic scattering. Positron (electron) proton charged current scattering provides a clear distinction
 770 between top (anti-top) quark production in Wb to t fusion. The rates of this process are very high, as is
 771 illustrated as a function of Q^2 in Fig. ?. Besides the rates and the charge tag it is notable that the absence
 772 of pile-up and underlying event effects, characteristic for LHC measurements, provide comfortable conditions
 773 for top quark physics at the LHeC.

774 Due to its large mass, the top quark may very well play a role in the mechanism of electroweak symmetry
 775 breaking (EWSB) both in the Standard Model as well as BSM physics. In the Standard Model, a precise
 776 measurement of single top production in DIS (see for example [?]) is sensitive to the b quark content of the
 777 proton. In a BSM EWSB scenario, the top quark will couple to the new physics sector and give rise to

²However, in non-perturbative QCD there may occur differences, for example between the strange and anti-strange quark distributions, for which there are some hints in DIS neutrino nucleon di-muon data and corresponding QCD fit analyses, see below.

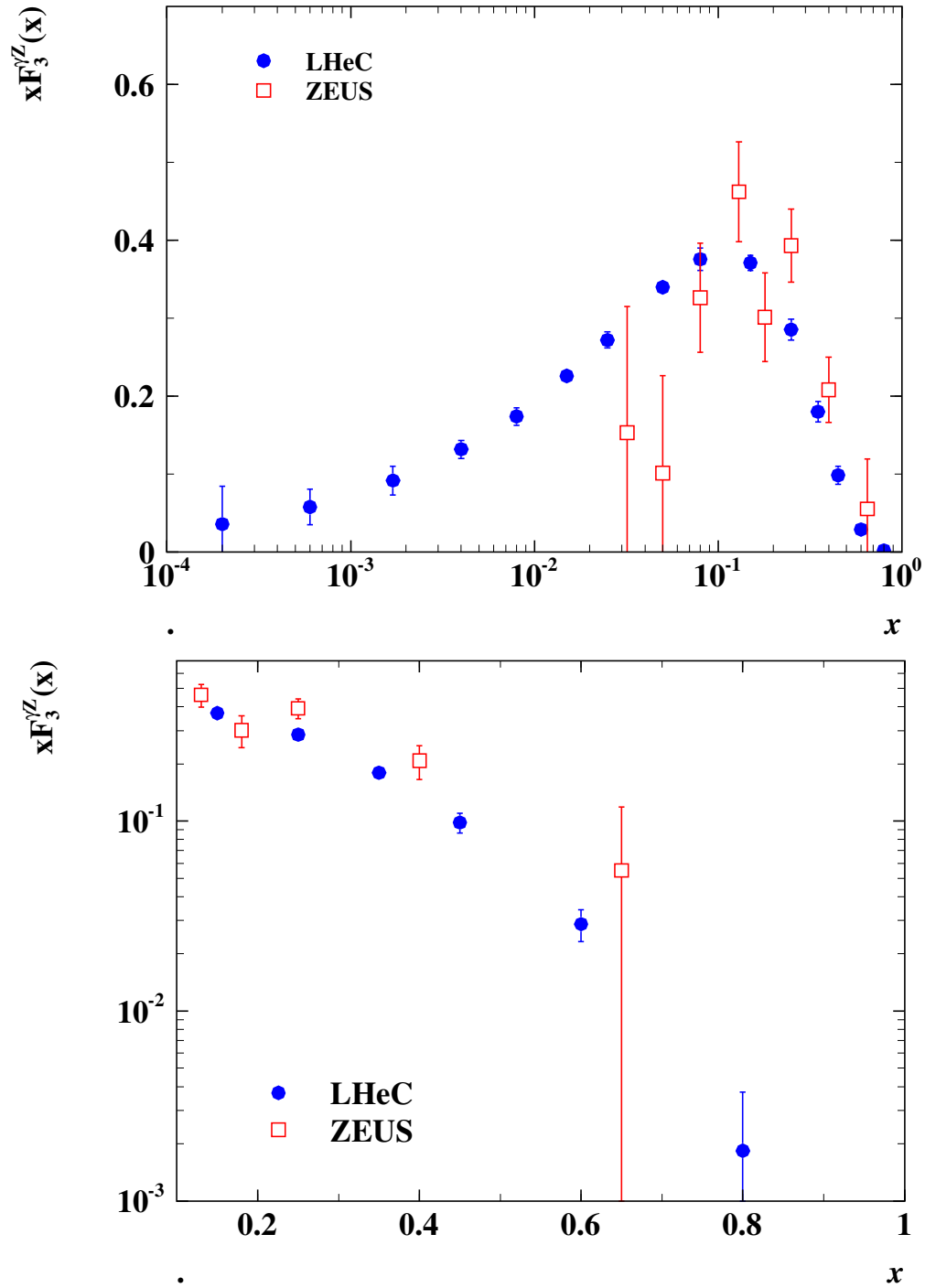


Figure 4.10: Simulation (top) of the LHeC measurement of the interference structure function $xF_3^{\gamma^Z}$ from unpolarised $e^\pm p$ scattering with 10 fb^{-1} luminosity per beam (blue, closed points) compared with the HERA II data as obtained by the ZEUS Collaboration with about 0.15 fb^{-1} luminosity per beam charge. This measurement at HERA is limited by its statistical accuracy mainly and therefore with the forthcoming H1 data added, only an about $1/\sqrt{2}$ improvement of the precision at HERA can be expected. One should notice that any significant deviation of sea from anti-quarks, see Eq. ??, would cause $xF_3^{\gamma^Z}$ at low x to not tend to zero. The top plot shows an average of $xF_3^{\gamma^Z}$ over Q^2 projected to a chosen Q^2 value of 1500 GeV^2 exploiting the fact that the valence quarks are approximately independent of Q^2 . The lower plot is a zoom into the high x region.

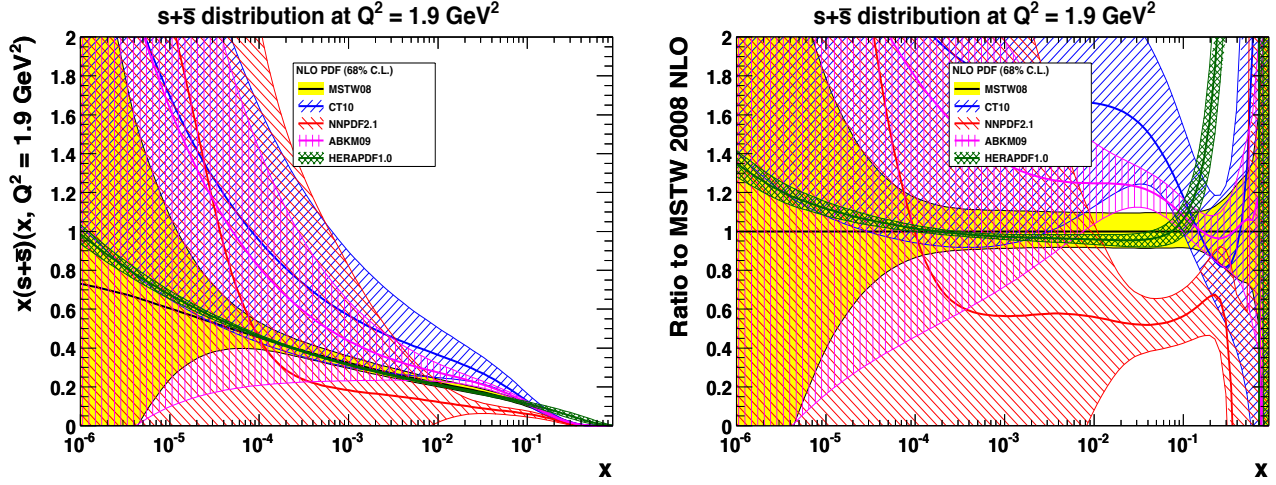


Figure 4.11: Sum of the strange and anti-strange quark distribution as embedded in the NLO QCD fit sets as noted in the legend. Left: $s + \bar{s}$ versus Bjorken x at $Q^2 = 1.9 \text{ GeV}^2$; right: ratio of $s + \bar{s}$ of various PDF determinations to MSTW08. In the HERAPDF1.0 analysis (green) the strange quark distribution is assumed to be a fixed fraction of the down quark distribution which is conventionally assumed to have the same low x behaviour as the up quark distribution, which results in a small uncertainty of $s + \bar{s}$.

778 anomalous production modes. The LHeC is expected to provide competitive sensitivity to flavor changing
 779 neutral currents (FCNC) especially anomalous $tu\gamma$ and tuZ couplings.

780 In the SM, top is produced dominantly in gluon-boson fusion at $x \lesssim 0.1$. In CC this leads to a top-beauty
 781 final state while in NC this gives rise to pair produced top-antitop quarks, with a cross section of order 10
 782 times lower than in CC [?]. The electron beam charge distinguishes top and anti-top quark production in
 783 CC. Thus a unique SM top physics program can be performed at the LHeC. This includes the consideration
 784 of a top-quark density which at very high scales may be considered “light”. Recently a six-flavour variable
 785 number scheme has been proposed [?], limited so far to leading order, in which it is predicted that the top
 786 contribution to proton structure has an on-set much below the threshold of its production in a massless
 787 scheme. This is illustrated in Fig. ?? . Due to the very high Q^2 and statistics, the LHeC opens top quark
 788 PDF physics as a new field of research.

789 Top, including anomalous couplings, has been considered for the CDR initially [?], based on some AN-
 790 OTOP and PYTHIA studies at generation level. With a detector now simulated in GEANT4 and in the
 791 light of the first top results provided by the LHC experiments [?], as well as further prospects, the CC and
 792 NC top physics at the LHeC deserves a more detailed study. This shall include an analysis about the possible
 793 precision measurement of the top (and anti) top quark mass, which at the LHC may be determined with
 794 an accuracy of 1 GeV and possibly be better in ep . Independently of whether one soon finds the SM Higgs
 795 particle or it remains elusive, a high precision measurement of m_t is of prime importance.

796 4.3 Gluon Distribution

797 There are many fundamental reasons to understand the gluon distribution and the gluon interactions deeper
 798 than hitherto. Half of proton’s momentum is carried by gluons. Gluon self-interaction is responsible for the
 799 creation of baryonic mass. The Higgs particle, should it exist, is predominantly produced by gluon-gluon

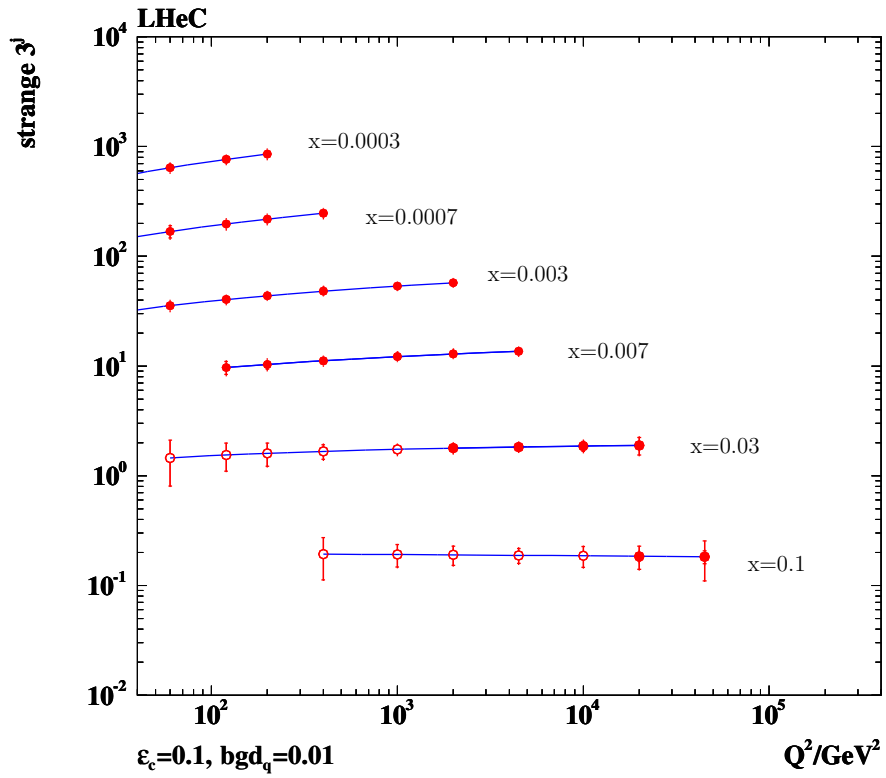


Figure 4.12: Simulated measurement of the strange quark density with the LHeC. Closed (open) points: tagging acceptance down to 10 (1°).

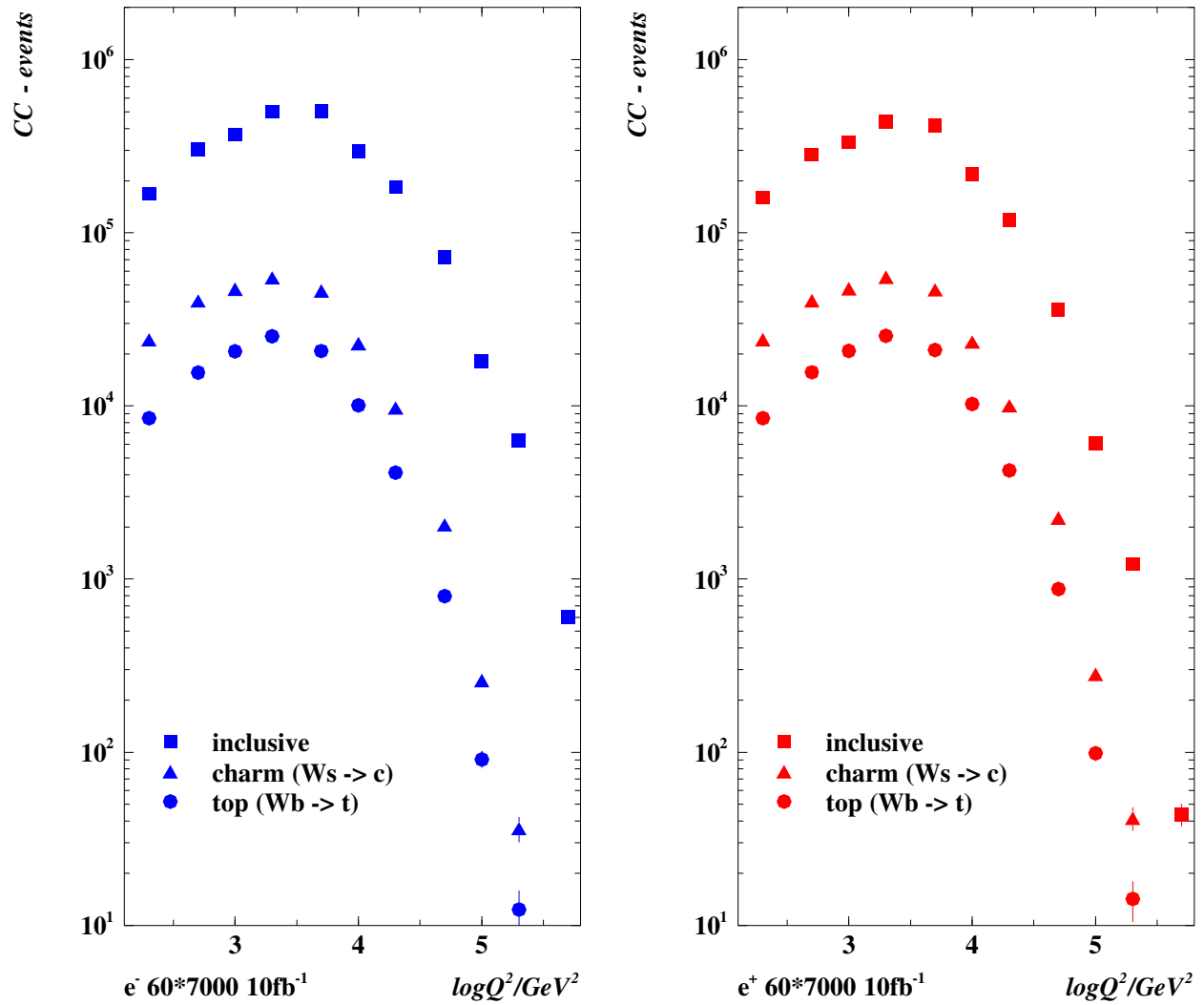


Figure 4.13: Charged current event rates for unpolarised e^-p (left) and e^+p (right) scattering in which \bar{t} and t is produced, respectively. Squares: inclusive CC rate vs. Q^2 ; triangles: charm production from Ws fusion; closed circles: top production from Wb fusion, estimated in a massless heavy flavour treatment. The rates are calculated for the default beam energies for 10 fb^{-1} of integrated luminosity. The errors are only statistical.

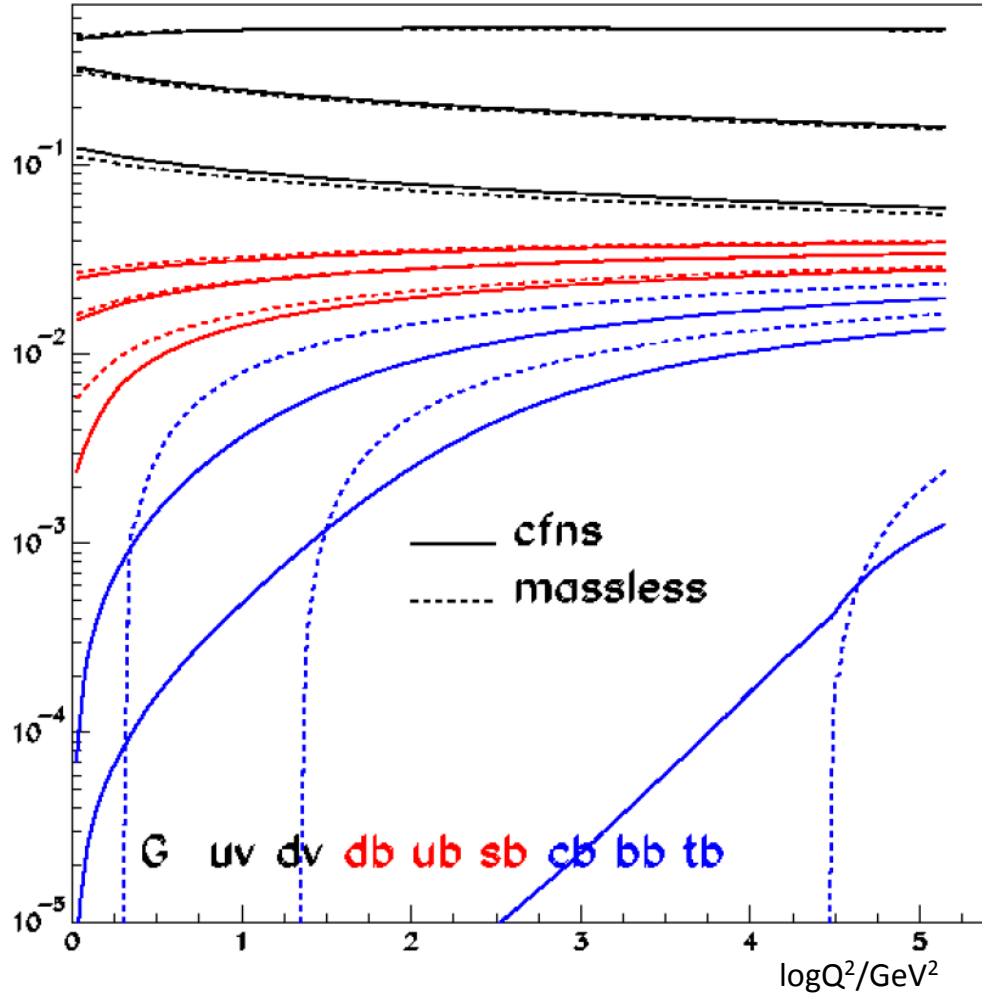


Figure 4.14: Parton momentum fractions as a function of Q^2 in a novel six-flavour variable number scheme (CFNS), solid curves, and in the massless scheme, dashed curves. At HERA one has observed beauty and charm production already below the conventional threshold of $\sqrt{Q^2} = m_Q$. The scheme of [?] suggests that there is a very early onset of top with measurable rates already at Q^2 values of only about one tenth of $m_t^2 \simeq 3 \cdot 10^4 \text{ GeV}^2$. With the LHeC the 'PDF' top physics is expected to commence.

800 interactions. The rise of the gluon density towards low Bjorken x must be tamed for unitarity reasons: there
 801 is a new phase of hadronic matter to be discovered, in which gluons interact non-linearly while α_s is smaller
 802 than 1.

803 The LHeC, with precision and range of the most appropriate process (DIS) to explore $xg(x, Q^2)$, will pin
 804 down the gluon distribution much more accurately than could be done before. This primarily comes from the
 805 extension of range and precision in the measurement of $\partial F_2/\partial \ln Q^2$ which at small x is a measure of xg . The
 806 inclusive NC and CC measurements together provide a fully constrained data base for the determination
 807 of the quark distributions, which strongly constrains xg . The addition of precision measurements of F_L ,
 808 discussed above and used in the small x chapter of this document, will unravel the saturating behaviour of
 809 xg . High precision measurements of boson-gluon fusion to heavy quark pairs will provide a complementary
 810 basis for understanding the gluon and its parton interactions.

811 The peculiarity of the gluon density is that it is defined and observable only in the context of a theory.
 812 Moreover, a crude data base and correspondingly rough fit ansatz can screen local deviations from an
 813 otherwise preferred smooth behaviour. It has yet not been settled whether there are gluonic “hot” spots in
 814 the proton or not. An example for possible surprises is provided by the analysis [?], in which Chebyshev
 815 polynomials have been used to parameterise the parton distributions in contrast to more conventional forms
 816 as in Eq. ???. Inspection of the gluon distribution obtained there reveals that it seems to be vanishing at
 817 $x \simeq 0.2$, i.e. at the point, in which scaling holds for $F_2(x, Q^2)$, which one might term a “cool” spot in
 818 the proton. Much more is still to be learned about the gluon, even when one is disregarding the yet to be
 819 explored role of the gluon in the theory of generalised and of unintegrated parton distributions.

820 The current knowledge of the gluon distribution in the proton is astonishingly limited as becomes clear
 821 from Fig. ?? showing the world determinations, and their uncertainties, of $xg(x, Q^2)$ at a typical initial, low
 822 scale, and from Fig. ?? expressing this information with ratios to one of the PDF sets. At low x and Q^2 most
 823 but not all of the PDF sets predict xg to be of valence like type with very large uncertainties for x below
 824 a few times 10^{-4} . At large x inclusive DIS has difficulties to pin down xg because the evolution of valence
 825 quarks as non-singlet quantities in QCD is not directly coupled to the gluon and very weak. Yet, even the
 826 information from jets, used in some of the PDF sets, does not lead to a clear understanding of xg at large
 827 x as is illustrated too. In fact, there is a tendency of obtaining a smaller xg at large x from HERA (I) data
 alone, see Fig. ??, as compared to the other determinations, albeit with large uncertainties.

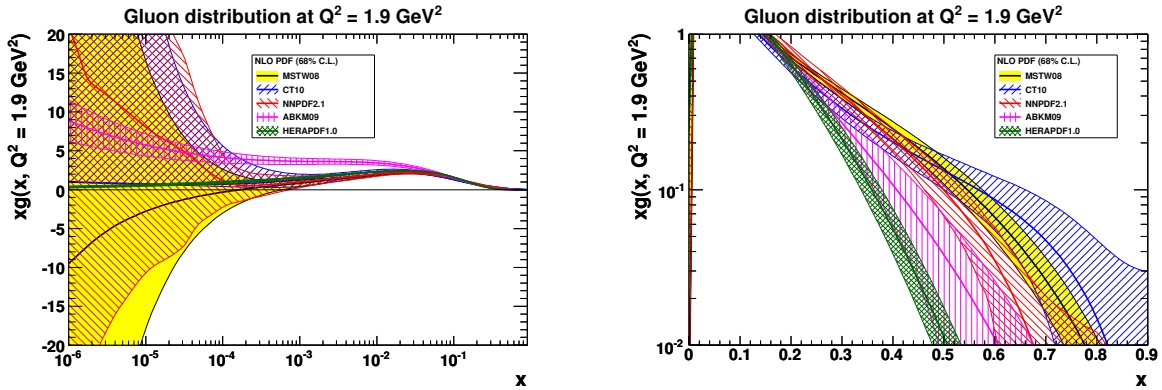


Figure 4.15: Gluon distribution and uncertainty bands, at $Q^2 = 1.9 \text{ GeV}^2$, for most of the available recent PDF determinations. Left: logarithmic x , right: linear x .

828
 829 The determination of xg is predicted to be radically improved with the LHeC precision data which extend
 830 up to lowest x near to 10^{-6} and large $x \geq 0.7$. The result of the QCD fit analysis for xg as described above
 831 in Sect. ?? is shown in Fig. ?. One observes a dramatic improvement at low x , as must be expected from the
 832 extension of the kinematic range, but also at high x , as attributed to the high x precision measurements

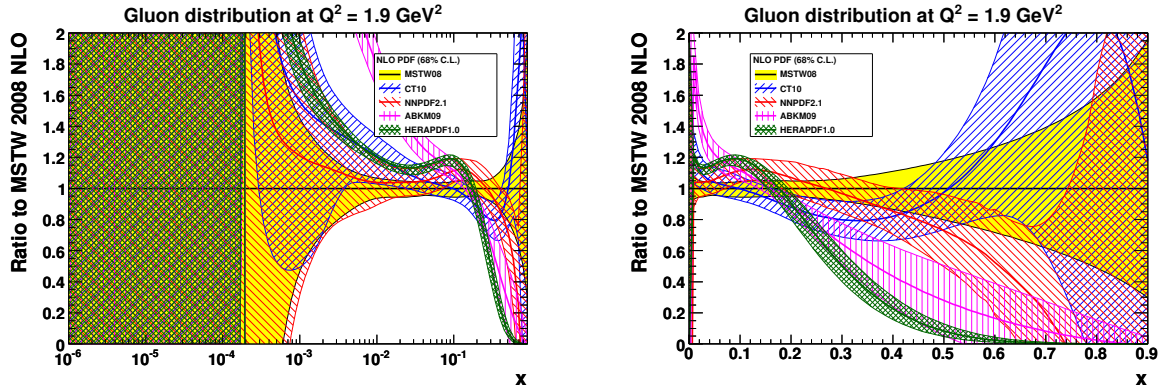


Figure 4.16: Ratios to MSTW08 of gluon distribution and uncertainty bands, at $Q^2 = 1.9 \text{ GeV}^2$, for most of the available recent PDF determinations. Left: logarithmic x , right: linear x .

833 of the NC and CC cross sections. At $x = 0.7$, for example, the predicted experimental uncertainty of xg is
 834 5%, which is about ten times more accurate than the results of MSTW08 or of the HERA fit indicate.

835 It is worth noting that the uncertainties considered here are restricted to those related to the genuine
 836 cross section measurement errors. There are further uncertainties, as discussed e.g. in [?], related to the
 837 difficulty of parameterising the PDFs and choosing the optimum solution in such a fit analysis. These will
 838 be also considerably reduced with the LHeC extended data base. Moreover, this analysis is not making
 839 use of the plethora of extra information on xg , which the LHeC will provide with F_L , $F_2^{c,b}$ and jet cross
 840 section measurements. The understanding of the gluon and its interactions is a primary task of the LHeC
 841 and undoubtedly a new horizon in strong interaction physics will be opened.

842 4.4 Prospects to Measure the Strong Coupling Constant

843 The precise knowledge of $\alpha_s(M_Z^2)$ is of instrumental importance for the correct prediction of the electro-
 844 weak gauge boson production cross sections and the Higgs boson cross section at Tevatron and the LHC
 845 [?]. Independently of such applications, the accurate determination of the coupling constants of the known
 846 fundamental forces is of importance in the search for their possible unification within a more fundamental
 847 theory. Among the coupling constants of the forces in the Standard Model, the strong coupling α_s exhibits
 848 the largest uncertainty, which is currently of the size of $\sim 1\%$. Any future improvement of this accuracy, along
 849 with the consolidation of the genuine central value, is one of the central issues of contemporary elementary
 850 particle physics. It demands deep experimental and theoretical efforts to obtain the required precision and
 851 especially to handle all essential systematic effects.

852 Experimentation at the LHeC will allow to measure the strong coupling constant $\alpha_s(M_Z^2)$ at much higher
 853 precision than hitherto, both from the scaling violations of the deep inelastic structure functions, as will be
 854 demonstrated below, and using ep multiple jet cross sections. For the final inclusion of jet data in global
 855 pdf analyses, both from ep and from hadron colliders, their description at NNLO is required. At the LHeC,
 856 similar to HERA, the measurement of the ep jet cross sections will form important data samples ³ for the
 857 measurement of $\alpha_s(M_Z^2)$.

³These are presented below but have not been used in this document for a determination of the strong coupling constant. One knows of course that the use of jet data in DIS helps resolving the α_s - xg correlation, especially at large x , and consequently leads to a significant reduction of the uncertainty on the coupling constant. This, however, tends to also change the central value. The LHeC as will be shown below determines α_s to permille precision already in inclusive scattering. Comparison with precise values from jets can be expected to shed light on the yet unresolved question as to whether there is a theoretical or systematic effect which leads to different values in inclusive DIS and jets or not.

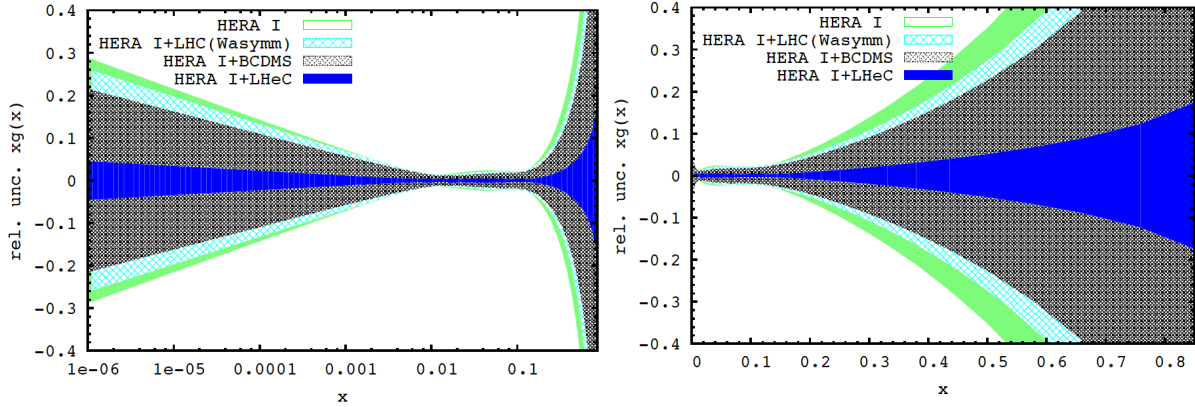


Figure 4.17: Relative uncertainty of the gluon distribution at $Q^2 = 1.9 \text{ GeV}^2$, as resulting from an NLO QCD fit to HERA (I) alone (green, outer), HERA and BCDMS (crossed), HERA and LHC (light blue, crossed) and the LHeC added (blue, dark). Left: logarithmic x , right: linear x .

858 Subsequently, a brief account will be given on the status and the complexity of determining α_s in DIS,
 859 followed by a presentation of the study of the α_s measurement uncertainty with the inclusive NC and CC
 860 data from the LHeC.

861 4.4.1 Status of the DIS Measurements of α_s

862 During the last 35 years the strong coupling constant has been measured with increasing accuracy in lepton-
 863 nucleon scattering in various experiments at CERN, FERMILAB and DESY. The precision, which has
 864 been reached currently, requires the description of the deep-inelastic scattering structure functions at $O(\alpha_s^3)$
 865 $[?, ?, ?]$.

	$\alpha_s(M_Z^2)$	
BBG	$0.1134^{+0.0019}_{-0.0021}$	valence analysis, NNLO [?]
GRS	0.112	valence analysis, NNLO [?]
ABKM	0.1135 ± 0.0014	HQ: FFNS $N_f = 3$ [?]
ABKM	0.1129 ± 0.0014	HQ: BSMN-approach [?]
JR	0.1124 ± 0.0020	dynamical approach [?]
JR	0.1158 ± 0.0035	standard fit [?]
MSTW	0.1171 ± 0.0014	[?]
ABM	0.1147 ± 0.0012	FFNS, incl. combined H1/ZEUS data [?]
BBG	$0.1141^{+0.0020}_{-0.0022}$	valence analysis, N ³ LO [?]
world average	0.1184 ± 0.0007	[?]

Table 4.3: Recent NNLO and N³LO determinations of the strong coupling $\alpha_s(M_Z)$ in DIS world data analyses.

866 As is well known [?], though also questioned [?], the fits at NLO exhibit scale uncertainties for both the

renormalization and factorization scales of $\Delta_{r,f}\alpha_s(M_Z^2) \sim 0.0050$, which are too large to cope with the experimental accuracy of $O(1\%)$. Therefore, NNLO analyses are mandatory. In Table 1 recent NNLO results are summarised. NNLO non-singlet data analyses have been performed in [?, ?]. The analysis [?] is based on an experimental combination of flavor non-singlet data referring to $F_2^{p,d}(x, Q^2)$ for $x < 0.35$ and using the respective valence approximations for $x > 0.35$. The $\bar{d}-\bar{u}$ distributions and the $O(\alpha_s^2)$ heavy flavor corrections were accounted for. The analysis could be extended to N³LO effectively due to the dominance of the Wilson coefficient in this order [?] if compared to the anomalous dimension, cf. [?, ?]. This analysis led to an increase of $\alpha_s(M_Z^2)$ by +0.0007 if compared to the NNLO value.

A combined singlet and non-singlet NNLO analysis based on the DIS world data, including the Drell-Yan and di-muon data, needed for a correct description of the sea-quark densities, was performed in [?]. In the fixed flavor number scheme (FFNS) the value of $\alpha_s(M_Z^2)$ is the same as in the non-singlet case [?]. The comparison between the FFNS and the BMSN scheme [?] for the description of the heavy flavor contributions induces a systematic uncertainty $\Delta\alpha_s(M_Z^2) = 0.0006$. One should note that also in the region of medium and lower values of x higher twist terms have to be accounted for within singlet analyses to cover data at lower values of Q^2 . Moreover, systematic errors quoted by the different experiments usually cannot be combined in quadrature with the statistical errors, but require a separate treatment. The NNLO analyses [?] are statistically compatible with the results of [?, ?, ?], while those of [?] yield a higher value.

In [?] the combined H1 and ZEUS data were accounted for in an NNLO analysis for the first time, which led to a shift of +0.0012. However, running quark mass effects [?] and the account of recent F_L data reduce this value again to the NNLO value given in [?]. Other recent NNLO analyses of precision data, as the measurement of $\alpha_s(M_Z^2)$ using thrust in high energy e^+e^- annihilation data [?, ?], result in $\alpha_s(M_Z^2) = 0.1153 \pm 0.0017 \pm 0.0023$, resp. $0.1135 \pm 0.0011 \pm 0.0006$. Also the latter values are lower than the 2009 world average [?] based on NLO, NNLO and N³LO results.

4.4.2 Simulation of α_s Determination

Since nearly twenty years, the α_s determination in DIS is dominated by the most precise data from the BCDMS Collaboration, which hint to particularly low values of $\alpha_s(M_Z) \simeq 0.113$ [?] and exhibit some peculiar systematic error effects, when compared to the SLAC data and in the pQCD analyses as are discussed in [?, ?]. Recent analyses seem to indicate that the influence of the BCDMS data is limited, which, however, is possible only when jet and nuclear fixed target data, extending to very low Q^2 , are used. Jet data sometimes tend to increase the value of α_s and certainly introduce extra theoretical problems connected with hadronisation effects in non-inclusive measurements. The use of fixed target data poses problems due to the uncertainty of corrections from higher twists and from nuclear effects, because what is required is an extraordinary precision if indeed one wants to unambiguously determine the strong coupling constant in DIS. These problems have been discussed in detail above, and recently also in presentations by MSTW [?] and in a phenomenological study of the NNPDF group [?].

The question, of how large α_s is, remains puzzling, as has been discussed at a recent workshop [?] and requires a qualitatively and quantitatively new level of experimental input if one wants to progress in DIS.

Following the description of the simulated LHeC data (Sec. ??) and the QCD fit technique (Sec. ??) a dedicated study has been performed to estimate the accuracy of an α_s measurement with the LHeC. In the fits, for the central values of the LHeC data, the SM expectation is used smeared within the above uncertainties assuming their Gaussian distribution and taking into account correlated uncertainties as well.

The QCD fit results are summarised in Tab. ?. The first two lines give the result of a fit to the HERA I data. One observes that the inclusion of DIS jet data reduces the uncertainty, by a factor of two, but it also increases the central value by more than the uncertainty. The LHeC alone, in sole inclusive DIS, reaches values of better than 0.2% which when complemented with HERA data reaches a one per mille precision. From inspecting the results one finds that enlarging the Q^2 minimum still leads to an impressive precision, as of two per mille in the LHeC plus HERA case, at values which safely are in the DIS region. A Q^2 cut of for example 10 GeV² excludes also the lowest x region in which non-linear gluon interaction effects may require to change the evolution equations.

case	cut [Q^2 in GeV ²]	α_s	\pm uncertainty	relative accuracy in %
HERA only (14p)	$Q^2 > 3.5$	0.11529	0.002238	1.94
HERA+jets (14p)	$Q^2 > 3.5$	0.12203	0.000995	0.82
LHeC only (14p)	$Q^2 > 3.5$	0.11680	0.000180	0.15
LHeC only (10p)	$Q^2 > 3.5$	0.11796	0.000199	0.17
LHeC only (14p)	$Q^2 > 20.$	0.11602	0.000292	0.25
LHeC+HERA (10p)	$Q^2 > 3.5$	0.11769	0.000132	0.11
LHeC+HERA (10p)	$Q^2 > 7.0$	0.11831	0.000238	0.20
LHeC+HERA (10p)	$Q^2 > 10.$	0.11839	0.000304	0.26

Table 4.4: Results of NLO QCD fits to HERA data (top, without and with jets) to the simulated LHeC data alone and to their combination. Here 10p or 14p denotes two different sets of parametrisations, one, with 10 parameters, the minimum parameter set used in [?] and the other one with four extra parameters added as has been described VOICAWHERE. The central values of the LHeC based results are obviously of no interest. The result quoted as relative accuracy includes all the statistical and the systematic error sources taking correlations as from the energy scale uncertainties into account.

916 It is obvious that the sole experimental uncertainty, while impressive and promising indeed, is not the only
917 problem in such a complex analysis. That requires all relevant parameters to be correspondingly tuned and
918 understood. For example, the charm mass has to be known at the 10 MeV level to allow an α_s uncertainty
919 of one per mille. The question of the uncertainty of the renormalisation and factorisation scales and their
920 effect on α_s will be posed newly and higher than NNLO approximations of pQCD appear to be necessary.
921 However, as mentioned above there already exist first N³LO results.

922 From an experimental and phenomenological point of view it appears extremely exciting that with the
923 LHeC the α_s determination in DIS will be put on much more solid grounds, by the high precision and
924 unprecedented kinematic range and but also by the resulting full constraints on the complete set of parton dis-
925 tributions, of light and heavy quarks, often by direct measurements, which hitherto had to be parameterised
926 in an often crude way.

927 In view of the importance of this result, this analysis has been performed independently twice with
928 separately generated NC and CC pseudodata under somewhat different assumption, albeit using the same
929 simulation program, and using different versions of the QCD fit program. The results obtained before [?]
930 are in good agreement with the numbers presented here.

931 4.5 Electron-Deuteron Scattering

932 The structure of the deuteron and of the neutron are experimental unknowns over most of the kinematic
933 region of deep inelastic scattering. The last time lepton-deuteron scattering was measured occurred in the
934 fixed target μD experiments at CERN [?, ?, ?], while it had only been considered at HERA [?, ?, ?]. The
935 LHeC so extends the range of these measurements by nearly four orders of magnitude in Q^2 and $1/x$, which
936 gives rise to a most exciting programme in QCD and in experimental physics.

937 DIS and Partons

938 Electron-deuteron scattering complements ep scattering in that it makes possible accurate measurements of
939 neutron structure in the new kinematic range accessed by the LHeC. In a collider configuration, in which
940 the hadron “target” has momentum much larger than the lepton probe, the spectator proton can be tagged
941 and its momentum measured with high resolution [?]. The resulting neutron structure function data are
942 then free of nuclear corrections which have plagued the interpretation of deuteron data, especially at larger

943 x , until now [?]. At low x , for the first time, since diffraction is related to shadowing, one will be able to
 944 control the shadowing corrections at the per cent level of accuracy as is also discussed below.

945 Accurate en cross section measurements will resolve the quark flavour decomposition of the sea, i.e. via
 946 isospin symmetry, unfolding \bar{u} from \bar{d} contributions to the rise of $F_2^p \propto x(4\bar{u} + \bar{d})$ towards low x , and, from
 947 the full set of $e^\pm p$ and $e^\pm n$ charged current cross section data, a full unfolding of the flavour content of the
 nucleon. For the study of the parton evolution with Q^2 , the measurement of $F_2^N = (F_2^p + F_2^n)/2$ is crucial

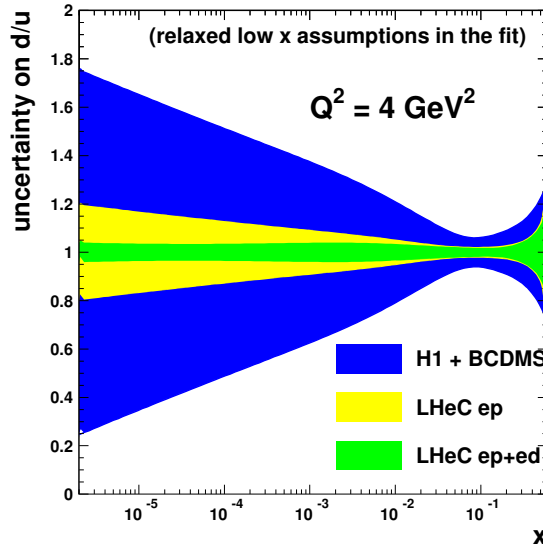


Figure 4.18: Uncertainty of the d/u ratio as a function of x from a QCD fit to H1 and BCDMS data (outer band, blue), to the LHeC proton data (middle band, yellow) and the combined simulated proton and deuteron data from the LHeC (inner band, green). In these fits the constraint of u and d to be the same at low x has been relaxed.

948 since it disentangles the evolution of the non-singlet and the singlet contributions. Down to x of about 10^{-3}
 949 the W^+/W^- LHC data will also provide important information on the up-down quark distributions, albeit
 950 at high Q^2 . With ep , eD and W^+/W^- data, the low x sea will be resolved for the first time, as all the low
 951 x light quark information from HERA has been restricted to F_2^p only.

952 A special interest in high precision neutron data at high Q^2 arises from the question of whether there
 953 holds charge symmetry at the parton level, as has been discussed recently [?]. It may be studied in the
 954 charged current ep and eD reactions, using both electrons and positrons, by measuring the asymmetry ratio
 955

$$R^- = 2 \frac{W_2^{-D} - W_2^{+D}}{W_2^{-p} + W_2^{+p}}, \quad (4.30)$$

956 which is directly sensitive to differences of up and down quark distributions in the proton and neutron,
 957 respectively, which conventionally are assumed to be equal. With the prospect of directly measuring the
 958 strange and anti-strange quark asymmetry in $e^\pm p$ CC scattering and of tagging the spectator proton and
 959 thus eliminating the Fermi motion corrections in eD , such a measurement becomes feasible at the LHeC. It
 960 requires high luminosity of order 1 fb^{-1} in eD scattering.

961 Hidden Colour

962 In nuclear physics nuclei are simply the composites of nucleons. However, QCD provides a new perspective [?,
 963 ?]. Six quarks in the fundamental 3_C representation of $SU(3)$ color can combine into five different color-

964 singlet combinations, only one of which corresponds to a proton and neutron. The deuteron wavefunction is a
965 proton-neutron bound state at large distances, but as the quark separation becomes smaller, QCD evolution
966 due to gluon exchange introduces four other “hidden color” states into the deuteron wavefunction [?]. The
967 normalization of the deuteron form factor observed at large Q^2 [?], as well as the presence of two mass
968 scales in the scaling behavior of the reduced deuteron form factor [?], suggest sizable hidden-color Fock state
969 contributions in the deuteron wavefunction [?]. The hidden-color states of the deuteron can be materialized
970 at the hadron level as $\Delta^{++}(uuu)\Delta^-(ddd)$ and other novel quantum fluctuations of the deuteron. These dual
971 hadronic components become important as one probes the deuteron at short distances, such as in exclusive
972 reactions at large momentum transfer. For example, the ratio $d\sigma/dt(\gamma d \rightarrow \Delta^{++}\Delta^-)/d\sigma/dt(\gamma d \rightarrow np)$ is
973 predicted to increase to a fixed ratio 2 : 5 with increasing transverse momentum p_T . Similarly, the Coulomb
974 dissociation of the deuteron into various exclusive channels $ed \rightarrow e' + pn, pp\pi^-, \Delta\Delta, \dots$ will have a changing
975 composition as the final-state hadrons are probed at high transverse momentum, reflecting the onset of
976 hidden-color degrees of freedom. The hidden color of the deuteron can be probed at the LHeC in electron
977 deuteron collisions by studying reactions such as $\gamma^*d \rightarrow npX$ where the proton and neutron emerge in the
978 target fragmentation region at high and opposite p_T . In principle, one can also study DIS reactions $ed \rightarrow e'X$
979 at very high Q^2 where $x > 1$. The production of high p_T anti-nuclei at the LHeC is also sensitive to hidden
980 color-nuclear components.

981 4.6 Electroweak physics

982 4.6.1 The context

983 Precision electroweak measurements at low energy have played a central role in establishing the Standard
984 Model (SM) as the theory of fundamental interactions. More recently, measurements at LEP, SLD, and
985 the Tevatron have confirmed the SM at the quantum level, verifying the existence of its higher-order loop
986 contributions. The sensitivity of these contribution to virtual heavy particles has allowed for an estimate of
987 the mass of the top quark prior to its actual discovery in 1995 by the CDF and DØ Collaborations. Now that
988 the determination of the top mass at the Tevatron has become quite accurate, reaching the 1% level, and
989 M_W is known with an error of 23 MeV, electroweak precision measurements imply significant constraints
990 on the mass of the last missing piece of the SM, the Higgs boson. The current situation has been analysed
991 for instance in [?, ?] taking into account the results of direct searches for the Higgs boson at LEP-2 and the
992 Tevatron, which currently exclude a SM Higgs boson with mass lower than 114GeV or in a narrow window
993 around 160GeV. At 95% CL, if the SM is correct, the Higgs boson must soon be found with mass below
994 155 GeV either at the Tevatron or at the LHC.

995 Electroweak precision measurements are also very effective in constraining the possible extensions of
996 the SM. In general, the observed good quality of the SM fit disfavors new physics at an energy scale of
997 $O(100\text{GeV})$ that modifies the Higgs mechanism in a drastic way. On the other hand, the fit does present
998 a few interesting deviations at the level of 2-3 σ . There is a significant tension between the FB asymmetry
999 of $Z \rightarrow b\bar{b}$ measured at LEP, which favors a heavy Higgs, and the LR asymmetry in $Z \rightarrow \ell\bar{\ell}$ and the W
1000 mass, which both favors a very light Higgs. Unfortunately, the present determination of M_H depends largely
1001 on these conflicting information, whose origin could be either statistical or rooted in new physics around
1002 the corner [?]. Another plausible $\sim 3\sigma$ hint of physics beyond the SM, without Higgs implications, is the
1003 discrepancy between the measured magnetic anomalous moment of the muon and its SM prediction [?].

1004 It is unlikely that operating experiments will change significantly the above picture of electroweak preci-
1005 sion measurements. The Tevatron and LHC will marginally improve the current precision on the top mass
1006 and reach a combined 15 MeV uncertainty on M_W , while LHCb might be able to achieve an interesting
1007 accuracy in the measurement of $\sin^2\theta_W$ [?, ?]. Two experiments at Jefferson Lab, Q-weak [?] and (later)
1008 MOLLER [?], will measure the weak mixing angle from parity violation in ep and e^-e^- scattering at low
1009 energy: these are interesting measurements complementary to the existing ones; MOLLER, in particular,
1010 may eventually reach an accuracy similar to that of LEP. It is widely expected that either the Higgs boson
1011 or further new physics will be discovered at the LHC, if not both. This is the context in which precision

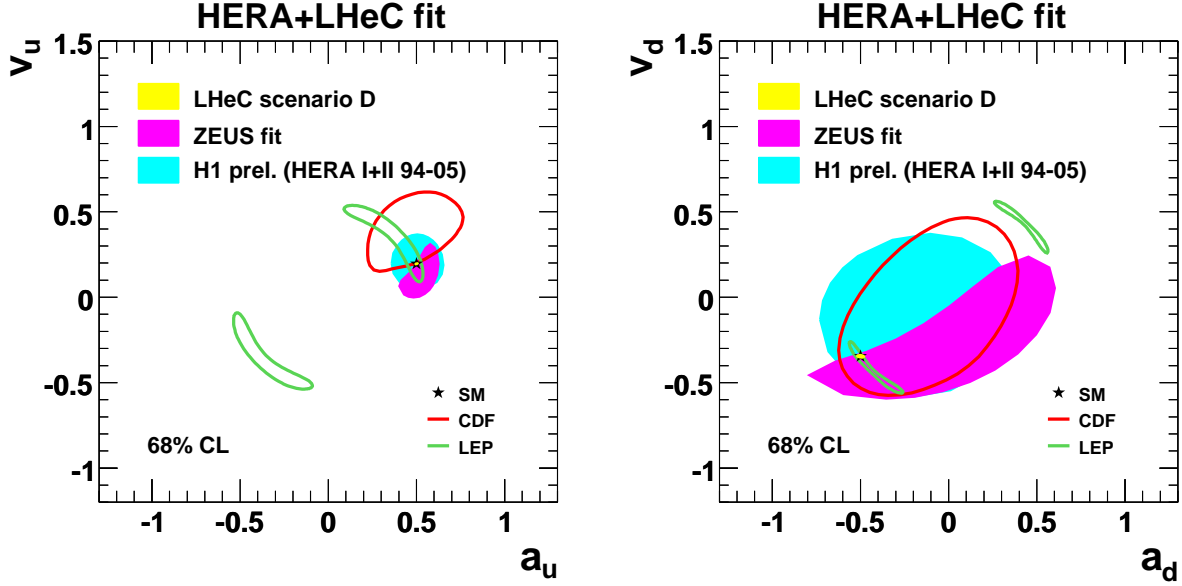


Figure 4.19: Determination of the vector and axial NC couplings of the light quarks at LEP, CDF, HERA and LHeC. - plot to be updated.

1012 electroweak measurements at LHeC are set.

1013 The electroweak measurements possible at LHeC are of the kind performed at HERA (see [?, ?] for an
 1014 overview). However, they will greatly benefit from the higher energy and larger luminosity, as well as from
 1015 highly polarized lepton beams, and therefore also include processes, as single standard model or anomalous
 1016 top quark production, which were impossible to study in ep before.

1017 A first class of measurements involves polarized charged currents (CC) only. They include a verification
 1018 of the left-handedness of CC from the polarization dependence of the CC cross-section. At HERA this has
 1019 led to a bound on possible right-handed currents, expressed in terms of the mass of a right-handed W_R boson
 1020 that couples to quarks with the same strength as the SM one. While the HERA result, $M_{W_R} > 210$ GeV
 1021 at 95% CL, can be significantly improved at the LHeC, low-energy flavour bounds and direct searches for
 1022 W type new bosons at the LHC are more sensitive. It yet is interesting to verify the universality of space-
 1023 and timelike interactions and thus to determine the propagator mass from the CC cross section through its
 1024 Q^2 dependence, $\propto (M_W^2/(M_W^2 + Q^2))^2 \phi(x, Q^2)$. At the LHeC, the HERA W propagator mass uncertainty
 1025 value may be improved by a factor of 10 to about 150 MeV.

1026 4.6.2 Light Quark Weak Neutral Current Couplings

1027 The LHeC will be able to measure the neutral current couplings of the light quarks at unprecedented
 1028 precision. As can be seen in Fig. ??, LEP has been able to constrain only an ambiguous combination of
 1029 them as the couplings enter as squares in pure weak NC reactions.

1030 DIS experiments with polarized electron and positron beams can completely disentangle the vector and
 1031 axial couplings of up and down type light quarks. As illustrated in Fig.??, the preliminary results by ZEUS
 1032 and H1 have improved on the LEP determination in the case of the up quarks [?, ?, ?]. Very recent $D0$
 1033 results somewhat improve on HERA constraints [?]. The sensitivity of the LHeC to the light quark NC
 1034 couplings has been studied with a QCD fit to the simulated data, in which the PDFs and the NC quark
 1035 couplings are simultaneously determined. Here the electron couplings are fixed, as they are very precisely
 1036 measured at LEP and SLD. The expected resolution for scenario D of LHeC is hardly visible on the scale

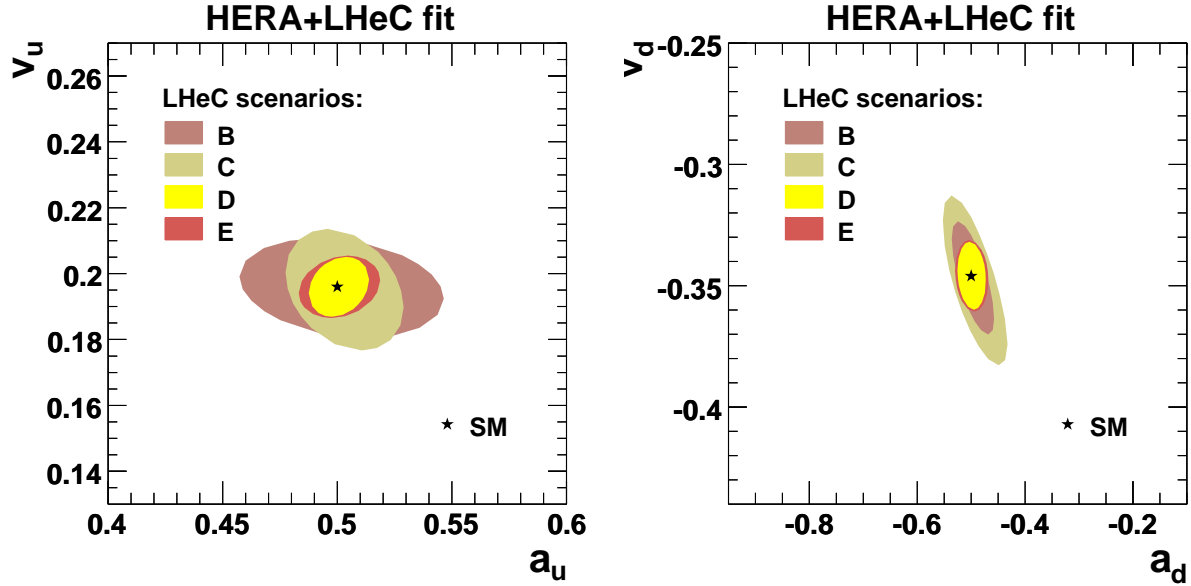


Figure 4.20: Determination of the vector and axial NC couplings of the light quarks at LHeC, comparison different scenarios.

1037 of Fig. ?? . A comparison among the various LHeC scenarios can be found in Fig. ?? The accuracy on
 1038 the vector and axial vector couplings of the u , d quarks ranges, in the best possible scenario, between 1
 1039 and 4%, with an improvement wrt HERA by a factor 10 to 40. A better determination of the light quark
 1040 NC couplings will particularly constrain New Physics models that modify significantly the light quark NC
 1041 couplings, without affecting the well-measured lepton and heavy quark couplings. It is not easy to realize
 1042 such an exotic scenario in a natural way, although family non-universal (leptophobic) Z' models (see for
 1043 instance [?, ?] and refs. therein), R-parity violating supersymmetry (see [?] for a review) and leptoquarks [?]
 1044 can in principle succeed. LHeC could therefore accurately test a spectrum of interesting new physics models.
 1045 A specific linear combination of the light quark NC vector couplings (v_u and v_d) might be measured at the
 1046 per cent level by the QWeak Collaboration [?]. Their results, combined with existing precise measurements
 1047 of Atomic Parity Violation and DIS, could provide a percent determination of v_u and v_d [?] and test the
 1048 same kind of models, but it will not probe the axial quark couplings.

1049 4.6.3 Determination of the Weak Mixing Angle

1050 Cross Section Asymmetries and Ratios

1051 The LHeC is a unique facility for electroweak physics because of the very high luminosity, high measurement
 1052 precision and the extreme range of momentum transfer Q^2 . Fig. ?? illustrates the reach and the size of
 1053 the electroweak effects in NC scattering. Depending on the charge and polarisation of the electron beam,
 1054 the contributions from γZ interference and pure Z exchange become comparable to or even exceed the
 1055 photon exchange contribution, i.e. of F_2 , which has dominated hitherto all NC DIS measurements. With the
 1056 availability of two charge and two polarisation states, of neutral and charged current measurements, proton
 1057 and isoscalar targets, a unique menu becomes available for testing the electroweak theory. For example,
 1058 one can very precisely measure light quark weak neutral current couplings, discussed above. One can also
 1059 test the universality of $\gamma - g$ and $Z - g$ fusion by extracting the heavy quark (c , b) contributions from γZ
 1060 interference. A remarkable measurement illustrated in the following regards the energy dependence of the

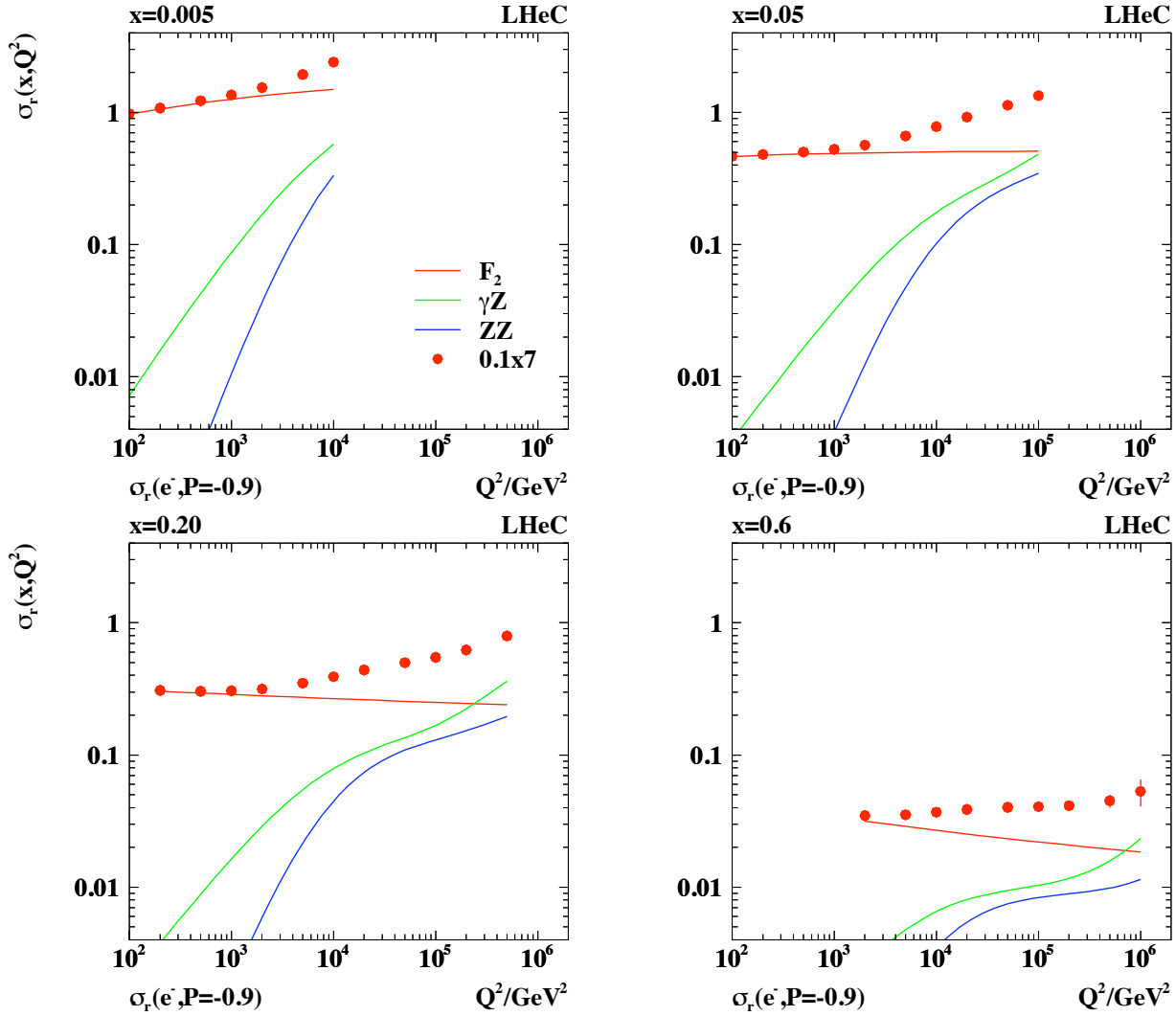


Figure 4.21: Simulated measurement of the neutral current DIS cross section (closed points) with statistical errors for 10 fb^{-1} shown as a function of Q^2 for different values of Bjorken x . The different curves represent the contributions of pure photon exchange (red), γZ interference (green) and pure Z exchange (blue) as prescribed in Eq. ???. Note the high precision of the reduced cross section measurement up to large x and Q^2 .

1061 weak mixing angle $\sin^2 \Theta$.

1062 Tests of the electroweak theory in DIS require to simultaneously control the parton distribution effects.
 1063 With the outstanding data base from the LHeC, joint QCD and electroweak fits become possible to high
 1064 orders perturbation theory. Cross section asymmetries and ratios can also be used to determine electroweak
 1065 parameters. Particularly useful examples are polarisation and charge asymmetries and also NC to CC cross
 1066 section ratios.

1067 In NC scattering, the polarisation asymmetry

$$A^\pm = \frac{1}{P_R - P_L} \cdot \frac{\sigma_{NC}^\pm(P_R) - \sigma_{NC}^\pm(P_L)}{\sigma_{NC}^\pm(P_R) + \sigma_{NC}^\pm(P_L)} \quad (4.31)$$

1068 served for the decisive confirmation of the left handed weak neutral current doublet structure as was predicted
 1069 by the GWS theory in 1979 [?]. The size of the electroweak asymmetries is given by the relative amount of
 1070 Z to photon exchange $O(10^{-4}Q^2/\text{GeV}^2)$, i.e. it becomes of order 1 at high Q^2 at the LHeC.

1071 To a good approximation the asymmetry measures the structure function ratio

$$A^\pm \simeq \mp \kappa_Z a_e \frac{F_2^{\gamma Z}}{(F_2 + \kappa_Z a_e Y_- x F_3^{\gamma Z} / Y_+)} \simeq \mp \kappa_Z a_e \frac{F_2^{\gamma Z}}{F_2}. \quad (4.32)$$

1072 Thus A^+ is expected to be about equal to $-A^-$ and to be only weakly dependent on the parton distributions.
 1073 The product of the axial coupling of the electron and the vector coupling of the quarks, inherent in $F_2^{\gamma Z}$,
 1074 determines the polarisation asymmetry to be parity violating. A measurement of A^\pm provides a unique and
 1075 precise measurement of the scale dependence of the weak mixing angle, as is discussed below (Sect. ??).
 1076 At large x the polarisation asymmetry provides an NC measurement of the d/u ratio of the valence quark
 1077 distributions, according to

$$A^\pm \simeq \pm \kappa \frac{1 + d_v/u_v}{4 + d_v/u_v}. \quad (4.33)$$

1078 Further asymmetries of NC cross sections have been discussed in [?].

1079 The neutral-to-charged current cross-section ratio

$$R^\pm = \frac{\sigma_{NC}^\pm}{\sigma_{CC}^\pm} = \frac{2}{(1 \pm P)\kappa_W^2} \cdot \frac{\sigma_{r,NC}^\pm}{\sigma_{r,CC}^\pm} \quad (4.34)$$

1080 is of interest for electroweak physics too as will be demonstrated below. At very high $Q^2 \gg M_Z^2$ and
 1081 neglecting terms in the NC part proportional to v_e it becomes approximately equal to

$$R^\pm \simeq \frac{2a_e^2}{(1 \pm P)\cos^2 \theta} \cdot \frac{Y_+ F_2^Z - Y_- P x F_3^Z}{Y_+ W_2^\pm + Y_- x W_3^\pm} \quad (4.35)$$

1082 which reveals the striking similarity of the neutral and charged weak interactions at high energies. One may
 1083 further consider, for example, a quantity which is the eN analogon to the Paschos-Wolfenstein relation [?]
 1084 in νN scattering

$$A_{NCC} = \frac{\sigma_{NC}^+ - \sigma_{NC}^-}{\sigma_{CC}^+ - \sigma_{CC}^-}. \quad (4.36)$$

1085 The very high luminosity and Q^2 range of the LHeC as compared even to HERA will open a completely
 1086 new era of electroweak physics in DIS.

1087 Measurement of the Weak Mixing Angle

1088 Further tests of the SM at the quantum level and indirect searches for new physics require ultimate precision.
 1089 Such corrections occur in the factor $1 - \Delta r$, see Eq. ??, which depends on the top mass, logarithmically on
 1090 the Higgs mass and possibly on new, heavy particles. A measurement of the weak mixing angle, $\sin^2 \theta$,

1091 to 0.01 % precision should fix the Higgs mass to 5 % accuracy. The so far most precise measurements of
 1092 $\sin^2 \theta$ have been performed at the Z pole in e^+e^- scattering, using the very high statistics, at LEP, and
 1093 in the case of the SLC, the large beam polarisation of 75 % too. The LHeC has the potential to measure
 1094 weak asymmetries and cross section ratios at, below and beyond the M_Z scale by precisely measuring their
 1095 dependence on $\sqrt{Q^2}$.

1096 The accuracy estimated for $\sin^2 \theta$ depends on its definition. The electroweak theory has three independent
 1097 parameters. For the subsequent study, as in a similar study of H1 [?], the values of α and M_Z are fixed,
 1098 which are best known, M_Z to 0.002 %. For the estimate of the sensitivity to electroweak effects as the third
 1099 parameter here $\sin^2 \theta$ is chosen, which is used, together with α and M_Z to calculate G and M_W and also
 1100 occurs in the weak neutral current couplings ⁴. This way both the NC and the CC cross sections are sensitive
 1101 to $\sin^2 \theta$. Equivalently one could have expressed all parameters using α , M_Z and M_W , and determine M_W .
 1102 Due to the relation $\sin^2 \theta = 1 - M_W^2/M_Z^2$, the error of such an indirect measurement of M_W is

$$\Delta M_W = \frac{M_W \delta \sin^2 \theta}{2 \sin^2 \theta}, \quad (4.37)$$

1103 i.e. a one permille accuracy on $\sin^2 \theta$ corresponds to $\Delta M_W = 40$ MeV.

1104 A simulation is done of the NC and CC cross sections depending on the lepton beam charges and
 1105 polarisations based on the formulae presented above. This allows to build a variety of asymmetries and cross
 1106 section ratios and derive their sensitivity to the weak mixing angle. An example is illustrated in Fig. ?? . Here
 1107 the polarisation asymmetry (left) and the NC/CC ratio (right) are calculated for different values of $\sin^2 \Theta$
 1108 using two recent sets of leading order parton distributions, CTEQ6LL and MSTW08. The measurement
 1109 accuracy of $\sin^2 \Theta$ has a statistical, a polarisation, a systematic and a pdf uncertainty. One derives that the
 1110 statistical precision is about 0.1 % for the NC asymmetry A^- and even 0.05 % for the NC/CC ratio R^- for
 1111 e^-p scattering with an assumed polarisation of -0.8 and a luminosity of 10 fb^{-1} for default beam energies.

1112 At this early stage of consideration one may not present a full error study. However, a few first con-
 1113 siderations are in order: The high luminosity and large Q^2 range move the electroweak physics at this ep
 1114 machine to the level of highest accuracy demands. Most of the systematic errors cancel in asymmetry and
 1115 ratio measurements. A 0.1 % electron energy scale uncertainty, as has been achieved with H1, for example,
 1116 translates at the LHeC to a 0.15 % change of A^- and a negligible change of R^- . This measurement samples
 1117 data in a region of very high cross section accuracy and can exclude the highest x region where uncertainties
 1118 grow like $1/(1-x)$. The desired level of polarisation measurement is obviously about a permille, which seems
 1119 to be possible as is discussed in the detector chapter.

1120 The requirements for A^- and R^- are different. The asymmetry A^- requires frequent changes of the
 1121 polarisation to control the time dependence of the measurement. It measures essentially a ratio of the
 1122 structure functions $F_2^{\gamma Z}/F_2$ and therefore it is rather insensitive to uncertainties related to the parton
 1123 distributions. In fact, one observes in Fig. ?? that the predictions of the two PDF sets considered differ
 1124 by less than the statistical uncertainty for A^- . The NC/CC ratio R is less sensitive to time drifts as the
 1125 NC and CC data are taken simultaneously. Its statistical power is highest, as had already been noticed for
 1126 HERA [?]. It yet is sensitive to the PDFs. For the two sets of PDFs considered here, an about two per cent
 1127 difference is calculated of the R^- ratios. This would spoil the extraction of $\sin^2 \Theta$. The high sensitivity of R
 1128 to the mixing angle can only be employed when the PDFs are much better known than so far. This, however,
 1129 is one of the major goals of the LHeC physics programme and large improvements are to be expected as
 1130 is discussed in Sec. ?? . The potential of measuring $\sin^2 \Theta$ from NC/CC ratios is observed to be particular
 1131 striking. However, for the evaluation of the scale dependence of $\sin^2 \Theta$ below, the results derived from A^-
 1132 are used due to its much smaller PDF sensitivity.

1133 The mixing angle, similar to α_s , is predicted to vary strongly as a function of the scale μ , which in DIS is
 1134 precisely known and given as $\sqrt{Q^2}$. This dependence results from higher order loop effects as calculated in [?].
 1135 Precise measurements to per mille uncertainty were performed at the Z pole by SLC and LEP experiments.

⁴An interesting test is also to fix α , M_Z and G and to determine derived electroweak parameters as M_W or $\sin^2 \Theta$ for precision consistency checks in the search for deviations from the SM. Such a study has b=not been undertaken so far for the LHeC.

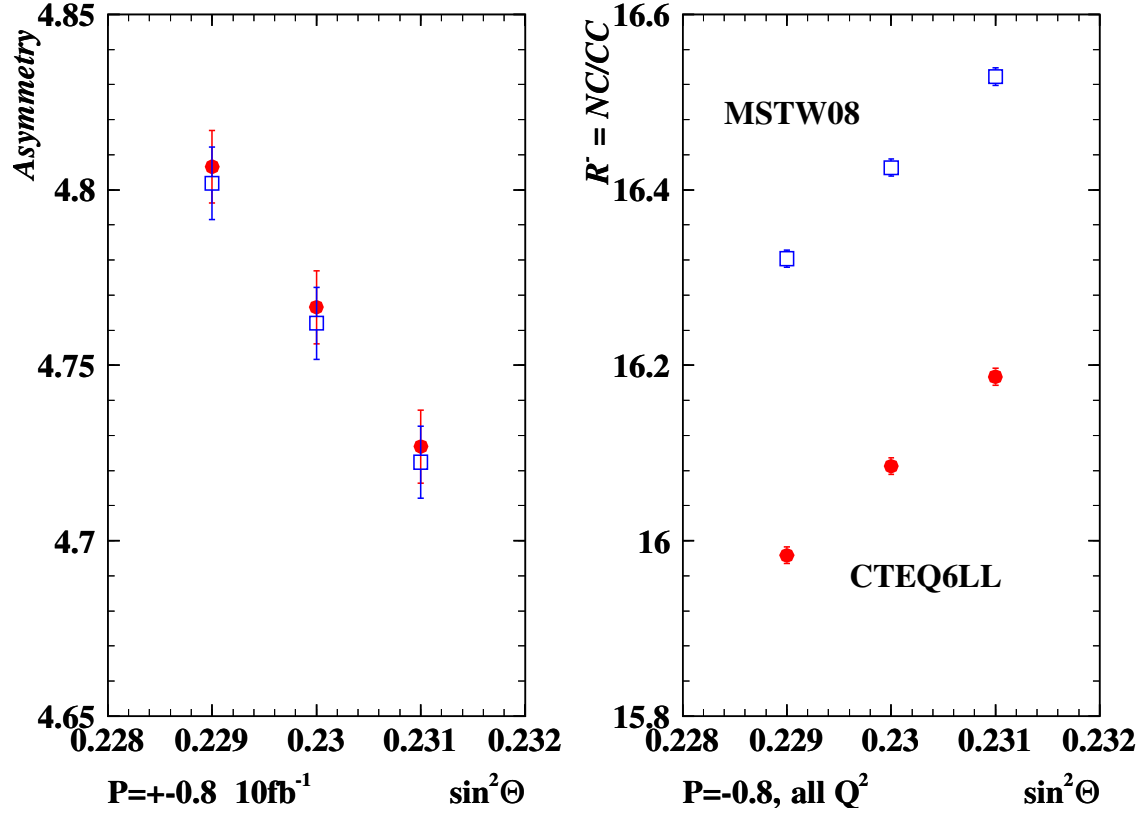


Figure 4.22: Simulated measurement of the polarisation NC cross section asymmetry A^- (left), in per cent for $P = \pm 0.8$, and the ratio of neutral-to-charged current cross sections, $R = NC/CC$ (right), for $P = -0.8$, for different values of $\sin^2 \theta$. The errors are statistical for luminosities of 10 fb^{-1} per beam for polarised electron scattering for $E_e = 60 \text{ GeV}$ and the nominal 7 TeV proton beam. The closed (open) symbols show the simulation for the CTEQ6LL (MSTW08) leading order parameterisations of the parton distributions. The average Q^2 is 1300 GeV^2 for the NC asymmetry A^- , while for the ratio R the average CC Q^2 is about 9500 GeV^2 . Consequently, the mean x in NC and CC differs by a factor of 6, which is at the origin of the large differences in R between the two PDF set predictions.

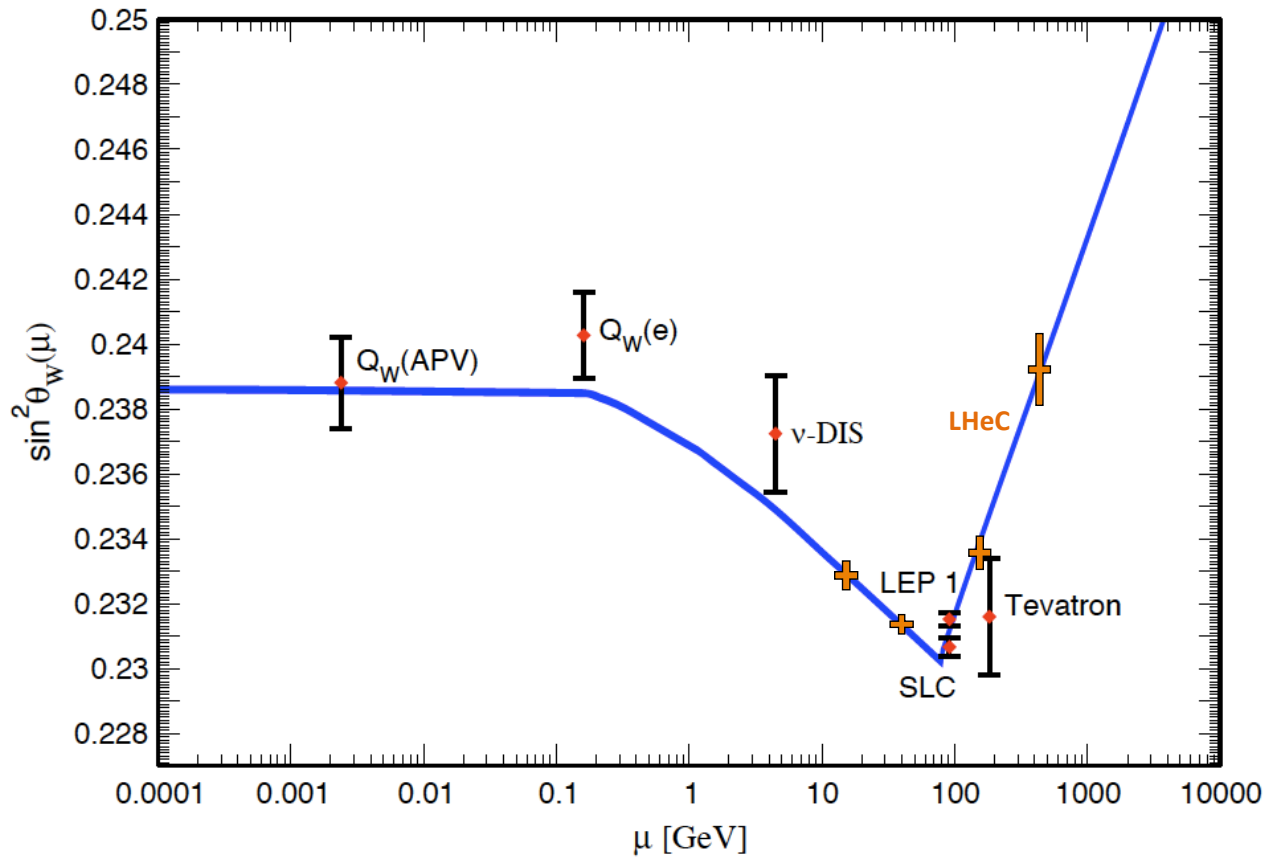


Figure 4.23: Dependence of the weak mixing angle on the energy scale μ , taken from [?]. Four simulated points have been added based on the estimated measurement accuracy using the polarisation asymmetry A^- binned in intervals of $\sqrt{Q^2}$, see text.

Type	Q_1	P_1	Q_2	P_2	$\delta s(A_{12})$	$\delta s(R_1)$	$\delta s(R_2)$
e^- Polarisation Conjugation	-1.	-0.8	-1.	0.8	0.00026	0.00009	0.00024
e^+ Polarisation Conjugation	+1.	-0.8	+1.	0.8	0.00027	0.00040	0.00015
e^- Low P Conjugation	-1.	-0.4	-1.	0.4	0.00052	0.00010	0.00015
Charge Conjugation $P=0$	+1.	0.	-1.	0.	0.01600	0.00019	0.00012
Charge Conjugation $P=\mp 0.8$	+1.	-0.8	-1.	0.8	—	0.00040	0.00024
Charge Conjugation $P=\pm 0.8$	+1.	+0.8	-1.	-0.8	0.00790	0.00015	0.00009
e^- PC Low $Q^2 \sim 300 \text{ GeV}^2$	-1.	-0.8	-1.	0.8	0.00068	0.00029	0.00083
e^- PC Med $Q^2 \sim 1500 \text{ GeV}^2$	-1.	-0.8	-1.	0.8	0.00027	0.00012	0.00029
e^- PC High $Q^2 \sim 22000 \text{ GeV}^2$	-1.	-0.8	-1.	0.8	0.00044	0.00071	0.00055
e^- PC vHigh $Q^2 \sim 130000 \text{ GeV}^2$	-1.	-0.8	-1.	0.8	0.00170	0.00460	0.00200

Table 4.5: Estimated accuracies of the weak mixing angle, $\delta \sin^2 \Theta$, in the on-mass shell scheme, from simulated measurements of the NC asymmetry and the NC/CC cross section ratio for different beam charge and polarisation conditions.

Recent low energy experiments have provided measurements of $\sin^2 \Theta$ at very low Q^2 as from the parity violation asymmetry due to polarisation conjugation in Moeller scattering at $Q^2 = 0.026 \text{ GeV}^2$ by the E158 experiment. At scale values of about 5 GeV the NuTeV Collaboration has determined the mixing angle which for some time created a substantial experimental and theoretical effort when it appeared to be above the theoretical expectation by a few standard deviations. Explanations of this “anomaly” included variations of the strange quark density, effects from QED or nuclear corrections. An ultraprecise measurement of $\sin^2 \Theta$ is envisaged, yet still at $\mu = M_Z$, if a new Z_0 factory was built.

The current measurements are summarised in Fig. ???. The plot also contains projected $\sin^2 \Theta$ uncertainty values from the LHeC, as listed in Table ??, which result from simulations of the parity violation asymmetry A^- in polarised $e^- p$ scattering, for scales between about 10 and 400 GeV . Due to the high statistics nature of the DIS NC process, the variation of $\sin^2 \Theta$ as a function of $\sqrt{Q^2}$ can be measured for a large range of $\sqrt{Q^2}$. At low scales the range limited by the sensitivity to the Z exchange effects and at high scales by the kinematic limit and luminosity. It may deserve a study to understand to how low values of Q^2 the asymmetry A^- can be determined in a meaningful measurement, which is related to time drifts, polarisation flip times etc. and likely can only be answered with real data. It is to be noted that previous and planned fixed target experiments measure this asymmetry at extremely small values of Q^2 as compared to the range of the LHeC.

From the range considered here, with $Q^2 > 300 \text{ GeV}^2$, it can be concluded, see Fig. ??, that the expected measurement accuracy would lead to a decisive test of the scale dependence of $\sin^2 \Theta$.

4.7 Charm and Beauty production

4.7.1 Introduction and overview of expected highlights

In this section it is shown that the measurements of charm and beauty production at LHeC provide high precision pQCD tests and are crucial to improve the knowledge of the proton structure. Historically the HERA charm and beauty studies extended by large amount results from previous fixed target experiments. This allowed a great advancement in the understanding of the dynamics of heavy quark production. The LHeC is the ideal machine for a further extension of similar historic importance because a higher centre of mass energy and a much larger integrated luminosity compared to HERA are available. On top of this the heavy flavour measurements will greatly benefit from the advanced detector design at LHeC with high precision (Silicon or similar) trackers all over the place. At HERA the tagging was restricted to central

1165 rapidities and effective efficiencies⁵ of only 0.1% (1%) for charm (beauty) were reached. At LHeC efficiencies
 1166 of 10% (50%) should be possible for charm (beauty) and a large rapidity range can be covered from the very
 1167 backward to the very forward regions. Before further elucidating the great measurement prospects the next
 1168 paragraph introduces the main heavy quark production processes, the relevant pQCD theoretical schemes
 1169 and some related open questions.

1170 In leading order, heavy quarks are produced in ep collisions via the Boson Gluon Fusion (BGF) process
 shown in Figure ?? on the left. This process provides direct access to the gluon density in the proton. BGF

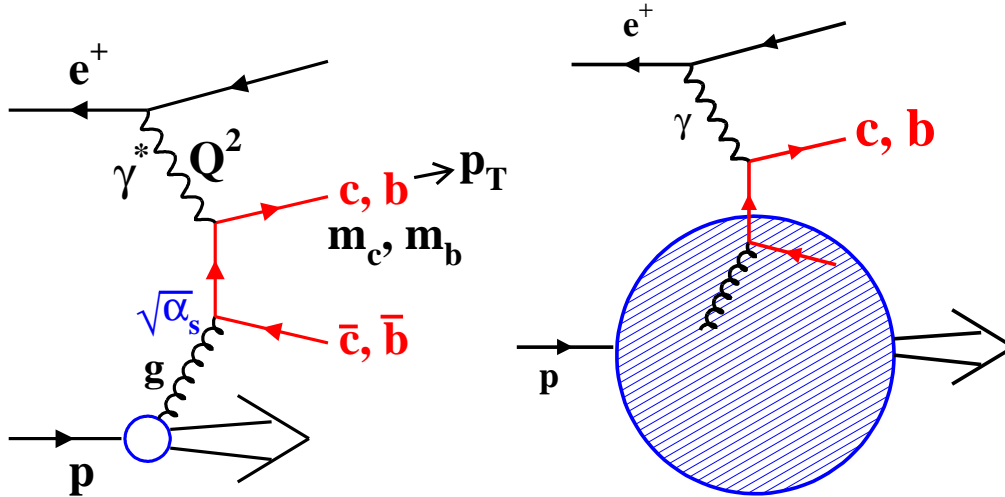


Figure 4.24: Left: Leading order Boson Gluon Fusion (BGF) diagram for charm and beauty production in ep -collisions. Right: Sketch of the leading order process in the massless approach where charm and beauty quarks are treated as massless sea quarks in the proton.

1171 type processes dominate DIS scattering towards lower x , due to the large gluon density. In the high Q^2
 1172 limit, the events with charm and beauty quarks are expected to account for $\sim 36\%$ and $\sim 9\%$ of the BGF
 1173 processes and hence contribute significantly to inclusive DIS. On the theoretical side, the description of heavy
 1174 quark production in the framework of perturbative QCD is complicated due to the presence of several large
 1175 scales like the heavy quark masses, the transverse momentum p_T of the produced quarks and the momentum
 1176 transfer Q^2 . Different calculation schemes have been developed to obtain predictions from pQCD. At low
 1177 scales p_T (or Q^2) the fixed-flavour number scheme (FFNS) [?, ?, ?] is expected to be most appropriate where
 1178 the quark masses are fully accounted for. At very high scales the NLO FFNS scheme predictions are expected
 1179 to break down since large logarithms $\ln(p_T^2/m^2)$ are neglected that represent collinear gluon radiations from
 1180 the heavy quark lines. These logarithms can be resummed to all orders in the alternative zero-mass variable
 1181 flavour number (ZM-VFNS) [?, ?, ?, ?] schemes. Here the charm and beauty quarks are treated above
 1182 kinematic threshold as massless and appear also as active sea quarks in the proton, as depicted in figure ??
 1183 in the sketch on the right. Most widespreadly used are nowadays the so-called generalised variable flavour
 1184 number schemes (GM-VFNS) [?, ?]. These mixed schemes converge to the massive and massless schemes at
 1185 low and high kinematical scales, respectively, and apply a suitable interpolation in the intermediate region.
 1186 However, the exact modelling of the interpolation and in general the treatment of mass dependent terms in
 1187 the perturbation series are still a highly controversial issue among the various theory groups. The different
 1188 treatments have profound implications for global PDF fits and influence the fitted densities of gluons and
 1189 other quark flavours in the proton. This has direct consequences for many important cross section predictions
 1190 at LHC, for instance for Z and W production. The value of the charm quark mass is also an important
 1191 uncertainty in the calculations. Recently the running charm mass has been fitted [?] to fixed target and
 1192

⁵The effective efficiency takes the background pollution into account. It is defined as the efficiency of an equivalent background free sample with the same signal precision as that obtained in the data.

HERA charm data obtaining a value $m_c(m_c) = 1.01 \pm 0.09(\text{exp}) \pm 0.03(\text{th})$ GeV.

The following main physics highlights are expected for heavy quark production measurements at LHeC:

- *Massive vs Massless scheme:* At HERA the charm and beauty production data were found to be well described by the NLO FFNS scheme calculations over the whole accessible phase space, up to the highest p_T and Q^2 scales. An LHeC collider would allow to extend these studies to a much larger kinematical phase space and thus to map the expected transition to the massless regime. Further improvements in the determination of the charm quark mass and in the tuning of the GM-VFNS schemes are possible and will have strong impacts on global PDF fits.

- *Gluon density determination:* At HERA the recorded charm data provide already some interesting sensitivity to the gluon density in the proton. However due to the small tagging efficiencies the precisions are far below those obtained from the scaling violations of F_2 or those from jet data. At LHeC this situation will highly improve and it will be possible to probe the gluon density via the BGF process down to proton momentum fractions $x_g \leq 10^{-5}$, where it is currently not well known.

At such low values of x_g a fixed-order perturbative computation becomes unreliable. It is then necessary to resum both evolution equations and hard matrix elements. In fact, heavy quark production is the first process for which all-order small x resummed terms were computed, and the high-energy factorization, on which the whole of perturbative small- x resummation is based, was proven in this context [?, ?]. Heavy quark production at the LHeC, with its high precision, energy and extended kinematic coverage, would thus provide an ideal setting for tests of high-energy factorization and small x resummation.

In this context it is also interesting to note that in the BGF process one can reach for charm production much smaller x_g values than with flavour inclusive jets since experimentally one can tag charm quarks with small transverse momenta. The studies of heavy flavour production sensitive to the gluon density can be done both in DIS and in the photoproduction kinematic regime.

- *Charm and beauty densities in the proton:* In general the measurements of the structure functions F_2^{cc} and F_2^{bb} are of highest interest for theoretical analyses of heavy flavour production in ep collisions. These structure functions are describing the parts of F_2 which are due to events with charm or beauty quarks in the final state. At sufficiently high $Q^2 \gg m_c^2, m_b^2$, the two structure functions can be directly related to effective densities of charm and beauty quarks in the proton, This can be used for predictions of many interesting processes at LHC with charm or beauty quarks in the initial state. For instance, as discussed in [?], in the minimal supersymmetric extension of the standard model the production of the neutral Higgs boson A is driven by $b\bar{b} \rightarrow A$ and for the calculation of this process the PDF uncertainties dominate over the theoretical uncertainties of the perturbative calculation. At HERA the measurements of F_2^{bb} barely reached the necessary high Q^2 regime and only with modest precision. Huge phase space extensions and precision improvements will be possible at LHeC.

- *Intrinsic charm component:* Since long it has been suggested [?, ?, ?, ?] that the proton wave function might contain an intrinsic charm component $uudc\bar{c}$. This would show up mainly at large $x > 0.1$. Unfortunately at HERA this large x region could not be studied mainly due to the limited detector acceptance in the forward region. Due to the even larger boost in the forward direction at LHeC the situation is also not easy there. However, with a forward tracking acceptance down to small polar angles there could be a chance to study this effect, in particular with the planned proton low energy runs.

- *Strange/antistrange densities:* Events with charm quarks in the final state can be also used as a tool for other purposes. The strange and antistrange quark densities in the proton can be analysed via the charge current process $sW \rightarrow c$, where the charm quark is tagged in the event. At HERA this was impossible due to the small cross sections, but at LHeC the cross sections for CC reactions are much higher and as noted before the other experimental conditions (luminosities, detector) will greatly improve. This leads to the first and precise measurement of both the strange and the anti-strange quark densities as is demonstrated in Sect. ??.

- *Electroweak physics:* There are intriguing possibilities for LHeC electroweak physics studies with charm and beauty quarks in the final state. For example one should be able to do a lepton beam polarisation asymmetry measurement for neutral current events, where the scattered quark is tagged as a beauty quark. This will provide direct access to the axial and vector couplings of the beauty quark to the Z boson. Similar measurements are possible for charm.

In summary the measurements of charm and beauty at an LHeC will be extremely useful for high precision pQCD tests, in particular for the understanding of the treatment of mass terms in pQCD, to improve the knowledge of the proton PDFs: directly for g, c, b, s, \bar{s} densities and indirectly also for u and d. Furthermore they provide a great potential for electroweak physics. At the time when the LHeC will be operated, the pQCD theory calculations are expected to have advanced considerably. In particular there is hope that full massive scheme NNLO calculations of order $o(\alpha_s^3)$ will be available by then. These will allow theory to data comparisons for heavy flavour production in ep collisions with unprecedented precision.

In the following subsections several dedicated simulation studies are presented which illustrate some of the expected highlights. First total cross sections are presented for various processes involving charm, beauty and also top quarks in the final state, showing that LHeC will be a genuine *multi heavy flavour factory*. Then the expected measurements of the structure functions F_2^{cc} and F_2^{bb} are discussed and compared to the existing HERA data. Next a study is presented of the possibility to measure intrinsic charm with dedicated low proton energy runs. Finally predictions for differential charm hadron production cross sections in the photoproduction kinematic regime are presented and compared to HERA, demonstrating the large phase space extension.

4.7.2 Total production cross sections for charm, beauty and top quarks

This section presents total cross sections for various heavy quark processes at LHeC (with 7 TeV proton beam energy) as a function of the lepton beam energy. Predictions are obtained for: charm and beauty production in photoproduction and DIS, the charged current processes $sW \rightarrow c$ and $bW \rightarrow t$ and top quark pair production in photoproduction and DIS. For comparison the flavour inclusive charged current total cross section is also shown. Table ?? lists the generated processes, the used Monte Carlo generators and the selected parton distribution functions. The resulting cross sections are shown in Figure ?. For comparison also the predicted cross sections for the HERA collider (with 920 GeV proton energy) are presented. The cross sections at LHeC are typically about one order of magnitude larger compared to HERA. Attached to the right of the plot are the number of events that are produced per 10 fb^{-1} of integrated luminosity. For instance for charm more than 10 billion events are expected in photoproduction and for beauty more than 100 million events. In DIS the numbers are typically a factor of five smaller. The strange and antistrange densities can be probed with some hundred thousands of charged current events with charm in the final state. The top quark production is dominated by the single production in the charged current reaction with beauty in the initial state and about one hundred thousands tops and a similar number of antitops are expected. In summary the LHeC will be the first ep collider which provides access to all quark flavours and with high statistics.

4.7.3 Charm and Beauty production in DIS

This section presents predictions for charm and beauty production in neutral current DIS, for Q^2 values of at least a few GeV^2 . The predictions are given for the structure functions $F_2^{c\bar{c}}$ and $F_2^{b\bar{b}}$ which denote the contributions from charm and beauty events to F_2 . As explained in section ?? the two structure functions are of large interest for theoretical analyses. Experimentally they are obtained by determining the total charm and beauty cross sections in two-dimensional bins of x and Q^2 . The LHeC projections shown here were obtained with the Monte Carlo programme RAPGAP [?] which generates charm and beauty production with massive leading order matrix elements supplemented by parton showers. The proton Parton Distribution Function set CTEQ5L [?] were used and the heavy-quark masses were set to $m_c = 1.5 \text{ GeV}$ and $m_b = 4.75 \text{ GeV}$, respectively. In general at HERA the RAPGAP predictions are known to provide a

Process	Monte Carlo	PDF
Charm γp Beauty γp tt γp	PYTHIA6.4 [?]	CTEQ6L [?]
Charm DIS Beauty DIS tt DIS	RAPGAP3.1 [?]	CTEQ5L [?]
CC e^+p CC e^-p $sW \rightarrow c$ $\bar{s}W \rightarrow \bar{c}$ $bW \rightarrow t$ $\bar{b}W \rightarrow \bar{t}$	LEPTO6.5 [?]	CTEQ5L
tt DIS	RAPGAP 3.1	CTEQ5L

Table 4.6: Used generator programmes for the predictions of total cross sections at LHeC, shown in Figure ???. For all processes with top quarks the top mass was set to a value of 170 GeV. For both photoproduction (labelled as γp) and DIS only direct photon processes were generated and no reactions with resolved photons.

1288 reasonable description of the measured charm and beauty DIS production data. The RAPGAP data were
1289 generated for an LHeC collider scenario with 100 GeV electrons colliding with 7 TeV protons. The statistical
1290 uncertainties have been evaluated such that they correspond to an integrated data luminosity of 10 fb^{-1} . All
1291 studies were done at the parton level, hadronisation effects were not taken into account. Tagging efficiencies
1292 of 10% for charm quarks and 50% for beauty quarks have been assumed, respectively. These efficiencies are
1293 about a factor 100 larger compared to the effective efficiencies (including the dilution due to background
1294 pollution) at HERA which may look surprisingly but is explainable. At HERA the charm quarks were tagged
1295 either with full charm meson reconstruction or with inclusive secondary vertexing of charm hadron decays.
1296 The first method suffered from very small branching ratios of suitable decay channels. The second technique
1297 which was also used for the beauty tagging was affected by a large pollution from light quark background
1298 events due to the limited detector capabilities to separate secondary from primary vertices. At LHeC one
1299 can expect a much better secondary vertex identification and thus a very strong background reduction. It is
1300 difficult to predict exactly how much background pollution will remain at LHeC, so for the purpose of this
1301 simulation study it was completely neglected. Systematic uncertainties were also neglected for the studies
1302 presented here. From the experiences at HERA the total systematic uncertainties for charm and beauty
1303 cross sections in the visible ranges can be expected to be of similar size as the statistical ones.

1304 Figures ?? and ?? show the resulting RAPGAP predictions at LHeC for the structure functions F_2^{cc} and
1305 F_2^{bb} , respectively, compared to recent measurements [?] from HERA. The data are shown as a function of
1306 x for various Q^2 values. The Q^2 values were chosen such that they cover a large fraction of the specific
1307 values for which HERA results are available. Some further values demonstrate the phase space extensions
1308 at LHeC. The projected LHeC data are presented as points with error bars which (where visible) indicate
1309 the estimated statistical uncertainties. For the open points the detector acceptance is assumed to cover the
1310 whole polar angle range. For the grey shaded and black points events are only accepted if at least one charm
1311 quark is found with polar angles $\theta_c > 2^\circ$ and $\theta_c > 10^\circ$, respectively. The selected results from HERA are
1312 shown as triangles with error bars indicating the total uncertainty. The HERA F_2^{cc} results in Figure ??
1313 are those of a recent weighted average [?] of almost all available measurements from H1 and ZEUS. In a
1314 large part of the covered phase space these results are already rather accurate, with precisions between 5%
1315 and 10%. The overlaid LHeC projections show a vast phase space increase to lower and larger x and also

Total cross sections in ep collisions

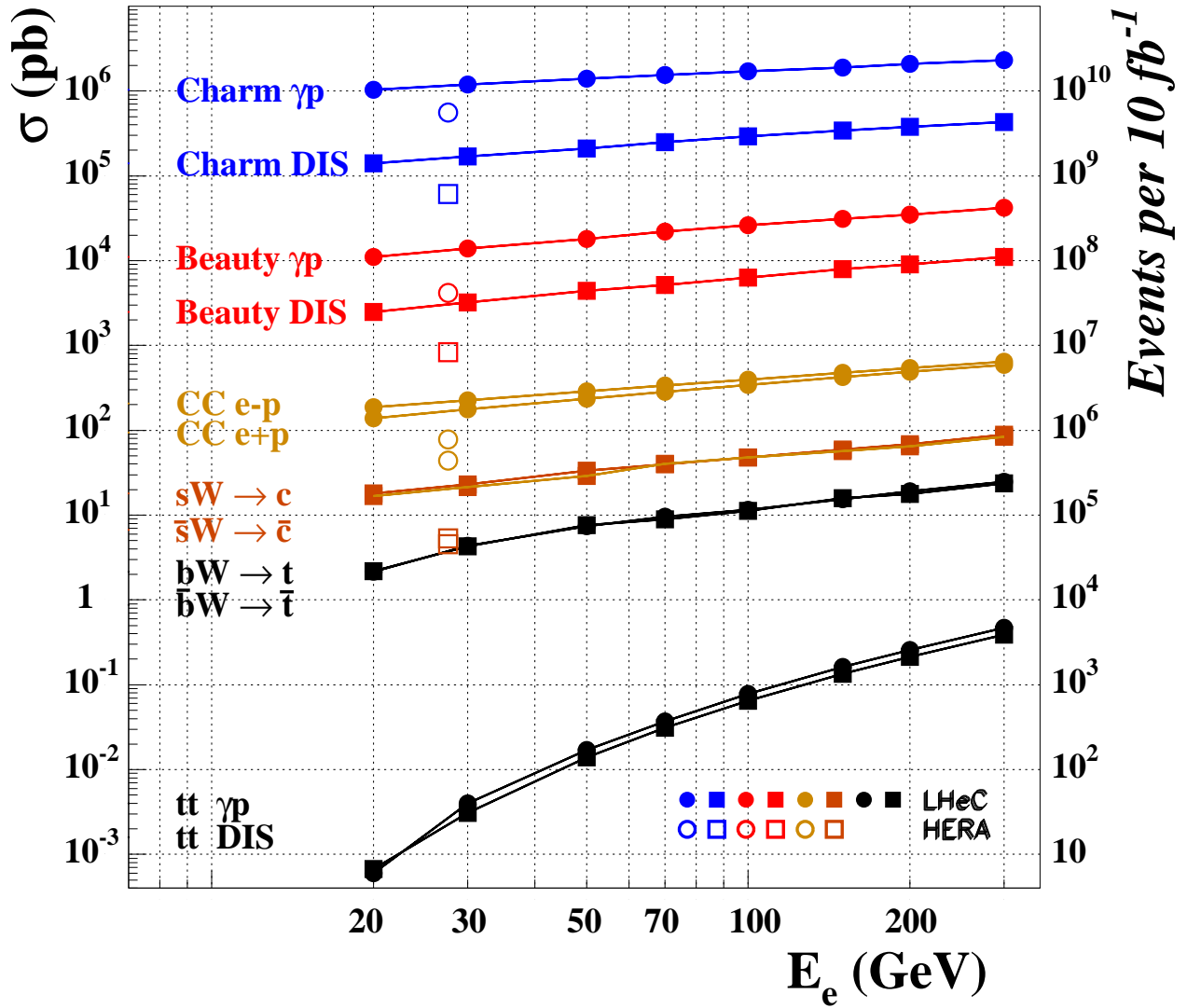


Figure 4.25: Total production cross section predictions for various heavy quark processes at the LHeC (with 7 TeV proton energy), as a function of the lepton beam energy. The following processes are covered: charm and beauty production in photoproduction and DIS, the charged current processes $sW \rightarrow c$ and $bW \rightarrow t$ and top pair production in photoproduction and DIS. The flavour inclusive charged current total cross section is also shown. All predictions are taken from Monte Carlo simulations, the details can be found in Table ???. For comparison also the predicted cross sections at HERA (with 920 GeV proton energy) are shown.

1316 to much higher Q^2 values. In the kinematic overlap region the expected statistical precisions at LHeC are
 1317 typically a factor ~ 40 better than at HERA which can be easily explained by the 20 times larger integrated
 1318 luminosity and the ~ 100 times better tagging efficiency. For the smaller x not covered by HERA the
 1319 precision even improves at LHeC due to the growing cross sections driven by the rise of the gluon density.
 1320 The best statistical precisions in the LHeC simulation are observed at smallest x values and small Q^2 and
 1321 reach down to 0.01%. As seen in the simulation (not shown here) the LHeC F_2^{sc} data provide access to the

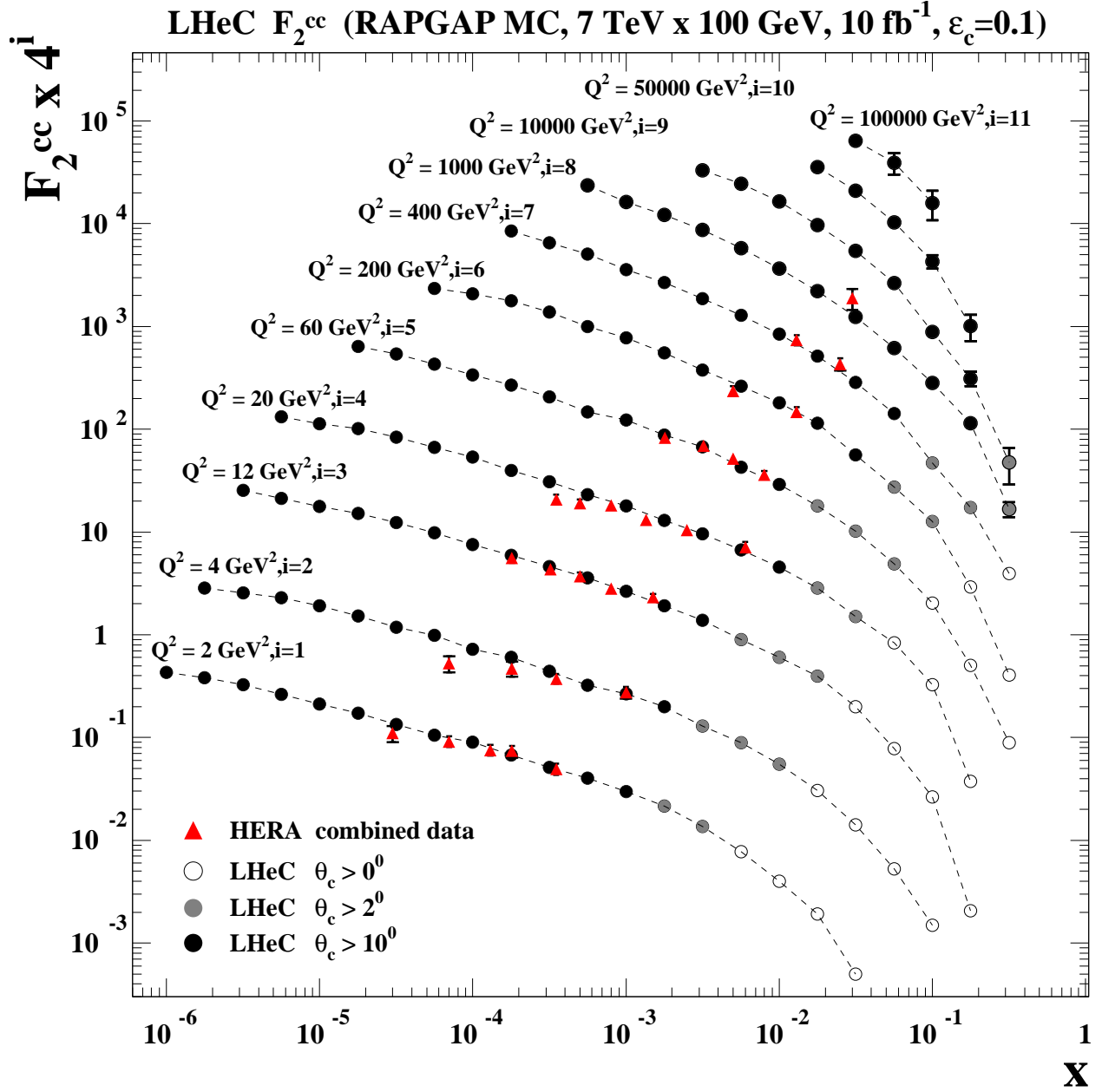


Figure 4.26: F_2^{cc} projections for LHeC compared to HERA data [?], shown as a function of x for various Q^2 values. The expected LHeC results obtained with the RAPGAP MC simulation are shown as points with error bars representing the statistical uncertainties. The dashed lines are interpolating curves between the points. For the open points the detector acceptance is assumed to cover the whole polar angle range. For the grey shaded and black points events are only accepted if at least one charm quark is found with polar angles $\theta_c > 2^0$ and $\theta_c > 10^0$, respectively. For further details of the LHeC simulation see the main text. The combined HERA results from H1 and ZEUS are shown as triangles with error bars representing their total uncertainty.

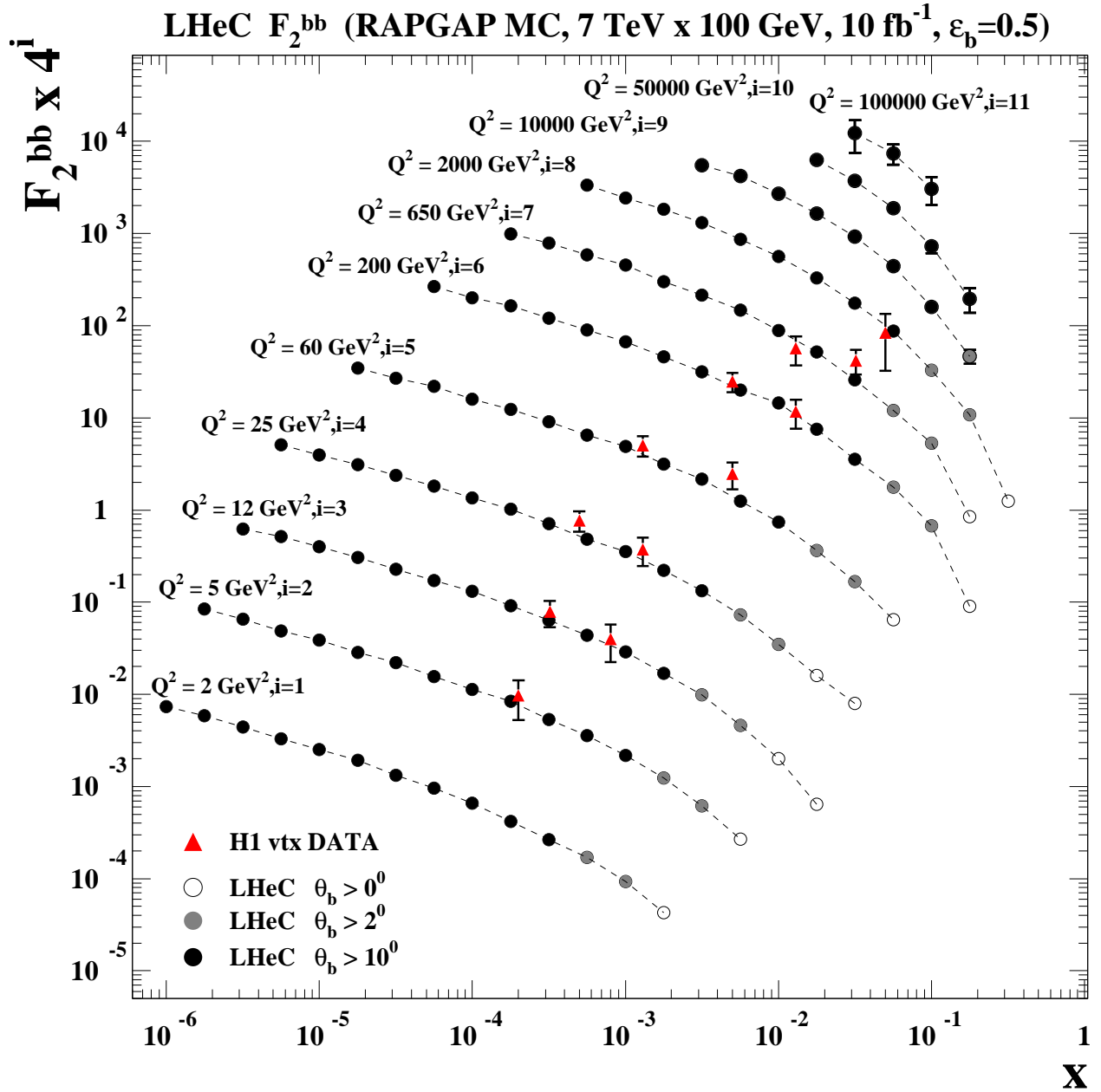


Figure 4.27: F_2^{bb} projections for LHeC compared to HERA data [?] from H1, shown as a function of x for various Q^2 values. The expected LHeC results obtained with the RAPGAP MC simulation are shown as points with error bars representing the statistical uncertainties. The dashed lines are interpolating curves between the points. For the open points the detector acceptance is assumed to cover the whole polar angle range. For the grey shaded and black points events are only accepted if at least one beauty quark is found with polar angles $\theta_b > 2^\circ$ and $\theta_b > 10^\circ$, respectively. For further details of the LHeC simulation see the main text. The HERA results from H1 are shown as triangles with error bars representing their total uncertainty.

1322 the gluon density in the BGF process down to proton momentum fractions $x_g \sim 10^{-5}$. The LHeC data can
 1323 also provide an substantial extension to higher x compared to HERA where the measurements reached x

values of a few percent. As evident from the simulated points with different polar angle cuts this necessitates an excellent forward tagging of charm quarks. In any case values of $x > 0.1$ should be accessible in the medium and large Q^2 domain.

Figure ?? show the RAPGAP predictions at LHeC for F_2^{bb} . Also shown are the results from the H1 analysis [?] based on inclusive secondary vertex tagging. Clearly these results and similar ones (not shown) from ZEUS are not very precise, the typical total uncertainties are 20-50%. Again, the LHeC F_2^{bb} projections demonstrate a vast phase space increase, similar as for charm. The best statistical precisions obtained at LHeC for F_2^{bb} are seen in the simulation towards low x and small and medium Q^2 and reach down to 1 permille. The measurements at LHeC will enable a precision mapping of beauty production from kinematic threshold to large Q^2 . In the context of the generalised variable flavour number schemes (GM-VFNS) this will allow to study in detail the onset of the beauty quark density in the proton and to compare it to the charm case. As mentioned in section ??, for high $Q^2 \gg m_b^2$ the F_2^{bb} results can be directly interpreted in terms of an effective beauty density in the proton. The measurement of this density is of large interest because it can be used to predict beauty quark initiated processes at the LHC. As visible in the figure, HERA covers only a small phase space in this region and with moderate precision. However, at LHeC the prospects for measuring F_2^{bb} in this region are very good.

4.7.4 Intrinsic Heavy Flavour

It is conventional to assume that the charm and bottom quarks in the proton structure function only arise from gluon splitting $g \rightarrow Q\bar{Q}$. In fact, the proton light-front wavefunction contains *ab initio* intrinsic heavy quark Fock state components such as $|uudc\bar{c}\rangle$ [?, ?, ?, ?]. The intrinsic heavy quarks carry most of the proton's momentum since this minimizes the off-shellness of the state. The heavy quark pair $Q\bar{Q}$ in the intrinsic Fock state is primarily a color-octet, and the ratio of intrinsic charm to intrinsic bottom scales as $m_c^2/m_b^2 \simeq 1/10$, as can easily be seen from the operator product expansion in non-Abelian QCD [?, ?]. Intrinsic charm and bottom explain the origin of high x_F open-charm and open-bottom hadron production, as well as the single and double J/ψ hadroproduction cross sections observed at high x_F . The factorization-breaking nuclear $A^\alpha(x_F)$ dependence of hadronic J/ψ production cross sections is also explained.

As emphasized recently [?], there are strong indications that the structure functions used to model charm and bottom quarks in the proton at large x have been underestimated, since they ignore intrinsic heavy quark fluctuations of hadron wavefunctions. Furthermore, the neglect of the intrinsic-heavy quark component in the proton structure function will lead to an incorrect assessment of the gluon distribution at larger x if it is assumed that sea quarks always arise from gluon splitting. The anomalous growth of the $p\bar{p} \rightarrow \gamma cX$ inclusive cross section observed by the D0 collaboration [?] at the Tevatron indicates that the charm distribution has been underestimated at $x > 0.1$.

In [?] a novel mechanism for inclusive and diffractive Higgs production $pp \rightarrow pHp$ is proposed, in which the Higgs boson carries a significant fraction of the projectile proton momentum. The production mechanism is based on the subprocess $(Q\bar{Q})g \rightarrow H$ where the $Q\bar{Q}$ in the $|uudQ\bar{Q}\rangle$ intrinsic heavy quark Fock state of the colliding proton has approximately 80% of the projectile protons momentum. A similar mechanism could produce the Higgs at large $x_F \sim 0.8$ in $\gamma p \rightarrow HX$ at the LHeC based on the mechanism $\gamma(Q\bar{Q}) \rightarrow H$ since the heavy quarks typically each carry light-cone momentum fractions $x \sim 0.4$ when they arise from the intrinsic heavy quark Fock states $|uudQ\bar{Q}\rangle$ of the proton.

The LHeC could establish the phenomenology of the charm and bottom structure functions at larger x . In addition to DIS measurements, one can test the charm (and bottom) distributions at the LHeC by measuring reactions such as $\gamma p \rightarrow cX$ where the charm jet is produced at high p_T in the reaction $\gamma c \rightarrow cg$.

In order to access the charm and bottom distributions towards larger Bjorken x , it is required to tag heavy flavour production in the forward direction. As this is difficult in the asymmetric electron-proton beam energy configuration such a measurement can favourably be done with a reduced proton beam energy. Approximately, as may be derived from Eq. ??, the small hadronic scattering angle, θ_h , is obtained from the relation, $\theta_h^2 \simeq 2\sqrt{Q^2}/E_p x$. Therefore a reduction by a factor of 7 of the proton beam energy E_p enhances x by 7 at fixed Q^2 and θ_h . One also notices that large x is reached at fixed θ_h and E_p only at high Q^2 . The attempt to access maximum x thus requires to find an optimum of high luminosity, to reach high Q^2 , and

1374
1375

low proton beam energy, to access large x . Fig. ?? shows a simulated measurement of the charm structure function for $E_p = 1$ TeV and a luminosity of 1 fb^{-1} . The two curves illustrate the difference between CTEQ66 PDF sets with and without an intrinsic charm component, based on [?]. The actual amount of intrinsic charm

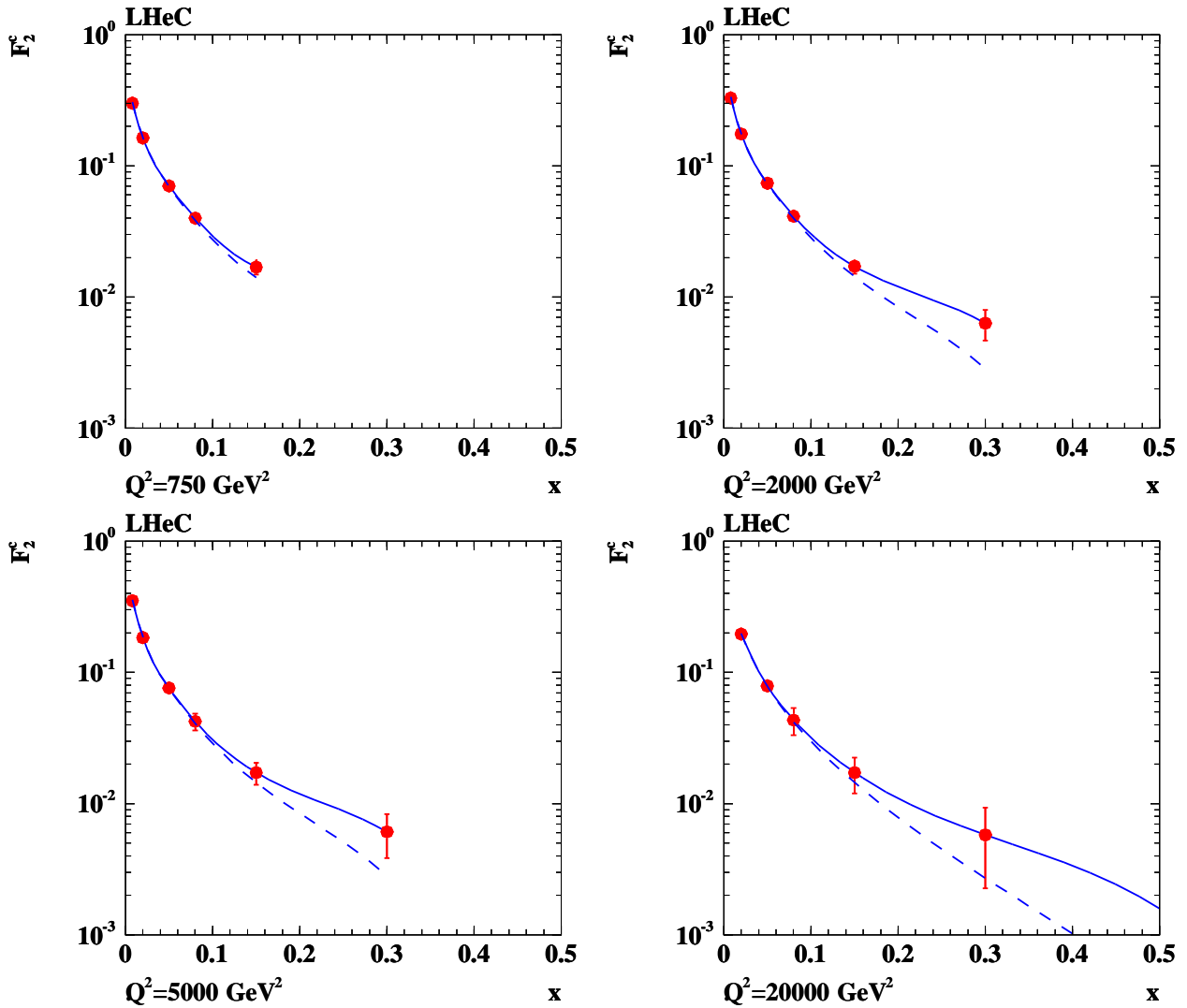


Figure 4.28: Simulation of measurement of the charm structure function at large x , see text. The errors are statistical, taking tagging and background efficiencies into account. The tagging efficiency for charm quarks was assumed to be 10% and the amount of background was estimated to be $0.01 \cdot N_{ev}$, where N_{ev} refers to the total number of expected NC events in the respective (Q^2, x) bin. Solide line: CTEQ66c predictions, including an intrinsic charm component, dashed line: ordinary CTEQ66m.

1376
1377
1378
1379
1380
1381

may be larger than in the CTEQ attempt, it may also be smaller. One so finds that a reliable detection of an intrinsic heavy charm component at the LHeC may be possible, but will be a challenge for forward charm detection and requires high luminosity. The result yet may be rewarding as it would have quite some theoretical consequences as sketched above. It would be obtained in a region of high enough Q^2 to be able to safely neglect any higher twist effects which may mimic such an observation at low energy experiments.

4.7.5 D^* meson photoproduction study

A study is presented of D^* meson photoproduction at LHeC compared to HERA. It is based on NLO predictions in the so-called general-mass variable-flavour-number scheme (GM-VFNS) [?, ?] for 1-particle inclusive heavy-meson production. Both direct and resolved photon contributions are taken into account. The cross section for direct photoproduction is a convolution of the proton PDFs, the cross section for the hard scattering process and the fragmentation functions FF for the transition of a parton to the observed heavy meson. For the resolved contribution, an additional convolution with the photon PDFs has to be performed. For the photoproduction predictions at the ep -colliders HERA and LHeC, the calculated photon proton cross sections are convoluted with the photon flux using the Weizsaecker-Williams approximation.

In the GM-VFNS approach the large logarithms $\ln(p_T^2/m^2)$, which appear due to the collinear mass singularities in the initial and final state, are factorized into the PDFs and the FFs and summed by the well known DGLAP evolution equations. The factorization is performed following the usual $\overline{\text{MS}}$ prescription which guarantees the universality of both PDFs and FFs. At the same time, mass-dependent power corrections are retained in the hard-scattering cross sections, as in the FFNS. For the photon PDF the parametrization of Ref. [?] with the standard set of parameter values is used and for the proton PDF the parametrization CTEQ6.5 [?] of the CTEQ group. For the FFs the set Belle/CLEO-GM of Ref. [?] is chosen. Various combinations of beam energies are studied. To compare with the situation at HERA, as

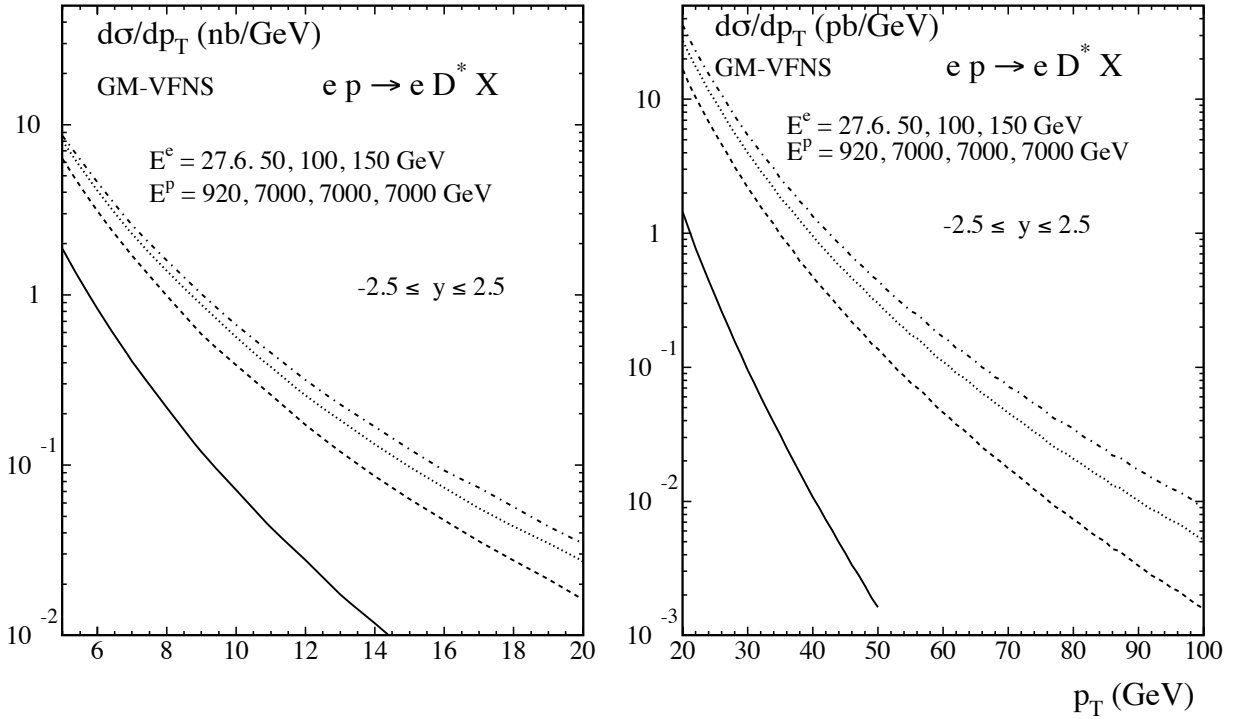


Figure 4.29: The p_T -differential cross section for the production of D^* mesons at LHeC for different beam energies integrated over rapidities $|\eta| \leq 2.5$, for the low- p_T range $5 \text{ GeV} \leq p_T \leq 20 \text{ GeV}$ (left) and for the high- p_T range $20 \text{ GeV} \leq p_T \leq 50 \text{ GeV}$ (right). The curves from bottom to top correspond to the combinations of beam energies as indicated in the figure.

a reference, the values $E^p = 920 \text{ GeV}$ and $E^e = 27.5 \text{ GeV}$ for proton and electron energies, respectively, are also included. For the LHeC the proton energy is taken to be always $E^p = 7 \text{ TeV}$ and the options $E^e = 50, 100$ and 150 GeV are considered. The exchanged photons are restricted to inelasticities y in the

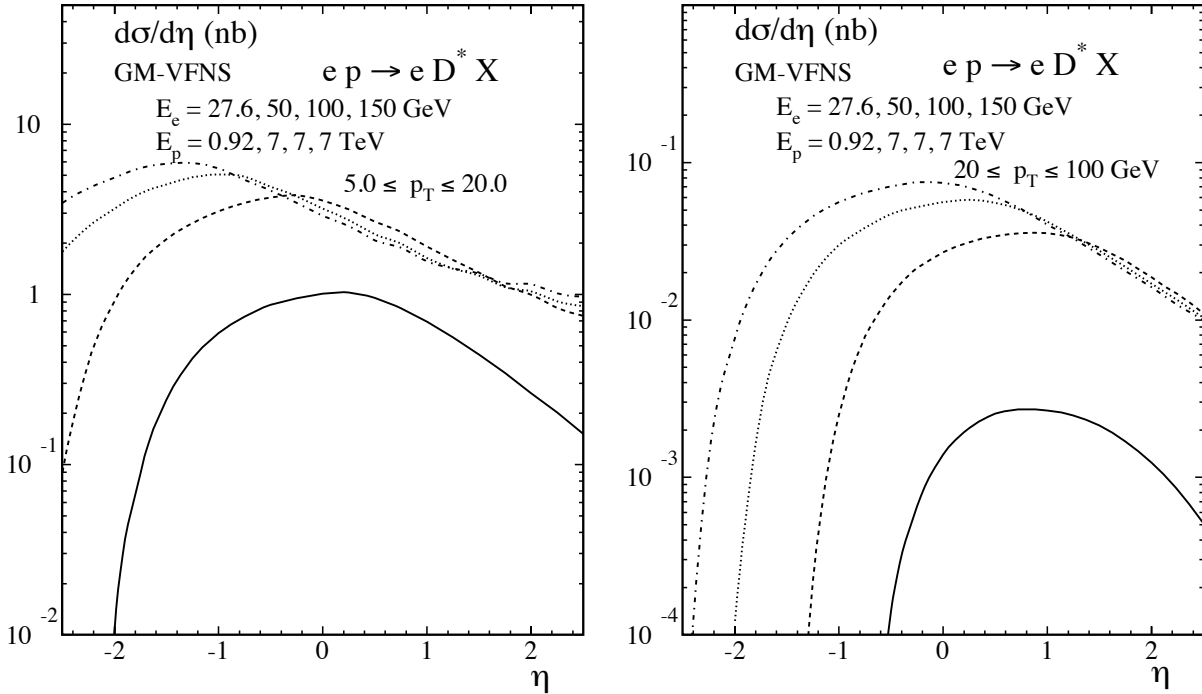


Figure 4.30: Rapidity distribution of the cross section for the production of D^* mesons at LHeC for different beam energies integrated over the low- p_T range $5 \text{ GeV} \leq p_T \leq 20 \text{ GeV}$ (left) and the high- p_T range $20 \text{ GeV} \leq p_T \leq 100 \text{ GeV}$ (right). The curves from bottom to top correspond to the combinations of beam energies as indicated in the figure.

1402 range $0.1 < y < 0.9$. The transverse momentum p_T and the rapidity η of the D^* -meson are varied in the
 1403 kinematic ranges $5 < p_T < 20 \text{ GeV}$ or $20 < p_T < 100$ and $|\eta| < 2.5$. Numerical results are shown in Fig.
 1404 ?? for the differential cross section $d\sigma/dp_T$ integrated over the rapidity $|\eta| \leq 2.5$ and in Fig. ?? for $d\sigma/d\eta$,
 1405 integrated over the p_T -ranges $5 \leq p_T \leq 20 \text{ GeV}$ and $20 \leq p_T \leq 100 \text{ GeV}$.

1406 The higher centre-of-mass energies available at the LHeC lead to a considerable increase of the cross
 1407 sections as compared to HERA. Obviously one can expect an increase in the precision of corresponding
 1408 measurements and much higher values of p_T , as well as higher values of the rapidity η , will be accessible.
 1409 Since theoretical predictions also become more reliable at higher p_T , measurements of heavy quark produc-
 1410 tion constitute a promising testing ground for perturbative QCD. One may expect that the experimental
 1411 information will contribute to an improved determination of the (extrinsic and intrinsic) charm content of
 1412 the proton and the charm fragmentation functions.

1413 4.8 High p_t jets

1414 4.8.1 Jets in ep

1415 The study of the jet final states in lepton-proton collisions allows the determination of aspects of the nucleon
 1416 structure which are not accessible in inclusive scattering. Moreover, jet production allows for probing pre-
 1417 dictions of QCD to a high accuracy. Depending on the virtuality of the exchanged photon, one distinguishes
 1418 processes in photoproduction (quasi-real photon) and deep inelastic scattering.

1419 The photoproduction cross section for di-jet final states can be studied in different kinematical regions,

1420 thereby covering a wide spectrum of physical phenomena, and probing the structure of the proton and the
 1421 photon. Two-jet production in deep inelastic scattering is a particularly sensitive probe of the gluon distri-
 1422 bution in the proton and of the strong coupling constant α_s . Both processes allow the study of potentially
 1423 large enhancement effects in di-jet and multi-jet production.

1424 Jet production in photoproduction proceeds via the direct processes, in which the quasi-real photon
 1425 interacts as a point-like particle with the partons from the proton, and the resolved processes, in which
 1426 the quasi-real photon interacts with the partons from the proton via its partonic constituents. The parton
 1427 distributions in the quasi-real photon are constrained mostly from the study of processes at e^+e^- colliders,
 1428 and are less well-determined than their counterparts in the proton. In both the direct and the resolved
 1429 process, there are two jets in the final state at lowest-order QCD. The jet production cross section is given in
 1430 QCD by the convolution of the flux of photons in the electron (usually estimated via the Weizacker-Williams
 1431 approximation), the parton densities in the photon, the parton densities in the proton and the partonic cross
 1432 section (calculable in pQCD). Therefore, the measurements of jet cross sections in photoproduction provide
 1433 tests of perturbative QCD and the structure of the photon and the proton.

1434 Owing to the large size of the cross section, photoproduction of di-jets can be used for precision physics
 1435 in QCD. A measurement at LHeC could improve upon previous HERA results and enter into a much larger
 1436 kinematical region. In measurements made by the ZEUS collaboration, the available photon-proton centre-of-
 1437 mass energy ranged from 142 to 293 GeV, and jets of a transverse energy of up to 90 GeV could be observed.
 1438 By comparing the measured cross section with the theoretical prediction in NLO pQCD, a value of $\alpha_s(M_Z)$
 1439 was extracted with a total uncertainty of $\pm 3\%$ and the running of α_s was tested over a wide range of E_t^{jet}
 1440 in a single measurement. The limiting factors in this measurement were the theoretical uncertainty inherent
 1441 to the NLO prediction (which could be improved by computing NNLO corrections to jet photoproduction)
 and the experimental systematic uncertainty in the detector energy calibration.

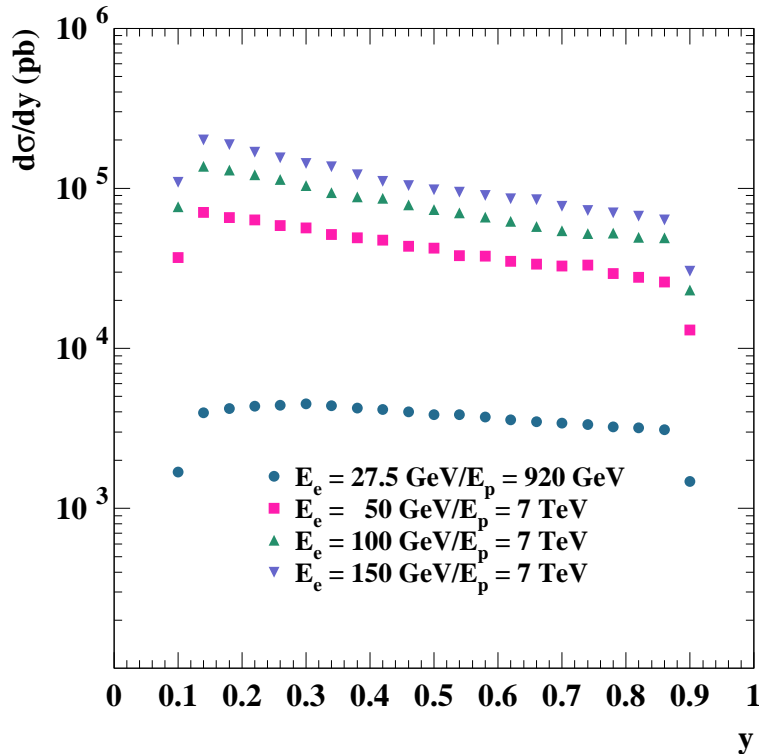


Figure 4.31: PYTHIA predictions for photoproduction cross section at HERA and for three LHeC scenarios.

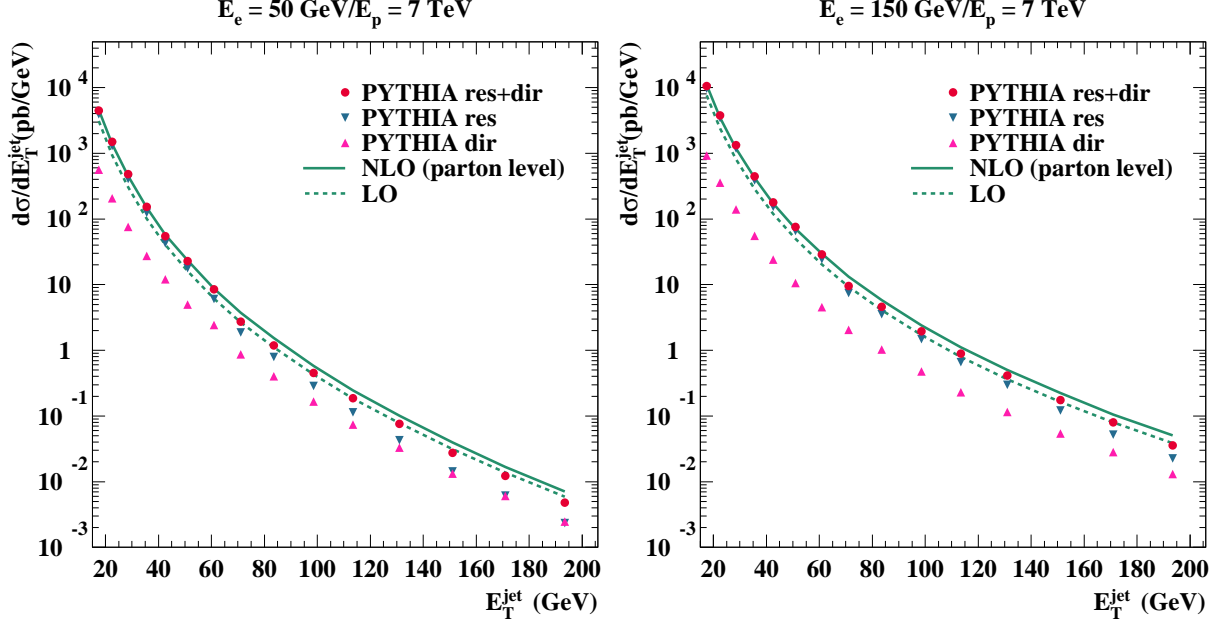


Figure 4.32: Parton level predictions for the inclusive transverse energy distribution in photoproduction.

1443 Another motivation for making new photoproduction experiments is to improve the knowledge of the
 1444 parton content of the photon. At present, most information on the photon structure is inferred from the
 1445 collision of quasi-real photons with electrons at e^+e^- colliders, resulting in a decent determination of the
 1446 total (charge weighted) quark content of the quasi-real photon. Its gluonic content, and the quark flavour
 1447 decomposition are on the other hand only loosely constrained. Improvements to the photon structure are of
 1448 crucial importance to physics studies at a future linear e^+e^- collider like the ILC or CLIC. Such a collider,
 1449 operating far above the Z -boson resonance, will face a huge background from photon-photon collisions.
 1450 This background can be suppressed only to a certain extent by kinematical cuts. Consequently, accurate
 1451 predictions of it (which require an improved knowledge of the photon's parton content) are mandatory for
 1452 the reliable interpretation of hadronic final states at the ILC or CLIC. Several parametrizations of the parton
 1453 distributions in the photon are available. They differ especially in the gluon content of the photon. For the
 1454 studies presented here, the GRV-HO parametrization [?] is used as default.

1455 The photoproduction studies performed at LHeC were done for three different electron energy scenarios:
 1456 $E_e=50, 100$ and 150 GeV. In all cases, the proton energy was set to 7 TeV. PYTHIA MC samples of
 1457 resolved and direct processes were generated for these three scenarios. Jets were searched using the k_t -
 1458 cluster algorithm in the kinematic region of $0.1 < y < 0.9$ and $Q^2 < 1$ GeV². Inclusive jet cross sections
 1459 were done for jets of $E_t^{\text{jet}} > 15$ GeV and $3 < \eta^{\text{jet}} < 3$. Figure ?? shows the PYTHIA MC cross sections as
 1460 functions of y for the three scenarios plus the corresponding cross section for the HERA regime. It can be
 1461 seen that the LHeC cross sections are one to two orders of magnitude larger than the cross section at HERA.

1462 The full study was complemented with fixed-order QCD calculations at order α_s and α_s^2 using the
 1463 program by Klasen et al. [?] with the CTEQ6.1 sets for the proton PDFs, GRV-HO sets for the photon
 1464 PDFs, $\alpha_s(M_Z) = 0.119$ and the renormalisation and factorisation scales were set to the transverse energy of
 1465 each jet.

1466 Figure ?? shows the inclusive jet cross sections at parton level as functions of E_t^{jet} for the three energy
 1467 scenarios for the PYTHIA res+dir (red dots), PYTHIA resolved (blue triangles) and PYTHIA direct (pink
 1468 triangles) together with the predictions from the NLO (solid curves) and LO (dashed curves) QCD calcu-
 1469 lations. The calculations predict a sizeable rate for Etjet of at least up to 200 GeV. Resolved processes

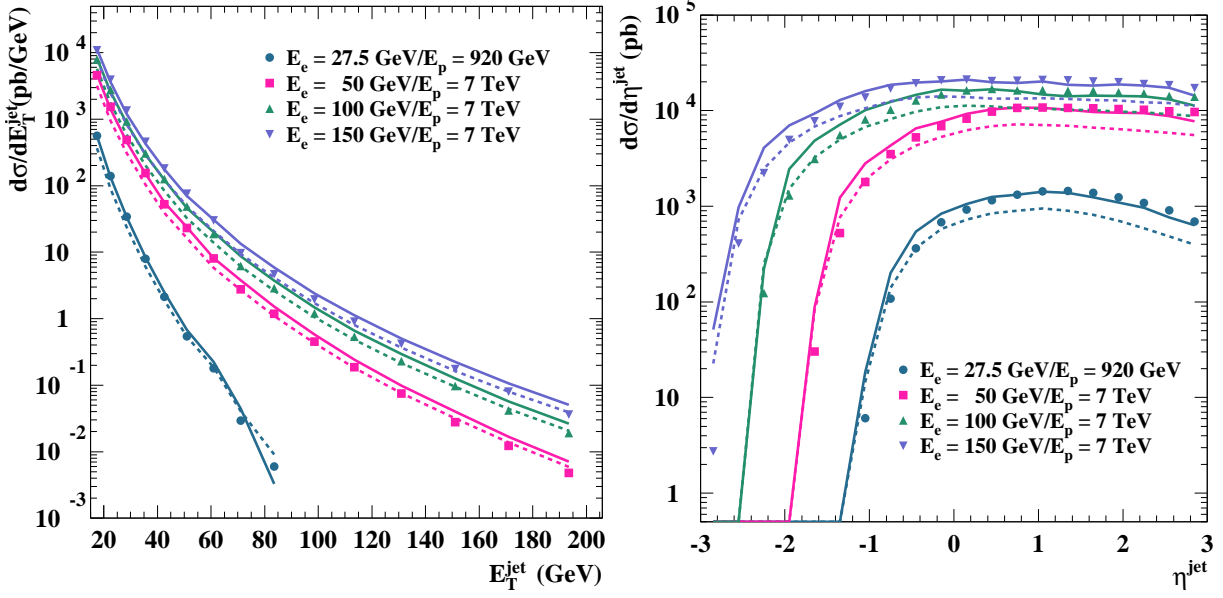


Figure 4.33: Dijet distributions in photoproduction as function of the jet transverse energy (left) and of the jet rapidity (right) for different LHeC energies compared to the HERA kinematic range.

1470 dominate at low E_t^{jet} , but the direct processes become increasingly more important as E_t^{jet} increases. The
 1471 PYTHIA cross sections (which have been normalised to the NLO integrated cross section) agree well in shape
 1472 with the NLO calculations. Investigating the η^{jet} distribution, we find that resolved processes dominate in
 1473 the forward region, while direct processes produce more central jets.

1474 Figure ?? show the inclusive jet cross sections at parton level as functions of E_t^{jet} (on the left) and η^{jet}
 1475 (on the right) for the PYTHIA resolved+direct (symbols) and the predictions from the NLO (solid curves)
 1476 and LO (dashed curves) QCD calculations together for the three energy scenarios. For comparison, the
 1477 calculations for the HERA regime are also included. It is seen that the cross sections at fixed E_t^{jet} increase
 1478 and that the jets tend to go more backward as the collision energy increases. The much larger photon-
 1479 proton centre-of-mass energies that could be available at LHeC provide a much wider reach in E_t^{jet} and η^{jet}
 1480 compared to HERA.

1481 Hadronisation corrections for the cross sections shown were investigated. The corrections are predicted
 1482 to be quite small, below +5% for the chosen scenarios. Since the hadronisation corrections are very small,
 1483 the features observed at parton level remain unchanged.

1484 Inclusive-jet and dijet measurements in deep-inelastic scattering (DIS) have since long been a tool to
 1485 test concepts and predictions of perturbative QCD. Especially at HERA, jets in DIS have been thoroughly
 1486 studied, and the results have provided deep insights, giving for example precise values for the strong coupling
 1487 constant, α_s and providing constraints for the proton PDFs.

1488 An especially interesting region for such studies has been the regime of large (for HERA) Q^2 values of, for
 1489 example, $Q^2 > 125 \text{ GeV}^2$. In this regime, the theoretical uncertainties, especially those due to the unknown
 1490 effects of missing higher orders in the perturbative expansion, are found to be small. Recently, both the H1
 1491 and ZEUS collaborations have published measurements of inclusive-jet and dijet events in this kinematic
 1492 regime.

1493 An extension of such measurements to the LHeC is interesting for two reasons: First, the provided high
 1494 luminosity will allow measurements in already explored kinematic regions with still increased experimental
 1495 precision. Second, the extension in centre-of-mass energy, \sqrt{s} , and thus in boson virtuality, Q^2 , and in jet
 1496 transverse energy, $E_{T,jet}$, will potentially allow to study pQCD at even higher scales, extending the scale

reach for measurements of the strong coupling or the precision of the proton PDFs at large values of x .

To explore the potential of such a measurement, we investigated DIS jet production for the following LHeC scenario: proton beam energy 7 TeV, electron beam energy 70 GeV and integrated luminosity 10 fb^{-1} . The study concentrates on the phase space of high boson virtualities Q^2 , with event selection cuts $100 < Q^2 < 500 \text{ GeV}^2$ and $0.1 < y < 0.7$, where y is the inelasticity of the event. Jets are reconstructed using the k_T clustering algorithm in the longitudinally invariant inclusive mode in the Breit reference frame. Jets were selected by requiring: a jet pseudorapidity in the laboratory of $-2 < \eta_{lab} < 3$, a jet transverse energy in the Breit frame of $E_{T,jet}^{Breit} > 20 \text{ GeV}$ for the inclusive-jet measurement and jet transverse energies in the Breit frame of 25(20) GeV for the leading and the second-hardest jet in the case of the dijet selection.

For inclusive-jet production we study cross sections in the indicated kinematic regime as functions of Q^2 , x_{Bj} , $E_{T,jet}^{Breit}$ and η_{jet}^{lab} , the jet pseudorapidity in the laboratory frame. For dijet production, studies are presented as functions of Q^2 , the logarithm of the proton momentum fraction ξ , $\log_{10} \xi$, the invariant dijet mass M_{jj} , the average transverse energy of the two jets in the Breit frame, $\overline{E_{T,jet}^{Breit}}$, and of half of the absolute difference of the two jet pseudorapidities in the laboratory frame, η' .

For the binning of the observables shown here, the statistical uncertainties for the indicated LHeC integrated luminosity can mostly be neglected, even at the highest scales. The systematic uncertainties were assumed to be dominated by the uncertainty on the jet energy scale which was assumed to be known to 1% or 3% (both scenarios are indicated with different colours in the following plots), leading to typical effects on the jet cross sections between 1 and 15%. A further relevant uncertainty is the acceptance correction that is applied to the data which was assumed to be 3% for all observables.

The theoretical calculations were performed with the DISJENT program [?] using the CTEQ6.1 proton PDFs [?,?]. The central default squared renormalisation and factorisation scales were set to Q^2 . The theory calculations for the LHeC scenario were corrected for the effects of hadronisation and Z^0 exchange using Monte Carlo data samples simulated with the LEPTO program [?].

Theoretical uncertainties were assessed by varying the renormalization scale up and down by a factor 2 (to estimate the potential effect of contributions beyond NLO QCD), by using the 40 error sets of the CTEQ6.1 parton distribution functions, and by varying α_s using the CTEQ6AB PDF [?]. The dominant theory uncertainty turned out to be due to the scale variations, resulting in effects of a few to up to 20% or more, for example for low values of Q^2 or, for the case of the dijet measurement, for low values of the invariant dijet mass, M_{jj} , or the logarithm of momentum fraction carried into the hard scattering, $\log_{10} \xi$.

Note that for the inclusive-jet results also the predictions for a HERA scenario with almost the same selection are shown in order to indicate the increased reach of the LHeC with respect to HERA. The only change is a reduction in centre-of-mass energy to 318 GeV and a reduced Q^2 reach, $125 < Q^2 < 45 \text{ GeV}^2$. The HERA predictions shown were also corrected for hadronisation effects and the effects of Z^0 exchange.

Figure ?? shows the inclusive jet cross section as function of Q^2 and of the jet transverse energy in the Breit frame, while Figure ?? shows the dijet cross section as function of Q^2 and of $\xi = x_{Bj}(1 + M_{jj}^2/Q^2)$. The top parts of the figures show the predicted cross sections together with the expected statistical and (uncorrelated) experimental systematic uncertainties as error bars. The correlated jet energy scale uncertainty is indicated as a coloured band; the inner, yellow band assumes an uncertainty of 1%, the outer, blue band one of 3%. Also shown as a thin hashed area are the theoretical uncertainties; the width of the band indicates the size of the combined theoretical uncertainty. In case of inclusive-jet production, also the predictions for HERA are indicated as a thin line.

The bottom parts of the figures show the relative uncertainties due to the jet energy scale (yellow band for 1%, blue band for 3%), the statistical and uncorrelated experimental systematic uncertainties as inner / outer error bars, and the combined theoretical uncertainties as hashed band. The inner part of this band indicates the uncertainty due to the variation of the renormalisation scale.

The inclusive-jet cross section as function of Q^2 shows a typical picture: In most region of the phase space, the uncertainties are dominated by the theory uncertainties, and here mainly by the renormalisation scale uncertainty. The typical size of experimental uncertainties is of the order of 10%, with larger values in regions with low relevant scales — i.e. low invariant dijet masses, low jet transverse energies or low Q^2 values. The theoretical uncertainties are typically between 5 and 20%, with partially strong variations over

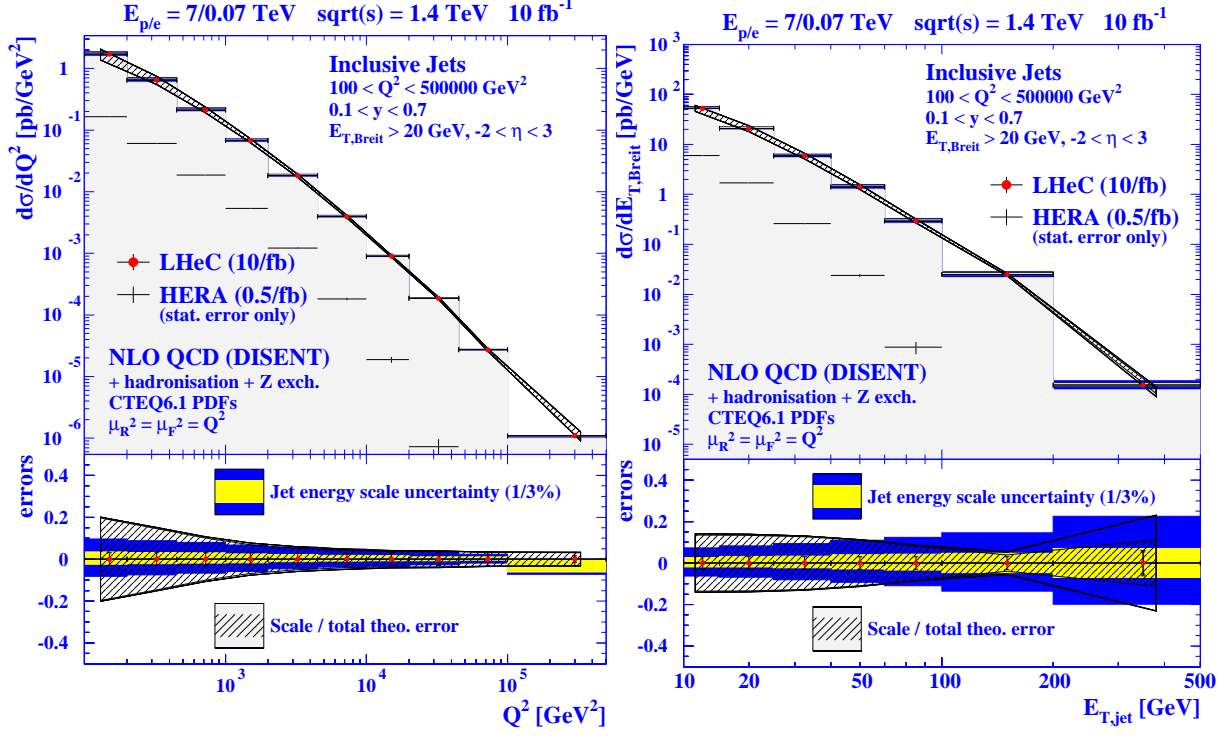


Figure 4.34: Predicted LHeC results for inclusive jet production as function of Q^2 and of E_T in the Breit frame. Predictions for HERA results are also shown.

1548 the typical range of the observable in question.

1549 A comparison with the HERA predictions for inclusive-jet production shows that the LHeC cross sections
 1550 is typically larger by 1 to 3 orders of magnitude. The dijet final state allows for a full reconstruction of the
 1551 partonic kinematics, and can thus be used to probe the parton distribution functions in Q^2 and ξ . It can
 1552 be seen that a measurement at LHeC covers a large kinematical range ranging down to $\xi \approx 10^{-3}$ and up to
 1553 $Q^2 = 10^5$ GeV². Potentially limiting factors in an extraction of parton distribution functions are especially
 1554 the jet energy scale uncertainty on the experimental side and missing higher order (NNLO) corrections on the
 1555 theory side. The jet energy scale uncertainty can be addressed by the detector design and by the experimental
 1556 setup of the measurement. NNLO corrections to dijet production in deep inelastic scattering are already
 1557 very much demanded by the precision of the HERA data, their calculation is currently in progress [?, ?].

1558 In summary, jet final states in photoproduction and deep inelastic scattering at the LHeC promise a wide
 1559 spectrum of new results on the partonic structure of the photon and the proton. They allow for precision tests
 1560 of QCD by independent determinations of the strong coupling constant over a kinematical range typically
 1561 one to two orders of magnitude larger than what was accessible at HERA. The resulting parton distributions
 1562 will have a direct impact for precision predictions at the LHC and a future linear collider.

1563 4.8.2 Jets in γA

1564 For photoproduction in eA collisions, jets provide an abundant yield of high-energy probes of the nuclear
 1565 medium. The expected cross sections have been computed using the calculations in [?, ?], for an electron
 1566 beam of 50 GeV colliding with the LHC beams. For the nuclear case the same integrated luminosity (2 fb^{-1})
 1567 was assumed per nucleon as for ep . Only jets with $E_{T,jet} > 20$ GeV are considered, and for the distribution
 1568 in $E_{T,jet}$ the pseudorapidity acceptance is $|\eta_{jet}| < 3.1$, corresponding to $5^\circ < \theta_{jet} < 175^\circ$ in polar angle. The

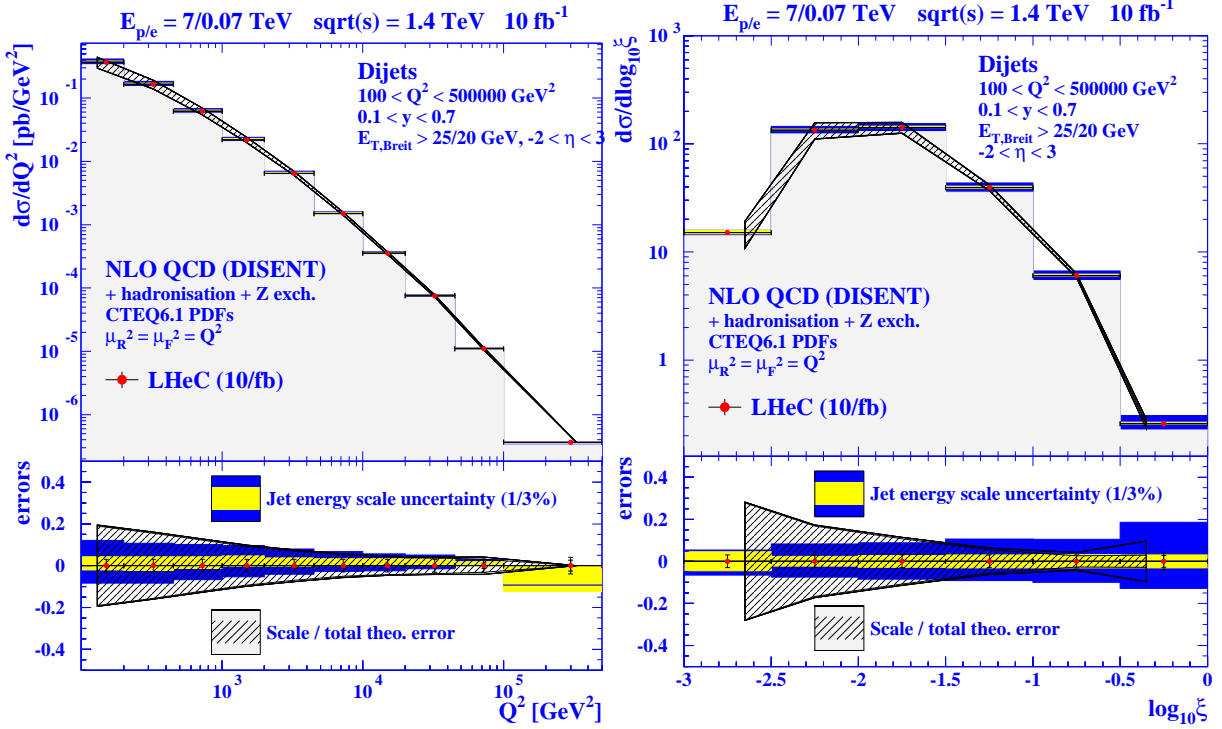


Figure 4.35: Predicted LHeC results for dijet production as function of Q^2 and of ξ .

1569 simulations use the Weizsäcker-Williams photon flux from the electron with the standard option in [?, ?].
 1570 The chosen photon, proton and nuclear modified PDFs are taken from GRV-HO [?], CTEQ6.1M [?] and
 1571 EPS09 [?], respectively - see Subsec. ?? for explanations on the nuclear modifications of PDFs. The
 1572 renormalization and factorization scales are taken to be $\mu_R = \mu_F = \sum_{jets} E_{T,jet}/2$ and the inclusive k_T jet
 1573 algorithm [?] is used with $D = 1$. The statistical uncertainty in the computation (i.e. in the Monte Carlo
 1574 integration) is smaller than 10 % for all results shown. This large statistical uncertainty is reached only for
 1575 the largest $E_{T,jet}$, with much smaller uncertainties at lower values of E_T . No attempt has been made to
 1576 estimate the uncertainties due to the choices of photons flux, photon or proton parton densities, scales or jet
 1577 algorithms (see [?, ?] for such considerations at HERA). The issues of background subtraction, experimental
 1578 efficiencies in the jet reconstruction or energy calibration have also yet to be addressed. The only uncertainty
 1579 studied thus far is that due to the nuclear parton densities, which is extracted in the EPS09 framework [?]
 1580 using the Hessian method.

1581 The results are shown in Fig. ?. One observes that yields of around 10^3 jets per GeV are expected with
 1582 $E_{T,jet} \sim 95$ (80) GeV in ep (ePb), for $|\eta_{jet}| < 3.1$ and the considered integrated luminosity of 2 fb^{-1} per
 1583 nucleon. The effects of the nuclear modification of parton densities and their uncertainties are smaller than
 1584 10 %. The two-peak structure in the η_{jet} -plot results from the sum of the direct plus resolved contributions,
 1585 each of which produce a single maximum, located in opposite hemispheres. Positive η_{jet} values are dominated
 1586 by direct photon interactions, whereas negative η_{jet} values are dominated by contributions from resolved
 1587 photons.

1588 4.9 Total photoproduction cross section

1589 Due to the $1/Q^4$ propagator term, the LHeC ep cross section is dominated by very low Q^2 quasi-real photons.
 1590 With a knowledge of the effective photon flux [?], measurements in this kinematic region can be used to

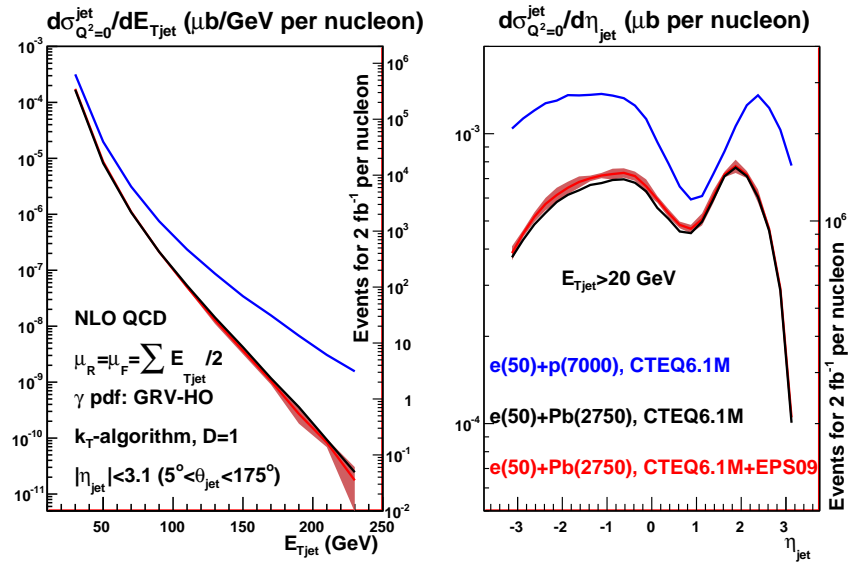


Figure 4.36: Predictions for the inclusive jet distribution in photoproduction, differential in $E_{T\text{jet}}$ (plot on the left) and η_{jet} (plot on the right) for $e(50)+p(7000)$ (blue lines), $e(50)+\text{Pb}(2750)$ without nuclear modification of the parton densities (black lines), and $e(50)+\text{Pb}(2750)$ with EPS09 nuclear modification of the parton densities (red lines for the central value and bands for the uncertainty coming from the nuclear modification factors). See the text and the legends on the plots for further details of the calculations and kinematic cuts. In both plots, the axis on the left corresponds to the cross section in μb , while the axis on the right provides the number of jets expected for an integrated luminosity of 2 fb^{-1} per nucleon, per unit of $E_{T\text{jet}}$ (η_{jet}) in the plot on the left (right).

1591 obtain real photoproduction (γp) cross sections. The real photon has a dual nature, sometimes interacting in
1592 a point-like manner and sometimes interacting through its effective partonic structure, resulting from $\gamma \rightarrow q\bar{q}$
1593 and higher multiplicity splittings well in advance of the target [?, ?], the details of which are fundamental to
1594 the understanding of QCD evolution.

1595 The behaviour of the total photoproduction cross section at high energy is a topic of a major interest. It
1596 is now firmly established experimentally that all hadronic cross sections rise with centre of mass energy for
1597 large energies. The Froissart-Martin bound has been derived for hadronic probes. It therefore remains to be
1598 seen whether this bound is applicable to γp scattering. For example in Refs. [?, ?] it has been argued that the
1599 bound for real photon-hadron interactions should be of a different functional form, namely $\ln^3 s$. This would
1600 imply that the universality of the asymptotic behaviour of hadronic cross sections does not hold. Therefore
1601 the measurement of the total photoproduction cross section at high energies will bring an important insight
1602 into the problems of universality of hadronic cross sections, unitarity constraints, the role of diffraction and
1603 the interface between hard and soft physics.

1604 In Fig. ??, available data on the total cross section are shown [?, ?, ?, ?]⁶, together with a variety of models.
1605 More specifically, the dot-dashed black line labelled ‘FF model GRS’ is a minijet model [?], the yellow band
1606 labelled ‘Godbole et al.’ is an eikonalized minijet model with soft gluon resummation [?] with the band
1607 defined by different choices of the parameters in the model, the red solid line labelled ‘Block & Halzen’ is
1608 based on a low energy parametrization of resonances joined with Finite Energy Sum Rules and asymptotic
1609 $\ln^2 s$ -behaviour [?, ?], and the dashed blue line labelled ‘Aspen model’ is a QCD inspired model [?].

1610 The theoretical predictions diverge at energies beyond those constrained by HERA data, where cross
1611 sections were obtained by tagging and measuring the energies of electrons scattered through very small
1612 angles in dedicated calorimeters located well down the beampipe in the outgoing electron direction [?, ?]. As
1613 discussed in Chapter ??, the most promising location for similar small angle electron detectors at the LHeC
1614 is in the region around 62 m from the interaction point, which could be used to tag scattered electrons in
1615 events with $Q^2 < 0.01 \text{ GeV}^2$ and $y \sim 0.3$. This naturally leads to measurements of the total photoproduction
1616 cross section at γp center-of-mass energies $W \sim 0.5\sqrt{s}$. The measurements would be strongly limited by
1617 systematics. In the absence of a detailed simulation of an LHeC detector these uncertainties are hard to
1618 estimate. For the simulated data in Fig. ??, uncertainties of 7% have been assumed, matching the precision
1619 of the H1 and ZEUS data. This would clearly be more than adequate to distinguish between many of the
1620 available models. The HERA uncertainties were dominated by the invisible contributions from diffractive
1621 channels in which the diffractive masses were too small to leave visible traces in the main detector. If detector
1622 acceptances to 1° are achieved at the LHeC, better precision is expected to be possible.

⁶The recent results by ZEUS [?] refer only to the energy behavior of the cross section in the range $194 < W < 296 \text{ GeV}$, but do not provide absolute values.

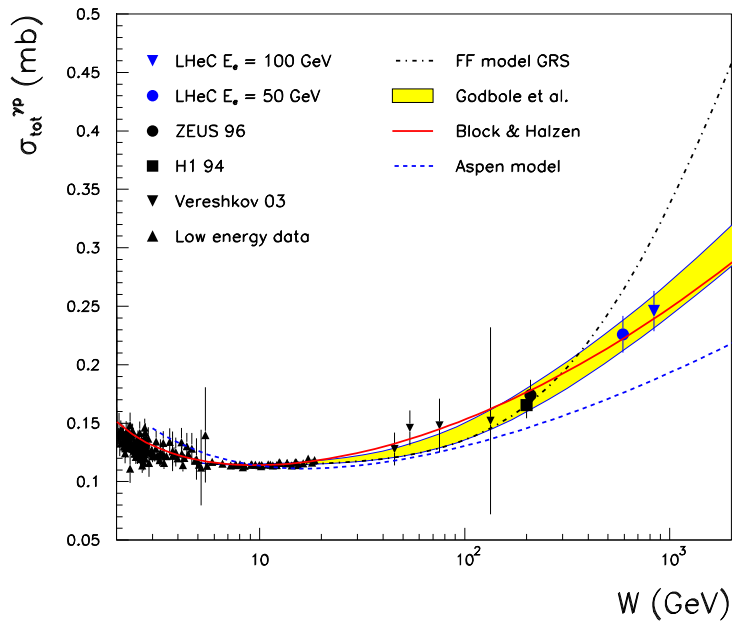


Figure 4.37: Simulated LHeC measurements of the total photoproduction cross section with $E_e = 50$ GeV or $E_e = 100$ GeV, compared with previous data and a variety of models (see text for details). This is derived from a similar figure in [?].

Chapter 5

New Physics at Large Scales

Although the LHC is expected to be the discovery machine for physics beyond the Standard Model at the TeV scale, it will not always be possible to measure with precision the parameters of the new physics. In this section, it is shown that in many cases the LHeC can probe in detail deviations from the expected electroweak interactions shared by leptons and quarks, thus adding essential information on the new physics. Previous studies [?, ?, ?, ?] of the potential of high-energy $e-p$ colliders for the discovery of exotic phenomena have considered a number of processes, most of which are reviewed here.

In some cases, Standard Model processes can also be better measured at the LHeC. Here, the charged and neutral current processes of SM Higgs production by vector boson fusion are investigated with the goal of measuring the $H-b-b$ coupling.

5.1 New Physics in inclusive DIS at high Q^2

The LHeC collider would enable the study of deep inelastic neutral current scattering at very high squared momentum transfers Q^2 , thus probing the structure of eq interactions at very short distances. At large scales new phenomena not directly detectable may become observable as deviations from the Standard Model predictions. A convenient tool to assess the experimental sensitivity beyond the maximal available center of mass energy and to parameterise indirect signatures of new physics is the concept of an effective four-fermion contact interaction. If the contact terms originate from a model where fermions have a substructure, a compositeness scale can be related to the size of the composite object. If they are due to the exchange of a new heavy particle, such as a leptoquark, the effective scale is related to the mass and coupling of the exchanged boson. Contact interaction phenomena are best observed as a modification of the expected Q^2 dependence and all information is essentially contained in the differential cross section $d\sigma/dQ^2$. An alternative way to parameterize the effects of fermion substructure makes use of form factors, which would also lead to deviations of $d\sigma/dQ^2$ with respect to the SM prediction. As a last example, low scale quantum gravity effects, which may be mediated via gravitons coupling to SM particles and propagating into large extra spatial dimensions, could also be observed as a modification of $d\sigma/dQ^2$ at highest Q^2 . These possible manifestations of new physics in inclusive DIS are addressed in this section.

5.1.1 Quark substructure

The remarkable similarities in the electromagnetic and weak interactions of leptons and quarks in the Standard Model, and their anomaly cancellations in the family structure, strongly suggest a fundamental connection. It would therefore be natural to conjecture that they could be composed of more fundamental constituents, or that they form a representation of a larger gauge symmetry group than that of the Standard Model, in a Grand Unified Theory.

1656
1657
1658
1659
1660

A possible method to investigate fermion substructures is to assign a finite size of radius R to the electroweak charges of leptons and/or quarks while treating the gauge bosons γ and Z still as pointlike particles [?]. A convenient parametrisation is to introduce ‘classical’ form factors $f(Q^2)$ at the gauge boson–fermion vertices, which are expected to diminish the Standard Model cross section at high momentum transfer

$$f(Q^2) = 1 - \frac{1}{6} \langle r^2 \rangle Q^2, \tag{5.1}$$

$$\frac{d\sigma}{dQ^2} = \frac{d\sigma^{SM}}{dQ^2} f_e^2(Q^2) f_q^2(Q^2). \tag{5.2}$$

1661
1662
1663
1664
1665
1666

The square root of the mean-square radius of the electroweak charge distribution, $R = \sqrt{\langle r^2 \rangle}$, is taken as a measure of the particle size. Since the pointlike nature of the electron/positron is already established down to extremely low distances in e^+e^- and $(g-2)_e$ experiments, only the quarks are allowed to be extended objects i.e. the form factor f_e can be set to unity in the above equation.

Figure.?? shows the sensitivity that an LHeC collider could reach on the ‘‘quark radius’’ [?]. Two configurations have been studied ($E_e = 70$ GeV and $E_e = 140$ GeV), and two values of the integrated luminosity, per charge, have been assumed in each case. A sensitivity to quark radius below 10^{-19} m could

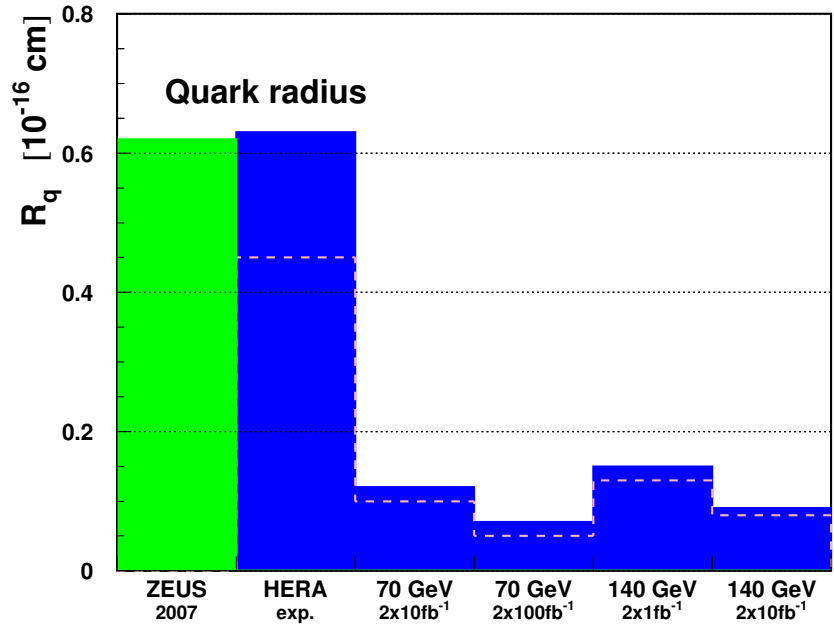


Figure 5.1: Sensitivity (95% confidence level limits) of an LHeC collider to the effective quark radius.

1667
1668
1669

be reached, which is one order of magnitude better than the current constraints, and comparable to the sensitivity that the LHC is expected to reach.

1670 5.1.2 Contact Interactions

1671
1672
1673

New currents or heavy bosons may produce indirect effects through the exchange of a virtual particle interfering with the γ and Z fields of the Standard Model. For particle masses and scales well above the available energy, $\Lambda \gg \sqrt{s}$, such indirect signatures may be investigated by searching for a four-fermion pointlike

1674 $(\bar{e}e)(\bar{q}q)$ contact interaction. The most general chiral invariant Lagrangian for neutral current vector-like
 1675 contact interactions can be written in the form [?, ?, ?]

$$\mathcal{L}_V = \sum_{q=u,d} \{ \eta_{LL}^q (\bar{e}_L \gamma_\mu e_L) (\bar{q}_L \gamma^\mu q_L) + \eta_{LR}^q (\bar{e}_L \gamma_\mu e_L) (\bar{q}_R \gamma^\mu q_R) + \eta_{RL}^q (\bar{e}_R \gamma_\mu e_R) (\bar{q}_L \gamma^\mu q_L) + \eta_{RR}^q (\bar{e}_R \gamma_\mu e_R) (\bar{q}_R \gamma^\mu q_R) \} , \quad (5.3)$$

1676 where the indices L and R denote the left-handed and right-handed fermion helicities and the sum extends
 1677 over up -type and $down$ -type quarks and antiquarks q . In deep inelastic scattering at high Q^2 the contributions
 1678 from the first generation u and d quarks completely dominate and contact terms arising from sea quarks s ,
 1679 c and b are strongly suppressed. Thus, there are eight independent effective coupling coefficients, four for
 1680 each quark flavour

$$\eta_{ab}^q \equiv \epsilon \frac{g^2}{\Lambda_{ab}^q} , \quad (5.4)$$

1681 where a and b indicate the L , R helicities, g is the overall coupling strength, Λ_{ab}^q is a scale parameter and ϵ
 1682 is a prefactor, often set to $\epsilon = \pm 1$, which determines the interference sign with the Standard Model currents.
 1683 The ansatz eq. (??) can be easily applied to any new phenomenon, *e.g.* (eq) compositeness, leptoquarks
 1684 or new gauge bosons, by an appropriate choice of the coefficients η_{ab} . Scalar and tensor interactions of
 1685 dimension 6 operators involving helicity flip couplings are strongly suppressed at HERA [?] and therefore not
 1686 considered.

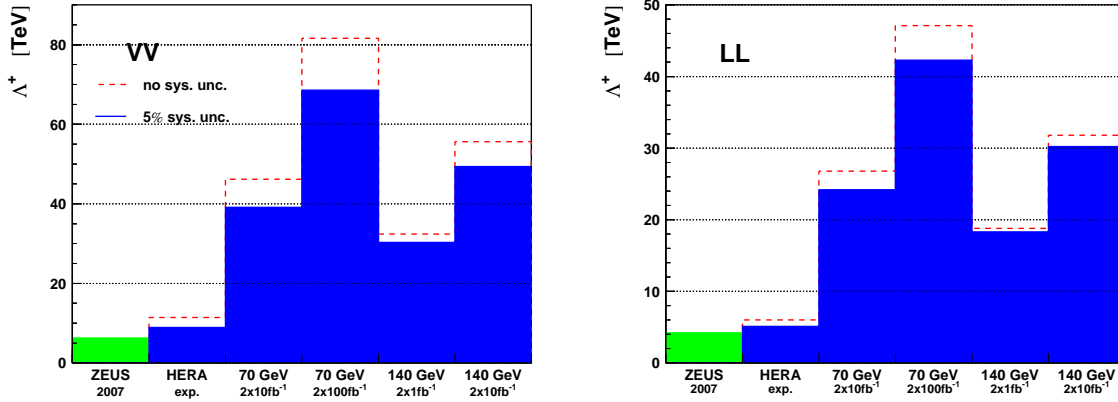


Figure 5.2: Sensitivity (95% confidence level limits) on the scale Λ for two example contact interactions.

1687 Figure ?? shows the sensitivity that an LHeC could reach on the scale Λ , for two example cases of contact
 1688 interactions [?]. In general, with 10 fb^{-1} of data, LHeC would probe scales between 25 TeV and 45 TeV,
 1689 depending on the model. The sensitivity of LHC to such $eeqq$ interactions, which would affect the di-electron
 1690 Drell-Yan (DY) spectrum at high masses, is similar.

1691 Figure ?? shows how the DY cross-section at LHC would deviate from the SM value, for three examples
 1692 of $eeqq$ contact interactions. In the “LL” model considered here, the sum in eq. (??) only involves left-
 1693 handed fermions and all amplitudes have the same phase ϵ . With only pp data, it will be difficult to
 1694 determine simultaneously the size of the contact interaction scale Λ and the sign of the interference of the
 1695 new amplitudes with respect to the SM ones: for example, for $\Lambda = 20 \text{ TeV}$ and $\epsilon = -1$, the decrease of the
 1696 cross-section with respect to the SM prediction for di-electron masses below $\sim 3 \text{ TeV}$, which is characteristic
 1697 of a negative interference, is too small to be firmly established when uncertainties due to parton distribution
 1698 functions are taken into account.

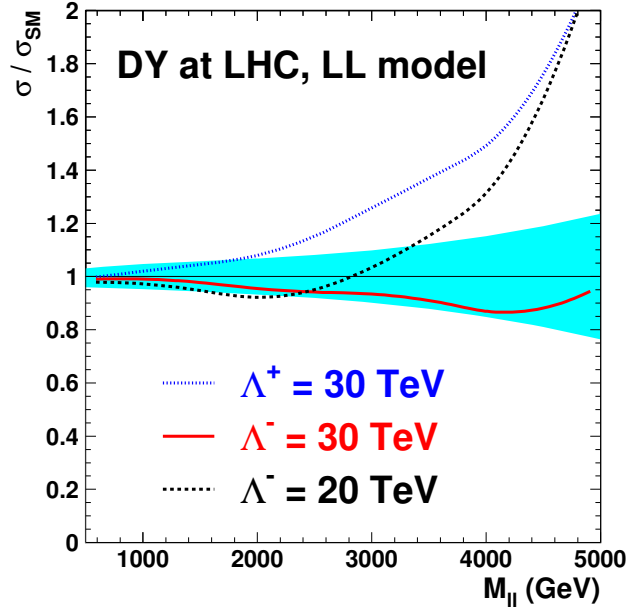


Figure 5.3: Example deviations, from its SM value, of the Drell-Yan cross-section at LHC as a function of the dilepton mass, in the presence of an $eeqq$ contact interaction. The blue band shows the relative uncertainty of the predicted SM cross-sections due to the current uncertainties of the parton distribution functions, as obtained from the CTEQ 6.1 sets.

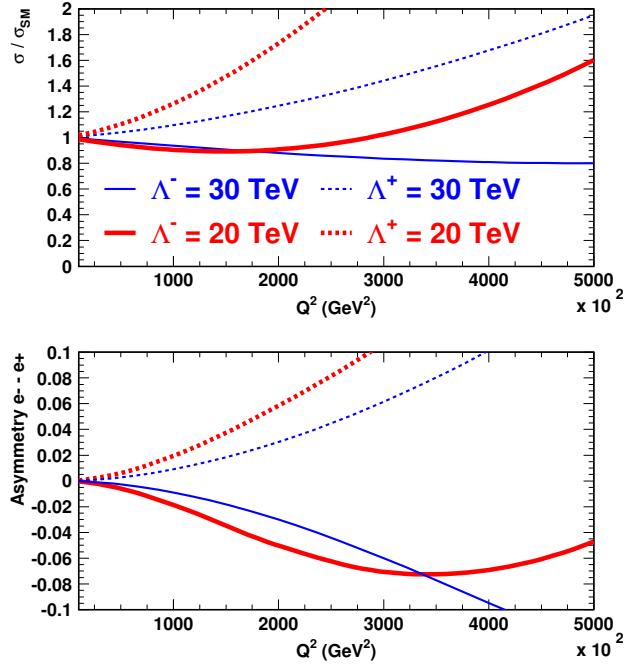


Figure 5.4: (top) Example deviations of the e^-p DIS cross-section at LHeC, in the presence of an $eeqq$ CI. The ratio of the “measured” to the SM cross-sections, $r = \sigma/\sigma_{SM}$, is shown. (bottom) Asymmetry $\frac{r(e^+) - r(e^-)}{r(e^+) + r(e^-)}$ between e^+p and e^-p measurements of σ/σ_{SM} .

1699 For the same “LL” model, the sign of this interference can be unambiguously determined at LHeC from
 1700 the asymmetry of σ/σ_{SM} in e^+p and e^-p data, as shown in Fig. ??.

1701
 1702 Moreover, with a polarised lepton beam, ep collisions would help determine the chiral structure of the
 1703 new interaction. More generally, it is very likely that both pp and ep data would be necessary to underpin the
 1704 structure of new physics which would manifest itself as an $eeqq$ contact interaction. Such a complementarity
 1705 of pp , ep (and also ee) data was studied in [?] in the context of the Tevatron, HERA and LEP colliders.

1706 5.1.3 Kaluza-Klein gravitons in extra-dimensions

1707 In some models with n large extra dimensions, the SM particles reside on a four-dimensional “brane”, while
 1708 the spin 2 graviton propagates into the extra spatial dimensions and appears in the four-dimensional world
 1709 as a tower of massive Kaluza-Klein (KK) states. The summation over the enormous number of Kaluza-Klein
 1710 states up to the ultraviolet cut-off scale, taken as the Planck scale M_S in the $4 + n$ space, leads to effective
 1711 contact-type interactions $ff'f'f'$ between two fermion lines, with a coupling $\eta = O(1)/M_S^4$. In ep scattering,
 1712 the exchange of such a tower of Kaluza-Klein gravitons would affect the Q^2 dependence of the DIS cross-
 1713 section $d\sigma/dQ^2$. At LHeC, such effects could be observed as long as the scale M_S is below 4 – 5 TeV. While
 1714 at the LHC, virtual graviton exchange may be observed for scales up to ~ 10 TeV, and the direct production
 1715 of KK gravitons, for scales up to 5 – 7 TeV depending on n , would allow this phenomenon to be studied
 1716 further, LHeC data may determine that the new interaction is universal by establishing that the effect in
 1717 the $eq \rightarrow eq$ cross-section is independent of the lepton charge and polarization, and, to some extent, of the
 1718 quark flavor.

1719 5.2 Leptoquarks and leptogluons

1720 The high energy of the LHeC extends the kinematic range of DIS physics to much higher values of electron-
 1721 quark mass $M = \sqrt{s}x$, beyond those of present ep colliders. By providing both baryonic and leptonic
 1722 quantum numbers in the initial state, it is ideally suited to a study of the properties of new bosons possessing
 1723 couplings to an electron-quark pair in this new mass range. Such particles can be squarks in supersymmetric
 1724 models with R -parity violation (\tilde{R}_p), or first-generation leptoquark (LQ) bosons which appear naturally in
 1725 various unifying theories beyond the Standard Model (SM) such as: E_6 [?], where new fields can mediate
 1726 interactions between leptons and quarks; extended technicolor [?, ?], where leptoquarks result from bound
 1727 states of technifermions; the Pati-Salam model [?], where the leptonic quantum number is a fourth color of
 1728 the quarks or in lepton-quark compositeness models. They are produced as single s -channel resonances via
 1729 the fusion of incoming electrons with quarks in the proton. They are generically referred to as “leptoquarks”
 1730 in what follows. The case of “leptogluons”, which could be produced in ep collisions as a fusion between the
 1731 electron and a gluon, is also addressed at the end of this section.

1732 5.2.1 Phenomenology of leptoquarks in ep collisions

1733 In ep collisions, LQs may be produced resonantly up to the kinematic limit of $\sqrt{s_{ep}}$ via the fusion of
 1734 the incident lepton with a quark or antiquark coming from the proton, or exchanged in the u -channel, as
 1735 illustrated in Fig. ??. The coupling λ at the $LQ - e - q$ vertex is an unknown parameter of the model.

1736 In the narrow-width approximation, the resonant production cross-section is proportional to $\lambda^2 q(x)$ where
 1737 $q(x)$ is the density of the struck parton in the incoming proton.

1738 The resonant production or t -channel exchange of a leptoquark gives $e + q$ or $\nu + q'$ final states leading to
 1739 individual events indistinguishable from SM NC and CC DIS respectively. For the process $eq \rightarrow LQ \rightarrow eq$,
 1740 the distribution of the transverse energy $E_{T,e}$ of the final state lepton shows a Jacobian peak at $M_{LQ}/2$,
 1741 M_{LQ} being the LQ mass. Hence the strategy to search for a LQ signal in ep collisions is to look, among
 1742 high Q^2 (i.e. high $E_{T,e}$) DIS event candidates, for a peak in the invariant mass M of the final $e - q$ pair.

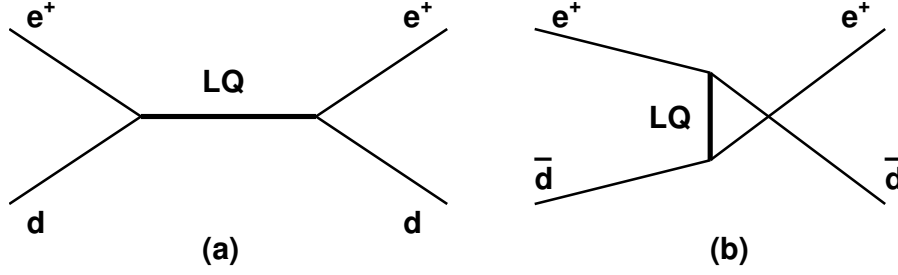


Figure 5.5: Example diagrams for resonant production in the s -channel (a) and exchange in the u -channel (b) of a LQ with fermion number $F = 0$. The corresponding diagrams for $|F| = 2$ LQs are obtained from those depicted by exchanging the quark and antiquark.

1743 Moreover, the significance of the LQ signal over the SM DIS background can be enhanced by exploiting the
 1744 specific angular distribution of the LQ decay products (see spin determination, below).

1745 5.2.2 The Buchmüller-Rückl-Wyler Model

1746 A reasonable phenomenological framework to study first generation LQs is provided by the BRW model [?].
 1747 This model is based on the most general Lagrangian that is invariant under $SU(3) \times SU(2) \times U(1)$, respects
 1748 lepton and baryon number conservation, and incorporates dimensionless family diagonal couplings of LQs
 1749 to left- and/or right-handed fermions. Under these assumptions LQs can be classified according to their
 1750 quantum numbers into 10 different LQ isospin multiplets (5 scalar and 5 vector), half of which carry a
 1751 vanishing fermion number $F = 3B + L$ (B and L denoting the baryon and lepton number respectively) and
 couple to $e^+ + q$ while the other half carry $|F| = 2$ and couple to $e^+ + \bar{q}$. These are listed in Table ??.

$F = -2$	Prod./Decay	β_e	$F = 0$	Prod./Decay	β_e
Scalar Leptoquarks					
$^{1/3}S_0$	$e_R^+ \bar{u}_R \rightarrow e^+ \bar{u}$	1/2	$^{5/3}S_{1/2}$	$e_R^+ u_R \rightarrow e^+ u$	1
	$e_L^+ \bar{u}_L \rightarrow e^+ \bar{u}$	1		$e_L^+ u_L \rightarrow e^+ u$	1
$^{4/3}\tilde{S}_0$	$e_L^+ \bar{d}_L \rightarrow e^+ \bar{d}$	1	$^{2/3}S_{1/2}$	$e_L^+ d_L \rightarrow e^+ d$	1
$^{4/3}S_1$	$e_R^+ \bar{d}_R \rightarrow e^+ \bar{d}$	1	$^{2/3}\tilde{S}_{1/2}$	$e_R^+ d_R \rightarrow e^+ d$	1
$^{1/3}S_1$	$e_R^+ \bar{u}_R \rightarrow e^+ \bar{u}$	1/2			
Vector Leptoquarks					
$^{4/3}V_{1/2}$	$e_L^+ \bar{d}_R \rightarrow e^+ \bar{d}$	1	$^{2/3}V_0$	$e_L^+ d_R \rightarrow e^+ d$	1
	$e_R^+ \bar{d}_L \rightarrow e^+ \bar{d}$	1		$e_R^+ d_L \rightarrow e^+ d$	1/2
$^{1/3}V_{1/2}$	$e_L^+ \bar{u}_R \rightarrow e^+ \bar{u}$	1	$^{5/3}\tilde{V}_0$	$e_L^+ u_R \rightarrow e^+ u$	1
$^{1/3}\tilde{V}_{1/2}$	$e_R^+ \bar{u}_L \rightarrow e^+ \bar{u}$	1	$^{5/3}V_1$	$e_R^+ u_L \rightarrow e^+ u$	1
			$^{2/3}V_1$	$e_R^+ d_L \rightarrow e^+ d$	1/2

Table 5.1: Leptoquark isospin families in the Buchmüller-Rückl-Wyler model. For each leptoquark, the superscript corresponds to its electric charge, while the subscript denotes its weak isospin. β_e denotes the branching ratio of the LQ into $e + q$.

1753
1754
1755
1756
1757

We use the nomenclature of [?] to label the different LQ states. In addition to the underlying hypotheses of BRW, we restrict LQs couplings to only one chirality state of the lepton, given that deviations from lepton universality in helicity suppressed pseudoscalar meson decays have not been observed [?, ?].

In the BRW model, LQs decay exclusively into eq and/or νq and the branching ratio $\beta_e = \beta(LQ \rightarrow eq)$ is fixed by gauge invariance to 0.5 or 1 depending on the LQ type.

1758 5.2.3 Phenomenology of leptoquarks in pp collisions

1759
1760
1761
1762
1763
1764
1765

Pair production In pp collisions leptoquarks would be mainly pair-produced via gg or qq interactions. As long as the coupling λ is not too strong (e.g. $\lambda \sim 0.3$ or below, corresponding to a strength similar to or lower than that of the electromagnetic coupling, $\sqrt{4\pi\alpha_{em}}$), the production cross-section is essentially independent of λ . At the LHC, LQ masses up to about 1.5 to 2 TeV will be probed [?], independently of the coupling λ . However, the determination of the quantum numbers of a first generation LQ in the pair-production mode is not possible (e.g. for the fermion number) or ambiguous and model-dependent (e.g. for the spin). Single LQ production is much better suited for such studies.

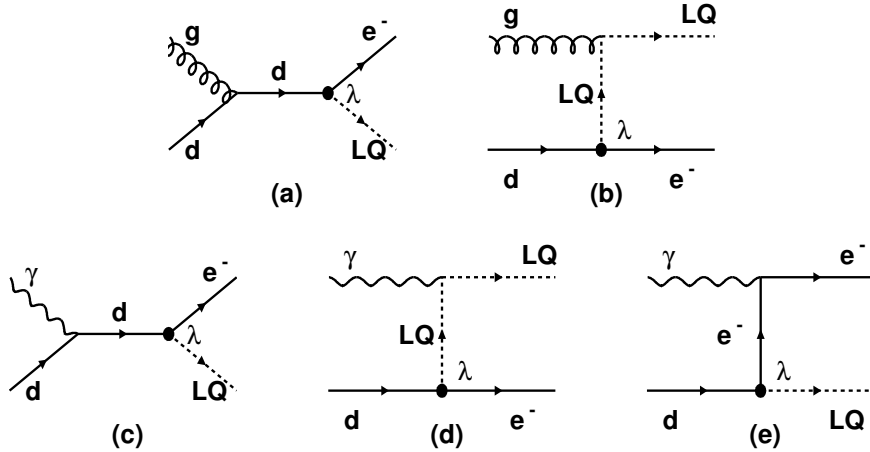


Figure 5.6: Diagrams for single LQ production in pp collisions, shown for the example case of the $\tilde{S}_{1/2}^L$ scalar leptoquark. The production may occur via qq interactions (a and b), or via $q\gamma$ interactions (c, d and e). In the latter case, the photon can be emitted by the proton (elastic regime) or by a quark coming from the proton (inelastic regime).

1766
1767
1768
1769

Single production Single LQ production at the LHC is also possible. So far, only the production mode $gq \rightarrow e + LQ$ (see example diagrams in Fig. ??a and b) has been considered in the literature (see e.g. [?]). In the context of this study, the additional production mode $\gamma q \rightarrow e + LQ$ has been considered as well (see example diagrams in Fig. ??c, d and e). This cross-section has been calculated by taking into account:

1770
1771
1772
1773
1774

- the inelastic regime, where the photon virtuality q^2 is large enough and the proton breaks up in a hadronic system with a mass well above the proton mass. In that case, the photon is emitted by a parton in the proton, and the process $qq' \rightarrow q + e + LQ$ is calculated.
- the elastic regime, in which the proton emitting the photon remains intact. This calculation involves the elastic form factors of the proton.

1775
1776

As the resonant LQ production in ep collisions, the cross-section of single LQ production in pp collisions approximately scales with the square of the coupling, $\sigma \propto \lambda^2$. Figure ?? (left) shows the cross-section for

1777 single LQ production at the LHC as a function of the LQ mass, assuming a coupling $\lambda = 0.1$. While the
 1778 inelastic part of the γq cross-section can be neglected, the elastic production plays an important role at high
 1779 masses; its cross-section is larger than that of LQ production via gq interactions for masses above ~ 1 TeV.
 1780 However, the cross-section for single LQ production at LHC is much lower than that at LHeC, in e^+p or e^-p
 1781 collisions, as shown in Fig.?? (right).

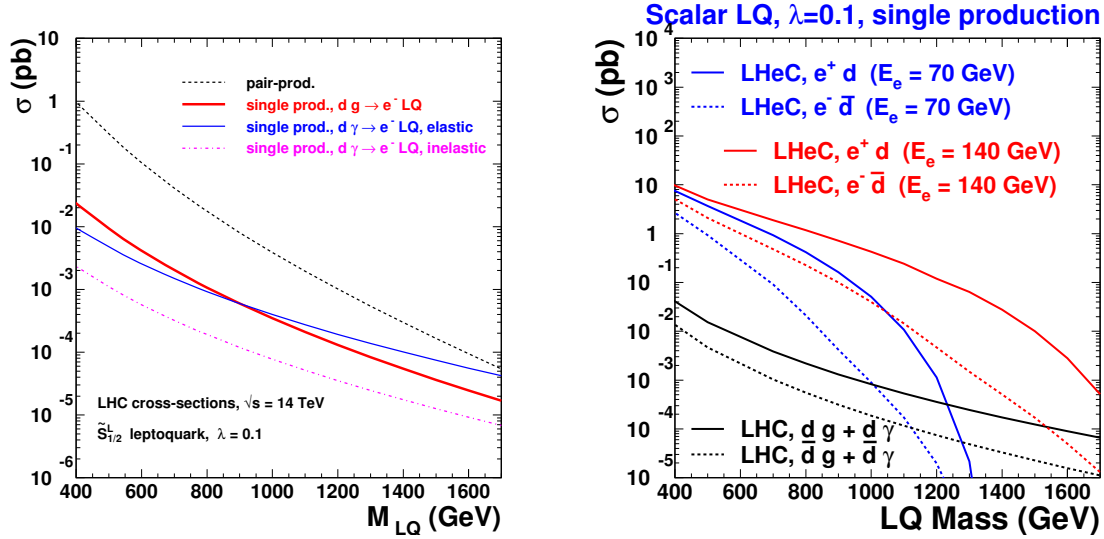


Figure 5.7: left: Single LQ production cross-section at the LHC. right: comparison of the cross-section for single LQ production, at LHC and at LHeC.

1782 **The Contact Term Approach** For LQ masses far above the kinematic limit, the contraction of the
 1783 propagator in the $eq \rightarrow eq$ and $qq \rightarrow ee$ amplitudes leads to a four-fermion interaction. Such interactions are
 1784 studied in the context of general contact terms, which can be used to parameterize any new physics process
 1785 with a characteristic energy scale far above the kinematic limit.

1786 In ep collisions, Contact Interactions (CI) would interfere with NC DIS processes and lead to a distortion
 1787 of the Q^2 spectrum of NC DIS candidate events. The results presented in section ?? can be re-interpreted
 1788 into expected sensitivities on high mass leptoquarks.

1789 5.2.4 Current status of leptoquark searches

1790 The H1 and ZEUS experiments at the HERA ep collider have constrained the coupling λ to be smaller than
 1791 the electromagnetic coupling ($\lambda < \sqrt{4\pi\alpha_{em}} \sim 0.3$) for first generation LQ s lighter than 300 GeV. The D0 and
 1792 CDF experiments at the Tevatron pp collider set constraints on first-generation LQ s that are independent of
 1793 the coupling λ , by looking for pair-produced LQ s that decay into eq (νq) with a branching ratio β ($1 - \beta$).
 1794 For a branching fraction $\beta = 1$, masses below 299 GeV are excluded by the D0 experiment [?]. The CMS
 1795 and ATLAS experiments have recently set tighter constraints [?, ?]. Fig. ?? shows the bounds obtained by
 1796 the CMS experiment with $\sim 32 \text{ pb}^{-1}$ collected in 2010, in the β versus M_{LQ} plane. For $\beta = 1$ ($\beta = 0.5$),
 1797 masses below 384 GeV (340 GeV) are ruled out.

1798 5.2.5 Sensitivity on leptoquarks at LHC and at LHeC

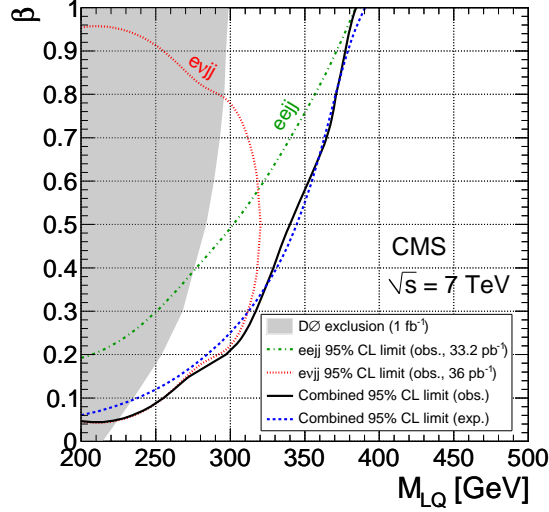


Figure 5.8: Constraints on first generation leptoquarks obtained by the CMS experiment.

1799 **Mass - coupling reach** Fig. ?? shows the expected sensitivity [?] of the LHC and LHeC colliders for
 1800 scalar leptoquark production. The single LQ production cross section depends on the unknown coupling λ
 1801 of the LQ to the electron-quark pair. For a coupling λ of $\mathcal{O}(0.1)$, LQ masses up to about 1 TeV could be
 1802 probed at the LHeC. In pp interactions at the LHC, such leptoquarks would be mainly produced via pair
 1803 production, or singly produced with a much reduced cross section.

1804 5.2.6 Determination of LQ properties

1805 In ep collisions LQ production can be probed in detail, taking advantage of the formation and decay of systems
 1806 which can be observed directly as a combination of jet and lepton invariant mass in the final state. It will
 1807 thereby be possible at the LHeC to probe directly and with high precision the perhaps complex structures
 1808 which will result in the lepton-jet system and to determine the quantum numbers of new states. Exam-
 1809 ples of the sensitivity of high energy ep collisions to the properties of LQ production follow. In particular,
 1810 a quantitative comparison of the potential of LHC and LHeC to measure the fermion number of a LQ is given.
 1811

Fermion number (F) Since the parton densities for u and d at high x are much larger than those for \bar{u}
 and \bar{d} , the production cross section at LHeC of an $F = 0$ ($F = 2$) LQ is much larger in e^+p (e^-p) than in
 e^-p (e^+p) collisions. A measurement of the asymmetry between the e^+p and e^-p LQ cross sections,

$$\mathcal{A}_{ep} = \frac{\sigma_{prod}(e^+p) - \sigma_{prod}(e^-p)}{\sigma_{prod}(e^+p) + \sigma_{prod}(e^-p)}$$

thus determines, via its sign, the fermion number of the produced leptoquark. Pair production of first
 generation LQs at the LHC will not allow this determination. Single LQ production at the LHC, followed
 by the LQ decay into e^\pm and q or \bar{q} , could determine F by comparing the signal cross sections with an e^+
 and an e^- coming from the resonant state. Indeed, for a $F = 0$ leptoquark, the signal observed when the
 resonance is made by a positron and a jet corresponds to diagrams involving a *quark* in the initial state (see
 Fig.??a). Hence the corresponding cross-section, $\sigma(e_{out}^+j)$ is larger than that of the signal observed when
 the resonance is made by an electron and a jet, $\sigma(e_{out}^-j)$, since a high x *antiquark* is involved in that latter

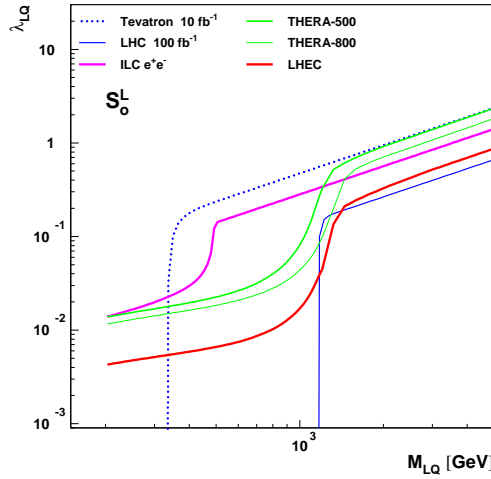


Figure 5.9: Mass-dependent upper bounds on the LQ coupling λ as expected at LHeC for a luminosity of 10 fb^{-1} (full red curve) and at the LHC for 100 fb^{-1} (full blue curve). These are shown for an example scalar LQ coupling to e^-u .

case (see Fig.??b). In contrast, for a $F = 2$ LQ, $\sigma(e_{out}^+j)$ is smaller than $\sigma(e_{out}^-j)$. The measurement of (the sign of) the asymmetry

$$\mathcal{A}_{pp} = \frac{\sigma(e_{out}^+j) - \sigma(e_{out}^-j)}{\sigma(e_{out}^+j) + \sigma(e_{out}^-j)}$$

should thus provide a determination of the LQ fermion number. However, the single LQ production cross

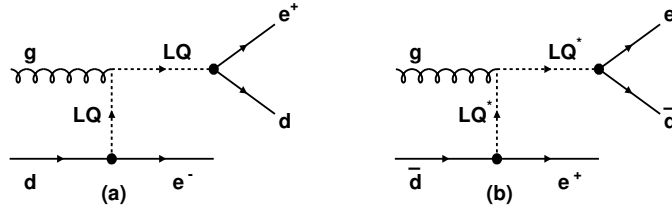


Figure 5.10: Single production of a $F = 0$ leptoquark decaying (a) into a positron and a jet and (b) into an electron and a jet. In (a) (resp. (b)), the jet comes from a quark (an antiquark); conservation of the baryon number implies that the parton involved in the initial state is a quark (an antiquark).

1812

1813 section at the LHC is two orders of magnitude lower than at the LHeC (Fig. ??), so that the asymmetry \mathcal{A}_{pp}
 1814 measured at the LHC may suffer from statistics in a large part of the parameter space. For a LQ coupling
 1815 to ed and $\lambda = 0.1$, no information on F can be extracted from 300 pb^{-1} of LHC data for a LQ mass above
 1816 $\sim 1 \text{ TeV}$, while the LHeC can determine F for LQ masses up to 1.5 TeV (Fig. ?? and Fig. ??). Details of
 1817 the determination of \mathcal{A}_{pp} at the LHC are given in the next paragraph.

1818

1819 An estimate of the precision with which the fermion number determination of a leptoquark can be
 1820 determined at the LHC was obtained from a Monte Carlo simulation. First, using the model [?] implemented
 1821 in CalcHep [?], samples were generated for the processes $g u \rightarrow e^+e^-u$ and $g \bar{u} \rightarrow e^+e^-\bar{u}$, keeping only

1822 diagrams involving the exchange of a scalar LQ exchange of charge 1/3, isospin 0 and fermion number 2.
 1823 This leptoquark ($^{1/3}S_0$ in the notation of Table ??) couples to $e_R^- u_R$. Assuming that it is chiral, only right-
 1824 handed coupling was allowed. The $^{1/3}S_0$ leptoquark was also assumed to couple only to the first generation.
 1825 Masses of 500 GeV, 750 GeV and 1 TeV were considered. The renormalization and factorization scales were
 1826 set at $Q^2 = m_{LQ}^2$ and the coupling parameter $\lambda = 0.1$. A center of mass energy of 14 TeV was assumed at
 1827 the LHC.

1828 High statistics background samples, corresponding to 150 fb^{-1} were also produced by generating the
 1829 same processes $pp \rightarrow e^+ e^- + \text{jet}$, including all diagrams except those involving the exchange of leptoquarks.
 1830 Kinematic preconditions were applied at the generation level to both signals and background: (i) $p_T(\text{jet}) >$
 1831 50 GeV , (ii) $p_T(e^\pm) > 20 \text{ GeV}$, (iii) invariant mass of jet- $e^+ - e^-$ system $> 200 \text{ GeV}$. The cross sections for
 1832 the signals and backgrounds under these conditions are: 19.7 fb, 3.4 fb and 0.87 fb for LQ's of mass 500 GeV,
 1833 750 GeV and 1 TeV respectively, and 1780 fb for the background. These events were subsequently passed
 1834 to Pythia [?] to perform parton showering and hadronization, then processed through Delphes [?] for a fast
 1835 simulation of the ATLAS detector. Finally, considering events with two reconstructed electrons of opposite
 1836 sign and, assuming that the leptoquark has already been discovered (at the LHC), the combination of the
 1837 highest p_T jet with the reconstructed e^- or e^+ with a mass closest to the known leptoquark mass is chosen
 1838 as the LQ candidate. The following cuts for $m_{LQ} = 500, 750$ and 1000 GeV , respectively, are applied:

- 1839 • dilepton invariant mass $m_{ll} > 150, 200, 250 \text{ GeV}$. This cut rejects very efficiently the $Z + \text{jets}$ back-
 1840 ground.
- 1841 • $p_T(e_1) > 150, 200, 250 \text{ GeV}$ and $p_T(e_2) > 75, 100, 100 \text{ GeV}$, where e_1 is the reconstructed e^\pm with
 1842 higher p_T and e_2 the lower p_T electron.
- 1843 • $p_T(j_1) > 100, 250, 400 \text{ GeV}$, where j_1 is the reconstructed jet with highest p_T , used for the reconstruc-
 1844 tion of the LQ.

1845 Table ?? summarizes the results of the simulation for an integrated luminosity of 300 fb^{-1} . The expected
 1846 number of signal events shown in the table is then simply the number of events due to the leptoquark
 1847 production and decay, falling in the resonance peak within a mass window of width (60, 100, 160 GeV) for
 1848 the three cases studied, respectively. Although this simple analysis can be improved by considering other
 1849 less dominant backgrounds and by using optimized selection criteria, it should give a good estimate of the
 1850 precision with which the asymmetry can be measured. This precision falls rapidly with increasing mass and,
 1851 above $\sim 1 \text{ TeV}$, it becomes impossible to observe simultaneously single production of both $^{1/3}S_0$ and $^{1/3}\bar{S}_0$.
 1852 It must be noted that the asymmetry at the LHC will be further diluted by the abundant leptoquark pair
 1853 production, not taken into account here.

LQ mass (GeV)	$^{1/3}S_1 \rightarrow e^+ \bar{u}$		$^{1/3}\bar{S}_1 \rightarrow e^- u$		Charge Asymmetry
	Signal	Background	Signal	Background	
500	121	431	771	478	0.73 ± 0.05
750	18.3	137	132	102	$0.76_{-0.14}^{+0.16}$
1000	4.9	57	44	42	$0.77_{0.24}^{+0.23}$

Table 5.2: Estimated number of events of signal and background, and the charge asymmetry measurement with 300 fb^{-1} at the LHC, for $\lambda = 0.1$.

1854 **Flavour structure of the LQ coupling** More generally, using the same charge asymmetry observable,
 1855 the LHeC will be sensitive to the flavour structure of the leptoquark, through the dependence on the parton
 1856 distribution functions of the interacting quark in the proton. Fig. ?? shows the calculated asymmetry for
 1857 scalar LQs. Provided that the coupling λ is not too small, the accuracy of the measurement of \mathcal{A}_{ep} at LHeC
 1858 (see Fig. ??) would allow the various LQ types to be disentangled, as different LQs lead to values of \mathcal{A}_{ep} that

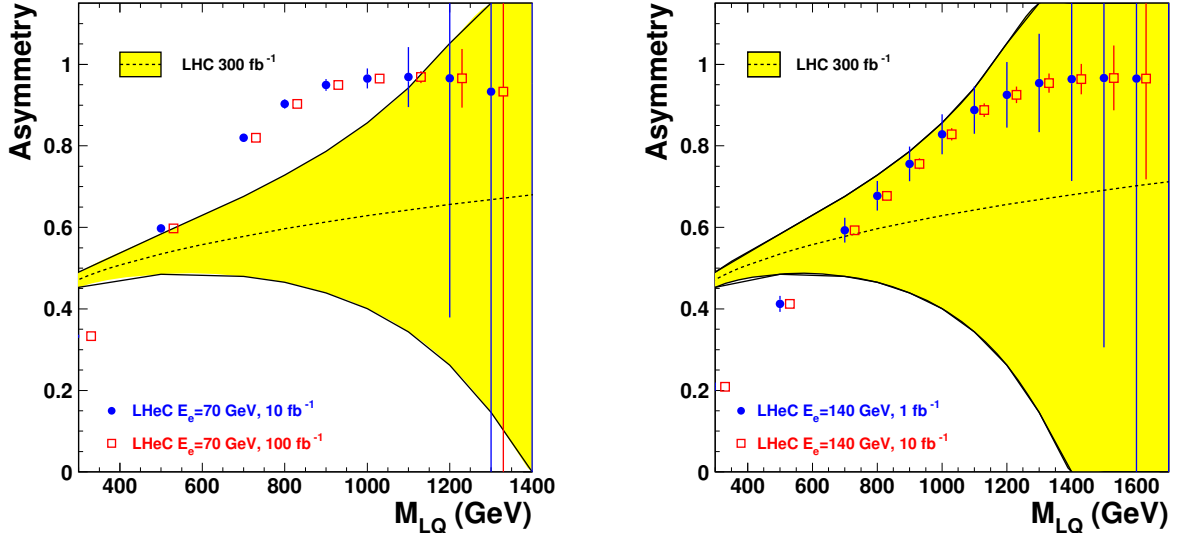


Figure 5.11: *Asymmetries which would determine the fermion number of a LQ, the sign of the asymmetry being the relevant quantity. The dashed curve shows the asymmetry that could be measured at the LHC; the yellow band shows the statistical uncertainty of this quantity, assuming an integrated luminosity of 300 fb^{-1} . The red and blue symbols, together with their error bars, show the asymmetry that would be measured at LHeC, assuming $E_e = 70 \text{ GeV}$ (left) or $E_e = 140 \text{ GeV}$ (right). Two values of the integrated luminosity have been assumed. These determinations correspond to the $\hat{S}_{1/2}^L$ (scalar LQ coupling to $e^+ + d$), with a coupling of $\lambda = 0.1$.*

1859 differ by typically 20 – 30%. A similar measurement at the LHC would be possible only in a very limited
 1860 part of the phase space (low masses and large couplings), where the statistics would be large enough to yield
 1861 an accuracy of about 20% on the measured asymmetry \mathcal{A}_{pp} .

1862 **Spin** At the LHeC, the angular distribution of the LQ decay products is unambiguously related to its spin.
 1863 Indeed, scalar LQs produced in the s -channel decay isotropically in their rest frame leading to a flat $d\sigma/dy$
 1864 spectrum where $y = \frac{1}{2}(1 + \cos\theta^*)$ is the Bjorken scattering variable in DIS and θ^* is the decay polar angle
 1865 of the lepton relative to the incident proton in the LQ centre of mass frame. In contrast, events resulting
 1866 from the production and decay of vector LQs would be distributed according to $d\sigma/dy \propto (1 - y)^2$. These
 1867 y spectra from scalar or vector LQ production are markedly different from the $d\sigma/dy \propto y^{-2}$ distribution
 1868 expected at fixed M for the dominant t -channel photon exchange in neutral current DIS events¹. Hence, a
 1869 LQ signal in the NC-like channel will be statistically most prominent at high y .

1870 The spin determination will be much more complicated, even possibly ambiguous, if only the LHC
 1871 leptoquark pair production data are available. Angular distributions for vector LQs depend strongly on the
 1872 structure of the $gLQ\overline{LQ}$ coupling, i.e. on possible anomalous couplings. For a structure similar to that of
 1873 the γWW vertex, vector LQs produced via $q\bar{q}$ fusion are unpolarised and, because both LQs are produced
 1874 with the same helicity, the distribution of the LQ production angle will be similar to that of a scalar LQ.
 1875 The study of LQ spin via single LQ production at the LHC will suffer from the relatively low rates and more
 1876 complicated backgrounds.

¹At high momentum transfer, Z^0 exchange is no longer negligible and contributes to less pronounced differences in the y spectra between LQ signal and DIS background.

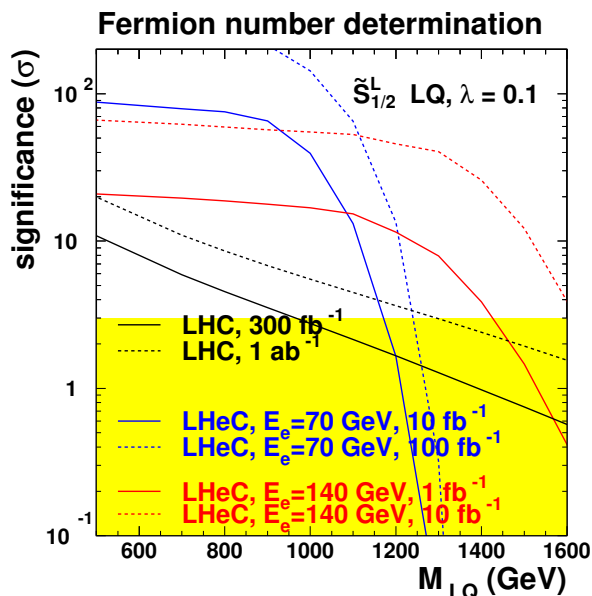


Figure 5.12: Significance of the determination of the fermion number of a LQ, at the LHC (black curve) and at the LHeC (blue and red curves). This corresponds to a $\tilde{S}_{1/2}^L$ leptoquark, assuming a coupling of $\lambda = 0.1$.

1877 **Neutrino decay modes** At the LHeC, there is similar sensitivity for LQ decay into both eq and νq . At
 1878 the LHC, in pp collisions, LQ decay into neutrino-quark final states is plagued by huge QCD background.
 1879 At the LHeC, production through eq fusion with subsequent νq decay is thus very important if the complete
 1880 pattern of LQ decay couplings is to be determined.

Coupling λ In the narrow-width approximation, the production cross-section of a LQ in ep collisions can be written as, depending on the LQ spin :

$$\sigma_{prod} = \frac{\lambda^2}{16\pi} q(x = M^2/s_{ep}) \quad (J = 0) \quad \text{or} \quad \sigma_{prod} = \frac{\lambda^2}{8\pi} q(x = M^2/s_{ep}) \quad (J = 1).$$

1881 At LHeC, the determination of:

- 1882 • the LQ spin, via the analysis of the angular distribution of its decay products;
- 1883 • the flavor of the quark q involved in the $e - q - LQ$ vertex, via the charge asymmetry described above;
- 1884 • the production cross-section, via the cross-sections measured in the eq and νq decay modes

1885 allows the value of the coupling λ to be determined, from the above formula.

1886 **Chiral structure of the LQ coupling** Chirality is central to the SM Lagrangian. Polarised electron and
 1887 positron beams² at the LHeC will shed light on the chiral structure of the LQ-e-q couplings. Measurements
 1888 of a similar nature at LHC are impossible.

1889
 1890 In summary, would a first generation leptoquark exist in the TeV mass range with a coupling λ of $\mathcal{O}(0.1)$,
 1891 the LHeC would allow a rich program of “spectroscopy” to be carried out, resulting in the determination of
 1892 most of the LQ properties.

²Whether it is possible to achieve longitudinal polarisation in a 70 GeV e^\pm beam in the LHC tunnel remains to be clarified.

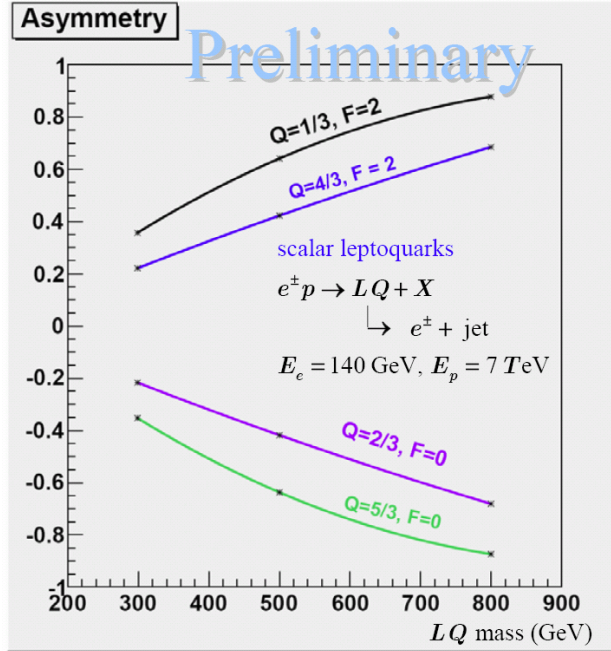


Figure 5.13: Charge asymmetry vs LQ mass for different types of scalar LQ's.

1893 5.2.7 Leptogluons

1894 While leptoquarks and excited fermions are widely discussed in the literature, leptogluons have not received
 1895 the same attention. However, they are predicted in all models with colored preons [?, ?, ?, ?, ?]. For
 1896 example, in the framework of fermion-scalar models, leptons would be bound states of a fermionic preon and
 1897 a scalar anti-preon $l = (F\bar{S}) = 1 \oplus 8$ (both F and S are color triplets), and each SM lepton would have its
 1898 own colour octet partner [?].

1899 A study of leptogluons production at LHeC is presented in [?]. It is based on the following Lagrangian:

$$L = \frac{1}{2\Lambda} \sum_l \{ \bar{l}_8^\alpha g_s G_{\mu\nu}^\alpha \sigma^{\mu\nu} (\eta_L l_L + \eta_R l_R) + h.c. \} \quad (5.5)$$

1900 where $G_{\mu\nu}^\alpha$ is the field strength tensor for gluon, index $\alpha = 1, 2, \dots, 8$ denotes the color, g_s is gauge coupling,
 1901 η_L and η_R are the chirality factors, l_L and l_R denote left and right spinor components of lepton, $\sigma^{\mu\nu}$ is the
 1902 anti-symmetric tensor and Λ is the compositeness scale. The leptonic chiral invariance implies $\eta_L \eta_R = 0$.

1903 The phenomenology of leptogluons at LHC and LHeC is very similar to that of leptoquarks, despite
 1904 their different spin (leptogluons are fermions while leptoquarks are bosons) and their different interactions.
 1905 Figure ?? shows typical cross-sections for single leptogluon production at the LHeC, assuming Λ is equal to
 1906 the leptogluon mass. It is estimated that, for example, a sensitivity of to a compositeness scale of 200 TeV,
 1907 at 3σ level can be achieved with LHeC having $E_e = 70$ GeV and with 1 fb^{-1} . The mass reach for M_{e8} is 1.1
 1908 TeV for $\Lambda = 10$ TeV.

1909 As for leptoquarks, would leptogluons be discovered at the LHC, LHeC data would be of highest value
 1910 for the determination of the properties of this new particle.

1911 5.3 Excited leptons and other new heavy leptons

1912 The three-family structure and mass hierarchy of the known fermions is one of the most puzzling charac-
 1913 teristics of the Standard Model (SM) of particle physics. Attractive explanations are provided by models

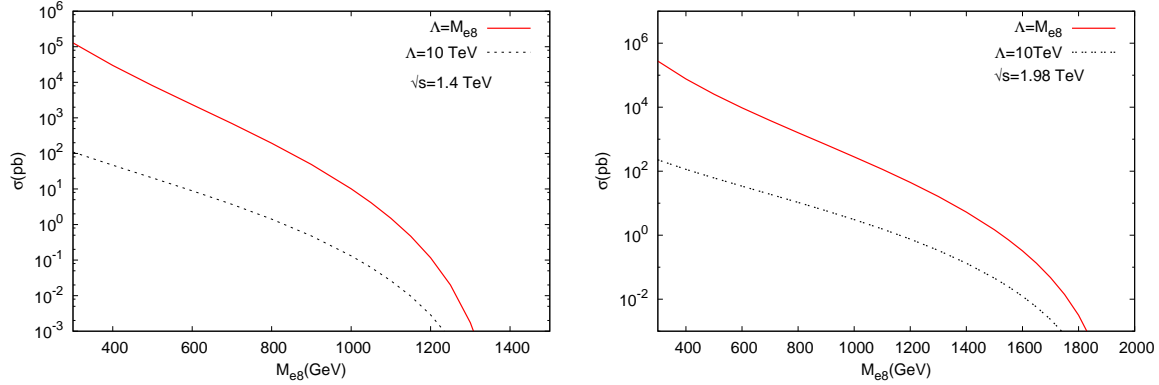


Figure 5.14: Resonant e_8 production at the LHeC, for two values of the center-of-mass energy.

1914 assuming composite quarks and leptons [?]. The existence of excited states of fermions (F^*) is a natural
 1915 consequence of compositeness models. More generally, various models predict the existence of fundamental
 1916 new heavy leptons, which can have similar experimental characteristics as excited leptons. They could, for
 1917 example, be part of a fourth Standard model family. They arise also in Grand Unified Theories, and appear
 1918 as colorless fermions in technicolor models.

1919 New heavy leptons could be pair-produced at the LHC up to masses of $\mathcal{O}(300)$ GeV. As for the case
 1920 of leptoquarks, pp data from pair-production of new leptons may not allow for a detailed study of their
 1921 properties and couplings. Single production of new leptons is also possible at the LHC, but is expected to
 1922 have a larger cross-section at LHeC, via $e\gamma$ or eW interactions. The case of excited electrons is considered
 1923 in the following, with more details being given in [?].

1924 Single production of excited leptons at the LHC (\sqrt{s} up to 14 TeV) may happen via the reactions
 1925 $pp \rightarrow e^\pm e^* \rightarrow e^+ e^- V$ and $pp \rightarrow \nu e^* + \nu^* e^\pm \rightarrow e^\pm \nu V$. The LHC should be able to tighten considerably the current
 1926 constraints on these possible new states and to probe excited lepton masses of up to 1 TeV [?]. A sensitivity
 1927 similar to the LHC could be reached at the ILC [?], with different e^+e^- , $e\gamma$ and $\gamma\gamma$ collisions modes and a
 1928 centre of mass energy of $\sqrt{s} \geq 500$ GeV.

1929 Recent results of searches for excited fermions [?, ?, ?] at HERA using all data collected by the H1 detector
 1930 have demonstrated that ep colliders are very competitive to pp or e^+e^- colliders. Indeed limits set by HERA
 1931 extend at high mass beyond the kinematic reach of LEP searches [?, ?] and to higher compositeness scales
 1932 than those obtained at the Tevatron [?] using 1 fb^{-1} of data. Therefore a future LHeC machine, with a
 1933 centre of mass energy of 1 – 2 TeV, much higher than at the HERA ep collider, would be ideal to search for
 1934 and study excited fermions. This has motivated us to examine excited electron production at a future LHeC
 1935 collider and compare it to the potential of other types of colliders at the TeV scale, the LHC and the ILC.

1936

1937 5.3.1 Excited Fermion Models

1938 Compositeness models attempt to explain the hierarchy of masses in the SM by the existence of a substructure
 1939 within the fermions. Several of these models [?, ?, ?] predict excited states of the known fermions, in which
 1940 excited fermions are assumed to have spin 1/2 and isospin 1/2 in order to limit the number of parameters
 1941 of the phenomenological study. They are expected to be grouped into both left- and right-handed weak
 1942 isodoublets with vector couplings. The existence of the right-handed doublets is required to protect the
 1943 ordinary light fermions from radiatively acquiring a large anomalous magnetic moment via F^*FV interaction
 1944 (where V is a γ , Z or W).

1945 Interactions between excited and ordinary fermions may be mediated by gauge bosons, as described by

1946 the effective Lagrangian:

$$\mathcal{L}_{GM} = \frac{1}{2\Lambda} \bar{F}_R^* \sigma^{\mu\nu} \left[g f \frac{\vec{\tau}}{2} W_{\mu\nu} + g' f' \frac{Y}{2} B_{\mu\nu} + g_s f_s \frac{\vec{\lambda}}{2} G_{\mu\nu} \right] F_L + h.c., \quad (5.6)$$

1947 where Y is the weak hypercharge, g_s , $g = \frac{e}{\sin\theta_W}$ and $g' = \frac{e}{\cos\theta_W}$ are the strong and electroweak gauge
 1948 couplings, where e is the electric charge and θ_W is the weak mixing angle; $\vec{\lambda}$ and $\vec{\tau}$ are the Gell-Mann
 1949 matrices and the Pauli matrices, respectively. $G_{\mu\nu}$, $W_{\mu\nu}$ and $B_{\mu\nu}$ are the field strength tensors describing
 1950 the gluon, the $SU(2)$, and the $U(1)$ gauge fields. f_s , f and f' are the coupling constants associated to each
 1951 gauge field. They depend on the composite dynamics. The parameter Λ has units of energy and can be
 1952 regarded as the compositeness scale which reflects the range of the new confinement force.

1953 In addition to gauge mediated (GM) interactions, novel composite dynamics may be visible as contact
 1954 interactions (CI) between excited fermions and ordinary fermions. Such interactions can be described by an
 1955 effective four-fermion Lagrangian [?]:

$$\mathcal{L}_{CI} = \frac{4\pi}{2\Lambda^2} j^\mu j_\mu, \quad (5.7)$$

1956 where Λ is here assumed to be the same parameter as in the gauge interaction Lagrangian (??) and j_μ is
 1957 the fermion current

$$j_\mu = \eta_L \bar{F}_L \gamma_\mu F_L + \eta'_L \bar{F}^*_L \gamma_\mu F^*_L + \eta''_L \bar{F}^*_L \gamma_\mu F_L + h.c. + (L \rightarrow R). \quad (5.8)$$

1958 By convention, the η factors of left-handed currents are set to ± 1 , while the factors of right-handed currents
 1959 are considered to be zero.

1960

1961 5.3.2 Simulation and Results

1962 In the following study, excited electron (e^*) production and decays via both GM and CI are considered. For
 1963 GM interactions, the e^* production cross section under the assumption $f = -f'$ becomes much smaller than
 1964 for $f = +f'$ and therefore only the case $f = +f'$ is studied.

1965 Considering pure gauge interactions, excited electrons could be produced in ep collisions at the LHeC
 1966 via a t -channel γ or Z bosons exchange. The Monte Carlo (MC) event generator COMPOS [?] is used for
 1967 the calculation of the e^* production cross section and the simulation of signal events. The production cross
 1968 sections of excited neutrinos at the LHeC is also shown in figure ??. These results are obtained with the
 1969 assumption $f = +f'$ and $M_{e^*} = \Lambda$ and are compared to production cross section at HERA and also at the
 1970 LHC [?]. In the mass range accessible by the LHeC, the e^* production cross section is clearly much higher
 1971 than at the LHC.

1972 Considering gauge and contact interactions together, formulae for the e^* production cross section via CI
 1973 and of the interference term between contact and gauge interactions have been incorporated into COMPOS [?,
 1974 ?]. For simplicity, the relative strength of gauge and contact interactions are fixed by setting the parameters
 1975 f and f' of the gauge interaction to one. Comparisons of the e^* production cross section via only gauge
 1976 interactions and via GM and CI together, as a function of the e^* mass, are presented in figure ??(a) for
 1977 $M_{e^*} = \Lambda$ and figure ??(b) for $\Lambda = 10$ TeV, respectively. These results for the LHeC at $\sqrt{s} = 1.4$ TeV
 1978 are compared to the cross section at an LHC operating at $\sqrt{s} = 14$ TeV. These plots demonstrate that at
 1979 the LHeC the ratio of the contact and gauge cross sections (proportional to \hat{s}/Λ^4 and $1/\Lambda^2$ respectively)
 1980 decreases as Λ and M_{e^*} increase differently than for the LHC where contact interactions may be an important
 1981 source of production of excited electrons. In the mass range accessed at the LHeC, e^* decays are dominated
 1982 by gauge decays, provided that Λ is large enough. Therefore, only gauge decays are looked for in the present
 1983 study.

1984 In order to estimate the sensitivity of excited electron searches at the LHeC, the e^* production followed
 1985 by its decay in the channel $e^* \rightarrow e\gamma$ is considered. This is the key channel for excited electron searches in ep
 1986 collisions as it provides a very clear signature and has a large branching ratio. Only the main sources of

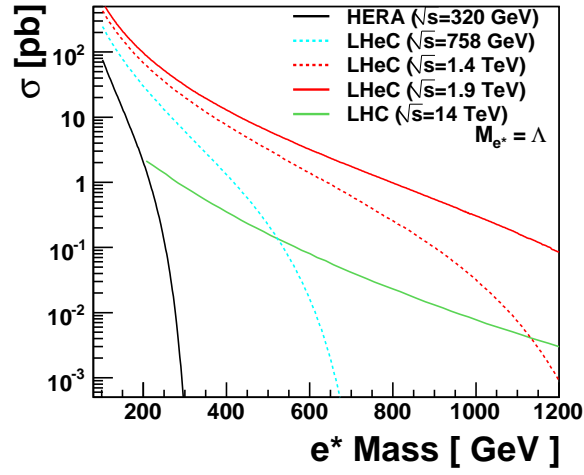


Figure 5.15: The e^* production cross section for different design scenarios of the LHeC electron-proton collider, compared to the cross sections at HERA and at the LHC.

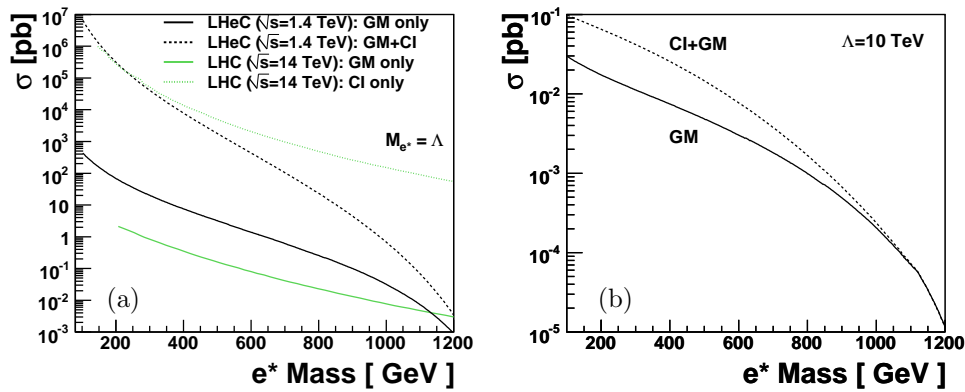


Figure 5.16: Comparison of the e^* production cross section via gauge and contact interactions. In figure (a), the results for the LHeC ($\sqrt{s} = 1.4$ TeV) and for the LHC ($\sqrt{s} = 14$ TeV) are compared. Production cross sections for a fixed Λ value of 10 TeV are shown in figure (b) for the LHeC.

1987 backgrounds from SM processes are considered here, namely neutral currents (NC DIS) and QED-Compton
1988 ($e\gamma$) events. Other possible SM backgrounds are negligible. The MC event generator WABGEN [?] is used
1989 to generate these background events. Figure ?? compares the e^* production cross section to the total cross
1990 section of SM backgrounds. Background events dominate in the low e^* mass region. Hence to enhance the
1991 signal, candidate events are selected with two isolated electromagnetic clusters with a polar angle between
1992 5° and 145° and transverse energies greater than 15 GeV and 10 GeV, respectively.

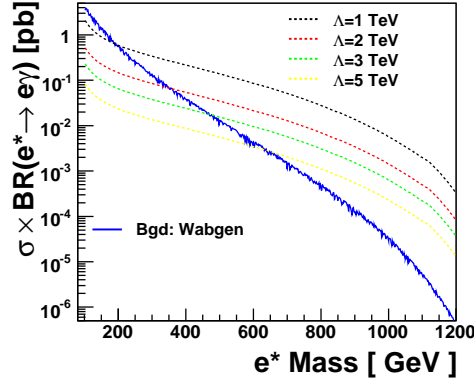


Figure 5.17: Electromagnetic production cross section for e^* ($e^* \rightarrow e\gamma$) for different values of Λ .

1993 To translate the results into exclusion limits, expected upper limits on the coupling f/Λ are derived at
1994 95% Confidence Level (CL) as a function of excited electron masses.

1995 In case of gauge interaction, the attainable limits at the LHeC on the ratio f/Λ are shown in figure ?? for
1996 excited electrons, for the hypothesis $f = +f'$ and different integrated luminosities $L = 10 \text{ fb}^{-1}$ for \sqrt{s} up to
1997 1.4 TeV and $L = 1 \text{ fb}^{-1}$ for \sqrt{s} up to 2 TeV. They are compared to the upper limits obtained at LEP [?,?],
1998 HERA [?] and also to the expected sensitivity of the LHC [?]. Considering the assumption $f/\Lambda = 1/M_{e^*}$
1999 and $f = +f'$, excited electrons with masses up to 1.2(1.5) TeV, corresponding to centre of mass energies of
2000 $\sqrt{s} = 1.4(1.9)$ TeV of the LHeC, are excluded. Under the same assumptions, LHC ($\sqrt{s} = 14$ TeV) could
2001 exclude e^* masses up to 1.2 TeV for an integrated luminosity of 100 fb^{-1} . In the accessible mass range
2002 of LHeC, the LHeC would be able to probe smaller values of the coupling f/Λ than the LHC. Similarly to
2003 leptoquarks (see section ??), if an excited electron is observed at the LHC with a mass of $\mathcal{O}(1 \text{ TeV})$, the
2004 LHeC would be better suited to study the properties of this particle, thanks to the larger single production
2005 cross-section (see Fig. ??).

2006 5.3.3 New leptons from a fourth generation

2007 New leptons from a fourth generation (l_4, ν_4) may have anomalous couplings to the standard leptons, as
2008 given by the following effective Lagrangian:

$$\begin{aligned}
\mathcal{L}_{nc} &= \left(\frac{\kappa_\gamma^{\ell_4 \ell_i}}{\Lambda} \right) e_\ell g_e \bar{\ell}_4 \sigma_{\mu\nu} \ell_i F^{\mu\nu} \\
&+ \left(\frac{\kappa_Z^{\ell_4 \ell_i}}{2\Lambda} \right) g_Z \bar{\ell}_4 \sigma_{\mu\nu} \ell_i Z^{\mu\nu} + \left(\frac{g_Z}{2} \right) \bar{\nu}_i \frac{i}{2\Lambda} \kappa_Z^{\nu_4 \nu_i} \sigma_{\mu\nu} q^\nu P_L \nu_4 Z^\mu + h.c. \\
\mathcal{L}_{cc} &= \left(\frac{g_W}{\sqrt{2}} \right) \bar{l}_i \left[\frac{i}{2\Lambda} \kappa_W^{\nu_4 l_i} \sigma_{\mu\nu} q^\nu \right] P_L \nu_4 W^\mu + h.c.
\end{aligned}$$

2009 In that case, the single production of l_4 and ν_4 would be similar to that of excited electrons and neutrinos. For
2010 a study of the properties and couplings of such a new lepton, an ep machine would offer the same advantages
2011 as presented above in the case of excited electrons. A study of the processes $ep \rightarrow l_4 X \rightarrow Ze(\gamma\mu)X$

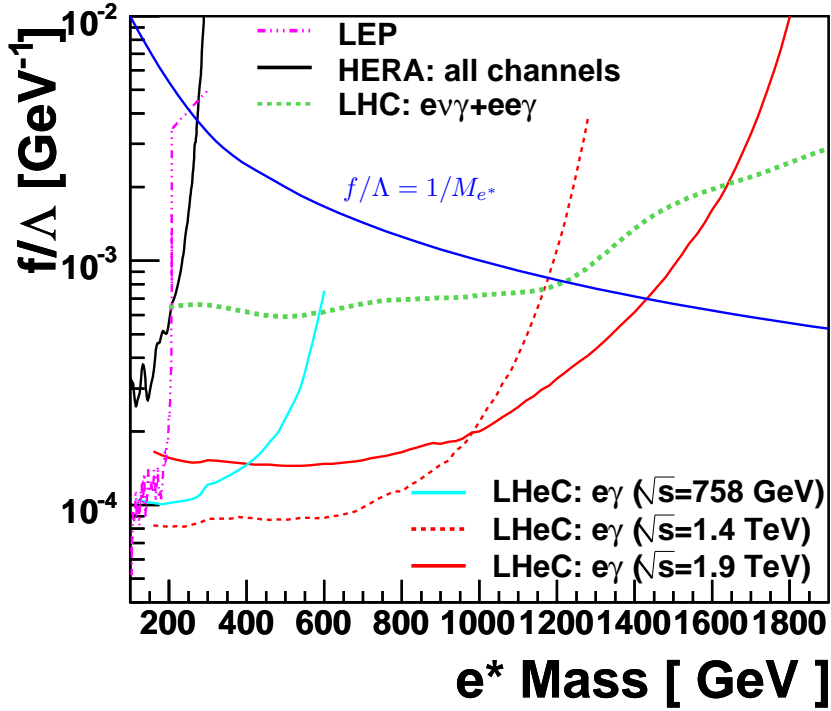


Figure 5.18: Sensitivity to excited electron searches for different design scenarios of the LHeC electron-proton collider, compared to the expected sensitivity of the LHC ($\sqrt{s} = 14$ TeV, $L = 100$ fb $^{-1}$). Different integrated luminosities at the LHeC ($L = 10$ fb $^{-1}$ for \sqrt{s} up to 1.4 TeV and $L = 1$ fb $^{-1}$ for \sqrt{s} up to 2 TeV) are assumed. The curves present the expected exclusion limits on the coupling f/Λ at 95% CL as a function of the mass of the excited electron with the assumption $f = +f'$. Areas above the curves are excluded. Present experimental limits obtained at LEP and HERA are also represented.

and $ep \rightarrow \nu_4 X \rightarrow W(e, \mu)X$ at the LHeC is presented in [?]. For example, for an anomalous coupling $\kappa/\Lambda = 1 \text{ TeV}^{-1}$, LHeC would be able to cover l_4 masses up to $\sim 900 \text{ GeV}$.

5.4 New physics in boson-quark interactions

Several extensions of the Standard Model predict new phenomena that would be directly observable in boson-quark interactions. For example, the top quark may have anomalous couplings to gauge bosons, leading to Flavour Changing Neutral Current (FCNC) vertices $tq\gamma$, where q is a light quark. Similarly, excited quarks (q^*) or quarks from a fourth generation (Q) could be produced via $\gamma q \rightarrow q^*$ or $\gamma q \rightarrow Q$. The transitions $\gamma q \rightarrow t, q^*, Q$ can be studied in ep collisions at the LHeC, but a much larger cross-section would be achieved at a γp collider, due to the much larger γp centre-of-mass energy. The single production of q^* , Q or of a top quark via anomalous couplings is also possible at the LHC, but it involves an anomalous coupling together with an electroweak coupling and the main background processes involve the strong interaction. The signal to background ratio will thus be much more challenging at the LHC, and any constraints on anomalous couplings would therefore be obtained from the decay channels of these quarks. The example of anomalous single top production is detailed in the following.

5.4.1 An LHeC-based γp collider

The possibility to operate the LHeC as a γp collider is described in [?]. If the electron beam is accelerated by a linac, it can be converted into a beam of high energy real photons, by backscattering off a laser pulse. The energy of these photons would be about 80% of the energy of the initial electrons.

5.4.2 Anomalous Single Top Production at the LHeC Based γp Collider

The top quark is expected to be most sensitive to physics beyond the Standard Model (BSM) because it is the heaviest available particle of the Standard Model (SM). A precise measurement of the couplings between SM bosons and fermions provides a powerful tool for the search of BSM physics allowing a possible detection of deviations from SM predictions [?]. Anomalous tqV ($V = g, \gamma, Z$ and $q = u, c$) couplings can be generated through dynamical mass generation [?], sensitive to the mechanism of dynamical symmetry breaking. They have a similar chiral structure as the mass terms, and the presence of these couplings would be interpreted as signals of new interactions. This motivates the study of top quark flavour changing neutral current (FCNC) couplings at present and future colliders.

Current experimental constraints at 95% C.L. on the anomalous top quark couplings are [?]: $BR(t \rightarrow \gamma u) < 0.0132$ and $BR(t \rightarrow \gamma c) < 0.0059$ from HERA; $BR(t \rightarrow \gamma q) < 0.041$ from LEP and $BR(t \rightarrow \gamma q) < 0.032$ from CDF. The HERA has much higher sensitivity to $u\gamma t$ than $c\gamma t$ due to more favorable parton density: the best limit is obtained from the ZEUS experiment.

The top quarks will be produced in large numbers at the Large Hadron Collider (LHC), allowing great precision measurement of the coupling. For a luminosity of 1 fb^{-1} (100 fb^{-1}) the expected ATLAS sensitivity to the top quark FCNC decay is $BR(t \rightarrow q\gamma) \sim 10^{-3}$ (10^{-4}) [?, ?]. The production of top quarks by FCNC interactions at hadron colliders has been studied in [?, ?, ?, ?, ?, ?, ?, ?, ?, ?, ?], e^+e^- colliders in [?, ?, ?, ?] and lepton-hadron collider in [?, ?, ?, ?]. LHC will give an opportunity to probe $BR(t \rightarrow ug)$ down to 5×10^{-3} [?]; ILC/CLIC has the potential to probe $BR(t \rightarrow q\gamma)$ down to 10^{-5} [?].

A linac-ring type collider presents the sole realistic way to TeV scale in γp collisions [?, ?, ?, ?, ?, ?]. Recently this opportunity has been widely discussed in the framework of the LHeC project [?]. Two stages of the LHeC were considered: QCD Explorer ($E_e = 50 - 100 \text{ GeV}$) and Energy Frontier ($E_e > 250 \text{ GeV}$). The potential of the LHeC as a γp collider to search for anomalous top quark interactions has been investigated [?]. The effective Lagrangian involving anomalous $t\gamma q$ ($q = u, c$) interactions is given by [?].

$$L = -g_e \sum_{q=u,c} Q_q \frac{\kappa_q}{\Lambda} \bar{t} \sigma^{\mu\nu} (f_q + h_q \gamma_5) q A_{\mu\nu} + h.c. \quad (5.9)$$

2054 where $A_{\mu\nu}$ is the usual photon field tensor, $\sigma_{\mu\nu} = \frac{i}{2}(\gamma_\mu\gamma_\nu - \gamma_\nu\gamma_\mu)$, Q_q is the quark charge, in general f_q and
 2055 h_q are complex numbers, g_e is the electromagnetic coupling constant, κ_q is a real and positive anomalous
 2056 FCNC coupling constant and Λ is the new physics scale. The neutral current magnitudes in the Lagrangian
 2057 satisfy $|(f_q)^2 + (h_q)^2| = 1$ for each term. The anomalous decay width can be calculated as

$$\Gamma(t \rightarrow q\gamma) = \left(\frac{\kappa_q}{\Lambda}\right)^2 \frac{2}{9} \alpha_{em} m_t^3 \quad (5.10)$$

2058 Taking $m_t = 173$ GeV and $\alpha_{em} = 0.0079$, the anomalous decay width ≈ 9 MeV for $\kappa_q/\Lambda = 1$ TeV $^{-1}$
 2059 while the SM decay width is about 1.5 GeV.

2060 For numerical calculations anomalous interaction vertices are implemented into the CalcHEP package [?]
 2061 using the CTEQ6M [?] parton distribution functions. The Feynman diagrams for the subprocess $\gamma q \rightarrow W^+ b$,
 2062 where $q = u, c$ are shown in Fig. ?? . The first three diagrams correspond to irreducible backgrounds and the
 2063 last one to the signal. The main background comes from associated production of W boson and the light
 2064 jets.

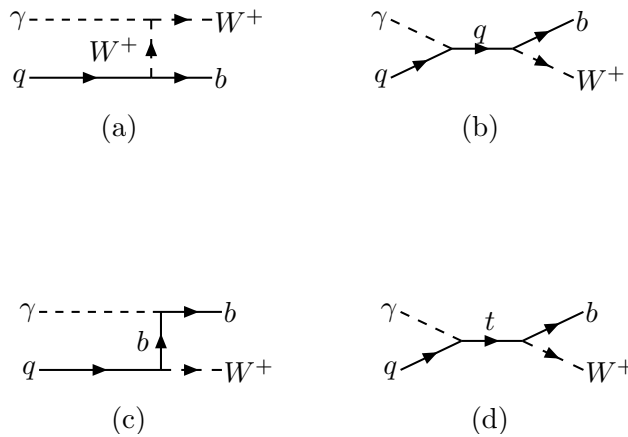


Figure 5.19: Feynman diagrams for $\gamma q \rightarrow W^+ b$, where $q = u, c$.

2065 The differential cross sections for the final state jets are given in Fig. ?? ($\kappa/\Lambda = 0.04$ TeV $^{-1}$) for $E_e = 70$
 2066 GeV and $E_p = 7000$ GeV assuming $\kappa_u = \kappa_c = \kappa$. It is seen that the transverse momentum distribution of
 2067 the signal has a peak around 70 GeV.

2068 Here, b-tagging efficiency is assumed to be 60% and the mistagging factors for light (u, d, s) and c quarks
 2069 are taken as 0.01 and 0.1, respectively. A p_T cut reduce the signal (by $\sim 30\%$ for $p_T > 50$ GeV), whereas
 2070 the background is essentially suppressed (by a factor 4-6) . In order to improve the signal to background
 2071 ratio further, one can apply a cut on the invariant mass of $W + jet$ around top mass. In Table ??, the cross
 2072 sections for signal and background processes are given after having applied both a p_T and an invariant mass
 2073 cuts ($M_{Wb} = 150 - 200$ GeV).

Table 5.3: The cross sections (in pb) according to the p_T cut and invariant mass interval ($M_{Wb} = 150 - 200$ GeV) for the signal and background at γp collider based on the LHeC with $E_e = 70$ GeV and $E_p = 7000$ GeV.

$\kappa/\Lambda = 0.01$ TeV $^{-1}$	$p_T > 20$ GeV	$p_T > 40$ GeV	$p_T > 50$ GeV
Signal	8.86×10^{-3}	7.54×10^{-3}	6.39×10^{-3}
Background: $W^+ b$	1.73×10^{-3}	1.12×10^{-3}	7.69×10^{-4}
Background: $W^+ c$	3.48×10^{-1}	2.30×10^{-1}	1.63×10^{-1}
Background: $W^+ jet$	1.39×10^{-1}	9.11×10^{-2}	6.38×10^{-2}

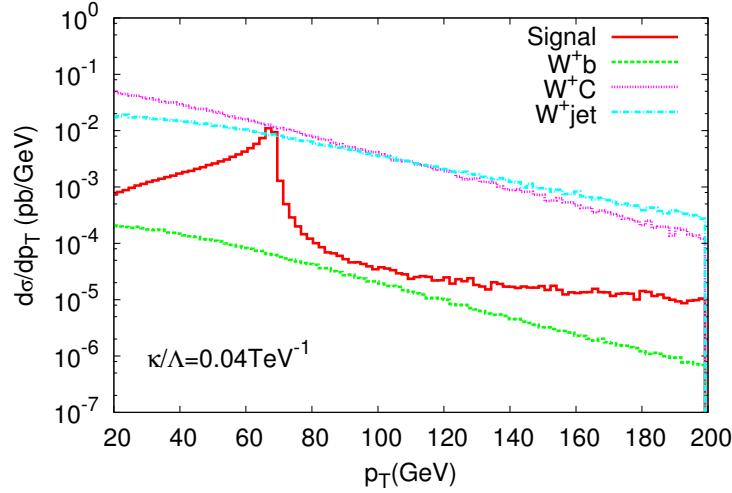


Figure 5.20: The transverse momentum distribution of the final state jet for the signal and background processes. The differential cross section includes the b -tagging efficiency and the rejection factors for the light jets. The center of mass energy $\sqrt{s_{ep}} = 1.4$ TeV and $\kappa/\Lambda = 0.04$ TeV $^{-1}$.

2074 In order to calculate the statistical significance (SS) we use following formula [?] :

$$SS = \sqrt{2 \left[(S + B) \ln\left(1 + \frac{S}{B}\right) - S \right]} \quad (5.11)$$

2075 where S and B are the numbers of signal and background events, respectively. Results are presented in Table
 2076 ?? for different κ/Λ and luminosity values. It is seen that even with 2 fb $^{-1}$ the LHeC based γp collider will
 2077 provide 5σ discovery for $\kappa/\Lambda = 0.02$ TeV $^{-1}$.

Table 5.4: The signal significance (SS) for different values of κ/Λ and integral luminosity for $E_e = 70$ GeV and $E_p = 7000$ GeV (the numbers in parenthesis correspond to $E_e = 140$ GeV).

SS	$L = 2$ fb $^{-1}$	$L = 10$ fb $^{-1}$
$\kappa/\Lambda = 0.01$ TeV $^{-1}$	2.58 (2.88)	5.79 (6.47)
$\kappa/\Lambda = 0.02$ TeV $^{-1}$	5.26 (5.92)	11.78 (13.25)

2078 Up to now, we have assumed $\kappa_u = \kappa_c = \kappa$. However, it would be interesting to analyze the case
 2079 $\kappa_u \neq \kappa_c$. Indeed, at HERA, valence u -quarks dominate whereas at LHeC energies the c -quark and u -quark
 2080 contributions become comparable. Therefore, the sensitivity to κ_c will be enhanced at LHeC comparing to
 2081 HERA. In Fig. ?? contour plots for anomalous couplings in $\kappa_u - \kappa_c$ plane are presented. For this purpose,
 2082 a χ^2 analysis was performed with

$$\chi^2 = \sum_{i=1}^N \left(\frac{\sigma_{S+B}^i - \sigma_B^i}{\Delta\sigma_B^i} \right)^2 \quad (5.12)$$

2083 where σ_B^i is the cross-section for the SM background in the i^{th} bin, including both b -jet and light-jet
 2084 contributions with their corresponding efficiency factors. In the σ_{S+B} calculations, we take into account
 2085 the different values for κ_u and κ_c as well as the signal-background interference. Figs. ??-?? show that the
 2086 sensitivity is enhanced by a factor of 1.5 when the luminosity changes from 2 fb $^{-1}$ to 10 fb $^{-1}$. Concerning the

2087 energy upgrade, increasing electron energy from 70 GeV to 140 GeV results in 20% improvement for κ_c [?].
 2088 Increasing the electron energy further (energy frontier ep collider) does not give an essential improvement in
 2089 the sensitivity to anomalous couplings [?].

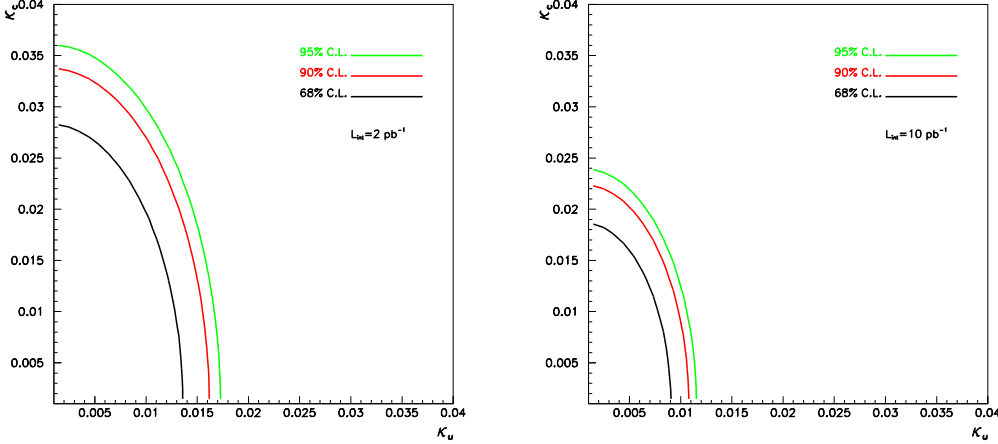


Figure 5.21: Contour plot for the anomalous couplings reachable at the LHeC based γp collider with the center of mass energy $\sqrt{s_{ep}} = 1.4$ TeV and integrated luminosity of $L_{int} = 2$ fb $^{-1}$ (left) or $L_{int} = 10$ fb $^{-1}$ (right)

2090 Table ?? shows that a sensitivity to anomalous coupling κ/Λ down to 0.01 TeV $^{-1}$ could be reached.
 2091 Noting that the value of $\kappa/\Lambda = 0.01$ TeV $^{-1}$ corresponds to $BR(t \rightarrow \gamma u) \approx 2 \times 10^{-6}$ which is two orders
 2092 smaller than the LHC reach with 100 fb $^{-1}$, it is obvious that even an upgraded LHC will not be competitive
 2093 with LHeC based γp collider in the search for anomalous $t\gamma q$ interactions. Different extensions of the SM
 2094 (SUSY, technicolor, little Higgs, extra dimensions etc.) predict branching ratio $BR(t \rightarrow \gamma q) = O(10^{-5})$, hence
 2095 the LHeC will provide an opportunity to probe these models. The top quark could provide very important
 2096 information for the Standard Model extensions due to its large mass close to the electroweak symmetry
 2097 breaking scale.

2098 5.4.3 Excited quarks in γp collisions at LHeC

2099 Excited quarks will have vertices with SM quark and gauge bosons (photon, gluon, Z or W bosons). They
 2100 can be produced at ep and γp colliders via quark photon fusion. Interactions involving excited quark are
 2101 described by the Lagrangian of eq. ?? (where F is now a quark q)

2102 A sizeable f_s coupling would allow for resonant q^* production at the LHC via quark-gluon fusion. In that
 2103 case, the LHC would offer a large discovery potential for excited quarks and would be well suited to study
 2104 the properties and couplings of these new quarks. However, if the coupling of excited quarks to gq happens
 2105 to be suppressed, the LHC would mainly produce q^* via pair-production and would have little sensitivity to
 2106 couplings f/Λ or f'/Λ . Such couplings would be better studied, or probed down to much lower values, via
 2107 single-production of q^* at the LHeC. A study of the LHeC potential for excited quarks is presented in [?].
 2108 An example of the 3σ discovery reach, assuming $f = f' = f_s$ and setting Λ to be equal to the q^* mass, is
 2109 given in Fig. ?. Both decays $q^* \rightarrow q\gamma$ and $q^* \rightarrow qg$ have been considered here.

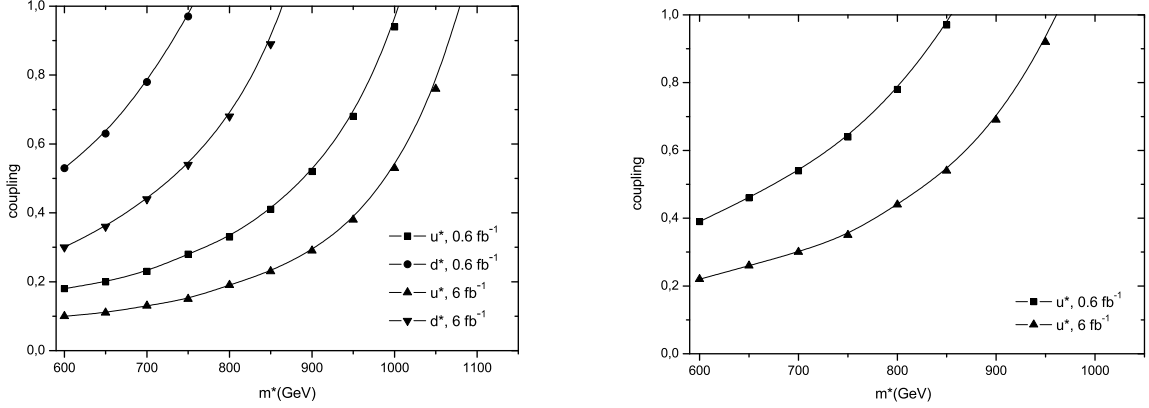


Figure 5.22: Observation reach at 3σ for coupling and excited quark mass at a γp collider with $\sqrt{s} = 1.27$ TeV from an analysis of (left) the jj channel and (right) the γj channel.

2110 5.4.4 Quarks from a fourth generation at LHeC

2111 The case of fourth generation quarks with magnetic FCNC interactions to gauge bosons and standard quarks,

$$\mathcal{L} = \left(\frac{\kappa_\gamma^{q_4 q_i}}{\Lambda} \right) e_q g_e \bar{q}_4 \sigma_{\mu\nu} q_i F^{\mu\nu} + \left(\frac{\kappa_Z^{q_4 q_i}}{2\Lambda} \right) g_Z \bar{q}_4 \sigma_{\mu\nu} q_i Z^{\mu\nu} + \left(\frac{\kappa_g^{q_4 q_i}}{\Lambda} \right) g_s \bar{q}_4 \sigma_{\mu\nu} T^a q_i G_a^{\mu\nu} + h.c. \quad (5.13)$$

2112 is very similar to that of excited quarks. A γp collider based on LHeC would have a better sensitivity than
 2113 LHC to anomalous couplings κ_γ and κ_Z . A detailed study is presented in [?] and example results are shown
 2114 in Fig. ?. These figures also show the clear advantage of a γp collider compared to an ep collider, for the
 2115 study of new physics in γq interactions.

2116 5.4.5 Diquarks at LHeC

2117 The case of diquark production at LHeC has been studied in [?]. The production cross-section can be
 2118 sizeable at a high energy ep machine, especially when operated as a γp collider. The measurement of the
 2119 $\gamma p \rightarrow DQ + X$ cross-section, for a diquark DQ of known mass and known coupling to the diquark pair³
 2120 would provide a measurement of the electric charge of the diquark. It would thus be complementary to
 2121 the pp data, which offer no simple way to access the DQ electric charge. However, the diquark masses and
 2122 couplings that could be accessible at LHeC appear to be already excluded by the recent search for dijet
 2123 resonances at the LHC [?].

2124 5.4.6 Quarks from a fourth generation in Wq interactions

2125 In case fourth generation quarks do not have anomalous interactions as in Eq. ??, they (or vector-like quarks
 2126 coupling to light generations [?, ?]) could be produced in ep collisions by Wq interactions provided that the
 2127 V_{Qq} elements of the extended CKM matrix are not too small, via the usual vector WqQ interactions. An
 2128 example of the sensitivity that could be reached at LHeC is presented in [?], assuming some values for the
 2129 V_{Qq} parameters. Measurements of single Q production at LHeC would provide complementary information
 2130 to the LHC data, that could help in determining the extended CKM matrix.

³The LHC would observe diquark as di-jet resonances, and could easily determine its mass, width and coupling to the quark pair.

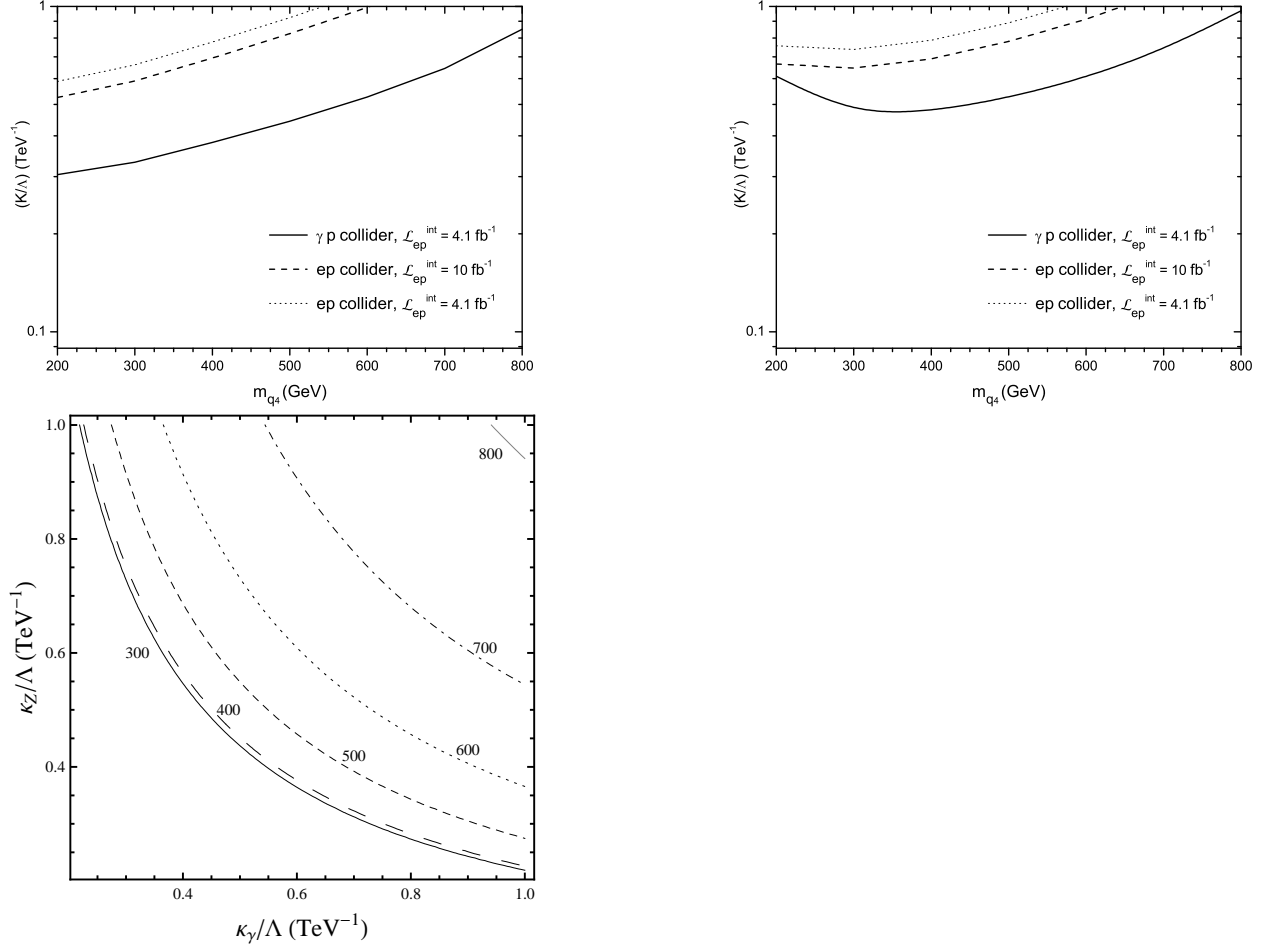


Figure 5.23: The achievable values of the anomalous coupling strength at ep and γp colliders for a) $q_4 \rightarrow \gamma q$ anomalous process and (b) $q_4 \rightarrow Zq$ anomalous process as a function of the q_4 mass; (c) the reachable values of anomalous photon and Z couplings with $L_{int} = 4.1 \text{ fb}^{-1}$.

2131 5.5 Sensitivity to a Higgs boson

2132 Understanding the mechanism of electroweak symmetry breaking is a key goal of the LHC physics programme.
 2133 In the SM, the symmetry breaking is realized via a scalar field (the Higgs field) which, at the minimum of the
 2134 potential, develops a non-zero vacuum expectation value. The breaking of the $SU(2)_L \times U(1)_Y$ symmetry
 2135 gives mass to the electroweak gauge bosons via the Higgs mechanism while the fermions obtain their mass
 2136 via Yukawa couplings with the Higgs field. The LHC experiments should be able to discover a Higgs boson
 2137 within the full allowable mass range, with an integrated luminosity of less than 10 fb^{-1} . Following its
 2138 discovery, it will be crucial to measure the couplings of this Higgs boson to the SM particles, in particular
 2139 to the fermions, in order to:

- 2140 • establish that the Higgs field is indeed accounting for the fermion masses, via Yukawa couplings $y_f H f \bar{f}$;
- 2141 • disentangle between the SM and (some of) its extensions. For example, despite the richer content of
 2142 the Higgs sector in the Minimal Supersymmetric Standard Model, only the light SUSY Higgs boson h
 2143 would be observable at the LHC in certain regions of parameter space. Its properties are very similar
 2144 to those of the SM Higgs H , and precise measurements of ratios $BR(\Phi \rightarrow VV)/BR(\Phi \rightarrow ff)$ will be
 2145 essential in determining whether or not the observed boson, Φ , is the SM Higgs scalar.

2146 Electroweak precision measurements strongly suggest that the SM Higgs boson should be light, in which case
 2147 it would decay into a $b\bar{b}$ pair with a branching ratio of $\sim 70\%$, but a measurement of the $Hb\bar{b}$ coupling will
 2148 be very challenging at the LHC [?, ?, ?]. Indeed, the observation of $H \rightarrow b\bar{b}$ in the inclusive production mode
 2149 is made very difficult by the huge QCD background, although a possible search channel would be associated
 2150 WH and ZH production, with highly boosted Higgs, leading to a high mass jet with substructure [?].
 2151 The observability of the signal in the $t\bar{t}H$ production mode also suffers from a large background, including
 2152 background of combinatorics origin, and from experimental systematic uncertainties.

2153 The signal $H \rightarrow b\bar{b}$ may be observed in the exclusive production mode, thanks to the much cleaner
 2154 environment in a diffractive process. However, the production cross-section in this mode suffers from large
 2155 theoretical uncertainties, such that this measurement, if feasible at all, would not translate into a precise
 2156 measurement of the $Hb\bar{b}$ coupling.

2157 At the LHeC, a light Higgs boson could be produced via WW or ZZ fusion with a sizeable cross-section.
 2158 This section focusses on the observability of the signal $ep \rightarrow H + X \rightarrow b\bar{b} + X$ at LHeC, which may be the
 2159 first observation of the $H \rightarrow b\bar{b}$ decay. A recent similar study can be found in [?].

2160 5.5.1 Higgs production at LHeC

2161 In ep collisions, the Higgs boson could be produced in neutral current (NC) interactions via the ZZH
 2162 coupling, and in charged current (CC) interactions via the WWH coupling. The corresponding diagrams
 2163 are shown in Fig. ??, and the production cross-sections, as a function of the Higgs mass, is displayed in
 2164 Fig. ?. The WWH production largely dominates the total cross-section. As is the case for the inclusive
 2165 CC DIS interactions, the cross-section is much larger in e^-p collisions than in e^+p collisions, due to the
 2166 more favorable density of the valence quark that is involved (u in e^-p , d in e^+p), and to the more favorable
 2167 helicity factors. Table ?? shows the Higgs production cross-section (at leading order) via CC interactions in
 2168 e^-p collisions, for various values of the Higgs mass and three example values of the electron beam energy.
 2169 The scale dependency of these leading order estimate is of $\mathcal{O}(10\%)$. Next-to-leading order corrections were
 2170 calculated in [?, ?]. They are small, but can affect within $\mathcal{O}(20\%)$ the shape of some kinematic distributions.

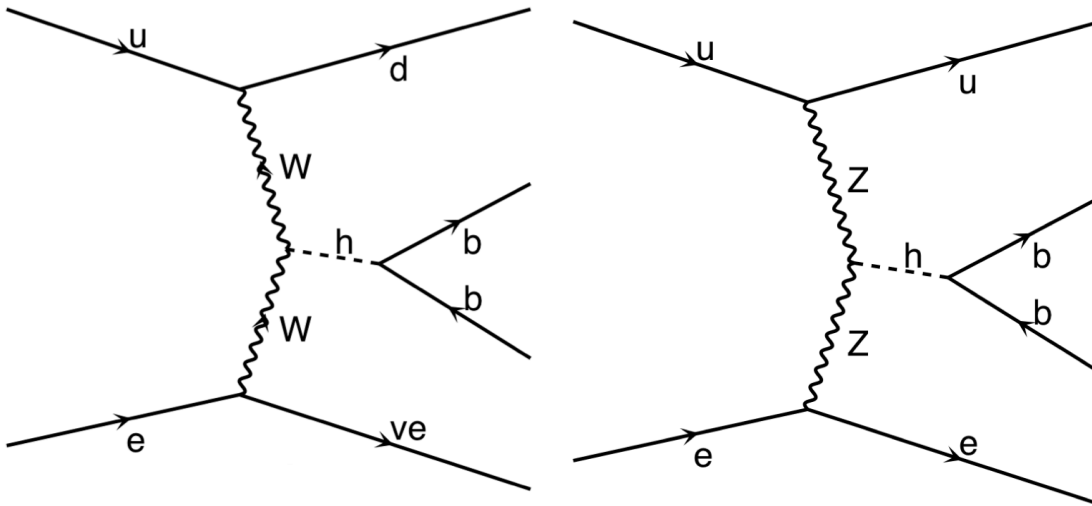


Figure 5.24: Feynman diagrams for CC(left) and NC(right) Higgs production at the LHeC.

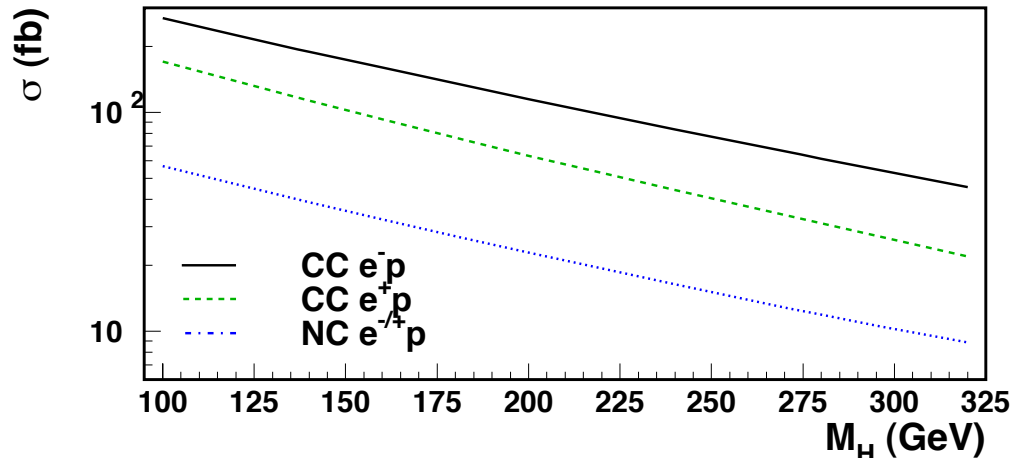


Figure 5.25: Production cross-section of a SM Higgs boson in ep collision with $E_e=150$ GeV and $E_p=7$ TeV, as a function of the Higgs mass.

M_H in GeV :	100	120	160	200	240	280
$E_e = 50$ GeV	102	81	50	32	20	12
$E_e = 100$ GeV	201	165	113	79	55	39
$E_e = 150$ GeV	286	239	170	123	90	67

Table 5.5: Production cross-section in fb of a SM Higgs boson via charged current interactions in e^-p collisions, for three example values of the electron beam energy.

2171 5.5.2 Observability of the signal

2172 The dominating source of background at large missing transverse energy is coming from multi-jet production
 2173 in CC DIS interactions. In particular, a good rejection of the background coming from single top production
 2174 ($e^-b \rightarrow \nu t$), where the top decays hadronically, puts severe constraints on the acceptance and the resolution
 2175 of the detector, as will be seen below. The background due to multijet production in NC interactions is also
 2176 considered.

2177 MadGraph [?] has been used to generate SM Higgs production, CC and NC DIS background events.
 2178 Calculations of cross-sections and generation of final states of outgoing particles are performed by MadGraph,
 2179 given the beam parameters, considering all possible tree-level Feynman diagrams in the SM. In the case of
 2180 NC, since the cross section is very high, diverging at low scattering angle, only processes producing two or
 2181 more b quarks were generated in order to have sufficient MC statistics. By artificially increasing the mistag
 2182 probability, it was possible to verify that, after the selection, essentially all the remaining NC background is
 2183 indeed due to events with two truly b-quark jets in the final state. Fragmentation and hadronization processes
 2184 were simulated by PYTHIA [?] with custom modifications to apply for ep collisions. Finally, particles were
 2185 passed through a generic detector using the PGS [?] fast detector simulation tool. We assumed tracking
 2186 coverage of $|\eta| < 3$ and calorimeter coverage of $|\eta| < 5$ with electromagnetic calorimeter resolution of
 2187 $5\%/\sqrt{E(\text{GeV})}$ (plus 1% of constant term) and hadronic calorimeter resolution of $60\%/\sqrt{E(\text{GeV})}$. Jets
 2188 were reconstructed by a cone algorithm with a cone size of $\Delta R = 0.7$. The efficiency of b-flavor tagging was
 2189 assumed to be 60% and flat within the calorimeter coverage, whereas mistagging probabilities of 10% and
 2190 1% for charm-quark jets and for light-quark jets, respectively, were taken into account.

2191 We set 150 GeV of electron beam energy with 7 TeV of proton beam energy as the reference beam

2192 configuration and assumed 120 GeV of SM Higgs boson mass in the MC simulation study. The results were
 2193 compared with those with a different beam energy and Higgs mass.

2194 The following selection criteria were applied, based on observable variables generated by the PGS detector
 2195 simulation, to distinguish $H \rightarrow b\bar{b}$ from the CC and NC DIS backgrounds.

2196 • **cut (1): Primary cuts**

- 2197 – Exclude electron-tagged events
- 2198 – $E_{T,miss} > 20$ GeV
- 2199 – $N_{jet}(P_{T,jet} > 20 \text{ GeV}) \geq 3$
- 2200 – $E_{T,total} > 100$ GeV
- 2201 – $y_{JB} < 0.9$, where $y_{JB} = \Sigma(E - p_z)/2E_e$
- 2202 – $Q_{JB}^2 > 400$ GeV, where $Q_{JB}^2 = E_{T,miss}^2/(1 - y_{JB})$

2203 • **cut (2): b-tag requirement**

- 2204 – $N_{b-jet}(P_{T,jet} > 20 \text{ GeV}) \geq 2$, where b-jet means a b-tagged jet

2205 • **cut (3): Higgs invariant mass cut**

- 2206 – $90 < M_H < 120$ GeV; due to the energy carried by the neutrino from b decays, the mass peaks
 2207 are slightly lower than the true Higgs mass

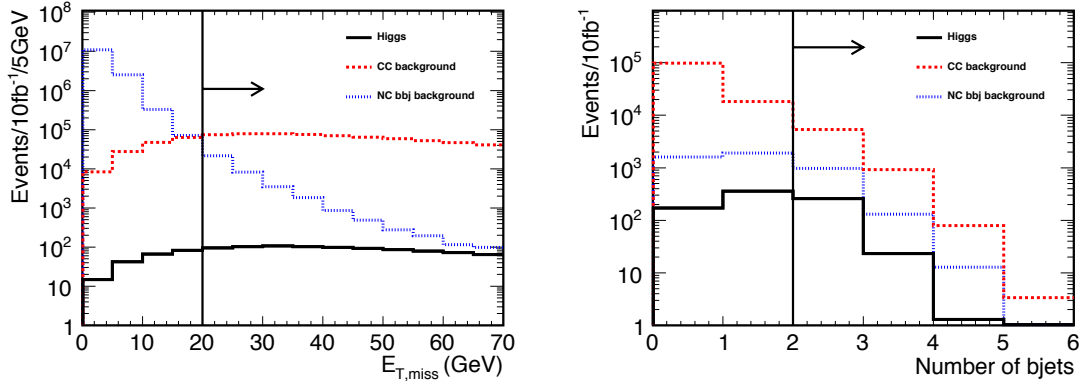


Figure 5.26: Missing E_T (left) and number of b-tagged jets (right). Solid (black), dashed (red) and dotted (blue) histograms show $H \rightarrow b\bar{b}$, CC and NC DIS background, respectively. The right plot is for events passing cut (1) in the text.

2208 Fig. ?? shows the missing E_T and number of b-tagged jets for $H \rightarrow b\bar{b}$ events together with the CC and
 2209 NC DIS background. The NC background is strongly suppressed by the missing E_T cut and electron-tag
 2210 requirement. We required at least two b-tagged jets, and reconstructed the Higgs invariant mass using the
 2211 two b-tagged jets with lowest and second lowest η . After cuts (1) + (2) + (3) were applied, 44.4% of the
 2212 remaining CC background was due to single top production. The following cuts were further applied.

- 2213 • **cut (4): rejection of single top production** Single top events result in a final state with two b-jets
 2214 and a W decaying into two light-quark jets. The following cuts were found to be efficient in suppressing
 2215 this background.

2216
2217
2218
2219
2220

- $M_{jjj,top} > 250$ GeV, where the three-jet invariant mass ($M_{jjj,top}$) was reconstructed from two b-jets with the lowest η and any third jet with the lowest η regardless of b-tag
- $M_{jj,W} > 130$ GeV, where di-jet invariant mass ($M_{jj,W}$) was reconstructed from one b-jet with the lowest η and any second jet with the lowest η regardless of b-tag but excluding the second lowest η b-jet

2221
2222

• cut (5): forward jet tagging

- $\eta_{jet} > 2$ for the lowest- η jet excluding the two b -jets

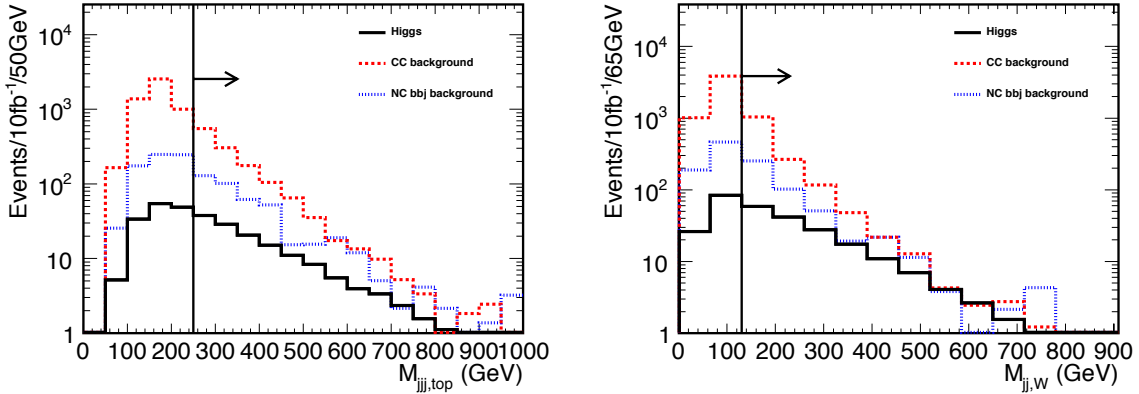


Figure 5.27: Three-jet (left) and di-jet (right) invariant masses. Solid (black), dashed (red) and dotted (blue) histograms show $H \rightarrow b\bar{b}$, CC and NC DIS background, respectively.

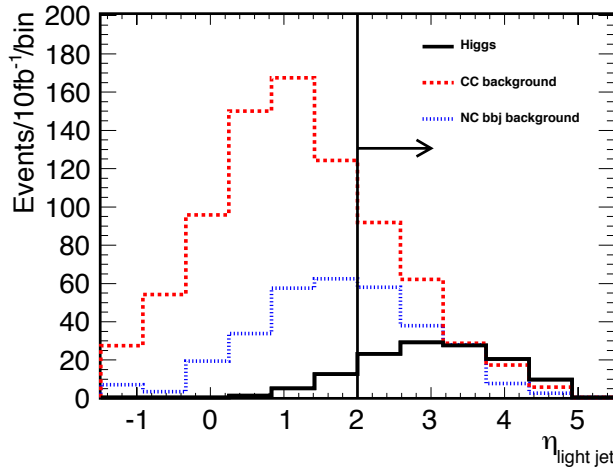


Figure 5.28: η_{jet} distribution for the lowest- η jet excluding the two b -tagged jets. Solid (black), dashed (red) and dotted (blue) histograms show $H \rightarrow b\bar{b}$, CC and NC DIS background, respectively.

2223
2224

Fig. ?? shows the reconstructed three-jet ($M_{jjj,top}$) and di-jet ($M_{jj,W}$) invariant masses after cuts (1) and (2) are applied. It is seen that, for CC background, the former peaks at the top mass and the latter peaks

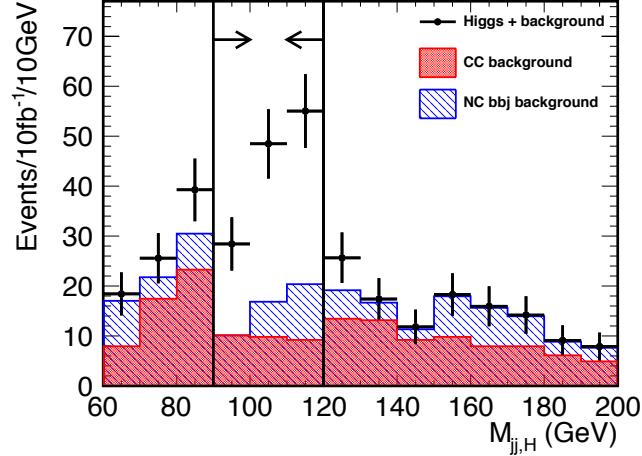


Figure 5.29: Reconstructed invariant Higgs mass after all selection criteria, except for the Higgs mass cut, have been applied. Points with error bars (black) show the $H \rightarrow b\bar{b}$ signal added to the CC (red histogram) and NC (hatched blue histogram) DIS background for an integrated luminosity of 10fb^{-1} .

at the W mass. The last cut is motivated by the fact that the jet from light quark participating in the CC reaction for the signal is kinematically boosted to forward rapidity (in the proton beam direction), as shown in Fig. ??.

Fig. ?? shows the reconstructed Higgs mass distribution for an integrated luminosity of 10fb^{-1} , after all selection criteria except for the Higgs mass cut have been applied. The results are summarized in Table ?. After the selection, 85 $H \rightarrow b\bar{b}$ events are expected for 10fb^{-1} luminosity with a 150 GeV electron beam. The signal to background ratio is 1.79 and the significance of the signal $S/\sqrt{N} = 12.3$. For a higher Higgs mass, $m_H=150$ GeV, the production cross section decreases and the $b\bar{b}$ branching ratio also decreases. The expected number of signal events becomes 25 and S/N and S/\sqrt{N} are 0.52 and 3.60, respectively. On the other hand, with 60 GeV electron beam and five times larger luminosity (50fb^{-1}), for 120 GeV Higgs, 124 $H \rightarrow b\bar{b}$ events are expected after the same cuts have been applied. Considering the CC and NC DIS background, S/N and S/\sqrt{N} are 1.05 and 11.4, respectively.

	Higgs production	CC DIS	NC bbj	S/N	S/\sqrt{N}
cut (1)	816	123000	4630	6.38×10^{-3}	2.28
cut (1) + (2) + (3)	178	1620	179	9.92×10^{-2}	4.21
All cuts	84.6	29.1	18.3	1.79	12.3

Table 5.6: Expected $H \rightarrow b\bar{b}$ signal and background events with 150 GeV electron beam for an integrated luminosity of 10fb^{-1} . Contents of the cuts are listed in text.

The results shown here are subject to large uncertainties. First, as mentioned above, the very large NC background cross section at forward scattering angles makes it impossible to simulate a sufficient number of events to limit the Monte Carlo statistical uncertainty. It is estimated that the background evaluation, with the above method where only events with at least two b quarks were simulated, has an uncertainty of about a factor 3. With a full simulation, it can be expected to be negligible when the true measurement is realized. Neglecting, therefore, this source of uncertainty, the systematic errors which will dominate are expected to be the theoretical estimates of signals and backgrounds and instrumental effects: efficiency and

2244 acceptance of lepton and jet reconstruction, b-tagging and mistagging probabilities. They are difficult to
 2245 estimate without real data and a real detector. The statistical uncertainty on the cross section can, however,
 2246 be estimated: 15% for the reference case of 150 GeV \times 7 TeV beams and a Higgs of mass 120 GeV. This
 2247 represents a direct measure of the statistical uncertainty on the product of the squares of couplings Hbb and
 2248 HWW .

2249 5.5.3 Probing Anomalous HWW Couplings at the LHeC

2250 The HWW vertex is an excellent handle on the quartic self-coupling of the scalar doublet. Its measurement
 2251 provides a direct insight into the nature of electroweak symmetry-breaking. Parametrising the $H(k) -$
 2252 $W^+(p) - W^-(q)$ vertex in the form $i\Gamma^{\mu\nu}(p, q) \epsilon_\mu(p) \epsilon_\nu^*(q)$, any deviations from the simple SM formula
 2253 $\Gamma_{(\text{SM})}^{\mu\nu}(p, q) = gM_W \lambda^{\mu\nu}$ at a level incompatible with SM loop corrections would immediately indicate the
 2254 presence of new physics. Following Ref. [?], we can parametrize these deviations using two dimension-5
 2255 operators

$$\Gamma_{\mu\nu}^{(\text{BSM})}(p, q) = \frac{-g}{M_W} [\lambda(p, q) \lambda_{\mu\nu} - p_\nu q_\mu] + i \lambda' \epsilon_{\mu\nu\rho\sigma} p^\rho q^\sigma \quad (5.14)$$

2256 where λ and λ' are, respectively, effective coupling strengths for the CP -conserving and the CP -violating
 2257 parts.

2258 An ep collider has a unique advantage in the fact that the HWW vertex gives rise to the process
 2259 $e + p \rightarrow \nu_e + X + H(b\bar{b})$ though the single Feynman diagram shown in Figure ??(left). The final state
 2260 has, therefore, missing transverse energy (MET) and three jets J_1, J_2 and J_3 , of which two (say J_2 and
 2261 J_3) are tagged as b -jets. It can be shown [?] that in the limit when there is practically no energy transfer
 2262 to the W bosons and the final states are very forward, the CP -conserving (CP -violating) coupling λ (λ')
 2263 contributes to the matrix element for this process a term of the form which goes through zero when the
 2264 missing transverse momentum is perpendicular to the p_T of the jet:

$$\mathcal{M} \sim +\lambda \vec{p}_T \cdot \vec{p}_T^{J_1} \quad \widetilde{\mathcal{M}} \sim -\lambda' \vec{p}_T \cdot \vec{p}_T^{J_1} . \quad (5.15)$$

2265 This explains the general trend illustrated in Figure ??, for an exact calculation of the $2 \rightarrow 3$ process
 2266 $eq \rightarrow \nu_e q' H$ at the parton level, with parton density functions from the CTEQ-6L1 set [?]. In the case
 2267 considered, 140 GeV electrons collide with 7 TeV protons and the Higgs boson mass is set to 120 GeV.

2268 A detailed simulation of the charged current process was discussed above in Sect. ?. Here, the analysis
 2269 is based on the kinematic cuts and efficiencies adopted in Ref. [?]. The azimuthal distribution has been
 2270 simulated in 10 bins, each of width $\pi/5$, and the signal and SM backgrounds have been calculated in each
 2271 bin using the same formulae used to create Figure ??, followed by a detailed simulation of fragmentation, jet
 2272 identification and detector effects. Assuming statistical errors dependent on the integrated luminosity L , we
 2273 then determine the sensitivity, for a given L , of the experiment to λ, λ' by making a log-likelihood analysis.
 2274 Our results are exhibited in Figure ??, where we present 95% exclusion plots for the λ and λ' couplings as a
 2275 function of L . It is clear from this figure that by the time the LHeC has collected 10 fb^{-1} of data, we will be
 2276 able to exclude the anomalous couplings to the level of 0.3 or lower. The experimental set-up is somewhat
 2277 more sensitive to the CP -even coupling, as evidenced by the narrower inaccessible region indicated on the
 2278 left panel.

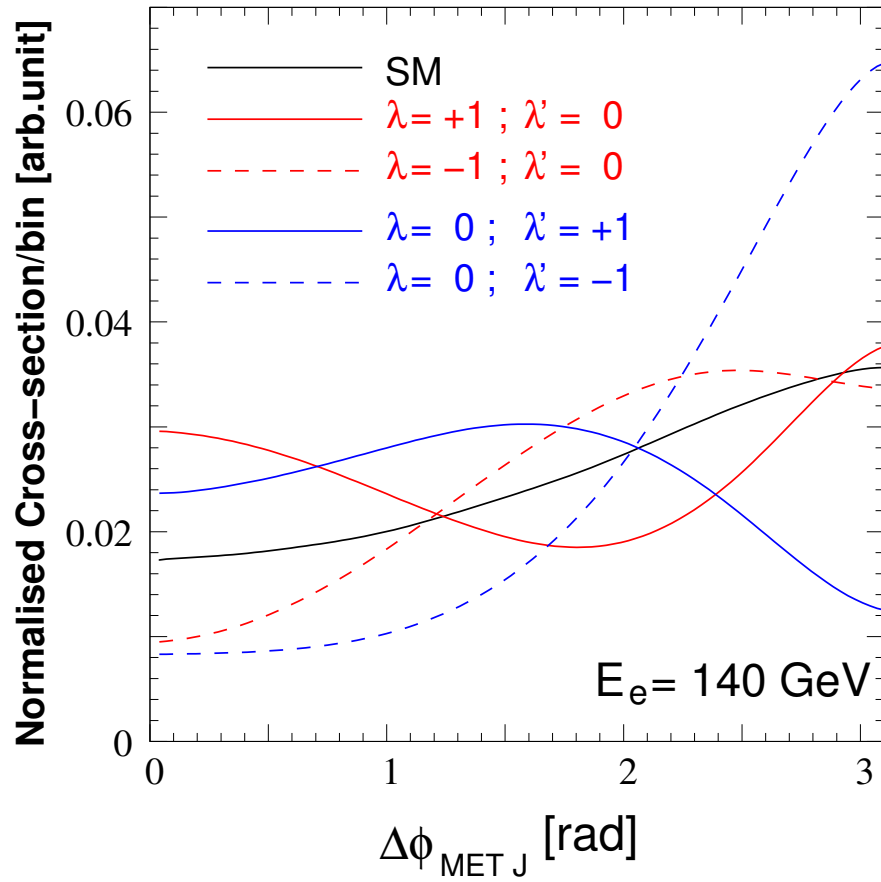


Figure 5.30: Illustrating the SM distribution in azimuthal angle and deviations therefrom which are due to anomalous HWW couplings.

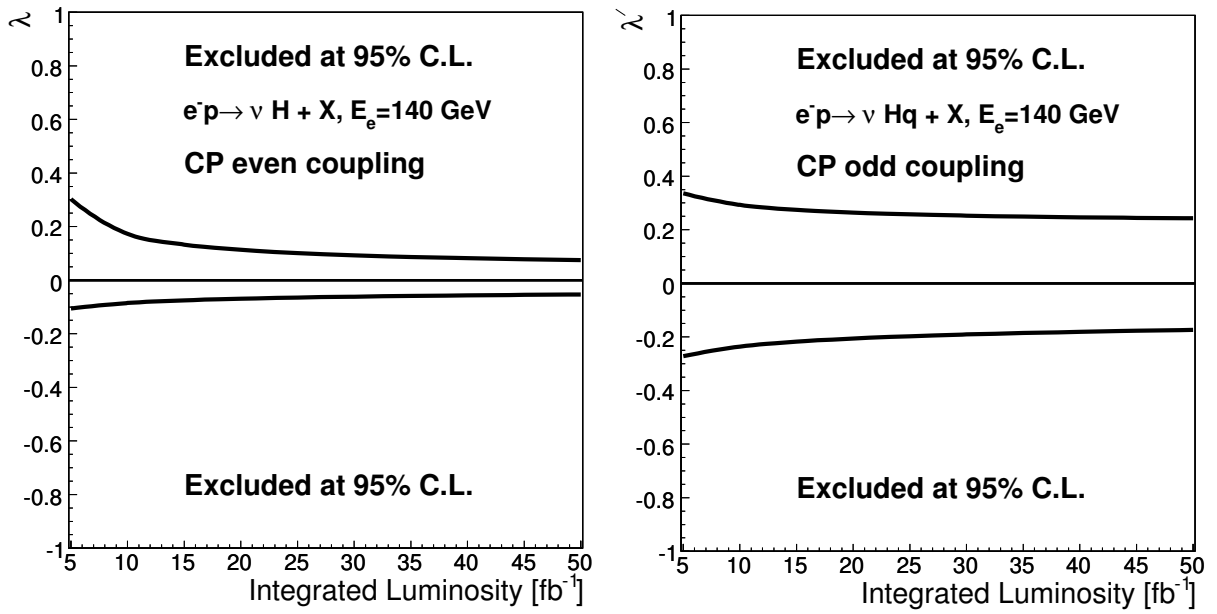


Figure 5.31: Exclusion plots obtainable by a study of the azimuthal angle distributions at the LHeC for the CP -even coupling λ and the CP -odd coupling λ' . Note that this study is for $M_H = 120$ GeV.

Chapter 6

Physics at High Parton Densities

6.1 Physics at small x

6.1.1 Unitarity and QCD

Introduction

QCD [?] is the fundamental theory of the strong interaction that has been extensively tested in the last 38 years. Still, many open questions remain to be solved. One of them, which can be addressed at high energies, is the transition between the regimes in which the strong coupling constant is either large or small - the so-called *strong and weak coupling* regimes. In the former, standard perturbation theory techniques are not applicable and exact analytical results are not yet within the reach of current knowledge. Therefore various models, *effective* theories, whose parameters cannot yet be derived from QCD, or numerical lattice computations, have to be employed. One example of such an effective theory which has been used through the years and actually predates QCD, is the Regge-Gribov [?, ?, ?] theory.

The weak coupling regime has been well tested in high-energy experiments through a selected class of measurements - often referred to as *hard processes* - where weak and strong coupling effects can be cleanly separated. There exists a well-defined theoretical concept which has been derived from first principles and probed in the weak coupling regime, namely the collinear factorization theorem (for a comprehensive review see [?] and references therein). It allows a separation of the cross sections involving hadrons into: (i) parts that can be computed within perturbation theory, corresponding to the cross section for parton scattering, and (ii) pieces which cannot be calculated using weak coupling techniques, but whose evolution is still perturbative. The latter are universal, process-independent distributions that either characterize the partonic content of the hadron - *parton densities* on which we will mainly focus the discussion - or the eventual projection of partons onto hadrons. Together with their corresponding (DGLAP) linear evolution equations [?, ?, ?], they have been used to describe experimental data to high accuracy. Examples include total DIS cross sections, the production of jets with large transverse momenta and final states with heavy quarks.

In recent years high-energy experiments have become sensitive to kinematic regions in which the coupling is small but the factorization assumption may no longer be valid. As an example, several HERA DIS measurements at small longitudinal momentum fractions x where parton densities are large, indicate deviations from the behavior expected within the standard collinear factorization. Similarly, hadronic or nuclear collisions involving partons with small x may also show such deviations. At the same time, in these small- x regions the cross sections grow rapidly, so contributions from such regions dominate hadronic cross sections in sufficiently high energy scattering. Experiments sensitive to this kinematic region thus provide a way to test QCD in the new regime where the parton densities become very large and novel effects are expected. We will refer to this region as the high parton density domain.

From a theoretical viewpoint, this situation offers both opportunities and challenges. The fact that, at

2315 small- x , there is no abrupt transition between the dilute and dense regimes, allows the use of techniques
 2316 which, while still being weak coupling, go beyond those used in the dilute limit. The usual parton multipli-
 2317 cation processes have to be supplemented by processes in which partons recombine - thus adding non-linear
 2318 terms to the evolution equations [?]. There are deep theoretical questions arising in this new dense par-
 2319 tonic regime of QCD. At high energies the scattering amplitudes are close to the unitarity limit, and one
 2320 expects that unitarity will be preserved by the taming of parton densities due to recombination effects -
 2321 this phenomenon is generically referred to as *saturation*. Thus, in the weak coupling limit the physics re-
 2322 sponsible for satisfying unitarity in QCD is expected to be describable in partonic language. Theoretical
 2323 calculations [?, ?, ?, ?] in high-energy QCD justify these generic expectations. Furthermore, the experi-
 2324 mental exploration of this transition region where the standard perturbative description based on collinear
 2325 factorization and linear evolution equations requires large corrections, provides new possibilities of further
 2326 understanding the strong coupling regime.

2327 Deep inelastic lepton-hadron scattering has already been shown to address these questions in the most
 2328 efficient manner. It provides the cleanest way of measuring the parton densities, including the small- x region
 2329 in which, as indicated above, the border between the dilute and dense regimes of QCD should occur within
 2330 the weak coupling region where calculations can be done. Approaching this transition region from the dilute
 2331 side by decreasing x or by increasing the number of nucleons in the target, one should observe features which
 2332 cannot be understood within the framework of linear QCD evolution equations but, using more elaborate
 2333 tools (non-linear evolution equations) can still be analyzed in terms of weak coupling techniques. In fact,
 2334 within the standard framework of the leading-twist linear QCD evolution equations (DGLAP) the parton
 2335 densities are predicted to rise at small x , and this rise has been seen very clearly at HERA. However, unitarity
 2336 prevents such a rise from continuing indefinitely, leading to saturation of gluon densities. In hadron-hadron
 2337 scattering it is unitarity which limits the growth of the total cross sections as a function of energy: according
 2338 to Froissart and Martin [?, ?]

$$\sigma_{\text{tot}} \leq \text{const.} \ln^2 s/s_0 , \quad (6.1)$$

2339 where s_0 is a typical hadronic scale. This bound comes from two fundamental assumptions. The first is that
 2340 the amplitude for the scattering at fixed value of impact parameter is bounded by unity and the second is
 2341 the finite range of the strong interaction. The bound on the amplitude has a simple physical interpretation
 2342 that the probability for the interaction becomes very high, so the target (or more precisely the interaction
 2343 region) is completely absorptive. This situation is usually referred to as a *black disk* regime. The description
 2344 of this regime is very challenging theoretically and it is expected that new phenomena will occur which are
 2345 direct manifestations of a new state in QCD which is characterized by a high parton density. The LHeC will
 2346 uniquely offer the possibility of exploring the transition towards this new state of dense QCD matter, as it
 2347 can pursue a two-pronged approach: high center-of-mass energy, extending the kinematic range to lower x ,
 2348 and the possibility of deep inelastic scattering off heavy nuclei.

2349 In the rest of this section we will present the different approaches that are currently under discussion to
 2350 describe the high-energy regime of QCD. We will recall the ideas that lead from linear evolution equations
 2351 to non-linear ones. On the former, we will discuss both cases in which the evolution equations are computed
 2352 within fixed-order perturbation theory (the DGLAP evolution equations) and where they include some kind of
 2353 resummation - thus going beyond any fixed order in the perturbative expansion in the QCD coupling constant.
 2354 The most famous example is the Balitsky-Fadin-Kuraev-Lipatov (BFKL) equation [?, ?]. Concerning the
 2355 latter, non-linear evolution leads to the phenomenon of saturation of partonic densities in the hadron or
 2356 nucleus. We will briefly review the realizations of saturation of parton densities both at strong coupling and,
 2357 mainly, at weak coupling. We will end by discussing the importance of diffractive observables and of the use
 2358 of nuclear targets for the investigation of the small- x behavior of the hadron or nucleus wave function.

2359 From DGLAP to non-linear evolution equations in QCD: saturation

2360 In DIS the structure function $F_2(x, Q^2)$ is proportional to the total cross section σ_{tot} for the scattering of a
 2361 virtual photon on a hadron h , $\gamma^* h \rightarrow X$. The growth of F_2 at small x translates into the rise of σ_{tot} as a
 2362 function of the energy of the virtual photon-hadron system. Although the Froissart-Martin bound, derived

for hadron-hadron scattering, cannot be applied to a process involving a virtual photon, direct calculations based on the evaluation of the QCD diagrams demonstrate unambiguously that, at small x , large corrections exist and need to be resummed. These corrections suppress the leading-twist results and there is no doubt that, for F_2 , the rise with $1/x$ predicted by DGLAP is modified by contributions which are not included in the framework of leading-twist linear evolution equations. The corrections which become numerically important in the small- x limit are also important for the restoration of the unitarity bound. As a result of these modifications parton saturation is reached for sufficiently large energies or small values of Bjorken- x .

In deep inelastic electron-proton scattering, the virtual photon emitted by the incoming electron interacts with partons inside the proton whose properties are specified by the kinematics of the photon. In particular, the transverse size of the partons is (roughly) inversely proportional to the square root of the virtuality of the photon, $\langle r_T^2 \rangle \sim 1/Q^2$. The deep inelastic cross section, parametrized through parton densities, thus counts the numbers of quarks and gluons per unit of phase space. For sufficiently large photon virtualities Q^2 and not too small x , the improved QCD parton model works well because the partons forming the hadron, on the distance scale defined by the small photon, are in a dilute regime, and they interact only weakly. This is a direct consequence of the property of asymptotic freedom, which makes the strong coupling constant small. This diluteness condition is not satisfied if the density of partons increases. This happens if either the number of partons increases (large structure function) or the interaction between the partons becomes strong (large α_s). The former situation is realized at small x , the latter for small photon virtuality Q^2 which sets the scale of the strong coupling $\alpha_s(Q^2)$. This simple qualitative argument shows that corrections to the standard QCD parton picture can be described in terms of quarks and gluons and their interactions as long as Q^2 is not too small ($\alpha_s(Q^2) \ll 1$) and the gluon density is large (small x). Combining these two conditions one arrives at the picture shown in Fig. ???: there is an approximately diagonal line in the $\ln Q^2 - \ln 1/x$ plane below which the parton distributions are dilute, and the standard QCD parton picture applies. In this regime linear evolution equations provide the correct description of parton dynamics. In the vicinity of the line, non-linear QCD corrections become important, and above the line partons are in a high-density state. Well above the line, interactions become strong, and standard perturbation theory is not valid. The division between the two regimes is usually defined in terms of a saturation line, which is specified by a dynamically generated saturation scale, growing with decreasing x . Within this picture one easily understands which type of corrections can be expected. Once the density of gluons increases sufficiently, it becomes probable that, prior to their interaction with the photon, gluons undergo recombination processes.

Saturation in perturbative QCD

While unitarity is an unavoidable feature of any quantum field theory, the microscopic dynamics which lead to it in QCD are not very well understood. There are several proposals to implement unitarity in strong interactions, which can be roughly classified into those which use non-perturbative models and those based on perturbative QCD calculations.

The usual non-perturbative framework to implement unitarity are Regge-Gribov based models [?, ?, ?]. Though they are quite successful in describing existing data on inclusive and diffractive ep and eA scattering (see e.g. [?, ?] and references therein), they lack theoretical foundations within QCD.

On the other hand, attempts have been going on for the last 30 years to implement parton rescattering or recombination¹ in perturbative QCD in order to describe its high-energy behaviour. In the pioneering work in [?, ?], a non-linear evolution equation in $\ln Q^2$ was proposed to provide the first correction to the linear equations. A non-linear term appeared, which was proportional to the local density of color charges seen by the probe (the virtual photon).

An alternative, independent approach was developed in [?], where the amplitudes for diffractive processes in the triple Regge limit were calculated. This resulted in the extraction of the triple Pomeron vertex in QCD at small x , which is responsible for the non-linear term in the evolution equations.

Later on these ideas were developed to include all corrections enhanced by the local density, to constitute what is called the Color Glass Condensate (CGC) [?, ?, ?, ?, ?, ?, ?, ?, ?, ?] (see also the most recent

¹Note that the rescattering and recombination concepts correspond to the same physical mechanism viewed in the rest frame and the infinite momentum frame of the hadron, respectively.

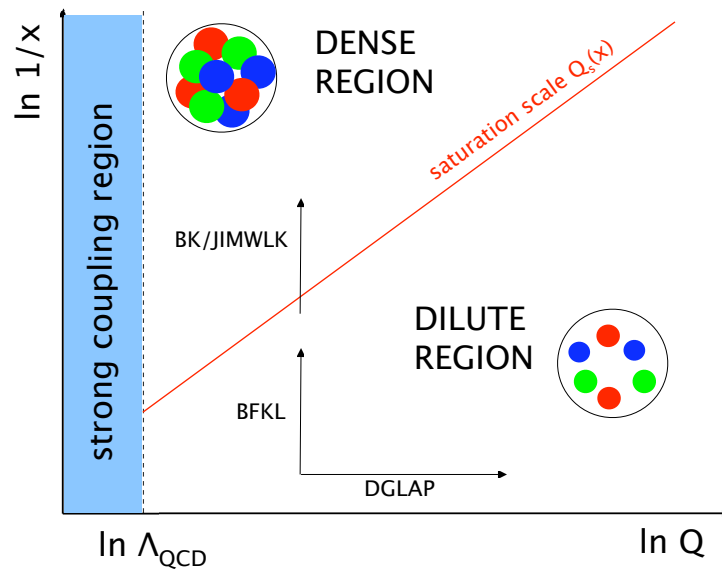


Figure 6.1: Schematic view of the different regions for the parton densities in the $\ln Q^2 - \ln 1/x$ plane. See the text for comments.

2411 developments in [?, ?, ?, ?]). The CGC provides a non-perturbative, but weak-coupling, realization of the
 2412 parton saturation ideas within QCD. The linear limit of the basic CGC equation is the BFKL equation,
 2413 which is the generally accepted linear evolution equation for the high-energy limit. As illustrated in Fig.
 2414 ??, the evolution in the $\ln Q^2 - \ln 1/x$ plane is driven by both linear equations: along $\ln Q^2$ for DGLAP and
 2415 along $\ln 1/x$ for BFKL.

2416 The basic framework in which saturation ideas are discussed is illustrated in Fig. ?. One is considering
 2417 the hadron wave function at high energy. Its partonic components can be separated into those with a
 2418 large momentum fraction x and those with small x . The large- x components are dilute and provide color
 2419 sources for the corresponding small- x components. Due to multiple splittings of the small- x gluons, a dense
 2420 system is eventually formed. One can then construct within this formalism an evolution equation for the
 2421 gluon correlators in the hadron wave function which is a renormalization group equation with respect to the
 2422 rapidity separating large- and small- x partons. This renormalization procedure assumes perturbative gluon
 2423 emissions from the large- x partons which imply a redefinition of the source at each step in rapidity.

2424 The mean field version of the CGC, the Balitsky-Kovchegov (BK) equation [?, ?], provides a non-linear
 2425 evolution equation for unintegrated gluon densities. It turns out that the BK approach results in a gluon
 2426 density which, for a fixed resolution of the probe, is saturated for small longitudinal momentum fractions
 2427 x , whereas at large values of x , the non-linear term is negligible. The separation between these two limits
 2428 is given by a dynamically generated saturation momentum $Q_s(x)$ which increases with decreasing x (c.f.
 2429 figure ??), and therefore saturation is determined by the condition $Q_s(x) > Q$. Then, for large energies or
 2430 small x , the system is in a dense regime of high gluon fields (thus non-perturbative) but the typical gluon
 2431 momentum, $\sim Q_s$, is large (thus the coupling constant which determines gluon interactions is weak). The
 2432 qualitative behavior of the saturation scale with energy and nuclear size can be argued as follows. The
 2433 transition from a dilute to a dense regime is marked by the packing factor (in this case, the product of the
 2434 density of gluons per unit transverse area times the gluon-gluon cross section) becoming of the order unity
 2435 i.e.

$$\frac{A \times xg(x, Q_s^2)}{\pi A^{2/3}} \times \frac{\alpha_s(Q_s^2)}{Q_s^2} \sim 1 \implies Q_s^2 \sim A^{1/3} Q_0^2 \left(\frac{1}{x}\right)^\lambda, \quad (6.2)$$

2436 where the growth of the gluon density at small x has been approximated by a power law, $xg(x, Q^2) \sim x^{-\lambda}$,
 2437 logarithms are neglected and the nucleus is considered a simple superposition of independent nucleons. The
 2438 exponent $\lambda \simeq 0.3$ can be derived from QCD, whereas the scale Q_0^2 has to be taken from experiment.

2439 The BK equation was derived under several simplifying assumptions such as the scattering of a dilute
 2440 projectile on a dense target, a large number of QCD colours and the absence of correlations in the target. At
 2441 present, the discussion is concentrated on how to overcome these difficulties [?, ?, ?]. Possible phenomenolog-
 2442 ical implications [?, ?, ?], are being considered. Also, the proposed relation between high-energy QCD and
 2443 Statistical Mechanics [?, ?] is under investigation.

2444 In the CGC formalism, the resummed terms are those enhanced by the energy and by the local density
 2445 of partons, and the saturation scale depends on the matter (colour charge) density at the impact parameter
 2446 probed by the virtual photon. For a nucleus, the nuclear size plays the role of an enhancement factor, see
 2447 Eq. (??), in a manner which is analogous to impact parameter scanning. Therefore, it is expected that when
 2448 scanning the impact parameter from the center to the periphery of the hadron at high energy, one should go
 2449 from a non-linear to a linear regime. Analogously, non-linear effects will become more important for large
 2450 nuclei than for smaller ones or for nucleons. Thus, a study of the variation of parton densities with impact
 2451 parameter and with the nuclear size, will provide an exacting test of our ideas on parton saturation.

2452 Resummation at low x

2453 The generic challenges that the small- x region bears in QCD are inherently related to the divergence of the
 2454 gluon number density with decreasing values of x . As is well known, deep-inelastic partonic cross sections
 2455 and parton splitting functions receive large corrections in the small- x limit due to the presence of powers
 2456 of $[\alpha_s \log x]$ to all orders in the perturbative expansion [?, ?, ?, ?, ?]. It thus suggests dramatic effects from
 2457 logarithmically enhanced corrections, so the success of fixed order NLO perturbation theory at HERA has

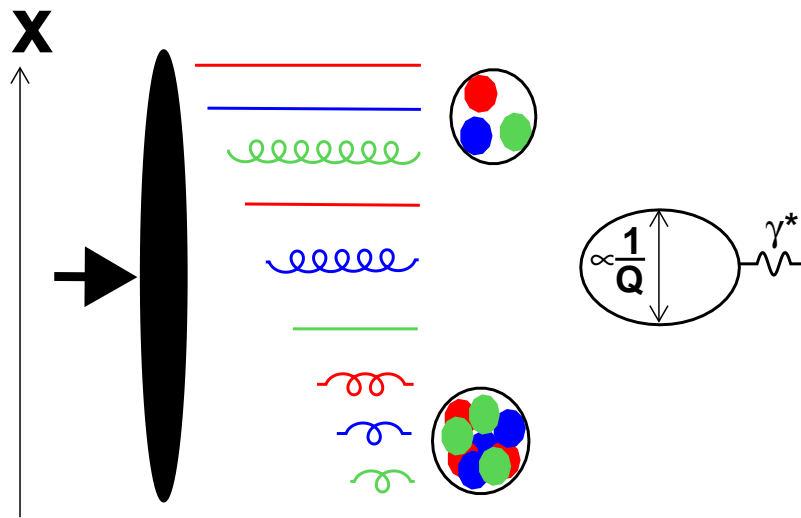


Figure 6.2: Illustration of saturation ideas. The hadron is moving very fast to the right, and its wave function contains many partonic components. Specifically, it includes partons with both large and small fractions of its longitudinal momentum x . The former are in a dilute regime, while the latter become densely packed due to multiple splitting. The photon with virtuality Q^2 is moving to the left and it constitutes a probe of the hadron wave function with a spatial resolution proportional to $1/Q$.

2458 been very hard to explain in regions where x becomes small. Recently, hints have been found that indeed
2459 the DGLAP fits tend to deteriorate systematically in the region of small x and Q^2 [?, ?]. Direct calculations
2460 at next-to-leading logarithmic accuracy in the BFKL framework were performed [?, ?], and showed a slow
2461 convergence of the perturbative series in the high-energy, or small- x regime. Therefore, generically one
2462 expects deviations from fixed-order DGLAP evolution in the small- x and small- Q regime which call for
2463 resummation of higher orders in perturbation theory.

2464 Extensive analyses have been performed in the last few years [?, ?, ?, ?, ?], which indeed point to the
2465 importance of resummation to all orders. Resummation should embody important constraints like kinematic
2466 effects, momentum sum rules and running coupling effects.

2467 Several important questions arise here, such as the relation and interplay of the resummation and the
2468 non-linear effects, and possibly the role of resummation in the transition between the perturbative and non-
2469 perturbative regimes in QCD. Precise experimental measurements in extended kinematic regions are needed
2470 to explore the deviations from standard DGLAP evolution and to quantify the role of resummation at small
2471 x .

2472 The importance of diffraction

2473 It was observed at HERA that a substantial fraction, about 10%, of deep inelastic interactions are diffractive
2474 events i.e. events in which the interacting proton stays intact, despite the inelasticity of the interaction.
2475 Moreover, the proton appears well separated from the rest of the hadronic final state by a large rapidity gap.
2476 The events otherwise look similar to normal deep inelastic events.

2477 Diffraction has been extensively analyzed at HERA, with a variety of measurements in bins of x and Q^2 ,
2478 as well as more differential analyses which include the dependence on the momentum transfer t . Physically,
2479 for the diffractive event to occur, there must be an exchange of a coherent, color neutral cluster of partons
2480 (a quasiparticle) which leaves the interacting proton intact. This color neutral cluster is often called the
2481 *pomeron*, and it can be characterised via a factorisation theorem [?] by a set of partonic densities analogous to
2482 those for the proton or nucleus. At lowest order, the QCD realisation of the pomeron is a pair of gluons [?, ?],
2483 which leads to enhanced sensitivity to saturation phenomena compared to the single gluon exchange in hte
2484 bulk of non-diffractive processes.

2485 There are strong theoretical indications that diffraction is closely linked with the phenomenon of partonic
2486 saturation. From a wide range of calculations, mostly based on the so-called dipole model, see for example
2487 [?, ?], it is known that diffractive DIS events involve softer effective scales than non-diffractive events at the
2488 same Q^2 . Thus, the exploration of diffractive phenomena offers a unique window to analyze the transition
2489 between perturbative and non-perturbative dynamics in QCD.

2490 LHeC will provide a widely extended kinematic coverage for diffractive events. By their study one could
2491 extract diffractive parton densities for a larger range in Q^2 than at HERA, and thus provide crucial tests
2492 of parton dynamics in diffraction as well as of the factorization theorems. The high energy involved also
2493 enables the production of diffractive states with large masses which could include W and Z bosons as well
2494 as states with heavy flavours or even exotic states with quantum numbers 1^- .

2495 Of particular importance is exclusive diffractive production of vector mesons, for which differential mea-
2496 surements as a function of squared four-momentum transfer, t , are most easily performed. It has been
2497 demonstrated that in this case, information about the momentum transfer of the cross section can be trans-
2498 lated into the dependence of the scattering amplitude on impact parameter. As a result, a profile in impact
2499 parameter of the interaction region, illustrated in Fig. ??, can be extracted. The precise determination of
2500 the dynamics governing the high parton density regime requires a detailed picture of the spatial distribution,
2501 in impact parameter space, of partons in the interaction region. As mentioned previously, by selecting small
2502 impact parameter values (large t), one is probing the regions of higher parton density where the saturation
2503 phenomenon is more likely to occur. One can then extract the value of the saturation scale as a function of
2504 energy and impact parameter.

2505 Even more inclusive measurements of the diffractive production of vector mesons can provide valuable
2506 information about parton dynamics. For example, the measurement of the energy dependence of the diffrac-
2507 tive cross section for the production of J/ψ at the LHeC can distinguish between different scenarios for

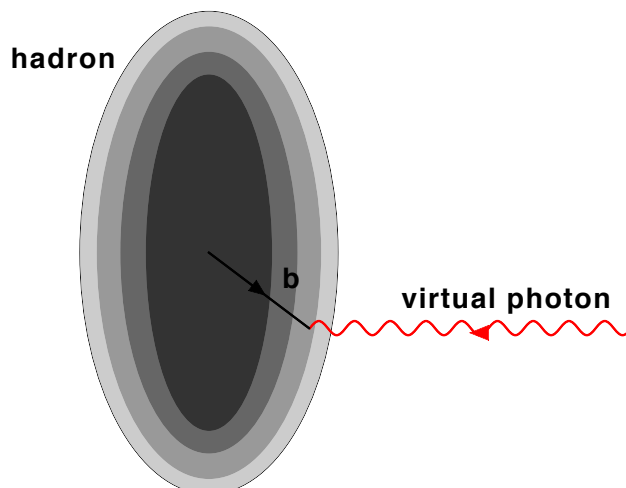


Figure 6.3: Illustration of the transverse profile of the hadron as explored by a virtual photon at impact parameter b .

parton evolution and thus explore parton saturation to a greater accuracy than ever before.

The importance of nuclei

In the context of small- x physics, studying lepton-nucleus collisions has a two-fold importance:

- On the one hand and as discussed in sections ?? and ??, the nuclear structure functions and parton densities are basically unknown at small x . The main reason for this lack of knowledge comes from the rather small area in the $\ln Q^2 - \ln 1/x$ plane covered by presently available experimental data, see Fig. ?. Current theoretical and phenomenological analyses [?] point to the importance of non-linear dynamics in DIS off nuclei at small and moderate Q^2 and small x , which needs to be tested experimentally. In this respect, a relation exists, as reviewed in Sec. ??, between diffraction in lepton-proton collisions and the small- x behavior of nuclear structure functions. Such relation relies on basic properties of Quantum Field Theory and its verification provides stringent tests of our understanding of these phenomena.
- Non-linear effects in parton evolution are enhanced by increasing the density of partons. Such an increase can be achieved (see Fig. ??) either by increasing the energy of the collision (decreasing x), or by increasing the nuclear mass number A . The latter can be accomplished by either using the largest nuclei possible, or by selecting subsets of collisions with small impact parameters b (i.e. more central collisions) between the relatively light nuclei and the virtual photon, such that more nucleons are involved. The ideal situation would be to Map out the dependence of the saturation scale on x , b and A as fully as possible (see Eq. (??)). This is a key observable in formulations which resum multiple interactions and result in parton saturation. As such it must be checked in experiment in order to clearly settle the mechanism underlying non-linear parton dynamics.

Also, the study of lepton-nucleus collisions has strong implications on the understanding of the experimental data from ultrarelativistic nucleus-nucleus collisions, as discussed later in Subsec. ??.

6.1.2 Status following HERA data

As discussed in the previous Section, in the low- x region a high parton density can be achieved in DIS and various novel phenomena are predicted. Ultimately, unitarity constraints become important and a ‘black

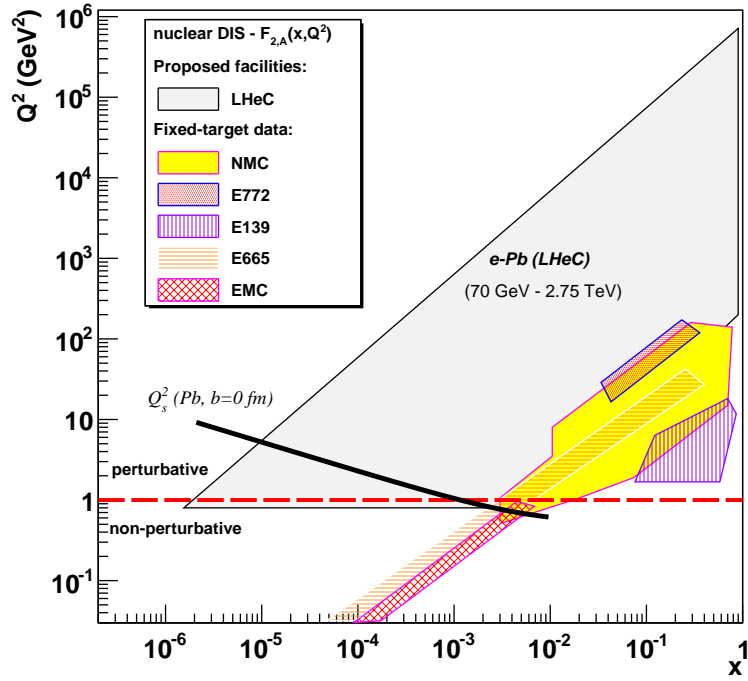


Figure 6.4: Kinematical coverage of the LHeC in the $\ln Q^2 - \ln 1/x$ plane for nuclear beams, compared with existing nuclear DIS and Drell-Yan experiments.

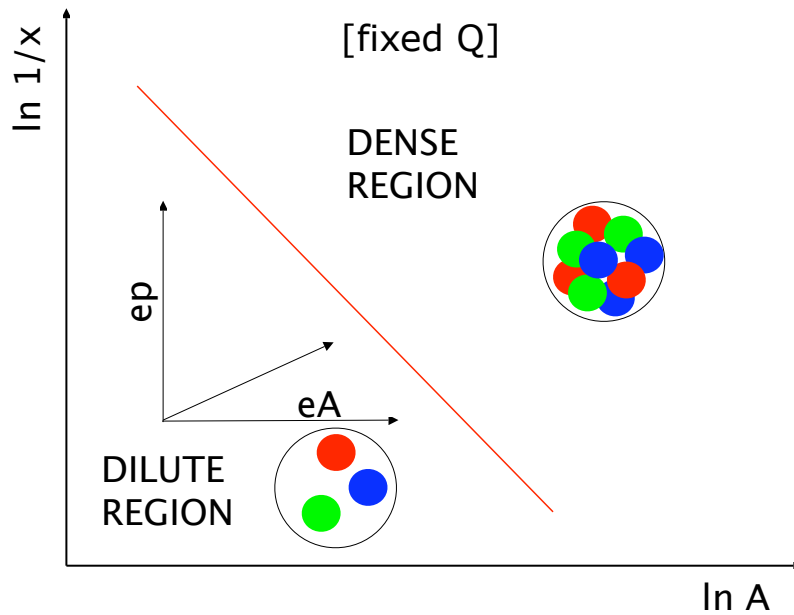


Figure 6.5: Schematic view of the different regions for the parton densities in the $\ln 1/x - \ln A$ plane, for fixed Q^2 . See the text for comments.

2534 disk' limit is approached [?], in which the cross section reaches the geometrical bound given by the transverse
 2535 proton or nucleus size. When α_s is small enough for quarks and gluons to be the right degrees of freedom,
 2536 parton saturation effects are therefore expected to occur within the theoretically controllable weak coupling
 2537 regime. In this small- x limit, many striking observable effects are predicted, such as Q^2 dependences of the
 2538 cross sections which differ fundamentally from the usual logarithmic variations, and diffractive cross sections
 2539 approaching 50% of the total [?]. This fairly good phenomenological understanding of the onset of unitarity
 2540 effects is, unfortunately, not very quantitative. In particular, the precise location of the saturation scale
 2541 line in the DIS kinematic plane (see Fig. ??) is to be determined experimentally. The search for parton
 2542 saturation effects has therefore been a major issue throughout the lifetime of the HERA project.

2543 Although no conclusive saturation signals have been observed in parton density fits to existing HERA
 2544 data, various hints have been obtained, for example, by studying the change in fit quality as low- x and Q^2
 2545 data are progressively omitted, in the NNPDF [?] and HERAPDF [?] analyses (see Subsec. ??).

2546 A more common approach is to fit the data to dipole models [?, ?, ?, ?], which are applicable at very low
 2547 Q^2 values beyond the range in which quarks and gluons can be considered to be good degrees of freedom.
 2548 The typical conclusion [?] is that HERA data in the perturbative regime exhibit at best weak evidence for
 2549 saturation. However, when data in the $Q^2 < 1 \text{ GeV}^2$ region are included, models which include saturation
 2550 effects are quite successful in the description of the wide variety of experimental data.

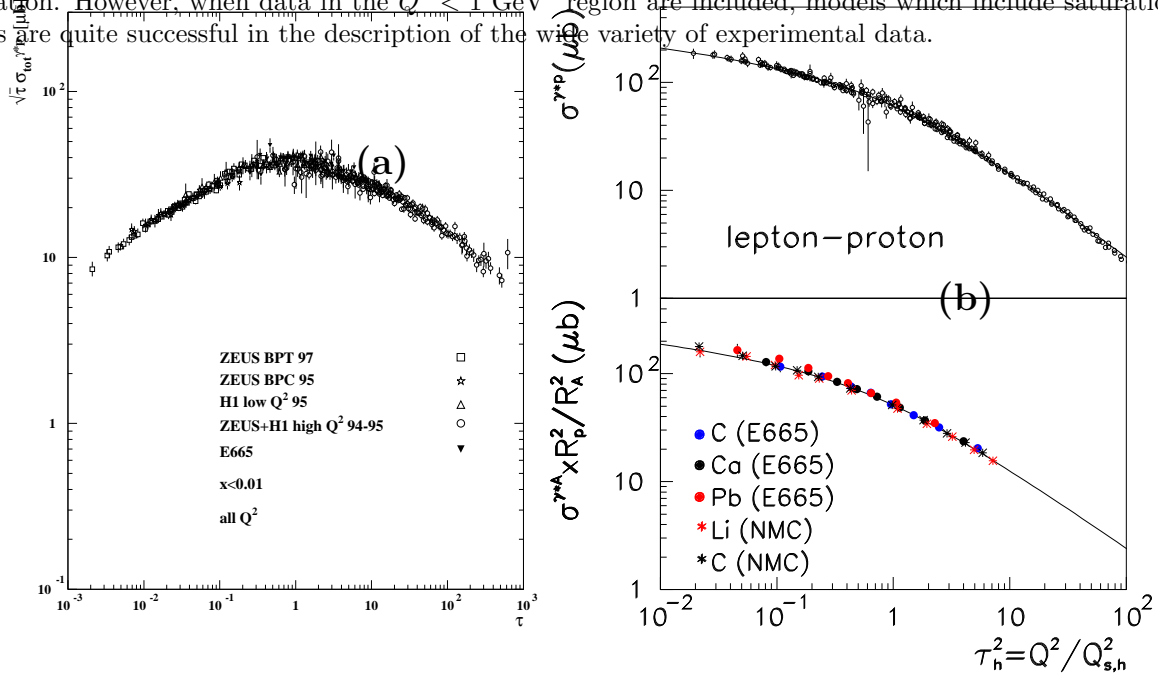


Figure 6.6: (a) Geometric scaling plot [?], in which low x data on the γ^*p cross section from HERA and E665 are plotted as a function of the dimensionless variable τ (see text). The cross sections are scaled by $\sqrt{\tau}$ for visibility. (b) Geometric scaling plot showing cross sections for electron scattering off nuclei as well as off protons [?].

2551 The 'geometric scaling' [?] feature of the HERA data (Fig. ??a) reveals that, to a good approximation,
 2552 the low- x cross section is a function of a single combined variable $\tau = Q^2 / Q_s^2(x)$, where $Q_s^2 = Q_0^2 x^{-\lambda}$ is
 2553 the saturation scale, see Eq. (??). This parameterisation works well for scattering off both protons and
 2554 ions, as shown in Fig. ??b [?, ?]. Geometric scaling is observed not only for the total γ^*p cross section, but
 2555 also for other, more exclusive observables in γ^*p collisions [?, ?] and even in hadron production in proton-
 2556 proton collisions at the LHC [?] and nucleus-nucleus collisions at RHIC [?]. This feature supports the view
 2557 (Subsec. ??) of the cross section as being invariant along lines of constant 'gluon occupancy'. When viewed
 2558 in detail (Fig. ??), there is a change in behaviour in the geometric scaling plot near $\tau = 1$, which has
 2559 been interpreted as a transition to the saturation region shown in Fig. ?. However, data with $\tau < 1$ exist
 2560 only at very low, non-perturbative, Q^2 values to date, precluding a partonic interpretation. Also, the fact

2561 that the scaling extends to large values of τ which characterize the dilute regime, has prompted theoretical
 2562 explanations of this phenomenon which do not invoke the physics of saturation [?].

2563 Dipole models

2564 As mentioned previously, one of the interesting observations at HERA is the success of the description of
 2565 many aspects of the experimental data within the framework of the so-called dipole picture [?, ?, ?] with
 2566 models that include unitarisation or saturation effects [?, ?]. These models are based on the assumption that
 2567 the relevant degrees of freedom at high energy are colour dipoles. Dipole models in DIS are closely related
 2568 to the Good-Walker picture [?] previously developed for soft processes in hadron-hadron collisions. In DIS,
 2569 dipoles are shown to be the eigenstates of high-energy scattering in QCD, and the photon wave function can
 2570 be expanded onto the dipole basis.

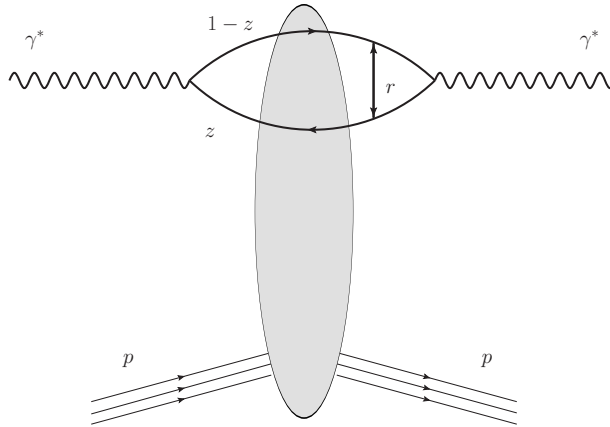


Figure 6.7: Schematic representation of dipole factorisation at small x in DIS. The virtual photon fluctuates into a quark-antiquark pair and subsequently interacts with the target. All the details of the dynamics of the interaction are encoded in the dipole scattering amplitude.

2571 The dipole factorization for the inclusive cross section in DIS is illustrated in Fig. ???. It differs from
 2572 the usual picture of the virtual photon probing the parton density of the target in that here the partonic
 2573 structure of the probed hadron is not evident. Instead, one chooses a particular Lorentz frame where the
 2574 photon fluctuates into a quark-antiquark pair with a transverse separation r and at impact parameter b with
 2575 respect to the target. For sufficiently small $x \ll (2m_N R_h)^{-1}$, with m_N the nucleon mass and R_h the hadron
 2576 or nuclear radius, the lifetime of the $q\bar{q}$ fluctuation is much longer than the typical time for interaction with
 2577 the target. The interaction of the $q\bar{q}$ dipole with the hadron or nucleus is then described by a scattering
 2578 matrix $S(r, b; x)$ such that $|S(r, b; x)| < 1$. The unitarity constraints can be incorporated naturally in this
 2579 picture [?] by the requirement that $|S(r, b; x)| \geq 0$, with $S(r, b; x) = 0$ corresponding to the black disk limit.
 2580 Integrating $1 - S(r, b; x)$ over the impact parameter b one obtains the dipole cross section $\sigma^{q\bar{q}}(r, x)$, which
 2581 depends on the dipole size and the energy (through the dependence on $x = x_{Bj}$). The transverse size of
 2582 the partons probed in this process is roughly proportional to the inverse of the virtuality of the photon
 2583 Q^2 . This statement is most accurate in the case of a longitudinally polarized photon, while in the case of a
 2584 transversely polarized one, the distribution of the probed transverse sizes of dipoles is broadened due to the
 2585 so-called aligned jet configurations.

2586 At small values of the dipole size, such that $r \ll 1/Q$, the dipole cross section can be shown to be related
 2587 to the integrated gluon distribution function

$$\sigma^{q\bar{q}}(r, x) \sim r^2 \alpha_s(C/r^2) xg(x, C/r^2), \quad (6.3)$$

2588 where C is a constant. In this regime, where r is small, the dipole cross section is small and consequently
 2589 the amplitude is far from the unitarity limits. With increasing energy the dipole cross section grows and
 2590 saturation corrections must be taken into account in order to guarantee the unitarity bound on $S(r, b; x)$. The
 2591 transition region between the two limits is characterised by the saturation scale $Q_s(x)$. Several models [?, ?, ?]
 2592 have been proposed which successfully describe the HERA data on the structure function F_2 .

2593 Once the dipole cross section has been constrained by the data on the inclusive structure functions, it
 2594 can be used to predict, with almost no additional parameters, the cross sections for diffractive production at
 2595 small x . Inclusive diffraction has been computed within the dipole picture in [?], and exclusive diffraction
 2596 of vector mesons in [?, ?]. One of the interesting aspects of these models is that they naturally lead to a
 2597 constant ratio of the diffractive to total cross sections as a function of energy [?]. In models with saturation
 2598 this is related to the fact that the saturation scale provides a natural x -dependent cut-off and gives the
 2599 same leading-twist behavior for inclusive and diffractive cross sections. As a result the ratio of inclusive to
 2600 diffractive cross sections is almost constant as a function of the energy.

2601 In spite of the fact that this approach has been able to successfully describe inclusive data and predict
 2602 diffraction at small values of x , there is still important conceptual progress to be made. Certainly there
 2603 are important hints from dipole models about the nature of the perturbative–non-perturbative transition in
 2604 QCD. Nevertheless, dipole models should be rather regarded as effective phenomenological approaches. As
 2605 such they only parametrize the essential dynamics at small x . For instance, the transverse impact parameter
 2606 dependence of the dipole scattering amplitude $S(r, b; x)$ is very poorly constrained. Indeed, it is possible
 2607 simultaneously to describe F_2 and F_2^D with a rather wide range of impact parameter dependences. On the
 2608 theoretical side, it has not been possible so far to fully predict the realistic profile of the interaction region in
 2609 transverse size. It is therefore of vital importance to measure accurately the t -dependencies of the diffractive
 2610 cross sections in an extended kinematic range to pin down the impact parameter distribution of the proton
 2611 at high energies.

2612 Hints of deviations from fixed-order linear DGLAP evolution in inclusive HERA data

2613 As discussed in previous sections, the experimental data on the inclusive structure functions F_2 and F_L
 2614 measured at HERA have been successfully described - with $\chi^2/d.o.f. \sim 1$ - by fits which use linear fixed-
 2615 order DGLAP evolution, see [?, ?, ?, ?, ?, ?, ?, ?, ?, ?]. The current status of the calculations is fixed order
 2616 at next-to-next-to-leading accuracy. On the other hand, see Subsec. ??, there are several theoretical reasons
 2617 to expect that at small x and/or at small Q^2 the fixed-order DGLAP framework needs to be extended.
 2618 Possible relevant phenomena predicted by perturbative QCD are linear small- x resummation, non-linear
 2619 evolution and parton saturation or other higher-twist effects. Although the exact kinematic regime in which
 2620 these effects should become important remains unclear, it is evident that at some point they will lead to
 2621 deviations from fixed-order DGLAP evolution. Therefore, an important question is whether these deviations
 2622 are already present in HERA data. Several analyses have been performed which aimed to address this
 2623 question.

2624 In one analysis [?], HERA $F_2(x, Q^2)$ data are subjected to three fits in the framework of a dipole model. In
 2625 one of the fits, the parameterisation of the dipole cross section does not contain saturation properties, whereas
 2626 in the other two, saturation effects are included using two rather different models [?, ?]. All three dipole
 2627 fits are able to describe the HERA data adequately in the perturbative region $Q^2 \geq 2 \text{ GeV}^2$. However,
 2628 a clear preference for the models containing saturation effects becomes evident when data in the range
 2629 $0.045 < Q^2 < 1 \text{ GeV}^2$ are added [?]. Similar conclusions are drawn when the same dipole cross section models
 2630 are applied to various less inclusive observables at HERA [?]. These observations provide an intriguing hint
 2631 that saturation effects may already be present in HERA data. However, due to the non-perturbative nature
 2632 of the low Q^2 kinematic region in which the effects appear, there is no clear interpretation in terms of
 2633 perturbative QCD degrees of freedom and firm conclusions cannot be drawn on the existence and nature of
 2634 parton recombination effects.

2635 In another analysis [?], possible indications of deviations from linear DGLAP evolution were discussed.
 2636 It was based on an unbiased PDF analysis of the inclusive HERA data. Here we present briefly an updated
 2637 version of this study which uses the most precise inclusive DIS data to date, the combined HERA–I dataset [?]

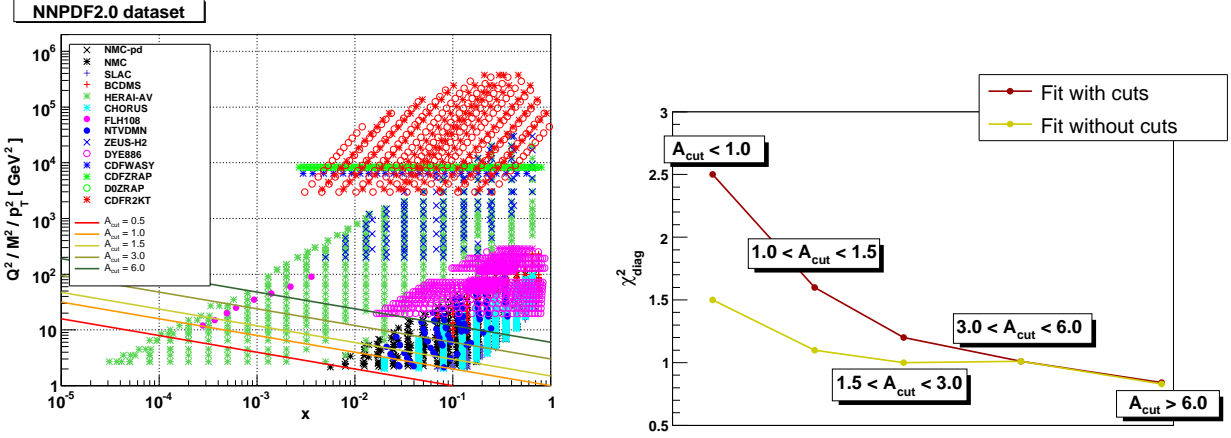


Figure 6.8: Left plot: the kinematic coverage of the data used in the NNPDF2.0 analysis, indicating the different choices of A_{cut} used to probe deviations from DGLAP. Right plot: the diagonal χ_{diag}^2 evaluated in kinematic slices corresponding to the different A_{cut} cuts, where χ_{diag}^2 has been computed using both the reference NNPDF2.0 fit without kinematic cuts (yellow line) and the NNPDF2.0 with the maximum $A_{\text{cut}} = 1.5$ cut (red line).

in the framework of the global NNPDF2.0 fitting framework. The key idea is to perform global fits only in the large- x , large- Q^2 region, where NLO DGLAP is expected to be reliable. This way one can determine *safe* parton distributions which are not contaminated by possible non-DGLAP effects. These PDFs are then evolved backwards into the potentially *unsafe* low- x and low- Q^2 kinematic region, and are used to compute physical observables, which are compared with data. A deviation between the predicted and observed behavior in this region can then provide a signal for effects beyond NLO DGLAP.

The PDFs were determined within the *safe* kinematic region in which $Q^2 \geq A_{\text{cut}} \cdot x^{-\lambda}$, where $\lambda = 0.3$ and A_{cut} is a variable parameter (see the left plot in Fig. ?? and [?] for details on the procedure). The NNPDF2.0 analysis [?] was repeated for different choices of the kinematic cuts, one for each choice of A_{cut} , and the results were compared with experimental data. As shown in Fig. ??, at high $Q^2 = 15 \text{ GeV}^2$ one does not see any significant deviation from NLO DGLAP. In this region all PDF sets agree with data and with one another, the only difference between them being that as A_{cut} increases the PDF uncertainty bands grow as expected due to the experimental information removed by the cuts. The situation is different at a lower $Q^2 = 3.5 \text{ GeV}^2$: the prediction obtained from the backwards evolution of the data above the cut exhibits a systematic downward trend, becoming more evident with increasing A_{cut} . These results are indicative of deficiencies in the description of HERA data at low- x and low- Q^2 by NLO DGLAP evolution². Specifically, the NLO DGLAP approach suggests a faster evolution with Q^2 than is present in the data. To be sure that one is observing a genuine small- x effect, one needs to check that it becomes less and less relevant as x and Q^2 increase. To this aim the diagonal χ_{diag}^2 was computed, see the right plot in Fig. ??, in different kinematic slices, both from the fit without cuts and from that with the maximum cut $A_{\text{cut}} = 1.5$. The expectation is that at larger x and Q^2 the difference between the two fits becomes smaller, as deviations from NLO DGLAP should become negligible. The data support this expectation: the contribution to the χ^2 from the region with $A_{\text{cut}} \geq 3$ is comparable for the fits with and without cuts, in contrast to the lower x and Q^2 region, where the χ^2 is substantially larger in the version of the fit with cuts applied. Nevertheless, it should be noted that there is no general consensus on the origins of these effects. e.g. in [?] it is suggested that their origin lies in bias due to the chosen initial conditions for DGLAP evolution

In summary, there are hints that the low- Q^2 –low- x region covered by HERA may exhibit deviations from fixed-order linear evolution. These hints are obtained from the success of dipole models with saturation features to describe the experimental data in this region, and from the fact that the quality of fixed-order

²This problem cannot be solved by NNLO corrections which work in the opposite direction, see in this respect [?]. Also, in the HERAPDF framework [?, ?] the fit quality tends to worsen when low- Q^2 data are included.

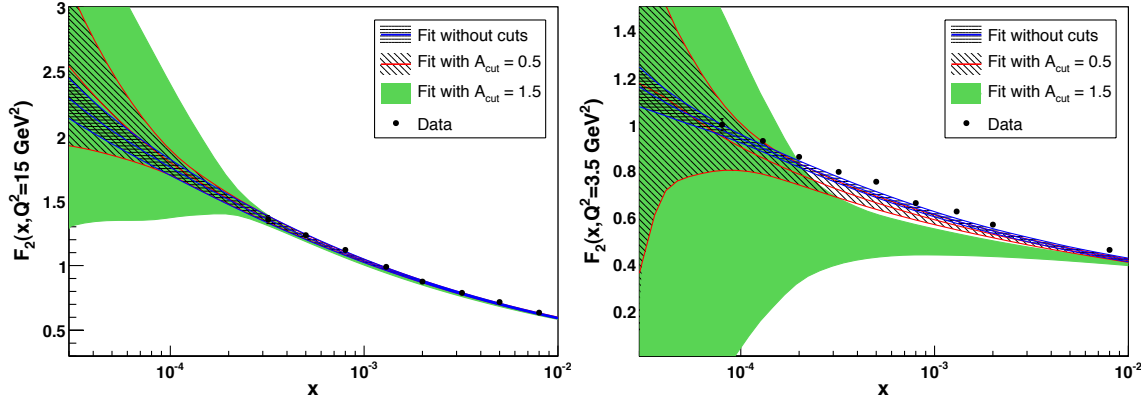


Figure 6.9: Left: the proton structure function $F_2(x, Q^2 = 15 \text{ GeV}^2)$ at small- x , computed from PDFs obtained from the NNPDF2.0 fits with different values of A_{cut} . Right: the same but at a lower $Q^2 = 3.5 \text{ GeV}^2$ scale.

2667 DGLAP fits seems to deteriorate there. However, the region in which such effects may be present corresponds
 2668 to rather small Q^2 , preventing a clear interpretation in terms of perturbative QCD degrees of freedom. In
 2669 addition, the overall quality of the fixed-order DGLAP fits to HERA data remains high. It is therefore
 2670 premature to draw any firm conclusion on the failure of fixed-order linear evolution as the appropriate tool
 2671 to describe all HERA data. In any case, it is clear that the methods discussed in this Subsection should be
 2672 used to analyse LHeC inclusive structure function data, and would allow a detailed characterization of any
 2673 new high-energy QCD dynamics unveiled by the LHeC. If the hints in the HERA data are correct, the novel
 2674 phenomena should appear at the LHeC in a higher Q^2 perturbative region where they can be established
 2675 cleanly and understood in terms of parton dynamics.

2676 Linear resummation schemes

2677 The deviations from DGLAP evolution could be caused by higher order effects at small x and small Q
 2678 which need to be resummed to all orders of perturbation theory. As mentioned previously, the problem
 2679 of resummation at small x has been extensively studied in recent years, see for example [?, ?, ?, ?, ?, ?].
 2680 It has been demonstrated that the small- x resummation framework accounts for running coupling effects,
 2681 kinematic constraints, gluon exchange symmetry and other physical constraints. The results were shown to
 2682 be very robust with respect to scale changes and different resummation schemes. As a result, the effect of
 2683 the resummation of terms which are enhanced at small x is perceptible but moderate - comparable in size
 2684 to typical NNLO fixed order corrections in the HERA region.

2685 A major development for high-energy resummation was presented in [?], where the full small- x resummation
 2686 of deep-inelastic scattering (DIS) anomalous dimensions and coefficient functions was obtained including
 2687 the quark contribution. This allowed for the first time a consistent small- x resummation of DIS structure
 2688 functions. These results are summarized in Fig. ??, taken from Ref. [?], where the K -factors for F_2 and F_L
 2689 for the resummed results are compared. As is evident from this figure, resummation is quite important in
 2690 the region of low x for a wide range of Q^2 values. One observes, for example, that the fixed order NNLO
 2691 contribution leads to an enhancement of F_2 with respect to NLO, whereas the resummed calculation leads
 2692 to a suppression. This means that a truncation at any fixed order is very likely to be insufficient for the
 2693 description of the LHeC data and therefore the fixed-order perturbative expansion becomes unreliable in the
 2694 low- x region, which calls for the resummation. Furthermore, the resummation of hard partonic cross sections
 2695 has been performed for several LHC processes such as heavy quark production [?], Higgs production [?, ?],
 2696 Drell-Yan [?, ?] and prompt photon production [?, ?]. The LHC is thus likely to provide a testing ground in
 2697 the near future.

2698 We refer to the recent review in Ref. [?] as well as to the HERA-LHC workshop proceedings [?] for a

2699 more detailed summary of recent theoretical developments in high-energy resummation.

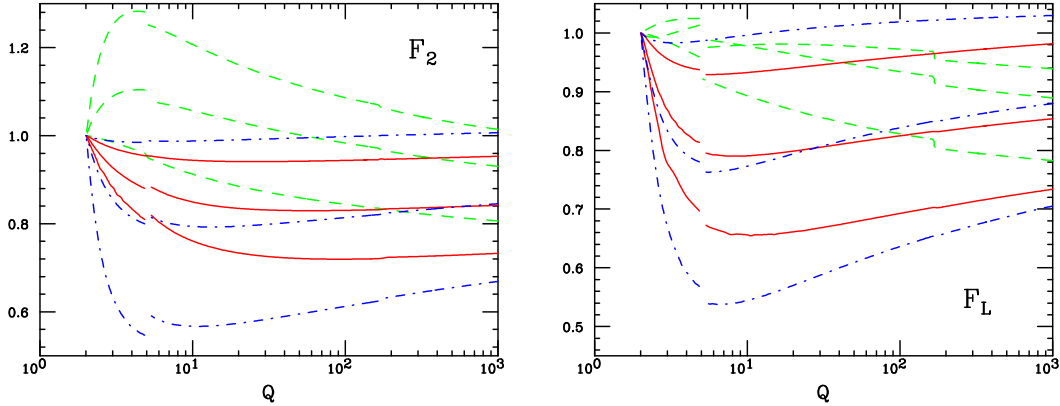


Figure 6.10: The K -factors, defined as the ratio of the fixed-order NNLO or resummed calculation to the NLO fixed-order results for the singlet F_2 and F_L structure functions, with F_2 and F_L kept fixed for all x at $Q_0 = 2$ GeV. Results are shown at fixed $x = 10^{-2}$, 10^{-4} or 10^{-6} as a function of Q in the range $Q = 2 - 1000$ GeV with α_s running and n_f varied in a zero-mass variable flavour number scheme. The breaks in the curves correspond to the b and t quark thresholds. The curves are: fixed order perturbation theory NNLO (green, dashed); resummed NLO in the $Q_0\overline{\text{MS}}$ scheme (red, solid), resummed NLO in the $\overline{\text{MS}}$ scheme (blue, dot-dashed). Curves with decreasing x correspond to those going from bottom to top for NNLO and from top to bottom in the resummed cases.

2700 To summarise, small- x resummation is becoming a very important component for precision LHC physics,
 2701 and will become a crucial ingredient of the LHeC small- x physics program [?, ?]. The LHeC extended
 2702 kinematic range will enhance the differences between the resummed predictions with respect to fixed-order
 2703 DGLAP calculations.

2704 6.1.3 Low- x physics perspectives at the LHC

2705 The low- x regime of QCD can also be analyzed in hadron and nucleus collisions at the LHC. The experimen-
 2706 tally accessible values of x range from $x \sim 10^{-3}$ to $x \sim 10^{-6}$ for central and forward rapidities respectively.
 2707 The estimates for the corresponding saturation scale at $x \sim 10^{-3}$, based on Eq. (??), result in $Q_s^2 \approx 1 \text{ GeV}^2$
 2708 for proton and $Q_s^2 \approx 5 \text{ GeV}^2$ for lead.

2709 The significant increase in the center-of-mass energy and the excellent rapidity coverage of the LHC
 2710 detectors will extend the kinematic reach in the x - Q^2 plane by orders of magnitude compared to previous
 2711 measurements at fixed-target and collider energies (see Fig. ??). Such measurements are particularly im-
 2712 portant in the nuclear case since, due to the scarcity of nuclear DIS data, the gluon PDF in the nucleus is
 2713 virtually unknown at fractional momenta below $x \approx 10^{-2}$ [?]. In addition, due to the dependence of the
 2714 saturation scale on the hadron transverse size, non-linear QCD phenomena are expected to play a central role
 2715 in the phenomenology of collisions involving nuclei. We succinctly review here the experimental possibilities
 2716 to study saturation physics in pp , pA and AA collisions at the LHC.

2717 Low- x studies in proton-proton collisions

2718 The LHC experiments feature detection capabilities at forward rapidities ($|\eta| \gtrsim 3$), which will allow mea-
 2719 surements of various perturbative processes sensitive to the underlying parton structure and its dynamical
 2720 evolution in the proton. The *minimum* parton momentum fractions probed in a $2 \rightarrow 2$ process with a particle

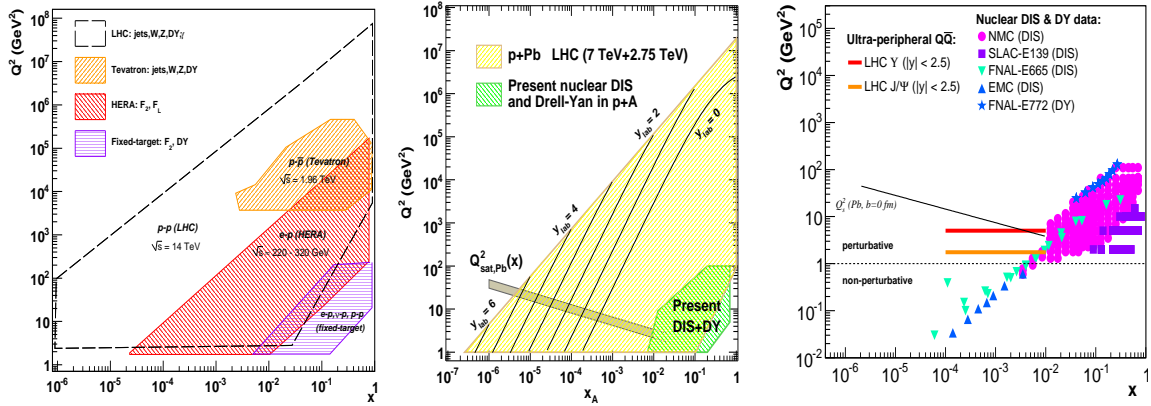


Figure 6.11: Kinematic reaches in the (x, Q^2) plane covered in proton-proton (left), proton-nucleus (center) [?] and ultraperipheral nucleus-nucleus (right) [?] collisions at the LHC. Also shown are the regions studied so far in collider and fixed-target experiments. Estimates of the saturation scale for lead are also shown.

2721 of momentum p_T produced at pseudo-rapidity η is

$$x_{min} = \frac{x_T e^{-\eta}}{2 - x_T e^{\eta}}, \quad \text{where } x_T = 2p_T/\sqrt{s}, \quad (6.4)$$

2722 i.e. x_{min} decreases by a factor ~ 10 every 2 units of rapidity. The extra e^{η} lever-arm motivates the interest in
 2723 *forward* particle production measurements to study the PDFs at small values of x . From Eq. (??) it follows
 2724 that the measurement at the LHC of particles with transverse momentum $p_T = 10$ GeV at rapidities $\eta \approx 5$
 2725 probes x values as low as $x \approx 10^{-5}$ (Fig. ??, left). Various experimental measurements have been proposed
 2726 at forward rapidities at the LHC to constrain the low- x PDFs in the proton and to look for possible evidence
 2727 for non-linear QCD effects. These include forward jets and Mueller-Navelet dijets in ATLAS and CMS [?];
 2728 and forward isolated photons [?] and Drell-Yan (DY) [?] in LHCb.

2729 Low- x studies in proton-nucleus collisions

2730 Until an electron-ion collider becomes available, proton-nucleus collisions will be the best available tool to
 2731 study small- x physics in a nuclear environment without the strong influence of the final-state medium, as
 2732 expected in the AA case. Though proton-nucleus collisions are not yet scheduled at the LHC, detailed fea-
 2733 sibility studies exist [?] and strategies to define the accessible physics programme are being developed [?].
 2734 The pA programme at the LHC serves a dual purpose [?]: to provide “cold QCD matter” benchmark mea-
 2735 surements for the physics measurements of the AA programme without significant final-state effects, and
 2736 to study the nuclear wavefunction in the small- x region. In Fig. ?? (center) we show how dramatically the
 2737 LHC will extend the region of phase space in the (x, Q^2) plane³ by orders of magnitude compared with
 2738 those studied at present. The same figure also shows the scarcity of nuclear DIS and DY measurements and,
 2739 correspondingly, the lack of knowledge of nuclear PDFs in the regions needed to constrain the initial state
 2740 for the AA programme - there is almost no information at present in the region $x \lesssim 10^{-2}$ [?].

2741
 2742 Nuclear PDF constraints, checks of factorization (universality of PDFs) and searches for saturation of
 2743 partonic densities will be performed in pA collisions at the LHC by studying different production cross

³Asymmetric colliding systems imply a rapidity shift in the two-in-one magnet design of the LHC. This shift has been taken into account in the figure: the quoted y values are those in the laboratory frame.

sections for e.g. inclusive light hadrons [?], heavy flavour particles [?], isolated photons [?], electroweak bosons [?] and jets. Additional opportunities also appear in the so-called ultra-peripheral collisions in which the coherent electromagnetic field created by the proton or the large nucleus effectively acts as one of the colliding particles with photon-induced collisions at centre of mass energies higher than those reached in photoproduction at the HERA collider [?] (see next subsection).

At this point it is worth mentioning that particle production in the forward (proton) rapidity region in dAu collisions at RHIC shows features suggestive of saturation effects, although no consensus has been reached so far, see [?, ?, ?, ?, ?] and references therein. The measurements at RHIC suffer from the limitation of working at the edge of the available phase space in order to study the small- x region in the nuclear wave function. This limitation will be overcome by the much larger available phase space at the LHC.

Low- x studies in nucleus-nucleus collisions

Heavy-ion (AA) collisions at the LHC aim at the exploration of collective partonic behaviour both in the initial wavefunction of the nuclei as well as in the final produced matter, the latter being a hot and dense QCD medium (see the discussions in Subsection ??). The nuclear PDFs at small x define the number of parton scattering centers and thus the initial conditions of the system which then thermalises.

A possible means of obtaining direct information on the nuclear parton distribution functions is through the study of final state particles which do not interact strongly with the surrounding medium, such as photons [?] or electroweak bosons [?]. Beyond this, global properties of the collision such as the total multiplicities or the existence of long-range rapidity structures (seen in AuAu collisions at RHIC [?] and in pp and PbPb collisions at the LHC [?, ?]) are sensitive to the saturation momentum which at the LHC is expected to be well within the weak coupling regime [?], $Q_{\text{sat,Pb}}^2 \approx 5 - 10 \text{ GeV}^2$. CGC predictions for charged hadron multiplicities in central Pb-Pb collisions at 5.5 TeV per nucleon are $dN_{ch}/d\eta|_{\eta=0} \approx 1500-2000$ [?]. (Note that the predictions done before the start of RHIC in 2000 were 3 times higher). Recent data from ALICE [?] give $dN_{ch}/d\eta|_{\eta=0} \approx 1600$ in central Pb-Pb at 2.76 TeV per nucleon, in rough agreement with CGC expectations.

As already noted for the pA case, one of the cleanest ways to study the low- x structure of the Pb nucleus at the LHC may be via ultra-peripheral collisions (UPCs) [?] in which the strong electromagnetic fields (the equivalent flux of quasi-real photons) generated by the colliding nuclei can be used for photoproduction studies at maximum energies $\sqrt{s_{\gamma N}} \approx 1 \text{ TeV}$, that is 3–4 times larger than at HERA. In particular, exclusive quarkonium photoproduction offers an attractive opportunity to constrain the low- x gluon density at moderate virtualities, since in such processes the gluon couples *directly* to the c or b quarks and the cross section is proportional to the gluon density *squared*. The vector meson mass M_V introduces a relatively large scale, amenable to a perturbative QCD treatment. In $\gamma A \rightarrow J/\psi(\Upsilon) A^{(*)}$ processes at the LHC, the gluon distribution can be probed at values as low as $x = M_V^2/W_{\gamma A}^2 e^y \approx 10^{-4}$, where $W_{\gamma A}$ is the γA centre of mass energy (Fig. ?? right). Full simulation studies [?, ?] of quarkonium photoproduction tagged with very-forward neutrons, show that ALICE and CMS can carry out detailed p_T, η measurements in the dielectron and dimuon decay channels.

In summary, pp , pA and AA collisions at the LHC have access to the small- x regime, and will certainly help to unravel the complex parton dynamics in this region. However, the excellent precision of a high energy electron-proton (ion) collider cannot be matched in hadronic collisions. The deep inelastic scattering process is much cleaner experimentally and under significantly better theoretical control. The description of hadron-hadron and heavy ion collisions in the regime of small x suffers from a variety of uncertainties, such as the question of the appropriate factorization, if any, and the large indeterminacy of fragmentation functions in the relevant kinematic region. Thus, the precise measurement of physical observables and parton densities and their interpretation in terms of QCD dynamics is only possible at an electron-hadron (ion) collider.

2790 6.1.4 Nuclear targets

2791 As discussed in Subsection ??, the use of nuclei offers a means of modifying the parton density both through
2792 colliding different nuclear species and by varying the impact parameter of the collision. Therefore, the study
2793 of DIS on nuclear targets is of the utmost importance for our understanding of the dynamics which control
2794 the behaviour of hadron and nuclear wave functions at small x . On the other hand, the characterization
2795 of parton densities inside nuclei and the study of other aspects of lepton-nucleus collisions such as particle
2796 production, are of strong interest both fundamentally and because they are crucial for a correct interpretation
2797 of the experimental results from ultrarelativistic ion-ion collisions. In the rest of this section we focus on
2798 these last two aspects.

2799 Additionally, nuclear effects have to be better understood in order to improve the constraints on nucleon
2800 PDF in analyses which include DIS data with neutrino beams (e.g. [?, ?]). Due to the smallness of the cross
2801 section, such neutrino experiments use nuclear targets, so corrections for nuclear effects are a significant
2802 source of uncertainty in the extraction of parton densities even for the proton.

2803 Comparing nuclear parton density functions

2804 The nuclear modification of structure functions has been extensively studied since the early 70's [?, ?]. It is
2805 usually characterized through the so-called nuclear modification factor which, for a given structure function
2806 or parton density f , reads

$$R_f^A(x, Q^2) = \frac{f^A(x, Q^2)}{A \times f^N(x, Q^2)}. \quad (6.5)$$

2807 In this equation, the superscript A refers to a nucleus of mass number A , while N denotes the nucleon (either
2808 a proton or a neutron, or their average as obtained from deuterium). The absence of nuclear effects would
2809 result in $R = 1$.

2810 The nuclear modification factor for F_2 shows a rich structure: an enhancement ($R > 1$) at large $x > 0.8$, a
2811 suppression ($R < 1$) for $0.3 < x < 0.8$, an enhancement for $0.1 < x < 0.3$, and a suppression for $x < 0.1$ where
2812 isospin effects can be neglected. The latter effect is called shadowing [?], and is the dominant phenomenon
2813 at high energies (the kinematical region $x < 0.1$ will determine particle production at the LHC, see Sec. ??
2814 and [?]).

2815 The modifications in each region are believed to be of different dynamical origin. In the case of shadowing,
2816 the explanation is usually given in terms of a coherent interaction involving several nucleons, which reduces
2817 the nuclear cross section from the totally incoherent situation, $R = 1$, towards a region of total coherence.
2818 In the region of very small x , small-to-moderate Q^2 and for large nuclei, the unitarity limit of the nuclear
2819 scattering amplitudes is expected to be approached and some mechanism of unitarisation such as multiple
2820 scattering should come into play. Therefore, in this region nuclear shadowing is closely related to the onset
2821 of the unitarity limit in QCD and the transition from coherent scattering of the probe off a single parton
2822 to coherent scattering off many partons. The different dynamical mechanisms proposed to deal with this
2823 problem should offer a quantitative explanation for shadowing, with the nuclear size playing the role of a
2824 density parameter in the way discussed in Subsection ??.

2825 At large enough Q^2 the generic expectation is that the parton system becomes dilute and the usual
2826 leading-twist linear DGLAP evolution equations should be applicable to nuclear PDFs. In this framework,
2827 global analyses of nuclear parton densities (in exact analogy to those of proton and neutron parton densities)
2828 have been developed up to NLO accuracy [?, ?, ?]. In these global analyses, the initial conditions for DGLAP
2829 evolution are parametrized by flexible functional forms but they lack theoretical motivation in terms of e.g.
2830 the dynamical mechanisms for unitarization mentioned above. On the other hand, the relation between
2831 diffraction and nuclear shadowing [?, ?] can in principle be employed to constrain the initial conditions for
2832 DGLAP evolution, as has been explored previously at both LO [?] and NLO [?]⁴ accuracy, see Subsec. ??.
2833 All nuclear PDF analyses [?, ?, ?] include data from NC DIS and DY experiments, and [?] also uses particle

⁴In the approach in [?] predictions are provided only for sea quarks and gluons, with the valence taken from the analysis in [?].

2834 production data at mid-rapidity in deuterium-nucleus collisions at RHIC. Error sets obtained through the
2835 Hessian method are provided in [?]. CC DIS data have been considered only recently [?, ?]⁵ in this context.

2836 Results from the different nuclear PDF analyses performed at NLO accuracy are shown in Fig. ??, with
2837 the band indicating the uncertainty obtained using the error sets in [?]. In addition to the discrepancies
2838 concerning the existence of an enhancement/suppression at large x , the different approaches lead to clear
2839 differences at small x , both in magnitude and in shape, usually within the large uncertainty band shown.
2840 With nuclear effects vanishing logarithmically in the DGLAP analysis, the corresponding differences and
2841 uncertainties diminish, although they remain sizable until rather large Q^2 .

2842 These large uncertainties are due to the lack of experimental data on nuclear structure functions for
2843 $Q^2 > 2 \text{ GeV}^2$ and x smaller than a few times 10^{-2} . The constraints on the small x gluon are particularly
2844 poor. Particle production data at mid-rapidity coming from deuterium-nucleus collisions at RHIC offer an
2845 indirect constraint on the small- x sea and glue [?], but these data are bound to contain sizable uncertainties
2846 intrinsic to particle production in hadronic collisions at small and moderate scales. Therefore, only high-
2847 accuracy data on nuclear structure functions at smaller x , with a large lever arm in Q^2 , as is achievable at
2848 the LHeC, will be able to substantially reduce the uncertainties and clearly distinguish between the different
2849 approaches.

2850 Requirements for the ultra-relativistic heavy ion programs at RHIC and the LHC

2851 The LHeC will offer extremely valuable information on several aspects of high-energy hadronic and nu-
2852 clear collisions. On the one hand, it will characterize hard scattering processes in nuclei through a precise
2853 determination of initial state. On the other hand, it will provide quantitative constraints on theoretical
2854 descriptions of initial particle production in ultra-relativistic nucleus-nucleus collisions and the subsequent
2855 evolution into the quark-gluon plasma, the deconfined partonic state of matter whose production and study
2856 offers key information about confinement. Such knowledge will complement that coming from pA collisions
2857 and self-calibrating hard probes in nucleus-nucleus collisions (see [?, ?, ?, ?, ?]) regarding the correct inter-
2858 pretation of the findings of the heavy-ion programme at RHIC (see e.g. [?, ?] and refs. therein) and at the
2859 LHC. Beyond the qualitative interpretation of such findings, the LHeC will greatly improve the quantitative
2860 characterization of the properties of QCD extracted from such studies. The relevant information can be
2861 classified into three items:

2862 a. Parton densities inside nuclei:

2863 The knowledge of parton densities inside nuclei is an essential piece of information for the analysis of the
2864 medium created in ultra-relativistic heavy-ion collisions using hard probes, i.e. those observables whose
2865 yield in nucleon-nucleon collisions can be predicted in pQCD (see [?, ?, ?, ?]). The comparison between
2866 the expectation from an incoherent superposition of nucleon-nucleon collisions and the measurement
2867 in nucleus-nucleus collision characterises the nuclear effects. However, we need to disentangle those
2868 effects which originate from the creation of a hot medium in nucleus-nucleus collisions, from effects
2869 arising only from differences in the partonic content between nucleons and nuclei.

2870 Our present knowledge of parton densities inside nuclei is clearly insufficient in the kinematic regions
2871 of interest for RHIC and, above all, for the LHC (see [?] and Subsection ??). Such ignorance reflects in
2872 uncertainties larger than a factor 3 – 4 for the calculation of different cross sections in nucleus-nucleus
2873 collisions at the LHC (see Fig. ?? and [?]), thus weakening strongly the possibility of extracting
2874 quantitative characteristics of the produced hot medium. While the pA program at the LHC will offer
2875 new constraints on the nuclear parton densities (e.g. [?, ?]), measurements at the LHeC would be far
2876 more constraining and would reduce the uncertainties in nucleus-nucleus cross sections to less than a
2877 factor two.

2878 b. Parton production and initial conditions for a heavy-ion collision:

⁵The analysis in [?] shows the compatibility of the nuclear corrections as extracted in [?] with CC DIS data on nuclear targets, while in [?] some tension is found between NC and CC DIS data.

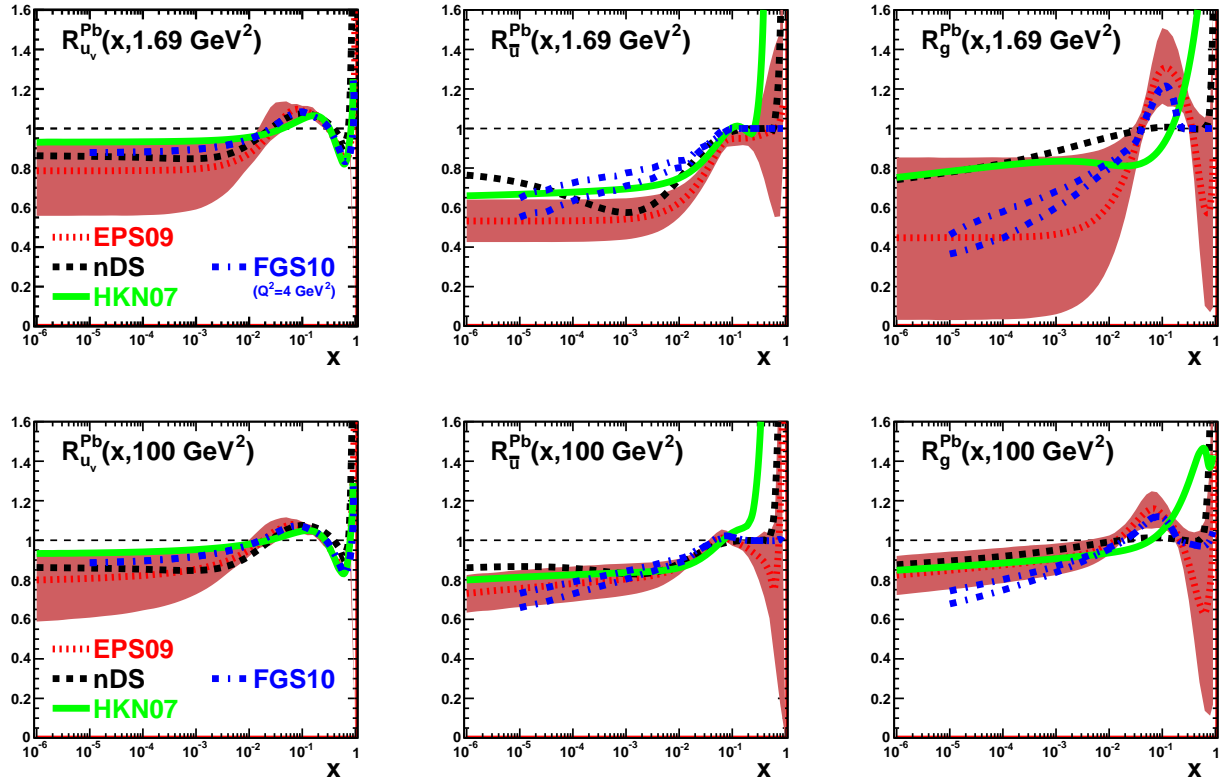


Figure 6.12: Ratio of parton densities in a bound proton in Pb to those in a free proton scaled by $A = 207$, for valence u (left), \bar{u} (middle) and g (right), at $Q^2 = 1.69$ (top) and 100 (bottom) GeV^2 . Results are shown from [?] (nDS, black dashed), [?] (HKN07, green solid), [?] (EPS09, red dotted) and [?] (FGS10, blue dashed-dotted; in this case the lowest Q^2 is 4 GeV^2 and two lines are drawn reflecting the uncertainty in the predictions). The red bands indicate the uncertainties according to the EPS09 analysis [?].

2879 The medium produced in ultra-relativistic heavy-ion collisions develops very early a collective behavior,
2880 usually considered as that of a thermalized medium and describable by relativistic hydrodynamics. The
2881 initial state of a heavy-ion collision for times prior to its eventual thermalization, and the thermalisation
2882 or isotropisation mechanism, play a key role in the description of the collective behavior. Such an
2883 initial condition for hydrodynamics or transport is presently modelled and fitted to data. But it
2884 should eventually be determined by a theoretical formalism of particle production within a saturation
2885 framework which embodies the both aspects: parton fluxes inside nuclei - discussed in the previous
2886 item, and particle production and evolution, eventually leading to isotropization.

2887 The CGC offers a well-defined framework in which the initial condition and thermalization mechanism
2888 can be computed from QCD, see Subsection ?? and e.g. [?] and refs. therein. Although our theoretical
2889 knowledge is still incomplete, electron-nucleus collisions are considerably less complex than the nucleus-
2890 nucleus collisions in which these CGC-based calculations already exist and can be tested. In this way,
2891 electron-ion collisions offer a testing ground for ideas on parton production in a dense environment,
2892 which is required for a first principles calculation of the initial conditions for the collective behavior in
2893 ultra-relativistic heavy-ion collisions. The LHeC offers the possibility of studying particle production
2894 in the kinematic region relevant for experiments at RHIC and the LHC.

2895 c. Parton fragmentation and hadronization inside the nuclear medium:

2896 The mechanism through which a highly virtual parton evolves from an off-shell coloured state to a final
2897 state consisting of colourless hadrons, is still subject to great uncertainties. Electron-ion experiments
2898 offer a testing ground for our ideas and understanding of such phenomena, see [?] and refs. therein,
2899 with the nucleus being a medium of controllable extent and density which modifies the radiation and
2900 hadronization processes.

2901 The LHeC will have capabilities for particle identification and jet reconstruction for both nucleon and
2902 nuclear targets. Its kinematic reach will allow the study of partons traveling through the nucleus
2903 from low energies, for which hadronization is expected to occur inside the nucleus, to high energies
2904 with hadronization outside the nucleus. Therefore the modification of the yields of energetic hadrons,
2905 observed at RHIC⁶ and usually attributed to in-medium energy loss - the so-called jet quenching
2906 phenomenon - will be investigated. With jet quenching playing a key role in the present discussions
2907 on the production and characterisation of the hot medium produced in ultra-relativistic heavy-ion
2908 collisions, the LHeC will offer most valuable information on effects in cold nuclear matter of great
2909 importance for clarifying and reducing the existing uncertainties.

2910 6.2 Prospects at the LHeC

2911 6.2.1 Strategy: decreasing x and increasing A

2912 As discussed previously, in order to analyse the regime of high parton densities at small x , we propose a
2913 two-pronged approach which is illustrated in Fig. ??. To reach an interesting novel regime of QCD one can
2914 either decrease x by increasing the center-of-mass energy or increase the matter density by increasing the
2915 mass number A of the nucleus. In addition, we will see that diffraction, and especially exclusive diffraction,
2916 will play a special role in unravelling the new dense partonic regime of QCD.

2917 The LHeC will offer a huge lever arm in x and also a possibility of changing the matter density at
2918 fixed values of x . This will allow us to pin down and compare the small x and saturation phenomena both
2919 in protons and nuclei and will offer an excellent testing ground for theoretical predictions. Thus, in the
2920 following, LHeC simulations of electron-proton collisions are paralleled by those in electron-lead wherever
2921 possible. For a complementary perspective on the opportunities for novel QCD studies offered by the LHeC,
2922 see [?].

⁶LHC experiments have already observed the jet quenching phenomenon both at the level of single-particle spectra [?] and through the study of jets [?,?], which will play a central role in heavy-ion physics at these energies.

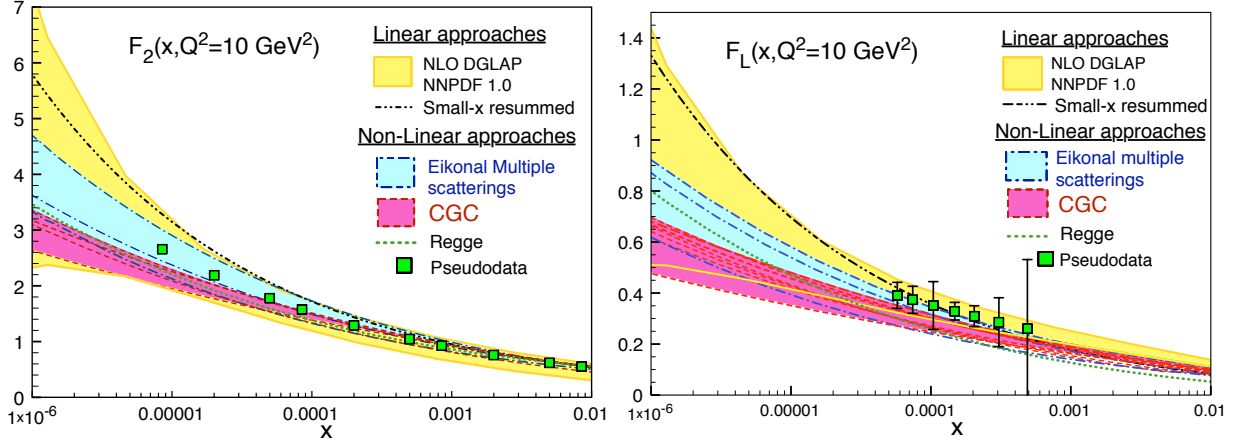


Figure 6.13: Predictions from different models for $F_2(x, Q^2 = 10 \text{ GeV}^2)$ (plot on the left) and $F_L(x, Q^2 = 10 \text{ GeV}^2)$ (plot on the right) versus x , together with the corresponding pseudodata. See the text for explanations.

6.2.2 Inclusive measurements

Predictions for the proton

The LHeC is expected to provide measurements of the structure functions of the proton with unprecedented precision, which will allow detailed studies of small- x QCD dynamics. In particular, it will be highly sensitive to departures of the inclusive observables, F_2 and F_L from the fixed-order DGLAP framework, in the region of small x and Q^2 . These deviations are expected by several theoretical arguments, as discussed in detail previously.

In Fig. ?? we show several predictions for the proton structure functions, F_2 and F_L , in ep collisions at $Q^2 = 10 \text{ GeV}^2$ and for $10^{-6} \leq x \leq 0.01$ i.e. $F_{2(L)}(x, Q^2 = 10 \text{ GeV}^2)$. The different curves correspond to the extrapolation of models that reproduce correctly the available HERA data for the same observables in the small- x region. They are classified into two categories: those based on linear evolution approaches and those that include non-linear small- x dynamics. Among the linear approaches we include extrapolation from the NLO DGLAP fit as performed by the NNPDF collaboration [?] (solid yellow bands) and the results from a combined DGLAP/BFKL approach, which includes resummation of small- x effects [?] (black-dotted-dotted lines). The non-linear calculations shown here are all formulated within the dipole model. We distinguish two categories: those based on the eikonalization of multiple scatterings together with DGLAP evolution of the gluon distributions [?, ?] (blue dashed-dotted lines) and those relying in the Color Glass Condensate effective theory of high-energy QCD scattering (red dashed lines). The latter include calculations based on solutions of the running coupling Balitsky-Kovchegov equation [?] and other more phenomenological models of the dipole amplitude without [?], or with [?] impact parameter dependence. Finally, we also include a hybrid approach, where initial conditions based on Regge theory and including non-linearities are evolved in Q^2 according to linear DGLAP evolution [?] (green dotted line). In all cases the error bands are generated by allowing variations of the free parameters in each subset of models. The green filled squares correspond to the subset of the simulated LHeC pseudodata at $Q^2 = 10 \text{ GeV}^2$ (see subsection ??).

Clearly, the accuracy of the data at the LHeC will offer huge possibilities for discriminating between different models and for constraining the dynamics underlying the small- x region.

Constraining small- x dynamics

The potential impact of the LHeC on low x parton densities within the framework of an NLO DGLAP analysis is assessed by adding the pseudodata introduced in subsection ?? into the NNPDF fitting analysis.

2952 The pseudodata are first generated at the extrapolated central values according to the existing NNPDF fits.

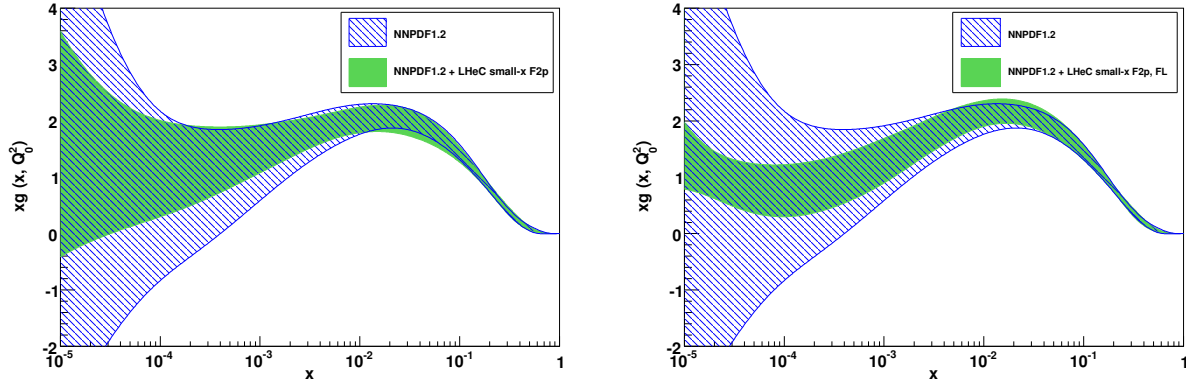


Figure 6.14: The results for the gluon distribution in the standard NNPDF1.2 DGLAP fit [?], together with the results when additionally including LHeC pseudodata for F_2 (left) and for both F_2 and F_L (right). The results are shown at the starting scale for DGLAP evolution, $Q_0^2 = 2 \text{ GeV}^2$.

2953 The extrapolated NNPDF1.2 gluon density and its uncertainty band are shown at the starting scale for
 2954 QCD evolution, $Q_0^2 = 2 \text{ GeV}^2$ in Fig. ??, where it can be seen that the lack of experimental constraints for
 2955 $x \lesssim 10^{-4}$ leads to an explosion in the uncertainties. When the LHeC F_2 pseudodata are included in addition,
 2956 the uncertainties improve considerably, but remain rather large at the lowest x values, due to the lack of a
 2957 large lever-arm in Q^2 to constrain the evolution. However, when the LHeC pseudodata on the longitudinal
 2958 structure function F_L are included in addition, the additional constraints lead to a much more substantial
 improvement in the uncertainties on the gluon density.

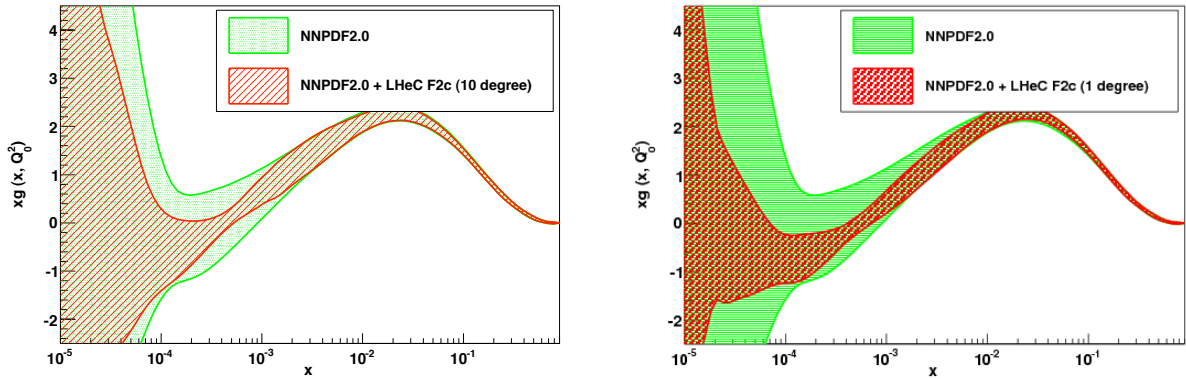


Figure 6.15: The effect on the extracted gluon distribution function of the inclusion of the LHeC pseudodata on the charmed structure function in the NNPDF global analysis. Left plot: scattered electron acceptance extending to within 10° of the beam pipe. Right plot: 1° acceptance. The results are shown at the starting scale for DGLAP evolution, $Q_0^2 = 2 \text{ GeV}^2$.

2959 As is well known from experience at HERA, the measurement of the longitudinal structure function
 2960 presents many experimental challenges and involves possibly undesirable modifications to the beam energies.
 2961 An alternative constraint on the gluon density from the charmed structure function F_2^c has therefore also been
 2962

investigated. As discussed in detail in Subsec. ??, the LHeC will offer unique precision in the determination of the charm and beauty structure functions, extending to very small x .

In Fig. ?? the gluon distribution function is shown, as obtained from the NNPDF2.0 analysis. The green band corresponds to the standard analysis. The red band shows the modified analysis where additionally F_2^c pseudodata from the LHeC are included, using a novel technique based on Bayesian reweighting [?]. It is observed that the charmed structure function considerably improves the constraints on the gluon density at small values of x , especially between $3 \times 10^{-5} - 10^{-2}$, provided that the scattered electron acceptance extends to within around 1° of the beampipe. With a sufficiently good theoretical understanding, heavy flavour production data from the LHeC may thus offer an alternative to F_L for precision constraints on the gluon density at all but the lowest x values.

Given that for all models considered in Fig. ?? there are significant flexibilities in the initial parametrisations, it is conceivable that upon suitable changes of parameters it would be possible to obtain satisfactory fits of a wide range of models to the LHeC data. It is therefore essential to analyse in more detail the ability of the LHeC to distinguish unambiguously between different evolution dynamics. With this aim, a PDF analysis is performed including LHeC pseudodata which are generated using different scenarios for small- x QCD dynamics. Pseudodata for $F_2(x, Q^2)$ and $F_L(x, Q^2)$ at small x are considered in a scenario in which the LHeC machine has electron energy $E_e = 70$ GeV and electron acceptance for $\theta_e \leq 179^\circ$, for an integrated luminosity of 1 fb^{-1} . The study is carried out in the framework of the NNPDF1.0 analysis [?] and includes all HERA and fixed target data used in that analysis, in addition to LHeC pseudodata. The kinematics of the LHeC pseudodata included in the fit (together with other data included in the original NNPDF1.0 analysis) are shown in Fig. ?. In order to avoid correlations between low x and high x data e.g. through the momentum sum rule constraint, only LHeC pseudodata with $x < 10^{-2}$ are considered. The average total uncertainty of the simulated F_2 pseudodata is $\sim 2\%$, while that of F_L is $\sim 8\%$.

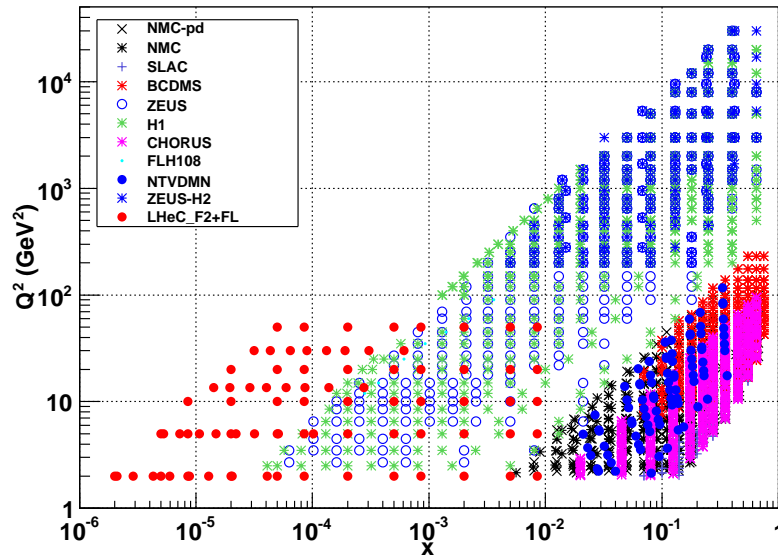


Figure 6.16: The kinematic coverage of the LHeC pseudodata used in the present studies, together with the data already included in the reference NNPDF1.0 dataset.

For the NNPDF fits, the input LHeC pseudodata are generated not within the DGLAP framework, but rather using two different models which include saturation effects in the gluon density: the AAMS09 model [?], which is based on non-linear Balitsky-Kovchegov evolution with a running coupling, and the FS04

2989 dipole model [?]. Both of these models deviate significantly from linear DGLAP evolution in the LHeC
 2990 regime.

2991 The global fit using the NNPDF1.0 framework with fixed-order DGLAP evolution is repeated, now in-
 2992 cluding LHeC pseudodata generated using the scenarios including saturation effects. By assessing the quality
 2993 of the fit with saturated LHeC pseudodata included, this study tests the sensitivity to parton dynamics be-
 2994 yond fixed-order DGLAP. The conclusions are the same for both the AAMS09 and the FS04 models. The
 2995 DGLAP analysis yields an acceptable fit when only the $F_2(x, Q^2)$ LHeC pseudodata are included. This
 2996 implies that although the underlying physical theories are different, the small- x extrapolations of AAMS09
 2997 and FS04 for F_2 are sufficiently similar to DGLAP-based extrapolations for the differences to be absorbed as
 2998 modifications to the shapes of the non-perturbative initial conditions for the PDFs at the starting scale Q_0^2
 2999 for DGLAP evolution. More sophisticated analyses, based for example on sequential kinematical cuts and
 3000 backwards DGLAP evolution, as presented in Subsec. ??, could still be applied. However, it seems likely
 3001 that it will not be possible unambiguously to establish non-linear effects using LHeC data on F_2 alone.

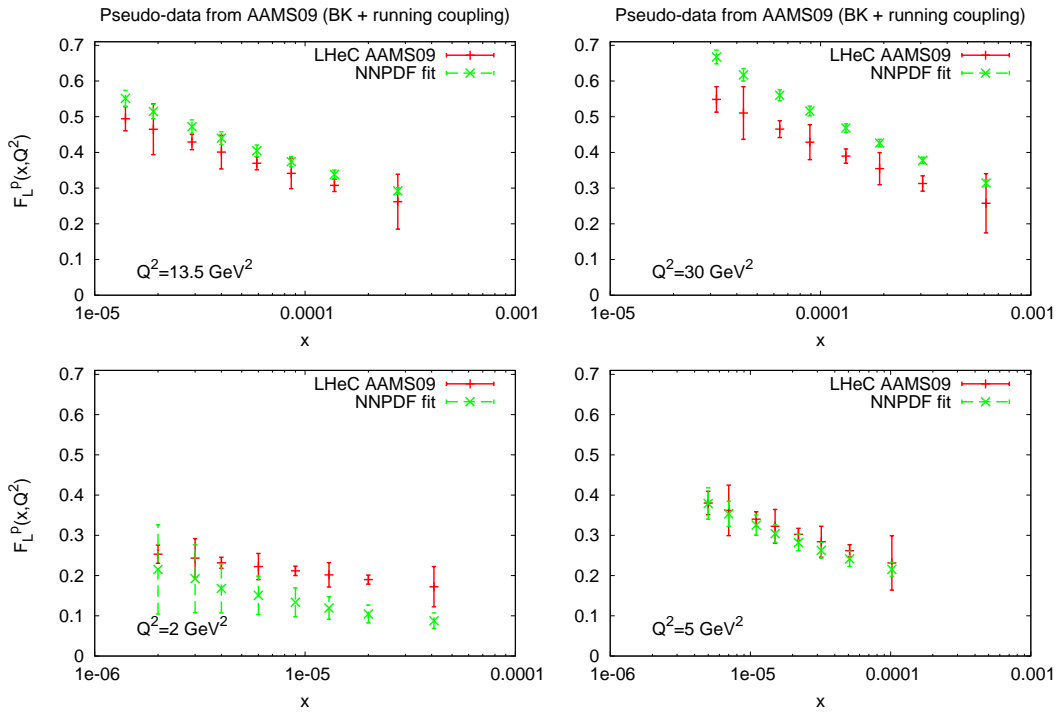


Figure 6.17: The results for F_L obtained from the best NLO DGLAP fit to the standard NNPDF1.2 data set, together with the LHeC pseudodata for $F_2(x, Q^2)$ and $F_L(x, Q^2)$ generated with the (saturating) AAMS09 model. The fit results are compared with the input AAMS09 F_L pseudodata.

3002 The situation is very different when data on the longitudinal structure function $F_L(x, Q^2)$ are included
 3003 in the NNPDF fit, provided the lever-arm in Q^2 is large enough for the gluon sensitivity through the Q^2
 3004 evolution of F_2 to conflict with that through F_L . The analysis based on linear DGLAP evolution fails to
 3005 reproduce simultaneously F_2 and F_L in all the Q^2 bins, and thus the overall χ^2 is very large. The effect is
 3006 illustrated in Fig. ??, where the best fits from the NNPDF DGLAP analysis are compared with the LHeC
 3007 F_L pseudodata generated from the AAMS09 model. This is a clear signal for a departure from fixed-order
 3008 DGLAP of the simulated pseudodata. This analysis shows that the combined use of F_2 and F_L data is
 3009 a very sensitive probe of novel small- x QCD dynamics, and that their measurement would be very likely

3010 to discriminate between different theoretical scenarios. Using F_2^c data in place of F_L may offer a similarly
 3011 powerful means of establishing deviations from fixed-order linear DGLAP evolution at small x .

3012 **Predictions for nuclei: impact on nuclear parton distribution functions**

3013 The LHeC, as an electron-ion collider in the TeV regime, will have an enormous potential for measuring the
 3014 nuclear parton distribution functions at small x . Let us start by a brief explanation of how the pseudodata
 3015 for inclusive observables in $e\text{Pb}$ collisions are obtained: To simulate an LHeC measurement of F_2 in electron-
 3016 nucleus collisions, the points (x, Q^2) , generated for $e(50) + p(7000)$ collisions for a high acceptance, low
 3017 luminosity scenario, as explained in subsection ??, are considered. Among them, we keep only those points
 3018 at small $x \leq 0.01$ and not too large $Q^2 < 1000 \text{ GeV}^2$ with $Q^2 \leq sx$, for a Pb beam energy of 2750 GeV per
 3019 nucleon. Under the assumption that the instantaneous luminosity per nucleon is the same in ep and eA [?],
 3020 the number of events is scaled by a factor $1/(5 \times 50 \times A)$, with 50 coming from the transition from a high
 3021 luminosity to a low luminosity scenario, and 5 being a crudely estimated reduction factor accounting for the
 3022 shorter running time for ions than for proton.

3023 At each point of the grid, σ_r and F_2 are generated using the dipole model of [?,?] to get the central value.
 3024 Then, for every point, the statistical error in ep is scaled by the previously mentioned factor $1/(5 \times 50 \times A)$,
 3025 and corrected for the difference in F_2 or σ_r between the (Glauberized) 5-flavor GBW model [?] and the
 3026 model used for the ep simulation. The fractional systematic errors are taken to be the same as for ep -
 3027 as has been achieved in previous DIS experiments on nuclear targets⁷. An analogous procedure is applied
 3028 when obtaining the nuclear pseudodata for F_2^c and F_2^b , considering the same tag and background rejection
 3029 efficiencies as in the ep simulation.

3030 To generate LHeC F_L pseudodata for a heavy ion target, a dedicated simulation of $e + p(2750)$ collisions
 3031 has been performed, at three different energies: 10, 25 and 50 GeV for the electron, with assumed luminosities
 3032 5, 10 and 100 pb^{-1} respectively, see subsec. ??. Then, for each point in the simulated grid, F_L values for
 3033 protons and nuclei are generated using the (Glauberized) 5-flavor GBW model [?]. The relative uncertainties
 3034 are taken to be exactly the same as in the ep simulation, as explained above.

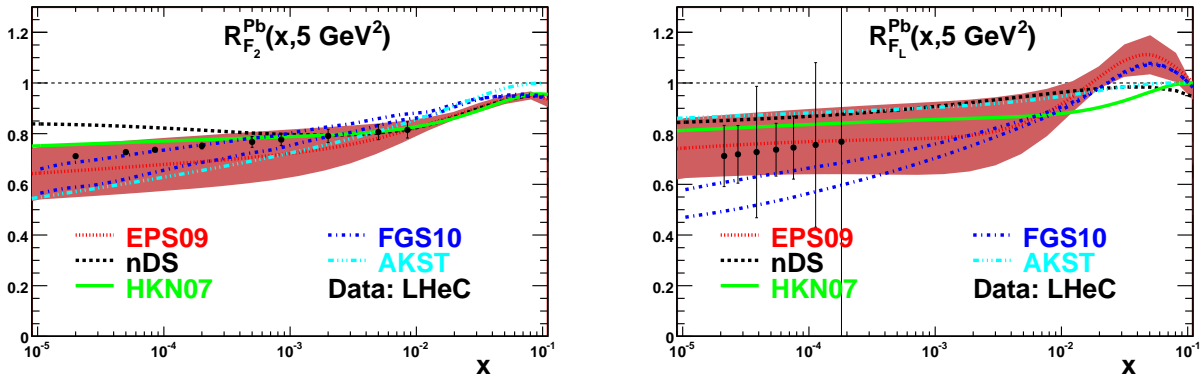


Figure 6.18: Predictions from different models for the nuclear modification factor, Eq. (??) for Pb with respect to the proton, for $F_2(x, Q^2 = 5 \text{ GeV}^2)$ (plot on the left) and $F_L(x, Q^2 = 5 \text{ GeV}^2)$ (plot on the right) versus x , together with the corresponding LHeC pseudodata. Dotted lines correspond to the nuclear PDF set EPS09 [?], dashed ones to nDS [?], solid ones to HKN07 [?], dashed-dotted ones to FGS10 [?] and dashed-dotted-dotted ones to AKST [?]. The band corresponds to the uncertainty in the Hessian analysis in EPS09 [?].

3035 In Fig. ?? we show several predictions for the nuclear suppression factor, Eq. (??), with respect to

⁷A significant difference in the systematics may eventually come from the different size of the QED radiative corrections for protons and nuclei, an important point which remains to be addressed in future studies.

3036 the proton, for the total and longitudinal structure functions, F_2 and F_L respectively, in ePb collisions
 3037 at an example $Q^2 = 5 \text{ GeV}^2$ and for $10^{-5} < x < 0.1$. Predictions based on global DGLAP analyses of
 3038 existing data at NLO: nDS, HKN07 and EPS09 [?, ?, ?], plus those from models using the relation between
 3039 diffraction and nuclear shadowing, AKST and FGS10 [?, ?], are shown together with the LHeC pseudodata.
 3040 Brief explanations on the different models can be found in Subsec. ???. Clearly, the accuracy of the data at
 3041 the LHeC will offer huge possibilities for discriminating between different models and for constraining the
 3042 dynamics underlying nuclear shadowing at small x .

3043 In order to better quantify how the LHeC would improve the present situation concerning nuclear PDFs
 3044 in global DGLAP analyses (see the uncertainty band in Fig. ??), nuclear LHeC pseudodata have been
 3045 included in the global EPS09 analysis [?]. The DGLAP evolution was carried out at NLO accuracy, in the
 3046 variable-flavor-number scheme (SACOT prescription) with the CTEQ6.6 [?] set for free proton PDFs as a
 3047 baseline. See [?] and references therein for further details. The only difference compared with the original
 3048 EPS09 setup is that one additional gluon parameter, x_a , has been varied (this parameter was originally
 3049 frozen in EPS09), and the only additionally weighted data set was the PHENIX data on π^0 production at
 3050 mid-rapidity [?] in dAu collisions at RHIC.

3051 Two different fits have been performed: the first one (Fit 1) includes pseudodata on the total reduced
 3052 cross section. The results of the fit are shown in Fig. ?? in terms of the nuclear modification factors for the
 3053 parton densities. A large improvement in the determination of sea quark and gluon densities at small x is
 3054 evident.

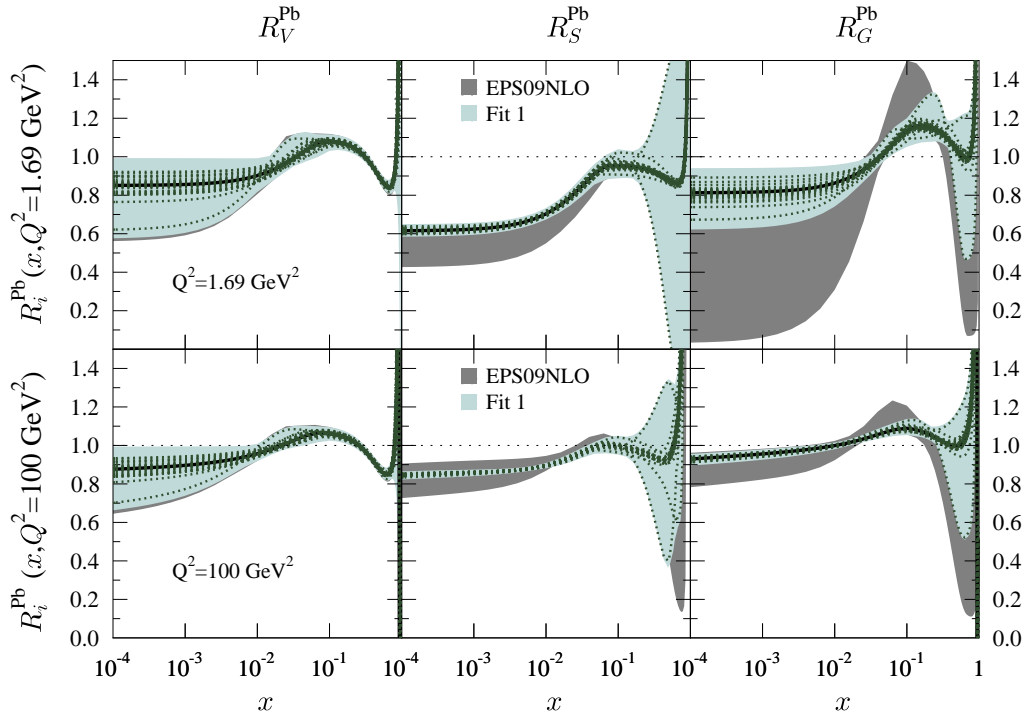


Figure 6.19: Ratio of parton densities for protons bound in Pb to those in a free proton, for valence u (left), \bar{u} (middle) and g (right), at $Q^2 = 1.69$ (top) and 100 (bottom) GeV^2 . The dark grey band corresponds to the uncertainty band using the Hessian method in the original EPS09 analysis [?], while the light blue band corresponds to the uncertainty obtained after including nuclear LHeC pseudodata on the total reduced cross sections (Fit 1). The dotted lines indicate the values corresponding to the different nPDF sets in the EPS09 analysis [?].

3055
3056
3057
3058
3059

The second fit (Fit 2) includes not only nuclear LHeC pseudodata on the total reduced cross section but also on its charm and beauty components. These data provide direct information on the nuclear effects on charm and beauty parton densities, which are generated mainly dynamically from the gluons through DGLAP evolution. Thus, the inclusion of such pseudodata further improves the determination of the nuclear effects on the gluon at small x , as illustrated in Fig. ??.

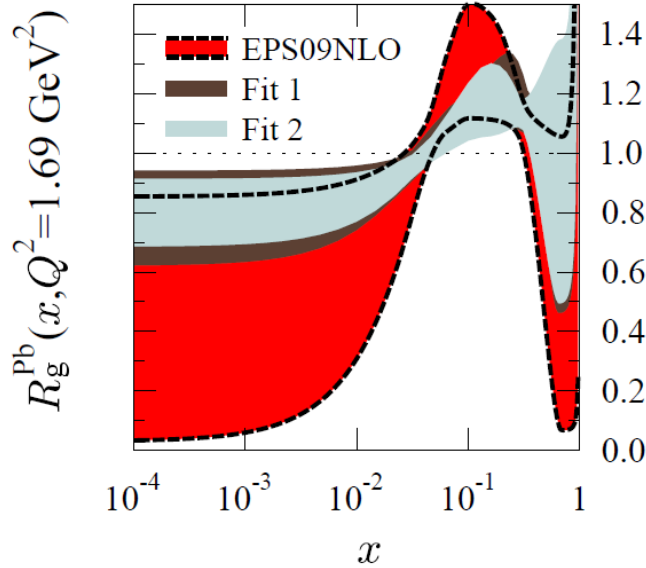


Figure 6.20: Ratio of the gluon density for protons bound in Pb to that of a free proton at $Q^2 = 1.69 \text{ GeV}^2$. The red band corresponds to the uncertainty using the Hessian method in the original EPS09 analysis [?], while the dark brown band corresponds to the uncertainty obtained after including nuclear LHeC pseudodata on the total reduced cross sections (Fit 1), and the light blue band shows the uncertainty obtained after further including pseudodata on charm and beauty reduced cross sections (Fit 2).

3060
3061
3062
3063
3064
3065
3066
3067
3068
3069
3070
3071
3072
3073
3074

In both Figs. ?? and ?? a sizable reduction of the uncertainties in the sea quark and gluon nuclear parton distributions at large $x > 0.1$ can also be observed. This improvement is basically due to the constraints imposed by sum rules and to the fact that DGLAP evolution links large and small x . Although the study of parton distributions at large x is not the subject of this chapter, it is worth commenting that F_2 could be measured in eA collisions at the LHeC with a statistical accuracy better than a few percent up to $x \sim 0.6$ but for large $Q^2 > 1000 \text{ GeV}^2$. On the other hand, flavor decomposition will only be accessible for $x < 0.1$. Therefore, the LHeC will provide additional information on the antishadowing ($R > 1, 0.1 < x < 0.3$) and - with less precision - on the EMC-effect ($R < 1, 0.3 < x < 0.8$) regions. The latter is valence-dominated and there exist data from fixed target experiments, though at much smaller Q^2 , so at the LHeC the validity of leading-twist DGLAP evolution will be tested.

Furthermore, the large lever-arm in Q^2 opens the possibility of measuring CC events in electron scattering on nuclear targets, thus helping to improve the loose constraints on the flavour decomposition of the nuclear parton densities coming from existing DIS and DY data. In this respect (see the comments in Subsec. ??) the LHeC may help to clarify the issue of the compatibility of the nuclear corrections extracted in neutrino-nucleus collisions with those coming from electron- or muon-nucleus collisions⁸.

⁸Note that the nuclear modifications of the structure function F_2 in these two types of process are expected to differ due to

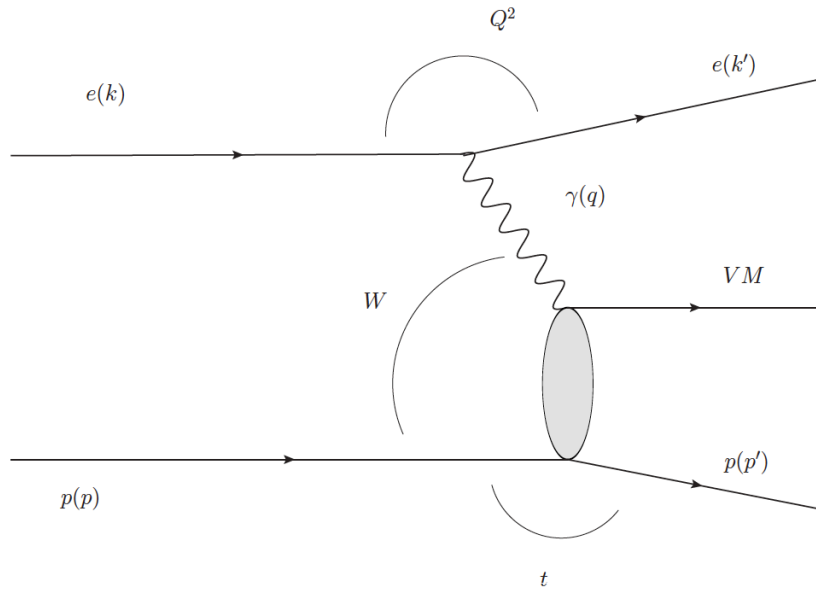


Figure 6.21: Schematic illustration of the exclusive vector meson production process and the kinematic variables used to describe it in photoproduction ($Q^2 \rightarrow 0$) and DIS (large Q^2). The outgoing particle labelled ‘VM’, may be either a vector meson with $J^{PC} = 1^{--}$ or a photon.

3075 In conclusion, the precision and large lever-arm in x and Q^2 of the nuclear data at the LHeC will offer huge
 3076 possibilities for discriminating different models and for constraining the parton densities in global DGLAP
 3077 analyses. Besides measurements of the reduced cross section, data on its charm and bottom components
 3078 and on F_L will help to constrain the nuclear effects on PDFs, see e.g. the recent work in [?, ?].

3079 6.2.3 Exclusive Production

3080 Introduction

3081 Exclusive processes such as the electroproduction of vector mesons and photons, $\gamma^* N \rightarrow VN (V = \rho^0, \phi, \gamma)$, or
 3082 photoproduction of heavy quarkonia, $\gamma N \rightarrow VN (V = J/\psi, \Upsilon)$ - see Fig. ?? - provide information on nucleon
 3083 structure and small- x dynamics which is complementary to that obtained in inclusive measurements [?]. The
 3084 exclusive production of J/ψ and ρ mesons in ep collisions and Deeply-Virtual Compton Scattering (DVCS,
 3085 $ep \rightarrow e\gamma p$), have been particularly prominent in the development of our understanding of HERA physics [?].

3086 Diffractive channels such as these are favourable, since the underlying exchange crudely equates to a
 3087 pair of gluons, making the process sensitive to the square of the gluon density [?], in place of the linear
 3088 dependence for F_2 or F_L . With a sufficiently good theoretical understanding of the exclusive production
 3089 mechanism, this may enhance substantially the sensitivity to non-linear evolution and saturation phenomena.
 3090 As already shown at HERA, J/Ψ production in particular is a potentially very clean probe of the gluonic
 3091 structure of the hadron [?, ?]. The same exclusive processes can be measured in deep inelastic scattering off
 3092 nuclei, where the gluon density is modified by nuclear effects [?]. In addition, exclusive processes give access
 3093 to the spatial distribution of the gluon density, parametrized by the impact parameter [?] of the collision.
 3094 The correlations between the gluons coupling to the proton contain information on the three-dimensional
 3095 structure of the nucleon or nucleus, which is encoded in the Generalised Parton Densities (GPDs). The

the different coupling to quarks [?].

3096 GPDs combine aspects of parton densities and elastic form factors and have emerged as a key concept for
3097 describing nucleon structure in QCD (see [?, ?, ?] for a review).

3098 Exclusive processes can be treated conveniently within the dipole picture described in Subsec. ???. In this
3099 framework, the cross section can be represented as a product of three factorisable terms: the splitting of an
3100 incoming photon into a $q\bar{q}$ dipole; the ‘dipole’ cross section for the interaction of this $q\bar{q}$ pair with the proton
3101 and, in the case of vector mesons, a wave function term for the projection of the dipole onto the meson. As
3102 discussed in Subsec. ?? the dipole formalism is particularly convenient since saturation effects can be easily
3103 incorporated.

3104 Generalised Parton Densities and Spatial Structure

3105 At sufficiently large Q^2 the exclusively produced meson or photon is in a configuration of transverse size
3106 much smaller than the typical hadronic size, $r_{\perp} \ll R_{\text{hadron}}$. As a result its interaction with the target
3107 can be described using perturbative QCD [?]. A QCD factorisation theorem [?] states that the exclusive
3108 amplitudes in this regime can be factorised into a perturbative QCD scattering process and certain universal
3109 process-independent functions describing the emission and absorption of the active partons by the target,
3110 the generalized parton distributions (GPDs).

3111 The Fourier transform of the GPDs with respect to the transverse momentum transferred to the nucleon
3112 describes the transverse spatial distribution of partons (illustrated in Fig. ??) with a given longitudinal
3113 momentum fraction x [?]. The transverse spatial distributions of quarks and gluons are fundamental char-
3114 acteristics of the nucleon, which reveal the size of the configurations in its partonic wave function and allow
3115 the study of the non-perturbative dynamics governing their change with x , such as Gribov diffusion, chiral
3116 dynamics, and other phenomena. The nucleon transverse gluonic size is also an essential input in studies of
3117 saturation at small x . It determines the initial conditions of the non-linear QCD evolution equations and
3118 thus directly influences the impact parameter dependence of the saturation scale for the nucleon [?, ?], which
3119 in turn predicates its nuclear enhancement [?]. Information on the nucleon transverse quark and gluon distri-
3120 butions is further required in the phenomenology of high-energy pp collisions with hard processes, including
3121 those with new particle production, where it determines the underlying event structure (centrality depen-
3122 dence) in inclusive scattering [?] and the rapidity gap survival probability in hard single diffraction [?] and
3123 central exclusive diffraction [?, ?]. In view of its considerable interest, the transverse quark/gluon imaging
3124 of the nucleon with exclusive processes has been recognized as an important objective of nucleon structure
3125 and small- x physics.

3126 Mapping the transverse spatial distribution of quarks and gluons requires measurement of the t -dependence
3127 of hard exclusive processes up to large values of $|t|$, of the order of 1 GeV^2 . Studies of the Q^2 -dependence
3128 and comparisons between different channels provide crucial tests of the reaction mechanism and the uni-
3129 versality of GPDs. Vector meson production at small x and heavy quarkonium photoproduction at high
3130 energies probe the gluon GPD of the target, while real photon production (DVCS) involves the singlet quark
3131 as well as the gluon GPDs. Measurements of exclusive J/ψ photo/electroproduction [?, ?] and ρ^0 and ϕ
3132 electroproduction at HERA have confirmed the applicability of the factorized QCD description through sev-
3133 eral model-independent tests, and have provided basic information on the nucleon gluonic size in the region
3134 $10^{-4} < x < 10^{-2}$ and its change with x [?]. Measurements of DVCS at HERA [?, ?] hint that the transverse
3135 distribution of singlet quarks may extend further than that of gluons. While these experiments have given
3136 important insight into transverse nucleon structure, the interpretation of the HERA data is limited by the
3137 low statistics which preclude a fully differential analysis. A major source of systematic uncertainty at larger
3138 t arises from the lack of a complete separation between elastically scattered protons and proton excitations,
3139 illustrating the importance of good scattered proton detection at the LHeC.

3140 As discussed in the following, the LHeC would enable a comprehensive program of gluon and singlet
3141 quark transverse imaging through exclusive processes, with numerous applications to nucleon structure and
3142 small- x physics. The high statistics would permit fully differential measurements of exclusive channels, as
3143 needed to understand the reaction mechanism. For example, measurements of the t -distributions for fixed
3144 x differentially in Q^2 are needed to confirm the dominance of small-size configurations. The LHeC would
3145 also push such measurements to the region $Q^2 \sim \text{few} \times 10 \text{ GeV}^2$ where finite-size (higher-twist) effects are

3146 small and the effects of QCD evolution can be cleanly identified. Measurements of gluonic exclusive channels
3147 ($J/\psi, \phi, \rho^0$) at the LHeC would provide gluonic transverse images of the nucleon down to $x \sim 10^{-6}$ with
3148 unprecedented accuracy, testing theoretical ideas about diffusion dynamics in the wave function. Because
3149 exclusive cross sections are proportional to the square of the gluon GPD (i.e. the gluon density), such
3150 measurements would also offer new insight into non-linear effects in QCD evolution, and enable new tests of
3151 the approach to saturation by measuring the impact parameter dependence of the saturation scale. Along
3152 these lines, saturation effects in the exclusive vector meson production on protons and nuclei have been
3153 studied in [?, ?, ?, ?]. Furthermore, measurements of DVCS would provide additional information on the
3154 nucleon singlet quark size and its dependence on x . Besides its intrinsic interest for nucleon structure and
3155 small- x physics, this information would greatly advance our theoretical understanding of the transverse
3156 geometry of high-energy pp collisions at the LHC. We note that these exclusive measurements at the LHeC
3157 would complement similar measurements at moderately small x ($0.003 < x < 0.2$) with the COMPASS
3158 experiment at CERN and in the valence region $x > 0.1$ with the JLab 12 GeV Upgrade, providing a
3159 comprehensive picture of the nucleon spatial structure.

3160 Further interesting information comes from hard exclusive measurements accompanied by the diffractive
3161 dissociation of the nucleon, $\gamma^* N \rightarrow V + Y$ ($Y =$ low-mass proton dissociation state). The ratio of inelastic to
3162 elastic diffraction in these processes provides information on the quantum fluctuations of the gluon density,
3163 which reveals the quantum-mechanical nature of the non-perturbative colour fields in the nucleon and can be
3164 related to dynamical models of low-energy nucleon structure [?]. HERA results are in qualitative agreement
3165 with such model predictions but do not permit a quantitative analysis. These measurements of exclusive
3166 diffraction at the LHeC, and similar ones for eA collisions, would allow for detailed quantitative studies of
3167 all these new aspects of nucleon and nuclear structure.

3168 Exclusive Production Formalism in the Dipole Approach

3169 For the exclusive production of vector mesons, a QCD factorization theorem has been demonstrated (for
3170 σ_L) in [?]. The dipole model follows from this QCD factorization theorem in the LO approximation. Within
3171 the dipole model, see Subsec. ??, the amplitude for the exclusive diffractive production of a particle E ,
3172 $\gamma^* p \rightarrow Ep$, shown in Fig. ??(a), can be expressed as

$$3173 \mathcal{A}_{T,L}^{\gamma^* p \rightarrow E+p}(x, Q, \Delta) = i \int d^2 \mathbf{r} \int_0^1 \frac{dz}{4\pi} \int d^2 \mathbf{b} (\Psi_E^* \Psi)_{T,L} e^{-i[\mathbf{b} - (1-z)\mathbf{r}] \cdot \Delta} \frac{d\sigma_{q\bar{q}}}{d^2 \mathbf{b}}. \quad (6.6)$$

3174 Here $E = V$ for vector meson production, or $E = \gamma$ for deeply virtual Compton scattering (DVCS). In Eq.
3175 (??), z is the fraction of the photon's light-cone momentum carried by the quark, $r = |\mathbf{r}|$ is the transverse size
3176 of the $q\bar{q}$ dipole, while \mathbf{b} is the impact parameter, that is, $b = |\mathbf{b}|$ is the transverse distance from the centre
3177 of the proton to the centre-of-mass of the $q\bar{q}$ dipole; see Fig. ??(a). The transverse momentum lost by the
3178 outgoing proton, Δ , is the Fourier conjugate variable to the impact parameter \mathbf{b} , and $t \equiv (p - p')^2 = -\Delta^2$.
3179 The forward overlap function between the initial-state photon wave function and the final-state vector meson
3180 or photon wave function in Eq. (??) is denoted $(\Psi_E^* \Psi)_{T,L}$, while the factor $\exp[i(1-z)\mathbf{r} \cdot \Delta]$ originates from the
3181 non-forward wave function [?]. The differential cross section for an exclusive diffractive process is obtained
3182 from the amplitude, Eq. (??), by

$$3183 \frac{d\sigma_{T,L}^{\gamma^* p \rightarrow E+p}}{dt} = \frac{1}{16\pi} \left| \mathcal{A}_{T,L}^{\gamma^* p \rightarrow E+p} \right|^2, \quad (6.7)$$

3184 up to corrections from the real part of the amplitude and from skewedness ($x' \ll x \ll 1$ for the variables
3185 shown in figure ??a). Taking the imaginary part of the forward scattering amplitude immediately gives the
3186 formula for the total $\gamma^* p$ cross section (or equivalently, the proton structure function $F_2 = F_T + F_L$) via the
3187 optical theorem:

$$3188 \sigma_{T,L}^{\gamma^* p}(x, Q) = \text{Im} \mathcal{A}_{T,L}^{\gamma^* p \rightarrow \gamma^* p}(x, Q, \Delta = 0) = \sum_f \int d^2 \mathbf{r} \int_0^1 \frac{dz}{4\pi} (\Psi^* \Psi)_{T,L}^f \int d^2 \mathbf{b} \frac{d\sigma_{q\bar{q}}}{d^2 \mathbf{b}}. \quad (6.8)$$

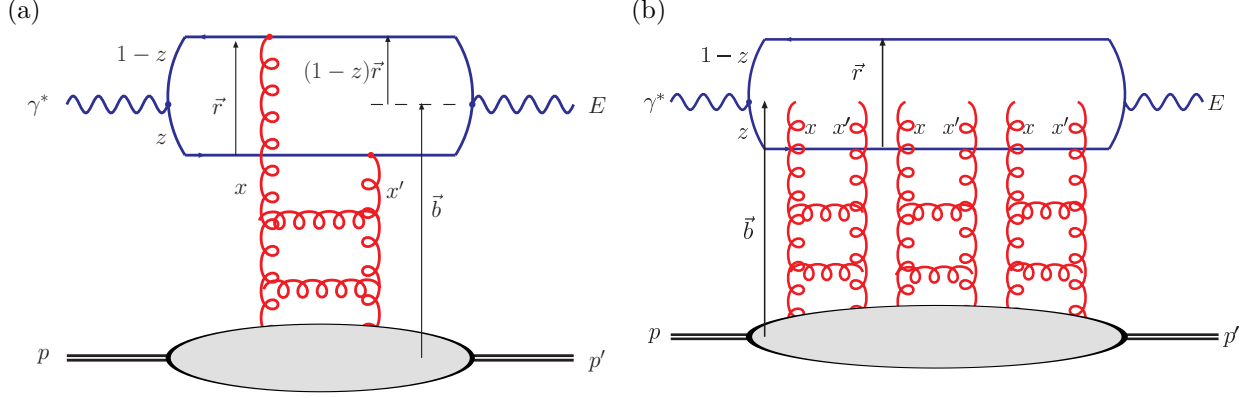


Figure 6.22: Parton level diagrams representing the γ^*p scattering amplitude proceeding via (a) single-Pomeron and (b) multi-Pomeron exchange, where the perturbative QCD Pomeron is represented by a gluon ladder. For exclusive diffractive processes, such as vector meson production ($E = V$) or DVCS ($E = \gamma$), we have $x' \ll x \ll 1$ and $t = (p - p')^2$. These diagrams are related through the optical theorem to inclusive DIS, where $E = \gamma^*$, $x' = x \ll 1$ and $p' = p$.

3186 The dipole picture therefore provides a unified description of both exclusive diffractive processes and inclusive
 3187 deep-inelastic scattering (DIS) at small x .

3188 The unknown quantity common to Eqs. (??) and (??) is the b -dependent dipole–proton cross section,

$$\frac{d\sigma_{q\bar{q}}}{d^2\mathbf{b}} = 2 \mathcal{N}(x, r, b), \quad (6.9)$$

3189 where \mathcal{N} is the imaginary part of the dipole–proton scattering amplitude, which can vary between zero and
 3190 one, with $\mathcal{N} = 1$ corresponding to the unitarity (“black disk”) limit. The scattering amplitude \mathcal{N} encodes the
 3191 information about the details of the strong interaction between the dipole and the target (proton or nucleus).
 3192 It is generally parameterised according to some theoretically-motivated functional form, with the paramete-
 3193 rs fitted to data. Most dipole models assume a factorised b dependence, $\mathcal{N}(x, r, b) = T(b)\mathcal{N}(x, r)$, with
 3194 $\mathcal{N}(x, r) \in [0, 1]$ and, for example, $T(b) = \Theta(R_p - b)$, so that the b -integrated $\sigma_{q\bar{q}} = (2\pi R_p^2)\mathcal{N}(x, r)$. However,
 3195 the “saturation scale” is strongly dependent on impact parameter and the chosen of b -dependence must be
 3196 made consistent with the t -dependence of exclusive diffraction at HERA. This matching is complicated by
 3197 the the non-zero effective “Pomeron slope” α'_p measured at HERA, which implies a correlation between the
 3198 x - and b - dependences of $\mathcal{N}(x, r, b)$. Therefore, for accurate results, $\mathcal{N}(x, r, b)$ should be determined from
 3199 the simultaneous description of inclusive DIS and exclusive diffractive processes.

3200 An impact-parameter-dependent saturation (“b-sat”) model [?, ?] has been shown to describe very suc-
 3201 cessfully a broad range of HERA data on exclusive diffractive vector meson (J/ψ , ϕ , ρ) production and DVCS
 3202 (see also the rather different approach in [?]), including almost all aspects of the Q^2 , W and t dependence
 3203 with the exception of α'_p , together with the inclusive structure functions F_2 , $F_2^{c\bar{c}}$, $F_2^{b\bar{b}}$ and F_L . The “b-Sat”
 3204 parameterisation is based on LO DGLAP evolution of an initial gluon density, $xg(x, \mu_0^2) = A_g x^{-\lambda_g} (1-x)^{5.6}$,
 3205 with a Gaussian impact parameter dependence, $T(b) \propto \exp(-b^2/2B_G)$. The dipole scattering amplitude is
 3206 parametrized as

$$\mathcal{N}(x, r, b) = 1 - \exp\left(-\frac{\pi^2}{2N_c} r^2 \alpha_S(\mu^2) xg(x, \mu^2) T(b)\right), \quad (6.10)$$

3207 where the scale $\mu^2 = 4/r^2 + \mu_0^2$, $B_G = 4 \text{ GeV}^{-2}$ was fixed from the t -slope of exclusive J/ψ photoproduction
 3208 at HERA, and the other three parameters ($\mu_0^2 = 1.17 \text{ GeV}^2$, $A_g = 2.55$, $\lambda_g = 0.020$) were fitted to ZEUS F_2
 3209 data with $x_{Bj} \leq 0.01$ and $Q^2 \in [0.25, 650] \text{ GeV}^2$ [?]. The eikonalised dipole scattering amplitude of Eq. (??)

3210 can be expanded as

$$3211 \quad \mathcal{N}(x, r, b) = \sum_{n=1}^{\infty} \frac{(-1)^{n+1}}{n!} \left[\frac{\pi^2}{2N_c} r^2 \alpha_S(\mu^2) xg(x, \mu^2) T(b) \right]^n, \quad (6.11)$$

3212 where the n -th term in the expansion corresponds to n -Pomeron exchange; for example, the case $n = 3$ is
 3213 illustrated in Fig. ??(b). The terms with $n > 1$ are necessary to ensure unitarity.

3213 Simulations of LHeC Elastic J/ψ and Υ Production

3214 Due to the extremely clean final states produced, the relatively low effective x -values ($x_{\text{eff}} \sim (Q^2 + m_V^2)/(Q^2 +$
 3215 $W^2)$) and scales ($Q_{\text{eff}}^2 \sim (Q^2 + m_V^2)/4$) accessed [?, ?], and the experimental possibility of varying both W
 3216 and t over wide ranges, J/ψ photoproduction ($Q^2 \rightarrow 0$) may offer the cleanest available signature to study
 3217 the transition between the dilute and dense regimes of small- x partons. It should be possible to detect the
 3218 muons from J/ψ or Υ decays with acceptances extending to within 1° of the beam pipe with dedicated muon
 3219 chambers on the outside of the experiment. Depending on the electron beam energy, this makes invariant
 3220 photon-proton masses W of well beyond 1 TeV accessible.

3221 For the analysis presented here we concentrate on the photoproduction limit, where the HERA data are
 3222 most precise due to the large cross sections and where unitarity effects are most important. Studies have
 3223 also been made at larger Q^2 [?], where the extra hard scale additionally allows a perturbative treatment of
 3224 exclusive light vector meson (e.g. ρ , ω , ϕ) production. Again, perturbative unitarity effects are expected to
 3225 be important for light vector meson production when $Q^2 \gtrsim 1 \text{ GeV}^2$ is not too large.

3226 LHeC pseudodata for elastic J/ψ and Υ photoproduction and electroproduction have been generated
 3227 using the DIFFVM Monte Carlo generator [?] under the assumption of 1° acceptance and a variety of lumi-
 3228 nosity scenarios. The DIFFVM generator involves a simple Regge-based parameterization of the dynamics
 3229 and a full treatment of decay angular distributions. Statistical uncertainties are estimated for each data
 3230 point. Systematic uncertainties are hard to estimate without a detailed simulation of the muon identification
 3231 and reconstruction capabilities of the detector, but are likely to be at least as good as the 10% measurements
 3232 typically achieved for the elastic J/ψ at HERA.

3233 The plots in Fig. ?? show t -integrated predictions for exclusive J/ψ photoproduction ($Q^2 = 0$) obtained
 3234 from Eqs. (??) and (??), using the eikonalised “b-Sat” dipole scattering amplitude given in Eq. (??) to-
 3235 gether with a “boosted Gaussian” vector meson wave function [?, ?]. Also shown is the single-Pomeron
 3236 exchange contribution obtained by keeping just the first ($n = 1$) term in the expansion of Eq. (??), such
 3237 that the scattering amplitude is linearly dependent on the gluon density, without refitting any of the input
 3238 parameters. The difference between the “eikonalised” and “1-Pomeron” predictions therefore indicates the
 3239 importance of unitarity corrections, which increase significantly with rising γp centre-of-mass energy W . The
 3240 maximum kinematic limit accessible at the LHeC, $W = \sqrt{s}$, is indicated with different options for electron
 3241 beam energies (E_e) and not accounting for the angular acceptance of the detector. The most precise HERA
 3242 data [?, ?] are overlaid, together with sample LHeC pseudodata points, assuming 1° muon acceptance, with
 3243 the errors (statistical only) given by an LHeC simulation with $E_e = 150 \text{ GeV}$. The central values of the
 3244 LHeC pseudodata points were obtained from a Gaussian distribution with the mean given by extrapolating
 3245 a power-law fit to the HERA data [?, ?] and the standard deviation given by the statistical errors from the
 3246 LHeC simulation. The plots in Fig. ?? show that the errors on the LHeC pseudodata are much smaller than
 3247 the difference between the “eikonalised” and “1-Pomeron” predictions. Therefore, exclusive J/ψ photopro-
 3248 duction at the LHeC may be an ideal observable for investigating unitarity corrections at a perturbative
 3249 scale provided by the charm-quark mass.

3250 Similar plots for exclusive Υ photoproduction are shown in Fig. ?. Here, the unitarity corrections are
 3251 smaller than for J/ψ production due to the larger scale provided by the bottom-quark mass and therefore the
 3252 smaller typical dipole sizes r being probed. The simulated LHeC pseudodata points also have larger statistical
 3253 errors than for J/ψ production due to the much smaller cross sections. Nonetheless, the simulations indicate
 3254 that a huge improvement in kinematic range and precision is possible compared with the very sparse Υ data
 3255 from HERA [?, ?, ?].

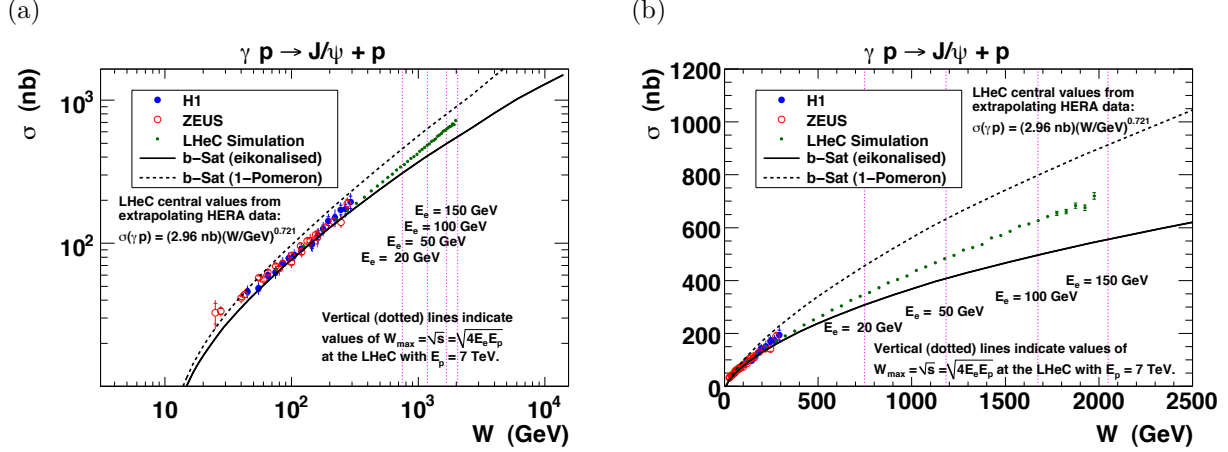


Figure 6.23: LHeC exclusive J/ψ photoproduction pseudodata, as a function of the γp centre-of-mass energy W , plotted on a (a) log–log scale and (b) linear–linear scale. The difference between the solid and dashed curves indicates the size of unitarity corrections according to the b-Sat dipole model.

3256 In order to achieve a satisfactory description of the experimental data on exclusive Υ photoproduction,
 3257 an additional normalization factor of ~ 2 has to be included in the dipole calculation (a similar factor is
 3258 required for other calculations using the dipole model, see for example Ref. [?]). This normalization factor
 3259 does not arise from any theoretical considerations. Therefore, the dipole model prediction for the Υ in
 3260 diffractive exclusive processes in DIS still poses significant theoretical questions which cannot be resolved
 3261 without LHeC data.

3262 The cross sections shown in Figs. ?? and ?? are integrated over $t \equiv (p-p')^2 = -\Delta^2$, where Δ is the Fourier
 3263 conjugate variable to the impact parameter \mathbf{b} . One expects that at high center-of-mass energies (small x),
 3264 saturation effects are most important close to the centre of the proton (small b), where the interaction region
 3265 is densest. This is illustrated in Fig. ??(a) where the b-Sat model dipole scattering amplitude is shown as a
 3266 function of b for various x values. By measuring exclusive diffraction in bins of $|t|$ one can extract the impact
 3267 parameter profile of the interaction region. This is illustrated in Fig. ??(b) where the integrand of Eq. (??)
 3268 is shown for different values of t as a function of impact parameter. Clearly for large values of $|t|$, small values
 3269 of b are probed in the impact parameter profile., corresponding to the most densely populated region, where
 3270 saturation effects should be most clearly visible. Indeed, the eikonalised dipole model of Eq. (??) leads to
 3271 “diffractive dips” in the t -distribution of exclusive J/ψ photoproduction at large $|t|$ (reminiscent of the dips
 3272 seen in the t -distribution of the proton-proton elastic cross section), departing from the exponential fall-off
 3273 in the t -distribution seen with single-Pomeron exchange [?]. The HERA experiments have only been able
 3274 to make precise measurements of exclusive J/ψ photoproduction at relatively small $|t| \lesssim 1 \text{ GeV}^2$, and no
 3275 significant departure from the exponential fall-off, $d\sigma/dt \sim \exp(-B_D|t|)$, has been observed.

3276 In Fig. ??, LHeC pseudodata on the differential cross section $d\sigma/dt$ is shown as a function of the energy
 3277 W in different bins of t for the case of exclusive J/Ψ production. Again two different b-Sat model scenarios
 3278 are shown, with unitarisation effects and with single Pomeron exchange. Already for small values of $|t| \sim$
 3279 0.2 GeV^2 and low values of electron energies there is a large discrepancy between the models. The LHeC
 3280 simulated data still have very small errors in this regime, and can clearly distinguish between the different
 3281 models. The differences are of course amplified for large t and large electron beam energies. However the
 3282 precision of the data deteriorates at large t .

3283 Summarising, it is clear that the precise measurements of large- $|t|$ exclusive J/ψ photoproduction at the
 3284 LHeC would have significant sensitivity to unitarity effects.

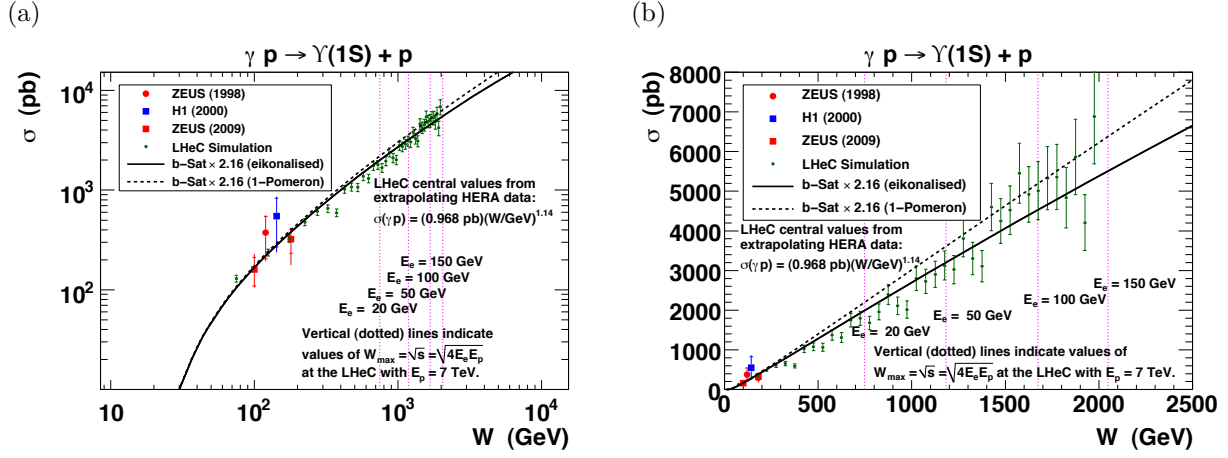


Figure 6.24: LHeC exclusive Υ photoproduction pseudodata, as a function of the γp centre-of-mass energy W , plotted on a (a) log–log scale and (b) linear–linear scale. The difference between the solid and dashed curves indicates the size of unitarity corrections according to the b-Sat model. The b-Sat theory predictions have been scaled by a factor 2.16 to best-fit the existing HERA data.

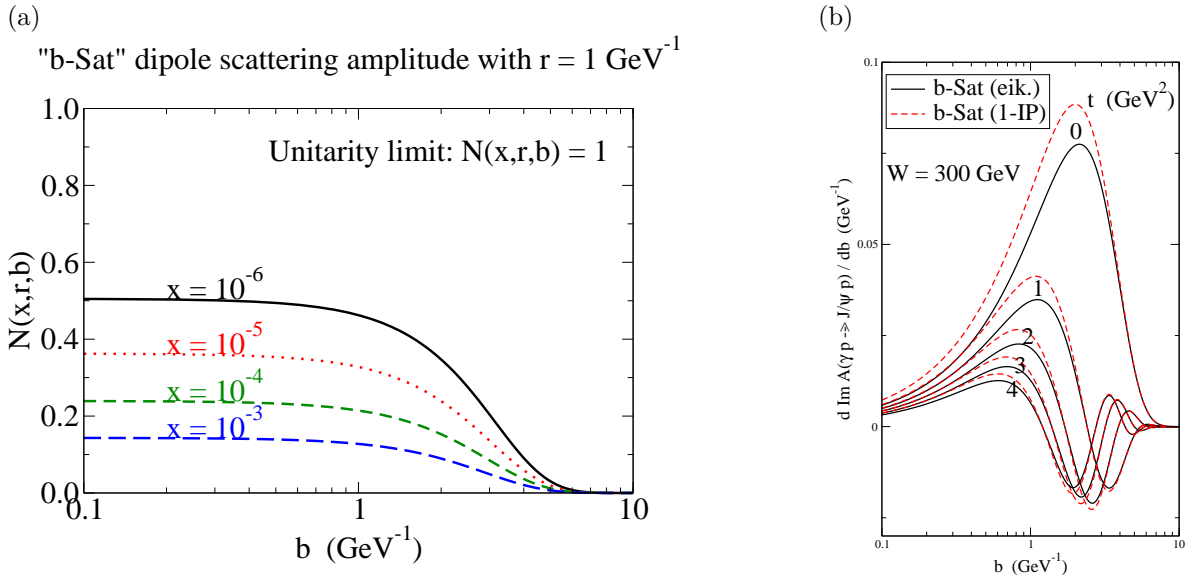


Figure 6.25: (a) The imaginary part of the dipole scattering amplitude, $\mathcal{N}(x, r, b)$, as a function of the impact parameter b , for fixed values of dipole size $r = 1 \text{ GeV}^{-1}$ (typical for exclusive J/ψ photoproduction) and different x values. (b) The $(r$ -integrated) amplitude - the integrand of Eq. (??) - for exclusive J/ψ photoproduction as a function of b , for $W = 300 \text{ GeV}$ and $|t| = 0, 1, 2, 3, 4 \text{ GeV}^2$.

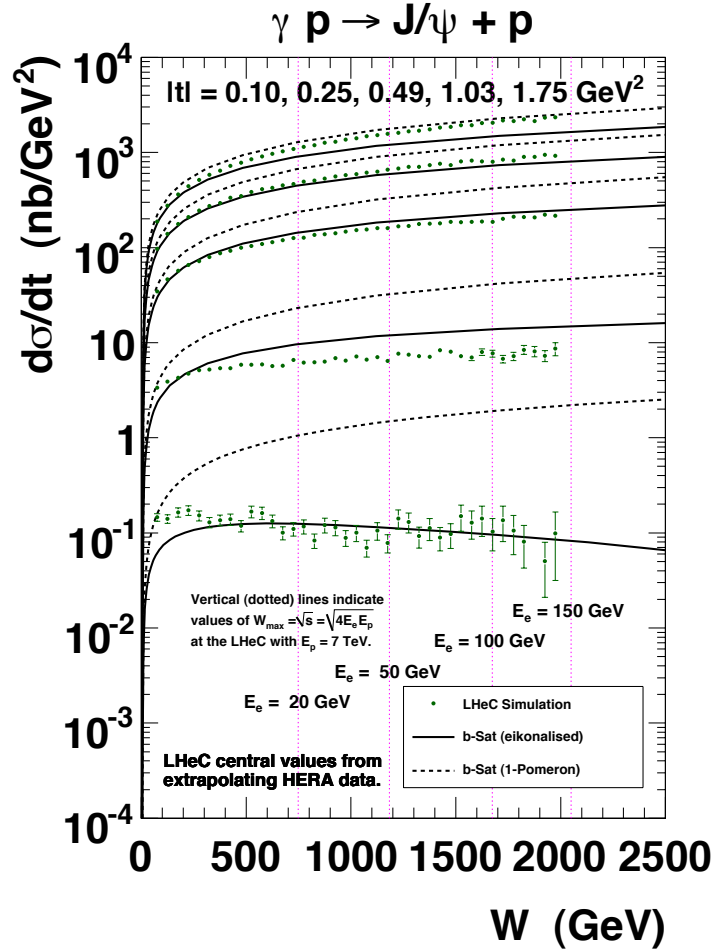


Figure 6.26: Simulated LHeC measurements of the W -dependence of exclusive J/ψ photoproduction at the LHeC, differentially in bins of $|t| = 0.10, 0.20, 0.49, 1.03, 1.75$ GeV². The difference between the solid and dashed curves indicates the size of unitarity corrections according to the b-Sat dipole model. The central values of the LHeC pseudodata points were obtained from a Gaussian distribution with the mean given by extrapolating a parameterization of HERA data and the standard deviation given by the statistical errors from the LHeC simulation with $E_e = 150$ GeV. The t -integrated cross section (σ) as a function of W for the HERA parameterization was obtained from a power-law fit to the data from both ZEUS [?] and H1 [?], then the t -distribution was assumed to behave as $d\sigma/dt = \sigma \cdot B_D \exp(-B_D|t|)$, with $B_D = [4.400 + 4 \cdot 0.137 \log(W/90 \text{ GeV})]$ GeV⁻² obtained from a linear fit to the values of B_D versus W given by both ZEUS [?] and H1 [?].

3285 **Simulations of Deeply Virtual Compton Scattering at the LHeC**

3286 Simulations of the DVCS measurement possibilities with the LHeC have been made using the Monte Carlo
 3287 generator MILOU [?], in the ‘FFS option’, for which the DVCS cross section is estimated using the model
 3288 of Frankfurt, Freund and Strikman [?]. A t -slope of $B = 6 \text{ GeV}^{-2}$ is assumed.

3289 The $ep \rightarrow e\gamma p$ DVCS cross section is estimated in various scenarios for the electron beam energy and
 3290 the statistical precision of the measurement is estimated for different integrated luminosity and detector
 3291 acceptance choices. Detector acceptance cuts at either 1° or 10° are placed on the polar angle of the final
 3292 state electron and photon. Based on experience with controlling backgrounds in HERA DVCS measurements
 3293 [?, ?, ?], an additional cut is placed on the transverse momentum P_T^γ of the final state photon.

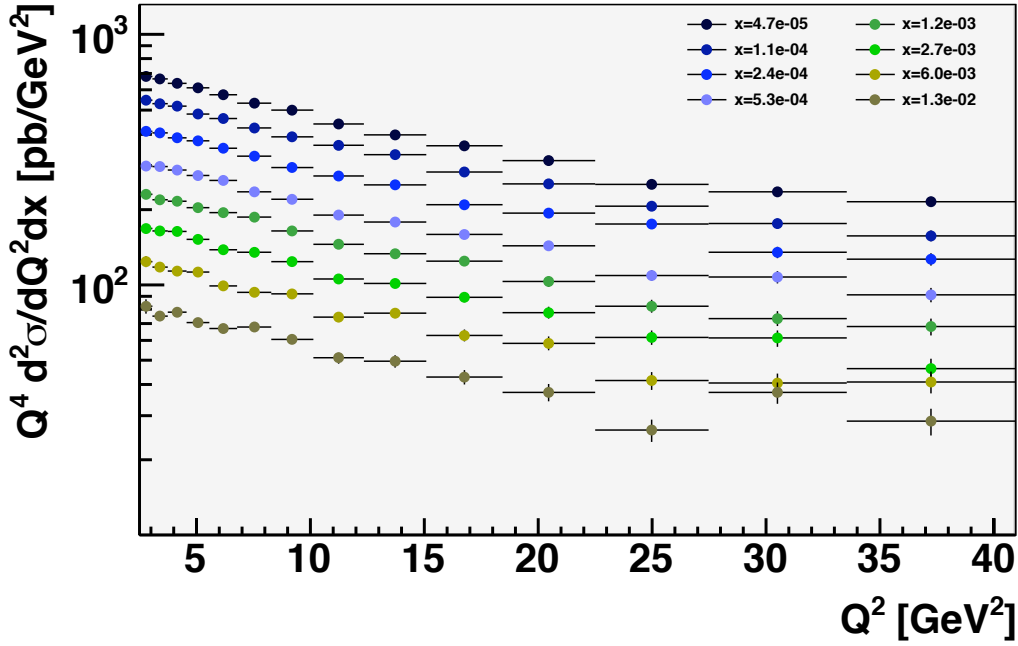


Figure 6.27: Simulated LHeC measurement of the DVCS cross section multiplied by Q^4 for different x values for a luminosity of 1 fb^{-1} , with $E_e = 50 \text{ GeV}$, and electron and photon acceptance extending to within 1° of the beampipe with a cut at $P_T^\gamma = 2 \text{ GeV}$. Only statistical uncertainties are considered.

3294 The kinematic limitations due to the scattered electron acceptance follow the same patterns as for the
 3295 inclusive cross section (see Subsec. ??). The photon P_T^γ cut is found to be a further important factor in the
 3296 Q^2 acceptance, with measurements at $Q^2 < 20 \text{ GeV}^2$ almost completely impossible for a cut at $P_T^\gamma > 5 \text{ GeV}$,
 3297 even in the scenario with detector acceptances reaching 1° . If this cut is relaxed to $P_T^\gamma > 2 \text{ GeV}$, it opens
 3298 the available phase space towards the lowest Q^2 and x values permitted by the electron acceptance.

3299 A simulation of a possible LHeC DVCS measurement double differentially in x and Q^2 is shown in Fig. ??
 3300 for a very modest luminosity scenario (1 fb^{-1}) in which the electron beam energy is 50 GeV , the detector
 3301 acceptance extends to 1° and photon measurements are possible down to $P_T^\gamma = 2 \text{ GeV}$. High precision is
 3302 possible throughout the region $2.5 < Q^2 < 40 \text{ GeV}^2$ for x values extending down to $\sim 5 \times 10^{-5}$. The need
 3303 to measure DVCS therefore places constraints on the detector performance for low transverse momentum
 3304 photons, which in practice translates into the electromagnetic calorimetry noise conditions and response
 3305 linearity at low energies.

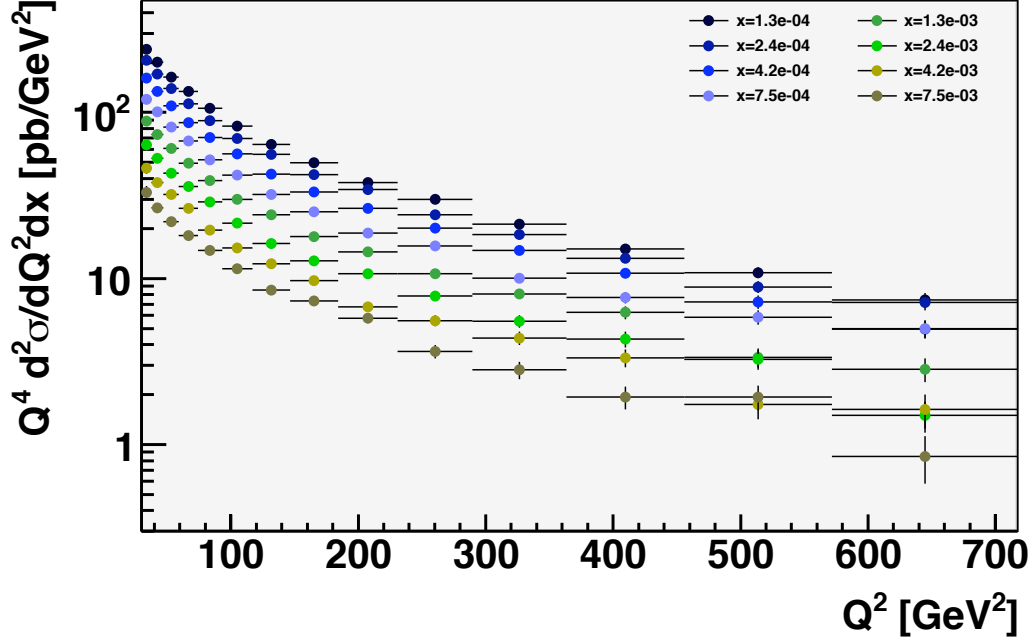


Figure 6.28: Simulated LHeC measurement of the DVCS cross section multiplied by Q^4 for different x values for a luminosity of 100 fb^{-1} , with $E_e = 50 \text{ GeV}$, and electron and photon acceptance extending to within 10° of the beampipe with a cut at $P_T^\gamma = 5 \text{ GeV}$. Only statistical uncertainties are considered.

3306 If the detector acceptance extends to only 10° , the P_T^γ cut no longer plays such an important role.
 3307 Although the low Q^2 acceptance is lost in this scenario, the larger luminosity will allow precise measurements
 3308 for $Q^2 \gtrsim 50 \text{ GeV}^2$, a region which is not well covered in the 1° acceptance scenario due to the small cross
 3309 section. In the simulation shown in Fig. ??, a factor of 100 increase in luminosity is considered, resulting
 3310 in precise measurements extending to $Q^2 > 500 \text{ GeV}^2$, well beyond the range explored for DVCS or other
 3311 GPD-sensitive processes to date.

3312 Maximising the lepton beam energy potentially gives access to the largest W and smallest x values,
 3313 provided the low P_T^γ region can be accessed. However, the higher beam lepton energy boosts the final state
 3314 photon in the scattered lepton direction, resulting in an additional acceptance limitation.

3315 Further studies of this process will require a better understanding of the detector in order to estimate
 3316 systematic uncertainties. A particularly interesting extension would be to investigate possible beam charge
 3317 [?, ?] and polarisation asymmetry measurements at lower x or larger Q^2 than was possible at HERA. With
 3318 the addition of such information, a full study of the potential of the LHeC to constrain GPDs could be
 3319 performed.

3320 Diffractive Vector Meson Production off Nuclei

3321 Exclusive diffractive processes are similarly promising as a source of information on the gluon density in the
 3322 nucleus [?]. Quasi-elastic scattering of photons from nuclei at small x can be treated within the same dipole
 3323 model framework as for ep scattering, making the comparisons with the proton case relatively straightforward.
 3324 The interaction of the dipole with the nucleus can be viewed as a sum of dipole scatterings off the nucleons
 3325 forming the nucleus. Nuclear effects can be incorporated into the dipole cross section by modifying the

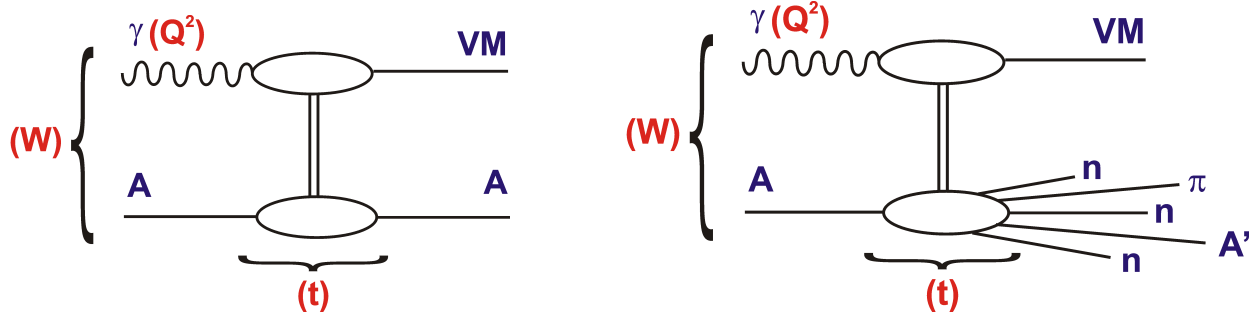


Figure 6.29: Diagrams illustrating the different types of exclusive diffraction in the nuclear case: coherent (plot on the left) and incoherent (plot on the right). While the diagrams have been drawn for the case of exclusive vector meson production, they equally apply to an arbitrary diffractively produced state.

3326 transverse gluon distribution and adding the corrections due to Glauber rescattering from multiple nucleons
 3327 [?, ?]. Previous experimental data on exclusive production from nuclei exist [?, ?], but are limited in both
 3328 kinematic range and precision.

3329 There is one aspect of diffraction which is specific to nuclei. The structure of incoherent diffraction with
 3330 nuclear break-up ($eA \rightarrow eXY$) is more complex than with a proton target, and it can also be more informative.
 3331 In the case of a target nucleus, we expect the following qualitative changes in the t -dependence. First, the
 3332 low- $|t|$ regime of coherent diffraction illustrated in Fig. ?? left, in which the nucleus scatters elastically and
 3333 remains in its ground state, will be dominant up to a smaller value of $|t|$ (about $|t| = 0.05 \text{ GeV}^2$) than in
 3334 the proton case, reflecting the larger size of the nucleus. The nuclear dissociation regime (incoherent case),
 3335 see Fig. ?? right, will consist of two parts: an intermediate regime in momentum transfer up to perhaps
 3336 $|t| = 0.7 \text{ GeV}^2$, where the nucleus will predominantly break up into its constituent nucleons, and a large- $|t|$
 3337 regime where the nucleons inside the nucleus will also break up, implying - for instance - pion production in
 3338 the Y system. While these are only qualitative expectations, it is crucial to study this aspect of diffraction
 3339 quantitatively in order to complete our understanding of the transverse structure of nuclei.

3340 Fig. ?? shows the diffractive cross sections for exclusive J/Ψ production off a lead nucleus with (b-Sat)
 3341 and without (b-NonSat) saturation effects. The figure shows both the coherent and incoherent cross sections.
 3342 According to both models shown, the cross section for $t \sim 0$ is dominated by coherent production, whereas the
 3343 nuclear break-up contribution becomes dominant for $|t| \gtrsim 0.01 \text{ GeV}^2$, leading to a relatively flat t distribution.
 3344 The coherent cross section exhibits a characteristic multiple-dip structure at these relatively large t values,
 3345 the details of which are sensitive to gluon saturation effects. Resolving these dips requires a clean separation
 3346 between the coherent and nuclear break-up contributions, which may be possible with sufficient forward
 3347 instrumentation. In particular, preliminary studies suggest that the detection of neutrons from the nuclear
 3348 break-up in the Zero Degree Calorimeter (Section ??) reduces the incoherent backgrounds dramatically.
 3349 Assuming that it is possible to obtain a relatively clean sample of coherent nuclear diffraction, resolving
 3350 the rich structure at large t should be possible based on the measurement of the transverse momentum of
 3351 the elastically produced J/ψ according to $t = -p_T^2(J/\psi)$. The resolution on the t measurement is thus
 3352 related to that on the J/ψ by $\Delta t = 2\sqrt{-t} \Delta p_T(J/\psi)$, amounting to $\Delta t < 0.01 \text{ GeV}^2$ throughout the range
 3353 shown in Fig. ?? assuming $\Delta p_T(J/\psi) < 10 \text{ MeV}$, as has been achieved at HERA. The pseudodata for the
 3354 coherent process shown in the figure are consistent with this resolution and correspond to a modest integrated
 3355 luminosity of order 10 pb^{-1} .

3356 Independently of the large $|t|$ behaviour, important information can be obtained from the low $|t|$ region
 3357 alone. Coherent production for $t \sim 0$ can easily be related to the properties of dipole-nucleon interactions,
 3358 because all nuclear effects can be absorbed into the nuclear wave functions, such that only the average gluon
 3359 density of the nucleus enters the calculation. For this forward cross section, the exact shape of the nuclear
 3360 wave function is not important, in contrast to what happens at larger $|t|$ where the distribution reflects the
 3361 functional form of the nuclear density.

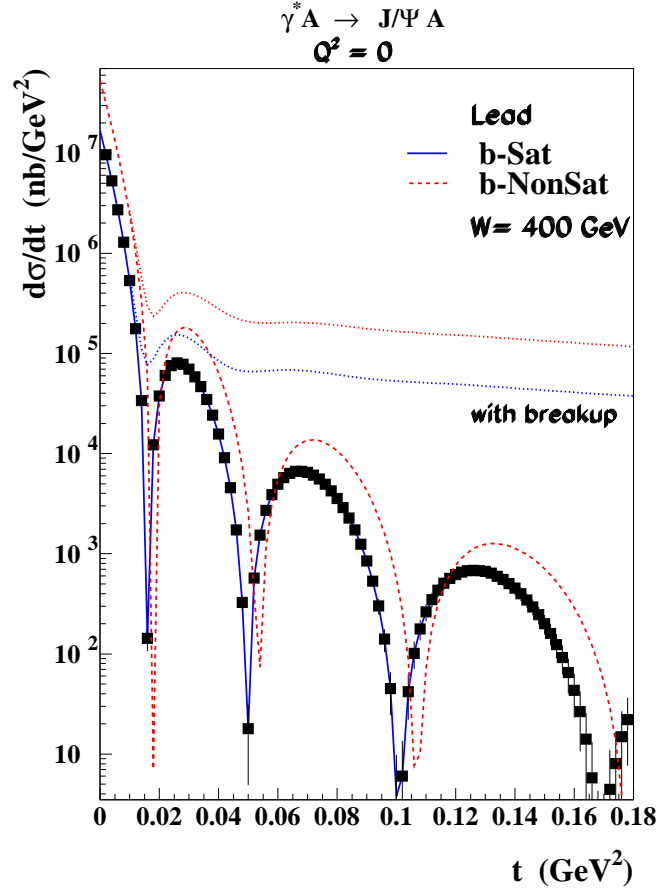


Figure 6.30: Differential cross section for the diffractive production of J/Ψ on a lead nucleus, as a function of the momentum transfer $|t|$. The dashed-red and solid-blue lines correspond to the b-Sat model predictions for coherent production without and with saturation effects, respectively. The dotted lines correspond to the predictions for the incoherent case. The pseudodata shown for the coherent case are explained in the text.

3362 Saturation effects can be studied in a very clean way using the t -averaged gluon density obtained in this
 3363 way from the forward coherent cross section. Fig. ?? shows this cross section for J/Ψ production as a
 3364 function of W for different nuclei. The cross section varies substantially as a function of the γ^*p centre of
 3365 mass energy W and the nuclear mass number A . It is also very sensitive to shadowing or saturation effects
 3366 due to the fact that the differential cross section at $t = 0$ has a quadratic dependence on the gluon density
 3367 and A . Due to this fact, the ratios of the cross sections for nuclei and protons are roughly proportional to
 3368 the ratios of the gluon densities squared. This has been exploited in the calculation [?] presented in Fig. ??,
 3369 where the nuclear modification factor R for the square of the gluon density is shown. The predictions are
 3370 consistent with those obtained from the b-Sat model (Fig. ??). Therefore, a precise measurement of the J/ψ
 3371 cross section around $t = 0$ is an invaluable source of information on the gluon density and in particular on
 3372 non-linear effects.

3373 Another region of interest is the measurement at larger $|t|$, $|t| \gtrsim 0.15 \text{ GeV}^2$. Here the reaction is fully
 3374 dominated by the incoherent processes in which the nucleus breaks up. The shadowing or saturation effects
 3375 should be stronger in this region than in the coherent case [?] and the shape of the diffractive cross section
 3376 should be only weakly sensitive to nuclear effects [?]. Finally, the intermediate region between $|t| \sim 0.01 \text{ GeV}^2$

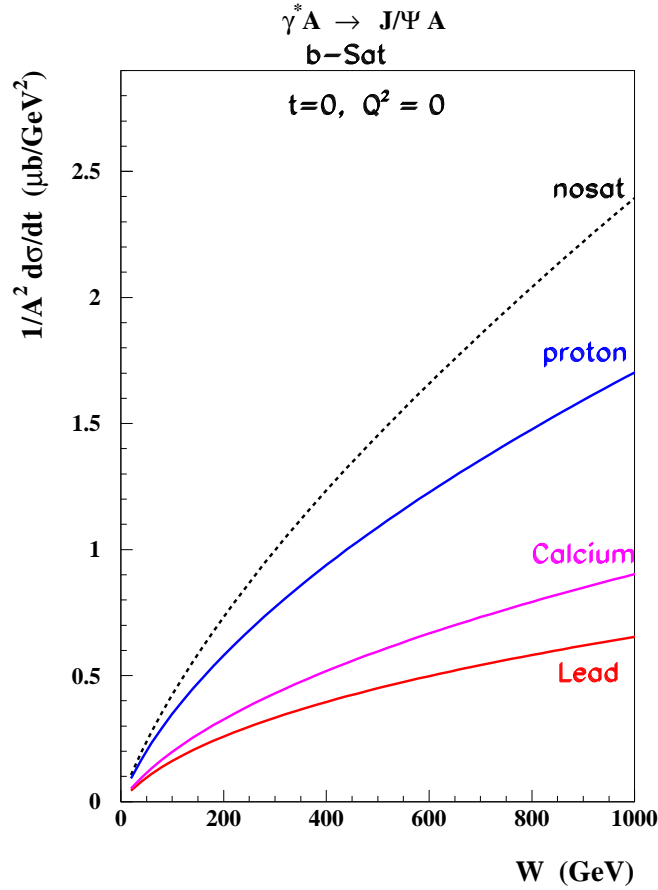


Figure 6.31: Energy dependence of the coherent photoproduction of the J/Ψ on a proton and different nuclei in the forward case $t = 0$ according to the b-Sat model. The cross sections are normalized by a factor $1/A^2$, corresponding to the dependence on the gluon density squared if no nuclear effects are present.

3377 and $|t| \sim 0.1 \text{ GeV}^2$ is also very interesting because here the barely known gluonic nuclear effects can be
3378 studied.

3379 Searching for the Odderon

3380 Exclusive processes in photoproduction and DIS offer unique sensitivity to rare exchanges in QCD. One
3381 prominent example is that of exclusive pseudoscalar meson production, which could proceed via the exchange
3382 of the Odderon. The Odderon is the postulated Reggeon which is the C-odd partner of the Pomeron. The
3383 exchange of an Odderon should contribute with different signs to particle-particle and particle-antiparticle
3384 scattering. Therefore, in the case of hadron-hadron collisions it could lead, via the optical theorem, to a
3385 finite difference between proton-proton and proton-antiproton total cross sections at high energies, provided
3386 the intercept of the Odderon is close to unity. Despite many searches, no evidence for Odderon exchange
3387 has been found so far, see for example [?]. Nevertheless, the existence of the Odderon is a firm prediction
3388 of high-energy QCD, for a comprehensive review see [?]. At lowest order in perturbation theory it can be
3389 described as a system of three non-interacting gluons. In the leading logarithmic approximation in x its
3390 evolution is governed by the Bartels-Kwieciński-Praszałowicz (BKP) equations [?, ?, ?]. Up to now, two

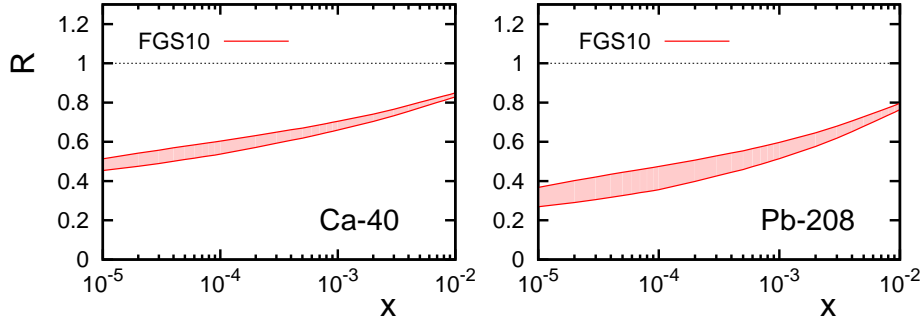


Figure 6.32: The x dependence of the nuclear modification ratio for the gluon density squared, from nuclei to protons (rescaled by A^2), for the scale corresponding to the exclusive production of the J/Ψ . Calculations obtained from the model described in [?].

3391 solutions to the BKP equations are known, one with intercept slightly below one [?] and the other with
 3392 intercept exactly equal to one [?].

3393 Several channels involving Odderon exchange are possible at the LHeC, leading to the exclusive production
 3394 of pseudoscalar mesons, $\gamma^{(*)}p \rightarrow Cp$, where $C = \pi^0, \eta, \eta', \eta_c \dots$. Searches for the Odderon in the reaction
 3395 $ep \rightarrow e\pi^0 N^*$ were performed by the H1 collaboration at HERA [?] at an average γp c.m.s energy $\langle W \rangle =$
 3396 215 GeV. No signal was found and an upper limit on the cross section was derived, $\sigma(ep \rightarrow e\pi^0 N^*, 0.02 <$
 3397 $|t| < 0.3 \text{ GeV}^2) < 49$ nb at the 95 % confidence level. Although the predicted cross sections for processes
 3398 governed by Odderon exchange are rather small, they are not suppressed with increasing centre-of-mass
 3399 energy and the large luminosities offered by the LHeC may be exactly what is required for a discovery. In
 3400 addition to π^0 production, Odderon searches at the LHeC could be based on other exclusive channels, for
 3401 example with heavier mesons η_c, η_b [?]. An even more sensitive test, ideal for study at the LHeC, is the
 3402 measurement of the difference between charm and anti-charm angular or energy distributions in $\gamma^* p \rightarrow c\bar{c}N^*$.
 3403 An asymmetry arises from the interference of pomeron and Odderon exchange amplitudes [?].

3404 6.2.4 Inclusive diffraction

3405 Introduction to Diffractive Deep Inelastic Scattering

3406 Approximately 10% of low- x DIS events are of the diffractive type, $ep \rightarrow eXp$, with the proton surviving
 3407 the collision intact despite the large momentum transfer from the electron (Fig. ??). This process is usually
 3408 interpreted as the diffractive dissociation of the exchanged virtual photon to produce any hadronic final state
 3409 system X with mass much smaller than W and the same net quantum numbers as the exchanged photon
 3410 ($J^{PC} = 1^{--}$). Due to the lack of colour flow, diffractive DIS events are characterised by a large gap in the
 3411 rapidity distribution of final state hadrons between the scattered proton and the diffractive final state X .

3412 As discussed in section ??, similar processes exist in electron-ion scattering, where they can be sub-divided
 3413 into fully coherent diffraction, where the nucleus stays intact ($eA \rightarrow eXA$) and incoherent diffraction, where
 3414 the nucleons within the nucleus are resolved and the nucleus breaks up ($eA \rightarrow eXY$, Y being a system
 3415 produced via nuclear or nucleon excitation, with the same quantum numbers as A).

3416 Theoretically, rapidity gap production is usually described in terms of the exchange of a net colourless
 3417 object in the t -channel, which is often referred to as a pomeron [?, ?]. In the simplest models [?, ?], this
 3418 pomeron has a universal structure and its vertex couplings factorise, such that it is applicable for example
 3419 to proton-(anti)proton scattering as well as DIS. One of the main achievements at HERA has been the
 3420 development of an understanding of diffractive DIS in terms of parton dynamics and QCD [?]. Events are
 3421 selected using the experimental signatures of either a leading proton [?, ?, ?] or the presence of a large rapidity
 3422 gap [?, ?]. The factorisable pomeron picture has proved remarkably successful for the description of most of
 3423 these data.

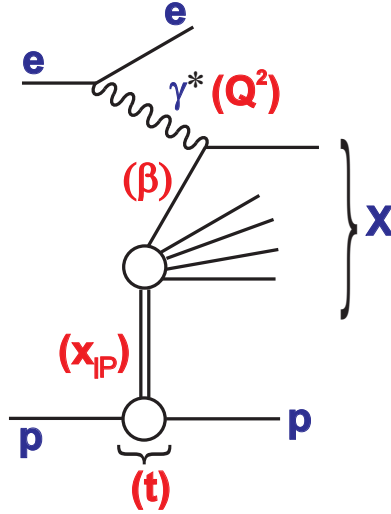


Figure 6.33: Illustration of the kinematic variables used to describe the inclusive diffractive DIS process $ep \rightarrow eXp$.

3424 The kinematic variables used to describe diffractive DIS are illustrated in Fig. ???. In addition to x , Q^2
 3425 and the squared four-momentum transfer t , the mass M_X of the diffractively produced final state provides
 3426 a further degree of freedom. In practice, the variable M_X is often replaced by

$$\beta = \frac{Q^2}{Q^2 + M_X^2 - t}. \quad (6.12)$$

3427 Small values of β refer to events with diffractive masses much bigger than the photon virtuality, while values
 3428 of β close to unity are associated with small M_X values. In models based on a factorisable pomeron, β may
 3429 be interpreted as the fraction of the pomeron longitudinal momentum which is carried by the struck parton.
 3430 The variable

$$x_{\mathbb{P}} = \frac{x}{\beta} = \frac{Q^2 + M_X^2 - t}{Q^2 + W^2 - M^2}, \quad (6.13)$$

3431 with M the nucleon mass, is then interpreted as the longitudinal momentum fraction of the Pomeron with
 3432 respect to the incoming proton or ion. It also characterises the size of the rapidity gap as $\Delta\eta \simeq \ln(1/x_{\mathbb{P}})$.

3433 Measuring Diffractive Deep Inelastic Scattering at the LHeC

3434 Diffractive DIS (DDIS) can be studied in a substantially increased kinematic range at the LHeC, which will
 3435 allow a whole new level of investigations of the factorisation properties of inclusive diffraction, will lead to
 3436 new insights into low- x dynamics and will provide a subset of final states with known quantum numbers for
 3437 use in searches for new physics and elsewhere.

3438 As shown in [?], collinear QCD factorisation holds in the leading-twist approximation in diffractive
 3439 DIS and can be used to define diffractive parton distribution functions for the proton or ion. That is,
 3440 within the collinear framework, the diffractive structure functions [?] can be expressed as convolutions of the
 3441 appropriate coefficient functions with diffractive quark and gluon distribution functions, which in general
 3442 depend on all of β , Q^2 , $x_{\mathbb{P}}$ and t . The diffractive parton distribution functions (DPDFs) are physically
 3443 interpreted as probabilities for finding a parton with a small fraction of the proton momentum $x = \beta x_{\mathbb{P}}$,
 3444 under the condition that the proton stays intact with a final state four-momentum which is specified up
 3445 to an azimuthal angle by $x_{\mathbb{P}}$ and t . The DPDFs may then be evolved in Q^2 with the DGLAP evolution
 3446 equations, with β playing the role of the Bjorken x variable. The other two variables $x_{\mathbb{P}}$ and t play the role
 3447 of external parameters to the DGLAP evolution.

3448 In various extractions using HERA DDIS data [?, ?, ?, ?] the DPDFs have been found to be dominated
 3449 by gluons. Proton vertex factorisation holds to good approximation, such that the DPDFs vary only in

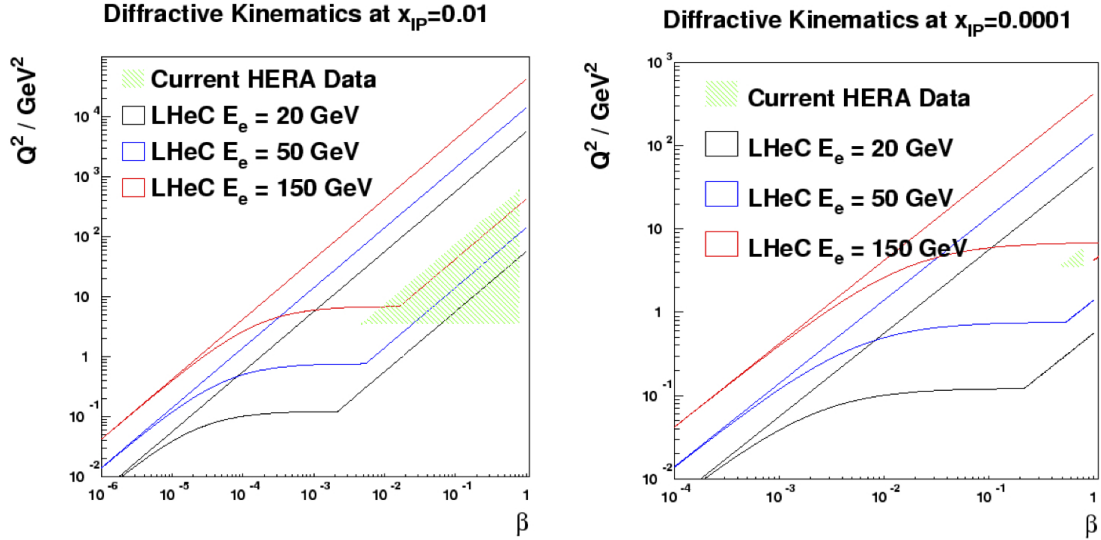


Figure 6.34: Diffractive DIS kinematic ranges in Q^2 and β of HERA and of the LHeC for different electron energies $E_e = 20, 50, 150$ GeV at $x_{\mathbb{P}} = 0.01$ (left plot), and $x_{\mathbb{P}} = 0.0001$ (right plot). In both cases, 1° acceptance is assumed for the scattered electron and the typical experimental restriction $y > 0.01$ is imposed. No rapidity gap restrictions are applied.

3450 normalisation with the four-momentum of the final state proton, the normalisation being well modelled
 3451 using Regge phenomenology [?].

3452 The LHeC will offer the opportunity to study diffractive DIS in an unprecedented kinematic range.
 3453 The diffractive kinematic plane is illustrated in Fig. ?? for two different values of the Pomeron momentum
 3454 fraction, $x_{\mathbb{P}} = 0.01$ and $x_{\mathbb{P}} = 0.0001$. In each plot, accessible kinematic ranges are shown for three different
 3455 electron energies in collision with the 7 TeV proton beam. Figure ??a corresponds to the coverage that
 3456 will be possible based on leading proton detection (see Chapter ??). Figure ??b is more representative of
 3457 the possibilities using the large rapidity gap technique (see the following). It is clear that the LHeC will
 3458 have a much increased reach compared with HERA towards low values of $x_{\mathbb{P}}$, where the interpretation of
 3459 diffractive events is not complicated by the presence of sub-leading meson exchanges, rapidity gaps are large
 3460 and diffractive event selection systematics are correspondingly small. The range in the fractional struck
 3461 quark momentum β extends by a factor of around 20 below that accessible at HERA.

3462 Figure ?? further illustrates the achievable kinematic range of diffractive DIS measurements at the LHeC
 3463 for the example of a 150 GeV electron beam combining large rapidity gap and proton tagging acceptance,
 3464 compared with an estimation of the final HERA performance. For ease of illustration, a binning scheme
 3465 is chosen in which the β dependence is emphasized and very large bins in $x_{\mathbb{P}}$ and Q^2 are taken. There
 3466 is a large difference between the kinematically accessible ranges with backward acceptance cuts of 1° and
 3467 10° . Statistical uncertainties are typically much smaller than 1% for a luminosity of 2 fb^{-1} , so a much finer
 3468 binning is possible, as required. The data points are plotted according to the H1 Fit B DPDF predictions [?],
 3469 which amounts to a crude extrapolation based on dependences in the HERA range.

3470 Systematic uncertainties are difficult to estimate without a detailed knowledge of the forward detectors
 3471 and their acceptances. At HERA, sub-5% systematics have been achieved in the bulk of the phase space
 3472 and it is likely that the LHeC could do at least as well.

3473 The limitations in the kinematic range accessible with the large rapidity gap technique are investigated
 3474 in Fig. ?. This shows the correlation between $x_{\mathbb{P}}$ and the pseudorapidity η_{max} of the most forward particle
 3475 in the hadronic final state system X , in simulated samples with LHeC and HERA beam energies, according
 3476 to the RAPGAP event generator [?]. This correlation depends only on the proton beam energy and is thus

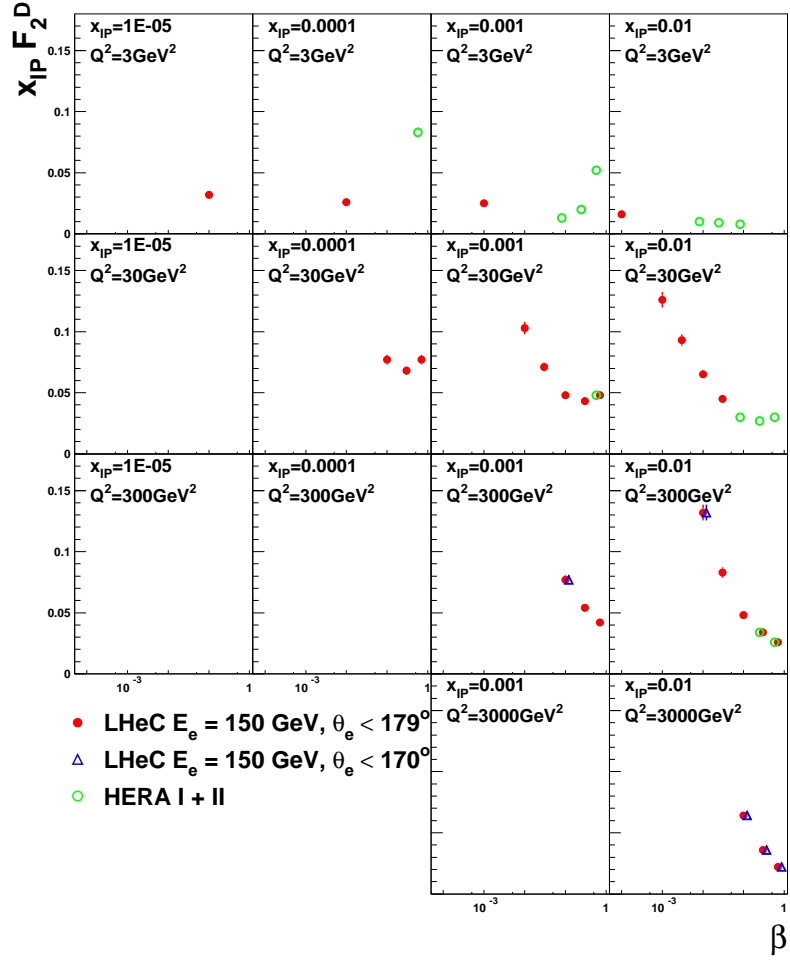


Figure 6.35: Simulation of a possible LHeC measurement of the diffractive structure function, F_2^D using a 2 fb^{-1} sample, compared with an estimate of the optimum results achievable at HERA using the full luminosity for a single experiment (500 pb^{-1}). The loss of kinematic region if the LHeC scattered electron acceptance extends to within 10° of the beam-pipe, rather than 1° is also illustrated.

3477 the same for all LHeC running scenarios. At HERA, a cut at $\eta_{\max} \sim 3.2$ has been used to select diffractive
 3478 events. Assuming LHeC forward instrumentation extending to around $\theta = 1^\circ$, a cut at $\eta_{\max} = 5$ may be
 3479 possible, which would allow measurements to be made comfortably up to $x_{\mathbb{P}} \sim 0.001$, with some limited
 3480 sensitivity at larger $x_{\mathbb{P}}$, a region where the proton tagging acceptance takes over (see Chapter ??). The
 3481 two methods are thus complementary, and offer some common acceptance in an overlap region of $x_{\mathbb{P}}$. This
 3482 redundancy could be used for cross-calibration of the two methods and their systematics, as has been done
 3483 at HERA.

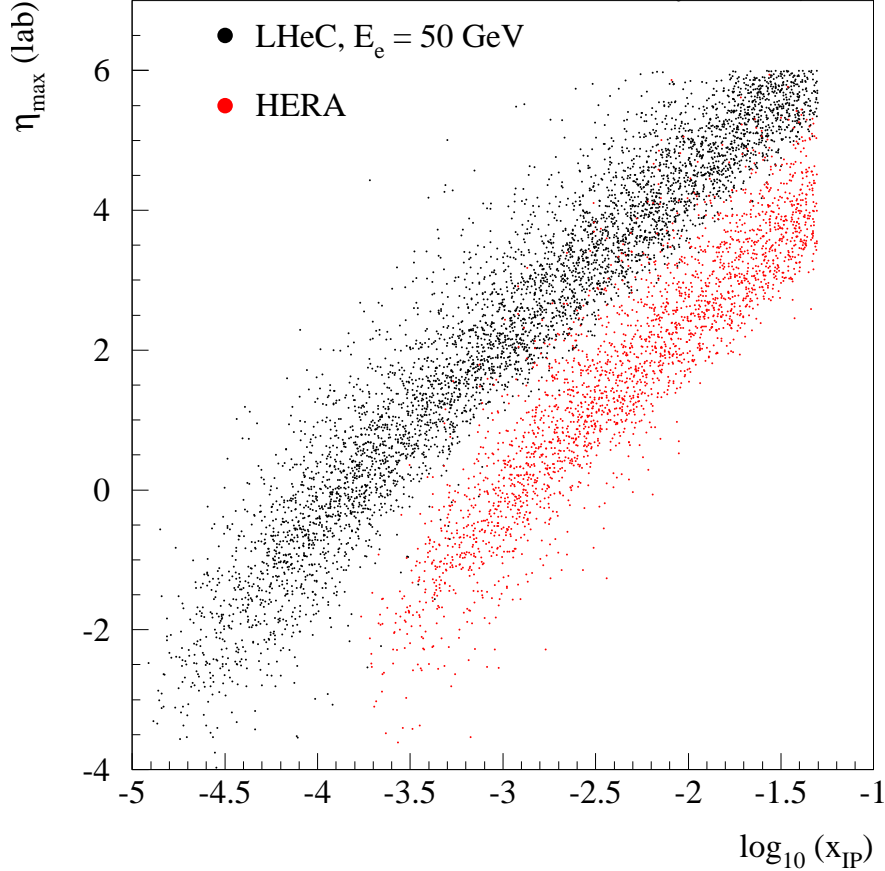


Figure 6.36: Comparison of the correlation between the rapidity gap selection variable, η_{\max} and $x_{\mathbb{P}}$ at HERA and at the LHeC, using events simulated with the RAPGAP Monte Carlo generator.

3484 Diffractive Parton Densities and Final States

3485 The previously unexplored diffractive DIS region of very low β is of particular interest. Here, diffractively
 3486 produced systems will be created with unprecedented invariant masses. Figure ??a shows a comparison
 3487 between HERA and the LHeC in terms of the M_X distribution which could be produced in diffractive
 3488 processes with $x_{\mathbb{P}} < 0.05$ (using the RAPGAP Monte Carlo model [?]). Figure ??a compares the expected
 3489 M_X distributions for one year of running at three LHeC electron beam energy choices. Diffractive masses
 3490 up to several hundred GeV are accessible with reasonable rates, such that diffractive final states involving
 3491 beauty quarks and W and Z bosons, or even exotic states with 1^- quantum numbers, could be produced.

3492 Large improvements in DPDFs are likely to be possible from NLO DGLAP fits to LHeC diffractive
 3493 structure function data. In addition to the extended phase space in β , the extension of the kinematic range
 3494 towards larger Q^2 increases the lever-arm for extracting the diffractive gluon density and opens the possibility
 3495 of significant weak gauge boson exchange, which would allow a quark flavour decomposition for the first time.

3496 Proton vertex factorisation can be tested precisely by comparing the LHeC β and Q^2 dependences at

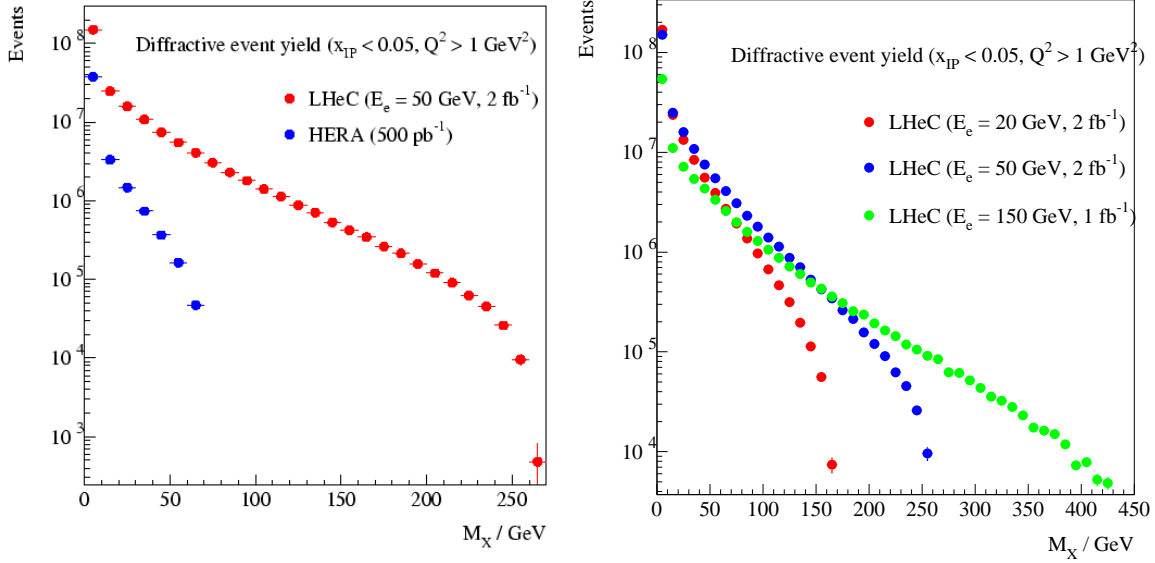


Figure 6.37: Simulated distributions in the invariant mass M_X according to the RAPGAP Monte Carlo model for samples of events obtainable with $x_{\text{IP}} < 0.05$ (a) One year of high acceptance LHeC running at $E_e = 50 \text{ GeV}$ compared with HERA (full luminosity for a single experiment). (b) Comparison between three different high acceptance LHeC luminosity and E_e scenarios.

3497 different small x_{IP} values in their considerable regions of overlap. The production of dijets or heavy quarks
 3498 as components of the diffractive system X will provide a means of testing QCD collinear factorisation.
 3499 These processes are driven by boson-gluon fusion ($\gamma^* g \rightarrow q\bar{q}$) and thus provide complementary sensitivity
 3500 to the diffractive gluon density to be compared with that from the scaling violations of the inclusive cross
 3501 section. Factorisation tests of this sort have been carried out on many occasions at HERA, with NLO
 3502 calculations based on DPDFs predicting jet and heavy flavour cross sections which are in good agreement
 3503 with data at large Q^2 [?, ?]. However, due to the relatively small accessible jet transverse momenta at
 3504 HERA, the precision is limited by scale uncertainties on the theoretical predictions. At the LHeC, much
 3505 larger diffractive jet transverse momenta are measurable ($p_T \lesssim M_X/2$), which should lead to much more
 3506 precise tests [?].

3507 The simulated measurement of the longitudinal proton structure function, F_L described in subsection ??,
 3508 could also be extended to extract the diffractive analogue, F_L^D . At small β , where the cross section for longi-
 3509 tudinally polarised photons is expected to be dominated by a leading twist contribution, an F_L^D measurement
 3510 provides further complementary constraints on the role of gluons in the diffractive PDFs. As $\beta \rightarrow 1$, a higher
 3511 twist contribution from longitudinally polarised photons, closely related to that driving vector meson elec-
 3512 troproduction, dominates the diffractive cross section in many models [?] and a measurement to even modest
 3513 precision would give considerable insight. A first measurement of this quantity has recently been reported
 3514 by the H1 Collaboration [?], though the precision is strongly limited by statistical uncertainties. The LHeC
 3515 provides the opportunity to explore it in much finer detail.

3516 In contrast to leading proton production, the production of leading neutrons in DIS ($ep \rightarrow eXn$) requires
 3517 the exchange of a net isovector system. Data from HERA have supported the view that this process is
 3518 driven dominantly by charged pion exchange over a wide range of neutron energies [?]. With the planned
 3519 emphasis on zero degree calorimetry for leading neutron measurements (see Chapter ??), LHeC data will
 3520 thus constrain the structure of the pion at much lower x and larger Q^2 values than has been possible hitherto.
 3521 Note also that the combination of rapidity gap detection and zero degree calorimetry offers the possibility

3522 of disentangling coherent from incoherent nuclear diffraction.

3523 **Diffractive DIS, Dipole Models and Sensitivity to Non-linear Effects**

3524 Diffractive DIS at the LHeC will give us an opportunity to test the predictions of collinear factorisation
 3525 and the possible onset of non-linear or higher-twist effects in the evolution. Of particular importance is the
 3526 semi-hard regime $Q^2 < 10 \text{ GeV}^2$ and x as small as possible. It is possible that the non-linear saturation
 3527 regime will be easier to reach with diffractive than with inclusive measurements, since diffractive processes
 3528 are mostly sensitive to quantum fluctuations in the proton wave function that have a virtuality of order of
 3529 the saturation scale Q_s^2 , instead of Q^2 . As a result, power corrections (not the generic Λ_{QCD}^2/Q^2 corrections,
 3530 but rather the sub-class of them of order Q_s^2/Q^2) are expected to come into play starting from a higher
 3531 value of Q^2 in diffractive than in inclusive DIS. Indeed, there is already a hint of this at HERA: collinear
 3532 factorization starts to fail below about 3 GeV^2 in the case of F_2 [?], while it breaks down already around
 3533 8 GeV^2 in the case of F_2^D [?]. This fact can alternatively be observed in the feature that models which
 3534 in principle should only work for small Q^2 , can in practice be used up to larger Q^2 for diffractive than for
 3535 inclusive observables (see e.g. [?]).

3536 With the sort of measurement precision for F_2^D possible at the LHeC, it ought to be possible to distinguish
 3537 between different models, as illustrated in Fig. ???. For the simulated data shown here, a conservative situation
 3538 is assumed, in which the electron beam energy is 50 GeV and only the rapidity gap selection method is used,
 3539 such that the highest $x_{\mathbb{P}}$ bin is at 0.001 . H1 Fit B [?] extrapolations (as in Fig. ??) are compared with
 3540 the “b-sat” [?, ?] and bCGC [?] dipole models. As has been found to be necessary to describe HERA data,
 3541 photon fluctuations to $q\bar{q}g$ states are included in addition to the usual $q\bar{q}$ dipoles used to describe inclusive
 3542 and vector meson cross sections. Both dipole models differ substantially from the H1 Fit B extrapolation.
 3543 The LHeC simulated precision and kinematic range are sufficient to distinguish between a range of models
 3544 with and without saturation effects and also between different models which incorporate saturation.

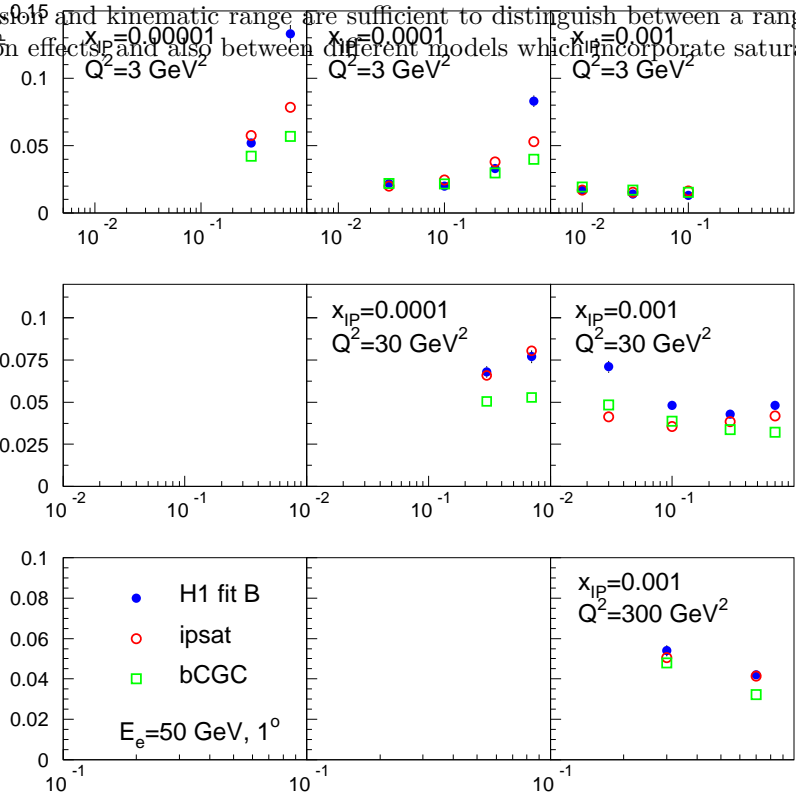


Figure 6.38: Simulated F_2^D measurements in selected $x_{\mathbb{P}}$, β and Q^2 bins. An extrapolation of the H1 Fit B DPDF fit to HERA data is compared with two different implementations of the dipole model, both of which contain saturation effects and include $q\bar{q}g$ photon fluctuations in addition to $q\bar{q}$ ones.

Predicting nuclear shadowing from inclusive diffraction in ep

The connection between nuclear shadowing and diffraction was established a long time ago by Gribov [?]. Its key approximation is that the nucleus can be described as a dilute system of nucleons in the nucleus rest frame. The accuracy of this approximation for hadron-nucleus interactions is on the level of a few %, which reflects the small admixture of non-nucleonic degrees of freedom in nuclei and the small off-shellness of the nucleons in nuclei as compared to the soft strong interaction scale. Gribov's result can be derived using the AGK cutting rules [?] and hence it is a manifestation of unitarity [?, ?]. The formalism can be used to calculate directly cross sections of $\gamma(\gamma^*)$ -nucleus scattering for the interaction with $N = 2$ nucleons, but has to be supplemented by additional considerations to account for the contribution of the interactions with $N \geq 3$ nucleons.

In this context, nuclear PDFs at small x can be calculated [?, ?] combining unitarity relations for different cuts of the shadowing diagrams corresponding to diffractive and inelastic final states, with the QCD factorisation theorem for hard diffraction [?]. A *model-independent* expression for the nuclear PDF at fixed impact parameter b , valid for the case $N = 2$ [?], reads:

$$\begin{aligned} \Delta [xf_{j/A}(x, Q^2, b)] &= xf_{j/N}(x, Q^2, b) - xf_{j/A}(x, Q^2, b) \\ &= 8\pi A(A-1)\Re e \left[\frac{(1-i\eta)^2}{1+\eta^2} \int_x^{0.1} dx_{\mathbb{P}} \beta f_j^{D(4)}(\beta, Q^2, x_{\mathbb{P}}, t_{\min}) \right. \\ &\quad \left. \times \int_{-\infty}^{\infty} dz_1 \int_{z_1}^{\infty} dz_2 \rho_A(\vec{b}, z_1) \rho_A(\vec{b}, z_2) e^{i(z_1-z_2)x_{\mathbb{P}}m_N} \right], \end{aligned} \quad (6.14)$$

where $f_{j/A}(x, Q^2)$, $f_{j/N}(x, Q^2)$ are nuclear and nucleon PDFs respectively, $f_j^{D(4)}(\beta, Q^2, x_{\mathbb{P}}, t_{\min})$ are diffractive nucleon PDFs, $\eta = \Re e A^{diff}/\Im m A^{diff} \approx 0.17$, $\rho_A(r)$ is the nuclear matter density, and $t_{\min} = -m_N^2 x_{\mathbb{P}}^2$ with m_N the nucleon mass. Eq. (??) satisfies the QCD evolution equations to all orders in α_s . Numerical studies indicate that the dominant contribution to the shadowing probed by present experiments - corresponding to not very small x - comes from the region of relatively large β , for which small- x approximations which involve resummation of $\ln x$ terms are not important.

In Eq. (??), the interaction of different configurations of the hard probe (e.g. $q\bar{q}$, $q\bar{q}g$, vector meson resonances, ...) are encoded in $f_j^{D(4)}(\beta, Q^2, x_{\mathbb{P}}, t_{\min})$. For the case of more than $N = 2$ nucleons, there are two or more intermediate nucleon diffractive states which may be different and thus result in a different interaction between the the virtual photon and the nucleus. Therefore the interaction of the hard probe with $N \geq 3$ nucleons is sensitive to finer details of the diffractive dynamics, namely the interplay between the interactions of the hard probe with N nucleons with different cross sections. This (colour) fluctuation effect is analogous to the inelastic shadowing phenomenon for the scattering of hadrons from nuclei, with the important difference that the dispersion of the interaction cross sections for the configurations in the projectile is much smaller in the hadronic case than in DIS.

In order to estimate this effect, one should note that, experimentally, the energy dependence of hard diffraction is close to that observed for soft Pomeron dynamics (the soft Pomeron intercept intercept $\alpha_{\mathbb{P}} \approx 1.11$) with the hard Pomeron contribution ($\alpha_{\mathbb{P}} \approx 1.25$) being a small correction. This fact indicates that hadron-like (aligned jet) configurations [?], evolved via DGLAP evolution to large Q^2 , dominate hard diffraction in DIS, while point-like configurations give an important, and increasing with Q^2 , contribution to small- x PDFs. This reduces the uncertainties in the treatment of $N \geq 3$ contributions [?, ?]. Calculations show that the difference between two extreme scenarios of colour fluctuations is $\leq 20\%$ for $A \sim 200$ and much smaller for lighter nuclei, see the two FGS10 curves in Figs. ?? and ?. Besides, fluctuations tend to reduce the shadowing somewhat compared with the approximations neglecting them [?, ?, ?, ?] (compare the FGS10 results in Fig. ?? left with those labelled AKST). The gluon density is more sensitive to the magnitude of fluctuations than F_2 , as can be inferred from Fig. ?? and Fig. ?? right.

Finally, the AGK technique also allows the calculation of the nuclear diffractive PDFs, see below, and fluctuations of multiplicity in non-diffractive DIS [?, ?, ?]. Both observables turn out to be sensitive to the pattern of colour fluctuations.

Predictions for inclusive diffraction on nuclear targets

Diffractive DIS events were first discovered in ep collisions at the HERA collider. Since no eA collider has ever been built, inclusive diffraction in eA has simply never been measured. Thus, DDIS off nuclei at the LHeC will be a completely unexplored territory throughout the whole kinematic domain accessed, implying a huge discovery potential.

Despite this lack of experimental information on DDIS off nuclei, we have expectations, based on our current understanding of QCD, of how it should look. For instance, the theory of nuclear shadowing allows us to construct nuclear diffractive PDFs for large Q^2 (see the previous item) while, within the Color Glass Condensate framework, nuclear diffractive structure functions can be predicted at small x . Depending on kinematics and the heavy ion species, different patterns of nuclear shadowing or antishadowing are expected as a function of β and $x_{\mathbb{P}}$. This is just one of many examples of what should be checked with an eA collider. Others are the impact parameter dependence introduced in the models, or the relation between nuclear shadowing and diffraction in ep which relies on what we know on DDIS from HERA. Therefore, in the larger kinematic domain accessible at the LHeC there are many things to discover about the structure of nuclei with diffractive measurements.

Predictions from a variety of models for nuclear coherent diffraction (see comments on different types of diffractive process on nuclei in Subsection on diffractive vector meson production), are shown in Figs. ?? and ?. The chosen models here are FGS10 [?] and KLMV [?, ?]. Both plots show selected LHeC pseudodata for $x_{\mathbb{P}}F_2^D$ as a function of β in bins of Q^2 and $x_{\mathbb{P}}$. Statistical and systematic errors are added in quadrature, with systematic errors estimated to be at the level of 5%. The models give very different predictions both in absolute value and in their detailed dependence on x_{IP} and Q^2 , which cannot be resolved without LHeC data.

Also shown in Fig. ?? are predicted diffractive-to-total ratios of the structure functions as a function of the collision energy W . It was demonstrated in [?] that the constancy with energy of this ratio for the proton can be naturally explained in the models which include saturation effects, because in the black disk regime the ratio of the diffractive to total cross sections tends to a constant value. At fixed impact parameter the ratio may grow as large as 50%, but the integration in impact parameter results in a smaller value. HERA data showed approximate energy independence of this ratio, which could be easily obtained within the GBW saturating dipole model [?]. Within the given energy range the models shown in figure ?? predict a slight variation with energy. Note however the rather substantial difference between predictions coming from the different models. The uncertainty in modelling the impact parameter is one of its main sources. LHeC data are required for clarification.

6.2.5 Jet and multi-jet observables, parton dynamics and fragmentation

Introduction

Inclusive measurements provide essential information about the integrated distributions of partons in a proton. However, as was discussed in previous sections, more exclusive measurements are needed to pin down the essential details of the small- x dynamics. For example, a central prediction of the BFKL framework at small x is the diffusion of the transverse momenta of the emitted partons between the photon and the proton. In the standard collinear approach with integrated parton densities the information about the transverse momentum is not accessible. However, it can be recovered within a different framework which utilizes unintegrated parton distribution functions, dependent on parton transverse momentum as well as x and Q^2 . Unintegrated PDFs are natural in the BFKL approach to small- x physics. A general, fundamental expectation is that as x decreases, the distribution in transverse momentum of the emitted partons broadens, resulting in diffusion.

The specific parton dynamics can be tested by a number of exclusive measurements. These in turn can provide valuable information about the distribution of transverse momentum in the proton. As discussed in [?], for many inclusive observables the collinear approximation with integrated PDFs is completely insufficient, and even just including parton transverse momentum effects by hand may not be sufficient to

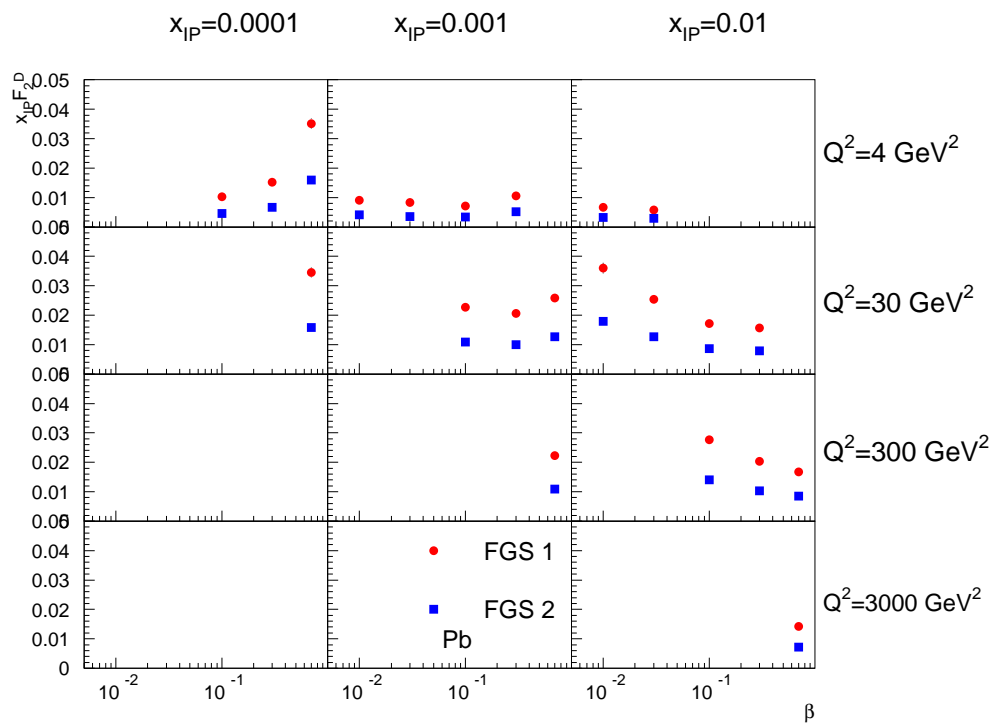


Figure 6.39: Diffractive structure function $x_{\mathbb{P}} F_2^D$ for Pb in bins of Q^2 and $x_{\mathbb{P}}$ as a function of β . Model calculations are taken from [?].

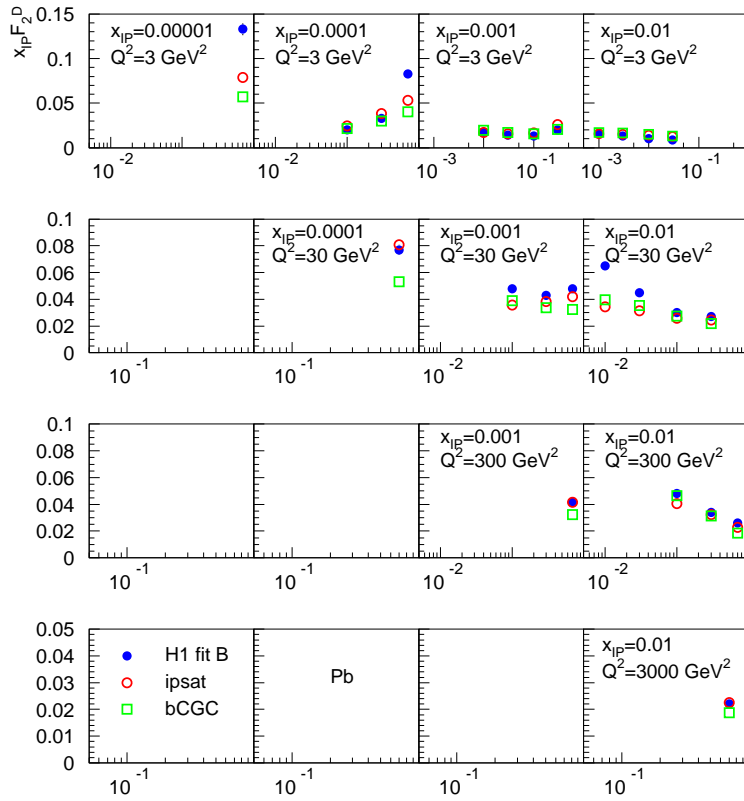


Figure 6.40: Diffractive structure function $x_{\mathbb{P}} F_2^D$ for Pb in bins of Q^2 and $x_{\mathbb{P}}$ as a function of β . Model calculations are based on the dipole framework [?, ?].

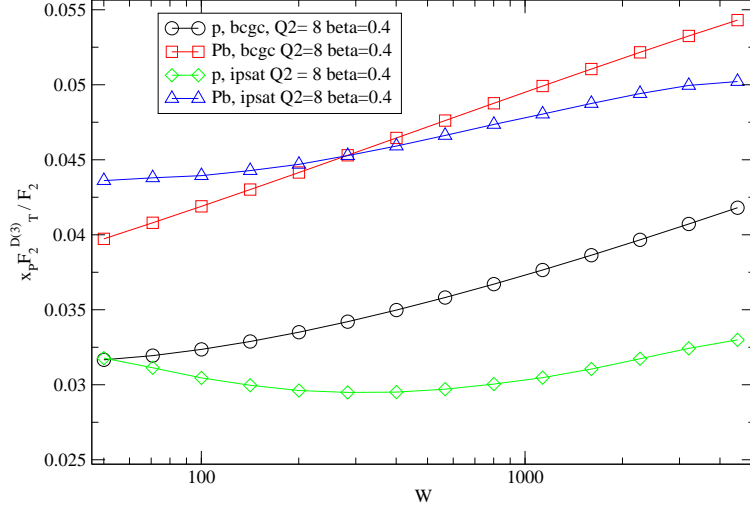


Figure 6.41: Ratio of the transversely polarised photon contribution to the diffractive structure function $x_p F_2^{D(3)}$ to the inclusive structure function in p and Pb for fixed values of Q^2 and β as a function of the energy W . The model calculations are based on the dipole framework [?, ?].

3636 describe many observables. In DIS, for example, processes needing unintegrated distributions include the
 3637 transverse momentum distribution of heavy quarks. Similar problems are encountered in hadron collisions
 3638 when studying heavy quark and Higgs production. The natural framework using unintegrated PDFs gives a
 3639 much more reliable description. Furthermore, lowest-order calculations in the framework with unintegrated
 3640 PDFs provide a much more realistic description of cross sections concerning kinematics. This may well lead
 3641 to NLO and higher corrections being much smaller numerically than they typically are at present in standard
 3642 collinear factorization, since the LO description is better.

3643 This approach, however, calls for precise measurements of a variety of relatively exclusive processes in
 3644 a wide kinematic range. As discussed below, measurements of dijets, forward jets and particles, as well as
 3645 transverse energy flow, are required to constrain the unintegrated PDFs and will give valuable information
 3646 about parton dynamics at small x . While we will discuss the case of DIS on a proton, all conclusions can be
 3647 paralleled for DIS on nuclei.

3648 Unintegrated PDFs

3649 The standard integrated parton densities are functions of the longitudinal momentum fraction of a parton
 3650 relative to its parent hadron, with an integral over the parton transverse momentum. In contrast, uninte-
 3651 grated, or transverse-momentum-dependent (TMD), parton densities depend on both parton longitudinal
 3652 momentum fraction and parton transverse momentum. Processes for which unintegrated densities are natural
 3653 include the Drell-Yan process (and its generalization to Higgs production), and semi-inclusive DIS (SIDIS).
 3654 In SIDIS, we need TMD fragmentation functions as well as TMD parton densities.

3655 In the literature there are several apparently different approaches to TMD parton densities, with varying
 3656 degrees of explicitness in the definitions and derivations.

- 3657 • The CSS approach [?, ?, ?, ?] and some further developments [?].
- 3658 • The CCFM approach [?, ?, ?, ?] for small x .
- 3659 • Related BFKL associated works [?, ?].

3660 Central to this subject is the concrete definition of TMD densities, and complications arise because QCD
 3661 is a gauge theory. A natural initial definition uses light-front quantization: the unintegrated density of

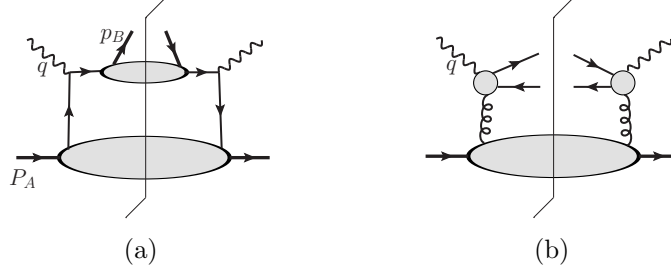


Figure 6.42: (a) Parton model factorisation for a SIDIS cross section. (b) Factorization for high-energy $q\bar{q}$ photoproduction.

3662 parton j in hadron h would be

$$f_{j/h}(x, \mathbf{k}_\perp) \stackrel{?}{=} \frac{1}{2x(2\pi)^3} \sum_\lambda \frac{\langle P, h | b_{k,\lambda,j}^\dagger b_{k,\lambda,j} | P, h \rangle_c}{\langle P, h | P, h \rangle} , \quad (6.15)$$

3663 where $b_{k,\lambda,j}$ and $b_{k,\lambda,j}^\dagger$ are light-front annihilation and creation operators, j and λ label parton flavor and
 3664 helicity, while $k = (k^+, \mathbf{k}_\perp)$ is its momentum, and only connected graphs ‘c’ are considered. The ‘?’ over the
 3665 equality sign warns that the formula does not apply literally in QCD. Expressing $b_{k,\lambda,j}$ and $b_{k,\lambda,j}^\dagger$ in terms
 3666 of fields gives the TMD density as the Fourier transform of a light-front parton correlator. For example, for
 3667 a quark

$$f_j(x, \mathbf{k}_\perp) \stackrel{?}{=} \int \frac{dw^- d^2\mathbf{w}_\perp}{(2\pi)^3} e^{-ixP^+w^- + i\mathbf{k}_\perp \cdot \mathbf{w}_\perp} \langle P | \bar{\psi}_j(0, w^-, \mathbf{w}_\perp) \frac{\gamma^+}{2} \psi_j(0) | P \rangle_c . \quad (6.16)$$

3668 One can similarly define a TMD fragmentation function [?] $d_{h/j}(z, \mathbf{p}_\perp)$, for the probability density of final-
 3669 state hadron h in an outgoing parton j .

3670 The corresponding factorization formula for SIDIS $e + A(P_A) \rightarrow e + B(p_B) + X$ is [?]

$$\frac{d\sigma}{dx dQ^2 dz d^2\mathbf{P}_{B\perp}} = \sum_j \int d^2\mathbf{k}_\perp H_j f_{j/A}(x, \mathbf{k}_\perp) d_{B/j}(z, \mathbf{P}_{B\perp} + z\mathbf{k}_\perp) , \quad (6.17)$$

3671 where z and $\mathbf{P}_{B\perp}$ are the fractional longitudinal momentum and the transverse momentum of the detected
 3672 hadron relative to the simplest parton-model calculation of the outgoing jet, while H_j is the hard-scattering
 3673 factor for electron-quark elastic scattering; see Fig. ??(a). In the fragmentation function $d_{B/j}$ in Eq. (??),
 3674 the use of $z\mathbf{k}_\perp$ with its factor of z is because the transverse-momentum argument of the fragmentation
 3675 function is a transverse momentum of the outgoing hadron relative to the parton initiating the jet, whereas
 3676 \mathbf{k}_\perp is the transverse momentum of a parton relative to a hadron.

3677 The most obvious way of applying (??) in QCD is to define the operators in light-cone gauge $A^+ = 0$,
 3678 or, equivalently, to attach Wilson lines to the quark fields with a light-like direction for the Wilson lines.
 3679 One minor problem in QCD is that, because the wave function is infinite (see below), the exact probability
 3680 interpretation of parton densities cannot be maintained.

3681 A much harder problem occurs because QCD is a gauge theory. Evaluating TMD densities defined by
 3682 (??) in light-cone gauge gives divergences where internal gluons have infinite negative rapidity [?]. These
 3683 cancel only in the integrated density. The physical problem is that any coloured parton entering (or leaving)
 3684 the hard scattering is accompanied by a cloud of soft gluons, and the soft gluons of a given transverse
 3685 momentum are distributed uniformly in rapidity. A parton density defined in light-cone gauge corresponds
 3686 to the asymptotic situation of infinite available rapidity.

3687 A quark in a realisable hard scattering can be considered as having a transverse recoil against the soft
 3688 gluons, but with a physically restricted range of rapidity. So a proper definition of a TMD density must
 3689 implement a rapidity cut-off in the gluon momenta. Evolution equations must take into account the rapidity

cut-off. The CSS formalism [?] has an explicit form of the rapidity cut-off and an equation for the dependence of TMD functions on the cut-off. But in any alternative formalism the need in the definitions for a cut-off to avoid rapidity divergences is non-negotiable.

Parton densities and fragmentation functions are only useful because they appear in factorisation theorems, so a useful definition must allow useful factorisation theorems to be formulated and derived. An improved definition involving Wilson line operators has recently been given in [?]; see also [?].

A second train of argument leads to a related kind of factorisation (the so-called k_{\perp} -factorisation) for processes at small x [?]. A classic process is photo- or electro-production of charm pairs $\gamma(p_1) + h(p_2) \rightarrow Q(p_3) + \bar{Q}(p_4) + X$, for which k_{\perp} -factorisation has the form

$$4M^2\sigma_{\gamma g}(\rho, M^2/Q_0^2) = \int d^2\mathbf{k}_{\perp} \int_0^1 \frac{dz}{z} \hat{\sigma}(\rho/z, \mathbf{k}_{\perp}^2/M^2) f_{g/h}(x, \mathbf{k}_{\perp}), \quad (6.18)$$

see Fig. ??(b). Here $\rho = M^2/(p_1 + p_2)^2 \ll 1$, and M is the mass of the heavy quark. The corresponding definition of the TMD gluon density [?] is said to use light-cone gauge, but there is in fact a hidden rapidity cut-off resulting from the use of the BFKL formalism.

Although both (??) and (??) use k_{\perp} -dependent parton densities, there are important differences. In (??), the hard scattering cross section $\hat{\sigma}$ has the incoming gluon *off-shell*, whereas in (??), the hard scattering H_j uses on-shell partons. This is associated with a substantial difference in the kinematics. In (??) for SIDIS, the transverse momenta of the partons relative to their hadrons are less than Q , which allows the neglect of parton virtuality in the hard scattering. This approximation fails at large partonic transverse momentum, $\mathbf{k}_{\perp} \sim Q$, but ordinary collinear factorisation is valid in that region. So the factorisation formula is readily corrected, by adding a suitable matching term [?].

In contrast, in the small- x formula (??), the gluon transverse momentum is comparable with the hard scale M . So it is not appropriate to neglect \mathbf{k}_{\perp} with respect to M , and the hard scattering is computed with an off-shell gluon. Factorisation is actually obtained from BFKL physics, where the gluons in Fig. ??(b) couple the charm quark subgraph to a subgraph where the lines have much larger rapidity.

The evolution equation of the CS-style TMD functions used in (??) gives the dependence of the TMD functions on the rapidity difference between the hadron and the virtual photon momenta. The results for TMD functions and for the cross sections can finally be obtained [?] in terms of (a) ordinary integrated parton densities and fragmentation functions, (b) perturbatively calculable quantities, and (c) a restricted set of non-perturbative quantities. The most important of these non-perturbative quantities is the distribution in recoil transverse momentum per unit rapidity against the emission of the soft interacting gluons, which is exponentiated after evolution. Importantly, it is independent of x and z , and it is universal between processes [?], and different only between gluons (color octet) and quarks (color triplet). There is also what can be characterised as a non-perturbative intrinsic transverse momentum distribution in both parton densities and fragmentation functions. In the quark sector, all but the fragmentation function are well measured in Drell-Yan processes [?].

On the other hand, evolution for the small- x formalism in (??) is given by the BFKL method.

The avenues for further improvement on this subject are both theoretical and experimental. On the theory side, these concern the relation between different formalisms for evolution [?, ?, ?, ?, ?], the extension of factorisation theorems to a larger number of particles in the final state, and the matching to Monte Carlo generators. On the experimental side, the sensitivity to TMD functions is linked to a sensitivity to parton transverse momentum. This is the case of SIDIS at low transverse momentum. Another interesting process which would enable the TMD gluon functions to be probed is $ep \rightarrow e\pi\pi X$, with the pions being in different directions (different jets), but such that they are close to back-to-back in the (q, p_i) (the so-called brick wall frame).

Finally, measuring SIDIS and dijet production off protons or nuclei at the LHeC will allow detailed investigations of non-linear parton evolution in QCD. In this respect, the SIDIS cross section [?] and dihadron production [?] have been studied in the CGC framework. It turns out that, for small x , one is sensitive to the saturation regime of the target (proton or nucleus) wave function if the transverse momentum of the produced hadron is of the order of the saturation momentum.

3738 **Dijet production and angular decorrelation**

3739 Dijet production in high energy deep inelastic electron-proton scattering is a very valuable process for the
 3740 study of small- x behavior in QCD. The dominant process is illustrated in Fig. ??, which is that of the
 3741 $\gamma^* g \rightarrow q\bar{q} \rightarrow$ dijet production. The incoming gluon can have sizeable transverse momentum accumulated
 3742 from diffusion in k_T along the gluon chain. As Bjorken- x becomes smaller, and therefore the longitudinal
 3743 momentum of the gluon also decreases, larger values of the transverse momentum k_T can be sampled. This
 3744 will lead to an azimuthal decorrelation between the jets which increases with decreasing x . The definition of
 3745 $\Delta\phi$ is indicated in Fig. ?. That is, the jets are no longer back-to-back since they must balance the sizable
 3746 transverse momentum k_T of the incoming virtual gluon.

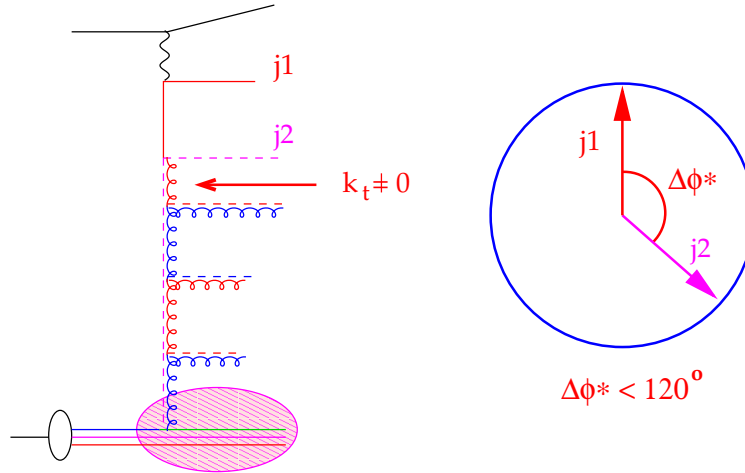


Figure 6.43: Schematic representation of the production of a system of two jets in the process of virtual photon-gluon fusion. The incoming gluon has non-vanishing transverse momentum $k_T \neq 0$ which leads to the decorrelation of the jets. $\Delta\phi$ is the angle between two jets.

3747 This picture of dijet production is to be contrasted with the conventional picture which uses integrated
 3748 parton distributions, and typically leads to a narrow distribution about the back-to-back jet configuration.
 3749 Higher orders usually broaden the distribution. However, as shown by direct measurements of DIS dijet
 3750 data [?], NLO DGLAP calculations are not able to accommodate the pronounced effect of the decorrelation.

3751 Explicit calculations for HERA kinematics show that the models which include the resummation of powers
 3752 of $\log 1/x$ compare favourably with the experimental data [?, ?, ?, ?]. The proposal and calculations to
 3753 extend such studies to diffractive DIS also exist [?, ?].

3754 In Fig. ?? we show the differential cross section as a function of $\Delta\phi$ for jets in the region $-1 < \eta_{jet} <$
 3755 2.5 with $E_{T,jet1} > 7$ GeV and $E_{T,jet2} > 5$ GeV found with the k_t jet algorithm in the kinematic range
 3756 $Q^2 > 5$ GeV, $0.1 < y < 0.6$ for different regions in x . The ‘MEPS’ prediction comes from a Monte Carlo
 3757 generator [?] using $\mathcal{O}(\alpha_s)$ matrix elements with a DGLAP-type parton shower. The ‘CDM prediction uses
 3758 the same generator [?], but with higher order parton radiation simulated with the Colour Dipole Model [?],
 3759 thus effectively including some k_t diffusion. Finally, the CASCADE Monte Carlo prediction [?], uses off-shell
 3760 matrix elements convoluted with an unintegrated gluon distribution (CCFM set A), with subsequent parton
 3761 showering according to the CCFM evolution equation.

3762 At large x all predictions agree reasonably well, in both shape and normalisation. At smaller x the
 3763 $\Delta\phi$ -distribution becomes flatter for CDM and CASCADE, indicating higher order effects leading to a larger
 3764 decorrelation of the produced jets. Whereas a decorrelation is observed, its size depends on the details of the
 3765 parton evolution and thus a measurement of the $\Delta\phi$ cross section provides a direct measurement of higher
 3766 order effects which need to be taken into account at small x .

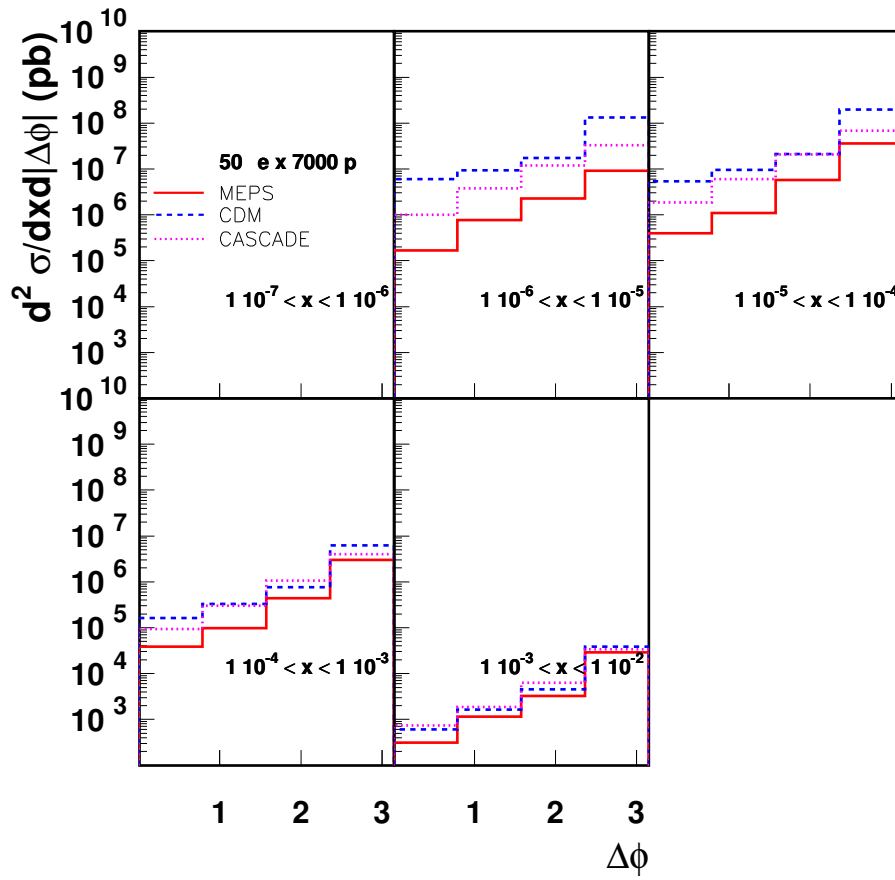


Figure 6.44: Differential cross section for dijet production as a function of the azimuthal separation $\Delta\phi$ for dijets with $E_{T,\text{jet}1} > 7$ GeV and $E_{T,\text{jet}2} > 5$ GeV.

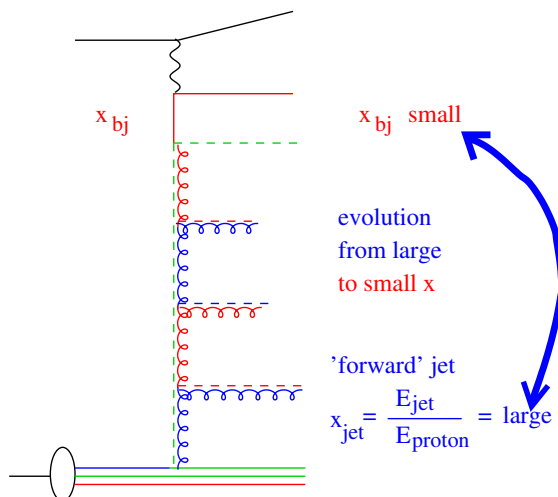


Figure 6.45: Schematic representation of the production of a high transverse momentum forward jet in DIS.

3767 Thus, in principle, a measurement of the azimuthal dijet distribution offers a direct determination of
 3768 the k_T -dependence of the unintegrated gluon distribution. When additionally supplemented by inclusive
 3769 measurements, it can serve as an important constraint for the precise determination of the fully unintegrated
 3770 parton distribution, with the transverse momentum dynamics in the proton completely unfolded.

3771 Forward observables

3772 It was proposed some time ago [?, ?] that a process which would be very sensitive to the parton dynamics
 3773 and the transverse momentum distribution was the production of forward jets in DIS. According to [?, ?],
 3774 DIS events containing identified forward jets provide a particularly clean window on small- x dynamics. The
 3775 schematic view of the process is illustrated in Fig. ???. The forward jet transverse momentum provides
 3776 the second hard scale p_T . Hence one has a process with two hard scales: the photon virtuality Q and
 3777 the transverse momentum of the forward jet p_T . As a result the collinear (DGLAP) configurations (with
 3778 no diffusion and strongly ordered transverse momenta) can be eliminated by choosing the scales to be
 3779 of comparable size, $Q^2 \simeq p_T^2$. Additionally, the jet is required to be produced in the forward direction
 3780 by demanding that x_J , the longitudinal momentum fraction of the produced jet, is as large as possible,
 3781 and x/x_J is as small as possible. This requirement selects events with a large sub-energy between the jet
 3782 and the virtual photon, such that the BFKL framework should be applicable. There have been dedicated
 3783 measurements of forward jets at HERA [?, ?, ?, ?, ?, ?], which demonstrated that DGLAP dynamics at NLO
 3784 are indeed incompatible with the experimental measurements. On the other hand, calculations based on
 3785 resummations of powers of $\log 1/x$ (BFKL and others) [?, ?, ?, ?, ?, ?, ?] are consistent with the data. The
 3786 azimuthal dependence of forward jet production has also been studied [?, ?] as a sensitive probe of the small- x
 3787 dynamics.

3788 Another observable that provides a valuable insight into the features of small- x physics is the transverse
 3789 energy (E_T -flow) accompanying DIS events at small x . The diffusion of the transverse momenta in this
 3790 region leads to a strongly enhanced distribution of E_T at small x . As shown in [?, ?], small- x evolution
 3791 results in a broad Gaussian E_T -distribution as a function of rapidity. This should be contrasted with the
 3792 much smaller E_T -flow obtained assuming strong k_T -ordering as in DGLAP-based approaches, which give an
 3793 E_T -distribution that narrows with decreasing x , for fixed Q^2 .

3794 The first experimental measurements of the E_T -flow in small- x DIS events indicate that there is signif-
 3795 icantly more E_T than is given by conventional QCD cascade models based on DGLAP evolution. Instead
 3796 we find that they are in much better agreement with estimates which incorporate dynamics beyond fixed-
 3797 order DGLAP [?, ?, ?] such as BFKL evolution. The latter dynamics are characterized by an increase of the

3798 E_T -flow in the central region with decreasing x .

3799 However, the experimental data from HERA do not enable a detailed analysis due to their constrained
 3800 kinematics. At the LHeC one could perform measurements with large separations in rapidity and for different
 3801 selections of the scales (Q, p_T) . In particular, there is a possibility of varying scales to test systematically
 3802 the parton dynamics from the collinear (strongly ordered) regime $Q^2 \gg p_T^2$ to the BFKL (equal scale, Regge
 3803 kinematics) regime $Q^2 \simeq p_T^2$. Measurements of the energy flow in different x -intervals, in the small- x regime,
 3804 should therefore allow a definitive check of the applicability of BFKL dynamics and of the eventual presence
 3805 of more involved, non-linear effects.

3806 A simulation of forward jet production at the LHeC is shown in Figs. ?? and ?. The jets are required
 3807 to have $E_T > 10$ GeV with a polar angle $\Theta_{jet} > 1^\circ$ or 3° in the laboratory frame. Jets are found with the
 3808 SISCone jet-algorithm [?]. The DIS phase space is defined by $Q^2 > 5$ GeV, $0.05 < y < 0.85$.

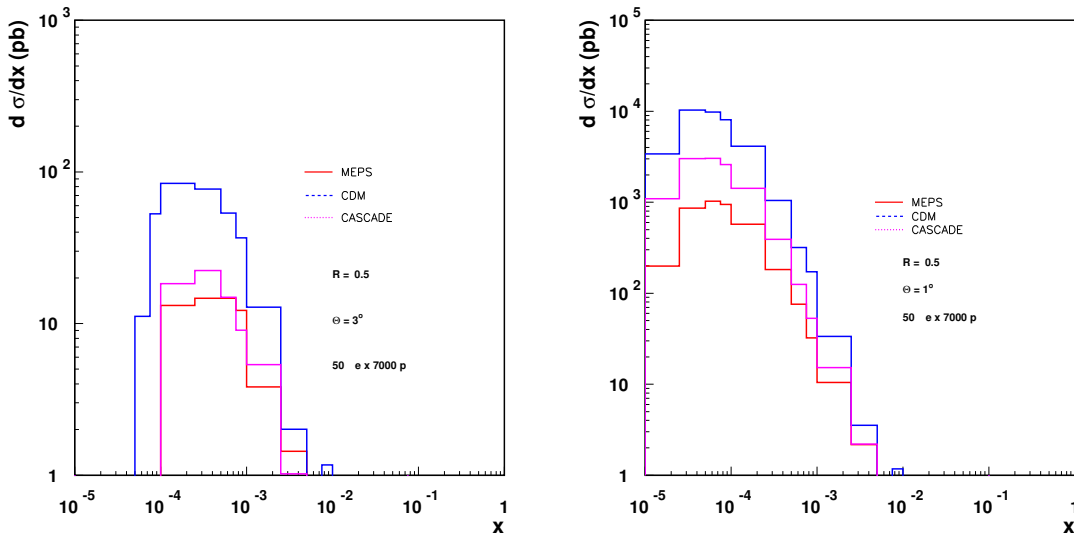


Figure 6.46: Cross section for forward jets with $\Theta_{jet} > 3^\circ$ (left) and $\Theta_{jet} > 1^\circ$ (right). Predictions from MEPS, CDM and CASCADE are shown. Jets are found with the SISCone algorithm using $R = 0.5$.

3809 In Fig. ?? the differential cross section is shown as a function of Bjorken x for an electron energy of
 3810 $E_e = 50$ GeV. The calculations are obtained from the MEPS [?], CDM [?] and CASCADE [?] Monte Carlo
 3811 models, as described in the previous section. Predictions for $\Theta_{jet} > 3^\circ$ and $\Theta_{jet} > 1^\circ$ are shown. One can
 3812 clearly see that the small- x range is explored in detail with the small angle scenario. In Fig. ?? the forward
 3813 jet cross section is shown when using $R = 1$ instead of $R = 0.5$ (Fig. ??). It is important to note that
 3814 good forward acceptance of the detector is crucial for the measurement of forward jets. The dependence of
 3815 the cross section on the acceptance angle is very strong as is evident from comparisons between the cross
 3816 sections for different Θ_{jet} cuts Figs. ?? and ??.

3817 A complementary reaction to that of forward jets is the production of forward π^0 mesons in DIS. Despite
 3818 having a lower rate, this process offers some advantages over forward jet production. By looking onto
 3819 single particle production the dependencies on the jet finding algorithms can be eliminated. Also, the
 3820 non-perturbative hadronisation effects can be effectively encompassed into fragmentation functions [?].

3821 Perturbative and non-perturbative aspects of final state radiation and hadronization

3822 The mechanism through which a highly virtual parton produced in a hard scattering gets rid of its virtuality
 3823 and colour and finally projects onto an observable final state hadron, is unknown to a great extent (see [?])

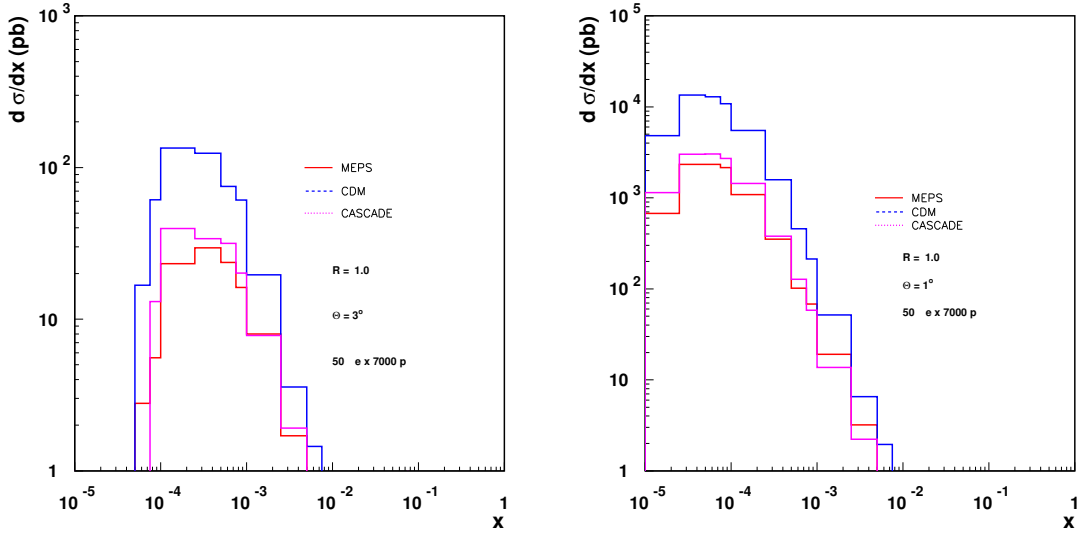


Figure 6.47: Cross section for forward jets with $\Theta_{jet} > 3^\circ$ (left) and $\Theta_{jet} > 1^\circ$ (right). Predictions from MEPS, CDM and CASCADE are shown. Jets are found with the SIScone algorithm using $R = 1.0$.

3824 and references therein). The different postulated stages of the process are illustrated in Fig. ???. The coloured
3825 parton undergoes QCD radiation before forming first a coloured excited bound state (pre-hadron), then a
3826 colourless pre-hadron and ultimately a final state hadron. These sub-processes are characterised by different
3827 time scales. While the first stage can be described in perturbative QCD [?], subsequent ones require models
3828 (e.g. the QCD dipole model for the pre-hadron stages) and non-perturbative information.

3829 The LHeC offers great opportunities to study these aspects and improve our understanding of all of
3830 them. The energy of the parton which is struck by the virtual photon implies a Lorentz dilation of the
3831 time scales for each stage of the radiation and hadronisation processes. All of them are influenced by the
3832 fact that they do not take place in the vacuum, but within the QCD field created by the other components
3833 of the hadron or nucleus. While at fixed target SIDIS or DY experiments, the lever arm in energy is
3834 relatively small (energy transfer to the struck parton in its rest frame, $\nu < 100$ GeV), at the LHeC this
3835 lever arm will be huge ($\nu < 10^5$ GeV; see also in Subsec. ?? the abundant yield of expected high transverse
3836 momentum jets in photoproduction), implying that the different stages can be considered to happen in or
3837 out of the hadron field depending on the parton energy. Furthermore, the fact that we can introduce a piece
3838 of coloured matter of known length and density - a nucleus - by doing ePb collisions at different centralities,
3839 allows a controllable variation of the influence of the different processes. The induced differences in the
3840 final distributions of hadrons, both in terms of their momenta and of their relative abundance, will provide
3841 important information about the time scales and the detailed physical mechanisms at work in each stage.
3842 Dramatic effects are predicted in some models [?], with a significant suppression of the forward hadron spectra
3843 due to the creation of the dense partonic system. Note that SIDIS experiments already provide information
3844 for the determination of standard fragmentation functions (see [?, ?] for a recent analysis). The other pieces
3845 of information, coming mainly from e^+e^- experiments, will not be improved until next-generation linear
3846 colliders become available.

3847 Furthermore, these studies will shed light on two aspects already discussed in Subsec. ??, related to the
3848 study of ultrarelativistic heavy-ion collisions: the characterization of the medium created in such collisions
3849 through hard probes, and the details of particle production in a dense situation which will define the initial
3850 conditions for the collective behavior of this medium. Concerning the latter, our theoretical tools for com-
3851 puting particle production in eA collisions are more advanced e.g. within the CGC framework, and on a

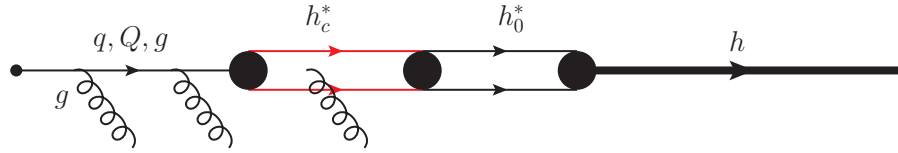


Figure 6.48: Sketch of the different postulated stages in the hadronisation of a highly virtual parton. From left to right: radiating parton; radiating coloured pre-hadron, colourless pre-hadron and final state hadron.

safer ground than in nucleus-nucleus collisions (see Subsec. ?? and e.g. [?] and refs. therein). The possibility of disentangling the different mechanisms through which the factorisation that is used in dilute systems - collinear factorisation [?] - becomes broken by density effects (e.g. initial and final state energy loss or final state absorption) will be possible at the LHeC and will complement existing studies done at much smaller energies in fixed target SIDIS and DY experiments [?].

6.2.6 Implications for ultra-high energy neutrino interactions and detection

The stringent constraints of the parton distributions at very small x from a future LHeC will have important implications for neutrino astronomy. Ultra-high energy neutrinos can provide important information about distant astronomical objects and the origin of the Universe. They have attracted a lot of attention during recent years, see the reviews [?, ?]. Neutrino astronomy has many advantages over conventional photon astronomy. This is due to the fact that neutrinos, unlike photons, interact only weakly, so they can travel long distances being practically undisturbed. The typical interaction lengths for neutrinos and photons at energy $E \sim 1$ TeV are about

$$\mathcal{L}_{int}^{\nu} \sim 250 \times 10^9 \text{ g/cm}^2, \quad \mathcal{L}_{int}^{\gamma} \sim 100 \text{ g/cm}^2.$$

Thus, very energetic photons with energy bigger than ~ 10 TeV cannot reach the Earth from the very distant corners of our Universe without being rescattered. In contrast, neutrinos can travel very long distances without interacting. They are also not deflected by galactic magnetic fields, and therefore at ultra-high energies the angular distortion of the neutrino trajectory is very small. As a result, highly energetic neutrinos reliably point back to their sources. The interest in the neutrinos at these high energies has led to the development of several neutrino observatories, see [?] and references therein.

For reliable observations based on neutrino detection, precise knowledge about their production rates and interactions is essential to estimate the background, the expected fluxes and the detection probabilities. Even though neutrinos interact only weakly with other particles, strong interactions play an essential role in the calculations of their production rates and interaction cross sections. This is due to the fact that neutrinos are produced in the decays of various mesons such as π , K , D and even B , which are produced in high-energy proton-proton (or proton-nucleus or nucleus-nucleus) collisions. These hadronic processes occur mainly in the atmosphere though possibly also in the accretion discs of remote Active Galactic Nuclei. Further, the interactions of highly energetic neutrinos with matter are dominated by the deep inelastic cross section with

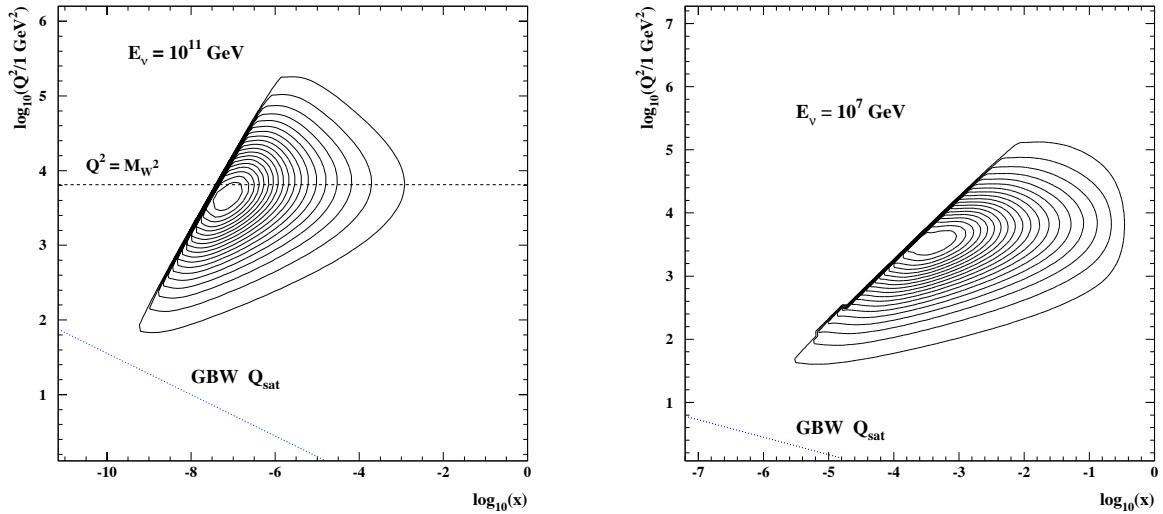


Figure 6.49: Contour plot showing the x, Q^2 domain of the dominant contribution to the differential cross section $d\sigma/d\ln(1/x)d\log Q^2$ for the total ν -nucleon interaction at neutrino laboratory energies of $E_\nu = 10^{11}$ GeV (left plot) and $E_\nu = 10^7$ GeV (right plot). The 20 contours enclose contributions of 5, 10, 15 \dots 100 % of the cross section. The saturation scale according to the model in [?] is shown as a dashed line. See the text for further explanation.

3872 nucleons or nuclei. Hence, low x information from high-energy collider experiments such as HERA, Tevatron,
 3873 LHC and, most importantly, the future LHeC, is invaluable.

3874 One of the main uncertainties (if not the dominant one) in the current limits on high-energy neutrino
 3875 production is due to the neutrino-nucleon (nucleus) cross section. In fact, event rates are proportional to
 3876 the neutrino cross section in many experiments. This cross section involves the gluon distribution probed
 3877 at very small values of Bjorken x , down to even $\sim 10^{-9}$, which corresponds to a very high centre of mass
 3878 energy.

3879 To visualize the kinematic regime probed in ultra-high energy neutrino-nucleon interactions, contour plots
 3880 of the differential cross section $\frac{d^2\sigma}{d\ln 1/x d\ln Q^2/\Lambda^2}$ in the (x, Q^2) plane are shown in Fig. ???. The contours enclose
 3881 regions with different contributions to the total cross section $\sigma(E_\nu)$. For very high energy $E_\nu = 10^{11}$ GeV the
 3882 dominant contribution comes from the domain $Q^2 \simeq M_W^2$ and $x_{\min} \simeq M_W^2/(2M_N E) \sim 10^{-8} - 10^{-7}$ where
 3883 M_N is the nucleon mass, inaccessible to any current or proposed accelerators. However, at lower neutrino
 3884 energy $E_\nu = 10^7$ GeV the relevant domain of (x, Q^2) could be very well covered by the LHeC, thus providing
 3885 important new constraints on the neutrino-nucleon cross section.

3886 On the other hand, another process which has been proposed for neutrino detection comes from the
 3887 discovery of neutrino flavor oscillations, which makes it possible that high rates of τ neutrinos reach the
 3888 Earth, despite being heavily suppressed in most postulated production mechanisms. The possibility to
 3889 search for ν_τ 's by looking for τ leptons that exit the Earth, Earth-skimming neutrinos, has been shown to be
 3890 particularly advantageous to detect neutrinos of energies in the EeV (10^{18} eV) range [?]. The short lifetime
 3891 of a τ lepton originating a neutrino charged current interaction allows the τ to decay in flight while still close
 3892 to the Earth's surface, producing an outgoing air shower, detectable in principle by various techniques. This
 3893 channel suffers from negligible contamination for other neutrino flavors. The sensitivity to ν_τ 's through the
 3894 Earth-skimming channel directly depends both on the neutrino charged current cross section and on the τ
 3895 range (the energy loss) which is determined by the amount of matter with which the neutrino has to interact
 3896 to produce an emerging τ . It turns out that the τ energy loss is also determined by the behavior of the

3897 proton and nucleus structure functions at very small values of x , see e.g. [?]. The average energy loss per
 3898 unit depth, X , is conveniently represented by:

$$-\left\langle \frac{dE}{dX} \right\rangle = a(E) + b(E)E, \quad b(E) = \frac{N_A}{A} \int dy y \int dQ^2 \frac{d\sigma^{LA}}{dQ^2 dy}, \quad (6.19)$$

3899 where the $a(E)$ term is due to ionization, $b(E)$ is the sum of fractional losses due to e^+e^- pair production,
 3900 Bremsstrahlung and photonuclear interactions, N_A is Avogadro's number and A is the mass number. The
 3901 parameter $a(E)$ is nearly constant and the term $b(E)E$ dominates the energy loss above a critical energy
 3902 that for τ leptons is a few TeV, with the photonuclear interaction being dominant for τ energies exceeding
 3903 $E = 10^7$ GeV (as already assumed in Eq. (??)). In Fig. ?? the relative contribution to $b(E)$ of different
 3904 x and Q^2 regions is shown. It can be observed that the energy loss is dominated by very small x and, in
 contrast to the case of the neutrino cross section, by small and moderate $Q^2 \lesssim m_\tau^2$.

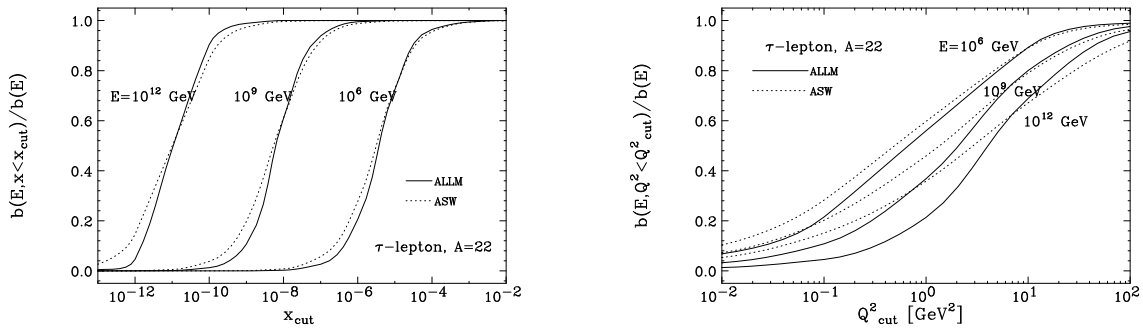


Figure 6.50: The relative contribution of $x < x_{cut}$ (plot on the left) and of $Q^2 < Q_{cut}^2$ (plot on the right) to the photonuclear energy loss rate, $b(E)$, for different neutrino energies $E = 10^6, 10^9$ and 10^{12} GeV, in two different models for the extrapolation of structure functions to very small x . See the text and [?] - from which these plots were taken - for explanations.

3905 As the LHeC will be able to explore a new regime of low x and high Q^2 and constrain the parton
 3906 distributions, the measurements performed at this collider will be invaluable for the precise evaluation of
 3907 the neutrino-nucleon (or nucleus) scattering cross sections and τ energy loss necessary for ultra-high energy
 3908 neutrino astronomy.
 3909

Part III

Accelerator

3910

3911

Chapter 7

Ring-Ring Collider

7.1 Baseline Parameters and Configuration

7.2 Geometry

All lattice descriptions in this chapter are based on the LHeC lattice Version 1.1.

7.2.1 General Layout

The general layout of the LHeC consists of eight arcs, six straight sections and two bypasses around the experiments in Point 1 and Point 5. The e-p collision experiment is assumed to be located in Point 2, the only foreseen interaction point of the electron and proton beams. All straight sections except those in the bypasses have the same length as the LHC straight sections: 538.8 m at even points and 537.8 m at odd points.

The insertions shared with the LHC are already used for the experiments or for LHC equipment. Therefore the RF for the electron ring is installed in the straight sections of the bypasses [?]. For the same reason the beam is injected in the bypass around Point 1. Point 1 is preferred over Point 5 for geological and infrastructural reasons. The overall layout of the LHeC is shown in Figure ??.

7.2.2 Electron Ring Circumference

The LHeC electron beam collides only in one point (assumed to be Point 2) with the protons of the LHC. This leaves the options to either exactly match the circumferences of the proton and electron rings or to allow a difference of a multiple of the LHC bunch spacing. In the case of different circumferences the proton beam could become unstable due to beam-beam interactions with the electrons [?]. To avoid this possible effect in the LHeC, the electron ring circumference is matched exactly to the proton ring circumference.

The circumference can be adjusted in two ways:

1. Different bypass designs, e.g. inner and outer bypass, which compensate each other in length.
2. Radial displacement of the electron ring to the inside or outside of the LHC in the places where the two rings share the same tunnel to compensate for the path length difference caused by the bypasses.

The various design possibilities for the bypasses are discussed in Sec. ?. Considering their characteristics, the best choice seems to be outer bypasses around both experiments.

7.2.3 Idealised Ring

In the following the average between LHC Beam1 and Beam2 is taken as reference geometry for the LHC.

3941 General Layout

3942 To compensate the path length differences from the bypasses, the electron ring is placed on average 61 cm
3943 to the inside of the LHC in the sections where both rings share the tunnel. For this a complete ring with an
3944 ideally constant radial offset of 61 cm to the LHC was designed. In the following we refer to this ring as the
3945 *Idealised Ring*.

3946 In addition to the horizontal displacement, the electron ring is set 1 m above the LHC in order to minimise
3947 the interference with the LHC elements. The main remaining conflicts in the arc are then the service modules
3948 as shown in Figure ?? and the DFBs in the insertions [?]. A representative cross section of the LHC tunnel
3949 is shown in Figure ??.

3950 In the main arcs the service modules have a length of 6.62 m and are installed at the beginning of each
3951 LHC arc cell. The insertions host a different number of DFBs with a varying placement and length. The
3952 idealised ring lattice is designed to avoid overlaps of magnet elements with all service modules in the main
3953 arcs. In order to show that it is possible to design an optics with no e-ring elements at any DFB positions in
3954 the insertions, the dispersion suppressors of the even and odd insertions were adapted to the DFB positions
3955 and lengths in IR2 and IR3 respectively. For simplicity all straight sections are filled with a regular FODO
3956 cell structure.

3957 Geometry

3958 To adjust the beam optics to the regular reappearance of the service modules at the beginning of each LHC
3959 arc cell it was suggested to use a multiple, n , or sub-multiple $1/n$ ($n \in \mathbb{N}$) of the LHC arc cell length as LHeC
3960 FODO cell length. Beside the integration constraints, the cell has to provide the right emittance. Taking
3961 half the LHC arc cell length as LHeC FODO cell length already fulfils this second criterion (Sec. ??).

3962 As the LHC arc cell is symmetric, the best geometrical alignment with the LHC main arc would be
3963 achieved, if the LHeC cell also had a symmetrical layout. Because of the service modules, no elements can
3964 be placed in the first 6.9 m of two consecutive cells. If all cells had the same layout, another 6.9 m would be
3965 lost in the second FODO cell. This would result in additional unwanted synchrotron radiation losses as the
3966 energy loss in a dipole magnet is proportional to the inverse length of the dipole

$$U_{\text{dipole}} = \frac{C_\gamma}{2\pi} E_0^4 \frac{\theta^2}{l}, \quad C_\gamma = \frac{4\pi}{3} \frac{r_e}{(m_e c^2)^3} \quad (7.1)$$

3967 where θ is the bending angle, l the length of the dipole and E_0 the beam energy. In order to avoid this, the
3968 LHeC arc cell is a double FODO cell, symmetric in the positioning of the quadrupoles but asymmetric in
3969 the placement of the dipoles (Figure ??).

3970 The bending angle in the arc cells and also in the DS is determined by the LHC geometry. In the
3971 following we refer to the LHC DS as the section from the end of the arc to the beginning of the LSS. With
3972 this definition the LHC DS consists of two cells. Keeping the same conversion rule as in the arc (one LHC
3973 FODO cell corresponds to two LHeC FODO cells), the LHeC DS would then ideally consist of 4 equal cells.
3974 For consistency the ratio between the LHeC DS and arc cell lengths is the same as between the LHC DS
3975 and arc cell. For the LHC this ratio is $2/3$. This leaves the following choices for the number of dipoles in
3976 the arc and DS cell:

$$N_{\text{Dipole, arc cell}} = \frac{3}{2} N_{\text{Dipole, DS cell}} = 3, 6, 9, 12, 15 \dots \quad (7.2)$$

3977 A good compromise between a reasonable dipole length and optimal use of the available space for the bending
3978 is 15 dipoles per arc cell. The dipoles are then split up in packages of $3 + 4 + 4 + 4$ in one arc cell and $2 + 3$
3979 in one DS cell.

3980 Beside the bending angle, the module length of the electron ring has to be matched to the LHC geometry.
3981 As the electron ring is radially displaced to the inside of the proton ring, all e-ring modules are slightly shorter
3982 than their proton ring equivalents (Table ??).

3983 The above considerations already fix the bending angle of the dipoles, which leaves only position and
3984 length as free parameters. Ideally the dipole length would be chosen as long as possible, but because of the

	Proton Ring	Electron Ring
Arc Cell Length	106.9 m	106.881 m
DSL Length (even points)	172.80 m	172.78 m
DSR Length (even points)	161.60 m	161.57 m
DSL Length (odd points)	173.74 m	173.72 m
DSR Length (odd points)	162.54 m	162.51 m

Table 7.1: Proton and Electron-Ring Module Lengths

3985 asymmetry of the arc cell, the dipoles have to be shortened and moved to the right in order to fit the LHC
3986 geometry.

3987 The LHeC DS layout would ideally be similar to the LHC DS layout (Figure ??), but has to be modified in
3988 order to leave space for the DFBs in the DS region. In the final design the dipoles are placed as symmetrically
3989 as possible between the regular arrangement of the quadrupoles (Figure ??, ??).

3990 The difference between the LHC proton ring and the idealised LHeC electron ring is shown in Figure ??
3991 and ??.

3992 7.2.4 Bypass Options

3993 In the design of the e-ring geometry, it is foreseen to bypass the LHC experiments at Point 1 and Point
3994 5. The main requirements for both bypasses are that all integration constraints are respected, synchrotron
3995 radiation losses are not significantly increased and that the change in circumference can be compensated by
3996 increasing or decreasing the radius of the ring.

3997 Three different options are considered as basic bypass designs:

3998 **Vertical Bypass:** A vertical bypass would have to be a vertically upward bypass as downward would
3999 imply crossing the LHC magnets and other elements. For this a separation of about 20 to 25 m is
4000 required [?]. This can only be achieved by strong additional vertical bending. In general a vertical
4001 bypass would therefore be rather long, increase the synchrotron radiation due to the additional vertical
4002 bends and decrease the polarization compared to a horizontal bypass. A vertical bypasses is therefore
4003 only considered as an option if horizontal bypasses are not possible.

4004 **Horizontal Inner Bypass:** A horizontal inner bypass can be constructed by simply decreasing the bending
4005 radius of the main bends. Consequently the synchrotron radiation losses for an inner bypass are larger
4006 than for a comparable outer bypass. The advantage of an inner bypass is, if used in combination with
4007 an outer one, that it reduces the circumference and the two bypasses could compensate each other's
4008 path length differences.

4009 **Horizontal Outer Bypass:** A horizontal outer bypass uses the existing curvature of the ring instead of
4010 additional or stronger dipoles and consequently does not increase the synchrotron radiation losses. In
4011 general this is the preferred option.

4012 7.2.5 Bypass Point 1

4013 The cavern in Point 1 reaches far to the outside of the LHC, so that a separation of about 100 m would be
4014 necessary in order to fully bypass the experimental hall. For a bypass on the inside, a smaller separation of
4015 about 39 m would be required. For an inner bypass with minimal separation, the bending strength in three
4016 normal arc cells would have to be doubled resulting in a bypass of more than 2 km length. A sketch of such
4017 an inner bypass is shown in Figure ??.

4018 Instead of a long inner bypass, an outer bypasses using the existing survey gallery is chosen as final
4019 design. With this design the separation is brought down to 16.25 m. The RF is installed in the straight

4020 section next to the straight section of the proton ring. The electron beam is injected into the arc on the
 4021 right side of the bypass. The design is shown in Figure ??.

4022 7.2.6 Bypasses Point 5

4023 Due to the compact design of the cavern in Point 5 a separation of only about 20 m is needed to completely
 4024 bypass the experiment on the outside (Figure ??). The separation in the case of an inner horizontal bypass
 4025 or a vertical bypass would be the same or larger and therefore, as in the case of Point 1, the horizontal outer
 4026 bypass is preferred over an inner or vertical one. The RF is installed in the centre straight section parallel
 4027 to the proton ring.

4028 7.2.7 Matching Proton and Electron Ring Circumference

4029 Both bypasses in Point 1 and Point 5 require approximately the same separation and a similar design was
 4030 chosen for both. To obtain the necessary separation Δ_{BP} a straight section of length s_{BP} is inserted into the
 4031 lattice of the idealised ring (Sec. ??) in front of the last two arc cells. The separation Δ_{BP} , the remaining
 4032 angle θ_{BP} and the inserted straight section s_{BP} are related by (Figure ??):

$$\Delta_{BP} = s_{BP} \sin \theta_{BP} \quad (7.3)$$

4033 As indicated in Figure ?? the separation could be increased by inserting a S-shaped chicane including negative
 4034 bends. The advantage of additional bends would be the faster separation of the electron and proton ring.
 4035 On the other hand the additional bends would need to be placed in the LHC tunnel, the straight sections of
 4036 the bypass would be reduced and the synchrotron radiation losses increased.

4037 In the following, estimates for the current bypass design, which does not include any extra bends, are
 4038 presented. Given the separation, angle and length of the inserted straight section, the induced change in
 4039 circumference is then:

$$\Delta s_{BP} = s_{BP} - x_{BP} = 2\Delta_{BP} \tan\left(\frac{\theta_{BP}}{2}\right) \quad (7.4)$$

4040 This change can be compensated by a change in radius of the idealised ring by:

$$\Delta s_{BP} = 2\pi\Delta R \quad (7.5)$$

4041 Taking the change in radius into account, the separation Δ_{BP} has to be substituted by $\Delta_{BP,tot} :=$
 4042 $\Delta_{BP} + \Delta R$. The radius change and the total separation are then related by:

$$\Delta R = \frac{\Delta_{BP}}{\pi \cot\left(\frac{\theta_{BP}}{2}\right) - 2}, \quad \text{with } \Delta_{BP} = \Delta_{BP1} + \Delta_{BP5} \quad (7.6)$$

4043 As the bypass in Point 1 passes through the existing survey gallery, the geometry and with it the separation
 4044 in Point 1, cannot be changed. The bypass in Point 5, on the other hand, is fully decoupled from the existing
 4045 LHC cavern and tunnel and is therefore used for the fine adjustment of the circumference. The design values
 4046 of both bypasses are summarised in Table ??.

	Point 1	Point 5
Total bypass length	1303.3 m	1303.7 m
Separation	16.25 m	20.56 m
Dispersion free straight section	172 m	297 m
Ideal radius change of the idealised ring	61 cm	

Table 7.2: Lengths characterising the bypasses.

7.3 Layout and Optics

Throughout the whole electron ring lattice, the choice of the optics is strongly influenced by the geometrical constraints and shortage of space in the LHC tunnel. The main interference with the LHC beside Point 1 and Point 5, which have to be bypassed, are the service modules and DFBs in the tunnel, where no electron ring elements can be placed.

7.3.1 Arc Cell Layout and Optics

The LHC service modules are placed at the beginning of each LHC main arc cell. In order to obtain a periodic solution of the lattice, the electron ring arc cell length can only be a multiple or $1/n$ th, $n \in \mathbf{N}$, of the LHC FODO cell length. Given the same phase advance and bending radius, the emittance increases with increasing cell length L of a FODO cell. In the case of the LHeC electron ring a FODO cell length corresponding to half the LHC FODO cell length delivers an emittance close to the design value. The emittance of a cell with the full LHC FODO cell length is about a factor of 4 too large.

Choosing half the LHC FODO cell length divides the arc into 23 equal double FODO cells with a symmetric configuration of the quadrupoles and an asymmetric distribution of the dipoles, namely 8 dipoles in the first FODO cell and 7 in the second. The dipole configuration is asymmetric in order to use all available space for the bending of the e-beam and consequently minimise the synchrotron radiation losses. With a phase advance of 180° horizontally and 120° vertically over the complete double FODO cell, which corresponds to a phase advance of $90^\circ/60^\circ$ per FODO cell, the horizontal emittance of 4.70 nm lies well below the design value of 5 nm. Because of the asymmetry of the dipole configuration, the phase advance in the horizontal plane is also not equally distributed. In the first half it is, at $90.6^\circ/60^\circ$, slightly larger than in the second half with $89.4^\circ/60^\circ$. The optics of one arc cell is shown in Figure ?? and the parameters are listed in Table ??.

Beam energy	60 GeV
Phase advance per cell	$180^\circ/120^\circ$
Cell length	106.881 m
Dipole fill factor	0.75
Damping partition $J_x/J_y/J_e$	1.5/1/1.5
Coupling constant κ	0.5
Horizontal emittance (no coupling)	4.70 nm
Horizontal emittance ($\kappa = 0.5$)	3.52 nm
Vertical emittance ($\kappa = 0.5$)	1.76 nm

Table 7.3: Optics parameters of one LHeC arc cell with a phase advance of $180^\circ/120^\circ$.

7.3.2 Insertion Layout and Optics

For simplicity all even and all odd insertions of the electron ring have the same layout as described in Sec. ???. Each insertion is divided in three parts: the dispersion suppressor on the left side (DSL), the straight section and the dispersion suppressor on the right side (DSR).

Dispersion Suppressor

Various well known standard DS designs like the missing bend or half bend scheme exist, but they are all based on specific placement of the dipoles. In the case of the LHeC the position of the dipoles is strongly determined by the LHC geometry and does not match any of the standard schemes. Therefore the dispersion

4077 matching is achieved by 8 individually powered quadrupoles and not with the positioning of the dipoles. The
4078 DS on the left side is split into two DS sections, reaching from the first DFB to the second and from the
4079 second to the beginning of the straight section. In the DSL the quadrupoles are distributed equally in each
4080 section. In the DSR they are placed with equal distances from each other throughout the complete DS. This
4081 layout turned out to be better for the right side due to the different arrangement of the DFBs. The DSs of
4082 the even and odd points differ slightly in their length but have the same general layout. The lengths of the
4083 DSs are listed in Table ???. The DS optics are shown in Figure ?? and ??.

4084 Straight Section

4085 For simplicity the straight sections consist of a regular FODO lattice with a phase advance of $90^\circ/60^\circ$. In a
4086 later stage the lattice and optics of the straight sections will have to be adjusted to the various insertions.

4087 7.3.3 Bypass Layout and Optics

4088 The general layout and nomenclature of the bypasses is illustrated in Figure ???. The straight sections LSSL,
4089 LSSR and IR are dispersion free sections reserved for the installation of RF, wiggler(s), injection etc. Two
4090 normal arc cells (4 FODO cells) with 8 individual quadrupoles are used as dispersion suppressor before the
4091 first straight section LSSL and after the last straight section LSSR. In the sections TLIR and TRIR the
4092 same configuration of dipoles is kept as in the idealised lattice for geometric reasons. Among this fixed
4093 arrangement of dipoles 14 matching quadrupoles per side are placed as equally as possible.

4094 The straight sections consist of a regular FODO lattice with a phase advance of $90^\circ/60^\circ$.
4095 The complete bypass optics in Point 1 and Point 5 are shown in Figure ?? and ??.

4096 7.3.4 Chromaticity Correction

4097 The phase advance of one LHeC FODO cell is approximately $90^\circ/60^\circ$. The traditional choice would be to
4098 correct the chromaticity with two interleaved families in the horizontal and three in the vertical plane, but
4099 this scheme leads to one strong and one weak sextupole in the horizontal plane, which is undesirable for the
4100 suppression of resonances. An interleaved scheme with 6 sextupoles yields to approximately similar strength
4101 for all sextupoles and should therefore lead to more stability. More detailed studies have to be carried out to
4102 find the best correction scheme, but chromaticity correction is not expected to be a problem in this machine.

4103 7.3.5 Working Point

4104 Because of the bypasses and the single interaction region, the LHeC lattice has no reflection or rotation
4105 symmetry. As 50% emittance ratio is required, betatron coupling resonances may be excited and must be
4106 taken into account for the choice of the working point. In addition the beam will suffer a maximum beam-
4107 beam tune shift of 0.086 in the horizontal and 0.088 in the vertical plane in the case of the 1° option and 0.085
4108 in the horizontal and 0.090 in the vertical plane in the case of the 10° option. Taking all this into account, a
4109 possible working point could be $Q_x = 122.1/Q_y = 83.13$ for the 1° optics and $Q_x = 122.1011/Q_y = 83.1283$
4110 for the 10° optics. The working point diagrams for both cases are shown in Figs. ?? and ??.

4111 7.3.6 Aperture

4112 The current LHeC e-ring magnet apertures [?] are based on the experience from LEP [?] applied on the
4113 LHeC arc cells. They correspond to minimum 23.0σ hor./ 39.9σ ver. in the arc dipoles, 31σ hor./ 59σ ver.
4114 in the arc quadrupoles, 9.7σ hor./ 34.3σ ver. in the insertion dipoles and 14.3σ hor./ 51.0σ ver. in the
4115 insertion quadrupoles. In the estimate all insertions were included except the interaction region. All values
4116 are summarised in Table ??, ??, ??, ??. The hor. aperture in the insertion dipoles could be slightly to tight,
4117 but can be probably extended without problems over the current 20 mm half aperture. In all calculations a

4118 gaussian profile in all three dimensions was assumed and the maximum beam size is consequently given by:

$$\sigma_{x,y} = \sqrt{\beta_{x,y}\epsilon_{x,y} + D_{x,y}^2\sigma_E^2} \quad (7.7)$$

4119 where $\epsilon_{x,y}$ are the design emittances of 5 respectively 2.5 nm.

Hor. half apert. dipole	30 mm
Ver. half apert. dipole	20 mm
Max. hor. beta function	82.7 m
Max. hor. dispersion	0.51 m
Max. ver. beta function	100.5 m
Max. hor. beam size	0.87 mm
Max. ver. beam size	0.50 mm
Hor. apert./max. beam size	34.5
Ver. apert./max. beam size	39.9

Table 7.4: Aperture and beam sizes for the arc dipoles

Hor. half aperture dipole	30 mm
Ver. half aperture dipole	20 mm
Max. hor. beta function	126.9 m
Max. hor. dispersion	1.64 m
Max. ver. beta function	136.2 m
Max. hor. beam size	2.06 mm
Max. ver. beam size	0.58 mm
Hor. aperture/max. beam size	14.6
Ver. aperture/max. beam size	34.3

Table 7.5: Aperture and beam sizes for the insertion dipoles

Apert. radius arc quad.	30 mm
Max. hor. beta function	99.2 m
Max. hor. dispersion	0.56 m
Max. ver. beta function	103.3 m
Max. hor. beam size	0.96 mm
Max. ver. beam size	0.51 mm
Hor. apert./max. beam size	31.4
Ver. apert./max. beam size	59.0

Table 7.6: Aperture and beam sizes for the arc quadrupoles

Apert. radius quad.	30 mm
Max. hor. beta function	141.9 m
Max. hor. dispersion	1.66 m
Max. ver. beta function	138.4 m
Max. hor. beam size	2.10 mm
Max. ver. beam size	0.59 mm
Hor. apert./max. beam size	14.3
Ver. apert./max. beam size	51.0

Table 7.7: Aperture and beam sizes for the insertion quadrupoles

4120 **7.3.7 Complete Lattice and Optics**

4121 Combining all the lattice parts discussed in section ?? to ?? one obtains a lattice with the parameters listed
 4122 in Table ??

Beam energy	60 GeV
No. of particles per bunch	1.98×10^{10}
No. of bunches	2808
Circumference	26658.8832 m
Syn. rad. loss per turn	437.2 mev
Power	43.72 MW
Damping partition $j_x/j_y/j_e$	1.5/1/1.5
Coupling constant κ	0.5
Damping time τ_x	0.016 s
Damping time τ_y	0.024 s
Damping time τ_e	0.016 s
Polarization time	61.7 min
Horizontal emittance (no coupling)	5.53 nm
Horizontal emittance ($\kappa = 0.5$)	4.15 nm
Vertical emittance ($\kappa = 0.5$)	2.07 nm
RF voltage V_{RF}	500 MV
RF frequency f_{RF}	721.421 MHz
Energy spread	0.00116
Momentum compaction	0.00008084
Synchrotron tune	0.058
Bunch length	6.88 mm
Max. hor. beta	141.94 m
Max. ver. beta	138.43 m
Max. hor. dispersion	1.66 m
Vert. dispersion	0 m
Max. hor. beam size (5/2.5 nm emittance)	2.1 mm
Max. ver. beam size (5/2.5 nm emittance)	0.59 mm

Table 7.8: LHeC Optics Parameters

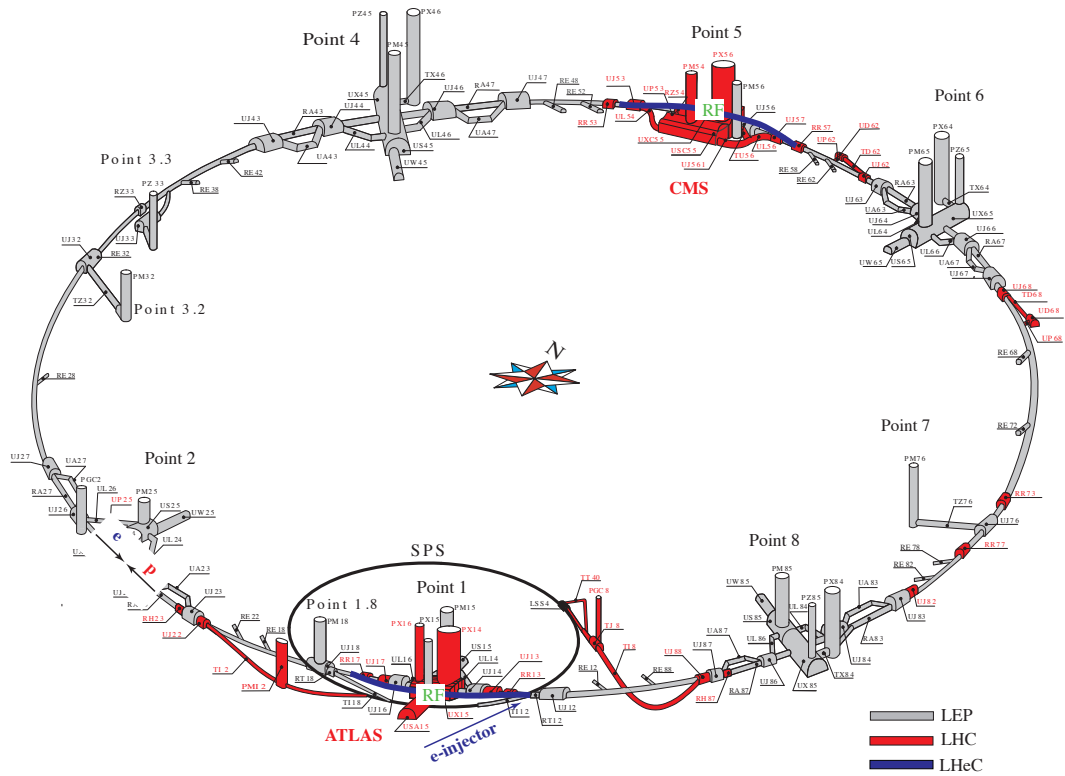


Figure 7.1: Schematic Layout of the LHeC: In grey the LEP tunnel now used for the LHC, in red the LHC extensions. The two LHeC bypasses are shown in blue. The RF is installed in the central straight section of the two bypasses. The bypass around Point 1 hosts in addition the injection.

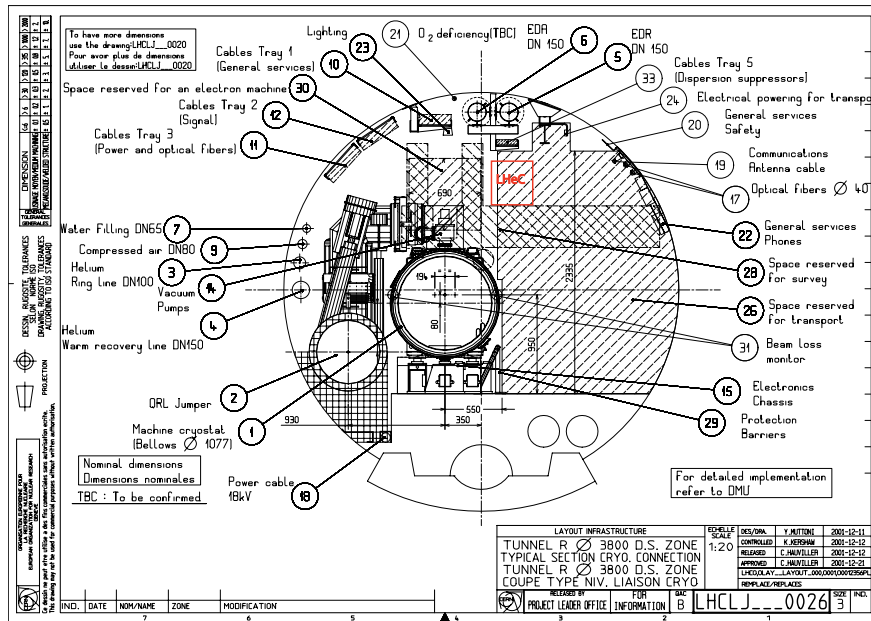


Figure 7.2: Representative cross section of the LHC tunnel. The location of the electron ring is indicated in red.

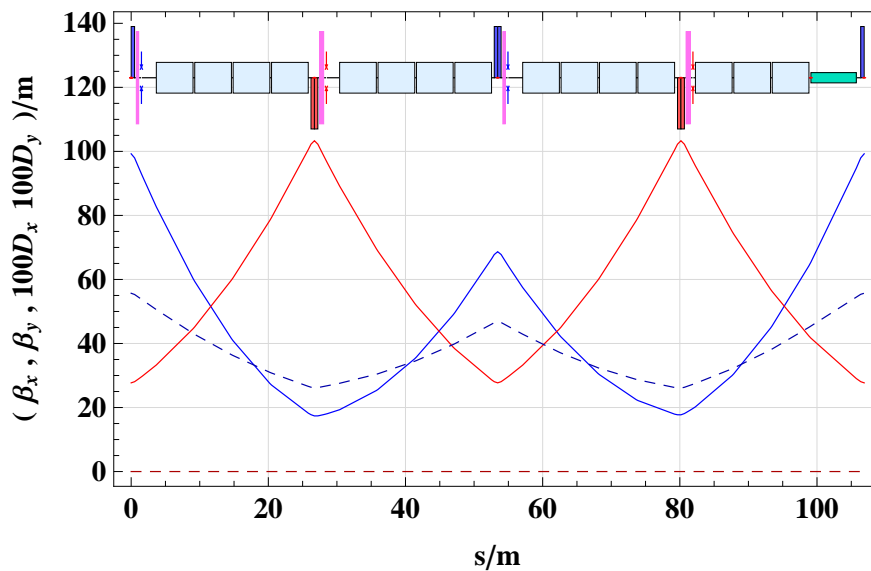


Figure 7.3: Electron ring arc cell optics. One arc cell consists of two FODO cells symmetric in the placement of the quadrupoles and asymmetric for the dipoles.

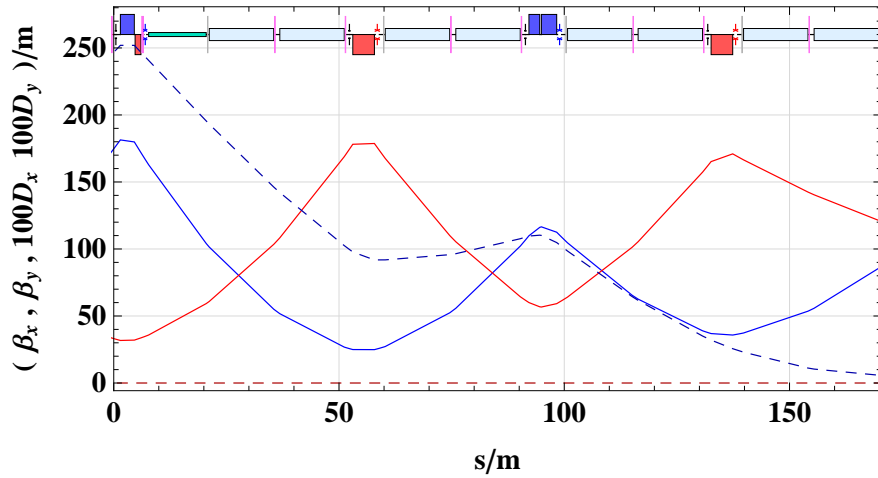


Figure 7.4: LHC DS on the left side of IP2.

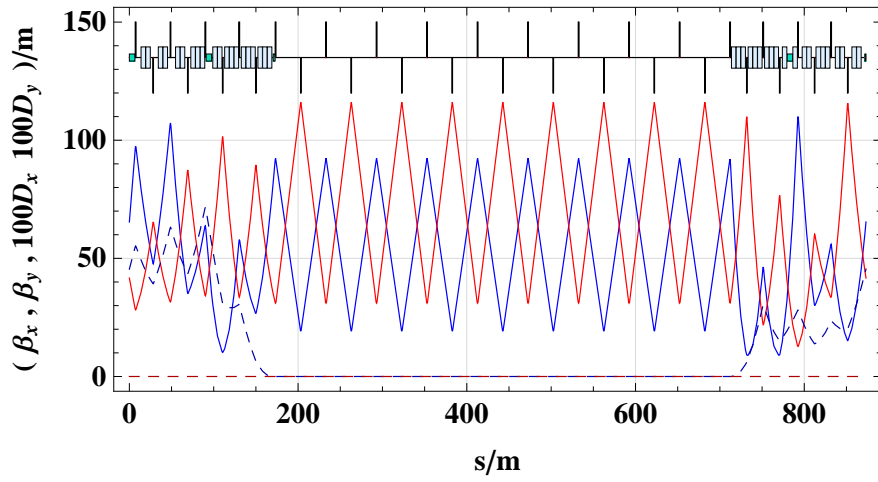


Figure 7.5: LHeC IR for even IRs, based on the DFB configuration in Point 2.

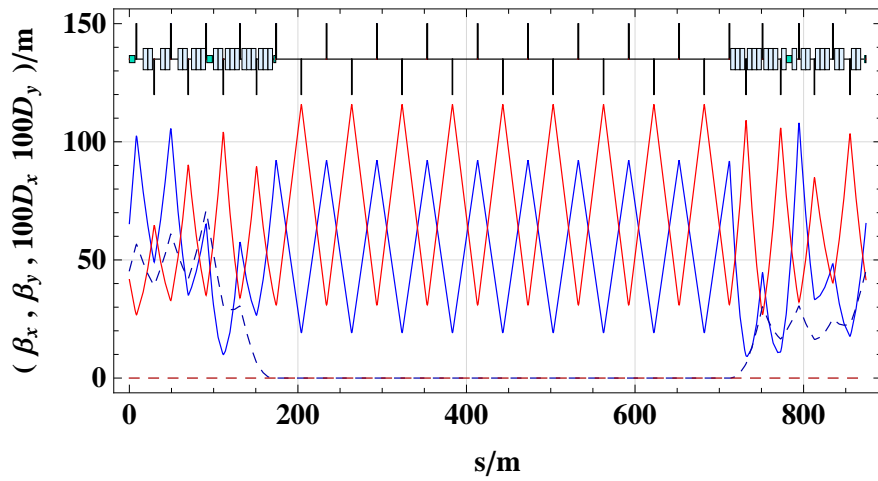


Figure 7.6: LHeC IR for odd IRs, based on the DFB configuration in Point 3.

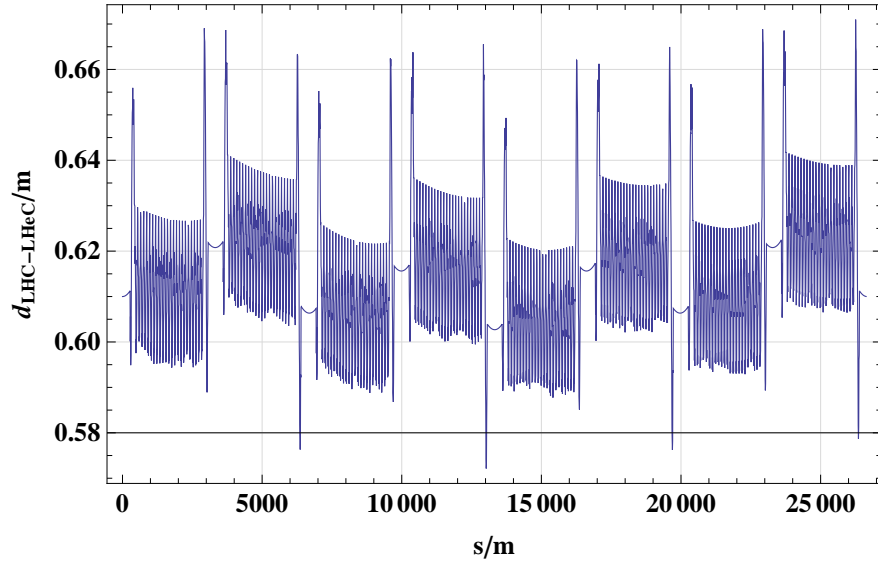


Figure 7.7: Radial distance between the idealised electron ring and the proton ring

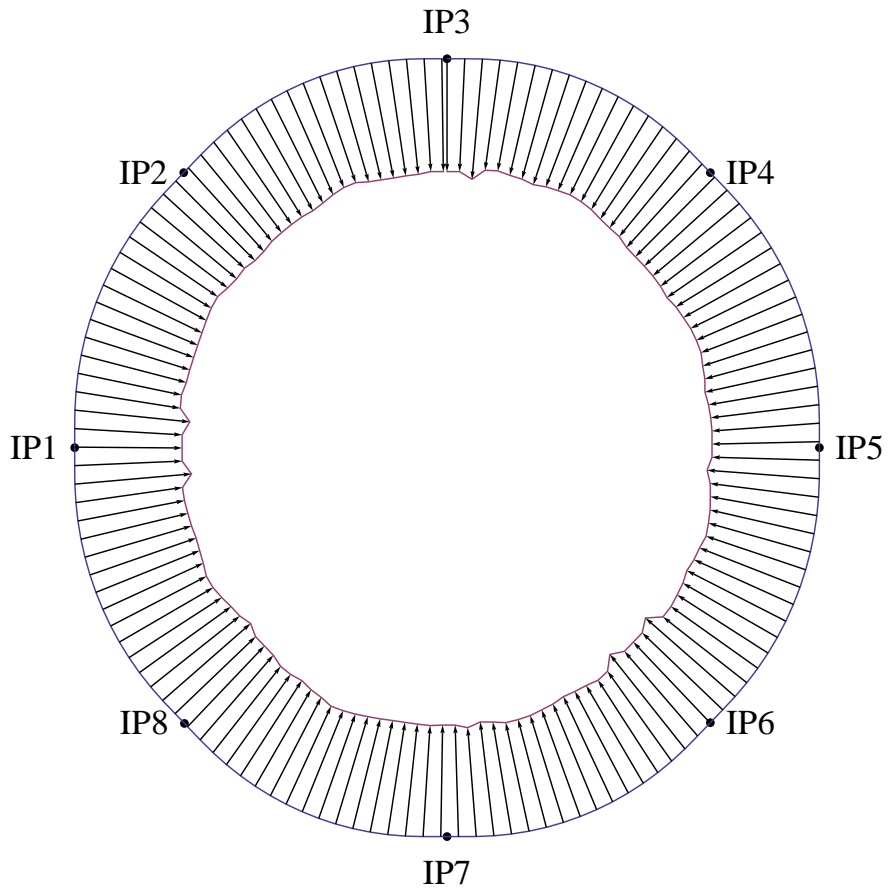


Figure 7.8: LHC and LHeC. The distance between the two rings is exaggerated by a factor 2000.

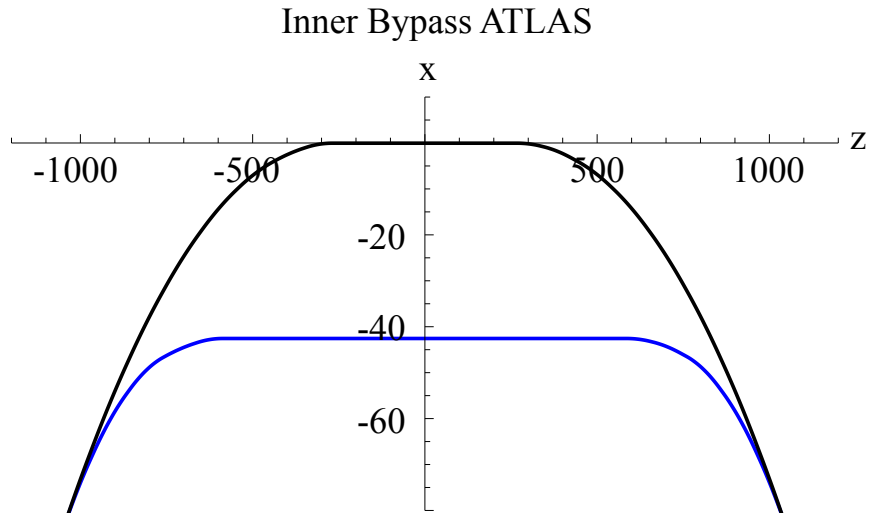


Figure 7.9: Example of an inner Bypass around Point 1. The Bypass is shown in blue, The LHC proton ring in black.

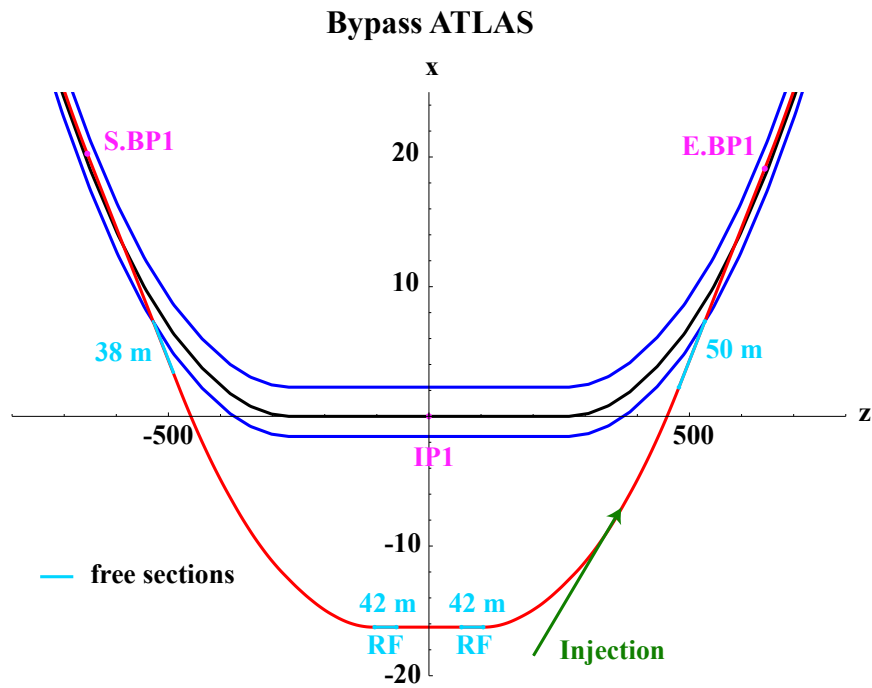


Figure 7.10: Final bypass design using the survey gallery in Point 1. The LHC proton ring is shown in black, the electron ring in red and the tunnel walls in blue. Dispersion free sections reserved for the installation of RF, wiggler(s), injection and other equipment are marked in light blue. The injection is marked in green and is located in the right arc of the bypass. Beginning and end of the bypass are marked with S.BP1 and E.BP1

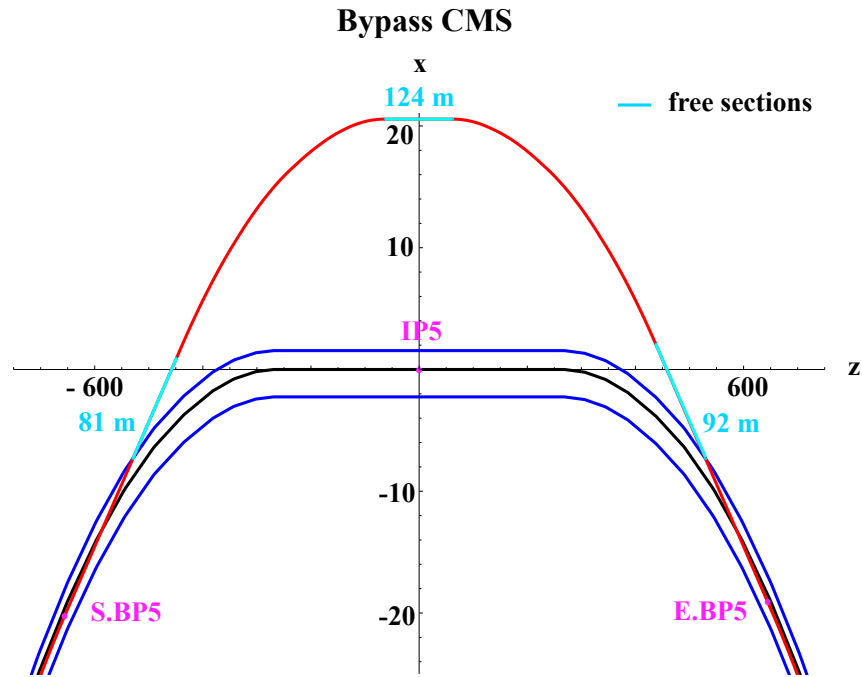


Figure 7.11: Horizontal outer bypass in Point 5. The LHC proton ring is shown in black, the electron ring in red and the tunnel walls in blue. Dispersion free sections reserved for the installation of RF, wiggler(s), injection and other equipment are marked in light blue. Beginning and end of the bypass are marked with S.BP5 and E.BP5

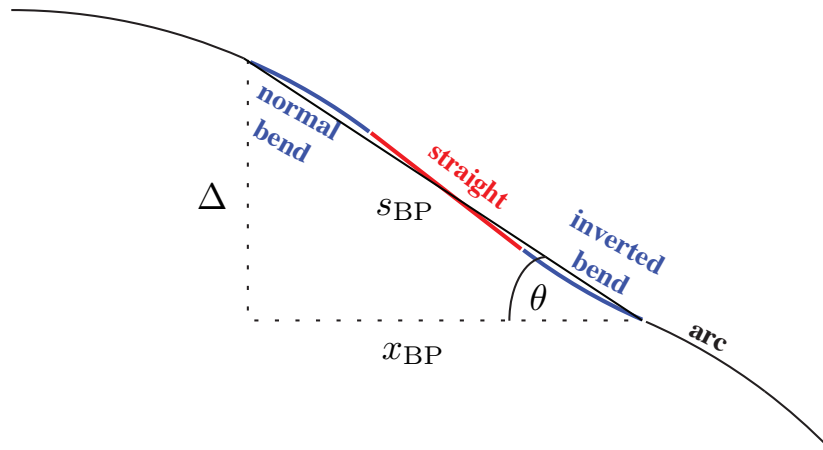


Figure 7.12: Outer bypass: a straight section is inserted to obtain the required separation. A larger separation could be achieved by inserting inverted bends.

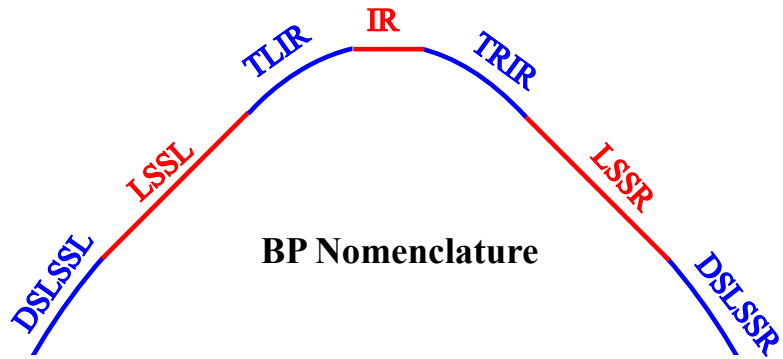


Figure 7.13: Bypass layout and nomenclature.

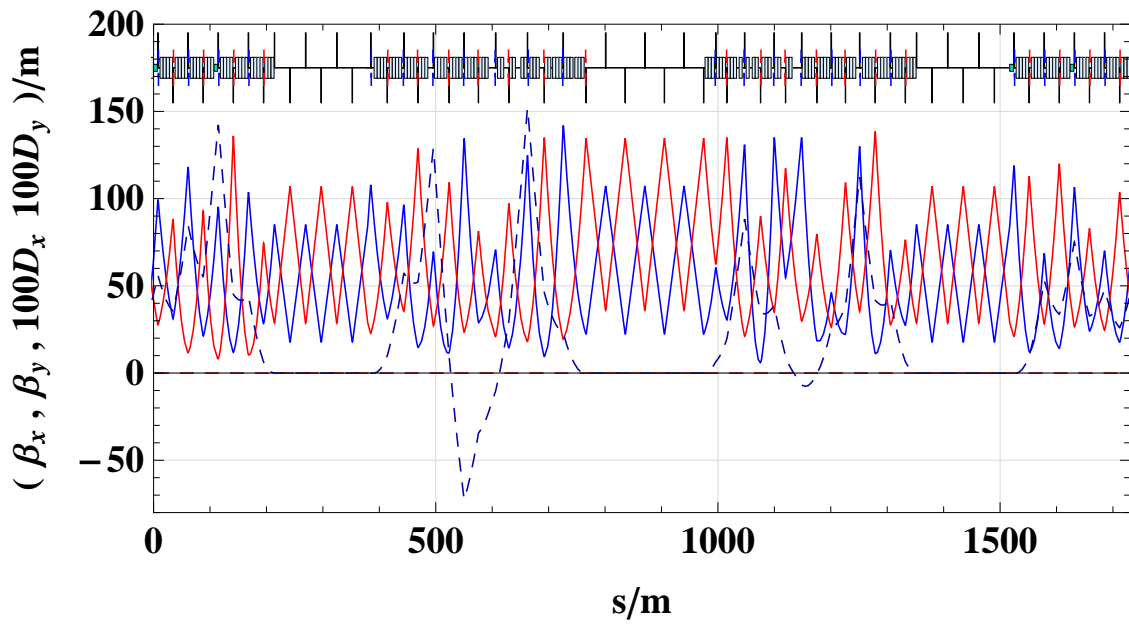


Figure 7.14: Bypass optics Point 1.

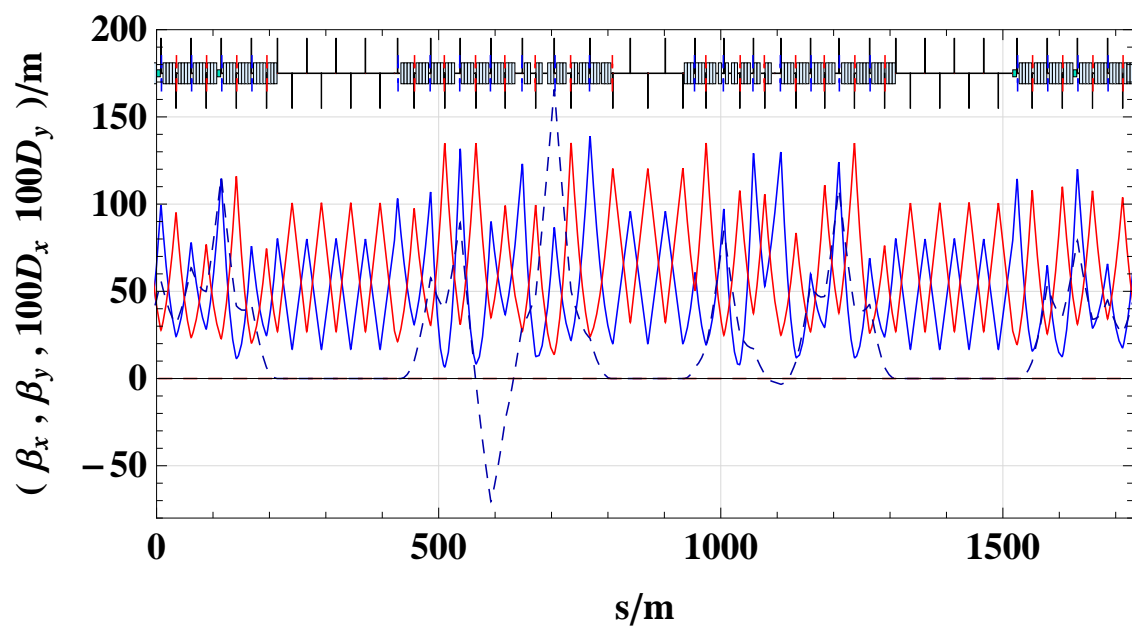


Figure 7.15: Bypass Optics Point 5.

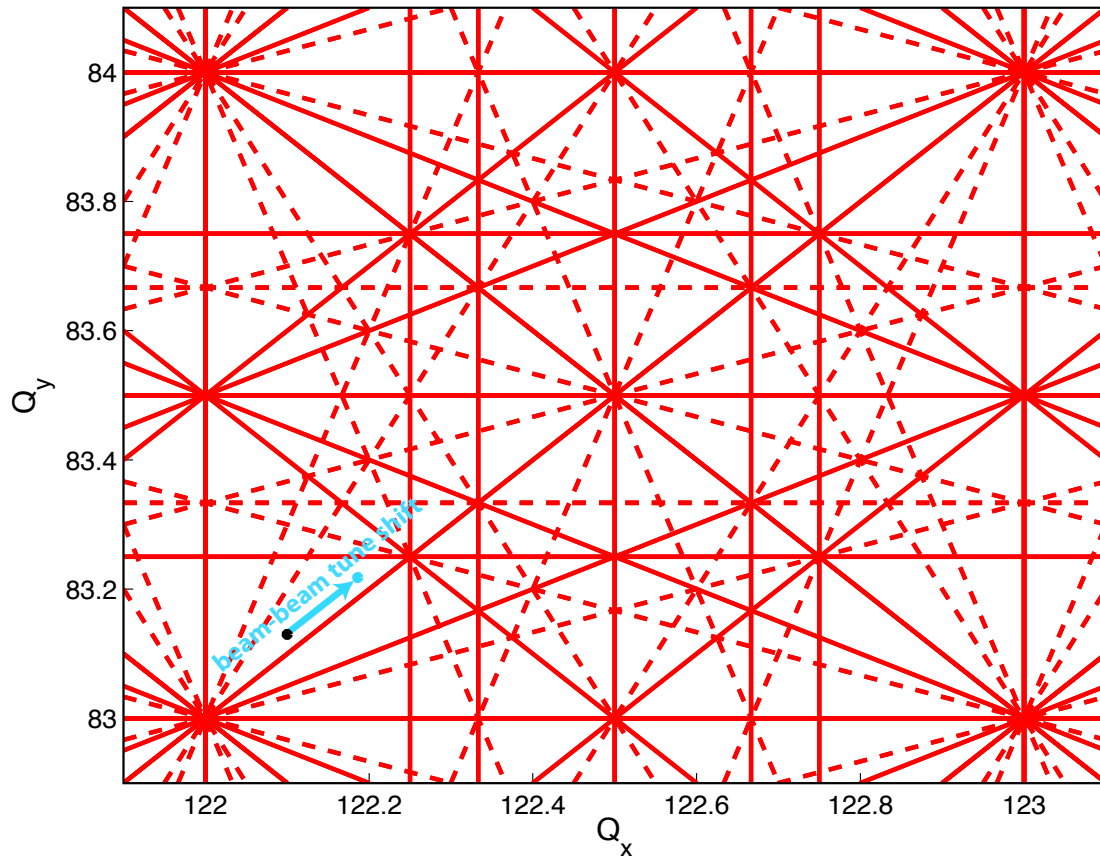


Figure 7.16: Working Point for the 1° optics. The dashed lines are the coupling resonances up to 4th order, the solid lines the constructive resonances up to 4th order. The black dot indicates the working point without beam-beam tune shift and the blue one with beam-beam tune shift.

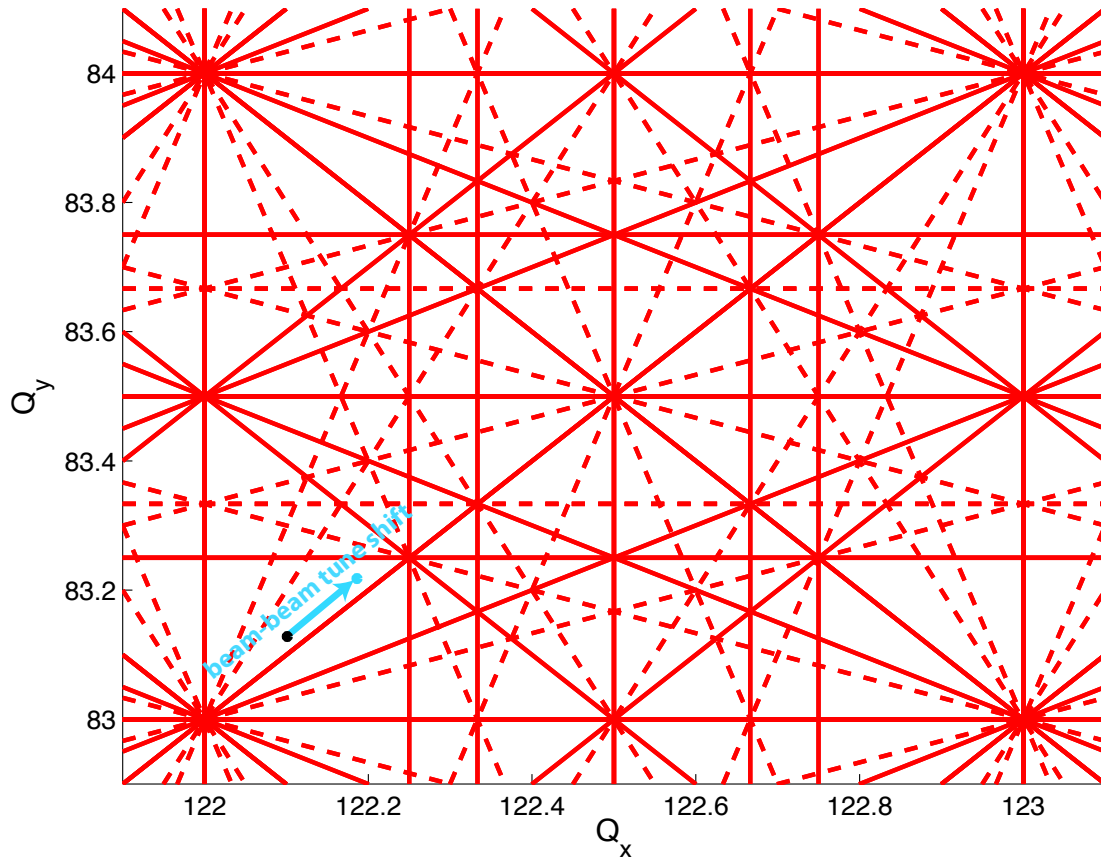


Figure 7.17: Working Point for the 10° optics. The dashed lines are the coupling resonances up to 4th order, the solid lines the constructive resonances up to 4th order. The black dot indicates the working point without beam-beam tune shift and the blue one with beam-beam tune shift.

7.4 Layout

The design of the Interaction Region (IR) of the LHeC is particularly challenging as it has to consider boundary conditions from

- The lattice design and beam optics of the electron and proton beam
- The geometry of the LHC experimental cavern and the tunnel
- The beam separation scheme which is determined by the bunch pattern of the LHC standard proton operation and related to this the optimisation of the synchrotron light emission and collimation
- The technical feasibility of the hardware.

Therefore the IR has to be optimised with respect to a well matched beam optics that adapts the optical parameters from the new electron-proton interaction point to the standard LHC proton beam optics in the arc and to the newly established beam optics of the electron ring. At the same time the two colliding beams as well as the non-colliding proton beam of LHC have to be separated efficiently and guided into their corresponding magnet lattices. As a general rule that has been established in the context of this study any modification in the standard LHC lattice and any impact on the LHC proton beam parameters had to be chosen moderately to avoid detrimental effects on the performance of the LHC proton-proton operation.

The layout and parameters of the new e/p interaction point are defined by the particle physics requirements. At present the physics programme that has been proposed for the LHeC [?] follows two themes - a high luminosity, high Q^2 programme requiring a forward and backward detector acceptance of around 10° and a low x, low Q^2 programme, which requires an increased detector acceptance in forward and backward direction of at least 1° and could proceed with reduced luminosity. Accordingly two machine scenarios have been studied for the interaction region design. Firstly, a design that has been optimised for high luminosity with an acceptance of 10° and secondly, a high acceptance design that allows for a smaller opening angle of the detector. In both cases the goal for the machine luminosity is in the range of $10^{33} \text{ cm}^{-2} \text{ s}^{-1}$ but the layouts differs in the magnet lattice, the achievable absolute luminosity and mainly the synchrotron radiation that is emitted during the beam separation process. Both options will be presented here in detail and the corresponding design luminosity, the technical requirements and the synchrotron radiation load will be compared. In both cases however, a well matched spot size of the electron and proton beam had to be established at the collision point: Experience in SPS and HERA [?] [?] showed that matched beam cross sections have to be established between the two colliding beams to guarantee stable beam conditions. Considering the different nature of the beams, namely the emittances of the electron beam in the two transverse planes, the interaction region design has to consider this boundary condition and the beam optics has to be established to achieve equal beam sizes $\sigma_x(p) = \sigma_x(e)$, $\sigma_y(p) = \sigma_y(e)$ at the IP.

The basic beam parameters however like energy, particle intensity and beam emittances are identical for both designs, determined by the electron and proton ring lattices and the pre-accelerators. They are summarised in Table ??.

Colliding two beams of different characteristics, the luminosity obtained is given by the equation

$$L = \sum_{i=1}^{n_b} (I_e * I_p) \frac{1}{e^2 f_0 2\pi \sqrt{\sigma_{xp}^2 + \sigma_{xe}^2} \sqrt{\sigma_{yp}^2 + \sigma_{ye}^2}}, \quad (7.8)$$

where $\sigma_{x,y}$ denotes the beam size of the electron and proton beam in the horizontal and vertical plane and I_e, I_p the electron and proton single bunch currents. In all IR layouts the electron beam size at the IP is matched to the proton beam size in order to optimise the delivered luminosity and minimise detrimental beam beam effects.

The main difference of the IR design for the electron proton collisions with respect to the existing LHC interaction regions is the fact that the two beams of LHeC cannot be focussed and / or guided at the same time: The different nature of the two beams, the fact that the electrons emit synchrotron radiation

Table 7.9: Main parameters for e/p collisions.

Quantity	unit	e	p
Beam energy	GeV	60	7000
Total beam current	mA	100	860
Number of bunches		2808	2808
Particles/bunch N_b	10^{10}	2.0	17
Horiz. emittance	nm	5.0	0.5
Vert. emittance	nm	2.5	0.5
Bunch distance	ns	25	

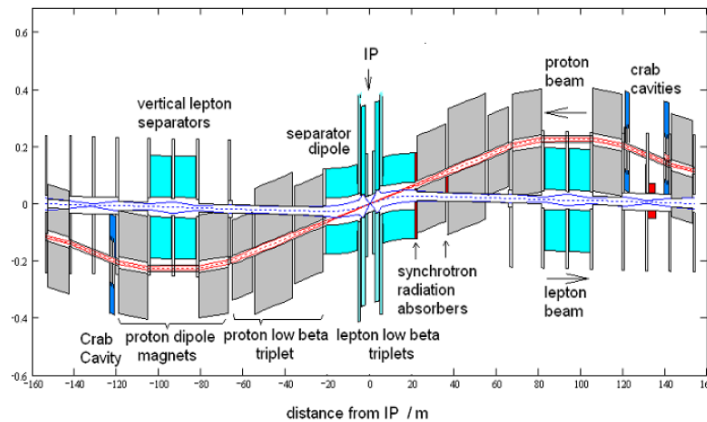


Figure 7.18: Schematic layout of the LHeC interaction region

4166 and mainly the large difference in the particle momentum make a simultaneous focusing of the two beams
 4167 impossible. The strong gradients of the proton quadrupoles in the LHC triplet structure cannot be tolerated
 4168 nor compensated for the electron lattice and a stable optical solution for the electrons is not achievable under
 4169 the influence of the proton magnet fields. The electron beam therefore has to be separated from the proton
 4170 beam after the collision point before any strong “7 TeV like” magnet field is applied.

4171 In order to obtain still a compact design and to optimize the achievable luminosity of the new e/p interaction
 4172 region, the beam separation scheme has to be combined with the electron mini-beta focusing structure.

4173 Figure ?? shows a schematic layout of the interaction region. It refers to the 10 degree option and shows
 4174 a compact triplet structure that is used for early focusing of the electron beam. The electron mini beta
 4175 quadrupoles are embedded into the detector opening angle and in order to obtain the required separation
 4176 effect they are shifted in the horizontal plane and act effectively as combined function magnets: Thus focusing
 4177 and separation of the electron beam are combined in a very compact lattice structure, which is the prerequisite
 4178 to achieve luminosity values in the range of $10^{33} \text{ cm}^{-2} \text{ s}^{-1}$.

4179 7.4.1 Beam Separation Scheme

4180 The separation scheme of the two beams has to be optimised with respect to an efficient (i.e. fast) beam
 4181 separation and a synchrotron radiation power and critical energy of the emitted photons that can be tolerated
 4182 by the absorber design. Two main issues have to be accomplished: a sufficient horizontal distance between
 4183 the beams has to be generated at the position of the first proton (half) quadrupole, located at a distance of s

Ring-ring option half-quadrupole, 4900 A, Gradient 137 T/m,
+ 2.5 T dipole field from feeddown

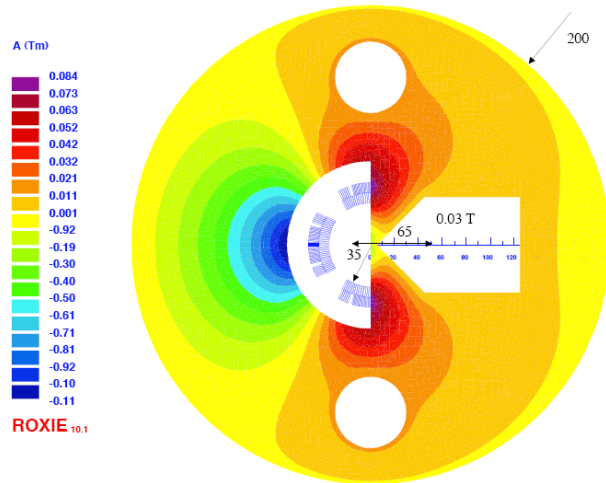


Figure 7.19: Super conducting half quadrupole in the proton lattice: The electron beam will pass on the right hand side of the mirror plate in a quasi field free region [?].

4184 = 22m from the interaction point (the nominal value of the LHC proton lattice). In addition to that, harmful
 4185 beam beam effects have to be avoided at the first parasitic bunch encounters which will take place at $s =$
 4186 3.75m, as the nominal bunch distance in LHC corresponds to $\Delta t = 25ns$. These so-called parasitic bunch
 4187 crossings have to be avoided as they would lead to intolerable beam-beam effects in the colliding beams. As
 4188 a consequence the separation scheme has to deliver a sufficiently large horizontal distance between the two
 4189 counter rotating bunches at these locations.

4190 To achieve the first requirement a separation effect is created inside the mini beta quadrupoles of the
 4191 electron beam: The large momentum difference of the two colliding beams provides a very elegant way to
 4192 separate the lepton and the hadron beams: Shifting the mini-beta quadrupoles of the electron beam and
 4193 installing a 15.8m long, but weak separator dipole magnet close to the IP provides the gentle separation that
 4194 is needed to keep the synchrotron radiation level in the IR within reasonable limits.
 4195 The nearest proton quadrupole to the IP is designed as a half-quadrupole to ease the extraction of the
 4196 outgoing electron beam. At this location (at $s=22m$) a minimum separation of $\Delta x = 55mm$ is needed to
 4197 guide the electron beam along the mirror plate of a sc. proton half quadrupole [?]. A first layout of this
 4198 magnet is sketched in figure ??

4199 The horizontal offsets of the mini beta lenses are chosen individually in such a way that the resulting
 4200 bending strength in the complete separation scheme (quadrupole triplet / doublet and separator dipole) is
 4201 constant. In this way a moderate separation strength is created with a constant bending radius of $\rho = 6757m$
 4202 for the 10 degree option. In the case of the 1 degree option the quadrupole lenses of the electron lattice
 4203 cannot be included inside the detector design as the opening angle of the detector does not provide enough
 4204 space for the hardware of the electron ring lattice. Therefore a much larger distance between the IP and the
 4205 location of the first electron lens had to be chosen ($\Delta s = 6.2m$ instead of $\Delta s = 1.2m$). As a consequence
 4206 - in order to achieve the same overall beam separation - stronger magnetic separation fields have to be
 4207 applied resulting in a bending radius of $\rho = 4057m$ in this case. In both cases the position of the electron
 4208 quadrupoles is following the design orbit of the electron beam to avoid local strong bending fields and keep
 4209 the synchrotron radiation power to a minimum. This technique has already been succesfully applied at the
 4210 layout of the HERA electron-proton collider [?].

4211
 4212 Still the separation at the location of the first proton magnet is small and a half quadrupole design for

Table 7.10: Parameters of the mini beta optics for the 1° and 10° options of the LHeC Interaction Region.

Detector Option Quantity	unit	1°		10°	
		electrons	protons	electrons	protons
Number of bunches		2808			
Particles/bunch N_b	10^{10}	1.96	17	1.96	17
Horiz. beta-function	m	0.4	4.0	0.18	1.8
Vert. beta-function	m	0.2	1.0	0.1	0.5
Horiz. emittance	nm	5.0	0.5	5.0	0.5
Vert. emittance	nm	2.5	0.5	2.5	0.5
Distance to IP	m	6.2	22	1.2	22
Crossing angle	mrad	1.0		1.0	
Synch. Rad. in IR	kW	51		33	
absolute Luminosity	$m^{-2} s^{-1}$	$8.54 * 10^{32}$		$1.8 * 10^{33}$	
Loss-Factor S		0.86		0.75	
effective Luminosity	$m^{-2} s^{-1}$	$7.33 * 10^{32}$		$1.34 * 10^{33}$	

4213 this super conducting magnet has been chosen at this point. The resulting beam parameters - including the
 4214 expected luminosity for this ring ring option - are summarised in Table 2.

4215 It has to be pointed out in this context that the arrangement of the off centre quadrupoles as well as
 4216 the strength of the separator dipole depend on the beam optics of the electron beam. The beam size at the
 4217 parasitic crossings and at the proton quadrupole will determine the required horizontal distance between the
 4218 electron and proton bunches. The strength and position of these magnets however will determine the optical
 4219 parameters, including the dispersion function that is created during the separation process itself. Therefore
 4220 a self-consistent layout concerning optics, beam separation and geometry of the synchrotron light absorbers
 4221 has to be found.

4222 It is obvious that these boundary conditions have to be fulfilled not only during luminosity operation of
 4223 the e/p rings. During injection and the complete acceleration procedure of the electron ring the influence
 4224 of the electron quadrupoles on the proton beam has to be compensated with respect to the proton beam
 4225 orbit (as a result of the separation fields) as well as to the proton beam optics: The changing deflecting
 4226 fields and gradients of the electron magnets will require correction procedures in the proton lattice that will
 4227 compensate this influence at any moment.

4228 7.4.2 Crossing Angle

4229 A central aspect of the LHeC IR design is the beam-beam interaction of the colliding electron and proton
 4230 bunches. The bunch structure of the electron beam will match the pattern of the LHC proton filling scheme
 4231 for maximal luminosity, giving equal bunch spacings of 25 ns to both beams. The IR design therefore
 4232 is required to separate the bunches as quickly as possible to avoid additional bunch interactions at these
 4233 positions and limit the beam-beam effect to the desired interactions at the IP. The design bunch distance
 4234 in the LHC proton bunch chain corresponds to $\Delta t = 25$ ns or $\Delta s = 7.5$ m. The counter rotating bunches
 4235 therefore meet after the crossing at the interaction point at additional, parasitic collision points in a distance
 4236 $s = 3.75$ m from the IP. To avoid detrimental effects from these parasitic crossings the above mentioned
 4237 separation scheme has to be supported by a crossing angle that will deliver a sufficiently large horizontal
 4238 distance between the bunches at the first parasitic bunch crossings. This technique is used in all LHC
 4239 interaction points. In the case of the LHeC however, the crossing angle is determined by the emittance of
 4240 the electron beam and the resulting beam size which is considerably larger than the usual proton beam size

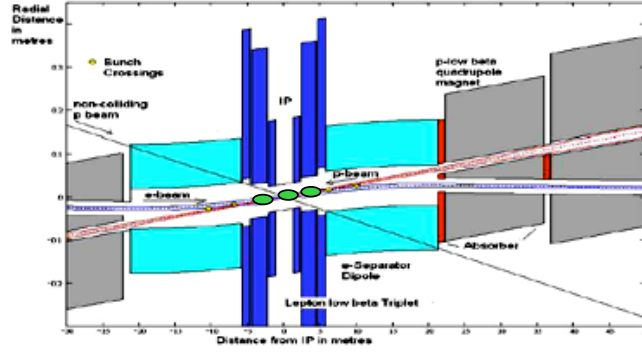


Figure 7.20: LHeC interaction region including the location of the first parasitic bunch encounters where a sufficient beam separation is achieved by a crossing angle of 1 mrad. The location of the parasitic encounters is indicated by green ovals.

4241 in the storage ring. In the case of the LHeC IR a crossing angle of $\theta = 1\text{mrad}$ is considered as sufficient
 4242 in the 1° as well as in the 10° option to avoid beam-beam effects from this parasitic crossings. Figure ??
 4243 shows the position of the first possible parasitic encounters and the effect of the crossing angle to deliver a
 4244 sufficient separation at these places.

4245 The detailed impact of one beam on another is evaluated by a dedicated beam-beam interaction study
 4246 which is included in this report, based on a minimum separation of $5\sigma_e + 5\sigma_p$ at every parasitic crossing node.
 4247 Due to the larger electron emittance the separation is mainly dominated by the electron beam parameters,
 4248 and as a general rule it can be stated that the rapid growth of the β -function in the drift around the IP,

$$\beta(s) = \beta^* + \frac{s^2}{\beta^*}, \quad (7.9)$$

4249 makes it harder to separate the beams if small β^* and a large drift space s is required in the optical design.

4250 In any design for the LHeC study, a crossing angle is used to establish an early beam separation, reduce
 4251 the required strength in the separation magnets and minimise the synchrotron radiation power that is created
 4252 inside the interaction region.

4253 As a draw back however the luminosity is reduced due to the fact that the bunches will not collide
 4254 anymore head on. This reduction is expressed in a geometric luminosity reduction factor “S”, that depends
 4255 on the crossing angle θ , the length of the electron and proton bunches σ_{ze} and σ_{zp} and the transverse beam
 4256 size in the plane of the bunch crossing σ_x^* :

$$S(\theta) = \left[1 + \left(\frac{\sigma_{sp}^2 + \sigma_{se}^2}{2\sigma_x^{*2}} \right) \tan^2 \frac{\theta}{2} \right]^{-\frac{1}{2}}. \quad (7.10)$$

4257

4258

4259 Accordingly, the effective luminosity that can be expected for a given IR layout is obtained by

$$L = S(\theta) * L_0 \quad (7.11)$$

4260

4261

4262 For the two beam optics that have been chosen for this design study (the 1° and the 10° option) and a
 4263 crossing angle of $\theta = 1\text{mrad}$ the loss factor amounts to $S = 74\%$ and $S = 85\%$ respectively.

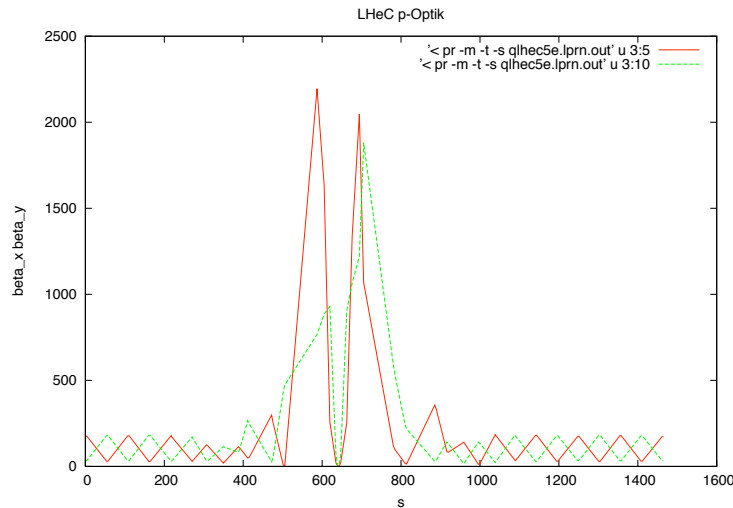


Figure 7.21: Proton optics for the LHeC interaction region. The gradients of the antisymmetric triplet lattice in the standard LHC have been modified to adopt for the requirements of the LHeC flat beam parameters.

4264 7.4.3 Beam Optics and Luminosity

4265 A special boundary condition had to be observed in the design of the proton beam optics of the LHeC:
 4266 For the layout of the four present proton-proton interaction regions in the LHC machine an anti-symmetric
 4267 option had been chosen: A solution that is appropriate for a round beam optics ($\sigma_x^* = \sigma_y^*$). An optimised
 4268 design for collisions with the flat e^\pm beams however requires unequal β -functions for the hadron beam at
 4269 the IP and the existing LHC optics can no longer be maintained. Therefore the optical layout of the existing
 4270 triplet structure in the LHC had to be modified to match the required beta functions ($\beta_x = 1.8\text{m}$, $\beta_y =$
 4271 0.5m) at the IP to the regular optics of the FODO structure in the arc (Figure ??).

4272 In the case of the electron beam optics, two different layouts of the interaction region are considered: One
 4273 optical concept for highest achievable luminosity and a solution for maximum detector acceptance. In the
 4274 first case an opening angle of 10° is available inside the detector geometry and allows to install an embedded
 4275 magnet structure where the first electron quadrupole lenses can be placed as close as $s = 1.2\text{m}$ from the IP.
 4276 This early focusing scheme leads to moderate values of the β function inside the mini beta quadrupoles and
 4277 therefore allows for a smaller spot size at the IP and larger luminosity values can be achieved. Still however
 4278 the quadrupoles require a compact design: While the gradients required by the optical solution are small
 4279 (for a super conducting magnet design) the outer radius of the first electron quadrupole has been limited to
 4280 $r_{max} = 210\text{mm}$.

4281 In the case of the 1° option the detector design is optimised for largest detector acceptance. Accordingly
 4282 the opening angle of the detector hardware is too small to deliver space for accelerator magnets. The mini
 4283 beta quadrupoles therefore have to be located outside the detector, and a distance $s = 6\text{m}$ from the IP had
 4284 to be chosen in this case. Even if the magnet dimensions are not limited by the detector design in this case,
 4285 the achievable luminosity is about a factor of two smaller than in the 10° case.

4286 The two beam optics that are based on these considerations are discussed in detail in the next chapter of
 4287 this report. In the case of the 10° option a triplet structure has been chosen to allow for moderate values of
 4288 the beta functions inside the mini beta quadrupoles. As a special feature of the optics that is shown in Figure
 4289 ?? the focusing effect of the first quadrupole magnet is moderate: Its gradient has been limited as it has to
 4290 deliver mainly the first beam separation. Table ?? includes as well the overall synchrotron radiation power

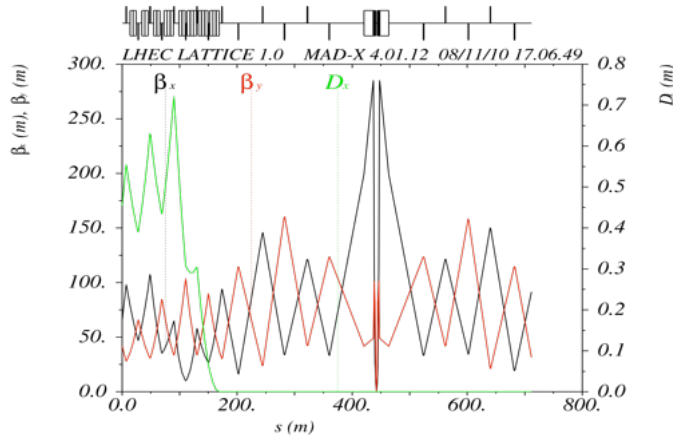


Figure 7.22: Electron optics for the LHeC interaction region. The plot corresponds to the 10 degree option where a triplet structure combined with a separation dipole has been chosen to separate the two beams.

4291 that is produced inside the IR. Due to the larger bending radius (i.e. smaller bending forces) in the case of
 4292 the 10° option the produced synchrotron radiation power is limited to about 30 kW, while the alternative -
 4293 high acceptance - option has to handle 50kW of synchrotron light.

4294 The details of the synchrotron light characteristics are covered in the next chapters of this report for both
 4295 cases, including the critical energies and the design of the required absorbers.

4296 For the 1° option the mini beta focusing is based on a quadrupole doublet as the space limitations in
 4297 the transverse plane are much more relaxed compared to the alternative option and the main issue here
 4298 was to find a compact design in the longitudinal coordinate: Due to the larger distance of the focusing
 4299 and separating magnets from the IP the magnet structure has to be more compact and the separating
 4300 field stronger to obtain the required horizontal beam distance at the location $s=22\text{m}$ of the first proton
 4301 quadrupole. The corresponding beam optics for both options are explained in full detail below.

4302 in the 1991 Luminosity Runs of

4303 7.5 Design Requirements of the Electron Beam Optics

4304 7.5.1 Optics Matching and IR Geometry

4305 Once the beams are separated into independent beam pipes, the electron beam must be transported into
 4306 the ring lattice. Quadrupoles are used in the electron machine LSS to transport the beam from the IP to
 4307 the dispersion suppressor and match twiss parameters at either end. This matching must be smooth and
 4308 not require infeasible apertures. In addition the first electron quadrupoles will be located inside the detector
 4309 hardware and therefore a compact design is required within the limited space available.

4310
 4311 The complete design of the long straight section "LSS", that includes the mini beta insertion, the matching
 4312 section and the dispersion suppressor must be designed around a number of further constraints. As well as
 4313 beam separation, the electron beam must be steered from the electron ring into the IR and back out again.
 4314 The colliding proton beam must be largely undisturbed by the electron beam. The non-colliding proton
 4315 beam must be guided through the IR without interacting with either of the other beams.

4316 7.6 High Luminosity IR Layout

4317 7.6.1 Parameters

4318 Table ?? details the interaction point parameters and other parameters for this design. To optimise for
 4319 luminosity, a small l^* is desired. An acceptance angle of 10° is therefore chosen, which gives an l^* of 1.2m
 4320 for final focusing quadrupoles of reasonable size.

$L(0)$	1.8×10^{33}
θ	1×10^{-3}
$S(\theta)$	0.746
$L(\theta)$	1.34×10^{33}
β_{x^*}	0.18 m
β_{y^*}	0.1 m
σ_{x^*}	3.00×10^{-5} m
σ_{y^*}	1.58×10^{-5} m
SR Power	33 kW
E_c	126 keV

Table 7.11: Parameters for the High Luminosity IR.

4321 SR calculations are detailed in section [??]. The total power emitted in the IR is similar to that in the
 4322 HERA-2 IR [reference] and as such appears to be reasonable, given enough space for absorbers.

4323 7.6.2 Layout

4324 Due to the relatively round beam spot aspect ratio of 1.8:1, a final quadrupole triplet layout has been chosen
 4325 for this design. The relatively weak horizontal focussing quadrupole used as first magnet lens is mainly
 4326 needed for beam separation, followed by two strong, nearly doublet like quadrupoles. The focusing strength
 4327 Figure ?? and table ?? detail the layout.

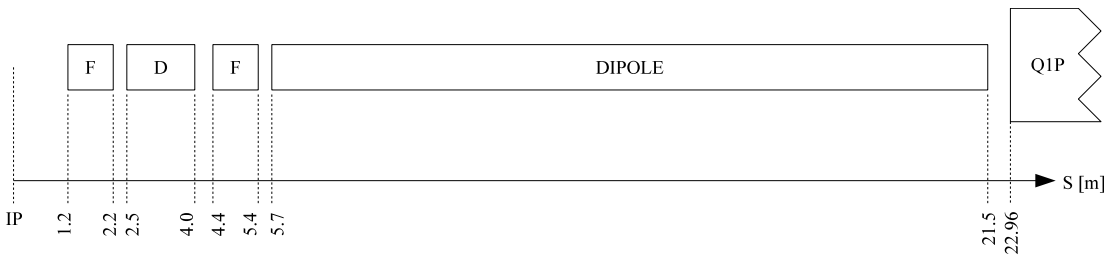


Figure 7.23: Layout of machine elements in the High Luminosity IR. Note that the left side of the IR is symmetric.

4329 The l^* of 1.2 m allows both strong focusing of the beam, and constant bending of the beam from 1.2 m to
 4330 21.5 m. This is achieved with offset quadrupoles and a separation dipole.

4331

4332 Figure ?? shows the β functions of the beam in both planes from the IP to the face of the final proton
 4333 quadrupole at $s = 23$ m.

Element	S_{entry} [m]	L [m]	Gradient [T/m]	Dipole Field [T]	Offset [m]
BS.L	-21.5	15.8	-	-0.0296	-
Q3E.L	-5.4	1.0	89.09228878	-0.0296	-3.32240×10^{-4}
Q2E.L	-4	1.5	-102.2013150	-0.0296	2.89624×10^{-4}
Q1E.L	-2.2	1.0	54.34070578	-0.0296	-5.44711×10^{-4}
IP	0.0	-	-	-	-
Q1E.R	1.2	1.0	54.34070578	0.0296	5.44711×10^{-4}
Q2E.R	2.5	1.5	-102.2013150	0.0296	-2.89624×10^{-4}
Q3E.R	4.4	1.0	89.09228878	0.0296	3.32240×10^{-4}
BS.R	5.7	15.8	-	-0.0296	-

Table 7.12: Machine elements for the High Luminosity IR. S_{entry} gives the leftmost point of the idealised magnetic field of an element. Note that S is relative to the IP.

7.6.3 Separation Scheme

As described above a quadrupole triplet configuration is used for the first focusing of the electron beam. This has the effect of generating a larger peak in β_x , between parasitic crossings but leads to smaller horizontal beam sizes at these locations and therefore reduces the necessary beam separation. The first F quadrupole reduces β_x at $s = 3.75$ m compared to an initial D quadrupole. The third F quadrupole then brings β_x down from the peak sufficiently to avoid large beam-beam interactions at the second parasitic crossing, $s = 7.5$ m.

This is provided by the bending effect of the offset quadrupoles, and also the IP crossing angle of 1 mrad. These elements ensure that the separation between the beams, normalised to beam size, increases at each parasitic crossing. Note that 1 mrad is not a minimum crossing angle required by beam-beam interaction separation criteria; it is however a chosen balance between luminosity loss and minimising bend strength. In theory, this layout could support an IP with no crossing angle; however the bend strength required to achieve this would generate an undesirable level of SR power.

7.6.4 Optics Matching and IR Geometry

The IR is matched into the ring arc lattice by means of matching quads in the LSS. The quads are roughly evenly placed, with sufficient space left after the IR section to accommodate the proton optics and the remaining electron ring geometry, which has yet to be designed fully. The solution is nearly symmetric about the IP; however due to the geometry of the LHC lattice, the electron ring itself is not exactly symmetric. As such the solution differs slightly on either side of the LSS. Table ?? details the layout of machine elements in the LSS. Five matching quadrupoles are used on either side of the IP. A sixth quadrupole is used on the left side, next to the dispersion suppressor. Due to the asymmetric design of the dispersion suppressors, a quadrupole (MQDSF.L2) is included at the same distance from the IP on the right side as part of the dispersion suppressor. MQDSF.L2 is required to match the optics, but is more constrained than the other matching quadrupoles. Figure ?? shows the β functions of the matching from the IP to the dispersion suppressor, on both sides of the IP (Figure ??)

A smooth matching is obtained, where the maximum beta functions are well controlled and continuously reduced to the values of the arc structure. The beam envelopes in the LSS are of reasonable size and do not require excessive aperture.

Note that this solution is not yet matched for dispersion as the rest of the ring geometry in the LSS and IR areas is yet to be designed.

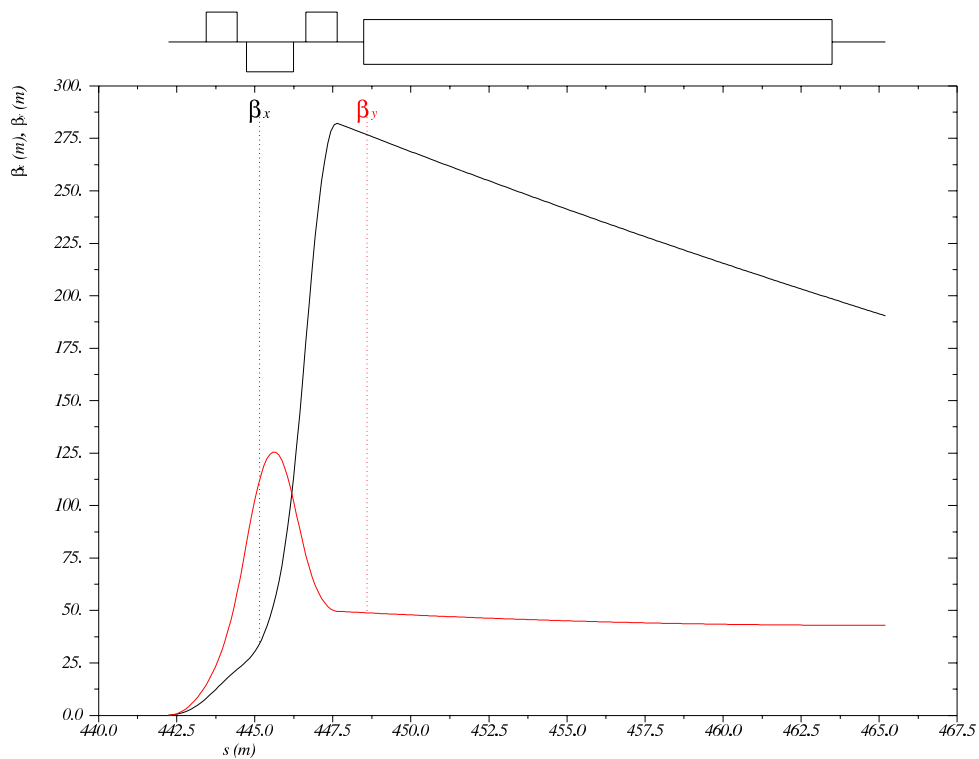


Figure 7.24: β functions in both planes for the High Luminosity IR layout, from the IP to the face of the final proton quadrupole at $s = 23$ m. Note that s is relative to the ring, which begins at the left side of the left dispersion suppressor of IP2.

4366 Plans for the remaining IR geometry include a second horizontal dipole, and quadrupoles, on either side to
 4367 turn each separation dipole into a dispersion-free S-shaped bend. This will be used to extract the beam into
 4368 the electron machine.

4369 7.7 High Acceptance IR Layout

4370 7.7.1 Parameters

4371 Table ?? details the design parameters for this option. The chosen detector opening angle for this layout
 4372 is 1° . All elements, especially the mini beta quadrupoles of the electron ring, therefore have to be placed
 4373 outside the limits of the detector, at $z = \pm 6.2$ m, where z is the longitudinal axis of the detector. As such,
 4374 the actual acceptance of the layout is limited by the beam pipe rather than the size of machine elements.
 4375 This also gives further flexibility in the strengths and designs of the final focusing quadrupoles, although
 4376 this flexibility is not exploited in the design.

4377
 4378 SR calculations are discussed in detail in section [??]. The total power emitted in the IR is similar to that in

Element	S_{entry} [m]	L [m]	Gradient [T/m]
MQDSF.L2	-268.8944	1.0	9.611358758
MQDM5.L2	-240.5	1.0	-7.435432612
MQFM4.L2	-198.5	1.0	7.148957108
MQDM3.L2	-160.5	1.0	-6.493088294
MQFM2.L2	-120.5	1.0	6.057685328
MQDM1.L2	-82.5	1.0	-4.962254798
MQDM1.R2	81.5	1.0	-4.977379112
MQFM2.R2	119.5	1.0	6.030944724
MQDM3.R2	159.5	1.0	-6.63145508
MQFM4.R2	197.5	1.0	6.884472924
MQDM5.R2	239.5	1.0	-7.439587356

Table 7.13: Machine elements for the High Luminosity LSS layout. S_{entry} gives the leftmost point of the idealised magnetic field of an element. Note that S is relative to the IP.

$L(0)$	8.54×10^{32}
θ	1×10^{-3}
$S(\theta)$	0.858
$L(\theta)$	7.33×10^{32}
β_x^*	0.4 m
β_y^*	0.2 m
σ_x^*	4.47×10^{-5} m
σ_y^*	2.24×10^{-5} m
SR Power	51 kW
E_c	163 keV

Table 7.14: Parameters for the High Acceptance IR.

4379 the HERA-2 IR [reference] and as such appears to be reasonable, given enough space for absorbers. However
4380 it is significantly higher than that in the high luminosity layout. As discussed in section [??], an option
4381 exists to reduce the total SR power by including a dipole field in the detector, thus mitigating the limitation
4382 imposed on dipole length by the larger l^* .

4383 7.7.2 Layout and separation scheme

4384 A symmetric final quadrupole doublet layout has been chosen for this design. The beam spot aspect ratio
4385 of 2:1 is marginally flatter than the High Luminosity layout, and as such a triplet is less suitable. Figure ??
4386 and table ?? detail the layout.

4387
4388 The l^* of 6.2m imposes limitations on focusing and bending in this layout. Focusing is limited by quadratic
4389 β growth through a drift space, which is increased for smaller β^* . As such, lower instantaneous luminosity
4390 is attainable.

4391
4392 As in the high luminosity option the beam separation will be achieved by a combination of a adequate
4393 crossing angle and the separation fields of off-centre quadrupole magnets. However, due to the large free

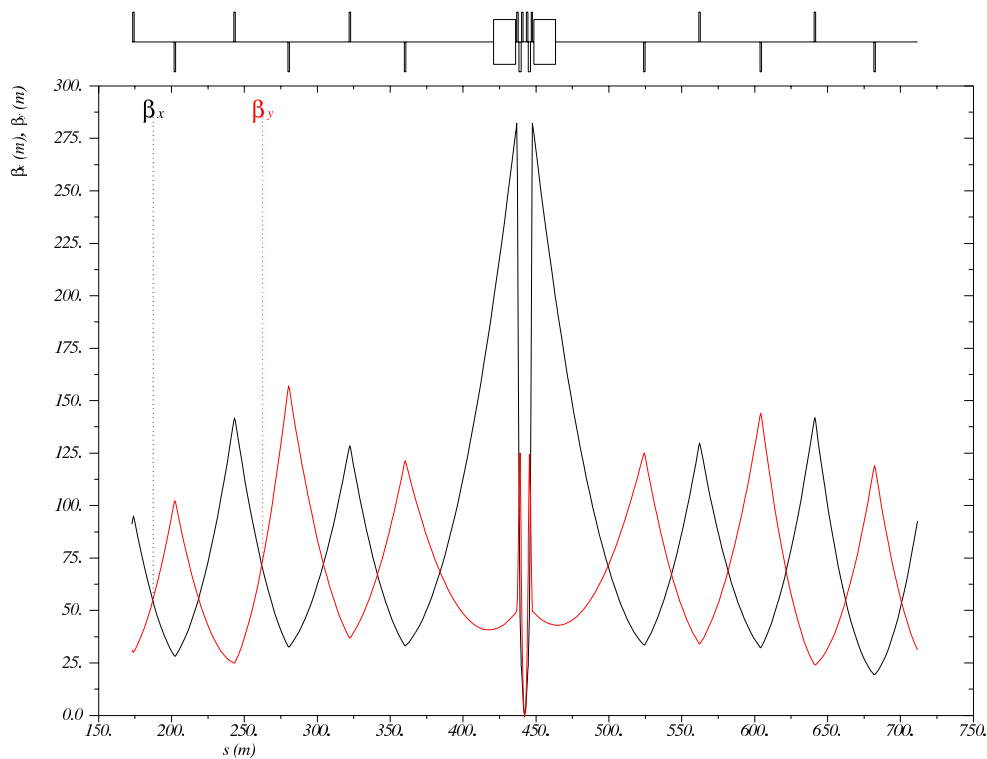


Figure 7.25: β functions in both planes for the High Luminosity IR layout, from the end of the left dispersion suppressor to the start of the right dispersion suppressor. Note that s is relative to the ring, which begins at the left side of the left dispersion suppressor of IP2.

Element	S_{entry} [m]	L [m]	Gradient [T/m]	Dipole Field [T]	Offset [m]
BS.L	-21.5	12.7	-	-0.0493	-
Q2E.L	-8.5	1.0	-77.31019000	-0.0493	6.37691×10^{-4}
Q1E.L	-7.2	1.0	90.40354154	-0.0493	-5.45333×10^{-4}
IP	0.0	-	-	-	-
Q1E.R	6.2	1.0	90.40354154	0.0493	5.45333×10^{-4}
Q2E.R	7.5	1.0	-77.31019000	0.0493	-6.37691×10^{-4}
BS.R	8.8	12.7	-	0.0493	-

Table 7.15: Machine elements for the High Acceptance IR. S_{entry} gives the leftmost point of the idealised magnetic field of an element. Note that S is relative to the IP.

4394 space of $z=6\text{m}$ to the IP, stronger fields have to be applied to obtain the same geometric separation at the
 4395 first proton quadrupole.

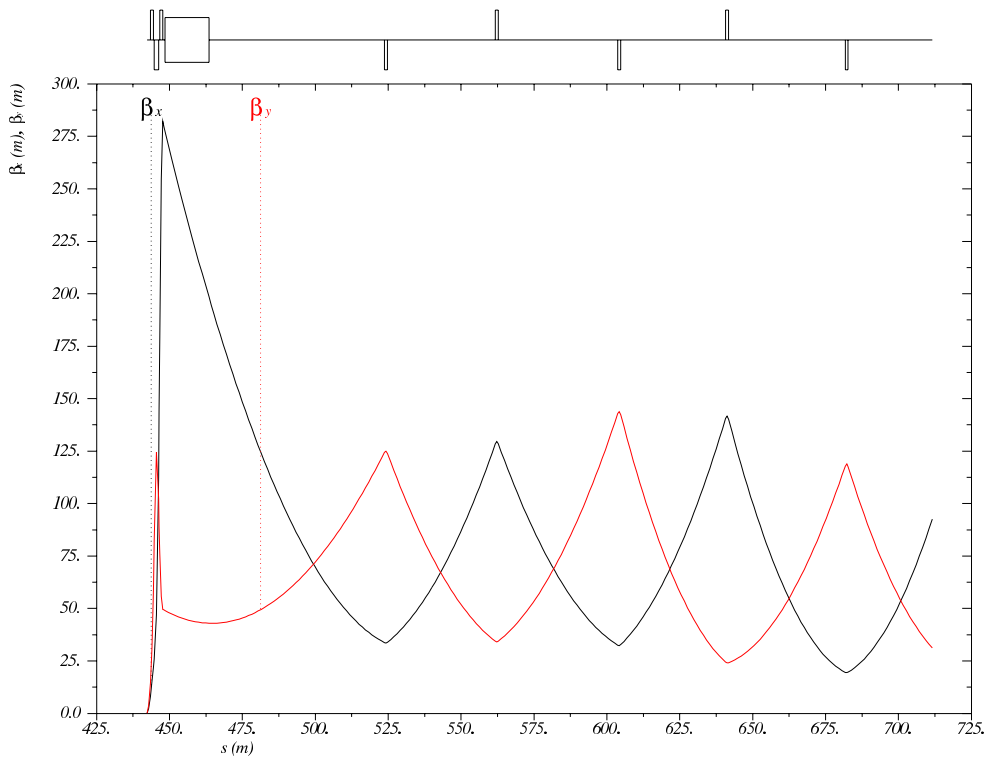


Figure 7.26: β functions in both planes for the High Luminosity IR layout, from the IP to the start of the right dispersion suppressor. Note that s is relative to the ring, which begins at the left side of the left dispersion suppressor of IP2.

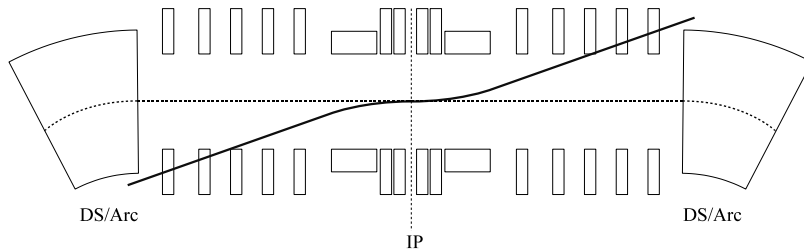


Figure 7.27: Graphical representation of misaligned LSS/IR geometry. With beam steering in the IR and no compensation in the LSS, the electron beam no longer lines up with the ring lattice reference orbit. Diagram is not to scale and does not represent the correct optical layout of the IR nor the LSS.

4396 Figure ?? shows the β functions of the beam in both planes from the IP to the face of the final proton
 4397 quadrupole at $s = 23$ m.

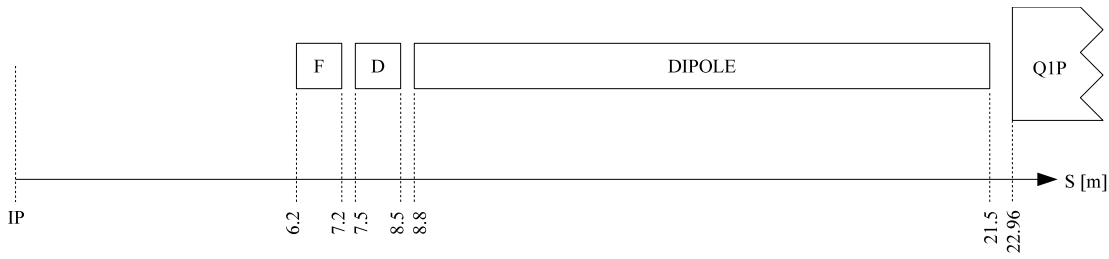


Figure 7.28: Layout of machine elements in the High Acceptance IR. Note that the left side of the IR is symmetric.

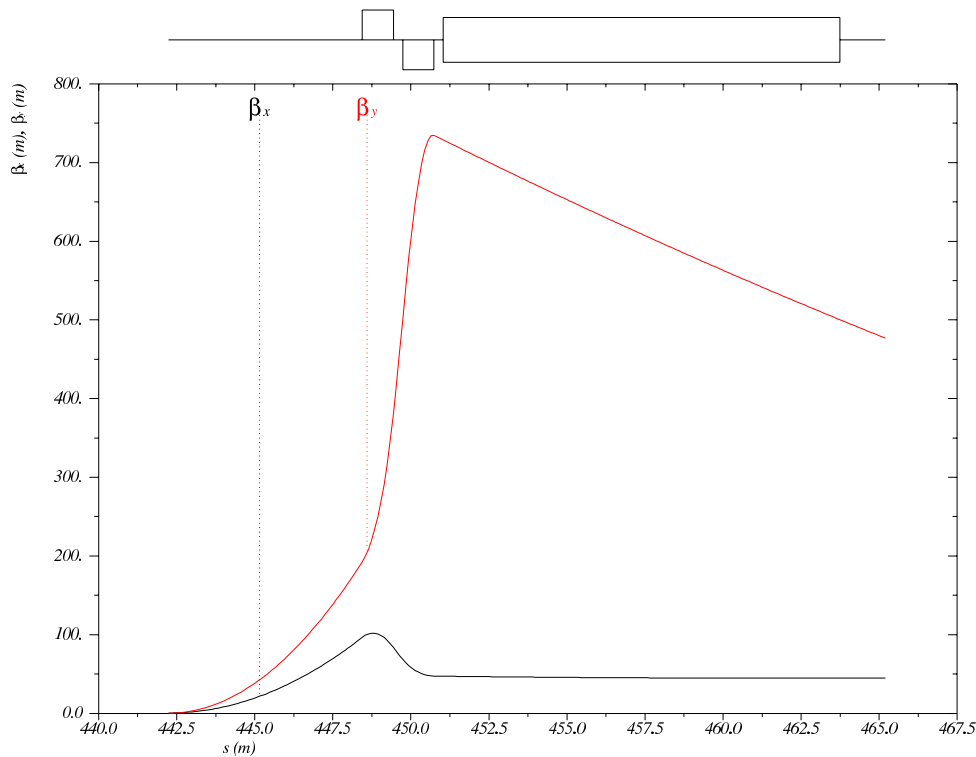


Figure 7.29: β functions in both planes for the High Acceptance IR layout, from the IP to the face of the final proton quadrupole at $s = 23$ m. Note that s is relative to the ring, which begins at the left side of the left dispersion suppressor of IP2.

4398 7.7.3 Optics Matching and IR Geometry

4399 The lattice that is used to match the IR optics to the periodic arc structure corresponds to a large extent
 4400 to the one presented for the high luminosity option. Figure ?? shows the β functions of the matching from

Element	S_{entry} [m]	L [m]	Gradient [T/m]
MQDSF.L2	-268.8944	1.0	9.643324144
MQFM6.L2	-237.5	1.0	-7.513288936
MQDM5.L2	-205.5	1.0	7.74537173
MQFM4.L2	-174.5	1.0	-6.18152704
MQDM3.L2	-143.5	1.0	6.475404012
MQFM2.L2	-111.5	1.0	-9.254556824
MQDM1.L2	-80.5	1.0	5.843405232
MQDM1.R2	79.5	1.0	5.843405232
MQFM2.R2	110.5	1.0	-9.254556824
MQDM3.R2	142.5	1.0	6.475404012
MQFM4.R2	173.5	1.0	-6.048380018
MQDM5.R2	204.5	1.0	7.360488416
MQFM6.R2	236.5	1.0	-7.225547436

Table 7.16: Machine elements for the High Acceptance LSS layout. S_{entry} gives the leftmost point of the idealised magnetic field of an element. Note that S is relative to the IP.

4401 the IP to the dispersion suppressor, on both sides of the IP (Figure ??).

4402

4403 As with the High Luminosity layout, a smooth matching is obtained, with the IR β peaks being brought
4404 down and controlled before being matched into the arc solution. The beam envelopes in the LSS are of
4405 reasonable size and do not require excessive aperture.

4406

4407 Other geometric issues must again be addressed, which are briefly discussed in section ??.

4408 7.7.4 Comparison of Layouts

4409 Table ?? shows a direct comparison of various parameters of the two layouts.

4410

Parameter	HL	HA
$L(0)$	1.8×10^{33}	8.54×10^{32}
θ	1×10^{-3}	1×10^{-3}
$S(\theta)$	0.746	0.858
$L(\theta)$	1.34×10^{33}	7.33×10^{32}
β_x^*	0.18 m	0.4 m
β_y^*	0.1 m	0.2 m
σ_x^*	3.00×10^{-5} m	4.47×10^{-5} m
σ_y^*	1.58×10^{-5} m	2.24×10^{-5} m
SR Power	33 kW	51 kW
E_c	126 keV	163 keV

Table 7.17: Parameters for the High Luminosity IR.

4411 The difference in luminosity after considering the loss factor S due to the crossing angle, is a factor of

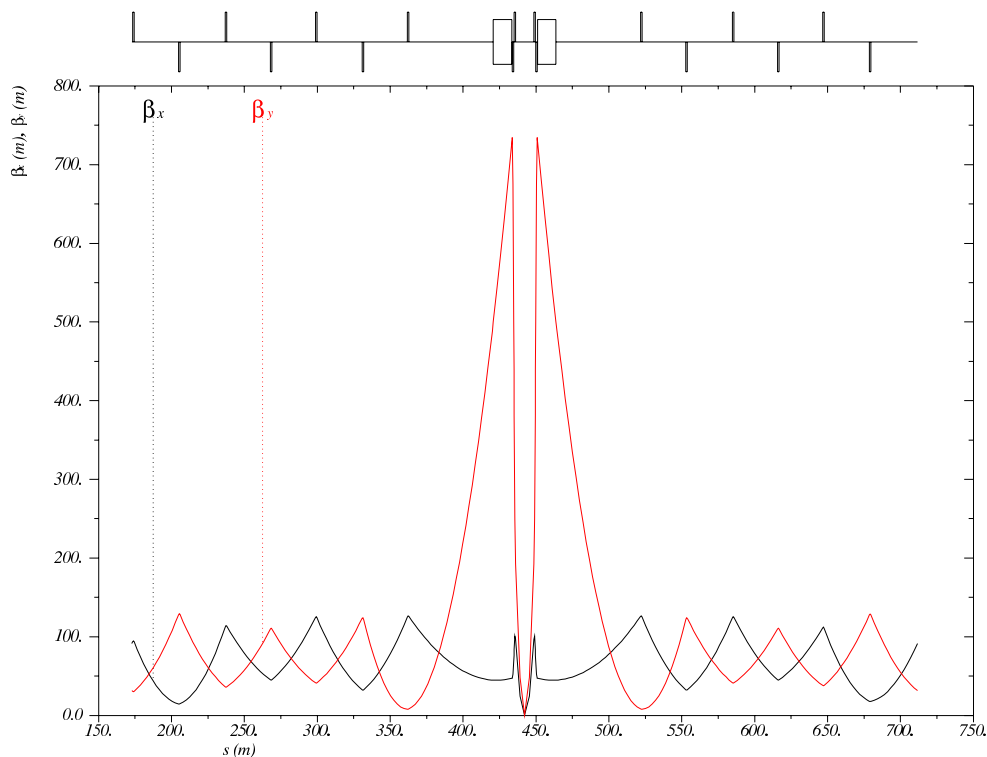


Figure 7.30: β functions in both planes for the High Acceptance IR layout, from the end of the left dispersion suppressor to the start of the right dispersion suppressor. Note that s is relative to the ring, which begins at the left side of the left dispersion suppressor of IP2.

4412 1.8. However it should be noted that this design strives for technical feasibility and both layouts could be
 4413 squeezed further to decrease β^* in both planes. The High Luminosity layout could likely be squeezed further
 4414 than the High Acceptance layout due to the large difference in l^* , as shown in figure ?? which compares the
 4415 two IR layouts. At this stage both designs deliver their required IP parameters of luminosity and acceptance
 4416 and appear to be feasible.

4417
 4418 The High Acceptance design generates a higher level of SR power. This still appears to be within rea-
 4419 sonable limits and is discussed in section [??]. Furthermore, an option is discussed to install a dipole magnet
 4420 in the detector. This early separation would reduce the required strength of the dipole fields in the IR,
 4421 significantly reducing total SR power.

4422 **Synchrotron radiation and absorbers**

4423 The synchrotron radiation (SR) in the interaction region has been analyzed in three ways. The SR was
 4424 simulated in depth using a program made with the Geant4 (G4) toolkit. In addition a cross check of the
 4425 total power and average critical energy was done in IRSYN, a Monte Carlo simulation package written by

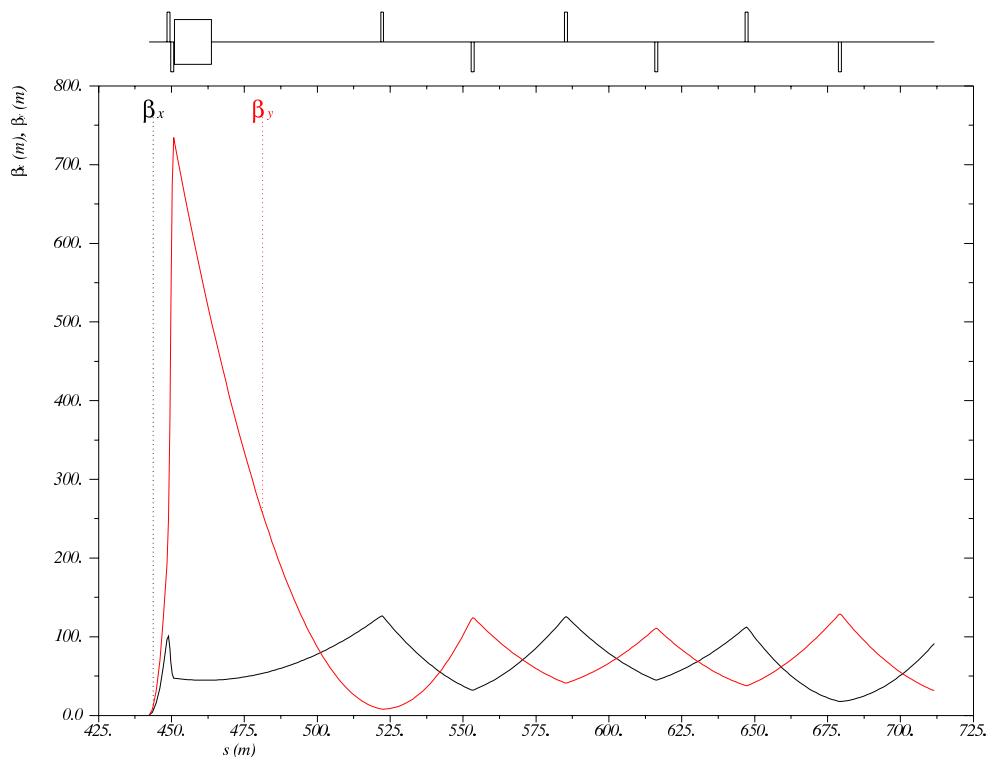


Figure 7.31: β functions in both planes for the High Luminosity IR layout, from the IP to the start of the right dispersion suppressor. Note that s is relative to the ring, which begins at the left side of the left dispersion suppressor of IP2.

4426 R. Appleby. [?] A final cross check has been made for the radiated power per element using an analytic
 4427 method. These other methods confirmed the results seen using G4. The G4 program uses Monte Carlo
 4428 methods to create gaussian spatial and angular distributions for the electron beam. The electron beam is
 4429 then guided through vacuum volumes that contain the magnetic fields for the separator dipoles and electron
 4430 final focusing quadrupoles.

4431 The SR is generated in these volumes using the appropriate G4 process classes. The G4 SR class was
 4432 written for a uniform magnetic field, and therefore the quadrupole volumes were divided such that the
 4433 field remained approximately constant in each volume. This created agreement between upstream and
 4434 downstream quadrupoles since for a downstream quadrupole the beta function at the entrance and exit are
 4435 reversed from its upstream counterpart. This agreement confirms that the field was approximately constant
 4436 in each volume.

4437 The position, direction, and energy of each photon created is written as ntuples at user defined Z values.
 4438 These ntuples are then used to analyze the SR fan as it evolves in Z. The analysis was done primarily
 4439 through the use of MATLAB scripts. It was necessary to make two versions of this program. One for the
 4440 high luminosity design and one for the high detector acceptance design.

4441 Before going further I will explain some conventions used for this section. I will refer to the electron

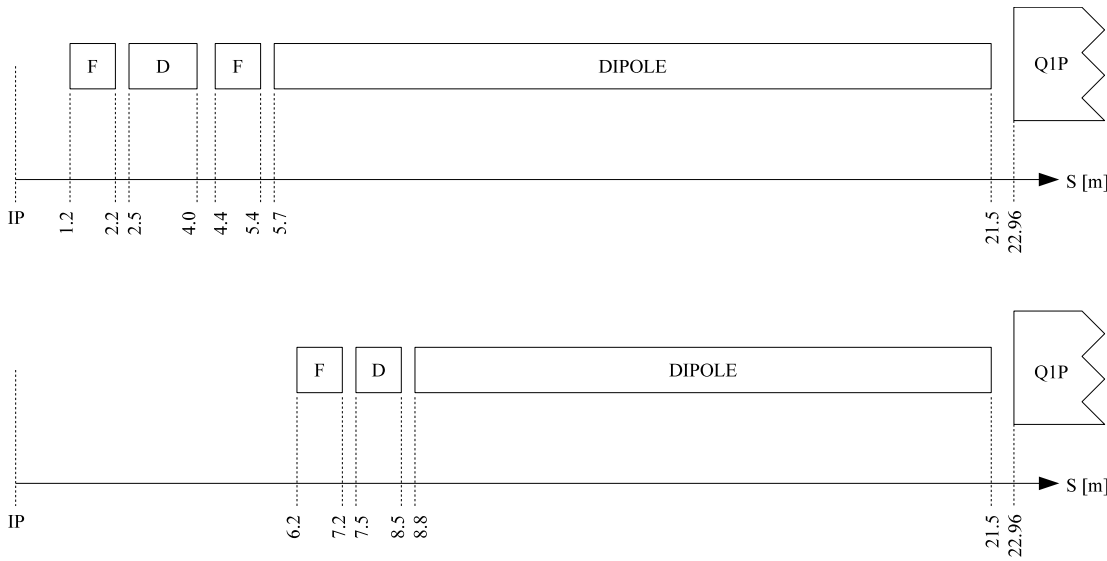


Figure 7.32: Scale comparison of the layouts for the High Luminosity and High Acceptance designs. Note the large difference in l^* .

4442 beam as *the beam* and the proton beams will be referred to as either the interacting or non interacting
 4443 proton beams. The beam propagates in the $-Z$ direction and the interacting proton beam propagates in the
 4444 $+Z$ direction, I will use a right handed coordinate system where the X axis is horizontal and the Y axis is
 4445 vertical. The beam centroid always remains in the $Y = 0$ plane. The *angle of the beam* will be used to refer
 4446 to the angle between the beam centroid's velocity vector and the Z axis, in the $Y = 0$ plane. This angle is
 4447 set such that the beam propagates in the $-X$ direction as it traverses Z.

4448 The SR fans extension in the horizontal direction is driven by the angle of the beam at the entrance
 4449 of the upstream separator dipole. Because the direction of emitted photons is parallel to the direction of
 4450 the electron that emitted it, the angle of the beam and the distance to the absorber are both greatest at
 4451 the entrance of the upstream separator dipole and therefore this defines one of the edges of the synchrotron
 4452 fan on the absorber. The other edge is defined by the crossing angle and the distance from the IP to the
 4453 absorber. The S shaped trajectory of the beam means that the smallest angle of the beam will be reached
 4454 at the IP. Therefore the photons emitted at this point will have the lowest angle and for this given angle the
 4455 smallest distance to the absorber. This defines the other edge of the fan in the horizontal direction.

4456 The SR fans extension in the vertical direction is driven by the beta function and angular spread of the
 4457 beam. The beta function along with the emittance defines the r.m.s. spot size of the beam. The vertical
 4458 spot size defines the Y position at which photons are emitted. On top of this the vertical angular spread
 4459 defines the angle between the velocity vector of these photons and the Z axis. Both of these values produce
 4460 complicated effects as they are functions of Z. These effects also affect the horizontal extension of the fan
 4461 however are of second order when compared to the angle of the beam. Since the beam moves in the $Y = 0$
 4462 plane these effects dominate the vertical extension of the beam.

4463 The number density distribution of the fan is a complicated issue. The number density at the absorber
 4464 is highest between the interacting beams. The reason for this is that although the separator dipoles create
 4465 significantly more photons the number of photons generated per unit length in Z is much lower for the dipoles
 4466 as opposed to the quadrupoles due to the high fields experienced in the quadrupoles. The position of the
 4467 quadrupole magnets then causes the light radiated from them to hit the absorber in the area between the
 4468 two interacting beams.

4469 **High Luminosity**

4470 **Parameters:** The parameters for the high luminosity option are listed in Table ?? . The separation refers
 4471 to the displacement between the two interacting beams at the face of the proton triplet.

Characteristic	Value
Electron Energy [GeV]	60
Electron Current [mA]	100
Crossing Angle [mrad]	1
Absorber Position [m]	-21.5
Dipole Field [T]	0.0296
Separation [mm]	55
γ/s	5.39×10^{18}

Table 7.18: High Luminosity: Parameters

4472 The energy, current, and crossing angle (θ_c) are common values used in all RR calculations. The dipole
 4473 field value refers to the constant dipole field created throughout all dipole elements in the IR. The direction
 4474 of this field is opposite on either side of the IP. The quadrupole elements have an effective dipole field created
 4475 by placing the quadrupole off axis, which is the same as this constant dipole field. The field is chosen such
 4476 that 55 mm of separation is reached by the face of the proton triplet. This separation was chosen based
 4477 on S. Russenschuck’s SC quadrupole design for the proton final focusing triplet. [?] The separation between
 4478 the interacting beams can be increased by raising the constant dipole field. However, for a dipole magnet
 4479 $P_{SR} \propto |B^2|$, [?] therefore an optimization of the design will need to be discussed. The chosen parameters
 4480 give a flux of 5.39×10^{18} photons per second at $Z = -21.5$ m.

4481 **Power and Critical Energy:** Table ?? shows the power of the SR produced by each element along with
 4482 the average critical energy produced per element. This is followed by the total power produced in the IR
 4483 and the average critical energy. Since the G4 simulations utilize Monte Carlo, multiple runs should be made
 4484 with various seeds to get an estimate for the standard error.

Element	Power [kW]	Critical Energy [keV]
DL	6.4	71
QL3	5.3	308
QL2	4.3	218
QL1	0.6	95
QR1	0.6	95
QR2	4.4	220
QR3	5.2	310
DR	6.4	71
Total/Avg	33.2	126

Table 7.19: High Luminosity: Power and Critical Energies as calculated with Geant4.

4485 The power from the dipoles is greater than any one quadrupole however the critical energies of the
 4486 quadrupoles are significantly higher than in the dipoles. It is expected that the dipole and quadrupole
 4487 elements can create power on the same order however have very different critical energies. This is because
 4488 the dipole is an order of magnitude longer than the quadrupole elements. Since the SR power created for

4489 both the quadrupole and dipoles are linearly dependent on length [?] one needs to have a much higher
 4490 average critical energy to create comparable amounts of power.

4491 **Comparison:** The IRSYN cross check of the power and critical energies is shown in Table ???. This
 4492 comparison was done for the total power and the average critical energy.

	Power [kW]		Critical Energy [keV]	
	Geant4	IRSYN	Geant4	IRSYN
Total/Avg	33.2	X	126	X

Table 7.20: High Luminosity: Geant4 and IRSYN comparison

4493 A third cross check to the G4 simulations was made for the power as shown in Table ???. This was done
 4494 using an analytic method for calculating power in dipole and quadrupole magnets. [?] This was done for
 4495 every element which provides confidence in the distribution of this power throughout the IR.

Element	Power [kW]	
	Geant4	Analytic
DL	6.4	6.3
QL3	5.3	5.4
QL2	4.3	4.6
QL1	0.6	0.6
QR1	0.6	0.6
QR2	4.4	4.6
QR3	5.2	5.4
DR	6.4	6.3
Total/Avg	33.2	33.8

Table 7.21: High Luminosity: Geant4 and Analytic method comparison

4496 **Number Density and Envelopes:** The number density of photons as a function of Z is shown in Figure
 4497 ??. Each graph displays the density of photons in the $Z = Z_o$ plane for various values of Z_o . The first three
 4498 figures give the growth of the SR fan inside the detector area. This is crucial for determining the dimensions
 4499 of the beam pipe. Since the fan grows asymmetrically in the -Z direction an asymmetric elliptical cone
 4500 geometry will minimize these dimensions, allowing the tracking to be placed as close to the beam as possible.
 4501 The horizontal extension of the fan in the high luminosity case is the minimum for the two Ring Ring options
 4502 as well as the Linac Ring option, which is most important inside the detector region. This is due to the
 4503 lower value of l^* . Because the quadrupoles are closer to the IP and contain effective dipole fields the angle
 4504 of the beam at the entrance of the upstream dipole can be lower as the angle of the beam doesnt need to
 4505 equal the crossing angle until $Z = l^*$. The number density of this fan appears as expected. There exists the
 4506 highest density between the two beams at the absorber.

4507 In Figure ?? the distribution was given at various Z values however a continuous envelope distribution is
 4508 also important to see everything at once. This can be seen in Figure ??, where the beam and fan envelopes
 4509 are shown in the $Y = 0$ plane. This makes it clear that the fan is antisymmetric which comes from the S
 4510 shape of the electron beam as previously mentioned.

4511 **Critical Energy Distribution:** The Critical Energy is dependent upon the element in which the SR is
 4512 generated, and for the quadrupole magnets it is also dependent upon Z. This is a result of the fact that the

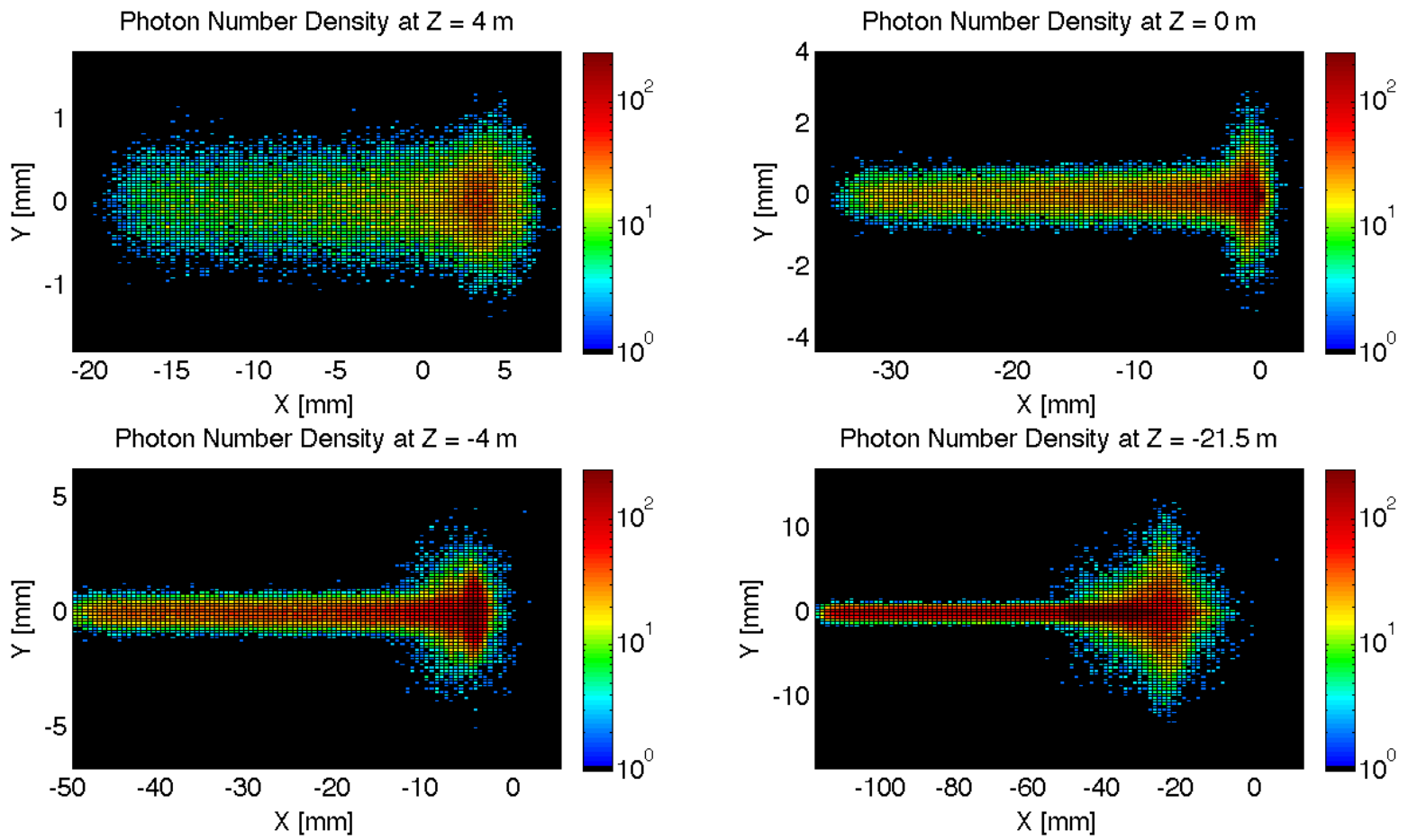


Figure 7.33: High Luminosity: Number Density Growth in Z

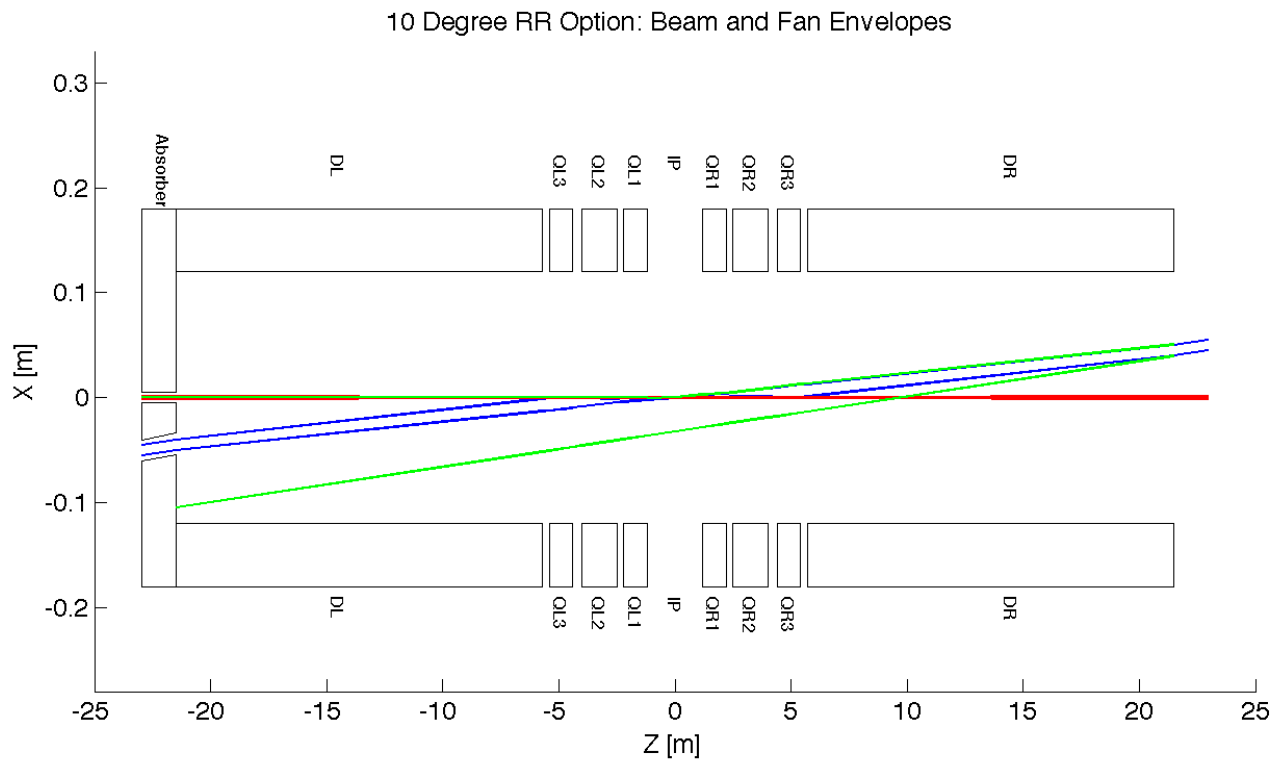


Figure 7.34: High Luminosity: Beam Envelopes in Z

4513 critical energy is proportional to the magnetic field component that is perpendicular to the particle direction.
 4514 i.e. $E_c \propto B_{\perp}$. [?] Since the magnitude of the magnetic field is dependent upon x and y, then for a gaussian
 4515 beam in position particles will experience different magnetic fields and therefore have a spectrum of critical
 4516 energies. In a dipole the field is constant and therefore regardless of the position of the particles as long as
 4517 they are in the uniform field area of the magnet they have a constant critical energy. Since the magnetic
 4518 field is dependent upon x and y it is clear that as the r.m.s. spot size of the beam decreases there will be a
 4519 decrease in critical energies. The opposite will occur for an increasing spot size. This is evident from Figure
 4520 ??.

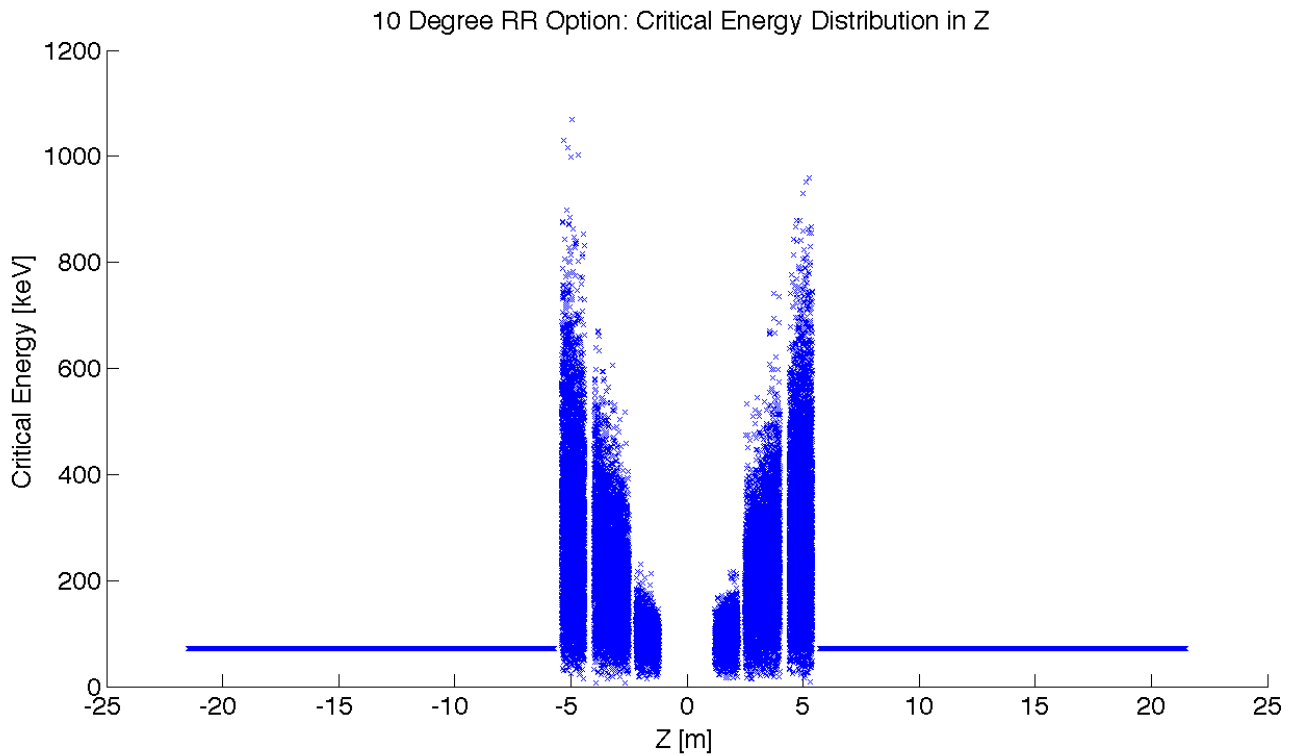


Figure 7.35: High Luminosity: Critical Energy Distribution in Z

4521 **Absorber:** The Photon distribution on the absorber surface is crucial. The distribution decides how the
 4522 absorber must be shaped. The shape of the absorber in addition to the distribution on the surface then
 4523 decides how much SR is backscattered into the detector region. In HERA backscattered SR was a significant
 4524 source of background that required careful attention. [?] Looking at Figure ?? it is shown that for the high
 4525 luminosity option 19.2 kW of power from the SR light will fall on the face of the absorber which is 58% of the
 4526 total power. This gives a general idea of the amount of power that will be absorbed. However, backscattering
 4527 and IR photons will lower the percent that is actually absorbed.

4528 **Proton Triplet:** The super conducting final focusing triplet for the protons needs to be protected from
 4529 radiation by the absorber. Some of the radiation produced upstream of the absorber however will either pass
 4530 through the absorber or pass through the apertures for the two interacting beams. This is most concerning
 4531 for the interacting proton beam aperture which will have the superconducting coils. A rough upper bound
 4532 for the amount of power the coils can absorb before quenching is 100W [?]. There is approximately 217 W
 4533 entering into the interacting proton beam aperture as is shown in Figure ?. This doesn't mean that all

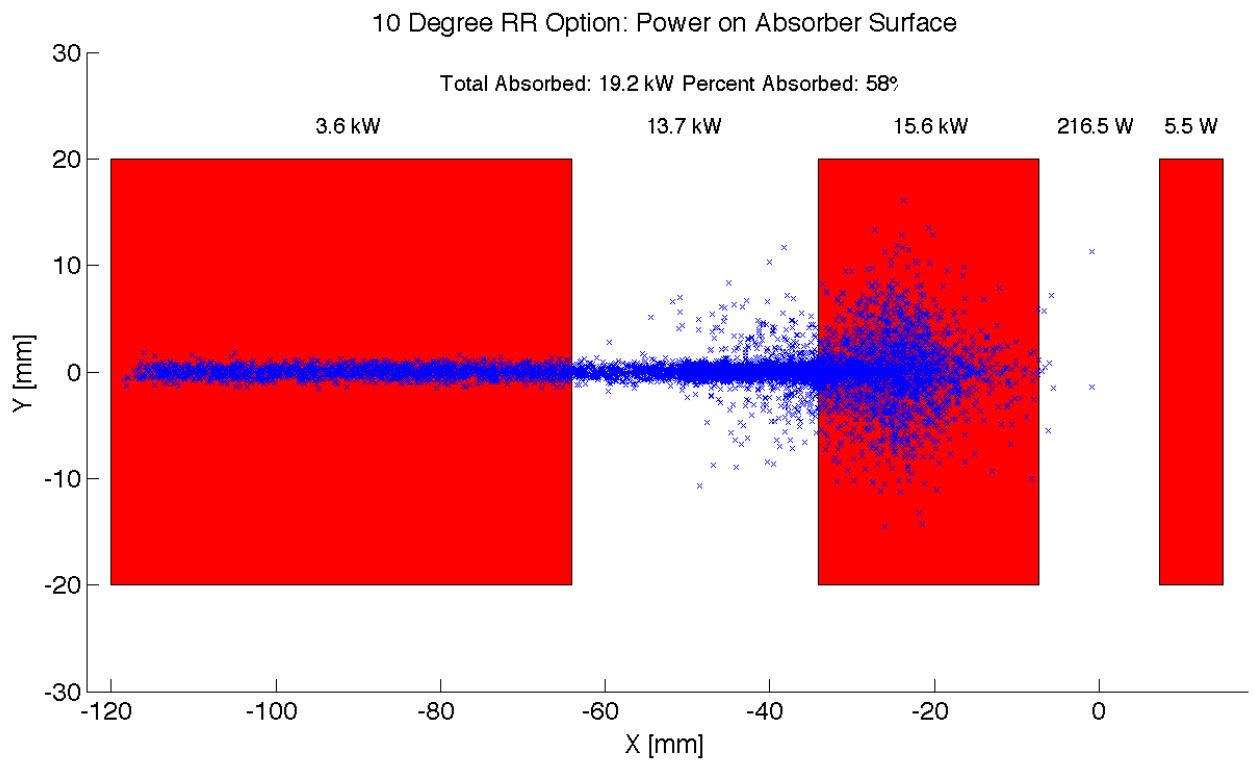


Figure 7.36: High Luminosity: Photon distribution on Absorber Surface

4534 this power will hit the coils but simulations need to be made to determine how much of this will hit the
 4535 coils. The amount of power that will pass through the absorber can be disregarded as it is not enough to
 4536 cause any effects. The main source of power moving downstream of the absorber will be the photons passing
 4537 through the beams aperture. This was approximately 13.7 kW as can be seen from Figure ???. Most of this
 4538 radiation can be absorbed in a secondary absorber placed after the first downstream proton quadrupole.
 4539 Overall protecting the proton triplet is important and although the absorber will minimize the radiation
 4540 continuing downstream this needs to be studied in depth.

4541 **Backscattering:** Another Geant4 program was written to simulate the backscattering of photons into the
 4542 detector region. The ntuple with the photon information written at the absorber surface is used as the
 4543 input for this program. An absorber geometry made of copper is described, and general physics processes
 4544 are set up. A detector volume is then described and set to record the information of all the photons which
 4545 enter in an ntuple. The first step in minimizing the backscattering was to optimize the absorber shape.
 4546 Although the simulation didnt include a beam pipe the backscattering for different absorber geometries was
 4547 compared against one another to find a minimum. The most basic shape was a block of copper that had
 4548 cylinders removed for the interacting beams. This was used as a benchmark to see the maximum possible
 4549 backscattering. In HERA a wedge shape was used for heat dissipation and minimizing backscattering [?].
 4550 The profile of two possible wedge shapes in the YZ plane is shown in Figure ???. It was found that this is
 4551 the optimum shape for the absorber. The reason for this is that a backscattered electron would have to have
 4552 its velocity vector be almost parallel to the wedge surface to escape from the wedge and therefore it works
 4553 as a trap. As can be seen from Table ??? utilizing the wedge shaped absorber did not reduce the power by
 4554 much. This appears to be a statistical limitation. This needs to be redone with higher statistics to get a
 4555 better opinion on the difference between the two geometries.

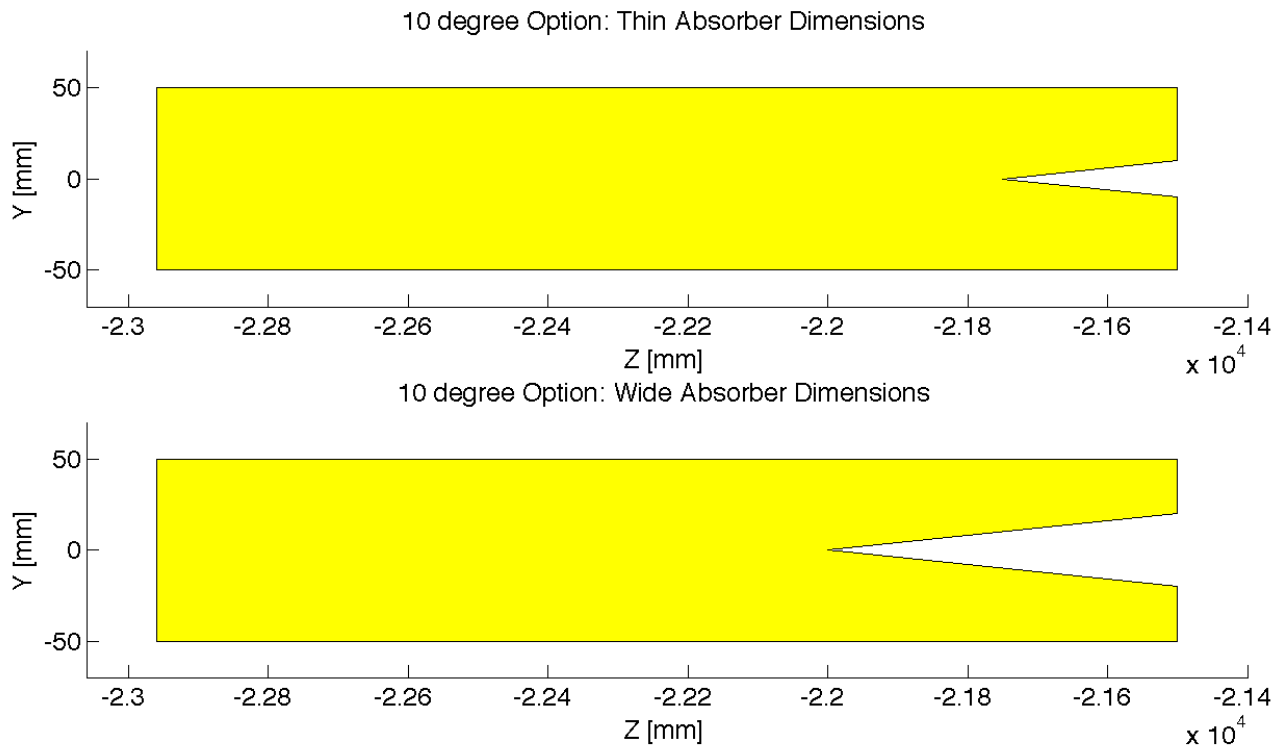


Figure 7.37: 10 deg: Absorber Dimensions

4556 After the absorber was optimized it was possible to set up a beam pipe geometry. An asymmetric
 4557 elliptical cone beam pipe geometry made of beryllium was used since it would minimize the necessary size
 4558 of the beam pipe as previously mentioned. The next step was to place the lead shield and masks inside this
 4559 beam pipe. To determine placement a simulation was run with just the beam pipe. Then it was recorded
 4560 where each backscattered photon would hit the beam pipe in Z. A histogram of this data was made. This
 4561 determined that the shield should be placed in the Z region ranging from -20 m until the absorber (-21.5
 4562 m). The shields were then placed at -21.2 m and -20.5 m. This decreased the backscattered power to zero
 4563 as can be seen from Table ???. Although this is promising this number should be checked again with higher
 4564 statistics to judge its accuracy. Overall there is still more optimization that can occur with this placement.

Absorber Type	Power [W]
Flat	22
Wedge	18.5
Wedge & Mask/Shield	0

Table 7.22: High Luminosity: Backscattering/Mask

4565 Cross sections of the beam pipe in the $Y = 0$ and $X = 0$ planes with the shields and masks included can
 4566 be seen in Figure ???.

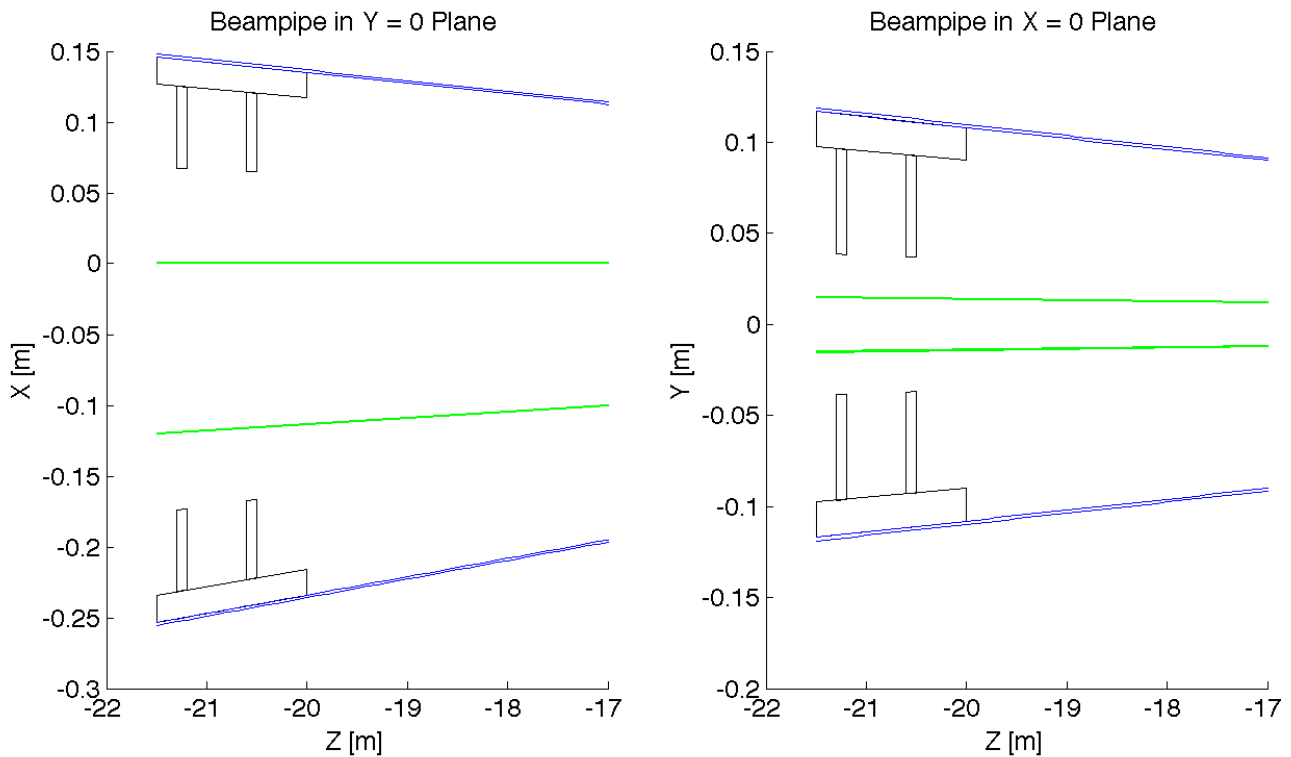


Figure 7.38: High Luminosity: Beampipe Cross Sections

4567 **High Detector Acceptance**

4568 **Parameters:** For the Ring Ring high acceptance option the basic parameters are listed in Table ?? . The
 4569 separation refers to the displacement between the two interacting beams at the face of the proton triplet.

Characteristic	Value
Electron Energy [GeV]	60
Electron Current [mA]	100
Crossing Angle [mrad]	1
Absorber Position [m]	-21.5
Dipole Field [T]	0.0493
Separation [mm]	55.16
γ/s	6.41×10^{18}

Table 7.23: High Acceptance: Parameters

4570 The energy, current, and crossing angle (θ_c) are common values used in all RR calculations. The dipole
 4571 field value refers to the constant dipole field created throughout all dipole elements in the IR. The separation
 4572 is the same as in the high luminosity case and can be altered for the same reasons with the same ramifica-
 4573 tions. The chosen parameters give a flux of 6.41×10^{18} photons per second at $Z = -21.5$ m, which is slightly
 4574 higher than in the high luminosity case. This is expected as the fields experienced in the high acceptance
 4575 case are higher.

4576 **Power and Critical Energy:** Table ?? shows the power of the SR produced by each element along with
 4577 the average critical energy produced per element. This is followed by the total power produced in the IR
 4578 and the average critical energy. Since the G4 simulations utilize Monte Carlo, multiple runs should be made
 4579 with various seeds to get an estimate for the standard error.

Element	Power [kW]	Critical Energy [keV]
DL	13.9	118
QL2	6.2	318
QL1	5.4	294
QR1	5.4	293
QR2	6.3	318
DR	13.9	118
Total/Avg	51.1	163

Table 7.24: High Acceptance: Power and Critical Energies [Geant4]

4580 The distribution of power and critical energy over the IR elements is similar to that of the high acceptance
 4581 option with the exception of the upstream and downstream separator dipole magnets. The power and
 4582 critical energies are significantly higher than before. This is due to the higher dipole field and the quadratic
 4583 dependence of power on magnetic field and linear dependence of critical energy on magnetic field. [?]

4584 **Comparison:** The IRSYN cross check of the power and critical energies is shown in Table ?? . This
 4585 comparison was done for the total power and the critical energy.

4586 A third cross check to the G4 simulations was also made for the power as shown in Table ?? . This was
 4587 done using an analytic method for calculating power in dipole and quadrupole magnets. [?] This comparison
 4588 provides confidence in the distribution of the power throughout the IR.

	Power [kW]		Critical Energy [keV]	
	Geant4	IRSYN	Geant4	IRSYN
Total/Avg	51.1	51.3	163	162

Table 7.25: High Acceptance: Geant4 and IRSYN comparison

	Power [kW]	
Element	Geant4	Analytic
DL	13.9	14
QL2	6.2	6.2
QL1	5.4	5.3
QR1	5.4	5.3
QR2	6.3	6.2
DR	13.9	14
Total	51.1	51

Table 7.26: High Acceptance: Geant4 and Analytic method comparison

4589 **Number Density and Envelopes:** The number density of photons as a function of Z is shown in Figure
4590 **??**. The horizontal extension of the fan in the high acceptance case is larger than in the high luminosity case
4591 however still lower than in the LR option. Since the beam stays at a constant angle for the first 6.2 m after
4592 the IP it requires larger fields to bend in order to reach the desired separation. This means that an overall
4593 larger angle is reached near the absorber, and since the S shaped trajectory is symmetric in Z the angle of
4594 the beam at the entrance of the upstream quadrupoles is also larger and therefore the fan extends further
4595 in X.

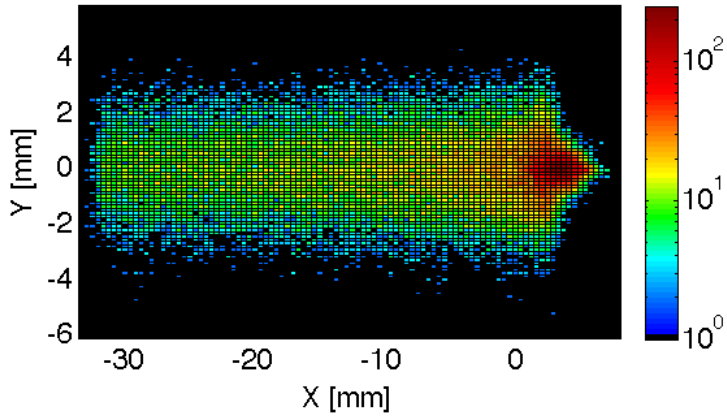
4596 The envelope of the SR fan can be seen in Figure **??**, where the XZ plane is shown at the value $Y = 0$.
4597 Once again the fan is antisymmetric due to the S shape of the electron beam.

4598 **Critical Energy Distribution:** The critical energy distribution in Z is similar to that of the high lumi-
4599 nosity case. This is due to the focusing of the beam in the IR. This is evident from Figure **??**.

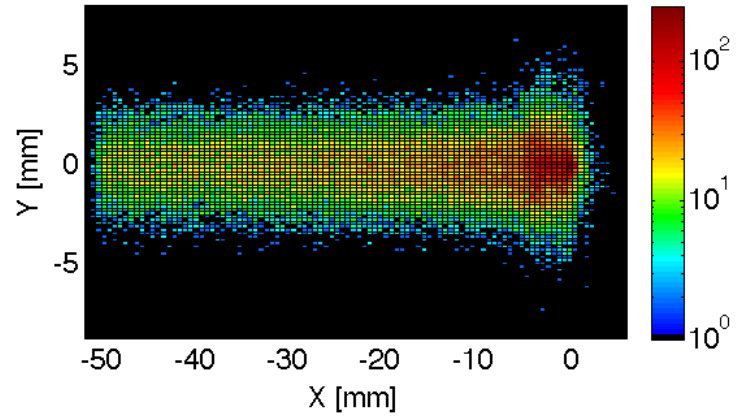
4600 **Absorber:** Looking at Figure **??** it is shown that for the high acceptance option 38.5 kW of power from
4601 the SR light will fall on the face of the absorber which is 75% of the total power. This gives a general idea of
4602 the amount of power that will be absorbed. However, backscattering and IR photons will lower the percent
4603 that is actually absorbed.

4604 **Proton Triplet:** The super conducting final focusing triplet for the protons needs to be protected from
4605 radiation by the absorber. Some of the radiation produced upstream of the absorber however will either pass
4606 through the absorber or pass through the apertures for the two interacting beams. This is most concerning
4607 for the interacting proton beam aperture which will have the superconducting coils. A rough upper bound
4608 for the amount of power the coils can absorb before quenching is 100 W. [?] In the high acceptance option
4609 there is approximately 0.4 W entering into the interacting proton beam aperture as is shown in Figure **??**.
4610 Therefore for the high acceptance option this is not an issue. The amount of power that will pass through
4611 the absorber can be disregarded as it is not enough to cause any significant effects. The main source of
4612 power moving downstream of the absorber will be the photons passing through the beams aperture. This
4613 was approximately 12.7 kW as can be seen from Figure **??**. Most of this radiation can be absorbed in
4614 a secondary absorber placed after the first downstream proton quadrupole. Overall protecting the proton

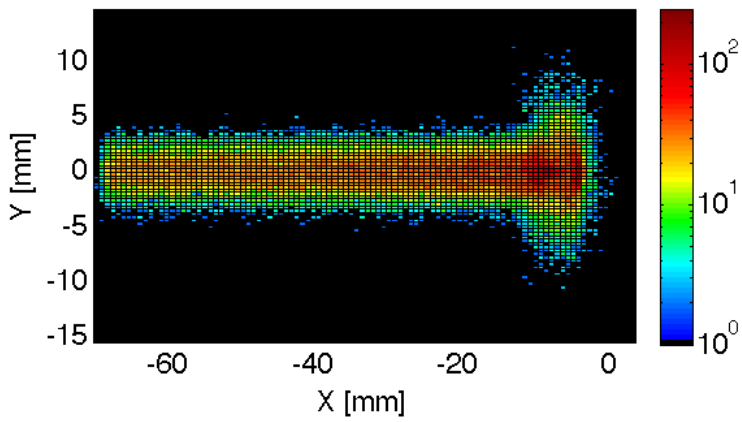
Photon Number Density at Z = 4 m



Photon Number Density at Z = 0 m



Photon Number Density at Z = -4 m



Photon Number Density at Z = -21.5 m

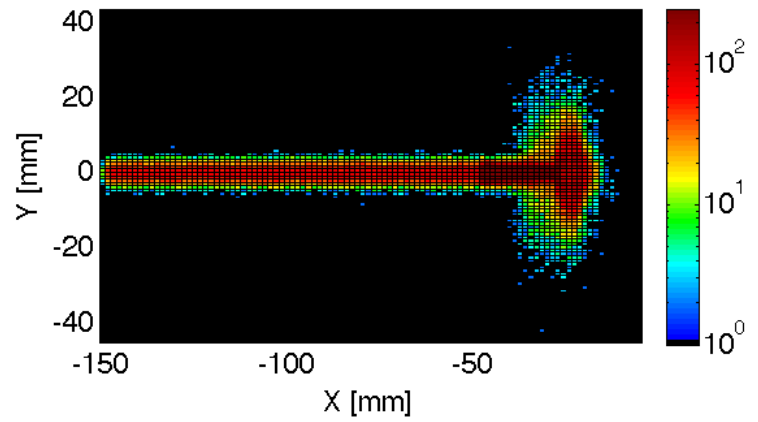


Figure 7.39: High Acceptance: Number Density Growth in Z

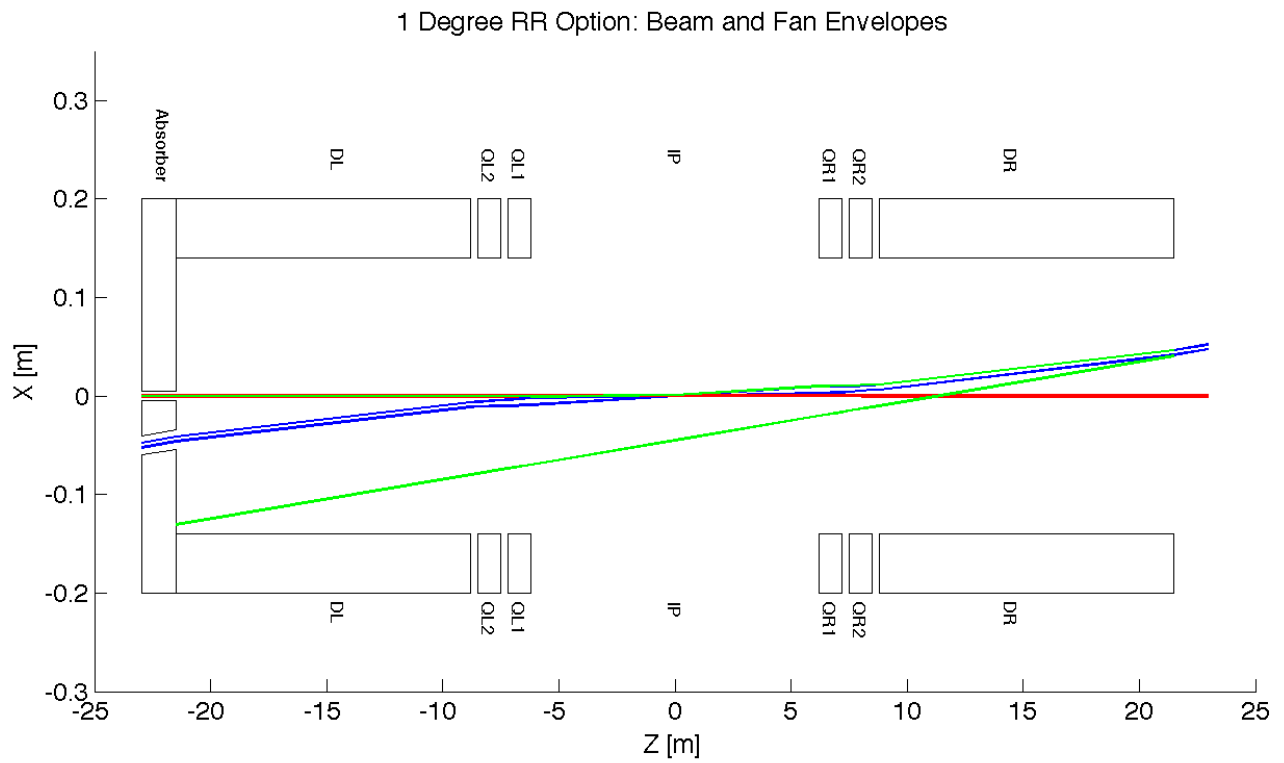


Figure 7.40: High Acceptance: Beam Envelopes in Z

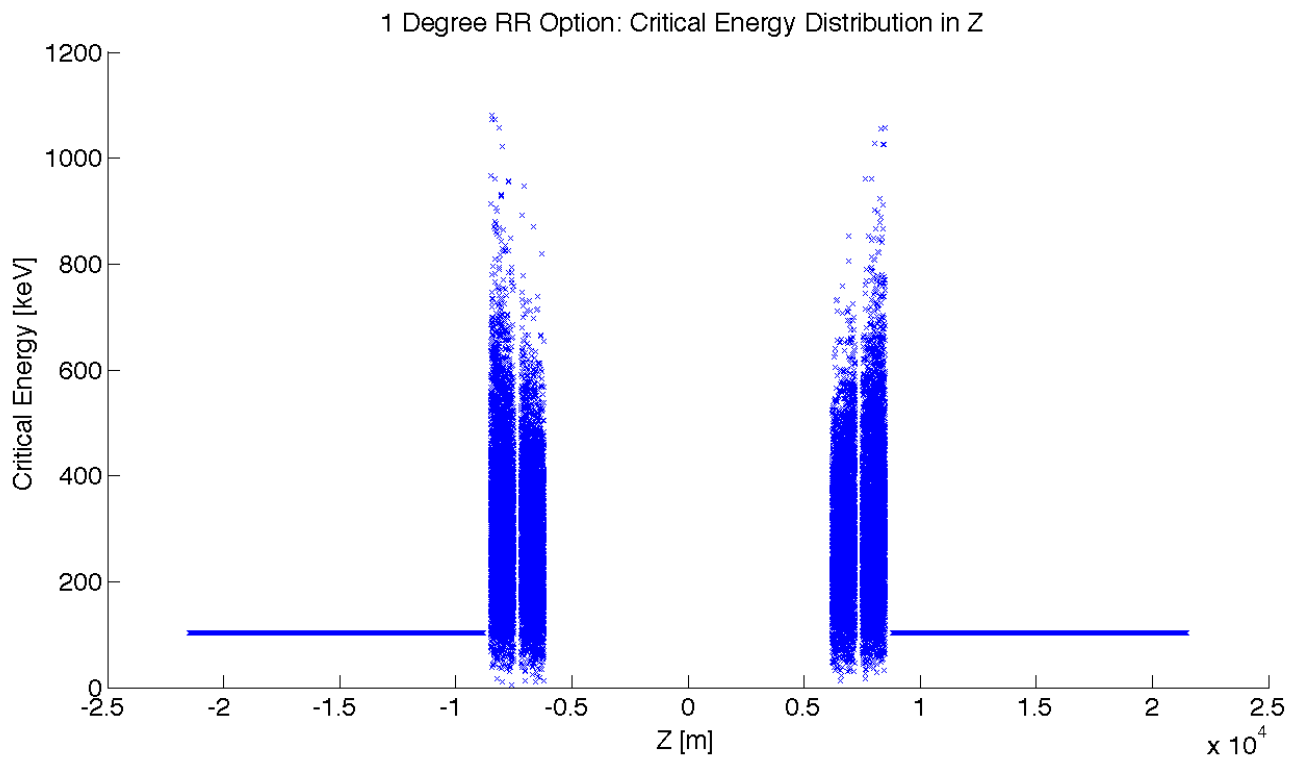


Figure 7.41: High Acceptance: Critical Energy Distribution in Z

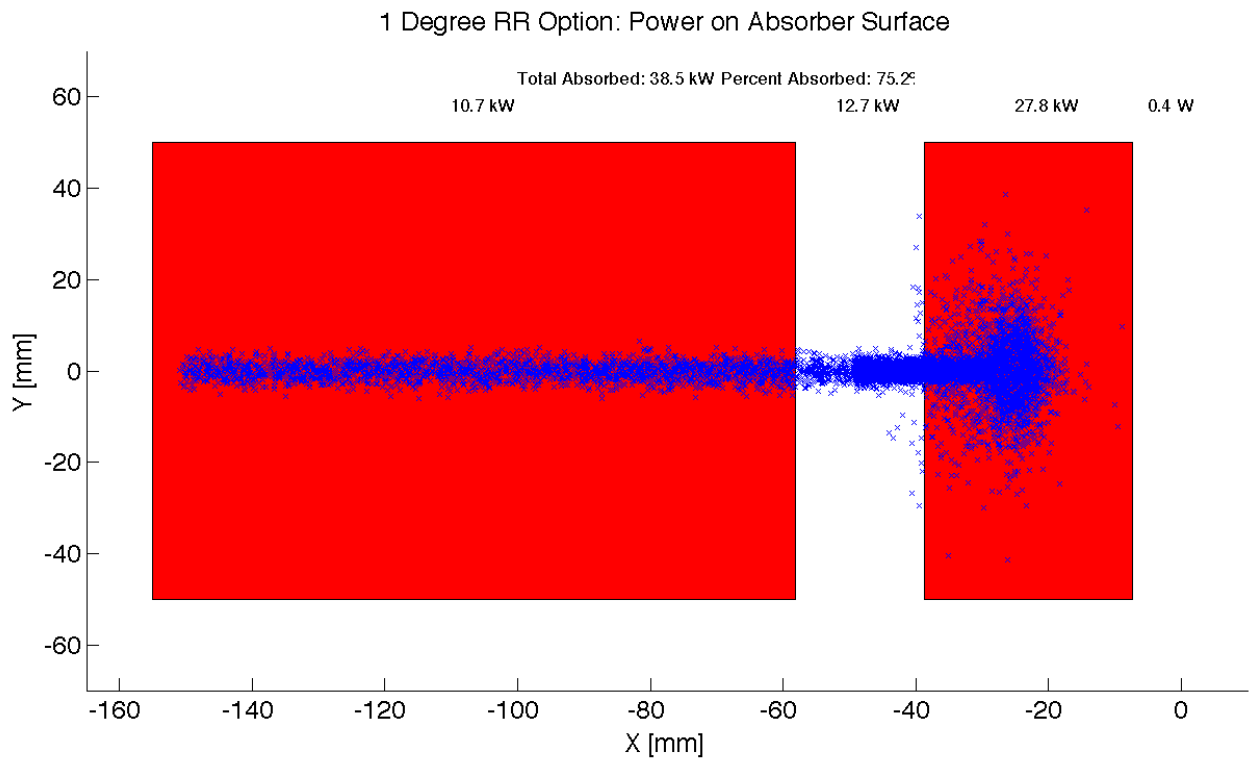


Figure 7.42: High Acceptance: Photon distribution on Absorber Surface

4615 triplet is important and although the absorber will minimize the radiation continuing downstream this needs
4616 to be studied in depth.

4617 **Backscattering:** Another Geant4 program was written to simulate the backscattering of photons into the
4618 detector region. The ntuple with the photon information written at the absorber surface is used as the
4619 input for this program. An absorber geometry made of copper is described, and general physics processes
4620 are set up. A detector volume is then described and set to record the information of all the photons which
4621 enter in an ntuple. The first step in minimizing the backscattering was to optimize the absorber shape.
4622 Although the simulation didnt include a beam pipe the backscattering for different absorber geometries was
4623 compared against one another to find a minimum. The most basic shape was a block of copper that had
4624 cylinders removed for the interacting beams. This was used as a benchmark to see the maximum possible
4625 backscattering. In HERA a wedge shape was used for heat dissipation and minimizing backscattering. [?]
4626 The profile of two possible wedge shapes in the YZ plane is shown in Figure ?? . It was found that this is the
4627 optimum shape for the absorber. The reason for this is that a backscattered electron would have to have its
4628 velocity vector be almost parallel to the wedge surface to escape from the wedge and therefore it works as a
4629 trap. As can be seen from Table ?? utilizing the wedge shaped absorber decreased the backscattered power
4630 by a factor of 9.

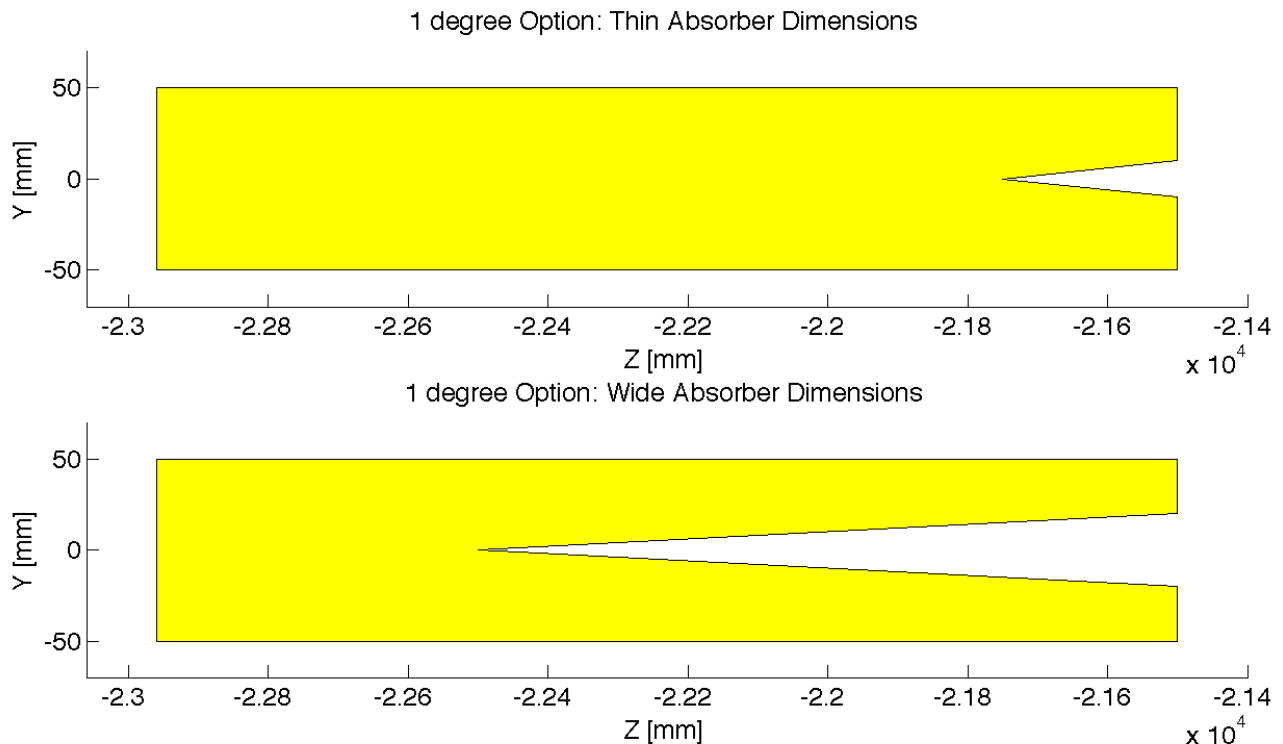


Figure 7.43: 1 deg: Absorber Dimensions

4631 After the absorber was optimized it was possible to set up a beam pipe geometry. An asymmetric
4632 elliptical cone beam pipe geometry made of beryllium was used since it would minimize the necessary size
4633 of the beam pipe as previously mentioned. The next step was to place the lead shield and masks inside this
4634 beam pipe. To determine placement a simulation was run with just the beam pipe. Then it was recorded
4635 where each backscattered photon would hit the beam pipe in Z. This determined that the shield should be
4636 placed in the Z region ranging from -20 m until the absorber (-21.5 m). The shields were then placed at -21.2

4637 m and -20.6 m. This decreased the backscattered power to zero as can be seen from Table ?? . Although
 4638 this is promising this number should be checked again with higher statistics to judge its accuracy. Overall
 4639 there is still more optimization that can occur with this placement.

Absorber Type	Power [W]
Flat	91.1
Wedge	10
Wedge & Mask/Shield	0

Table 7.27: High Acceptance: Backscattering/Mask

4640 Cross sections of the beam pipe in the $Y = 0$ and $X = 0$ planes with the shields and masks included can
 4641 be seen in Figure ??.

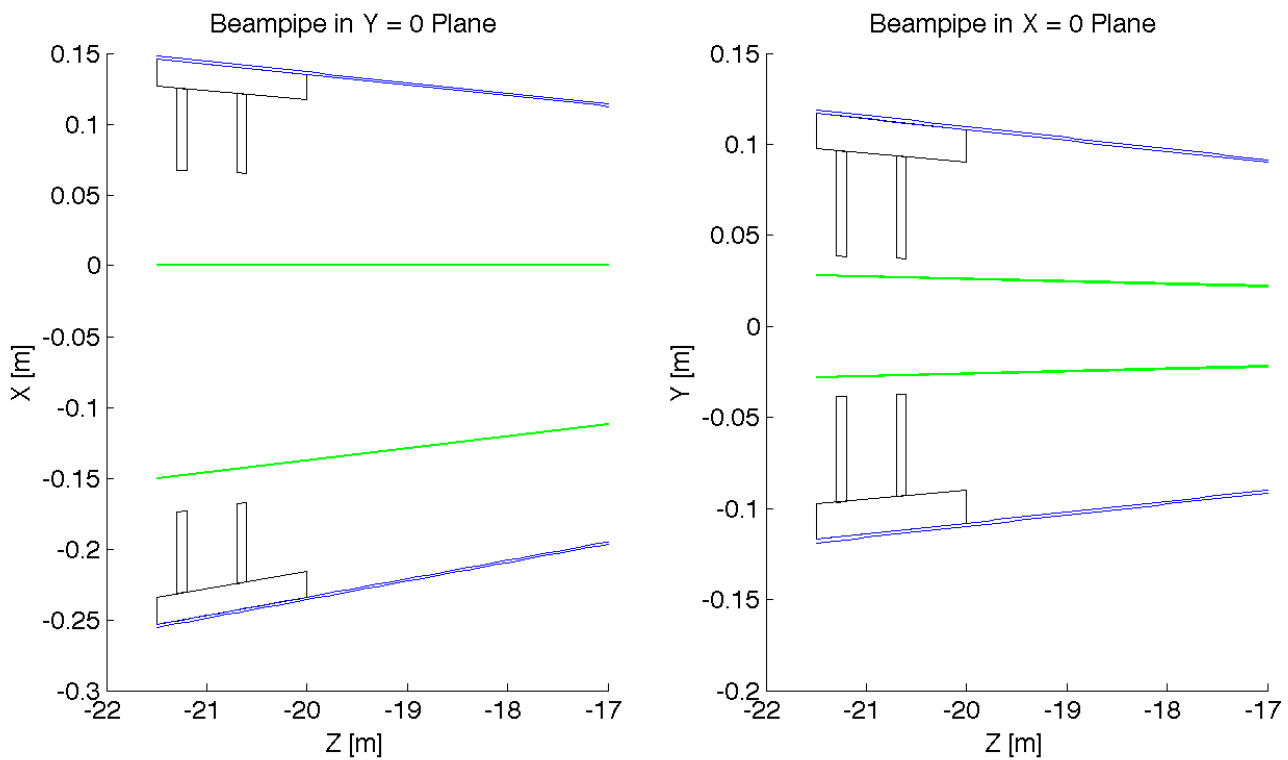


Figure 7.44: High Acceptance: Beampipe Cross Sections

4642 7.8 Beam-beam effects in the LHeC

4643 In the framework of the Large Hadron electron Collider a ring-ring option is considered where protons of
 4644 one beam collide with the protons of the second proton beam as well as with leptons from a separate ring.
 4645 To deduce possible limitations the present knowledge of the LHC beam-beam effects from proton-proton
 4646 collisions are fundamental to define parameters of an interaction point with electron-proton collisions. From
 4647 past experience it is known that the maximum achievable luminosity in a collider is limited by beam-beam
 4648 effects. These are often quantified by the maximum beam-beam tune shifts in each of the two beams. An

4649 important aspect in electron-proton collisions is that the proton beam, more sensitive to transverse noise,
 4650 could be perturbed by a higher level of noise in the electron beam. In this section we will assess some limits
 4651 to the possible tune shift achievable in collision based on experience from past colliders as CESR [?] and
 4652 LEP [?] and more recent ones like the LHC [?].

4653 7.8.1 Head-on beam-beam effects

4654 A first important performance issue in beam-beam interaction comes from the restricted choice of the β -
 4655 function at the interaction point to keep the transverse beam sizes equal for the two beams since proton and
 4656 electron emittances are different. The choice of beta functions at the interaction point has to be different
 4657 for the two beams in order to keep $\sigma_x^e = \sigma_x^p$ and $\sigma_y^e = \sigma_y^p$ for the reasons explained in detail in [?]. In a
 4658 mismatched collision the larger bunch may suffer more because a large part of the particle distribution will
 4659 experience the non-linear beam-beam force of the other bunch. With this in mind it is preferable to keep
 4660 the electron beam slightly larger than the proton beam since the electron beam may be less sensitive due
 4661 to strong radiation damping. This matching implies that the electron emittances must be controlled during
 4662 operation and kept as constant as possible (i.e. H/V coupling). For the proton beam the beam-beam effects
 4663 from the electron beam will be different for the two planes. Optical matching of the beam sizes at the IP is
 4664 the first constraint for any interaction region layout proposed.

4665
 4666 Another important issue is the achievable tune shift and how this relates to the linear beam-beam pa-
 4667 rameter which is normally the parameter used to evaluate the strength of the beam-beam interaction.

4668
 4669 The linear beam-beam parameter is defined as ξ_{bb} and is expressed for the case of round beams like in
 4670 proton-proton collision at the LHC as:

$$\xi_{bb} = \frac{Nr_p\beta^*}{4\pi\gamma\sigma^2} \quad (7.12)$$

4671 where r_p is the proton classical radius, β^* is the optical amplitude function (β -function) at the interaction
 4672 point, $\sigma = \sigma_{x,y}$ is the transverse beam size in meters at the interaction point, N_p is the bunch intensity and
 4673 γ is the relativistic factor. For proton-proton collisions where ξ_{bb} does not reach too large values and the
 4674 operational tune is far enough away from linear resonances, this parameter is about equal to the linear tune
 4675 shift ΔQ expected from the head-on beam-beam interaction. This is the case for the LHC proton-proton
 4676 collisions at IP1 and IP5 where the linear tune shift per IP is of the order of 0.0034/0.0037 for nominal beam
 4677 parameters as summarized in Table ?? and corresponds to the linear beam-beam parameter ξ_{bb} . This is in
 4678 general not true for lepton colliders where the operational scenario differs from hadron colliders and other
 4679 effects become dominant and have to be taken into account.

4680 In the case of electron beams the transverse shape of the beams is normally elliptical with $\sigma_x > \sigma_y$. In this
 4681 configuration one can generalize the linear beam-beam parameter calculation with the following formula [?]:

$$\xi_{x,y} = \frac{Nr_e\beta_{x,y}^*}{2\pi\gamma\sigma_{x,y}(\sigma_x + \sigma_y)} \quad (7.13)$$

4682 with r_e is the electron classical radius.

4683 In the case of electron-proton collisions one has to also take into account the different species during
 4684 collision and the beam-beam parameters become:

$$\xi_{(x,y),b_1} = \frac{N_{b_2}r_{b_1}\beta_{(x,y),b_1}^*}{2\pi\gamma_{b_1}\sigma_{(x,y),b_2}(\sigma_{x,b_2} + \sigma_{y,b_2})} \quad (7.14)$$

4685 Here b_1 and b_2 refer to Beam1 and Beam2 respectively. The linear beam-beam parameter ξ is often used
 4686 to quantify the strength of the beam-beam interaction, however it does not reflect the non-linear nature of
 4687 the electromagnetic interaction. Nevertheless, it can be used for comparison and as a scaling parameter.

Parameter	LEP	LHC (nominal)
Beam sizes	160 μm \cdot 4 μm ?	16.6 μm \cdot 16.6 μm
Intensity N	4.0 \cdot 10 ¹¹ /bunch	1.15 \cdot 10 ¹¹ /bunch
Energy	100 GeV	7000 GeV
$\beta_x^* \cdot \beta_y^*$	1.25 m \cdot 0.05 m	0.55 m \cdot 0.55 m
Crossing angle	0.0	0/285 μrad
Beam-beam parameter(ξ)	0.0700	0.0037/0.0034

Table 7.28: Comparison of parameters for the LEP collider and the LHC.

4688 Since a general beam-beam limit cannot be found and will be different from one collider to the next, the
4689 interpretation should be conservative.

4690 In Table ?? we compare LEP and LHC beam parameters and achieved linear beam-beam parameters.
4691 Some of the differences are striking: while the beams in the LHC are round at the interaction point, they are
4692 very flat in LEP. This is due to the excitation of the beam in the horizontal plane by the strong synchrotron
4693 radiation and damping in the vertical plane. Another observation is the much larger beam-beam parameter
4694 in LEP.

4695 One reason for the larger achievable beam-beam parameter in lepton colliders is due to a significant
4696 dynamic beta effect when operating at a working point close to integer tune. This is considered more
4697 difficult with proton beams. In Equation ?? the perturbed β^* is expressed as a function of the beam-beam
4698 parameter and the phase advance between two interaction points $2\pi Q^i$. The tune shift becomes a function
4699 of the tune which can be chosen to keep the actual shift small.

$$\beta^*(Q) = \frac{\beta}{\sqrt{1 + 4\pi\xi(\cot(2\pi Q^i)) - 4\pi^2\xi^2}} \quad (7.15)$$

4700 From experience it is known that electrons have a bigger range for the linear head-on beam-beam param-
4701 eter: LEP II has proved a beam-beam parameter of 0.07 corresponding to a measured ΔQ of 0.03 as also
4702 confirmed in other lepton colliders. CESR demonstrated the possibility to achieve tune shifts of the order
4703 of 0.09. A second and most important reason for a higher acceptable tune shift in lepton colliders is the
4704 synchrotron radiation damping. Furthermore, while for lepton colliders a clear indication for a "beam-beam
4705 limit" exists, not such criteria can be easily defined for hadron machines [?]. With this brief resume on the
4706 head-on linear beam-beam parameters reached so far it is clear that the beam which will have some limits
4707 on the choice of beam-beam parameters ξ_{bb} is the proton beam.

4708 The LHC as a proton-proton collider has confirmed previous experience from SppS and Tevatron that
4709 a total linear tune shift of 0.018 (0.006 per IP) is tolerable with neither important losses nor reduction of
4710 beam lifetime during normal operation. It is generally admitted that ξ_{bb} could reach a value of 0.01 per
4711 interaction point. Recent experiments at the LHC with very high intensity beams beyond ultimate and
4712 reduced beam transverse sizes demonstrated the possibility of reaching head-on tune shifts well beyond the
4713 nominal values [?]. At the LHC tune shifts per IP close to 0.02 have been achieved. Total tune shift exceeding
4714 0.034 have also been achieved with stable beams for two symmetric crossings at IP1 and IP5. These latest
4715 experiments demonstrate the possibility to operate with larger than nominal beam-beam parameters.

4716 The calculated beam-beam parameters for the electron and proton beams due to an electron-proton
4717 collision in the LHeC are summarized in Table ?? for the two interaction region options (1 Degree Option
4718 and 10 Degree Option).

4719 The two proposed interaction region options will give for the proton beams a maximum beam-beam
4720 parameter in the horizontal plane of about $8 \cdot 10^{-4}$. This effect is in the shadow of the proton-proton
4721 collision at IP1 and IP5 which will give a beam-beam parameter of $5.5 \cdot 10^{-3}$ per single IP for nominal
4722 beam emittances and assuming intensities of $1.7 \cdot 10^{11}$ protons/bunch which was already achieved during
4723 2010 operation at the LHC with reduced emittances and nominal beam intensities. One should not expect

IR Option	1 degree		10 degree	
	Electrons	Protons	Electrons	Protons
Beams	Electrons	Protons	Electrons	Protons
Energy	60 GeV	7 TeV	60 GeV	7 TeV
Intensity	$2 \cdot 10^{10}$	$1.7 \cdot 10^{11}$	$2 \cdot 10^{10}$	$1.7 \cdot 10^{11}$
β_x^*	0.4 m	4.05 m	0.18 m	1.8 m
β_y^*	0.2 m	0.97 m	0.1 m	0.5 m
ϵ_x	5 nm	0.5 nm	5 nm	0.5 nm
ϵ_y	2.5 nm	0.5 nm	2.5 nm	0.5 nm
σ_x	45 μm		30 μm	
σ_y	22 μm		15.8 μm	
Cross angle	1 mrad		1 mrad	
$\xi_{bb,x}$	0.086	0.0008	0.085	0.0008
$\xi_{bb,y}$	0.088	0.0004	0.090	0.0004
Luminosity	$7.33 \cdot 10^{32} \text{ cm}^{-2} \text{ s}^{-1}$		$1.34 \cdot 10^{33} \text{ cm}^{-2} \text{ s}^{-1}$	

Table 7.29: Beam parameters for the interaction region options and the relative linear beam-beam parameter ξ .

	Nominal		Upgrade	
	Electrons	Protons	Electrons	Protons
$\xi_{bb,x}$	0.016	0.0013	0.027	0.0017
$\xi_{bb,y}$	0.018	0.0012	0.041	0.0005

Table 7.30: Linear beam-beam parameters for HERA, nominal machine and upgrade parameters.

IR Option	1 degree		10 degree	
Beams	Electrons	Protons	Electrons	Protons
β_x^*	0.4 m	4.05 m	0.18 m	1.8 m
β_y^*	0.2 m	0.97 m	0.1 m	0.5 m
ϵ_x	5 nm	0.5 nm	5 nm	0.5 nm
ϵ_y	2.5 nm	0.5 nm	2.5 nm	0.5 nm
Cross angle	1 mrad		1 mrad	
d_x	90 σ_e	8.94 σ_p	60 σ_e	6.0 σ_p

Table 7.31: Normalized distance of beam-beam long range encounter for the two interaction region options.

important effects of the head-on tune shifts coming from the electron beam apart from a potential coupling of noise from the electron into the proton beam. For the electron beam, on the contrary, the beam-beam parameter of $8.6 \cdot 10^{-2}$ is large and represents a value at the limit of what has been achieved so far in other lepton machines (LEP at 90 GeV energy achieved a beam-beam parameter of 0.07 while KEK and HERA a maximum $\xi_{bb} = 0.04$ during operation, CESR achieved a beam-beam parameter of 0.09 for single IP but with lower luminosity). The beam-beam tuneshifts achieved at HERA for the nominal and upgrade version are summarized in Table ?? for comparison.

7.8.2 Long range beam-beam effects

So far we have discussed head-on beam-beam interactions but an important issue are the long range interactions which will occur at the electron-proton collision and their interplay with the proton-proton crossings at IP1 and IP5. The two interaction points IP1 and IP5 will give up to 60 proton-proton long-range interactions which should be added to the two interaction region options which will give two additional parasitic encounters. The beam separation at this encounters should be as large as possible to reduce any non-linear perturbation. The parasitic encounters occur every 3.75 m from the interaction point for a bunch spacing of 25 ns. The proposed optics will then lead to parasitic beam-beam interactions which will occur at a transverse separation d as:

$$d(s)_{x,y} = \alpha \frac{s}{\sqrt{\epsilon_{x,y} \beta(s)_{x,y}}} \quad (7.16)$$

with $\epsilon_{x,y}$ are the beam emittance in the separation plane and $\beta(s)$ is the betatron function at a distance s from the interaction point.

In Table ?? the distances of the parasitic encounters in units of the transverse beam sizes are shown for both interaction region layouts.

The 1 degree option gives long range interactions at larger separation with respect to the 10 degree option which results in small separations of $\approx 6 \sigma$ for the proton beam. Particles in the tail of the proton beam particles will experience the non linearity of the electron beam electromagnetic force. The presence of two long range at 6σ separation may be acceptable since it is shown experimentally that few encounters also at smaller separation do not affect the beams dramatically [?]. However, the interplay of these two encounters with the long-range interactions from IP1 and IP5 should be studied in detail with numerical simulation to highlight possible limitations. In this framework future experiments at the LHC will help defining a possible beam parameters space for the control of the long-range effects from proton-proton collisions. If encounters at 6σ present a limitation to the collider performance then a possible cure to increase the long-range separation could be a further increase of the crossing angle and using crab cavities can recover the increased geometric luminosity reduction factor. In this case a study of the crab cavities effects on the proton beam would be essential to define the effects of transverse noise on colliding beams.

For any reliable study of the LHeC project one has to address other possible beam-beam issues with extensive numerical simulations of the operational scenario of the LHeC. This is fundamental since there is no other

4758 possible simplification which can be adopted in evaluating the non-linear parts of the beam-beam forces.
4759 For this reason a detailed and full interaction layout with crossing schemes matched in thin lens version
4760 is needed. With the complete optic layout beam-beam effects which still need further studies by means of
4761 numerical simulation campaign are the following:

- 4762 • Long-range tune shifts and orbit effects.
- 4763 • Self-consistent study of the proton-proton and electron-proton beam dynamics interplay.
- 4764 • Dynamic aperture tracking studies.
- 4765 • Multi-bunch effects.
- 4766 • Noise coupling from the electron to the proton beam.

4767 The evaluation of the non-linear effects of the beam-beam interactions with self-consistent calculations will
4768 define a set of parameters for operation [?].

4769 7.9 Performance as an electron-ion collider

4770 7.9.1 Heavy nuclei, e-Pb collisions

4771 With the first collisions of lead nuclei ($^{208}\text{Pb}^{82+}$) in 2010 [?, ?], the LHC has already demonstrated its
4772 capability as a heavy-ion collider and this naturally opens up the possibility of electron-nucleus (e-A) collisions
4773 in the LHeC.

4774 This mode of operation would obviously fall into the annually scheduled ion operation period of the LHC
4775 in order not to interfere with the high luminosity proton-proton operation. In principle, the CERN complex
4776 could provide A-A (or even p-A) collisions to the LHC experiments while the LHeC operates with e-A
4777 collisions. The lifetime of the nuclear beam would depend mainly on whether it was exposed to the losses
4778 from A-A luminosity in the LHC (in this case it would be at least a few hours).

4779 In the first decade or so of LHC operation, the ion injector chain is expected to provide mainly $^{208}\text{Pb}^{82+}$,
4780 but also other species such as $^{40}\text{Ar}^{18+}$ or $^{129}\text{Xe}^{54+}$, either to the LHC or from the SPS to fixed target exper-
4781 iments in the North Area. These beams could also be collided with electrons in the LHeC but solid intensity
4782 estimates are not yet available for the lighter ions. For simplicity, we shall estimate LHeC performance
4783 in e-Pb collisions with the design performance values of the ion injector chain as described in [?] and the
4784 assumption of a single nuclear beam in one ring of the LHC with parameters as recalled from [?] in Table ??.
4785 It is assumed that present uncertainties about the Pb intensity limits at full energy in the LHC will have
4786 been resolved, if necessary, by installation of new collimators in the dispersion suppressors of the collimation
4787 insertions in the LHC. This simplifies the discussion because the design emittances of Pb and proton beams
4788 in the LHC are such that both species have the same geometric beam sizes and considerations of optics
4789 and aperture can be taken over directly. The “Ultimate Pb” value of the Pb single bunch intensity was
4790 already attained in 2010 [?] using a simplified injection scheme but not yet with the nominal filling scheme
4791 for 592 bunches; it can be considered an optimistic goal. At present, there are no prospects for increasing
4792 the number of bunches significantly. Lower Pb emittances may be possible but would not increase e-Pb
4793 luminosity unless matched with smaller optical functions or emittances for the electron beam.

4794 Assume that the injection system can create an electron bunch train matching the 592-bunch train of Pb
4795 nuclei in the LHC so that every Pb bunch finds a collision partner in the electron beam. Assuming further
4796 that the hadron optics can be adjusted to match the sizes of the electron and Pb beams, the luminosity can
4797 be expressed in terms of the interaction point optical functions and emittances of the electron beam. Since
4798 the e-A physics is focused on low- x these are taken from Table ?? describing the Ring-Ring High Acceptance
4799 optics, which reduces the luminosity by a factor 2 as compared with the High-Luminosity optics.

4800 In e-p mode, the intensity of the 2808 electron bunches, N_e is limited for the Ring-Ring version of the
4801 LHeC by the total RF power available to compensate the synchrotron radiation loss. For the same power

		Design Pb	Ultimate Pb
Energy	E_{Pb}	574. TeV	
Energy per nucleon	E_N	2.76 TeV	
No. of bunches	n_b	592	
Ions per bunch	N_{Pb}	$7. \times 10^7$	1.2×10^8
Normalised emittance	ε_n	1.5 μm	

Table 7.32: Parameters for the $^{208}\text{Pb}^{82+}$ beam according to Chapter 21 of [?].

4802 (some 44 MW for $N_e = 2 \times 10^{10}$ of Table ??), the intensity of the $n_b = 592$ bunches required to collide
4803 with the Pb nuclei can be increased by a factor 2808/592 to $N_e = 9.5 \times 10^{10}$. Electron beam parameters
4804 for the LHeC Ring-Ring option other than the single bunch intensity can be taken from Table ?. Present
4805 experience with beam-beam effects in the LHC suggests that the additional electron intensity would not
4806 present any problem for the proton beam. The single-bunch intensity is still well below that achieved in
4807 LEP although the feasibility of these values should be confirmed by further analysis of the ring impedance
4808 and collective effects.

4809 Neglecting the geometric reduction factor due to the crossing angle and the Hourglass effect, the *electron-*
4810 *nucleon* luminosity, $L_{eN} = AL_{eA}$, is then given by

$$L_{eN} = \frac{n_b f_0 N_e (A N_{\text{Pb}})}{4\pi \sqrt{\beta_{xe}^* \varepsilon_x} \sqrt{\beta_{ye}^* \varepsilon_y}} = \begin{cases} 2.6 \times 10^{31} \text{ cm}^{-2}\text{s}^{-1} & \text{(Nominal Pb)} \\ 4.5 \times 10^{31} \text{ cm}^{-2}\text{s}^{-1} & \text{(Ultimate Pb)} \end{cases} \quad (7.17)$$

4811 This gives an indication of the range of peak luminosities that can be expected. A factor of 2 could be gained
4812 by switching to the high-luminosity interaction region optics.

4813 By the time the LHeC comes into operation, it is not unreasonable to hope that ways to increase the
4814 number of Pb bunches and perhaps to reduce their emittance (by cooling) may be implemented. Therefore,
4815 on an optimistic view, the luminosity could be even higher than the value quoted here.

4816 Finally, we note that the dependence of luminosity on electron beam energy ($\propto E_e^{-6}$) is very strong at
4817 the power limit so that a trade-off between energy and luminosity may be of interest.

4818 7.9.2 Electron-deuteron collisions

4819 As discussed in [?], deuteron beams are not presently available in the CERN complex. Meanwhile it has been
4820 clearly demonstrated [?] that it would not be feasible to set up a D^- source and accelerate them via Linac4.
4821 The present proton Linac2 is due to be shut down so the only way to accelerate them would be via the
4822 heavy ion Linac3. However this would require a new source, RFQ and switch-yard at the input to Linac3.
4823 The study of practical feasibility, space limitations, design and potential performance of these modifications
4824 to the injector complex will start only in late 2011 with a view to supplying D and other light ions to fixed
4825 target experiments and the LHC in several years' time.

4826 Assuming that a practical design can be implemented, the intensity of bunches in the LHC ring can be
4827 estimated as follows.

4828 The present GTS-LHC source delivers $^{208}\text{Pb}^{29+}$ ions with a charge-to-mass ratio $Q/A = 1/7.2$. A
4829 safe estimate of the space-charge limit at the entrance of Linac3 is 200 μA . To accelerate deuterons with
4830 $Q/A = 1/2$, all magnetic and electric fields would have to be reduced by a factor 3.6, leading to a space-charge
4831 limited current of 55 μA .

4832 However there is then a very comfortable margin in the electric and magnetic fields and deuterons are
4833 not subject to the loss factors associated with the subsequent stripping stages for Pb. If enough deuteron
4834 current is available from the source (say 5 mA), and one accepts losses in the linac and a somewhat degraded

4835 beam quality at the end, then a current in the range of 200-500 μA would probably be available at the end
 4836 of the linac.

4837 As a caveat, early measurements of poor transmission of helium ions in Linac3 [?] should be mentioned.
 4838 However the explanation is unclear due to the lack of appropriate diagnostics.

4839 The bunch number and filling pattern in the LHC would be similar to that of the Pb beam. A naive
 4840 transposition of the scaling of the ratios of Linac3 output current (50 μA) to LHC bunch intensity (7×10^7)
 4841 from Pb to deuterons would suggest that the deuteron single-bunch intensity in the LHC could be $N_D \approx$
 4842 1.5×10^{10} .

4843 However this does not consider the differences in performance of the remainder of the injector chain (the
 4844 LEIR cooling ring, PS and SPS synchrotrons). A proper evaluation of these requires a more detailed study.
 4845 To be safe, we can apply a factor 5 reduction to this value.

4846 Then, assuming that we collide such a beam with the electron beam described in the preceding sub-
 4847 section, we see that *electron-nucleon* luminosities of order $L_{eN} \gtrsim 10^{31} \text{ cm}^{-2}\text{s}^{-1}$ could be accessible in e-D
 4848 collisions at the LHeC.

4849 7.10 Spin polarisation – an overview

4850 Before describing concepts for attaining electron and positron spin polarisation for the ring-ring option of
 4851 the LHeC we present a brief overview of the theory and phenomenology. We can then draw on this later as
 4852 required. This overview is necessarily brief but more details can be found in [?, ?].

4853 7.10.1 Self polarisation

4854 The spin polarisation of an ensemble of spin-1/2 fermions with the same energies travelling in the same
 4855 direction is defined as

$$\vec{P} = \langle \frac{2}{\hbar} \vec{\sigma} \rangle \quad (7.18)$$

4856 where $\vec{\sigma}$ is the spin operator in the rest frame and $\langle \rangle$ denotes the expectation value for the mixed spin
 4857 state. We denote the single-particle rest-frame expectation value of $\frac{2}{\hbar} \vec{\sigma}$ by \vec{S} and we call this the “spin”.
 4858 The polarisation is then the average of \vec{S} over an ensemble of particles such as that of a bunch of particles.

4859 Relativistic e^\pm circulating in the (vertical) guide field of a storage ring emit synchrotron radiation and
 4860 a tiny fraction of the photons can cause spin flip from up to down and vice versa. However, the up-to-
 4861 down and down-to-up rates differ, with the result that in ideal circumstances the electron (positron) beam
 4862 can become spin polarised anti-parallel (parallel) to the field, reaching a maximum polarisation, P_{st} , of
 4863 $\frac{8}{5\sqrt{3}} = 92.4\%$. This, the Sokolov-Ternov (S-T) polarising process, is very slow on the time scale of other
 4864 dynamical phenomena occurring in storage rings, and the inverse time constant for the exponential build up
 4865 is [?]:

$$\tau_{\text{st}}^{-1} = \frac{5\sqrt{3}}{8} \frac{r_e \gamma^5 \hbar}{m_e |\rho|^3} \quad (7.19)$$

4866 where r_e is the classical electron radius, γ is the Lorentz factor, ρ is the radius of curvature in the magnets
 4867 and the other symbols have their usual meanings. The time constant is usually in the range of a few minutes
 4868 to a few hours.

4869 However, even without radiative spin flip, the spins are not stationary but precess in the external fields.
 4870 In particular, the motion of \vec{S} for a relativistic charged particle travelling in electric and magnetic fields is
 4871 governed by the Thomas-BMT equation $d\vec{S}/ds = \vec{\Omega} \times \vec{S}$ where s is the distance around the ring [?, ?]. The
 4872 vector $\vec{\Omega}$ depends on the electric (\vec{E}) and magnetic (\vec{B}) fields, the energy and the velocity (\vec{v}) which evolves

4873 according to the Lorentz equation:

$$\vec{\Omega} = \frac{e}{m_e c} \left[- \left(\frac{1}{\gamma} + a \right) \vec{B} + \frac{a\gamma}{1+\gamma} \frac{1}{c^2} (\vec{v} \cdot \vec{B}) \vec{v} + \frac{1}{c^2} \left(a + \frac{1}{1+\gamma} \right) (\vec{v} \times \vec{E}) \right] \quad (7.20)$$

$$= \frac{e}{m_e c} \left[- \left(\frac{1}{\gamma} + a \right) \vec{B}_\perp - \frac{g}{2\gamma} \vec{B}_\parallel + \frac{1}{c^2} \left(a + \frac{1}{1+\gamma} \right) (\vec{v} \times \vec{E}) \right]. \quad (7.21)$$

4874 Thus $\vec{\Omega}$ depends on s and on the position of the particle $u \equiv (x, p_x, y, p_y, l, \delta)$ in the 6-D phase space of
 4875 the motion. The coordinate δ is the fractional deviation of the energy from the energy of a synchronous
 4876 particle (“the beam energy”) and l is the distance from the centre of the bunch. The coordinates x and y are
 4877 the horizontal and vertical positions of the particle relative to the reference trajectory and $p_x = x', p_y = y'$
 4878 (except in solenoids) are their conjugate momenta. The quantity g is the appropriate gyromagnetic factor
 4879 and $a = (g - 2)/2$ is the gyromagnetic anomaly. For e^\pm , $a \approx 0.0011596$. \vec{B}_\parallel and \vec{B}_\perp are the magnetic fields
 4880 parallel and perpendicular to the velocity.

4881 In a simplified picture, the majority of the photons in the synchrotron radiation do not cause spin flip but
 4882 tend instead to randomise the e^\pm orbital motion in the (inhomogeneous) magnetic fields. Then, if the ring is
 4883 insufficiently-well geometrically aligned and/or if it contains special magnet systems like the “spin rotators”
 4884 needed to produce longitudinal polarisation at a detector (see below), the spin-orbit coupling embodied in
 4885 the Thomas-BMT equation can cause spin diffusion, i.e. depolarisation. Compared to the S-T polarising
 4886 effect the depolarisation tends to rise very strongly with beam energy. The equilibrium polarisation is then
 4887 less than 92.4% and will depend on the relative strengths of the polarisation and depolarisation processes. As
 4888 we shall see later, even without depolarisation certain dipole layouts can reduce the equilibrium polarisation
 4889 to below 92.4 %.

4890 Analytical estimates of the attainable equilibrium polarisation are best based on the Derbenev-Kondratenko
 4891 (D-K) formalism [?, ?]. This implicitly asserts that the value of the equilibrium polarisation in an e^\pm storage
 4892 ring is the same at all points in phase space and is given by

$$P_{\text{dk}} = \mp \frac{8}{5\sqrt{3}} \frac{\oint ds \left\langle \frac{1}{|\rho(s)|^3} \hat{b} \cdot \left(\hat{n} - \frac{\partial \hat{n}}{\partial \delta} \right) \right\rangle_s}{\oint ds \left\langle \frac{1}{|\rho(s)|^3} \left(1 - \frac{2}{9} (\hat{n} \cdot \hat{s})^2 + \frac{11}{18} \left| \frac{\partial \hat{n}}{\partial \delta} \right|^2 \right) \right\rangle_s} \quad (7.22)$$

4893 where $\langle \rangle_s$ denotes an average over phase space at azimuth s , \hat{s} is the direction of motion and $\hat{b} = (\hat{s} \times \dot{\hat{s}})/|\dot{\hat{s}}|$.
 4894 \hat{b} is the magnetic field direction if the electric field vanishes and the motion is perpendicular to the magnetic
 4895 field. $\hat{n}(u; s)$ is a unit 3-vector field over the phase space satisfying the Thomas-BMT equation along particle
 4896 trajectories $u(s)$ (which are assumed to be integrable), and it is 1-turn periodic: $\hat{n}(u; s + C) = \hat{n}(u; s)$ where
 4897 C is the circumference of the ring.

4898 The field $\hat{n}(u; s)$ is a key object for systematising spin dynamics in storage rings. It provides a reference
 4899 direction for spin at each point in phase space and it is now called the “invariant spin field” [?, ?, ?]. At
 4900 zero orbital amplitude, i.e. on the periodic (“closed”) orbit, the $\hat{n}(0; s)$ is written as $\hat{n}_0(s)$. For e^\pm rings and
 4901 away from spin-orbit resonances (see below), \hat{n} is normally at most a few milliradians away from \hat{n}_0 .

4902 A central ingredient of the D-K formalism is the implicit assumption that the e^\pm polarisation at each
 4903 point in phase space is parallel to \hat{n} at that point. In the approximation that the particles have the same
 4904 energies and are travelling in the same direction, the polarisation of a bunch measured in a polarimeter at
 4905 s is then the ensemble average

$$\vec{P}_{\text{ens,dk}}(s) = P_{\text{dk}} \langle \hat{n} \rangle_s. \quad (7.23)$$

4906 In conventional situations in e^\pm rings, $\langle \hat{n} \rangle_s$ is very nearly aligned along $\hat{n}_0(s)$. The *value* of the ensemble
 4907 average, $P_{\text{ens,dk}}(s)$, is essentially independent of s .

4908

Equation ?? can be viewed as having three components. The piece

$$P_{\text{bk}} = \mp \frac{8}{5\sqrt{3}} \frac{\oint ds \left\langle \frac{1}{|\rho(s)|^3} \hat{b} \cdot \hat{n} \right\rangle_s}{\oint ds \left\langle \frac{1}{|\rho(s)|^3} \left(1 - \frac{2}{9} (\hat{n} \cdot \hat{s})^2\right) \right\rangle_s} \approx \mp \frac{8}{5\sqrt{3}} \frac{\oint ds \frac{1}{|\rho(s)|^3} \hat{b} \cdot \hat{n}_0}{\oint ds \frac{1}{|\rho(s)|^3} \left(1 - \frac{2}{9} n_{0s}^2\right)}. \quad (7.24)$$

4909

4910

4911

4912

4913

4914

4915

4916

gives the equilibrium polarisation due to radiative spin flip. The quantity n_{0s} is the component of \hat{n}_0 along the closed orbit. The subscript “bk” is used here instead of “st” to reflect the fact that this is the generalisation by Baier and Katkov [?, ?] of the original S-T expression to cover the case of piecewise homogeneous fields. Depolarisation is then accounted for by including the term with $\frac{11}{18} \left| \frac{\partial \hat{n}}{\partial \delta} \right|^2$ in the denominator. Finally, the term with $\frac{\partial \hat{n}}{\partial \delta}$ in the numerator is the so-called kinetic polarisation term. This results from the dependence of the radiation power on the initial spin direction and is not associated with spin flip. It can normally be neglected but is still of interest in rings with special layouts.

In the presence of radiative depolarisation the rate in Eq. ?? must be replaced by

$$\tau_{\text{dk}}^{-1} = \frac{5\sqrt{3}}{8} \frac{r_e \gamma^5 \hbar}{m_e C} \oint ds \left\langle \frac{1 - \frac{2}{9} (\hat{n} \cdot \hat{s})^2 + \frac{11}{18} \left| \frac{\partial \hat{n}}{\partial \delta} \right|^2}{|\rho(s)|^3} \right\rangle_s. \quad (7.25)$$

4917

This can be written in terms of the spin-flip polarisation rate, τ_{bk}^{-1} , and the depolarisation rate, τ_{dep}^{-1} , as:

$$\frac{1}{\tau_{\text{dk}}} = \frac{1}{\tau_{\text{bk}}} + \frac{1}{\tau_{\text{dep}}}, \quad (7.26)$$

4918

where

$$\tau_{\text{dep}}^{-1} = \frac{5\sqrt{3}}{8} \frac{r_e \gamma^5 \hbar}{m_e C} \oint ds \left\langle \frac{\frac{11}{18} \left| \frac{\partial \hat{n}}{\partial \delta} \right|^2}{|\rho(s)|^3} \right\rangle_s \quad (7.27)$$

4919

and

$$\tau_{\text{bk}}^{-1} = \frac{5\sqrt{3}}{8} \frac{r_e \gamma^5 \hbar}{m_e C} \oint ds \left\langle \frac{1 - \frac{2}{9} (\hat{n} \cdot \hat{s})^2}{|\rho(s)|^3} \right\rangle_s. \quad (7.28)$$

4920

The time dependence for build-up from an initial polarisation P_0 to equilibrium is

$$P(t) = P_{\text{ens,dk}} \left[1 - e^{-t/\tau_{\text{dk}}} \right] + P_0 e^{-t/\tau_{\text{dk}}}. \quad (7.29)$$

4921

4922

4923

4924

4925

4926

4927

4928

4929

4930

4931

4932

In perfectly aligned e^\pm storage rings containing just horizontal bends, quadrupoles and accelerating cavities, there is no vertical betatron motion and $\hat{n}_0(s)$ is vertical. Since the spins do not “see” radial quadrupole fields and since the electric fields in the cavities are essentially parallel to the particle motion, \hat{n} is vertical, parallel to the guide fields and to $\hat{n}_0(s)$ at all u and s . Then the derivative $\frac{\partial \hat{n}}{\partial \delta}$ vanishes and there is no depolarisation. However, real rings have misalignments. Then there is vertical betatron motion so that the spins also see radial fields which tilt them from the vertical. Moreover, $\hat{n}_0(s)$ is also tilted and the spins can couple to vertical quadrupole fields too. As a result \hat{n} becomes dependent on u and “fans out” away from $\hat{n}_0(s)$ by an amount which usually increases with the orbit amplitudes. Then in general $\frac{\partial \hat{n}}{\partial \delta}$ no longer vanishes in the dipoles (where $1/|\rho(s)|^3$ is large) and depolarisation occurs. In the presence of skew quadrupoles and solenoids and, in particular, in the presence of spin rotators, $\frac{\partial \hat{n}}{\partial \delta}$ can be non-zero in dipoles even with perfect alignment. The deviation of \hat{n} from $\hat{n}_0(s)$, and the depolarisation, tend to be particularly large near to the spin-orbit resonance condition

$$\nu_0 = k_0 + k_I Q_I + k_{II} Q_{II} + k_{III} Q_{III}. \quad (7.30)$$

4933

4934

Here $k_0, k_I, k_{II}, k_{III}$ are integers, Q_I, Q_{II}, Q_{III} are the three tunes of the synchrotron motion and ν_0 is the spin tune on the closed orbit, i.e. the number of precessions around $\hat{n}_0(s)$ per turn, made by a spin on

4935 the closed orbit ¹. In the special case, or in the approximation, of no synchrotron coupling one can make
4936 the associations: $I \rightarrow x$, $II \rightarrow y$ and $III \rightarrow s$, where, here, the subscript s labels the synchrotron mode.
4937 In a simple flat ring with no closed-orbit distortion, $\nu_0 = a\gamma$ where γ is the Lorentz factor for the nominal
4938 beam energy. For e^\pm , $a\gamma$ increments by 1 for every 441 MeV increase in beam energy. In the presence of
4939 misalignments and special elements like rotators, ν_0 is usually still approximately proportional to the beam
4940 energy. Thus an energy scan will show peaks in τ_{dep}^{-1} and dips in $P_{\text{ens,dk}}(s)$, namely at around the resonances.
4941 Examples can be seen in figures ?? and ?? below. The resonance condition expresses the fact that the
4942 disturbance to spins is greatest when the $|\vec{\Omega}(u; s) - \vec{\Omega}(0; s)|$ along a trajectory is coherent (“in step”) with
4943 the natural spin precession. The quantity $(|k_I| + |k_{II}| + |k_{III}|)$ is called the order of the resonance. Usually,
4944 the strongest resonances are those for which $|k_I| + |k_{II}| + |k_{III}| = 1$, i.e. the first-order resonances. The next
4945 strongest are usually the so-called “*synchrotron sideband resonances*” of parent first-order resonances, i.e.
4946 resonances for which $\nu_0 = k_0 \pm Q_{I,II,III} + \bar{k}_{III} Q_{III}$ where \bar{k}_{III} is an integer and mode III is associated with
4947 synchrotron motion. All resonances are due to the non-commutation of successive spin rotations in 3-D and
4948 they therefore occur even with purely linear orbital motion.

4949 We now list some keys points.

- 4950 • The approximation on the r.h.s. of Eq. ?? makes it clear that if there are dipole magnets with fields
4951 not parallel to \hat{n}_0 , as is the case, for example, when spin rotators are used, then P_{bk} can be lower than
4952 the 92.4% achievable in the case of a simple ring with no solenoids and where all dipole fields and $\hat{n}_0(s)$
4953 are vertical.
- 4954 • If, as is usual, the kinetic polarisation term makes just a small contribution, the above formulae can
4955 be combined to give

$$P_{\text{ens,dk}} \approx P_{\text{bk}} \frac{\tau_{\text{dk}}}{\tau_{\text{bk}}} . \quad (7.31)$$

4956 From Eq. ?? it is clear that $\tau_{\text{dk}} \leq \tau_{\text{bk}}$.

- 4957 • The underlying rate of polarisation due to the S-T effect, τ_{bk}^{-1} , increases with the fifth power of the
4958 energy and decreases with the third power of the bending radii.
- 4959 • It can be shown that as a general rule the “normalised” strength of the depolarisation, $\tau_{\text{dep}}^{-1}/\tau_{\text{bk}}^{-1}$,
4960 increases with beam energy according to a tune-dependent polynomial in even powers of the beam
4961 energy. So we expect that the attainable equilibrium polarisation decreases as the energy increases.
4962 This was confirmed LEP, where with the tools available, little polarisation could be obtained at 60
4963 GeV [?].

4964 7.10.2 Suppression of depolarisation – spin matching

4965 Although the S-T effect offers a convenient way to obtain stored high energy e^\pm beams, it is only useful in
4966 practice if there is not too much depolarisation. Depolarisation can be significant if the ring is misaligned,
4967 if it contains spin rotators or if it contains uncompensated solenoids or skew quadrupoles. Then if $P_{\text{ens,dk}}$
4968 and/or τ_{dk} are too small, the layout and the optic must be adjusted so that $(|\frac{\partial \hat{n}}{\partial \delta}|)^2$ is small where $1/|\rho(s)|^3$
4969 is large. So far it is only possible to do this within the linear approximation for spin motion. This technique
4970 is called “*linear spin matching*” and when successful, as for example at HERA [?], it immediately reduces
4971 the strengths of the first-order spin-orbit resonances. Spin matching requires two steps: “*strong synchrobeta*
4972 *spin matching*” is applied to the optics and layout of the perfectly aligned ring and then “*harmonic closed-*
4973 *orbit spin matching*” is applied to soften the effects of misalignments. This latter technique aims to adjust
4974 the closed orbit so as to reduce the tilt of \hat{n}_0 from the vertical in the arcs. Since the misalignments can
4975 vary in time and are usually not sufficiently well known, the adjustments are applied empirically while the
4976 polarisation is being measured.

4977 Spin matching must be approached on a case-by-case basis. An overview can be found in [?].

¹In fact the resonance condition should be more precisely expressed in terms of the so-called amplitude dependent spin tune [?, ?, ?]. But for typical e^\pm rings, the amplitude dependent spin tune differs only insignificantly from ν_0 .

4978 7.10.3 Higher order resonances

4979 Even if the beam energy is chosen so that first-order resonances are avoided and in linear approximation
 4980 $P_{\text{ens,dk}}$ and/or τ_{dk} are expected to be large, it can happen that that beam energy corresponds to a higher
 4981 order resonance. As mentioned above, in practice the most intrusive higher order resonances are those for
 4982 which $\nu_0 = k_0 \pm Q_k + \tilde{k}_s Q_s$ ($k \equiv I, II$ or III). These synchrotron sideband resonances of the first-order
 4983 parent resonances are due to modulation by energy oscillations of the instantaneous rate of spin precession
 4984 around \hat{n}_0 . The depolarisation rates associated with sidebands of isolated parent resonances ($\nu_0 = k_0 \pm Q_k$)
 4985 are related to the depolarisation rates for the parent resonances. For example, if the beam energy is such
 4986 that the system is near to a dominant Q_y resonance we can approximate τ_{dep}^{-1} in the form

$$\tau_{\text{dep}}^{-1} \propto \frac{A_y}{(\nu_0 - k_0 \pm Q_y)^2}. \quad (7.32)$$

4987 This becomes

$$\tau_{\text{dep}}^{-1} \propto \sum_{\tilde{k}_s=-\infty}^{\infty} \frac{A_y B_y(\zeta; \tilde{k}_s)}{(\nu_0 - k_0 \pm Q_y \pm \tilde{k}_s Q_s)^2}$$

4988 if the synchrotron sidebands are included. The quantity A_y depends on the beam energy and the optics and
 4989 is reduced by spin matching. The proportionality constants $B_y(\zeta; \tilde{k}_s)$ are called *enhancement factors*, and
 4990 they contain modified Bessel functions $I_{|\tilde{k}_s|}(\zeta)$ and $I_{|\tilde{k}_s|+1}(\zeta)$ which depend on Q_s and the energy spread σ_δ
 4991 through the *modulation index* $\zeta = (a\gamma \sigma_\delta / Q_s)^2$. More formulae can be found in [?, ?].

4992 Thus the effects of synchrotron sideband resonances can be reduced by doing the spin matches described
 4993 above. Note that these formulae are just meant as a guide since they are approximate and explicitly neglect
 4994 interference between the first-order parent resonances. To get a complete impression, the Monte-Carlo
 4995 simulation mentioned later must be used. The sideband strengths generally increase with the energy spread
 4996 and the beam energy and the sidebands are a major contributor to the increase of $\tau_{\text{dep}}^{-1} / \tau_{\text{bk}}^{-1}$ with energy.

4997 7.10.4 Spin rotators

4998 The LHeC, like all analogous projects involving spin, needs longitudinal polarisation at the interaction point.
 4999 However, if the S-T effect is to be the means of producing and maintaining the polarisation, then as is clear
 5000 from Eq. ??, \hat{n}_0 must be close to vertical in most of the dipoles. We have seen at Eq. ?? that the polarisation
 5001 is essentially parallel to \hat{n}_0 . So to get longitudinal polarisation at a detector, it must be arranged that \hat{n}_0
 5002 is longitudinal at the detector but vertical in the rest of the ring. This can be achieved with magnet systems
 5003 called spin rotators which rotate \hat{n}_0 from vertical to longitudinal on one side of the detector and back to
 5004 vertical again on the other side.

5005 Spin rotators use sequences of magnets which generate large spin rotations around different axes and
 5006 exploit the non-commutation of successive large rotations around different axes. According to the T-BMT
 5007 equation, the rate of spin precession in longitudinal fields is inversely proportional to the energy. However,
 5008 for motion perpendicular to a magnetic field spins precess at a rate essentially proportional to the energy:
 5009 $\delta\theta_{\text{spin}} = (a\gamma + 1)\delta\theta_{\text{orb}}$ in obvious notation. Thus for the high-energy ring considered here, spin rotators
 5010 should be based on dipoles as in HERA [?]. In that case the rotators consisted of interleaved horizontal and
 5011 vertical bending magnets set up so as to generate interleaved, closed, horizontal and vertical bumps in the
 5012 design orbit. The individual orbit deflections were small but the spin rotations were of the order of a radian.
 5013 The success in obtaining high longitudinal polarisation at HERA attests to the efficacy of such rotators.

5014 Eq. ?? shows that P_{bk} essentially scales with the cosine of the angle of tilt of \hat{n}_0 from the vertical in the
 5015 arc dipoles. Thus a rotation error resulting in a tilt of \hat{n}_0 of even a few degrees would not reduce P_{bk} by
 5016 too much. However, as was mentioned above, a tilt of \hat{n}_0 in the arcs can lead to depolarisation. In fact the
 5017 calculations below show that at 60 GeV, tilts of more than a few milliradians cause significant depolarisation.
 5018 Thus well-tuned rotators are essential for maintaining polarisation.

7.10.5 Calculations of the e^\pm polarisation in the LHeC

As a first step towards assessing the attainable polarisation we have considered an early version of the LHeC lattice: a flat ring with no rotators, no interaction point and no bypasses. The tunes are $Q_x = 123.83$ and $Q_y = 85.62$. The horizontal emittance is 8 nm which agrees well with the on-momentum emittance calculated by MadX. The ring is therefore typical of the designs under consideration. With perfect alignment, \hat{n}_0 is vertical everywhere and there is no vertical dispersion. The polarisation will then reach 92.4%. At ≈ 60 GeV, $\tau_{bk} \approx 60$ minutes.

For the simple flat ring these values can be obtained by hand from Eq. ?? and Eq. ?. However, in general, e.g., in the presence of misalignments or rotators, the calculation of polarisation requires special software and for this study, the thick-lens code SLICKTRACK was used [?]. This essentially consists of four sections which carry out the following tasks:

- (1) Simulation of misalignments followed by orbit correction with correction coils.
 - (2) Calculation of the optical properties of the beam and the beam sizes.
 - (3) Calculation of $\partial\hat{n}/\partial\delta$ for linearised spin motion with the thick-lens version (SLICK [?]) of the SLIM algorithm [?].
- The equilibrium polarisation is then obtained from Eq. ?. This provides a first impression and only exhibits the first order resonances.
- (4) Calculation of the rate of depolarisation beyond the linear approximation of item 3.

In general, the numerical calculation of the integrand in Eq. ? beyond first order represents a difficult computational problem. Therefore a pragmatic approach is adopted, whereby the rate of depolarisation is obtained with a Monte-Carlo spin-orbit tracking algorithm which includes radiation emission. The algorithm employs full 3-D spin motion in order to see the effect of the higher order resonances. The Monte-Carlo algorithm can also handle the effect on the particles and on the spins of the non-linear beam-beam forces. An estimate of the equilibrium polarisation is then obtained from Eq. ?.

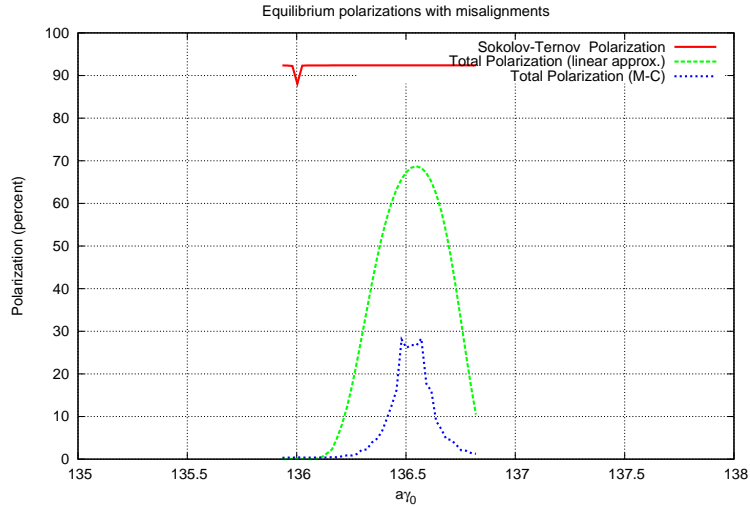


Figure 7.45: Estimated polarisation for the LHeC without spin rotators, $Q_s = 0.06$.

Some basic features of the polarisation for the misaligned flat ring are shown in figures ?? and ?? where polarisations are plotted against $a\gamma$ around 60 GeV. In both cases the r.m.s. vertical closed-orbit deviation

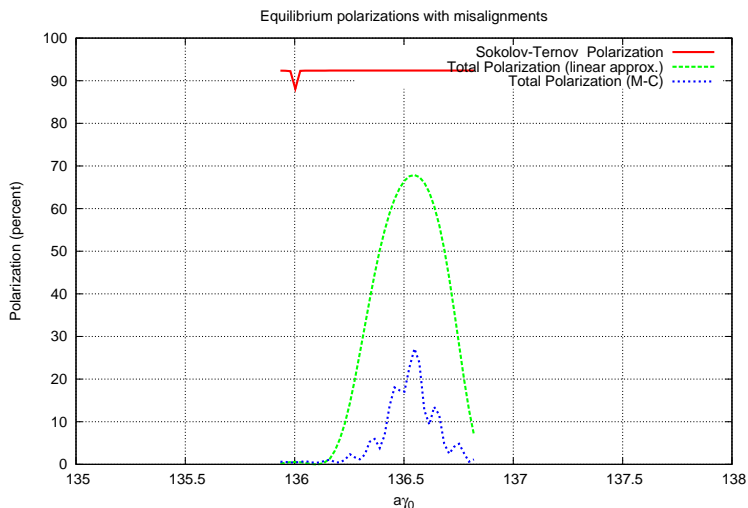


Figure 7.46: Estimated polarisation for the LHeC without spin rotators, $Q_s = 0.1$.

5045 is about $75\mu\text{m}$. This is obtained after giving the quadrupoles r.m.s. vertical misalignments of $150\mu\text{m}$ and
 5046 assigning a correction coil to every quadrupole. The vector \hat{n}_0 has an r.m.s. tilt of about 4 milliradians from
 5047 the vertical near $a\gamma = 136.5$. For figure ?? the synchrotron tune, Q_s , is 0.06 so that $\xi \approx 5$. For figure ??,
 5048 $Q_s = 0.1$ so that $\xi \approx 1.9$.

5049 The red curves depict the polarisation due to the Sokolov-Ternov effect alone. The dip to below 92.4
 5050 % at $a\gamma = 136$ is due to the characteristic very large tilt of \hat{n}_0 from the vertical at an integer value of $a\gamma$.
 5051 See [?].

5052 The green curves depict the equilibrium polarisation after taking into account the depolarisation associ-
 5053 ated with the misalignments and the consequent tilt of \hat{n}_0 . The polarisation is calculated with the linearised
 5054 spin motion as in item 3 above. In these examples the polarisation reaches about 68 %. The strong fall off
 5055 on each side of the peak is mainly due to first-order ‘‘synchrotron’’ resonances $\nu_0 = k_0 \pm Q_s$. Since Q_s is
 5056 small these curves are similar for the two values of Q_s .

5057 The blue curves show the polarisation obtained as in item 4 above. Now, by going beyond the linearisation
 5058 of the spin motion, the peak polarisation is about 27 %. The fall from 68 % is mainly due to synchrotron
 5059 sideband resonances. With $Q_s = 0.06$ (Fig. ??) the resonances are overlapping. With $Q_s = 0.1$, (Fig. ??) the
 5060 sidebands begin to separate. In any case these curves demonstrate the extreme sensitivity of the attainable
 5061 polarisation to small tilts of \hat{n}_0 at high energy. Simulations for $Q_s = 0.1$ with a series of differently misaligned
 5062 rings, all with r.m.s. vertical closed-orbit distortions of about $75\mu\text{m}$, exhibit peak equilibrium polarisations
 5063 ranging from about about 10 % to about 40 %. Experience at HERA suggests that harmonic closed-orbit
 5064 spin matching can eliminate the cases of very low polarisation.

5065 Figure ?? shows a typical energy dependence of the peak equilibrium polarisation for a fixed rf voltage
 5066 and for one of the misaligned rings. The synchrotron tune varies from $Q_s = 0.093$ at 40 GeV to $Q_s = 0.053$
 5067 at 65 GeV due to the change in energy loss per turn. As expected the attainable polarisation falls steeply
 5068 as the energy increases. However, although with this good alignment, a high polarisation is predicted at 45
 5069 GeV, τ_{bk} would be about 5 hours as at LEP. A small τ_{bk} is not only essential for a programme of particle
 5070 physics, but essential for the application of empirical harmonic closed-orbit spin matching.

5071 As mentioned above it was difficult to get polarisation at 60 GeV at LEP. However, these calculations
 5072 suggest that by adopting the levels of alignment that are now standard for synchrotron-radiation sources
 5073 and by applying harmonic closed-orbit spin matching, there is reason to hope that high polarisation in a flat
 5074 ring can still be obtained.

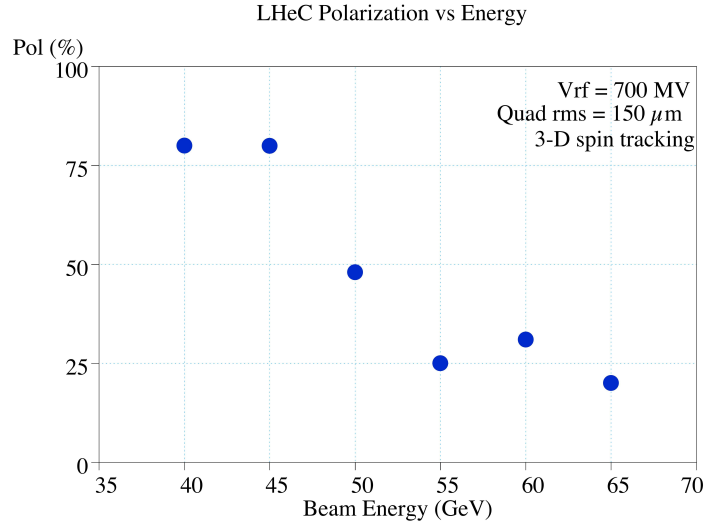


Figure 7.47: Equilibrium polarisation *vs* ring energy, full 3-D spin tracking results

5075 7.10.6 Further work

5076 We now list the next steps towards obtaining longitudinal polarisation at the interaction point.

5077 (1) A harmonic closed-orbit spin matching algorithm must be implemented for the LHeC to try to correct
 5078 the remaining tilt of \hat{n}_0 and thereby increase the equilibrium polarisation.

5079 (2) Practical spin rotators must be designed and appropriate strong synchrobeta spin matching must be
 5080 implemented. The design of the rotators and spin matching are closely linked. Some preliminary
 5081 numerical investigations (below) show, as expected, that without this spin matching, little polarisation
 5082 will be obtained.

5083 (3) If synchrotron sideband resonances are still overwhelming after items 1 and 2 are implemented, a
 5084 scheme involving Siberian Snakes could be tried. Siberian Snakes are arrangements of magnets which
 5085 manipulate spin on the design orbit so that the closed-orbit spin tune is independent of beam energy.
 5086 Normally the spin tune is then 1/2 and heuristic arguments suggest that the sidebands should be
 5087 suppressed. However, the two standard schemes [?] either cause \hat{n}_0 to lie in the machine plane (just
 5088 one snake) or ensure that it is vertically up in one half of the ring and vertically down in the other
 5089 half (two snakes). In both cases Eq. ?? shows that P_{bk} vanishes. In principle, this problem can be
 5090 overcome for two snakes by again appealing to Eq. ?? and having short strong dipoles in the half of
 5091 the ring where \hat{n}_0 points vertically up and long weaker dipoles in the half of the ring where \hat{n}_0 points
 5092 vertically down (or vice versa). Of course, the dipoles must be chosen so that the total bend angle is
 5093 π in each half of the ring. Moreover, Eq. ?? shows that the pure Sokolov-Ternov polarisation would
 5094 be much less than 92.4%. One version of this concept [?] uses a pair of rotators which together form
 5095 a snake while a complementary snake is inserted diametrically opposite to the interaction point. Each
 5096 rotator comprises interleaved strings of vertical and horizontal bends which not only rotate the spins
 5097 from vertical to horizontal, but also bring the e^\pm beams down to the level of the proton beam and then
 5098 up again. However, the use of short dipoles in the arcs increases the radiation losses.

5099 Note that because of the energy dependence of spin rotations in the dipoles, \hat{n}_0 is vertical in the arcs
 5100 at just one energy. This concept has been tested with SLICKTRACK but in the absence of a strong

synchrobeta spin match, the equilibrium polarisation is very small as expected. Nevertheless the effects of misalignments and the tilt of \hat{n}_0 away from design energy, have been isolated by imposing an artificial spin match using standard facilities in SLICKTRACK. The snake in the arc has been represented as a thin element that has no influence on the orbital motion. Then it looks as if the synchrotron sidebands are indeed suppressed in the depolarisation associated with tilts of \hat{n}_0 . In contrast to the rotators in HERA, this kind of rotator allows only one helicity for electrons and one for positrons.

- (4) If a scheme can be found which delivers sufficient longitudinal polarisation, the effect of non-linear orbital motion, the effect of beam-beam forces and the effect of the magnetic fields of the detector must then be studied.

7.10.7 Summary

We have investigated the possibility of polarisation in the LHeC electron ring. At this stage of the work it appears that a polarisation of between 25 and 40% at 60 GeV can be reasonably aimed for, assuming the efficacy of harmonic closed-orbit spin matching. Attaining this degree of polarisation will require precision alignment of the magnets to better than $150\mu\text{m}$ rms, a challenging but achievable goal. The spin rotators necessary at the IP need to be properly spin matched to avoid additional depolarisation and this work is in progress. An interesting alternative involving the use of Siberian Snakes to try to avoid the depolarising synchrotron sideband resonances is being investigated. At present, this appears to potentially yield a similar degree of polarisation, at the expense of increased energy dissipation in the arcs arising from the required differences of the bending radii in the two halves of the machine.

7.11 Integration and machine protection issues

7.11.1 Space requirements

The integration of an additional electron accelerator into the LHC is a difficult task. For once, the LEP tunnel was designed for LEP and not for the LHC, which is now using up almost all space in the tunnel. It is not evident, how to place another accelerator into the limited space. Secondly, the LHC will run for several years, before the installation of a second machine can start. Meanwhile the tunnel will be irradiated and all installation work must proceed as fast as possible to limit the collective and individual doses. The activation after the planned high-luminosity-run of the LHC and after one month of cool-down is expected to be around $0.5 \dots 1 \mu\text{Sv/h}$ [?] on the proton magnets and many times more at exposed positions. Moreover the time windows for installation will be short and other work for the LHC will be going on, maybe with higher priority. Nevertheless, with careful preparation and advanced installation schemes an electron accelerator can be fitted in.

For the installation of the LHC machine proper, all heavy equipment had to pass the UJ2, while entering the tunnel. There the equipment had to be moved from TI2, which comes in from the outside, to the transport zone of LHC, which is on the inner side of the ring. Clearly, applying this procedure to the installation of the LHeC everything above the cold dipoles has to be removed. The new access shafts and the smaller size of the equipment for the electron ring may render this operation unnecessary.

General The new electron accelerator will be partially in the existing tunnel and partially in specially excavated tunnel sections and behind the experiments in existing underground areas. The excavation work will need special access shafts in the neighborhood of the experiments from where the stub-tunnels can be driven. The connection to the existing LEP tunnels will be very difficult. The new tunnel enters with a very small grazing angle, which means over a considerable length. Very likely the proton installation will have to be removed while the last meters of the new tunnel is bored.

Figure ?? shows a typical cross section of the LHC tunnel, where the two machines are together. The LHC dipole dominates the picture. The transport zone is indicated at the right (inside of the ring). The cryogenic installations (QRL) and various pipes and cable trays are on the left. The dipole cross section

5146 shows two concentric circles. The larger circle corresponds to the largest extension at the re-enforcement
 5147 rings and marks a very localized space restriction on a very long object. The inner circle is relevant for
 5148 items shorter than about 10 m longitudinally. A hatched square above the dipole labeled 30 indicates the
 5149 area, which was kept free in the beginning for an electron machine. Unfortunately, the center of this space
 5150 is right above the proton beam. Any additional machine will, however, have to avoid the interaction points
 5151 1 and 5. In doing so additional length will be necessary, which can only be compensated for by shifting
 5152 the electron machine in the arc about 60 cm to the inside (right), as indicated by the red square in Figure
 5153 ???. The limited space for compensation puts a constraint on the extra length created by the bypasses.
 5154 The transport zone will, however, be affected. This requires an unconventional way to mount the electron
 machine. Nevertheless, there is clearly space to place an electron ring into the LHC, for most of the arc.

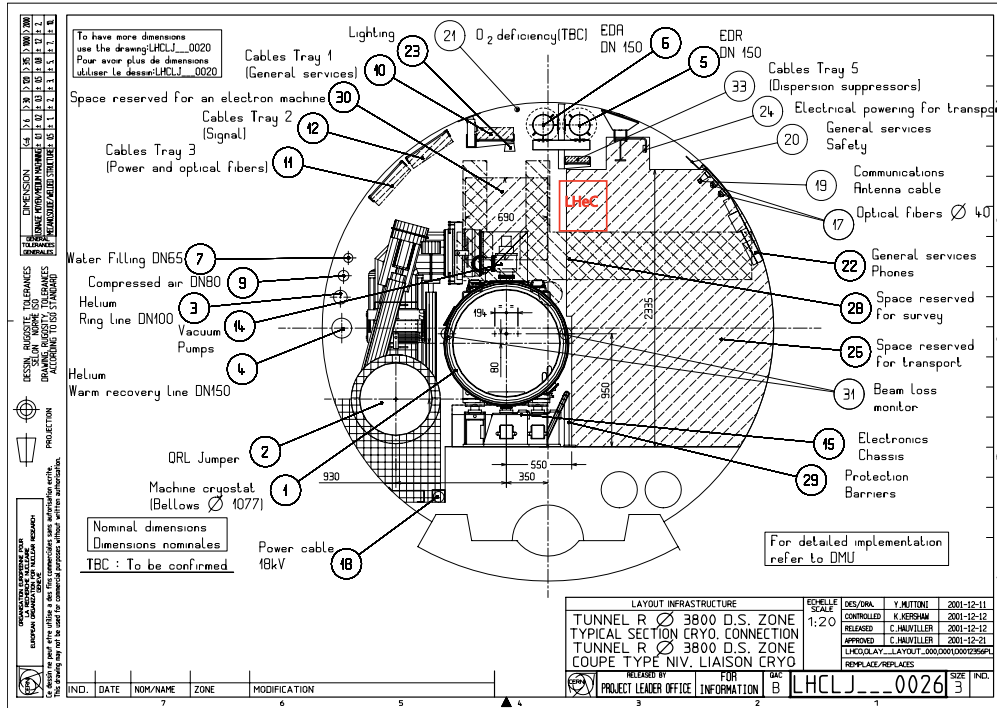


Figure 7.48: Cross-section of the LHC tunnel with the original space holder for the electron beam installation directly above the LHC cryostat and the shifted new required space due to the additional bypass in IR1 and IR5 and the need to keep the overall circumference of the electron ring identical to that of the proton beams.

5155 Figure ?? gives the impression that the tunnel for most of its length is not too occupied.
 5156

5157 **In the arc** In Fig. ?? one sees the chain of superconducting magnets and in the far distances the *QRL*
 5158 *Service Module* with its jumper, the cryogenic connection between the superconducting machine and the
 5159 cryogenic distribution line. The service modules come always at the position of every second quadrupole and
 5160 have a substantial length. The optics of the LHeC foresees no e-ring magnet at these positions. A photo of
 5161 service modules in the workshop is shown in figure ?? (courtesy CERN) illustrating that the QRL extends
 5162 substantially in the vertical direction above the LHC arc cryostat and cryo line. The picture ??, taken in
 5163 sector 3, shows also the critical tunnel condition in this part of the machine. Clearly, heavy loads cannot
 5164 be suspended from the tunnel ceiling. The limit is set to 100 kg per meter along the tunnel. The e-ring
 5165 components have to rest on stands from the floor wherever possible. See ?? on page ?. Normally there
 5166 is enough space between the LHC dipoles and the QRL to place a vertical 10 cm quadratic or rectangular



Figure 7.49: View of sector 4 showing the chain of superconducting magnets in the arc.



Figure 7.50: Sideview of a QRL service module with the jumper that extends vertically above the LHC cryostat and the cryogenic distribution line.

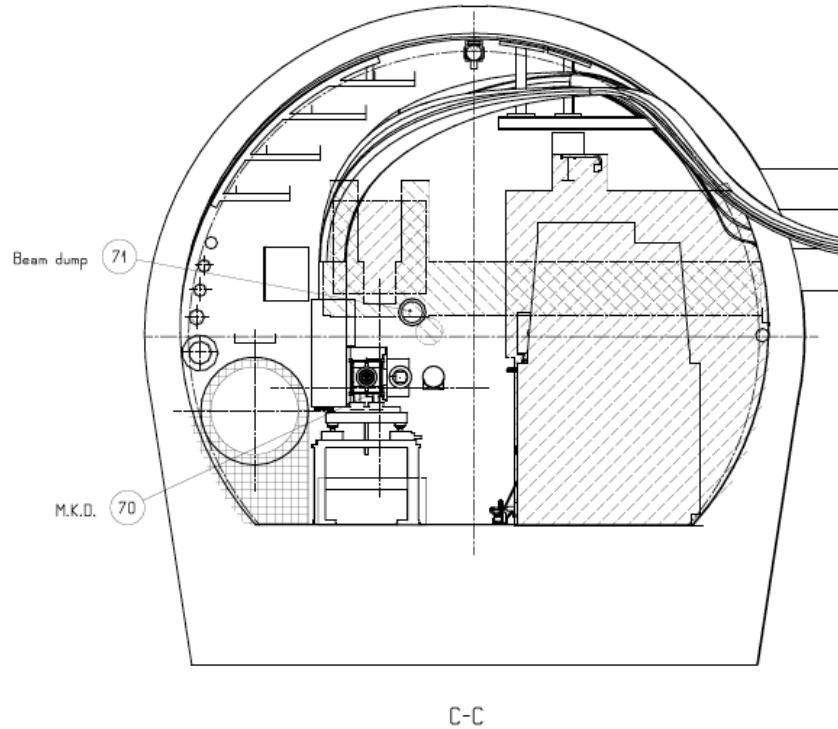


Figure 7.51: Dump kicker [?]

5167 support. Alternatively a steel arch bolted to the tunnel walls and resting on the floor can support the
 5168 components from above. This construction is required wherever the space for a stand is not available.

5169 The electron machine, though partially in the transport zone, will be high up in the tunnel, high enough
 5170 not to interfere with the transport of a proton magnet or alike. The transport of cryogenic equipment may
 5171 need the full height. Transports of that kind will only happen, when part of the LHC are warmed up. This
 5172 gives enough time to shift the electron ring to the outside by 30 cm, if the stands are prepared for this
 5173 operation. The outside movement causes also a small elongation of the inter-magnet connections. This effect
 5174 is locally so small that the expansion joints, required anyway, can accommodate it. One could even think
 5175 of moving large sections of the e-machine outwards in a semi-automatic way. Thus the time to clear the
 5176 transport path can be kept in the shadow of the warm-up and cool-down times.

5177 **Dump area** The most important space constraints for the electron machine are in the proton dump area,
 5178 the proton RF cavities, point 3, and in particular the collimator sections.

5179 Figure ?? [?] shows the situation at the dump kicker. The same area is also shown in a photo in Figure ??,
 5180 while Figure ?? shows one of the outgoing dump-lines. The installation of the e-machine requires the proper
 5181 rerouting of cables (which might be damaged by radiation and in need of exchange anyhow), eventually
 5182 turning of pumps by 90 degrees or straight sections in the electron optics to bridge particularly difficult
 5183 stretches with a beam pipe only.

5184 **Point 4, proton RF** The Figures ?? [?] and ?? illustrate the situation at the point 4, where the LHC RF
 5185 is installed. Fortunately, the area is not very long. A short straight section could be created for the electron
 5186 ring. This would allow to pass the area with just a shielded beam pipe.

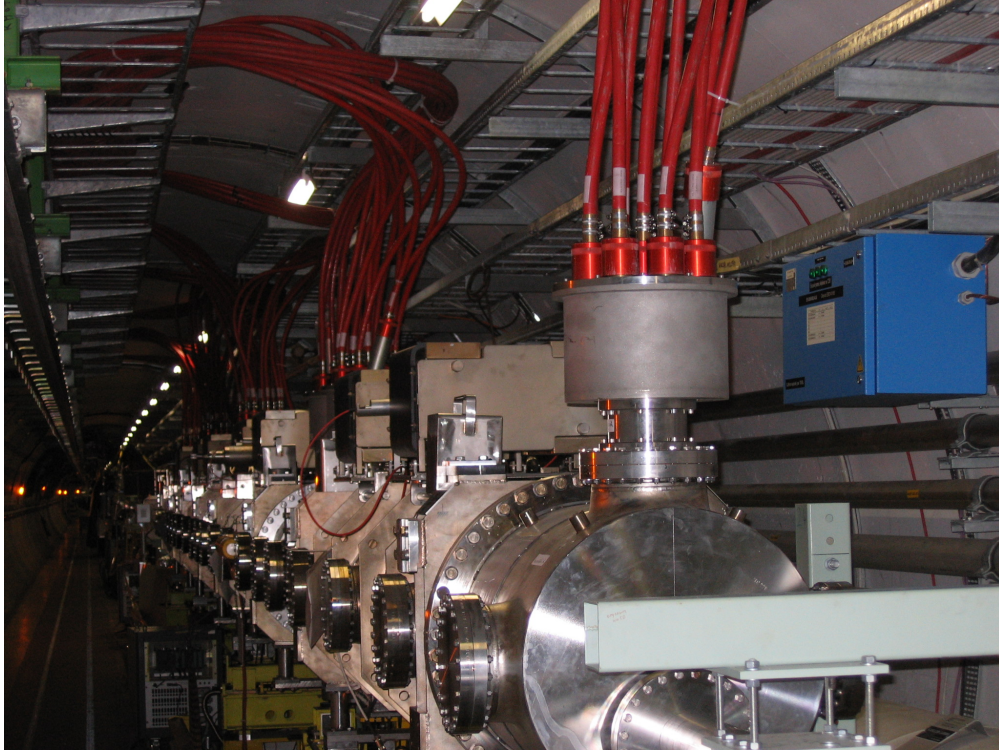


Figure 7.52: Dump kicker installation in IR6 for one of the two LHC proton rings.

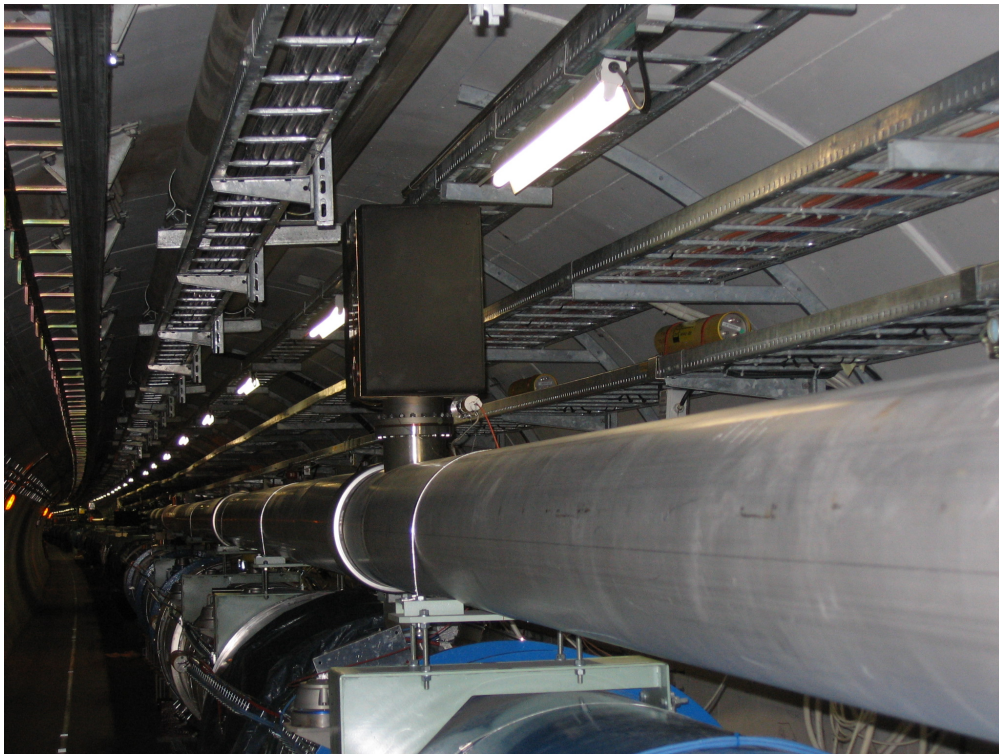
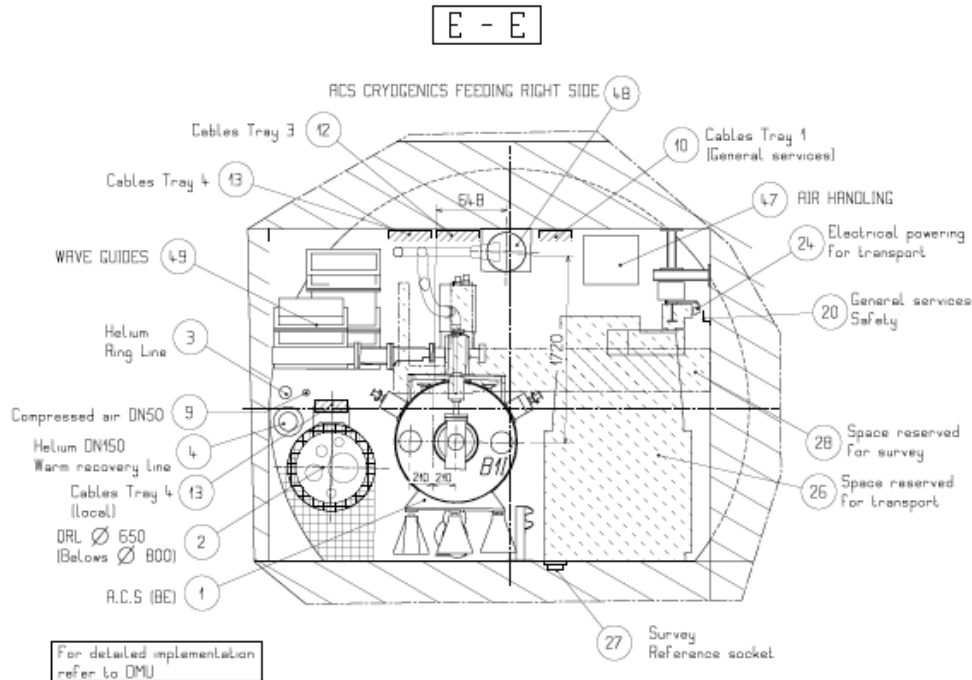


Figure 7.53: Dump line of one of the LHC proton rings.



h

Figure 7.54: Schematic tunnel cross section with the LHC Proton Proton RF in point 4 [?].

5187 **Cryolink in point 3** The geography around point 3 did not permit to place there a cryoplant. The
 5188 cryogenic cooling for the feedboxes is provided by a cryolink, as is shown in the figures ?? and ??. In
 5189 particular above the Q6 proton quadrupole changes have to be made. There are other interferences with
 5190 the cryogenics, as for example at the DFBA's (main feedboxes). An example is shown in figure ??. Eventually
 5191 the electron optics has to be adapted to allow the beampipe to pass the cables, which may have to be moved
 5192 a bit.

5193 **Long straight section 7** An extra air duct is mounted in the long straight section 7 (LSS7) as is indicated
 5194 in Fig. ?? (labelled Plenum de ventilation) avoiding the air pollution of the area above point 7. The duct
 5195 occupies the space planned for the electron machine. The air duct has to be replaced by a slightly different
 5196 construction mounted further outside (to the right in the figure). There are also air ducts at points 1 and 5,
 5197 but they are not an issue. The electron ring is passing behind the experiments in these points

5198 **Proton collimation** The areas around Point 3 (-62...+177m) and Point 7 (-149...+205m) [?] are heavily
 5199 used for the collimation of the proton beam. The high dose rate in the neighborhood of a collimator
 5200 makes special precautions for the installation of new components or the exchange of a collimator necessary.
 5201 Moreover, the collimator installation needs the full height of the tunnel. Hence, the electron ring installation
 5202 has to be suspended from the re-enforced tunnel roof. The electron machine components must be removable
 5203 and installable, easy and fast. The re-alignment must be well prepared and fast, possibly in a remote fashion.
 5204 It is uncommon to identify fast mounting and demounting as a major issue. However, with sufficient emphasis
 5205 during the R&D phase of the project, this problem can be solved.

5206 7.11.2 Impact of the synchrotron radiation on tunnel electronics

5207 It is assumed that the main power converters of the LHC will have been moved out of the RRs because of
 5208 the single event upsets, caused by proton losses.

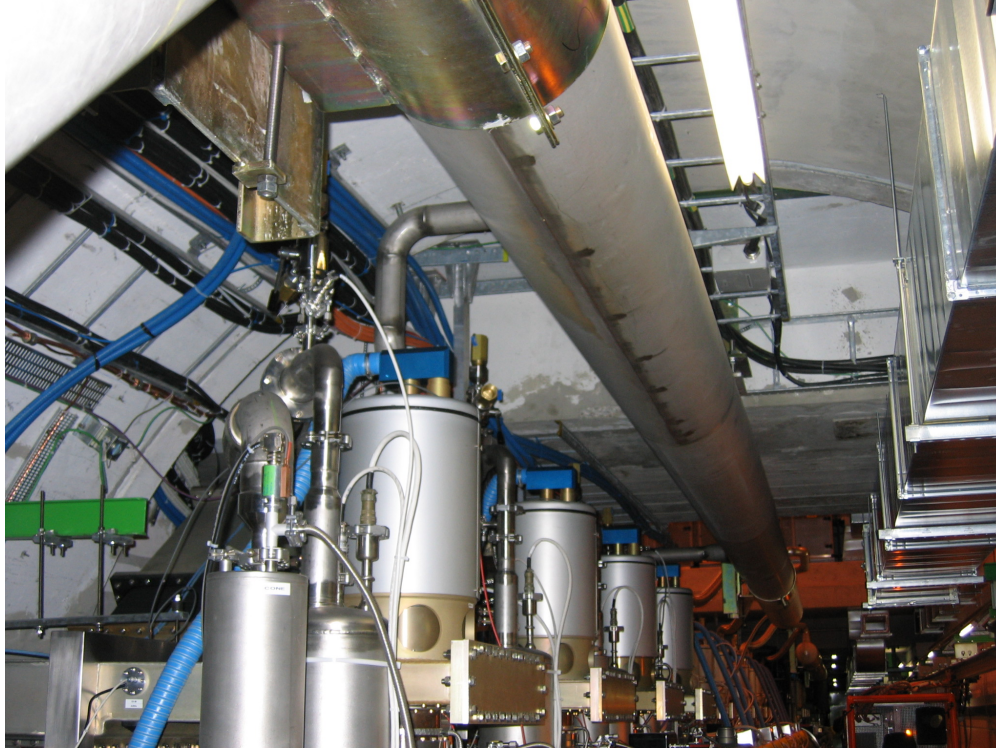


Figure 7.55: Tight space restriction in Point 4 due to the LHC proton RF installation.

5209 The synchrotron radiation has to be intercepted at the source, as in all other electron accelerators. A few
5210 millimeter of lead are sufficient for the relatively low (critical) energies around 100 to 200 keV. The K-edge
5211 of lead is at 88 keV, the absorption coefficient is above 80/cm at this energy [?]. One centimeter of lead is
5212 sufficient to suppress 300 keV photons by a factor of 100. Detailed calculations of the optics will determine
5213 the amount of lead needed in the various places. The primary shielding needs an effective water cooling to
5214 avoid partial melting of the lead.

5215 The electronics is placed below the proton magnets. Only backscattered photons with correspondingly
5216 lower energy will reach the electronics. If necessary, a few millimeter of extra shielding could be added here.

5217 The risk for additional single event upsets due to synchrotron radiation is negligible.

5218 7.11.3 Compatibility with the proton beam loss system

5219 The proton beam loss monitoring system works very satisfactory. It has been designed to detect proton
5220 losses by observing secondaries at the outside of the LHC magnets. The sensors are ionization chambers.
5221 Excessive synchrotron radiation (SR) background will presumably trigger the system and dump the proton
5222 beam. The SR background at the monitors has to be reduced by careful shielding of either the monitors or
5223 the electron ring. Alternatively, the impact of the photon background can be reduced by using a new loss
5224 monitoring system which is based on coincidences (as was done elsewhere [?]).

5225 7.11.4 Space requirements for the electron dump

5226 The electron beam of the LHeC installation requires a dedicated dump section. Potential interference of
5227 the losses during or after an electron beam dump with equipment of the LHC proton rings still needs to be
5228 studied and a suitable space still needs to be found in the LHC tunnel.

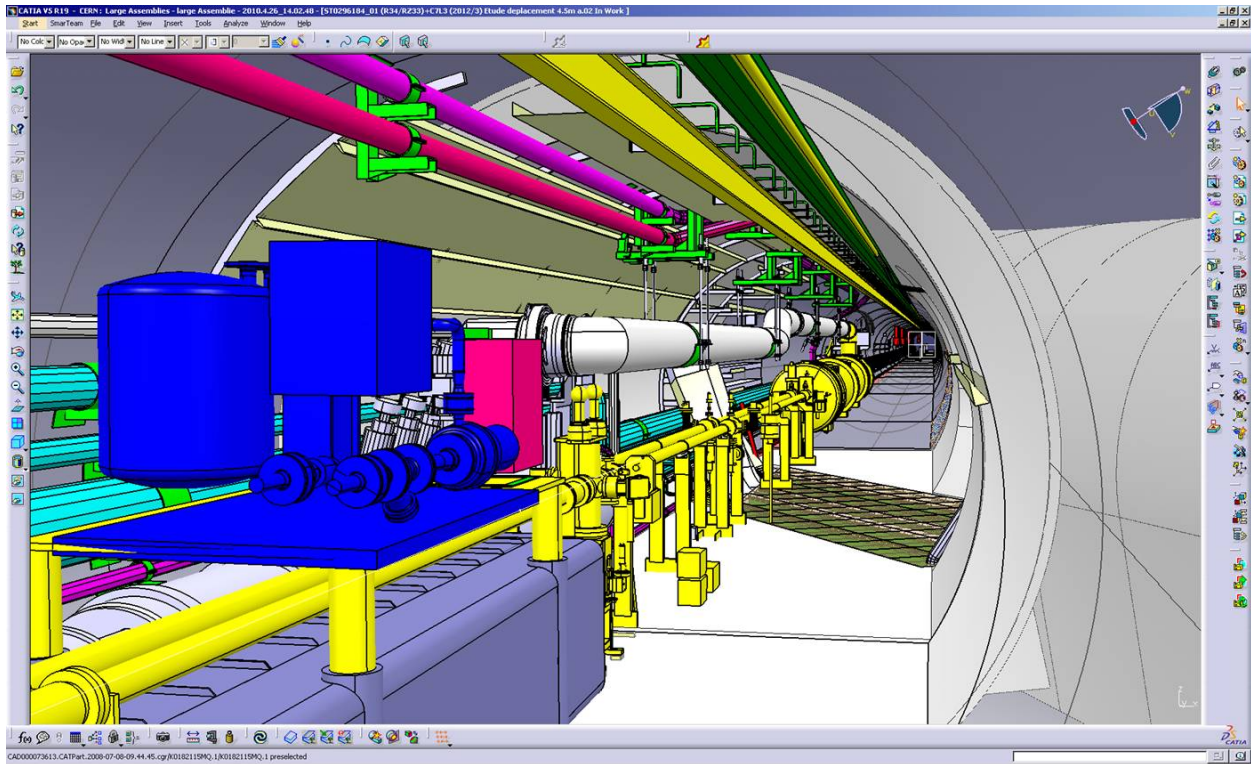


Figure 7.56: The cryogenic connection in point 3

5229 7.11.5 Protection of the p-machine against heavy electron losses

5230 The existing proton loss detectors are placed, as mentioned above, at the LHC magnets. The trigger threshold
 5231 requires certain number of detectors to be hit by a certain number of particles. The assumption is that the
 5232 particles come from the inside of the magnets and the particle density there is much higher. Electron losses,
 5233 creating a similar pattern in the proton loss detectors will result in a much lower particle density in the
 5234 superconducting coils. Hence, still tolerable electron losses will unnecessarily trigger the proton loss system
 5235 and dump the proton beam. The proton losses are kept at a low level by installing an advanced system of
 5236 collimators and masks. Fast changes of magnet currents, which will result in a beam loss, are detected. A
 5237 similar system is required for the electrons. An electron loss detection system, like the one mentioned in
 5238 Ref. [?], combined with the proton loss system can be used to identify the source of the observed loss pattern
 5239 and to minimize the electron losses by improved operation. It seems very optimistic to think of a hardware
 5240 discrimination system, which determines very fast the source of the loss and acts correspondingly. Such a
 5241 system could be envisaged only after several years of running.

5242 7.11.6 How to combine the Machine Protection of both rings?

5243 The existing machine-protection system combines many different subsystems. The proton loss system, the
 5244 quench detection system, cryogenics, vacuum, access, and many other subsystems may signal a dangerous
 5245 situation. This requirement lead to a very modular architecture, which could be expanded to include the
 5246 electron accelerator.

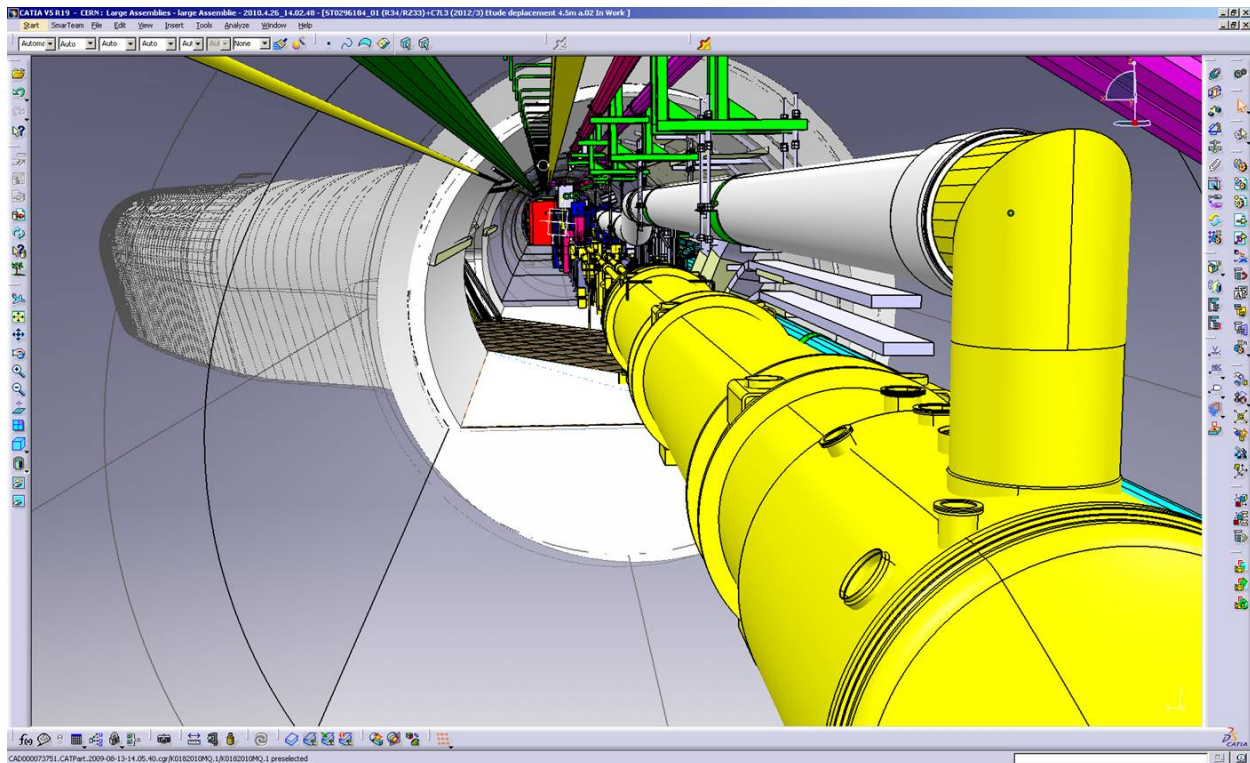


Figure 7.57: The cryogenic connection in point 3 (grey tube passing above the two LHC proton beam vacuum tubes [yellow]).

7.12 LHeC Injector for the Ring-Ring option

7.12.1 Injector

The LEP pre-injectors have been dismantled and the infrastructure re-used for the CLIC test facility CTF3. The RF cavities that accelerated leptons in the SPS have been removed to reduce its impedance. Re-installation of an injector chain similar to LEP's through the PS and SPS would be costly and potentially limit the proton performance.

The LHeC e-ring therefore requires new lepton injectors.

In the 30 years from the design of the LEP injectors, there has been substantial progress in accelerator technology. This is particularly true in the field of superconducting radio frequency technology which was very successfully used for LEP2 on a large scale and which has been further developed for TESLA and the ILC. It makes it feasible to design a very compact and efficient 10 GeV injector based on the principle of a recirculating LINAC and to take advantage of the studies for ELFE at CERN [?].

7.12.2 Required performance

The main requirements for the LHeC ring-ring electron and positron injectors are summarized in Table ??.

Polarization is not required from the ring injectors. It would be very difficult to maintain the polarization during the acceleration in the main ring. Instead, polarization can be built up at top energy from synchrotron radiation.

The electron bunch intensity for nominal LHeC performance is 1.4×10^{10} . The target intensity for the injector is taken as 2×10^{10} which includes a safety factor and allows for losses at injection and during the

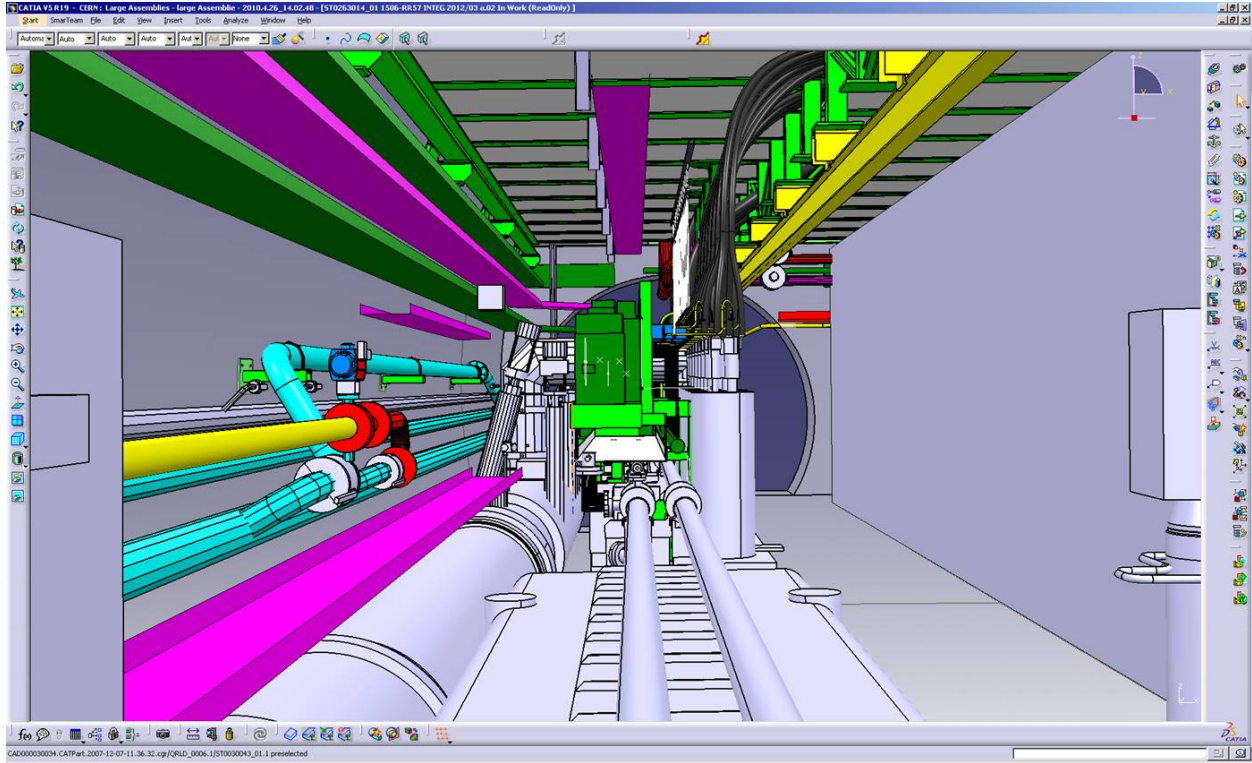


Figure 7.58: A typical big current feed-box (DFBA) on top of (green) and next to (grey shafts with black power lines) the two proton beam pipes.

5266 ramp. Higher single-bunch intensities may be useful, with a smaller number of bunches, for the e-A mode of
 5267 operation. LEP was operated with much higher bunch intensities up to 4×10^{11} limited by the transverse
 5268 mode coupling instability (TMCI). The TMCI threshold current can be estimated from [?]

$$I_{th} = \frac{\omega_s E}{e \sum \beta k_{\perp}(\sigma_s)} \quad (7.33)$$

5269 where $\omega_s = 2\pi Q_s f_{rev}$ is the synchrotron frequency, e the elementary charge, E is the beam energy, β the
 5270 beta function value at the location of the impedance and k_{\perp} the loss factor which accounts for the transverse
 5271 impedance of the machine. LEP had a design injection energy of 20 GeV. It was raised to 22 GeV to increase
 5272 the TMCI threshold.

5273 The relatively low bunch intensity required for the LHeC allows for direct injection without accumulation
 5274 and for a lower injection energy compared to LEP. The LHeC transverse impedance will be similar to LEP,
 5275 with a smaller contribution from the reduced number of cavities and an increased impedance contribution
 5276 from the more compact beam-pipe cross-section. Lowering the beam energy results in weak bending fields
 5277 and loss of synchrotron radiation damping. A beam energy of a few GeV may still be tolerable for transverse
 5278 mode coupling but would not be practical for magnet stability and require strong wigglers to get a significant
 5279 radiation damping (otherwise this requires a minimum beam energy of the order of 10 GeV).

5280 A pulse frequency of on average 5 Hz is required, to fill the LHeC electron ring with 2808 bunches in
 5281 10 minutes.

5282 The injector requirements summarized in Table ?? are within the reach of proven technology and concepts.
 5283 An example is the FACET facility at SLAC which provides 2×10^{10} electrons of 23 GeV energy at 30 Hz
 5284 repetition frequency [?].

5285 The intensities and repetition frequency required here match well with the performance of the LIL, the

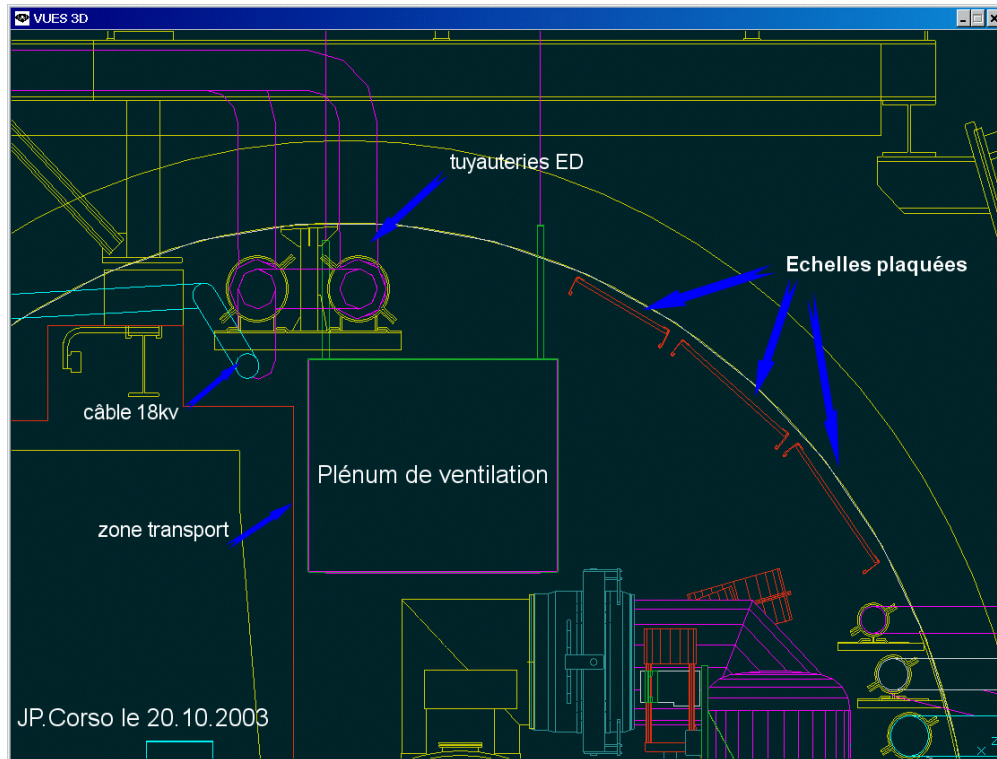


Figure 7.59: Air-duct in LSS7 indicated by the box labelled 'Plenum de ventilation' [?].

5286 first part of the LEP pre-injectors, which we reconsider here for the source, positron accumulation and pre-
 5287 acceleration to 0.6 GeV. For the acceleration to 10 GeV we propose a new, superconducting recirculating
 5288 LINAC.

5289 7.12.3 Source, accumulator and acceleration to 0.6 GeV

5290 Figure ?? shows the layout of the LPI (LEP Pre-Injector) as it was working in 2000. The LPI was composed
 5291 of the LIL (LEP Injector Linac) and the EPA (Electron Positron Accumulator).

5292 Table ?? gives the beam characteristics at the end of LIL.

5293 Table ?? gives the electron and positron beam parameters at the exit of EPA.

5294 With 8 bunches in the EPA for a 1.14 s cycle, the 2808 bunches required for the LHeC could be filled in
 5295 6.7 min which is perfectly adequate. According to the original LEP injector design report [?] Vol.I, the cycle
 5296 length for positrons is 11.22 s which would allow the 2808 bunches to be filled in 66 minutes. We conclude
 5297 that the LIL+EPA performance is fully adequate for the LHeC. A reduction of the cycle length for positrons
 5298 would be useful to reduce the filling time.

5299 Timing considerations

5300 EPA was planned for 1 to 8 bunches compatible with the LEP RF-frequency. The EPA circumference of
 5301 125.665 m corresponds to $t_{rev} = 419.173$ ns, which is 16.75×25 ns and would in theory allow for 16 bunches
 5302 spaced by 25 ns as relevant for the LHeC. Injection in batches of 72 bunches as possible for protons into the
 5303 LHC would require a five times larger damping ring which would be rather expensive.

5304 EPA had an RF-frequency $f_{rf} = 19.0852$ MHz. It will be increased to 40 MHz to allow for a bunch spacing
 5305 of 25 ns. For the injection into the LHC we propose a fast kicker system with a kicker rise-time below 25 ns.

Table 7.33: Main parameters for the LHeC RR injector

particle types	e^+, e^-
polarized	no
injection energy	$E_b = 10 \text{ GeV}$
bunch intensity	$2 \times 10^{10} e = 3.2 \text{ nC}$
pulse frequency	$\geq 5 / \text{s}$

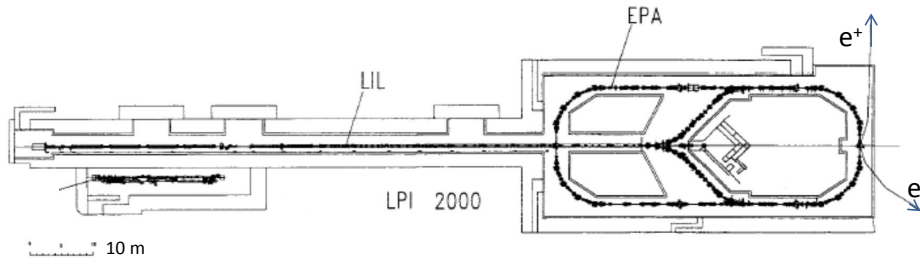


Figure 7.60: Layout of the LPI in 2000.

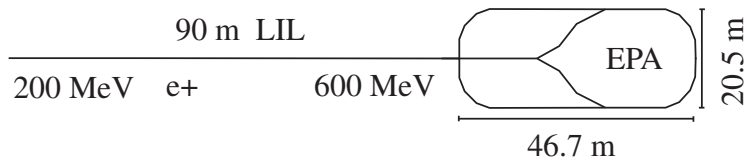


Figure 7.61: LIL and EPA

Beam energy	200 to 700 MeV
Charge	5×10^8 to $2 \times 10^{10} e^-$ / pulse
Pulse length	10 to 40 ns (FWHM)
Repetition frequency	1 to 100 Hz
Beam sizes (rms)	3 mm

Table 7.34: LIL beam parameters.

Energy	200 to 600 MeV
Charge	up to $4.5 \times 10^{11} e^\pm$
Intensity	up to 0.172 A
Number of bunches	1 to 8
Emittance	0.1 mm.mrad
Tune	$Q_x = 4.537, Q_y = 4.298$

Table 7.35: The electron and positron beam parameters at the exit of EPA.

5306 This conserves the dimensions of EPA and gives full flexibility to place the bunches into the LHeC electron
5307 ring as required to collide with the proton or ion bunches [?, ?].

5308 7.12.4 10 GeV injector

5309 For the acceleration to 10 GeV we propose a re-circulating LINAC, designed as a downscaled, low energy
5310 version of the 25 GeV ELFE at CERN design [?] using modern ILC-type RF-technology.

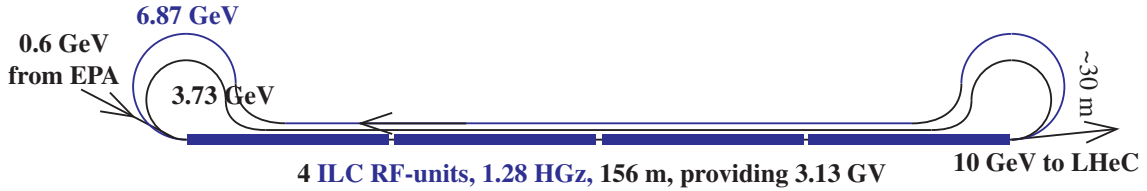


Figure 7.62: Recirculator using 4 ILC modules.

5311 A sketch of the proposed machine is shown in Fig. ???. The acceleration is provided by 4 RF-units of the
5312 ILC type, providing together 3.13 GV acceleration.

5313 The acceleration from 0.6 GeV to 10 GeV is achieved in three passages through the LINAC. This requires
5314 only two re-circulation arcs which can be constructed in the horizontal plane. The maximum energy in the
5315 last re-circulation arc is $10 - 3.13 = 6.87$ GeV.

5316 For a beam energy E and bending radius ρ , the energy loss U_0 by synchrotron radiation in the single
5317 passage through a re-circulation arc is

$$U_0 = C_\gamma \frac{E^4}{\rho} \quad (7.34)$$

5318 where

$$C_\gamma = \frac{e^2}{3\epsilon_0} \frac{1}{(mc^2)^4} = 8.846 \times 10^{-5} \text{ m GeV}^{-3} .$$

5319 where e is the elementary charge and m the electron mass. The relative energy spread is increased by the

5320 synchrotron radiation in a single passage by

$$\sigma_e = r_e c_f \frac{\gamma^{5/2}}{\rho} \tag{7.35}$$

5321 where r_e is the classical electron radius and

$$c_f = \frac{3}{2} \sqrt{\frac{55\pi}{27\sqrt{3}\alpha}} = 33.75. \tag{7.36}$$

5322 A bending radius of $\rho = 2$ m at $E = 6.87$ GeV would result in an energy loss by recirculation of $U_0 = 98$ MeV
 5323 and an energy spread of 10^{-3} . This would both be tolerable, but require very strong superconducting 11 tesla
 5324 magnets for the 6.87 GeV recirculation.

5325 At this stage, we propose the use of warm 2 tesla magnets, resulting in a bending radius of $\rho = 11.5$ m
 5326 for the 6.87 GeV recirculation and $\rho = 6.2$ m for the 3.73 GeV recirculation. The values for the energy loss
 5327 and spread are listed in Table ??.

Table 7.36: Energy, bending field and radius, energy loss and energy spread in the recirculator magnets.

E GeV	B tesla	ρ m	U_0 MeV	σ_e
6.87	2	11.45	17.1	1.7×10^{-4}
3.73	2	6.23	2.8	7×10^{-5}

5328 To save space and allow for a single LINAC tunnel, we propose a dogbone-like shape for the recirculators
 5329 as shown in Fig. ??.

Chapter 8

Linac-Ring Collider

8.1 Basic Parameters and Configurations

8.1.1 General Considerations

A high-energy electron-proton collider can be realized by accelerating electrons (or positrons) in a linear accelerator (linac) to 60–140 GeV and colliding them with the 7-TeV protons circulating in the LHC. Except for the collision point and the surrounding interaction region, the tunnel and the infrastructure for such a linac are separate and fully decoupled from the LHC operation, from the LHC maintenance work, and from other LHC upgrades (e.g., HL-LHC and HE-LHC).

The technical developments required for this type of collider can both benefit from and be used for many future projects. In particular, to deliver a long or continuous beam pulse, as required for high luminosity, the linac must be based on superconducting (SC) radio frequency (RF) technology. The development and industrial production of its components can exploit synergies with numerous other advancing SC-RF projects around the world, such as the European XFEL at DESY, eRHIC, ESS, ILC, CEBAF upgrade, CESR-ERL, JLAMP, and the CERN HP-SPL.

For high luminosity operation at a beam energy of 50–70 GeV the linac should be operated in continuous wave (CW) mode, which restricts the maximum RF gradient through the associated cryogenics power, to a value of about 20 MV/m or less. In order to limit the active length of such a linac and to keep its construction and operating costs low, the linac should, and can, be recirculating. For the sake of energy efficiency and to limit the overall site power, while boosting the luminosity, the SC recirculating CW linac can be operated in energy-recovery (ER) mode. A 60-GeV recirculating energy-recovery linac represents the baseline scenario for a linac-ring LHeC.

Electron-beam energies higher than 70 GeV, e.g. 140 GeV, can be achieved by a pulsed SC linac, similar to the XFEL, ILC or SPL. In this case the accelerating gradient can be larger than for CW operation, i.e. above 30 MV/m, which minimizes the total length, but recirculation is no longer possible at this beam energy due to prohibitively high synchrotron-radiation energy losses in any return arc of reasonable dimension. As a consequence the standard energy recovery scheme using recirculation cannot be implemented and the luminosity of such a higher-energy lepton-hadron collider would be more than an order of magnitude lower than the one of the lower-energy CW ERL machine, at the same wall-plug power. An advanced energy-recovery option for the pulsed straight linac would employ two-beam technology, as developed for CLIC, in this case based on a decelerating linac and multiple energy-transfer beams, to boost the luminosity potentially by several orders of magnitude [?]. Such novel type of energy-recovery linac could later be converted into a linear collider, or vice versa.

While for a linac it is straightforward to deliver a 80–90% polarized electron beam, the production of a sufficient number of positrons is extremely challenging for a linac-ring collider. A conceivable path towards decent proton-positron luminosities would include a recycling of the spent positrons, together with the recovery of their energy.

5367 The development of a CW SC recirculating energy-recovery linac (ERL) for LHeC would prepare the
5368 ground, the technology and the infrastructure for many possible future projects, e.g., for an International
5369 Linear Collider, for a Muon Collider¹, for a neutrino factory, or for a proton-driven plasma wake field
5370 accelerator. A ring-linac LHeC would, therefore, promote any conceivable future high-energy physics project,
5371 while pursuing an attractive forefront high-energy physics programme in its own right.

5372 8.1.2 ERL Performance and Layout

5373 Particle physics imposes the following performance requirements. The lepton beam energy should be 60
5374 GeV or higher and the electron-proton luminosity of order $10^{33} \text{ cm}^{-2}\text{s}^{-1}$. Positron-proton collisions are
5375 also required, with at least a few percent of the electron-proton luminosity. Since the LHeC should operate
5376 simultaneously with LHC pp physics, it should not degrade the pp luminosity. Both electron and positron
5377 beams should be polarized. Lastly, the detector acceptance should extend down to 1° or less. In addition,
5378 the total electrical power for the lepton branch of the LHeC collider should stay below 100 MW.

5379 For round-beam collisions, the luminosity of the linac-ring collider [?] is written as

$$L = \frac{1}{4\pi e} \frac{N_{b,p}}{\epsilon_p} \frac{1}{\beta_p^*} I_e H_{hg} H_D, \quad (8.1)$$

5380 where e denotes the electron charge, $N_{b,p}$ the proton bunch population, β_p^* the proton IP beta function, I_e the
5381 average electron beam current, H_{hg} the geometric loss factor arising from crossing angle and hourglass effect,
5382 and H_D the disruption enhancement factor due to the electron pinch in collision, or luminosity reduction
5383 factor from the anti-pinch in the case of positrons. In the above formula, it is assumed that the electron
5384 bunch spacing is a multiple of the proton beam bunch spacing. The latter could be equal to 25, 50 or 75 ns,
5385 without changing the luminosity value.

5386 The ratio $N_{b,p}/\epsilon_p$ is also called the proton beam brightness. Among other constraints, the LHC beam
5387 brightness is limited by the proton-proton beam-beam limit. For the LHeC design we assume the brightness
5388 value obtained for the ultimate bunch intensity, $N_{p,p} = 1.7 \times 10^{11}$, and the nominal proton beam emittance,
5389 $\epsilon_p = 0.5 \text{ nm}$ ($\gamma\epsilon_p = 3.75 \mu\text{m}$). This corresponds to a total pp beam-beam tune shift of 0.01. More than two
5390 times higher values have already been demonstrated, with good pp luminosity lifetime, during initial LHC
5391 beam commissioning, indicating a potential for higher ep luminosity.

5392 To maximize the luminosity the proton IP beta function is chosen as 0.1 m. This is considerable smaller
5393 than the 0.55 m for the pp collisions of the nominal LHC. The reduced beta function can be achieved by
5394 reducing the free length between the IP and the first proton quadrupole (10 m instead of 23 m), and by
5395 squeezing only one of the two proton beams, namely the one colliding with the leptons, which increases the
5396 aperture available for this beam in the last quadrupoles. In addition, we assume that the final quadrupoles
5397 could be based on Nb₃Sn superconductor technology instead of Nb-Ti. The critical field for Nb₃Sn is almost
5398 two times higher than for Nb-Ti, at the same temperature and current density, allowing for correspondingly
5399 larger aperture and higher quadrupole gradient. Nb₃Sn quadrupoles are presently under development for
5400 the High-Luminosity LHC upgrade (HL-LHC).

5401 The geometric loss factor H_{hg} needs to be optimized as well. For round beams with $\sigma_{z,p} \gg \sigma_{z,e}$ (well
5402 fulfilled for $\sigma_{z,p} \approx 7.55 \text{ cm}$, $\sigma_{z,e} \approx 300 \mu\text{m}$) and $\theta_c \ll 1$, it can be expressed as²

$$H_{hg} = \frac{\sqrt{\pi} z e^{z^2} \text{erfc}(z)}{S}, \quad (8.2)$$

5403 where

$$z \equiv 2 \frac{(\beta_e^*/\sigma_{z,p})(\epsilon_e/\epsilon_p)}{\sqrt{1 + (\epsilon_e/\epsilon_p)^2}} S$$

¹The proposed Muon Collider heavily relies on SC recirculating linacs for muon acceleration as well as on a SC-linac proton driver.

²The derivation of this formula is similar to the one for the LHC in Ref. [?], with the difference that here the two beams have different emittances and IP beta functions, and the electron bunch length is neglected. Curves obtained with formula (??) were first reported in [?].

5404 and

$$S \equiv \sqrt{1 + \frac{\sigma_{x,p}^2 \theta_c^2}{8\sigma_p^{*2}}}.$$

5405 Luminosity loss from a crossing angle is avoided by head-on collisions. The luminosity loss from the hourglass
5406 effect, due to the long proton bunches and potentially small electron beta functions, is kept small, thanks
5407 to a “small” linac electron beam emittance of 0.43 nm ($\gamma\epsilon_e = 50 \mu\text{m}$). We note that the assumed electron-
5408 beam emittance, though small when compared with a storage ring of comparable energy, is still very large
5409 by linear-collider standards.

5410 The disruption enhancement factor for electron-proton collisions is about $H_D \approx 1.35$, according to
5411 Guinea-Pig simulations [?] and a simple estimate based on the fact that the average rms size of the electron
5412 beam during the collision approaches a value equal to $1/\sqrt{2}$ of the proton beam size. This additional
5413 luminosity increase from disruption is not taken into account in the numbers given below. On the other
5414 hand, for positron-proton collisions the disruption of the positrons leads to a significant luminosity reduction,
5415 by roughly a factor $H_D \approx 0.3$, similar to the case of electron-electron collisions [?].

5416 The final parameter determining the luminosity is the average electron (or positron) beam current I_e . It
5417 is closely tied to the total electrical power available (taken to be 100 MW).

5418 Crossing Angle and IR Layout

5419 The colliding electron and proton beams need to be separated by 7 cm at a distance of 10 m from the
5420 IP in order to enter through separate holes in the first proton quadrupole magnet. This separation could
5421 be achieved with a crossing angle of 7 mrad and crab cavities. The required crab voltage would, however,
5422 need to be of order 200 MV, which is 20–30 times the voltage needed for pp crab crossing at the HL-LHC.
5423 Therefore, crab crossing is not considered an option for the L-R LHeC. Without crab cavities, any crossing
5424 angle should be smaller than 0.3 mrad, as is illustrated in Fig. ???. Such small a crossing angle is not useful,
5425 compared with the 7 mrad angle required for the separation. The R-L interaction region (IR), therefore, uses
5426 detector-integrated dipole fields around the collision point, to provide head-on ep collisions ($\theta_c = 0$ mrad)
5427 and to separate the beams by the required amount. A dipole field of about 0.3 T over a length of ± 9 m
5428 accomplishes these goals.

5429 The IR layout with separation dipoles and crossing angle is sketched in Fig. ???. Significant synchrotron
5430 radiation, with 48 kW average power, and a critical photon energy of 0.7 MeV, is emitted in the dipole
5431 fields. A large portion of this radiation is extracted through the electron and proton beam pipes. The SC
5432 proton magnets can be protected against the radiation heat load by an absorber placed in front of the first
5433 quadrupole and by a liner inside the beam pipe. Backscattering of synchrotron radiation into the detector
5434 is minimized by shaping the surface of absorbers and by additional masking.

5435 The separation dipole fields modify, and enhance, the geometric acceptance of the detector. Figure ??
5436 illustrates that scattered electrons with energies of 10–50 GeV might be detected at scattering angles down
5437 to zero degrees.

5438 Electron Beam and the Case for Energy Recovery

5439 The electron-beam emittance and the electron IP beta function are not critical, since the proton beam size is
5440 large by electron-beam standards (namely about $7 \mu\text{m}$ rms compared with nm beam-sizes for linear colliders).
5441 The most important parameter for high luminosity is the average beam current, I_e , which linearly enters
5442 into the luminosity formula (??). In addition to the electron beam current, also the bunch spacing (which
5443 should be a multiple of the LHC 25-ns proton spacing) and polarization (80–90% for the electrons) need
5444 to be considered. Having pushed all other parameters in (??), Fig. ?? illustrates that an average electron
5445 current of about 6.4 mA is required to reach the target luminosity of $10^{33} \text{ cm}^{-2}\text{s}^{-1}$.

5446 For comparison, the CLIC main beam has a design average current of 0.01 mA [?], so that it falls short
5447 by a factor 600 from the LHeC requirement. For other applications it has been proposed to raise the CLIC

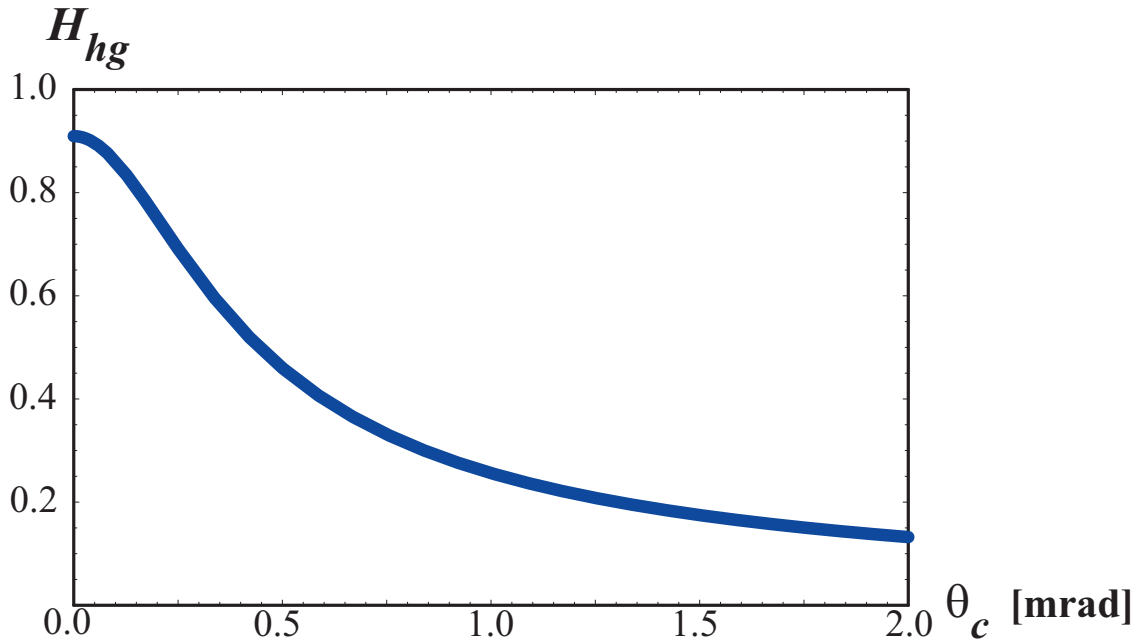


Figure 8.1: Geometric luminosity loss factor H_{hg} , (??), as a function of the total crossing angle

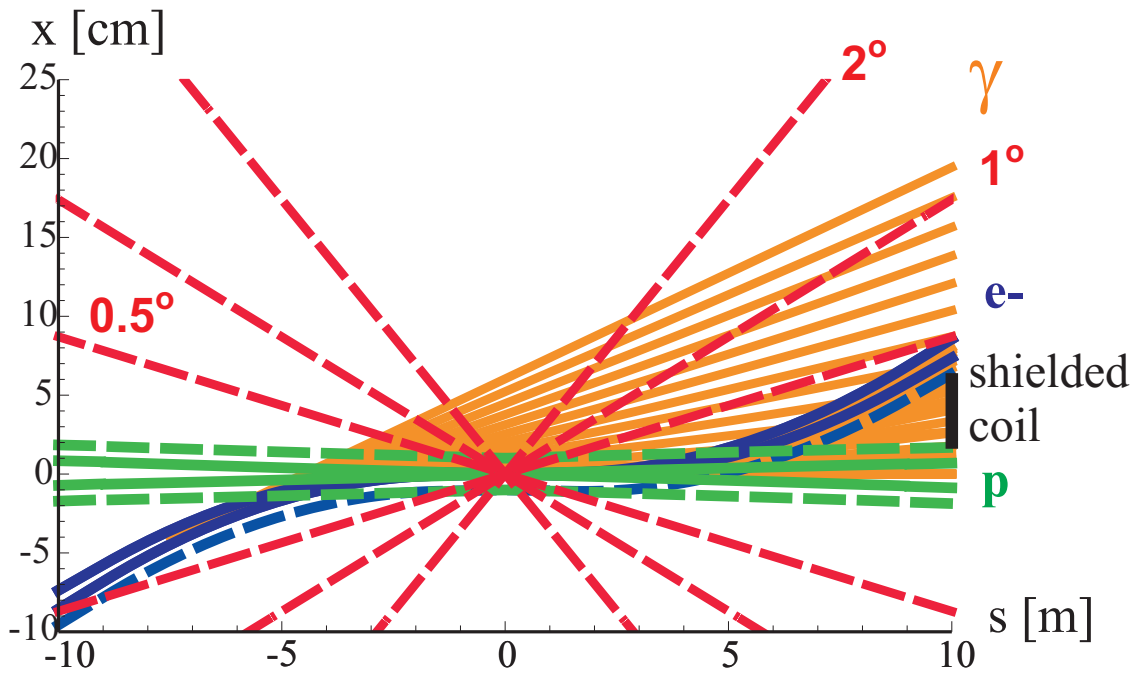


Figure 8.2: Linac-ring interaction-region layout. Shown are the beam envelopes of 10σ (electrons) [solid blue] or 11σ (protons) [solid green], the same envelopes with an additional constant margin of 10 mm [dashed], the synchrotron-radiation fan [orange], the approximate location of the magnet coil between incoming protons and outgoing electron beam [black], and a “1 degree” line.

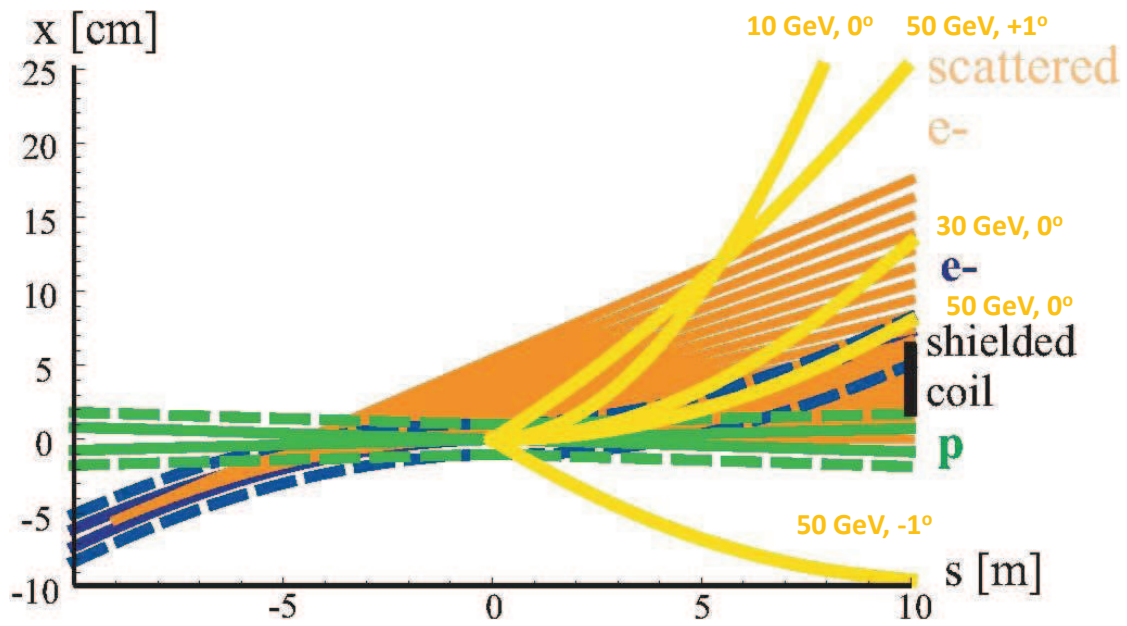


Figure 8.3: Example trajectories in the detector dipole fields for electrons of different energies and scattering angles, demonstrating an enhancement of the detector acceptance by the dipoles.

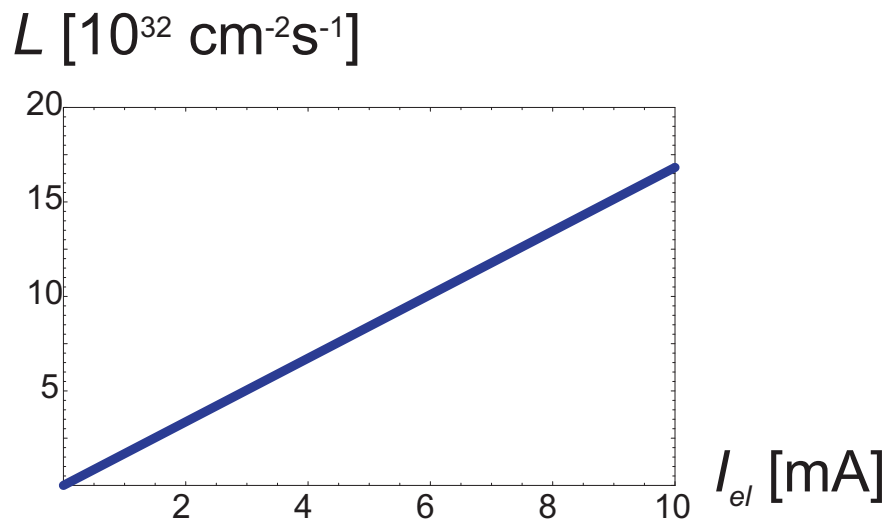


Figure 8.4: Linac-ring luminosity versus average electron beam current, according to (??).

5448 beam power by lowering the accelerating gradient, raising the bunch charge by a factor of two, and increasing
5449 the repetition rate up to three times, which raises the average beam current by a factor 6 to about 0.06 mA
5450 (this type of CLIC upgrade is described in [?]). This ultimate CLIC main beam current is still a factor 100
5451 below the LHeC target. On the other hand, the CLIC drive beam would have a sufficiently high current,
5452 namely 30 mA, but at the low energy 2.37 GeV, which would not be useful for high-energy *ep* physics. Due
5453 to this low energy, also the drive beam power is still a factor of 5 smaller than the one required by LHeC.
5454 Finally, the ILC design current is about 0.04 mA [?], which also falls more than a factor 100 short of the
5455 goal.

5456 Fortunately, SC linacs can provide higher average current, e.g. by increasing the linac duty factor 10–100
5457 times, or even running in continuous wave (CW) mode, at lower accelerating gradient. Example average
5458 currents for a few proposed designs illustrate this point: The CERN High-Power Superconducting Proton
5459 Linac aims at about 1.5 mA average current (with 50 Hz pulse rate) [?], the Cornell ERL design at 100 mA
5460 (cw) [?], and the eRHIC ERL at about 50 mA average current at 20 GeV beam energy (cw) [?]. All these
5461 designs are close to, or exceed, the LHeC requirements for average beam current and average beam power
5462 (6.4 mA at 60 GeV). It is worth noting that the JLAB UV/IR 4th Generation Light Source FEL is routinely
5463 operating with 10 mA average current (135 pC pulses at 75 MHz) [?].

5464 The target LHeC IP electron-beam power is 384 MW. With a standard wall-plug-power to RF conversion
5465 efficiency around 50%, this would imply about 800 MW electrical power, far more than available. This
5466 highlights the need for energy recovery where the energy of the spent beam, after collision, is recuperated
5467 by returning the beam 180° out of phase through the same RF structure that had earlier been used for its
5468 acceleration, again with several recirculations. An energy recovery efficiency η_{ER} reduces the electrical power
5469 required for RF power generation at a given beam current by a factor $(1 - \eta_{\text{ER}})$. We need an efficiency η_{ER}
5470 above 90% or higher to reach the beam-current goal of 6.4 mA with less than 100 MW total electrical power.

5471 The above arguments have given birth to the LHeC Energy Recovery Linac high-luminosity baseline
5472 design, which is being presented in this chapter.

5473 Choice of RF Frequency

5474 Two candidate RF frequencies exist for the SC linac. One possibility is operating at the ILC and XFEL RF
5475 frequency around 1.3 GHz, the other choosing a frequency of about 720 MHz, close to the RF frequencies of
5476 the CERN High-Power SPL, eRHIC, and the European Spallation Source (ESS).

5477 The ILC frequency would have the advantage of synergy with the XFEL infrastructure, of profiting from
5478 the high gradients reached with ILC accelerating cavities, and of smaller structure size, which could reduce
5479 the amount of high-purity niobium needed by a factor 2 to 4.

5480 Despite these advantages, the present LHeC baseline frequency is 720 MHz, or, more precisely, 721 MHz
5481 to be compatible with the LHC bunch spacing. The arguments in favor of this lower frequency are the
5482 following:

- 5483 • A frequency of 721 MHz requires less cryo-power (about two times less than at 1.3 GHz according to
5484 BCS theory; the exact difference will depend on the residual resistance [?]).
- 5485 • The lower frequency will facilitate the design and operation of high-power couplers [?], though the
5486 couplers might not be critical [?].
- 5487 • The smaller number of cells per module (of similar length) at lower RF frequency is preferred with
5488 regard to trapped modes [?].
- 5489 • The lower-frequency structures reduce beam-loading effects and transverse wake fields.
- 5490 • The project can benefit from synergy with SPL, eRHIC and ESS.

5491 In case the cavity material costs at 721 MHz would turn out to be a major concern, they could be reduced
5492 by applying niobium as a thin film on a copper substrate, rather than using bulk niobium. The thin film
5493 technology may also enhance the intrinsic cavity properties, e.g. increase the Q value.

5494 Linac RF parameters for both 720 MHz and 1.3 GHz in CW mode as well as for a pulsed 1.3-GHz option
 5495 are compared in Table ???. The 721 MHz parameters are derived from eRHIC [?]. Pulsed-linac applications
 5496 for LHeC are discussed in subsections ?? and ??.

Table 8.1: Linac RF parameters for two different RF frequencies and two modes of operation.

	ERL 721 MHz	ERL 1.3 GHz	Pulsed
duty factor	CW	CW	0.05
RF frequency [GHz]	0.72	0.72	1.3
cavity length [m]	1	~1	~1
energy gain / cavity [MeV]	18	18	31.5
R/Q [100Ω]	400–500	1200	1200
Q_0 [10^{10}]	2.5–5.0	2?	1
power loss stat. [W/cav.]	5	< 0.5	< 0.5
power loss RF [W/cav.]	8–32 ¹	13–27 ²	< 10
power loss total [W/cav.]	13–37	13–27	11
“W per W” (1.8 K to RT)	700	700	700
power loss / GeV at RT [MW]	0.51–1.44	0.6–1.1	0.24
length / GeV [m] (filling=0.57)	97	97	56

5497 ERL Electrical Site Power

5498 The cryopower for two 10-GeV accelerating SC linacs is 28.9 MW, assuming pessimistically 37 W/m heat
 5499 load at 1.8 K and 18 MV/m cavity gradient (this is a pessimistic estimate since the heat load could be up to
 5500 3 times smaller; see Table ??), and 700 “W per W” cryo efficiency as for the ILC. The RF power needed to
 5501 control microphonics for the accelerating RF is estimated at 22.2 MW, considering that 10 kW/m RF power
 5502 may be required, as for eRHIC, with 50% RF generation efficiency. The electrical power for the additional
 5503 RF compensating the synchrotron-radiation energy loss is 24.1 MW, with an RF generation efficiency of 50%.
 5504 The cryo power for the compensating RF is 2.1 MW, provided in additional 1.44 GeV linac sections, and
 5505 the microphonics control for the compensating RF requires another 1.6 MW. In addition, with an injection
 5506 energy of 50 MeV, 6.4 mA beam current, and as usual 50% efficiency, the electron injector consumes about
 5507 6.4 MW. A further 3 MW is budgeted for the recirculation-arc magnets [?]. Together this gives a grand total
 5508 of 88.3 MW electrical power, some 10%.below the 100 MW limit.

5509 ERL Configuration

5510 The ERL configuration is depicted in Fig. ??. The shape, arc radius and number of passes have been
 5511 optimized with respect to construction cost and with respect to synchrotron-radiation effects [?].

5512 The ERL is of racetrack shape. A 500-MeV electron bunch coming from the injector is accelerated in each
 5513 of the two 10-GeV SC linacs during three revolutions, after which it has obtained an energy of 60 GeV. The
 5514 60-GeV beam is focused and collided with the proton beam. It is then bent by 180° in the highest-energy arc
 5515 beam line before it is sent back through the first linac, at a decelerating RF phase. After three revolutions
 5516 with deceleration, re-converting the energy stored in the beam to RF energy, the beam energy is back at its

¹The range of heat-load values quoted for 721 MHz reflects the measured parameters of eRHIC prototype cavity BNL-I and an extrapolation to the improved cavity BNL-III [?].

²The range of heat-load values indicated for 1.3 GHz refers to different assumptions on the cavity Q at 18 MV/m (or to two different extrapolations from [?]).

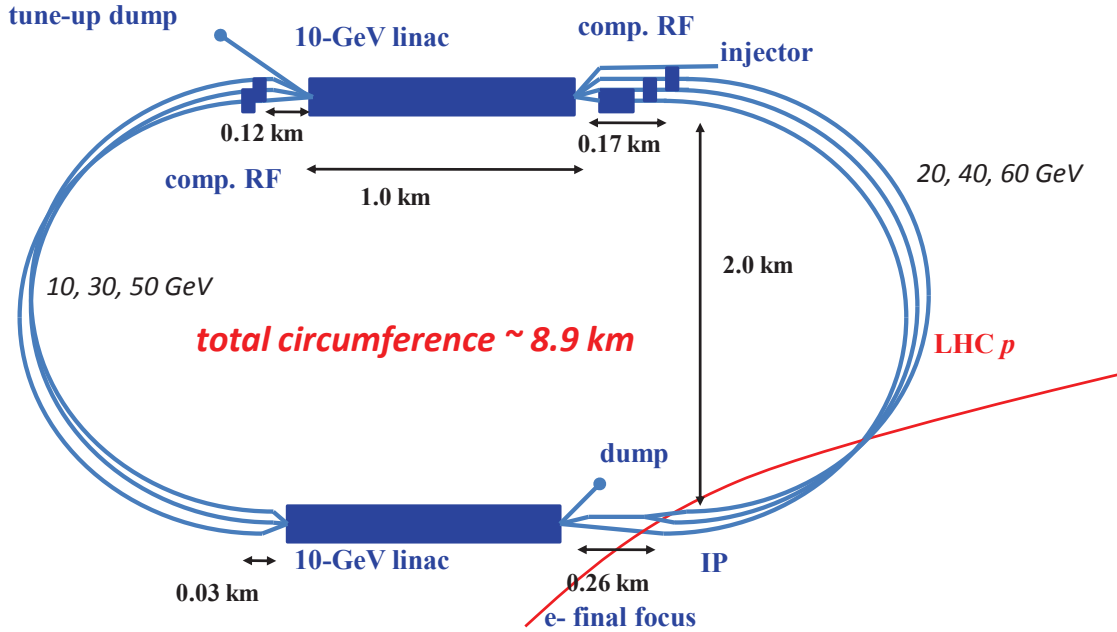


Figure 8.5: LHeC ERL layout including dimensions.

5517 original value of 500 MeV, and the beam is now disposed in a low-power 3.2-MW beam dump. A second,
 5518 smaller (tune-up) dump could be installed behind the first linac.

5519 Strictly speaking, with an injection energy into the first linac of 0.5 GeV, the energy gain in the two
 5520 accelerating linacs need not be 10 GeV each, but about 9.92 GeV, in order to reach 60 GeV after three
 5521 passages through each linac. Considering a rough value of 10 GeV means that we overestimate the electrical
 5522 power required by about 1%.

5523 Each arc contains three separate beam lines at energies of 10, 30 and 50 GeV on one side, and 20, 40 and
 5524 60 GeV on the other. Except for the highest energy level of 60 GeV, at which there is only one beam, in
 5525 each of the other arc beam lines there always co-exist a decelerating and an accelerating beam. The effective
 5526 arc radius of curvature is 1 km, with a dipole bending radius of 764 m [?].

5527 The two straight sections accommodate the 1-km long SC accelerating linacs. In addition to the 1km
 5528 linac section, there is an additional space of 290 m in each straight section of the racetrack. In one straight
 5529 of the racetrack 260 m of this additional length is allocated for the electron final focus (plus matching and
 5530 splitting), the residual 30 m on the other side of the same straight allows for combining the beam and
 5531 matching the optics into the arc. In the second straight section of the racetrack the additional length of
 5532 the straight sections houses the additional linacs for compensating the 1.44 GeV energy loss in the return
 5533 arcs [?]. For the highest energy, 60 GeV, there is a single beam and the compensating RF (750 MV) can
 5534 have the same frequency, 721 MHz, as in the main linac [?]. For the other energies, a higher harmonic RF
 5535 system, e.g. at 1.442 GHz, can compensate the energy loss for both decelerating and accelerating beams,
 5536 which are 180° out of phase at 721 MHz. On one side of the second straight one must compensate a total
 5537 of about 907 MV (=750+148+9 MV, corresponding to the energy loss at 60, 40 and 20 GeV, respectively),
 5538 which should easily fit within a length of 170 m. On the other side one has to compensate 409 MV (=362+47
 5539 MV), corresponding to SR energy losses at 50 and 30 GeV), for which a length of 120 m is available.

5540 The total circumference of the ERL racetrack is chosen as 8.9 km, equal to one third of the LHC
 5541 circumference. This choice has the advantage that one could introduce ion-clearing gaps in the electron
 5542 beam which would match each other on successive revolutions (e.g. for efficient ion clearing in the linacs
 5543 that are shared by six different parts of the beam) and which would also always coincide with the same proton

bunch locations in the LHC, so that in the latter a given proton beam would either always collide or never collide with the electrons [?]. Ion clearing may be necessary to suppress ion-driven beam instabilities. The proposed implementation scheme would remove ions while minimizing the proton emittance growth which could otherwise arise when encountering collisions only on some of the turns. In addition, this arrangement can be useful for comparing the emittance growth of proton bunches which are colliding with the electrons and those which are not.

The length of individual components is as follows. The exact length of the 10-GeV linac is 1008 m. The individual cavity length is taken to be 1 m. The optics consists of 56-m long FODO cells with 32 cavities. The number of cavities per linac is 576. The linac cavity filling factor is 57.1%. The effective arc bending radius is set to be 1000 m. The bending radius of the dipole magnets is 764 m, corresponding to a dipole filling factor of 76.4% in the arcs. The longest SR compensation linac has a length of 84 m (replacing the energy lost by SR at 60 GeV). Combiners and splitters between straights and arcs require about 20–30 m space each. The electron final focus may have a length of 200–230 m.

IP Parameters and Beam-Beam Effects

Table ?? presents interaction-point (IP) parameters for the electron and proton beams.

Table 8.2: IP beam parameters

	protons	electrons
beam energy [GeV]	7000	60
Lorentz factor γ	7460	117400
normalized emittance $\gamma\epsilon_{x,y}$ [μm]	3.75	50
geometric emittance $\epsilon_{x,y}$ [nm]	0.40	0.43
a IP beta function $\beta_{x,y}^*$ [m]	0.10	0.12
rms IP beam size $\sigma_{x,y}^*$ [μm]	7	7
initial rms IP beam divergence $\sigma_{x',y'}^*$ [μrad]	70	58
beam current [mA]	≥ 430	6.4
bunch spacing [ns]	25 or 50	(25 or) 50
bunch population [ns]	1.7×10^{11}	(1 or) 2×10^9

Due to the low charge of the electron bunch, the proton head-on beam-beam tune shift is tiny, namely $\Delta Q_p = +0.0001$, which amounts to only about 1% of the LHC pp design tune shift (and is of opposite sign). Therefore, the proton-beam tune spread induced by the ep collisions is negligible. In fact, the electron beam acts like an electron lens and could conceivably increase the pp tune shift and luminosity, but only by about 1%. Long-range beam-beam effects are equally insignificant for both electrons and protons, since the detector-integrated dipoles separate the electron and proton bunches by about $36\sigma_p$ at the first parasitic encounter, 3.75 m away from the IP.

One further item to be looked at is the proton beam emittance growth. Past attempts at directly simulating the emittance growth from ep collisions were dominated by numerical noise from the finite number of macroparticles and could only set an upper bound [?], nevertheless indicating that the proton emittance growth due to the pinching electron beam might be acceptable for centered collisions. Proton emittance growth due to electron-beam position jitter and simultaneous pp collisions is another potential concern. For a 1σ offset between the electron and proton orbit at the IP, the proton bunch receives a deflection of about 10 nrad (approximately $10^{-4}\sigma_{x',y'}^*$). Beam-beam simulations for LHC pp collisions have determined the acceptable level for random white-noise dipole excitation as $\Delta x/\sigma_x \leq 0.1\%$ [?]. This translates into a very relaxed electron-beam random orbit jitter tolerance of more than 1σ . The tolerance on the orbit jitter will

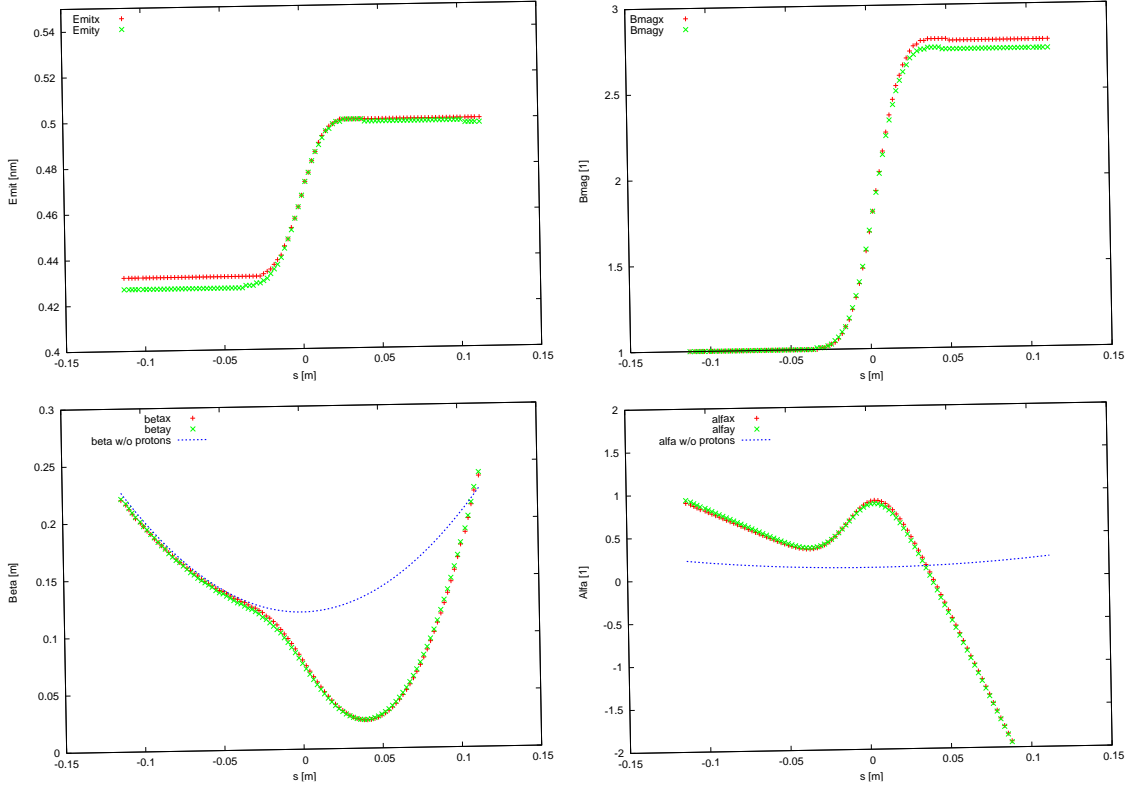


Figure 8.6: Simulated evolution of the electron beam emittance (top left), mismatch factor B_{mag} (top right) beta function (bottom left) and alpha function (bottom right) during the collision with a proton bunch, as a function of distance from the IP.

5575 then not be set by beam-beam effects, but by the luminosity loss resulting from off-center collisions, which,
 5576 without disruption, scales as $\exp(-(\Delta x)^2/(4\sigma_{x,y}^2))$. The random orbit jitter observed at the SLAC SLC had
 5577 been of order $0.3\text{--}0.5\sigma$ [?, ?]. A 0.1σ offset at LHeC would reduce the luminosity by at most 0.3%, a 0.3σ
 5578 offset by 2.2%. Disruption further relaxes the tolerance.

5579 The strongest beam-beam effect is encountered by the electron beam, which is heavily disrupted. The
 5580 electron disruption parameter is $D_{x,y} \equiv N_{b,p}r_e\sigma_{z,p}/(\gamma_e\sigma^{*2}) \approx 6$, and the “nominal disruption angle” $\theta_0 \equiv$
 5581 $D\sigma^*/\sigma_{z,p} = N_{b,p}r_e/(\gamma_e\sigma^*)$ [?] is about $600 \mu\text{rad}$ (roughly $10\sigma_{x',y'}$), which is huge. Simulations show that
 5582 the actual maximum angle of the disrupted electrons is less than half θ_0 .

5583 Figure ?? illustrates the emittance growth and optics-parameter change for the electron beam due to
 5584 head-on collision with a “strong” proton bunch. The intrinsic emittance grows by only 15%, but there is a
 5585 180% growth in the mismatch parameter “ B_{mag} ” (defined as $B_{\text{mag}} = (\beta\gamma_0 - 2\alpha\alpha_0 + \beta_0\gamma)/2$, where quantities
 5586 with and without subindex “0” refer to the optics without and with collision, respectively. Without adjusting
 5587 the extraction line optics to the parameters of the mismatched beam the emittance growth will be about
 5588 200%. This would be acceptable since the arc and linac physical apertures have been determined assuming
 5589 up to 300% emittance growth for the decelerating beam [?]. However, if the optics of the extraction line is
 5590 rematched for the colliding electron beam (corresponding to an effective β^* of about 3 cm rather than the
 5591 nominal 12 cm; see Fig.?? bottom left), the net emittance growth can be much reduced, to only about 20%.
 5592 The various optics parameters shown in Fig. ?? vary by no more than 10–20% for beam-beam orbit offsets
 5593 up to 1σ .

5594 Figure ?? presents the average electron deflection angle as a function of the beam-beam offset. The
 5595 extraction channel for the electron beam must have sufficient aperture to accommodate both the larger

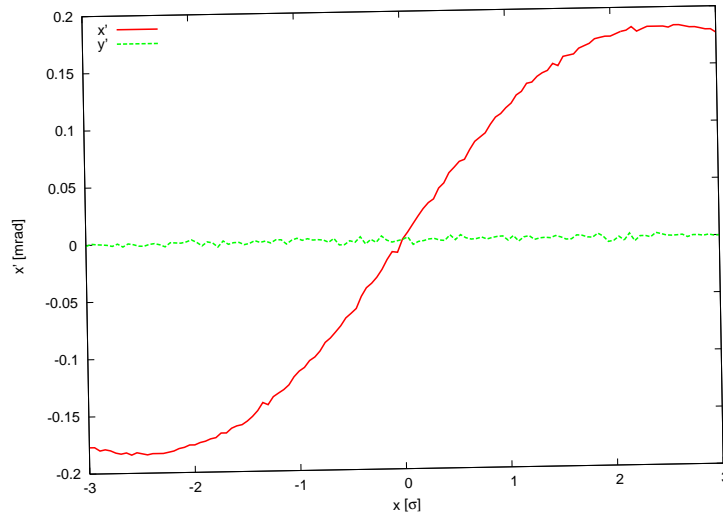


Figure 8.7: Simulated electron horizontal center-of-mass deflection angle as a function of the horizontal beam-beam offset.

5596 emittance due to disruption and the average trajectory change due to off-center collisions.

5597 8.1.3 Polarization

5598 The electron beam can be produced from a polarized DC gun with about 90% polarization, and with,
 5599 conservatively, 10–50 μm normalized emittance [?]. Spin-manipulation tools and measures for preserving
 5600 polarization, like Wien filter and/or spin rotators, and polarimeters should be included in the optics design
 5601 of the injector, the final focus, and the extraction line.

5602 As for the positrons, up to about 60% polarization can be achieved either with an undulator [?] or with
 5603 a Compton-based e^+ source [?, ?]³.

5604 8.1.4 Pulsed Linacs

5605 For beam energies above about 140 GeV, due to the growing impact of synchrotron radiation, the construction
 5606 of a single straight linac is cheaper than that of a recirculating linac [?]. Figure ?? shows the schematic of
 5607 an LHeC collider based on a pulsed straight 140-GeV linac, including injector, final focus, and beam dump.
 5608 The linac could be either of ILC type (1.3 GHz RF frequency) or operate at 721 MHz as the preferred ERL
 5609 version. In both cases, ILC values are assumed for the cavity gradient (31.5 MV/m) and for the cavity
 5610 unloaded Q value ($Q_0 = 10^{10}$). This type of linac would be extendable to ever higher beam energies and
 5611 could conceivably later become part of a linear collider. In its basic, simplest and conventional version no
 5612 energy recovery is possible for this configuration, since it is impossible to bend the 140-GeV beam around.
 5613 The lack of energy recovery leads to significantly lower luminosity. For example, with 10 Hz repetition rate,
 5614 5 ms pulse length (longer than ILC), a geometric reduction factor $H_g = 0.94$ and $N_b = 1.5 \times 10^9$ per bunch,
 5615 the average electron current would be 0.27 mA and the luminosity $4 \times 10^{31} \text{ cm}^{-2}\text{s}^{-1}$.

5616 The construction of the 140-GeV pulsed straight linac could be staged, e.g. so as to first feature a pulsed
 5617 linac at 60 GeV, which could also be used for γ - p/A collisions (see subsection ??). The linac length decreases
 5618 directly in proportion to the beam energy. For example, at 140-GeV the pulsed linac measures 7.9 km, while
 5619 at 60 GeV its length would be 3.4 km. For a given constant wall-plug power, of 100 MW, both the average
 5620 electron current and the luminosity scale roughly inversely with the beam energy. At 60 GeV the average

³The primary challenge for positrons is to produce them in sufficient number and with a small enough emittance.

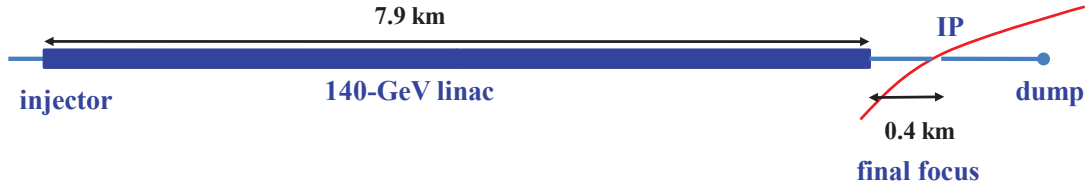


Figure 8.8: Pulsed single straight 140-GeV linac for highest energy ep collisions.

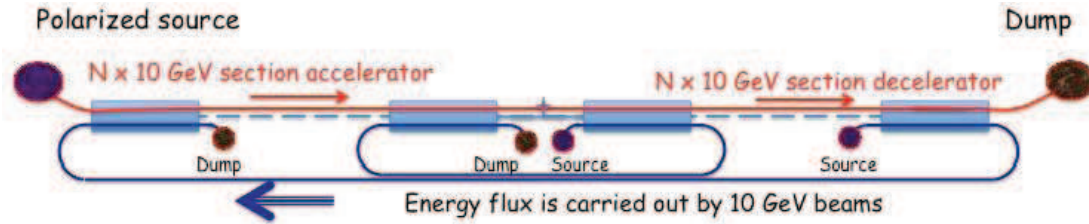


Figure 8.9: Highest-energy high-luminosity ERL option based on two straight linacs and multiple 10-GeV energy-transfer beams [?].

5621 electron current becomes 0.63 mA and the pulsed-linac luminosity, without any energy recovery, would be
 5622 more than $9 \times 10^{31} \text{ cm}^{-2}\text{s}^{-1}$.

5623 8.1.5 Highest-Energy LHeC ERL Option

5624 The simple straight linac layout of Fig. ?? can be expanded as shown in Fig. ?? [?]. The main electron
 5625 beam propagates from the left to the right. In the first linac it gains about 150 GeV, then collides with
 5626 the hadron beam, and is then decelerated in the second linac. By transferring the RF energy back to the
 5627 first accelerating linac, with the help of multiple, e.g. 15, 10-GeV “energy-transfer beams,” a novel type
 5628 of energy recovery is realized without bending the spent beam. With two straight linacs facing each other
 5629 this configuration could easily be converted into a linear collider, or vice versa, pending on geometrical and
 5630 geographical constraints of the LHC site. As there are no synchrotron-radiation losses the energy recovery
 5631 can be nearly 100% efficient. Such novel form of ERL could push the LHeC luminosity to the $10^{35} \text{ cm}^{-2}\text{s}^{-1}$
 5632 level. In addition, it offers ample synergy with the CLIC two-beam technology.

5633 8.1.6 γ -p/A Option

5634 In case of a (pulsed) linac without energy recovery the electron beam can be converted into a high-energy
 5635 photon beam, by backscattering off a laser pulse, as is illustrated in Fig. ??. The rms laser spot size at the
 5636 conversion point should be similar to the size of the electron beam at this location, that is $\sigma_\gamma \approx 10\mu\text{m}$.

5637 With a laser wavelength around $\lambda_\gamma \approx 250 \text{ nm}$ ($E_{\gamma,0} \approx 5 \text{ eV}$), obtained e.g. from a Nd:YAG laser with
 5638 frequency quadrupling, the Compton-scattering parameter x [?, ?],

$$x \approx 15.3 \left[\frac{E_{e,0}}{\text{TeV}} \right] \left[\frac{E_{\gamma,0}}{\text{eV}} \right], \quad (8.3)$$

5639 is close to the optimum value 4.8 for an electron energy of 60 GeV (for $x > 4.8$ high-energy photons get
 5640 lost due to the creation of e^+e^- pairs). The maximum energy of the Compton scattered photons is given by
 5641 $E_{\gamma,\text{max}} = x/(x+1)E_0$, which is larger than 80% of the initial electron-beam energy $E_{e,0}$, for our parameters.
 5642 The cross section and photon spectra depend on the longitudinal electron polarization λ_e and on the circular

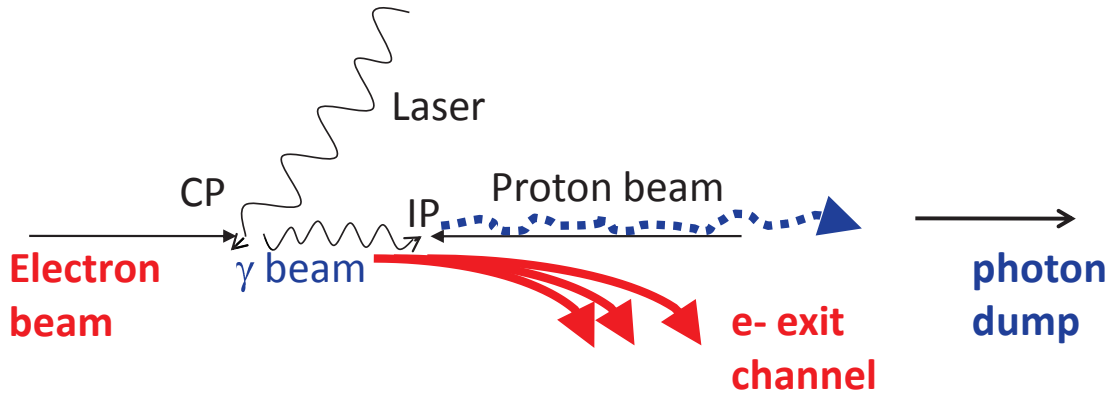


Figure 8.10: Schematic of γ - p/A collision; prior to the photon-hadron interaction point (IP), the electron beam is scattered off a several-J laser pulse at the conversion point (CP).

5643 laser polarization P_c . With proper orientation ($2\lambda_e P_c = -1$) the photon spectrum is concentrated near the
 5644 highest energy $E_{\gamma,\max}$.

5645 The probability of scattering per individual electron is [?]

$$n_\gamma = 1 - \exp(-q) \quad (8.4)$$

5646 with

$$q = \frac{\sigma_c A}{E_{\gamma,0} 2\pi\sigma_\gamma^2}, \quad (8.5)$$

5647 where σ_c denotes the (polarized) Compton cross section and A the laser pulse energy. Using the formulae
 5648 in [?], the Compton cross section for $x = 4.8$ and $2\lambda_e P_c = -1$ is computed to be $\sigma_c = 3.28 \times 10^{-25} \text{ cm}^2$. The
 5649 pulse energy corresponding to $q = 1$, i.e. to a conversion efficiency of 65%, is estimated as $A \approx E_{\gamma,0} 2\pi\sigma_\gamma^2 / \sigma_c \approx$
 5650 16 J. To set this into perspective, for a $\gamma\gamma$ collider at the ILC, Ref. [?] considered a pulse energy of 9 J at a
 5651 four times longer wavelength of $\lambda \approx 1 \mu\text{m}$.

5652 The energies of the leftover electrons after conversion extend from about 10 to 60 GeV. This spent
 5653 electron beam, with its enormous energy spread, must be safely extracted from the interaction region. The
 5654 detector-integrated dipole magnets will assist in this process. They will also move the scattered electrons
 5655 away from the interaction point. A beam dump for the neutral photons should also be installed, behind the
 5656 downstream quadrupole channel.

5657 Figure ?? presents an example photon energy spectrum after the conversion and a luminosity spectrum [?],
 5658 obtained from a simulation with the Monte-Carlo code CAIN [?].

5659 Differently from $\gamma\gamma$ collisions at a linear collider, thanks to the much larger IP spot size and smaller
 5660 beam energy, the conversion point can be a much larger distance $\Delta s \approx \beta^* \sim 0.1 \text{ m}$ away from the interaction
 5661 point, which could simplify the integration in the detector, and is also necessary as otherwise, with e.g. a
 5662 mm-distance between CP and IP, the conversion would take place inside the proton bunch.

5663 To achieve the required laser pulse energy, external pulses can be stacked in a recirculating optical cavity.
 5664 For an electron bunch spacing of e.g. 200 ns, the path length of the recirculation could be 60m. A schematic
 5665 of a possible mirror system is sketched in Fig. ?? (adapted from [?]).

5666 8.1.7 Summary of Basic Parameters and Configurations

5667 The baseline 60-GeV ERL option presented here can provide a ep luminosity of $10^{33} \text{ cm}^{-2}\text{s}^{-1}$, at less than
 5668 100 MW total electrical power for the electron branch of the collider, and with less than 9 km circumference.
 5669 The 21 GV of SC-RF installation represents its main hardware component.

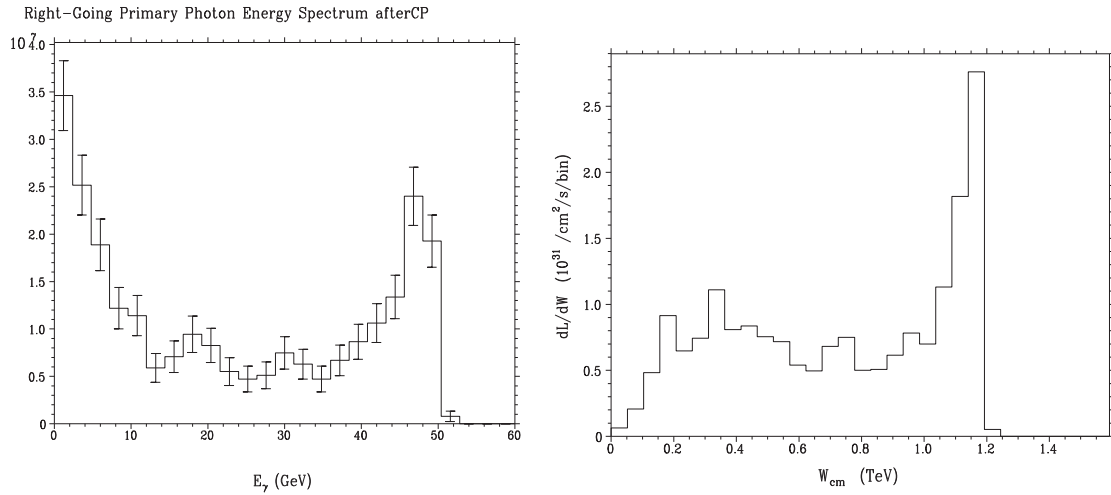


Figure 8.11: Simulated example photon spectrum after the conversion point (left) and γ - p luminosity spectrum [?].

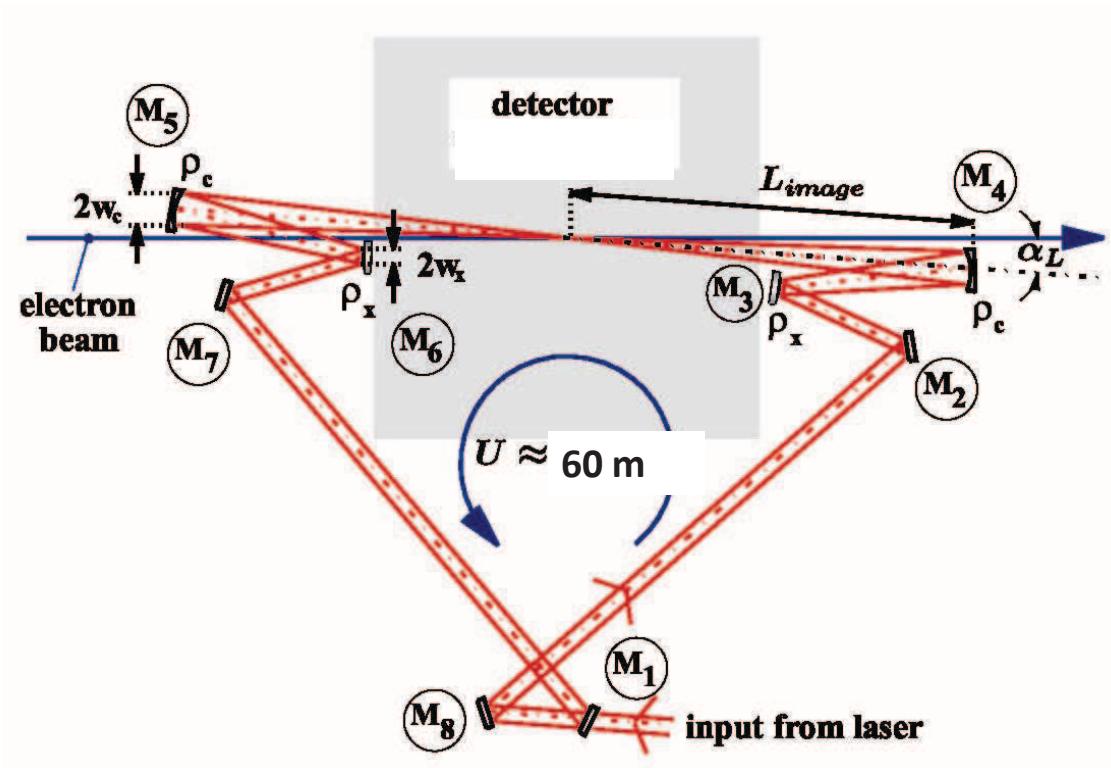


Figure 8.12: Recirculating mirror arrangement providing a laser-pulse path length of 60 m for pulse stacking synchronously with the arriving electron bunches (adapted from [?]).

5670 A pulsed 140-GeV linac, without energy recovery, could achieve a luminosity of $1.4 \times 10^{31} \text{ cm}^{-2}\text{s}^{-1}$, at
5671 higher c.m. energy, again with less than 100 MW electrical power, and shorter than 9 km in length. The
5672 pulsed linac can accommodate a γ - p/A option. An advanced, novel type of energy recovery, proposed for
5673 the single straight high-energy linac case, includes a second decelerating linac, and multiple 10-GeV “energy-
5674 transfer beams”. This type of collider could potentially reach luminosities of $10^{35} \text{ cm}^{-2}\text{s}^{-1}$.

5675 High polarization is possible for all linac-ring options. Beam-beam effects are benign, especially for the
5676 proton beam, which will not be affected by the presence of the electron beam.

5677 Producing the required number of positrons needed for high-luminosity proton-positron collisions is the
5678 main open challenge for a linac-ring LHeC. Recovery of the positrons together with their energy, as well as
5679 fast transverse cooling schemes, are likely to be essential ingredients for any linac-based high-luminosity ep
5680 collider involving positrons.

5681 8.2 Interaction region

5682 This section presents a first conceptual design of the LHeC linac-ring Interaction Region (IR). The merits of
5683 the IR are a very low β^* of 0.1m with proton triplets as close as possible to the IP to minimize chromaticity.
5684 Head-on proton-electron collisions are achieved by means of dipoles around the Interaction Point (IP). The
5685 Nb₃Sn superconductor has been chosen for the proton triplets since it provides the largest gradient. If this
5686 technology proves not feasible in the timescale of the LHeC a new design of the IR can be pursued using
5687 standard technology.

5688 The main goal of this first design is to evaluate potential obstacles, decide on the needs of special
5689 approaches for chromaticity correction and evaluate the impact of the IR synchrotron radiation.

5690 8.2.1 Layout

5691 A crossing angle of 6 mrad between the non-colliding proton beams allows enough separation to place the
5692 proton triplets. Only the proton beam colliding with the electrons is focused. A possible configuration in
5693 IR2 could be to inject the electrons parallel to the LHC Beam1 and collide them head-on with Beam2, see
5694 Fig. ???. The signs of the separation and recombination dipoles (D1 and D2) have to be changed to allow
5695 for the large crossing angle at the IP. The new D1 has one aperture per beam and is 4.5 times stronger
5696 than the LHC design D1. The new D2 is 1.5 times stronger than the LHC design D2. Both dipoles feature
5697 about a 6 T field. The lengths of the nominal LHC D1 and D2 dipoles have been left unchanged, 23 m and
5698 9 m, respectively. However the final IR design will need to incorporate a escape line for the neutral particles
5699 coming from the IP, probably requiring to split D1 into two parts separated by tens of meters.

5700 Bending dipoles around the IP are used to make the electrons collide head-on with Beam2 and to safely
5701 extract the disrupted electron beam. The required field of these dipoles is determined by the L^* and the
5702 minimum separation of the electron and the focused beam at the first quadrupole (Q1). A 0.3 T field
5703 extending over 9 m allows for a beams separation of 0.07 m at the entry of Q1. This separation distance
5704 is compatible with mirror quadrupole designs using Nb₃Sn technology; see Section ???. The electron beam
5705 radiates 48 kW in the IR dipoles. A sketch of the 3 beams, the synchrotron radiation fan and the proton
5706 triplets is shown in Fig. ???.

5707 8.2.2 Optics

5708 Colliding proton optics

5709 The colliding beam triplet starts at $L^*=10\text{m}$ from the IP. It consists of 3 quadrupoles with main parameters
5710 given in Table ???. The quadrupole aperture is computed as $11\max(\sigma_x, \sigma_y)+5$ mm. The 5 mm split into
5711 1.5 mm for the beam pipe, 1.5 mm for mechanical tolerances and 2 mm for the closed orbit. The magnet
5712 parameters for the first two quadrupoles correspond to Nb₃Sn design described in Section ???. The total
5713 chromaticity from the two IP sides amounts to 960 units. The optics functions for the colliding beam are
5714 shown in Fig. ???

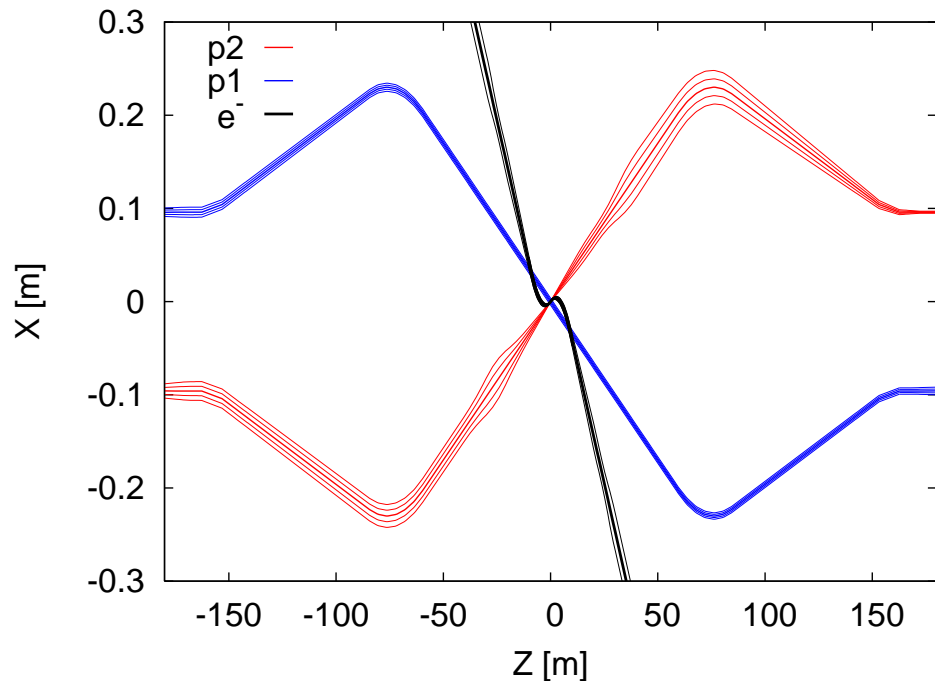


Figure 8.13: LHeC interaction region displaying the two proton beams and the electron beam trajectories with 5σ and 10σ envelopes.

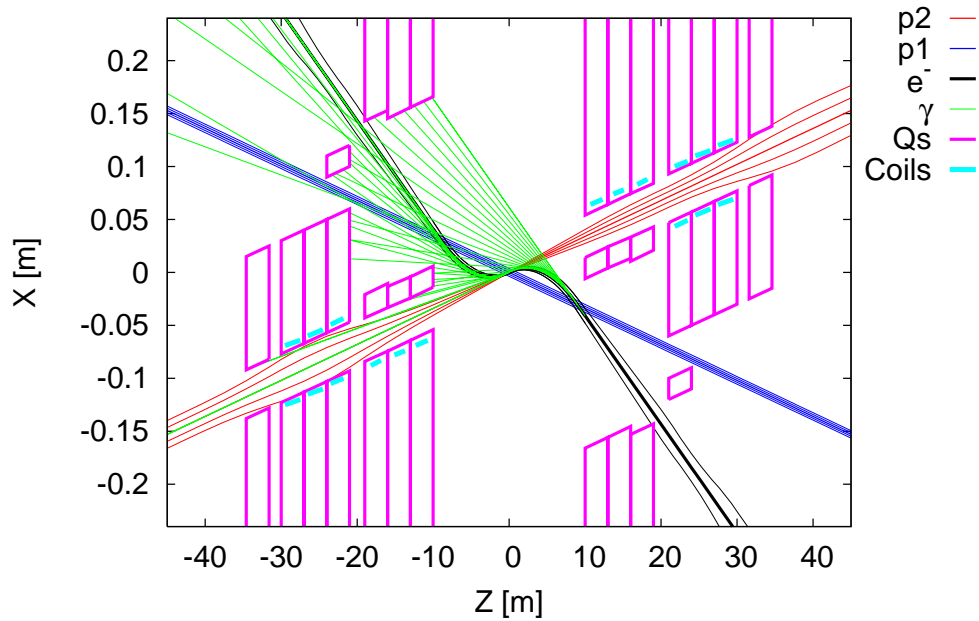


Figure 8.14: LHeC interaction region with a schematic view of synchrotron radiation. Beam trajectories with 5σ and 10σ envelopes are shown. The parameters of the Q1 and Q2 quadrupole segments correspond to the Nb₃Sn half-aperture and single-aperture (with holes) quadrupole of Fig. ??.

Name	Gradient [T/m]	Length [m]	Radius [mm]
Q1	187	9	22
Q2	308	9	30
Q3	185	9	32

Table 8.3: Parameters of the proton triplet quadrupoles. The radius is computed as $11\max(\sigma_x, \sigma_y) + 5$ mm.

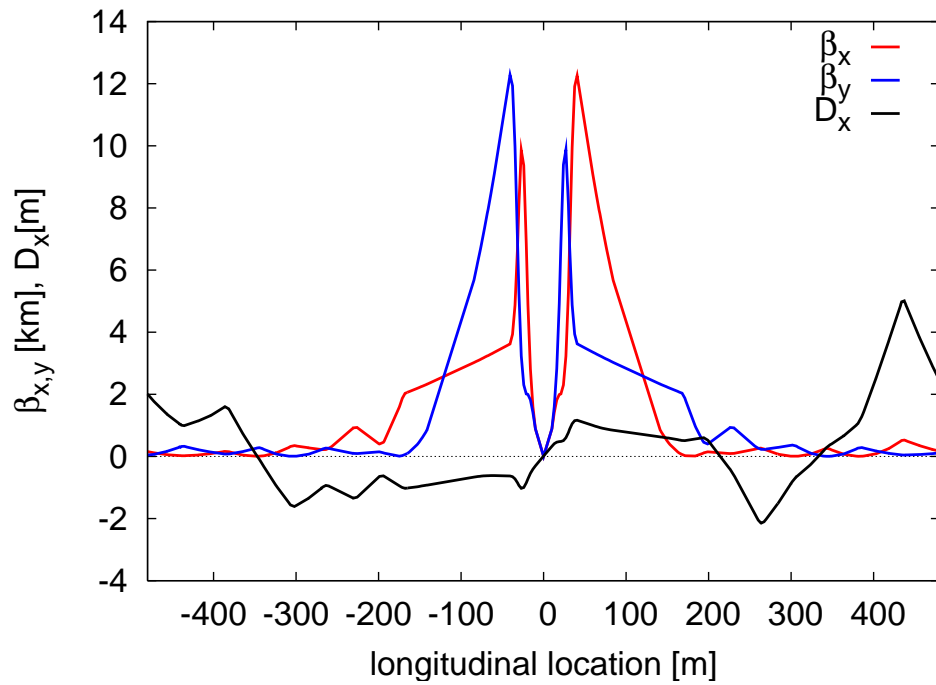


Figure 8.15: Optics functions for main proton beam.

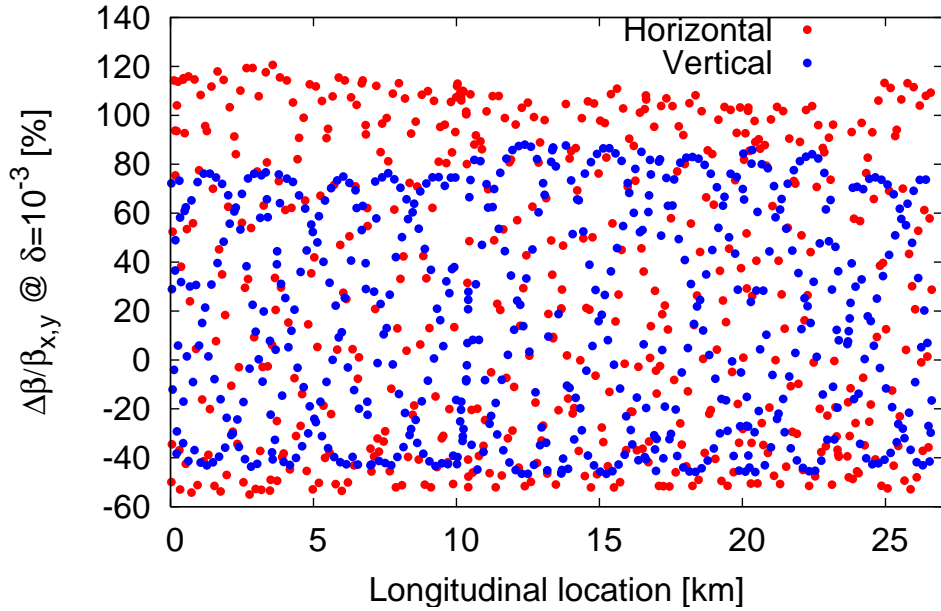


Figure 8.16: Chromatic beta-beating at $dp/p=0.001$.

5715 It was initially hoped that a compact Nb₃Sn triplet with $L^*=10\text{m}$ would allow for a normal chromaticity
 5716 correction using the arc sextupoles. However after matching this triplet to the LHC and correcting linear
 5717 chromaticity the chromatic β -beating at $dp/p=0.001$ is about 100% (see Fig. ??). This is intolerable regard-
 5718 ing collimation and machine protection issues. Therefore a dedicated chromaticity correction scheme has to
 5719 be adopted. A large collection of studies exist showing the feasibility of correcting even larger chromaticities
 5720 in the LHC [?, ?, ?]. Other local chromatic correction approaches as [?], where quadrupole doublets are used
 5721 to provide the strong focusing, could also be considered for the LHeC.

5722 Since LHeC anyhow requires a new dedicated chromaticity correction scheme, current NbTi technology
 5723 could be pursued instead of Nb₃Sn and the L^* could also be slightly increased. The same conceptual three-
 5724 beam crossing scheme as in Fig. ?? could be kept.

5725 To achieve L^* below 23 m requires a cantilever supported on a large mass as proposed for the CLIC QD0 [?]
 5726 to provide sub-nanometer stability at the IP. The LHeC vibration tolerances are much more relaxed, being
 5727 on the sub-micrometer level.

5728 Non-colliding proton optics

5729 The non-colliding beam has no triplet quadrupoles since it does not need to be focused. The LHC “alignment
 5730 optics” [?] was used as a starting point. Figure ?? shows the optics functions around the IP. The LHeC IP
 5731 longitudinal location can be chosen so as to completely avoid unwanted proton-proton collisions.

5732 The non-colliding proton beam travels through dedicated holes in the proton triplet quadrupoles, in Q1
 5733 together with the electron beam. The Q1 hole dimensions are determined by the electron beam, see below.
 5734 By contrast, the non-colliding proton beam travels alone through the first module of the Q2, requiring about
 5735 30 mm full aperture. No fields are assumed in these apertures but the possible residual fields could easily
 5736 be taken into account for the proton optics.

5737 Electron optics

5738 The electron $L^*=30\text{ m}$ has been chosen to allow for enough separation between the proton and the electron
 5739 final focusing quadrupoles. A first design of the optics already matched to the exit of the linac is shown in

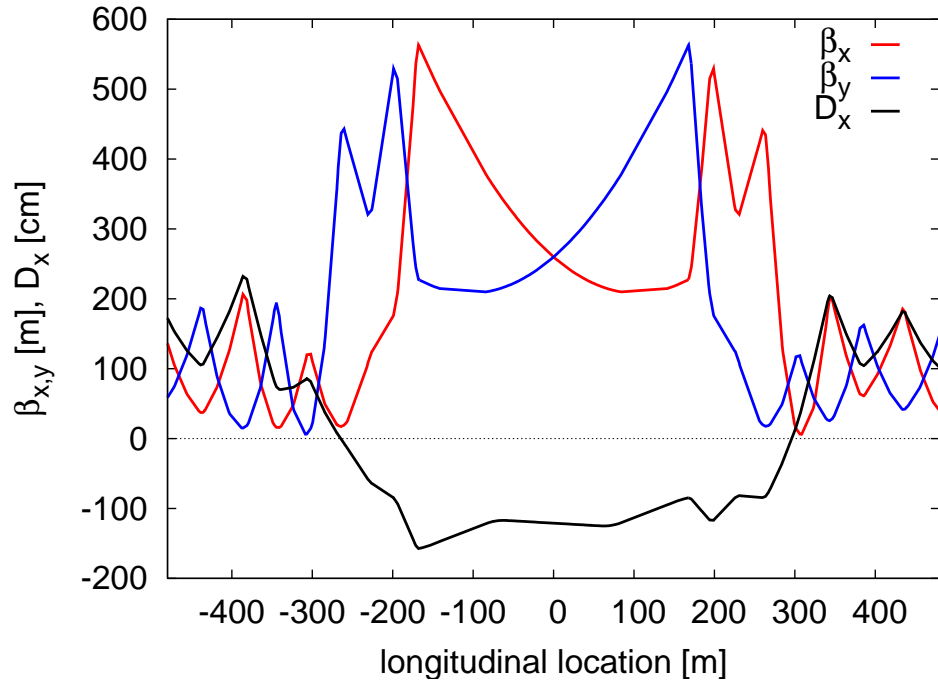


Figure 8.17: Optics functions for the non-colliding proton beam without triplets.

Name	Gradient [T/m]	Length [m]	Radius [mm]
Q1	19.7	1.34	20
Q2A	38.8	1.18	32
Q2B	3.46	1.18	20
Q3	22.3	1.34	22

Table 8.4: Parameters of the electron triplet quadrupoles. The radius is computed as $11\max(\sigma_x, \sigma_y) + 5$ mm.

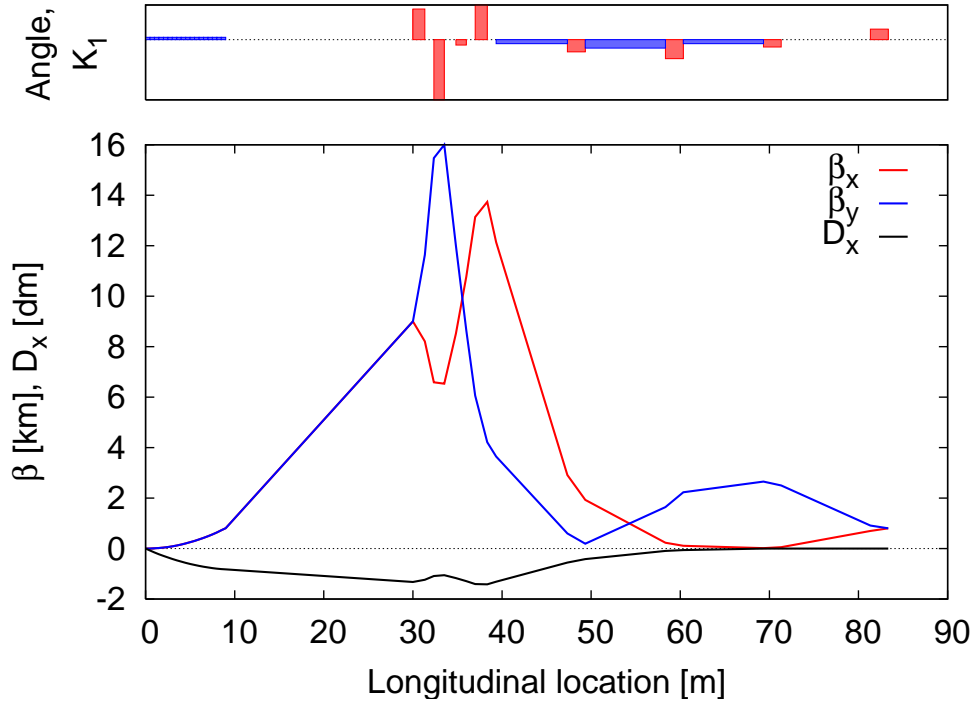


Figure 8.18: Optics of the electron beam.

5740 Fig. ???. The electron focusing quadrupoles feature moderately low gradients as shown in Table ??. The
 5741 IP beam size aberration versus the relative rms energy spread of the beam is shown in Fig. ??. Chromatic
 5742 correction is mandatory for relative energy spreads above 3×10^{-4} . It is recommended to design a chromatic
 5743 correction section. About 200 m are available between the exit of the linac and the IP while the current
 5744 electron final focus is using only 90 m, leaving space for collimation and beam diagnostics.

5745 The electrons shares a hole with the non-colliding proton beam in the first half-quadrupole, Q1, and
 5746 then travels through a dedicated hole in the cryostat of Q2. The common hole in the proton Q1 must
 5747 have about 160 mm full horizontal aperture to allow for the varying separation between the electron and
 5748 non-colliding proton orbit (120 mm) with the usual electron-beam aperture assumptions (± 20 mm). First
 5749 design of mirror magnets for Q1 feature a field of 0.5 T in the electron beam pipe. This value is considered
 5750 too large when compared to the IR dipole of 0.3 T, but new designs with active isolation or dedicated coils
 5751 could considerably reduce this field. Migrating to NbTi technology would automatically reduce this field
 5752 too.

5753 Spent electron beam

5754 The proton electromagnetic field provides extra focusing to the electron beam. This increases the divergence
 5755 of the electron. Figure ?? shows the horizontal distribution of the electrons at 10 m from the IP (entry of
 5756 Q1) as computed by Guineapig [?]. The contribution of dispersion and energy spread to the transverse size
 5757 of the exiting collided beam can be neglected. Therefore, it is possible to linearly scale the sigmas at 10 m to
 5758 estimate both the horizontal and vertical sigmas at any other longitudinal location. The simulation used 10^5
 5759 particles. No particles are observed beyond 4.5 mm from the beam centroid at 10 m from the IP and beyond
 5760 9 mm at 20 m. A radial aperture of 10 mm has been reserved for the beam size at the incoming electron Q1
 5761 hole. The same value of 10 mm seem to be enough to also host the spent electron beams, although it might
 5762 be worth to allocate more aperture margin in the last block of Q1.

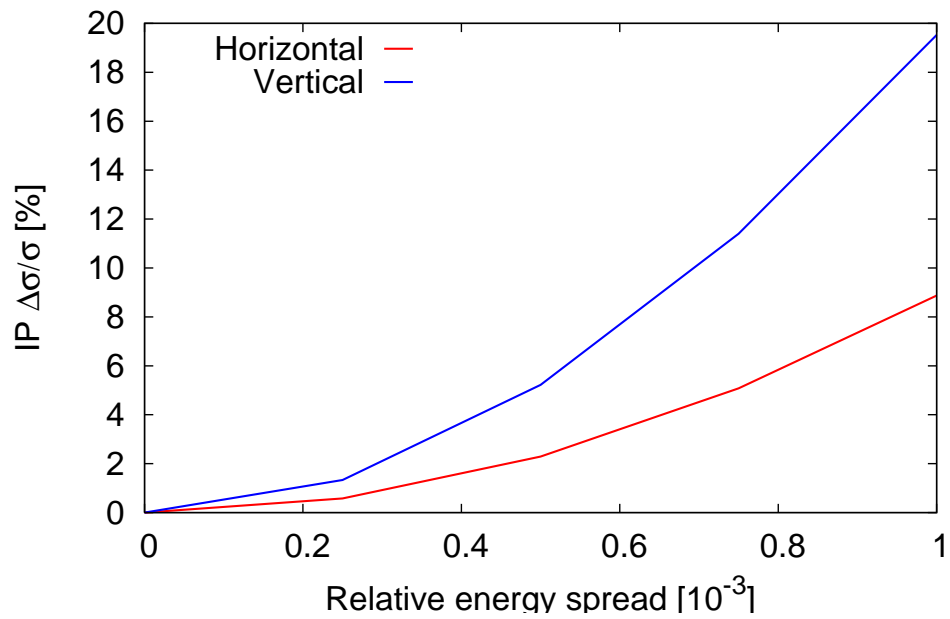


Figure 8.19: IP electron beam size versus relative energy spread of the beam.

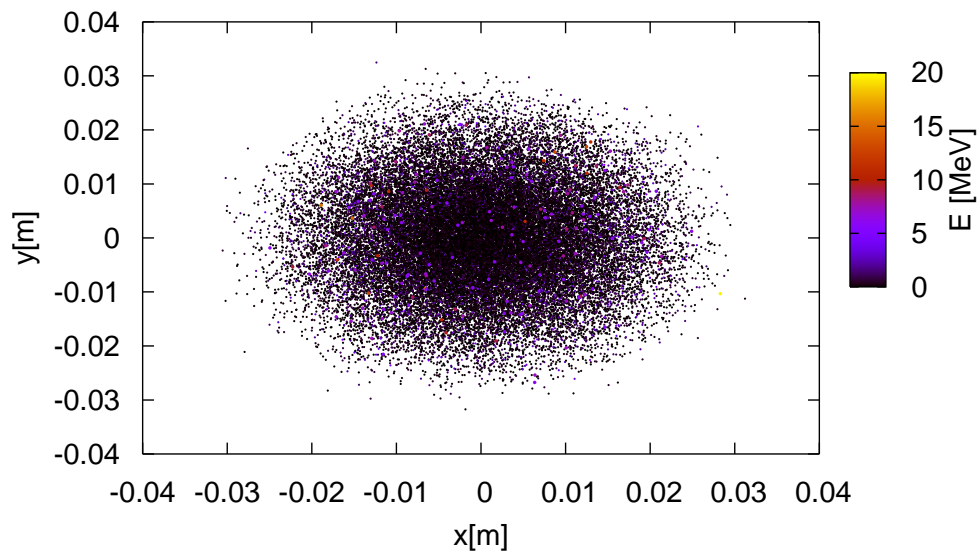


Figure 8.20: Distribution of the spent electron beam at 10 m from the IP. The Gaussian and rms sigmas are shown on the plot.

5763 8.2.3 Modifications for γp or γ -A

5764 The electron beam can be converted into photons by Compton scattering off a high-power laser pulse, as
5765 discussed Section ???. For this option a laser path and high-finesse optical cavities must be integrated into
5766 the interaction region. A multiple mirror arrangement has been sketched in Fig. ??. The 0.3-T dipole field
5767 after the (now) γ -p interaction point will help to separate the Compton-scattered spent electron beam from
5768 the high-energy photons. The high-energy photons propagate straight into the direction of the incoming
5769 proton beam through the main openings of Q1 and Q2, while the spent electrons will be extracted through
5770 the low-field exit holes shared with the non-colliding proton beam, as for electron-proton collisions.

5771 8.2.4 Synchrotron radiation and absorbers

5772 Introduction

5773 The synchrotron radiation (SR) in the linac-ring interaction region has been analyzed by three different
5774 approaches. The SR was simulated using a program made with the Geant4 (G4) toolkit. In addition, a cross
5775 check of the total power and average critical energy was done in IRSYN, a Monte Carlo simulation package
5776 written by R. Appleby [?]. A final cross check of the radiated power has been performed using an analytic
5777 method. The latter two checks confirmed the results obtained from G4. The G4 program uses Monte Carlo
5778 methods to create the desired Gaussian spatial and angular distributions of an electron beam. This electron
5779 beam distribution is then transported through a “vacuum system,” including the magnetic fields for the
5780 separator dipoles. In a non-zero magnetic field SR is generated using the appropriate G4 process classes.
5781 The position, direction, and energy of each photon emitted is written as ntuples at user defined longitudinal
5782 positions (Z values). These ntuples are then used to analyze the SR fan as it evolves in Z . The latter
5783 analysis was done primarily through MATLAB scripts.

5784 This section uses the following conventions. The electron beam is being referred to as *the beam* and the
5785 proton beams will be called either the interacting or non interacting proton beams. The (electron) beam
5786 propagates in the $-Z$ direction and the interacting proton beam propagates in the $+Z$ direction. At the
5787 collision point both beams propagate up the straight Z (or $-Z$) direction. A right-handed coordinate system
5788 is used where the X axis is horizontal and the Y axis vertical. The beam centroid always remains in the
5789 $Y = 0$ plane. The *angle of the beam* will be used to refer to the angle between the beam centroid’s direction
5790 and the Z axis, in the $Y = 0$ plane. This angle is defined such that the beam propagates in the $-X$ direction
5791 when it passes through the dipole field as it moves along Z .

5792 The SR fans extension in the horizontal direction is determined by the angle of the beam at the entrance
5793 of the upstream separator dipole. Because the direction of the photons is parallel to the direction of the
5794 electron from which it is emitted, the angle of the beam and the X -distance to the interacting proton beam
5795 at the Z location of the last proton quadrupole are both greatest for photons generated at the entrance of
5796 the upstream separator dipole and, therefore, this angle defines one of the edges of the synchrotron fan on
5797 the absorber in front of the proton quadrupole. The other edge is defined by the crossing angle, which is
5798 zero for the linac-ring option. The S shaped trajectory of the beam means that the smallest angle of the
5799 beam will be reached at the IP. Therefore, the photons emitted at this point will move exactly along the Z
5800 axis. This defines the other edge of the fan in the horizontal direction.

5801 The SR fans extent in the vertical direction is determined by the beta function and angular spread of
5802 the beam. The beta function along with the emittance defines the local rms beam size. The vertical rms
5803 beam size characterizes the range of Y positions at which photons are emitted. Possibly more importantly,
5804 the vertical angular spread defines the angle between the velocity vector of these photons and the Z axis.
5805 Both of these dependencies are functions of Z . Similar effects also affect the horizontal extension of the SR
5806 fan, however, in the horizontal plane they are of second order when compared to the horizontal deflection
5807 angle in the strong dipole field.

5808 The number density distribution of the SR fan is inferred from the simulations. The number density at
5809 the location of the absorber is highest in the region between the two interacting beams. This is due to the
5810 S shaped trajectory of the beam.

5811 **Parameters**

5812 The parameters for the Linac Ring option are listed in Table ?? . The separation refers to the displacement
 5813 between the two interacting beams at the face of the proton triplet.

Characteristic	Value
Electron Energy [GeV]	60
Electron Current [mA]	6.6
Crossing Angle [mrad]	0
Absorber Position [m]	-9
Dipole Field [T]	0.3
Separation [mm]	75
γ/s	1.37×10^{18}

Table 8.5: LR: Parameters

5814 The energy, current, and crossing angle (θ_c) are the common values used in all LR calculations. The B
 5815 value refers to the constant dipole field created throughout the two dipole magnets in the IR. The direction
 5816 of this field is opposite on either side of the IP. The field is chosen such that 75 mm of separation is reached
 5817 by the face of the proton triplet. This separation was chosen based on S. Russenschuck’s SC quadrupole
 5818 design. [?] The separation between the interacting beams can be increased by raising the constant dipole
 5819 field however for a dipole magnet $P_{SR} \propto |B^2|$, [?] therefore an optimization of the design will need to be
 5820 discussed. The chosen parameters give a flux of 1.37×10^{18} photons per second at Z = -9 m.

5821 **Power and Critical Energy**

5822 Table ?? shows the power of the SR produced in the IR along with the critical energy. This is followed by
 5823 the total power produced in the IR and the critical energy. Since the G4 simulations utilize Monte Carlo,
 5824 multiple runs were used to provide a standard error. This only caused fluctuations in the power since the
 5825 critical energy is static for a constant field and constant energy.

Element	Power [kW]	Critical Energy [keV]
DL	24.4 +/- 0.1	718
DR	24.4 +/- 0.1	718
Total	48.8 +/- 0.1	718

Table 8.6: LR: Power and Critical Energies as calculated with Geant4.

5826 These magnets have strong fields and therefore produce high critical energies and a substantial amount
 5827 of power. Although the power is similar to that of the RR design the critical energy is much larger. This
 5828 comes from the linear dependence of critical energy on magnetic field (*i.e.* $E_c \propto B$) [?]. With the dipole field
 5829 in the LR case being an order of magnitude larger than the dipole fields in the RR case the critical energies
 5830 from the dipole magnets are also an order of magnitude larger in the LR case.

5831 **Comparison**

5832 The IRSYN cross check of the power and critical energies is shown in Table ?? . This comparison was done
 5833 for the total power and the critical energy.

5834 A third cross check to the Geant4 simulations was made for the power as shown in Table ?? . This was
 5835 done using an analytic method for calculating power in dipole magnets [?].

	Power [kW]		Critical Energy [keV]	
	Geant4	IRSYN	Geant4	IRSYN
Total	48.8 +/- 0.1	X	718	718

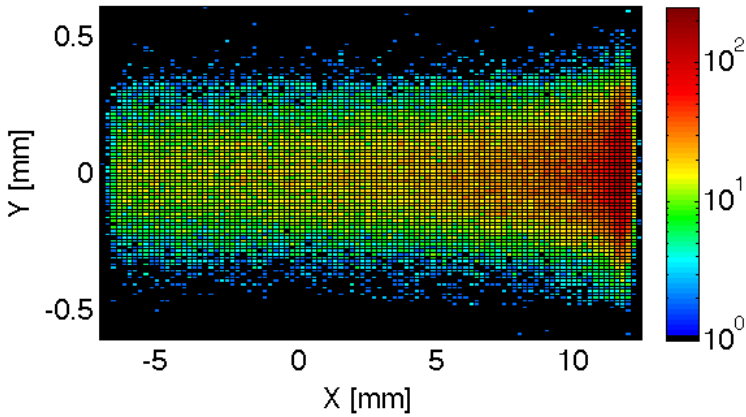
Table 8.7: LR: Geant4 and IRSYN comparison.

	Power [kW]	
Element	Geant4	Analytic
DL	24.4 +/- 0.1	24.4
DR	24.4 +/- 0.1	24.4
Total/Avg	48.8 +/- 0.1	48.8

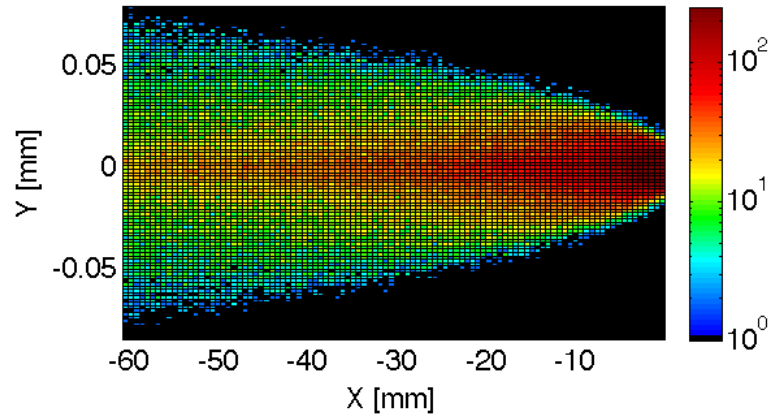
Table 8.8: LR: Geant4 and Analytic method comparison.

5836 **Number Density and Envelopes**

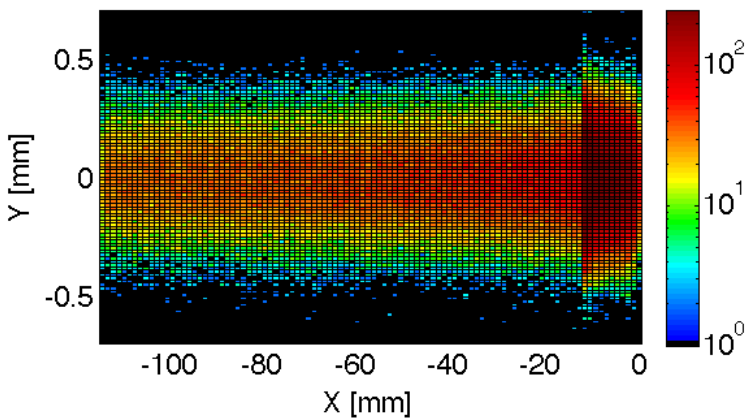
Photon Number Density at Z = 4 m



Photon Number Density at Z = 0 m



Photon Number Density at Z = -4 m



Photon Number Density at Z = -9 m

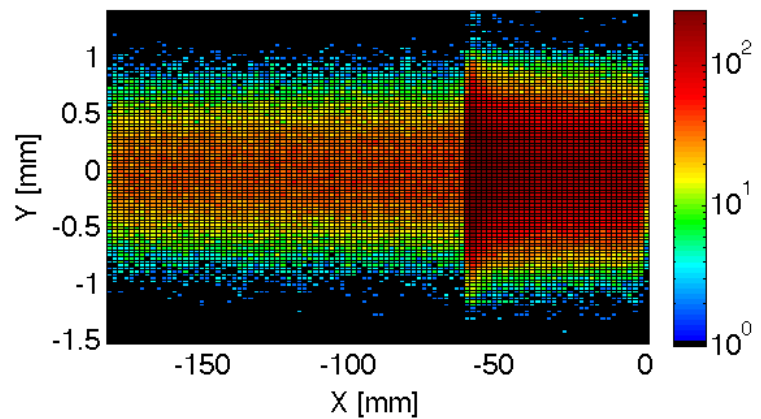


Figure 8.21: LR: Number Density of photons Growth in Z direction.

5837 The number density of photons at different Z values is shown in Figure ???. Each graph displays the
 5838 density of photons in the $Z = Z_o$ plane for various values of Z_o . The first three graphs give the growth
 5839 of the SR fan inside the detector area. This is crucial for determining the dimensions of the beam pipe
 5840 inside the detector area. Since the fan grows asymmetrically in the $-Z$ direction an asymmetric elliptical
 5841 cone shaped beam pipe will minimize these dimensions, allowing the tracking to be placed as close to the
 5842 beam as possible. The horizontal extension of the fan in the LR option is larger than in the RR case. This
 5843 is due to the large angle of the beam at the entrance of the upstream separator dipole. As mentioned in
 5844 the introduction this angle defines the fans extension, and in the LR case this angle is the largest, hence the
 5845 largest fan. The number density of this fan appears as expected. There exists the highest density between
 5846 the two beams at the absorber.

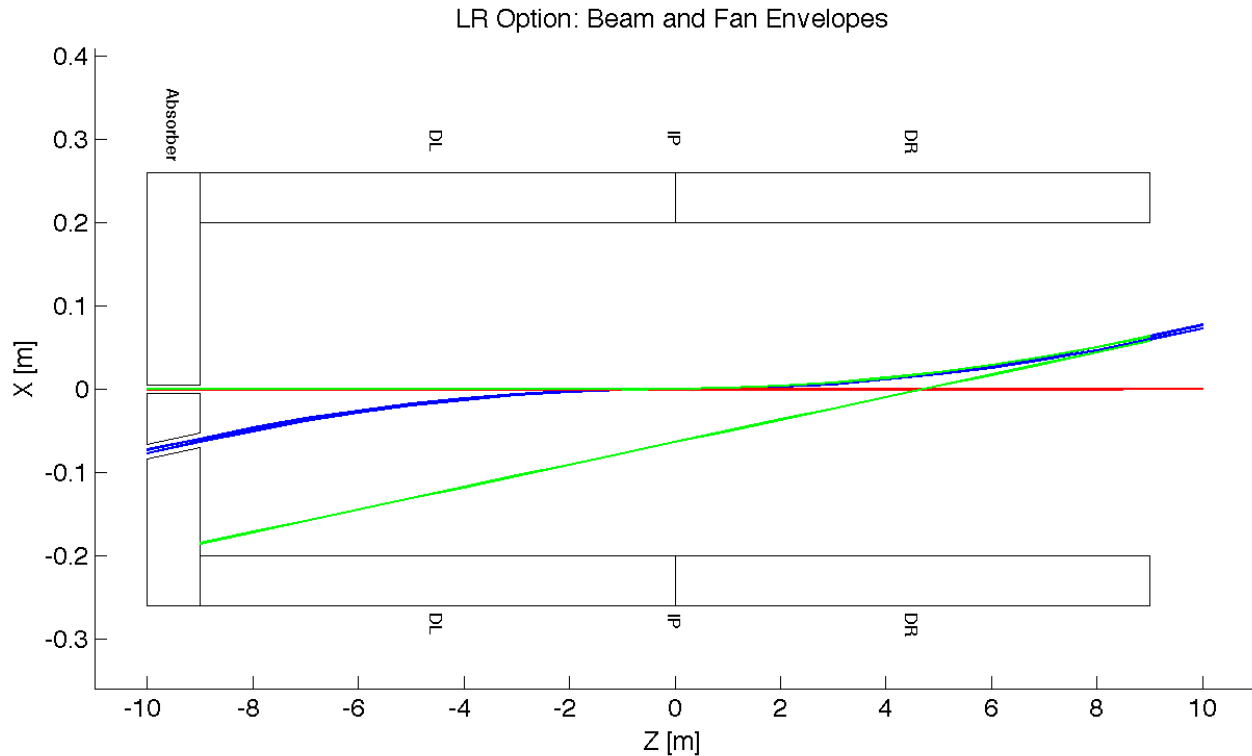


Figure 8.22: LR: Beam Envelopes in Z direction.

5847 In Figure ?? the distribution was given at various Z values however a continuous envelope distribution is
 5848 also important to see everything at once. This can be seen in Figure ??, where the beam and fan envelopes
 5849 are shown in the $Y = 0$ plane. This makes it clear that the fan is antisymmetric which comes from the S
 5850 shape of the electron beam as previously mentioned.

5851 Absorber

5852 The Photon distribution on the absorber surface is crucial. The distribution decides how the absorber must
 5853 be shaped. The shape of the absorber in addition to the distribution on the surface then decides how
 5854 much SR is backscattered into the detector region. In HERA backscattered SR was a significant source of
 5855 background that required careful attention [?]. Looking at Figure ?? it is shown that for the LR option
 5856 35.15 kW of power from the SR light will fall on the face of the absorber which is 73% of the total power.
 5857 This gives a general idea of the amount of power that will be absorbed. However, backscattering and IR

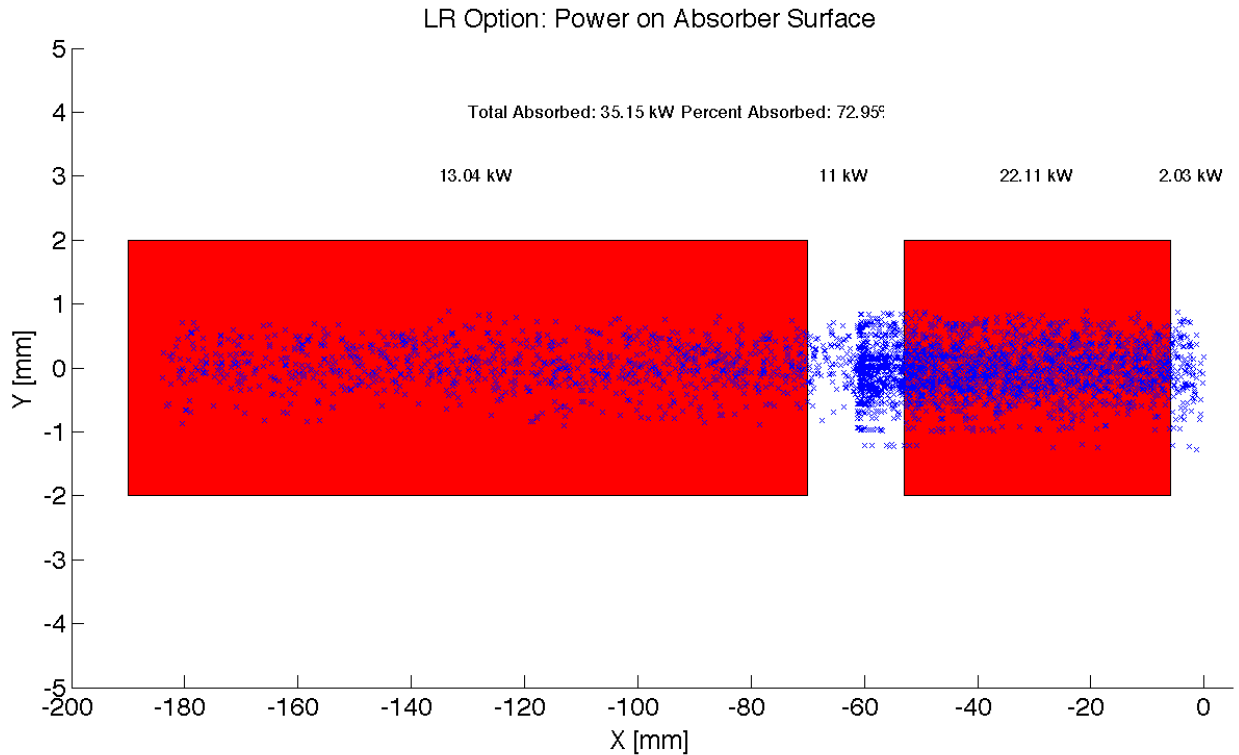


Figure 8.23: LR: Photon distribution on the Absorber Surface.

5858 photons will lower the percent that is actually absorbed.

5859 **Proton Triplet:** The super conducting final focusing triplet for the protons needs to be protected from
 5860 radiation by the absorber. Some of the radiation produced upstream of the absorber however will either pass
 5861 through the absorber or pass through the apertures for the two interacting beams. This is most concerning
 5862 for the interacting proton beam aperture which will have the superconducting coils. A rough upper bound
 5863 for the amount of power the coils can absorb before quenching is 100 W. [?] There is approximately 2 kW
 5864 entering into the interacting proton beam aperture as is shown in Figure ???. This doesnt mean that all this
 5865 power will hit the coils but simulations need to be made to determine how much of this will hit the coils.
 5866 The amount of power that will pass through the absorber (0.25 W) can be disregarded as it is not enough
 5867 to cause any significant effects. The main source of power moving downstream of the absorber will be the
 5868 photons passing through the beams aperture. This was approximately 11 kW as can be seen from Figure
 5869 ???. Most of this radiation can be absorbed in a secondary absorber placed after the first downstream proton
 5870 quadrupole. Overall protecting the proton triplet is important and although the absorber will minimize the
 5871 radiation continuing downstream this needs to be studied in depth.

5872 **Beamstrahlung** The beamstrahlung photons travel parallel to the proton beam until the entrance of D1
 5873 without impacting the triplets. Figure ?? shows the transverse and energy distributions of the beamstrahlung
 5874 photons at the entry of D1 as computed with Guineapig [?]. The maximum photon energy is about 20 MeV
 5875 the average photon energy is 0.4 MeV. The beamstrahlung power is 980 W. D1 has to be designed to properly
 5876 dispose the neutral debris from the IP. Splitting D1 into two parts could allow an escape line for the neutral
 5877 particles.

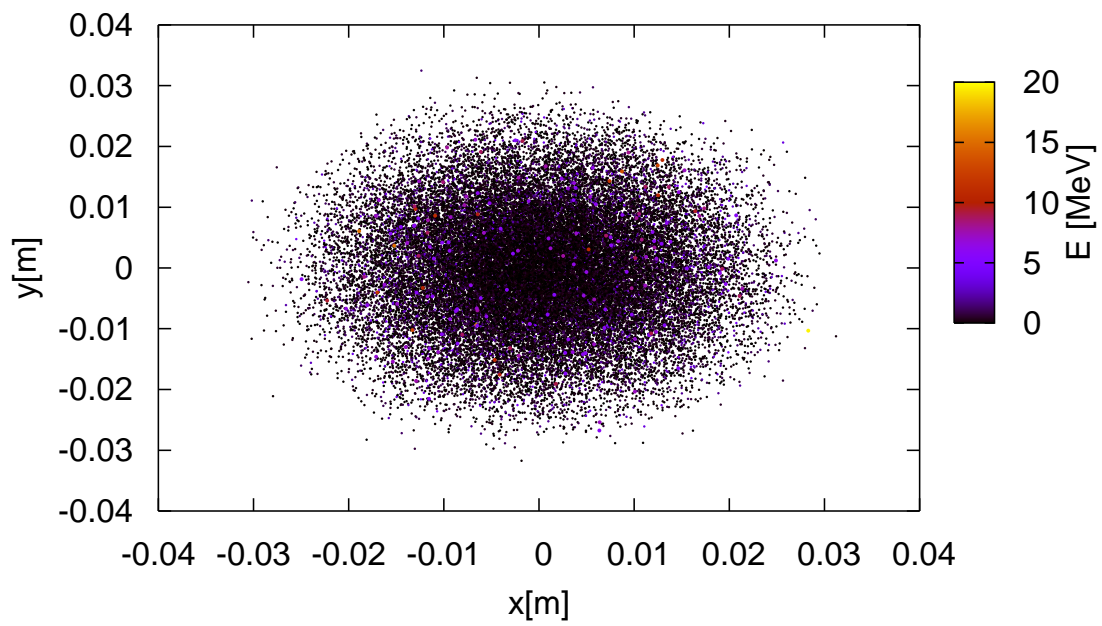


Figure 8.24: Beamstrahlung photons at the entrance of D1.

5878 **Backscattering** Another G4 program was written to simulate the backscattering of photons into the
 5879 detector region. The ntuple with the photon information written at the absorber surface is used as the
 5880 input for this program. An absorber geometry made of copper is described, and general physics processes
 5881 are set up. A detector volume is then described and set to record the information of all the photons which
 5882 enter in an ntuple. The first step in minimizing the backscattering was to optimize the absorber shape.
 5883 Although the simulation didnt include a beampipe the backscattering for different absorber geometries was
 5884 compared against one another to find a minimum. The most basic shape was a block of copper that had
 5885 cylinders removed for the interacting beams. This was used as a benchmark to see the maximum possible
 5886 backscattering. In HERA a wedge shape was used for heat dissipation and minimizing backscattering [?].
 5887 The profile of this geometry in the YZ plane is shown in Figure ???. It was found that this is the optimum
 5888 shape for the absorber. The reason for this is that a backscattered electron would have to have to have its
 5889 velocity vector be almost parallel to the wedge surface to escape from the wedge and therefore it works as a
 5890 trap. One can be seen from Table ??? utilizing the wedge shaped absorber decreased the backscattered power
 5891 by a factor of 4. The energy distribution for the backscattered photons can be seen in Figure ???.

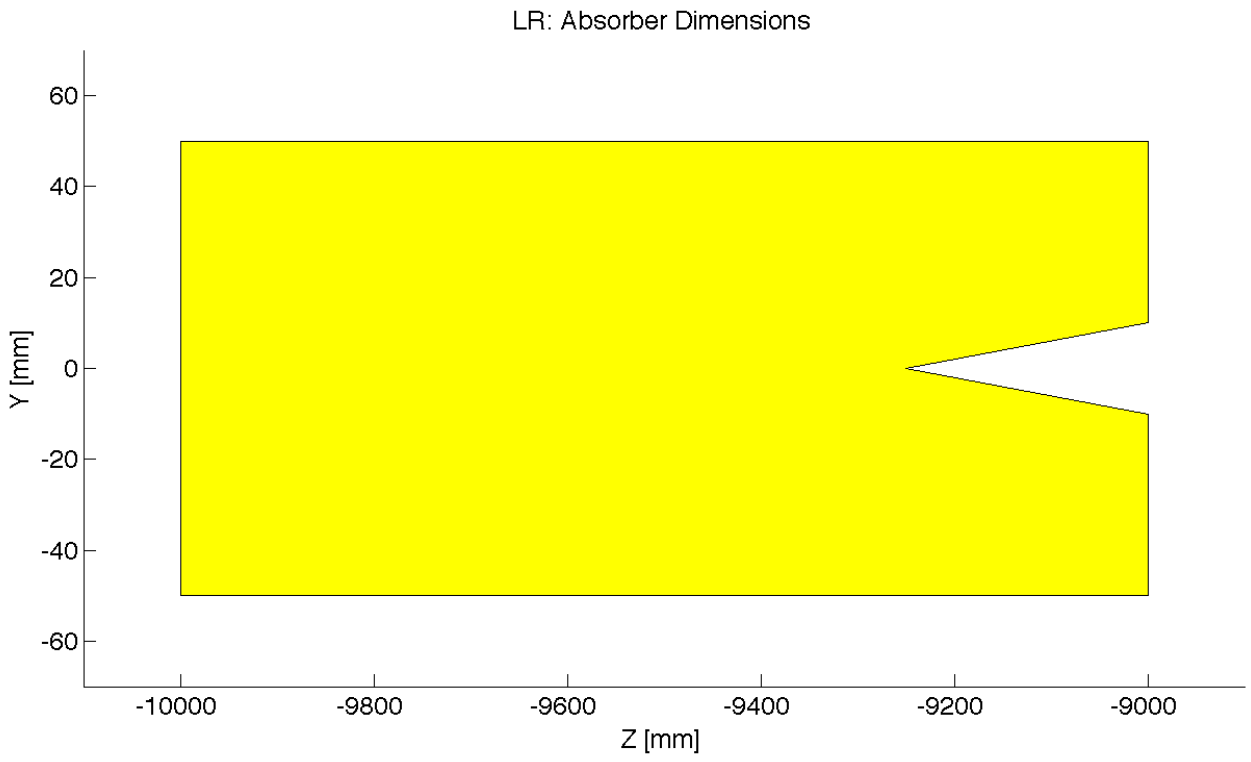


Figure 8.25: LR: Absorber Dimensions.

5892 After the absorber was optimized it was possible to set up a beam pipe geometry. An asymmetric
 5893 elliptical cone beam pipe geometry made of beryllium was used since it would minimize the necessary size
 5894 of the beam pipe as previously mentioned. The next step was to place the lead shield and masks inside this
 5895 beam pipe. To determine placement a simulation was run with just the beam pipe. Then it was recorded
 5896 where each backscattered photon would hit the beam pipe in Z. A histogram of this data was made as shown
 5897 in Figure ???. This determined that the shield should be placed in the Z region ranging from -8 m until the
 5898 absorber (-9 m). The masks were then placed at -8.9 m and -8.3 m. This decreased the backscattered power
 5899 by a factor of 40 as can be seen from Table ???. Overall there is still more optimization that can occur with
 5900 this placement.

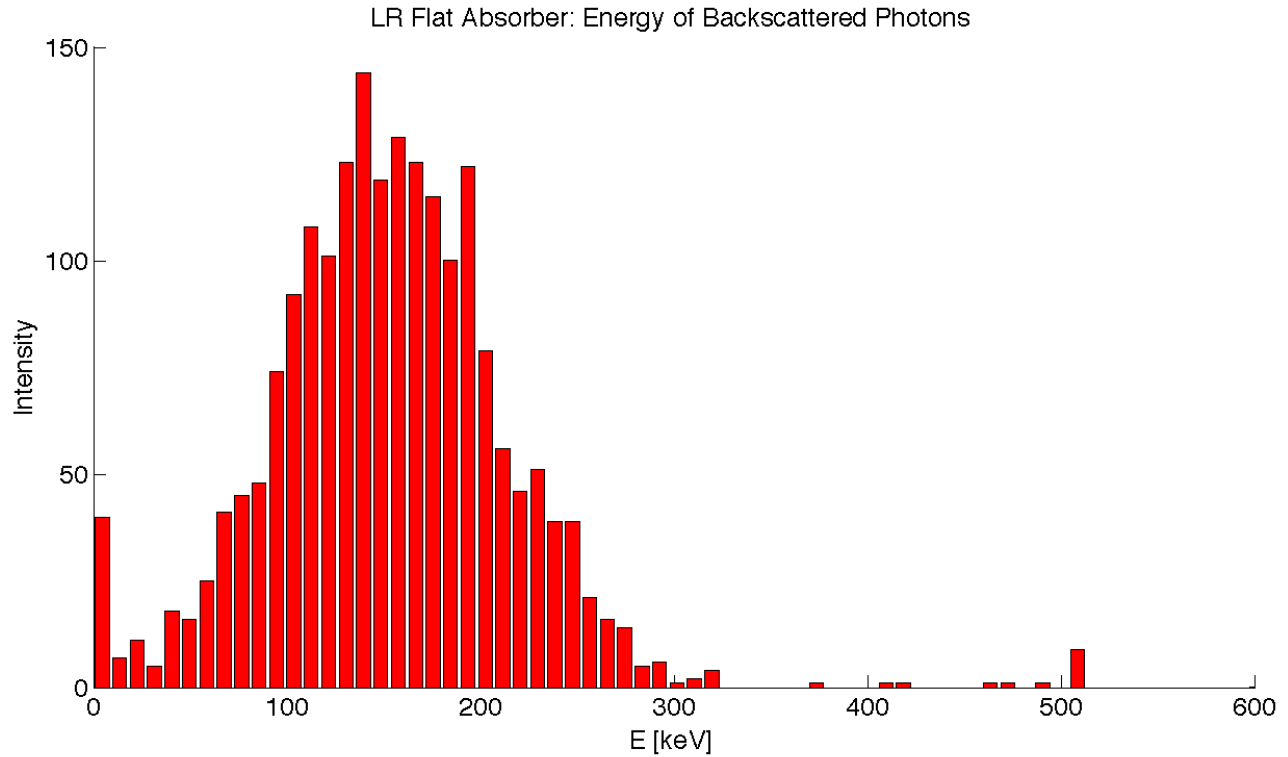


Figure 8.26: LR: Backscattered Energy Distribution.

Absorber Type	Power [W]
Flat	645.9
Wedge	159.1
Wedge & Mask/Shield	4.3

Table 8.9: LR: Power deposition due to Backscattered photons.

5901 Cross sections of the beam pipe in the $Y = 0$ and $X = 0$ planes with the shields and masks included can
 5902 be seen in Figure ??.

5903 8.3 Linac Lattice and Impedance

5904 8.3.1 Overall Layout

5905 The proposed layout of the recirculating linear accelerator complex (RLA) is illustrated schematically in
 5906 Fig. ??. It consists of the following components:

- 5907 • A 0.5 GeV injector with an injection chicane.
- 5908 • A pair of 721.44MHz SCRF linacs. Each linac is one kilometer long with an energy gain 10GeV per
 5909 pass.
- 5910 • Six 180° arcs. Each arc has a radius of one kilometer.

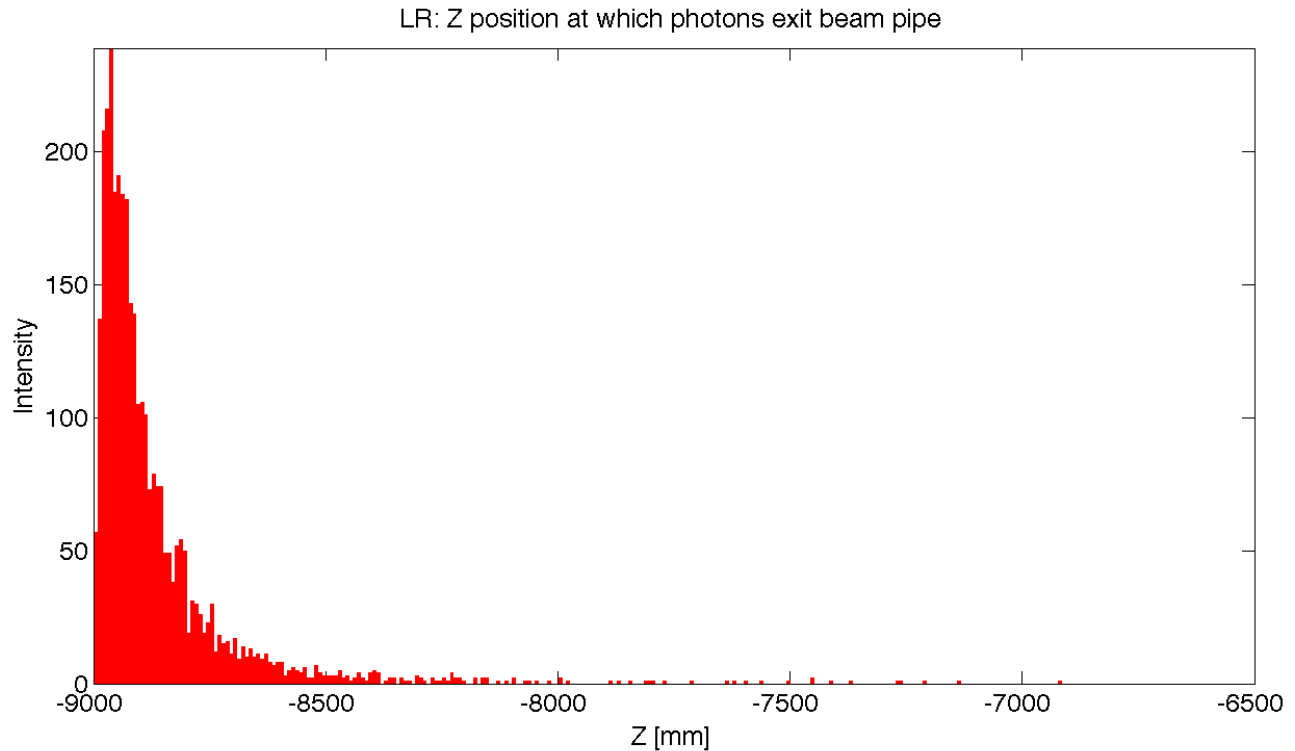


Figure 8.27: LR: Backscattered Photons Exiting the Beam Pipe.

- 5911 • For each arc one re-accelerating station that compensates the synchrotron radiation emitted in this
5912 arc.
- 5913 • A switching station at the beginning and end of each linac to combine the beams from different arcs
5914 and to distribute them over different arcs.
- 5915 • An extraction dump at 0.5 GeV.

5916 After injection, the beam makes three passes through the linacs before it collides with the LHC beam.
5917 The beam will then perform three additional turns in which the beam energy is almost completely extracted.
5918 The size of the complex is chosen such that each turn has the same length and that three turns correspond
5919 to the LHC circumference. This choice is motivated by the following considerations:

- 5920 • To avoid the build-up of a significant ion density in the accelerator complex, clearing gaps may be
5921 required in the beam.
- 5922 • The longitudinal position of these gaps must coincide for each of the six turns that a beam performs.
5923 This requires that the turns have the same length.
- 5924 • Due to the gaps some LHC bunches will collide with an electron bunch but some will not. It is
5925 advantageous to have each LHC bunch either always collide with an electron bunch or to never collide.
5926 The choice of length for one turn in the RLA allows to achieve this.

5927 Some key beam parameters are given in table ??.

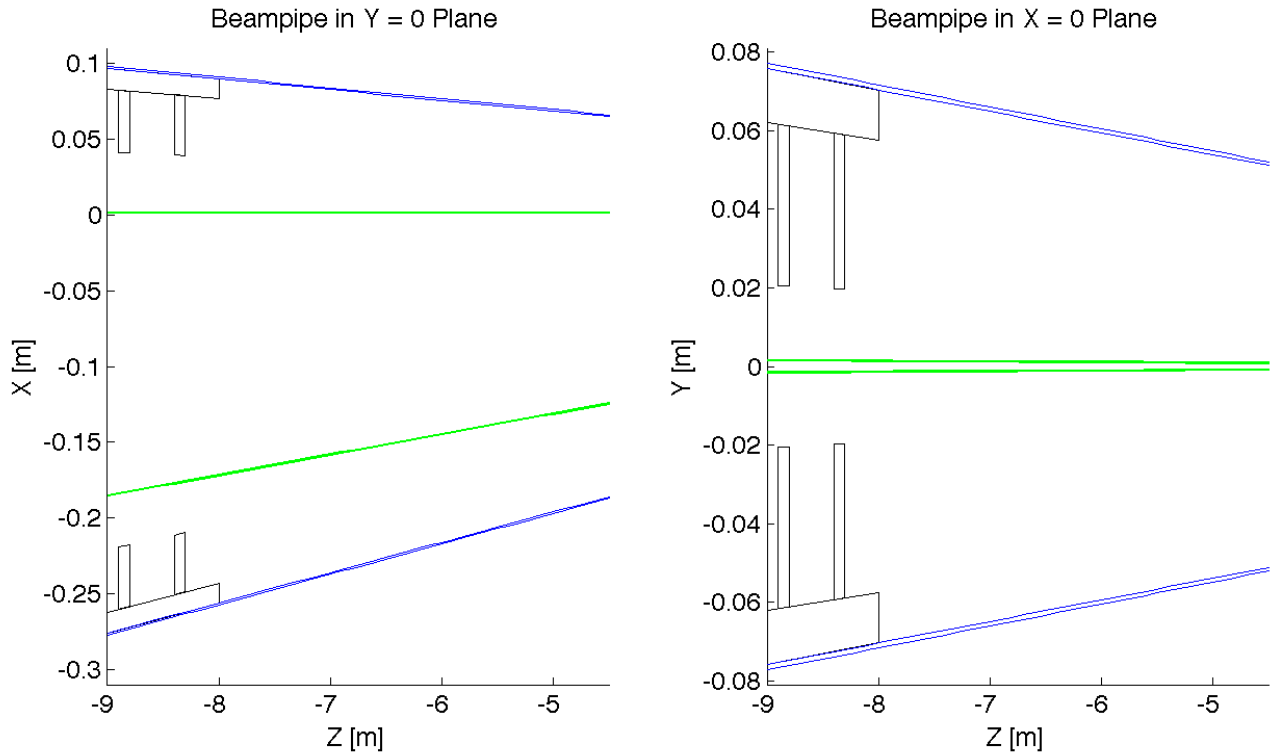


Figure 8.28: LR: Beampipe Cross Sections.

Parameter	Symbol	Value
Particles per bunch	N	$2 \cdot 10^9$
Initial normalised transverse emittance	ϵ_x, ϵ_y	$30 \mu\text{m}$
Normalised transverse emittance at IP	ϵ_x, ϵ_y	$50 \mu\text{m}$
Bunch length	σ_z	$600 \mu\text{m}$

Table 8.10: Key beam parameters.

5928 8.3.2 Linac Layout and Lattice

5929 The key element of the transverse beam dynamics in a multi-pass recirculating linac is an appropriate choice
 5930 of multi-pass linac optics. The focusing strength of the quadrupoles along the linac needs to be set such
 5931 that one can transport the beam at each pass. Obviously, one would like to optimize the focusing profile to
 5932 accommodate a large number of passes through the RLA. In addition, the requirement of energy recovery
 5933 puts a constraint on the exit/entrance Twiss functions for the two linacs. As a baseline we have chosen a
 5934 FODO lattice with a phase advance of 130° for the beam that passes with the lowest energy and a quadrupole
 5935 spacing of 28m [?]. Alternative choices are possible. An example is an optics that avoids any quadrupole in
 5936 the linacs [?].

5937 Linac Module Layout

5938 The linac consists of a series of units, each consisting of two cryomodules and one quadrupole pack. See
 5939 Fig. ?? for the layout. Each cryomodule is 12.8m and contains eight 1m-long accelerating cavities. The

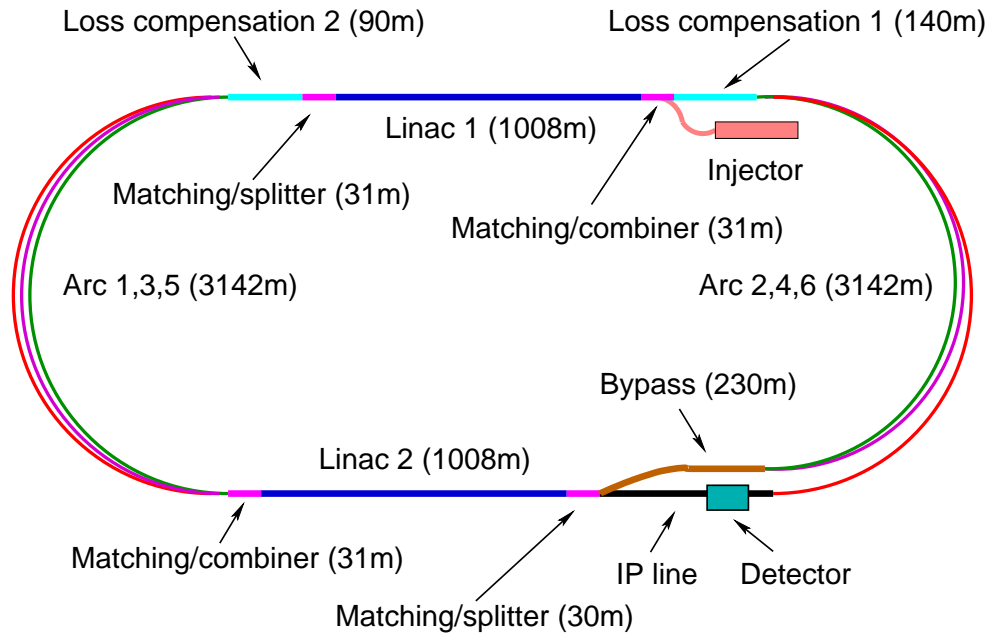


Figure 8.29: The schematic layout of the recirculating linear accelerator complex.

Figure 8.30: The schematic layout of a linac unit.

5940 interconnect between two adjacent cryomodules is 0.8m long. The quadrupole pack is 1.6m long, including
 5941 the interconnects to the adjacent cryomodules. The whole unit is 28m long.

5942 Each quadrupole pack contains a quadrupole, a beam position monitor and a vertical and horizontal
 5943 dipole corrector, see section 2.9.

5944 Linac Optics

5945 The linac consists of 36 units with a total length of 1008m. In the first linac, the strength of the quadrupoles
 5946 has been chosen to provide a phase advance per cell of 130° for the beam in its first turn. In the second
 5947 linac, the strength has been set to provide a phase advance of 130° for the last turn of the beam. The initial
 5948 Twiss parameters of the beam and the return arcs are optimised to minimise the beta-functions of the beams
 5949 in the following passages. The criterion used has been to minimise the integral

$$\int_0^L \frac{\beta}{E} ds \quad (8.6)$$

5950 Single bunch transverse wakefield effects and multi-bunch effects between bunches that have been injected
 5951 shortly after each other are proportional to this integral [?]. The final solution is shown in Fig. ???. A
 5952 significant beta-beating can be observed due to the weak focusing for the higher energy beams.

5953 Return Arc Optics

5954 At the ends of each linac the beams need to be directed into the appropriate energy-dependent arcs for
 5955 recirculation. Each bunch will pass each arc twice, once when it is accelerated before the collision and once
 5956 when it is decelerated after the collision. The only exception is the arc at highest energy that is passed
 5957 only once. For practical reasons, horizontal rather than vertical beam separation was chosen. Rather than

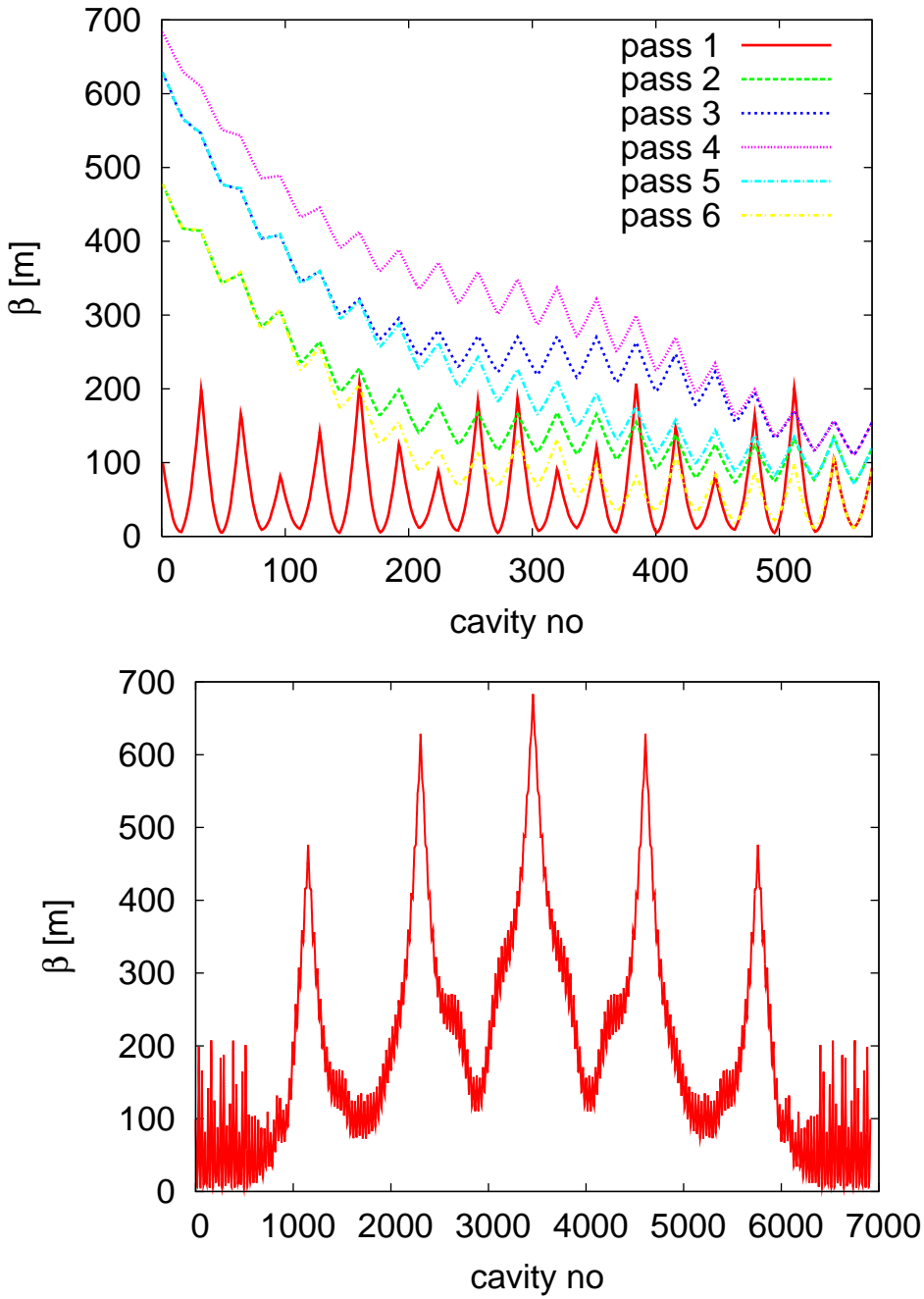


Figure 8.31: Beta-functions in the first linac. On the top, the beta-functions of the six different beam passages in the first linac are shown. On the bottom, the beta-function as seen by the beam during his stay in the linacs are shown.

turn no	E [GeV]	ΔE [MeV]	σ_E/E [%]
1	10.5	0.7	0.00036
2	20.5	10.2	0.0019
3	30.5	49.8	0.0053
4	40.5	155	0.011
5	50.5	375	0.020
6	60.5	771	0.033
7	50.5	375	0.044
8	40.5	155	0.056
9	30.5	49.8	0.074
10	20.5	10.2	0.11
11	10.5	0.7	0.216
dump	0.5	0.0	4.53

Table 8.11: Energy loss due to synchrotron radiation in the arcs as a function of the arc number. The integrated energy spread induced by synchrotron radiation is also shown.

5958 suppressing the horizontal dispersion created by the spreader, the horizontal dispersion can be smoothly
5959 matched to that of the arc, which results in a very compact, single dipole, spreader/recombiner system.

5960 The initial choice of large arc radius (1 km) was dictated by limiting energy loss due to synchrotron
5961 radiation at top energy (60.5 GeV) to less than 1%. However other adverse effects of synchrotron radiation
5962 on beam phase-space such as cumulative emittance and momentum growth due to quantum excitations are
5963 of paramount importance for a high luminosity collider that requires normalized emittance of 50 mm mrad.

5964 Three different arc designs have been developed [?]. In the design for the lowest energy turns, the beta-
5965 functions are kept small in order to limit the required vacuum chamber size and consequently the magnet
5966 aperture. At the highest energy, the lattice is optimised to keep the emittance growth limited, while the
5967 beta-functions are allowed to be larger. A cell of the lowest and one of the highest energy arc is shown in
5968 Fig. ?? All turns have a bending radius of 764m. The beam pipe diameter is 25mm, which corresponds to
5969 more than 12σ aperture.

5970 An interesting alternative optics, which pushes towards a smaller beam pipe, has also been developed [?].

5971 Synchrotron Radiation in Return Arcs

5972 Synchrotron radiation in the arcs leads to a significant beam energy loss. This loss is compensated by the
5973 small linacs that are incorporated before or after each arc when the beams are already or still separated
5974 according to their energy, see Fig. ?. The energy loss at the 60GeV turn-round can be compensated by a
5975 linac with an RF frequency of 721.44MHz. The compensation at the other arcs is performed with an RF
5976 frequency of 1442.88MHz. In this way the bunches that are on their way to the collision point and the ones
5977 that already collided can both be accelerated. This ensures that the energy of these bunches are the same
5978 on the way to and from the interaction point, which simplifies the optics design. If the energy loss were not
5979 compensated the beams would have a different energy at each turn, so that the number of return arcs would
5980 need to be doubled.

5981 The synchrotron radiation is also generating an energy spread of the beam. In Tab. ?? the relative energy
5982 spread is shown as a function of the arc number that the beam has seen. At the interaction point, the
5983 synchrotron radiation induced RMS energy spread is only 2×10^{-4} , which adds to the energy spread of the
5984 wakefields. At the final arc the energy spread reaches about 0.22%, while at the beam dump it grows to a
5985 full 4.5%.

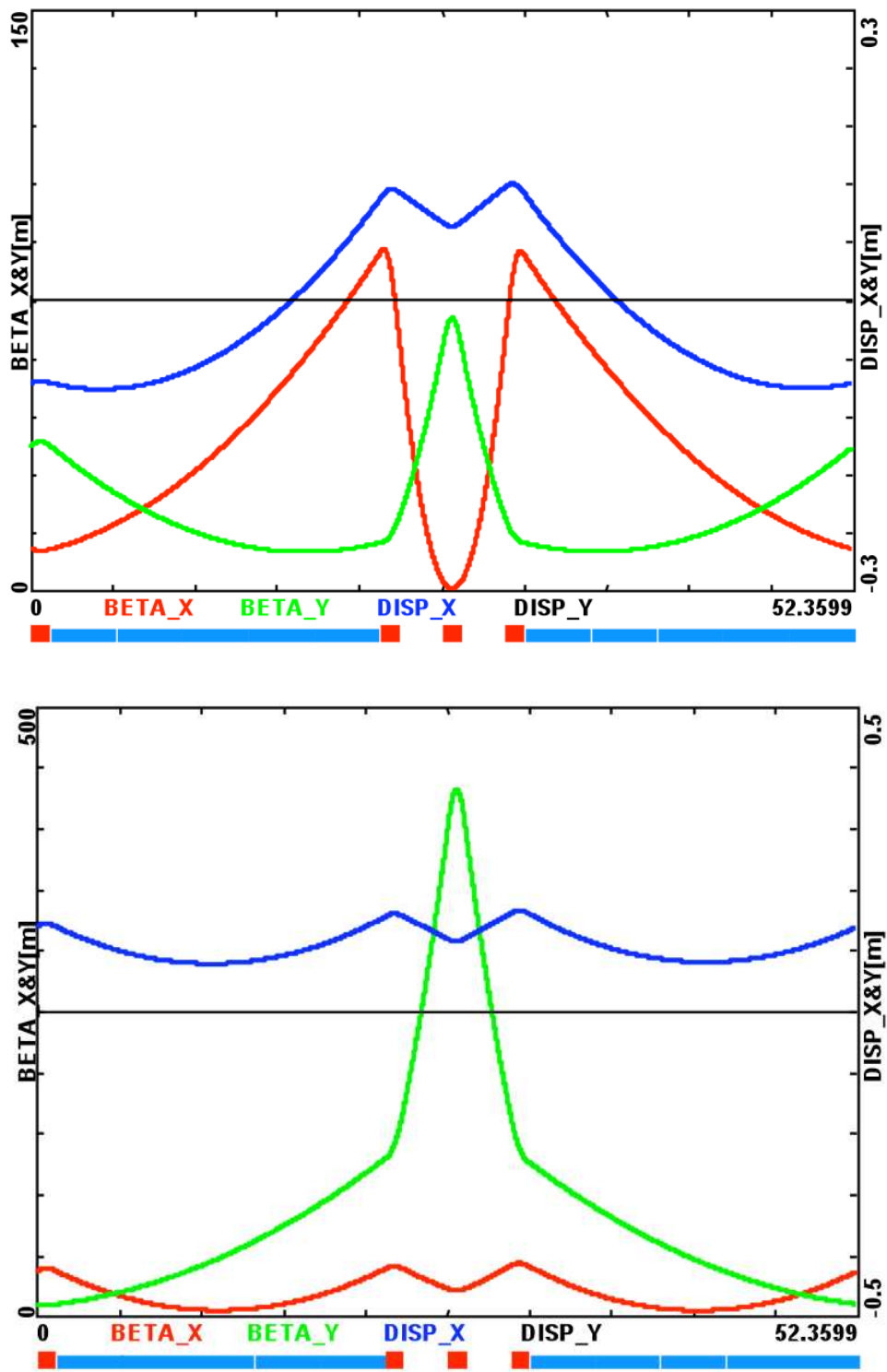


Figure 8.32: The optics of the lowest (top) and the highest (bottom) energy return arcs.

turn no	E [GeV]	$\Delta\epsilon_{arc}$ [μm]	$\Delta\epsilon_t$ [μm]
1	10.5	0.0025	0.0025
2	20.5	0.140	0.143
3	30.5	0.380	0.522
4	40.5	2.082	2.604
5	50.5	4.268	6.872
6	60.5	12.618	19.490
5	50.5	4.268	23.758
4	40.5	2.082	25.840
3	30.5	0.380	26.220
2	20.5	0.140	26.360
1	10.5	0.0025	26.362

Table 8.12: The emittance growth due to synchrotron radiation in the arcs.

5986 The growth of the normalised emittance is given by

$$\Delta\epsilon = \frac{55}{48\sqrt{3}} \frac{\hbar c}{mc^2} r_e \gamma^6 I_5 \quad (8.7)$$

5987 Here, r_e is the classical electron radius, and I_5 is given by

$$I_5 = \int_0^L \frac{H}{|\rho|^3} ds = \frac{\langle H \rangle \theta}{\rho^2} \quad H = \gamma D^2 + 2\alpha DD' + \beta D'^2 \quad (8.8)$$

5988 For a return arc with a total bend angle $\theta = 180^\circ$ one finds

$$\Delta\epsilon = \frac{55}{48\sqrt{3}} \frac{\hbar c}{mc^2} r_e \gamma^6 \pi \frac{\langle H \rangle \theta}{\rho^2} \quad (8.9)$$

5989 The synchrotron radiation induced emittance growth is shown in table ???. Before the interaction point
5990 a total growth of about $7\mu\text{m}$ is accumulated. The final value is $26\mu\text{m}$. While this growth is significant
5991 compared to the target emittance of $50\mu\text{m}$ at the collision point, it seems acceptable.

5992 Matching Sections and Energy Compensation

5993 Currently we do not have a design of the matching sections. However, we expect these sections to be
5994 straightforward. For the case of the linac optics without quadrupoles and the alternative return arc lattice
5995 design matching sections designs exist and exhibit no issues [?]. Also the sections that compensate the energy
5996 loss in the arcs have not been designed. But this again should be straightforward.

5997 8.3.3 Beam Break-Up

5998 Single-Bunch Wakefield Effect

5999 In order to evaluate the single bunch wakefield effects we used PLACET [?]. The full linac lattice has
6000 been implemented for all turns but the arcs have each been replaced by a simple transfer matrix, since the
6001 matching sections have not been available.

6002 Single bunch wakefields were not available for the SPL cavities. We therefore used the wakefields in
6003 the ILC/TESLA cavities [?]. In order to adjust the wakefields to the lower frequency and larger iris radius

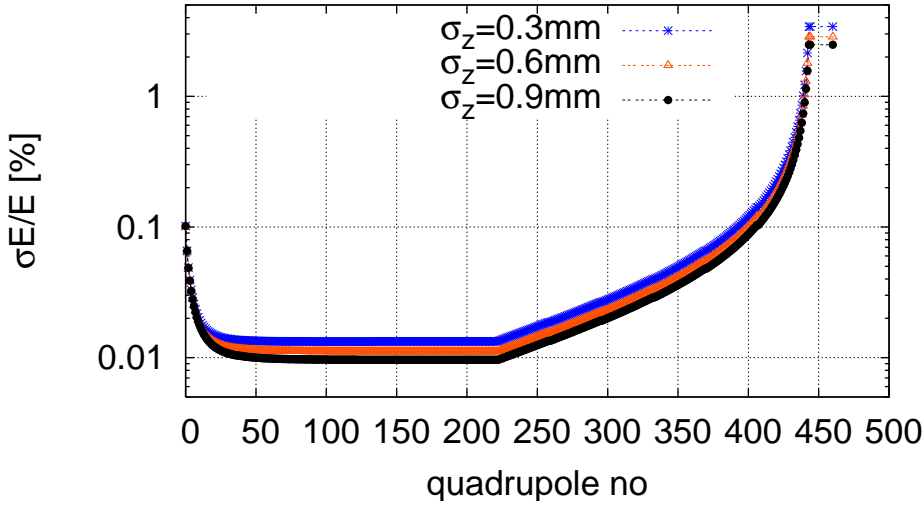


Figure 8.33: The RMS energy spread due to single bunch wakefields along the linacs. The bunch has been cut longitudinally at $\pm 3\sigma_z$ and at $\pm 3\sigma_E$ in the initial uncorrelated energy spread.

6004 (70mm vs. 39mm for the central irises) we used the following scaling

$$W_{\perp}(s) \approx \frac{1}{(70/39)^3} W_{\perp,ILC}(s/(70/39)) \quad W_L(s) \approx \frac{1}{(70/39)^2} W_{L,ILC}(s/(70/39)) \quad (8.10)$$

6005 First, the RMS energy spread along the linacs is determined. An initial uncorrelated RMS energy spread
 6006 of 0.1% is assumed. Three different bunch lengths were studied, i.e. $300\mu\text{m}$, $600\mu\text{m}$ and $900\mu\text{m}$. This longest
 6007 value yields the smallest final energy spread. The energy spread along during the beam life-time can be seen
 6008 in Fig. ???. The wakefield induced energy spread is between 1×10^{-4} and 2×10^{-4} at the interaction point,
 6009 $1-2 \times 10^{-3}$ at the final arc and 3.5–4.5% at the beam dump.

6010 Second, the single bunch beam-break-up is studied by tracking a bunch with an initial offset of $\Delta x = \sigma_x$.
 6011 The resulting emittance growth of the bunch is very small, see Fig. ???.

6012 Multi-Bunch Transverse Wakefield Effects

6013 For a single pass through a linac the multi-bunch effects can easily be estimated analytically [?]. Another
 6014 approach exists in case of two passes through one cavity [?]. It is less straightforward to find an analytic
 6015 solution for multiple turns in linacs with wakefields that vary from one cavity to the next. In this case the
 6016 also phase advance from one passage through a cavity to the next passage depends on the position of the
 6017 cavity within the linac.

6018 We therefore have developed a code to simulate the multi-bunch effect in the case of recirculation and
 6019 energy recovery [?]. It assumes point-like bunches and takes a number of dipole wake field modes into
 6020 account. A cavity-to-cavity frequency spread of the wakefield modes can also be modeled. The arcs are
 6021 replaced with simple transfer matrices. In the simulation, we offset a single bunch of a long train by one
 6022 unit and determine the final position in phase space of all other bunches.

6023 We evaluated the beam stability using the wakefield modes that have been calculated for the SPL cavity
 6024 design [?]. The level of the Q -values of the transverse modes is not yet known. We assume $Q = 10^5$ for all
 6025 modes, which is comparable to the larger of the Q -values found in the TESLA cavities. A random variation
 6026 of the transverse mode frequencies of 0.1% has been assumed, which corresponds to the target for ILC [?].
 6027 The results in Fig. ??? indicate that the beam remains stable in our baseline design. Even in the alternative
 6028 lattice with no focusing in the linacs, the beam would remain stable but with significantly less margin.

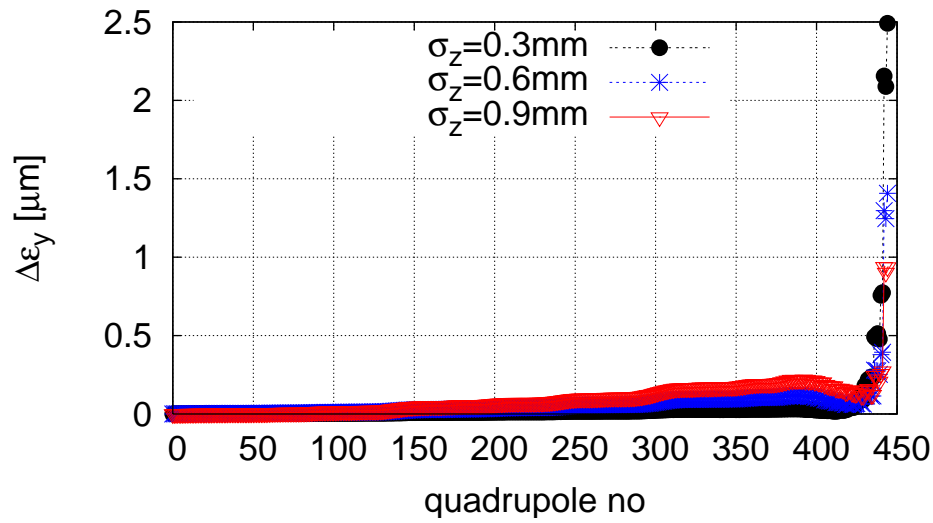


Figure 8.34: The single-bunch emittance growth along the LHeC linacs for a bunch with an initial offset of $\Delta x = \sigma_x$. The arcs have been represented by a simple transfer matrix.

f [GHz]	k [V/pCm ²]	f [GHz]	k [V/pCm ²]
0.9151	9.323	1.675	4.160
0.9398	19.095	2.101	1.447
0.9664	8.201	2.220	1.427
1.003	5.799	2.267	1.377
1.014	13.426	2.331	2.212
1.020	4.659	2.338	11.918
1.378	1.111	2.345	5.621
1.393	20.346	2.526	1.886
1.408	1.477	2.592	1.045
1.409	23.274	2.592	1.069
1.607	8.186	2.693	1.256
1.666	1.393	2.696	1.347
1.670	1.261	2.838	4.350

Table 8.13: The considered dipole modes of the SPL cavity design.

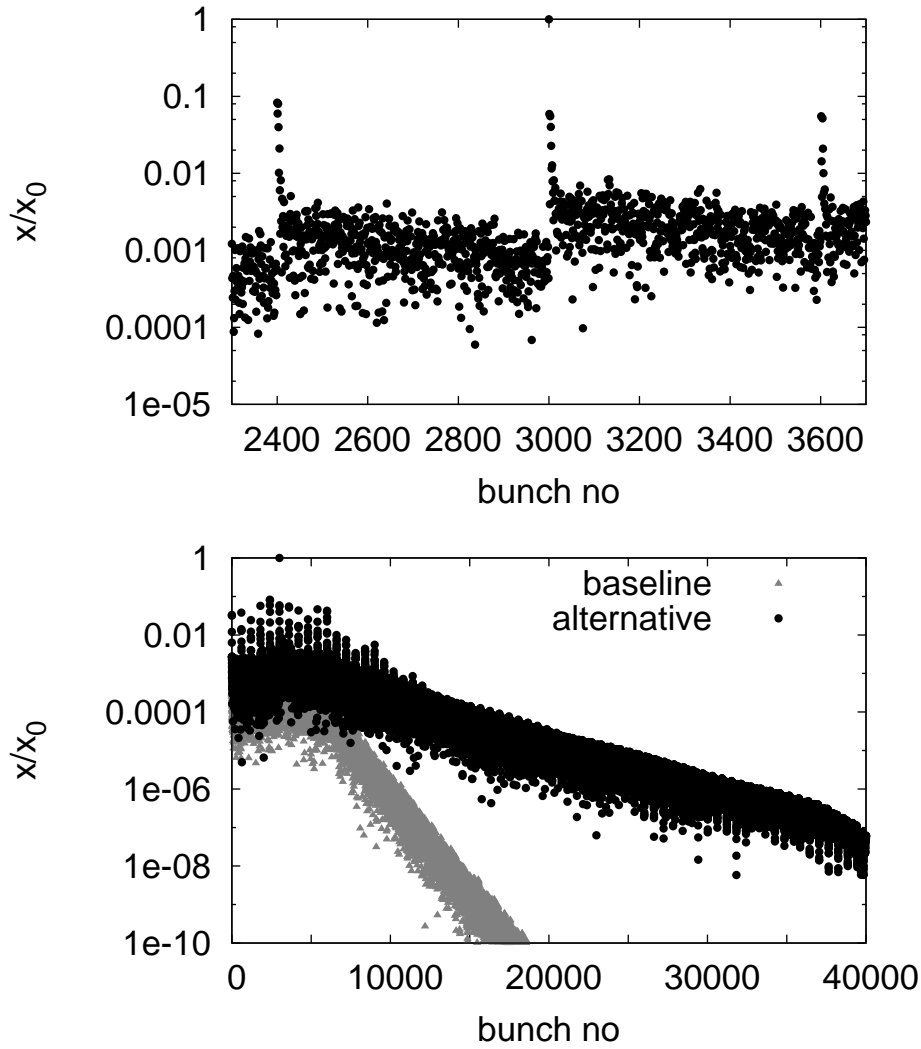


Figure 8.35: Multi-bunch beam break-up assuming the SPL cavity wakefields. One bunch has been offset at the beginning of the machine and the normalised amplitudes of the bunch oscillations are shown along the train at the end of the last turn. The upper plot shows a small number of bunches before and after the one that has been offset (i.e. bunch 3000). The lower plot shows the amplitudes along the full simulated train for the baseline lattice and the alternative design with no quadrupole focusing. One can see the fast decay of the amplitudes.

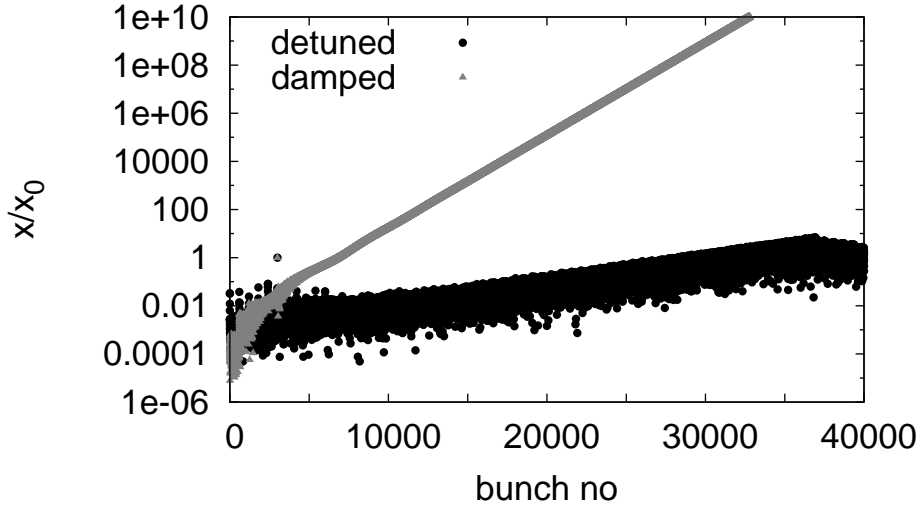


Figure 8.36: Multi-bunch beam break-up for the SPL cavities. In one case only damping, in the other case only cavity-to-cavity mode detuning is present.

6029 We also performed simulations, assuming that either only damping or detuning were present, see Fig. ??.
 6030 The beam is unstable in both cases. Based on our results we conclude

- 6031 • One has to ensure that transverse higher order cavity modes are detuned from one cavity to the next.
 6032 While this detuning can naturally occur due to production tolerances, one has to find a method to
 6033 ensure its presence. This problem exists similarly for the ILC.
- 6034 • Damping of the transverse modes is required.

6035 Further studies can give more precise limits on the maximum required Q and minimum mode detuning.

6036 Multi-Pass Beam Breakup Instability (BBU)

6037 **BBU model for ERL** To gain confidence that electron current of 6.5 mA, required for the LHeC lumi-
 6038 nosity is feasible, one needs to look into multi-pass beam breakup stability for our ERL design. Here, we will
 6039 summarize results of a recent numerical study of 6-pass (3 passes “up” and 3 passes “down”) BBU due to
 6040 the transverse higher order modes (HOMs) excited in the RF cavities. The beam travelling along each linac
 6041 experiences cumulative transverse deflection from each cavity HOMs. They add up for all 3 accelerating
 6042 passes in both linacs and continue for another 3 decelerating passes (energy recovery). Therefore, one needs
 6043 to study transverse dynamics of the beam interacting with cavity HOMs for the entire passage through ERL
 6044 using specific linac optics for each of six passes, as well as linear transfer maps of the 6 return arcs. In case
 6045 of BBU instability the transverse particle positions would increase exponentially and finally the particles
 6046 would hit a beam pipe.

6047 The following analytic formula describes the BBU threshold current for a single cavity with one HOM
 6048 excitation only, and one recirculation (one pass in each linac):

$$I_{th} = -\frac{2pc}{q} \frac{1}{(R/Q)Q_l M^* k \sin(\omega T_r)} \quad (8.11)$$

6049 where

- 6050 • $M^* = M_{12} \cos^2 \alpha + (M_{14} + M_{32}) \sin \alpha \cos \alpha + M_{34} \sin^2 \alpha$

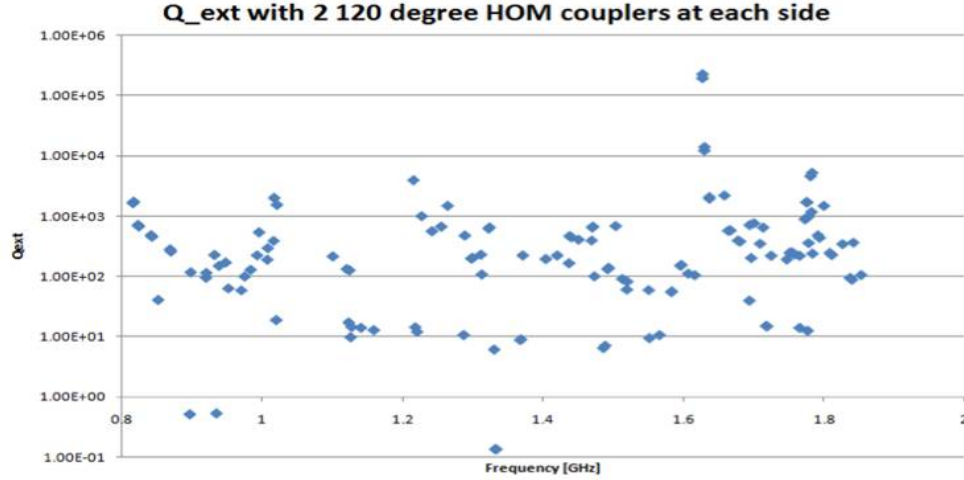


Figure 8.37: Quality factor of BNL3 cavity per “High Current SRF Cavity Design for SPL and eRHIC”, S. Belomestnykh et al., Proceedings of 2011 Particle Accelerator Conference, New York, NY, USA.

- 6051 • p - particle momentum on the second pass
- 6052 • q - particle charge
- 6053 • R/Q - shunt impedance of the dipole mode
- 6054 • Q_l - quality factor of the dipole mode
- 6055 • k - wave number of dipole mode
- 6056 • T_r - recirculation time
- 6057 • α - polarization angle (0 - horizontal, 90 - vertical)

6058 The TDBBU code applies the above formalism, formulated in the time domain (TD), for each cavity
 6059 along the entire ERL.

6060 **HOM Data** LHeC ERL is designed with 720 MHz RF cavities. Since such cavities have not been fabri-
 6061 cated yet, the BNL3 5-cell SRF cavity data would serve as close reference for the HOM data even though
 6062 BNL3 fundamental mode frequency, 703.79 MHz, is slightly different. The summary of measured HOMs is
 6063 illustrated in Figure ??.

6064 One can notice that all the Q values are less than $1 \cdot 10^6$ and most of them are smaller than $1 \cdot 10^4$. For
 6065 our BBU simulation, we consider the worst case of $Q_l = 1 \cdot 10^6$. Out of all HOMs collected in Figure ??, we
 6066 selected three most offending HOMs with relatively high R/Q values. They are summarized in table ??.

Frequency[MHz]	Q_l	R/Q[Ohm]
1003	$1 \cdot 10^6$	32
1337	$1 \cdot 10^6$	32
1820	$1 \cdot 10^6$	32

Table 8.14: The most offending HOMs selected into BBU simulation.

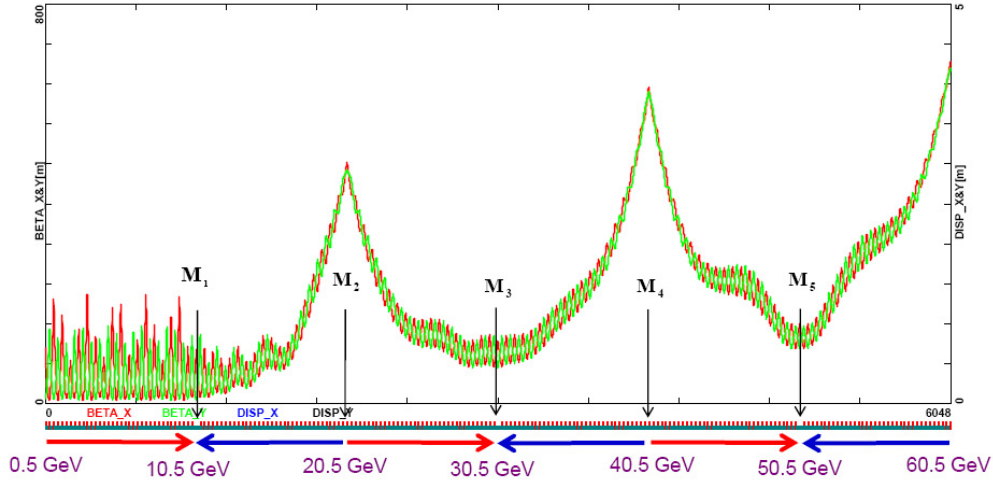


Figure 8.38: Multi-pass linac optics optimized for 3-pass ERL As a virtue of ER, Linac 2 Optics is a mirror reflection of Linac 1.

ERL multi-pass Optics A concise representation of multi-pass ERL linac Optics for all six passes, with constraints imposed on Twiss functions by “sharing” the same return arcs by the accelerating and decelerating passes is presented in Figure ??.

All six return arcs have to satisfy, by design, the following features:

- No coupling
- Double Achromat ($D_{x,y} = 0 = D'_{x,y}$)
- Isochronous ($M_{56} = 0$)
- Mirror symmetric ends ($\beta_{x,y}^1 = \beta_{x,y}^2$ and $\alpha_{x,y}^1 = \alpha_{x,y} = -\alpha_{x,y}^2$)

Assuming the above design features of arc optics and knowing the Twiss parameters at the end of each linac, as well as, the betatron phase advances, f_x and f_y , we can construct the arc Transfer matrices ad hoc using the following formula:

$$M^i = \begin{pmatrix} M_x^i & 0 & 0 \\ 0 & M_y^i & 0 \\ 0 & 0 & 1 \end{pmatrix}, M_{x,y}^i = \begin{pmatrix} \cos \phi_{x,y}^i + \alpha_{x,y}^i \sin \phi_{x,y}^i & \beta_{x,y}^i \sin \phi_{x,y}^i \\ \frac{2\alpha_{x,y}^i}{\beta_{x,y}^i} \cos \phi_{x,y}^i - \frac{1 - (\alpha_{x,y}^i)^2}{\beta_{x,y}^i} \sin \phi_{x,y}^i & \cos \phi_{x,y}^i + \alpha_{x,y}^i \sin \phi_{x,y}^i \end{pmatrix} \quad (8.12)$$

TDBBU Simulation For each cavity along the linac, the three offending HOM frequencies are randomly distributed with the full width of 2 MHz. In practice, the HOM frequencies are generated using random numbers in that range and these are distributed at each cavity. Twenty samples for different HOM frequency distributions are generated. The plots below show the beam behavior near the threshold. The horizontal axis corresponds to a bunch number and can be considered as an axis of time (if the bunch numbers are divided by frequencies). The vertical axis represents the transverse beam position at the end of the second linac. We plot the transverse positions of every 1117th particles. The number 1117 is somehow arbitrary; however it is a large prime number chosen to avoid an unexpected sub-harmonic redundancy in the data sampling. The simulation results for various beam currents: 4, 5 and 6 mA are illustrated in Figure ??.

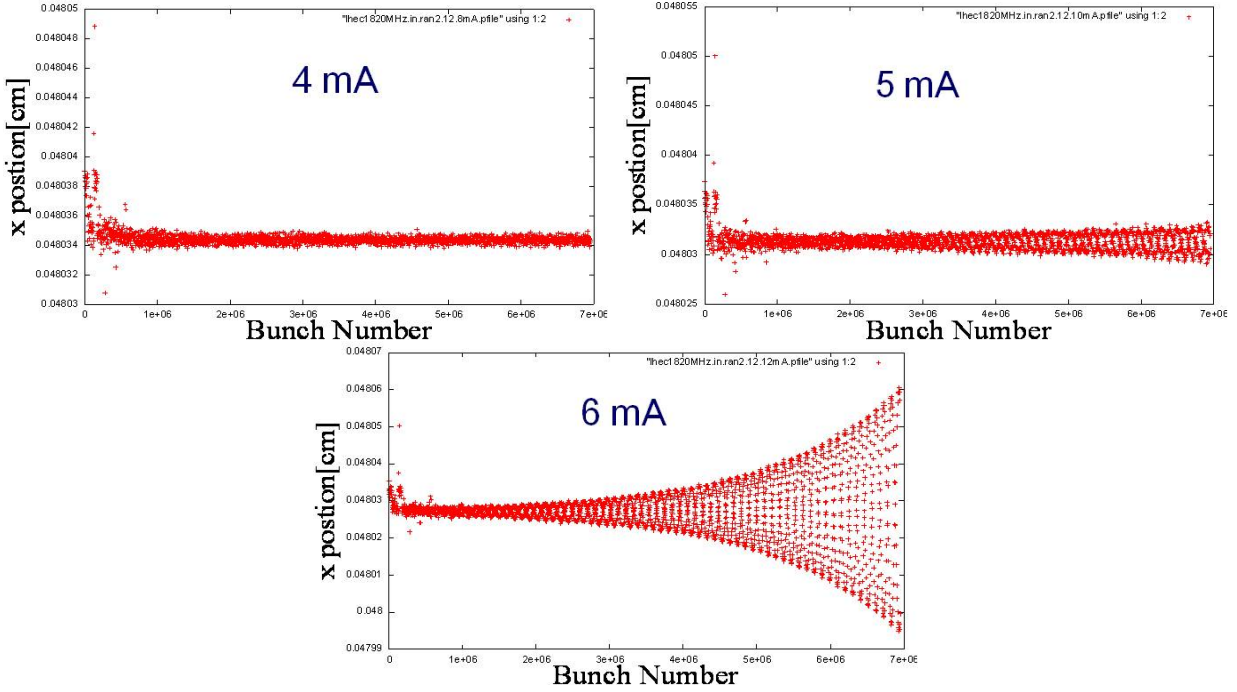


Figure 8.39: Large scale TDBBU simulation results for various beam currents: 4 (top left), 5 (top right) and 6 mA.

6087 **BBU stability** As illustrated in Figure ??, the beam is stable at 4 mA. At 5 mA the transverse position
 6088 is increasing, which indicate onset of the instability. Finally, at 6 mA one explicitly observes an exponential
 6089 increase in transverse beam position - a vivid case of beam instability. Therefore, we could infer that the
 6090 BBU threshold current is somewhere around 5 mA. One needs to keep in mind, our study assumed the worst
 6091 case interpretation of HOM's measurement for a cavity with limited HOM suppression, only one pair 1200
 6092 HOM dampers per cavity. This suggests more extended HOM damping will bring the stability threshold
 6093 above 6.5 mA. Further BBU study with more realistic HOM selection extracted from the same measurement,
 6094 summarized in Figure ??, is under way.

6095 Fast Beam-Ion Instability

6096 Collision of beam particles with the residual gas in the beam pipe will lead to the production of positive
 6097 ions. These ions can be trapped in the beam. Their presence modifies the betatron function of the beam
 6098 since the ions focus the beam. They can also lead to beam break-up, since bunches with an offset will induce
 6099 a coherent motion in the ions. This can in turn lead to a kick of the ions on following bunches.

6100 **Trapping Condition in the beam pulse** In order to estimate whether ions are trapped or not, one can
 6101 replace each beam with a thin focusing lens, with the strength determined by the charge and transverse
 6102 dimension of the beam. In this case the force is assumed to be linear with the ion offset, which is a good
 6103 approximation for small offsets.

6104 The coherent frequency f_i of the ions in the field of a beam of with bunches of similar size is given by [?]:

$$f_i = \frac{c}{\pi} \sqrt{\frac{Q_i N r_e \frac{m_e}{A m_p}}{3 \sigma_y (\sigma_x + \sigma_y) \Delta L}} \quad (8.13)$$

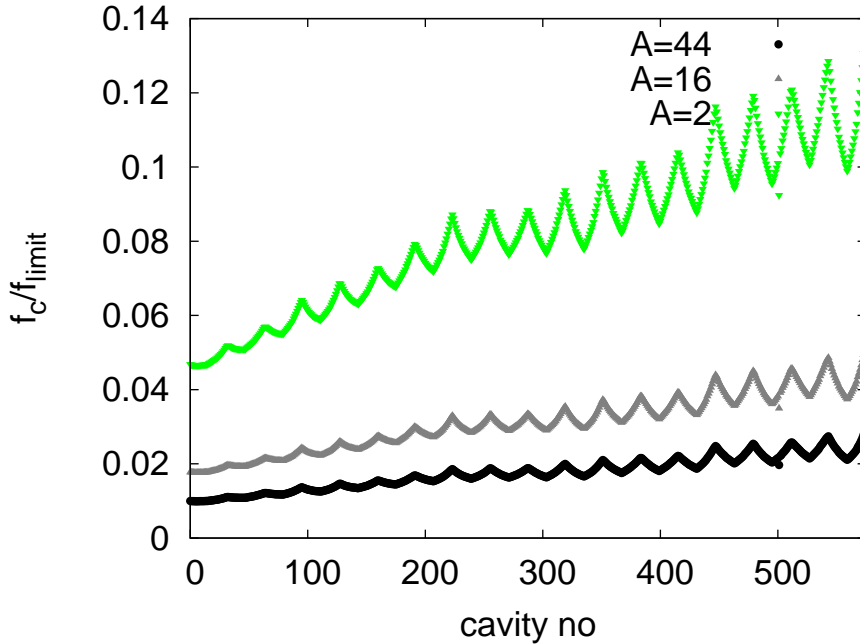


Figure 8.40: The oscillation frequency f_c of ions of different mass number A in the linacs using the average focusing strength of the bunches at different energy. The frequency is normalised to the limit frequency f_{limit} above which the ions would not be trapped any more.

6105 Here, N is the number of electrons per bunch, ΔL the bunch spacing, r_e the classical electron radius, m_e
 6106 the electron mass, Q_i the charge of the ions in units of e and A is their mass number and m_p the proton
 6107 mass. The beam transverse beam size is given by σ_x and σ_y . The ions will be trapped in the beam if

$$f_i \leq f_{limit} = \frac{c}{4\Delta L} \quad (8.14)$$

6108 In the following we will use $\Delta L \approx 2.5\text{m}$, i.e. assume that the bunches from the different turns are almost
 6109 evenly spaced longitudinally.

6110 In the linacs, the transverse size of the beam changes from one passage to the next while in each of the
 6111 return arcs the beams have (approximately) the same size at both passages. But the variation from one turn
 6112 to the next is not huge, so we use the average focusing strength of the six turns. The calculation shows that
 6113 ions will be trapped for a continuous beam in the linacs. Since we are far from the limit of the trapping
 6114 condition, the simplification in our model should not matter. As can be seen in Fig. ?? CO_2^+ ions are trapped
 6115 all along the linacs. Even hydrogen ions H_2^+ would be trapped everywhere. If one places the bunches from
 6116 the six turns very close to each other longitudinally, the limit frequency f_{limit} is reduced. However, the ratio
 6117 f_c/f_{limit} is not increased by more than a factor 6, which is not fully sufficient to remove the H_2^+ .

6118 **Impact and Mitigation of Ion Effects** Without any methods to remove ions, a continuous beam would
 6119 collect ions until they neutralise the beam current. This will render the beam unstable. Hence one needs to
 6120 find methods to remove the ions. We will first quickly describe the mitigation techniques and then give a
 6121 rough estimate of the expected ion effect.

6122 A number of techniques can be used to reduce the fast beam-ion instability:

- 6123 • An excellent vacuum quality will slow down the build-up of a significant ion density.

6124
6125

- Clearing gaps can be incorporated in the electron beam. During these gaps the ions can drift away from the beam orbit.

6126
6127

- Clearing electrodes can be used to extract the ions. They would apply a bias voltage that lets the ions slowly drift out of the beam.

6128
6129
6130
6131
6132
6133
6134
6135

Clearing Gaps In order to provide the gap for ion cleaning, the beam has to consist at injection of short trains of bunches with duration τ_{beam} separated by gaps τ_{gap} . If each turn of the beam in the machine takes τ_{cycle} , the beam parameters have to be adjusted such that $n(\tau_{beam} + \tau_{gap}) = \tau_{cycle}$. In this case the gaps of the different turns fall into the same location of the machine. This scheme will avoid beam loading during the gap and ensure that the gaps are fully empty. By choosing the time for one round trip in the electron machine to be an integer fraction of the LHC roundtrip time $\tau_{LHC} = m\tau_{cycle}$, one ensures that each bunch in the LHC will either always collide with an electron bunch or never. We chose to use $\tau_{cycle} = 1/3\tau_{LHC}$ and to use a single gap with $\tau_{gap} = 1/3\tau_{cycle} \approx 10 \mu s$.

6136
6137
6138

In order to evaluate the impact of a clearing gap in the beam, we model the beam as a thick focusing lens and the gap as a drift. The treatment follows [?], except that we use a thick lens approach and correct a factor two in the force. The focusing strength of the lens can be calculated as

$$k = \frac{2Nr_e m_e}{A_{ion} m_p \sigma_y (\sigma_x + \sigma_y) \Delta L} \quad (8.15)$$

6139

The ions will not be collected if the following equation is fulfilled

$$\left| 2 \cos(\sqrt{k}(L_{erl} - L_g)) - \sqrt{k} L_g \sin(\sqrt{k}(L_{erl} - L_g)) \right| \geq 2 \quad (8.16)$$

6140
6141

Since the beam size will vary as a function of the number of turns that the beam has performed, we replace the above defined k with the average value over the six turns using the average bunch spacing ΔL ,

$$k = \frac{1}{n} \sum_{i=1}^n \frac{2Nr_e m_e}{A_{ion} m_p \sigma_{y,i} (\sigma_{x,i} + \sigma_{y,i}) \Delta L}. \quad (8.17)$$

6142
6143
6144
6145

The results of the calculation can be found in Fig. ???. As can be seen, in most locations the ions are not trapped. But small regions exist where ions will accumulate. More study is needed to understand which ion density is reached in these areas. Longitudinal motion of the ions will slowly move them into other regions where they are no longer trapped.

6146
6147
6148
6149
6150

Ion Instability While the gap ensures that ions will be lost in the long run, they will still be trapped at least during the full train length of $20 \mu s$. We therefore evaluate the impact of ions on the beam during this time. This optimistically ignores that ions will not be completely removed from one turn to the next. However, the stability criteria we employ will be pessimistic. Clearly detailed simulations will be needed in the future to improve the predictive power of the estimates.

6151
6152
6153

Different theoretical models exist for the rise time of a beam instability in the presence of ions. A pessimistic estimate is used in the following. The typical rise time of the beam-ion instability for the n th bunch can be estimated to be [?]

$$\tau_c = \frac{\sqrt{27}}{4} \left(\frac{\sigma_y (\sigma_x + \sigma_y)}{Nr_e} \right)^{\frac{3}{2}} \sqrt{\frac{A_{ion} m_p}{m} \frac{kT}{p \sigma_{ion} \beta_y c n^2 \sqrt{L_{sep}}}} \gamma \quad (8.18)$$

6154
6155

This estimate does not take into account that the ion frequency varies with transverse position within the bunch and along the beam line.

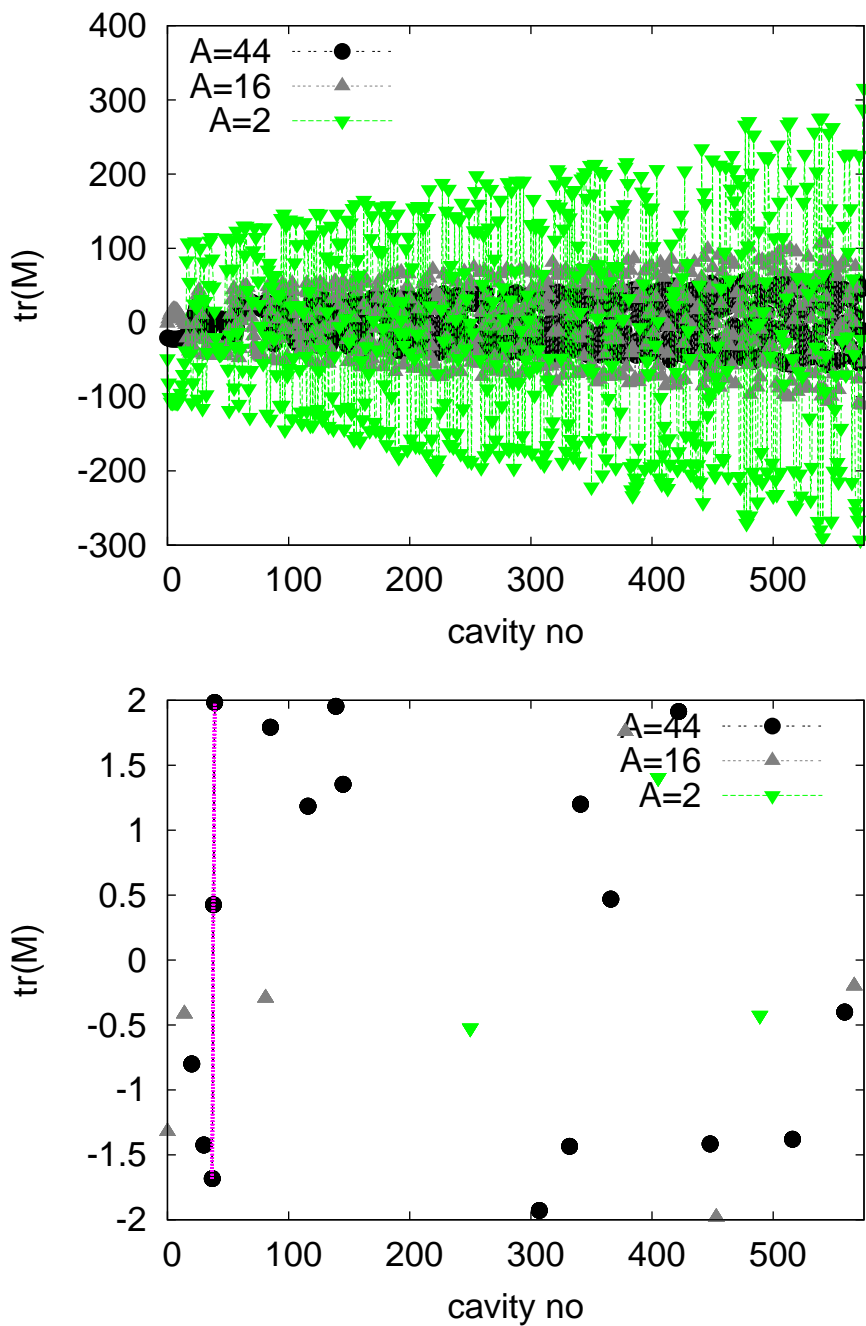


Figure 8.41: The trace of the transfer matrix for H_2^+ , CH_4^+ and CO_2^+ ions in presence of a clearing gap. Values above 2 or below -2 indicate that the ions will not be trapped.

6156 We calculate the local instability rise length $c\tau_c$ for a pressure of $p = 10^{-11}$ hPa at the position of the
6157 beam. As can be seen in Fig. ?? this instability rise length ranges from a few kilometers to several hundred.
6158 One can estimate the overall rise time of the ion instability by averaging over the local ion instability rates:

$$\left\langle \frac{1}{\tau_c} \right\rangle = \frac{\int \frac{1}{\tau_c(s)} ds}{\int ds} \quad (8.19)$$

6159 For the worst case in the figure, i.e. CH_4^+ , one finds $c\tau_c \approx 14$ km and for H_2^+ $c\tau_c \approx 25$ km. The beam
6160 will travel a total of 12km during the six passes through each of the two linacs. So the typical time scale
6161 of the rise of the instability is longer than the life time of the beam and we expect no issue. This estimate
6162 is conservative since it does not take into account that ion frequency varies within the beam and along the
6163 machine. Both effects will stabilise the beam. Hence we conclude that a partial pressure below 10^{-11} hPa is
6164 required for the LHeC linacs.

6165 In the cold part of LEP a vacuum level of 0.5×10^{-9} hPa has been measured at room temperature, which
6166 corresponds to 0.6×10^{-10} hPa in the cold [?]. This is higher than required but this value “represents more
6167 the outgassing of warm adjacent parts of the vacuum system” [?] and can be considered a pessimistic upper
6168 limit. Measurements in the cold at HERA showed vacuum levels of 10^{-11} hPa [?], which would be sufficient
6169 but potentially marginal. Recent measurements at LHC show a hydrogen pressure of 5×10^{-12} hPa measured
6170 at room temperature, which corresponds to about 5×10^{-13} hPa in the cold [?]. For all other gasses a pressure
6171 of less than 10^{-13} hPa is expected measured in the warm [?], corresponding to 10^{-14} hPa in the cold. These
6172 levels are significantly better than the requirements. The shortest instability rise length would be due to
6173 hydrogen. With a length of $c\tau_c \approx 500$ km which is longer than 40 turns. Hence we do not expect a problem
6174 with the fast beam-ion instability in the linacs provided the vacuum system is designed accordingly.

6175 The effect of the fast beam-ion instability in the arcs has been calculated in a similar way, taking into
6176 account the reduced beam current and the baseline lattice for each arc. Even H_2^+ will be trapped in the
6177 arcs. We calculate the instability rise length $c\tau_c$ for a partial pressure of 10^{-9} hPa for each ion mass and find
6178 $c\tau_c \approx 70$ km for H_2^+ , $c\tau_c \approx 50$ km for N_2^+ and CO^+ and $c\tau_c \approx 60$ km for CO_2^+ . The total distance the beam
6179 travels in the arcs is 15km. Hence we conclude that a partial pressure below 10^{-9} hPa should be sufficient
6180 for the arcs. More detailed work will be needed in the future to fully assess the ion effects in LHeC but we
6181 remain confident that they can be handled.

Ion Induced Phase Advance Error The relative phase advance error along a beam line can be calculated using [?] for a round beam:

$$\frac{\Delta\phi}{\phi} = \frac{1}{2} \frac{Nr_e}{\Delta L \epsilon_y} \frac{\theta}{\langle \beta_y^{-1} \rangle}$$

6182 Here θ is the neutralisation of the beam by the ions. We use the maximum beta-function in the linac to
6183 make a conservative approximation $\langle \beta^{-1} \rangle = 1/700$ m. At the end of the train we find $\rho \approx 3.3 \times 10^{-5}$ for
6184 $p = 10^{-11}$ hPa in the cold and $p = 10^{-9}$ hPa in the warm parts of the machine. This yields $\Delta\Phi/\Phi \approx 7 \times 10^{-4}$.
6185 Hence the phase advance error can be neglected.

6186 **Impact of the Gap on Beam Loading** It should be noted that the gaps may create some beam-loading
6187 variation in the injector complex. We can estimate the associated gradient variation assuming that the same
6188 cavities and gradients are used in the injector as in the linacs. We use

$$\frac{\Delta G}{G} \approx \frac{1}{2} \frac{R}{Q} \omega \frac{\tau_{gap} \tau_{beam} I}{\tau_{gap} + \tau_{beam}} \frac{1}{G} \quad (8.20)$$

6189 In this case the 10μ s gaps in the bunch train correspond to a gradient variation of about 0.6%. This seems
6190 very acceptable.

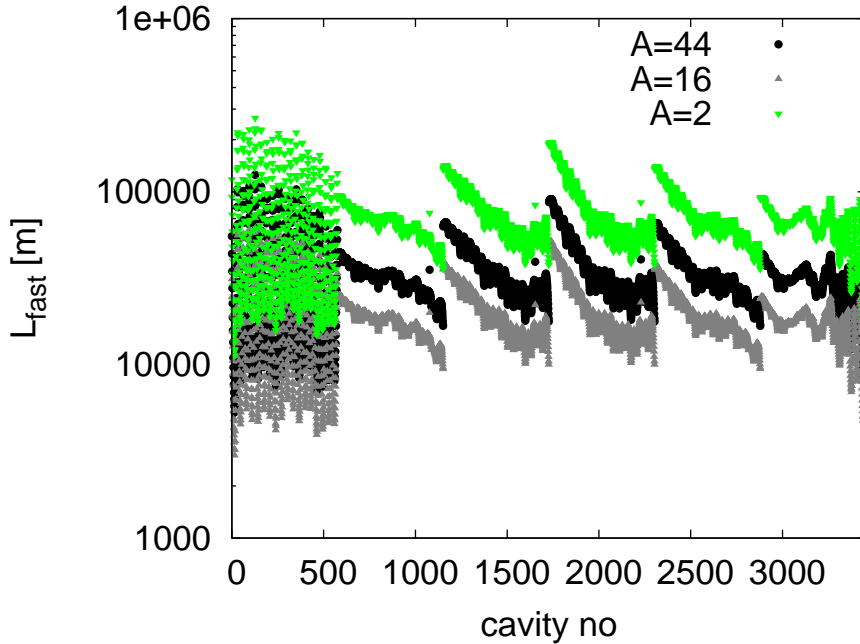


Figure 8.42: The instability length of the beam-ion instability assuming a very conservative partial pressure of 10^{-11} hPa for each gas.

8.3.4 Imperfections

Static imperfections can lead to emittance growth in the LHeC linacs and arcs. However, one can afford an emittance budget that is significantly larger than the one for the ILC, i.e. $10\mu\text{m}$ vs. 20nm . If the LHeC components are aligned with the accuracy of the ILC components, one would not expect emittance growth to be a serious issue. In particular in the linacs dispersion free steering can be used and should be very effective, since the energies of the different probe beams are much larger than they would be in ILC.

Gradient Jitter and Cavity Tilt

Since the cavities have tilts with respect to the beam line axis, dynamic variations of the gradient will lead to transverse beam deflections. This effect can be easily calculated using the following expression:

$$\frac{\langle y^2 \rangle}{\sigma_y^2} = \frac{\langle (y')^2 \rangle}{\sigma_{y'}^2} = \frac{1}{2} \frac{1}{\epsilon} \int \frac{\beta}{E} ds \frac{L_{cav} \langle \Delta G^2 \rangle \langle (y'_{cav})^2 \rangle}{mc^2}$$

For an RMS cavity tilt of $300\mu\text{radian}$, an RMS gradient jitter of 1% and an emittance of $50\mu\text{m}$ we find

$$\frac{\langle y^2 \rangle}{\sigma_y^2} = \frac{\langle (y')^2 \rangle}{\sigma_{y'}^2} \approx 0.0125$$

i.e. an RMS beam jitter of $\approx 0.07\sigma_y$. At the interaction point the beam jitter would be $\approx 0.05\sigma_{y'}$.

8.4 Polarized-Electron Injector for the Linac-Ring LHeC

We present the injector for the polarized electron beam. The issue of producing a sufficient number of polarized or unpolarized positrons is discussed in section ??.

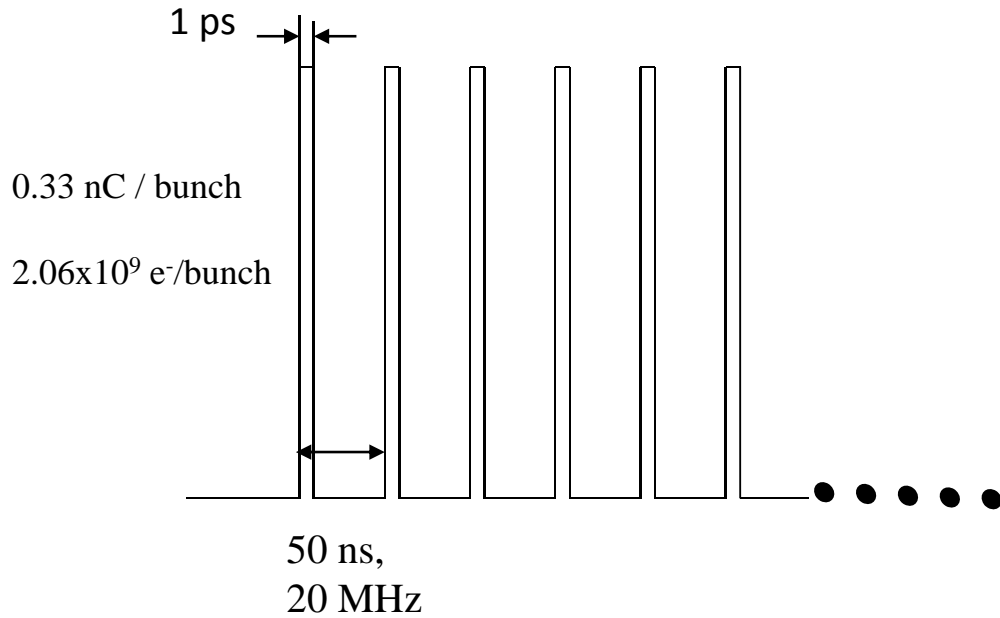


Figure 8.43: Beam pattern at IP

6202 The Linac-Ring option is based on an ERL machine where the beam pattern, at IP, is shown in Figure
 6203 ??.

6204 With this bunch spacing, one needs 20×10^9 bunches/second and with the requested bunch charge, the
 6205 average beam current is 20×10^9 b/s \times 0.33 nC/b = 6.6 mA.

6206 Figure ?? shows a possible layout for the injector complex, as source of polarized electron beam.

6207 The injector is composed of a DC gun where a photocathode is illuminated by a laser beam. Then a linac
 6208 accelerates electron beam up to the requested energy before injection into the ERL. Downstream a bunch
 6209 compressor system allows to compress the beam down to 1 ps and finally a spin rotator, brings the spin in
 6210 the vertical plane.

6211 Assuming 90% of transport efficiency between the source and the IP, the bunch charge at the photo-
 6212 cathode should be 2.2×10^9 e⁻/b. According to the laser and photocathode performance, the laser pulse width,
 6213 corresponding to the electron bunch length, will be between 10 and 100 ps.

6214 Table ?? summarises the electron beam parameters at the exit of the DC gun.

6215 The challenges to produce the 7 mA beam current are the following:

- 6216 • a very good vacuum ($< 10^{-12}$ mbar) is required in order to get a good lifetime.
- 6217 • the issues related to the space charge limit and the surface charge limit should be considered. A peak
 6218 current of 10 A with 4 ns pulse length has been demonstrated. Assuming a similar value for the DC
 6219 gun, a laser pulse length of 35 ps would be sufficient to produce the requested LHeC charge.
- 6220 • the high voltage (100 kV to 500 kV) of the DC gun could induce important field emissions.
- 6221 • the design of the cathode/anode geometry is crucial for a beam transport close to 100%.
- 6222 • the quantum efficiency should be as high as possible for the photocathode ($\sim 1\%$ or more).
- 6223 • the laser parameters (300 nJ/pulse on the photocathode, 20 MHz repetition rate) will need some R&D
 6224 according to what is existing today on the market.
- 6225 • the space charge could increase the transverse beam emittances.

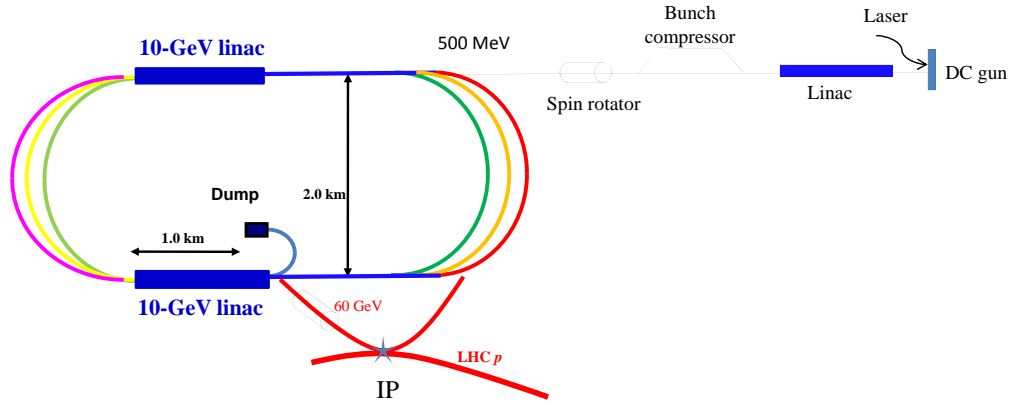


Figure 8.44: Layout of the injector (not to scale).

Parameters	60 GeV ERL
Electrons /bunch	2.2×10^9
Charge /bunch	0.35 nC
Number bunches / s	20×10^9
Bunch length	10 – 100 ps
Bunch spacing	50 ns
Pulse repetition rate	CW
Average current	7 mA
Peak current of the bunch	3.5 – 350 A
Current density (1 cm)	1.1 – 110 A/cm ²
Polarization	> 90%

Table 8.15: Beam parameters at the source.

6226 In conclusion, a tradeoff between the photocathode, the gun and the laser seems reachable to get accept-
 6227 able parameters at the gun exit. A classical Pre-Injector Linac accelerates electron beam to the requested
 6228 ERL energy. Different stages of bunch compressor are used to compensate the initial laser pulse and the
 6229 space charge effects inducing bunch lengthening. A classical spin rotator system rotates the spin before
 6230 injection into the ERL.

6231 8.5 Spin Rotator

6232 The LHeC physics requires polarized electrons with spin aligned longitudinally at the collision point [?]. In
 6233 the electron accelerator of LHeC, consisting of two 10-GeV superconducting linear accelerators linked with
 6234 six 180° arc paths, the depolarization due to the arcs is negligible if the spin is aligned vertically in the arcs.

6235 The motion of the spin vector \vec{S} is governed by Thomas-BMT equation [?, ?] shown in Eq. ??

$$\frac{d\vec{S}}{dt} = \frac{e}{m\gamma} \vec{S} \times [(1 + G\gamma)\vec{B}_\perp + (1 + G)\vec{B}_\parallel] \quad (8.21)$$

6236 where e , m and γ are the electric charge, mass and Lorentz factor of the particle. G is the anomalous
 6237 g-factor. For protons, $G = 1.7928474$ and for electrons, $G = 0.00115$. \vec{B}_\perp and \vec{B}_\parallel are the magnetic field
 6238 perpendicular and parallel to the particle velocity direction, respectively. In Eq. ??, magnetic field is in the

laboratory frame while the spin vector \vec{S} is in the particle's rest frame. In a bending dipole, a spin vector precesses $G\gamma$ times of the particle's orbital rotation in the particle's moving frame. It is also evident that solenoid field is less effective to manipulate spin motion at high energies.

For the LHeC physics program, the polarization of 60 GeV electron beam needs to be aligned longitudinally at the collision point which is after the last arc and the acceleration. The most economical way to control the spin direction at the collision point is to control the spin direction of the low energy electron beam at the early stage of injector using a Wien Filter, a traditional low energy spin rotator. Since spin vector rotates $G\gamma\pi$ each time it passes through a 180° arc, the goal of the Wien Filter is to put the spin vector in the horizontal plane with an angle to the direction of the particle's velocity to compensate the amount of spin rotations before collision.

For the layout of LHeC, i.e. two linear accelerators linked with two arcs, spin vector rotates

$$\phi_{arc} = G\pi[\gamma_i(2n - 1) + \Delta\gamma n(2n - 1)] \quad (8.22)$$

after its n th path. Here, γ_i is the initial Lorentz factor of the beam and $\Delta\gamma$ is the energy gain of each linear accelerator. In addition, LHeC also employs two horizontal bending dipoles on either side of the collision point to separate the electrons from the protons. Each of this bending dipole is 0.3 T and spans 9 m from the collision point. For 60 GeV electron beam, it rotates the spin vector by $\phi_{IP} = 104.4^\circ$. For initial energy of 10 GeV and each linear accelerator energy gain of 10 GeV, Table ?? lists the amount of spin rotation through the arcs and the amount of spin rotation through the final bending dipole at the collision point for 20 GeV, 40 GeV and 60 GeV beam, respectively. Here, the amount of spin rotation is the net spin

Table 8.16: total spin rotation from arcs and final bending dipole at collision point

beam energy [GeV]	# of path n	ϕ_{arc} [degrees]	ϕ_{IP} [degrees]
20	1	8101.8	34.8
40	2	36457.9	69.6
60	3	81017.6	104.4

rotations in the range of 2π . Since the spin rotation is proportional to beam energy, for a beam of particles with non-zero momentum spread, different amount of spin rotation then generates a spread of spin vector directions. This results in an effective polarization loss due to the spread of the spin vector. Fig. ?? shows the angle spread of the spin vector for an off-momentum particle at 20GeV, 40GeV and 60GeV. The calculation assumes the initial energy before the electron beam enters the arc is 10 GeV and energy gain of each linear accelerator is 10 GeV. It shows that for 60 GeV electron beam, a momentum spread of 3×10^{-4} can cause about 10% polarization loss effectively due to the spread of the spin vectors. This may not be able to satisfy the requirement on high polarization.

In order to provide the desirable polarization direction without sacrificing polarization, one can take the traditional approach of high energy polarized beams at HERA and RHIC, i.e. to rotate the spin vector to vertical direction before it gets accelerated to high energy. Since the spin vector aligns with the main bending magnetic fields' direction, this prevents the spread of the spin vector due to the momentum spread. After the last arc and acceleration, at 60 GeV beam energy, the spin vector must be rotated back so as to be longitudinally aligned at the collision point. To this end, for the current compact LHeC design, we propose to use a RHIC type spin rotator [?, ?] at the LHeC. Besides saving space of being compact, this approach also provides the advantage of independent control of the spin vector orientation, as well as nearly energy independent spin rotation for the same magnetic field. The four helical dipoles are arranged in a similar fashion as the RHIC spin rotator, i.e. with alternating helicity. Fig. ?? shows the schematic layout. Each helical dipole is 3.3 m long and the helicity alternates between right hand to left hand between each helical dipole. The two inner helical dipoles have the same magnetic field but opposite helicity. Same applies to the two outer helical dipoles.

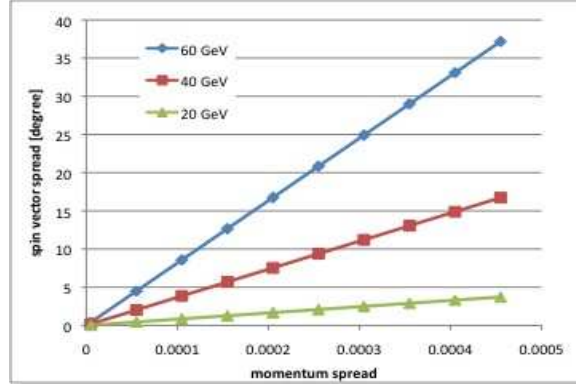


Figure 8.45: Calculated spin vector spread as function of momentum spread. The effective polarization loss is the cosine of spin vector spread angle, i.e. for an angle of 30 degrees, the effective polarization is 86% of initial beam polarization

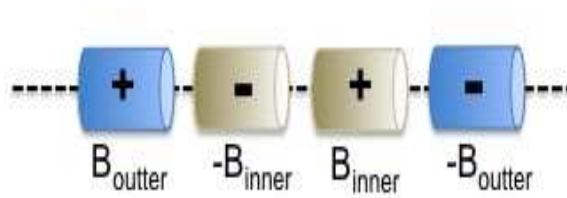


Figure 8.46: Schematic layout of LHeC spin rotator. A total of four helical dipoles with alternating helicity marked as + and -. The polarity of two outer helical dipole fields are also opposite. And so is the polarity of the two inner helical dipoles.

6278 For each helical dipole, the magnetic field is given by

$$B_x = B \cos kz; B_y = B \sin kz; B_z = 0.0 \quad (8.23)$$

6279 where, $B_{x,y,z}$ are the horizontal, vertical and longitudinal component of the magnetic field, respectively. Z
 6280 is the longitudinal distance along the helical dipole axis. $|k| = \frac{2\pi}{\lambda}$ and λ are wave number and wave length
 6281 of the helical field, respectively.

6282 For spin roator, all helical dipoles are chosen to be one period, i.e. $\lambda = L$, where L is the length of each
 6283 helical dipole. Depending on the direction of the helicity, $\frac{k}{|k|} = \pm 1$. Fig. ?? shows the correlation of the
 6284 magnetic field for the inner and outer helical magnets of a spin rotator which brings the spin vector from
 6285 vertical direction to be in the horizontal plane. Fig. ?? shows the calculated angle of the spin vector for
 6286 each outer helical magnet field. Both plots show that this design provides a flexible choice of the direction
 6287 of spin vector by adjusting the outer and inner helical magnetic fields respectively.

6288 This rotator will be placed in the straight section of between LINAC and final focusing section (FFS).
 6289 This is upstream of the final bending dipole at the collision point as well as three bends right upstream
 6290 of the triplet. The 0.3 T final bending dipole rotates spin vector by 104.4 degrees for 60 GeV electron
 6291 beam, while the other three bends rotates spin vector by -1.8 degrees. In order to bring the spin vector
 6292 of polarized electron along longitudinal direction, it requires that spin rotator to put the spin vector from
 6293 vertical direction to the horizontal plane with an angle of 102.6 degrees away from longitudinal direction.
 6294 This requirement then yields the magnetic field of the inner pair and outer pair to be 1.92 T and 0.93 T,
 6295 respectively. The maximum orbital excursion is 17 mm in horizontal and 8.5mm in vertical. The fine tuning
 6296 of the direction of spin vector can be achieved by empirically adjusting the helical dipole magnetic field

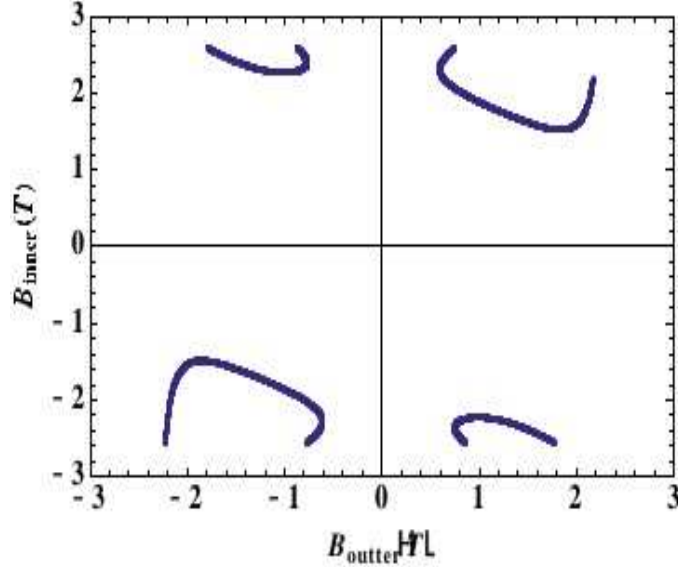


Figure 8.47: correlation of the outer and inner helical dipole magnetic field strength for a spin rotator which is designed to bring a vertically aligned spin vector to the horizontal plane.

6297 strength based on the measurements of the polarimeters before and after the collision point.

6298 Detailed calculations including helical dipole design, orbital and spin tracking of spin rotator are in
6299 working progress.

6300 8.6 Positron Options for the Linac-Ring LHeC

6301 8.6.1 Motivation

6302 To accomplish the full particle physics programme of the LHeC it is important to provide both positron-
6303 proton (nucleon) and electron-proton (nucleon) collisions. In case of the Linac-Ring LHeC this implies that
6304 a challenging rate of positrons must be maintained at the interaction point.

6305 8.6.2 LHeC Linac-Ring e^+ Requirements

6306 Table ?? compares the e^+ beam flux foreseen for LHeC with those obtained at the SLC, and targeted for
6307 CLIC and the ILC.

6308 The SLC (Stanford Linear Collider) was the only linear-collider type machine which has produced e^+ for
6309 a high-energy particle physics experiment. The flux for the CLIC project (a factor 20 compared to SLC)
6310 is already considered challenging and possible options with hybrid targets are under investigation on paper.
6311 Even more positrons would be required for the ILC. The requested LHeC flux for pulsed operation at 140
6312 GeV (a factor 300 compared to SLC) could be obtained, in a first approximation, with 10 e^+ target stations
6313 working in parallel. Several more advanced solutions are proposed to meet the requested LHeC flux for the
6314 CW option (a factor 7300 compared to SLC).

6315 8.6.3 Mitigation Schemes

6316 Two main approaches can be considered to reduce the rate of positrons that needs to be produced at the
6317 source, namely

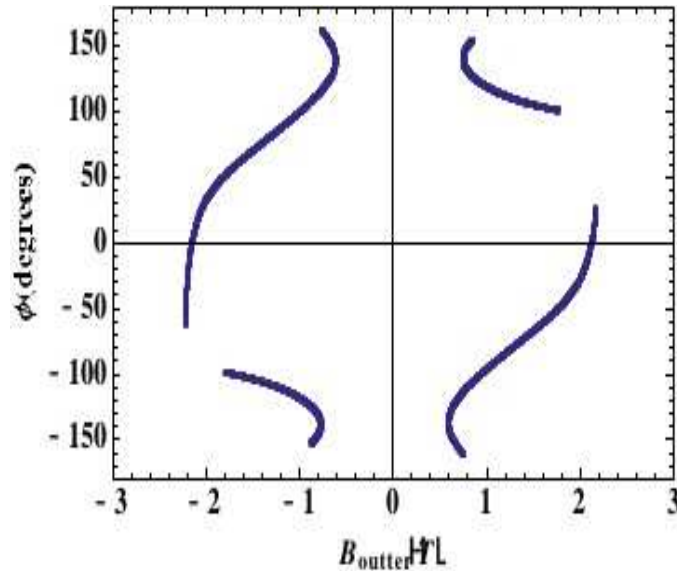


Figure 8.48: spin vector direction in the horizontal plane as function of outer helical magnet field strength

- 6318 • Recycling the positrons after the collision, with implied considerations on e^+ emittance after collision,
 6319 emittance growth in the 60-GeV return arc due to synchrotron radiation, and the possible introduction
 6320 of a cooling scheme, e.g. laser cooling à la Telnov at lower beam energy, introducing a tri-ring recovery
 6321 scheme with fast laser cooling in central ring. (see below), or a using a large damping ring. If 90% of
 6322 the positrons are recycled the requirement for the source drops by an order of magnitude.

- 6323 • Repeated collisions on multiple turns, e.g. using a (pulsed) 180-degree phase-shift chicane in order to
 6324 recover 60 GeV in the second return arc after the collision.

6325 Reuse and Cooling of Positrons

6326 One of the most challenging problems associated with the continuous production of positrons is cooling
 6327 (damping) of the positron beam emerging from a source or recycled after the collision. The cooling process
 6328 in a storage ring requires many synchrotron and betatron oscillation periods as well as the emission of many
 6329 photons. The direct connection of the ERL's output and input aiming at a reuse of the positron beam does
 6330 not solve the problem of beam cooling, since the electron suffers from noticeable disruption.

6331 Beam cooling, that is at least an e-fold reduction of energy spread and transverse emittances, usually
 6332 requires at least thousand turns of beam in a damping ring. The employment of a novel idea of fast cooling [?]
 6333 may reduce this period, down to 200...500 turns. Even further reduction of the cooling period might be
 6334 attained by designing a damping ring with multiple, S , superperiods, each of which of the double chicane
 6335 scheme (to provide about $S/2$ synchrotron oscillations per full turn). In this latter case, the number of turns
 6336 needed for cooling would be reduced by another factor of S .

6337 The next section present consideration on the pushed performance of a conventional damping ring, and it
 6338 estimates the damping that could be obtained in a ring with the size of the SPS. An elegant complementary or
 6339 alternative solution to relax the damping requirements — the tri-ring scheme — is described in the following
 6340 section.

	SLC	CLIC (3 TeV)	ILC (500 GeV)	LHeC (p= 140)	LHeC (ERL)
Energy (GeV)	1.19	2.86	4	140	60
e^+ /bunch at IP ($\times 10^9$)	40	3.72	20	1.6	2
Norm. emittance (mm.mrad)	30 (H)	0.66 (H)	10 (H)	100	50
	2 (V)	0.02 (V)	0.04 (V)		
Longit. rms emittance (eV-m)	7000	5000	60000	10000	5000
e^+ /bunch after capture ($\times 10^9$)	50	7.6	30	1.8	2.2
Bunches / macropulse	1	312	2625	10^5	NA
Macropulse repetition rate	120	50	5	10	CW
Bunches / second	120	15600	13125	10^6	20×10^6
e^+ / second ($\times 10^{14}$)	0.06	1.1	3.9	18	440

Table 8.17: Comparison of the e^+ flux.

6341 Damping-Ring Considerations

6342 The main parameter driving the circumference choice of a positron damping ring for the LHeC complex is
6343 the train length (for the pulsed option) and the structure. For 10^5 bunches with separation of 25 ns the
6344 damping ring has to be unreasonably long (around 750 km). The bunch train has thus to be compressed
6345 in the damping ring and uncompressed by extracting individual bunches every 25 ns using a fast extraction
6346 kicker or RF deflector. The minimum bunch spacing in the ring is determined by the fastest achievable rise
6347 time of the extraction systems. A fast kicker can probably pulse with rise/fall times of around 2.5 ns and an
6348 RF deflector may be reduced even further (0.5 ns). Both systems have to present a stability of the order of
6349 a few 10^{-4} . Given the larger emittance the kicker stability requirement may be relaxed compared with the
6350 damping rings of CLIC and ILC. Considering a 2.5-ns bunch spacing, the ring circumference can be reduced
6351 by a factor of 10 but remains still very large. A further order-of-magnitude reduction can be obtained by
6352 considering either ten times less bunches (with correspondingly higher charge) or an order of magnitude
6353 increase of the repetition rate, i.e. 100 Hz instead of 10 Hz. Indeed, with a 100-Hz repetition rate, the ring
6354 becomes 7.5 km, which is very close to the circumference of the SPS of $C = 2200\pi = 6911.5$ m.

6355 In this respect, a parameter set can be deduced by taking as base a damping ring in the SPS tunnel ⁴,
6356 where a train of 9221 bunches with 2.5 ns can fit. The high repetition rate option demands that the bunches
6357 are damped and then extracted within 10 ms. Considering that at least 5 damping times are needed to
6358 reach equilibrium, the transverse damping time should be less than 2 ms. This number is assumed in the
6359 following. We note, however, that a damping time of 10 or 20 ms, with much relaxed constraints on the ring,
6360 may already be sufficient for recycling spent positrons and recovering their original emittance.

6361 The transverse damping time is given by

$$\tau_{x,y} = \frac{2EC}{cJ_{x,y}U} \quad , \quad (8.24)$$

6362 with E the energy, $J_{x,y} \approx 1$ the damping partition numbers, c the speed of light and U the energy loss per
6363 turn:

$$U = \frac{C_\gamma E^4}{\rho} (1 + F_w) \quad , \quad (8.25)$$

6364 with $\rho = E/(eB)$ the bending radius and F_w the wiggler damping factor:

$$F_w = \frac{L_w B_w^2}{4\pi B^2 \rho} \quad , \quad (8.26)$$

⁴A damping ring in the SPS tunnel has already been considered as early as 1988 by L. Evans and R. Schmidt, in CLIC Note 58, although their parameter set has been far away from present LHeC and CLIC requirements.

6365 with L_w and B_w the wiggler length and field respectively. The transverse damping time can be rewritten as

$$\tau = \frac{8\pi C}{ceC_\gamma E(eB_w^2 L_w + 4\pi BE)} \quad , \quad (8.27)$$

6366 connecting it directly with the ring energy and radiating magnet characteristics. Considering a maximum
 6367 bending field of 1.8 T and wiggler field of 1.9 T, there is a parametric interdependence between beam energy,
 6368 the total wiggler length and the damping time. Figure ?? shows the dependence of the damping ring energy
 6369 on the total wiggler length for a damping time of 2 ms (red curve). Without wigglers, the ring has to
 6370 run at 22 GeV, whereas for around 10 GeV, wigglers with a total length of 800 m are needed. The blue
 6371 curve represents the same dependence when the low repetition rate is considered which indeed increases the
 6372 damping time by an order of magnitude. In that case, the ring energy without any wigglers can be reduced
 6373 to 7 GeV and it can be dropped to less than 4 GeV for a total wiggler length of 200 m.

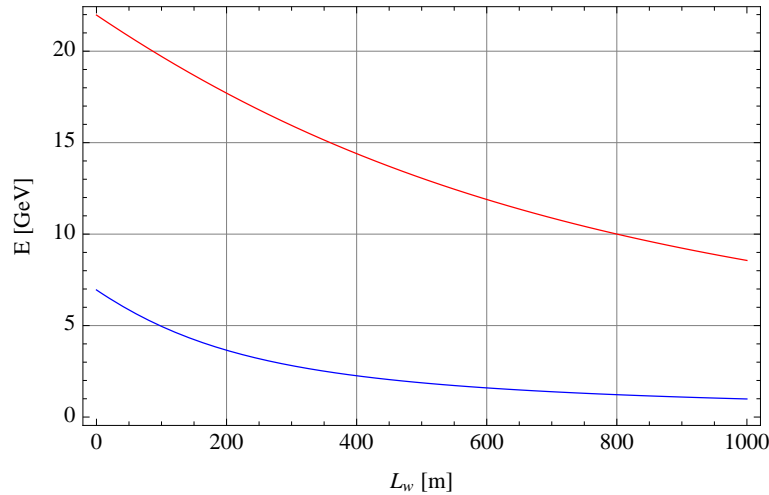


Figure 8.49: Dependence of the damping ring energy on the total wiggler length for a transverse damping time of 2 ms (red curve) and 20 ms (blue curve).

6374 A tentative parameter list for the low and high repetition rate option can be found in table ?? . This
 6375 example considers for both cases, 234 bending magnets of 0.5m-long dipoles with 1.8T bending field. The
 6376 wiggler field of 1.9 T and a period of 5 cm is within the reach of modern hybrid wiggler technology. A big
 6377 challenge is the longitudinal parameters driven from the high energy loss per-turn, especially in the high
 6378 repetition rate case, where around 300 MV of total RF voltage is needed to restore the high-energy loss/turn.
 6379 In addition, the bunch has to be kept short (around 5 mm) in order to achieve the longitudinal emittance
 6380 target of 10 keV-m, which necessitates a quasi-isochronous ring, with momentum compaction factor, close
 6381 to 10^{-6} . This may be a challenge for lattice design as low momentum compaction factors are achieved for
 6382 strong focusing conditions, which increase chromaticity, and necessitate strong sextupoles with detrimental
 6383 effects for the dynamic aperture of the ring. The average beam power of 25 MW indicates that the wall-plug
 6384 power would be quite high and may necessitate the use of super-conducting RF system to increase efficiency.
 6385 In the low repetition case, the RF voltage and power are an order of magnitude more relaxed.

6386 **Tri-Ring Scheme**

6387 A possible solution to cool down a continuous positron beam, both the recycled beam and/or a new beam
 6388 from a source, is the tri-ring scheme illustrated in Fig. ??.

6389 The operation cycle of the system is as follows:

- 6390 • The basic cycle lasts N turns

- 6391 – N -turn injection from ERL into the accumulating ring (bottom)
- 6392 – N -turn cooling in the cooling ring (middle); fast laser cooling may be employed here
- 6393 – N -turn slow extraction from the extracting ring (top) into rgw ERL
- 6394 • One-turn transfer from the cooling ring into the extracting ring
- 6395 • One-turn transfer from the accumulating ring into the cooling ring

6396 The average current in the cooling ring is $N \times$ average ERL current. The number of turns of the main cycle is
 6397 limited by the efficiency of multiturn injection and the maximum current wgiuch can be stored (and cooled)
 6398 in the cooling ring.

6399 Laser cooling may generate a new low-emittance positron beams to compensate for losses.and emittance
 6400 growth of the recycled beam.

6401 Reusing and/or cooling of positrons relaxes the requirements for all types of positron source discussed in
 6402 the following. The cooling period is limited by the maximal stored current in the ring and by the multiturn
 6403 injection. Fast laser cooling may be employed for compensating positron emittance growth when reusing
 6404 positrons or to compensate losses (without a dedicated high-current positron source). The slow extraction
 6405 process is also able to further reduce the energy spread (chromatic extraction) or, alternatively, the transverse
 6406 emittance (resonant extraction).

6407 8.6.4 Positron Production Schemes

6408 Positrons can be produced by pair creation when high-energy electrons or photons hit a target. Conventional
 6409 sources, as used at the SLC, sent a high-energy electron beam on a conversion target. Alternatively, a high-

Table 8.18: CLIC versus NLC parameters driving the DRs design.

Parameter [unit]	High Rep-rate	Low Rep-rate
Energy [GeV]	10	7
Bunch population [10^9]	1.6	1.6
Bunch spacing [ns]	2.5	2.5
Number of bunches/train	9221	9221
Repetition rate [Hz]	100	10
Damping times trans./long. [ms]	2/1	20/10
Energy loss/turn [MeV]	230	16
Horizontal norm. emittance [μm]	20	100
Optics detuning factor	80	80
Dipole field [T]	1.8	1.8
Dipole length [m]	0.5	0.5
Wiggler field [T]	1.9	-
Wiggler period [cm]	5	-
Total wiggler length [m]	800	-
Dipole length [m]	0.5	0.5
Longitudinal norm. emittances [keV.m]	10	10
Momentum compaction factor	10^{-6}	10^{-6}
RF voltage [MV]	300	35
rms energy spread [%]	0.20	0.17
rms bunch length [mm]	5.2	8.8
average power [MW]	23.6	3.6

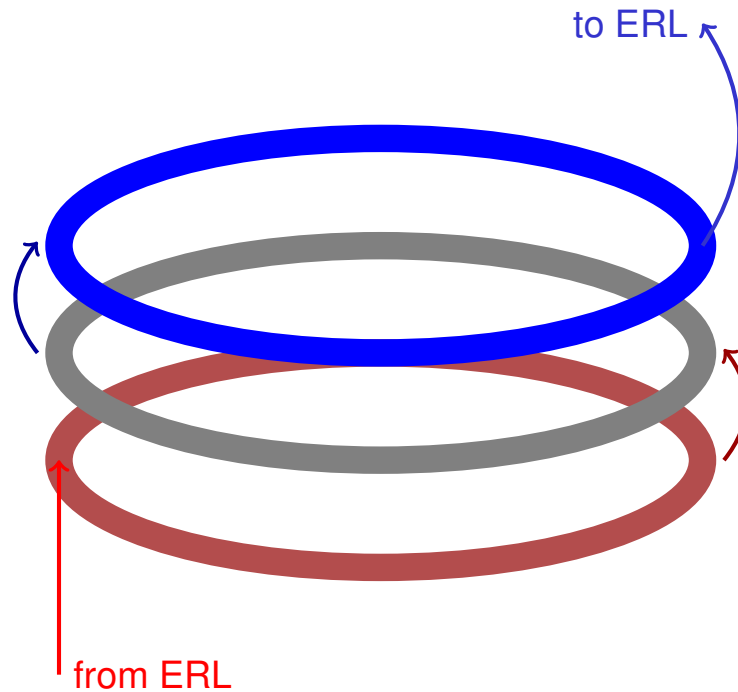


Figure 8.50: Tri-ring scheme

6410 energy electron beam can first be used to create high-energy photons, and these photons are then sent onto
 6411 a target. The prior conversion into photons reduces the heat load of the target, for a given output intensity,
 6412 and it may also improve the emittance of the generated positrons.

6413 There exist a number of schemes that can accomplish the conversion of electrons into photons. Several
 6414 of them employ Compton scattering off a high-power laser pulse stacked in an optical cavity. According to
 6415 the electron-beam accelerator employed, one distinguishes Compton rings, Compton linacs, and Compton
 6416 ERLs. An alternative scheme uses the photons emitted by an electron beam of very high energy (of order
 6417 100 GeV) when passing through a short-period undulator.

6418 Finally, there even exists a simpler scheme where a high-power laser pulse itself serves as the target for
 6419 (coherent) pair creation.

6420 Applications of the various possible schemes to the LHeC are discussed in the following sections.

6421 8.6.5 Targets

6422 For the positron flux considered the heating and possible destruction of the target are important concerns.
 6423 Different target schemes and types can address these challenges:

- 6424 • Multiple targets operating in parallel (Section ??).
- 6425 • He-cooled granular W-sphere targets (Section ??).

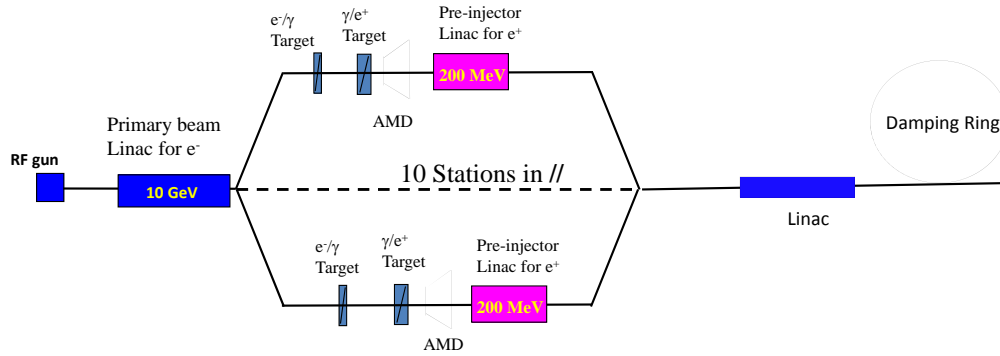


Figure 8.51: Possible layout with unpolarised e^+ for the LHeC injector (p-140 GeV).

- 6426 • Rotating-wheel targets (Section ??).
- 6427 • Sliced-rod W tungsten conversion targets (Section ??);
- 6428 • Liquid mercury targeta (Section ??).
- 6429 • Running tape with annealing process (Section ??).

6430 8.6.6 Conventional Scheme based on e^- Beam Hitting Target

6431 The LHeC ERL option requires a positron current of 6 mA or $4 \times 10^{16} e^+/s$, with normalized emittance of
 6432 $\leq 50 \mu\text{m}$ and longitudinal emittance $\leq 5 \text{ MeV}\cdot\text{mm}$.

6433 For a conversion target with optimized length the power of the primary beam is converted as follows
 6434 $P_{\text{primary}}(100\%) = P_{\text{thermal}}(30\%) + P_{\gamma}(50\%) + P_{e^-}(12\%) + P_{e^+}(8\%)$. The average kinetic energy of the
 6435 newly generated positrons is $\langle T_{e^+} \rangle \approx 5 \text{ MeV}$, which allows estimating the total power incident omn the
 6436 target as $P_{\text{target}} = 5 \text{ MV} \times 6 \text{ mA} / 0.08 = 375 \text{ kW}$. Assuming an electron linac efficiency of $\eta_{\text{acc}} \approx 20\%$ we
 6437 find $P_{\text{wall}} = P_{\text{target}}/0.2 = 1.9 \text{ MW}$. This wall-plug power level looks feasible and affordable.

6438 Figure ?? illustrates a possible option, which alone would already meet the requirements for the 140-GeV
 6439 single-linac case, where the repetition rate is 10 Hz. The idea is to use 10 e^+ target stations in parallel. This
 6440 implies installing 2 RF deflectors upstream and the same downstream. Experience exists for RF deflectors
 6441 at 3 GHz and with operating 2 lines in parallel. Assuming that this configuration is acceptable from the
 6442 beam-optics point-of-view, it would be necessary to implement a fast damping scheme because the bare
 6443 emittances from the target will be too high for the injection into the ERL.

6444 Table ?? shows the beam characteristics at the end of the 10 GeV Primary beam Linac for electrons,
 6445 before splitting the beam.

Primary beam energy (e^-)	10 GeV
Number e^- / bunch	1.2×10^9
Number of bunches / pulse	100000
Number e^- / pulse	1.2×10^{14}
Pulse length	5 ms
Beam power	1900 kW
Bunch length	1 ps

Table 8.19: Electron beam parameters before splitting.

6446 Table ?? shows the beam parameters at each e^+ target. Energy of 5.6 kW is deposited in each target and
 6447 the Peak Energy Deposition Density (PEDD) is around 30 J/g. This value has been chosen, in order to be
 6448 below the breakdown limit for tungsten (W) target. It is based on recent simulations [?] with conventional
 6449 W targets. A new study has been done [?], assuming a target made out of an assembly of densely packed W
 6450 spheres (density about 75% of solid tungsten) with diameters of 1–2 mm. The cooling is provided by blowing
 6451 He-gas through the voids between the spheres. Such He-cooled granular targets have been considered for
 6452 neutrino factories and recently for the European Spallation Source ESSS.

Yield (e^+/e^-)	1.5
Beam power (for e^-)	190 kW
Deposited power / target	5.6 kW
PEDD	30 J/g
Number e^+ / bunch	1.8×10^9
Number bunches / pulse	10,000
Number e^+ / pulse	1.8×10^{13}

Table 8.20: Beam parameters at each e^+ target.

6453 To achieve the required cooling and the corresponding mass flow of the cooling fluid, we consider pres-
 6454 surized He at 10 bar entering the target volume at a velocity of 10 m/s, i.e. a mass flow 1.8 g/s is required
 6455 for each target. From this a convection coefficient of about $\alpha = 1 \text{ W/cm}^2/\text{K}$ can be expected and a cooling
 6456 time constant τ (exponential decay time after an adiabatic temperature rise of a sphere) of 185 ms will
 6457 result. Clearly, not much cooling during a pulse of 5 ms duration will occur, but cooling will set in during
 6458 the off-beam time of 95 ms between the pulses. The peak temperature after each pulse will stabilize at about
 6459 500 K above that of the cooling fluid. An average exit temperature of the He-gas of about 600 °C will have
 6460 still to be added, which drives the maximum temperature of the spheres up to about 1100 °C. Although
 6461 compatible with W in an inert atmosphere, it should be attempted to reach lower temperatures. This could
 6462 be achieved by increasing the He-pressure to 20 bar and the velocity of He to 20 m/s which might reduce
 6463 the maximum temperature in a sphere to 500 °C. Thus, a He-cooled granular 10-W-target system could be
 6464 a viable solution.

6465 Another approach has been considered. To achieve, as in the previous case, a reduction of the energy
 6466 deposition density by a factor of 10, a fast rotating wheel could be designed. The beam pulse of 5 ms duration
 6467 is spread over the rim of the rotating wheel and a linear velocity of the rotating rim of 20 m/s would be
 6468 required. This would lead to repetition rate of about 1000 rpm, assuming a wheel diameter of 0.4 m. Such
 6469 a solution is actually under investigation for the ILC with a rotation speed of 1800 rpm.

6470 Here tungsten spheres, again, are contained in a structure, similar to a care tyre, as is illustrated in
 6471 Fig. ???. The container is possibly made of light Ti-alloy where the sides, facing the beam entrance and exit
 6472 should be made of Beryllium, compatible with the beam heating. The helium for the cooling is injected from
 6473 the rotating axle through spokes into the actual target ring and is recuperated in the same way.

6474 If the beam pulse duration is extended by a factor 10, i.e. 50 ms duration, maintaining of course the
 6475 same average power, then the rotation time could be reduced. The velocity of the wheel is such that over
 6476 the duration of 5 ms the rim is displaced by one beam width, i.e. 1 cm. This leads to much reduced rotation
 6477 speeds of 2 m/s, which can readily be achieved in a wheel with a diameter of 16 cm, rotating at 240 rpm.

6478 By choosing appropriately the rotation velocity, the average time between two hits of the same spot on
 6479 the rim of the wheel, is about 0.5 s. With the aforementioned cooling time constant for the He-circuit of
 6480 185 ms, the adiabatic temperature rise during one hit over 5 ms of 211 K will have dropped to close to zero
 6481 before the next hit. Since we assume to simultaneously cool the whole rim of the wheel, a He-flow of 90 g/s
 6482 must be provided. Taking into account the temperature increase in the cooling fluid, a maximum tungsten
 6483 temperature in the W-spheres of about 350°C can be expected, which is rather comfortable.

6484 Using a continuous D.C.-beam with no gaps will further alleviate the structure and performance of the

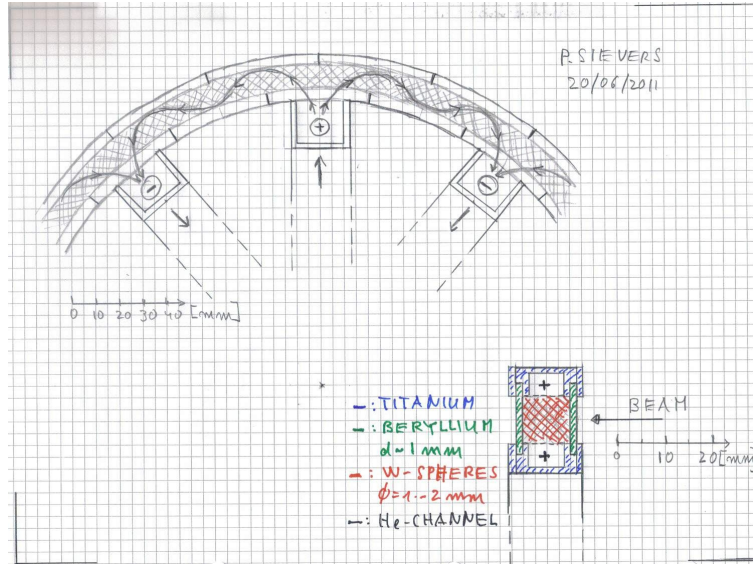


Figure 8.52: Artist's view of rotating wheel containing W spheres with He cooling.

6485 target wheel.

6486 The interference of the rotating wheel with the downstream flux concentrator will have to be assessed. One
 6487 may, however, expect considerably less forces than presently considered for the ILC, due to the much lower
 6488 velocity of the wheel. Moreover, proper choice of materials with high electrical resistivity and laminating
 6489 the structure may be considered.

6490 Clearly, the W-granules must be contained inside the beam vacuum within a structure which is He-leak
 6491 tight at the selected He-pressure. As material for the upstream and downstream beam windows, Beryllium
 6492 must be considered which, due to its large radiation length (34 cm as compared to W with 0.34 cm), should
 6493 resist to the thermal loads. This, however, has to be verified.

6494 Also, radiation damage and life time issues will still have to be assessed.

6495 It is believed that rotating “Air to Vacuum” seals at 240 rpm are commercially available or can be
 6496 adapted to the radiation environment. Rotating “High Pressure He to Air” seals may have to be developed,
 6497 where small He-leaks can be tolerated.

6498 This last approach is focused on e^+ targets. Presently with conventional targets, the transverse normal-
 6499 ized rms beam emittances, in both planes, are in the range of 6000 to 10 000 mm.mrad. With the new type
 6500 of target, we do not know yet by how much the transverse emittances will be changed. In any case, a strong
 6501 reduction of emittances is mandatory for the requested LHeC performance.

6502 Assuming that large or small emittances could be recombined, Table ?? shows a possible e^+ flux after
 6503 recombination.

6504 Finally, if a solution is found for the emittances, it will be necessary to design and implement a linac
 6505 accelerating the positron beam up to 500 MeV, the energy for the ERL injection.

6506 8.6.7 Compton Sources

6507 In Compton sources, (polarized) positrons are produced as a result of the following processes:

- 6508 1. Electron beam (current I_{e^-}) scatters off polarized laser photons (energy in pulse W).
- 6509 2. Gamma flux, $\sim I_{e^-} \times W$, is first collimated and then impinging on a conversion target.
- 6510 3. Produced positrons lose a fraction of energy while traversing the target.

Secondary beam energy (e^+)	200 MeV
Number e^+ bunch	1.8×10^9
Number of bunches / pulse	100000
Number of e^+ / pulse	1.8×10^{14}
Bunch spacing	50 ns
Repetition rate	10 Hz

Table 8.21: Positron beam parameters after recombination.

6511 4. Postselection: low-energy positrons are discarded to attain the required polarization.

6512 Three principal factors limit the performance of polarized positron sources based on Compton scattering.
6513 They are:

- 6514 1. Limited average current of electrons scattering off laser photons (world record $I_{e^-} = 5$ A – PEP ring).
- 6515 2. Limited energy of pulses stored in optical resonators (fast progress, an array of resonators may be
6516 employed, 1...5 J assumed maximal accepted: higher energy of pulses violates electron dynamics).
- 6517 3. Limited power density of gammas, to which the conversion target is tolerable (sliced-rod convertor
6518 reduces positron losses and increases the current).

6519 The polarization degree of positrons is determined by the cut-off energy of positrons exiting from the target:
6520 the higher the polarization required the higher the energy threshold for discarding low-energy positrons (and
6521 the lower the yield). The optimal target thickness that maximizes the yield also decreases with the increase
6522 of the polarization requested, along with a decrease in the yield of positrons (but with an improved quality
6523 of the positron beam: a smaller energy spread, and a smaller transverse emittance).

6524 For a CLIC source of polarized positrons [?] (1 GeV electron energy, 1 μ m YAG laser system, and,
6525 correspondingly, 20 MeV maximal energy of the Compton spectrum) “envelopes” describing the limiting
6526 number of positrons from the conversion target per scattered gamma and the associated polarization are
6527 presented in Fig. ??.

6528 Compton Ring

6529 A typical Compton-ring gamma source (the CLIC ring) with the parameters listed in [?], and modified to
6530 accommodate an entire array of optical resonators, namely 10 units with 50 mJ of laser energy stored in each,
6531 installed in the dispersive section, is capable of producing 0.01 gammas per electron-turn. This scheme can
6532 be enhanced by increasing the laser energy by a factor of 10, up to 5 J, and by halving the collision angle,
6533 to 4 degrees, which increases the yield by an order of magnitude, up to 0.1 gammas per electron-turn.

6534 A typical tungsten convertor optimized for Compton gammas with a maximal energy of 20 MeV can de-
6535 livered 0.01 positrons with 60% polarization per incident scattered gamma. The convertor can be enhanced
6536 as well: a sliced-rod convertor target produces 0.07/0.13 positrons per gammas for a 1 m or 3 m long rod,
6537 respectively [?].

6538 Including a 50% overhead, for either the standard scheme and with teh two types of enhancements,
6539 various projects require the minimal circulating currents in Compton rings listed in Table ??.

6540 Table ?? illustrates that a Compton-ring source equipped with an array of optical resonators yielding a
6541 total laser-pulse energy of 5 Joule, together with a sliced-rod conversion raget, will produce the desired flux
6542 of polarized positrons even for the LHeC ERL option.

6543 In conclusion, according to the present understanding and simulations, a Compton positron source
6544 may produce sufficient average positron beam current for all LHeC options. The conversion of gammas to
6545 positrons is a bottleneck, which requires a study and optimization of effective convertor targets such as the
6546 sliced-rod converter.

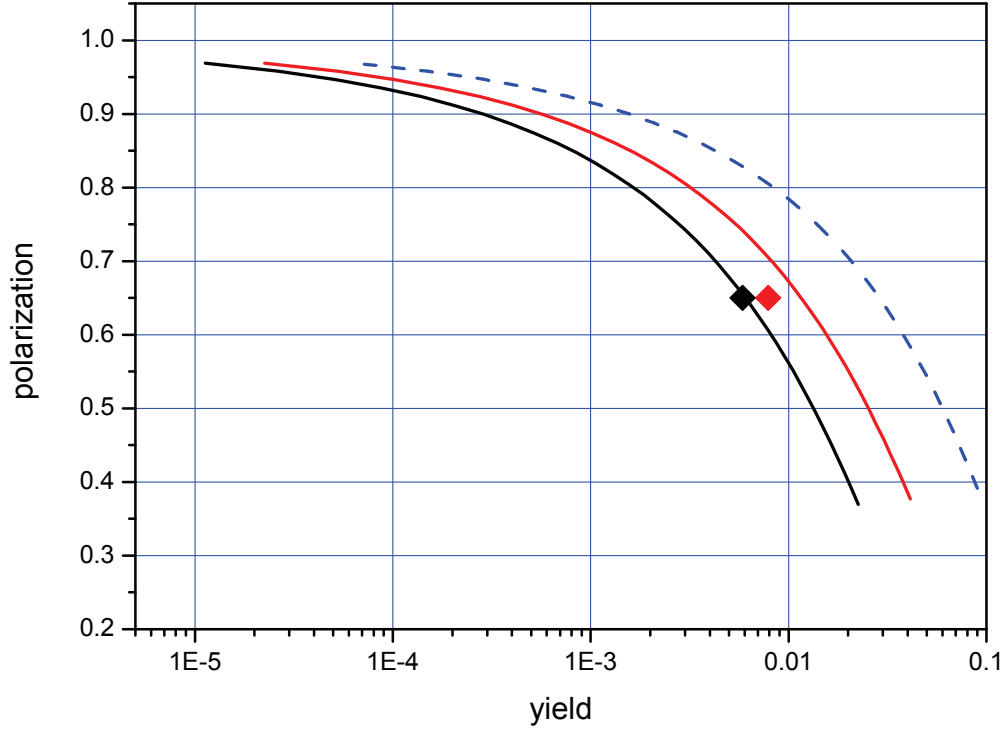


Figure 8.53: Limits for Ti (black) and W (red) conversion targets. Diamonds: simulations (A.Schalicke, S.Riemann). Blue Dashed curve: a sliced-rod conversion target.

Table 8.22: IP positron current and the implied minimum electron beam current in a Compton Ring

	unit	SLC	CLIC (3TeV)	LHeC p-140	LHeC ERL
I_{e+} at IP	μA	0.96	18	290	7050
typical I_{e-}	A	1.4E-2	0.26	4.3	105.7
I_{e-} with 5 J	A	1.5E-3	2.8E-2	0.46	11.2
I_{e-} with 5 J+1 m rod	A	2.2E-4	4.0E-3	6.5E-2	1.6

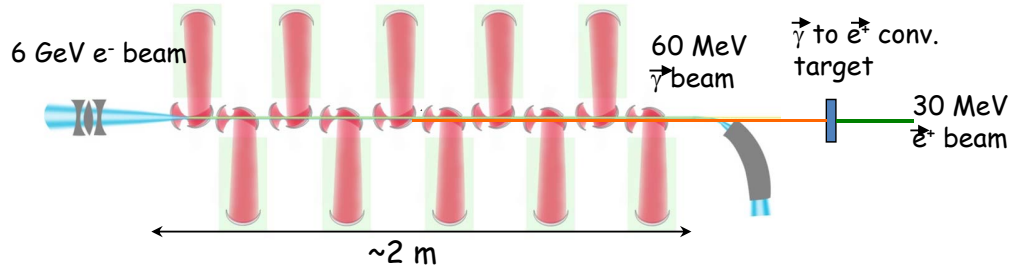


Figure 8.54: Layout based on Compton Linac.

6547 **Compton Linac**

6548 Positrons, even polarized, can be generated by the Compton scattering process of high-power laser pulses
 6549 stacked in optical cavities with a high-energy electron beam from a linac. Figure ?? present a possible layout
 6550 for such configuration.

6551 At BNL, a ratio photon/electron close to 1 has been demonstrated. Assuming that a ratio pho-
 6552 ton/positron close to 2% is achievable, then 50 photons are required to produce 1 e⁺. For LHeC, one
 6553 needs 0.35 nC/bunch (for the e⁺ to be produced). Based on above estimations, it implies ~18 nC/bunch
 6554 (for the e⁻ beam). Then with 10 optical cavities, the requested e⁻ charge is about 1.8 nC / bunch which is
 6555 a reasonable value.

6556 **Power Analysis for Compton Schemes and Compton ERL**

6557 A number of pertinent technologies have been investigated, but are not yet established:

- 6558 1. 1.3 Ampere ERL (R&D at BNL)
- 6559 2. Mercury target or annealing target (Muon collider collaboration)
- 6560 3. High finesse optical stacking cavities with factor 1000 enhancement, 1 kW pump (France, KEK, ...)

6561 This section considers different Compton-based options for an LHeC positron source including power con-
 6562 siderations. The following source requirements were taken into account:

- 6563 • 6mA average current or 4×10^{16} e⁺/sec
- 6564 • 2×10^7 bunches with 2×10^9 e⁺/bunch
- 6565 • Normalized rms emittance of 50 microns
- 6566 • Longitudinal emittance 5 MeV-mm or 10 mm normalized.

6567 The **power analysis** for the different schemes can be done backwards:

- 6568 1. power of the captured positron beam
- 6569 2. → power of the gamma beam entering the conversion target and generating electron positron pairs
- 6570 3. → drive electron beam generating gamma beam
- 6571 4. → klystron generating drive electron beam
- 6572 5. → wall plug power

6573 Scattering of the multi MeV gammas on the target produces the electrons and positrons. The optimal
 6574 gamma beam energy range of 30-60 MeV is selected as a compromise between conversion efficiency and
 6575 capture efficiency as well as longitudinal emittance. Beam power of the captured positron beam is estimated
 6576 at $6 \text{ mA} \times 30 \text{ MeV}$ or 180 kW.

6577 The conversion efficiency of gamma beam into captured positrons ranges from 0.3 to 2% for different
 6578 schemes of the ILC positron source. This (optimistically) sets a requirement for the gamma beam entering
 6579 the target at 9 MW. A 2–6 GeV electron beam is used in different schemes to generate a gamma beam by
 6580 Compton scattering of the powerful laser beam. The efficiency of electron beam power conversion is at most
 6581 10%, for the scheme with a CO2 laser. This puts a lower limit on the drive beam power at 90 MW. A CLIC
 6582 type driver can optimistically generate the drive beam at approximately 50 percent efficiency and, therefore,
 6583 an overall power requirement to generate a 6 mA positron beam with pulsed linac (CLIC type) and the CO2
 6584 laser can be estimated at 180 MW.

6585 To summarize:

- 6586 • $6 \text{ mA} \times 30 \text{ MeV} \rightarrow 180 \text{ kW } e^+$ beam (Output of conversion target)
- 6587 • $\gamma \rightarrow e^+$ efficiency about 2% $\rightarrow 9 \text{ MW } \gamma$ beam (conversion efficiency)
- 6588 • $e^- \rightarrow \gamma$ about 10%, 90 MW e^- beam
- 6589 • Wall $\rightarrow e^-$ about 50% or 180 MW wall power

6590 The wall plug power for the electron beam alone exceeds the limit of 100 MW set for the entire project.
 6591 On the other hand, the energy spread of the circulating beam would be prohibitive in a Compton ring scheme
 6592 subjected to the requirement to generate 9 MW from a 30-MeV gamma beam. Both issues can be handled
 6593 by exploring the energy recovery linac option. A 3-GeV 1.3-Ampere ERL with 2 micron laser enhancement
 6594 cavities has the potential of generating the required positron beam with only 50 MW of wall plug power, as
 6595 follows:

- 6596 • $6 \text{ mA} \times 30 \text{ MeV} = 180 \text{ kW } e^+$ beam (Output of conversion target)
- 6597 • $\gamma \rightarrow e^+$ about 1% $\rightarrow 18 \text{ MW } \gamma$ beam (Conversion efficiency)
- 6598 • $e^- \rightarrow \gamma$ about 0.5% 4 GW e^- beam (99.9% efficient ERL)
- 6599 • Wall $\rightarrow e^-$ about 50% of $0.001 \times 4 \text{ GW} + 18 \text{ MW}$
- 6600 • Total $\approx 50 \text{ MW}$ wall power

6601 The major challenge of a pulsed linac scheme is in the cost of driving the linac. A high wall power require-
 6602 ment combined with long pulse format make the CO2 laser/pulse linac combination an unlikely solution.
 6603 The challenge of the ERL scheme lies in the development of the recirculating cavities and target/capture
 6604 system that would be able to perform the CW mode of operation.

6605 **Emittances:** The upper estimate on the transverse and longitudinal emittances in the case of 2 GeV
 6606 ERL for the captured positron beams can be estimated as follows:

- 6607 • Normalized positron beam emittance, expressed through its energy, RMS beam size and angular di-
 6608 vergence at the target exit: $\epsilon_N \approx \gamma_{e^+} \sigma \sigma'$.
- Acquired angular spread in the length target (typically selected at 0.4 radiation length) can be estimated
 as

$$\sigma_{e^+} \approx \frac{1}{\sqrt{2}} \frac{14 \text{ MeV}}{E_{e^+}} \sqrt{\frac{L_{\text{target}}}{X_0}} \approx \frac{10}{\gamma_{e^+}} .$$

- 6609 • Three components contribute to the beam size:

1. Scattering in the target:

$$\sigma_{e^+,sc} \approx \frac{\sqrt{2}}{3} \sigma'_{e^+} L_{\text{target}} \approx \frac{\sqrt{2}}{3} 0.3 \cdot 1.2 \text{ mm} \approx 150 \text{ } \mu\text{m} .$$

2. Beam size due to gamma beam divergence:

$$\sigma_{\gamma,div} \approx \frac{1}{2\gamma_{e^-}} \frac{L_{IR}}{\sqrt{2}} \approx \frac{1}{2 \times 4000} \frac{0.1 \text{ m}}{\sqrt{2}} \approx 15 \text{ } \mu\text{m} .$$

3. and e- beam size on target:

$$\sigma_{\gamma e^-} \approx \sqrt{\frac{\epsilon_{Ne^-}}{\gamma_{e^-}} \beta_{e^-}} \approx \sqrt{\frac{10 \text{ } \mu\text{m}}{4000}} 1 \text{ m} \approx 50 \text{ } \mu\text{m} .$$

This results in the normalized transverse emittance of 1.5 mm. The strong magnetic field in which the target would likely be immersed will lower this estimate. The estimate for the longitudinal emittance is:

$$\epsilon_{||,N} \approx \Delta\gamma_{e^+} \sigma_{\tau e^-} \approx \frac{60 - 30}{4} 60 \text{ } \mu\text{m} \approx 450 \text{ } \mu\text{m} .$$

6610 **Compton-ERL Target:** Charged particle beams exiting the conversion target generate most of the
 6611 heat. The deposited power can be estimated (roughly) as $6 \text{ mA} \times 5 \text{ MeV} \times 2 \times 2$, or 120 kW. 5 MeV is
 6612 estimated for the energy loss and factors of 2 are attributed to equal parts of captured and non-captured low
 6613 energy positrons, and to the equal number of electrons and positrons. This suggests that a liquid mercury
 6614 target may be an important candidate.

6615 **Compton ERL Summary:** High current ERL seems the most promising approach, e.g. a 3-GeV 1.3-A
 6616 ERL with 2-micron wavelength optical enhancement cavities.

6617 Target is going to be a very difficult consideration (candidates would be a liquid mercury target or running
 6618 tape with annealing process). The desired emittances are not reached from any Compton scheme source,
 6619 even if the target is immersed in a strong magnetic field. Therefore, cooling or scraping would be required.

6620 Laser Pulses and Optical Cavities

6621 Different experimental programs presently underway aim at achieving a very important photon pulse intensity
 6622 by direct production in a laser system and stacking in a passive optical resonator. This laser-stacking scheme
 6623 allows increasing the available average power in the optical cavity without requiring impossible performances
 6624 to the drive laser system. As far as Compton-source developments are concerned, depending on the purpose
 6625 of the application, the stored pulse length ranges from a few hundreds of femtoseconds to a few picoseconds,
 6626 the repetition frequency (which determines the cavity length) from 20 to 200 MHz, and the wavelength from
 6627 0.5 to 1.1 μm .

6628 When trying to achieve storing a very high power in a Fabry-Perot optical resonator the state of the
 6629 art of the present technology has to be taken into account. As far as the laser is concerned, in the last
 6630 years an impressive increase in the available average power has been provided by the development of the
 6631 fiber amplifiers. The best performances have been obtained by combining the development of large core
 6632 single mode photonic crystal fibers with the chirped-pulse amplification (CPA) technique. For example, a
 6633 200-fs, 1048-nm wavelength, 78-MHz oscillator pulse after a first stretching to 800 ps, has been amplified
 6634 in a system composed of a two-stage double-clad photonic crystal fiber preamplifier (30 μm mode field and
 6635 170 μm pump cladding diameter) pumped at 976-nm wavelength, and a main-amplifier double-clad water
 6636 cooled fibre (27- μm mode field and 500 μm air clad). After this phase a recompression of the pulse to 640
 6637 fs has yielded an “incredible” average power of 830 W and about 10 μJ per puls [?].

6638 To stack many short laser pulses in a Fabry Perot resonator, and obtain an important pulse enhancement,
 6639 it is necessary to lock the cavity characteristic comb with the laser one. This implies to act on two degrees
 6640 of freedom given by the repetition frequency and by the carrier to phase envelope (Φ_{ce}). In this context the

6641 Pound Driver Hall locking techniques is employed in the LAL cavity [?]. This technique has attained the
6642 best performances in gain, as far as pulses of few ps are concerned. A gain of about 10000 was achieved,
6643 storing a laser pulse of close to 20 kW in a confocal two mirror cavity. However, the best result, as far as the
6644 stored power is concerned, has been achieved by the MPQ laboratory using the Hansch-Couillaud locking
6645 technique [?]. With a pulse length of 200 fs an average power of 18 kW was obtained in a 78-MHz tie bow
6646 cavity with an enhancement factor of 1800. After this achievement, thermal problems were noticed due to
6647 the very high-power density of the pulse. Stretching the pulse to 2 ps the stacking process was efficient up
6648 to 72 kW with an estimated gain of 1400. In the cavity waist this corresponded to a 10^{14} W/cm² power
6649 density. At this power level the coupling between the laser power and the cavity was near 50%.

6650 In the framework of the Compton facilities another important experimental effort is carried out jointly by
6651 LAL Orsay (France) and KEK Tsukuba (Japan) [?]. In fact, to validate the use of optical passive cavities,
6652 different tests have to be performed also taking into account the reliability and the compatibility of a given
6653 optical cavity with the accelerator environment. A 176 MHz, a four-mirror vacuum-compatible optical
6654 cavity has been designed, realized and installed in the KEK-ATF ring. A four-mirror configuration was
6655 chosen instead of a two-mirror one, because with the former it is possible to achieve very small laser-waists
6656 without losing in mechanical stability. An estimated stored power of 2 kW has been achieved during the
6657 commissioning of the system at the end of 2010. A future program to explore the 100kW range is envisaged.
6658 At the ATF beam energy, Compton collision will produce gamma rays near 20 MeV resulting in the world-s
6659 first beam-driven gamma factory.

6660 8.6.8 Undulator Source

6661 Another positron production option would be an undulator process, based on the main high-energy electron
6662 (or positron) beam. The LHeC undulator scheme can benefit from the pertinent development work done
6663 for the ILC. The beam energy at LHeC would be lower, e.g. 60 GeV, which might possibly be compensated
6664 by more ambitious undulator magnets, e.g. ones based on Nb₃Sn or HTS. However, the requested photon
6665 flux calls for a careful investigation. The undulator parameters needed for 60 GeV, the expected positron
6666 production rate, and technical feasibility all require further study.

6667 8.6.9 Source based on Coherent Pair Creation

6668 The normalized transverse emittance of all positrons from a target is of order $\epsilon_N \approx 1 - 10$ mm, to be
6669 compared with a a requested emittance of $\epsilon_N = 0.05$ mm. Therefore, a factor 100 emittance reduction is
6670 required.

6671 Solution 1 would be to simply cut the phase space. However, this would give rise to an unrealistic increase
6672 of the primary beam power.

6673 Solution 2 would be to collect all positrons, accelerate them to 1 GeV and damp them for $\text{Log}(100) \sim 5$
6674 damping times, with an implied RF power of $P_{RF} = 1 \text{ GeV} \times 5 \text{ mA} \times 5/0.6 = 60 \text{ MW}$, where an RF efficiency
6675 of 50% was assumed.

6676 Solution 3 would be to produce positrons in a smaller phase space volume. Indeed the inherent transverse
6677 emittance from pair production is small. The large phase space volume only comes from multiple scattering
6678 in the production target.

6679 Pair production from relativistic electrons in a strong laser field would not need any solid target, since
6680 the laser itself serves as the target, and it would not suffer from multiple scattering. This process has been
6681 studied in the 1960's and 1990's [?, ?, ?]. It should be reconsidered with 2011 state of the art TiSa lasers and
6682 X-ray FELs [?].

6683 8.6.10 Conclusions

6684 The challenging requirements for the LHeC Linac-Ring positron source are relaxed if positrons can be collided
6685 several times before deceleration, if they can be reused over several acceleration/deceleration cycles, and/or

6686 if they can be cooled. The compact tri-ring scheme is an attractive proposal for recooling the spent and
6687 recycled positrons. A conventional damping ring in the SPS tunnel would be an alternative.

6688 Assuming some of the aforementioned measures are taken to reduce the required positron intensity, which
6689 needs to be generated, by at least an order of magnitude, and also assuming that an advanced target, e.g.
6690 W-granules, rotating wheel, sliced-rod converter, or liquid metal jet, can be used, several of the proposed
6691 source and cooling concepts could provide the intensity and the beam quality required by the LHeC ERL.

6692 For example, the Compton-ring source and the Compton ERL are viable candidates for the Linac-
6693 Ring LHeC positron source. Coherent pair production and an advanced undulator represent other possible
6694 schemes, still to be explored for LHeC in greater detail. The coherent pair production would have the
6695 appealing feature of generating positrons with an inherently small emittance.

6696 In conclusion, it does seem technically possible to meet the very demanding requirements for the LHeC
6697 positron source by a combination of approaches. A serious and concerted R&D effort will be required to
6698 determine the optimum linac-ring positron configuration.

Chapter 9

System Design

9.1 Magnets for the Interaction Region

9.1.1 Introduction

The technical requirements for the ring-ring options are easily achieved with superconducting magnets of proven technology. It is possible to make use of the wire and cable development for the LHC inner triplet magnets. We have studied all-together seven variants of which two are selected for this CDR. Although these magnets will require engineering design efforts, there are no challenges because the mechanical design will be very similar to the MQXA [?] magnet built for the LHC [?].

The requirements in terms of aperture and field gradient are much more difficult to obtain for the linac-ring option. We reverse the arguments and present the limitations for the field gradient and septum size, that is, the minimum distance between the proton and electron beams, for both Nb-Ti and Nb₃Sn superconducting technology. Here we limit ourselves to the two most promising conceptual designs.

9.1.2 Magnets for the ring-ring option

The interaction region requires a number of focussing magnets with apertures for the two proton beams and field-free regions to pass the electron beam after the collision point. The lattice design was presented in Section xx; the schematic layout is shown in Fig. ??.

The field requirements for the ring-ring option (gradient of 127 T/m, beam stay clear of 13 mm (12 σ), aperture radius of 21 mm for the proton beam, 30 mm for the electron beam) allow a number of different magnet designs using the well proven Nb-Ti superconductor technology and making use of the cable development for the LHC. In the simulations presented here, we have used the parameters (geometrical, critical surface, superconductor magnetization) of the cables used in the insertion quadrupole MQY of the LHC.

Fig. ?? shows a superferric magnet as built for the KEKb facility [?]. This design comes to its limits due to the saturation of the iron poles. Indeed, the fringe field in the aperture of the electron beam exceeds the limit tolerable for the electron beam optics, and the field quality required for proton beam stability, on the order of one unit in 10^{-4} at a reference radius of 2/3 the aperture, is difficult to achieve.

The magnetic flux density in the low-field region of the design shown in Fig. ?? (right) is about 0.3 T. We therefore disregard this design as well. Moreover, the engineering design work required for the mechanical structure of this magnet would be higher than for the proven designs shown in Fig. ??.

Fig. ?? shows the three alternatives based on LHC magnet technology. In the case of the double aperture version the aperture for the proton beams is 21 mm in diameter, in the single aperture version the beam pipe is 26 mm. In all cases the 127 T/m field gradient can be achieved with a comfortable safety margin to quench (exceeding 30%) and using the cable(s) of the MQY magnet of the LHC. The operation temperature is supposed to be 1.8 K, employing superfluid helium technology. The cable characteristic data are given in

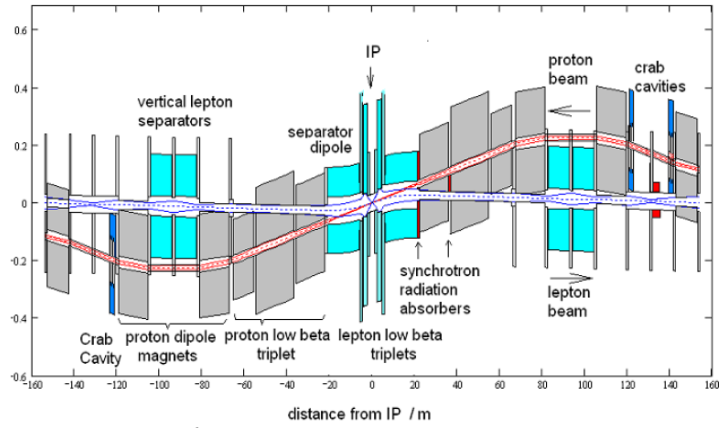


Figure 9.1: Layout of the LHeC interaction region (ring-ring option).

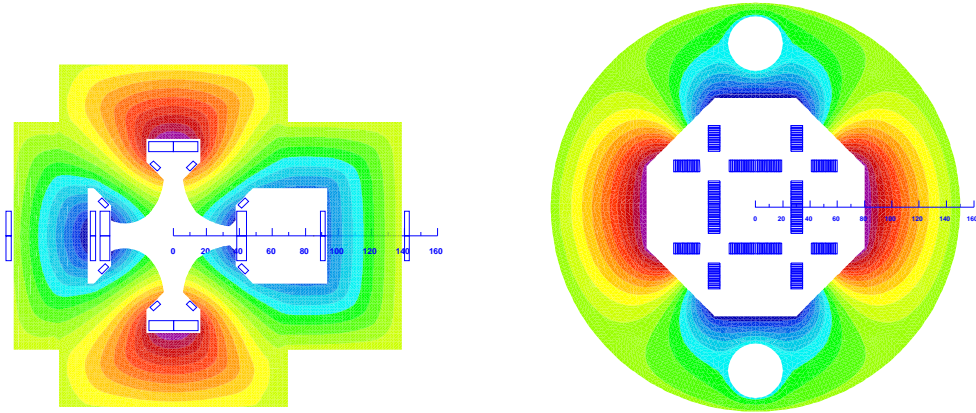


Figure 9.2: Cross-sections of insertion quadrupole magnets with iso-surfaces of the magnetic vector potential (field-lines). Left: Super-ferric, similar to the design presented in [?]. Right: Superconducting block-coil magnet as proposed in [?] for a coil-test facility.

6734 Table ???. The outer radii of the magnet coldmasses do not exceed the size of the triplet magnets installed
 6735 in the LHC (diameter of 495 mm). The fringe field in the aperture of the electron beam is in all cases below
 6736 0.05 T.

6737 Fig. ?? shows half-aperture quadrupoles (single and double-aperture versions for the proton beams) in a
 6738 similar design as proposed in [?]. The reduced aperture requirement in the double-aperture version makes it
 6739 possible to use a single layer coil and thus to reduce the beam-separation distance between the proton and
 6740 the electron beams. The field-free regions is large enough to also accommodate the counter rotating proton
 6741 beam. The version shown in Fig. ?? (left) employs a double-layer coil. In all cases the outer diameter of the
 6742 coldmasses do not exceed the size of the triplet magnets currently installed in the LHC tunnel.

6743 For this CDR we retain only the single aperture version for the Q2 (shown in Fig. ??, left) and the half-
 6744 aperture quadrupole for the Q1 (shown in Fig. ??, top left). The separation distance between the electron and
 6745 proton beams in Q1 requires the half-aperture quadrupole design to limit the overall synchrotron radiation
 6746 power emitted by bending of the 60 GeV electron beam. The single aperture version for Q2 is retained in

Table 9.1: Characteristic data for the superconducting cables and strands. OL = outer layer, IL = inner layer

Magnet	MQY (OL)	MQY (IL)
Diameter of strands (mm)	0.48	0.735
Copper to SC area ratio	1.75	1.25
Filament diameter (μ m)	6	6
B_{ref} (T) @ T_{ref} (K)	8 @ 1.9	5 @ 4.5
$J_c(B_{\text{ref}}, T_{\text{ref}})$ (A mm^{-2})	2872	2810
$-dJ_c/dB$ ($\text{A mm}^{-2} \text{T}$)	600	606
$\rho(293 \text{ K})/\rho(4.2 \text{ K})$ of Cu	80	80
Cable width (mm)	8.3	8.3
Cable thickness, thin edge (mm)	0.78	1.15
Cable thickness, thick edge (mm)	0.91	1.40
Keystone angle (degree)	0.89	1.72
Insulation thicken. narrow side (mm)	0.08	0.08
Insulation thicken. broad side (mm)	0.08	0.08
Cable transposition pitch length (mm)	66	66
Number of strands	34	22
Cross section of Cu (mm^2)	3.9	5.2
Cross section of SC (mm^2)	2.2	4.1

6747 the present layout, because the counter rotating proton beam can be guided outside the Q2 triplet magnet.
6748 The design of Q3 follows closely that of Q2, except for the size of the septum between the proton and the
6749 electron beams.

6750 The coils in all three triplet magnets are made from two layers, using both Nb-Ti composite cables as
6751 specified in Table ???. The layers are individually optimized for field quality. This reduces the sensitivity
6752 to manufacturing tolerances and the effect of superconductor magnetization [?]. The mechanical design will
6753 be similar to the MQXA magnet where two kinds of interleaved yoke laminations are assembled under a
6754 hydraulic press and locked with keys in order to obtain the required pre-stress of the coil/collar structure.
6755 The main parameters of the magnets are given in Table ???.

6756 9.1.3 Magnets for the linac-ring option

6757 The requirements in terms of aperture and field gradient are more difficult to obtain for the linac-ring option.
6758 Consequently we present the limitations for the field gradient and septum size achievable with both Nb-Ti
6759 and Nb_3Sn superconducting technologies. We limit ourselves to the two conceptual designs already chosen
6760 for the ring-ring option. For the half quadrupole, shown in Fig. ?? (right), the working points on the
6761 load-line are given for both superconducting technologies in Fig. ??.

6762 However, the conductor size must be increased and in case of the half quadrupole, a four layer coil must
6763 be used; see Fig. ???. The thickness of the coil is limited by the flexural rigidity of the cable, which will
6764 make the coil-end design difficult. Moreover, a thicker coil will also increase the beam separation between
6765 the proton and the electron beams. The results of the field computation are given in Table ??, column 3
6766 and 4. Because of the higher iron saturation, the fringe fields in the electron beam channel are considerably
6767 higher than in the magnets for the ring-ring option.

6768 For the Nb_3Sn option we assume composite wire produced with the internal Sn process (Nb rod extru-

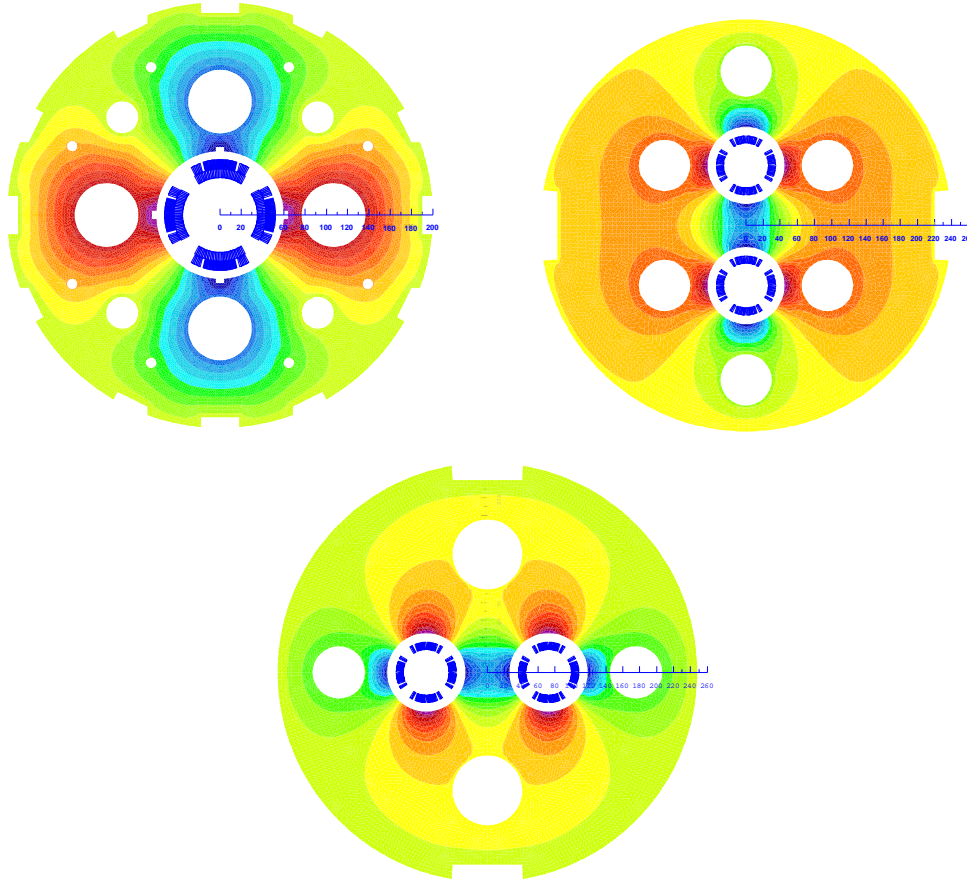


Figure 9.3: Cross-sections with field-lines of insertion quadrupole magnets. Classical designs similar to the LHC magnet technology. Top left: Single aperture with a double layer coil employing both cables listed in Table ???. Design chosen for Q2. Top right: Double aperture vertical. Bottom: Double aperture horizontal. The double-aperture magnets can be built with a single layer coil using only the MQY inner layer cable; see the right column of Table ???.

sions), [?]. The non-Cu critical current density is 2900 A/mm^2 at 12 T and 4.2 K. The filament size of $46 \mu\text{m}$ in Nb_3Sn strands give rise to higher persistent current effects in the magnet. The choice of Nb_3Sn would impose a considerable R&D and engineering design effort, which is however, not more challenging than other accelerator magnet projects employing this technology [?].

Fig. ?? shows the conceptual design of the mechanical structure of these magnets. The necessary prestress in the coil-collar structure, which must be high enough to avoid unloading at full excitation, cannot be exerted with the stainless-steel collars alone. For the single aperture magnet as shown in Fig. ?? left, two interleaved sets of yoke laminations (a large one comprising the area of the yoke keys and a smaller, floating lamination with no structural function) provide the necessary mechanical stability of the magnet during cooldown and excitation. Preassembled yoke packs are mounted around the collars and put under a hydraulic press, so that the keys can be inserted. The sizing of these keys and the amount of prestress before the cooldown will have to be calculated using mechanical FEM programs. This also depends on the elastic modulus of the coil, which has to be measured with a short-model equipped with pressure gauges. Special care must be taken to avoid nonallowed multipole harmonics because the four-fold symmetry of the

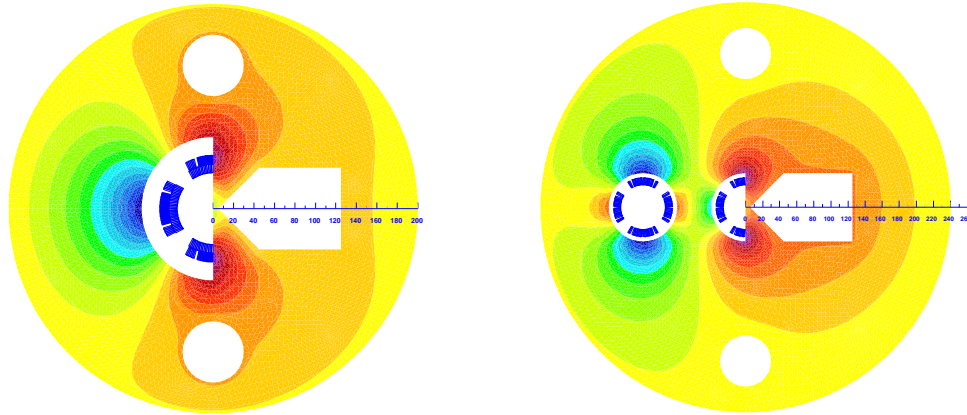


Figure 9.4: Cross-sections of insertion quadrupole magnets with field-lines. Left: Single half-aperture quadrupole with field-free domain [?]; design selected for Q1. Right: Double-aperture magnet composed of a quadrupole and half quadrupole.

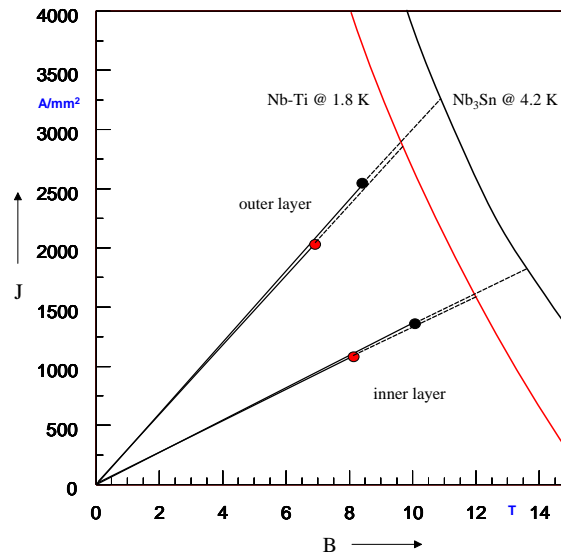


Figure 9.5: Working points on the load-line for both Nb-Ti and Nb₃Sn variants of the half quadrupole for Q1.

6783 quadrupole will not entirely be maintained.

6784 The mechanical structure of the half-quadrupole magnet is somewhat similar, however, because of the
 6785 left/right asymmetry four different yoke laminations must be produced. The minimum thickness of the
 6786 septum will also have to be calculated with structural FEM programs.

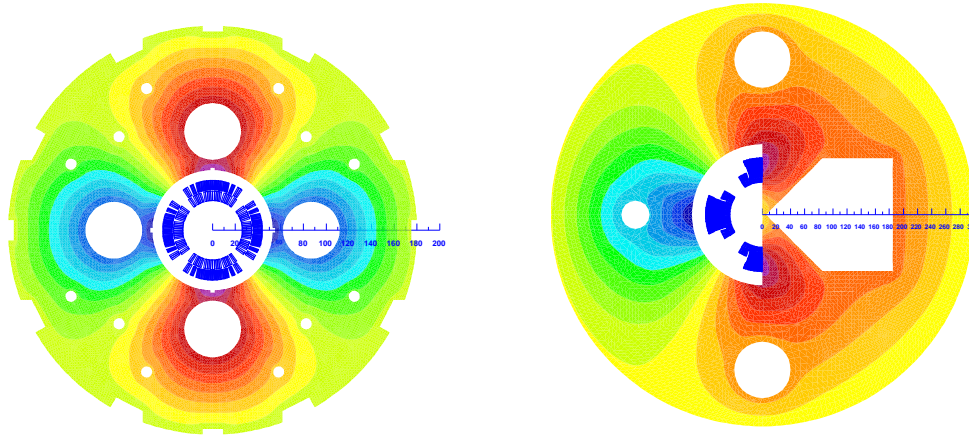


Figure 9.6: Cross-sections of the insertion quadrupole magnets for the linac-ring option. Left: Single aperture quadrupole. Right: Half quadrupole with field-free region.

Table 9.2: SC = type of superconductor, g = field gradient, R = radius of the aperture (without coldbore and beam-screen), LL = operation percentage on the load line of the superconductor material, I_{nom} = operational current, B_0 = main dipole field, S_{beam} = beam separation distance, B_{fringe} = fringe field in the aperture for the electron beam, g_{fringe} = gradient field in the aperture for the electron beam.

Type		Ring-ring single aperture	Ring-ring half-quad	Linac-ring single aperture	Linac-ring half-quad
Function		Q2	Q1	Q2	Q1
SC		Nb-Ti at 1.8 K			
R	mm	36	35	23	46
I_{nom}	A	4600	4900	6700	4500
g	T/m	137	137	248	145
B_0	T	-	2.5	-	3.6
LL	%	73	77	88	87
S_{beam}	mm	107	65	87	63
B_{fringe}	T	0.016	0.03	0.03	0.37
g_{fringe}	T/m	0.5	0.8	3.5	18
SC		Nb ₃ Sn at 4.2 K			
I_{nom}	A			6700	4500
g	T/m			311	175
B_0	T			-	4.7
LL	%			83	82
B_{fringe}	T			0.09	0.5
g_{fringe}	T/m			9	25

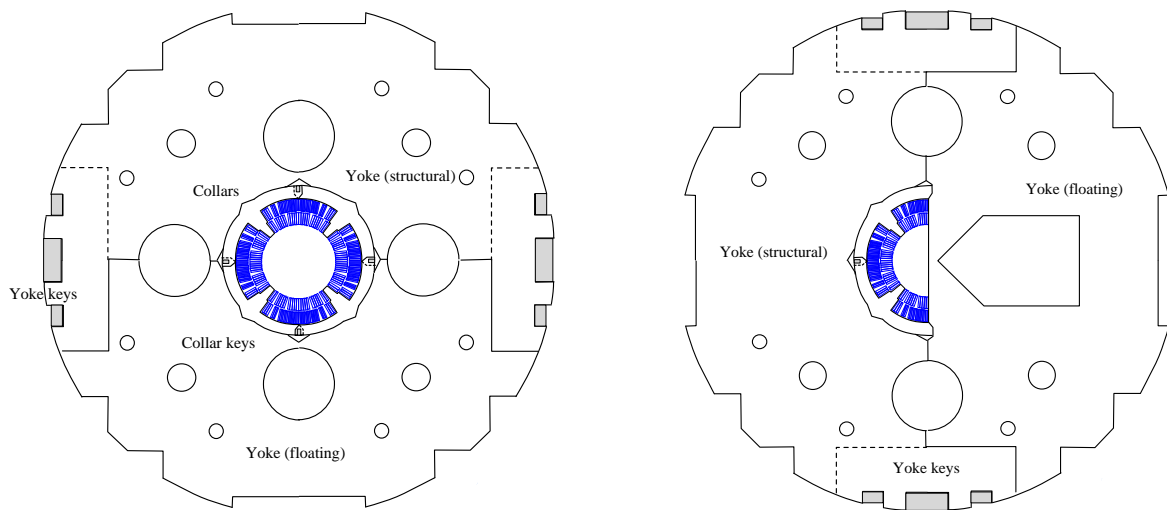


Figure 9.7: Sketch of the mechanical structure. Left: Single aperture magnet. Right: Half quadrupole with field-free region.

6787 **9.1.4 Dipole Magnets**

6788 Two different types of bending magnets are considered in this document: the ones for the LR Option, used
 6789 in the arcs of the recirculator, and the ones for the RR Option, to be installed in the LHC ring.

6790 **Dipole Magnets for the LR Option**

6791 Each of the 6 arcs of the recirculator needs 600 four-meter-long bending magnets, providing a magnetic field
 6792 from 0.046 T to 0.264 T depending on the arc energy from 10.5 GeV to 60.5 GeV.

6793 Considering the relatively low field strength required even for the highest energy arc, and the small
 6794 required physical aperture of 25 mm only, it is proposed here to adopt the same cross section for all magnets,
 6795 possibly with smaller conductors for the lowest energies.

6796 This allows the design of very compact and relatively cheap magnets, running at low current densities to
 6797 minimize the power consumption.

6798 Table ?? summarizes the main parameters of the proposed magnet design illustrated in Figure ??.

Parameter	Value	Units
Beam Energy	10.5-60.5	GeV
Magnetic Length	4.0	Meters
Magnetic Field	0.046-0.264	Tesla
Number of magnets	6 x 600 = 3600	
Vertical aperture	25	mm
Pole width	80	mm
Number of turns	2	
Current @ 0.264 T	2200	Ampere
Conductor material	copper	
Magnet inductance	0.10	milli-Henry
Magnet resistance	0.10	milli-Ohm
Power @ 10.5 GeV	15	Watt
Power @ 20.5 GeV	55	Watt
Power @ 30.5 GeV	125	Watt
Power @ 40.5 GeV	225	Watt
Power @ 50.5 GeV	350	Watt
Power @ 60.5 GeV	500	Watt
Total power consumption 10-60 GeV	762	kW
Cooling	air or water	depends on energy

Table 9.3: Main parameters of bending magnets for the LR recirculator. Resistance and power refer to the same conductor size, however for the lowest energies conductors may be smaller.

6799 **Dipole Magnets for the RR Option**

6800 3040 bending magnets, 5.35-meter-long each, are needed in the LHC tunnel for the RR option. They shall
 6801 provide a magnetic field ranging from 0.0127 T at 10 GeV to 0.0763 T at 60 GeV. Additionally, about 40
 6802 magnets will be needed in the Interaction Regions totalling about 3080 magnets. The main issues in the
 6803 design of these magnets are:

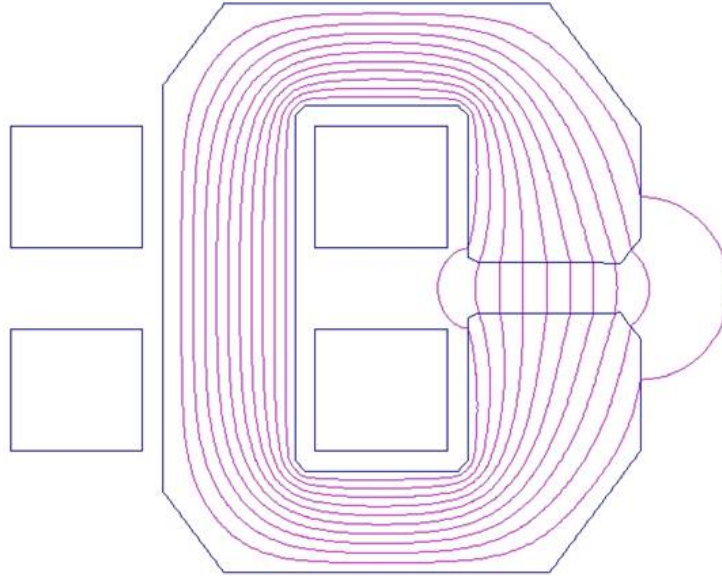


Figure 9.8: Bending magnets for the LR recirculator

- 6804 • the field range, situated in low field region, and in particular the very low injection field constitute
6805 a challenge for achieving a satisfactory field reproducibility from cycle to cycle and for making field
6806 quality relatively constant during the field ramp. These specific issues will be discussed further in the
6807 paragraphs dealing with the experimental work carried out at BINP and at CERN
- 6808 • compactness, to fit in the present LHC
- 6809 • compatibility with synchrotron radiation power

6810 The proposed design is constituted by compact C-Type dipoles, with the C-aperture on the external side
6811 of the ring to possibly allow the use of a vacuum pre-chamber and in any case to avoid the magnet intercepts
6812 the synchrotron radiation. The unusual poles shape allows minimizing the difference of flux lines length
6813 over the horizontal aperture, making magnetic field quality less dependent on the iron characteristics than
6814 in a C-type dipole of conventional shape. The coils are constituted by solid single bars of conductor, which
6815 after insulation are individually slit inside the magnet. The conductor can be in aluminium or in copper
6816 depending from economical reasons coming from a correct balance between investment cost and operation.
6817 The present design is based on an aluminium conductor, which among other has the advantage of making
6818 the magnet lighter than with a copper conductor. The conductor size is sufficiently large to reduce the
6819 dissipated power within levels which can be dealt by ventilation in the LHC tunnel: this is a considerable
6820 advantage in terms of simplicity of magnet manufacture, connections, reliability and of course of avoiding
6821 the installation of a water cooling circuit in the LHC arcs.

6822 Table ?? summarizes the main parameters of the proposed magnet design illustrated in Figure ??.

6823 9.1.5 BINP Model

6824 Two different types of models have been manufactured, both aiming at demonstrating that a cycle-to-cycle
6825 reproducibility of the relatively low injection field (only 127 Gauss at an injection energy of 10 GeV) better
6826 than 0.1 Gauss can be achieved. Both models, pictured in Figure ??, showed a magnetic field reproducibility
6827 at injection field within +/- 0.075 Gauss when cycled between injection and maximum field. To achieve such
6828 results both models make use of the same iron laminations, which are 3408 type silicon steel grain oriented

Parameter	Value	Units
Beam Energy	10-60	GeV
Magnetic Length	5.35	Meters
Magnetic Field	0.0127-0.0763	Tesla
Number of magnets	3080	
Vertical aperture	40	mm
Pole width	150	mm
Number of turns	2	
Current @ 0.763 T	1300	Ampere
Conductor material	copper	
Magnet inductance	0.15	milli-Henry
Magnet resistance	0.16	milli-Ohm
Power @ 60 GeV	270	Watt
Total power consumption @ 60 GeV	0.8	MW
Cooling	air or water	depends on tunnel ventilation

Table 9.4: Main parameters of bending magnets for the RR Option.

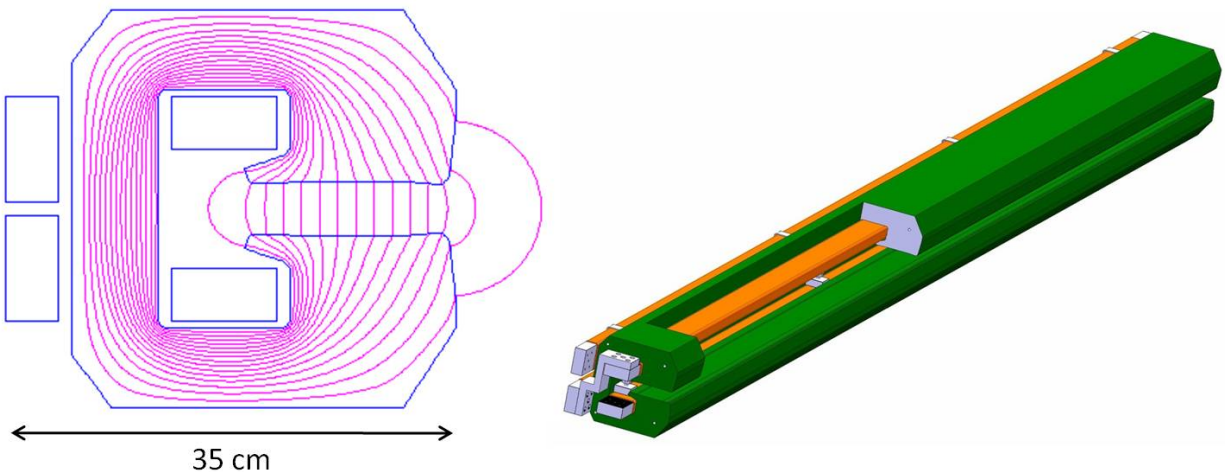


Figure 9.9: Bending magnets for the RR Option

6829 0.35 mm thick. Their coercive force in the direction of the orientation is about 6 A/m, and perpendicular
6830 to the direction of the orientation remains relatively low at about 22 A/m. The C-type model has been
6831 assembled in two variants, with the central iron part with grains oriented vertically and with grain oriented
6832 horizontally (both blocks are as shown in the picture). The relevant magnetic measurements did not show
6833 differences between the two versions.

6834 9.1.6 CERN Model

6835 As a complementary study to the one made by BINP, the CERN model explores the manufacture of lighter
6836 magnets, with the yoke made by interleaved iron and plastic laminations. The magnetic flux produced in the
6837 magnet aperture is concentrated in the iron only, with a thickness ratio between plastic and iron of about

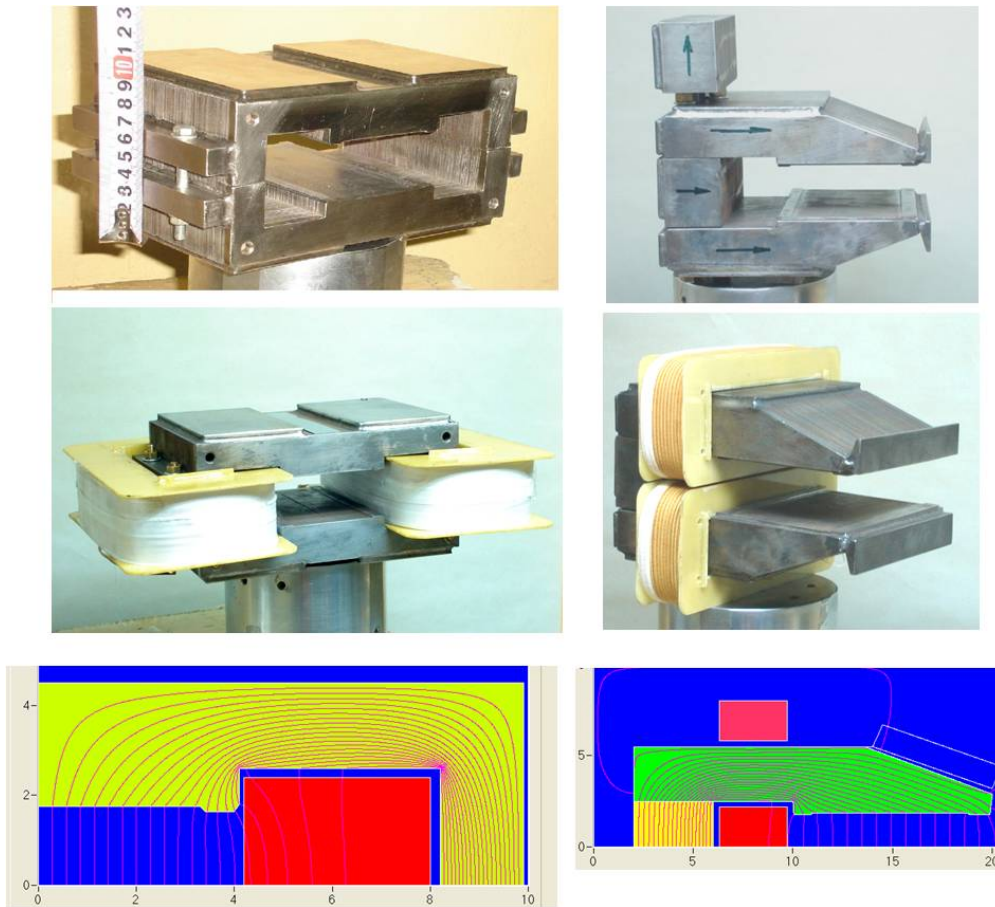


Figure 9.10: H and C-Type model magnets made by BINP

6838 2:1 the magnetic field in the iron is about 3 times that in the magnet gap. In addition to a lighter assembly,
 6839 this solution has the advantage of increasing the magnetic working point of the iron at injection fields, thus
 6840 being less sensitive to the quality of the iron and in particular to the coercive force. To explore the whole
 6841 potential of this solution three different lamination materials have been explored: an expensive NiFe 50 steel
 6842 (H_c 3A/m) which will act as reference, a conventional grain oriented steel with similar characteristics as the
 6843 one used by BINP, and a conventional low carbon steel with H_c 70 A/m. The model cross section reproduces
 6844 the reference one described for the RR dipoles.

6845 9.1.7 Quadrupole and Corrector Magnets

6846 In case of the RR option we need, in the LHC tunnel:

- 6847 • in the arcs, 336 QF each providing 10.28T integrated strength, and 336 QD each providing 8.40T
 6848 integrated strength
- 6849 • in the insertion and by-pass, 97 QF each providing 18T integrated strength, and 97 QD each providing
 6850 12.6T integrated strength

6851 In case of the LR option we need:

- 6852 • in the two 10 GeV linacs, 37+37 quadrupoles each providing 2.5T integrated strength

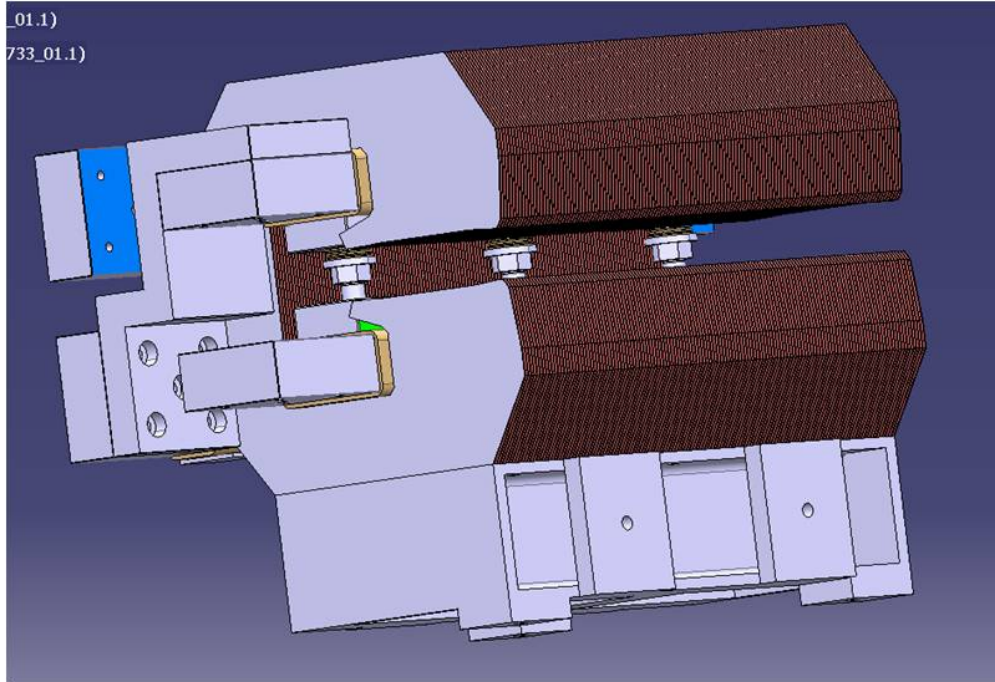


Figure 9.11: 400 mm long RR dipole model with interleaved laminations

- 6853 • again in the two 10 GeV linacs, 37+37 correctors each providing 10mTm integrated strength in both
- 6854 vertical and horizontal direction

- 6855 • in the recirculator arcs 4 different quadrupole types, the Q0, Q1 and Q3 each providing about 35 T
- 6856 integrated strength, and the Q2 each providing about 50T integrated strength

6857 **RR: 336+336 quadrupoles in the arcs**

6858 Considering the integrated strength of QD and QF are not much different, we propose having the same type

6859 of magnets: the relevant parameters are summarized in Table ?? and the cross section is illustrated in Figure

6860 ??.

6861 **RR: 148 + 148 quadrupoles in the insertion and by-pass**

6862 In total 148 QF and 148 QD quadrupoles are needed in the insertion and by-pass. The required integrated

6863 strength is 18T for the QF and 13T for the QD. We propose having the same magnet cross section with two

6864 different length, 1.0 m the QF and 0.7 m the QD, capable of producing a gradient of up to 19 T/m. The

6865 relevant parameters are summarized in table ?? and the cross section is illustrated in Figure ??.

6866 **LR: 37 + 37 quadrupoles for the two 10 GeV Linacs**

6867 The present design solution considers 70 mm aperture radius magnets to be compatible with any possible

6868 aperture requirement. The relevant parameters are summarized in table ?? and the cross section is illustrated

6869 in Figure ??.

Parameter	Value	Units
Beam Energy	10-60	GeV
Magnetic Length	1.0	Meters
Field gradient @ 60 GeV	10.28 (QF) - 8.40 (QD)	T/m
Number of magnets	336 + 336	
Aperture radius	30	mm
Total length	1.2	meters
Weight	700	kg
Number of turns/pole	10	
Current @ 10.28 T/m	390	Ampere
Conductor material	copper	
Current density	4	A/mm ²
Magnet inductance 3	milli-Henry	
Magnet resistance	16	milli-Ohm
Power @ 60 GeV	2500	Watt
Cooling	water	

Table 9.5: Main parameters of arc quadrupole magnets for the RR Option.

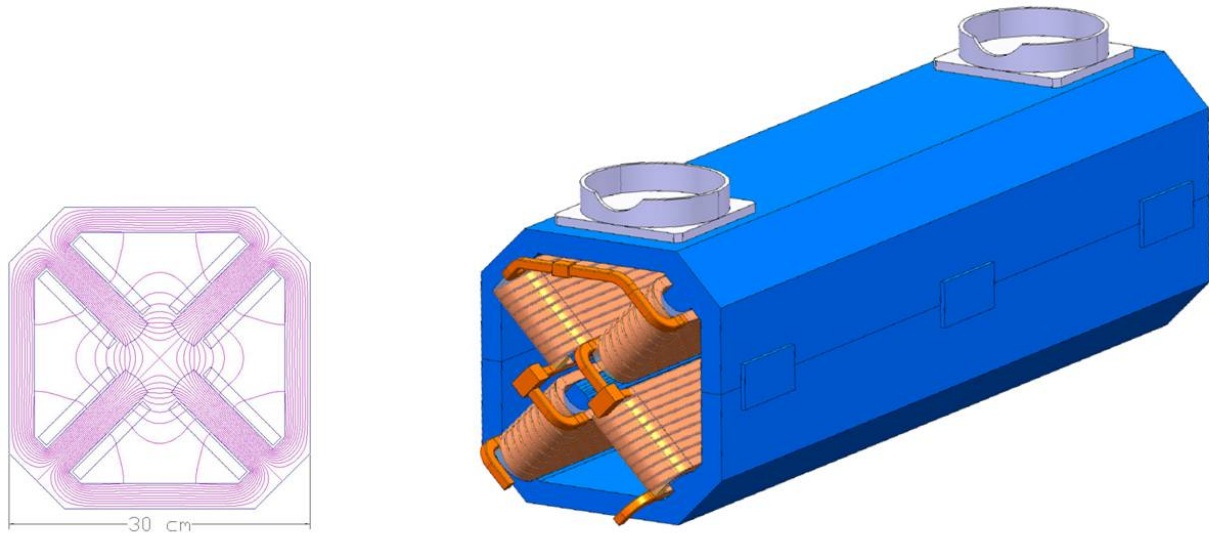


Figure 9.12: Arc quadrupole magnets for the RR Option

6870 **LR: 37 + 37 correctors for the two 10 GeV Linacs**

6871 The combined function correctors shall provide an integrated field of 10 mTm in an aperture of 140 mm.

6872 The relevant parameters are summarized in table ?? and the cross section is illustrated in Figure ??.

Parameter	Value	Units
Beam Energy	10-60	GeV
Magnetic Length (QD/QF)	1.0/0.7	Meters
Field gradient @ 60 GeV	19	T/m
Number of magnets (QD+QF)	148 + 148	
Aperture radius	30	mm
Total length (QD/QF)	1.2/0.9	meters
Weight (QD/QF)	700/500	kg
Number of turns/pole	17	
Current @ 19 T/m	410	Ampere
Conductor material	copper	
Current density	5	A/mm ²
Magnet inductance (QD/QF)	12/9	milli-Henry
Magnet resistance (QD/QF)	40/30	milli-Ohm
Power @ 60 GeV (QD/QF)	7/5	kWatt
Cooling	water	

Table 9.6: Main parameters of insertion and by-pass quadrupole magnets for the RR Option.

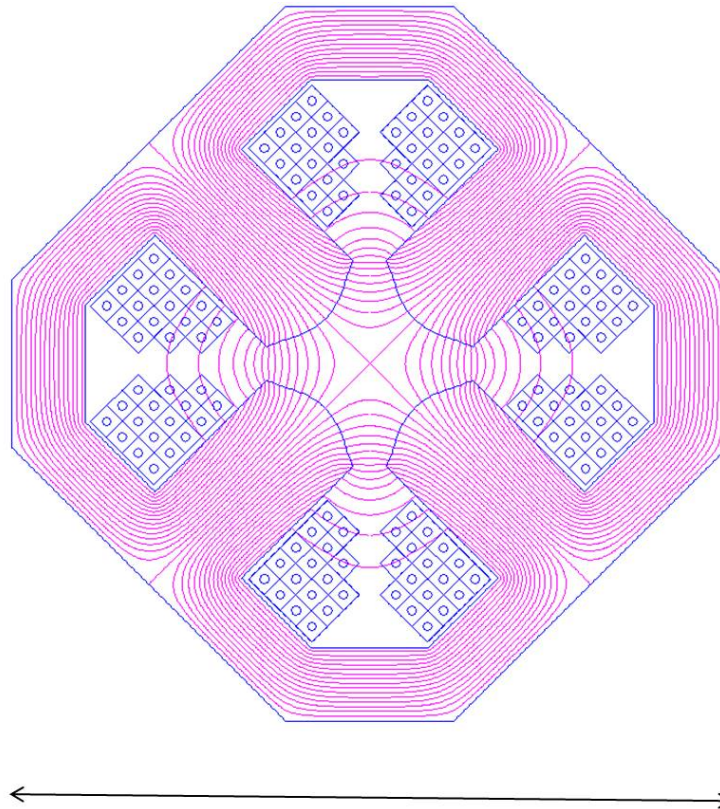


Figure 9.13: Insertion and by-pass quadrupole magnets for the RR Option

Parameter	Value	Units
Magnetic Length	250	mm
Field gradient	10	T/m
Number of magnets	37 + 37	
Aperture radius	70	mm
Weight (QD/QF)	300	kg
Number of turns/pole	44	
Current @ 10 T/m	500	Ampere
Conductor material	copper	
Current density	5	A/mm ²
Magnet inductance	12	milli-Henry
Magnet resistance	24	milli-Ohm
Power @ 500 A	6	kWatt
Cooling	water	

Table 9.7: Main parameters of quadrupoles for the 10 GeV linacs of the LR option

Parameter	Value	Units
Magnetic Length	400	mm
Field induction	25	mT
Number of magnets (QD+QF)	37 + 37	
Free aperture	140 x 140	mm x mm
Yoke length	250	mm
Total length	350	mm
Weight	100	kg
Number of turns/circuit	2x100	
Current	40	Ampere
Conductor material	copper	
Current density	1.5	A/mm ²
Magnet inductance per circuit	10	milli-Henry
Magnet resistance per circuit	0.1	Ohm
Power per circuit	160	Watt
Cooling	air	

Table 9.8: Main parameters of combined function corrector magnets for the LR Option.

6873 **LR: 360 Q0 + 360 Q1+ 360 Q2 + 360 Q3 quadrupoles for the recirculator arcs**

6874 In each of the 6 arcs there are 4 types of quadrupoles, each type in 60 units, making 240 quadrupoles per
6875 arc. The required integrated strength can be met with one type of quadrupole manufactured in two different
6876 length: 1200 mm the Q2 and 900 mm the Q0-Q1-Q3. The quadrupoles of the low energy arcs may use
6877 a smaller conductor or less turns or the same conductor as the higher energy quadrupoles showing then
6878 ecological friendly power consumption. The relevant parameters are summarized in table ?? and the cross
6879 section is illustrated in Figure ??.

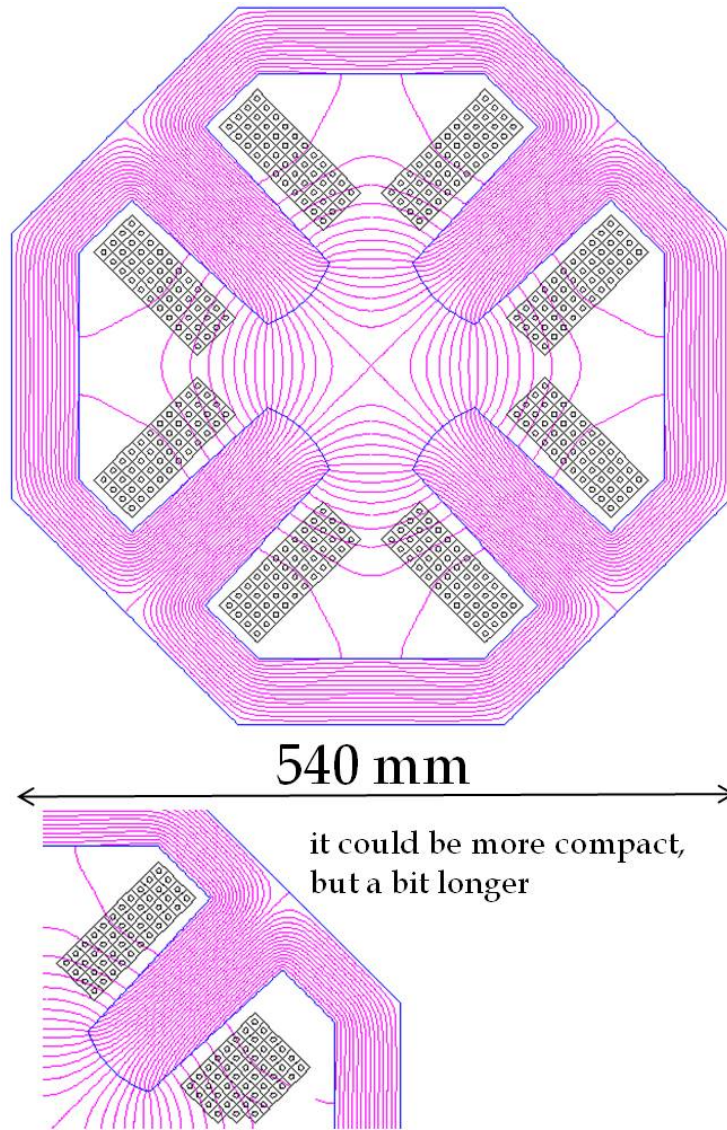


Figure 9.14: Quadrupoles for the 10 GeV linacs of the LR option

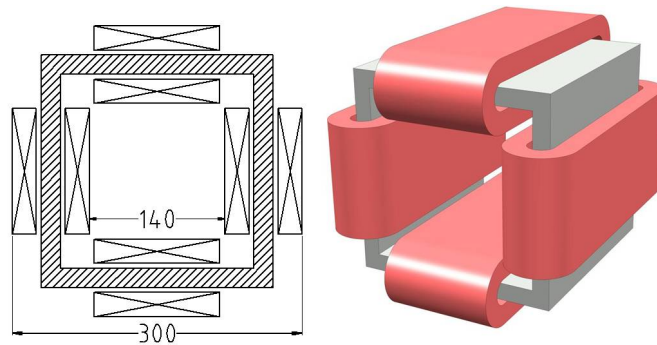


Figure 9.15: Combined function corrector magnets for the LR Option

Parameter	Value	Units
Beam Energy	10-60	GeV
Magnetic Length	0.9/1.2	Meters
Field gradient	41	T/m
Number of magnets (Q0+Q1+Q2+Q3)	1440	
Aperture radius	20	mm
Weight (QD/QF)	550/750	kg
Number of turns/pole	17	
Current @ 41 T/m	410	Ampere
Conductor material	copper	
Current density	5	A/mm ²
Magnet inductance	15/20	milli-Henry
Magnet resistance	30/40	milli-Ohm
Power @ 410 A	5/7	kWatt
Cooling	water	

Table 9.9: Main parameters of quadrupoles for the recirculators of the LR option

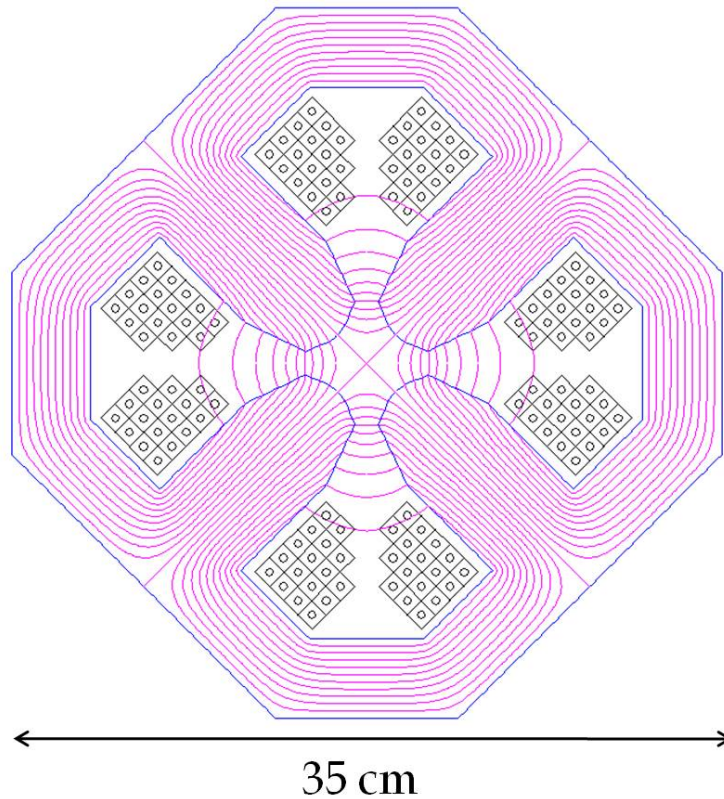


Figure 9.16: Quadrupoles for the recirculators of the LR option

9.2 Ring-Ring RF Design

9.2.1 Design Parameters

The RF system parameters for the e-ring are listed in Table ?? . For a beam energy of 60 GeV the synchrotron losses are 437 MeV/turn. With a nominal beam current of 100 mA the rather significant amount power of 47.3 MW is lost due to synchrotron radiation. For the voltages needed superconducting RF is the only choice.

9.2.2 Cavities and klystrons

Cavity design

The most important issue determining the RF design is not so much in achieving high accelerating gradient but rather the need to handle large powers through the power coupler. The choice of RF frequency is based on relatively compact cavities which are able to handle the relatively high beam intensities and allowing fitting of power couplers of sufficient dimensions to handle the RF power. A frequency in the range 600 to 800 MHz is the most appropriate. Cavities of frequency of 704 MHz are currently being developed at CERN in the context of the study of a Superconducting Proton Linac (SPL) [?] [?] [?]. The same frequency is also used at BNL for ERL cavities for the RHIC upgrade project [?]. Both cavities are 5-cell and can achieve gradients greater than 20 MV/m. For the present study we take an RF frequency of 721.42 MHz, which is compatible with LHC \tilde{O} s minimum 25 ns bunch spacing. An RF voltage of 500 MV gives a quantum lifetime of 50 hours; this is taken as the minimum operating voltage. An RF voltage of 560 MV gives infinite quantum lifetime and a margin of 60 MV which permits feedback system voltage excursions and provides tolerance to temporary failure of part of the RF system without beam loss.

5-cell cavities would require too much RF power transferred through the power coupler, therefore we use 2-cell cavities here in keeping the cell shape. Then with a total of 112 cavities, the power per cavity supplied to the beam to compensate the synchrotron radiation losses is 390 kW. This level of power handling is only just reached for the power couplers of the larger 400 MHz cavities of the LHC. It is therefore proposed to use two power couplers per cavity and split the power. In terms of voltage, only 5 MV per cavity is required to make 560 MV, hence it is sufficient to use cavities with two cells instead of five. The resulting cavity active length is 0.42 m and the gradient is a conservative 11.9 MV/m. Under these conditions the matched loaded Q is $2.8 \cdot 10^5$. Over-coupling by 50 % to $1.9 \cdot 10^5$ provides a stability margin and incurs relatively small power overhead. Under this condition the average forward power through the coupler is just under 200 kW. This nevertheless remains challenging for the design of power coupler.

Cryomodule layout

With 8 cavities per cryomodule there are a total of 14 cryomodules. The estimated cryomodule length, scaled from the 8 5-cell cavity of SPL to two cells per cavity is 10 m. There are 8 double cell cavities in 14 10m cryomodules, the total RF cryomodule length is therefore 140 m, but space must be allowed for quadrupoles, vacuum equipment and beam instrumentation. A total of 208 m is available in the by-passes: 124 m at CMS and 2 x 42m at ATLAS. Eight cryomodules can therefore be installed in the CMS bypass and six, three on each side, in the ATLAS by-passes. The distance between the modules can be taken as 3 m to allow space for the other equipment. The positioning of the RF tunnels in the CMS and ATLAS bypasses is shown in Figure ??.

RF Power System

The configuration for powering of one eight cavity cryomodule is shown in figure ?? . Each klystron feeds two cavities with power being split near the cavity to its two couplers. Taking two cavities per klystron with an estimated 7 % losses in the waveguide system gives a mean required klystron output power of 870 kW. A 15 % margin for the feedbacks gives a klystron rated power of 1 MW. The total number of klystrons is 56,

Energy	GeV	60
Beam current	mA	100
Synchrotron losses	MeV/turn	437
Power loss to synchrotron radiation	MW	43.70
Bunch frequency (25 ns spacing)	MHz	40.08
Multiplying factor		18
RF frequency	MHz	721.42
Harmonic number		64152
RF Voltage for 50 hour quantum lifetime	MV	500.00
Nominal RF voltage (MV)	MV	560.00
Synchronous phase angle	degrees	129
Quantum lifetime at nominal RF voltage	hrs	infinite
Number of cavities		112
Number of 8-cavity cryomodules		14
Power couplers per cavity		2
Average RF power to beam per power coupler	kW	195
Voltage per cavity at nominal voltage	MV	5.00
Cells per cavity		2
Cavity active length	m	0.42
Cavity R/Q		114
Cavity Gradient	MV/m	11.90
Cavity loaded Q (Matched)		$2.8 \cdot 10^5$
Cavity forward power (nom. current, nom. voltage) for matched condition	kW	390
Nominal cavity loaded Q (matched for 50 % more beam)		$1.9 \cdot 10^5$
Cavity forward power (nominal current, voltage & loaded Q)	kW	406
Forward power per coupler	kW	203
Number of cavities per klystron		2
Waveguide losses	%	7
Klystron output power	kW	870
Feedbacks & detuning power margins	%	15
Klystron rated power	kW	1000
Total number of klystrons		56
Total average operating klystron RF power	MW	49
DC power to klystrons assuming 65% klystron efficiency	%	75
Grid power for RF, assuming 95% efficiency of power converters	MW	79

Table 9.10: RF system parameters for the electron ring.

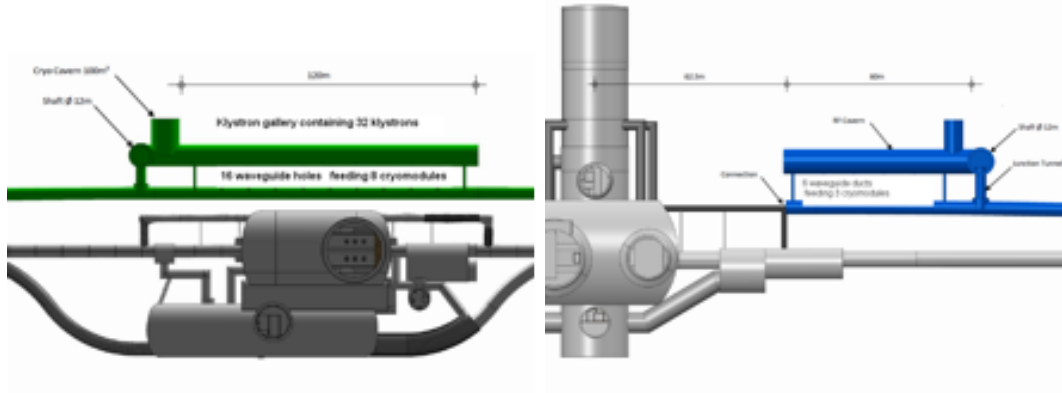


Figure 9.17: RF tunnel Layouts at CMS and ATLAS bypasses. Note only the right hand side at ATLAS shown.

6924 delivering an average total RF power of 49 MW. Taking 65 % klystron efficiency and 95 % efficiency in the
 6925 power converters gives roughly 79 MW grid power needed for the RF power system.

6926 RF Power System Layout

6927 The klystrons are installed in the additional tunnels parallel to the by-passes. An estimated surface area of
 6928 100m² is needed for the two klystrons, circulators, HV equipment and Low Level RF and controls racks for
 6929 each 8 cavity module in adjacent RF gallery. This defines the tunnel width over the 13 m module interval
 6930 (length + spacing) to be 8 m. Waveguide ducts are needed between the by-passes and the RF tunnels. With
 6931 one waveguide per klystron into the tunnel, and two waveguides per duct, there are 16 ducts in the CMS
 6932 tunnels, spaced roughly 6.5 m apart. At ATLAS there would be six ducts on either side with the same
 6933 spacing. The required diameter of the duct tunnel is 90cm.

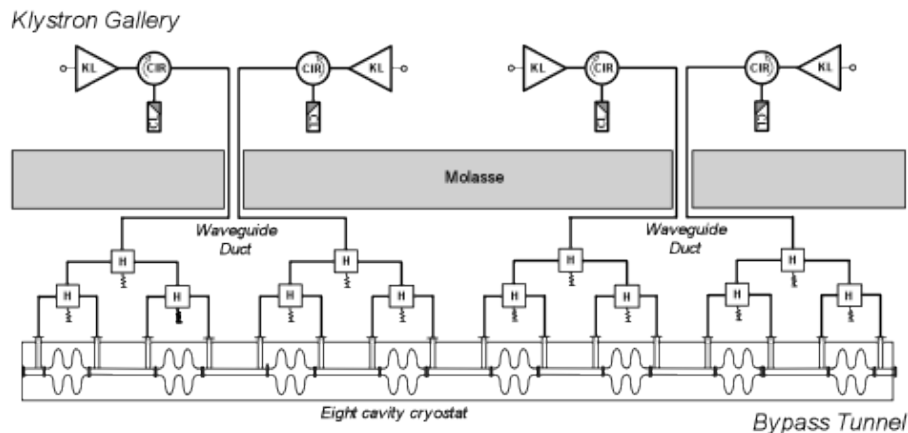


Figure 9.18: Layouts of RF power equipment in bypass and in RF gallery for one cryomodule.

6934 Surface Installations

6935 One HV Power Converter rated at 6 MVA is needed per 4 klystrons. These are housed in surface buildings:
 6936 eight converters at CMS, and six at ATLAS.

Arc	Arc energy [GeV]	Energy loss per arc passage [MeV]	Number of passages	Total energy loss per arc [MeV]
6	60	570.0	1	570.0
5	50	275.0	2	550.0
4	40	115.0	2	230.0
3	30	35.0	2	70.0
2	20	7.0	2	14.0
1	10	0.4	2	0.8
				1434.8

Table 9.11: Energy losses in the arcs on a half circle of 1 km radius

6937 Conclusions

6938 721.4 MHz RF systems can be just fitted in the two bypasses nearest ATLAS and CMS. Detailed studies need
6939 to be done on the optimization of the cavity geometry for the high beam current and ensuring acceptable
6940 transverse impedance. The RF power system is large. Further work is needed on integration to exactly define
6941 tunnel and cavity cavern layouts and quantify the space requirements. Phased installation with gradual
6942 energy build-up, as was done for LEP, is an interesting possibility. The power needed for RF is 79 MW. To
6943 this must be added power for RF controls, for power converters, cryogenics and all other machine equipment.

6944 9.3 Linac-Ring RF Design

6945 9.3.1 Design Parameters

6946 The ERL design [?] [?] [?] is based on two 10 GeV linacs, with 0.3 GeV injection and 6 linac passes to reach
6947 60 GeV. This is shown in Figure ??.

6948 The overall parameters are given in table [Frank]. With a beam current of 6.6 mA produced, there are
6949 currents of nearly 20 mA in both directions in the linacs. Significant power, greater than the injection energy,
6950 is lost in the passages through the arcs due to synchrotron radiation as shown in Table ??.

6951 The energy loss in the arcs can be compensated by independent RF systems operating at twice the normal
6952 RF frequency. As proposed by [?] it could be envisaged to let the main linacs replace the energy lost to
6953 synchrotron radiation. However, this scheme significantly restricts operational freedom and is not tested yet.
6954 Therefore we keep it only as one possible option. For the present report both options are presented - Case 1
6955 for additional RF systems in the arcs to compensate synchrotron losses and Case 2 for this energy supplied
6956 by the linacs.

6957 Linac design

6958 High accelerating gradient is needed. First tests on cavities at similar frequency at BNL have already reached
6959 20 MV at Q_0 of $1 \cdot 10^{10}$. Improved cavity design and careful cavity processing should allow meeting the
6960 specifications. The optimum number of cavities and the gradient is an overall compromise taking into account
6961 cost, cryogenics consumption and operational reliability. The RF power system needs to compensate energy
6962 loss and non-ideal energy recovery due to beam losses, phasing errors, transients, ponderomotive effects and
6963 noise. It also needs to allow testing and processing of the cavities at full gradient without circulating beam.
6964 The main RF parameters are given in Table ??, for the two cases described above.

6965 The linac RF design is based on 5-cell cavities operating at 721.42 MHz, this frequency being compatible
6966 with 25 ns bunch spacing in LHC, as for the electron ring option. A gradient of 20 MV/m can be taken.

Parameter	Unit	Separate Arc RF	No Arc RF
Beam energy	GeV	60.0	60.0
Injection energy	GeV	0.3	0.3
Average beam current out	mA	6.6	6.6
Av. accelerated beam current in linacs	mA	19.8	19.8
Required total voltage in both linacs	GV	20.0	20.0
Energy recovery efficiency	%	96	96
Total power needed to compensate recovery losses	MW	15.8	15.8
Total energy loss per cycle in arcs	MeV	1434.8	1434.8
Total power needed to compensate arc losses	MW	0.0	9.5
RF frequency	MHz	721.42	721.42
Gradient	MV/m	20	20
Cells per cavity		5	5
Cavity length	m	1.06	1.06
Cavity voltage	MV	21.2	21.2
Number of cavities		944	944
Power to compensate recovery losses per cavity	kW	16.8	16.8
Power to compensate synch. rad. losses per cavity	kW	0.0	10.0
Cavity R/Q	circuit Ω	285	285
Cavity unloaded Q [Q_o]	10^{10}	2.5	2.5
Loaded Q [Q_{ext}]	10^6	47	29
Cavity forward power	kW	16.8	26.8
Cavity forward power - no beam		4.2	6.7
Number of cavities per solid state amp.		1	1
Transmission losses	%	7	7
Amplifier output power per cavity	kW	17.9	28.7
Feedbacks power margin	%	15	15
Amplifier rated power	kW	21	33
Total number of amplifiers		944	944
Total average amplifier output power	MW	17	27
Assumed overall conversion efficiency grid to amplifier RF output	%	70	70
Grid power for linacs RF	MW	24	39

Table 9.12: Linac RF parameters.

Parameter	Unit	Value
Cavities per cryomodule		8
Number of cavities		472
Number of cryomodules per linac		59
Cryomodule length	m	14
Spacing of cryomodules	m	2
Linac length	m	944

Table 9.13: ERL cryomodule numbers, length and spacing.

6967 This is a conservative estimate based on SPL type cavities presently being developed, with a design aim of
6968 25 MV/m. The unloaded Q (Q_0) is taken as $2.5 \cdot 10^{10}$. This is presently a challenging figure, but recent
6969 tests on cavities at this frequency for e-RHIC have been very encouraging. With an active cavity length of
6970 1.06 m the voltage is 21.2 MV per cavity. This requires 944 cavities in total, or 472 cavities per linac. The
6971 cavity external Q (Q_{ext}) is derived from optimum coupling to the required beam power to compensate the
6972 4 energy losses in Case 1 and this plus the synchrotron radiation losses in the arcs in Case 2. It should be
6973 noted that the 300 MeV injection linac, with nearly 2 MW beam power will also take grid power of between
6974 3 and 4 MW.

6975 9.3.2 Layout and RF powering

6976 Cryomodule and RF power system layout

6977 With eight cavities in a cryomodule of 14 m length, there are 59 cryomodules per linac. Allowing a further
6978 2 m per cryomodule for other linac equipment the total linac length is 944 m. This is summarized in table
6979 ??.

6980 RF power system

6981 Assuming optimum coupling the forward power per cavity is approximately 17.9 kW and 28.7 kW for Cases
6982 1 and 2 respectively. The available power per cavity must be somewhat higher to allow margin for operation
6983 of RF the feedback systems; i.e. 21 kW and 33 kW per cavity. These levels can certainly be achieved with
6984 solid state amplifiers, avoiding the need for high voltage power supplies and associated protection equipment.
6985 The grid to RF conversion efficiency is also somewhat higher; 70 % can be taken. The total supplied average
6986 RF powers are approximately 17 MW and 27 MW for the two cases and the grid power required for powering
6987 of the linacs is 24 MW and 39 MW respectively.

6988 RF Power system layout

6989 The RF amplifiers and RF feedback and controls racks are housed in a separate parallel powering gallery.
6990 There is one RF amplifier per cavity, the power being fed by WR1150 standard waveguides, each 11.5 inches
6991 by 5.75 inches (30 cm by 15 cm). The number of holes between the powering and linac tunnels can be limited
6992 to one per four cavities, i.e. two per cryomodule, spaced 8 m apart giving 118 holes per linac. The diameter
6993 is 90cm. The diameters could be reduced if half height waveguides or coax lines are used.

6994 9.3.3 Arc RF systems

6995 Table ?? shows the synchrotron radiation losses in the arcs; they are negligible in the 10 GeV arc. In the
6996 20, 30, 40 and 50 GeV arc both the accelerated and decelerated beams pass the same arc RF system with
6997 180° phase shift at the basic frequency of 721.42 MHz; hence to accelerate both beams, the arc RF system

Parameter	Unit	Value
Total energy loss in 20-60GeV arcs	MeV	1434
Power loss in 20-60GeV arcs	MW	9.5
Arc RF frequency	MHz	1442/721
Number of cavities		49/28
Number of klystrons		25/7
Total average supplied klystron RF power	MW	10.8
Assumed overall conversion efficiency - grid to klystrons RF out	%	60
Grid power for arc RF systems	MW	18

Table 9.14: Arc RF systems overall parameters.

6998 is operated at twice the frequency, i.e. at 1442.82 MHz. The 60 GeV arc carries only the decelerated beam
6999 and there one can use the linac RF cavities at 721.42 MHz. However, since here the required power per
7000 cavity is much larger the solid state amplifiers of the main linac cannot be used but a klystron or IOT must
7001 be applied. Overall parameters for these RF systems are given in Table ??.

7002 The arc systems provide very different voltages. Parameters for the individual systems are given in table
7003 ??. Use of cavities and cryostats scaled to those in the linacs is assumed; however short cryostats containing
7004 four cavities could be used in the 20 and 40 GeV arc systems. Powering would be by klystrons, a total of 36
7005 rated at a maximum of 360 kW, with one klystron supplying up to four cavities.

7006 It can be noted that the overall grid power is less if the arc energy recovery is supplied by the main linacs.
7007 (39 MW compared to 24 plus 18 = 42 MW). This is partly due to the assumed higher efficiency of the solid
7008 state amplifiers in the linacs compared to the klystrons in the arc RF systems.

7009 9.4 Crab crossing for the LHeC

7010 Due to the very high electron beam energies for the LHeC, the required RF power and the interaction
7011 region design due to synchrotron radiation are challenging. The IR layout for the RR option consists
7012 of a crossing angle to mitigate parasitic interactions and allows for a simple scheme to accomodate the
7013 synchrotron radiation fan. A crab crossing scheme for the proton beam is highly desirable to recover the
7014 geometric luminosity loss due to this crossing angle. The complex interaction region in the LHeC and the
7015 issues associated with the sychrotron radiation can be relaxed with an implementation of crab crossing. In
7016 addition to the luminosity gain, the issues associated with the synchrotron radiation can be relaxed with an
7017 implementation of crab crossing near the IR. It is also a natural knob to regulate the beam-beam parameter
7018 if desired. Although the linac-ring option plans to employ separation dipoles and mirrors for sychrotron
7019 radiation, crab crossing can prove to be a simpler option if the technology is viable.

7020 9.4.1 Luminosity Reduction

7021 In the nominal LHC with proton-proton collision, the two beams share a common vaccum chamber for
7022 approximately a 100m from the IP. Therefore, a crossing angle is required in the IRs to avoid parasitic inter-
7023 actions. Consequently, the luminosity is reduced by a geometrical reduction factor which can be expressed
7024 as

$$R = \frac{1}{\sqrt{1 - \Phi^2}} \quad (9.1)$$

7025 where $\Phi = \sqrt{\theta\sigma_z/2\sigma_x}$ is the Piwinski parameter, which is propotional to ratio of the longitudinal and
7026 transverse beam sizes in the plane of the crossing.

Parameter	Unit	Arc 2	Arc 3	Arc 4	Arc 5	Arc 6	Totals
Arc energy	GeV	20	30	40	50	60	
Energy lost per arc passage	MeV	7	35	115	275	570	
Number of passes		2	2	2	2	1	
Total energy loss in arc	MeV	14	70	230	550	570	1434
Power loss in arc	MW	0.1	0.5	1.5	3.6	3.8	9.5
RF frequency 1442 MHz	MHz	x	x	x	x		
RF frequency 721 MHz	MHz					x	
Cavities at 1442 MHz		1	4	12	32		49
Cavities at 721 MHz						28	28
Required voltage/cavity	MV	7.2	9.1	9.9	8.9	21.1	
RF Power/cavity	kW	92	116	127	113	134	
Nominal RF power/cavity	kW	96	120	132	118	140	
Klystron output power/cavity	kW	103	129	141	126	150	
Kl. rated power/cavity	kW	120	150	170	150	180	
Cavities/klystron		1	2	2	2	4	
Klystron rated power	kW	120	300	340	300	720	
Klystrons at 1442 MHz		1	2	6	16		25
Klystrons at 721 MHz						7	7
Total average supplied klystron RF power	MW	0.1	0.5	1.7	4.0	4.2	10.5
Assumed overall conversion efficiency grid to klystrons total RF power	%	60	60	60	60	60	
Grid power arc RF systems	MW	0.2	0.9	2.8	6.7	7.0	18

Table 9.15: Parameters of the individual arc RF systems.

7027 With reducing β^* for the upgrade and a constant beam-to-beam separation in the IRs ($\sim 10\sigma$), the
 7028 luminosity reduction factor becomes significant. To compensate this crossing angle, a crab crossing scheme
 7029 is proposed and R&D is moving rapidly to realize the technology [?, ?]. In addition to crossing angle
 7030 compensation, it allows a natural knob to regulate the beam-beam parameter which can valuable while
 7031 operating close to the beam-beam limit.

7032 For the electron-proton collisions, the Piwinski parameter can be redefined as

$$\Phi_p = \frac{\theta_c}{2\sqrt{2}\sigma_x^*} \sqrt{\sigma_{z,p}^2 + \sigma_{z,e}^2} \quad (9.2)$$

7033 where $\sigma_{z,p}$ and $\sigma_{z,e}$ are the proton and electron bunch lengths. Table ?? lists the relevant parameters of the
 crossing schemes in the LHeC as compared to some other machines.

Table 9.16: Relevant parameters of the crossing schemes in the LHeC compared to LHC, KEK-B and eRHIC.
 Note † corresponds to electrons and * corresponds vertical plane.

	KEK-B	LHC		LHeC		eRHIC
		Nominal	Upgrade	RR	LR	
θ_c [mrad]	22.0	0.285	0.4-0.6	1.0	0.0 (4.0)	0.0 (5.0)
σ_z [cm]	0.7	7.55		7.55 (0.7†)		20/1.2†
σ_x^* [μm]	103	16.6	11.2	30 (15.8*)	-	32
Φ	0.75	0.64	1-1.4	0.9 (1.6*)	0.0	0.0 (11.0)

7034

7035 9.4.2 Crossing Schemes

7036 Since the bunch length of the electrons are significantly smaller (at least factor 10) than that of the protons,
 7037 the geometrical overlap due to crossing angle is mainly dominated by the angle of the proton bunches. Four
 7038 different cases (see Fig. ??) were simulated to determine the luminosity gain in the different cases with crab
 cavities and comparing it to the nominal case (see Table ??).

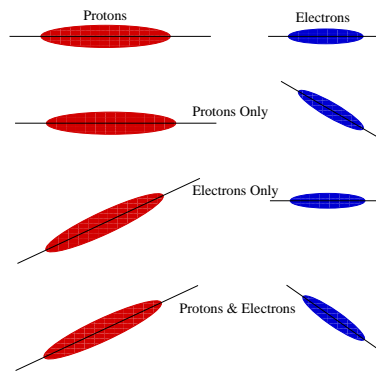


Figure 9.19: Schematic of different crossing schemes using crab cavities on either proton or electron beams as compared to the head-on collision.

7039

7040 The luminosity gains strongly depend on the choice of RF frequency as the reduction factor due to the
 7041 RF curvature at frequencies of interest (0.4-0.8 GHz) is non-negligible.

Table 9.17: Luminosity gains computed for different crossing schemes with crab cavities and a crossing angle of 1 mrad.

Scenario	L/L ₀	
	400 MHz	800 MHz
X-Angle (1 mrad)	1.0	
Uncross both e^- and p^+	1.88%	1.48
Uncross only e^-	1.007	
Uncross only p^+	1.88	1.48

9.4.3 RF Technology

The cavity voltage required for can be calculated using

$$V_{crab} = \frac{2cE_0 \tan(\theta_c/2) \sin(\mu_x/2)}{\omega_{RF} \sqrt{\beta_{crab} \beta^*} \cos(\psi_{cc \rightarrow ip}^x - \mu_x/2)} \quad (9.3)$$

where E_0 is the beam energy, ω_{RF} is the RF frequency of the cavity, β_{crab} and β^* are the beta-functions at the cavity and the IP respectively, $\psi_{cc \rightarrow ip}^x$ is the phase advance from the cavity to the IP and μ_x is the betatron tune. The nominal scenarios for both proton-proton and electron-proton IRs are anticipated to have local crab crossing with two cavities per beam to create a local crab-bump within the IR. Since the β -functions are typically large in the location of the crab cavities, a voltage of approximately 20 MV should suffice for crossing angles of approximately 1-2 mrad. The exact voltage will depend on the final interaction region optics of the both the proton and the electron beams.

To accomodate the crab cavities within the IR region, deflecting structures with a compact footprint are required. Conventional pill-box type elliptical cavities at frequencies of 400 MHz are too large to fit within the LHC interection region constraints. The effort to compress the cavity footprint recently resulted in several TEM type deflecting mode geometries [?]. Apart from being significantly smaller than its elliptical counterpart, the deflecting mode is the primary mode thus giving paving way to a new class of cavities at lower frequencies (400 MHz) which is preferred from the RF curvature point of view

Demonstration of novel RF concepts providing high kick gradients and robust operation within the LHC constraints are mandatory to realize the benefits of crab crossing. R&D on novel concepts are already underway for the LHC upgrade. The issues of impedance, collimation and machine protection are similar to that of the implementation of the proton-proton IRs.

9.5 Vacuum

9.5.1 Vacuum requirements

In particle accelerators, beams are travelling under vacuum to reduce beam-gas interactions i.e. the scattering of beam particles on the molecules of the residual gas. The beam-gas interaction is dominated by the bremsstrahlung on the nuclei of gas molecules therefore depends on partial pressure, weight of the gas species and radiation length [g/cm²]. In presence of a photon-stimulated desorption, the residual gas is dominated by hydrogen (75%) followed by CO/CO₂ (24%) and 1% CH₄. Argon normally represents less than 1% of the residual gas if welding best practice for UHV applications is applied. To be noted that Argon is 67 times more harmful than hydrogen (H₂), CO₂, CO and N₂ are about 30 times worst and is 10 times worst.

The beam-gas interactions are responsible for machine performance limitations such as reduction of beam lifetime (nuclear scattering), machine luminosity (multiple coulomb scattering), intensity limitation by pressure instabilities (ionisation) and for positive beams only, electron (ionisation) induced instabilities

7074 (beam blow up). The heat load induced by scatted protons and ions can also be an issue for the cryomagnets
 7075 since local heat loads can lead to a magnet quench i.e. a transition from the superconducting to the normal
 7076 state. The heavy gases are the most dangerous because of their higher ionisation cross-sections. In the case
 7077 of the LHeC, this limitation exists only in the experimental areas where the two beams travel in the same
 7078 beampipe. The beam-gas interactions can also increase the background to the detectors in the experimental
 7079 areas (non-captured particles or nuclear cascade generated by the lost particles upstream the detectors)
 7080 and the radiation dose rates in the accelerator tunnels. Thus, leading to material activation, dose rates to
 7081 intervention crews, premature degradation of tunnel infrastructures like cables and electronics and finally
 7082 higher probability of electronic single events induced by neutrons which can destroy the electronics in the
 7083 tunnel but also in the service galleries.

7084 The design of the vacuum system is also driven by severe additional constraints which have to be consid-
 7085 ered at the design stage since retrofitting mitigation solutions is often impossible or very expensive. Among
 7086 them, the vacuum system has to be designed to minimise beam impedance and higher order modes (HOM)
 7087 generation while optimising beam aperture in particular in the magnets. It has to provide also enough ports
 7088 for the pumps and vacuum diagnostics. For accelerators with cryogenic magnets, the beampipe has to be
 7089 designed to intercept heat loads induced by synchrotron radiation, energy loss by nuclear scattering, image
 7090 currents, energy dissipated during the development of electron clouds, the later building up only in presence
 7091 of positively charged beams.

7092 The integration of all these constraints often lead to a compromise in performances and in the case of
 7093 the LHeC, the compromise will differ between the Linac-Ring and the Ring-Ring options.

7094 9.5.2 Synchrotron radiation

7095 The presence of a strong synchrotron radiation has two major implications for the vacuum system: it has to
 7096 be designed to operate under the strong photon-induced stimulated desorption while being compatible with
 7097 the significant heat loads onto the beampipes. In the common beampipe, the photo-electrons generated by
 7098 the synchrotron radiation will dramatically enhanced the electron cloud build-up and mitigation solutions
 7099 shall be included at the design stage.

7100 Synchrotron radiation power

7101 The synchrotron radiation power is an issue for the heat load deposited on the beampipes and for its
 7102 evacuation and will be the driving factor for the mechanical engineering of the beampipes. Indeed, the
 7103 heated surfaces will have a higher outgassing rates, the increase being exponentially dependent with the
 7104 surface temperature (factor 10 for a $\Delta T = 50^\circ\text{C}$ increase). The synchrotron radiation power can be calculated
 7105 with equation ???. Since scaling linearly with the beam intensity, I , with the power of 4 for energy, E , and
 7106 inversely to power of 2 of the bending radius, the synchrotron radiation power in the Ring-Ring option is
 7107 expected to be 45 times higher than LEP and locally at the by-passes, the power can be about 180 times
 7108 higher. To be compared with the factor 10 expected in the bending and injection sections of the Linac-Ring
 7109 option.

$$7100 P[\text{W}/\text{m}] = 1.24 \times 10^3 \frac{E^4 I}{\rho^2} \quad (9.4)$$

7110 Photon-induced desorption

7111 The desorption rate depends on critical energy of the synchrotron light, ϵ_c , the energy which divides in two
 7112 the emitted power. For most materials, the desorption rates vary quasi linearly with the critical energy
 7113 (equation ??).

$$7110 \epsilon_c(\text{eV}) = \frac{3 \cdot 10^{-7}}{R} \left(\frac{E_B}{E_0} \right)^3 \quad (9.5)$$

7114
7115
7116
7117
7118
7119

$E_0 = 5 \cdot 10^{-4}$ GeV for electrons, E_B is the energy of the beam and R the bending radius.

For the LHeC, the beam energies will be equivalent to the LEP at start. Then, a similar value of the critical energy can be assumed allowing the comparison with LEP pressure observations. Figure ?? shows typical photo-desorption yields measured on copper and stainless steel samples. But the beam intensities being by far larger, the linear photon flux which scales linearly (equation 3) with energy and intensity and inversely with bending radius will increase significantly.

$$\Gamma[\text{photons/s/m}] = 7 \times 10^{19} \frac{EI}{\rho} \quad (9.6)$$

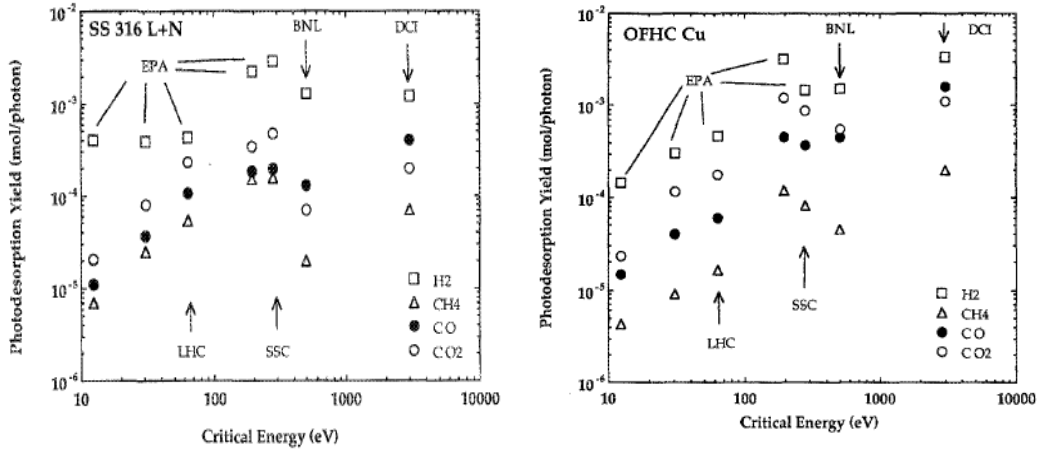


Figure 9.20: Photodesorption yields measured on copper and stainless steel surfaces. To be noted that the desorption yields of methane, η_{CH_4} , is 50 times lower than η_{H_2} .

7120
7121
7122
7123
7124
7125

For the Ring-Ring option (bending sections and by-passes), the linear photon flux is expected to be 45 times larger than in LEP, to be compared to the factor 5 expected for the Linac-Ring option.

The photon stimulated pressure rise, ΔP , depends linearly on the critical energy, on the beam energy and beam intensity as shown by equation ???. The temperature affecting the dependence of the desorption yield (equation ?? and ??), η , to the critical energy, ϵ_c the pressure rises will differ between surfaces at ambient temperature (equation ??) and at cryogenic temperature (equation ??).

$$\Delta P \propto \eta(\epsilon_c) EI \quad (9.7)$$

$$\text{at room temperature : } \eta \propto \epsilon_c \text{ and } \epsilon_c \propto E^3 \text{ such that } \Delta P \propto E^4 I \quad (9.8)$$

$$\text{at cryogenic temperature : } \eta \propto \epsilon_c^{2/3} \text{ and } \epsilon_c \propto E^3 \text{ such that } \Delta P \propto E^3 I \quad (9.9)$$

7126
7127

Therefore, the photon stimulated pressure rise is expected to be 45 times higher than LEP for the Ring-Ring option, to be compared with the factor 30 for the Linac-Ring option.

7128 Vacuum cleaning and beam scrubbing

7129
7130
7131

The dynamic pressure i.e. the pressure while operating the accelerator with beams will be dominated by the beam-induced dynamic effects like stimulated desorption due to beam losses or synchrotron radiations or by electron stimulated desorption in case an electron cloud is building-up.

7132
7133

In presence of synchrotron radiation, the vacuum cleaning process which characterises the reduction of the desorption yields (η) of a surface resulting from the bombardment of the surface by electrons, photons

7134 or ions, significantly decreases the induced gas loads (3 – 4 orders of magnitude observed in LEP) improving
 7135 the dynamic pressure at constant pumping speed. This results in a progressive increase of the beam lifetime.

7136 In presence of an electron cloud, the beam scrubbing which characterises the reduction of the secondary
 7137 electron yield (SEY, δ) of a surface resulting from the bombardment of the surface by electrons, photons or
 7138 ions, significantly decreases the induced gas loads (2 – 3 orders of magnitude observed in SPS) improving
 7139 the dynamic pressure at constant pumping speed. Similarly to what happens with the vacuum cleaning, this
 7140 results also in a progressive increase of the beam lifetime.

7141 By default and mainly driven by costs and integration issues, the vacuum system of an accelerator
 7142 dominated by beam-induced dynamic effects is never designed to provide the nominal performances as from
 7143 “day 1”. Indeed, vacuum cleaning and beam scrubbing are assumed to improve the beampipe surface
 7144 characteristics while the beam intensity and beam energy are progressively increased during the first years
 7145 of operation.

7146 This implies accepting a shorter beam lifetime or reduced beam current during the initial phase; about
 7147 500 h of operation with beams were required for LEP to achieve the nominal performances. New technical
 7148 developments such as Non-Evaporable Coatings (NEG) shall be considered since significantly decreasing the
 7149 time required to achieve the nominal performances (Figures ?? and ??).

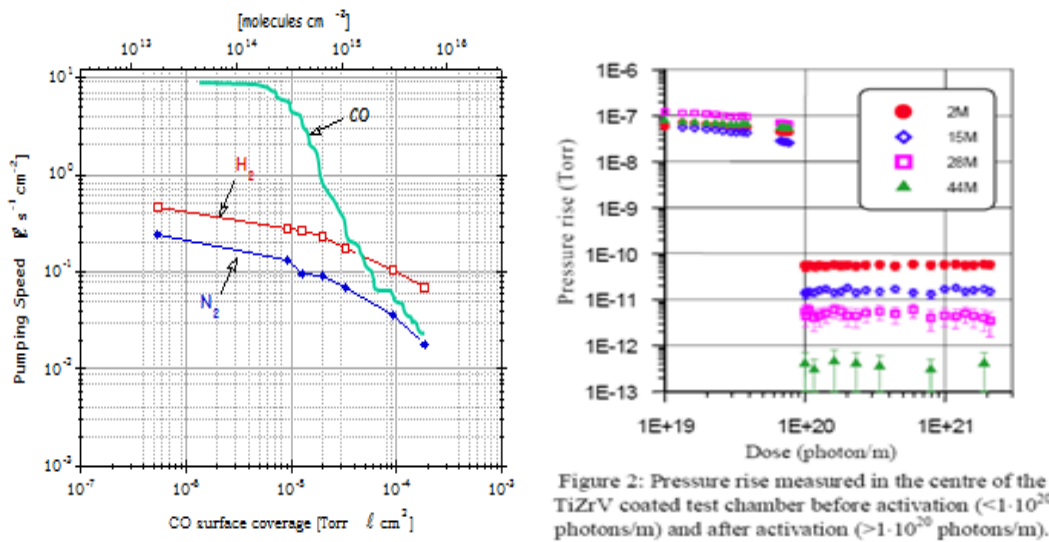


Figure 9.21: NEG pumping speed for different gas species and pressure rises measured in presence of a photon flux before and after NEG activation.

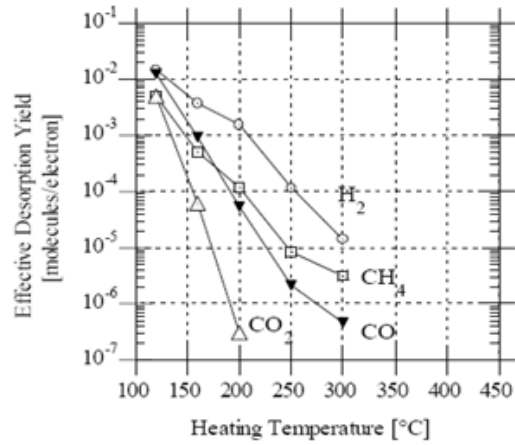
7150 9.5.3 Vacuum engineering issues

7151 The engineering of the vacuum system has to be integrated right from the beginning of the project. This
 7152 becomes imperative for the Ring-Ring option since it has to take into account the constraints of the LHC and
 7153 allow for future consolidations and upgrades. For the Linac-Ring option, the tangential injection and dump
 7154 lines will be in common with the LHC beam vacuum over long distances. The experience has shown that
 7155 the vacuum engineering shall proceed in parallel on the following topics: expertise provided to beam-related
 7156 components (magnets, beam instrumentation, radio-frequency systems, etc.), engineering of vacuum related
 7157 components (beampipes, bellows, pumping ports, etc.) and machine integration including the cabling and
 7158 the integration of the services.

7159 Basically, the vacuum system is designed to interconnect the beam related equipments installed on the
 7160 beam line (magnets, kickers, RF cavities, beam absorbers, beam instrumentation, etc.) and to provide

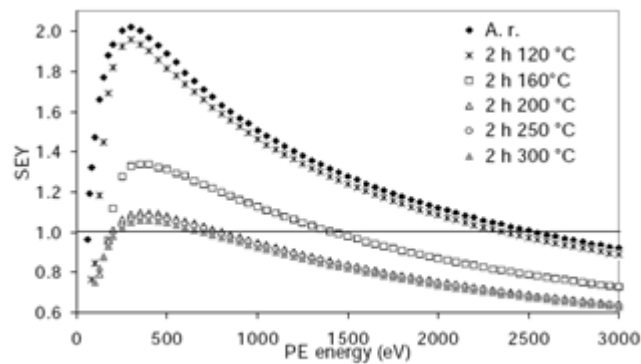
Table 2: Summary of results from the activated test chamber

Gas	Sticking probability	Photodesorption yield (molecules/photon)
H ₂	~0.007	~1.5·10 ⁻⁵
CH ₄	0	2·10 ⁻⁷
CO (28)	0.5	<1·10 ⁻⁵
C _x H _y (28)	0	<3·10 ⁻⁸
CO ₂	0.5	<2·10 ⁻⁶



•C. Benvenuti et al. J.Vac.Sci.Technol.A 16(1) 1998

Figure 9.22: Photon (left) and Electron (right) desorption yields.



C. Scheuerlein et al. Appl.Surf.Sci 172(2001)

Figure 9.23: Reduction of the secondary electron yield (SEY, δ) by Photons a) and Electron b) desorption yields.

7161 the adequate pumping speed and vacuum instrumentation. The vacuum components are often composed
7162 by vacuum pipes, interconnection bellows, diagnostics, pumping ports and sector valves. The number of
7163 pumps, vacuum diagnostics, bellows and ports will differ significantly between the two options discussed in
7164 this CDR and also between vacuum sectors of the same accelerator.

7165 **Vacuum pumping**

7166 The vacuum system of the LHeC will be mainly operated at ambient temperature. These systems rely more
7167 and more on NEG coatings since they provide a distributed pumping and huge pumping speed (Fig.2) and
7168 capacity and reduce the outgassing and desorption yields (Fig.3-4). These coatings are compatible with
7169 copper, aluminium and stainless steel beampipes. An alternative could be to use the LEP configuration
7170 with NEG strips. This alternative solution has only the advantage of avoiding the bake out constraints for
7171 the activation of the NEG coatings. A configuration of a distributed ion pumps is not considered since less
7172 performing and only applicable in dipole magnets i.e. bending sections. In any case, ion pumps are required
7173 as a complement of the NEG coatings to pump the noble gasses and methane to avoid the ion beam-induced
7174 instability. Sublimation pumps are not excluded in case of local huge outgassing rates, NEG cartridges being
7175 an interesting alternative since recent developments made by manufacturers include an ion pump and a NEG
7176 cartridge in the same body.

7177 The roughing from atmosphere down to the UHV range will be obtained using mobile turbomolecular
7178 pumping stations. These pumps are dismantled prior to beam circulations.

7179 The part of the vacuum system operated at cryogenic temperature, if any, could rely on gas condensation if
7180 the operating temperatures are below 2 K. Additional cryosorbing material could be required if an important
7181 hydrogen gas load is expected. This issue still needs to be addressed. As made for the LHC, the parts at
7182 cryogenic temperature must be isolated from the NEG coated part by sector valves when not at their
7183 operating temperature to avoid the premature saturation of the NEG coatings.

7184 The pumping layout will be simpler for the Ring-Ring option since more space is available around the
7185 beampipes. The tighter tolerances for the Linac-Ring option make the integration and pumping layout more
7186 delicate. However, the vacuum stability will be easier to ensure in the Linac-Ring option since only the
7187 bending sections are exposed to the synchrotron radiation.

7188 **Vacuum Diagnostics**

7189 For both options, the radiation level expected will be too high to use pressure sensors with onboard electron-
7190 ics. Therefore, passive gauges shall be used, inducing additional cabling costs and need for gauge controllers.

7191 **Vacuum Sectorisation**

7192 The sectorisation of the beam vacuum system results from the integration of various constraints, the major
7193 being: venting and bake-out requirements, conditioning requirements (RF and HV devices), protection
7194 of fragile and complex systems (experimental areas and ceramic chambers), decoupling of vacuum parts at
7195 room temperature from upstream and downstream parts at cryogenic temperature thus non-baked, radiation
7196 issues, etc.

7197 For UHV beam vacuum systems, all-metal gate valves shall be preferred in order to allow for bake-out at
7198 temperature above 250°C. VITON-sealed valves even though the VITON has been submitted to a special
7199 treatment are not recommended nearby NEG coatings or NEG pumps since minor outgassing of Fluor will
7200 degrade the pump characteristics.

7201 In the injection and extraction regions, the installation of the sector valves will lead to integration issues
7202 since the space left between the beampipes with a tangential injection/extraction and the circulating beams
7203 is often limited. This could result in a long common beam vacuum which implies that the LHC beam vacuum
7204 requirements will apply to the LHeC part shared with LHC.

7205 Vacuum protection

7206 The distribution of the vacuum sector valves will be made in order to provide the maximum protection to
7207 the beam vacuum in case of failure (leak provoked or not). Interlocking the sector valves is not an obvious
7208 task. Indeed, increasing the number of sensors will provide more pressure indications but often results in
7209 a degradation of the overall reliability. The protection at closure (pressure rise, leaks) is treated differently
7210 from the protection while recovering from a technical stop with parts of the accelerator beampipe vented or
7211 being pumped down.

7212 The vacuum protections of the common beampipes between LHeC and LHC shall fulfill the strong LHC
7213 requirements. Indeed, any failure in the LHeC propagating to the LHC could lead to long machine downtime
7214 (several months) in case of an accidental venting of an LHC beam vacuum sector.

7215 HOM and Impedance implications

7216 The generation and trapping of higher order mode (HOM) resulting from the changes in beampipe cross-
7217 sections are severe issues for high intensity electron machines. Thus, the engineering design of LHeC must
7218 be inspired on new generation of synchrotron radiation light sources instead of the simple LEP design. All
7219 bellows and gaps shall be equipped with optimised RF fingers, designed to avoid sparking resulting from bad
7220 electrical continuity. Indeed, these effects could induce pressure rises and machine performance limitations.

7221 Bake-out of vacuum system

7222 An operating pressure in the UHV range (10^{-10} Pa) will be required for both options. This implies the use
7223 of a fully baked-out beam vacuum system. Two options are possible: permanent and dismountable bake out.
7224 The permanent solution could be an option for the Linac-Ring but has to be excluded for the Ring-Ring
7225 option for cost reasons. As done for the dipole chambers (bending sections) of LEP, hot pressurised water can
7226 be used but the limit at 150°C is a constraint for the activation of NEG coatings. Developments are being
7227 carried on at CERN to lower the activation temperature from 180°C down to 150°C but this technology is
7228 not yet available.

7229 Shielding issues

7230 The synchrotron radiation power is an engineering challenge for the beampipes. Indeed, 50% of the radiation
7231 power hitting the vacuum chamber is absorbed in the beampipe chamber (case of LEP aluminum chamber).
7232 The remainder 50%, mainly the high-energy part of the spectrum, escapes into the tunnel and creates severe
7233 problems like degradation of organic material and electronics due to high dose rates and formation of ozone
7234 and nitric acid could lead to severe corrosion problems in particular with aluminum and copper materials.

7235 In this respect, the Ring-Ring option is less favorable since the synchrotron radiation will be localised at
7236 the plane of the existing LHC cable trays and electrical distribution boxes in the tunnel. Similar constraints
7237 exist also for the Linac-Ring option but these zones are localised at the bending sections of the LHeC.

7238 Detailed calculations are still to be carried on but based on LEP design, a lead shielding of 3 to 8 mm
7239 soldered directly on the vacuum chamber would be required for 70 GeV beams. Higher energies could require
7240 more thickness. The evacuation of the synchrotron radiation induced heat load on the beampipe wall and
7241 on lead shielding is a critical issue which needs to be studied. In case of insufficient heat propagation and
7242 cooling, the lead will get melted as observed in LEP in the injection areas. The material fatigue shall also
7243 be investigated since running at much higher beam current as compared to LEP, will increase the induced
7244 stress to the material and welds of the beampipes.

7245 As made in LEP, the best compromise to fulfill the above mentioned constraints is the use of aluminum
7246 beampipes, covered by a lead shielding layer. The complex beampipe cross-section required to optimise
7247 the water cooling of the beampipe and shielding is feasible by extrusion of aluminum billets and the costs
7248 are acceptable for large productions. The large heat conductivity helps also the heat exchange. However,
7249 extruded aluminum beampipes induce limitations for the maximum bake out temperature and therefore
7250 for the NEG coatings activation. Special grades of aluminum shall be used. The reliability of vacuum

interconnections based on aluminum flanges is a concern at high temperature ($>150^{\circ}\text{C}$) and corrosion issues shall be addressed. The stainless steel beampipes do not have these limitations but they have poorer heat conductivity and they are more difficult and costly to machine and shape.

The LEP 110 GeV operation has shown the criticality of unexpected synchrotron radiations heating vacuum components and in particular the vacuum connections between pipes or equipments. Indeed, the flanges, by “offering” a thick path, are behaving as photon absorbers and heat up very quickly. Hence, at cool down and due to the differential dilatation, leaks are opening. In LEP, these unexpected SR induced heat loads resulted from orbit displacement in quadrupoles during the ramp in energy and of the use of the wigglers also during the ramp. In LHeC, resulting from the much higher beam current, these issues shall be carefully studied.

Corrosion issues

In vacuum systems, feedthroughs and bellows are particularly exposed to corrosion. The feedthroughs, particularly those of the ion pumps where high voltage is permanently present, are critical parts. A demonstrated and cheap solution to prevent the risk of corrosion consists in heating directly the protective cover to reduce the relative humidity around the feedthrough.

The bellows are critical due to their thickness, often between 0.1 – 0.15 mm. PVC material must be prohibited in the tunnel. Indeed, in presence of radiations, it can generate hydrochloric acid (HCl) which corrodes stainless steel materials. This corrosion has the particularity to be strongly penetrating, once seen at the surface, it is often too late to mitigate the effects. Aluminum bellows are exposed to corrosion by nitric acid (HNO_3) which is generated by the combination of O_3 and NO.

Humidity is the driving factor and shall be kept 50%. However, in the long term, accidental spillage can compromise locally the conditions and therefore, corrosion-resistant design are strongly recommended.

9.6 Beam Pipe Design

9.6.1 Requirements

The vacuum system inside the experimental sector has a number of different and sometimes conflicting requirements. Firstly, it must allow normal operation of the LHC with two circulating beams in the chamber. This implies conformity with aperture, impedance, RF, machine protection as well as dynamic vacuum requirements. The addition of the incoming electron beam adds constraints in terms of geometry for the associated synchrotron radiation (SR) fan and the addition of SR masks in the vacuum. Finally, optimization of the surrounding detector for high acceptance running means that all materials for chambers, instrumentation and supports must be optimized for transparency to particles and the central chamber must be as small and well aligned as possible to allow detectors to approach the beam aperture limit at the interaction point.

9.6.2 Choice of Materials for beampipes

LHC machine requirements imply an inner beampipe wall that has low impedance (good electrical conductivity) along with low desorption yields for beam stimulated emissions and resistance to radiation damage.

Ideal materials for transparency to particles have low radiation length (Z) and hence low atomic mass. These materials either have poor (i.e. high) desorption yields (eg. aluminium, beryllium) or are not vacuum and impedance compatible (eg. carbon). Solutions to this problem typically include thin film coatings to improve desorption yields and composite structures to combine good mechanical properties with vacuum and electrical properties.

The LHC experimental vacuum systems, along with most other colliders currently use metallic beryllium vacuum chambers around the interaction points due to a very favourable combination of Z , electrical conductivity, vacuum tightness, radiation resistance, plus mechanical stiffness and strength. High desorption yields are suppressed by a thin film TiNiV non-evaporable getter (NEG) coating. This coating also gives a high

7296 distributed vacuum pumping speed, allowing long, small aperture vacuum chambers to be used that would
 7297 otherwise be conductance-limited. Activation of this coating requires periodic heating of the chamber to
 7298 180–220°C under vacuum for a few hours. This means that the chamber and environment must be designed
 7299 for these temperatures. This activation is scheduled in annual LHC shutdowns. Long-term development is
 7300 in progress for low desorption yield coatings that do not require high temperature activation [?]. These may
 7301 have applications for LHeC.

7302 Production technology developed for the LHC uses beryllium sections machined from hot-pressed blocks
 7303 and electron beam welded to produce chambers. This has the advantage that a wide range of vacuum
 7304 chamber forms can be manufactured. Cylindrical and conical chamber sections are installed in the LHC
 7305 experiments.

7306 Disadvantages of beryllium include high cost, fragility and toxicity in the powder form, as well as limited
 7307 availability. For this reason, long-term development of other technologies for experimental beampipes is
 7308 under way at CERN which may yield applications for LHeC.

7309 Composite beampipe structures made from carbon and other low-Z materials have been developed for
 7310 colliders. These typically use a thin inner membrane to comply with vacuum and impedance requirements.
 7311 Composite structure pipes were eventually rejected for LHC application for reasons of temperature and
 7312 radiation resistance and the risk of delamination due to mismatch of thermal expansion coefficients. Lower
 7313 luminosity in LHeC experiments combined with new low temperature coatings may allow these materials to
 7314 be re-evaluated.

7315 9.6.3 Beampipe Geometries

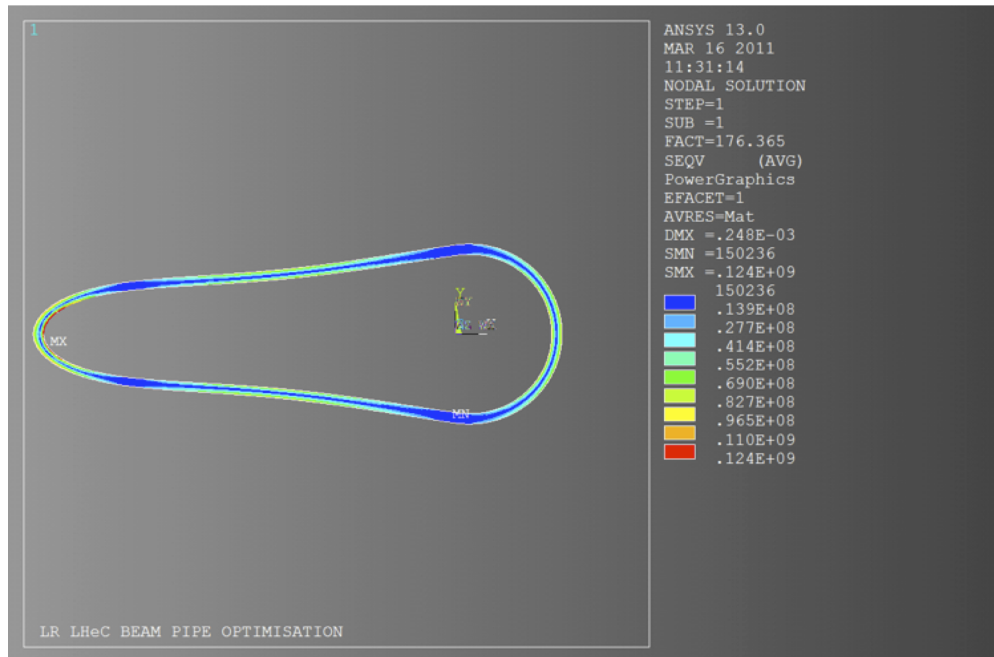


Figure 9.24: Section through the LR geometry showing contours of Von Mises equivalent stress (Pa).

7316 The proposed geometry has a cross section composed of a half-circle intersecting with a half-ellipse. Cylindrical
 7317 cross-sections under external pressure fail by elastic instability (buckling) whereas elliptical sections
 7318 can (depending on the geometry) fail by plastic collapse (yielding).

7319 Figure ?? and ?? show optimizations of the proposed geometries for the LINAC-Ring (LR) and Ring-Ring
 7320 (RR) beampipes assuming a long chamber of constant cross section made from beryllium metal. Preliminary

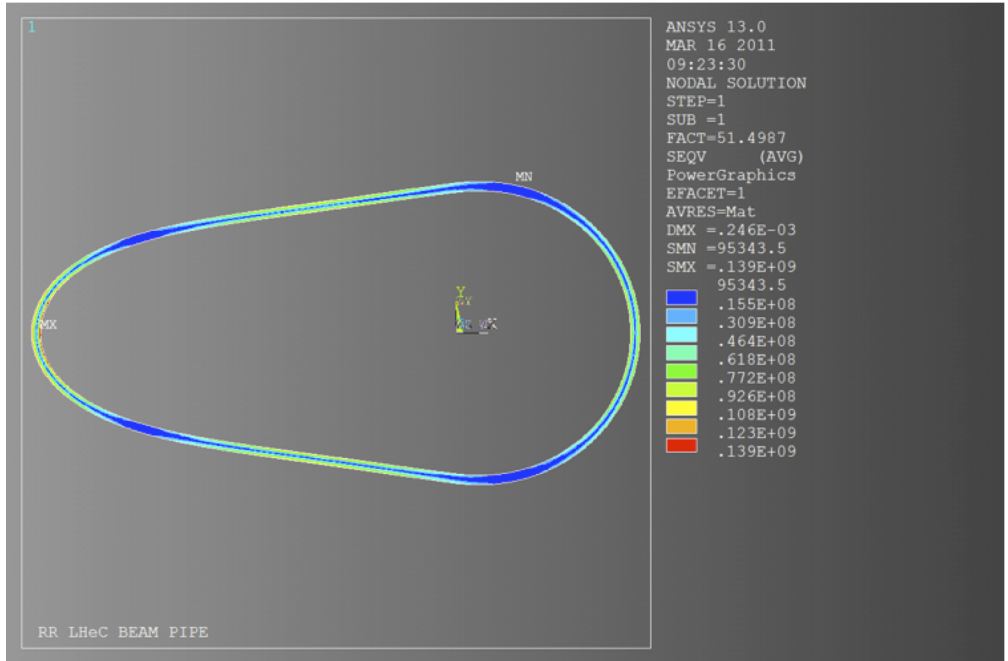


Figure 9.25: Section through the RR geometry showing contours of Von Mises equivalent stress (Pa).

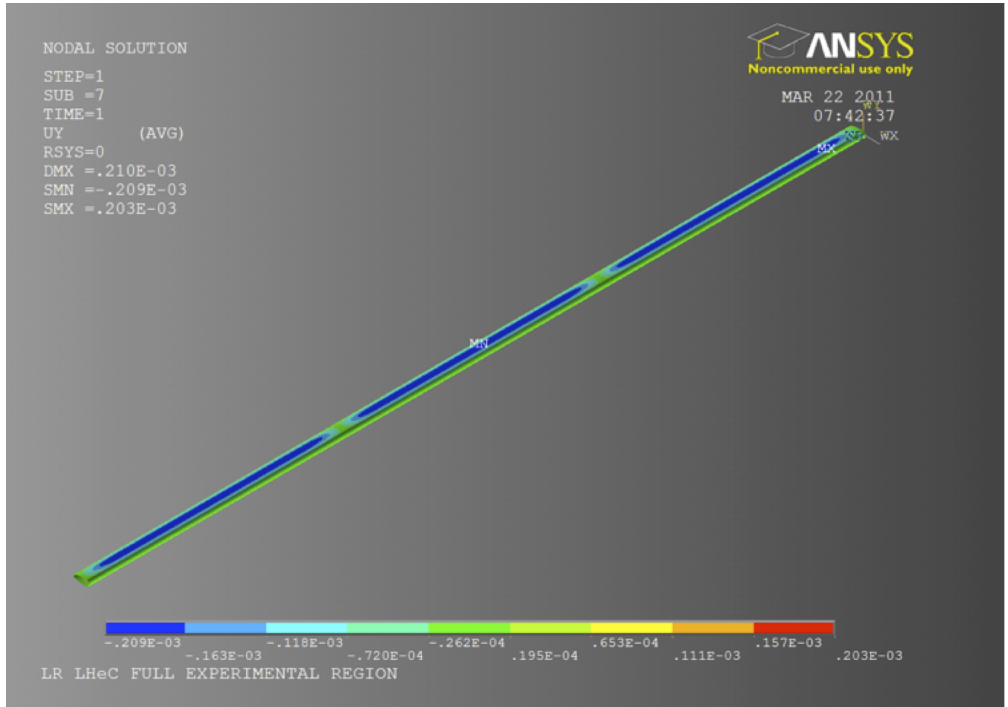


Figure 9.26: 3-D view of the LR geometry showing contours of bending displacement [m].

7321 analyses have been performed using the ANSYS finite element code. The wall thickness was minimized for
7322 the criteria of yield strength and buckling load multiplier. The LR geometry considered has a circular section
7323 radius of 22 mm and elliptical major radius of 100 mm. The RR geometry has a circular section radius of 22
7324 mm and elliptical major radius of 55 mm. This preliminary analysis suggests that a constant wall thickness
7325 of 2.5 – 3 mm for the LR and 1.3 to 1.5 mm for the RR would be sufficient to resist the external pressure.
7326 Failure for both of these sections would be expected to occur by plastic collapse.

7327 At this stage of the project, these geometries represent the most optimized forms that fulfill the LHC
7328 machine requirements. However, for 1 degree tracks this corresponds to $X/X_0 \approx 21\text{-}25\%$ for the LR and
7329 $\approx 41\text{-}49\%$ for the RR designs. This suggests that additional effort must be put into beampipe geometries
7330 optimized for low angles. Composite beampipe concepts suggested for machines such as the LEP [?] should
7331 be re-considered in the light of advances in lightweight materials and production techniques.

7332 The optimized section of the experimental chamber is 6.1 m in length. This length will require a number of
7333 optimized supports. These supports function to reduce bending deflection and stresses to within acceptable
7334 limits and to control the natural frequency of chamber vibration. The non-symmetric geometry will lead to
7335 a torsional stress component between supports which must be considered in their design. Figure ?? shows a
7336 preliminary analysis of bending displacement for the LR chamber geometry. With 2 intermediate supports
7337 the maximum calculated displacement (without bakeout equipment) is 0.21 mm.

7338 9.6.4 Vacuum Instrumentation

7339 If, as assumed, this chamber is coated with a NEG film on the inner surfaces, then a high pumping speed of
7340 chemically active gasses will be available. Additional lumped pumps will be required for non-gettered gasses
7341 such as CH_4 and noble gasses; however, outgassing rates for these gasses are typically very low.

7342 The vacuum sector containing the experiment will be delimited from the adjacent machine by sector
7343 valves. These will be used to allow independent commissioning of machine and experiment vacuum. The
7344 experimental vacuum sector will require pressure gauges covering the whole range from atmospheric to UHV,
7345 these are used both for monitoring the pressure in the experimental chamber and as interlocks for the machine
7346 control system.

7347 9.6.5 Synchrotron Radiation Masks

7348 LHeC experimental sector will require a moveable SR mask upstream of the interaction. From the vacuum
7349 perspective, this implies a system for motion separated from atmosphere by UHV bellows. The SR flux on
7350 the mask will generate a gas load that should be removed by a local pumping system dedicated to the mask.
7351 As the load due to thermally stimulated desorption increases exponentially with the temperature, cooling
7352 may be required. However, cooling the mask would significantly complicate the vacuum system design. The
7353 generation of photo-electrons must also be avoided since these photo-electrons can interact with the proton
7354 beam and lead to an electron cloud build-up.

7355 9.6.6 Installation and Integration

7356 The installation of the vacuum system is closely linked to the detector closure sequence. Therefore, the
7357 design has to be validated in advance to prevent integration issues which would lead to significant delay
7358 and increase of costs. Temporary supports and protections are required at each stage of the installation.
7359 Indeed, as compared to the size of the detectors, the beam pipe are small, fragile and need to be permanently
7360 supported and protected while moving the detector components. Leak tightness and bake-out testing are
7361 compulsory at each step of the installation since all vacuum systems are subsequently enclosed in the detector,
7362 preventing any access or repair. Their reliability is therefore critical. Precise survey procedures must also
7363 be developed and incorporated in the beampipe design to minimize the mechanical component of the beam
7364 aperture requirement. Engineering solutions for bakeout also has to be studied in details since the equipment
7365 (heaters, probes and cables) must fit within the limited space available between beampipes and the detector
7366 components.

9.7 Cryogenics

9.7.1 Ring-Ring Cryogenics Design

Introduction

The Ring-Ring version foresees the 60 GeV accelerator to be installed in the existing LHC tunnel. Acceleration of the particles is done with 0.42 m long 5 MV superconducting (SC) cavities housed in fourteen 10 m long cryomodules. They will be placed at two opposite locations in by-passes of point 1 (ATLAS) and, point 5 (CMS). While at CMS a continuous straight by-pass can be built, at ATLAS two straight sections are conceived on each side of the detector cavern (“left” and “right”) with a connecting beam pipe crossing the detector hall. Lay-outs and detailed RF description see chapter XXXXXXXX. The three separate cryomodules locations require three dedicated 2 K cryo-systems. Injection to the Ring at 10 GeV is done with a 1.3 GHz pulsed three-pass re-circulating high field injector. A dedicated cryoplant provides 2 K cooling of its SC cavities. In total four independent cryoplants with their respective distribution systems are needed for the Ring-Ring version. For the LHeC detector the high gradient focusing insertion magnets will be SC and housed in LHC dipole type cryostats. The cooling principle is the same as for LHC dipoles and, the existing cryogenic infrastructure can be used with comparatively small adaptations of the feedboxes. More detailed engineering studies are beyond the scope of this report. This chapter describes the cryosystems of the e-Ring accelerator and the related injector.

Ring-Ring cryogenics

The cavities operate at 2 K superfluid helium temperatures and dissipate an estimated 4 W per cavity at 5 MV. The 8-cavity cryomodule has three temperature levels; a 2 K saturated bath containing the cavities, a 5 – 8 K combined thermal shield and heat intercept for couplers and other equipment and, a 40 – 80 K thermal shield. The thermal loss estimates are listed in Table ?? . With efficiencies of modern state of the art cryoplants reaching 1/COP values of 1000 W/W at 2 K, 250 W/W at 5 K and 20 W/W at 40 – 80 K the minimum plant powers are calculated. To the equivalent cooling power at 4.5 K we add a 50% contingency for the distribution system with transfer lines running parallel to the cryomodules. In Table ?? the equivalent cooling powers of the three cryoplants are given.

Temperature (K)	2	5 – 8	40 – 80
One cryomodule			
Static loss (W)	5	15	100
Dynamic loss (W)	32	15	80
Sum (W)	37	30	180
8 modules (CMS site) (W)	296	240	1440(2160)
3 modules (ATLAS left) (W)	111	90	720(1080)
3 modules (ATLAS right) (W)	111	90	720(1080)

Table 9.18: Thermal loss estimate of cryomodules. In brackets the values with ultimate thermal losses (50% contingency) which are taken into account for the cryoplant sizing.

At CMS site a dedicated 3 kW @4.2 K cryoplant is needed. Except for some general infrastructure equipment like e.g. gas tanks it will be separated from the existing CMS cryoplant used to cool the solenoid magnet. Comparatively modest cooling powers suggest the use of a single compact refrigerator cold box, in contrast to split versions as proposed in this CDR for the Linac-Ring version described below. (The split version is based on LHC technology with a combined surface and underground cold box.) The cold box will be installed directly in the underground cavern at proximity to the cryomodule string. Ambient temperature high and low pressure lines make the link to the compressor stations on surface. For the 2 K

Site	Plant power @4.2 K (kW)
CMS site	3.0
ATLAS left	1.2
ATLAS right	1.2

Table 9.19: Cryoplant equivalent cooling powers.

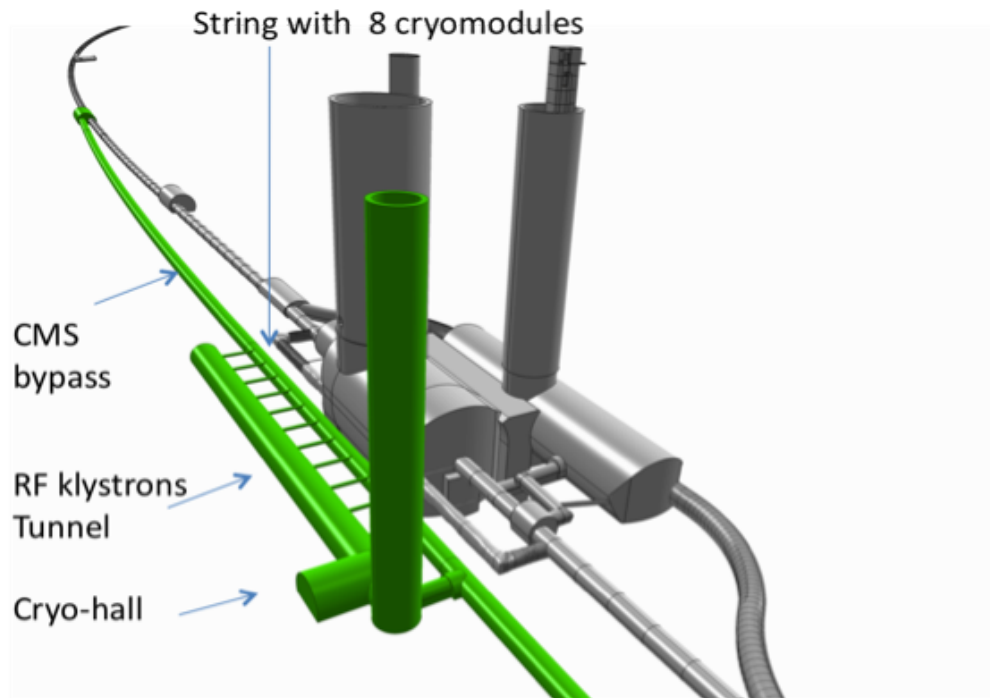


Figure 9.27: Lay-out of the CMS by-pass with location of the cryomodules and the 3 kW @4.5 K cryoplant.

7400 temperature level two cold compressors with a total compression ratio of 10 are proposed followed by warm
7401 compressors to compress the gas to ambient pressure. Figure ?? shows the lay-out of the CMS by-pass
7402 region. At the two ATLAS sites (left, right) with three cryomodules each, two options are conceivable. The
7403 first consists of connecting to the LHC QRL transfer lines and their terminal feedboxes at vicinity for a
7404 “parasitic” use of excessive cooling power of the LHC cryoplants. For this two additional 10 – 15 m long
7405 perpendicular tunnels to connect the LHC tunnel with the LHeC by-pass would have to be constructed. The
7406 feasibility of this option and potential (negative) impacts have to be studied in more detail in a subsequent
7407 report. The second option is to use two dedicated cryoplants as proposed for the CMS site, however, with
7408 reduced capacity. Also in this case the cold box will be installed at proximity to the cryomodule strings in
7409 the cryo-hall. The two refrigerators are of the same design principle as for CMS, except for their size and
7410 capacity which is smaller. Their location will be on ATLAS terrain which allows to potentially use already
7411 existing cryogenic infrastructure of the large cryo-system for the cooling of the ATLAS toroidal and solenoid
7412 magnets. Among these are the gas storage tanks, the compressor hall and control rooms. Figure ?? shows
7413 the lay-out of the ATLAS by-pass region.

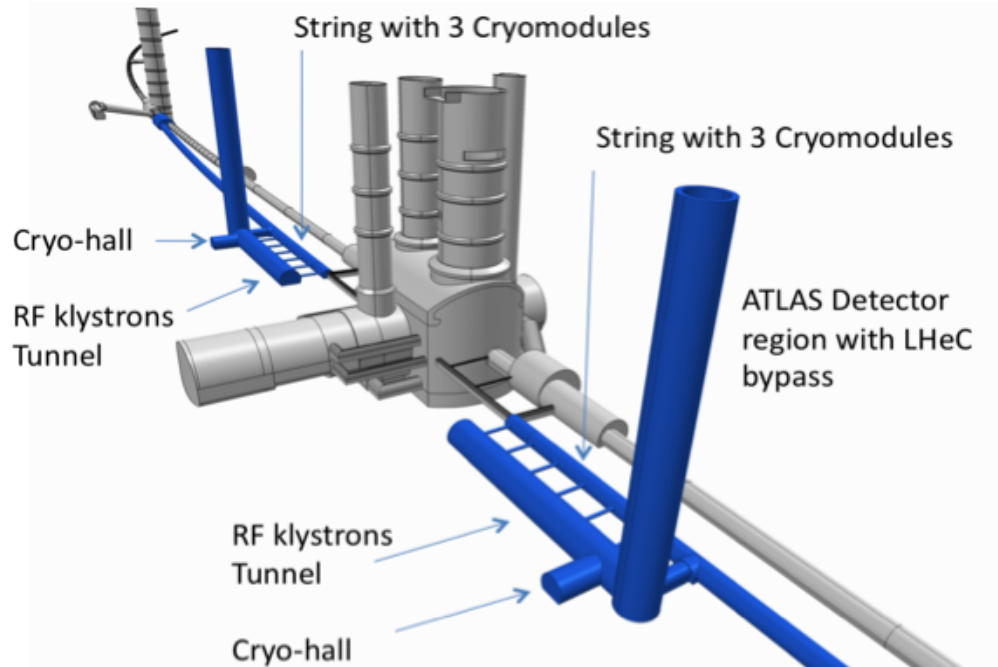


Figure 9.28: Lay-out of the ATLAS by-pass with locations of the cryomodules and the two 1.2 kW @4.5 K cryoplants.

7414 **Cryogenics for the 10 GeV Injector**

7415 The injector is a three-pass recirculating pulsed 10 Hz machine providing leptons at injection energies of
 7416 10 GeV to the LHeC Ring machine. Figure ?? shows its basic principle. Cryomodules of the XFEL (ILC)
 7417 type with 1.3 GHz superconducting cavities are proposed which allow the application of already existing
 7418 technology requiring little adaptation effort for LHeC. A 146 m long string will be composed of in total
 7419 12 cryomodules each 12.2 m long. Cryogen distribution is done within the volume of the cryostats. Bath
 7420 cooling is at 2 K saturated superfluid helium. Adopted from XFEL the common pump line of 300 mm
 7421 runs within the cryomodules envelope to collect vapor of all individual cavity baths. Therefore no external
 7422 transfer line is required which simplifies the overall design. The suction pressure of 30 mbar is provided by
 7423 cold compressors in the cold box and subsequent ambient temperature compressors. Two more temperature
 7424 levels of 5 – 8 K and 40 – 80 K are used for intercepts and thermal shielding. The operation of the injector at
 7425 LHeC is in part comparable to XFEL, this during the injection and loading phase of leptons into the LHeC
 7426 ring. During all other operation phases of a complete LHeC cycle (ramping to final particle energies in the
 7427 LHC/LHeC tunnel and subsequent physics runs) the injector machine is “idle”. Only static heat losses of
 7428 the cryomodules and the cryogenic infrastructure have to be intercepted during this time period. Principly
 7429 a reduced power cryogenic system operating with an “economizer” could be

7430 conceived, i.e. a large liquid helium storage is filled during low demands which in turn boosts the
 7431 cryomodules during the injection phases. A simpler approach, however, is the design for constant (maximum)
 7432 cooling power when active and, during idle periods, internal electric heaters in the 2 K bath are switched on
 7433 to keep the load constant. This principle is adopted for these initial studies. A compact single refrigerator
 7434 cold box providing temperatures from 300 K to 2 K will be installed in a protected area at vicinity to the
 7435 extraction region of the cryomodule string while the compressor set is at surface. For the estimation of
 7436 power consumption and cooling performances we shall use the experience gained at DESY during testing of
 7437 XFEL cryomodules. With a final energy of 10 GeV and three pass operation the acceleration field required

Temperature (K)	2	5 – 8	40 – 80
Static loss (W)	5	15	100
Dynamic loss (W)	8	3	40
Sum (W)	11	18	140
Sum 12 modules (W)	132(198)	216(324)	1680(2520)

Table 9.20: Thermal loss estimate of the 146 m long string built of 12 XFEL type cryo-modules. In brackets values with 50% contingency. Cryoplant equivalent cooling power; 2 kW @4.5 K.

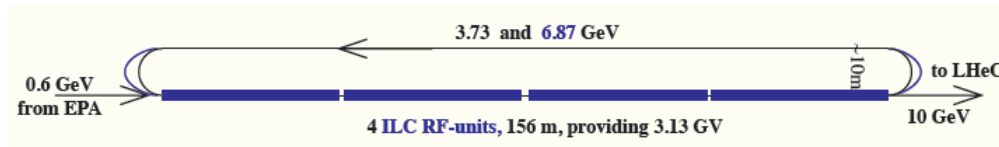


Figure 9.29: Principle of the 10 GeV re-circulating Injector with high gradient pulsed SC cavities (23 MV/m) and 12 cryomodules of the ILC/XFEL type operating at 2 K.

7438 is 23 MV/m. At DESY power consumption measurements have been made with cryomodules for a similar
 7439 acceleration field of 23.8 MV/m and 10 Hz operation. Our estimates as shown in the Table ?? are based on
 7440 these recent data. With 1/COP values as used in above chapter and a 50% margin for additional thermal
 7441 losses we estimate the required cooling power of the plant to 2 kW @4.5 K.

9.7.2 Linac-Ring Cryogenics Design

Location and basic lay-out

7442 The ERL (Energy Recovery Linac) is of racetrack shape with two 1 km long straight SC acceleration sections
 7443 and, two arcs of 1 km radius with normal conducting magnets. Location and lay-out studies made are
 7444 described in chapter XXXXXXXXXXXXXXXXXXXX Civil Engineering and Services. The currently favored
 7445 position is within the LHC perimeter (see figure XXXXXXXXXXXX) versus the external version being largely
 7446 under St. Genis community. For the “inside” version more of the newly required surface areas could be
 7447 located on existing CERN grounds comprising SM18, North Area and, Point 2. Next steps following this
 7448 CDR will require more detailed combined studies of civil engineering, RF, cryogenics and other services to try
 7449 optimize the lay-out also, and in particular, for the cryogenic equipment having impact on its own complexity
 7450 and costs. As base in this study we propose a symmetric lay-out with a sub-division of the respective 1 km
 7451 long straight sections in four equally spaced sections each housing four 250 m long cryomodule strings. As
 7452 indicated in chapter 9 the ERL will be inclined towards the Lake of Geneva by 1.4%, however, due to its
 7453 orientation the tilt in longitudinal direction relevant to the cryogenics is smaller.
 7454
 7455

Cryomodules

7456 Eight 721 MHz SC 5-cell cavities of length 1.04 m long will be housed in 14 m long cryomodules. Bath cooling
 7457 of the cavities is done with slightly subcooled saturated superfluid helium at 2 K. Each cryostat is equipped
 7458 with a J.T. valve located upstream to expand the 2 K supply helium to the 30 mbar bath pressure and the
 7459 liquid is brought gravity assist to the downstream individual 8 cavity bath volumes via an interconnecting
 7460 header pipe. This principle is similar to the SPL preliminary design which has to cope with a tilt of 1.7 %
 7461 [1]. Heat intercept and thermal shielding is at 5-8 K and 40-80 K. The final LHeC L-R cryomodule design
 7462 can be based on extensive previous work and studies of both existing SC linear accelerators and, such being
 7463 under construction or planned ones. Among these are CEBAF, ILC, XFEL, SPL, e-RHIC. For this study
 7464 adapted TESLA/XFEL type cryomodules are proposed. Figure ?? shows a design proposal of a module with
 7465

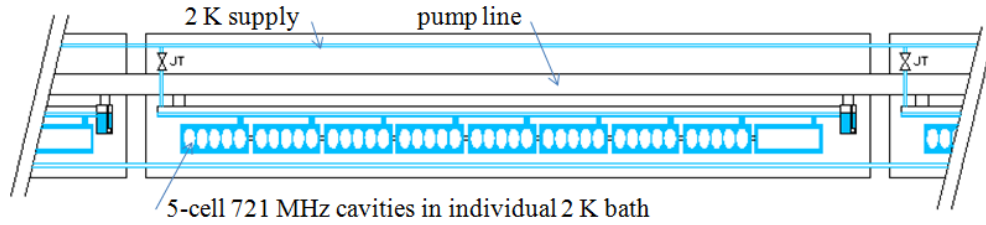


Figure 9.30: Schematic proposal of the 14 m long cryomodules with eight 5-cell 721 MHz cavities operating at 2 K. Supply pipes and the 30 mbar pump line are within cryostat envelope. For the case with inclination right part is lower. (only 2 K circuits are shown) .

7466 the eight cavities and the cold correction magnets in their individual bath. All cryogen distribution is done
 7467 within the cryostat module which interconnects to the adjacent ones with the pipe runs throughout a 250 m
 7468 long cryomodule string. Also the pump line is proposed to be within the cryostat envelope. The expected
 7469 mass flow rate of 180 g/s at 2 K of a 250 m long section with 15 cryomodules (see calculations next chapter)
 7470 is approximately comparable to XFEL for its entire machine for which the corresponding pump line diameter
 7471 has been designed and tested [2]. The parameters of the LHeC SC cavities and cooling requirements are
 7472 listed in Table ??.

Parameter	Value
Two linacs	length 1 km
5-cell cavities	length 1.04 m
Number	944
Cavities/ cryomodule	8
Number cryomodules	118
Length cryomodule	14 m
Voltage per cavity	21.2 MV
R/Q	285Ω
Cavity Q0	$2.5 \cdot 10^{10}$
Operation	CW
Bath cooling	2 K
Cooling power/cav.	32 W @2 K
Total cooling power (2 linacs)	30 kW @2 K

Table 9.21: Parameters and cooling requirements of the ERL (Linac-Ring version).

7473 Cryogenic System

7474 The estimated thermal loads per cavity are based on a voltage of 21.2 MV, an R/Q of 285Ω and a Q0
 7475 of $2.5 \cdot 10^{10}$. With CW operation the dissipated heat per cavity will be 32 W, respectively 256 W per
 7476 cryomodule. This consists of a very high load. The 1 km long straight sections are sub-divided in four 250 m
 7477 long sub-sections each with 15 interconnecting cryomodules forming a string which are individually supplied
 7478 by a respective refrigerator through local distribution boxes. Eight dedicated refrigerators supply the eight
 7479 strings. Figure ?? gives a basic lay-out of the cryo-system with its sectorisation. The refrigerator cold boxes
 7480 will be of the so-called “split” type with a surface cold box and a connecting underground cold box as explored

7481 and implemented first for LEP2 and later at a larger scale for LHC. The surface cold box will be installed
7482 close to the compressor set and produce temperature levels between 300 K and 4.5 K. The underground
7483 cold box will be installed at proximity to the respective cryomodule string in a protected area and produce
7484 the 2 K with cold compressors. Figure ?? gives a principle lay-out of the refrigerator configuration. The
7485 final location of the ERL will dictate civil engineering constraints and the “ideal” symmetric configuration
7486 of placement of the refrigerators as done here will have to be reviewed accordingly and, hence, partially
7487 deviate from this proposal. Also in case only one access shaft per linac can be conceived the four surface
7488 cold boxes may be installed in form of clusters around the pit while the four related 2 K underground cold
7489 boxes will be installed remotely close to the respective cryomodule string to be supplied as described above
7490 and shown in figure ?. The total dynamic cooling power of the ERL with 944 cavities amounts to 30 kW
7491 @2 K. For the calculation of the cooling performances of the refrigerators in this document only the largely
7492 dominating dynamic thermal loads of the cavities are taken into account dwarfing all other thermal losses
7493 of the cryomodules which become negligible in a first order approach. Recent developments and industrial
7494 design of large scale refrigerator systems as for LHC [3] indicate the feasibility of a 1/COP of 700 W/W
7495 for 2 K large scale cryoplants. Hence, with this figure the total electric grid power amounts to 21 MW.
7496 The total equivalent refrigerator power at 4.5 K is estimated to 80 kW. This corresponds to about ? of the
7497 installed cooling power at LHC. In case contingencies are taken into account in the engineering design the
7498 cooling capacity could approach LHC. For this preliminary study contingencies are omitted, this also in view
7499 of expected future improved cavity performances. Eight cryoplants with 10 kW @4.5 K each are proposed
7500 for the ERL. The technology to design and construct such units as well as the overall systems engineering is
7501 largely available today and can be based on experience from LHC, CEBAF, XFEL. Nevertheless it consists
7502 of an engineering challenge due to its sheer size and the large performance capacities required. Development
7503 work will have to be done for the cold compressors units together with detailed combined CERN/industrial
7504 engineering design of the refrigerator cold boxes. Implementation and operation of such large systems will
7505 consist of a complex task. Further cavities and cryomodules will require a limited R&D program. From this
7506 we expect improved quality factors with respect to today’s state of the art. The cryogenics of the L-R version
7507 consists of a formidable engineering challenge, however, it is feasible and, CERN disposes of the respective
7508 know-how.

Parameter	Value
Number of Refrigerators	1/COP @2 K
8	700
Minimum cooling capacity/refrigerator	10 kW @4.5 K
Contingency	none
Minimum total cooling power	80 kW @4.5 K
Grid power consumption	21 MW

Table 9.22: Refrigerator cooling capacity and power consumption (minimum cooling power).

7509 9.7.3 General Conclusions Cryogenics for LHeC

7510 These conclusions reference to the complete cryogenic contributions, i.e. for the detector cryogenics, the R-R
7511 and the L-R version;

7512 The striking advantage of an extension from LHC to a LHeC lies, apart from the new physics, in the
7513 comparatively small investment cost, the possibility of quasi undisturbed continuation of LHC hadron physics
7514 and the fact that the technologies are largely already at hand today. This applies also to the cryogenic part.
7515 No so-called “show-stoppers” could be detected during these studies. For the detector SC magnet and
7516 LArgon cryogenics technologies developed and implemented at the ATLAS experiment can be used in a
7517 “down-scaled” way. For the accelerator cryogenics the two options Ring-Ring and Linac-Ring differ strongly
7518 in principle and investment. While for the R-R only four small to medium sized 2 K refrigerators are

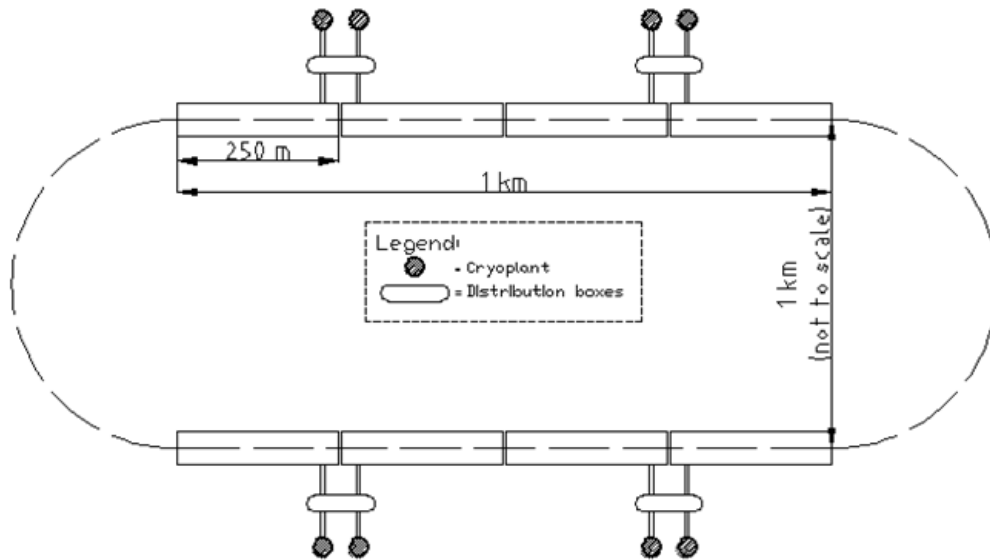


Figure 9.31: Basic lay-out of the 6 pass ERL. Two 1 km long SC acceleration sections with a 10 GeV linac each. Eight 10 kW @2 K cryoplants. Configuration such that each plant supplies a cryomodule string of 250 m length. (figure not to scale).

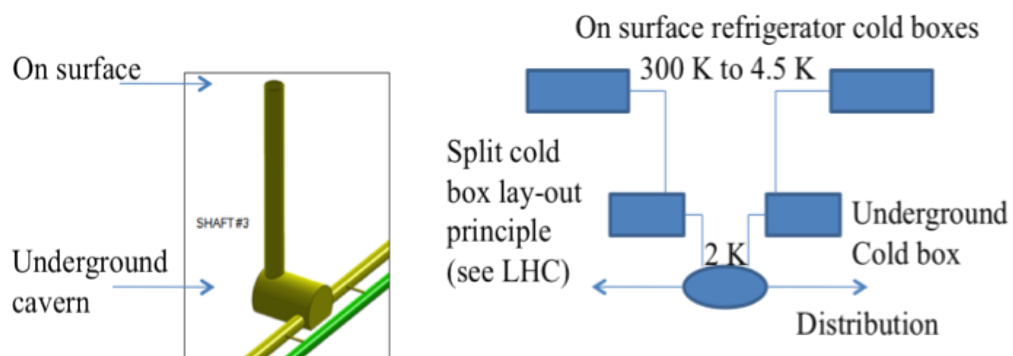


Figure 9.32: Basic principle of a Split Cold Box lay-out (comparable to LHC accelerator cryogenics).

7519 required, for the cryomodules of the injector and the three LHC tunnel bypasses, the L-R option with two
7520 1 km long CW operated 2 K SC cavities is extremely demanding. The total installed cryogenic power will
7521 likely exceed 100 kW @4.5 K equivalent, approaching values of the LHC. However, these estimates are only
7522 based on currently proved data of the cavity Q0. The development of high Q SC cavities is being pursued
7523 in several laboratories and new encouraging results are on the horizon indicating improvement of quality
7524 having positive and direct impact for cryogenic requirements and respective plant sizes.

9.8 Beam dumps

9.8.1 Post collision line for 140 GeV option

The post collision line for the 140 GeV Linac option has to be designed taking care of minimising beam losses and irradiation. The production of beamsstrahlung photons and e^-e^+ pairs is negligible and the energy spread limited to 2×10^{-4} . A standard optics with FODO cells and a long field-free region allowing the beam to naturally grow before reaching the dump can be foreseen. The aperture of the post collision line is defined by the size of the spent beam and, in particular, by its largest horizontal and vertical angular divergence (to be calculated). A system of collimators could be used to keep losses below an acceptable level. Strong quadrupoles and/or kickers should be installed at the end of the line to dilute the beam in order to reduce the energy deposition at the dump window. Extraction line requirements:

- Acceptable radiation level in the tunnel
- Reasonably big transverse beam size at the dump window and energy dilution
- Beam line aperture big enough to host the beam: beta function and energy spread must be taken into account
- elements of the beam line must have enough clearance.

9.8.2 Absorber for 140 GeV option

Nominal operation with the 140 GeV Linac foresees to dump a 50 MW beam. This power corresponds to the average energy consumption of 69000 Europeans. An *Eco Dump* could be used to recover that energy; detailed studies are needed and are not presented here. Another option is to start from the concept of the ILC water dump and scale it linearly to the LHeC requirements. The ILC design is based on a water dump with a vortex-like flow pattern and is rated for 18 MW beam of electrons and positrons [?]. Cold pressurized water (18 m³ at 10 bar) flows transversely with respect to the direction of the beam. The beam always encounters fresh water and dissipates the energy into it. The heat is then transmitted through heat exchangers. Solid material plates(Cu or W) are placed beyond the water vessel to absorb the tail of the beam energy spectrum and reduce the total length of the dump. This layer is followed by a stage of solid material, cooled by air natural convection and thermal radiation to ambient, plus several meters of shielding. The size of the LHeC dump, including the shielding, should be 36 m longitudinally and 21 m transversely and it should contain 36 m³ of water. The water is separated from the vacuum of the extraction line by a thin Titanium Alloy (Ti-6Al-4V) window which has high temperature strength properties, low modulus of elasticity and low coefficient of thermal expansion. The window is primarily cooled by forced convection to water in order to reduce temperature rise and thermal stress during the passage of the beam. The window must be thin enough to minimise the energy absorption and the beam spot size of the undisrupted beam must be sufficiently large to prevent window damage. A combination of active dilution and optical means, like strong quadrupoles or increased length of the transfer line, can be use on this purpose. Further studies and challenges related to the dump design are:

- pressure wave formation and propagation into the water vessel
- remotely operable window exchange
- handling of tritium gas and tritiated water.

9.8.3 Energy deposition studies

Preliminary estimates, of the maximum temperature increase in the water and at the dump window, have been defined according to FLUKA simulation results performed for the ILC dump [?]. A 50 MW steady state power should induce a maximum temperature increase ΔT of 90° corresponding to a peak temperature

7567 of 215°. The water in the vessel should be kept at a pressure of about 35 bar in order to insure a 25° margin
 7568 from the water boiling point.

7569 FLUKA studies have been carried out for a 1 mm thick Ti window with a hemispherical shape. The beam
 7570 size at the ILC window is $\sigma_x = 2.42$ mm and $\sigma_y = 0.27$ mm; an extraction line with 170 m drift and 6 cm
 7571 sweep radius for beam dilution have been considered. A beam power of 25 W with a maximum heat source
 7572 of 21 W/cm³ deposited on the window have been calculated. This corresponds to a maximum temperature
 7573 of 77° for the minimum ionisation particle ($dE/dx = 2$ MeV \times cm²/g), no shower is produced because the
 7574 thickness of the window is significantly smaller than the radiation length. A maximum temperature lower
 7575 than 100° would require a minimum beam size of $\sigma_{x,y} = 1.8$ mm. A minimum β function of 8877 m would
 7576 be needed being the beam emittance $\varepsilon_{x,y} = 0.37$ nm for the undisturbed beam. The radius of the dump
 7577 window depends on the size of the disrupted beam. The emittance of the disrupted beam is $\varepsilon_{x,y} = 0.74$ nm
 7578 corresponding to a beam size $\sigma_{x,y}$ of 2.56 mm (for $\beta = 8877$ m); a radius R = 5 cm could then fit a 10 σ
 7579 envelope. The yield strength of the Ti alloy used for the window is $\sigma_{Ti} = 830$ MPa, this, according to the
 7580 formula:

$$\sigma_{Ti} = 0.49 \times \Delta P \frac{R^2}{d^2} \quad (9.10)$$

7581 where $\Delta P = 3.5$ MPa, imposes that the thickness of the window d is bigger than 2.3 mm.

7582 Length of the transfer line drift space and possible dilution have to be estimated together with possible
 7583 cooling.

7584 9.8.4 Beam line dump for ERL Linac-Ring option

7585 The main dump for the ERL Linac-ring option will be located downstream of the interaction point. Splitting
 7586 magnets and switches have to be installed in the extraction region and the extracted beam has to be tilted
 7587 away from the circulating beam by 0.03 rad to provide enough clearance for the first bending dipole of the
 7588 LHeC arc (see Fig. ??). A 90 m transfer line, containing two recombination magnets and dilution kickers,
 is considered to be installed between the LHeC and the LHC arcs(see Fig. ??). The beam dump will be

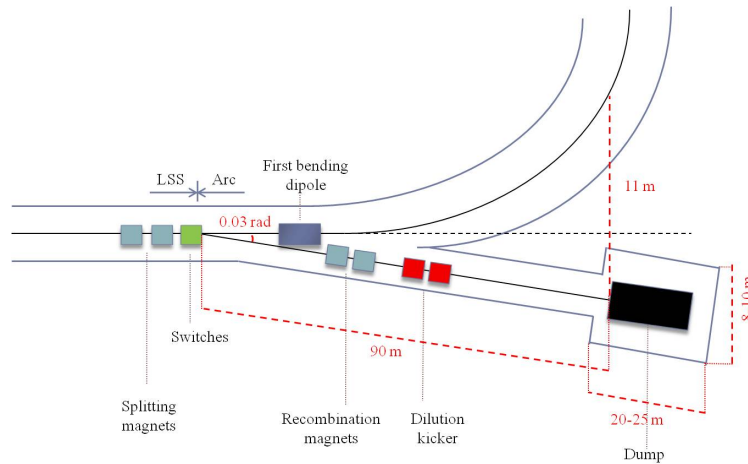


Figure 9.33: Scheme of the transfer line from end of long straight section of the linac and beam dump.

7589 housed in a UD62/UD68 like cavern at the end of the TL and the option of having service caverns for water
 7590 treatment and heat exchange is explored. An additional dump, and its extraction line, could be installed at
 7591 the end of the first linac(see Fig. ??) for beam setup purposes at intermediate energy. The same design as
 7592 for the nominal dump and extraction line would be applied.

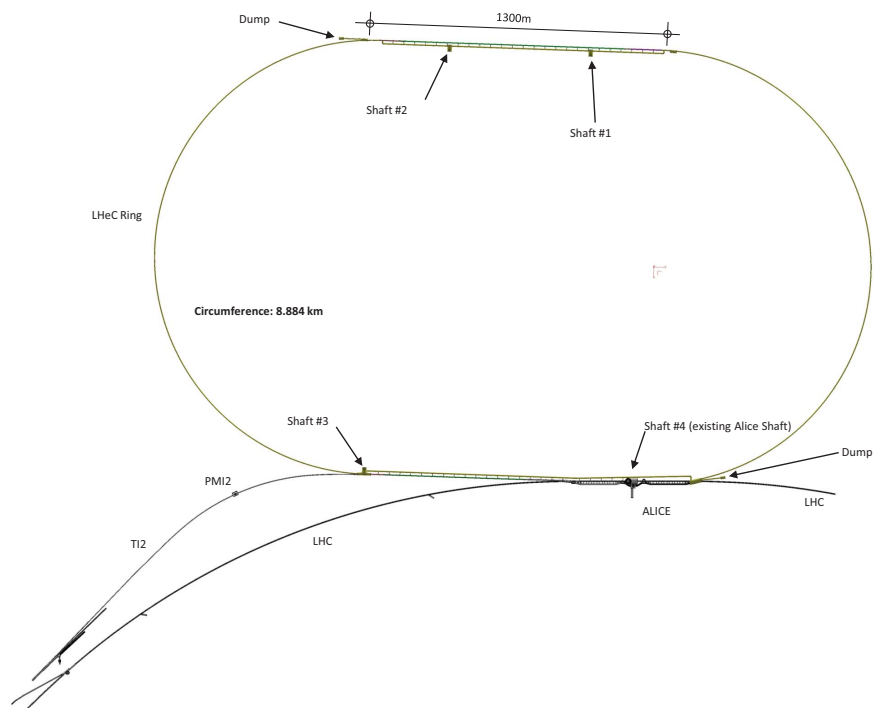


Figure 9.34: Two beam dumps are installed 90 m downstream the end of the long straight section of each linac for nominal operation and beam setup.

9.8.5 Absorber for ERL Linac-Ring option

During nominal operation a 0.5 GeV beam has to be dumped with a current of 6.6 mA. The setup beam will have a maximum current of 0.05 mA and an energy varying from 10 GeV to 60 GeV (10 GeV step size). Globally, a maximum beam power of 3 MW has to be dumped. The same design as for the 140 GeV option can be used by scaling linearly. In this case, a 3 m³ water dump (0.5 m diameter and 8 m length) with a 3 m × 3 m × 10 m long shielding has to be implemented. No show stopper has been identified for the 18 MW ILC dump, same considerations are valid in this less critical case.

9.8.6 Injection Region Design for Ring-Ring Option

A 10 GeV recirculating Linac will be used to inject the electrons in the LHeC. This will be built on the surface or underground and a transfer line will connect the linac to the LHeC injection region. At this stage a purely horizontal injection is considered, since this will be easier to integrate into the accelerator. The electron beam will be injected in the bypass around ATLAS, with the baseline being injection into a dispersion free region (at the right side of ATLAS). Bunch-to-bucket injection is planned, as the individual bunch intensities are easily reachable in the injector and accumulation is not foreseen. Two options are considered: a simple septum plus kicker system where single bunches or short trains are injected directly onto the closed orbit; and a mismatched injection, where the bunches are injected with either a betatron or dispersion offset.

Injection onto the closed orbit

The baseline option is injection onto the orbit, where a kicker and a septum would be installed in the dispersion free region at the right side of ATLAS bypass (see Fig. ??). Injecting the beam onto the closed orbit has the advantage that the extra aperture requirements around the rest of the machine from injection oscillations or mismatch are minimised. The kicker and septum can be installed around a Defocusing quadrupole to minimise the kicker strength required. The kicker-septum phase advance is 75°.

Some assumptions made to define the required element apertures are made in Table ??.

For the septum, an opening between injected and circulating beam of 47 mm is required, taking into account some pessimistic assumptions on orbit, tolerances and with a 4 mm thick septum. This determines the kicker strength of about 1 mrad.

Orbit variation	± 4 mm
Injection precision	± 3 mm
Mechanical/alignment tolerance	± 1 mm
Horizontal normalised emittance $\varepsilon_{n,x}$	0.58 mm
Vertical normalised emittance $\varepsilon_{n,y}$	0.29 mm
Injection mismatch (on emittance)	100 %
β_x, β_y @ Kicker	61.3 m, 39.7 m
β_x, β_y @ Septum	57.3 m, 42.3 m
σ_x, σ_y @ Kicker and Septum	0.8 mm, 0.4 mm

Table 9.23: Assumptions for beam parameters used to define the septum and kicker apertures

The septum strength should be about 33 mrad to provide enough clearance for the injected beam at the upstream lattice quadrupole, the yoke of which is assumed to have a full width of 0.6 m. This requires about 1.1 T m, and a 3.0 m long magnet at about 0.37 T is reasonable, of single turn coil construction with a vertical gap of 40 mm and a current of 12 kA.

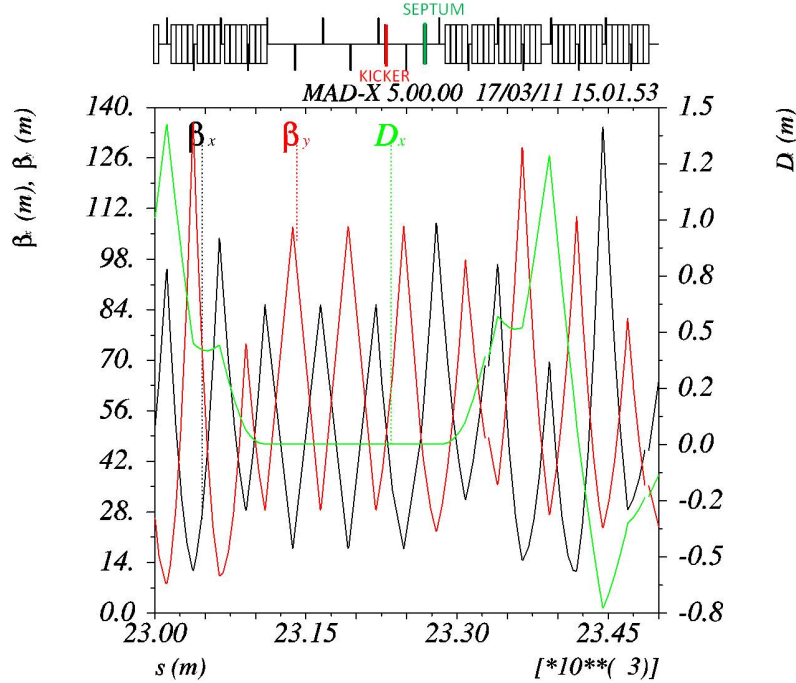


Figure 9.35: Injection optics is shown. The sequence starts ($s=0$) at the beginning of the dispersion suppressor at the left side of IP2 and proceeds clockwise, while the electron beam rotates counterclockwise (from right to left in the figure). The injection kicker and septum are installed in the dispersion free region of the bypass at the right side of ATLAS.

7625 The RF frequency of the linac is 1.3 GHz and a bunch spacing of 25 ns is considered, as the LHeC electron
 7626 beam bunch structure is assumed to match with the LHC proton beam structure. Optimally a train of 72
 7627 bunches would be injected, which would require a 1.8 μs flattop for the kickers and a very relaxed 0.9 μs rise
 7628 time (as for the LHC injection kickers [?]). However, this train length is too long for the recirculating linac
 7629 to produce, and so the kicker rise time and fall time requirements are therefore assumed to be about 23 ns,
 7630 to allow for the bunch length and some jitter.

7631 For a rise time $t_m = 23$ ns, a system impedance Z of 25 Ω is assumed, and a rather conservative system
 7632 voltage U of 60 kV.

7633 Assuming a full vertical opening h of 40 mm, and a full horizontal opening w of 60 mm (which allow ± 6
 7634 σ beam envelopes with pessimistic assumptions on various tolerances and orbit), the magnetic length l_m of
 7635 the individual magnets is:

$$l_m = ht_m Z / \mu_0 w = 0.31 \text{ m}$$

7636 For a terminated system the gap field B is simply:

$$B = \frac{\mu_0 U}{2hZ} = 0.037 \text{ T}$$

7637 As 0.03 Tm are required, the magnetic length should be 0.8 m, which requires 3 magnets. Assuming each
 7638 magnet is 0.5 m long, including flanges and transitions the total installed kicker length is therefore about
 7639 1.5 m.

7640 **Mismatched injection**

7641 A mismatched injection is also possible, Figure ?? with a closed orbit bump used to bring the circulating
 7642 beam orbit close to the septum, and then switched off before the next circulating bunch arrives.

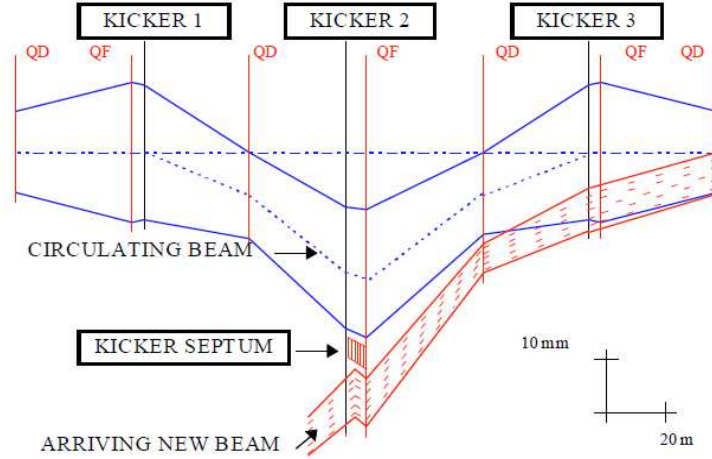


Figure 9.36: layout of mismatched injection system. To minimise kicker strengths the magnets are located near focusing quadrupoles.

7643 The injected beam then performs damped betatron or synchrotron oscillations, depending on the type of
 7644 mismatch used. In LHeC the damping time is about 3 seconds, so that to achieve the suggested 0.2 s period
 7645 between injections, a damping wiggler would certainly be needed - the design of such a wiggler needs to be
 7646 investigated.

Magnet	θ_x [mrad]	B dl [Tm]
KICKER1	1.35	0.04
KICKER2	2.37	0.08
KICKER3	0.55	0.02

Table 9.24: Kickers strength and integrated magnetic field needed to generate an orbit bump of 20 mm at the injection point.

7647 Three kickers (KICKER 1, KICKER 2 and KICKER 3 in Fig. ??) are used to generate a closed orbit
 7648 bump of 20 mm at the injection point. The kicker parameters are summarized in table ?. In case of betatron
 7649 mismatch, the bumpers can be installed in the dispersion free region considered for the injection onto the
 7650 closed orbit case discussed in the previous section (see Fig. ??). The installed magnet lengths of the kickers
 7651 should be 2 m, 3.5 m and 1 m respectively, for the kickers size, Z and U parameters given above. Overall the
 7652 kicker system is not very different to the system needed to inject onto the orbit.

7653 To allow for the possibility of synchrotron injection, the injection kicker-septum would need to be located
 7654 where the horizontal dispersion D_x is large. The beam is then injected with a position offset x and a
 7655 momentum offset δp , such that:

$$x = D_x \delta p$$

7656 The beam then performs damped synchrotron oscillations around the ring, which can have an advantage
 7657 in terms of faster damping time and also smaller orbit excursions in the long straight sections, particularly
 7658 experimental ones, where the dispersion functions are small.

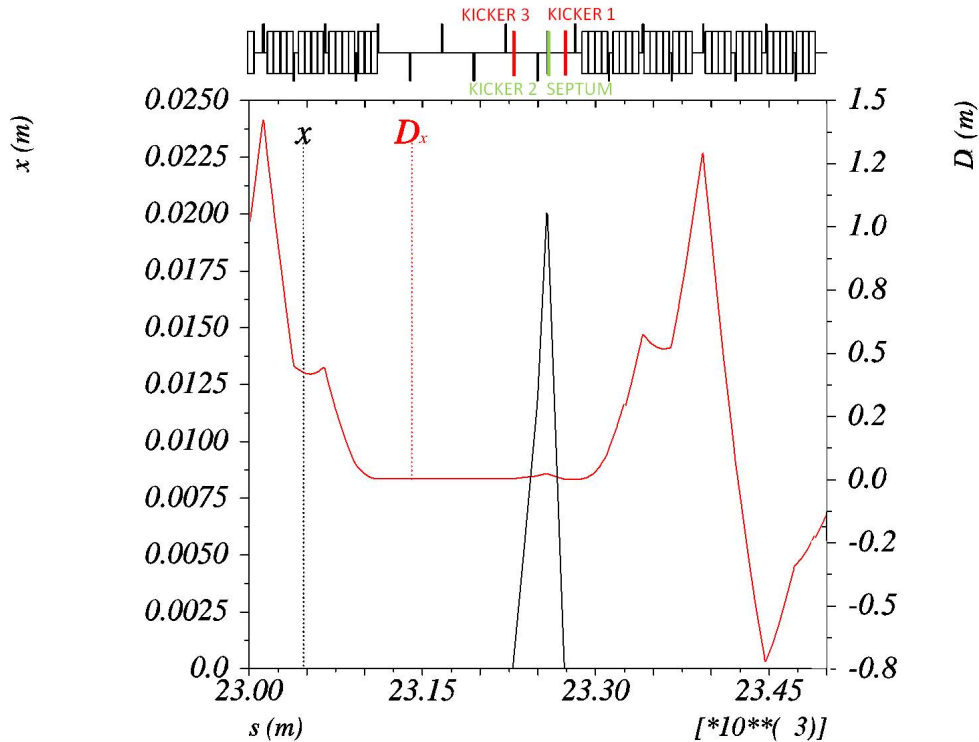


Figure 9.37: A closed orbit bump of 20 mm is generated by three kickers installed in the dispersion free region located at the right side of the bypass around ATLAS (electron beam moves from right to left in the Figure).

7659 As an alternative to the fast (23 ns rise time) kicker for both types of mismatched injection, the kicker
 7660 rise- and fall-time could be increased to almost a full turn, so that the bump is off when the mismatched
 7661 bunch arrives back at the septum. This relaxes considerably the requirements on the injection kicker in
 7662 terms of fall time. However, this does introduce extra complexity in terms of synchronizing the individual
 7663 kicker pulse lengths and waveform shapes, since for the faster kicker once the synchronization is reasonably
 7664 well corrected only the strengths need to be adjusted to close the injection bump for the single bunch.

7665 9.8.7 Injection transfer line

7666 The injection transfer line from the 10 GeV injection recirculating linac is expected to be straightforward.
 7667 A transfer line of about 900 m, constituted by 15 FODO cells, has been considered. The phase advance of
 7668 each cell corresponds to about 100° .

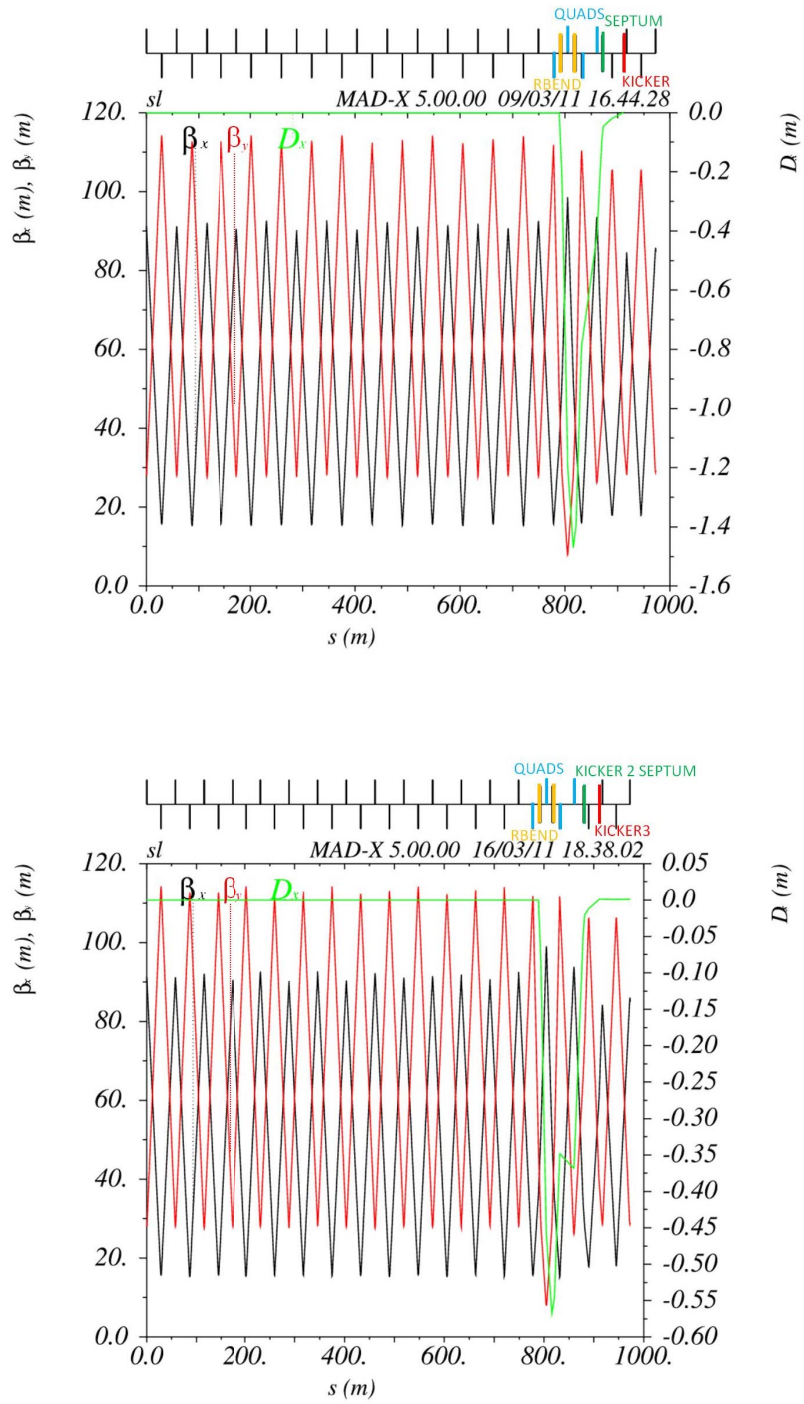


Figure 9.38: Transfer line optics for the injection onto orbit case (top) and mismatched injection case (bottom).

7669 The last two cells are used for optics matching. In particular, four quadrupoles, 1 m long each, are used
 7670 for β_x and β_y matching, while two rectangular bending magnets, 5 m long each, are used for matching the
 7671 horizontal dispersion D_x to 0 (maximum $D_x = -1.48$ m for the injection onto closed orbit case and maximum
 7672 $D_x = -0.57$ m for the mismatched injection case). The “good field region” for a 6σ beam envelope requires
 7673 a minimum half-aperture, in the matching insertion, of 15 mm and 10 mm for the focusing and defocusing
 7674 quadrupoles respectively, corresponding to a pole tip field of about 0.02 T. The maximum strength of the
 7675 bending magnets, which are used for dispersion matching, corresponds to about 39 mrad. This requires
 7676 1.3 T m and a maximum field of 0.3 T. A single turn coil of 9.5 kA with a vertical gap of 40 mm could be
 7677 used.

7678 9.8.8 60 GeV internal dump

7679 An internal dump will be needed for electron beam abort. The design for LEP [?] consisted of a boron carbide
 7680 spoiler and an Aluminum alloy (6% copper, low magnesium) absorbing block (0.4 m \times 0.4 m \times 2.1 m long).
 7681 A fast kicker was used to sweep eight bunches, of 8.3×10^{11} electrons at 100 GeV, onto the absorber. The
 7682 first bunch was deflected by 65 mm and the last by 45 mm, inducing a temperature increase ΔT of 165°.

7683 The bunch intensity for the LHeC is about a factor of 20 lower than for LEP and beam size is double (σ
 7684 = 0.5 mm in LEP and $\sigma = 1$ mm in LHeC).

7685 The lower energy (60 GeV) and energy density permit to dump 160 bunches in 20 mm to obtain the
 7686 same ΔT as for LEP. However, in total LHeC will be filled with 2808 bunches, which means that significant
 7687 additional dilution will be required. A combination of a horizontal and a vertical kicker magnet can be used,
 7688 as an active dilution system, to paint the beam on the absorber block and increase the effective sweep length.
 7689 The kickers and the dump can be located in the bypass around CMS, in a dispersion free region (see fig. ??).

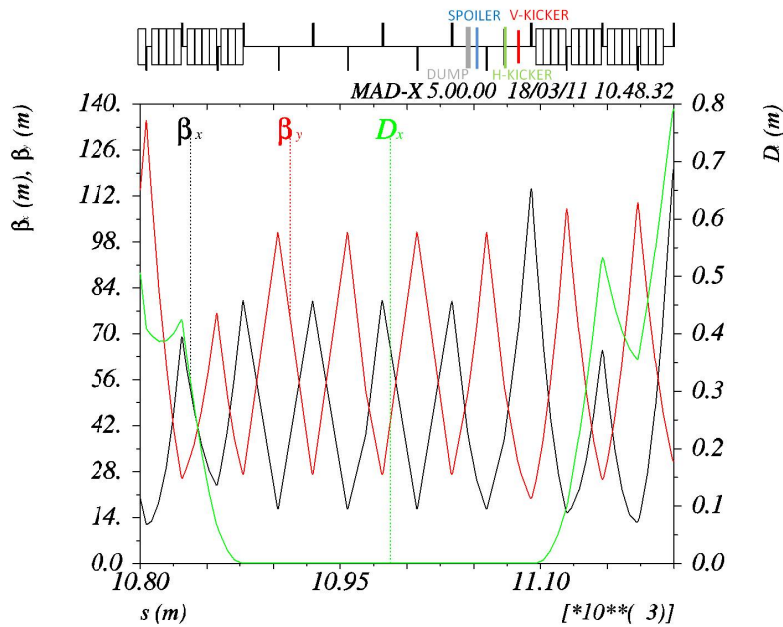


Figure 9.39: The optics in the region of the CMS bypass where the beam dump system could be installed is shown. The system consists of two kickers, one spoiler and a Carbon-composite absorber which are installed in the dispersion free region of the bypass at the right side of CMS (beam proceeds from right to left in the Figure).

7690 It is envisaged to use Carbon-composite for the absorber block, since this has much better thermal and
 7691 mechanical properties than aluminum. The required sweep length is then assumed to be about 100 mm,

7692 from scaling of the LEP design. The minimum sweep speed in this case is about 0.6 mm per μs , which
 7693 means about 54 bunches per mm. Taking into account the energy and the beam size, this represents less
 7694 than a factor 2 higher energy density on the dump block, compared to the average determined by the simple
 7695 scaling, that should be feasible using carbon. More detailed studies are required to optimise the diluter and
 7696 block designs. Vacuum containment, shielding and a water cooling system has to be incorporated. A beam
 7697 profile monitor can be implemented in front of each absorber to observe the correct functioning of the beam
 7698 dump system.

7699 The vertical kicker would provide a nominal deflection of about 55 mm (see fig. ??), modulated by $\pm 13\%$
 7700 for three periods during the 100 μs abort (see fig. ??), while the horizontal kicker strength would increase
 7701 linearly from zero to give a maximum deflection at the dump of about 55 mm (see Fig. ?? and Fig. ??). This
 7702 corresponds to system kicks of 2.7 and 1.6 mrad respectively.

7703 Parameters characterizing the kicker magnets are presented in Table ??.

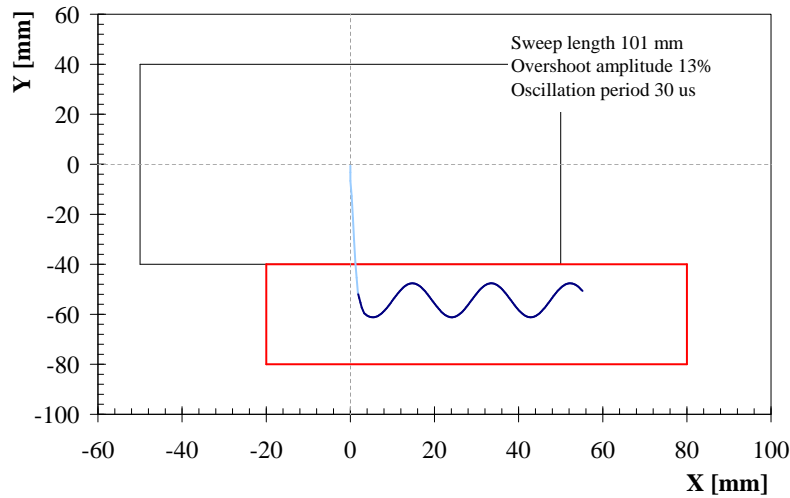


Figure 9.40: A vertical and a horizontal kicker are used to dilute the beam on the dump absorbing block.

7704 In the present lattice the dump is placed ~ 30 m downstream of the kickers, corresponding to a phase
 7705 advance of about 63° in the horizontal plane and 35° in the vertical plane. The minimum horizontal and
 7706 vertical aperture at the dump are 26 mm and 22 mm respectively (at the dump: $\beta_x = 37$ m and $\beta_y = 55$ m,
 7707 using the same beam and machine parameter assumptions, as presented in Table ??). The kicker system
 7708 field rise time is assumed to be at most 3 μs (abort gap) and the kicker field flat-top at least 90 μs as for the
 7709 LHC proton beam. Same design as for the LHC dump kicker magnets MKD can be used: a steel yoke with
 7710 a one-turn HV winding. These magnets can provide a magnetic field in the gap of 0.34 T. For a magnetic
 7711 length of 0.31 m ($Z = 25 \Omega$ and $U = 60$ kV), a total installed kicker length of 1.5 m for the horizontal system
 7712 and 2.5 m for the vertical system has to be considered.

7713 A spoiler (one-side single graphite block: 0.3 m \times 0.10 m \times 0.5 m long) can be installed 5 m upstream
 7714 of the dump at the extraction side to provide further dilution.

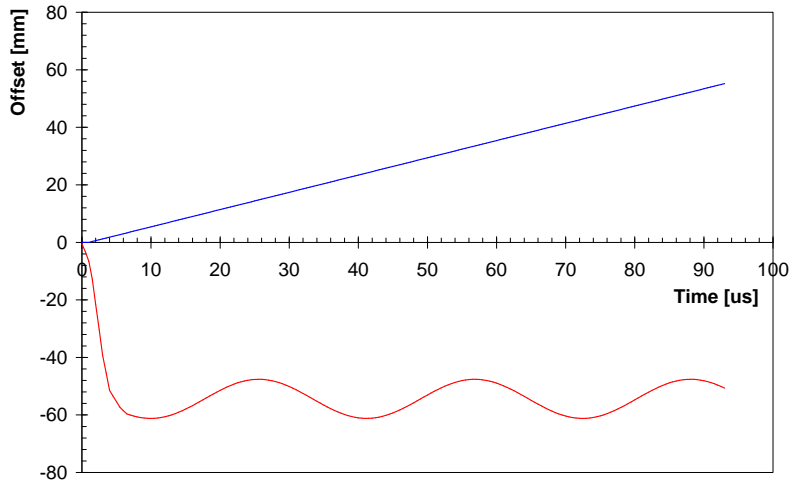


Figure 9.41: The strength of the vertical kicker oscillates in time by $\pm 13\%$ around its nominal value. The deflection provided by the horizontal kicker increases almost linearly in time.

	MKDV	MKDH
Length [m]	2.5	1.5
Maximum angle [mrad]	2.7	1.6
Maximum field [T]	0.34	0.34
Rise/Fall time [ns]	800	800
Flat top length [μ s]	90	90

Table 9.25: Parameters characterising vertical and horizontal kicker magnets of the extraction system.

Chapter 10

Civil Engineering and Services

10.1 Overview

Infrastructure costs for projects such as LHeC, typically represent approximately one third of the overall budget. For this reason, particular emphasis has been placed on Civil Engineering and Services studies, to ensure a cost efficient conceptual design. This chapter provides an overview of the designs adopted for the key infrastructure cost driver, namely, civil engineering. The costs for the other infrastructure items such as cooling & ventilation, electrical supply, transport & installation will be pro-rated for the CDR and studied in further detail during the next phase of the project. For the purposes of this conceptual design report, the civil engineering (CE) studies have assumed that the Interaction Region (IR) for LHeC will be at LHC Point 2, which currently houses the ALICE detector. As far as possible, any surface facilities have been situated on existing CERN land. Both the Ring-Ring and Linac-Ring underground works will be discussed in this Chapter. Surface buildings/structures have not been considered for the CDR.

10.2 Location, Geology and Construction Methods

This section describes the general situation and geology that can be expected for both the Ring-Ring and Linac Ring options.

10.2.1 Location

The proposed siting for the LHeC project is in the North-Western part of the Geneva region at the existing CERN laboratory. The proposed Interaction Region is fully located within existing CERN land at LHC Point 2, close to the village of St.Genis, in France. The CERN area is extremely well suited to housing such a large project, with the very stable and well understood ground conditions having several particle accelerators in the region for over 50 years. The civil engineering works for the most recent machine, the LHC were completed in 2005, so excellent geological records exist and have been utilised for this study to minimise the costs and risk to the project. Any new underground structures will be constructed in the stable Molasse rock at a depth of 100-150m in an area with little seismic activity. CERN and the Geneva region have all the necessary infrastructure at their disposal to accommodate such a project. Due to the fact that Geneva is the home of many international organizations excellent transport and communication networks already exist. Geneva Airport is only 5km from the CERN site, with direct links and a newly constructed tramway, shown in Figure ??, gives direct access from the Meyrin Site to the city centre.

The governments of France and Switzerland have long standing agreements concerning the support of particle accelerators in the Geneva region, which make it very likely that the land could be made available free of charge, as it was for previous CERN projects.



Figure 10.1: Tram stop outside CERN Meyrin Site.

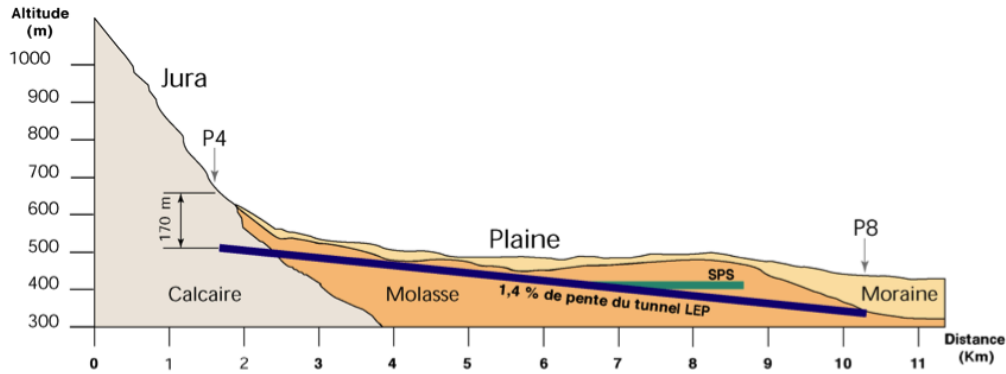


Figure 10.2: Simplified cross section of the LHC housed mostly in Molasse Rock

10.2.2 Land Features

The proposed location for the accelerator is situated within the Swiss midlands embedded between the high mountain chains of the Alps and the lower mountain chain of the Jura. CERN is situated at the feet of the Jura mountain chain in a plain slightly inclined towards the lake of Geneva. The surface terrain was shaped by the Rhone glacier which once extended from the Alps to the valley of the Rhone. The water of the area flows to the Mediterranean Sea. The absolute altitude of the surface ranges from 430 to 500m with respect to sea level. The physical positioning for the project has been developed based on the assumption that the maximum underground volume possible should be housed within the Molasse Rock and should avoid as much as possible any known geological faults or environmentally sensitive areas. The shafts leading to any on-surface facilities have been positioned in the least populated areas, however, as no real discussions have taken place with the local authorities, the presented layouts can only be regarded as indicative, for costing purposes only.

10.2.3 Geology

The LHeC project is within the Geneva Basin, a sub-basin of the large North Alpine Foreland (or Molasse) Basin. This is a large basin which extends along the entire Alpine Front from South-Eastern France to Bavaria, and is infilled by Molasse deposits of Oligocene and Miocene age. The basin is underlain by crystalline basement rocks and formations of Triassic, Jurassic and Cretaceous age. The Molasse, comprising an alternating sequence of marls and sandstones (and formations of intermediate compositions) is overlain by Quaternary glacial moraines related to the Würmian and Rissian glaciations. Figure ?? shows a simplified layout of the LHC.

10.2.4 Site Development

As most of the new works are on a close to existing facilities, it is assumed for the CDR that the existing facilities such as restaurant, main access, road network etc are sufficient and have not been costed. However, for the parts located outside the existing fenceline, but within CERN property, the following items will have to be included in the costs:

- Roads and car parks
- Drainage networks
- Landscaping and planting
- Spoil dumps



Figure 10.3: TBM Gripper type machine used for Neutrino tunnel at CERN (left) and roadheader type machine (right).

7776 All temporary facilities needed for the construction works have also been included in the cost estimate.

7777 10.2.5 Construction Methods

7778 It is envisaged that Tunnel Boring Machines (TBMs) will be utilised for the main tunnel excavation greater
 7779 than approximately 2km in length. In the Molasse rock, a shielded TBM will be utilised, with single pass pre-
 7780 cast segmental lining, followed by injection grouting behind the lining. For planning and costing exercises,
 7781 an average TBM advancement of 25m per day, or 150m per week is predicted.

7782 The second phase excavation will be executed using a roadheader type machine. Both machines types are
 7783 shown in figure ?? . Any new shafts that have to pass through substantial layers of water bearing moraines
 7784 (for example at CMS) will have to utilize the ground freezing technique. This involves freezing the ground
 7785 with a primary cooling circuit using ammonia and a secondary circuit using brine at -23C, circulating in
 7786 vertical tubes in pre-drilled holes at 1.5 metre intervals. This frozen wall allows excavation of the shafts in
 7787 dry ground conditions and also acts as a retaining wall. Figure ?? shows this method being utilized for LHC
 7788 shaft excavation at CMS.

7789 10.3 Civil Engineering Layouts for Ring-Ring

7790 The Ring-Ring solution will require new bypass tunnels at both Point 1 (currently housing the LHC Atlas
 7791 detector) and Point 5 (CMS). Both of the bypass tunnels are on the outside of the LHC ring. Figure ?? shows
 7792 the bypass tunnel in blue needed around Point 1. This tunnel is 730m long and has an internal diameter
 7793 of 4.5m. Two new 12m diameter shafts are required to allow access to construct the underground areas
 7794 with minimum disruption to LHC operations. Underground areas are made available for RF/Cryogenic and
 7795 general services. Two junction caverns will be excavated to create a liaison with the LHC tunnel.

7796 Waveguides ducts (0.9m diameter) will connect the LHeC Bypass tunnel to the RF cavern, as shown in
 7797 Figure ?? . In order to position the bypass as close as possible to the LHC ring, it has been assumed that
 7798 the LHeC beampipe can be accommodated within the existing survey gallery, and pass through the ATLAS
 7799 experimental hall.

7800 The Bypass around CMS Point 5 is 1km long with an internal tunnel diameter of 4.5m. Only one new
 7801 shaft is required for excavation works. A roadheader type machine will be used for excavation, with the new
 7802 tunnel position as close as possible to the LHC tunnel as not to induce movements or create operational
 7803 problems to the existing facilities. Figure ?? shows the new bypass tunnel and service cavern required around
 7804 CMS.

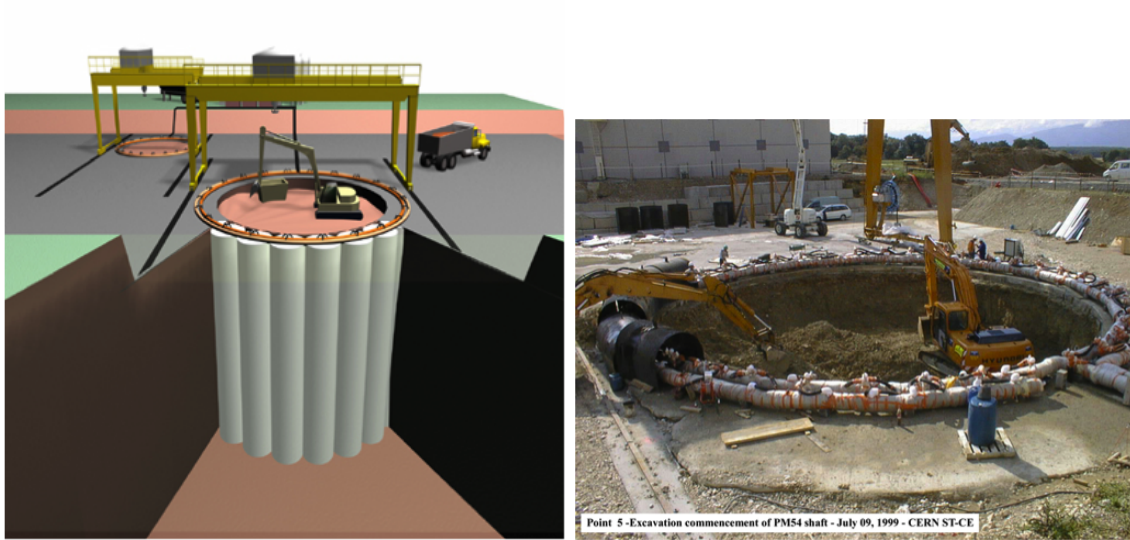


Figure 10.4: LHC Shaft PM54, linking up cylinders of ice to construct a temporary wall.

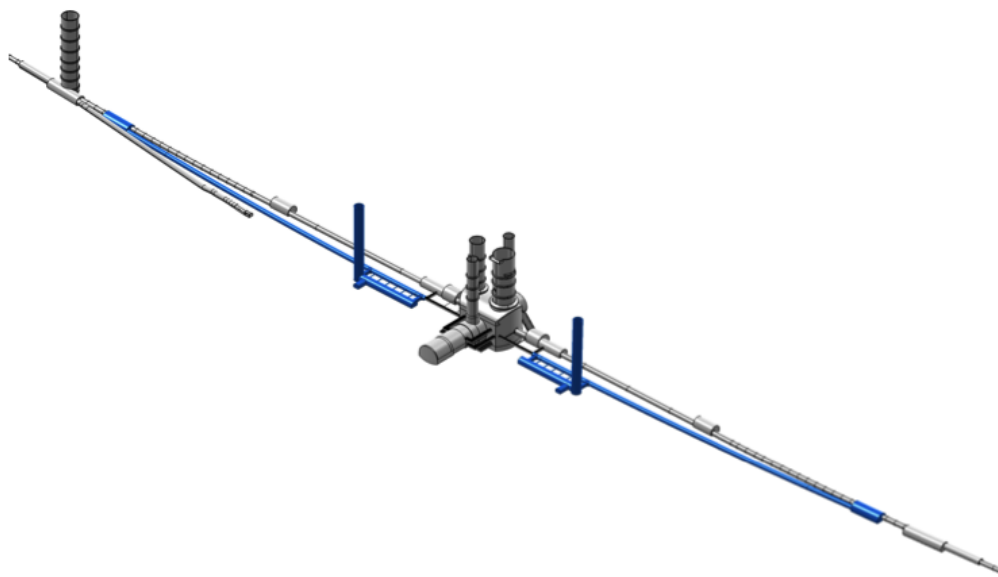


Figure 10.5: Ring-Ring Bypass around ATLAS Point 1.

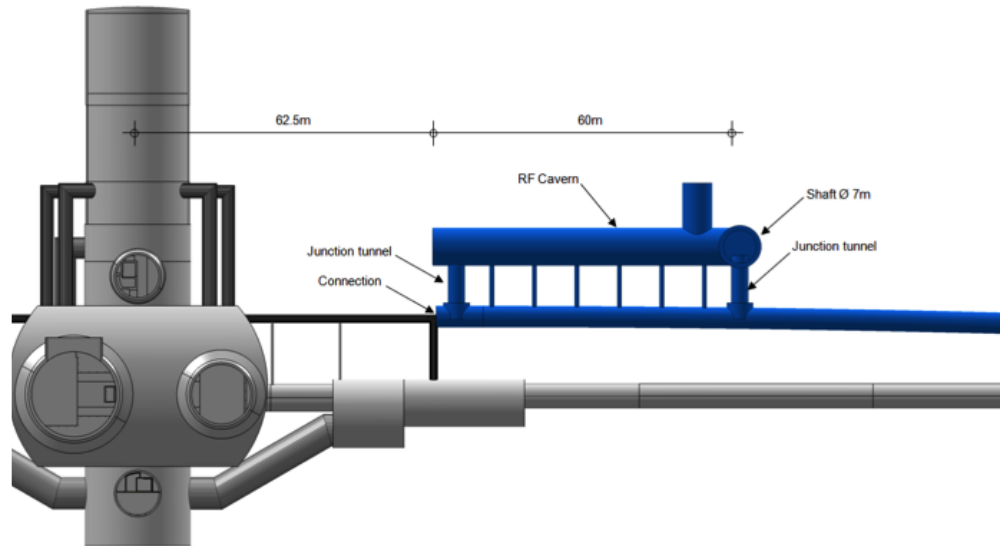


Figure 10.6: Cryo and RF Caverns at Point 1.

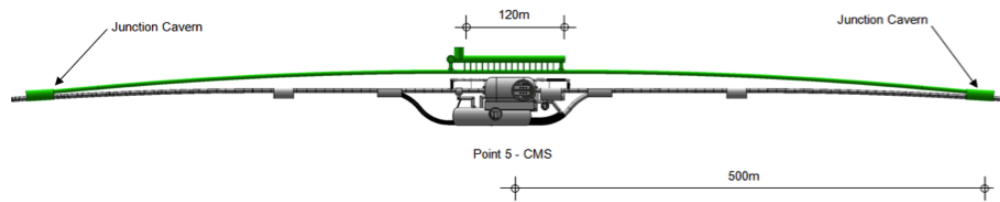


Figure 10.7: Ring-Ring Bypass around CMS Point 5.

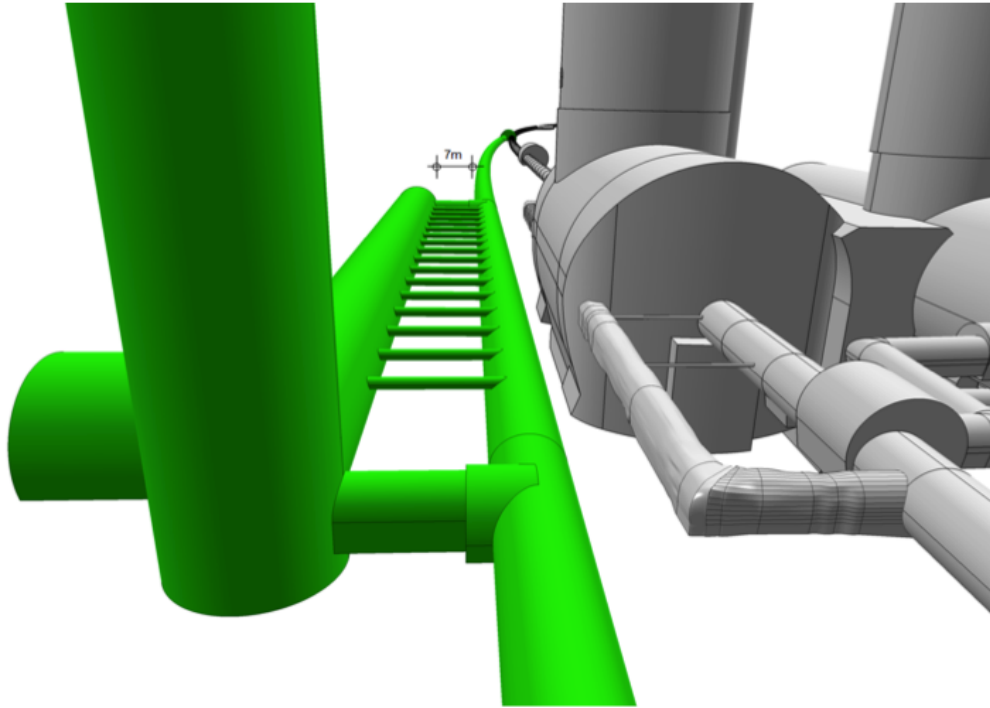


Figure 10.8: 3d model of Ring-Ring Bypass around CMS Point 5 The civil engineering for the e- injection complex for the Ring-Ring option has not been studied for the CDR.

7805 Figure ?? shows a 3d model of the bypass around the CMS Point 5. The new excavations will have a
 7806 minimum of 7m of Molasse rock separating the new works from existing LHC structures. This is to avoid
 7807 any unwanted deformation or vibration problems on the existing LHC structures.

7808 10.4 Civil Engineering Layouts for Linac-Ring

7809 For the CDR it has been assumed that the 60 GeV Energy Recovery Linac (ERL) will be located around the
 7810 St.Genis area of France, injecting directly into the LHC ALICE Cavern at point 2. Approximately 10km of
 7811 new tunnels (5m and 6m diameter), 2 shafts and 9 caverns will be required. The majority of civil engineering
 7812 works can be completed while LHC is operational. Figure ?? highlights the area on the LHC where the new
 7813 ERL will be situated.

7814 The ERL will be positioned inside the LHC Ring, in order to ensure that new surface facilities are located,
 7815 as much as possible, on existing CERN land. Secondary tunnels running alongside the long straight sections
 7816 will house RF, Cryogenic and Services for the machine. One of the long straight sections is shown in Figure
 7817 ??. The entire ERL will be tilted in order to follow a suitable layer of Molasse rock. On average the ERL
 7818 will be tilted approximately 1.4%, dipping towards Lake Geneva, as per LHC.

7819 10.5 Summary

7820 From a civil engineering point of view, both the Ring-Ring and Linac-Ring options are feasible. The Ring-
 7821 Ring option will provide a cheaper solution, however, with a marginally increased risk to LHC activity, due
 7822 to the fact that most of the excavation works being in close proximity to the existing installations. The
 7823 Linac-Ring option is the cleaner solution from a civil engineering point of view, with much less risk to LHC,
 7824 but with substantial extra cost and greater time needed for environmental and building permit procedures.

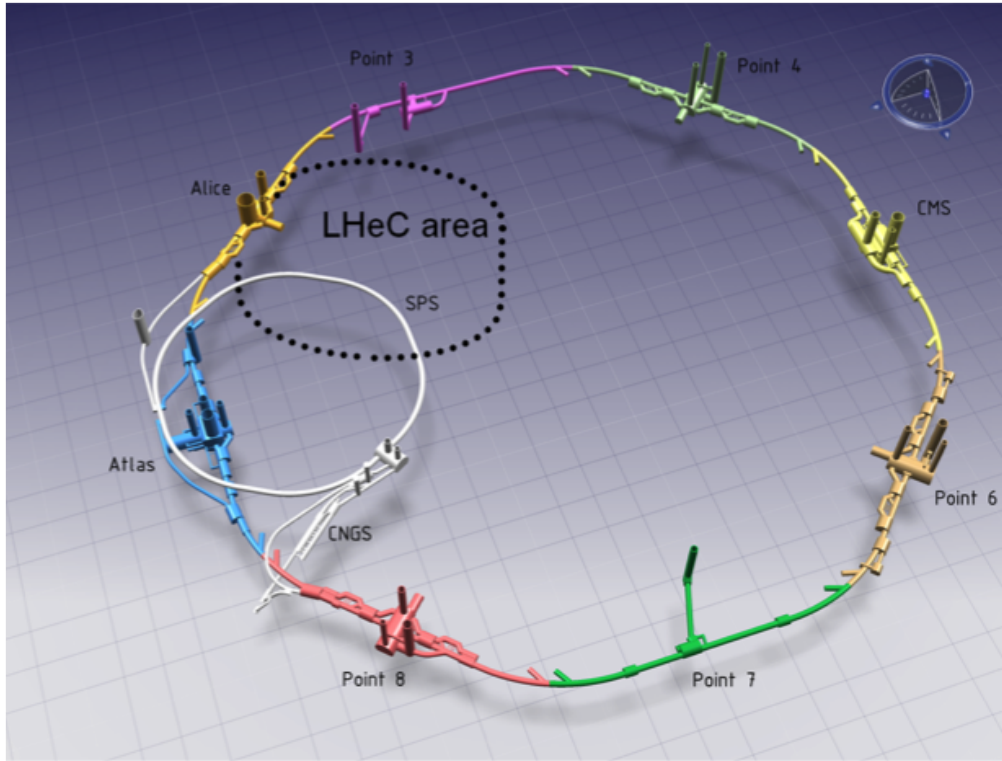


Figure 10.9: Schematic model of ERL position injecting into ALICE.

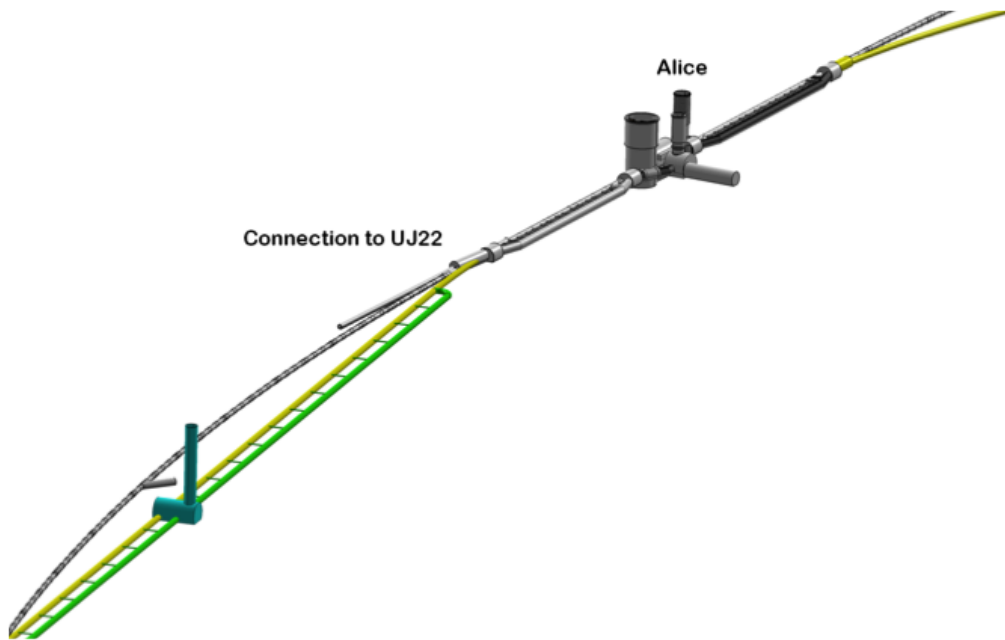


Figure 10.10: ERL Injection area into ALICE and RF/Cryo/Services Cavern (yellow & green).

Chapter 11

Project Planning

We base the planning of the LHeC project on the assumption that the LHC machine will reach the end of its lifetime when the High Luminosity LHC project reaches its design goal of $3000 fb^{-1}$. Figure ?? shows the current status of the CERN planning for the LHC related upgrade projects. The current planning foresees three long shutdowns:

- Long Shutdown 1 (LS1) for repairing the faulty splice connections in the LHC and allowing operations at nominal energy of 7 TeV.
- Long Shutdown 2 (LS2) for consolidating the LHC for operation above nominal beam intensities
- Long Shutdown 3 (LS3) for implementing the HL-LHC upgrade installations.

Figure ?? shows the resulting evolution of the integrated luminosity per experiment over time assuming the LHC performance stabilizes at nominal luminosity after LS1. Figure ?? shows a similar evolution of the integrated luminosity assuming the LHC performance stabilizes at ultimate luminosity after LS1.

In both scenarios, the LHC reaches a total integrated luminosity of ca. $200 fb^{-1}$ before LS3 and the installation of the HL-LHC upgrade. The HL-LHC project aims at a generation of $200 fb^{-1}$ to $300 fb^{-1}$ per year [?] and one can assume that the HL-LHC design goal can be reached by between 9 and 13 years after the LS3. Assuming a one year long shutdown for LS3, this implies the accumulation of $3000 fb^{-1}$ by ca. 2030 to 2035. Aiming for the LHeC at an exploitation time of 10 years the LHeC operation should therefore start together with the HL-LHC operation after the LS3 in 2022.

We base our estimates for the project time line on the experience of other projects, such as (LEP, LHC and LINAC4 at CERN and the European XFEL at DESY and the PSI XFEL). In the following we will analyze separately the required time line for the project construction for the RF system development, the production of the magnet system, the required civil engineering and the installation of the accelerator components in the tunnel.

The superconducting RF development for LEP and LHC both required approximately 2 to 3 years for the cavity prototyping and testing and approximately 5 to 6 years of test stand operation of the superconducting RF cavity modules adding up to a total time of approximately 6 to 8 years from first prototype to final installation. The first LHC cavity prototypes were constructed in 2000 with a final installation of the 4 cryo modules in the LHC tunnel in 2006. The first LEP superconducting RF cavity was tested in LEP in 1991. LEP2 operation started in 1996 but still required 2 years of progressively commissioning all cryo modules in building B180 before their final installation in the LEP tunnel. The last cryo module of the 73 4-cell LEP cryo modules was installed in the LEP tunnel in 1999. Both RF installations featured extensive test stand operations. The LEP RF system had cavity test stands in building SM18 and a separate power test in building B180 which were operated from 1994 until 1999. The LHC RF system had both, the cavity and the power test stands, in SM18. The LHC test stands were operated from 2002 until 2006 (the test stand operation was slowed down at the end due to difficulties with the RF coupler design). In both cases, LEP



Figure 11.1: Draft version of the CERN MTP as of June 2011.

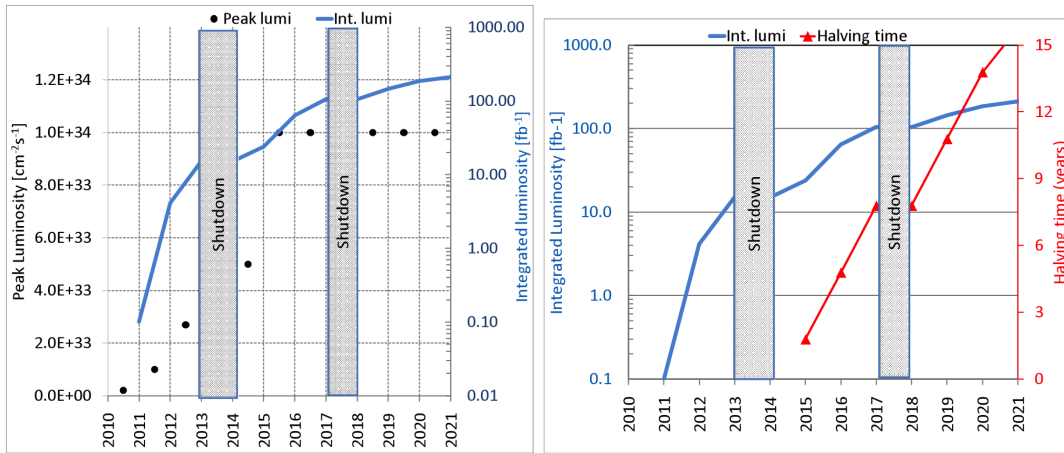


Figure 11.2: Left: Projected luminosity evolution for the LHC assuming the LHC reaches nominal performance levels after the first long shutdown (LS1) and then remains at nominal performance after 2016. Right: The resulting evolution of the integrated luminosity for the LHC experiments. [?].

7861 and LHC, the RF system installation was therefore accompanied by a 5 to 6 year test stand operation which
 7862 overlapped with the actual installation period in the tunnel [?].

7863 The LHeC linac-ring RF system requires 118 cryomodules of eight 721 MHz 5-cell superconducting RF
 7864 structures, amounting to a total of approximately 950 structures or thirteen times the number of LEP RF
 7865 structures. It seems therefore reasonable to assume for the LHeC linac-ring RF system a total time of
 7866 10 years from first prototype construction to final installation in the tunnel with a dedicated test stand
 7867 operation for approximately 8 years. ¹ The LHeC ring-ring RF system corresponds approximately to the
 7868 LEPII RF system in terms of total power and overall length of the RF installation and it seems reasonable
 7869 to assume for the LHeC ring-ring RF system a slightly shorter time scale. Here we assume the same time
 7870 scale as for LEPII: a total time of 8 years from first prototype construction to final installation in the tunnel
 7871 with a dedicated test stand operation for approximately 6 years.

7872 For the magnet system we base a first order estimate of the required timescale for the magnet production
 7873 and installation on the experience with LHC transfer lines. The LHC transfer lines have a total length of
 7874 6 km and feature a total of ca. 350 normal conducting magnets. The magnet production extended over 3
 7875 years with a production rate of ca. 10 magnets per month [?]. It is, however, important to underline that the
 7876 production rate was not limited by production capacity but rather, was following the project requirements
 7877 and the CERN ability for magnet testing after reception at CERN. Both LHeC options feature a relatively
 7878 large number of magnets, approximately 4000 magnets. Compared to the LHC transfer line magnets, these
 7879 magnets are much more compact and one can assume that the magnet production rate can be significantly
 7880 larger than that for the LHC transfer lines. The LHeC magnet production requires therefore industrial
 7881 production rates featuring several contractors and production lines. The price to pay for such an industrial
 7882 production scheme will be the requirement for a pre-series production and a thorough quality assurance

¹Faster production rates could be possible by using several manufacturers in parallel as it is, for example, planned for the ILC. The ILC project requires approximately 15000 cavities and aims at a 10 to 15 times faster production rate as compared to the XFEL cavity production. But such an approach requires long preparation studies for the industrialization (the ILC assumes more than 3 years for such studies [?]), dedicated production test facilities (the ILC has production test facilities at three different laboratories: DESY, KEK and FNAL), an extensive pre-series production and test bench operation for verifying the cavity and cryomodule design before launching the mass production (the ILC project has more than 20 years experience of pre-series production and test bench operation in form of the TTF, FLASH and XFEL installations) and a large production volume so that it is lucrative for several manufacturers to split the overall production while still undertaking significant investments for the production lines. Such an approach can not be applied to a 'small' project like the LHeC and can therefore not lead to an overall faster production time line (unless one uses the ILC cavities and joins the production contracts for the ILC).

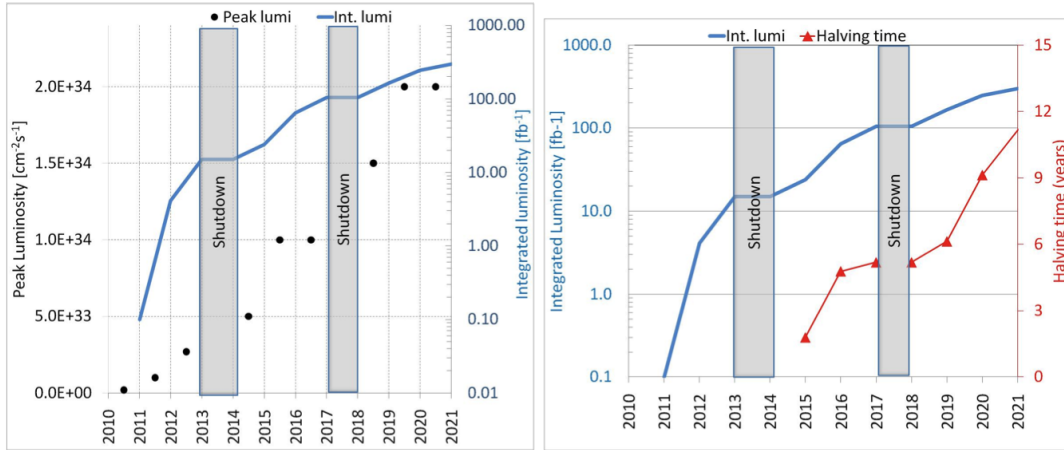


Figure 11.3: Left: Optimistic projection of the luminosity evolution for the LHC assuming the LHC reaches ultimate performance levels after the first long shutdown (LS2). Right: The resulting evolution of the integrated luminosity for the LHC experiments. [?].

7883 over the whole production process. All LHeC magnets will require furthermore a detailed geometry and
 7884 field quality measurement program after reception at CERN. In the following we assume 1-2 years for the
 7885 pre-series production and first testing followed by potential design modifications and a peak production rate
 7886 of ca. 60 dipoles and 20 quadrupoles per month (ca. ten times the production rate of the LHC transfer
 7887 lines). These assumptions lead to a total construction time of ca. 4 to 6 years and a total of 6 to 8 years
 7888 from magnet design to final installation in the tunnel.

7889 For the civil engineering we base our first order estimate for the time line on the estimates for the CLIC
 7890 500 GeV option which features a total length that is comparable to the 60 GeV linac-ring option. The
 7891 civil engineering work requires for the LHeC linac-ring option the construction of ca. 10 km underground
 7892 installations which is estimated to take approximately 4 years construction time (the required underground
 7893 construction for the ring-ring solution is smaller but will occur in the direct vicinity of the main LHC tunnel).
 7894 The installation of the technical infrastructure (water, electricity etc.) will take approximately 2 years and
 7895 the final installation of the machine elements in the tunnel another 2 years. All three activities can partially
 7896 overlap, leading to an estimate of the total construction time of ca. 6 years [?].

7897 For all other components (cryogenics, injector complex, detector etc.) we assume for the moment that
 7898 their development and installation can be done in the shadow of the three components mentioned above.

7899 In summary, we estimate:

- 7900 • Between 8 and 10 years for the production of the RF system (time from prototype to final installation
 7901 in the tunnel) with dedicated test stand operation over 6 to 8 years.
- 7902 • Between 6 and 8 years for the production of the magnet system (time from prototype to final installation
 7903 in the tunnel) with several production lines and test facilities for the quality assurance during the
 7904 magnet production.
- 7905 • Approximately 6 years for the civil engineering work and actual installation in the tunnel.
- 7906 • All other components such as injector complex, cryogenics installation, detector construction etc, are
 7907 assumed to lie in the shadow of the above components.

7908 The above time estimates appear as reasonable estimates compared to the planning of other projects like
 7909 the European XFEL at DESY, the European Spallation Source (ESS) in Sweden, LINAC4 at CERN and
 7910 the PSI XFEL facilities:

- 7911 • The European XFEL project features a 3 km long superconducting linear accelerator (comparable in
7912 size to the linac section of the LHeC linac-ring option) started the civil engineering in January 2009
7913 and plans for completing the civil engineering work in end 2012 (\rightarrow 4 years of bare civil engineering
7914 work) [?]. The project had in form of the FLASH (TTF) installation a pre-series production of 150
7915 1.3 GHz 9-cell cavity modules that went from 1993 to 2005 (12 years) and an extended test stand
7916 operation. The XFEL project plans for an industrial production of more than 600 1.3 GHz 9-cell
7917 cavity module from 2010 until 2014 (4 to 5 year production time) [?].
- 7918 • The ESS facility features ca. 300 m superconducting RF sections and plans for a construction phase
7919 of 9 years (2009 until 2017) with first operation in 2018 and full performance reach in 2025 [?].
- 7920 • The LINAC4 project is a ca. 200 m long normal conducting linac installation which has a ca. 3 year
7921 long civil engineering construction period, followed by one year of infrastructure installation and 1.5
7922 years of waveguide and accelerator component installation, amounting to a total construction period of
7923 ca. 5.5 years (start of civil engineering in beginning 2008 and end of the accelerator installation by mid
7924 2013) which seems rather long compared to the civil engineering estimates for the LHeC (installation
7925 length of ca. 10 km and ca. 100 m underground; ca. 50 times the LINAC4 installation length which
7926 is mainly above surface) [?].
- 7927 • The PSI XFEL project features an approximately 1 km long normal conducting linac and plans for
7928 2 years for the generation of a TDR, a 5 year test stand operation, a 4 year construction period and
7929 an installation period of 3 years leading to a total project time line of 6 years from start of the test
7930 facilities to the start of the actual project [?].

7931 Except for the European XFEL project, which has a longer superconducting RF section than both LHeC
7932 versions, all of the above reference facilities are smaller in scale than the LHeC project and plan between
7933 6 and 9 years from beginning of construction (civil engineering) until the start of operation. All facilities
7934 with superconducting cavities plan for an RF production time of ca. 5 years for their key components and a
7935 substantial period of test bench operation and pre-series production for critical elements (5 years or more).

7936 Figure ?? summarizes the above considerations in form of a schematic outline of the project planning.
7937 The planning in Fig. ?? addresses only aspects related to the accelerator complex and does not address
7938 additional constraints coming from the detector installation in the cavern. Furthermore, it does not include
7939 additional constraints arising from the LHC operation, logistics constraints and resource limitations due to
7940 the planning for the long shutdowns of the LHC and does therefore certainly not attempt to be an accurate
7941 project projection. Rather than presenting an accurate timeline for the LHeC installation, the presented
7942 planning aims at illustrating that a start of the LHeC operation in 2023 requires the start of first prototype
7943 development and testing already by 2012. Meeting the milestone of an LHeC operation start in 2023 requires
7944 a rather swift project launch starting with the generation of a proper TDR and the launch of first RF R&D
7945 activities by 2012. This ambitious goal can only be achieved if the project receives adequate resource
7946 allocations in 2012. Potential first activities for the prototype development and testing could focus around
7947 the development of superconducting RF cavities, where synergies with ESS and SPL studies exist, with the
7948 goal of setting up an ERL test facility. It could also include the development of electron and positron sources
7949 where synergies with the CLIC and ILC projects exist. Because of their synergies with the ESS, SPL and
7950 the linear collider projects, a start of R&D activities for the LHeC by 2012 appears to be quite timely. In
7951 case the Ring-Ring installation turns out to be the better option for the LHeC, a ERL test facility could in
7952 the end also serve as an injector complex for the Ring-Ring option of the LHeC. It represents therefore a
7953 reasonable investment into the LHeC project independent of a the final implementation choice.

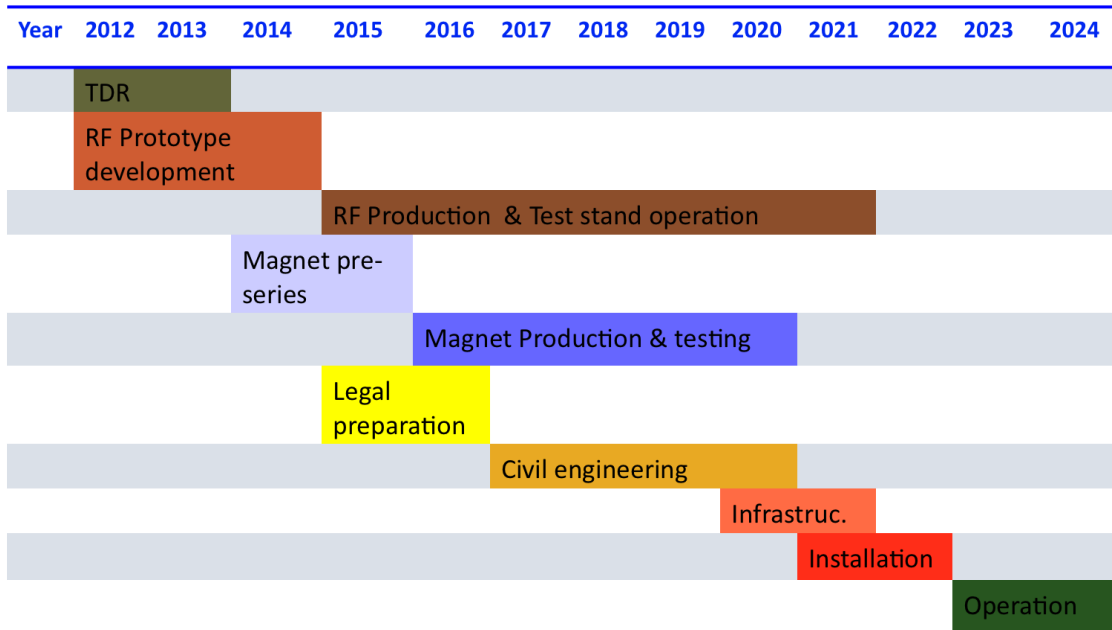


Figure 11.4: Planning considerations for the LHeC, where we assumed a partial overlap of the time lines for the various LHeC project steps (for example a partial overlap of the civil engineering for the tunnel construction and the installation of the technical infrastructure and accelerator components). The overall planning goal of completion by the LS3 seems quite ambitious even with such a partial overlap of individual activities and requires first prototype development as soon as by 2012. The presented planning discusses only aspects related to the accelerator complex and does not address additional constraints coming from the detector installation in the cavern.

Part IV

Detector

7954

7955

Chapter 12

Detector Requirements

12.1 Requirements on the LHeC Detector

The new ep/A detector at the LHeC has to basically be a precision instrument of maximum acceptance. The physics program depends on a high level of precision, as for the measurement of α_s , and in the reconstruction of complex final states, like the charged current single top production and decay or the precision measurement of the b -quark density. The acceptance has to extend as close as possible to the beam axis because of the interest in the physics at low and at large Bjorken x . The dimensions of the detector are constrained by the radial extension of the beam pipe in combination with maximum polar angle coverage¹, desirably down to about 1° and 179° for forward going final state particles and backward scattered electrons at low Q^2 , respectively. A further general demand is a high modularity enabling much of the detector construction to be performed above ground for keeping the installation time at a minimum, and to be able to access inner detector parts within reasonable shut down times.

The time schedule of the project demands to have a detector ready within about ten years. This prevents any significant R&D program to be performed. The choice of components fortunately can rely on the vast experience obtained at HERA, the LHC, including its detector upgrades to come, and on ILC detector development studies. The next few sections outline the acceptance and measurement requirements on the detector in detail. Then follow more detailed technical considerations, including alternative solutions, which taken together illustrate the feasibility of experimentation at the LHeC.

12.1.1 Installation and Magnets

The LHeC project represents an upgrade of the LHC. The experiment would be the fifth large experiment, and the detector the third multi-purpose 4π acceptance detector. It requires a cavern, which for the purpose of the design study has been considered to be the ALICE cavern in IP2, see Fig. ???. The installation of the detector has to proceed as fast as possible in order not to introduce large extra delays to the LHC program. High modularity and pre-assembly above ground are therefore inevitable demands for the design.

The cost has to be limited in order for the project to be fundable in parallel to when the large upgrade investments are presumably made for the ATLAS and CMS detectors in the high luminosity phase of the LHC. The cost is related to technology choices, the detector granularity and its size. Crucial parameters of the detector are the beam pipe dimensions, when combined with the small angle acceptance constraint, see below, and the parameters of the solenoid. The cost C of a solenoid can be represented as a function of the

¹This CDR adopts the HERA convention of the coordinate system, which has been defined with the z axis given by the proton beam direction. This implies that Rutherford "backscattering" of the electron is viewed as scattering into small angles. When the partons are essentially at rest, at very small x , the electrons are scattered "forward" as in fixed target forward spectrometers. The somewhat unfortunate HERA convention calls this backwards. The x and y coordinates are defined such that there is a right handed coordinate system formed with y pointing upwards and x to the center of the proton ring.

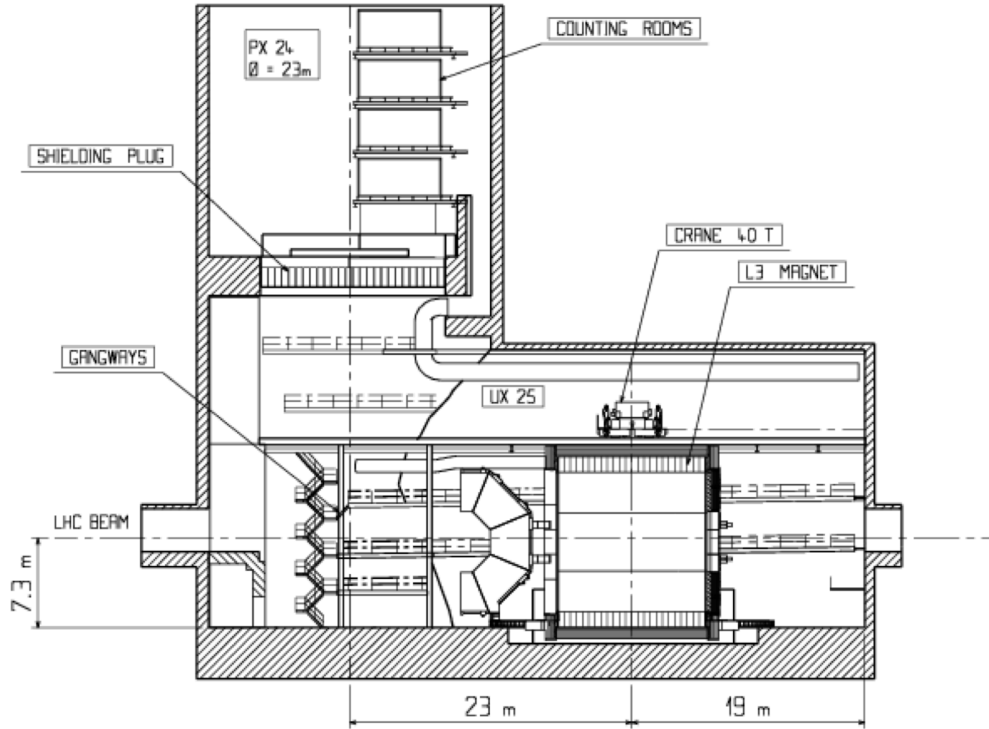


Figure 12.1: Cross section of the IP2 cavern with the ALICE detector inside the L3 magnet. Round access shaft of 23m diameter, cavern about 50m along the beam-line.

7986 energy density, ρ_E , $C \simeq 0.5(\rho_E/MJ)^{0.66}$ [?], which is determined as

$$\rho_E = \frac{1}{2\mu_0} \cdot \int B^2 dV \simeq \frac{1}{2\mu_0} \cdot \pi r^2 \cdot l \cdot B^2. \quad (12.1)$$

7987 From these relations one derives roughly that the solenoid cost scales linearly with the radius r and field
 7988 strength B and with the length l to the power 0.66. The solenoid radius influences the track length in the
 7989 transverse plane, which determines $\propto r^{-2}$ the transverse momentum resolution whereas field strength enters
 7990 linearly $\propto B^{-1}$.

7991 The Linac-Ring version of the LHeC requires to put an extended dipole field of 0.3 T into the detector
 7992 for ensuring head-on ep collisions and for separating the beams.

7993 A balance between a strong magnetic field for optimal tracking resolution and an affordable sized magnet
 7994 has to be found, knowing that the magnets themselves represent one source of inactive material and that
 7995 the energy stored in the magnets and their return flux require an outer shielding proportional to the field
 7996 and to the square of the solenoid radius.

7997 In the current design the solenoid is placed in between the electromagnetic and the hadron calorimeter²
 7998 at a radius of about 1 m. The field strength is set to 3.5 T in order to compensate the small radial extension
 7999 of the tracker, the focus of which in the LHeC environment is on the forward direction. The chosen design po-
 8000 sition with dipoles and solenoid placed outside the electromagnetic calorimeter ensures good electromagnetic
 8001 calorimetry and high dipole field quality near to the beam line. Fig. ?? shows such the magnet arrangement
 8002 inside the detector volume schematically. The total material budget of the solenoid and the dipole, at per-
 8003 pendicular crossing, may be represented by about 16 cm of Aluminum, corresponding to about one quarter

²An option is also considered of placing the solenoid outside the calorimeters, at about 2.5 m radius, combined with a second, bigger solenoid for the flux return, with the muon detector in between. A two-solenoid solution was considered already in the fourth detector concept for the ILD [?].

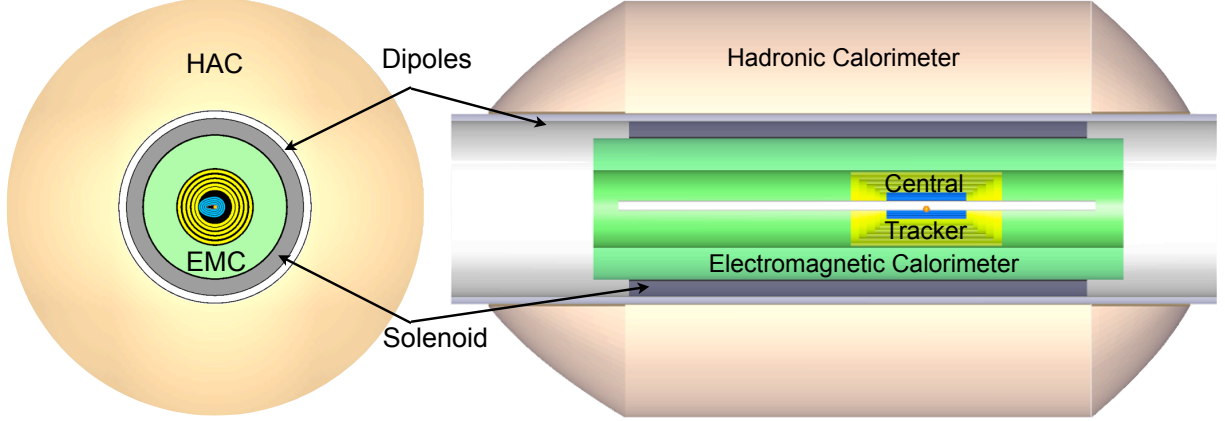


Figure 12.2: Schematic xy and rz views of the magnets and barrel calorimeter arrangement for the baseline layout.

8004 of an interaction length (λ_I) and about 1 radiation length (X_0). This further supports the choice of the
 8005 magnets located outside of the electromagnetic calorimeter, yet placed before the hadronic calorimeter in
 8006 order to limit the radial dimensions. More details on the design study of the detector magnets are addressed
 8007 in Sect.??.

8008 12.1.2 Kinematic reconstruction

8009 The inclusive ep DIS kinematics are defined by the negative four-momentum transfer squared, Q^2 , and
 8010 Bjorken x . Both are related to the cms energy squared s via the inelasticity y through the relation $Q^2 = sxy$,
 8011 which implies $Q^2 \leq s$. The energy squared s is determined by the product of the beam energies, $s = 4E_p E_e$,
 8012 for head-on collisions and large energies compared to the proton mass.

8013 The kinematics are determined from the scattered electron with energy E'_e and polar angle θ_e and from
 8014 the hadronic final state of energy E_h and scattering angle θ_h . The variables Q^2 and y can be calculated from
 8015 the scattered electron kinematics as

$$\begin{aligned}
 Q_e^2 &= 4E_e E'_e \cos^2\left(\frac{\theta_e}{2}\right) \\
 y_e &= 1 - \frac{E'_e}{E_e} \sin^2\left(\frac{\theta_e}{2}\right)
 \end{aligned}
 \tag{12.2}$$

8016 and from the hadronic final state kinematics as

$$\begin{aligned}
 Q_h^2 &= \frac{1}{1 - y_h} \cdot E_h^2 \sin^2(\theta_h) \\
 y_h &= \frac{E_h}{E_e} \sin^2\left(\frac{\theta_h}{2}\right)
 \end{aligned}
 \tag{12.3}$$

8017 and x is given as Q^2/sy . The kinematic reconstruction in neutral current scattering therefore is redundant,
 8018 which is one reason why DIS experiments at ep colliders are precise. An important example is the calibration
 8019 of the electromagnetic energy scale from the measurements of the electron and the hadron scattering angles.
 8020 At HERA, this led to energy calibration accuracies for E'_e at the per mil level. In a large part of the phase
 8021 space, around $x = E_e/E_p$, the scattered electron energy is approximately equal to the beam energy, $E'_e \simeq E_e$,
 8022 which causes a large “kinematic peak” in the scattered electron energy distribution. The hadronic energy
 8023 scale can be obtained from the transverse momentum balance in neutral current scattering, $p_t^e \simeq p_t^h$. It is
 8024 determined to about 1% at HERA.

8025 Following Eq.??, the kinematics in charged current scattering is reconstructed from the transverse and
 8026 longitudinal momenta and energy of the final state particles according to

$$\begin{aligned} Q_h^2 &= \frac{1}{1 - y_h} \sum p_t^2 \\ y_h &= \frac{1}{2E_e} \sum (E - p_z). \end{aligned} \quad (12.4)$$

8027 There have been many refinements used in the reconstruction of the kinematics, as discussed e.g. in [?],
 8028 which for the principle design considerations, however, are of less importance.

8029 12.1.3 Acceptance regions - scattered electron

8030 The positions of isolines of constant energy and angle of the scattered electron in the (Q^2, x) plane are given
 8031 by the relations:

$$\begin{aligned} Q^2(x, E'_e) &= sx \cdot \frac{E_e - E'_e}{E_e - xE_p} \\ Q^2(x, \theta_e) &= sx \cdot \frac{E_e}{E_e + xE_p \tan^2(\theta_e/2)}. \end{aligned} \quad (12.5)$$

8032 Following these relations, an acceptance limitation of the scattered electron angle, as due to the beam pipe
 8033 or focussing magnets, to a maximum value θ_e^{max} defines a constant minimum Q^2 which independently of E_p
 8034 is given as

$$Q_{min}^2(x, \theta_e^{max}) \simeq [2E_e \cot(\theta_e^{max}/2)]^2. \quad (12.6)$$

8035 apart from the smallest x . This is illustrated in Fig.???. There follows that a $179^\circ(170^\circ)$ angular cut
 8036 corresponds to a minimum Q^2 of about 1 (100) GeV^2 at nominal electron beam energy. One easily recognizes
 8037 in Fig.?? that the physics at low x and Q^2 requires to measure electrons scattered backwards from about
 8038 135° up to 179° . Their energy in this θ_e region does not exceed E_e significantly. At lower x to very good
 8039 approximation $y = E'_e/E_e$ (as can be seen from the lines $y = 0.5$ and $E'_e = 30 \text{ GeV}$ in Fig.??).

8040 Following Eq.??, Q_{min}^2 varies $\propto E_e^2$. It thus is as small as 0.03 GeV^2 for $E_e = 10 \text{ GeV}$, the injection
 8041 energy of the ring accelerator but increases to 6.0 GeV^2 for $E_e = 140 \text{ GeV}$, the maximum electron beam
 8042 energy considered in this design report, apart from smallest x , if $\theta_e^{max} = 179^\circ$. While Q_{min}^2 decreases $\propto E_e^2$,
 8043 the acceptance loss towards small x is only $\propto E_e$. The measurement of the transition region from hadronic
 8044 to partonic behavior, from 0.1 to 10 GeV^2 , therefore requires to take data at lower electron beam energies³.
 8045 These variations are illustrated in Fig.?? for an electron beam energy of 10 GeV , the injection energy for
 8046 the ring and a one-pass linac energy, and for the highest E_e of 140 GeV considered in this report.

8047 Electrons scattered forward correspond to scattering at large $Q^2 \geq 10^4 \text{ GeV}^2$, as is illustrated in the
 8048 zoomed kinematic region plot Fig.???. The energies in the very forward region, $\theta_e \lesssim 10^\circ$, exceed 1000 GeV .
 8049 For large E_e and x , Eq.?? simplifies to $Q^2 \simeq 4E_e E'_e$, i.e. a linear relation of Q^2 and E'_e which is independent
 8050 of x and of E_p , apart from the fact that $Q_{max}^2 = s$.

³The requirement of acceptance up to 179° determines the length of the backward detector. It could be tempting to utilize this E_e dependence in the design: if one limited the backward electron acceptance to for example 178° instead of 179° this would reduce the backward detector extension in $-z$. With data taken at reduced E_e one would come back to lower Q^2 . From Eq.?? one derives that $E_e = 30 \text{ GeV}$ and 178° is leading to the same Q_{min}^2 of about 1.1 GeV^2 , at not extremely small x , as is $E_e = 60 \text{ GeV}$ and 179° . However, one would loose in acceptance to the lowest x , linearly with E_e . Moreover, for the present design the (inner) beam pipe radius in vertical direction is 2.2 cm . This results in an extension of about 1.5 m for the first tracker plane to register an electron scattered at 179° . If one adds about 1 m for the tracker length, and 1 m for the backward calorimeter following the tracker, one arrives at about 3.5 m backward detector length. Obviously for 178° one could reduce the first 1.5 m to say 80 cm but one would still like to have a sizable tracker length for achieving some sagitta to determine the charge of the scattered electron and perhaps arrive at an overall backward detector length of about 2.5 m . While this is an interesting reduction one looses the lowest x corner which opens $\propto E_e$. The access to lowest x in the DIS region is a fundamental part of the LHeC physics program and thus the about 179° design requirement has been kept. There are reasons to take data with reduced E_e as for F_L , thus the LHeC detector will access the region below 1 GeV^2 too.

LHeC - electron kinematics

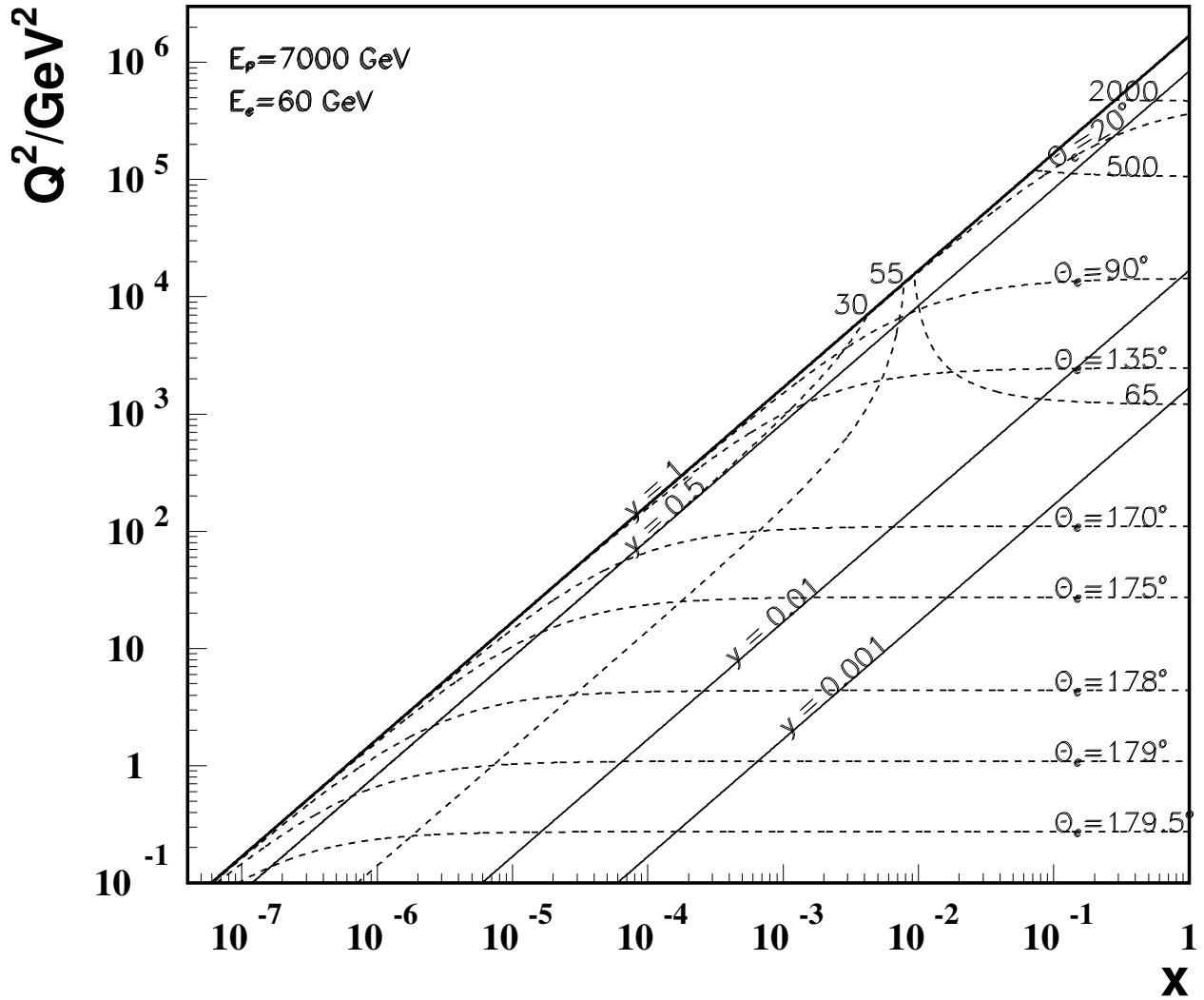


Figure 12.3: Kinematics of electron detection at the LHeC. Lines of constant scattering angle θ_e and energy, in GeV, are drawn. The region of low $Q^2 \lesssim 10^2 \text{ GeV}^2$, comprising the lowest x region, requires to measure electrons scattered backwards with energies not exceeding E_e . At small energies, for $y \lesssim 0.5$ a good e/h separation is important to suppress hadronic background, as from photoproduction. The barrel calorimeter part, of about $90 \pm 45^\circ$, measures scattered electrons of energy not exceeding a few hundreds of GeV, while the forward calorimeter has to reconstruct electron energies of a few TeV. Both the barrel and the forward calorimeters measure the high x part, which requires very good scale calibration as the uncertainties diverge $\propto 1/(1-x)$ towards large x .

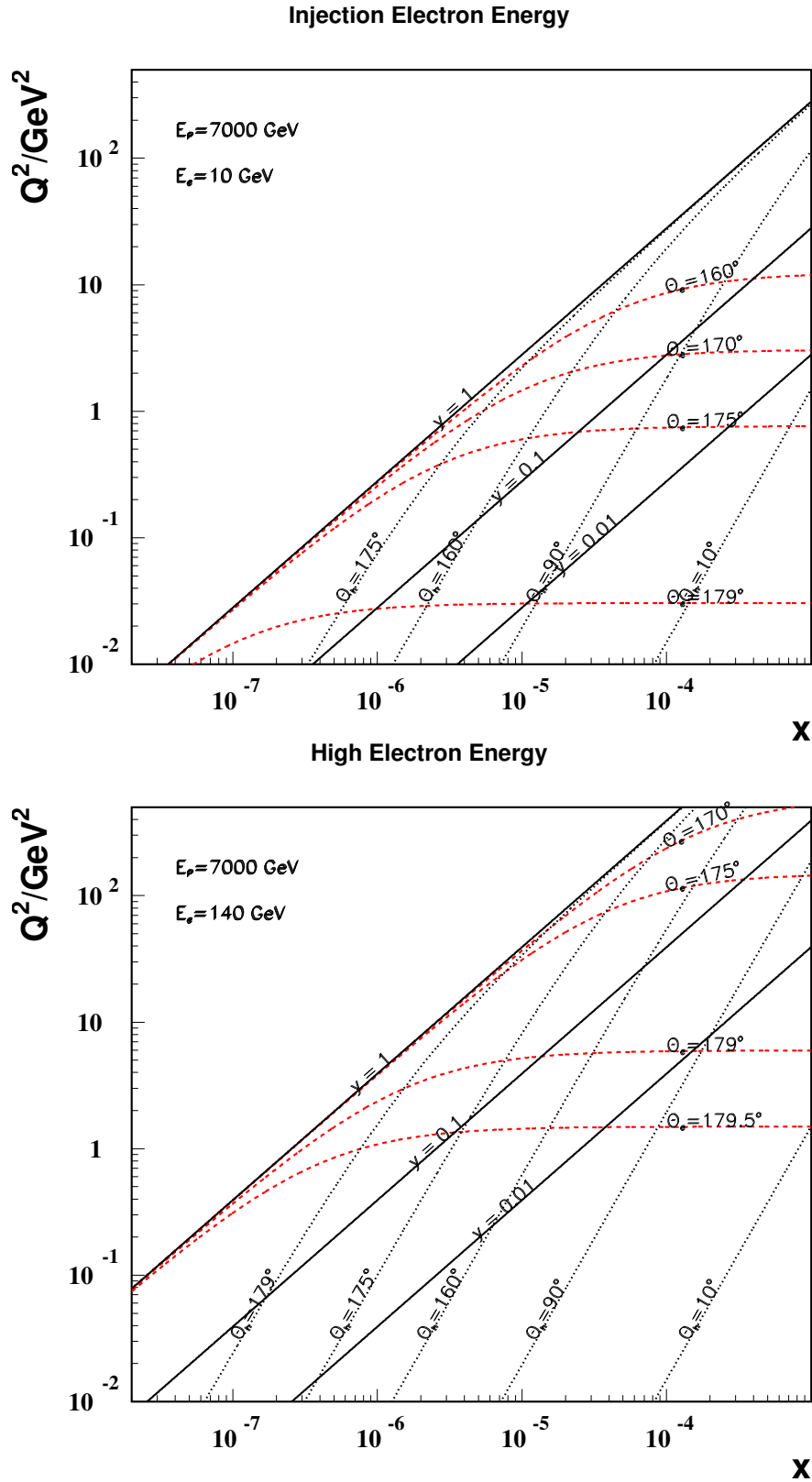


Figure 12.4: Kinematics at low x and Q^2 of electron and hadronic final state detection at the LHeC with an electron beam energy of 10 GeV (top) as compared to 140 GeV (bottom). At larger x , the iso- θ_e lines are at about constant $Q^2 \propto E_e^2$. At low x , the scattered energies, not drawn here, are approximately $E'_e \simeq (1 - y) \cdot E_e$, and at lower Q^2 and x one has $E_h \simeq E_e - E'_e \simeq y \cdot E_e$. At very high E_e part of the very low Q^2 region may be accessible with the electron tagged along the e beam direction, outside the central detector, and the kinematics measured with the hadronic final state.

LHeC - electron kinematics

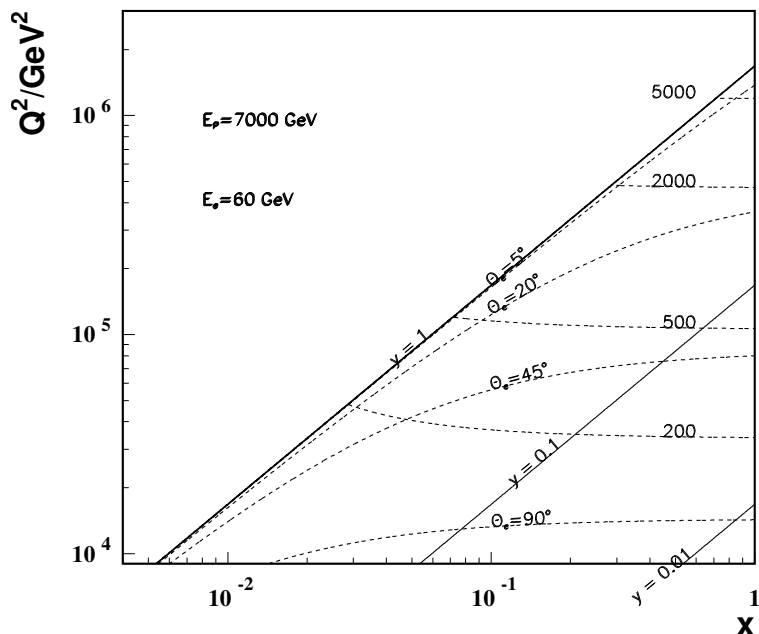


Figure 12.5: Kinematics of electron detection in the forward detector region corresponding to large $Q^2 \geq 10^4 \text{ GeV}^2$. The energy values are given in GeV. At very high Q^2 the iso- E'_e lines are rather independent of x , i.e. $Q^2(x, E'_e) \simeq 4E_e E'_e$.

12.1.4 Acceptance regions - hadronic final state

The positions of isolines in the (Q^2, x) plane of constant energy and angle of the hadronic final state, approximated here by the current jet or struck quark direction, are given by the relations:

$$\begin{aligned}
 Q^2(x, E_h) &= sx \cdot \frac{x E_p - E_h}{x E_p - E_e} \\
 Q^2(x, \theta_h) &= sx \cdot \frac{x E_p}{x E_p + E_e \cot^2(\theta_h/2)}
 \end{aligned}
 \tag{12.7}$$

and are illustrated in Fig. ???. At low $x \lesssim 10^{-4}$, the hadronic final state is emitted backwards, $\theta_h > 135^\circ$, with energies of a few GeV to a maximum of E_e . Lines at constant y at low x are approximately at $y = 1 - E'_e/E_e$ and $E'_e + E_h = E_e$, i.e. $y = E_h/E_e$. Final state physics at lowest $x \lesssim 3 \cdot 10^{-6}$ requires access to the backward region within a few degrees of the beam pipe (Fig. ??). This is the high y region in which the longitudinal structure function is measured.

The x range accessed with the barrel calorimeter region, of θ_h between 135° and 45° , is typically around 10^{-4} and smaller than a decade for each Q^2 , as can be seen in Fig. ???. The hadronic energies in this part do not exceed typically 200 GeV. The detector part which covers this region is quite large but the requirements are modest. One might even be tempted to consider a two-arm spectrometer only. However, the measurement of missing transverse energy and the importance of using the longitudinal momentum conservation for background and radiative correction reductions, with the $E - p_z$ criterion, demand the detector to be hermetic and complete.

For the measurement of the hadronic final state the forward detector is most demanding. Due to the high luminosity, the large x region will be populated and a unique physics program at large x and high Q^2 may be pursued. In this region the relative systematic error increases like $1/(1-x)$ towards large x , see

LHeC - hadronic final state kinematics

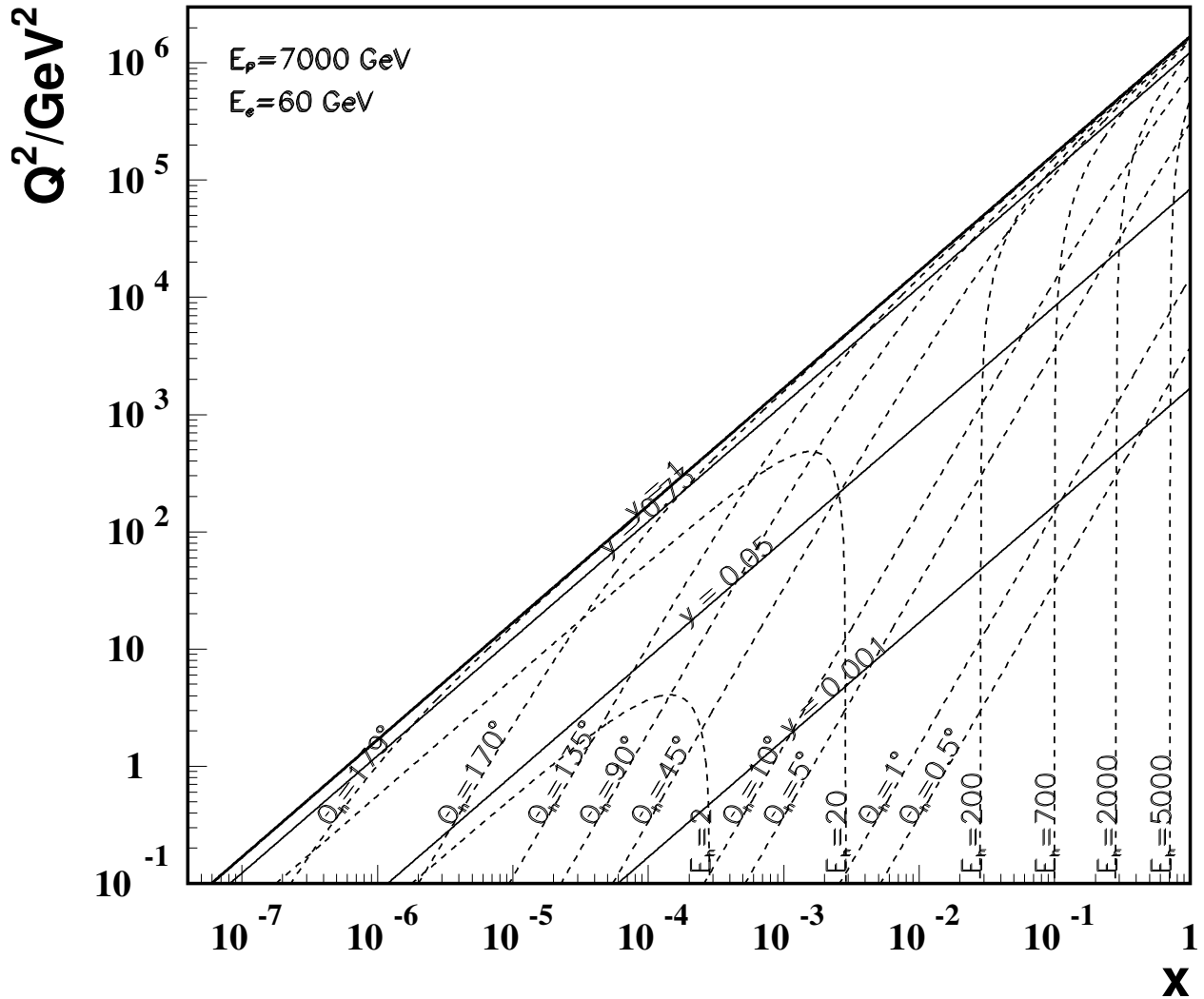


Figure 12.6: Kinematics of hadronic final state detection at the LHeC. Lines of constant energy and angle of the hadronic final state are drawn, as represented by simple kinematics of the struck quark. One easily recognizes that the most demanding region is the large x domain, where very high energetic final state particles are scattered close to the (forward) direction of the proton beam. The barrel region, of about $90 \pm 45^\circ$, is rather modest in its requirements. At low x the final state is not very energetic, $E_h + E'_e \simeq E_e$, and scattered into the backward detector region.

below. At high x and not extreme Q^2 the $Q^2(x, E_h)$ line degenerates to a line $x = E_h/E_p$ as can be derived from Eq. ?? and be seen in Fig. ?. High x coverage thus demands the registration of up to a few TeV of energy close to the beam pipe, i.e. a dedicated high resolution calorimeter is mandatory for the region below about $5 - 10^\circ$ extending to as small angles as possible. A minimum angle cut $\theta_{h,min}$ in the forward region, the direction of the proton beam, would exclude the large x region from the hadronic final state acceptance (Fig. ??), along a line

$$Q^2(x, \theta_{h,min}) \simeq [2E_p x \tan^2(\theta_{h,min}/2)]^2, \quad (12.8)$$

which is linear in the $\log Q^2$, $\log x$ plot and depends on E_p only. Thus at $E_p = 7 \text{ TeV}$ the minimum Q^2 is roughly $(1000[100]x)^2$ at a minimum angle of $10[1]^\circ$. Since the dependence in Eq. ?? is quadratic with E_p , lowering the proton beam energy is of considerable interest for reaching the highest possible x and overlapping with the large x data of previous experiments or searches for specific phenomena as intrinsic heavy flavour.

12.1.5 Acceptance at the High Energy LHC

Presently one considers to build a high energy (HE) LHC in the thirties with proton beam energies of 16 TeV [?]. Such an accelerator would better be combined with an electron beam of energy exceeding the 60 GeV, considered as default here, in order to profit from the doubled proton beam energy and to limit the asymmetry of the two beam energies. Choosing the 140 GeV beam mentioned above as an example, Figure ?? displays the kinematics and acceptance regions for given scattering angles and energies of the electron (dashed green and red) and of the hadronic final state (black, dotted and dashed dotted). The cms energy in this case is enhanced by about a factor of five. The maximum Q^2 reaches 10 TeV^2 , which is 10^6 times higher than the typical momentum transfer squared covered by the pioneering DIS experiment at SLAC. The kinematic constraints in terms of angular acceptance would be similar to the present detector design as can be derived from the Q^2, x plot. At very high x (Q^2) the energy E_h (E'_e) to be registered would be doubled. With care in the present design, one would probably be able to use the main LHeC detector components also in the HE phase of the LHC.

12.1.6 Energy Resolution and Calibration

The LHeC detector is dedicated to most accurate measurements of the strong and electroweak interaction and to the investigation of new phenomena. The calorimetry therefore requires:

- Optimum scale calibrations, as for the measurement of the strong coupling constant. This is much helped by the redundant kinematic reconstruction and kinematic relations, as $E'_e \simeq E_e$ at low Q^2 , $E'_e + E_h \simeq E_e$ at small x , the double angle reconstruction [?] of E'_e and the transverse momentum balance of p_T^e and p_T^h . From the experience with H1 and the much increased statistics it is assumed that E'_e may be calibrated to $0.1 - 0.5\%$ and E_h to $1 - 2\%$ accuracy. The latter precision will be most crucial in the forward, high x part of the calorimeter because the uncertainties diverge $\propto 1/(1-x)$ towards large x .
- High resolution, for the reconstruction of multi-jet final states as from the $H \rightarrow b\bar{b}$ decay. This is a particular challenge for the forward calorimeter. While detailed simulations are still ongoing one may assume that $(10 - 15)/\sqrt{E/GeV}\%$ resolutions for E'_e and $(40 - 50)/\sqrt{E/GeV}\%$ for E_h are appropriate, with small linear terms. These requirements are very similar to the ATLAS detector which quotes electromagnetic resolutions of $10/\sqrt{E/GeV} \oplus 0.007\%$ and hadronic energy resolutions of $50/\sqrt{E/GeV} \oplus 0.03\%$. The basic electromagnetic calorimeter choice for the LHeC can be for Liquid Argon (LAr)⁴. The hadronic calorimeter is outside the magnets and serving also for the magnetic flux

⁴In H1 very good experience has been collected with the longterm stability of the LAr calorimeter. A special demand is the low noise performance because the measurements at small inelasticity y are crucial for reaching large Bjorken x . In this region a small misidentified deposition of energy in the backward part of the detector can spoil the measurement at low $y \lesssim 0.01$, as can be seen from Eq. ??.

Kinematics at HE-LHeC

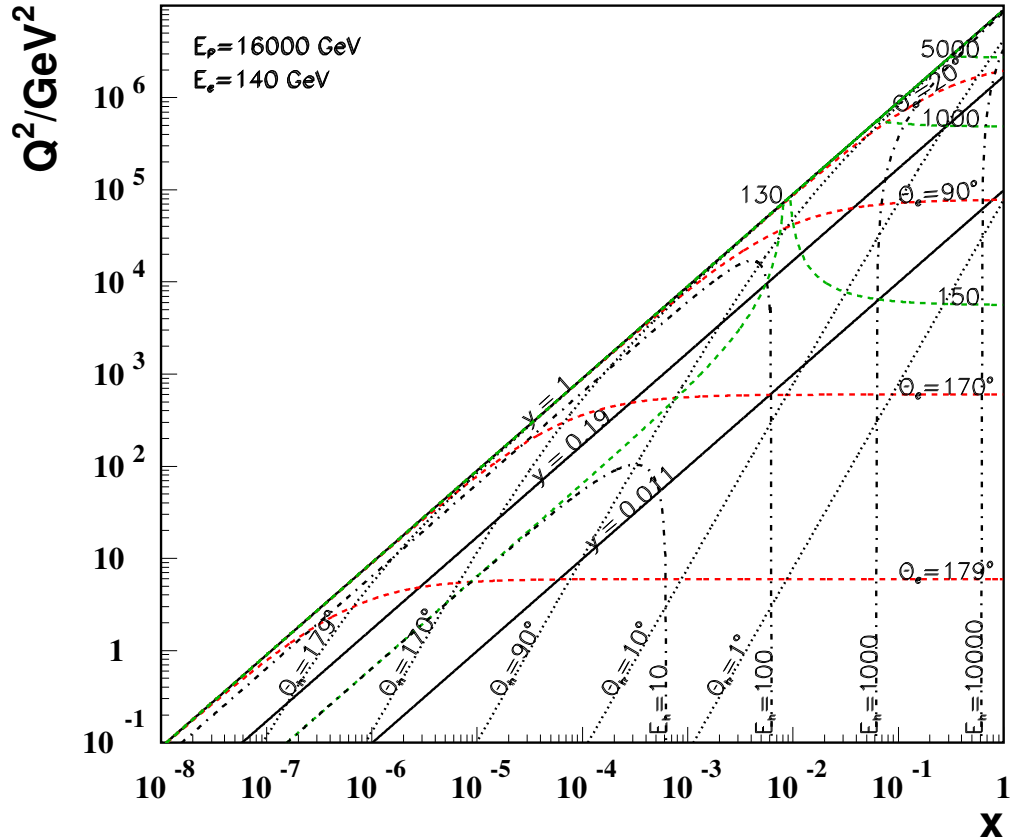


Figure 12.7: Scattered electron and hadronic final state kinematics for the HE-LHC at $E_p = 16$ TeV coupled with a 140 GeV electron beam. Lines of constant scattering angles and energies are plotted. The line $y = 0.011$ defines the edge of the HERA kinematics and $y = 0.19$ defines the edge of the default machine considered in this report ($E_e = 60$ GeV and $E_p = 7$ TeV).

8110 return may be built as a tile calorimeter with the additional advantage of supporting the whole detector.
 8111 The first year of operating the ATLAS combined LAr/TileCal calorimeter has been encouraging. Some
 8112 special calorimeters are needed in the small angle forward region ($\theta \lesssim 5^\circ$) where the deposited energies
 8113 are extremely large, and also in the backward region ($\theta \geq 135^\circ$) where the electron detection of modest
 8114 energy is a special task.

- 8115 • Good electron-hadron separation, as for the electron identification at high y and low Q^2 (backwards)
 8116 or high Q^2 (in the extreme forward direction). This is a requirement on the segmentation of the
 8117 calorimeters and on building trackers in front also of the forward and backward calorimeters to support
 8118 the energy measurements and the electron identification in particular.

8119 Obviously the calorimetry needs to be hermetic for the identification of the charged current process and
 8120 good measurement of $E_{T,miss}$. These considerations are also summarised in Tab. ??.

8121 12.1.7 Tracking Requirements

8122 The tracking detector has to enable

region of detector approximate angular range / degrees	backward 179 - 135	barrel 135 -45	forward 45-1
scattered electron energy/GeV	3-100	10-400	50-5000
x_e	$10^{-7} - 1$	$10^{-4} - 1$	$10^{-2} - 1$
elm scale calibration in %	0.1	0.2	0.5
elm energy resolution $\delta E/E$ in % $\cdot \sqrt{E/GeV}$	10	15	15
hadronic final state energy/GeV	3-100	3-200	3-5000
x_h	$10^{-7} - 10^{-3}$	$10^{-5} - 10^{-2}$	$10^{-4} - 1$
hadronic scale calibration in %	2	1	1
hadronic energy resolution in % $\cdot \sqrt{E/GeV}$	60	50	40

Table 12.1: Summary of calorimeter kinematics and requirements for the default design energies of $60 \times 7000 \text{ GeV}^2$, see text. The forward (backward) calorimetry has to extend to 1° (179°).

- 8123 • Accurate measurements of the transverse momenta and polar angles
- 8124 • Secondary vertexing in a maximum polar angle acceptance range
- 8125 • Resolution of complex, multiparticle and highly energetic final states in forward direction
- 8126 • Charge identification of the scattered electron
- 8127 • Distinction of neutral and charged particle production
- 8128 • Measurement of vector mesons, as the J/ψ or Υ decay into muon pairs

8129 The transverse momentum resolution in a solenoidal field can be approximated by

$$\frac{\delta p_T}{p_T^2} = \frac{\Delta}{0.3BL^2} \cdot \sqrt{\frac{720}{N+4}} \quad (12.9)$$

8130 where B is the field strength, Δ is the spatial hit resolution and L the track length in the plane transverse
8131 to the beam direction, and N being the number of measurements on a track, which enters as prescribed
8132 in [?]. As an example, for $B = 3.5 \text{ T}$, $\Delta = 10 \mu\text{m}$, $N = 4 + 5$ and $L = 0.42 \text{ m}$ one obtains a transverse
8133 momentum measurement accuracy of about $3 \cdot 10^{-4}$. A simulation, using the LICTOY program [?], of the
8134 transverse momentum, transverse impact parameter and polar angle resolutions is shown in Fig. ???. One
8135 can see that the estimate following Eq. ??? is approximately correct for larger momenta where the multiple
8136 scattering becomes negligible. This momentum resolution, in terms of $\delta p_T/p_T^2$ is about ten times better
8137 than the one achieved with the H1 central drift chamber. It is similar to the ATLAS momentum resolution
8138 for central tracks and thus considered to be adequate for the enlarged momenta at LHeC as compared to
8139 HERA and the goal of high precision vertex tagging. One finds that the impact parameter resolution, for
8140 high momenta, is a factor of eight improved over the H1 or ZEUS result.

8141 In backward direction, a main tracking task is to determine the charge of the scattered electron or
8142 positron, which has momenta $E'_e \leq E_e$, down to a few GeV for DIS at high $y \simeq 1 - E'_e/E_e$. With a beam
8143 spot as accurate as about $10 \times 30 \mu\text{m}^2$ and the beam pipe radius of a few cm only, the backward Silicon strip
8144 tracker will allow a precise E/p determination when combined with the backward calorimeter, even better
8145 than has been achieved with the H1 backward silicon detector [?].

8146 In the forward region, $\theta < 5^\circ$, as may be deduced from Figs. ???, ???, the hadronic final state, for all Q^2 ,
8147 and the scattered electron, when scattered "back" at high Q^2 , are very energetic. This requires a dedicated
8148 calorimeter. Depending on the track path and momentum, the track sagitta becomes very small, for example
8149 about $10 \mu\text{m}$ for a 1 TeV track momentum and a 1 m track length. In such extreme cases of high momenta,

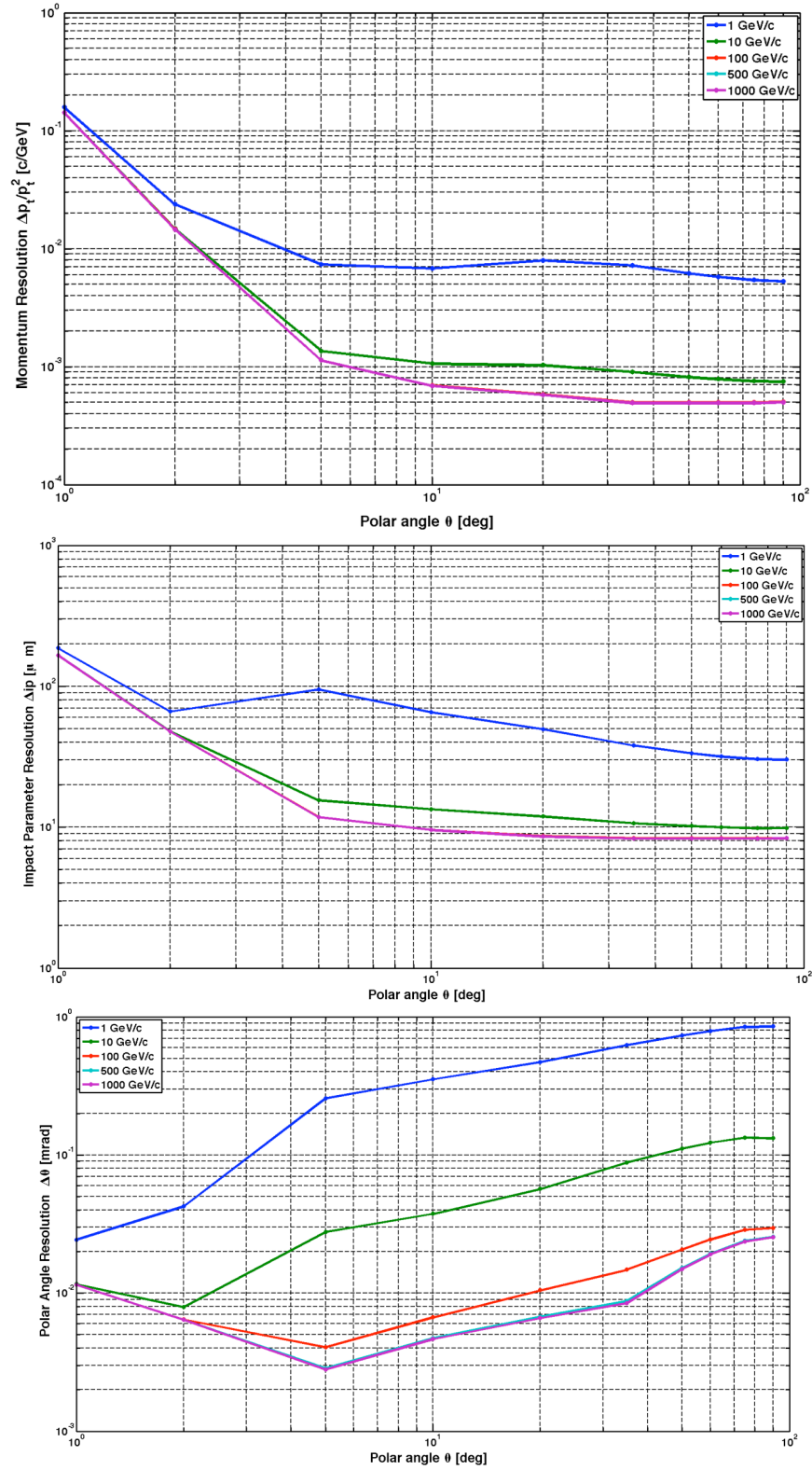


Figure 12.8: Transverse momentum (top), impact parameter (middle) and polar angle (bottom) measurement resolutions as function of the polar angle for the default detector design for four values of track transverse momentum.

8150 the functionality of the tracker will be difficult to achieve: the sagitta becoming small means that there will
8151 be limits to the transverse momentum measurement while the ability to distinguish photons and electrons
8152 will be compromised by the high probability of showering and conversion when the pipe is passed under very
8153 small angles. A forward tracker yet is considered to be useful down to small angles for the reconstruction
8154 of the event structure, the rejection of beam induced background and the reconstruction of forward going
8155 muons. This region requires detailed simulation studies in a next phase of the project.

8156 12.1.8 Particle Identification Requirements

8157 The requirements on the identification of particles focus on the identification of the scattered electron, a
8158 reliable missing energy measurement and precision tracking for measuring the decay of charm and beauty
8159 particles, the latter rather on a statistical basis than individually. Classic measurements as the identification
8160 of the D meson from the $K\pi\pi$ decay with a slow pion or the identification of B production from high p_T
8161 leptons require a very precise track detector. The tracker should determine some dE/dX properties but
8162 there is no attempt to distinguish strange particles, as kaons from pions, as the measurement of the strange
8163 quark distribution is traced back to charm tagging in CC events. The identification of muons, apart from
8164 some focus on the forward and backward direction, is similar to that of pp detectors. In addition a number
8165 of taggers is foreseen to tag

- 8166 • electrons scattered near the beam pipe in backward direction to access low Q^2 events and control the
8167 photoproduction background;
- 8168 • photons scattered near the beam pipe in backward direction to measure the luminosity from Bethe
8169 Heitler scattering;
- 8170 • protons scattered in forward direction to measure diffractive DIS in ep scattering and to tag the
8171 spectator proton in en scattering in electron-deuteron runs;
- 8172 • neutrons scattered in forward direction to measure pion exchange in ep scattering and to tag the
8173 spectator neutron in ep scattering in electron-deuteron runs;
- 8174 • deuterons scattered in forward direction in order to discover diffraction in lepton-nucleus scattering.

8175 From the perspective of particle identification therefore no unusual requirements are derived. One needs a
8176 state of the art tracker with a very challenging forward part and a tagger system with the deuteron as a new
8177 component in forward direction.

8178 12.1.9 Summary of the Requirements on the LHeC Detector

8179 The above considerations along with the constraints from machine operation and the physics program can
8180 be summarized in the following detector requirements.

- 8181 1. The LHeC experiment has to be operated in parallel to the other LHC experiments and has to be set
8182 up in accordance to CERN regulations.
- 8183 2. The detector realization requires a modular design and construction with the assembly process done in
8184 parallel partly at surface level and partly in the experimental area following the LHC machine running
8185 and maintenance periods.
- 8186 3. The beam pipe will host the electron beam along with the two LHC counter rotating proton beams.
8187 The non interacting proton/ion beam has to bypass the IP region guided through the same beam pipe
8188 housing the electron and interacting proton/ion beam (see chapter ??).
- 8189 4. The detector should be modular and flexible to accommodate the high acceptance as well as the high
8190 luminosity running foreseen for the two main physics programs. The flexibility should accommodate
8191 reducing/enhancing the energy asymmetry of the beams - chapter ??.

- 8192 5. The detector design can profit from the experience at HERA and the LHC and will be based on the
8193 recent detector developments in order to meet the ambitious physics requirements, summarized in pre-
8194 vious chapter, using settled technology, avoiding extended R&D programs and being of comparatively
8195 reasonable cost.
- 8196 6. Mechanics/services have to be optimized minimizing the amount of material in sensitive regions of the
8197 experimental setup.
- 8198 7. The detector has to be operated in a high luminosity environment L . High \bar{L} is anticipated with small
8199 beam spot sizes ($\sigma_x \approx 30\mu m$, $\sigma_y \approx 16\mu m$), small β^* and relatively large IP angles (see acc. part). On
8200 the other hand β^* has to be chosen to eliminate effects of parasitic bunch crossings. The machine and
8201 detector requirements near the IP is an optimization problem.
- 8202 8. The detector must experience acceptable backgrounds. The design has to be background insensitive as
8203 far as possible and the machine has to incorporate masks, shielding's and an appropriate optics design
8204 that minimizes background sources and a vacuum profile that reduces backgrounds.
- 8205 9. It might be necessary to have insertable/removable shielding protecting the detector against injection
8206 and poor machine performance.
- 8207 10. Special Interaction Region (IR) instrumentation for tuning of the machine with respect to background
8208 and luminosity is needed. Radiation detectors e.g. near mask and tight apertures are useful for fast
8209 identification of background sources. Fast bunch related informations are useful for beam optimization
8210 in that context.
- 8211 11. Good vertex resolution for decay particle secondary vertex tagging is required, which implies a small
8212 radius and thin beam pipe optimized in view of synchrotron radiation and background production -
8213 see section ??.
- 8214 12. The detector will have one solenoid in its default version building a homogenous field in the tracking
8215 area of 3.5 T extending over $z = +370cm, -200cm$. Solenoid options are described in section ??.
- 8216 13. The tracking and calorimetry in the forward and backward direction has to be set up such that the
8217 extreme asymmetry of the production kinematics are taken into account by layout and choice of
8218 technology for the detector design and ensure high efficiency measurements. The detectors have to be
8219 radiation hard.
- 8220 14. Very forward/backward detectors have to be set up to access the diffractive produced events and
8221 measuring the luminosity with high precision, respectively - section ??.

Chapter 13

Central Detector

13.1 Basic Detector Description

Following the considerations of the physics requirements and the technical and operational constraints outlined above, a detector design for high precision and large acceptance Deep Inelastic Scattering is presented. The detectors for the Linac-Ring or the Ring-Ring options are nearly identical: the two notable differences are the dipoles in the Linac-Ring case for separating the e and the p beams and the larger beam pipe due to the wider synchrotron radiation fan. For practical reasons of this report the more complicated Linac-Ring detector has been chosen as the baseline, termed version A. This evidently affects the solenoid-dipole configuration and the inner shape of the tracker but is of no severe concern. For the Ring-Ring case the luminosity may be maximised by inserting focussing quadrupoles near to the IP. This causes the inner detector to be designed modular such that a transition could be made between the two phases, with the quadrupoles to achieve maximum luminosity and without, to ensure maximum polar angle acceptance ¹.

The LHeC detector is asymmetric in design, reflecting the beam energy asymmetry and reducing cost. It is a general purpose 4π detector, which consists of an inner silicon tracker, with extended forward and backward parts, surrounded by an electromagnetic calorimeter, which is separated from the hadronic calorimeter by a solenoid with 3.5 T field incorporating dipoles, in the Linac-Ring case, Fig. ??, or not, in the Ring-Ring case, Fig. ?. The hadron calorimeter is enclosed in a muon tracker system, not shown here but discussed below. The main detector is complemented by hadron tagging detectors in the forward direction and a polarimeter and luminosity measurement system backwards, as is also presented below. Its longitudinal extension is determined by the need to cover polar angles down to 1° at the given beam pipe dimension. Its radial size is mainly determined by the requirement of full energy containment of hadronic showers in the calorimeter.

The dipoles for the Linac-Ring IR cannot be of a too large radius to act on the beam and be affordable. Their bulk material should also not compromise tracking and electromagnetic energy measurements and thus have to be placed outside the electromagnetic calorimeter, chosen to be Liquid Argon. The solenoid cost scales, as discussed above, approximately with its radius which in absolute allows some ten millions CHF to be economised, with the solenoid placed inside the hadronic calorimeter ². In order to minimize cost and material, it appears appropriate to foresee a single cryostat housing the electromagnetic calorimeter and the solenoid and dipole magnets. This leads also to some modification of the forward and backward calorimeter inserts, which can be seen comparing the Linac-Ring Fig. ?? with the Ring-Ring Fig. ??.

¹The very recent optics design results suggest that there is only a factor of two difference between the luminosity achievable with and without the quadrupoles. That is not enough to justify considering two measurement phases, in particular having in mind that such a transition, as happened at HERA, may take much more time than one would estimate beforehand. If the Ring-Ring solution was chosen, therefore, it would most likely only require one unchanged main detector configuration. The baseline considered here would be fully adequate for this case, with less complication of the magnets and a narrower pipe.

²Since for the physics performance it is evidently advantageous to place the solenoid outside the hadronic calorimeter, this option, termed B, has also been studied and is discussed below. The radius of the large coil would be about 2.5 m which still compares well with for example the H1 and the CMS coils.

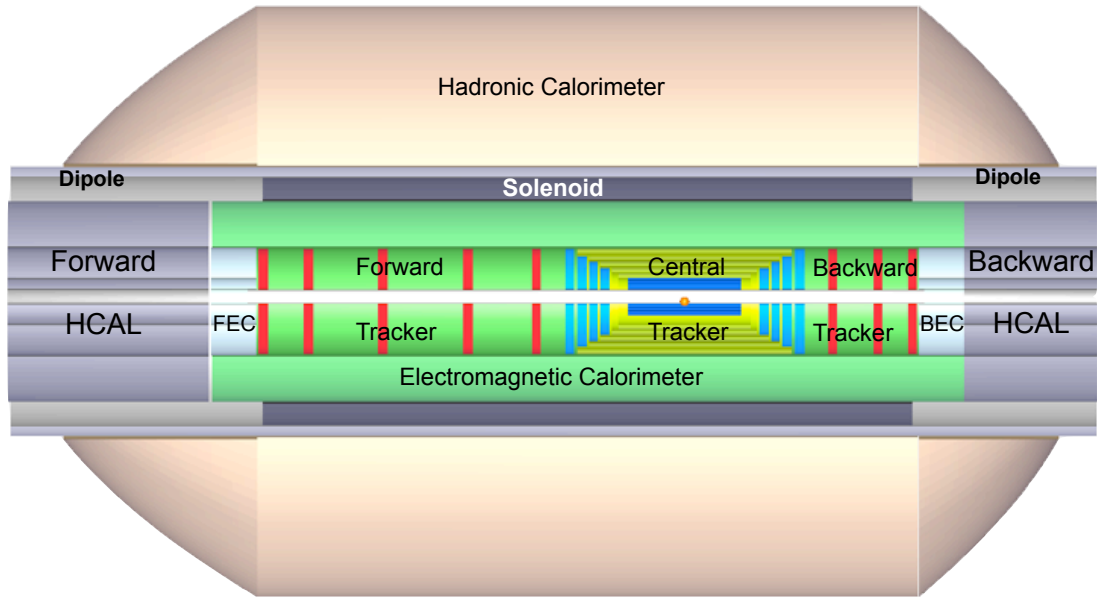


Figure 13.1: Schematic rz view of the detector design for the Linear-Ring machine option showing the characteristic dipole and solenoid placement between the electromagnetic and the hadronic calorimeters. The proton beam, from the right, collides with the electron beam, from the left, at the IP which is surrounded by a central tracker system complemented by large forward and backward tracker telescopes followed by sets of calorimeters. The detector as sketched here, i.e. without the muon tracking system, has a radius of 2.6 m and extends from about $z = -3.6$ m to $z = +5.9$ m in the direction of the proton beam.

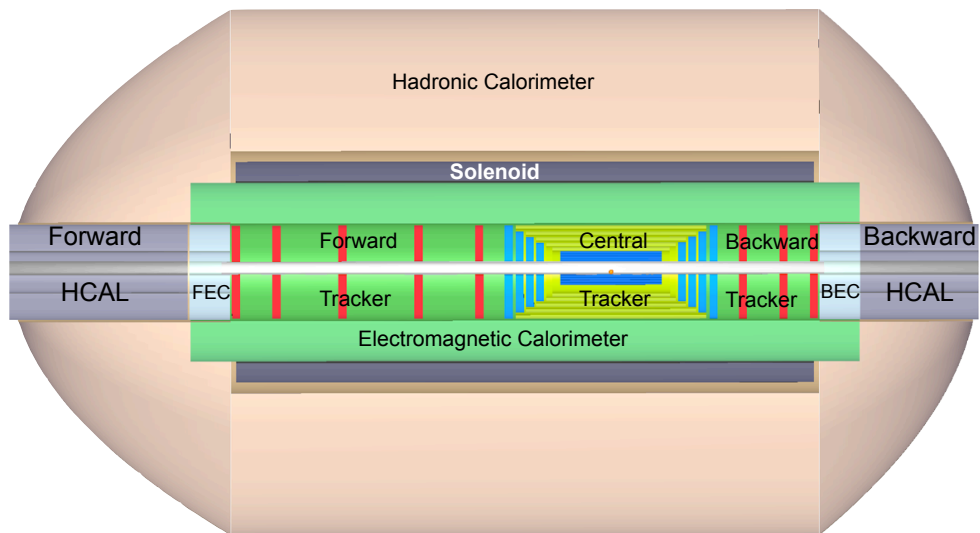


Figure 13.2: Schematic rz view of the detector design for the Ring-Ring machine option. Note that the outer part of the forward and backward calorimeters ends at smaller radii, as compared to the Linac-Ring case, since there are no dipole magnets foreseen.

8252
8253
8254
8255
8256
8257
8258
8259

The Ring-Ring configuration possibly requires separate data taking phases with maximum polar angle acceptance, for physics at low and high x , and with ultimate luminosity, for electroweak physics and the search for rare phenomena. Correspondingly, the LHeC inner detector is designed here with a modular structure as is illustrated in Figs. ?? and ?? which show the detector without and with the low β quadrupoles inserted to accommodate for either configuration, respectively. This requires the removal of the forward/backward tracking setup (shown in red in Fig. ??) and the subsequent reinstallation of the external forward/backward electromagnetic and hadronic calorimeter plugins near to the vertex. The high luminosity apparatus would have a polar angle acceptance coverage of about 8° - 172° for an estimated gain in luminosity of slightly higher than a factor of two with respect to the large acceptance configuration.

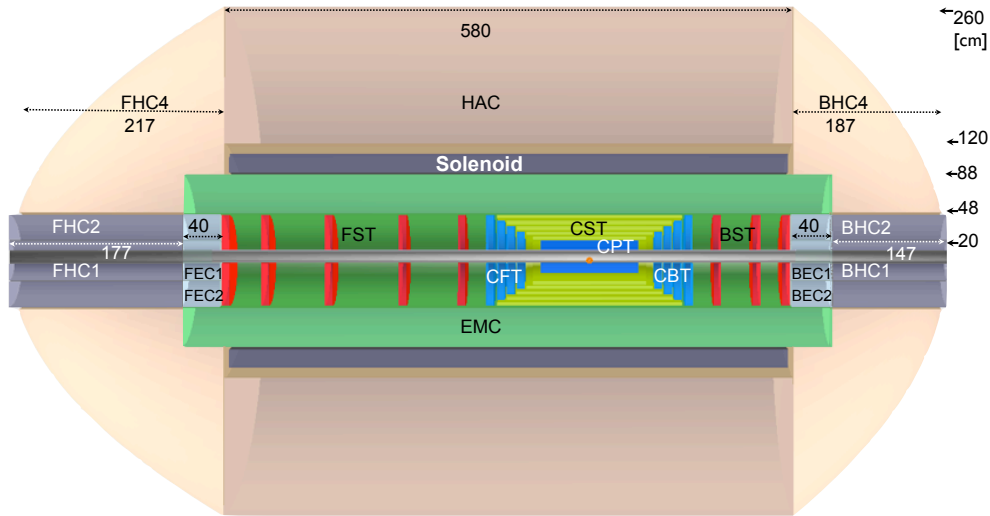


Figure 13.3: An rz cross section and dimensions of the main detector (muon detector not shown) for the Ring-Ring detector version (no dipoles) extending the polar angle acceptance to about 1° in forward and 179° in backward direction.

8260
8261
8262
8263
8264
8265
8266
8267
8268
8269
8270
8271
8272
8273
8274
8275
8276
8277
8278
8279
8280

The Ring-Ring and Linac-Ring detectors also differ due to the different optics and the beam pipe geometry.

In the Ring-Ring design the e and p/A beams collide with a small non-zero crossing angle, large enough to avoid parasitic crossings, which for a 25 ns bunch crossing occur at ± 3.75 m from the IP. Additional masks are used to shield the inner part of the detector from synchrotron radiation generated upstream of the detector.

For the Linac-Ring design, the dipole field in the detector area which allow for head-on collisions and provide the required separation, produces additional synchrotron radiation which has to pass through the interaction region requiring a larger beam pipe. This difference results in a factor of two wider extension of the horizontal beam pipe in the outer region in the Linac-Ring case, which in this regard is the unfavourable solution. The radius of the circular part has been chosen according to tentative choices of the LHC upgrade beam pipe dimensions.

According to a first estimate of the synchrotron radiation and an initial placement of masks, shielding the Ring-Ring detector from direct and backscattered photons, the beam pipe geometries have been chosen as shown in Fig. ?? for the Ring-Ring case and in Fig. ?? for the Linac-Ring case.

As already mentioned, the necessity to register particle production down to 1 and 179° poses severe constraints on the material and the thickness of the pipe. In the design as shown here, a beryllium pipe would have 3.0 (1.5) mm thickness in the Linac-Ring (Ring-Ring) case. An extensive R&D program is needed aiming for higher stability of the beam pipe at given dimensions and for thinner/lighter beam wall construction resulting in higher transparency for all final state particles. This R&D program is necessary

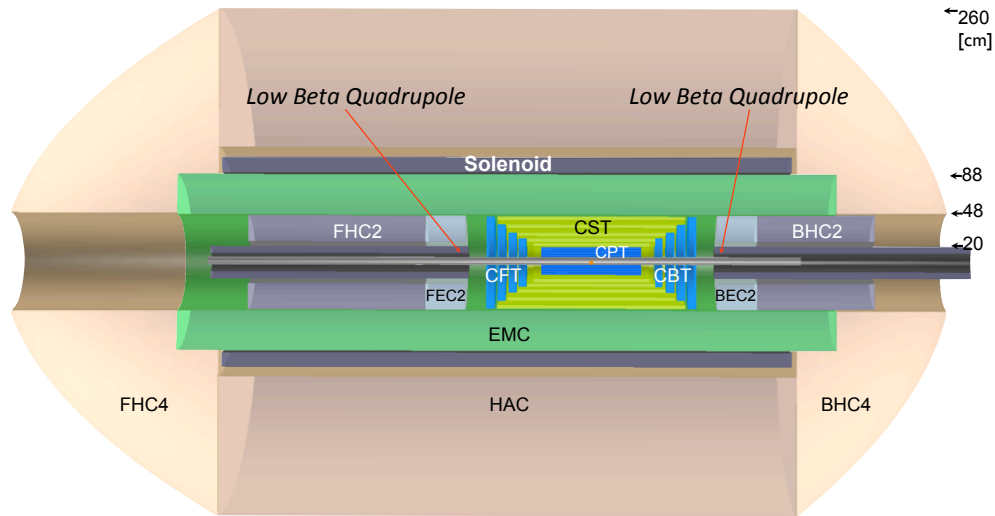


Figure 13.4: An rz cross section and dimensions of the main detector (muon detector not shown) for the Ring-Ring detector version (no dipoles) in which the luminosity is maximised by replacing the forward and backward tracker telescopes by focusing, low β quadrupole magnets at $\pm 1.2\text{m}$ away from the nominal interaction point. The polar angle acceptance is thus reduced to about $8 - 172^\circ$. As compared to the high acceptance detector (Fig. ??), the outer forward/backward calorimeter inserts have been moved nearer to the interaction point.

RR - Inner Dimensions
 Circular(x)=2.2cm; Elliptical(-x)=-5.5, y=2.2cm

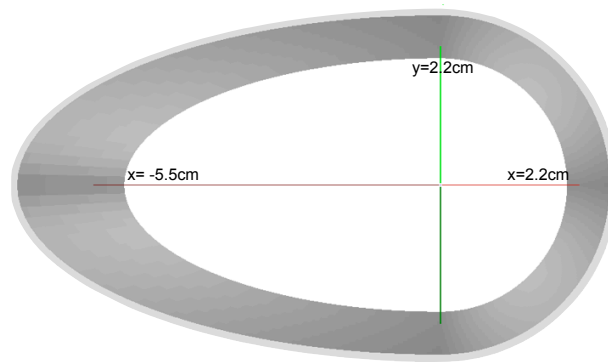


Figure 13.5: Perspective drawing of the beam pipe and its dimensions in the ring-ring configuration. The dimensions consider a 1 cm safety margin around the synchrotron radiation envelope with masks (not shown) for primary synchrotron radiation suppression placed at $z = 6, 5, 4\text{m}$.

LR - Inner Dimensions
 Circular(x)=2.2cm; Elliptical(-x)=-10., y=2.2cm

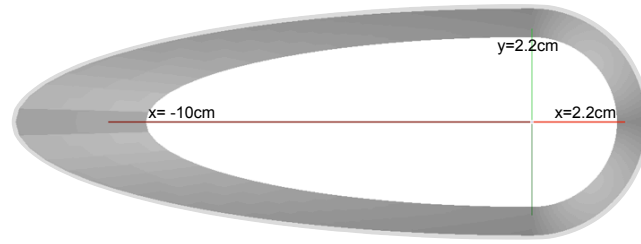


Figure 13.6: Perspective drawing of the beam pipe and its dimensions in the linac-ring configuration. The dimensions consider a 1 cm safety margin around the synchrotron radiation envelope.

8281 regardless of which machine option for the LHeC facility is selected. It may also turn out to be advantageous
 8282 to use a trumpet shaped beampipe when this problem gets revisited in a more advanced phase of the LHeC
 8283 design when more detailed simulations will be available and results of pipe material developments become
 8284 known.

8285 In order to ensure optimal polar angle acceptance coverage, the innermost subdetector dimensions have
 8286 to be adapted to the beam pipe shape. Fig. ?? illustrates the disposition that a circular silicon tracker would
 8287 imply and the corresponding acceptance losses. These can be reduced as is shown in Fig. ?? if the detector
 8288 acceptance follows as close as possible the elliptic-circular shape of the pipe. Electrons scattered at high polar
 8289 angle, corresponding to small $Q^2 \sim 1 \text{ GeV}^2$, will only be registered in the inner part of the azimuthal angle
 8290 region for the nominal electron beam energy. As had been shown above, the lowering of the electron beam
 8291 energy effectively reduces the strong requirement of measuring up to about 179° , at the expense however, of
 8292 a somewhat reduced acceptance towards lowest Bjorken x .

8293 The optimum configuration of the inner detector will be revisited when the choice between the Linac-Ring
 8294 and the Ring-Ring option is made. It represents in any case one of the most challenging problems to be
 8295 solved for the LHeC.

8296 13.2 Baseline Detector Layout

8297 The baseline configuration (A) of the main detector has the solenoid in between the two calorimeters,
 8298 combined with a dipole field in the Linac-Ring case. It is subdivided into a central barrel and the forward
 8299 and backward end-cap regions, which differ in their design because the forward region sees the remnant
 8300 and the highly energetic ($E_h \lesssim E_p$) jet from the struck quark while the backward region sees the scattered
 8301 electron of energy $E'_e \leq E_e$. The detector configuration is sketched in Fig. ?? with component abbreviations
 8302 and some dimensions given. More detailed dimensions are given in Fig. ??.

8303 For the purpose of this design, technologies had to be chosen in line with the detector requirements,
 8304 see Sect. ??, and based on an evaluation of the technologies available or under development for the LHC
 8305 experiments or foreseen for a linear collider detector. The complete inner tracker is considered to be made
 8306 of Silicon. This enables to keep the radius of the magnets small, at about 1 m. Based on experience with
 8307 H1 and ATLAS the EMC is chosen to be a Liquid Argon (LAr) Calorimeter. The super conducting dipoles
 8308 (light grey in Fig. ??) are placed in a common cryostat with the detector solenoid (dark grey) and the LAr
 8309 EMC (green). The common cryostat is optimum for reducing the amount of material present in front of the
 8310 hadronic barrel calorimeter. The HAC is an iron-scintillator tile calorimeter, which also guides the return
 8311 flux of the magnetic field, as in ATLAS [?, ?]. In the baseline design (A) the muon detectors are placed
 8312 outside of the magnetic field with the function of tagging muons, the momentum of which is determined by
 8313 the inner tracker.

8314 For the Ring-Ring machine, in order to maximize the luminosity, extra focusing magnets must be placed

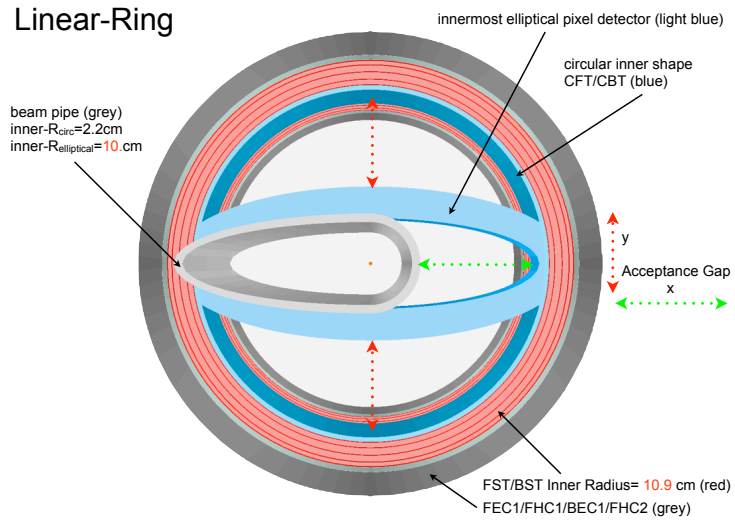


Figure 13.7: Linac-Ring beam pipe design and acceptance gap's due to deviations of inner shapes of the forward/backward tracking detectors FST/BST (circular) and the innermost central pixel detector layer (elliptical) from the pipe shape.

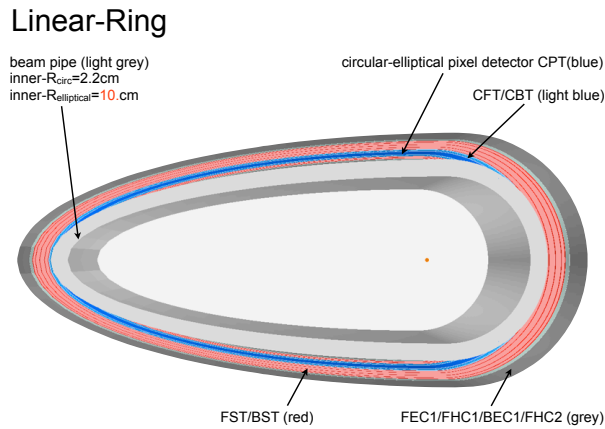


Figure 13.8: Beam pipe design for Linac-Ring and optimized circular-elliptical shape following the beam pipe for all adjacent detector parts.

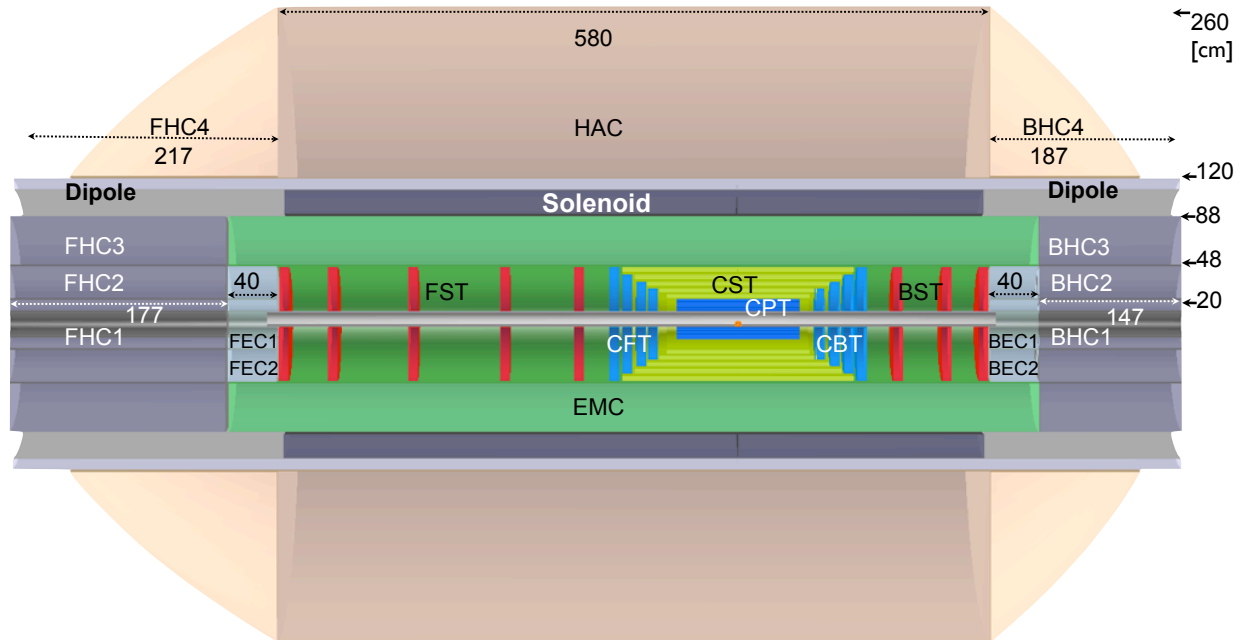


Figure 13.9: An rz cross section of the LHeC detector, in its baseline configuration (A). In the central barrel, the following components are considered: a central Silicon pixel detector (CPT); silicon tracking detectors (CST,CFT/CBT) of different technology; an electromagnetic calorimeter (EMC) surrounded by the magnets and followed by a hadronic calorimeter (HAC). Not shown is the muon detector. The electron at low Q^2 is scattered into the backward silicon tracker (BST) and its energy measured in the BEC and BHC calorimeters. In the forward region similar components are placed for tracking (FST) and calorimetry (FEC, FHC).

8315 near to the interaction point ³. This would mean replacing the FST and the BST tracking detectors by the
 8316 low- β quadrupoles (see Fig. ??), at the expense of losing about 8° of polar angle acceptance. The modular
 8317 design of the forward and backward trackers and the corresponding calorimeter modules allow the trackers
 8318 to be mounted/unmounted and the calorimeter inserts to be moved in and out of position as required. The
 8319 inner electromagnetic and hadronic endcap inserts, FEC1/BEC1 and FHC1/BHC1, respectively, will be
 8320 removed allowing the insertion of the low β -magnets and only partially put back in. Particular attention is
 8321 needed for the mechanical support structures of the quadrupoles. The structure must ensure the stability of
 8322 reproducible beam steering, while interfering as little as possible with the detector. The presence of strong
 8323 focussing magnets close to the interaction point was one issue experienced during HERA2 running [?].

8324 13.2.1 An Alternative Solenoid Placement - Option B

8325 The configuration A is determined by the intention to keep the detector ‘small’: it uses the HAC as flux
 8326 return for an inside solenoid which, for the Linac-Ring case, is combined with long dipoles. This is not ideal
 8327 for the hadronic energy measurement. Therefore a second configuration (B) has been considered, to much
 8328 less detail, in which the solenoid is placed outside the HAC. Option B might be of interest only for the
 8329 Ring-Ring case as otherwise, the requirement of the bending dipoles to be placed right after the EMC would
 8330 anyhow compromise the design requiring anyhow similar cryogenics and support structures as in option A.

8331 In considering a solenoid around the HAC one finds, as from the CMS geometry, that the return iron

³See above for an evaluation of that possibility.

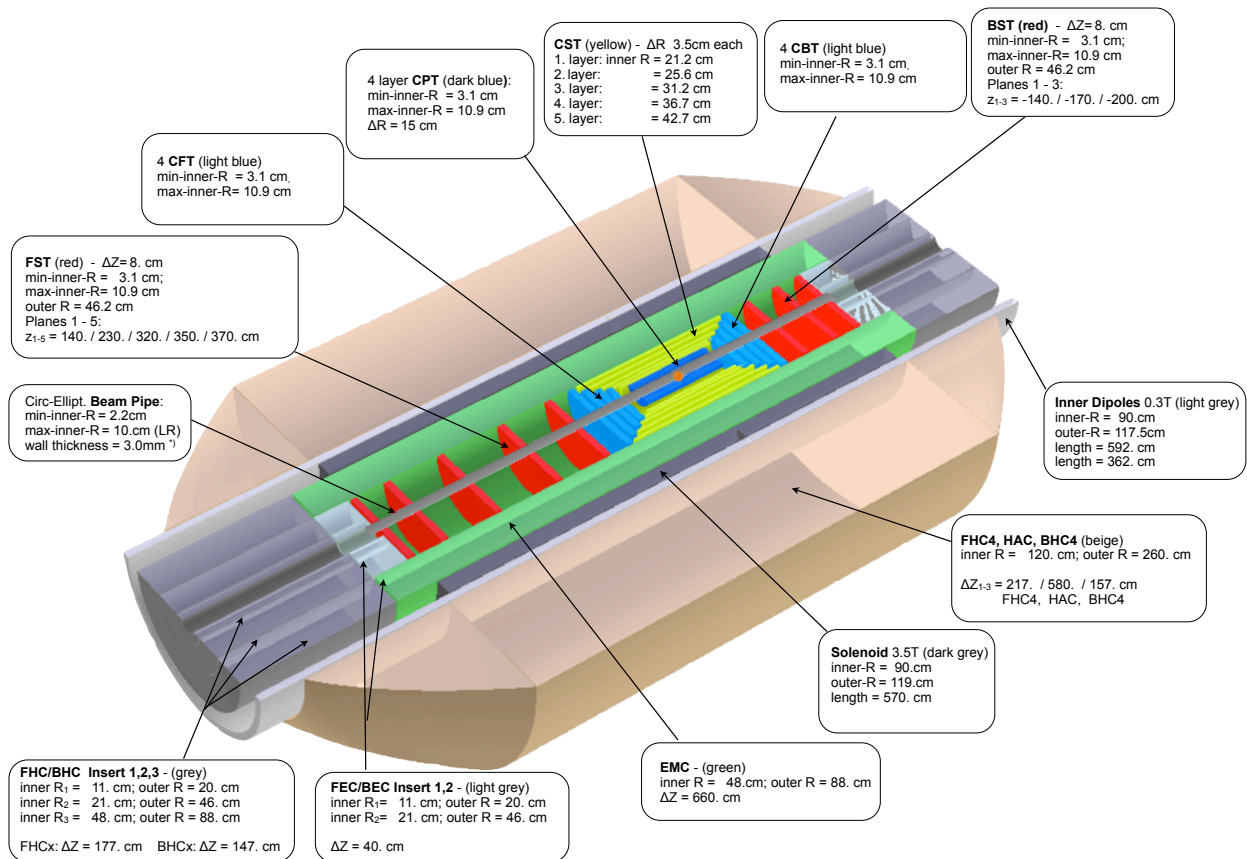


Figure 13.10: View of the baseline detector configuration (A) with some dimensions for each of the main detector components.

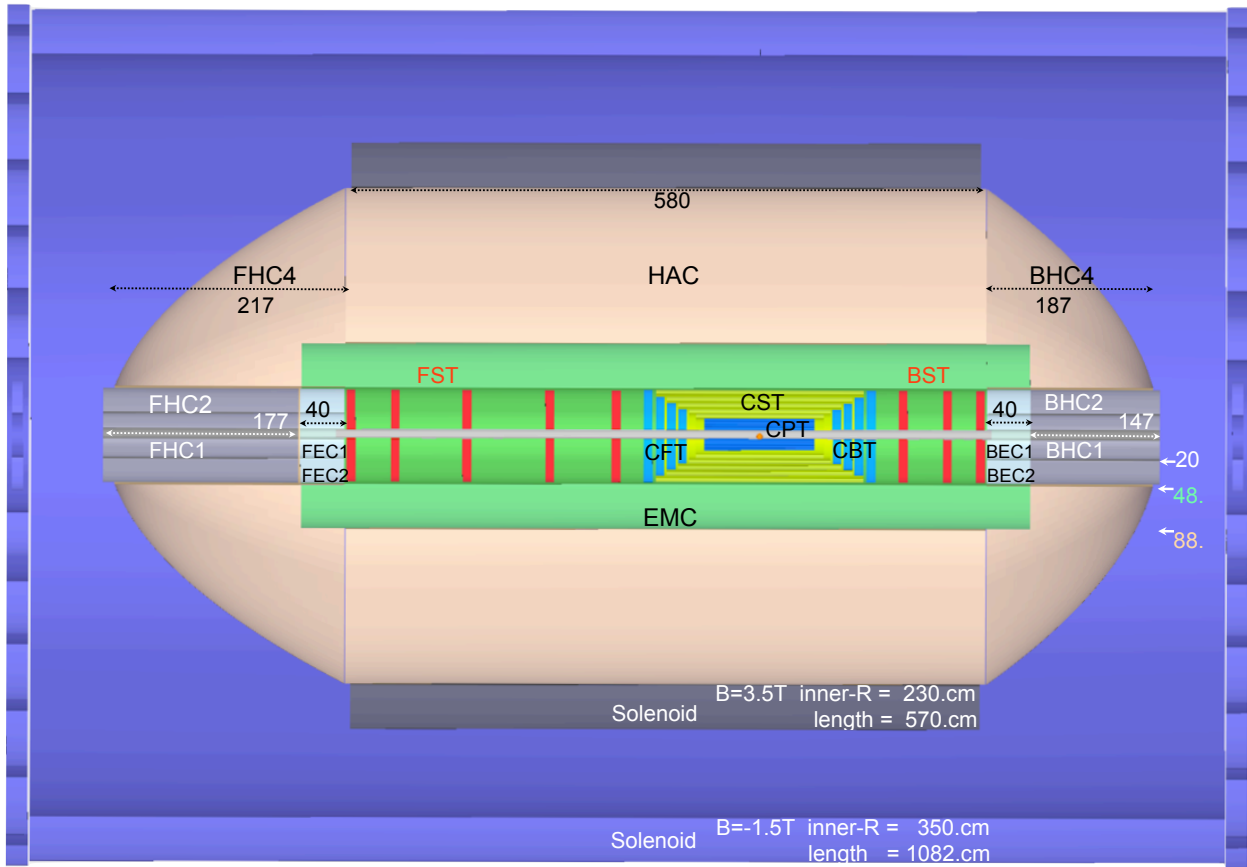


Figure 13.11: An rz cross section of the LHeC detector, option B, in which the solenoid is placed outside the HAC. A compensating larger solenoid is considered, see text. The muon detector is not shown but would be placed inside the second solenoid. The overall dimensions of this detector configuration are about 10 m length and 8 m diameter.

would be massive, of order 10000 tons [HERMANN??], and extend by several meters further out in radius, which may pose problems when one has the IP2 cavern in mind. One then is lead to consider using a second solenoid for an active flux return, which gives a good muon momentum reconstruction. A strong magnetic field of 3.5 T covering the barrel calorimeter (HAC) leads to a better separation of charged hadron induced showers in the HAC area compared to the sole fringe field effect in case of the inner solenoid baseline design A. The HAC would have to be designed very carefully as there would be no muon-iron return yoke following for catching shower tails. A warm EMC design with no need for a cryostat would become an option worth considering. Also extending the tracker by an extra more conventional layer of tracking chambers in front of the EMC would be an interesting possibility, with which the amount and radius of the Silicon detector may be somewhat reduced.

An overview of the detector configuration B is given in Fig. ?? . A two solenoid configuration is the 4th Concept for an ILC Detector [?]. The second outer solenoid keeps the overall dimensions of the detector limited. A detailed consideration of option B has not been intended at this stage of the project.

13.3 Magnet Design

The principle magnet configuration in the Linac-Ring baseline option is introduced and the principle design of solenoid and dipole magnets as well as their cryogenic services are described. In section ?? , the twin solenoid system option (detector option B) providing 3.5 T in the entire calorimeter space in combination with a 1.5 T space for a high precision muon tracking detector is addressed briefly.

13.3.1 Magnets configuration

The LHeC magnet system comprises for the bending of the particles produced in the collisions a 3.5 T solenoid with a free bore of 1.8 m and a coil length of 5.7 m. The bore size to provide space for the Pixel (CPT) and Strip (CST) detectors as well as the electromagnetic Liquid Argon calorimeter (EMC) with magnetic field while the hadronic tile calorimeter (HAC) and muon tagging detectors are left outside. The layout of the magnets in the baseline detector is shown in Figure 4.1. The iron present in the hadronic calorimeter also provides the return path for the solenoid magnetic field. In the Linac-Ring option also a set of 18 m long e-beam bending dipoles are required that provide 0.3 T on axis, a plus and a minus dipole of 9 m length each, respectively. The first dipole is to bring the e-beam into the collision point and the second to guide the beam away after the collision point. In the Ring-Ring option this set is obsolete. The Linac-Ring option obviously is more demanding and thus taken as the reference design and presented here. The introduction of the set of dipoles requires choosing a radial position and radial gap for these coils. Since space is required for the solenoid as well, an elegant solution is to combine within the detector volume the dipoles and the solenoid in one cryostat thereby minimizing the total radial gap as well as maximizing particle transparency. A second combination of cryogenic objects can be made by also housing the Li Argon electromagnetic calorimeter in the same cryostat which would reduce the radial built up of material significantly. Since a combination is easier the separate option is more demanding and therefore engineered and described here. Since the set of dipoles is 18 m long to provide the 2·2.5 Tm magnetic field integral, and the detector is 10 m long, each of the two dipoles are split in two sections. The inner superconducting sections sit with the solenoid in the same cryostat and the outer normal conducting iron based electromagnetic sections with much smaller bore of 0.3 m are positioned on the beam line at either side of the detectors, see Figure ?? .

13.3.2 Detector Solenoid

The conceptual design of the solenoid is presented and where necessary some details on the dipoles are mentioned as well. The position of the solenoid with respect to the other detector components and the envelopes respected have been shown before in Figure ?? . The longitudinal section of the LHeC baseline detector for the default detector configuration and the Linac-Ring option are shown; indicated are the position of the 3.5 T solenoid and the 0.3 T inner superconducting dipole sections. Solenoid and dipoles are

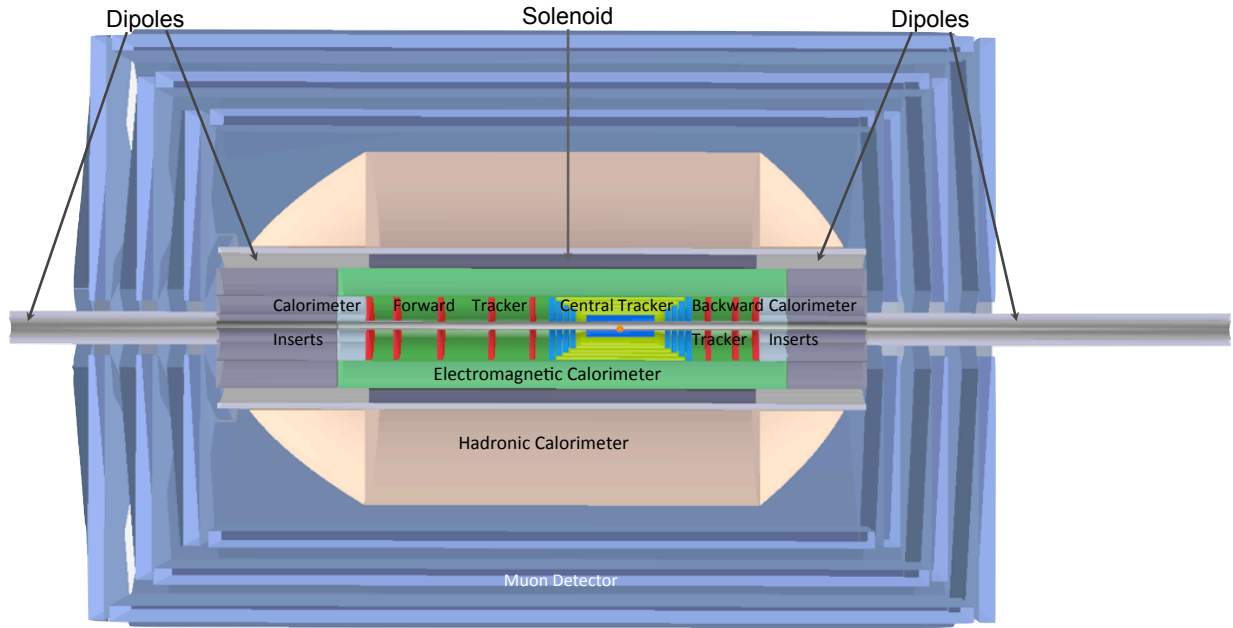


Figure 13.12: Configuration of the solenoid and electron beam bending dipoles in the baseline Linac-Ring detector. Longitudinal r-z section showing the position to solenoid and the two dipoles, each split in two sections, a superconducting inner section incorporated with the solenoid in one cryostat and a normal conducting iron based outer section magnet with smaller bore.

8377 on a common support cylinder and housed in a single cryostat with a free bore of 1.8 m and extending along
 8378 the entire detector with a length of ≈ 10 m.

8379 The design of the solenoid is based on the very successful experience with the many detector magnets
 8380 built over the past 30 years, in particular the most recent ATLAS and CMS solenoids [?], [?], [?], [?]. The
 8381 dimensions of the LHeC solenoid (3.5 T, 5.7 m long and 0.96 m inner radius) are about those of the ATLAS
 8382 solenoid (2.0 T, 5.3 m long with 1.25 m radius) while it has to provide the magnetic field of the much larger
 8383 CMS solenoid. Since the requested magnetic field is 1.75 times higher than in the ATLAS solenoid a double
 8384 layer coil will be needed. Using well established design codes with proven records on earlier detector magnets,
 8385 the main solenoid parameters are determined and are listed in Table ??.

8386 The solenoid is wound in two layers internally in an Al5083 alloy support cylinder with 30 mm wall
 8387 thickness and a length of about 6 m. When finished two extensions cylinders are flanged to the central
 8388 solenoid section at either end for supporting the inner superconducting dipole sections, see Figure ??. In
 8389 this way the solenoid can be produced as a 6 m long coil unit in a company, transported to the integration
 8390 site where the adjacent sections are coupled and the dipoles sections can be introduced.

8391 The magnetic field generated by the system of solenoid and internal dipoles is shown in Figure ??. The
 8392 peaks in magnetic field in the solenoid and dipole windings as results of their combined operation at nominal
 8393 current are 4.1 and 2.3 T respectively. The B_z and B_y components of the magnetic field are shown in
 8394 Figure ??.

8395 The superconductor used for the solenoid is an Al stabilized NbTi/Cu Rutherford cable based on state-of-
 8396 the-art NbTi strands featuring 3000 A/mm^2 critical current density at 5 T and 4.2 K. A 20 strands Rutherford
 8397 cable carries the nominal current of 10 kA which is 30% of its critical current. The conductor has a comfort-
 8398 able temperature margin of 2.0 K when operating the coil with a forced Helium flow enabling 4.6 K in the
 8399 solenoid windings. The high purity Al used for the co-extrusion of Al and cable is mechanically reinforced
 8400 by micro-alloying with either Ni or Zn, or another qualified material, a technology qualified for the ATLAS
 8401 solenoid. Two conductor units of 5.4 km would be perfect, corresponding to the two layers in the coil wind-

Property	Parameter	value	unit
Dimensions	Cryostat inner radius	0.900	m
	Length	10.000	m
	Outer radius	1.140	m
	Coil windings inner radius	0.960	m
	Length	5.700	m
	Thickness	60.0	mm
	Support cylinder thickness	0.030	m
	Conductor section, Al-stabilized NbTi/Cu + insulation	30.0×6.8	mm^2
	Length	10.8	km
	Superconducting cable section, 20 strands	12.4×2.4	mm^2
Masses	Superconducting strand diameter Cu/NbTi ratio = 1.25	1.24	mm
	Conductor windings	5.7	t
	Support cylinder, solenoid section + dipole sections	4.1	t
	Total cold mass	10.0	t
	Cryostat including thermal shield	6.5	t
Electro-magnetics	Total mass of cryostat, solenoid and small parts	17.0	t
	Central magnetic field	3.50	T
	Peak magnetic field in windings (dipoles off)	3.53	T
	Peak magnetic field in solenoid windings (dipoles on)	4.1	T
	Nominal current	10.0	kA
	Number of turns, 2 layers	1683	
	Self-inductance	1.6	H
	Stored energy	81.5	MJ
	E/m, energy-to-mass ratio of windings	14.2	kJ/kg
	E/m, energy-to-mass ratio of cold mass	9.2	kJ/kg
Margins	Charging time	1.0	hour
	Current rate	2.8	A/s
	Inductive charging voltage	2.3	V
	Coil operating point, nominal / critical current	0.3	
	Temperature margin at 4.6 K operating temperature	2.0	K
Mechanics	Cold mass temperature at quench (no extraction)	~ 80	K
	Mean hoop stress	~ 55	MPa
Cryogenics	Peak stress	~ 85	MPa
	Thermal load at 4.6 K, coil and cryosystem with 50% margin	~ 90	W
	Radiation shield load width 30% margin	~ 550	W
	Cooling down time / quench recovery time	4 and 1	day
	Use of liquid helium	~ 10	g/s

Table 13.1: Main parameters of the baseline LHeC Solenoid providing 3.5 T in a free bore of 1.8 m.

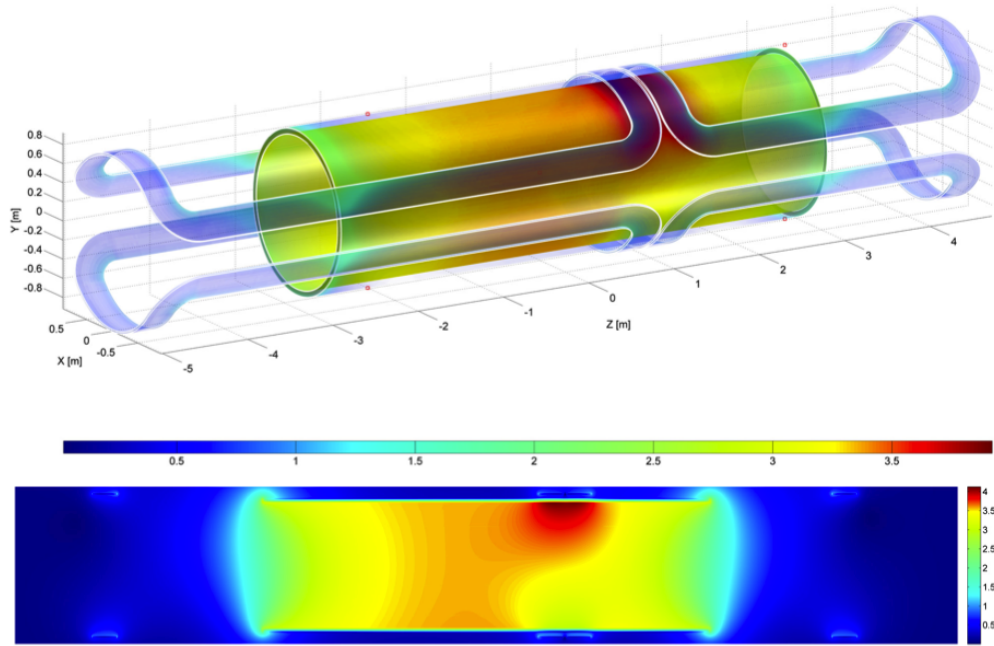


Figure 13.13: Magnetic field of the magnet system of solenoid and the two internal superconducting dipoles at nominal currents (effect of iron ignored). The position of the peak magnetic field of 4.1 T is local due to the adjacent current return heads on top of the solenoid where all magnetic fields add up.

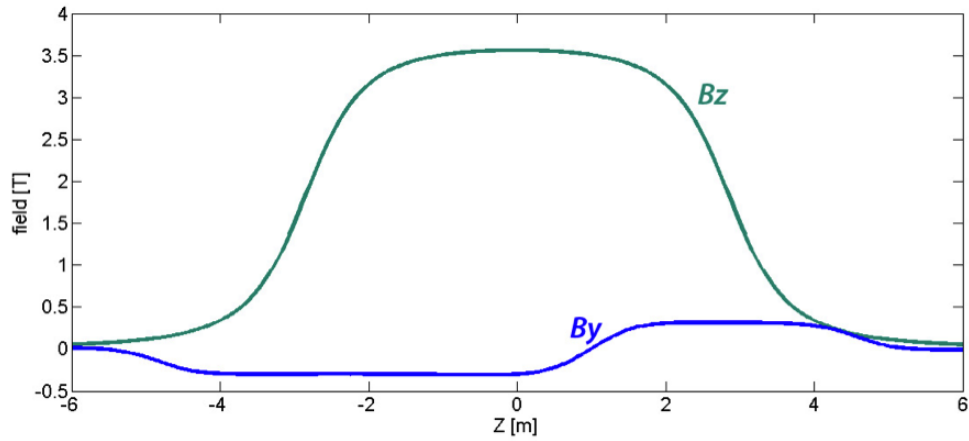


Figure 13.14: Magnetic field components B_z (solenoid) and B_y (set of internal dipoles) on the beam axis across 12 m in z . Note, the magnetic field of the external electromagnets are not included here.

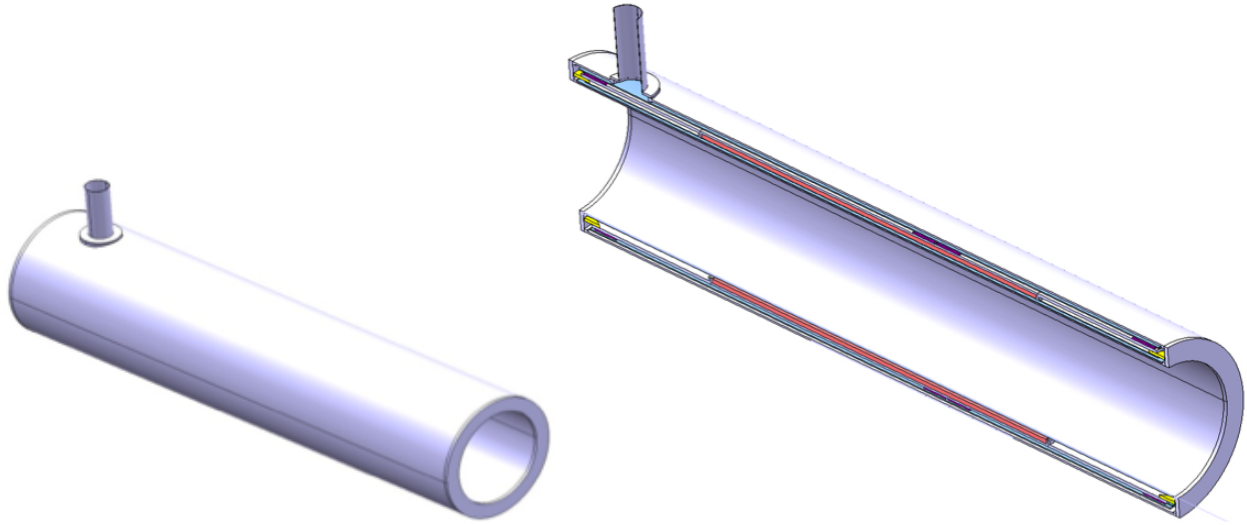


Figure 13.15: Cryostat of the magnet system. Left: the integrated cryostat, and right: longitudinal cut through the cryostat comprising a single cold mass of solenoid and internal superconducting dipole sections.

8402 ings. Eventually internal splices are acceptable and can be made reliably by overlapping a full turn and
 8403 performing welding on the two adjacent thin edges of the conductors. The conductor insulation is a double
 8404 layer of 0.3 mm thick polyimide/glass tape (or similar product) featuring a high breakdown voltage of more
 8405 than 2 kV and robustness for coil winding damage in order to limit the risk of turn-to-turn shorts. Coil
 8406 winding can be performed either using the wet winding technique with pre-impregnated tape or a vacuum
 8407 impregnation technique may be applied. Both techniques are appropriate provided fully qualified with the
 8408 coil winding contractor. Once the solenoid windings are finished and delivered to the coil integration site, the
 8409 dipole coil sections are inserted in slots milled into the outer surface of the support cylinder, see section ??.
 8410 The four dipole upper and lower coil sections are separately produced as flat racetrack coils and then bent
 8411 onto the fully assembled support cylinder. Next all interconnections and bus connections to the current leads
 8412 are laid down and the cold mass is inserted in the cryostat. The cryostat design is shown in Figure ??. The
 8413 cold mass is supported from the cryostat with a system of triangle brackets, a proven technique providing a
 8414 very compact solution [?], [?]. The cryostat is equipped with thermal shields and multi-layer super-insulation
 8415 in the usual way. The coil windings of both solenoid and dipole sections are cooled by conduction by forced
 8416 flow liquid helium circulating in 14 mm sized cooling tubes that are attached to the outer surface of the
 8417 integrated support cylinder. The two layer winding pack of 60 mm radial built and fully bonded to the
 8418 support cylinder is sufficiently thin to warrant a thermal gradient in the winding pack of less than 0.1 K.

8419 13.3.3 Detector integrated e-beam bending dipoles

8420 The two e-beam bending dipoles are positioned symmetrically around the beams intersection point. As
 8421 outlined before each 9 m long dipole is split into a superconducting section integrated with the central
 8422 solenoid and a normal conducting iron based electro-magnet positioned around the beam outside the main
 8423 detector envelope. The external dipole magnets are conventional and will not be further detailed here. The
 8424 principle parameters of the superconducting dipole sections are listed in Table ??.

8425 13.3.4 Cryogenics for magnets and calorimeter

8426 The cryogenic operating conditions achieved by circulating forced flow two-phase helium in cooling pipes
 8427 attached to the Al-alloy coil support cylinder. Electric powering of the magnets at 10 kA is through two
 8428 pairs of low-loss high-temperature superconducting current leads. The current leads are housed in a separate

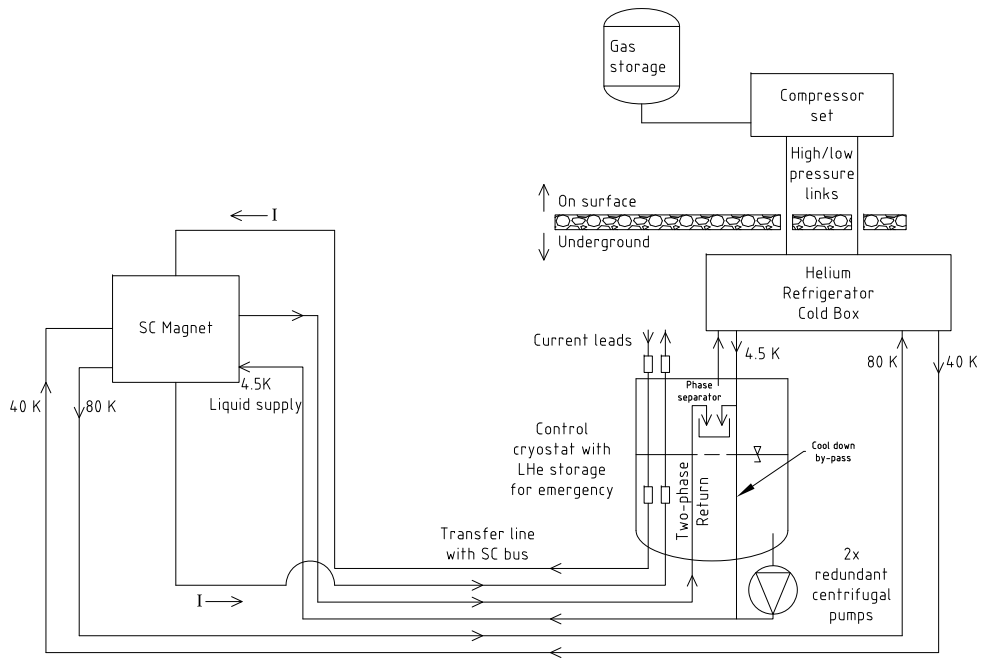


Figure 13.16: Basic cryogenic flow scheme for the cooling of the superconducting magnets.

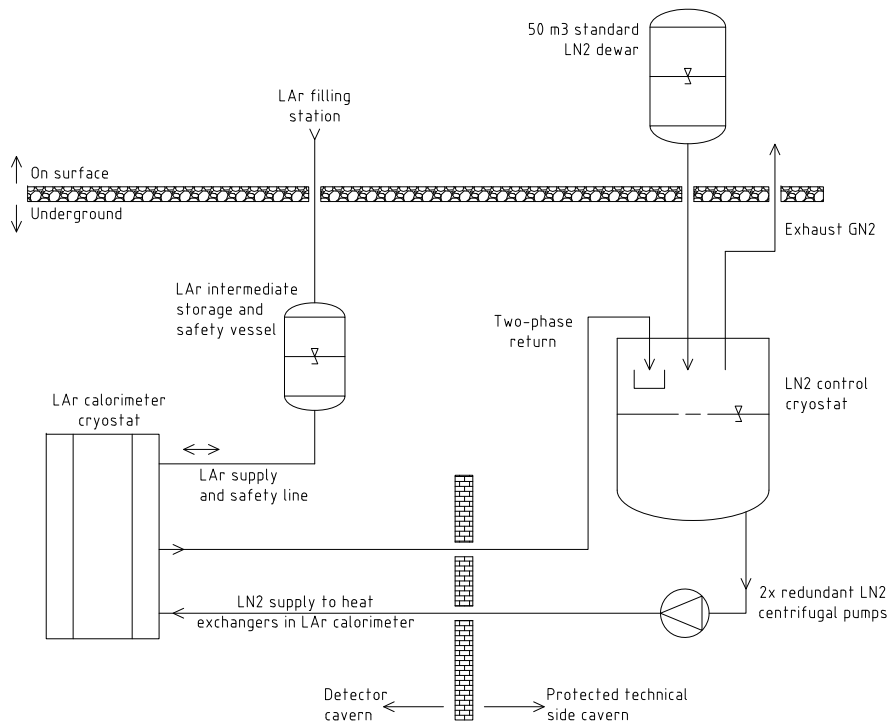


Figure 13.17: Basic cryogenic flow scheme for the cooling of the liquid argon calorimeter.

	Plus coil	Minus coil	
Magnetic field on axis		0.3	T
Peak magnetic field in windings (solenoid off)		0.7	T
Peak magnetic field in windings (solenoid on)		2.6	T
Dipole length (including external sections)		9.0	m
Field integral internal section (sc dipole)	1.6	1.0	Tm
Field integral external section (iron magnet)	1.1	1.7	Tm
Operating current		2.0	kA
Stored Energy	1.9	1.2	MJ
Coil inductance	?	?	H
Windings engineering current density	?	?	A/mm ²
Coil inner / outer radius		1.042/1052	m
Coil length	6.00	3.70	m
NbTi/Cu cable (12 strands Rutherford cable)		1.44×4.31	mm ²
Conductor length	5.4	3.6	km

Table 13.2: Main design parameters of the set of superconducting electron beam bending dipoles.

8429 service cryostat installed at distance in a side cavern, a non-radiation environment. This current leads
8430 cryostat contains a larger amount of helium sufficient for a safe 1-2 hours ramp down in the case of refrigerator
8431 failure as well as to maintain the magnets at operating temperature for a few hours. Redundant centrifugal
8432 pumps provide for circulation of the slightly sub-cooled liquid helium to the magnets. The two-phase return
8433 flow is brought to a phase separator in the cryostat. A combined superconducting link and helium transfer
8434 line connects the service cryostat with the current leads and helium buffer to the magnets. The refrigerator
8435 is at proximity to the cryostat and the compressor set is installed on surface. The expected modest thermal
8436 loss of the magnet system amounts to some 60 W@4.5 K, the use of low loss current leads and, the estimated
8437 overall system loss suggest a small sized standard refrigerator in the class of 200 to 300 W@4.5 K. Figure ??
8438 shows the simplified flow scheme of the helium cryogenic system.

8439 A liquid Argon calorimeter is envisaged as part of an EMC. As mentioned before, it can be installed
8440 in a separate cryostat or preferably share the cryostat with the solenoid. In the latter case the systems
8441 compactness is increased and the inner thermal shield can be omitted. The calorimeter will have an overall
8442 18 m³ volume from which approximately 12 m³ will be slightly sub-cooled liquid argon. Cooling is with two-
8443 phase liquid nitrogen in longitudinal pipe runs and its circulation is provided by two redundant small sized
8444 liquid nitrogen pumps. The liquid nitrogen is supplied from a standard dewar on surface to an intermediate
8445 cryostat which serves also as the phase separator. For the liquid argon filling, a line connects from the surface
8446 to an intermediate dewar from which it is transferred to the LAr cryostat in the detector. This dewar also
8447 serves as emergency volume in the case of vacuum loss or leak problems to which the liquid argon can be
8448 transferred from the cryostat. Figure ?? shows the functional principle of the Argon cooling units.

8449 The cooling principles of both cryogenic systems proposed in this paper are based on previous design and
8450 experience from the much more complex ATLAS detector cryogenics.

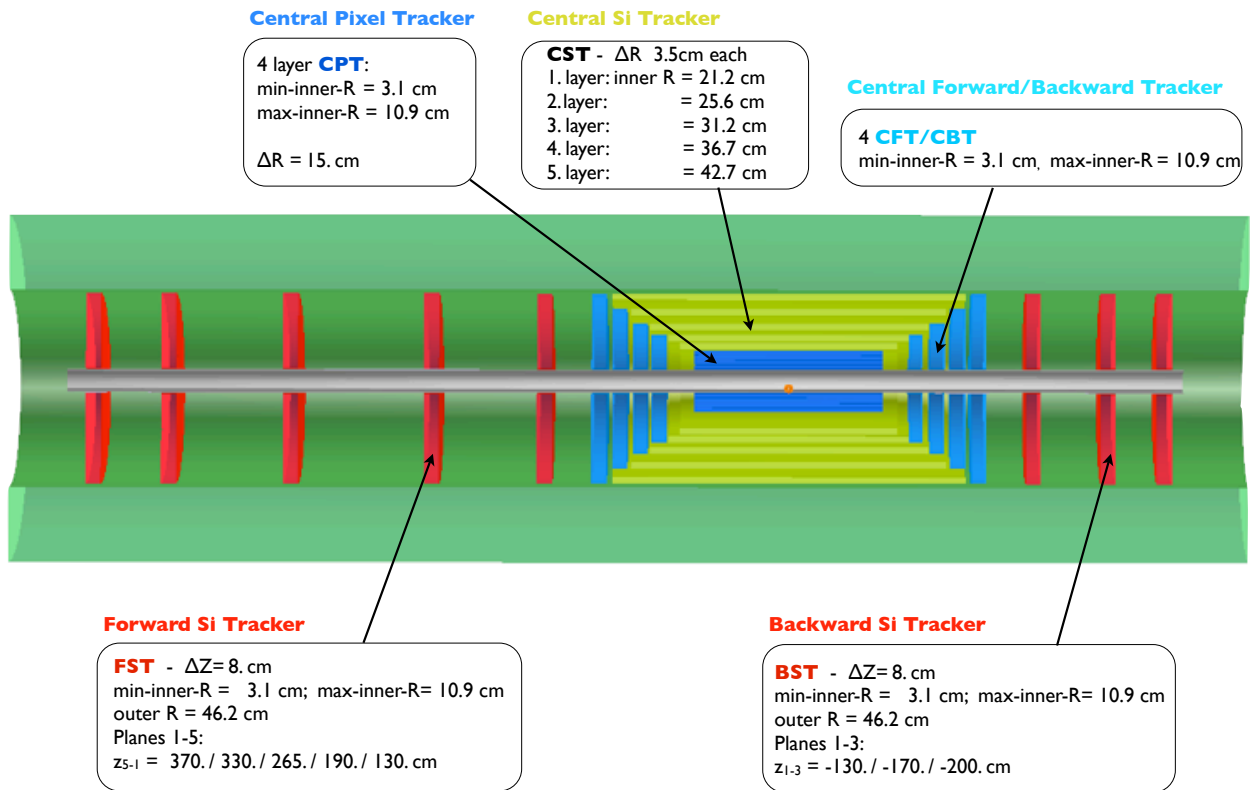


Figure 13.18: Tracker and barrel Electromagnetic-Calorimeter r_z view of the baseline detector (Linac-Ring case).

13.3.5 Twin Solenoid System

13.4 Tracking Detector

13.4.1 Tracking Detectors Layout - Baseline Detector

The tracking detectors (Fig. ??) inside the electromagnetic calorimeter are Si-sensor only devices. The tracker system has to provide precise tracking, momentum determination as far as possible, vertex reconstruction and pattern recognition. It covers the pseudorapidity range $-4.8 < \eta < 5.5$ and is located inside the solenoidal field of 3.5T. Additionally a dipole field of 0.3T is superposed resulting from the beam steering dipoles housed inside the same cryostat as the solenoid. For 1° tracks the bending solenoidal field component (0.36T) is of the same order as the dipole field and the resulting track Sagitta reaches the [mm] range when particles of momentum $< 100\text{GeV}$ pass 250cm (track length measured) Fig. ?. The tracker described here (FST) measure 1° tracks over a distance of $\approx 180\text{cm}$ (forward direction). Therefore a momentum determination for $\approx 1^\circ$ and high momentum tracks is unlikely but with precision tracking the analysis will rely on the tagged energy measurement. The backward measurement is characterised by even shorter track length's. There the analysis will rely on the energy measurement in calorimeters combined with a well defined track definition. That approach is supported by the fact that the particle flux in backward compared to forward direction is lower due to kinematics. The well separated charged tracks in backward direction are usually easier to measure and will allow the precision tagging of corresponding calorimeter signals. Very low Q^2 /low x processes will be better accessible by reducing the electron beam energy thus measured at larger angles in backward direction (see Fig. ?? and Fig. ?? and discussion in chapter ??).

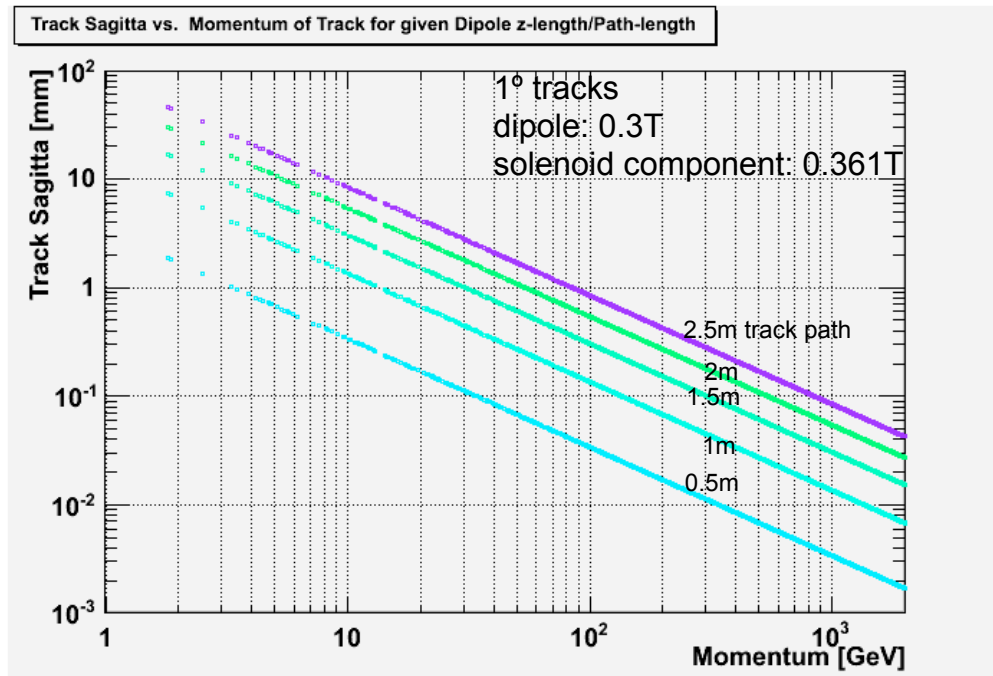


Figure 13.19: Track Sagitta vs. Momentum of 1° tracks in a superposed dipole/solenoidal field.

The tracker is subdivided into central (CPT, CST, CFT/CBT) and forward/backward parts (FST, BST). Fig. ?? shows the tracker configuration for the high acceptance running of solution (A) of the detector design. More details are summarized in Tab. ?? ⁴.

⁴The item *project area* in table ?? describes the area which has to be equipped with appropriate Si-sensors (e.g. single-sided

Central Barrel	CPT1	CPT2	CPT3	CPT4	CST1	CST2	CST3	CST4	CST5
Min. Radius R [cm]	3.1	5.6	8.1	10.6	21.2	25.6	31.2	36.7	42.7
Min. Polar Angle θ [°]	3.6	6.4	9.2	12.0	20.0	21.8	22.8	22.4	24.4
Max. $ \eta $	3.5	2.9	2.5	2.2	1.6	1.4	1.2	1.0	0.8
ΔR [cm]	2	2	2	2	3.5	3.5	3.5	3.5	3.5
$\pm z$ -length [cm]	50	50	50	50	58	64	74	84	94
Project Area [m ²]	1.4				8.1				
Central Endcaps	CFT4	CFT3	CFT2	CFT1		CBT1	CBT2	CBT3	CBT4
Min. Radius R [cm]	3.1	3.1	3.1	3.1		3.1	3.1	3.1	3.1
Min. Polar Angle θ [°]	1.8	2.0	2.2	2.6		177.4	177.7	178	178.2
at z [cm]	101	90	80	70		-70	-80	-90	-101
Max./Min. η	4.2	4.0	3.9	3.8		-3.8	-3.9	-4.0	-4.2
Δz [cm]	7	7	7	7		7	7	7	7
Project Area [m ²]	1.8					1.8			
Fwd/Bwd Planes	FST5	FST4	FST3	FST2	FST1		BST1	BST2	BST3
Min. Radius R [cm]	3.1	3.1	3.1	3.1	3.1		3.1	3.1	3.1
Min. Polar Angle θ [°]	0.48	0.54	0.68	0.95	1.4		178.6	178.9	179.1
at z [cm]	370	330	265	190	130		-130	-170	-200
Max./Min. η	5.5	5.4	5.2	4.8	4.5		-4.5	-4.7	-4.8
Outer Radius R [cm]	46.2	46.2	46.2	46.2	46.2		46.2	46.2	46.2
Δz [cm]	8	8	8	8	8		8	8	8
Project Area [m ²]	3.3						2.0		

Table 13.3: Summary of tracker dimensions.

The 4 Si-Pixel-Layers CPT1-CPT4 (resolution of $\sigma_{\text{pix}} \approx 8\mu\text{m}$) positioned as close to the beam pipe as possible.

Si-strixel (CST1-CST5) (resolution of $\sigma_{\text{strixel}} \approx 12\mu\text{m}$) forming the central barrel layers. An alternative is the of 2_in_1 single sided Si-strip solution for these barrel cylinders ($\sigma_{\text{strip}} \approx 15\mu\text{m}$) (Ref. [?]).

The endcap Si-strip detectors CFT/CBT(1-4) complete the central tracker.

The tracker inserts, 5 wheels of Si-Strip detectors in forward direction (FST) and 3 wheels in backward direction (BST), are based on single sided Si-strip detectors of 2_in_1-design ($\sigma_{\text{strip}} \approx 15\mu\text{m}$). They have to be removed in case of high luminosity running for the Ring-Ring option of the accelerator configuration see Fig. ??.

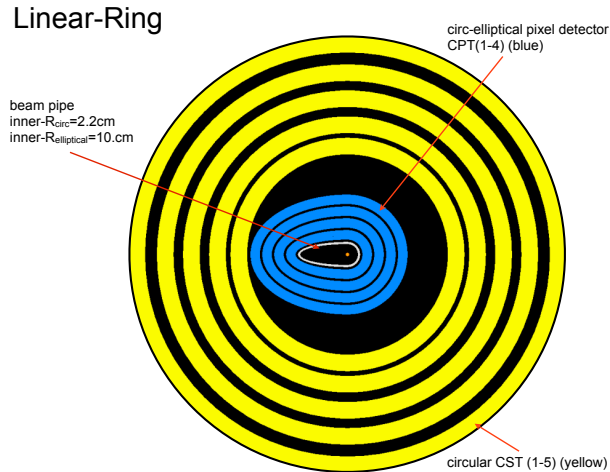


Figure 13.20: XY cut away view of the Central Pixel (CPT) and Central Strixel Tracker (CST) (Linac-Ring layout).

8473 Acceptance coverage down to 1° and 179° , respectively, and the tagging of secondary vertices originating
 8474 from the decay of heavy particles over a wide range of $|\eta|$ are requirements vital for the physics program
 8475 for the LHeC experiment. Measuring close to the beam line for maximal polar angle coverage and to the
 8476 vertex are major requests. The shape of the CPT and the inner dimensions of all near-beam detectors have
 8477 been chosen accordingly (Fig. ?? show the xy view of the circular-elliptical CPT and the cylindrical CST
 8478 detectors).

8479 The *All-Silicon* based tracking devices allow high resolution track space points measurement and hence
 8480 sufficient pattern recognition even at both angle acceptance limits in forward and in backward direction,
 8481 respectively. The expected jet angular and energy distribution for some selected physics processes simulated
 8482 using *RAPGAP* (Ref. [?]) is shown in Fig. ?. That figures illustrate once again the importance of the
 8483 forward acceptance down to 1° .

8484
 8485 Some results of preliminary tracker performance simulations using the LicToy-2.0 program [?] for the
 8486 tracker setup (see table ?? and Fig. ??), are summarized in Fig. ?. The geometrical arrangement of the
 8487 tracking detectors together with the pre-defined resolution settings for those parts, perform as expected at
 8488 least within that simplified framework. ⁵

8489 13.4.2 Tracking Detector Design Criteria and possible Solutions

8490 The experience of former attempts for an optimal detector setup suggest that some criteria should be
 8491 discussed as early as possible.

8492 Some arguments for the design will predominantly be (see Ref. [?], [?]):

- 8493 • Optimizing of cost for all components. Making use of technology developments for HL-LHC/ILC exper-
 8494 iments (Ref. [?], [?], [?], [?], [?], [?], [?], [?], [?], [?], [?], [?], [?]) but rely on technologies available

or double-sided sensors). An alternative would be the usage of Si-Gas detectors providing track segment information instead of track points, e.g. in the CST cylinders (Ref. [?], [?], [?])

⁵It might be necessary to set up an analog readout tracking system or implement fairly small strip sizes to keep the spatial resolution at high level maintaining the accuracy of momentum measurement. Alternatively or in addition one could install more tracking layers/planes. That has to be clarified by a more elaborated simulation.

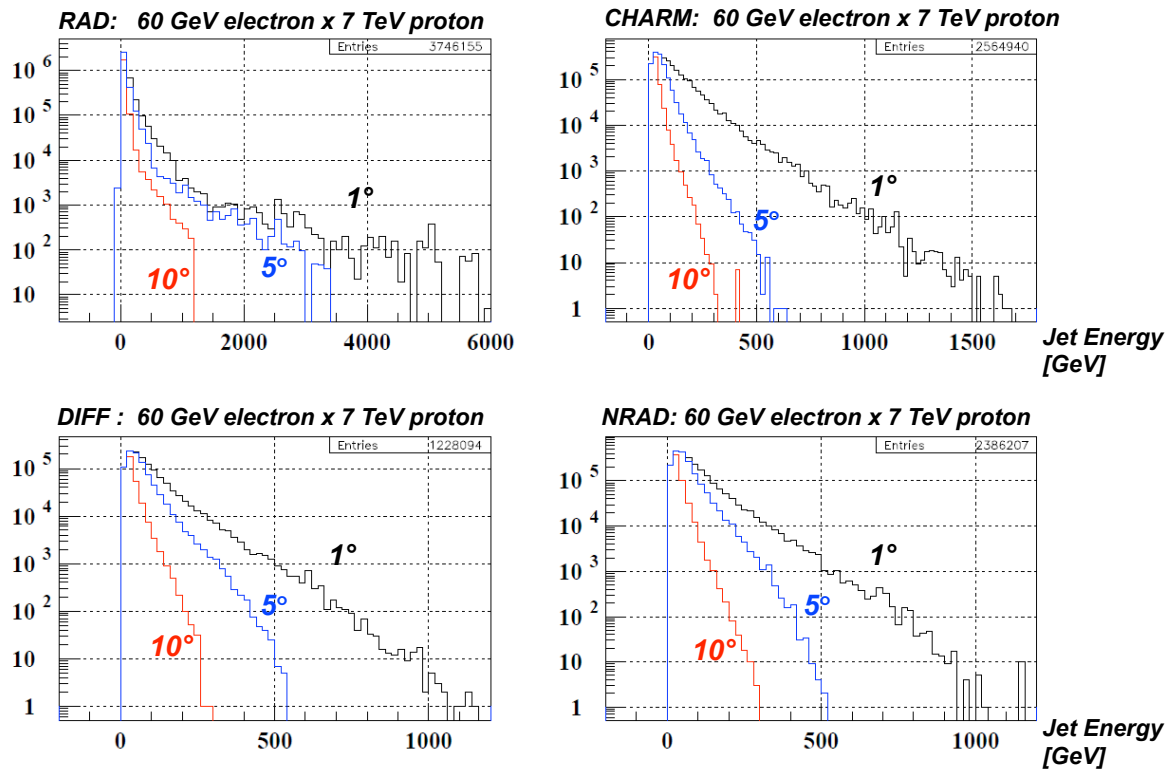


Figure 13.21: Radiative, diffractive, charm and non-radiative Jet production for polar angle $\theta = 1^\circ, 5^\circ$ and 10° .

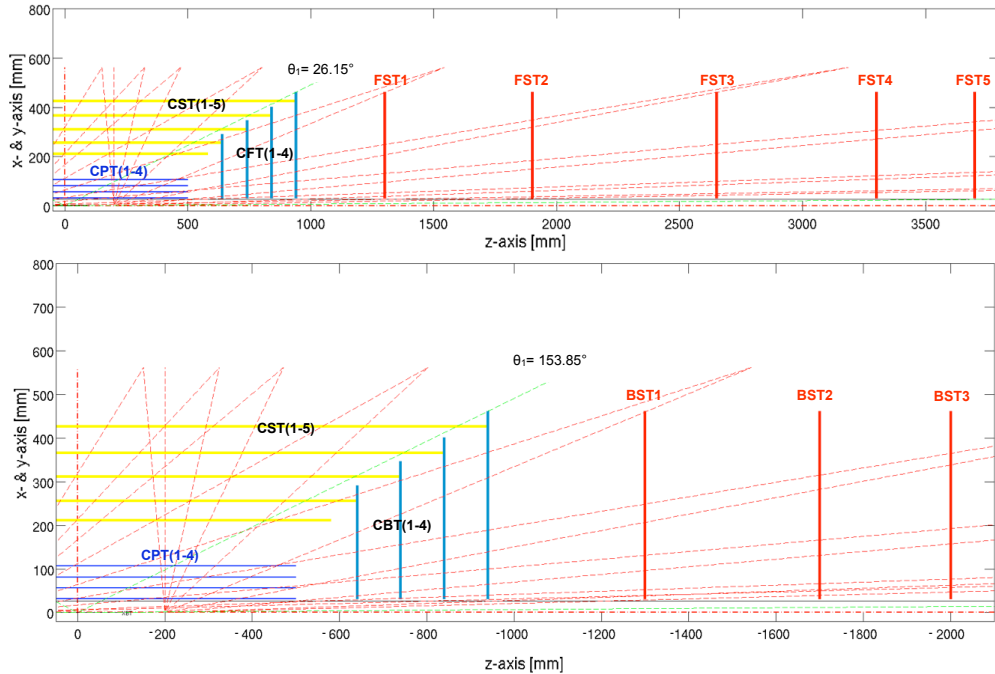


Figure 13.22: LicToy2.0 tracker design of the central/forward FST(top) and central/backward direction BST(bottom).

8495 today because of time constraints. Today's accessible sensors, integrated electronics, readout/trigger
 8496 circuitry, mechanics, cooling etc. have to be used to meet the goal: installation in the 2020's.

- 8497 • The default tracker setup is based on the silicon microstrip detector technology developed for the big
 8498 experiments at LHC, ILC, TEVATRON, b-factories, etc. within the last 20 years. The decisions for
 8499 sensor types (pixel, strip) operation depend on many factors and will be taken according to its
 8500 functionality finally:

8501 The expected radiation load is defined and influenced by the interaction rate (25ns), luminosity
 8502 ($\approx 10^{33} \text{ cm}^{-2} \text{ s}^{-1}$), particle rate per angle interval, fluence n_{eq} and ionisation dose over 1 years running.
 8503 Some data will be better defined after evaluation of more detailed simulations. Specifically the radiation
 8504 impact on tracker wheels, calorimeter inserts and inner pixel-barrel layer has to be studied. The tools
 8505 for those simulations are being prepared. Very first estimates will be discussed in section ?? in more
 8506 detail, but no indication for extremely high radiation load into the detectors adjacent to the beam
 8507 pipe have been obtained so far. The expected levels are far below what the LHC experiments have to
 8508 sustain.

8509 A side remark is related to the active parts of the forward/backward calorimeter. For safety rea-
 8510 sons those calorimeter inserts should be equipped with radiation hard Si-based sensors according to
 8511 LHC/HL-LHC standards. Relatively small in volume but still large in terms of layer area (m^2), the
 8512 equipment of calo-inserts Si-strip/Si-pad based is a sizeable investment but might be needed for safety
 8513 reasons. A final decision will be possible after more cross checks (some FLUKA simulations are pend-
 8514 ing).⁶

⁶On physics event generation level appropriate instruments are missing or of limited use; e.g. ep interactions are not incorporated into PYTHIA8 currently

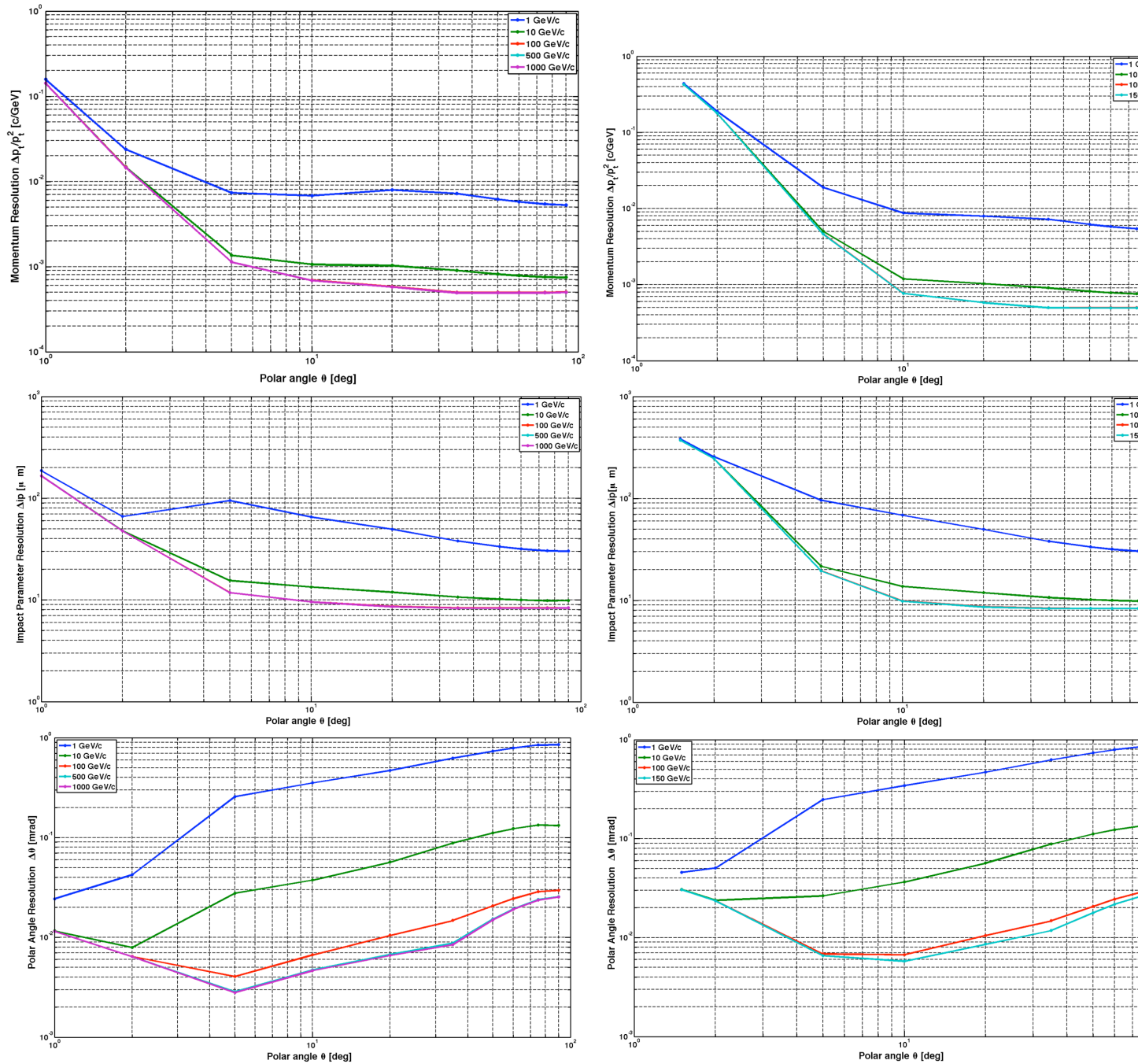


Figure 13.23: Scaled momentum, impact parameter and polar angle resolution as function of polar angle θ resulting from tracker design simulation using LiCToy2 for the FST(left) and BST(right) side. Tracker setup used as shown in Fig. ??,

Basic parameters:

$B=3.5T$, $X/X_0^{\text{beam pipe}} = 0.002$, $X/X_0^{\text{det-parts}} = 0.005$, efficiency=0.99%, Resolutions(σ): $\sigma_{\text{CPT}} = 8\mu\text{m}$, $\sigma_{\text{CST,CFT,CBT}} = 12\mu\text{m}$, $\sigma_{\text{FST,BST}} = 15\mu\text{m}$, minimal inner radius $R_{\text{min}}^{\text{CPT,CFT,CBT,FST,BST}} = 3.15\text{cm}$.

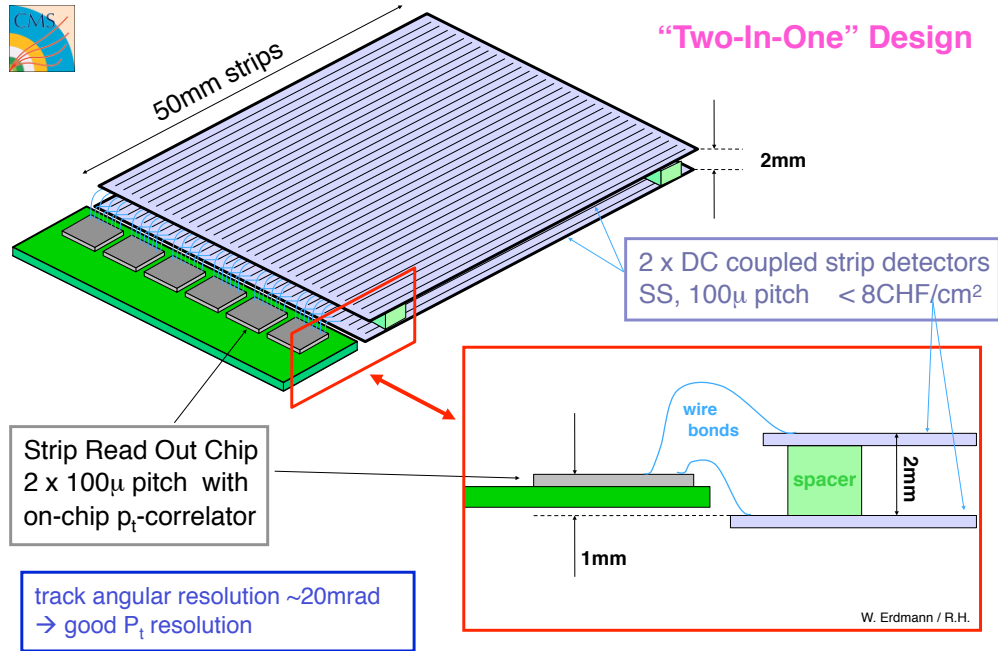


Figure 13.24: Layout of the 2_in_1 strip sensor design used as p_t -trigger setup for the CMS experiment.

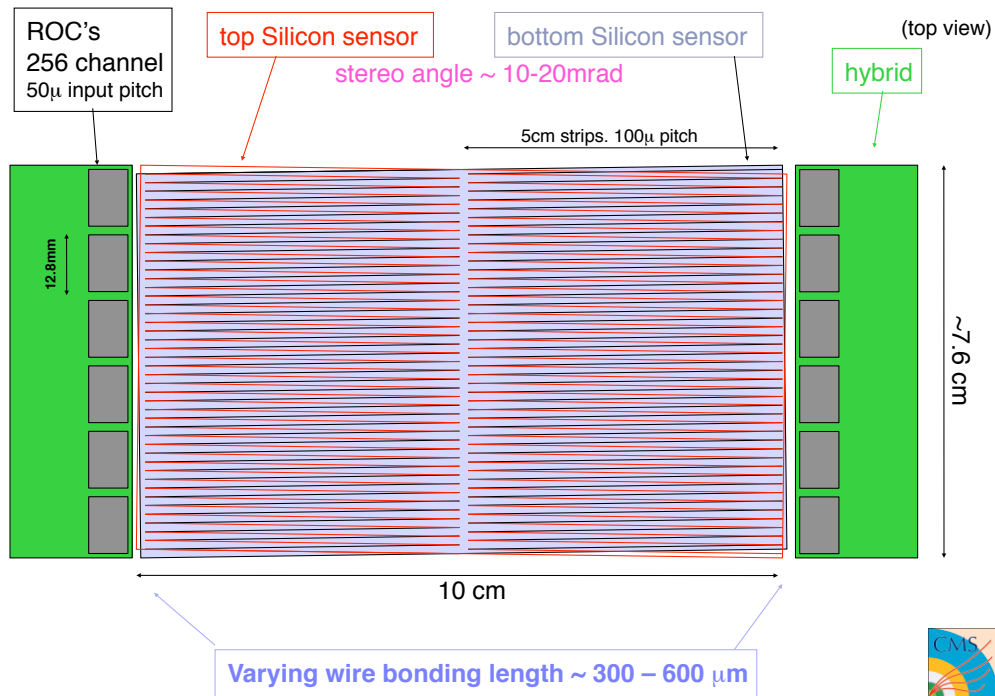


Figure 13.25: Layout of the 2_in_1 strip sensor design used as tracker module. Double use of e.g. power and cooling.

Decisions have to define the trigger capabilities/options, here in the context of tracking only, which have a direct impact on sensor choice, arrangement and attached electronics. It might be that very recent developments of 3D integration semiconductor layers interconnected to form monolithic unities of sensor&electronic circuitry are in time for the installation in the 2020's but conventional wire bonded or bump bonded solutions may be more cost efficient and rely on components available today. E.g. using the 2_in_1 strip sensor design as p_t -trigger discussed by the CMS upgrade design group Fig. ??, Refs. [?] will have, e.g., direct impact on a muon-trigger definition. The sensor, hybrid and readout modules are available and interconnected by wire bonds. On the other hand the 2_in_1 sensor design is a very elegant way saving resources when setting up a tracker (CMS design Fig. ??, Refs. [?]).

Candidates of readout chips attached to the sensors are e.g. the ATLAS FE-I4 ($50\mu m * 250\mu m$) and CMS ROC ($100\mu m * 150\mu m$) (see Refs. [?], [?]). The sensor pitch has to be matched and the electronics scheme defined before.

- The size of the largest stave structure to be installed (half z-length $\approx 94cm$) is smaller then the stave length used e.g. by ATLAS ($\approx 120cm$). Powering and in that respect cooling per stave are therefore less demanding then for the current LHC installations. Minimization of cooling effort reduces the material budget directly; cooling is related to power consumption issues and it might be a criterion for technology selection. A decision on powering concept is needed (seriell, parallel powering). It will depend on the template chosen for readout and services. The obvious suggestion is to re-apply one scheme used by a current LHC experiment inline with the sensor & electronic & readout option selected.

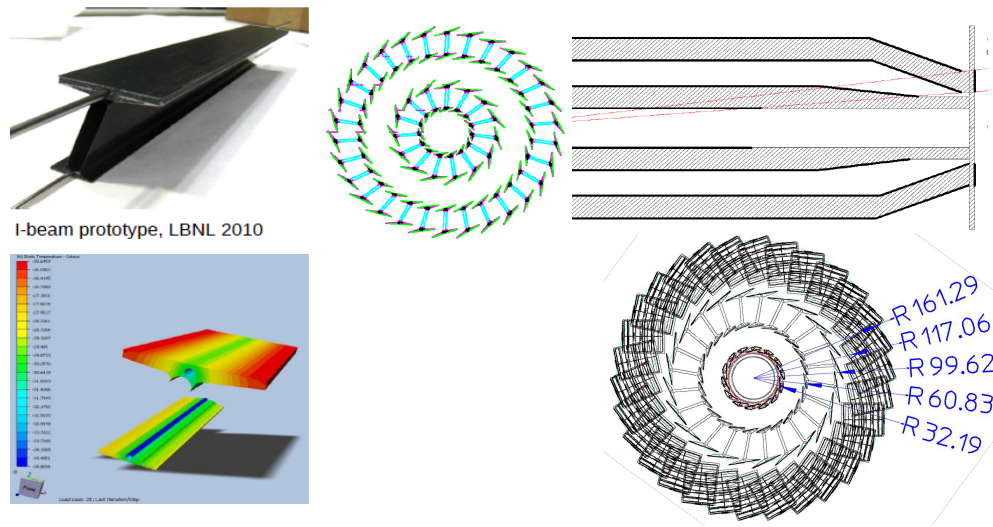


Figure 13.26: Proposed mechanics and sensor layout for the ATLAS pixel upgrade.

- The mechanical support and cooling elements have to be chosen to minimize the material budget of the setup and hence to diminish the impact of Coulomb multiple-scattering on track resolution by the tracker material. The HL-LHC upgrade developments of e.g. ATLAS and CMS show the relevance of that topic for the future physics program at the second phase of LHC. Rigid but very light mechanics in connection with improved sensor arrangement, incorporation of cooling systems and all other services into the support structure are the main design criteria for HL-LHC and should be for LHeC as well. In Figs. ??, ?? and ?? are possible mechanical solution for the ATLAS and CMS tracker upgrade in the barrel as well as in the forward/backward tracker region shown (Refs. [?], [?], [?]). Those designs may well serve as templates for the LHeC experiment. An artist view in Fig. ?? shows the implementation

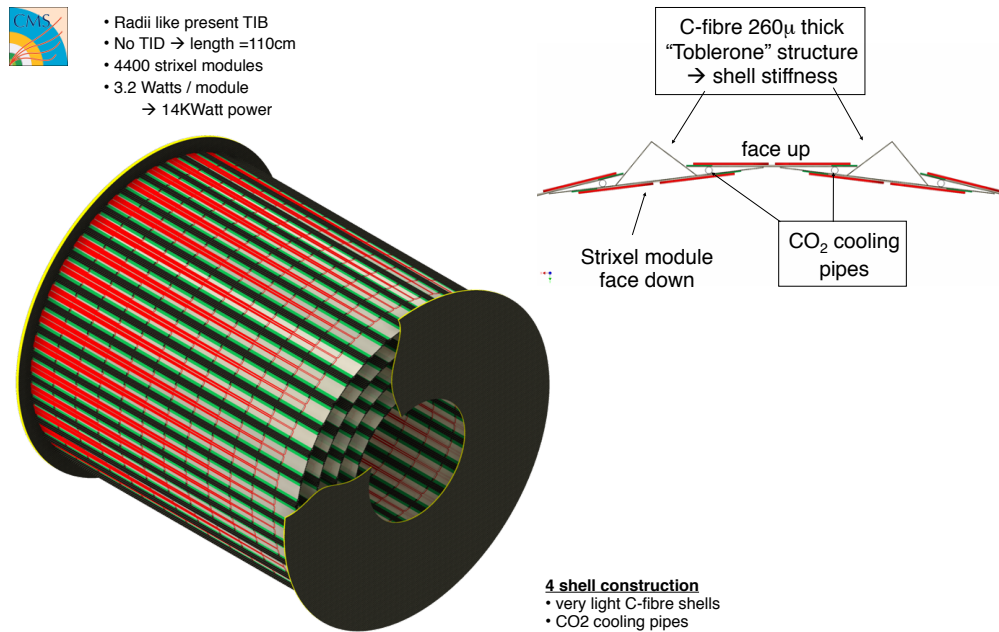


Figure 13.27: Proposed mechanics layout for the CMS inner barrel tracker upgrade.

Inner & outer ring of blades

CO₂ tubes embedded in half disk support:

- support cylinder:
 - Carbon carbon
 - Grooves for cooling tube
 - Stainless steel tube:
 - 1.8mm OD, 100 μ m wall

Blades:

- all identical
- Rotated by 20° radial
- Tilted by 12° (inner ring)
- 2 modules per blade (ϕ overlap)
- individually replaceable

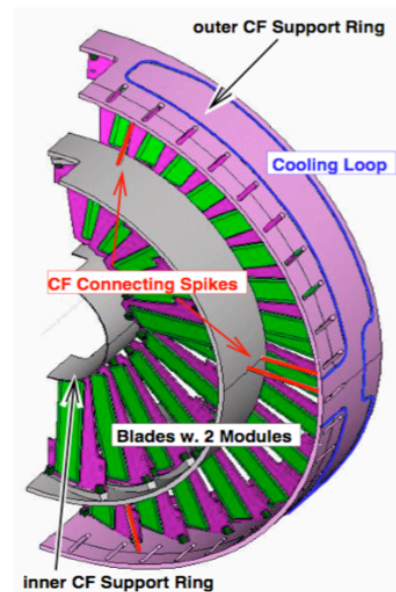
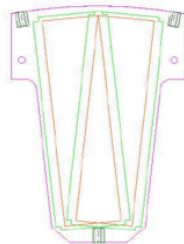


Figure 13.28: Proposed mechanics layout for the CMS tracker wheel upgrade.

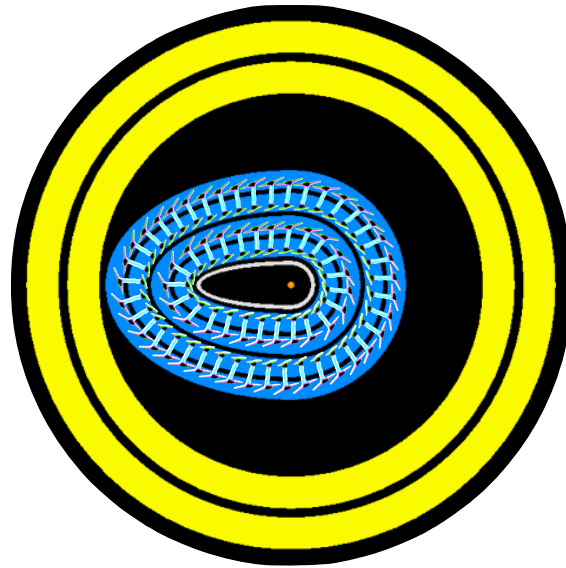


Figure 13.29: Artist view of the pixel sensor arrangement using the double-I ATLAS layout as template (Fig. ??).

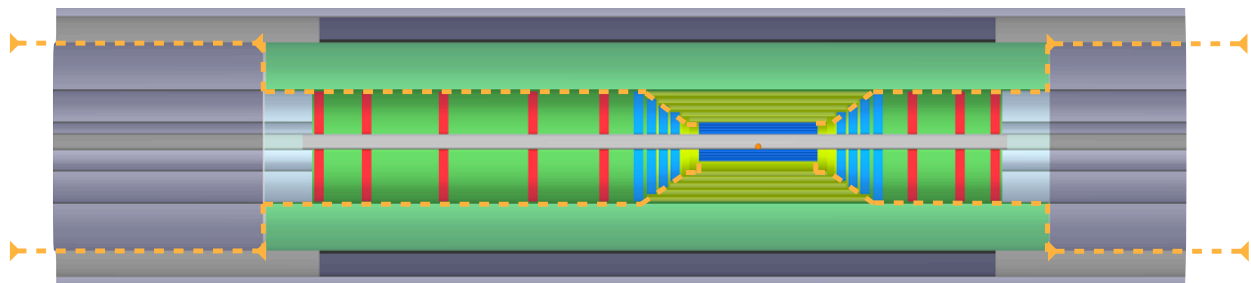


Figure 13.30: Path of services for all tracking detectors (orange). The services are integrated into support structures whenever possible

8544 of the double-I ATLAS pixel arrangement into the 4 layer pixel structure of the LHeC experiment.
8545 That could be an installation template. The goal is the design of a tracker which is transparent enough
8546 and reaches in terms of radiation length thickness the range $\approx 1.5 - 2\%X_0$. Possible pathes (orange)
8547 for the IN/OUT services of the tracking detectors are sketched in Fig. ?? . The cables and tubes are as
8548 far as possible integrated into the support structures of the sub-detectors.

- 8549 • Optimization of detector Read-Out reducing the cost and material impact of cables. An example
8550 is discussed in detail for the ATLAS/CMS HL-LHC opto-link upgrade in Ref. [?]. The front end
8551 electronics buffer depth will depend on bunch crossing rate (25ns) and trigger/readout speed capability.
- 8552 • Special Interaction Region instrumentation for tuning of the machine minimizing the background and
8553 optimizing the luminosity is needed. Radiation detectors e.g. near mask and tight apertures are useful
8554 for fast identification of background sources. Fast bunch related informations are collected efficiently
8555 e.g. by dedicated diamond detectors (like for CMS: [?], [?], [?], [?]).

8556 First and preliminary **GEANT4** studies using minimum bias events generated with **Pythia6** (Ref. [?])
8557 will be discussed in the following section. The simulation of detector responds is important because it may
8558 have impact on technology decisions and will be evaluated further. A more refined simulation will provide, a
8559 more differential picture of the detector responds. Of course the performance of the detector in line with the
8560 software algorithms used define how accurate the particle flow tracking in jets, the reseed after interactions
8561 and conversions can be solved. That implies that the software solutions play a major role to come up with
8562 the optimized detector finally.

8563 13.5 Geant4 Event Simulations - General Detector Description

8564 13.5.1 Introduction

8565 Minimum bias events in the LHeC Detector have been simulated using the **GEANT4** Toolkit [?]. In
8566 addition **ROOT** [?], **GDML** [?], **AIDA** [?] and **Pythia6** [?] have also been incorporated. A **ROOT** macro
8567 has been written which gives a general description of the LHeC Detector geometry and materials. This
8568 description is then transported from **ROOT** to **GEANT4** in XML format via **GDML**. A **Pythia6** program
8569 has also been used to create minimum bias ep events. **Pythia6** outputs the events in HEPEVT format. This
8570 is then run through a subroutine to produce a format readable by **GEANT4**. The actual simulations are
8571 completed natively in **GEANT4** once the geometry, materials and events are loaded. The Analysis is done
8572 with **ROOT** (and the Java Analysis Studio **JAS** [?]) which is interfaced to **GEANT4** via **AIDA**. The flow
8573 of these simulations is outlined in Figure ??.

8574 13.5.2 Pythia6

8575 The **Pythia6** event used in the **GEANT4** simulations contains γ^*P interactions convoluted with the $\gamma/e-$
8576 flux. This setup contains non vanishing cross sections including semihard QCD, elastic scattering, single/
8577 double diffractive among others (The listed interactions dominate σ_{tot}). In order for the events to be
8578 minimum bias no restrictions are placed on the W or Q^2 range.

8579 Table ?? gives the **Pythia6** parameters used for the minimum bias events. The logarithm of the variables
8580 W and Q^2 are given. Since these variables obey amplitudes given by $P(x) \propto \frac{1}{x^2}$ then $P(\text{Log}(x)) \propto e^{-x^2}$
8581 showing that $\text{Log}(x)$ produces mean and rms values following normal statistics.

8582 The tools available for ep event generation are not current. The frontier of high energy physics is focused
8583 on hadron collisions due to the LHC. The numerous problems present in a new energy scale require developers
8584 to focus in this area. This results in a lack of development of event generation tools for a new energy scale of
8585 ep collisions. This is the reason we are using **Pythia6** as opposed to its C++ successor. Although it works
8586 fine for an approximation it would be advantageous to have development here.

8587 The parameters used to scale the results of the simulation in order to find annual quantities are given in
8588 Table ??.

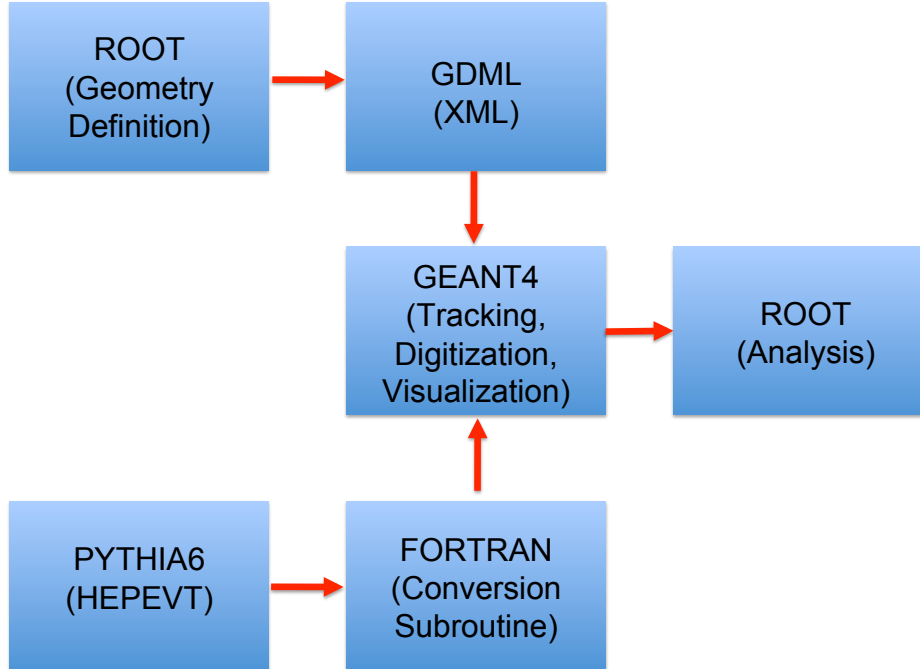


Figure 13.31: Simulation Framework Flow Chart

Characteristic	Value
$Log(W)_{mean}$ [GeV]	2.09
$Log(W)_{rms}$ [GeV]	0.55
$Log(Q^2)_{mean}$ [GeV^2]	-4.98
$Log(Q^2)_{rms}$ [GeV^2]	3.15
Electron Energy [GeV]	60
Proton Energy [GeV]	7000

Table 13.4: Pythia6 Parameters

Characteristic	Value
Total Cross Section [mb]	0.0686
Luminosity [$mb^{-1}s^{-1}$]	10^6
$\frac{dN}{dt}$ [int/yr]	2.57×10^{12}

Table 13.5: Scaling Parameters

13.5.3 1 MeV Neutron Equivalent

NEIL Scaling

In order to find the 1 MeV Neutron Equivalent one must find the appropriate displacement damage functions $[D(E)]$ for the particles. By scaling the damage functions by the reciprocal of $D(n, 1 \text{ MeV})$ one arrives at a weight which will turn a fluence of random particles into the 1 MeV Neutron Equivalent fluence. $D(E)$ is not only dependent on particle type but also on the material in which the particles are traversing. The $D(E)$

8595 functions used in the simulations can be found in Figure ?? [?].

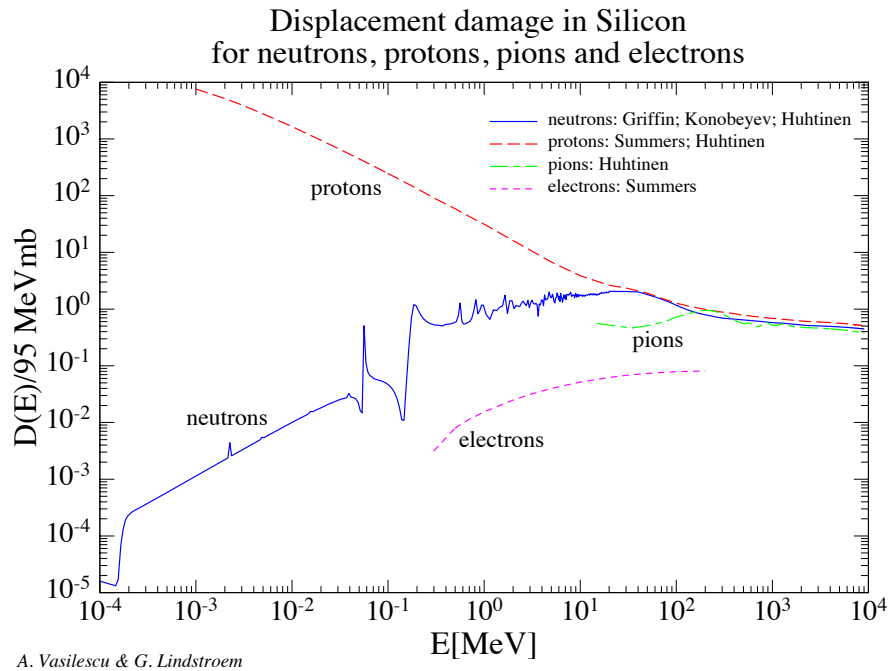


Figure 13.32: Displacement Damage for various particles in Silicon

8596 Scoring

8597 In order to find the 1 MeV Neutron Equivalent fluence through the tracking portion of the detector scoring
8598 was incorporated into the **GEANT4** simulations. A user defined scorer was used that would calculate the
8599 number of hits on the surface of a detector component, weight the hits according to the appropriate damage
8600 functions and finally divide the sum of these weighted hits by the inner surface area of the detector component.
8601 The flux was then scaled by the number of events per year using the mentioned scaling parameters given in
8602 Table ???. The total 1 MeV Neutron Equivalent fluences are given in Table ??.

8603 Histogramming

8604 A different approach was used in order to find the 1 MeV Neutron Equivalent fluence distribution in R_{polar}
8605 and Z . In order to retain data generated on the event level instead of the run level a set up of Sensitive
8606 Detectors [SD] must be initialized that will measure user defined quantities for traversing particles. The
8607 entire tracking region was set as one SD, with each hit containing the position information, and the current
8608 $D(E)$ value of the given track. A 2D histogram is generated for the variables R_{polar} and Z . The intensity
8609 (each hit weighted by its $D(E)$ value) is then scaled by the number of events in the run, the number of events
8610 per year, and a fluence weighting function. This function divides the number of entries in each bin by the
8611 average surface area the bin represents (i.e. $2\pi R_{mean}\Delta Z$ where R_{mean} is the mean R value which the bin
8612 spans and ΔZ is the width of the Z bins). By this weighting process the resulting 2D histogram (Figure ??)
8613 displays the 1 MeV Neutron Equivalent Fluence in $\frac{cm^{-2}}{year}$.

Central Barrel			
Region	ΔZ [cm]	R_{min} [cm]	Fluence [$\frac{N}{cm^2 yr}$]
CPT1	100	3.1	1.38×10^{10}
CPT2	100	5.6	9.99×10^9
CPT3	100	8.1	8.26×10^9
CPT4	100	10.6	7.25×10^9
CST1	116	21.2	6×10^9
CST2	128	25.6	5.66×10^9
CST3	148	31.2	5.38×10^9
CST4	168	36.7	5.25×10^9
CST5	188	42.7	5.16×10^9
Central Endcaps			
Region	Z [cm]	ΔR [cm]	Fluence [$\frac{N}{cm^2 yr}$]
CFT1	70	26	8×10^9
CFT2	80	31.6	7.42×10^9
CFT3	90	37.1	7.08×10^9
CFT4	101	43.1	6.93×10^9
CBT1	-70	26	2.77×10^9
CBT2	-80	31.6	2.48×10^9
CBT3	-90	37.1	2.26×10^9
CBT4	-101	43.1	2.09×10^9
Fwd/Bwd Planes			
Region	Z [cm]	ΔR [cm]	Fluence [$\frac{N}{cm^2 yr}$]
FST1	130	43.1	8.2×10^9
FST2	190	43.1	1.14×10^{10}
FST3	265	43.1	1.63×10^{10}
FST4	330	43.1	2.29×10^{10}
FST5	370	43.1	2.75×10^{10}
BST1	-130	43.1	1.96×10^9
BST2	-170	43.1	1.91×10^9
BST3	-200	43.1	1.99×10^9

Table 13.6: 1 MeV Neutron Equivalent Fluence

8614 13.5.4 Nearest Neighbor

8615 The **Geant4** simulations were also used to find the resolution required in the forward tracking. Firstly, the
8616 flux through the surface of CFT1, CFT4, FST1, and FST5 was found. A minimization algorithm is then
8617 used to find the nearest neighboring hit at the $Z = constant$ surface for each hit. This distance scale is
8618 characteristic of the resolution required for the tracking component in question. The nearest neighboring
8619 hit distribution is calculated on the event level. This implies that only the hits from the same event are
8620 compared. This will have to be studied further to take pileup into account, however information on the event
8621 level is a nice approximation. The nearest neighbor distribution for CFT4 is shown in Figure ?? and for

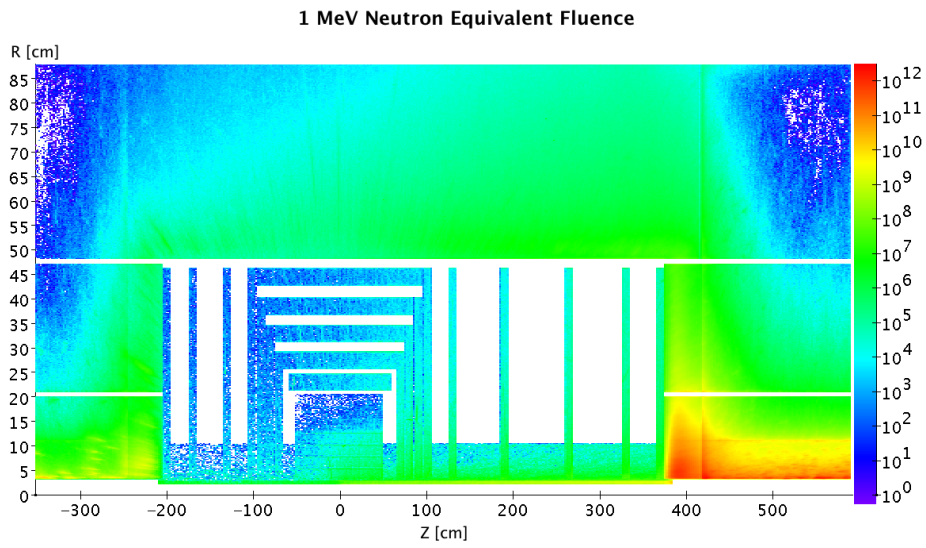


Figure 13.33: 1 MeV Neutron Equivalent Fluence [$\text{cm}^{-2}/\text{year}^{-1}$].

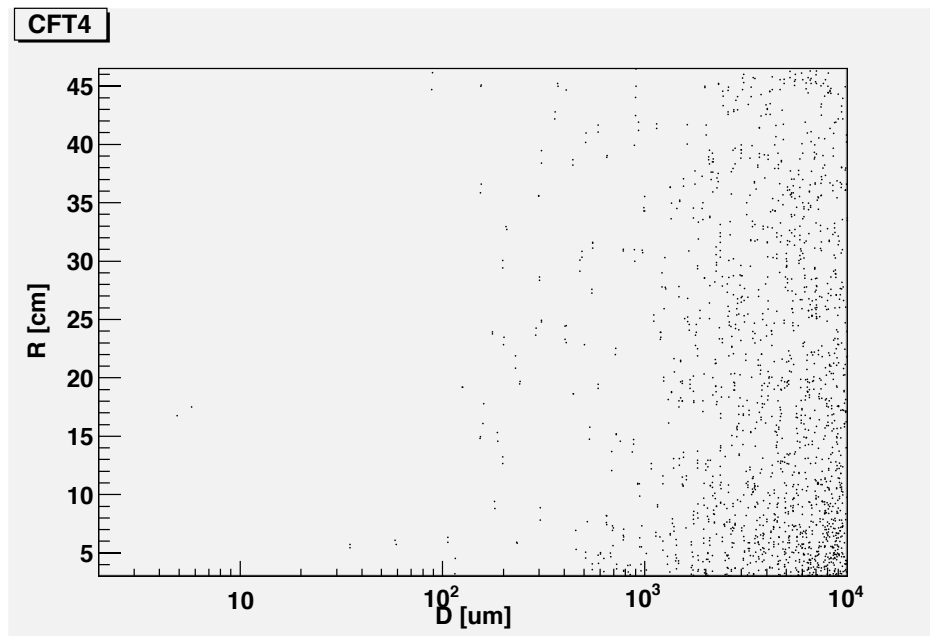


Figure 13.34: Nearest Neighbor distribution for CFT4

Tracking Component	Hits under 10 μm [%]
CFT1	0.18
CFT4	0.23
FST1	0
FST5	0.1

Table 13.7: Nearest Neighbor under 10 μm

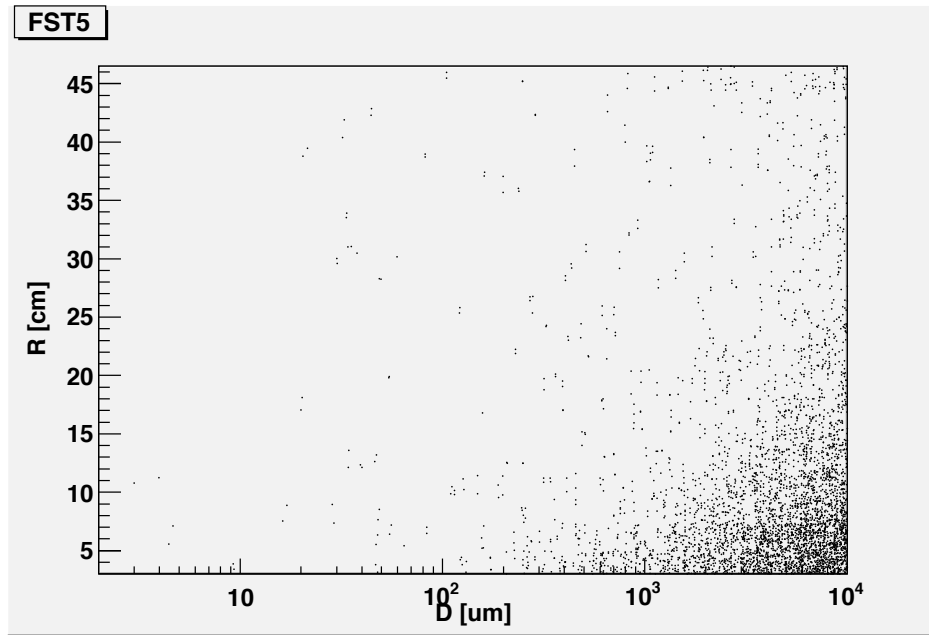


Figure 13.35: Nearest Neighbor distribution for FST5

8622 FST5 in Figure ?? . The x axis contains the value of the nearest neighbor for each hit in terms of μm while
8623 the y axis contains R in terms of cm. A required resolution of 10 or less μm would require pixel detectors
8624 instead of strip detectors. The CFT4 and FST5 Figures display a very low hit density in this area. The
8625 percentage of hits with $D < 10 \mu m$ for the four tracking components in question are given in Table ?? .

8626 13.5.5 Cross Checking

8627 DAWN was used for visualization of the detector. This was able to produce clear pictures which was one
8628 way to make sure the translation of geometry from ROOT to GEANT4 went as expected. An event in the
8629 central tracking region is presented in Figure ?? .

8630 In addition to the minimum bias events, **Pythia6** was also used to create some Leptoquark events. This
8631 was one method of checking the **Pythia6** input (i.e. that the events produced describe the given kinematic
8632 range and cross sections available). However it was also utilized to determine the detector response at various
8633 kinematic ranges. Since $\sigma_{EM} \propto \frac{1}{Q^4}$ The minimum bias events have very low Q^2 and therefore very forward
8634 jets, which leaves almost no activity in the barrel HCAL. By looking at some high Q^2 events it is possible
8635 to see the response of the hadronic calorimetry in the barrel region, making sure it is showering correctly.
8636 Some pictures of the Leptoquark events are given in Figure ?? and Figure ?? .

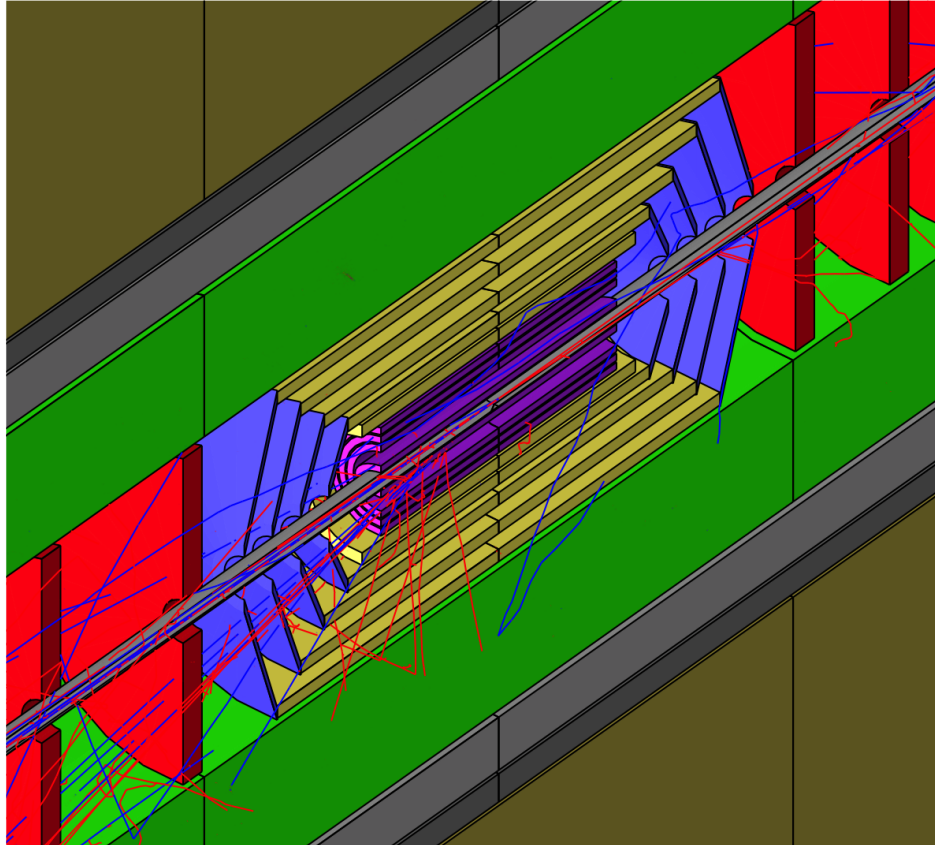


Figure 13.36: G4 Event

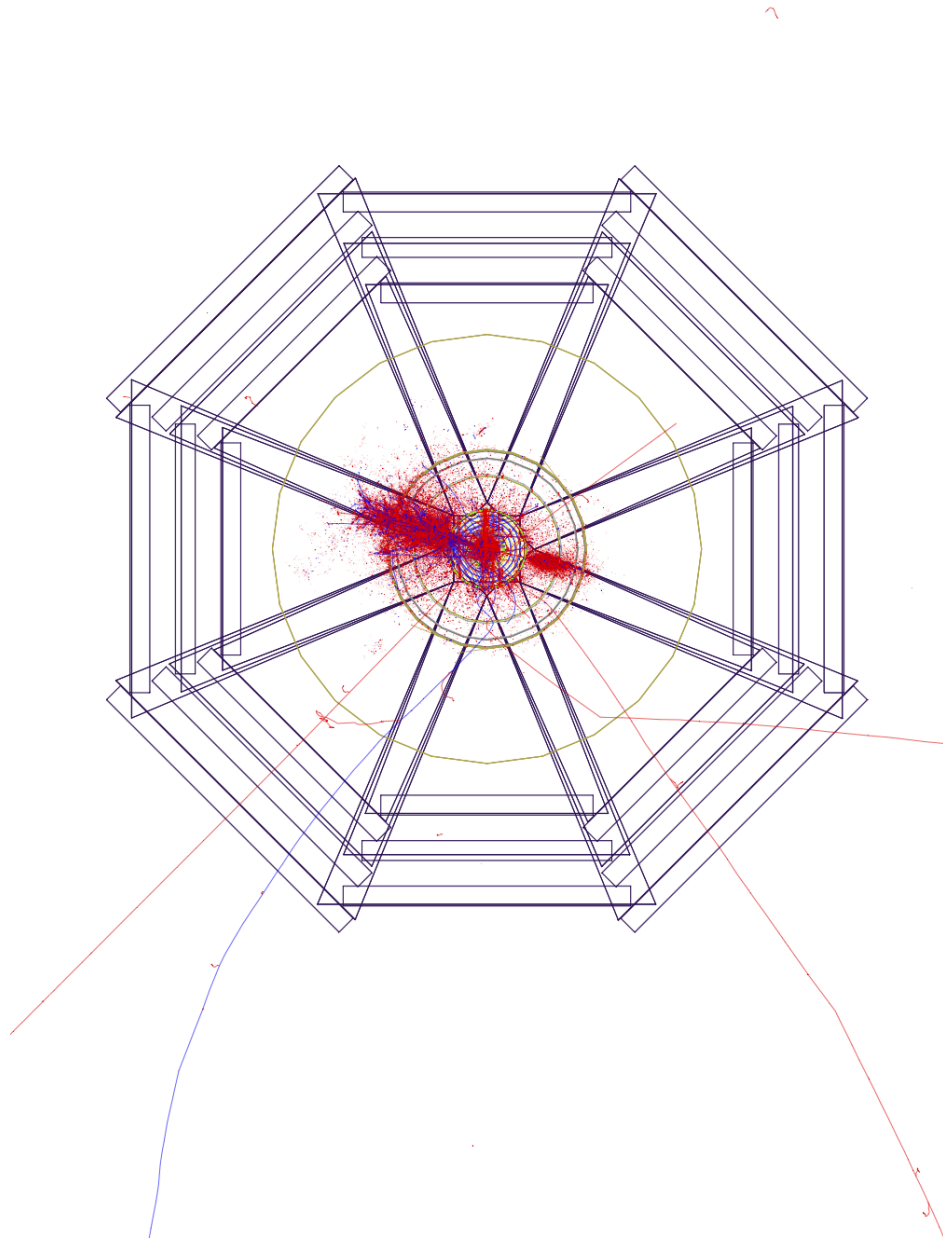


Figure 13.37: Leptoquark Event XY

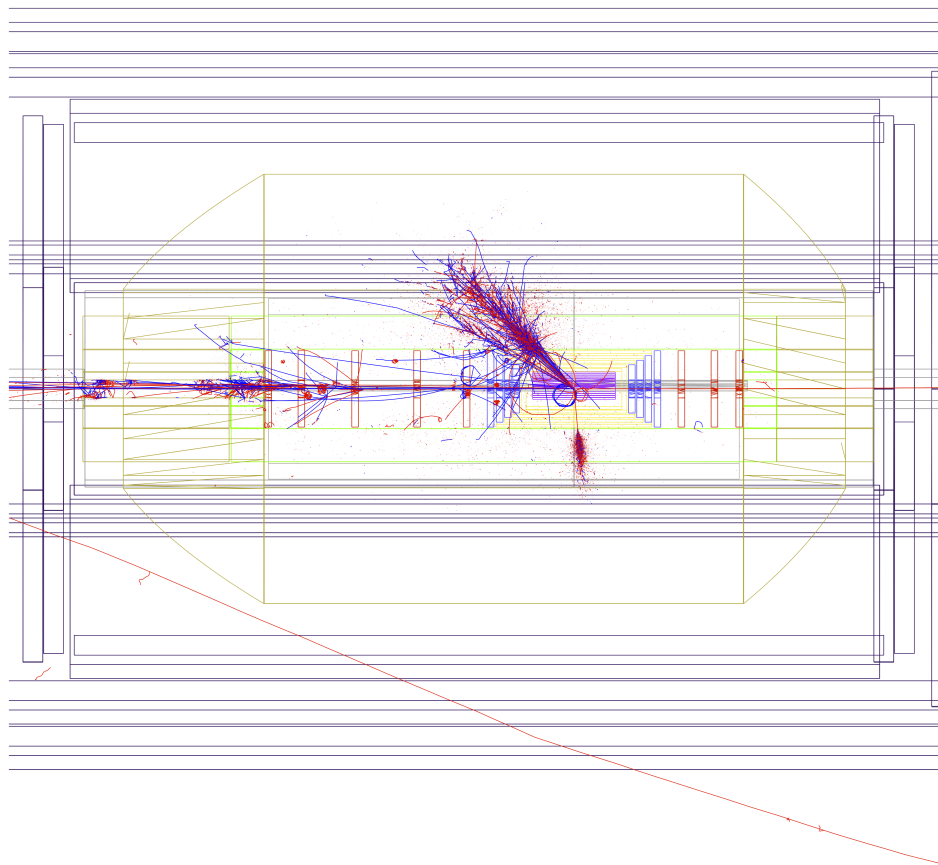


Figure 13.38: Leptoquark Event RZ

8637 13.5.6 Future Goals

8638 There are many goals still to be accomplished by the LHeC Detector Simulations. The set up needs to be
8639 modified to include a detailed calorimeter description. Currently the calorimeter volumes contain a mixture
8640 of FR4, Krypton, Active and Passive material which is weighted according to a realistic set up. This design
8641 must be replaced with a realistic setup of the calorimeters. This also needs to be done for the tracking
8642 which is currently composed of single silicon pieces instead of smaller modules. The majority of the work in
8643 making these changes comes from the required read out geometry and sensitive detector set up that would
8644 be required for analysis of a complicated geometrical structure. This also might require a restructuring of
8645 the simulation package. Since the detector description was done first in **ROOT**, **GDML** was an option to
8646 allow utilizing **GEANT4** without recoding the geometry. However if the geometry will significantly change
8647 then this might benefit from being done natively in **GEANT4**. Of course the Geometry needs to be iterated
8648 until it actually describes the exact detector (service pipes, read out, etc...). However this will come with
8649 the TDR.

8650 Finally the stability of the simulations needs to be assessed. Eventually a complex multifunctional
8651 detector simulation package needs to be produced. This is best done by wrapping numerous simulation
8652 toolkits into a single package utilizing **ROOT**, such as **AliROOT** [?], [?], [?] or **ILCROOT** [?]. The LHeC
8653 simulations at some point need to make a shift towards creating a package like this, in order to promote
8654 greater functionality and greater accessibility.

8655 13.6 Calorimetry

8656 The LHeC calorimetry has to fulfill the requirements described in ???. The goal is a powerful level 1 trigger
8657 and detector able to resolve shower development in 3D space with no or minimal punch through. High
8658 transverse and longitudinal segmentation are necessary along with a good matching to tracking devices for
8659 particle identification and separation of neutral and charged particles. The calorimetry needs to be hermetic
8660 for the identification of the charged current process and good measurement of E_T^{miss} ⁷. These considerations
8661 are summarized in Tab. ???.

8662 The baseline design foresees a modular structure of independent electromagnetic and hadronic calorimeter
8663 components. In order to fully contain electromagnetic showers a thickness of about $25 \sim 30X_0$ is required.
8664 The design of the EMC modules will vary when moving from the very forward region, where energies up to
8665 $\mathcal{O}(1\text{TeV})$ are expected, to the barrel and the rear region, where the detection of the scattered low energy
8666 electron has to be precisely tagged and measured.

8667 Following the option A of the baseline design, the EMC is surrounded by the coil providing the magnetic
8668 field for momentum measurement in the tracking.

8669 The hadronic calorimetry, naturally surrounding the EMC is also foreseen to have a sufficient depth and
8670 a projective modular design to precisely measure over the full energy range high energetic jets and provide
8671 a granularity such to faithfully separate multiple jet events. Given the energies available at the LHeC, the
8672 forward part will be more extended (up to $10\lambda_I$) for good containment of energies up to few TeV.

8673 In the next sections the baseline design for the EMC and HAC components is presented and discussed
8674 along with a comparison of technologies and the experience from other HEP detectors e.g. [?], [?], [?], [?], [?].
8675 A brief outlook towards ongoing R&D and new technologies which would even extend the precision and the
8676 scope of the detector are briefly addressed.

8677 13.6.1 The Barrel Electromagnetic Calorimeter

8678 Due to the very asymmetric energy and particle multiplicity distribution over the azimuthal angle, the
8679 detector design foresees a composite electromagnetic calorimeter with diverse requirements in the forward,

⁷Each cell in the calorimeter is given a four-vector, with an energy equal to the measured energy in the cell, a direction pointing from the interaction vertex to the center of the cell, and a zero mass. The transverse components of these vectors are summed over all the calorimeter cells. This sum, with a sign change, defines the *calorimeter missing energy*, $E_T^{miss} = -\sum_i \vec{E}_T^i$

8680 barrel and backward region. In the barrel region a Liquid Argon calorimeter (LAr) with *accordion-shaped*
 8681 electrodes as in use for ATLAS is foreseen covering the pseudorapidity interval $2.8 < \eta < -2.3$. The principle
 8682 of LAr sampling calorimetry is to arrange many layers of passive material, in our case lead given its short
 8683 radiation length ($X_0=0.56$ cm), alternated with layers of active material, here LAr with $X_0=14.0$ cm. The
 8684 choice of liquid argon calorimetry follows from its intrinsic excellent linearity, stability in time and radiation
 8685 tolerance [?], [?], [?], [?], [?], [?], [?], [?].

8686 At the LHeC, LAr would provide the required energy resolution, detector granularity and projective
 8687 design. The detector with an outer diameter of 88 cm would share the same cryostat of the main solenoid
 8688 which in case of a Linac-Ring design would include the bending dipoles. Size and construction details of the
 8689 cryogenics are described in ???. At larger radii, where most of the calorimeter weight is located and where
 8690 the radiation levels are low, a less expensive technology based on absorber-scintillator hadronic calorimeter
 8691 can be used. The performance of the LAr calorimetry system has been extensively addressed [?] and here
 8692 only specific design issues and detector simulation will be discussed.

8693 Fig. ?? shows a x - y and r - z view of the LHeC Barrel EM calorimeter. As for the ATLAS LAr Calorimeter,
 8694 the detector volume is filled with a projective accordion structure based on lead absorber. This layout allows
 8695 for the extraction of the detector signals without significantly degrading the high-frequency components
 8696 which are vital for fast shaping. The flexibility in the longitudinal and transverse segmentation, and the
 8697 possibility of implementing a section with narrow strips to measure the shower shape in its initial part,
 represent additional advantages. It is worth noticing that due to the asymmetric design, the projective

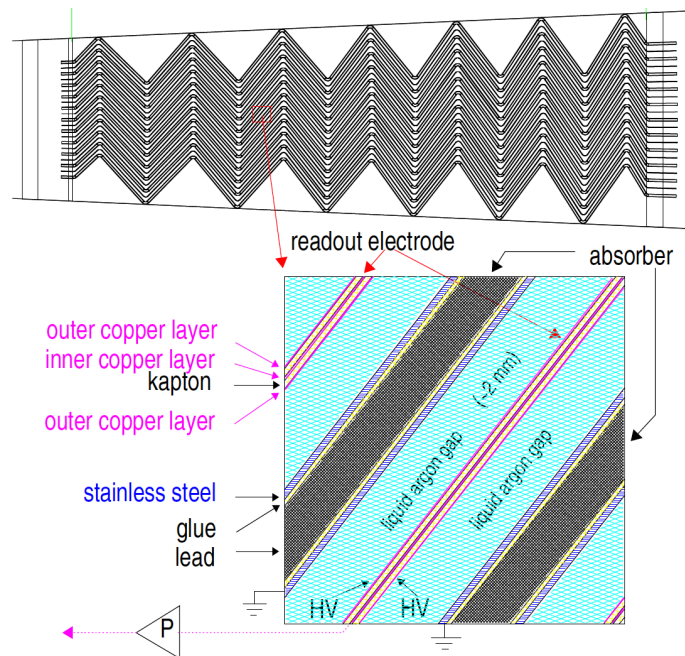


Figure 13.39: Longitudinal view of the accordion structure of the ATLAS LAr Calorimeter

8698 structure is not fully symmetric as the calorimeter and the solenoid center are shifted forward with respect
 8699 to the interaction point. Fig. ?? shows a detail of the accordion-electrode structure. A basic cell consists
 8700 of an absorber plate, a liquid argon gap, a readout electrode and a second liquid argon gap. The mean
 8701 thickness of the liquid argon gap is constant along the whole barrel and along the calorimeter depth. The
 8702 readout granularity would be subdivided in 3 cylindrical sections of increasing size in $\Delta\eta \times \Delta\phi$. As shown
 8703 in Fig. ??, the first sampling section of the electromagnetic calorimeter would have a very fine granularity
 8704 ($\Delta\eta \times \Delta\phi = 0.003 \times 0.1$), to optimize the ability to separate photons from π^0 energy deposits. The second
 8705

8706 sampling section, mainly devoted to energy measurement, would have a granularity of about 0.025×0.025 ,
 8707 and the back sampling has a slightly coarser granularity of $\Delta\eta \times \Delta\phi = 0.050 \times 0.025$.

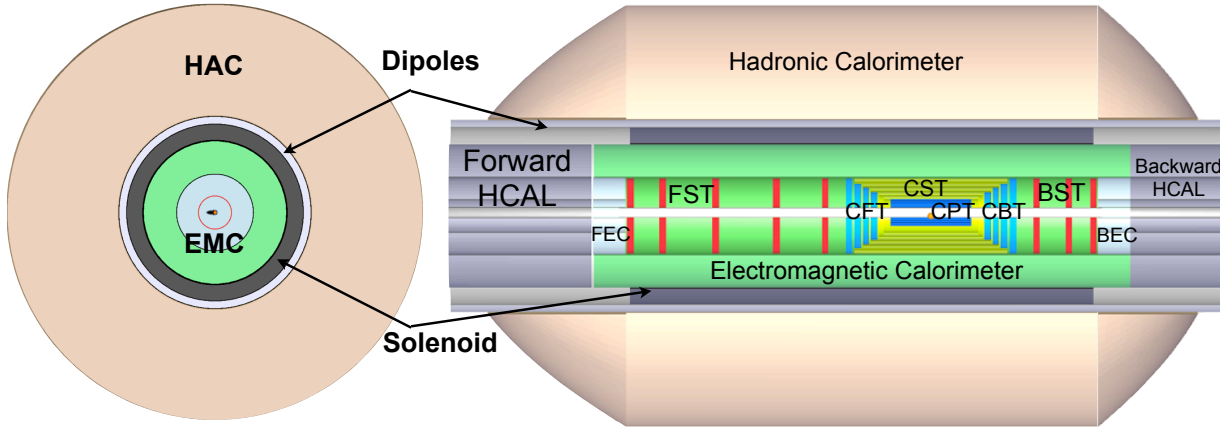


Figure 13.40: x - y and r - z view of the LHeC Barrel EM calorimeter (green).

8708 13.6.2 The Hadronic Barrel Calorimeter

8709 The LHeC baseline hadronic calorimeter in the barrel region is foreseen to be a sampling device made out
 8710 of steel and scintillating tiles, as absorber and active material. The detector, from now on indicated as *Tile*
 8711 *Calorimeter*, would provide the required mechanical stability for the inner LAr and Magnet cryostat along
 8712 with the iron required for the return flux of the solenoidal field. The simple and well proven idea [?] of
 8713 calorimetry is particularly suited for the LHeC environment since also in use in ATLAS [?].

8714 The absorber structure is a laminate of steel plates of various dimensions, connected to a massive structural
 8715 element referred to as a girder. The highly periodic structure of the system allows the construction of
 8716 a large detector by assembling smaller sub-modules together. Since the mechanical assembly is completely
 8717 independent from the optical instrumentation, the design becomes simple and cost effective. Simplicity has
 8718 been the guideline for the light collection scheme used as well: the fibers are coupled radially to the tiles
 8719 along the outside faces of each module. The laminated structure of the absorber allows for channels in which
 8720 the fibers run. The use of fibers for the readout allows to define a tridimensional cell read-out, creating a
 8721 projective geometry for triggering and energy reconstruction. A compact electronics read-out is housed in
 8722 the girder of each module. Finally, the read-out of the two sides of each of the scintillating tiles into two
 8723 separate photomultipliers provides the redundancy needed during the expected period of operation.

8724 In the baseline design the calorimeter consists of a cylindrical structure with inner and outer radius of
 8725 120 and 260 cm respectively (Tab.??). The central HAC barrel part is 580 cm in length along the beam
 8726 axis. Endcaps extend the calorimetry further in the forward and backward direction in order to guarantee
 8727 sufficient energy containment. The detector cylinder would be built of several independent wedges along the
 8728 azimuthal direction while the modularity and segmentation might vary depending on the adopted machine
 8729 design (Ring-Ring or Linac-Ring). The Tile calorimeter forms the shell of the inner part of the LHeC
 8730 detector. Within its volume, once the barrel and the extended barrels are assembled, all the sub-detectors,
 8731 except the muon system, will be placed. The massive iron structure is rigid enough to support their weight,
 8732 the most important components being the full liquid argon cryostat and the solenoid.

8733 The main function of the Tile Calorimeter is to contribute to the energy reconstruction of the jets
 8734 produced in e - p interactions and, with the addition of the end-cap and forward calorimeters, to provide
 8735 a good E_T^{miss} measurement. Achieving this at the LHeC is not straightforward as the large proton beam
 8736 energy and the electron proton energy imbalance center requires good performance over an extremely large
 8737 range extending from a few GeV up to several TeV.

E-Calo Parts	FEC1	FEC2		EMC		BEC2	BEC1
Min. Inner radius R [cm]	3.1	21		48		21	3.1
Min. polar angle θ [°]	0.48	3.2		6.6/168.9		174.2	179.1
Max. pseudorapidity η	5.5	3.6		2.8/-2.3		-3.	-4.8
Outer radius [cm]	20	46		88		46	20
z -length [cm]	40	40		660		40	40
Volume [m ³]	0.3			11.3		0.3	
H-Calo Parts barrel			FHC4	HAC	BHC4		
Inner radius [cm]			120	120	120		
Outer radius [cm]			260	260	260		
z -length [cm]			217	580	157		
Volume [m ³]			121.2				
H-Calo Parts Inserts	FHC1	FHC2	FHC3		BHC3	BHC2	BHC1
Min. inner radius R [cm]	11	21	48		48	21	11
Min. polar angle θ [°]	0.43	2.9	6.6		169.	175.2	179.3
Max/min pseudorapidity η	5.6	3.7	2.9		-2.4	-3.2	-5.
Outer radius [cm]	20	46	88		88	46	20
z -length [cm]	177	177	177		117	117	117
Volume [m ³]	4.2				2.8		

Table 13.8: Summary of calorimeter dimensions.

The electromagnetic barrel calorimeter is currently represented by the barrel part EMC (LAr-Pb module); the setup reaches $X_0 \approx 25$ radiation length) and the movable inserts forward FEC1, FEC2 (Si-W modules ($X_0 \approx 30$) and the backward BEC1, BEC2 (Si-Pb modules; $X_0 \approx 25$).

The hadronic barrel parts are represented by FHC4, HAC, BHC4 (forward, central and backward - Scintillator-Fe Tile modules; $\lambda_I \approx 8$ interaction length) and the movable inserts FHC1, FHC2, FHC3 (Si-W modules; $\lambda_I \approx 10$), BHC1, BHC2, BHC3 (Si-Cu modules, $\lambda_I \approx 8$) see Fig. ??.

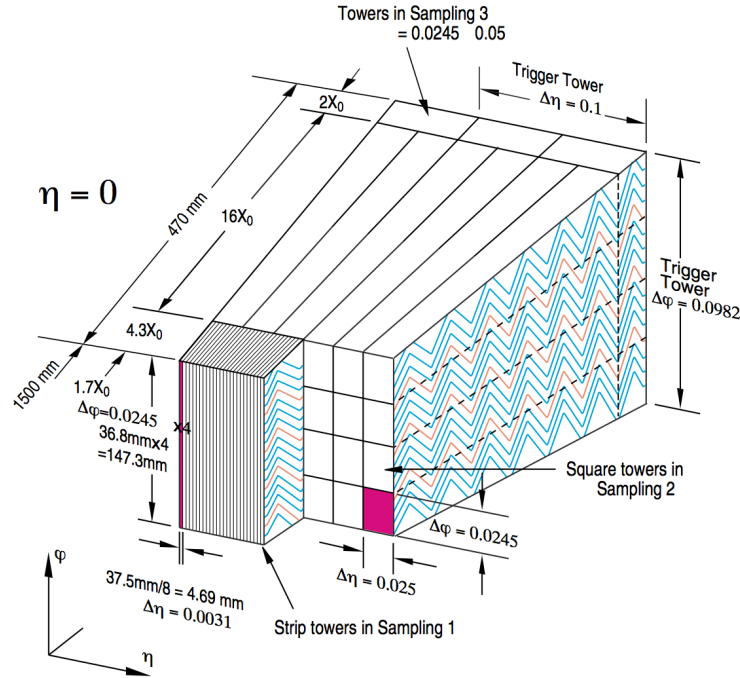


Figure 13.41: 3D view of the accordion structure of the ATLAS LAr Calorimeter

8738 The guidelines for the design of this device are derived from the required overall physics performance
 8739 which call for an intrinsic resolution for jets in the barrel region of $50\% \cdot \sqrt{E/GeV}$ with a segmentation of
 8740 $\Delta\eta \times \Delta\phi = 0.1 \times 0.1$ (??).

8741 The granularity of the Tile Calorimeter is important to finely match the electromagnetic LAr calorimeter
 8742 in front and correct for the dead material of the magnet complex. The proposed hadronic segmentation for
 8743 the cells behind the electromagnetic section, will allow an efficient hadron leakage cut, needed for electron
 8744 and photon identification. A reasonable longitudinal segmentation, especially around the maximum depth
 8745 of the shower, favours an appropriate weighting technique to restore, at the level of 1-2%, the linearity of the
 8746 energy response to hadrons, which is intrinsically non-linear because of the non-compensating nature of the
 8747 calorimeter. At the highest energies expected, the resolution of the calorimetry is dominated by the constant
 8748 term, for which the largest contribution comes from the detector non-linearity and from the calibration. An
 8749 attempt is made to keep the constant term below the 2% level.

8750 13.6.3 Endcap Calorimeters

8751 Calorimetry in the forward and backward direction at the LHeC is of extreme importance: in the forward
 8752 region highest energy deposits require high granularity and very good scale calibration, in the backward
 8753 region high sensitivity to low energy electrons and a good e/h separation is important to precisely measure
 8754 the scattered electron and suppress hadronic background.

8755 As seen from Fig. ?? the very forward and to less extend also the backward parts of the calorimeter
 8756 are specifically exposed to dense particle radiation and have to be radiation hard by design. Synchrotron
 8757 radiation and any further background radiation has to be tolerated additionally.

8758 Fig. ?? shows in detail the encap calorimeters for the Ring-Ring design. The two-phase experimental
 8759 program requires the endcaps to be modular as these components will be either moved along the beam line
 8760 or removed to allow the placement of the strong focussing magnets for the high luminosity run. Relevant
 8761 dimensions and specifications are summarised in Tab. ??.

8762 For the Linac-Ring design, where no additional magnets along the beampipe will be required, the sub-
8763 components FHC2/FHC3 and BHC2/BHC3, can be unified in single modules for the forward and backward
8764 direction, respectively.

8765 We envisage excellent performance regarding:

- 8766 • Level one triggering
- 8767 • electron identification in jets (tagging and e from heavy quark production); precision measurement of
8768 showers
- 8769 • identifying heavy flavour production by partial reconstruction
- 8770 • good γ separation by identified impact, thus discriminating γ/π^0
- 8771 • hadronic and electromagnetic signatures, also in case of e^\pm -*Ion* interactions
- 8772 • jet finding, jet energy and impact position measurements

8773 The tight geometry of the insert calorimeters require a non conventional and challenging design based
8774 on former developments [?], [?], [?], [?], [?], [?], [?], [?]. The choice of tungsten (W) as absorber specifically
8775 for the forward inserts is driven by its very short radiation length and a large absorption to radiation length
8776 ratio. About 26 cm of tungsten will absorb the electromagnetic showers completely and will contain the
8777 hadronic shower to a large extent and over a large range of energy ($\approx 30X_0 + \approx 10\lambda_I$). The electromagnetic
8778 and the hadronic part can be combined even in the same compartment to minimize boundary effects.

8779 An alternative to tungsten for the hadronic absorber is copper (Cu). Simulations have been performed
8780 to compare the different absorbers. Since the backward inserts have more relaxed requirements, the material
8781 for the absorbers are lead (Pb) for the electromagnetic part and copper for the hadronic one. For the Ring-
8782 Ring option, where no dipole field along the beampipe is required, a further and more economical choice
8783 of steel (Fe) instead of copper can be considered. The active signal sensors for both the forward as the
8784 backward calorimeter arrangements have been chosen to be silicon-strip (electromagnetic fwd/bwd parts)
8785 and silicon-pad (hadronic fwd/bwd parts), respectively.

8786 13.7 Calorimeter Simulation

8787 In this section preliminary results on simulations of the barrel and endcap calorimeters are illustrated. The
8788 detector components presented above have been simulated using **GEANT4.9.2** [?] with single and multiple
8789 particle events along with full e - p events from the **QGSP-3.3** [?] physics list. The Quark-Gluon String Pre-
8790 compound (**QGSP**) is based on theory-driven models and uses the quark-gluon-string model for interactions
8791 and a pre-equilibrium decay model for fragmentation.

8792 The detector geometry, including the various layers of active, absorbing and support material were coded
8793 and inserted in the simulation. Energy resolutions for electromagnetic and hadronic deposits were studied
8794 along with concepts for optimal trigger and signal reconstruction. Particular attention was put into the key
8795 features and the construction constraints of the detector, namely the beam optics and the magnets (the
8796 solenoid and the Linac-Ring dipoles). Where a similar design from an existing or developing detector are
8797 available, the results are presented complemented by referenced studies.

8798 The energy resolution of a calorimeter is parameterized by the following quadratic sum:
8799
8800

$$\frac{\sigma_E}{E} = \frac{a}{\sqrt{E}} \oplus b \quad (13.1)$$

8801 where E is the particle energy in GeV , a is the stochastic term, which is arising from fluctuations in the
8802 number of signal producing processes, b is the constant term, which describes imperfections in calorimeter
8803 construction, fluctuations in longitudinal energy containment, non-uniformities in signal collection etc. A

8804 third term c (left out here) is often also added which would represent the noise in experimental data de-
 8805 scription. The energy deposition of primary and secondary particles in the calorimeter was obtained using
 8806 **GEANT4**, and fitted to extract a and b . Effects due to the readout process were not considered at this
 8807 stage.

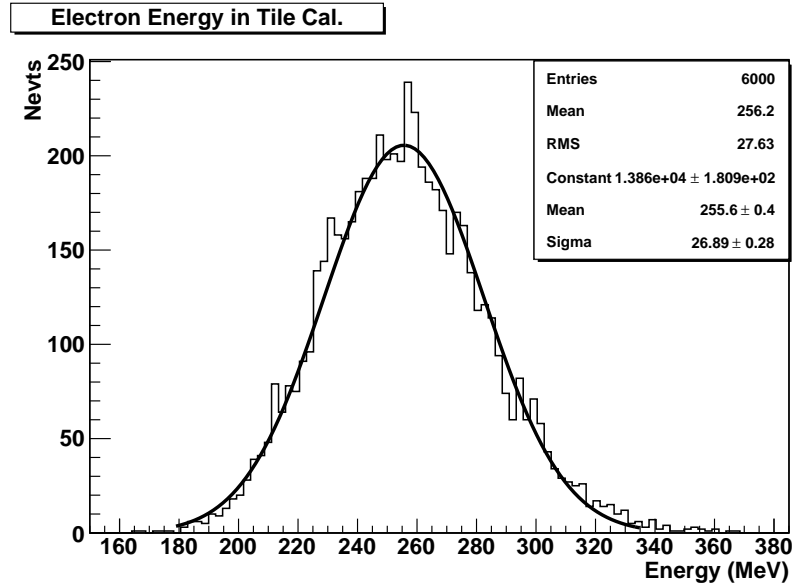


Figure 13.42: Example for a pion energy distribution and the Gaussian fit. The resulting σ and mean values are estimated for pions of an incident angle $\theta = 70^\circ$ and 10 GeV energy.

8808

8809 Each energy distribution was fitted with a Gaussian, $\pm 2\sigma$ around the mean and the energy depended
 8810 resolution was calculated using those mean values fitted. An example of the energy distribution and Gaus-
 8811 sian fit applied is shown in Fig. ???. The a and b parameters are then calculated from the fit of σ/E .

8812

8813 13.7.1 The Barrel LAr Calorimeter Simulation

8814 A simplified layout, adapted from the ATLAS LAr calorimeter [?], has been implemented in a **GEANT4**
 8815 simulation and used to extract the main characteristics of the LHeC barrel electromagnetic calorimeter.

8816 The accordion shaped absorber sheets are 2.2 mm thick lead layers intermediated by 3.8 mm wide gaps
 8817 filled with liquid argon. In the present model the electrodes which in the case for ATLAS are 2×0.275 mm
 8818 thick, where not considered. Both absorber and the liquid argon gap have an accordion fold length of
 8819 40.1 mm and 13 bend angles of 90° . A total of 62 absorber sheets each 250 cm wide in z-direction have been
 8820 incorporated into the simulation (Fig. ??-left). A 20 GeV incident single electron showering in the stack is
 8821 shown in Fig. ??-right). The energy resolution for electrons was obtained from the ratio of the mean and
 8822 the standart deviation of the electron response, both obtained by fitting a gaussian to the energy spectrum.
 8823 Figure ?? shows the energy resolution for electrons of energy between 10 and 400 GeV. These results are in
 8824 agreement with [?]. In the simulation the energy deposited in the active material is normalized to the energy
 8825 of the incident particle.

Tile Rows	Height of Tiles in Radial Direction	Scintillator Thickness
1-3	97 mm	3 mm
4-6	127 mm	3 mm
7-11	147 mm	3 mm
<i>x</i> -depth	1407 mm	

Table 13.9: Longitudinal (into *x*-direction) segmentation of the hadronic tile calorimeter (HAC).

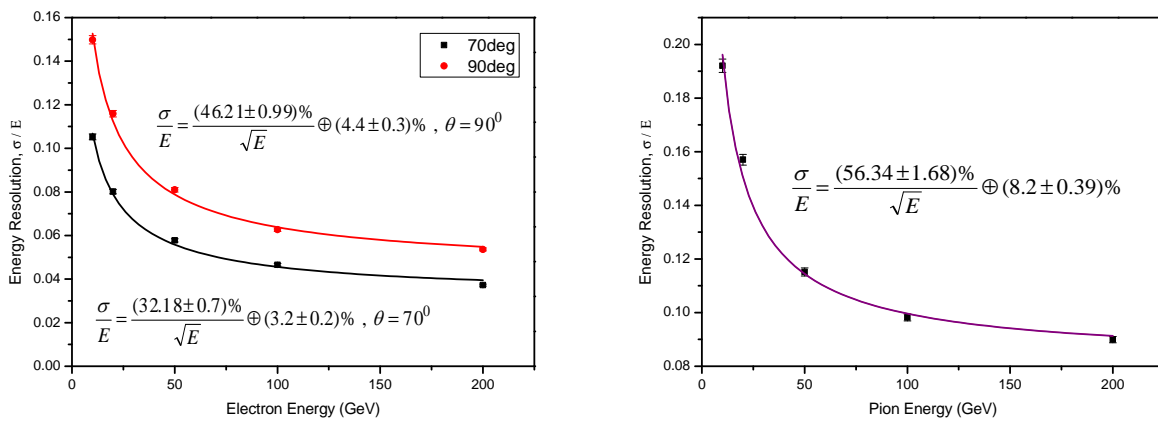


Figure 13.43: Tile Calorimeter energy resolution for electrons at $\theta = 70^\circ$ and 90° (left) and for pions at $\theta = 90^\circ$ (right).

13.7.2 The Barrel Tile Calorimeter Simulation

The HAC is a scintillator-steel tile calorimeter: 4 mm thick steel plates are interspaced by 3 mm thick scintillator tiles. The tiles are placed in planes perpendicular to the z -direction. The absorber structure consist of 262 repeated periods, each of which spans 19 mm in z and consist of 16 mm of steel and 3 mm of scintillator tile. 11 transverse rows of tiles are used in a module. The total interaction depth of the HAC prototype correspond to $\lambda_I = 7$. The longitudinal segmentation of the HAC module is described in Tab. ??.

In this section the performance of the hadron calorimeter alone has been investigated. in the later sections the combined use of EMC and HAC parts has been studied. The energy resolution of the tile calorimeter was simulated with electrons and pions within the energy range 3-200 GeV (Fig. ??). The obtained stochastic term values are consistent with results obtained for ATLAS [?]. The response to electrons show the general good resolution thus that any leakage from the electromagnetic calorimetry in front of HAC would be resolved safely.

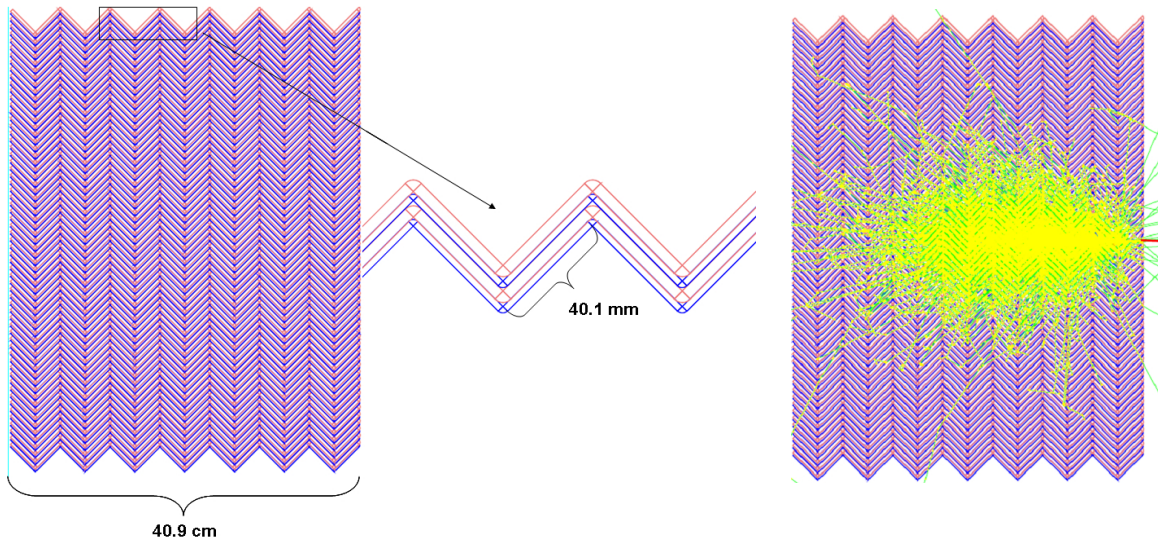


Figure 13.44: View of the parallel geometry accordion calorimeter (left) and simulation of a single electron shower with initial energy of 20 GeV (right).

13.7.3 Combined Liquid Argon and Tile Calorimeter Simulation

The combined system (accordion and tile calorimeter) has been studied. The effect of the dead material due to the magnet and the cryostat between the EMC and HAC has been studied in first approximation. The energy resolution of the combined system has been simulated. The effect of the solenoid and the cryostat infrastructure has been simulated by adding a thick Aluminum layer (14 cm) in between EMC and HAC. The study has been performed with particles in a wide range of energy and for different incident angle in order to obtain information about the detector response for particles entering the calorimeters at different z .

The hadronic shower simulations have been obtained in the energy range 3 GeV-200 GeV. First results of the energy resolutions as a function of energy for pions are shown in Fig. ??.

13.7.4 Electromagnetic (warm) Calorimeter Simulation - Pb-Scintillator Option

Along with the baseline liquid argon calorimeter, a more conservative option, not requiring a dedicated cryogenic system, has been considered for the barrel electromagnetic calorimetry. For this purpose a

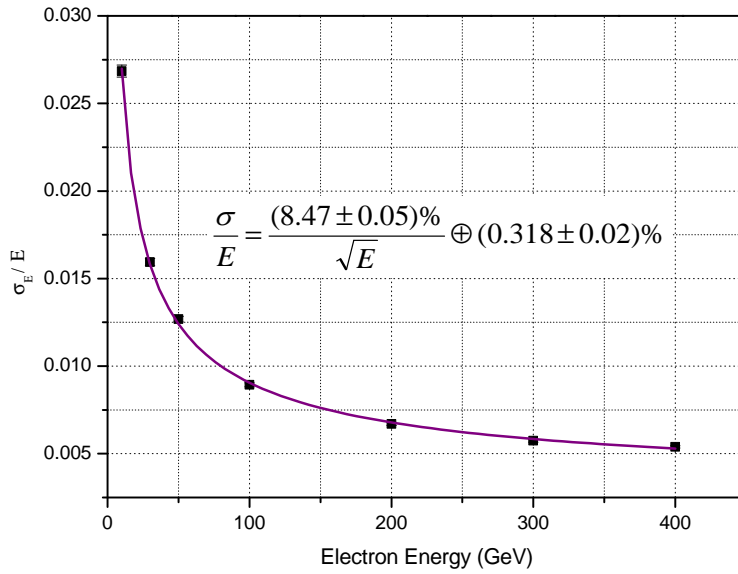


Figure 13.45: LAr accordion calorimeter energy resolution for electrons between 10 and 400 GeV.

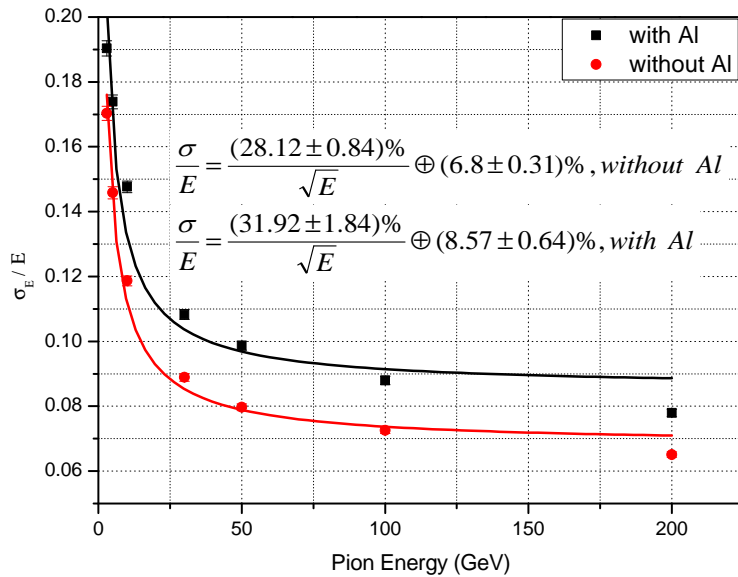


Figure 13.46: Accordion and Tile Calorimeter energy resolution for pions with and without 14cm Al block.

8852 lead-scintillator sampling calorimeter, composed of 20×0.85 cm thick Pb layers interspaced by 4 mm plas-
 8853 tic scintillator plates was setup for simulation. The radiation length of this systems correspond to $30X_0$
 8854 ($X_0(Pb)=0.56$ cm). All dimensions of the calorimeter systems have been kept according to the default solu-
 tion summarized in Tab. ??.

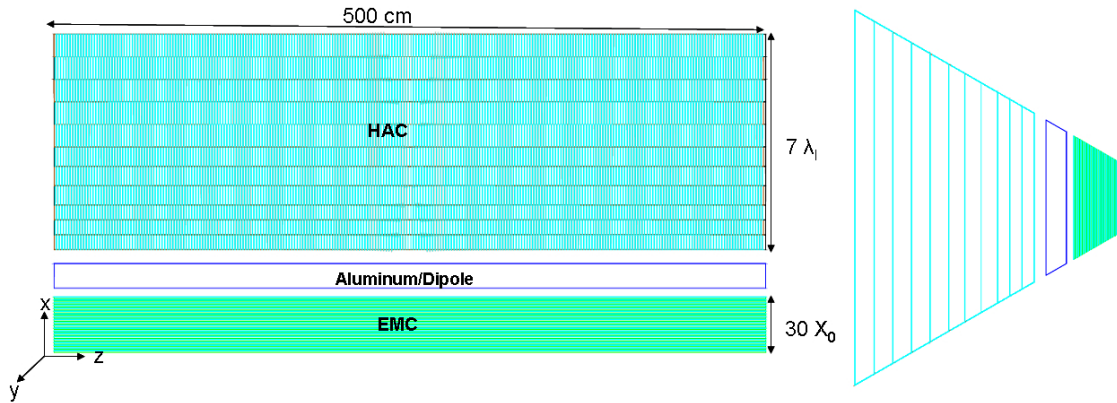


Figure 13.47: Simulation - barrel calorimeter module EMC/solenoid-dipole-system($\propto 16$ cm Al-block)/HAC.

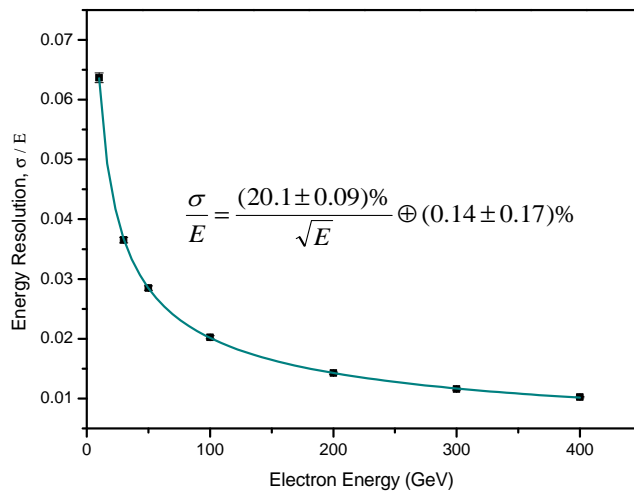


Figure 13.48: EM-Calorimeter energy resolution for electrons at $\theta = 90^\circ$.

8855

8856 The lead-scintillator EMC stack was placed 30 cm in front of the HAC. Again an aluminum block of 16 cm
 8857 was inserted between EMC and HAC representing the magnet/cryostat system as illustrated in Fig. ??. The
 8858 sketched module would be one out of 6 azimuthal segments of the complete barrel EMC and HAC. The energy
 8859 resolution of the electromagnetic lead-scintillator calorimeter as obtained with electrons of 10-400 GeV is
 8860 shown in Fig. ??.

8861

8862 As the energy loss for electrons and pions differs in shape, normalization and depth, it is worth looking
 more in detail to their shower profiles when traversing the calorimeter. At detector level, this information,

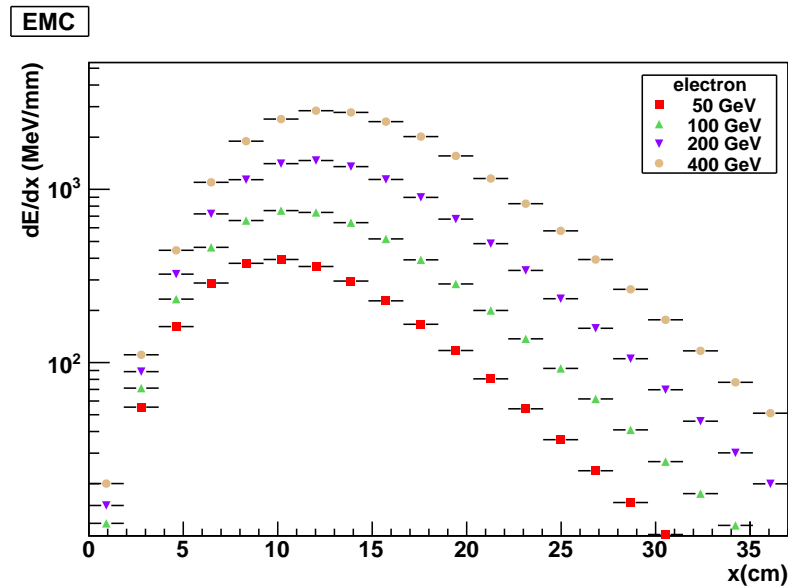


Figure 13.49: Electron longitudinal shower profile for EMC at various energies. Only the statistical uncertainties are shown.

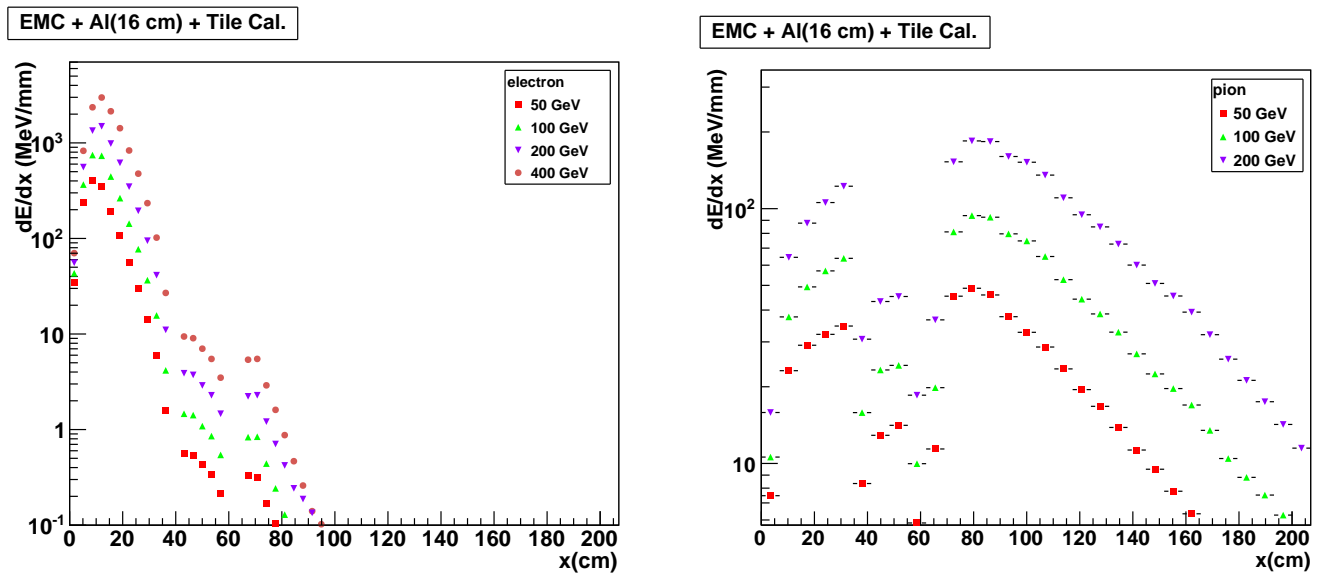


Figure 13.50: Electron (left) and Pion (right) longitudinal shower profile for the EMC/solenoid-dipole-system (Al-block)/HAC at various energies.

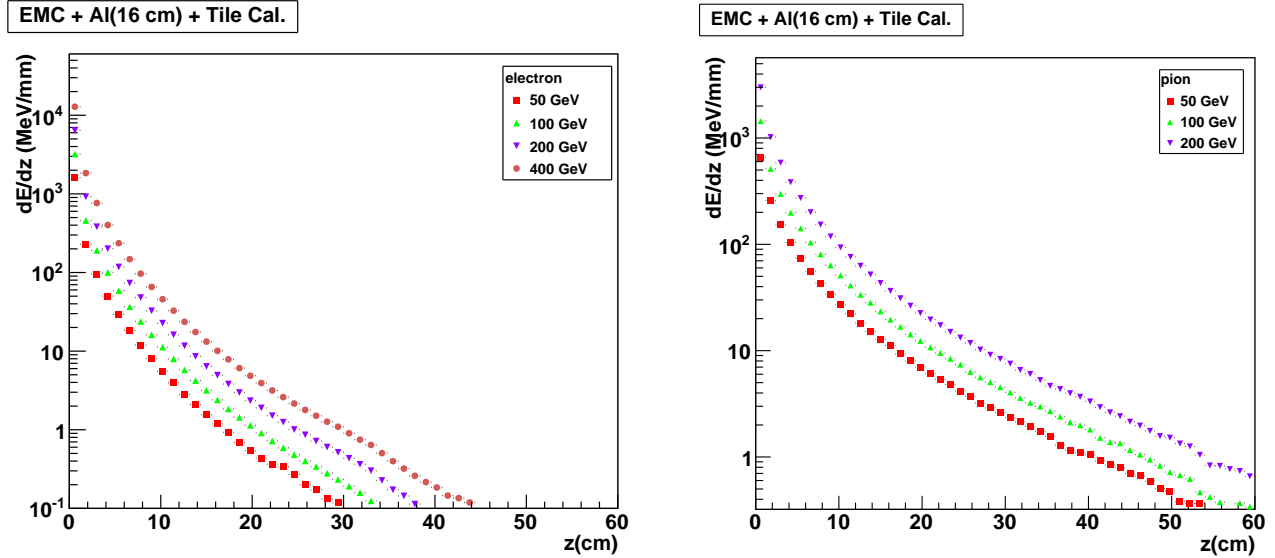


Figure 13.51: Energy deposit and transverse shower profiles for electron (left) and pion (right).

8863 if available, can be used to identify and discriminate particles and improve the energy resolution. For this a
 8864 high granularity, necessary to separate jets and energy deposits coming from different products, along with
 8865 a longitudinal segmentation and software reweighting are essential.

8866 Longitudinal and transverse shower profiles have been studied with electrons and pions of different energies.
 8867 As the detector structure, constrained by the presence of the cylindrical volumes of the tracking detector
 8868 and the magnet systems, which are not projective, the same study was repeated with electrons and pions
 8869 sent into the calorimeter system with incident angles between 30° and 90° . The calorimeter depth (37 cm for
 8870 the EMC and 140 cm for the barrel HAC) for particles with $\theta = 90^\circ$ increases (for particles with smaller
 8871 or larger θ . The longitudinal shower profiles for electrons and pions are summarized in Fig. ?? and Fig. ??.
 8872 They show the mean deposited energy as a function of the calorimeter stack depth. The longitudinal shower
 8873 profile of electrons is shorter than for pions. The energy deposition of the electrons has its maximum in
 8874 the EMC (Fig. ??). The leakage into the hadronic part of the calorimeter system is small and sums up
 8875 to $\mathcal{O}(10)$ MeV. Pions penetrate deeper into the calorimeter and the maximum of energy deposition is seen
 8876 consistently in the HAC region (Fig. ??-right). Less energy deposition occurs between in the region between
 8877 37 and 67 cm because of the aluminum layer which represents the cryostat-wall, the solenoid and the dipole
 8878 magnet structures. The containment of the hadronic showers is complete.

8879 Transverse profiles are usually expressed as a function of the transverse coordinates and are integrated
 8880 over the longitudinal coordinate. Fig. ?? shows the transverse shower profiles for electrons and pions. Since
 8881 the electromagnetic showers are compact, the electromagnetic energy is deposited relatively close to the core
 8882 of the shower. As expected the hadronic profiles show a larger transverse spread.

8883 13.7.5 Forward and Backward Inserts Calorimeter Simulation

8884 The very important forward/backward instrumentation for calorimetric measurement has been chosen such
 8885 that from the point of view of performance and availability of the technology all currently known boundary
 8886 conditions could be met. More detailed studies towards a technical design will clarify open issues. The
 8887 details of the stack constructions are summarized in Table ??. The following options have been considered
 8888 for the insert calorimeters:

- 8889 • The forward electromagnetic calorimeter (FEC) inserts (i.e. FEC1 and FEC2) are tungsten-silicon
 8890 sampling calorimeters for compact and radiation hard stack design matching the tracking system

	Calo Module	Layer	Absorber	Thickness	Instrumented Gap	Total Depth
	FEC($W-Si$)	1-25	1.4 mm	16 cm		
	$30X_0$	26-50	2.8 mm	19.5 cm	5 mm	35.5 cm
	FHC($W-Si$)	1-15	1.2 cm	39 cm		
		16-31	1.6 cm	48 cm		
	$10\lambda_I$	32-46	3.8 cm	78 cm	14 mm	165 cm
	FHC($Cu-Si$)	1-10	2.5 cm	30 cm		
		11-20	5 cm	55 cm		
	$10\lambda_I$	21-30	7.5 cm	80 cm	14 mm	165 cm
	BEC($Pb-Si$)	1-25	1.8 mm	17 cm		
	$25X_0$	26-50	3.8 mm	22 cm	5 mm	39 cm
	BHC($Cu-Si$)	1-15	2.0 cm	39.75 cm		
		16-27	3.5 cm	49.8 cm		
	$7.9\lambda_I$	28-39	4.0 cm	55.8 cm	6.5 mm	145.35 cm

Table 13.10: Layer material choice and dimension of electromagnetic and hadronic calorimeter modules simulated. X_0 denotes the radiation length and λ_I the interaction length for the whole stack, respectively. Additional to each absorber layer, layers are placed inside the gap describing the instrumentation (support and readout, respectively): Si-sensors ($525\mu m$), Si-support structures (FR4; 0.65 mm) and Kapton based circuits (1.15 mm). Constants used: $X_0(W)=0.3504$ cm, $\lambda_I(W)=9.946$ cm, $\lambda_I(Cu)=15.06$ cm and $X_0(Pb) = 0.5612$ cm.

8891

towards the interaction point with high granularity.

8892

- The forward hadronic calorimeter (FHC) inserts (i.e. FHC1, FHC2 and FHC3) have been simulated using two different absorber materials, Copper (Cu) and Tungsten (W). Using W only would make the forward insert calorimeters FEC&FHC very homogenous. The electromagnetic and the hadronic part could be combined in the same compartment. On the other hand using Cu is probably more economical.

8893

8894

8895

8896

8897

- The backward electromagnetic calorimeter (BEC) inserts (i.e. BEC1 and BEC2) are lead-silicon sampling calorimeters, with silicon as sensitive media because of the synchrotron radiation risk, specifically in the backward direction. The energy of particles, predominantly the "kinematical peak electrons" scattered backward, is expected to be low enough such that a smaller integrated radiation length X_0 installed and the use of Pb as absorber material is justified.

8898

8899

8900

8901

8902

- The backward hadronic calorimeter (BHC) inserts (i.e. BHC1, BHC2 and BHC3) have been setup as copper-silicon sampling calorimeters.

8903

8904

The BEC, BHC and BEC&BHC composite calorimeter are generally structured as their forward electromagnetic and hadronic calorimeter counterparts sketched in Figure ??.

8905

8906

The lateral size of a shower is due to the multiple scattering of electrons and positrons and characterized by the Molière radius (ρ_M) of the setup. The lateral development of the electromagnetic showers initiated by electrons or photons scales with the Molière radius. The Molière radii of tungsten and lead are $\rho_M=0.9327$ cm and $\rho_M=1.602$ cm [?], respectively. ⁸ ρ_M has to be low enough to separate showers, thus that argument is in favour of W specifically for the construction of the forward insert calorimeters (Fig. ??).

8907

8908

8909

8910

⁸The Molière radius, ρ_M , is the radius of a cylinder containing on average 90% of the electromagnetic shower's energy deposition.

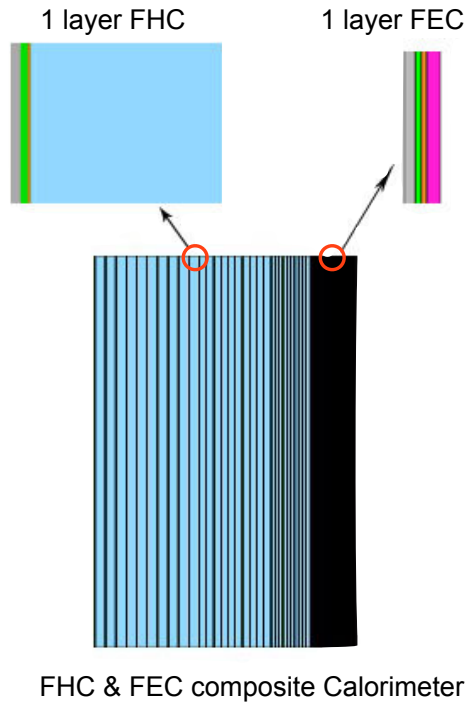


Figure 13.52: Cross section in rz of FHC+FEC. Color coding: the absorber of the FHC is in blue. The absorber of the FEC is in pink. The silicon detectors, silicon support and kapton circuits of FEC and FHC are in brown, green and gray respectively.

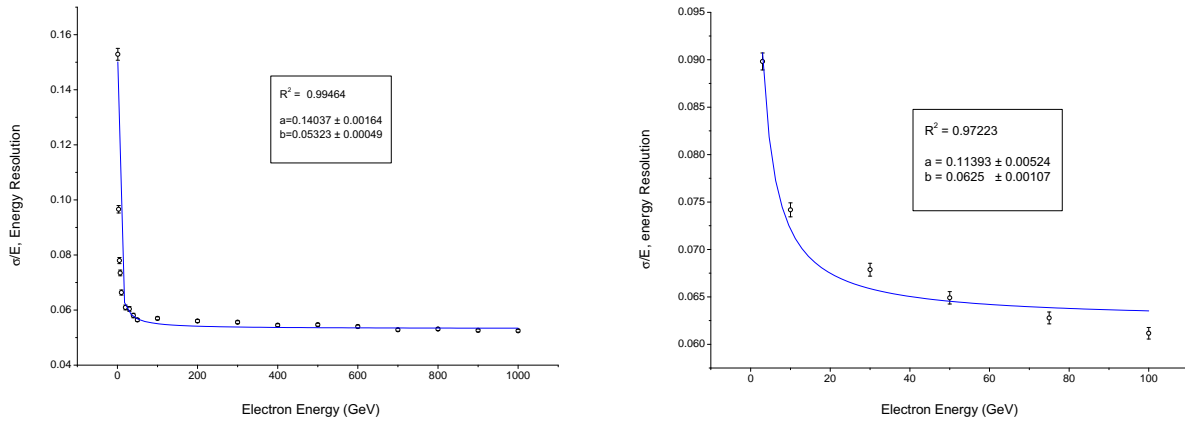


Figure 13.53: Energy resolution spectra simulated for electrons in the energy range 1 GeV-1 TeV in the FEC_(W-Si) (left) and for electrons (energy range 3 GeV-100 GeV) in the BEC_(Pb-Si) stacks (right).

Calo Module (Composition)	Parameterized Energy Resolution
Electromagnetic Response	
FEC _(W-Si)	$\frac{\sigma_E}{E} = \frac{(14.0 \pm 0.16)\%}{\sqrt{E}} \oplus (5.3 \pm 0.049)\%$
BEC _(Pb-Si)	$\frac{\sigma_E}{E} = \frac{(11.4 \pm 0.5)\%}{\sqrt{E}} \oplus (6.3 \pm 0.1)\%$
Hadronic Response	
FEC _(W-Si) & FHC _(W-Si)	$\frac{\sigma_E}{E} = \frac{(45.4 \pm 1.7)\%}{\sqrt{E}} \oplus (4.8 \pm 0.086)\%$
FEC _(W-Si) & FHC _(Cu-Si)	$\frac{\sigma_E}{E} = \frac{(46.0 \pm 1.7)\%}{\sqrt{E}} \oplus 6.1 \pm 0.073\%$
BEC _(Pb-Si) & BHC _(Cu-Si)	$\frac{\sigma_E}{E} = \frac{(21.6 \pm 1.9)\%}{\sqrt{E}} \oplus (9.7 \pm 0.4)\%$

Table 13.11: Energy resolution parametrization for electrons in the electromagnetic stacks (FEC/BEC) and for pions in the composite FEC&FHC and BEC&BHC stack structures, respectively. The energy ranges fitted has been chosen to:

FEC_(W-Si) 1 GeV-5 TeV electrons,
 BEC_(Pb-Si) 3 GeV-100 GeV electrons,
 FEC_(W-Si) & FHC_(Cu-Si) and FEC_(W-Si) & FHC_(W-Si) 50 GeV-1 TeV pions,
 BEC_(Pb-Si) & BHC_(Cu-Si) 3 GeV-100 GeV pions.

The energy resolution spectra simulated are summarized in Figs. ?? and ??.

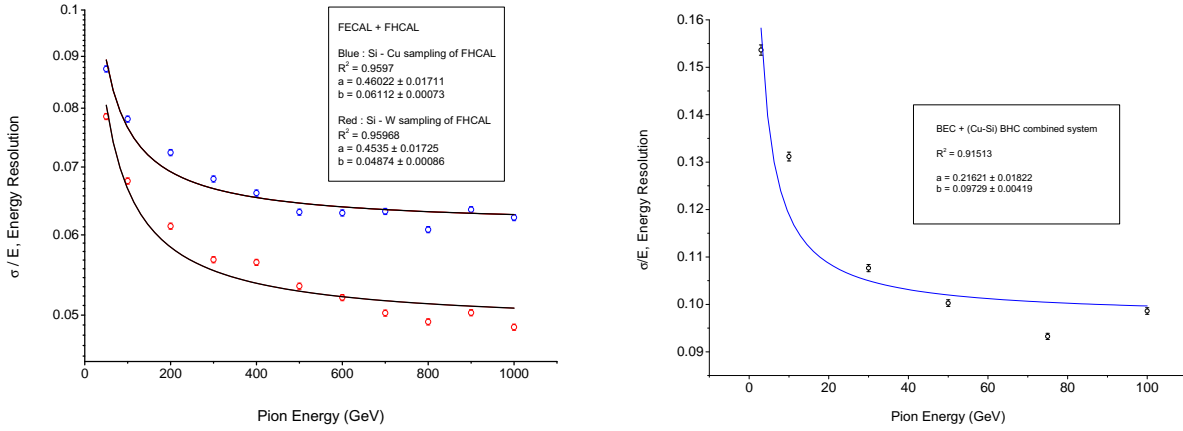


Figure 13.54: Comparison of energy resolution spectra for pions (energy range 50 GeV-1 TeV) in FEC_(W-Si)&FHC_(Cu-Si) and FEC_(W-Si)&FHC_(W-Si) composite system, respectively (left) and energy resolution spectrum for pions (energy range 3 GeV-100 GeV) in the BEC_(Pb-Si)&BHC_(Cu-Si) composite system (right).

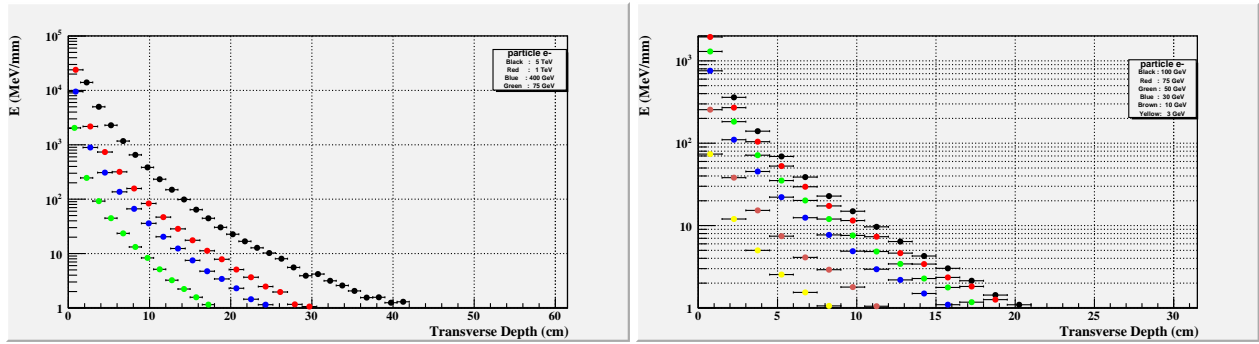


Figure 13.55: Comparison of transverse shower profiles for electrons with energies 75 GeV-5 TeV on $FEC_{(W-Si)}$ (left) and 3 GeV-100 GeV on $BEC_{(Pb-Si)}$ (right).

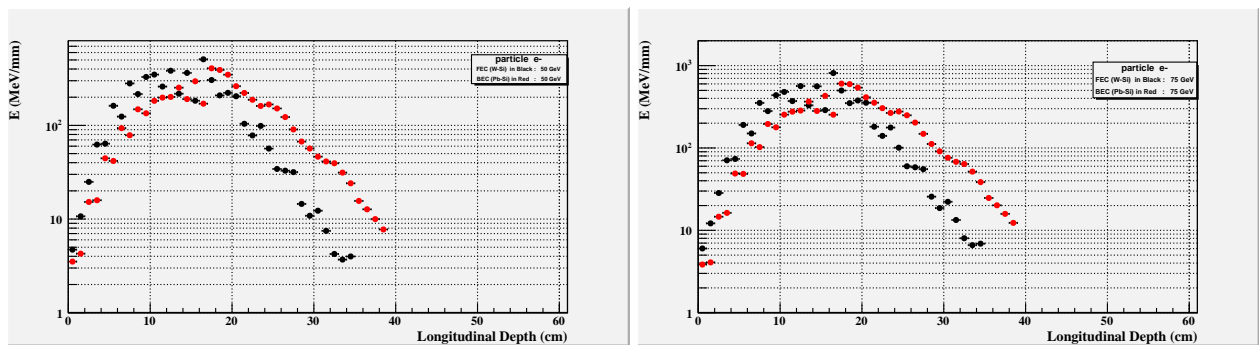


Figure 13.56: Comparison of average energy deposition as a function of longitudinal shower extension for electrons energies of 50 GeV (left) and 75 GeV (right) in $FEC_{(W-Si)}$ (black) and $BEC_{(Pb-Si)}$ (red).

8911 The simulated maximum longitudinal shower profiles for electrons in the FEC and BEC (Fig ??) are in
 8912 agreement with former results [?]. In average 99.4% and 98.8% of the incident energy for simulated elec-
 8913 tron energies in the range of 1 GeV-1 TeV for $FEC_{(W-Si)}$ and 3 GeV-100 GeV for $BEC_{(Pb-Si)}$, respectively,
 8914 are contained in the electromagnetic calorimeters. Thus the high energy electromagnetic showers are suffi-
 8915 ciently well contained in the $30X_0^{FEC}$ and $25X_0^{BEC}$ stack construction, respectively, taking into account the
 8916 considerably lower energies expected in backward direction.

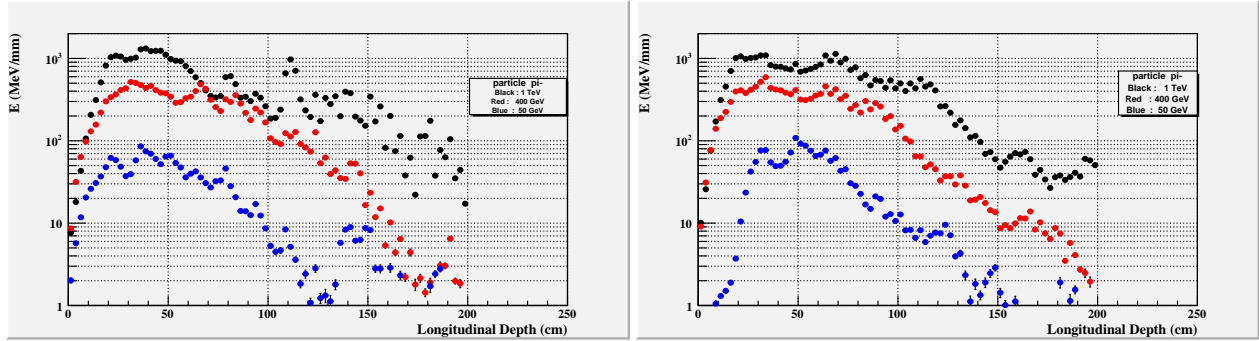


Figure 13.57: Average energy deposition as a function of depth for pions in the energy range 50 GeV-1 TeV in the $FEC_{(W-Si)}$ & $FHC_{(W-Si)}$ system (left) and in the $FEC_{(W-Si)}$ & $FHC_{(Cu-Si)}$ composite stack system (right).

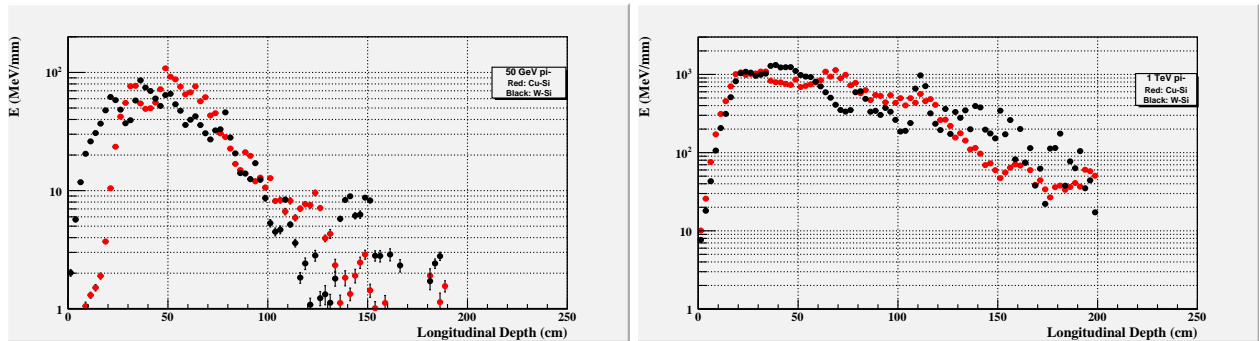


Figure 13.58: Comparison of $FEC_{(W-Si)}$ & $FHC_{(Cu-Si)}$ (red) and $FEC_{(W-Si)}$ & $FHC_{(W-Si)}$ (black) stack systems in terms of average energy depositions as a function of stack depth for pions of energy 50 GeV (left) and the same comparison for pions with energy 1 TeV (right).

8917 The longitudinal distribution of the hadronic calorimeters and shower maxima of the longitudinal dis-
 8918 tribution scales with the nuclear interaction length λ_I . For copper is λ_I by $\approx 51\%$ larger than for tungsten.
 8919 Indeed we observed that showers in the $FHC_{(W-Si)}$ stack (Fig. ??-left) reaches the energy deposition max-
 8920 imum already earlier in the calorimeter, i.e. at smaller depth values. That effect is more pronounced for
 8921 lower energetic pions (Fig. ??-left). The thickness of $10\lambda_I$ provides sufficient containment of the hadronic
 8922 cascades for precision measurements both of jet properties and of E_T^{miss} . The overall containment when
 8923 using $FHC_{(W-Si)}$ instead of $FHC_{(Cu-Si)}$ for the configurations described in Tab. ?? seems to be better.

8924 Some leakage for the hadronic calorimeter $BEC_{(Pb-Si)}$ & $BHC_{(Cu-Si)}$ in backward direction have been
 8925 observed. But the main emphasis in backward direction is the analysis of the electromagnetic component of
 8926 the $e^\pm p/e^\pm Ion$ scattering.

8927 It should be mentioned that essential design details are not defined yet and will affect the performance of
 8928 the real calorimeter. Essential are granularity definitions optimized for shower separation and dead regions

8929 for cables or mechanical structures unavoidable and not contributing to any energy estimation [?], [?]. A
 8930 detailed simulation will take that into account.

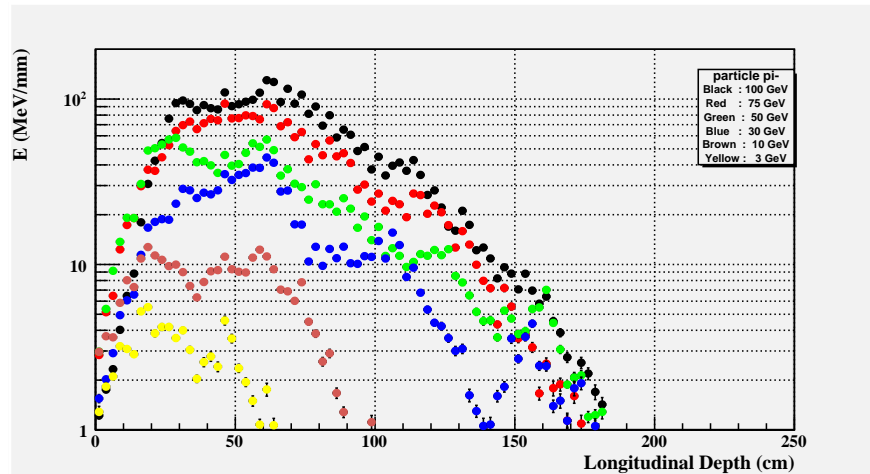


Figure 13.59: Average energy deposition as a function of depth for pions in the energy range 3 GeV-100 GeV incident on the $BEC_{(Pb-Si)}$ & $BHC_{(Cu-Si)}$ composite system.

8931 13.8 Calorimeter Summary

8932 Choosing the sampling calorimeter principle for all calorimeter parts is motivated by good experience in the
 8933 past and constraints given by:

- 8934 • dimensions
- 8935 • costs
- 8936 • experience in the context of e/h compensation and energy-weighting function approximating the linear
 8937 responds of the electromagnetic/hadronic calorimeter system (H1/ATLAS)
- 8938 • the lateral/longitudinal granularity has to be chosen accordingly

8939 Specifically the silicon-absorber based inserts in the forward and backward directions, have to be compact
 8940 and efficiently matched to the tracking devices in front of the calorimeter but *NOT* aiming for a **Particle-
 8941 Flow Calorimeter** [?] [?] [?] which would require a longer/deeper hadronic calorimeter stack construction
 8942 and very high granularity for safe identification of all charged and neutral hadronic particles as well as
 8943 photons. In any case the projective design of the calorimeter stack cells has to be ensured making use of
 8944 signal weighting for good space resolutions (of the order of 1 mm).

8945 An alternative calorimeter design would be the implementation of the **Double Readout Calorimeter**
 8946 concept [?] ⁹. The dual readout calorimeters measure each shower twice and in two different ways. The
 8947 major component, dE/dx contributions of all charged particles (e^\pm, π^\pm, K^\pm , spallation p, recoil p, nuclear
 8948 fragments, etc.), is measured in scintillating material and the electromagnetic part, predominantly coming
 8949 from subshowers from $\pi^0 \rightarrow \gamma\gamma$ decays, is measured by the Čerenkov light generated in clear fibres/plates by
 8950 the relativistic e^\pm passing through [?]. Making use of a obviously constant ratio of $(e/h)_C$ (for Čerenkov light
 8951 emitting material) and $(e/h)_S$ (for Scintillation light emitting material), respectively, the energy response

⁹using plates/fibres in the double readout calorimeter stack for both signal components which are radiation hard

8952 of the calorimeter to electrons e and to hadrons h at all energies can be controlled by construction with
 8953 convincing results [?] [?].

8954 The preliminary simulations and the results shown indicate the validity of the proposed design concepts as
 8955 a baseline solution for the given dimensions of the LHeC detector. A more elaborated design will be possible
 8956 as soon as general decisions on the accelerator concept and therefore magnet design have been taken.

8957 13.9 Muon Detector

8958 Muon detection is an important aspect of the physics program covered by the LHeC. In particular the muon
 8959 detector can improve the scope and the spectrum of measurements, here only a few are listed:

- 8960 • Higgs decay, leptoquarks, lepton flavor violation
- 8961 • PDF fits from semileptonic decay of hadrons and heavy flavors.
- 8962 • Vector meson production

8963 The penetrative power of muons would be exploited by several layers of muon chambers ensuring good
 8964 tracking resolution and hermetic coverage, in particular towards small angles in the forward and backward
 8965 regions. These regions, particular challenging for central tracking detector due to the accelerator infrastruc-
 8966 ture, are more accessible at larger distance from the interaction region as is done for travelling minimum
 8967 ionizing particles as muons are.

8968 Fig. ?? shows the muon polar distributions at the LHeC coming from the decay elastic $ep \rightarrow J/\psi \rightarrow \mu^+ \mu^-$
 8969 production. The improvement by enlarging the coverage towards small angles is evident as shown in Fig. ??
 8970 where the coverage as a function of the γp system center of mass energy W is shown for the cases of 10° and
 8971 1° detector acceptance.

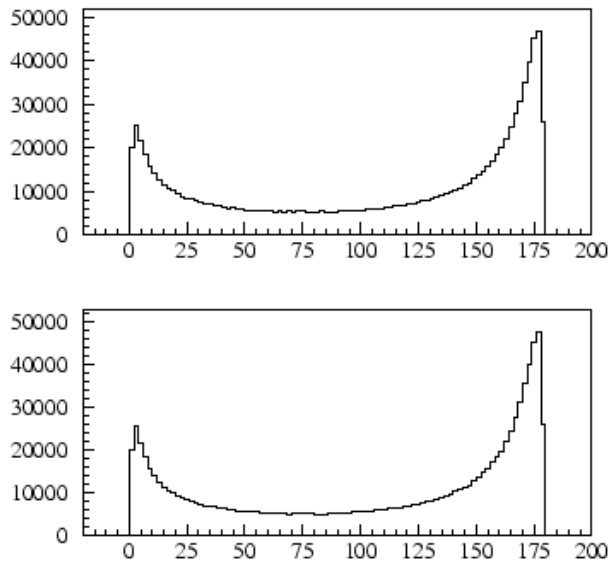


Figure 13.60: Distribution for J/ψ with $E_e = 50$ GeV. Polar angle of positive (top) and negative (bottom) muon respectively.

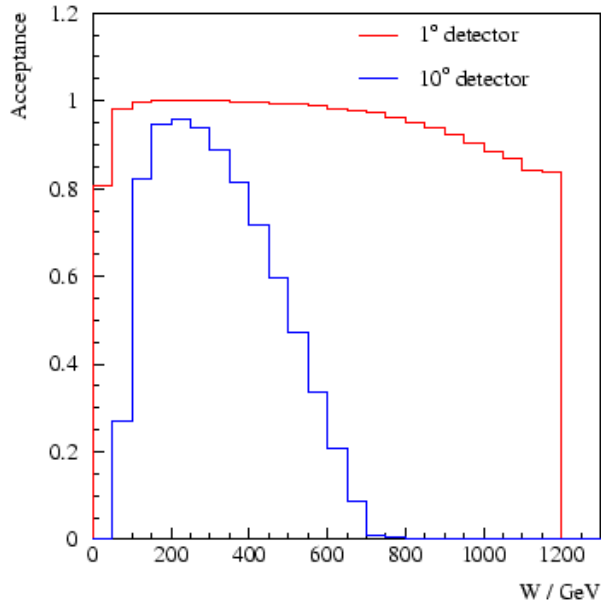


Figure 13.61: Acceptance for J/ψ with $E_e = 50$ GeV as a function of W , the center of mass energy of the γp system. A detector with larger coverage both in the forward and in the rear region allows for measurements on a much wider W range.

8972 13.9.1 Muon detector design

8973 The LHeC main detector will be surrounded by multiple layers of muon detectors. Fig. ?? shows a 3d
 8974 view of the baseline detector (option A). Three muon double detector layers mechanically attached to an
 8975 iron structure which could provide either the return flux of residual B field from the inner solenoid or an
 8976 additional field from warm magnets.

8977 Following the state of the art of present muon detector as implemented in the LHC experiments and
 8978 in similar high energy physics experiments, several options providing the required tracking resolution, rate
 8979 sustainability and prompt trigger and readout are available.

8980 The two LHC general purpose detectors, ATLAS and CMS, combine Drift Tubes and Cathode Strip
 8981 Chambers for precision measurements along with with Resistive Plates Chambers and Thing Gap Chambers
 8982 for Trigger and second coordinate measurements [?, ?]. A similar approach can be considered for the LHeC
 8983 muon detector with 2 or 3 superlayers each one composed of a double layer of 2d trigger detector and a
 8984 precision measurement as shown in Fig.??.

8985 Other technologies (as for instance micromegas [?], gem etc.) along with further developments of the
 8986 existing ones (thin gap RPC [?], smaller monitored drift tubes [?], thin strip TGC), might also be considered
 8987 for the LHeC. It is anyhow evident that the requirements from the LHC would also satisfy the running at
 8988 the LHeC where backgrounds and luminosity are expected to be lower.

8989 To provide at this stage a complete design of the muon detector is beyond the scope of this document
 8990 as too many options are available and depend on the choices to be taken in the accelerator and the main
 8991 detector design. Only a few options are discussed below with the aim to demonstrate, for the baseline design,
 8992 the feasibility and scope of a detector using available technologies. More studies and design optimization
 8993 will follow in the next steps.

8994 13.9.2 The LHeC muon detector options

8995 Neglecting for the moment the detector technologies to be used, depending on the experimental weight the
 8996 muon detector will have within the LHeC detector, few different approaches satisfying increasing requirements

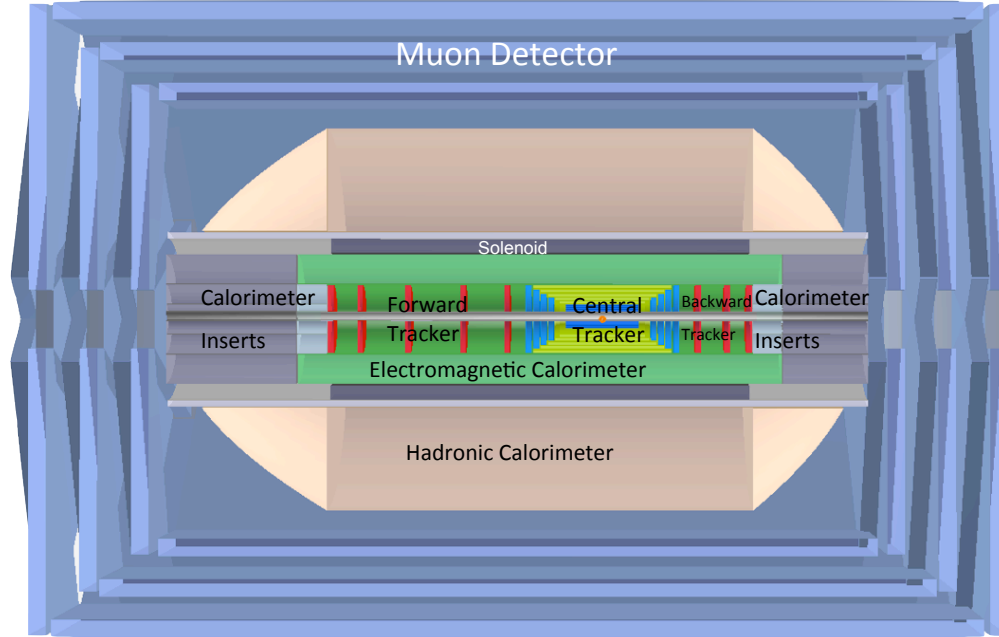


Figure 13.62: A full view of the baseline detector in the r - z plane with all components shown. The detector dimensions are ≈ 14 m in z with a diameter of ≈ 9 m.

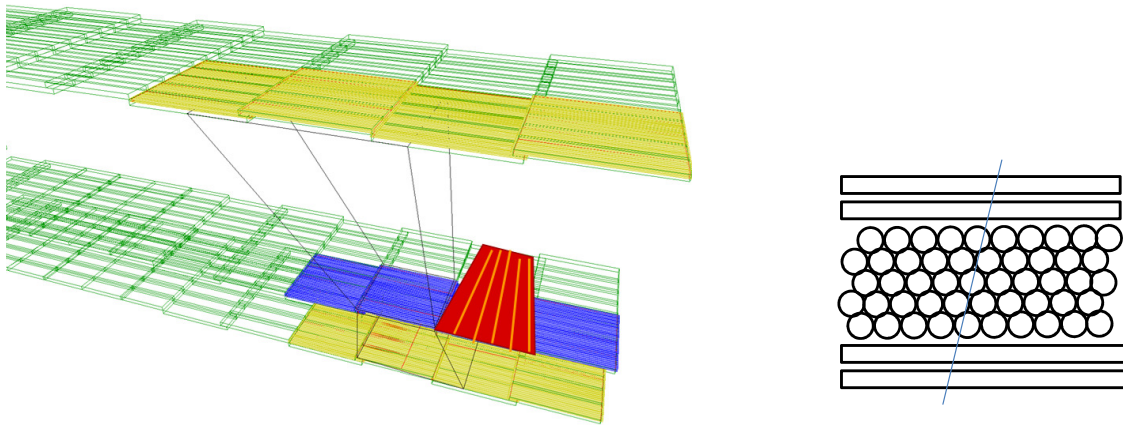


Figure 13.63: Artist 3d view of the projective arrangement of the layers barrel muon chambers (left). A schematic view of the cross section of one of the chambers which include a double layer of $\eta\phi$ trigger measurement used also for level one triggering along with the precision measurement obtained by drift tubes

8997 can be considered.

- 8998 1. Muon tagging
- 8999 2. Combined muon momentum measurement
- 9000 3. Standalone momentum measurement

9001 With “muon tagging” (1) we indicate a muon detector built with at least 2 layers of muon chambers that
9002 provide $\eta\phi$ measurement and a fast coincidence for trigger purposes. No additional magnetic field would be
9003 set up and the muon detector, using only the return flux of the central solenoid would be able to provide only
9004 a very rough estimate of the particle momentum. The multiple layers and the fast detector response would
9005 allow a pointing trigger to reject non prompt particles. Muon Momentum measurements would be done
9006 using mainly the tracking detector and possibly complemented by the energy deposits in the calorimeter
9007 (that have to be compatible with those of a minimum ionizing particle) and the muon tag.

9008 The next step (2) would be to enhance the muon momentum measurement by adding an extra magnetic
9009 field, embedding the muon chambers in an iron yoke. The amount of iron and the size of the yoke can be
9010 optimized in order maximize the resolution in the energy range required.

9011 Both options (1) and (2) can be considered for the baseline design option A and. It is worth noticing that
9012 for low energy muons (as expected in the barrel and rear region) an instrumented yoke might not be required
9013 as the momentum resolution of the tracking system will be far superior. For muon momenta of 20 GeV and
9014 above the presence of an additional magnetic field or an instrumented iron yoke could improve especially in
9015 the forward and backward region, where the momentum resolution is worse due to the solenoidal field being
9016 parallel to the beamline.

9017 Although the presence of an iron mass serves four good purposes, namely:

- 9018 • return the magnetic flux
- 9019 • serve as a hadron (π^\pm, K, p, n) particle filter so that predominantly μ^\pm emerge at a large radius
- 9020 • provide excellent mechanical support for all detector systems, especially the massive calorimeter
- 9021 • serve as a radiation shield for the area and the electronics

9022 as soon as the solenoid field and its size increase, the required shielding also increases proportionally and its
9023 density, weight and costs pose important limitations which might be overcome by the use of a twin solenoid
9024 system as discussed in ??.

9025 This novel approach which would guarantee a “standalone momentum measurement ” (3). The outer
9026 solenoid allows for a very smooth and constant field in an iron free region. As shown in Fig. ??, the muon
9027 detector is immersed in a strong constant field (~ 1.5 T) which would allow precise momentum measurement
9028 of momenta up to 500 GeV with $\delta p/p$ $x.x$. A strong advantage of an air muon spectrometer is the significant
9029 reduction of the the uncertainty due to multiple Coulomb scattering. Additionally, the use of forward
9030 and backward coils can improve the field quality also in the endcap regions allowing the field to line up
9031 transversely to the beam line, for an improved longitudinal momentum measurement.

9032 13.9.3 Forward Muon Extensions

9033 Detection of muons in the forward hemisphere is extremely relevant at the LHeC where the kinematics of
9034 important physical phenomena (production of heavy flavours, high x physics, leptoquarks etc.) requires a
9035 coverage down to the smallest possible angle with respect to the beam axis. Since the tracking momentum
9036 resolution deteriorates at small angles an independent measurement in the forward region would provide a
9037 completely independent tool for the measurement of the muon momentum.

9038 Given the high particle, and specifically, muons flux expected in the forward region, the use of a dedicated
9039 forward muon toroid would allow the measurement of muon charge and momentum. In Fig.?? a sketch of a
9040 possible design for a “small” forward muon toroid is given. For the baseline detector A, a more conventional,

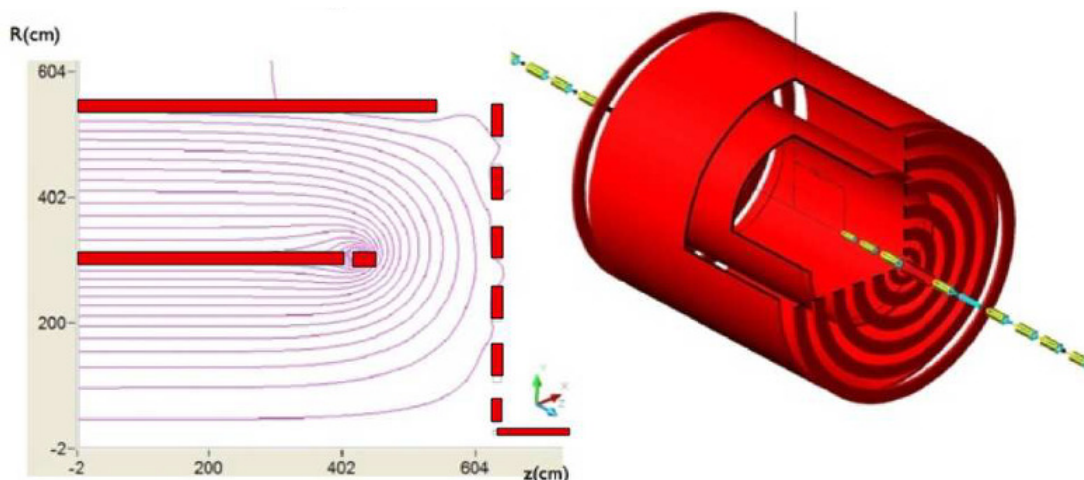


Figure 13.64: Magnetic field lines for the dual solenoid and wall of coil [?]. The whole detector is enclosed in a second return solenoid; forward and rear coils which allow for a smooth field at the detector muon encaps

9041 iron based solution (as in HERA for H1 and ZEUS) could be adopted incorporated or located outside of the
 9042 the muon iron-yoke. The option of an air core forward toroid combined, either with the option A detector
 9043 inside the iron yoke system or in the larger twin solenoid option B would even more enhance the forward
 9044 muon momentum resolution especially for very small angles with respect to the beam line.

9045 The insertion of a forward air core based toroid closer to the central tracking system was also consid-
 9046 ered and rejected as the bulk material of the required coils, located between the tracking planes and the
 9047 calorimeters would compromise the calorimetry measurements.

9048 13.9.4 Muon Detector Summary

9049 Several options for the LHeC muon detector are available.

9050 These range from a simple muon tagging detector which, combined with the baseline detector A would
 9051 already be sufficient for a clean muon trigger, allowing to remove beam gas background and non pointing
 9052 tracks. The precision of the momentum resolution would depend mostly on the main detector (tracking and
 9053 calorimetry) which anyhow would degrade at small forward and backward angle.

9054 Improvements by means of a iron yoke and conventional forward muon toroids would allow improved
 9055 performance especially for higher momenta and for muon spectroscopy in the forward region. The experience
 9056 from HERA indicate that a solution lacking of a standalone muon trigger could be acceptable for most of
 9057 the physics program.

9058 The ultimate design nevertheless appears to be the the twin solenoid option. This more challenging
 9059 design, shown in Fig.?? naturally follows the option B of the baseline design: the larger main solenoid is
 9060 located outside of the hadronic calorimeter and together with a second active shielding solenoid provides a
 9061 wide material free region for precise standalone muon momentum measurement. The higher energies available
 9062 in the forward region and the interesting physics channels also push for a leading edge design towards use
 9063 of additional forward muon toroid. The detector acceptance for the muon channel physics could be largely
 9064 extended.

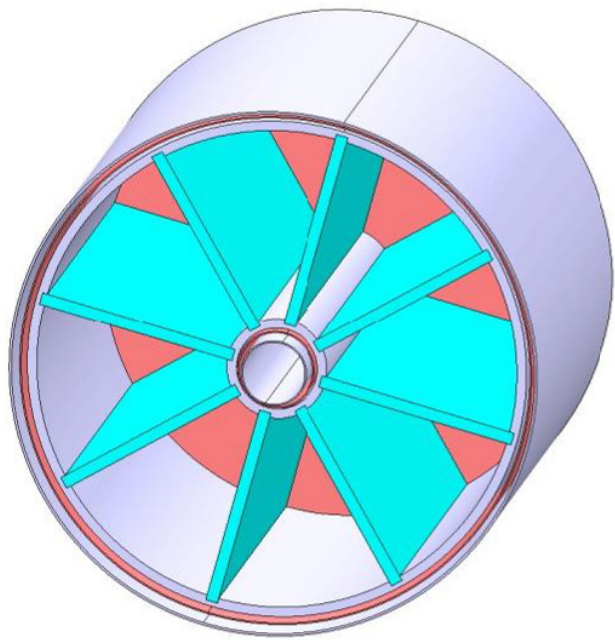


Figure 13.65: CAD drawing for a 2T air core toroid with 20 cm bore and a size about 1 m³

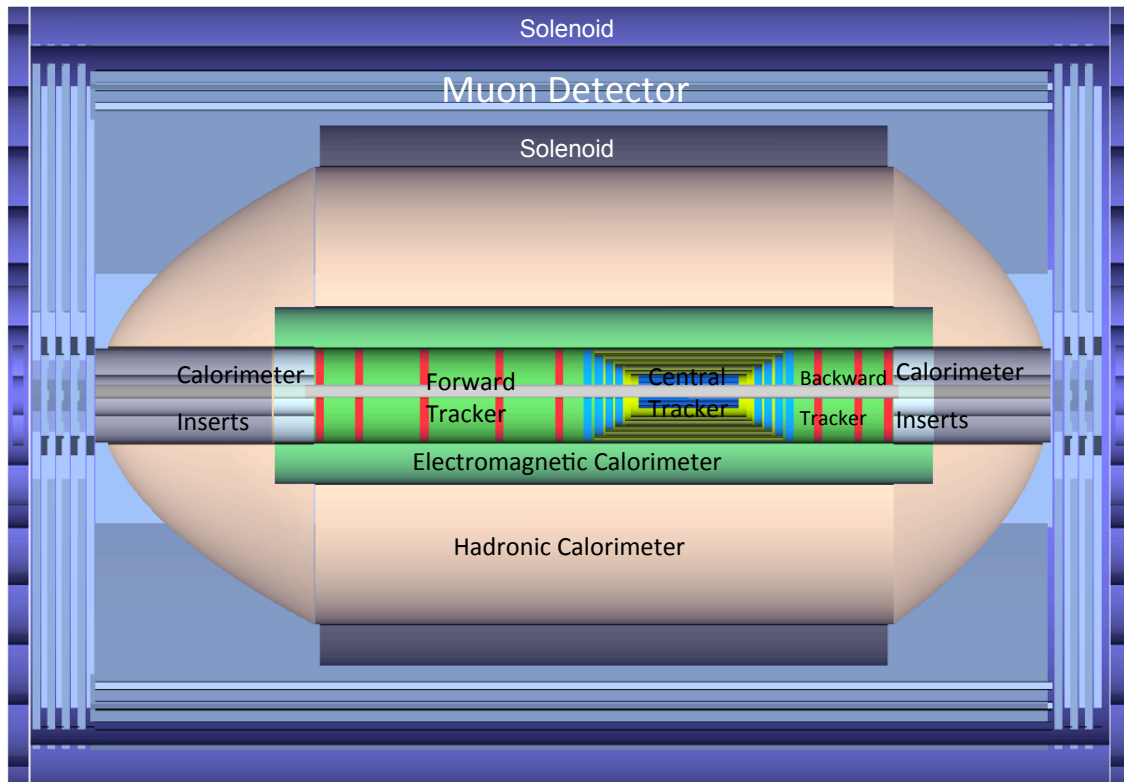


Figure 13.66: The option B of the LHeC baseline detector. The larger solenoid surrounds the hadronic calorimetry. The volume outside the solenoid is filled with an approximately uniform magnetic field of 1.5 T and is instrumented with 3-4 multilayers of Muon chambers.

Chapter 14

Forward and Backward Detectors

14.1 Luminosity Measurement and Electron Tagging

Luminosity measurement is an important issue for any collider experiment. At the LHeC, where precision measurements constitute a significant part of the physics programme, the design requirement is $\delta\mathcal{L} = 1\%$.

In addition to an accurate determination of integrated luminosity, \mathcal{L} , for the normalisation of physics cross sections, the luminosity system should allow for fast beam monitoring with a typical statistical precision of 1%/sec for tuning and optimisation of ep -collisions and to provide good control of the mid-term variations of instantaneous luminosity, L .

Rich experience gained by H1 [?, ?] and ZEUS [?, ?] Collaborations at HERA was used in the design studies of the luminosity system for the LHeC. In particular, one important lesson to be learnt from HERA is to prepare several alternative methods for luminosity determination.

For the LHeC we consider both Linac-Ring (LR) and Ring-Ring (RR) options as well as high Q^2 ($10^\circ - 170^\circ$ acceptance) and low Q^2 ($1^\circ - 179^\circ$ acceptance) detector setups. This spans over a wide range of instantaneous luminosity¹ $L = (10^{32} - 2 \cdot 10^{33})\text{cm}^{-2}\text{s}^{-1}$. Hence suitable processes for the three tasks outlined above should have the following minimal visible cross sections²:

- fast monitoring ($\delta\mathcal{L} = 1\%/ \text{sec} \Rightarrow 10 \text{ kHz}$) – $\sigma_{\text{vis}} \gtrsim 100\mu\text{b}$,
- mid-term control ($\delta\mathcal{L} = 0.5\%/ \text{hour} \Rightarrow 10 \text{ Hz}$) – $\sigma_{\text{vis}} \gtrsim 100\text{nb}$,
- physics sample normalisation ($\delta\mathcal{L} = 0.5\%/ \text{week} \Rightarrow 0.1 \text{ Hz}$) – $\sigma_{\text{vis}} \gtrsim 1\text{nb}$.

The best candidate for luminosity determination is the purely electromagnetic *bremsstrahlung reaction* $ep \rightarrow e\gamma + p$ shown in Figure ??a, which has a large and precisely known cross section. Depending on the photon emission angle it is called either Bethe-Heitler process (collinear emission) or QED Compton scattering (wide angle bremsstrahlung). In addition, Neutral Current DIS events in a well understood (x, Q^2) range can be used for the *relative* normalisation and mid-term yield control.

While QED Compton and NC DIS processes can be measured in the main detector dedicated ‘tunnel detectors’ are required to register Bethe-Heitler events. For the latter, additional challenges as compared to HERA are related to the LHeC specifics: non-zero beam crossing angle in IP for RR option, and severe aperture limitation for LR option. Finally, for the high luminosity LHeC running one should not forget about significant pileup (L/bunch is $\sim 2 - 3$ times bigger as compared to HERA-II running).

¹This also takes into account exponential reduction of L during the data taking in every luminosity fill.

²Statistical error has to be small in comparison with total error δL_{tot} in order not to spoil overall accuracy.

14.1.1 Options

The huge rate of ‘zero angle’ electrons and photons from Bethe-Heitler reaction³ makes a dedicated luminosity system in the tunnel ideal for fast monitoring purposes. However, it is usually very sensitive to the details of the beam optics at the IP, may suffer from synchrotron radiation (SR) and requires, for accurate absolute normalisation, a large and precisely known geometrical acceptance which is often difficult to ensure. On the contrary, the main detector has stable and well known acceptance and is safely shielded against SR. Therefore, although QED Compton events in the detector acceptance have significantly smaller rates they may be better suited for overall global normalisation of the physics samples. Thus the two methods are complementary, having very different systematics and providing useful redundancy and cross check for the luminosity determination.

To evaluate the main LHeC detector acceptance for NC DIS events and for the elastic QED Compton process DJANGOH [?] and COMPTON [?] event generators were used respectively. Different options for dedicated luminosity detectors in the LHC tunnel have been studied with help of the special H1LUMI program package [?], which contains Monte Carlo generation of the ‘collinear’ photons and electrons from various processes (Bethe-Heitler reaction, quasi-real photoproduction, e-beam scattering on the rest gas) as well as a simple tracking through the beamline.⁴

14.1.2 Use of the Main LHeC Detector

To estimate visible cross sections for NC DIS and elastic QED Compton events a typical HERA analysis strategy was used. That is: safe fiducial cuts against energy leakage over the backward calorimeter boundaries at small radii, safe (Q^2, y) cuts for NC DIS events to restrict measurement to the phase space where F_2 is known to good precision of 1 – 2% and the F_L contribution is negligible, and elasticity cuts for QEDC events to reject the less precisely known inelastic contribution. In addition basic cuts against major backgrounds were applied (photoproduction in case of NC DIS and DVCS, elastic VM production and low mass diffraction in case of QED Compton).

The visible NC DIS cross section, $\sigma_{\text{vis}}^{\text{DIS}}(Q^2 > 10\text{GeV}^2, 0.05 < y < 0.6) \simeq 10$ nb for 10° setup and $\simeq 150$ nb for 1° setup. This corresponds to a 10 – 15 Hz rate which is comfortable enough for mid-term yield control.

For elastic QED Compton events, the visible cross section, $\sigma_{\text{vis}}^{\text{QEDC}} \simeq 0.03$ nb for 10° setup and $\simeq 3.5$ nb for 1° setup. Hence while for the latter sufficiently high rate is possible even for $L = 10^{32}\text{cm}^{-2}\text{s}^{-1}$, in case of ‘high Q^2 ’ setup the QEDC event rate is 4 – 5 times smaller, thus only providing acceptable statistical precision for large samples, of the order 0.5%/month.

In order to improve this a special small dedicated calorimeter could eventually be added after the strong focusing quadrupole, at $z = -6\text{m}$. Such ‘QEDC tagger’ should consist of two movable stations approaching the beam-pipe from the top and the bottom in the vertical direction, as sketched in Figure ??b. This way detector sections will be safe with respect to SR fan confined in the median plane. The visible elastic QED Compton cross section for such a device is 4.3 ± 0.2 nb which significantly improves statistics for the luminosity measurement. The angular acceptance of the ‘QEDC tagger’ corresponds to the range $\theta = 0.5^\circ - 1^\circ$ which lies outside the tracking acceptance. Therefore calorimeter sections should be supplemented by small silicon detectors in order to make it possible to reconstruct the event vertex from the final state containing only one electron and one photon. These silicon trackers are also useful for e/γ separation and rejection of the potential background. Actual dimensions and parameters of this optional ‘QEDC tagger’ requires extra design studies.

³Total cross section, $\sigma_{BH} \simeq 870$ mb for 60×7000 GeV² ep collisions at the LHeC.

⁴The tracking has been performed by interfacing H1LUMI to GEANT3 [?] having LHeC beamline implemented up to $\sim 110\text{m}$ from the IP.

14.1.3 Dedicated Luminosity Detectors in the tunnel

In case of the RR-option which implies non-zero crossing angle for early e/p beam separation, the dominant part of the Bethe-Heitler photons will end up at $z \simeq -22\text{m}$, between electron and proton beam-pipes (see Figure ??c). This is the hottest place where also a powerful SR flux must be absorbed. On the first glance this makes luminosity monitoring based upon the bremsstrahlung photons impossible.

There is however an interesting possibility. SR absorber needs good cooling system. The most natural cooling utilises circulating water. This cooling water can be used at the same time as an active media for Čerenkov radiation from electromagnetic showers initiated by the energetic Bethe-Heitler photons. The idea is based on two facts:

1. The dominant part of the SR spectrum lies below the Čerenkov threshold for water, $E_{\text{thr}} = 260 \text{ keV}$, and hence will not produce light signal. Low intensity tail of the energetic synchrotron photons can be further suppressed by few radiation lengths of the absorber material in front of the water volume.
2. Water is absolutely radiation resistant media and hence such simple Čerenkov counter can stand any dose without performance deterioration.

The Čerenkov light can be collected and read out by two photo-multipliers as sketched on Figure ??d. The geometric acceptance depends on the details of the e -beam optics. For the actual RR design with the crossing angle $\sim 1 \text{ mrad}$ the acceptance to the Bethe-Heitler photons is up to 90%, thus allowing fast and reliable luminosity monitoring with 3 – 5% systematic uncertainty.

Of course, such an active SR absorber is not a calorimeter with good energy resolution, but just a simple counter. It is worth noting, that similar water Čerenkov detector has been successfully used in the H1 Luminosity System during HERA-I operation.

In case of LR-option, electrons collide with protons head-on, with zero crossing angle. This makes the situation very similar to HERA, where Bethe-Heitler photons travel along the proton beam direction and can be caught at around $z = -120\text{m}$, after the first proton bending dipole. Essential difference is that unlike HERA, LHC protons are deflected horizontally at this place rather than vertically. Thus the luminosity detector should be placed in the median plane next to the interacting proton beam, p_1 , as shown on Figure ??e. In this case energy measurement with good resolution is not a problem, so major uncertainty will come from the knowledge of the limited geometric acceptance. This limitation is defined by the proton beam-line aperture, in particular by the aperture of the quadrupoles Q1-Q3 of the low-beta proton triplet. Moreover, it might be necessary to split D1 dipole into two parts in order to provide escape path for the photons with sufficient aperture. First estimates show that the geometric acceptance of the Photon Detector up to 95% is possible at the nominal beam conditions. HERA experience tells, that the uncertainty can be estimated as $\delta A = 0.1 \cdot (1 - A)$ leading to the total luminosity error of $\delta L = 1\%$ in this case.

14.1.4 Small angle Electron Tagger

The Bethe-Heitler reaction can be tagged not only by detecting a final state photon, but also by detecting the outgoing electron. Since all other competing processes have much smaller cross sections measuring inclusive rate of the scattered electrons under zero angle will provide a clean enough sample for luminosity monitoring. The remaining small background (mainly due to off-momentum electrons from e -beam scattering on the rest gas) can be precisely controlled and statistically subtracted using non-colliding (*pilot*) electron bunches.

In order to determine the best positions for the Electron taggers the LHeC beamline simulation has been performed in the vicinity of the Interaction Region for the RR-option. Several positions for the e -tagger stations were tried:⁵ $z = -14\text{m}$, -22m and -62m . As one can see on the top part of Figure ?? all places provide reasonable acceptances, reaching approximately (20 – 25)% at the maximum. However, $z = -14\text{m}$ and $z = -22\text{m}$ most likely will suffer from SR flux, making e -tagger operation problematic at those positions.

⁵For the station at $z = -14\text{m}$ the electron dipole magnet should be split into two parts, while the region around $z = -62\text{m}$ has sufficiently comfortable place for the Electron tagger, before the e -beam is bended vertically.

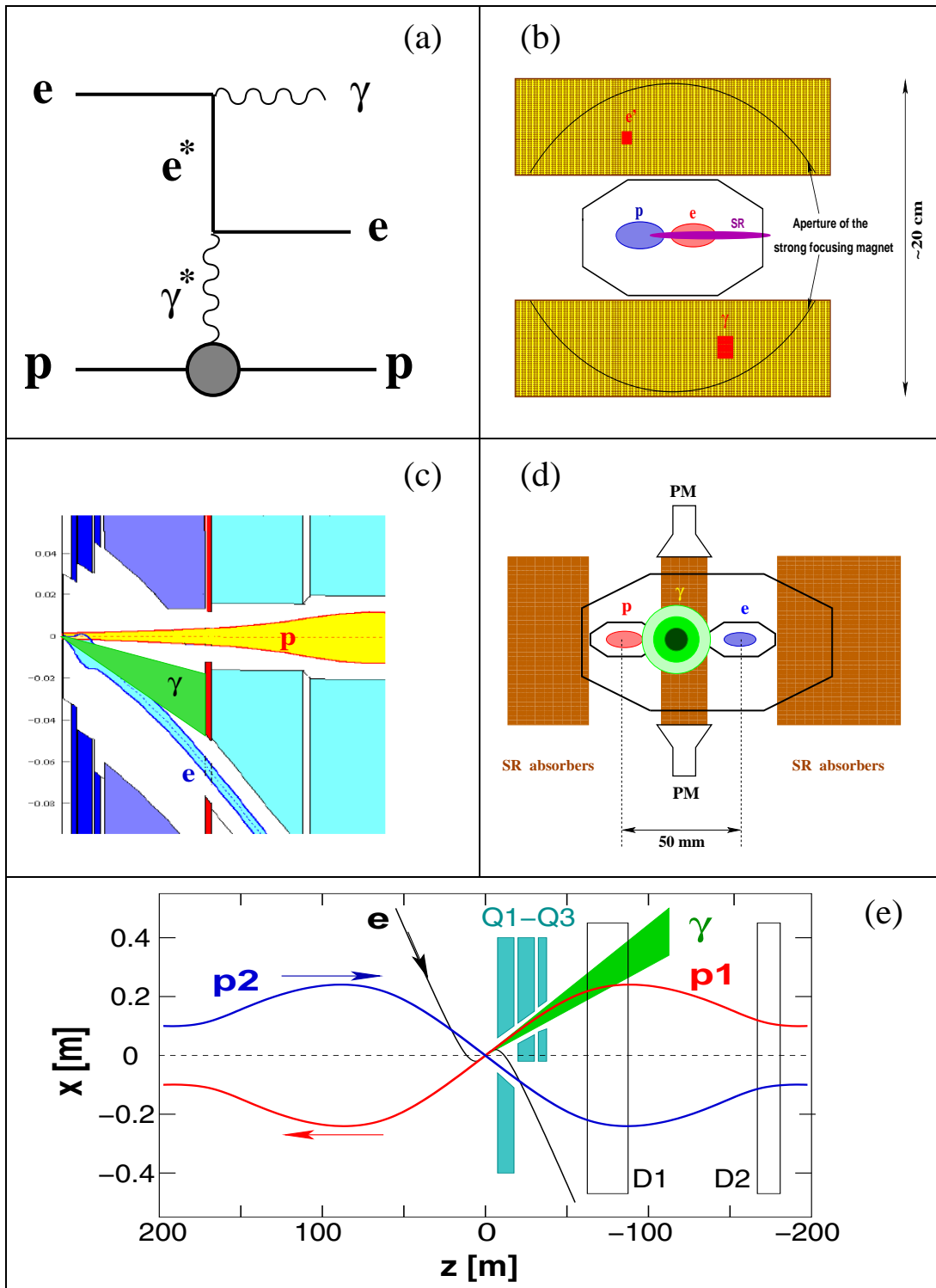


Figure 14.1: Options for the luminosity monitoring at the LHeC. (a) Feynman diagram for QEDC (γ^* pole) or BH (γ^* , e^* poles) processes; (b) QEDC tagger at $z = -6$ m; (c,d) active SR absorber at $z = -22$ m for RR-option (circles show 1-, 2- and 3- σ contours for BH photons); (e) schematic view for the LR-option with 3- σ fan of BH photons.

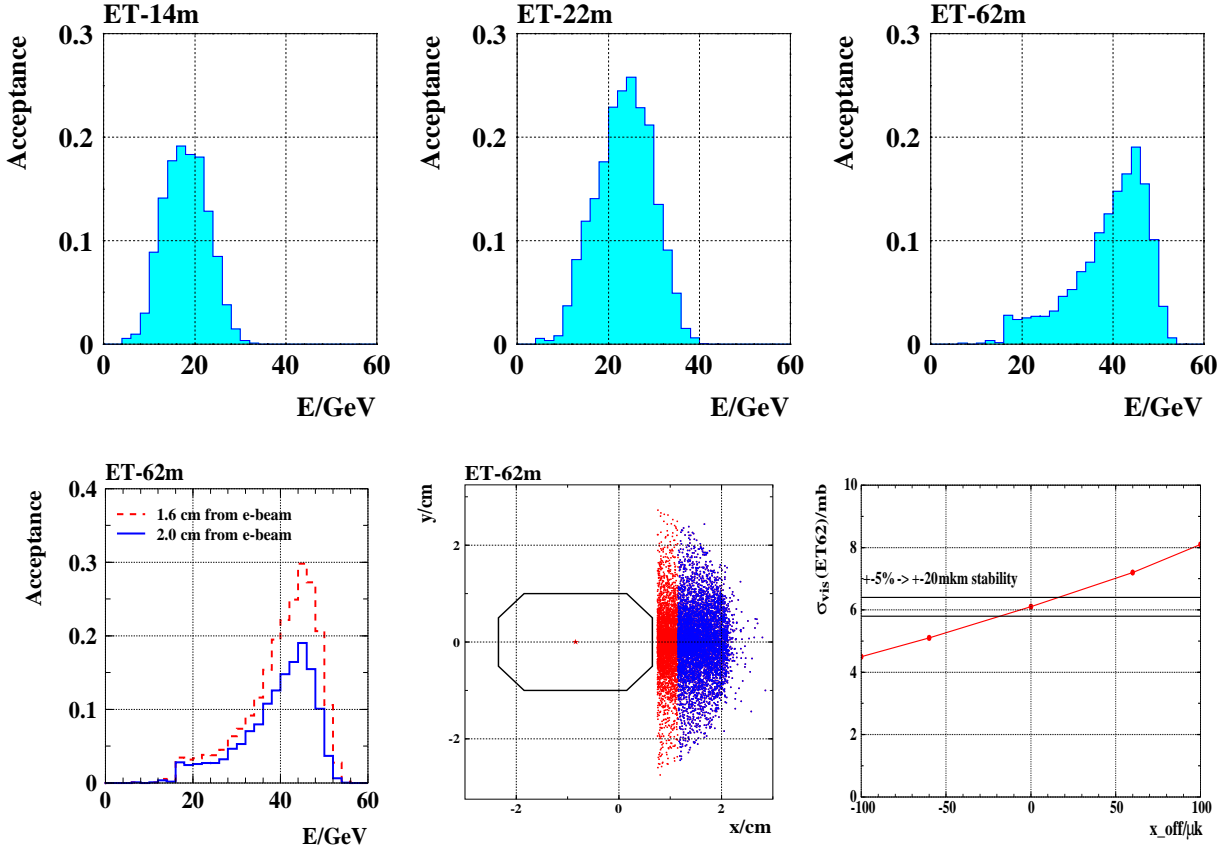


Figure 14.2: Top: acceptances of the e -taggers for Bethe-Heitler events at different z -positions from IP (RR-option). Bottom: variations in the acceptance of the e -tagger at $z = -62\text{m}$ as a function of its position with respect to the e -beam axis and on the horizontal offset of the beam orbit at the IP.

9180 The most promising position for the Electron tagger is at $z = -62\text{m}$. The actual acceptance strongly
 9181 depends both on the distance of the sensitive detector volume from the e -beam axis and on the details of the
 9182 electron optics at the IP, such as beam tilt or small trajectory offset, as illustrated on the bottom part of
 9183 Figure ???. Therefore a precise independent monitoring of beam optics and accurate position measurement
 9184 of the e -tagger are required in order to control geometrical acceptance to a sufficient precision. For example,
 9185 instability in the horizontal trajectory offset at IP, x_{off} , of $\pm 20\mu\text{m}$ leads to the systematic uncertainty of 5%
 9186 in the visible cross section, $\sigma_{\text{vis}}(\text{ET62})$.

9187 It is fair to note, that the magnetic field of the main LHeC detector was not taken into account in the
 9188 simulation. The influence of this field is expected to be very small and will not alter basic conclusions of this
 9189 section. Also, for the LR-option a similar acceptance is expected, although it may differ in shape somewhat.

9190 In order to demonstrate that the ideas described in Sec. ?? and ?? are realistic a typical example of
 9191 the online rates variations for the H1 Luminosity System at HERA is shown on Figure ???. The system
 9192 utilised all three types of the detectors discussed above: a total absorption electromagnetic calorimeter for
 9193 the Bethe-Heitler photons (PD), a water Čerenkov counter (VC) and the Electron tagger (ET6). One can
 9194 see, that online luminosity estimate by every of those detectors is well within 5% in spite of significant
 9195 changes in the acceptance due to electron beam tilt jumps and adjustments at the IP.

9196 **14.1.5 Summary and Open Questions**

9197 Accurate luminosity measurement at the LHeC is highly non-trivial task. As follows from HERA experience
 9198 unexpected surprises are possible, hence it is important to consider several scenarios from the beginning and
 9199 to prepare alternative methods for luminosity determination.

9200 Statistical precision and systematic uncertainties for different methods of luminosity measurement are
 9201 summarised in Table ??.

Method	Stat. error	Syst.error	Systematic error components	Application
BH (γ)	0.05%/sec	1–5%	$\sigma(E \gtrsim 10\text{GeV})$ acceptance, A E -scale, pileup	0.5% 10%(1– A) 0.5 – 4% Monitoring, tuning, short term variations
BH (e)	0.2%/sec	3–6%	$\sigma(E \gtrsim 10\text{GeV})$ acceptance background E -scale	0.5% 2.5 – 5% 1% 1% Monitoring, tuning, short term variations
QEDC	0.5%/week	1.5%	σ (el/inel) acceptance vertex eff. E -scale	1% 1% 0.5% 0.3% Absolute \mathcal{L} , global normalisation
NC DIS	0.5%/h	2.5%	σ ($y < 0.6$) acceptance vertex eff. E -scale	2% 1% 1% 0.3% Relative \mathcal{L} , mid-term variations

Table 14.1: Dominant systematics for various methods of luminosity measurement.

9202 Precise determination of integrated luminosity, \mathcal{L} , is possible with the main detector utilising the QEDC
 9203 process. $\delta\mathcal{L} = 1.5 - 2\%$ is within reach. Further improvement requires in particular more accurate theoretical
 9204 calculation of the elastic QED Compton cross section, with $\delta\sigma_{\text{el}}^{\text{QEDC}} \lesssim 0.5\%$. To enhance statistical precision
 9205 a dedicated QEDC tagger at $z = -6\text{m}$ might be useful. This device could also be used to access very low
 9206 Q^2 region, interpolating between DIS and photoproduction regimes.

9207 Fast instantaneous luminosity monitoring is challenging, but several options do exist which are based
 9208 upon detection of the photons and/or electrons from the Bethe-Heitler process.

- 9209 • Photon Detector at $z = 110\text{m}$ for LR option requires properly shaped proton beam-pipe at $z =$
 9210 $-68 - 120\text{m}$ from IP2.
- 9211 • In case of RR option Bethe-Heitler photons can be detected using a water Čerenkov counter integrated
 9212 with SR absorber at $z = -22\text{m}$.
- 9213 • Electron tagger at $z = -62\text{m}$ is very promising for both LR and RR schemes. It can be used not only
 9214 for luminosity monitoring, but also to enhance photoproduction physics capabilities and to provide
 9215 extra control of the γp background to DIS, by tagging quasi-real photoproduction events.

9216 Good monitoring of the e -optics at the IP is required to control acceptances of the tunnel detectors to a
 9217 level of 2 – 5%.

14.2 Polarimeter

The most powerful technique to measure the polarisation of the electrons and positrons of LHeC is Compton polarimetry. At high electron beam energies, this technique has been successfully used in the past at SLC [?] and at HERA [?] for example. The experimental setup consists of a laser beam which provides the electron/positron beam, and a calorimeter to measure the scattered gamma ray. At SLC, the scattered electron was also measured in a dedicated spectrometer. From the kinematics of Compton scattering one can get the expression for the maximum scattered photon energy:

$$E_{\gamma,max} \approx E_0 \frac{x}{1+x}$$

and the minimum scattered electron energy

$$E_{e,min} \approx E_0 \frac{1}{1+x},$$

9219 where E_0 is the electron/positron beam energy and $x = 4kE_0/m_e^2$ with k being the laser photon beam
 9220 energy. At LHeC and for a $\approx 1\mu\text{m}$ laser beam wavelength, one gets $E_{\gamma,max} \approx 29\text{GeV}$ and $E_{e,min} \approx 31\text{GeV}$.
 9221 Providing that the laser beam is circularly polarised, the electron/positron beam longitudinal polarisation is
 9222 obtained from a fit to the scattered photon and/or to the electron energy spectrum. From an experimental
 9223 point of view, both measurements can be complementary since the high energy region of the scattered
 9224 photon energy spectrum is sensitive to the electron/positron beam longitudinal polarisation, whereas it is
 9225 the opposite for the scattered electron/positron energy spectrum. Indeed, the high measurement precision of
 9226 SLC was achieved thanks to the measurement of the scattered electrons. The measurement of both scattered
 9227 photon and electron/positron spectra was therefore foreseen for a very high precision polarimetry at future
 9228 electron-positron high energy colliders [?,?].

9229 For LHeC, we may follow the work done for the future linear colliders [?]. In order to reach the per
 9230 mille level on the longitudinal polarisation measurement, one may measure both the scattered photon and
 9231 electron energy spectrum.

14.2.1 Polarisation from the scattered photons

9232 The photons are scattered within a very narrow cone of half aperture $\approx 1/\gamma$. It is therefore impossible
 9233 to distinguish the photons reaching the calorimeter. As for the extraction of the longitudinal polarisation
 9234 from the scattered photon beam energy, one may then distinguish three dynamical regimes [?]. The single
 9235 and few scattered photons regimes, where one can extract the polarisation from a first principle fit to the
 9236 scattered photon energy spectrum; the multi-photon regime where the central limit theorem holds for the
 9237 energy spectra and where the longitudinal polarisation is extracted from an asymmetry between the average
 9238 scattered energies corresponding to a circularly left and right laser beam polarisation [?]. Both regimes
 9239 have positive and negative experimental features. In the single and few photon regimes the energy spectra
 9240 exhibits kinematical edges which allow an in situ calibration of the detector energy response but the physical
 9241 accelerator photon background which is difficult to model precisely, e.g. synchrotron radiation, limits the
 9242 final precision on the polarisation measurement [?]. In the multi-photon regime, the background is negligible
 9243 since it is located at low energy but one cannot measure the energy calibration of the detector in situ and one
 9244 must rely on some high energy extrapolation of calibrations obtained at low energy [?] (e.g. for 100 scattered
 9245 photon/bunch the deposited energy in the calorimeter would be more than 1TeV at LHeC). However, the
 9246 laser technology has improved in the last ten years and one can consider at present a very stable pulsed
 9247 laser beam with adjustable pulse energy allowing to operate in single, few and multi photon regimes. In this
 9248 way, one can calibrate the calorimeter in situ and optimise the dynamical regime, a multi-photon regime as
 9249 close as possible to the few photon regime, in order to minimise the final uncertainty on the polarisation
 9250 measurement.
 9251

14.2.2 Polarisation from the scattered electrons

The nice feature of the scattered electron/positron is that one can use a magnetic spectrometer to distinguish them from each other. Following [?] one may carefully design a Compton interaction region in order to implement a dedicated electron spectrometer followed by a segmented electron detector in order to measure the scattered electron angular spectrum, itself related to the electron energy spectrum. A precise particle tracking is needed but this experimental method also allows a precise control of the systematic uncertainties [?].

Common to both techniques is the control and measurement of the laser beam polarisation. It was shown in [?] that a few per mille precision can be achieved in an accelerator environment. Therefore, with a redundancy in measuring the electron/positron beam longitudinal polarisation from both the electron and photon scattered energy spectra, a final precision at the per mille level will be reachable at LHeC.

14.3 Zero Degree Calorimeter

The goal of Zero Degree Calorimeter (ZDC) is to measure the energy and angles of very forward particles. At HERA experiments, H1 and ZEUS, the forward neutral particles scattered at polar angles below 0.75 mrad have been measured in the dedicated Forward Neutron Calorimeters (FNC) [?, ?]. The LHC experiments, CMS, ATLAS, ALICE and LHCf, have the ZDC calorimeters for detection of forward neutral particles, ALICE has also the ZDC calorimeter for the measurements of spectator protons [?, ?, ?, ?, ?].

The ZDC calorimeter will be an important addition to the future LHeC experiment as many physics measurements in ep , ed and eA collisions can be made possible with the installation of ZDC.

14.3.1 ZDC detector design

The position of the Zero Degree Calorimeter in the tunnel and the overall dimensions depend mainly on the space available for the installation. At the LHC the beams are deflected by two separating dipoles. These dipoles also deflect the spectator protons, separating them from the neutrons and photons, which scatter at $\sim 0^\circ$.

The ZDC detector will be made of two calorimeters: one for the measurement of neutral particles at 0° and another one positioned externally to the outgoing proton beam for the measurement of spectator protons from eD and eA scattering. The geometry, technical specifications and proposed design of ZDC detectors are to large extent similar to the ZDCs of the LHC experiments. There the ZDC calorimeter for detection of neutral particles are placed at $z = 115 - 140$ m in a 90 mm narrow space between two beam pipes. (The photo of neutron calorimeter of ALICE experiment [?, ?] is shown in Figure ??). In the case of the LHeC, the ZDC calorimeter can be placed in the space available at about 90 – 100 m next to the interacting proton beam pipe, as indicated in Figure ??.

Below the general considerations for the design are presented. In order to finalise the study of the geometry of detectors, a detailed simulation of the LHeC interaction region and the beamline must be performed.

14.3.2 Neutron Calorimeter

The design of ZDC has to satisfy various technical issues. Detector has to be capable of detecting neutrons and photons produced with scattering angles up to 0.3 mrad or more and energies between some hundreds GeV to the proton beam energy (7 TeV) with a reasonable resolution of few percents. It should be able to distinguish hadronic and electromagnetic showers (i.e. separate neutrons from photons) and to separate showers from two or more particle entering the detector (i.e. needs position resolution of $\mathcal{O}(1\text{mm})$ or better).

The condition, that at least 95% of hadronic shower of $\mathcal{O}(\text{TeV})$ is contained within the calorimeter, requires 9.5–10 nuclear interaction lengths of absorber. The neutron ZDC will be made of two sections. The front part of calorimeter (electromagnetic section) with $1.5\text{--}2 \lambda$ length and fine granularity is needed for precise determination of the position of impact point, discrimination of electromagnetic and hadronic showers

9297 and separation of showers from two or more particles entering the detector. The hadronic section of the ZDC
 9298 can be built with coarser sampling, which gives an increase of average density and, consequently, the increase
 9299 of effective nuclear interaction length. The ZDC will be operating in a very hard radiation environment,
 9300 therefore it has to be made of radiation resistant materials. Since the different parts of calorimeter undergo
 9301 different intensity of radiation (higher for front part), it is advantageous to have longitudinal segmentation
 9302 of 4-5 identical sections, which will allow to control the change of energy response due to radiation damage.
 9303 Comparison of the energy spectrum from the showers which start in different sections can be used for
 9304 correction of changes in energy response.

9305 A possible solution to build a compact device with good radiation resistance is to use spaghetti calorimeter
 9306 with tungsten absorbers and quartz fibres. The principle of operation is based on the detection of Cherenkov
 9307 light produced by the shower's charged particles in the fibres. These detectors are proven to be fast (\sim few ns),
 9308 radiation hard and have good energy resolution. Using tungsten as a passive material allows the construction
 9309 of compact devices. One can also consider option to use thick gaseous electron multipliers (THGEM) [?, ?]
 9310 as active media.

9311 14.3.3 Proton Calorimeter

9312 In analogy to ALICE experiment, the second ZDC for detection of spectator protons can be positioned at
 9313 about a same distance from IP as neutron ZDC [?, ?]. The size of proton ZDC has to be small, due to the
 9314 few cm small size of spectator proton spot, but sufficient to obtain shower containment. This calorimeter
 9315 will be made with same technique as the neutron ZDC.

9316 14.3.4 Calibration and monitoring

9317 After initial calibration of the ZDCs with test-beams, it is essential to have regular online and offline control
 9318 of the stability of the response, in particular due to hard radiation and temperature environment. The
 9319 stability of the gain of the PMTs and the radiation damage in fibres can be monitored using the laser or
 9320 LED light pulses. The stability of absolute calibration can be monitored using the interactions of the proton
 9321 beam and residual gas molecules in the beam-pipe and comparison with the results of Monte Carlo simulation
 9322 based on pion exchange, as used at HERA [?, ?]. A useful tool for absolute energy calibration will be the
 9323 reconstruction of invariant masses, e.g. $\pi^0 \rightarrow 2\gamma$ or $\Lambda, \Delta \rightarrow n\pi^0$, with decay particles produced at very small
 9324 opening angles and reconstructed in ZDC. This will however require the possibility to reconstruct several
 9325 particles in the ZDC within one event.

9326 14.4 Forward Proton Detection

9327 In diffractive interactions between protons or between an electron and a proton, the proton may survive a
 9328 hard collision and be scattered at a low angle θ along the beam line while losing a small fraction ξ (\sim 1%)
 9329 of its energy. The ATLAS and CMS collaborations have investigated the feasibility to install detectors along
 9330 the LHC beam line to measure the energy and momentum of such diffractively scattered protons [?]. Since
 9331 the proton beam optics is primarily determined by the shape of the accelerator - which will not change for
 9332 proton arm of the LHeC - the conclusions reached in this R&D study are still relevant for an LHeC detector.

In such a setup, diffractively scattered protons are separated from the nominal beam when traveling
 through dipole magnets with a slightly lower momentum. This spectroscopic behavior of the accelerator is
 described by the energy dispersion function, D_x , which, when multiplied with the actual energy loss, ξ , gives
 the additional offset of the trajectory followed by the off-momentum proton:

$$x_{\text{offset}} = D_x \times \xi.$$

9333 The acceptance window in ξ is therefore determined by the closest possible approach of the proton
 9334 detectors to the beam for low ξ and by the distance of the beam pipe walls from the nominal proton
 9335 trajectory for high ξ . The closest possible approach is often taken to be equal to 12σ with σ equal to the

9336 beam width at a specific point. At the point of interest, 420m from the interaction point, the beam width
9337 is approximately equal to $250 \mu\text{m}$. On the other hand, the typical LHC beam pipe radius at large distances
9338 from the interaction point is approximately 2 cm. Even protons that have lost no energy, will eventually
9339 hit the beam pipe wall if they are scattered at large angles. This therefore fixes the maximally allowed
9340 four-momentum-transfer squared t , which is approximately equal to the square of the transverse momentum
9341 p_T of the scattered proton at the interaction point.

9342 At 420 m from the interaction point, the dispersion function at the LHC reaches 1.5 m, which results in an
9343 optimal acceptance window for diffractively scattered protons (roughly $0.002 < \xi < 0.013$). The acceptance
9344 as function of ξ and t is shown in Fig. ??, using the LHC proton beam optics [?]. The small corrections
9345 to be applied for the LHeC proton beam optics are not considered to be relevant for the description of the
9346 acceptance.

9347 When the proton's position and angle w.r.t. the nominal beam can be accurately measured by the
9348 detectors, it is in principle possible to reconstruct the initial scattering angles and momentum loss of the
9349 proton at the interaction point. Even with an infinitesimally small detector resolution, the intrinsic beam
9350 width and divergence will still imply a lower limit on the resolution of the reconstructed kinematics. As the
9351 beam is typically maximally focussed at the interaction point in order to obtain a good luminosity, it will
9352 be the beam divergence that dominates the resolution on reconstructed variables.

9353 Figure ?? show the relation of position and angle w.r.t. the nominal beam and the proton scattering
9354 angle and momentum loss in both the horizontal and vertical plane as obtained from the LHC proton beam
9355 optics [?]. Clearly, in order to distinguish angles and momentum losses indicated by the curves in Fig. ??,
9356 the detector must have a resolution better than the distance between the curves.

9357 As stated above, protons with the same momentum loss and scattering angles will still end up at different
9358 positions and angles due to the intrinsic width and divergence of the beam. Lower limits on the resolution
9359 of reconstructed kinematics can therefore be determined. These are typically of the order of 0.5‰ for ξ and
9360 $0.2 \mu\text{rad}$ for the scattering angle θ . Figure ?? show the main dependences of the resolution on ξ , t and the
9361 azimuthal scattering angle ϕ .

9362 A crucial issue in the operation of near-beam detectors is the alignment of the detectors w.r.t. the nominal
9363 beam. Typically, such detectors are retracted when beams are injected and moved close to the beam only
9364 when the accelerator conditions are declared to be stable. Also the beam itself, may not always be reinjected
9365 at the same position. It is therefore important to realign the detectors at for each accelerator run and to
9366 monitor any drifts during the run. At HERA, a kinematic peak method section was used for alignment:
9367 as the reconstructed scattering angles depend on the misalignment, one may extract alignment constants
9368 by requiring that the observed cross section is maximal for forward scattering. In addition, this alignment
9369 procedure may be cross-checked by using a physics process with an exclusive system produced in the central
9370 detector such that the proton kinematics is fixed by applying energy-momentum conservation to the full set
9371 of final state particles. The feasibility of various alignment methods at the LHeC remains to be studied.

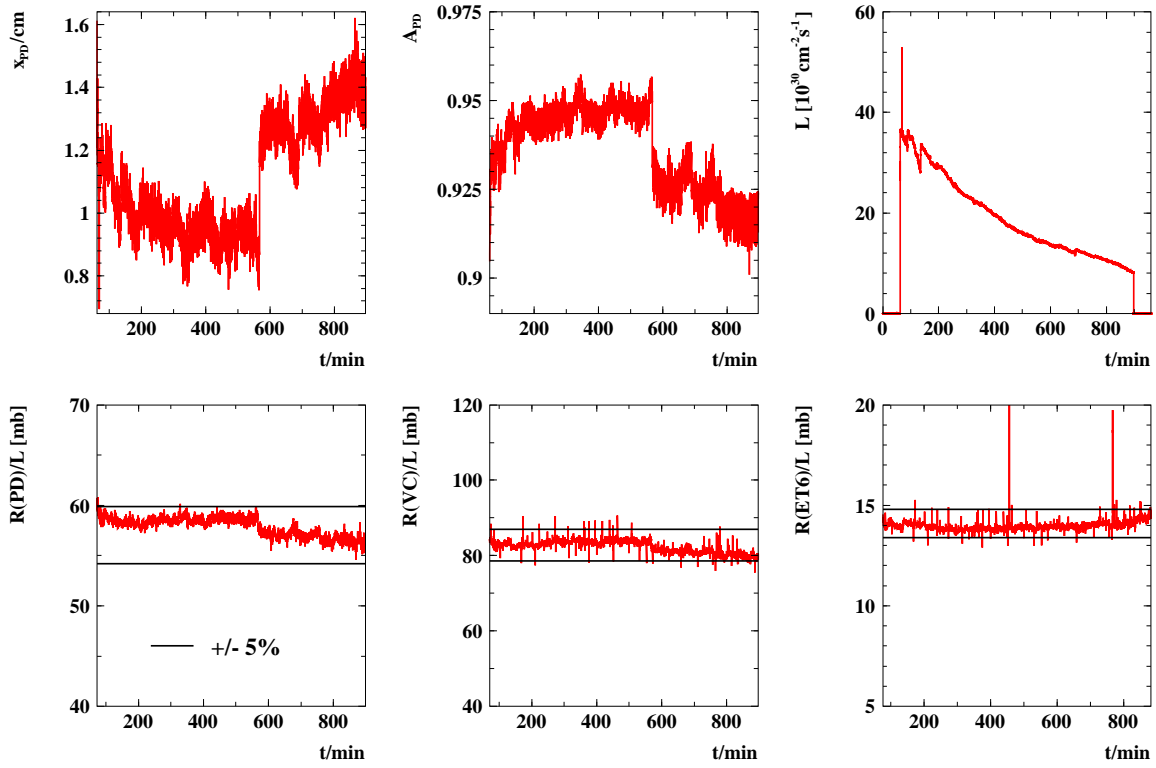


Figure 14.3: Online H1 Lumi System acceptance and rates variations in a typical HERA luminosity fill.

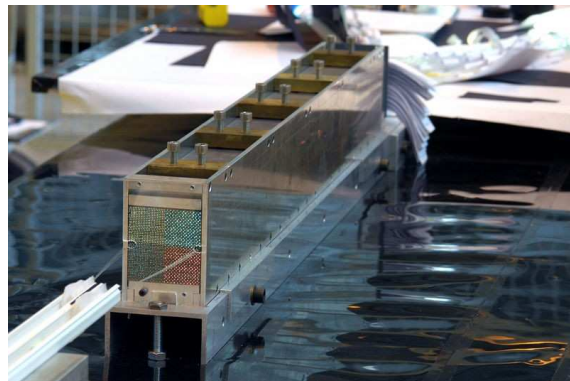


Figure 14.4: Photo of the Zero Degree Neutron Calorimeter (ZN) of ALICE experiment.

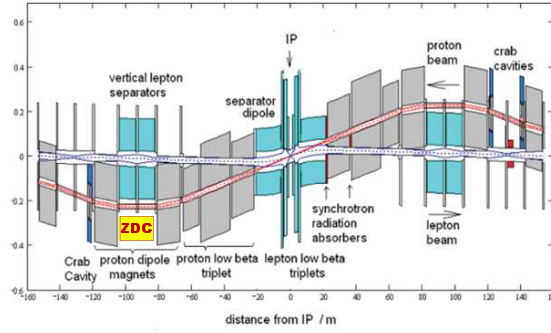


Figure 14.5: Schematic layout of the LHeC interaction region. The possible position of the ZDC is indicated.

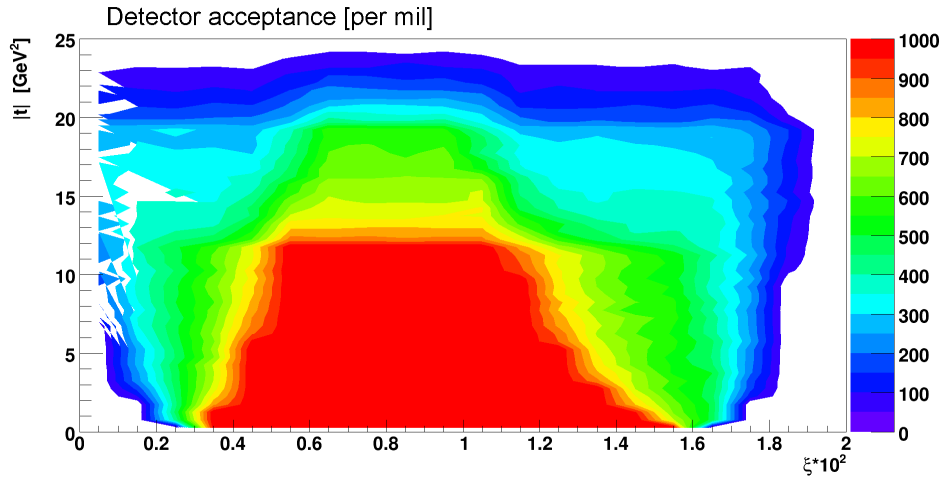


Figure 14.6: The acceptance for a proton detector placed at 420m from the interaction point is shown as function of the momentum loss ξ and the fourmomentum-transfer squared t . The color legend runs from 0% (no acceptance) to 1000% (full acceptance).

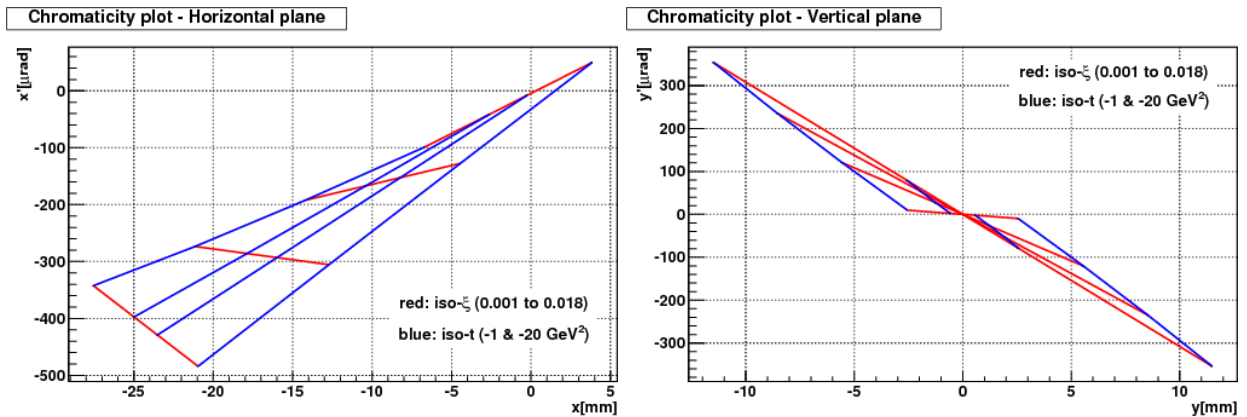


Figure 14.7: Lines of constant ξ and $t \approx (1 - \xi)E_{\text{beam}}\theta^2$ are shown in the plane of proton position and angle w.r.t. the nominal proton beam in the horizontal (left) and vertical (right) plane.

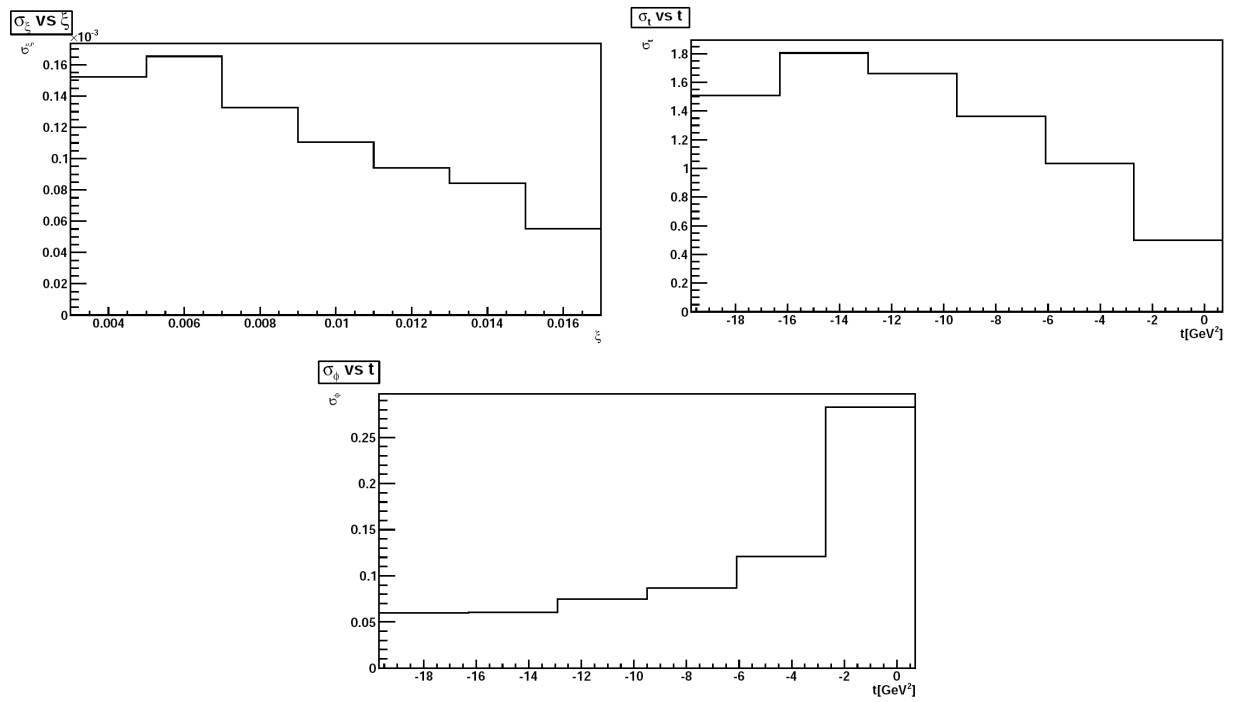


Figure 14.8: The lower limit due to the intrinsic beam width and divergence on the resolution of kinematic variables is shown for ξ as function ξ (top left), t as function t (top right) and ϕ as function of t (bottom).

Part V

9372

Summary

9373

⁹³⁷⁴ Acknowledgement

⁹³⁷⁵ Many thanks to many – still to be written

Bibliography

9376

- 9377 [1] G. Altarelli, B. Mele, and R. Ruckl, *PHYSICS OF $e p$ COLLISIONS IN THE TeV ENERGY RANGE*, . Presented at
9378 ECFA-CERN Workshop on Feasibility of Hadron Colliders in LEP Tunnel, Lausanne and Geneva, Switzerland, Mar
9379 26-27, 1984.
- 9380 [2] A. Febel, H. Gerke, M. Tigner, H. Wiedemann, and B. Wiik, *The proposed desy proton-electron colliding beam*
9381 *experiment. (talk)*, IEEE Trans.Nucl.Sci. **20** (1973) 782–785.
- 9382 [3] CHEEP Study Groups Collaboration, J. R. Ellis, B. Wiik, and K. Hubner, *CHEEP: AN $e-p$ FACILITY IN THE SPS*, .
- 9383 [4] M. A. e. a. SLAC-LBL Study Group, *Particle Physics with electron-positron-proton beams*, SLAC-146.
- 9384 [5] J. e. a. T. Kamae, *Tristan ep Working Group Report*, UTPN-165, University of Tokyo.
- 9385 [6] E. Blackmore, R. Carnegie, S. Conetti, M. Dixit, K. Edwards, et al., *Electron - proton collisions at Fermilab*, .
9386 Spokesperson: W.R. Frisken.
- 9387 [7] A. Verdier, *An $e p$ insertion for LHC and LEP*, 1990.
- 9388 [8] W. Bartel, *$e p$ experiments in LEP/LHC interaction regions*, 1990.
- 9389 [9] R. Ruckl, *$e p$ physics at LEP x LHC*, Proc. Aachen LHC Workshop, CERN-90-10-B, MPI-PAE-PTH-76-90.
- 9390 [10] E.Keil, *LHC ep Option*, LHC Report **93**, CERN 1996.
- 9391 [11] M. Tigner, B. Wiik, and F. Willeke, *An Electron - proton collider in the TeV range*, .
- 9392 [12] L. A. K. M. Katz, U. and e. Schlenstedt, S., *Physics and experimentation at a linear electron positron collider. Vol. 4:*
9393 *The THERA book. Electron proton scattering at $s^{**}(1/2)$ approx. 1-TeV, 445p.*, .
- 9394 [13] D. Schulte and F. Zimmermann, *QCD explorer based on LHC and CLIC-1*, . Prepared for 9th European Particle
9395 Accelerator Conference (EPAC 2004), Lucerne, Switzerland, 5-9 Jul 2004.
- 9396 [14] J. B. Dainton, M. Klein, P. Newman, E. Perez, and F. Willeke, *Deep inelastic electron nucleon scattering at the LHC*,
9397 JINST **1** (2006) P10001, arXiv:hep-ex/0603016.
- 9398 [15] M. Klein, *Physics at HERA and beyond*, AIP Conf.Proc. **792** (2005) 1065–1076.
- 9399 [16] M. Breidenbach, J. I. Friedman, H. W. Kendall, E. D. Bloom, D. Coward, et al., *Observed Behavior of Highly Inelastic*
9400 *electron-Proton Scattering*, Phys.Rev.Lett. **23** (1969) 935–939.
- 9401 [17] E. D. Bloom, D. Coward, H. DeStaabler, J. Drees, G. Miller, et al., *High-Energy Inelastic $e p$ Scattering at 6-Degrees*
9402 *and 10-Degrees*, Phys.Rev.Lett. **23** (1969) 930–934.
- 9403 [18] M. f. t. L. S. G. Klein, *Status of the LHeC Design*, CERN, Geneva and SLAC, Stanford.
- 9404 [19] S. Myers, *Invited Talk at ICHEP, Paris*, 2010.
- 9405 [20] F. Wilczek, *Talk at the 50 Years of the PS Nobel Prize Winner Colloquium, CERN*, 2009.
- 9406 [21] H. Geiger and E. Marsden, *On a Diffuse Reflection of the α Particles*, Proc. Royal Society **A82** (1909) 495–500.
- 9407 [22] E. Rutherford, *The scattering of the α and β Particles by Matter and the Strcuture of the Atom*, Philosophical
9408 Magazine, Series 6 **21** (1911) 669–688.
- 9409 [23] R. Hofstadter and R. McAllister, *ELECTRON SCATTERING FROM THE PROTON*, Phys.Rev. **98** (1955) 217–218.
- 9410 [24] D. J. Gross and F. Wilczek, *ULTRAVIOLET BEHAVIOR OF NON-ABELIAN GAUGE THEORIES*, Phys. Rev. Lett.
9411 **30** (1973) 1343–1346.
- 9412 [25] H. D. Politzer, *RELIABLE PERTURBATIVE RESULTS FOR STRONG INTERACTIONS?*, Phys. Rev. Lett. **30**
9413 (1973) 1346–1349.
- 9414 [26] R. Feynman, *Photon-hadron interactions*, . 1973.
- 9415 [27] H. Fritzsch, M. Gell-Mann, and H. Leutwyler, *Advantages of the Color Octet Gluon Picture*, Phys.Lett. **B47** (1973)
9416 365–368.

- 9417 [28] H1 and ZEUS Collaboration, F. Aaron et al., *Combined Measurement and QCD Analysis of the Inclusive e^+p*
9418 *Scattering Cross Sections at HERA*, JHEP **1001** (2010) 109, [arXiv:0911.0884](https://arxiv.org/abs/0911.0884) [[hep-ex](#)].
- 9419 [29] A. De Rujula, *Charm is found*, . Proceedings of XVIII ICHEP Conference, Tbilissi, 1976.
- 9420 [30] A. Salam, *The Unconfined Quarks and Gluons*, . Proceedings of XVIII ICHEP Conference, Tbilissi, 1976.
- 9421 [31] J. L. Hewett and T. G. Rizzo, *Low-Energy Phenomenology of Superstring Inspired $E(6)$ Models*, Phys. Rept. **183**
9422 (1989) 193.
- 9423 [32] J. C. Pati and A. Salam, *Lepton Number as the Fourth Color*, Phys. Rev. **D10** (1974) 275–289.
- 9424 [33] B. Andersson, G. Gustafson, G. Ingelman, and T. Sjostrand, *Parton Fragmentation and String Dynamics*, Phys. Rept.
9425 **97** (1983) 31–145.
- 9426 [34] J. Kuti and V. F. Weisskopf, *Inelastic lepton - nucleon scattering and lepton pair production in the relativistic quark*
9427 *parton model*, Phys.Rev. **D4** (1971) 3418–3439.
- 9428 [35] S. Brodsky, P. Hoyer, C. Peterson, and N. Sakai, *The Intrinsic Charm of the Proton*, Phys.Lett. **B93** (1980) 451–455.
- 9429 [36] D. Mueller, D. Robaschik, B. Geyer, F. M. Dittes, and J. Horejsi, *Wave functions, evolution equations and evolution*
9430 *kernels from light-ray operators of QCD*, Fortschr. Phys. **42** (1994) 101, [arXiv:hep-ph/9812448](https://arxiv.org/abs/hep-ph/9812448).
- 9431 [37] A. V. Belitsky and A. V. Radyushkin, *Unraveling hadron structure with generalized parton distributions*, Phys. Rept.
9432 **418** (2005) 1–387, [arXiv:hep-ph/0504030](https://arxiv.org/abs/hep-ph/0504030).
- 9433 [38] V. N. Gribov, *Interaction of gamma quanta and electrons with nuclei at high-energies*, Sov. Phys. JETP **30** (1970)
9434 709–717.
- 9435 [39] M. Klein and T. Riemann, *ELECTROWEAK INTERACTIONS PROBING THE NUCLEON STRUCTURE*, Z.Phys.
9436 **C24** (1984) 151.
- 9437 [40] E. Derman, *Tests for a weak neutral current in lN to $l^+ anything$ at high energy*, Phys.Rev. **D7** (1973) 2755–2775.
- 9438 [41] J. Callan, Curtis G. and D. J. Gross, *High-energy electroproduction and the constitution of the electric current*,
9439 Phys.Rev.Lett. **22** (1969) 156–159.
- 9440 [42] G. Altarelli and G. Martinelli, *Transverse Momentum of Jets in Electroproduction from Quantum Chromodynamics*,
9441 Phys.Lett. **B76** (1978) 89.
- 9442 [43] A. Argento, A. Benvenuti, D. Bollini, G. Bruni, T. Camporesi, et al., *MEASUREMENT OF THE INTERFERENCE*
9443 *STRUCTURE FUNCTION $xG(3)(x)$ IN MUON - NUCLEON SCATTERING*, Phys.Lett. **B140** (1984) 142.
- 9444 [44] A. Arbuzov, D. Y. Bardin, J. Blumlein, L. Kalinovskaya, and T. Riemann, *Hector 1.00: A Program for the calculation*
9445 *of QED, QCD and electroweak corrections to $e p$ and lepton $^+ - N$ deep inelastic neutral and charged current scattering*,
9446 Comput.Phys.Commun. **94** (1996) 128–184, [arXiv:hep-ph/9511434](https://arxiv.org/abs/hep-ph/9511434) [[hep-ph](#)].
- 9447 [45] Particle Data Group Collaboration, K. Nakamura, *Review of particle physics*, J. Phys. **G37** (2010) 075021.
- 9448 [46] J. Blumlein and M. Klein, *On the cross calibration of calorimeters at $e p$ colliders*, Nucl. Instrum. Meth. **A329** (1993)
9449 112–116.
- 9450 [47] M. Klein, *Scenarios and Measurements with the LHeC*, Talk given at the LHeC Meeting at DIS 2009, Madrid, Spain,
9451 April 2009.
- 9452 [48] ZEUS Collaboration, S. Chekanov et al., *Measurement of the Longitudinal Proton Structure Function at HERA*,
9453 Phys.Lett. **B682** (2009) 8–22, [arXiv:0904.1092](https://arxiv.org/abs/0904.1092) [[hep-ex](#)].
- 9454 [49] F. Aaron, C. Alexa, V. Andreev, S. Backovic, A. Baghdasaryan, et al., *Measurement of the Inclusive $e^{\pm}p$ Scattering*
9455 *Cross Section at High Inelasticity y and of the Structure Function FL* , Eur.Phys.J. **C71** (2011) 1579, [arXiv:1012.4355](https://arxiv.org/abs/1012.4355)
9456 [[hep-ex](#)].
- 9457 [50] M. Botje, *QCDNUM manual*. <http://www.nikhef.nl/~h24/qcdnum/>. <http://www.nikhef.nl/~h24/qcdnum/>.
- 9458 [51] E. Rizvi and T. Sloan, *$x F^{**}(\gamma Z)(3)$ in charged lepton scattering*, Eur.Phys.J.direct **C3** (2001) N2,
9459 [arXiv:hep-ex/0101007](https://arxiv.org/abs/hep-ex/0101007) [[hep-ex](#)].
- 9460 [52] HERMES Collaboration, A. Airapetian et al., *Measurement of Parton Distributions of Strange Quarks in the Nucleon*
9461 *from Charged-Kaon Production in Deep-Inelastic Scattering on the Deuteron*, Phys. Lett. **B666** (2008) 446–450,
9462 [arXiv:0803.2993](https://arxiv.org/abs/0803.2993) [[hep-ex](#)].
- 9463 [53] U. Baur and J. van der Bij, *TOP QUARK PRODUCTION AT HERA*, Nucl.Phys. **B304** (1988) 451.
- 9464 [54] H. Fritzsch and D. Holtmannspotter, *The Production of single t quarks at LEP and HERA*, Phys. Lett. **B457** (1999)
9465 186–192, [arXiv:hep-ph/9901411](https://arxiv.org/abs/hep-ph/9901411).
- 9466 [55] C. Pascaud, *CFNS*, Talk given at DIS 2011, Newport News, USA, April 2011.
- 9467 [56] G. Brandt, *Single top production of diquarks at LHeC*, Talk given at the 1st CERN-ECFA Workshop on the LHeC,
9468 Divonne-les-Bains, France, 1-3 September 2008.
- 9469 [57] CMS Collaboration, S. Chatrchyan et al., *Measurement of the t -channel single top quark production cross section in pp*
9470 *collisions at $\sqrt{s} = 7$ TeV*, [arXiv:1106.3052](https://arxiv.org/abs/1106.3052) [[hep-ex](#)]. * Temporary entry *.

- 9471 [58] A. Glazov, S. Moch, and V. Radescu, *Parton Distribution Uncertainties using Smoothness Prior*, Phys.Lett. **B695**
9472 (2011) 238–241, [arXiv:1009.6170 \[hep-ph\]](#).
- 9473 [59] S. Alekhin, J. Blumlein, P. Jimenez-Delgado, S. Moch, and E. Reya, *NNLO Benchmarks for Gauge and Higgs Boson*
9474 *Production at TeV Hadron Colliders*, Phys. Lett. **B697** (2011) 127–135, [arXiv:1011.6259 \[hep-ph\]](#).
- 9475 [60] S. Moch, J. Vermaseren, and A. Vogt, *The Three loop splitting functions in QCD: The Nonsinglet case*, Nucl.Phys.
9476 **B688** (2004) 101–134, [arXiv:hep-ph/0403192 \[hep-ph\]](#).
- 9477 [61] J. A. M. Vermaseren, A. Vogt, and S. Moch, *The third-order QCD corrections to deep-inelastic scattering by photon*
9478 *exchange*, Nucl. Phys. **B724** (2005) 3–182, [arXiv:hep-ph/0504242](#).
- 9479 [62] I. Bierenbaum, J. Blumlein, and S. Klein, *Mellin Moments of the $O(\alpha^{*3}(s))$ Heavy Flavor Contributions to*
9480 *unpolarized Deep-Inelastic Scattering at $Q^{*2} \gg m^{*2}$ and Anomalous Dimensions*, Nucl.Phys. **B820** (2009) 417–482,
9481 [arXiv:0904.3563 \[hep-ph\]](#).
- 9482 [63] J. Blumlein, H. Bottcher, and A. Guffanti, *Non-singlet QCD analysis of deep inelastic world data at $O(\alpha(s)^{*3})$* ,
9483 Nucl.Phys. **B774** (2007) 182–207, [arXiv:hep-ph/0607200 \[hep-ph\]](#).
- 9484 [64] M. Gluck, E. Reya, and C. Schuck, *Non-singlet QCD analysis of $F(2)(x, Q^{*2})$ up to NNLO*, Nucl.Phys. **B754** (2006)
9485 178–186, [arXiv:hep-ph/0604116 \[hep-ph\]](#).
- 9486 [65] S. Alekhin, J. Blumlein, S. Klein, and S. Moch, *The 3, 4, and 5-flavor NNLO Parton from Deep-Inelastic-Scattering*
9487 *Data and at Hadron Colliders*, Phys.Rev. **D81** (2010) 014032, [arXiv:0908.2766 \[hep-ph\]](#).
- 9488 [66] P. Jimenez-Delgado and E. Reya, *Dynamical NNLO parton distributions*, Phys. Rev. **D79** (2009) 074023,
9489 [arXiv:0810.4274 \[hep-ph\]](#).
- 9490 [67] A. D. Martin, W. J. Stirling, R. S. Thorne, and G. Watt, *Uncertainties on alphas in global PDF analyses and*
9491 *implications for predicted hadronic cross sections*, Eur. Phys. J. **C64** (2009) 653–680, [arXiv:0905.3531 \[hep-ph\]](#).
- 9492 [68] S. Alekhin, J. Blumlein, and S.-O. Moch, *Update of the NNLO PDFs in the 3-, 4-, and 5-flavour scheme*, PoS
9493 **DIS2010** (2010) 021, [arXiv:1007.3657 \[hep-ph\]](#).
- 9494 [69] S. Bethke, *The 2009 World Average of $\alpha(s)$* , Eur.Phys.J. **C64** (2009) 689–703, [arXiv:0908.1135 \[hep-ph\]](#).
- 9495 [70] J. Blumlein, S. Riemersma, W. van Neerven, and A. Vogt, *Theoretical uncertainties in the QCD evolution of structure*
9496 *functions and their impact on α -s ($M(Z)^{*2}$)*, Nucl.Phys.Proc.Suppl. **51C** (1996) 97–105, [arXiv:hep-ph/9609217](#)
9497 [\[hep-ph\]](#).
- 9498 [71] S. J. Brodsky, *Novel QCD Phenomenology at the LHeC*, [arXiv:1106.5820 \[hep-ph\]](#). LHeC-Note-2011-002 PHY and
9499 SLAC-PUB-14487.
- 9500 [72] M. Buza, Y. Matiounine, J. Smith, and W. van Neerven, *Charm electroproduction viewed in the variable flavor number*
9501 *scheme versus fixed order perturbation theory*, Eur.Phys.J. **C1** (1998) 301–320, [arXiv:hep-ph/9612398 \[hep-ph\]](#).
- 9502 [73] S. Alekhin and S. Moch, *Heavy-quark deep-inelastic scattering with a running mass*, Phys. Lett. **B699** (2011) 345–353,
9503 [arXiv:1011.5790 \[hep-ph\]](#).
- 9504 [74] T. Gehrmann, M. Jaquier, and G. Luisoni, *Hadronization effects in event shape moments*, Eur.Phys.J. **C67** (2010)
9505 57–72, [arXiv:0911.2422 \[hep-ph\]](#).
- 9506 [75] R. Abbate, M. Fickinger, A. H. Hoang, V. Mateu, and I. W. Stewart, *Thrust at N3LL with Power Corrections and a*
9507 *Precision Global Fit for α s(m_Z)*, Phys.Rev. **D83** (2011) 074021, [arXiv:1006.3080 \[hep-ph\]](#).
- 9508 [76] M. Virchaux and A. Milsztajn, *A Measurement of α -s and higher twists from a QCD analysis of high statistics F-2*
9509 *data on hydrogen and deuterium targets*, Phys.Lett. **B274** (1992) 221–229.
- 9510 [77] H1 Collaboration, C. Adloff et al., *Deep-inelastic inclusive e p scattering at low x and a determination of α (s)*, Eur.
9511 Phys. J. **C21** (2001) 33–61, [arXiv:hep-ex/0012053](#).
- 9512 [78] R. Wallny, *A Measurement of the Gluon Distribution in the Proton and of the Strong Coupling Constant α s from*
9513 *Inclusive Deep-Inelastic Scattering*, H1 PhD Thesis 2001, Zurich, Switzerland, 2001.
- 9514 [79] A. Martin, W. Stirling, R. Thorne, and G. Watt, *alphas in MSTW Analyses*, Talk given in [?], February 2011.
- 9515 [80] S. Lionetti, R. D. Ball, V. Bertone, F. Cerutti, L. Del Debbio, et al., *Precision determination of α_s using an unbiased*
9516 *global NLO parton set*, [arXiv:1103.2369 \[hep-ph\]](#).
- 9517 [81] S. Bethke et al., *Workshop on Precision Measurements on alphas*, MPI Munich, Germany, February, 2011.
- 9518 [82] T. Kluge, *Prospects of α s Determinations in DIS*, Talks given at the CERN-ECFA-NuPECC Workshops on the
9519 LHeC, Divonne-les-Bains, France, September 2008/09.
- 9520 [83] BCDMS Collaboration, A. Benvenuti et al., *A COMPARISON OF THE STRUCTURE FUNCTIONS F2 OF THE*
9521 *PROTON AND THE NEUTRON FROM DEEP INELASTIC MUON SCATTERING AT HIGH Q^{*2}* , Phys.Lett.
9522 **B237** (1990) 599.
- 9523 [84] BCDMS Collaboration, A. C. Benvenuti et al., *A HIGH STATISTICS MEASUREMENT OF THE DEUTERON*
9524 *STRUCTURE FUNCTIONS F2 (x, Q^{*2}) AND R FROM DEEP INELASTIC MUON SCATTERING AT HIGH*
9525 *Q^{*2}* , Phys. Lett. **B237** (1990) 592.

- 9526 [85] European Muon Collaboration, J. Aubert et al., *Measurements of the nucleon structure functions F_2^n in deep inelastic muon scattering from deuterium and comparison with those from hydrogen and iron*, Nucl.Phys. **B293** (1987) 740.
- 9527
- 9528 [86] T. A. et al., *eD Scattering with H1, A Letter of Intent DESY 03-194*, .
- 9529 [87] T. A. et al., *A New experiment For HERA, MPP-2003-62*, .
- 9530 [88] T. Greenshaw and M. Klein, *The Future of lepton nucleon scattering: A Summary of the Durham Workshop, December 2001*, J.Phys.G **G28** (2002) 2503–2508, arXiv:hep-ex/0204032 [hep-ex].
- 9531
- 9532 [89] I. Schienbein, J. Yu, K. Kovarik, C. Keppel, J. Morfin, et al., *PDF Nuclear Corrections for Charged and Neutral Current Processes*, Phys.Rev. **D80** (2009) 094004, arXiv:0907.2357 [hep-ph].
- 9533
- 9534 [90] T. Hobbs, J. Londergan, D. Murdock, and A. Thomas, *Testing Partonic Charge Symmetry at a High-Energy Electron Collider*, Phys.Lett. **B698** (2011) 123–127, arXiv:1101.3923 [hep-ph].
- 9535
- 9536 [91] S. J. Brodsky and B. Chertok, *The Asymptotic Form-Factors of Hadrons and Nuclei and the Continuity of Particle and Nuclear Dynamics*, Phys.Rev. **D14** (1976) 3003–3020.
- 9537
- 9538 [92] V. A. Matveev and P. Sorba, *Is Deuteron a Six Quark System?*, Lett.Nuovo Cim. **20** (1977) 435.
- 9539 [93] S. J. Brodsky, C.-R. Ji, and G. Lepage, *Quantum Chromodynamic Predictions for the Deuteron Form-Factor*, Phys.Rev.Lett. **51** (1983) 83.
- 9540
- 9541 [94] R. Arnold, B. Chertok, E. Dally, A. Grigorian, C. Jordan, et al., *Measurement of the electron-Deuteron Elastic Scattering Cross-Section in the Range $0.8 \text{ GeV}^{*2} \leq q^2 \leq 6 \text{ GeV}^{*2}$* , Phys.Rev.Lett. **35** (1975) 776.
- 9542
- 9543 [95] G. R. Farrar, K. Huleihel, and H.-y. Zhang, *Deuteron form-factor*, Phys.Rev.Lett. **74** (1995) 650–653.
- 9544 [96] H. Flacher, M. Goebel, J. Haller, A. Hocker, K. Monig, et al., *Gfitter - Revisiting the Global Electroweak Fit of the Standard Model and Beyond*, Eur.Phys.J. **C60** (2009, see <http://gfitter.desy.de/>) 543–583, arXiv:0811.0009 [hep-ph].
- 9545
- 9546
- 9547 [97] J. Erler, *The Mass of the Higgs Boson in the Standard Electroweak Model*, Phys.Rev. **D81** (2010) 051301, arXiv:1002.1320 [hep-ph].
- 9548
- 9549 [98] P. Gambino, *The top priority: Precision electroweak physics from low to high energy*, Int. J. Mod. Phys. **A19** (2004) 808–820, arXiv:hep-ph/0311257.
- 9550
- 9551 [99] M. Davier, A. Hoecker, B. Malaescu, and Z. Zhang, *Reevaluation of the Hadronic Contributions to the Muon $g-2$ and to $\alpha(MZ)$* , Eur.Phys.J. **C71** (2011) 1515, arXiv:1010.4180 [hep-ph].
- 9552
- 9553 [100] S. Haywood, P. Hobson, W. Hollik, Z. Kunszt, G. Azaelos, et al., *Electroweak physics, hep-ph/0003275*, arXiv:hep-ph/0003275 [hep-ph].
- 9554
- 9555 [101] K. Rabbertz, *QCD and Electroweak Physics at LHC*, PoS **RADCOR2009** (2010) 016, arXiv:1002.3628 [hep-ph].
- 9556 [102] S. <http://www.jlab.org/qweak/>, , .
- 9557 [103] S. <http://hallaweb.jlab.org/12GeV/Moller/>, , .
- 9558 [104] R. Cashmore, E. Elsen, B. A. Kniehl, and H. Spiesberger, *Electroweak physics at HERA: Introduction and summary*, arXiv:hep-ph/9610251 [hep-ph].
- 9559
- 9560 [105] H1 and ZEUS Collaboration, Z. Zhang, *Electroweak and beyond the Standard Model results from HERA*, Nucl.Phys.Proc.Suppl. **191** (2009) 271–280, arXiv:0812.4662 [hep-ex].
- 9561
- 9562 [106] H1 Collaboration, A. Aktas et al., *A Determination of electroweak parameters at HERA*, Phys.Lett. **B632** (2006) 35–42, arXiv:hep-ex/0507080 [hep-ex].
- 9563
- 9564 [107] H1 Collaboration, Z.-Q. Zhang, *Combined electroweak and QCD fits including NC and CC data with polarised electron beam at HERA-2*, PoS **DIS2010** (2010) 056.
- 9565
- 9566 [108] E. Salvioni, A. Strumia, G. Villadoro, and F. Zwirner, *Non-universal minimal Z' models: present bounds and early LHC reach*, JHEP **1003** (2010) 010, arXiv:0911.1450 [hep-ph].
- 9567
- 9568 [109] J. Erler and P. Langacker, *Indications for an extra neutral gauge boson in electroweak precision data*, Phys.Rev.Lett. **84** (2000) 212–215, arXiv:hep-ph/9910315 [hep-ph].
- 9569
- 9570 [110] R. Barbier, C. Berat, M. Besancon, M. Chemtob, A. Deandrea, et al., *R-parity violating supersymmetry*, Phys.Rept. **420** (2005) 1–202, arXiv:hep-ph/0406039 [hep-ph].
- 9571
- 9572 [111] M. Carpentier and S. Davidson, *Constraints on two-lepton, two quark operators*, Eur.Phys.J. **C70** (2010, and refs. therein) 1071–1090, arXiv:1008.0280 [hep-ph].
- 9573
- 9574 [112] J. Erler, A. Kurylov, and M. J. Ramsey-Musolf, *The Weak charge of the proton and new physics*, Phys.Rev. **D68** (2003) 016006, arXiv:hep-ph/0302149 [hep-ph].
- 9575
- 9576 [113] C. Prescott, W. Atwood, R. Cottrell, H. DeStaebler, E. L. Garwin, et al., *Further Measurements of Parity Nonconservation in Inelastic electron Scattering*, Phys.Lett. **B84** (1979) 524.
- 9577
- 9578 [114] E. A. Paschos and L. Wolfenstein, *Tests for neutral currents in neutrino reactions*, Phys. Rev. **D7** (1973) 91–95.

- 9579 [115] J. Blumlein, M. Klein, and T. Riemann, *TESTING THE ELECTROWEAK STANDARD MODEL AT HERA*, .
- 9580 [116] A. Czarnecki and W. J. Marciano, *Polarized Moller scattering asymmetries*, Int.J.Mod.Phys. **A15** (2000) 2365–2376,
9581 [arXiv:hep-ph/0003049](#) [[hep-ph](#)].
- 9582 [117] B. W. Harris and J. Smith, *Charm quark and D^{*+} - cross sections in deeply inelastic scattering at HERA*, Phys. Rev.
9583 **D57** (1998) 2806–2812, [arXiv:hep-ph/9706334](#).
- 9584 [118] S. Frixione, M. L. Mangano, P. Nason, and G. Ridolfi, *Total Cross Sections for Heavy Flavour Production at HERA*,
9585 Phys. Lett. **B348** (1995) 633–645, [arXiv:hep-ph/9412348](#).
- 9586 [119] S. Frixione, P. Nason, and G. Ridolfi, *Differential distributions for heavy flavor production at HERA*, Nucl. Phys. **B454**
9587 (1995) 3–24, [arXiv:hep-ph/9506226](#).
- 9588 [120] J. Binnewies, B. A. Kniehl, and G. Kramer, *Inclusive B meson production in $e^+ e^-$ and p anti- p collisions*, Phys. Rev.
9589 **D58** (1998) 034016, [arXiv:hep-ph/9802231](#).
- 9590 [121] J. Binnewies, B. A. Kniehl, and G. Kramer, *Coherent description of D^{*+} - production in $e^+ e^-$ and low- Q^{*2} $e p$*
9591 *collisions*, Z. Phys. **C76** (1997) 677–688, [arXiv:hep-ph/9702408](#).
- 9592 [122] B. A. Kniehl, G. Kramer, and M. Spira, *Large $p(T)$ photoproduction of D^{*+} - mesons in $e p$ collisions*, Z. Phys. **C76**
9593 (1997) 689–700, [arXiv:hep-ph/9610267](#).
- 9594 [123] M. Cacciari and M. Greco, *Charm Production via Fragmentation*, Z. Phys. **C69** (1996) 459–466, [arXiv:hep-ph/9505419](#).
- 9595 [124] G. Kramer and H. Spiesberger, *Inclusive photoproduction of D^* mesons with massive charm quarks*, Eur. Phys. J. **C38**
9596 (2004) 309–318, [arXiv:hep-ph/0311062](#).
- 9597 [125] B. A. Kniehl, G. Kramer, I. Schienbein, and H. Spiesberger, *Inclusive D^{*+} - production in p anti- p collisions with*
9598 *massive charm quarks*, Phys. Rev. **D71** (2005) 014018, [arXiv:hep-ph/0410289](#).
- 9599 [126] S. Catani, M. Ciafaloni, and F. Hautmann, *GLUON CONTRIBUTIONS TO SMALL x HEAVY FLAVOR*
9600 *PRODUCTION*, Phys. Lett. **B242** (1990) 97.
- 9601 [127] S. Catani, M. Ciafaloni, and F. Hautmann, *High-energy factorization and small x heavy flavor production*, Nucl. Phys.
9602 **B366** (1991) 135–188.
- 9603 [128] A. Belyaev, J. Pumplin, W.-K. Tung, and C. P. Yuan, *Uncertainties of the inclusive Higgs production cross section at*
9604 *the Tevatron and the LHC*, JHEP **01** (2006) 069, [arXiv:hep-ph/0508222](#).
- 9605 [129] S. J. Brodsky, J. C. Collins, S. D. Ellis, J. F. Gunion, and A. H. Mueller, *INTRINSIC CHEVROLETS AT THE SSC*, .
- 9606 [130] B. Harris, J. Smith, and R. Vogt, *Reanalysis of the EMC charm production data with extrinsic and intrinsic charm at*
9607 *NLO*, Nucl.Phys. **B461** (1996) 181–196, [arXiv:hep-ph/9508403](#) [[hep-ph](#)].
- 9608 [131] M. Franz, M. V. Polyakov, and K. Goeke, *Heavy quark mass expansion and intrinsic charm in light hadrons*, Phys.Rev.
9609 **D62** (2000) 074024, [arXiv:hep-ph/0002240](#) [[hep-ph](#)].
- 9610 [132] T. Sjostrand, S. Mrenna, and P. Z. Skands, *PYTHIA 6.4 Physics Manual*, JHEP **05** (2006) 026, [arXiv:hep-ph/0603175](#).
- 9611 [133] J. Pumplin et al., *New generation of parton distributions with uncertainties from global QCD analysis*, JHEP **07** (2002)
9612 012, [arXiv:hep-ph/0201195](#).
- 9613 [134] H. Jung, *Hard diffractive scattering in high-energy $e p$ collisions and the Monte Carlo generator RAPGAP*, Comp.
9614 Phys. Commun. **86** (1995) 147–161.
- 9615 [135] CTEQ Collaboration, H. L. Lai et al., *Global QCD analysis of parton structure of the nucleon: CTEQ5 parton*
9616 *distributions*, Eur. Phys. J. **C12** (2000) 375–392, [arXiv:hep-ph/9903282](#).
- 9617 [136] G. Ingelman, A. Edin, and J. Rathsman, *LEPTO 6.5 - A Monte Carlo Generator for Deep Inelastic Lepton-Nucleon*
9618 *Scattering*, Comput. Phys. Commun. **101** (1997) 108–134, [arXiv:hep-ph/9605286](#).
- 9619 [137] H1 and Z. Collaborations, *Combination of F_2^{cc} from DIS measurements at HERA*, Preliminary measurements
9620 H1prelim-09-171,ZEUS-prel-09-015.
- 9621 [138] H1 Collaboration, F. D. Aaron et al., *Measurement of the Charm and Beauty Structure Functions using the H1 Vertex*
9622 *Detector at HERA*, Eur. Phys. J. **C65** (2010) 89–109, [arXiv:0907.2643](#) [[hep-ex](#)].
- 9623 [139] J. Pumplin, H. L. Lai, and W. K. Tung, *The charm parton content of the nucleon*, Phys. Rev. **D75** (2007) 054029,
9624 [arXiv:hep-ph/0701220](#).
- 9625 [140] D0 Collaboration, V. Abazov et al., *Measurement of $\gamma + b + X$ and $\gamma + c + X$ production cross sections in*
9626 *p anti- p collisions at $s^{*2} = 1.96$ -TeV*, Phys.Rev.Lett. **102** (2009) 192002, [arXiv:0901.0739](#) [[hep-ex](#)].
- 9627 [141] S. J. Brodsky, B. Kopeliovich, I. Schmidt, and J. Soffer, *Diffractive Higgs production from intrinsic heavy flavors in the*
9628 *proton*, Phys.Rev. **D73** (2006) 113005, [arXiv:hep-ph/0603238](#) [[hep-ph](#)].
- 9629 [142] P. Aurenche, M. Fontannaz, and J. P. Guillet, *New NLO parametrizations of the parton distributions in real photons*,
9630 Eur. Phys. J. **C44** (2005) 395–409, [arXiv:hep-ph/0503259](#).
- 9631 [143] W. K. Tung et al., *Heavy quark mass effects in deep inelastic scattering and global QCD analysis*, JHEP **02** (2007) 053,
9632 [arXiv:hep-ph/0611254](#).

- 9633 [144] T. Kneesch, B. A. Kniehl, G. Kramer, and I. Schienbein, *Charmed-Meson Fragmentation Functions with Finite-Mass*
9634 *Corrections*, Nucl. Phys. **B799** (2008) 34–59, [arXiv:0712.0481 \[hep-ph\]](#).
- 9635 [145] M. Gluck, E. Reya, and A. Vogt, *Photonic parton distributions*, Phys. Rev. **D46** (1992) 1973–1979.
- 9636 [146] M. Klasen and G. Kramer, *Inclusive two-jet production at HERA: Direct and resolved cross sections in next-to-leading*
9637 *order QCD*, Z. Phys. **C76** (1997) 67–74, [arXiv:hep-ph/9611450](#).
- 9638 [147] S. Catani and M. H. Seymour, *A general algorithm for calculating jet cross sections in NLO QCD*, Nucl. Phys. **B485**
9639 (1997) 291–419, [arXiv:hep-ph/9605323](#).
- 9640 [148] D. Stump et al., *Inclusive jet production, parton distributions, and the search for new physics*, JHEP **10** (2003) 046,
9641 [arXiv:hep-ph/0303013](#).
- 9642 [149] J. Pumplin, A. Belyaev, J. Huston, D. Stump, and W. K. Tung, *Parton distributions and the strong coupling:*
9643 *CTEQ6AB PDFs*, JHEP **02** (2006) 032, [arXiv:hep-ph/0512167](#).
- 9644 [150] T. Gehrmann and E. W. N. Glover, *Two-Loop QCD Helicity Amplitudes for (2+1)-Jet Production in Deep Inelastic*
9645 *Scattering*, Phys. Lett. **B676** (2009) 146–151, [arXiv:0904.2665 \[hep-ph\]](#).
- 9646 [151] A. Daleo, A. Gehrmann-De Ridder, T. Gehrmann, and G. Luisoni, *Antenna subtraction at NNLO with hadronic initial*
9647 *states: initial-final configurations*, JHEP **01** (2010) 118, [arXiv:0912.0374 \[hep-ph\]](#).
- 9648 [152] S. Frixione, Z. Kunszt, and A. Signer, *Three jet cross-sections to next-to-leading order*, Nucl. Phys. **B467** (1996)
9649 399–442, [arXiv:hep-ph/9512328](#).
- 9650 [153] S. Frixione, *A General approach to jet cross-sections in QCD*, Nucl. Phys. **B507** (1997) 295–314,
9651 [arXiv:hep-ph/9706545](#).
- 9652 [154] M. Gluck, E. Reya, and A. Vogt, *Parton structure of the photon beyond the leading order*, Phys. Rev. **D45** (1992)
9653 3986–3994.
- 9654 [155] K. J. Eskola, H. Paukkunen, and C. A. Salgado, *EPS09 - a New Generation of NLO and LO Nuclear Parton*
9655 *Distribution Functions*, JHEP **04** (2009) 065, [arXiv:0902.4154 \[hep-ph\]](#).
- 9656 [156] S. D. Ellis and D. E. Soper, *Successive combination jet algorithm for hadron collisions*, Phys. Rev. **D48** (1993)
9657 3160–3166, [arXiv:hep-ph/9305266](#).
- 9658 [157] H1 Collaboration, C. Adloff et al., *Measurement of inclusive jet cross-sections in photoproduction at HERA*, Eur. Phys.
9659 J. **C29** (2003) 497–513, [arXiv:hep-ex/0302034](#).
- 9660 [158] S. Frixione and G. Ridolfi, *Jet photoproduction at HERA*, Nucl. Phys. **B507** (1997) 315–333, [arXiv:hep-ph/9707345](#).
- 9661 [159] V. M. Budnev, I. F. Ginzburg, G. V. Meledin, and V. G. Serbo, *The Two photon particle production mechanism.*
9662 *Physical problems. Applications. Equivalent photon approximation*, Phys. Rept. **15** (1975) 181–281.
- 9663 [160] T. H. Bauer, R. D. Spital, D. R. Yennie, and F. M. Pipkin, *The Hadronic Properties of the Photon in High-Energy*
9664 *Interactions*, Rev. Mod. Phys. **50** (1978) 261.
- 9665 [161] J. M. Butterworth and M. Wing, *High energy photoproduction*, Rept. Prog. Phys. **68** (2005) 2773–2828,
9666 [arXiv:hep-ex/0509018](#).
- 9667 [162] L. Frankfurt, V. Guzey, M. McDermott, and M. Strikman, *Revealing the black body regime of small x DIS through final*
9668 *state signals*, Phys. Rev. Lett. **87** (2001) 192301, [arXiv:hep-ph/0104154](#).
- 9669 [163] T. C. Rogers and M. I. Strikman, *Hadronic interactions of ultra-high energy photons with protons and light nuclei in*
9670 *the dipole picture*, J. Phys. **G32** (2006) 2041–2063, [arXiv:hep-ph/0512311](#).
- 9671 [164] ZEUS Collaboration, S. Chekanov et al., *Measurement of the photon proton total cross section at a center-of-mass*
9672 *energy of 209-GeV at HERA*, Nucl. Phys. **B627** (2002) 3–28, [arXiv:hep-ex/0202034](#).
- 9673 [165] H1 Collaboration, S. Aid et al., *Measurement of the total photon-proton cross-section and its decomposition at 200-GeV*
9674 *center-of-mass energy*, Z. Phys. **C69** (1995) 27–38, [arXiv:hep-ex/9509001](#).
- 9675 [166] G. M. Vereshkov, O. D. Lalakulich, Y. F. Novoseltsev, and R. V. Novoseltseva, *Total cross section for photon nucleon*
9676 *interaction in the energy range $\sqrt{s} = 40\text{-GeV} - 250\text{-GeV}$* , Phys. Atom. Nucl. **66** (2003) 565–574.
- 9677 [167] Z. Collaboration, *Measurement of the energy dependence of the total photon-proton cross section at HERA*, Phys.Lett.
9678 **B697** (2011) 184–193, [arXiv:1011.1652 \[hep-ex\]](#). * Temporary entry *.
- 9679 [168] R. M. Godbole, A. Grau, G. Pancheri, and Y. N. Srivastava, *Total photoproduction cross-section at very high energy*,
9680 Eur. Phys. J. **C63** (2009) 69–85, [arXiv:0812.1065 \[hep-ph\]](#).
- 9681 [169] M. M. Block and F. Halzen, *Evidence for the saturation of the Froissart bound*, Phys. Rev. **D70** (2004) 091901,
9682 [arXiv:hep-ph/0405174](#).
- 9683 [170] M. M. Block and F. Halzen, *New evidence for the saturation of the Froissart bound*, Phys. Rev. **D72** (2005) 036006,
9684 [arXiv:hep-ph/0506031](#).
- 9685 [171] M. M. Block, E. M. Gregores, F. Halzen, and G. Pancheri, *Photon - proton and photon-photon scattering from nucleon-*
9686 *nucleon forward amplitudes*, Phys. Rev. **D60** (1999) 054024, [arXiv:hep-ph/9809403](#).

- 9687 [172] J. A. Bagger and M. E. Peskin, *EXOTIC PROCESSES IN HIGH-ENERGY $e p$ COLLISIONS*, Phys. Rev. **D31** (1985)
9688 2211.
- 9689 [173] R. J. Cashmore et al., *EXOTIC PHENOMENA IN HIGH-ENERGY $E P$ COLLISIONS*, Phys. Rept. **122** (1985)
9690 275–386.
- 9691 [174] G. Jarlskog, (Ed.) and D. Rein, (Ed.), *ECFA Large Hadron Collider Workshop, Aachen, Germany, 4-9 Oct 1990:*
9692 *Proceedings.1*, . CERN-90-10-V-1.
- 9693 [175] G. Kopp, D. Schaile, M. Spira, and P. M. Zerwas, *Bounds on radii and magnetic dipole moments of quarks and leptons*
9694 *from LEP, SLC and HERA*, Z. Phys. **C65** (1995) 545–550, [arXiv:hep-ph/9409457](#).
- 9695 [176] A. F. Zarnecki, *Leptoquarks and Contact Interactions at LeHC*, [arXiv:0809.2917 \[hep-ph\]](#).
- 9696 [177] E. Eichten, K. D. Lane, and M. E. Peskin, *New Tests for Quark and Lepton Substructure*, Phys. Rev. Lett. **50** (1983)
9697 811–814.
- 9698 [178] R. Ruckl, *PROBING LEPTON AND QUARK SUBSTRUCTURE IN POLARIZED $e+ N$ SCATTERING*, Nucl.
9699 Phys. **B234** (1984) 91.
- 9700 [179] P. Haberl, F. Schrempp, and H. U. Martyn, *Contact interactions and new heavy bosons at HERA: A Model*
9701 *independent analysis*, . In *Hamburg 1991, Proceedings, Physics at HERA, vol. 2* 1133-1148. (see HIGH ENERGY
9702 PHYSICS INDEX 30 (1992) No. 12988).
- 9703 [180] A. F. Zarnecki, *Global analysis of eeqq contact interactions and future prospects for high-energy physics*, Eur. Phys. J.
9704 **C11** (1999) 539–557, [arXiv:hep-ph/9904334](#).
- 9705 [181] E. Farhi and L. Susskind, *Technicolor*, Phys. Rept. **74** (1981) 277.
- 9706 [182] C. T. Hill and E. H. Simmons, *Strong dynamics and electroweak symmetry breaking*, Phys. Rept. **381** (2003) 235–402,
9707 [arXiv:hep-ph/0203079](#).
- 9708 [183] W. Buchmuller, R. Ruckl, and D. Wyler, *Leptoquarks in lepton quark collisions*, Phys. Lett. **B191** (1987) 442–448.
- 9709 [184] B. Schrempp, *Leptoquarks and leptogluons at HERA: Theoretical perspectives*, . In *Hamburg 1991, Proceedings,
9710 Physics at HERA, vol. 2* 1034-1042. (see HIGH ENERGY PHYSICS INDEX 30 (1992) No. 12988).
- 9711 [185] S. Davidson, D. C. Bailey, and B. A. Campbell, *Model independent constraints on leptoquarks from rare processes*, Z.
9712 Phys. **C61** (1994) 613–644, [arXiv:hep-ph/9309310](#).
- 9713 [186] M. Leurer, *A Comprehensive study of leptoquark bounds*, Phys. Rev. **D49** (1994) 333–342, [arXiv:hep-ph/9309266](#).
- 9714 [187] A. Belyaev, C. Leroy, R. Mehdiev, and A. Pukhov, *Leptoquark single and pair production at LHC with*
9715 *CalcHEP/CompHEP in the complete model*, JHEP **09** (2005) 005, [arXiv:hep-ph/0502067](#).
- 9716 [188] D0 Collaboration, V. M. Abazov et al., *Search for pair production of first-generation leptoquarks in $p \bar{p}$ collisions at*
9717 *$\sqrt{s}=1.96$ TeV*, Phys. Lett. **B681** (2009) 224–232, [arXiv:0907.1048 \[hep-ex\]](#).
- 9718 [189] T. A. Collaboration, *Search for pair production of first or second generation leptoquarks in proton-proton collisions at*
9719 *$\sqrt{s}=7$ TeV using the ATLAS detector at the LHC*, [arXiv:1104.4481 \[hep-ex\]](#). * Temporary entry *.
- 9720 [190] CMS Collaboration, S. Chatrchyan et al., *Search for First Generation Scalar Leptoquarks in the $e\nu jj$ channel in pp*
9721 *collisions at $\sqrt{s} = 7$ TeV*, [arXiv:1105.5237 \[hep-ex\]](#). * Temporary entry *.
- 9722 [191] A. Belyaev and A. Pukhov.
- 9723 [192] A. Pukhov, *Calcchep 2.3: MSSM, structure functions, event generation, 1, and generation of matrix elements for other*
9724 *packages*, [arXiv:hep-ph/0412191](#).
- 9725 [193] S. Ovyn, X. Rouby, and V. Lemaitre, *Delphes, a framework for fast simulation of a generic collider experiment*,
9726 [arXiv:0903.2225 \[hep-ph\]](#).
- 9727 [194] H. Harari, *A Schematic Model of Quarks and Leptons*, Phys. Lett. **B86** (1979) 83.
- 9728 [195] H. Fritzsch and G. Mandelbaum, *Weak Interactions as Manifestations of the Substructure of Leptons and Quarks*,
9729 Phys. Lett. **B102** (1981) 319.
- 9730 [196] O. W. Greenberg and J. Sucher, *A Quantum Structure Dynamic Model of Quarks, Leptons, Weak Vector Bosons, and*
9731 *Higgs Mesons*, Phys. Lett. **B99** (1981) 339.
- 9732 [197] R. Barbieri, R. N. Mohapatra, and A. Masiero, *Compositeness and a Left-Right Symmetric Electroweak Model Without*
9733 *Broken Gauge Interactions*, Phys. Lett. **B105** (1981) 369–374.
- 9734 [198] U. Baur and K. H. Streng, *COLORED LEPTON MASS BOUNDS FROM p anti- p COLLIDER DATA*, Phys. Lett.
9735 **B162** (1985) 387.
- 9736 [199] A. Celikel, M. Kantar, and S. Sultansoy, *A search for sextet quarks and leptogluons at the LHC*, Phys. Lett. **B443**
9737 (1998) 359–364.
- 9738 [200] S. S. M. Sahin and S. Turkoz, *Resonant production of color octet electrons at the LHeC*, . CERN-LHeC-Note-2010-015
9739 PHY.
- 9740 [201] H. Harari, *COMPOSITE MODELS FOR QUARKS AND LEPTONS*, Phys. Rept. **104** (1984) 159.

- 9741 [202] N. T. E. Sauvan, *Single production of excited fermions at LHeC*, . CERN-LHeC-Note-2010-011 PHY.
- 9742 [203] O. J. P. Eboli, S. M. Lietti, and P. Mathews, *Excited leptons at the CERN Large Hadron Collider*, Phys. Rev. **D65**
9743 (2002) 075003, arXiv:hep-ph/0111001.
- 9744 [204] E. M. Gregores, M. C. Gonzalez-Garcia, and S. F. Novaes, *Discriminating new physics scenarios at NLC: The Role of*
9745 *polarization*, Phys. Rev. **D56** (1997) 2920–2927, arXiv:hep-ph/9703430.
- 9746 [205] H1 Collaboration, F. D. Aaron et al., *Search for Excited Electrons in ep Collisions at HERA*, Phys. Lett. **B666** (2008)
9747 131–139, arXiv:0805.4530 [hep-ex].
- 9748 [206] H1 Collaboration, F. D. Aaron et al., *A Search for Excited Neutrinos in e-p Collisions at HERA*, Phys. Lett. **B663**
9749 (2008) 382–389, arXiv:0802.1858 [hep-ex].
- 9750 [207] H1 Collaboration, F. D. Aaron et al., *Search for Excited Quarks in ep Collisions at HERA*, Phys. Lett. **B678** (2009)
9751 335–343, arXiv:0904.3392 [hep-ex].
- 9752 [208] OPAL Collaboration, G. Abbiendi et al., *Search for charged excited leptons in e+ e- collisions at s**(1/2) = 183-GeV*
9753 *- 209-GeV*, Phys. Lett. **B544** (2002) 57–72, arXiv:hep-ex/0206061.
- 9754 [209] DELPHI Collaboration, J. Abdallah et al., *Determination of the e+ e- -j gamma gamma (gamma) cross- section at*
9755 *LEP 2*, Eur. Phys. J. **C37** (2004) 405–419, arXiv:hep-ex/0409058.
- 9756 [210] D0 Collaboration, V. M. Abazov et al., *Search for excited electrons in pp collisions at sqrt(s) = 1.96-TeV*, Phys. Rev. **D77**
9757 (2008) 091102, arXiv:0801.0877 [hep-ex].
- 9758 [211] K. Hagiwara, D. Zeppenfeld, and S. Komamiya, *Excited Lepton Production at LEP and HERA*, Z. Phys. **C29** (1985)
9759 115.
- 9760 [212] F. Boudjema, A. Djouadi, and J. L. Kneur, *Excited fermions at e+ e- and e P colliders*, Z. Phys. **C57** (1993) 425–450.
- 9761 [213] U. Baur, M. Spira, and P. M. Zerwas, *EXCITED QUARK AND LEPTON PRODUCTION AT HADRON*
9762 *COLLIDERS*, Phys. Rev. **D42** (1990) 815–824.
- 9763 [214] T. Kohler, *Exotic processes at HERA: The Event generator COMPOS*, . In *Hamburg 1991, Proceedings, Physics at
9764 HERA, vol. 3* 1526-1541. (see HIGH ENERGY PHYSICS INDEX 30 (1992) No. 12988).
- 9765 [215] M. Spira. private communication.
- 9766 [216] C. Berger and P. Kandel, *A new generator for wide angle bremsstrahlung*, . Prepared for Workshop on Monte Carlo
9767 Generators for HERA Physics (Plenary Starting Meeting), Hamburg, Germany, 27-30 Apr 1998.
- 9768 [217] A. C. et al., *Production of the Fourth SM Family Fermions at the Large Hadron Electron Collider*, .
9769 CERN-LHeC-Note-2010-016 PHY.
- 9770 [218] J. A. Aguilar-Saavedra, *A minimal set of top anomalous couplings*, Nucl. Phys. **B812** (2009) 181–204, arXiv:0811.3842
9771 [hep-ph].
- 9772 [219] Particle Data Group Collaboration, C. Amsler et al., *Review of particle physics*, Phys. Lett. **B667** (2008) 1.
- 9773 [220] The ATLAS Collaboration, G. Aad et al., *Expected Performance of the ATLAS Experiment - Detector, Trigger and*
9774 *Physics*, arXiv:0901.0512 [hep-ex].
- 9775 [221] *ATLAS detector and physics performance. Technical design report. Vol. 2*, . CERN-LHCC-99-15.
- 9776 [222] T. Han, K. Whisnant, B. L. Young, and X. Zhang, *Searching for t -> c g at the Fermilab Tevatron*, Phys. Lett. **B385**
9777 (1996) 311–316, arXiv:hep-ph/9606231.
- 9778 [223] E. Malkawi and T. M. P. Tait, *Top-Charm Strong Flavour-Changing Neutral Currents at the Tevatron*, Phys. Rev. **D54**
9779 (1996) 5758–5762, arXiv:hep-ph/9511337.
- 9780 [224] T. M. P. Tait and C. P. Yuan, *Anomalous t-c-g coupling: The connection between single top production and top decay*,
9781 Phys. Rev. **D55** (1997) 7300–7301, arXiv:hep-ph/9611244.
- 9782 [225] T. Han, M. Hosch, K. Whisnant, B.-L. Young, and X. Zhang, *Single top quark production via FCNC couplings at*
9783 *hadron colliders*, Phys. Rev. **D58** (1998) 073008, arXiv:hep-ph/9806486.
- 9784 [226] T. M. P. Tait and C. P. Yuan, *Single top quark production as a window to physics beyond the standard model*, Phys.
9785 Rev. **D63** (2001) 014018, arXiv:hep-ph/0007298.
- 9786 [227] J. J. Liu, C. S. Li, L. L. Yang, and L. G. Jin, *Single top quark production via SUSY-QCD FCNC couplings at the*
9787 *CERN LHC in the unconstrained MSSM*, Nucl. Phys. **B705** (2005) 3–32, arXiv:hep-ph/0404099.
- 9788 [228] J. J. Liu, C. S. Li, L. L. Yang, and L. G. Jin, *Next-to-leading order QCD corrections to the direct top quark production*
9789 *via model-independent FCNC couplings at hadron colliders*, Phys. Rev. **D72** (2005) 074018, arXiv:hep-ph/0508016.
- 9790 [229] J.-j. Cao, G.-l. Liu, J. M. Yang, and H.-j. Zhang, *Top-quark FCNC productions at LHC in topcolor-assisted technicolor*
9791 *model*, Phys. Rev. **D76** (2007) 014004, arXiv:hep-ph/0703308.
- 9792 [230] J. J. Cao et al., *SUSY-induced FCNC top-quark processes at the Large Hadron Collider*, Phys. Rev. **D75** (2007)
9793 075021, arXiv:hep-ph/0702264.

- 9794 [231] P. M. Ferreira, R. B. Guedes, and R. Santos, *Combined effects of strong and electroweak FCNC effective operators in*
9795 *top quark physics at the CERN LHC*, Phys. Rev. **D77** (2008) 114008, [arXiv:0802.2075 \[hep-ph\]](#).
- 9796 [232] J. M. Yang, *Probing New Physics from Top Quark Processes at LHC: A Mini Review*, Int. J. Mod. Phys. **A23** (2008)
9797 3343, [arXiv:0801.0210 \[hep-ph\]](#).
- 9798 [233] X.-F. Han, L. Wang, and J. M. Yang, *Top quark FCNC decays and productions at LHC in littlest Higgs model with*
9799 *T-parity*, [arXiv:0903.5491 \[hep-ph\]](#).
- 9800 [234] J. Cao, Z. Heng, L. Wu, and J. M. Yang, *R-parity violating effects in top quark FCNC productions at LHC*, Phys. Rev.
9801 **D79** (2009) 054003, [arXiv:0812.1698 \[hep-ph\]](#).
- 9802 [235] V. F. Obraztsov, S. R. Slabospitsky, and O. P. Yushchenko, *Search for anomalous top quark interaction at LEP-2*
9803 *collider*, Phys. Lett. **B426** (1998) 393–402, [arXiv:hep-ph/9712394](#).
- 9804 [236] T. Han and J. L. Hewett, *Top charm associated production in high-energy e^+e^- collisions*, Phys. Rev. **D60** (1999)
9805 074015, [arXiv:hep-ph/9811237](#).
- 9806 [237] J.-j. Cao, Z.-h. Xiong, and J. M. Yang, *SUSY-induced top quark FCNC processes at linear colliders*, Nucl. Phys. **B651**
9807 (2003) 87–105, [arXiv:hep-ph/0208035](#).
- 9808 [238] J. A. Aguilar-Saavedra, *Top flavor-changing neutral interactions: Theoretical expectations and experimental detection*,
9809 Acta Phys. Polon. **B35** (2004) 2695–2710, [arXiv:hep-ph/0409342](#).
- 9810 [239] A. T. Alan and A. Senol, *Single top production at HERA and THERA*, Europhys. Lett. **59** (2002) 669–673,
9811 [arXiv:hep-ph/0202119](#).
- 9812 [240] A. A. Ashimova and S. R. Slabospitsky, *The Constraint on FCNC Coupling of the Top Quark with a Gluon from ep*
9813 *Collisions*, Phys. Lett. **B668** (2008) 282–285, [arXiv:hep-ph/0604119](#).
- 9814 [241] H1 Collaboration, F. D. Aaron et al., *Search for Single Top Quark Production at HERA*, Phys. Lett. **B678** (2009)
9815 450–458, [arXiv:0904.3876 \[hep-ex\]](#).
- 9816 [242] O. Cakir and S. A. Cetin, *Anomalous single top quark production at the CERN LHC*, J. Phys. **G31** (2005) N1–N8.
- 9817 [243] G. A. Moortgat-Pick et al., *The role of polarized positrons and electrons in revealing fundamental interactions at the*
9818 *linear collider*, Phys. Rept. **460** (2008) 131–243, [arXiv:hep-ph/0507011](#).
- 9819 [244] S. Sultansoy, *Linac-ring type colliders: Second way to TeV scale*, Eur. Phys. J. **C33** (2004) s1064–s1066,
9820 [arXiv:hep-ex/0306034](#).
- 9821 [245] S. F. Sultanov, *Prospects of the future e p and gamma p colliders: Luminosity and physics*, . IC/89/409.
- 9822 [246] S. I. Alekhin et al., *PHYSICS AT gamma p COLLIDERS OF TeV ENERGIES*, Int. J. Mod. Phys. **A6** (1991) 21–40.
- 9823 [247] A. K. Ciftci, S. Sultansoy, S. Turkoz, and O. Yavas, *Main parameters of TeV energy gamma p colliders*, Nucl. Instrum.
9824 Meth. **A365** (1995) 317–328.
- 9825 [248] A. K. Ciftci, S. Sultansoy, and O. Yavas, *TESLA*HERA based gamma p and gamma A colliders*, Nucl. Instrum. Meth.
9826 **A472** (2001) 72–78, [arXiv:hep-ex/0007009](#).
- 9827 [249] H. Aksakal, A. K. Ciftci, Z. Nergiz, D. Schulte, and F. Zimmermann, *Conversion efficiency and luminosity for gamma*
9828 *proton colliders based on the LHC-CLIC or LHC-ILC QCD Explorer scheme*, Nucl. Instrum. Meth. **A576** (2007)
9829 287–293, [arXiv:hep-ex/0612041](#).
- 9830 [250] I. T. Cakir, O. Cakir, and S. Sultansoy, *Anomalous Single Top Production at the Large Hadron electron Collider Based*
9831 *gamma p Collider*, Phys. Lett. **B685** (2010) 170–173, [arXiv:0911.4194 \[hep-ph\]](#).
- 9832 [251] CMS Collaboration, G. L. Bayatian et al., *CMS technical design report, volume II: Physics performance*, J. Phys. **G34**
9833 (2007) 995–1579.
- 9834 [252] O. Cakir, *Anomalous production of top quarks at CLIC + LHC based γp colliders*, J. Phys. **G29** (2003) 1181–1192,
9835 [arXiv:hep-ph/0301116](#).
- 9836 [253] R. Ciftci, *Production of Excited Quark at γp Collider Based on the Large Hadron Electron Collider*, .
9837 CERN-LHeC-Note-2010-017 PHY.
- 9838 [254] O. Çakır and M. Şahin, *Diquarks in γp Collisions at LHeC*, . CERN-LHeC-Note-2010-012 PHY.
- 9839 [255] CMS Collaboration, V. Khachatryan et al., *Search for Dijet Resonances in 7 TeV pp Collisions at CMS*, Phys. Rev.
9840 Lett. **105** (2010) 211801, [arXiv:1010.0203 \[hep-ex\]](#).
- 9841 [256] A. Atre, M. Carena, T. Han, and J. Santiago, *Heavy Quarks Above the Top at the Tevatron*, Phys. Rev. **D79** (2009)
9842 054018, [arXiv:0806.3966 \[hep-ph\]](#).
- 9843 [257] A. Atre et al., *Model-Independent Searches for New Quarks at the LHC*, [arXiv:1102.1987 \[hep-ph\]](#).
- 9844 [258] O.Cakir, *Single Production of Fourth Family Quarks at LHeC*, . CERN-LHeC-Note-2010-013 PHY.
- 9845 [259] M. Dührssen, *Measurement of Higgs boson parameters at the LHC*, Czech. J. Phys. **55** (2005) B145–B152.
- 9846 [260] J. M. Butterworth, A. R. Davison, M. Rubin, and G. P. Salam, *Jet substructure as a new Higgs search channel at the*
9847 *LHC*, Phys. Rev. Lett. **100** (2008) 242001, [arXiv:0802.2470 \[hep-ph\]](#).

- 9848 [261] T. Han and B. Mellado, *Higgs Boson Searches and the Higgs Coupling at the LHeC*, Phys. Rev. **D82** (2010) 016009,
9849 [arXiv:0909.2460 \[hep-ph\]](#).
- 9850 [262] B. Jager, *Next-to-leading order QCD corrections to Higgs production at a future lepton-proton collider*, Phys.Rev. **D81**
9851 (2010) 054018, [arXiv:1001.3789 \[hep-ph\]](#).
- 9852 [263] J. Blumlein, G. van Oldenborgh, and R. Ruckl, *QCD and QED corrections to Higgs boson production in charged
9853 current e p scattering*, Nucl.Phys. **B395** (1993) 35–59, [arXiv:hep-ph/9209219 \[hep-ph\]](#).
- 9854 [264] J. Alwall et al., *MadGraph/MadEvent v4: The New Web Generation*, JHEP **09** (2007) 028, [arXiv:0706.2334 \[hep-ph\]](#).
- 9855 [265] PGS. <http://www.physics.ucdavis.edu/~conway/research/software/pgs/pgs4-general.htm>.
- 9856 [266] T. Plehn, D. L. Rainwater, and D. Zeppenfeld, *Determining the structure of Higgs couplings at the LHC*, Phys. Rev.
9857 Lett. **88** (2002) 051801, [arXiv:hep-ph/0105325](#).
- 9858 [267] T. Regge, *Introduction to complex orbital momenta*, Nuovo Cim. **14** (1959) 951.
- 9859 [268] V. N. Gribov, *A REGGEON DIAGRAM TECHNIQUE*, Sov. Phys. JETP **26** (1968) 414–422.
- 9860 [269] H. D. I. Abarbanel, J. B. Bronzan, R. L. Sugar, and A. R. White, *Reggeon Field Theory: Formulation and Use*, Phys.
9861 Rept. **21** (1975) 119–182.
- 9862 [270] J. C. Collins, D. E. Soper, and G. F. Sterman, *Factorization of Hard Processes in QCD*, Adv. Ser. Direct. High Energy
9863 Phys. **5** (1988) 1–91, [arXiv:hep-ph/0409313](#).
- 9864 [271] V. N. Gribov and L. N. Lipatov, *Deep inelastic ep scattering in perturbation theory*, Sov. J. Nucl. Phys. **15** (1972)
9865 438–450.
- 9866 [272] G. Altarelli and G. Parisi, *Asymptotic Freedom in Parton Language*, Nucl. Phys. **B126** (1977) 298.
- 9867 [273] Y. L. Dokshitzer, *Calculation of the Structure Functions for Deep Inelastic Scattering and e+ e- Annihilation by
9868 Perturbation Theory in Quantum Chromodynamics*, Sov. Phys. JETP **46** (1977) 641–653.
- 9869 [274] L. V. Gribov, E. M. Levin, and M. G. Ryskin, *Semihard Processes in QCD*, Phys. Rept. **100** (1983) 1–150.
- 9870 [275] A. H. Mueller, *Small x Behavior and Parton Saturation: A QCD Model*, Nucl. Phys. **B335** (1990) 115.
- 9871 [276] J. Jalilian-Marian, A. Kovner, A. Leonidov, and H. Weigert, *The Wilson renormalization group for low x physics:
9872 Towards the high density regime*, Phys. Rev. **D59** (1999) 014014, [arXiv:hep-ph/9706377](#).
- 9873 [277] I. Balitsky, *Operator expansion for high-energy scattering*, Nucl. Phys. **B463** (1996) 99–160, [arXiv:hep-ph/9509348](#).
- 9874 [278] Y. V. Kovchegov, *Small-x F2 structure function of a nucleus including multiple pomeron exchanges*, Phys. Rev. **D60**
9875 (1999) 034008, [arXiv:hep-ph/9901281](#).
- 9876 [279] M. Froissart, *Asymptotic behavior and subtractions in the Mandelstam representation*, Phys. Rev. **123** (1961)
9877 1053–1057.
- 9878 [280] A. Martin, *Unitarity and high-energy behavior of scattering amplitudes*, Phys. Rev. **129** (1963) 1432–1436.
- 9879 [281] E. A. Kuraev, L. N. Lipatov, and V. S. Fadin, *The Pomernanchuk Singularity in Nonabelian Gauge Theories*, Sov. Phys.
9880 JETP **45** (1977) 199–204.
- 9881 [282] I. I. Balitsky and L. N. Lipatov, *The Pomernanchuk Singularity in Quantum Chromodynamics*, Sov. J. Nucl. Phys. **28**
9882 (1978) 822–829.
- 9883 [283] V. N. Gribov, *Glauber corrections and the interaction between high- energy hadrons and nuclei*, Sov. Phys. JETP **29**
9884 (1969) 483–487.
- 9885 [284] N. Armesto, A. B. Kaidalov, C. A. Salgado, and K. Tywoniuk, *A unitarized model of inclusive and diffractive DIS with
9886 Q2-evolution*, Phys. Rev. **D81** (2010) 074002, [arXiv:1001.3021 \[hep-ph\]](#).
- 9887 [285] N. Armesto, A. B. Kaidalov, C. A. Salgado, and K. Tywoniuk, *Nuclear shadowing in Glauber-Gribov theory with Q2-
9888 evolution*, Eur. Phys. J. **C68** (2010) 447–457, [arXiv:1003.2947 \[hep-ph\]](#).
- 9889 [286] A. H. Mueller and J.-w. Qiu, *Gluon Recombination and Shadowing at Small Values of x*, Nucl. Phys. **B268** (1986) 427.
- 9890 [287] J. Bartels and M. Wusthoff, *The Triple Regge limit of diffractive dissociation in deep inelastic scattering*, Z. Phys. **C66**
9891 (1995) 157–180.
- 9892 [288] L. D. McLerran and R. Venugopalan, *Computing quark and gluon distribution functions for very large nuclei*, Phys.
9893 Rev. **D49** (1994) 2233–2241, [arXiv:hep-ph/9309289](#).
- 9894 [289] L. D. McLerran and R. Venugopalan, *Gluon distribution functions for very large nuclei at small transverse momentum*,
9895 Phys. Rev. **D49** (1994) 3352–3355, [arXiv:hep-ph/9311205](#).
- 9896 [290] L. D. McLerran and R. Venugopalan, *Green's functions in the color field of a large nucleus*, Phys. Rev. **D50** (1994)
9897 2225–2233, [arXiv:hep-ph/9402335](#).
- 9898 [291] J. Jalilian-Marian, A. Kovner, and H. Weigert, *The Wilson renormalization group for low x physics: Gluon evolution at
9899 finite parton density*, Phys. Rev. **D59** (1999) 014015, [arXiv:hep-ph/9709432](#).

- 9900 [292] A. Kovner, J. G. Milhano, and H. Weigert, *Relating different approaches to nonlinear QCD evolution at finite gluon*
9901 *density*, Phys. Rev. **D62** (2000) 114005, [arXiv:hep-ph/0004014](#).
- 9902 [293] H. Weigert, *Unitarity at small Bjorken x*, Nucl. Phys. **A703** (2002) 823–860, [arXiv:hep-ph/0004044](#).
- 9903 [294] E. Iancu, A. Leonidov, and L. D. McLerran, *Nonlinear gluon evolution in the color glass condensate. I*, Nucl. Phys.
9904 **A692** (2001) 583–645, [arXiv:hep-ph/0011241](#).
- 9905 [295] E. Ferreiro, E. Iancu, A. Leonidov, and L. McLerran, *Nonlinear gluon evolution in the color glass condensate. II*, Nucl.
9906 Phys. **A703** (2002) 489–538, [arXiv:hep-ph/0109115](#).
- 9907 [296] T. Altinoluk, A. Kovner, M. Lublinsky, and J. Peressutti, *QCD Reggeon Field Theory for every day: Pomeron loops*
9908 *included*, JHEP **03** (2009) 109, [arXiv:0901.2559 \[hep-ph\]](#).
- 9909 [297] F. Gelis, E. Iancu, J. Jalilian-Marian, and R. Venugopalan, *The Color Glass Condensate*, Ann.Rev.Nucl.Part.Sci. **60**
9910 (2010) 463–489, [arXiv:1002.0333 \[hep-ph\]](#).
- 9911 [298] Y. V. Kovchegov and H. Weigert, *Triumvirate of Running Couplings in Small-x Evolution*, Nucl.Phys. **A784** (2007)
9912 188–226, [arXiv:hep-ph/0609090 \[hep-ph\]](#).
- 9913 [299] I. Balitsky and G. A. Chirilli, *Next-to-leading order evolution of color dipoles*, Phys. Rev. **D77** (2008) 014019,
9914 [arXiv:0710.4330 \[hep-ph\]](#).
- 9915 [300] E. Iancu, A. Mueller, and S. Munier, *Universal behavior of QCD amplitudes at high energy from general tools of*
9916 *statistical physics*, Phys.Lett. **B606** (2005) 342–350, [arXiv:hep-ph/0410018 \[hep-ph\]](#).
- 9917 [301] Y. V. Kovchegov, J. Kuokkanen, K. Rummukainen, and H. Weigert, *Subleading- $N(c)$ corrections in non-linear small-x*
9918 *evolution*, Nucl.Phys. **A823** (2009) 47–82, [arXiv:0812.3238 \[hep-ph\]](#).
- 9919 [302] A. Dumitru and J. Jalilian-Marian, *Forward dijets in high-energy collisions: Evolution of QCD n-point functions*
9920 *beyond the dipole approximation*, Phys.Rev. **D82** (2010) 074023, [arXiv:1008.0480 \[hep-ph\]](#).
- 9921 [303] C. Marquet and H. Weigert, *New observables to test the Color Glass Condensate beyond the large- N_c limit*, Nucl.Phys.
9922 **A843** (2010) 68–97, [arXiv:1003.0813 \[hep-ph\]](#).
- 9923 [304] Y. Hatta, E. Iancu, C. Marquet, G. Soyez, and D. Triantafyllopoulos, *Diffusive scaling and the high-energy limit of deep*
9924 *inelastic scattering in QCD at large $N(c)$* , Nucl.Phys. **A773** (2006) 95–155, [arXiv:hep-ph/0601150 \[hep-ph\]](#).
- 9925 [305] S. Munier, *Quantum chromodynamics at high energy and statistical physics*, Phys.Rept. **473** (2009) 1–49,
9926 [arXiv:0901.2823 \[hep-ph\]](#). * Temporary entry *.
- 9927 [306] S. Catani and F. Hautmann, *High-energy factorization and small x deep inelastic scattering beyond leading order*, Nucl.
9928 Phys. **B427** (1994) 475–524, [arXiv:hep-ph/9405388](#).
- 9929 [307] F. Caola, S. Forte, and J. Rojo, *Deviations from NLO QCD evolution in inclusive HERA data*, Phys. Lett. **B686**
9930 (2010) 127–135, [arXiv:0910.3143 \[hep-ph\]](#).
- 9931 [308] V. S. Fadin and L. N. Lipatov, *BFKL pomeron in the next-to-leading approximation*, Phys. Lett. **B429** (1998) 127–134,
9932 [arXiv:hep-ph/9802290](#).
- 9933 [309] M. Ciafaloni and G. Camici, *Energy scale(s) and next-to-leading BFKL equation*, Phys. Lett. **B430** (1998) 349–354,
9934 [arXiv:hep-ph/9803389](#).
- 9935 [310] G. Altarelli, R. D. Ball, and S. Forte, *An anomalous dimension for small x evolution*, Nucl. Phys. **B674** (2003)
9936 459–483, [arXiv:hep-ph/0306156](#).
- 9937 [311] G. Altarelli, R. D. Ball, and S. Forte, *Perturbatively stable resummed small x evolution kernels*, Nucl. Phys. **B742**
9938 (2006) 1–40, [arXiv:hep-ph/0512237](#).
- 9939 [312] G. Altarelli, R. D. Ball, and S. Forte, *Small x Resummation with Quarks: Deep-Inelastic Scattering*, Nucl. Phys. **B799**
9940 (2008) 199–240, [arXiv:0802.0032 \[hep-ph\]](#).
- 9941 [313] M. Ciafaloni, D. Colferai, G. P. Salam, and A. M. Stasto, *Renormalisation group improved small-x Green’s function*,
9942 Phys. Rev. **D68** (2003) 114003, [arXiv:hep-ph/0307188](#).
- 9943 [314] M. Ciafaloni, D. Colferai, G. P. Salam, and A. M. Stasto, *The gluon splitting function at moderately small x*, Phys.
9944 Lett. **B587** (2004) 87–94, [arXiv:hep-ph/0311325](#).
- 9945 [315] M. Ciafaloni, D. Colferai, G. P. Salam, and A. M. Stasto, *A matrix formulation for small-x singlet evolution*, JHEP **08**
9946 (2007) 046, [arXiv:0707.1453 \[hep-ph\]](#).
- 9947 [316] J. C. Collins, *Proof of factorization for diffractive hard scattering*, Phys. Rev. **D57** (1998) 3051–3056,
9948 [arXiv:hep-ph/9709499](#).
- 9949 [317] F. Low, *A Model of the Bare Pomeron*, Phys. Rev. **D12** (1975) 163.
- 9950 [318] S. Nussinov, *Colored Quark Version of Some Hadronic Puzzles*, Phys. Rev. Lett. **34** (1975) 1286.
- 9951 [319] K. J. Golec-Biernat and M. Wusthoff, *Saturation effects in deep inelastic scattering at low Q^{*2} and its implications on*
9952 *diffraction*, Phys. Rev. **D59** (1998) 014017, [arXiv:hep-ph/9807513](#).

- 9953 [320] K. J. Golec-Biernat and M. Wusthoff, *Saturation in diffractive deep inelastic scattering*, Phys. Rev. **D60** (1999) 114023,
9954 [arXiv:hep-ph/9903358](#).
- 9955 [321] N. Armesto, *Nuclear shadowing*, J. Phys. **G32** (2006) R367–R394, [arXiv:hep-ph/0604108](#).
- 9956 [322] L. Frankfurt, M. Strikman, and C. Weiss, *Small- x physics: From HERA to LHC and beyond*, Ann. Rev. Nucl. Part. Sci. **55** (2005) 403–465, [arXiv:hep-ph/0507286](#).
9957
- 9958 [323] E. Iancu, K. Itakura, and S. Munier, *Saturation and BFKL dynamics in the HERA data at small x* , Phys. Lett. **B590**
9959 (2004) 199–208, [arXiv:hep-ph/0310338](#).
- 9960 [324] J. R. Forshaw and G. Shaw, *Gluon saturation in the colour dipole model?*, JHEP **12** (2004) 052, [arXiv:hep-ph/0411337](#).
- 9961 [325] A. M. Stasto, K. J. Golec-Biernat, and J. Kwiecinski, *Geometric scaling for the total $\gamma^* p$ cross-section in the low
9962 x region*, Phys. Rev. Lett. **86** (2001) 596–599, [arXiv:hep-ph/0007192](#).
- 9963 [326] N. Armesto, C. A. Salgado, and U. A. Wiedemann, *Relating high-energy lepton hadron, proton nucleus and nucleus
9964 nucleus collisions through geometric scaling*, Phys. Rev. Lett. **94** (2005) 022002, [arXiv:hep-ph/0407018](#).
- 9965 [327] C. Marquet and L. Schoeffel, *Geometric scaling in diffractive deep inelastic scattering*, Phys. Lett. **B639** (2006)
9966 471–477, [arXiv:hep-ph/0606079](#).
- 9967 [328] V. Goncalves and M. Machado, *Geometric scaling in inclusive charm production*, Phys.Rev.Lett. **91** (2003) 202002,
9968 [arXiv:hep-ph/0307090](#) [[hep-ph](#)].
- 9969 [329] L. McLerran and M. Praszalowicz, *Saturation and Scaling of Multiplicity, Mean p_T and p_T Distributions from 200
9970 GeV $lt\ sqrt(s)$ $lt\ 7\ TeV$* , Acta Phys.Polon. **B41** (2010) 1917–1926, [arXiv:1006.4293](#) [[hep-ph](#)].
- 9971 [330] F. Caola and S. Forte, *Geometric Scaling from GLAP evolution*, Phys. Rev. Lett. **101** (2008) 022001, [arXiv:0802.1878](#)
9972 [[hep-ph](#)].
- 9973 [331] N. N. Nikolaev and B. G. Zakharov, *Colour transparency and scaling properties of nuclear shadowing in deep inelastic
9974 scattering*, Z. Phys. **C49** (1991) 607–618.
- 9975 [332] N. Nikolaev and B. G. Zakharov, *Pomeron structure function and diffraction dissociation of virtual photons in
9976 perturbative QCD*, Z. Phys. **C53** (1992) 331–346.
- 9977 [333] A. H. Mueller and B. Patel, *Single and double BFKL pomeron exchange and a dipole picture of high-energy hard
9978 processes*, Nucl. Phys. **B425** (1994) 471–488, [arXiv:hep-ph/9403256](#).
- 9979 [334] A. H. Mueller, *Unitarity and the BFKL pomeron*, Nucl. Phys. **B437** (1995) 107–126, [arXiv:hep-ph/9408245](#).
- 9980 [335] M. L. Good and W. D. Walker, *Diffraction dissociation of beam particles*, Phys. Rev. **120** (1960) 1857–1860.
- 9981 [336] A. H. Mueller, *Parton saturation: An overview*, [arXiv:hep-ph/0111244](#).
- 9982 [337] J. Bartels, K. J. Golec-Biernat, and H. Kowalski, *A modification of the saturation model: DGLAP evolution*, Phys.
9983 Rev. **D66** (2002) 014001, [arXiv:hep-ph/0203258](#).
- 9984 [338] H. Kowalski and D. Teaney, *An impact parameter dipole saturation model*, Phys. Rev. **D68** (2003) 114005,
9985 [arXiv:hep-ph/0304189](#).
- 9986 [339] H. Kowalski, L. Motyka, and G. Watt, *Exclusive diffractive processes at HERA within the dipole picture*, Phys. Rev.
9987 **D74** (2006) 074016, [arXiv:hep-ph/0606272](#).
- 9988 [340] A. D. Martin, R. G. Roberts, W. J. Stirling, and R. S. Thorne, *Uncertainties of predictions from parton distributions. I:
9989 Experimental errors. ((T))*, Eur. Phys. J. **C28** (2003) 455–473, [arXiv:hep-ph/0211080](#).
- 9990 [341] A. D. Martin, W. J. Stirling, R. S. Thorne, and G. Watt, *Update of Parton Distributions at NNLO*, Phys. Lett. **B652**
9991 (2007) 292–299, [arXiv:0706.0459](#) [[hep-ph](#)].
- 9992 [342] P. M. Nadolsky et al., *Implications of CTEQ global analysis for collider observables*, Phys. Rev. **D78** (2008) 013004,
9993 [arXiv:0802.0007](#) [[hep-ph](#)].
- 9994 [343] G. Watt, A. D. Martin, W. J. Stirling, and R. S. Thorne, *Recent Progress in Global PDF Analysis*, [arXiv:0806.4890](#)
9995 [[hep-ph](#)].
- 9996 [344] A. Martin, W. Stirling, R. Thorne, and G. Watt, *Parton distributions for the LHC*, Eur.Phys.J. **C63** (2009) 189–285,
9997 [arXiv:0901.0002](#) [[hep-ph](#)].
- 9998 [345] H.-L. Lai, J. Huston, Z. Li, P. Nadolsky, J. Pumplin, et al., *Uncertainty induced by QCD coupling in the CTEQ global
9999 analysis of parton distributions*, Phys.Rev. **D82** (2010) 054021, [arXiv:1004.4624](#) [[hep-ph](#)].
- 10000 [346] R. D. Ball et al., *A first unbiased global NLO determination of parton distributions and their uncertainties*, Nucl. Phys.
10001 **B838** (2010) 136–206, [arXiv:1002.4407](#) [[hep-ph](#)].
- 10002 [347] J. R. Forshaw, R. Sandapen, and G. Shaw, *Further success of the colour dipole model*, JHEP **11** (2006) 025,
10003 [arXiv:hep-ph/0608161](#).
- 10004 [348] H.-L. Lai, M. Guzzi, J. Huston, Z. Li, P. M. Nadolsky, et al., *New parton distributions for collider physics*, Phys.Rev.
10005 **D82** (2010) 074024, [arXiv:1007.2241](#) [[hep-ph](#)].
- 10006 [349] R. D. Ball and R. K. Ellis, *Heavy quark production at high-energy*, JHEP **05** (2001) 053, [arXiv:hep-ph/0101199](#).

- 10007 [350] S. Marzani, R. D. Ball, V. Del Duca, S. Forte, and A. Vicini, *Higgs production via gluon-gluon fusion with finite top mass beyond next-to-leading order*, Nucl. Phys. **B800** (2008) 127–145, arXiv:0801.2544 [hep-ph].
- 10008
- 10009 [351] S. Marzani, R. D. Ball, V. Del Duca, S. Forte, and A. Vicini, *Finite-top-mass effects in NNLO Higgs production*, Nucl. Phys. Proc. Suppl. **186** (2009) 98–101, arXiv:0809.4934 [hep-ph].
- 10010
- 10011 [352] S. Marzani and R. D. Ball, *High Energy Resummation of Drell-Yan Processes*, Nucl. Phys. **B814** (2009) 246–264, arXiv:0812.3602 [hep-ph].
- 10012
- 10013 [353] S. Marzani and R. D. Ball, *Drell-Yan processes in the high-energy limit*, arXiv:0906.4729 [hep-ph].
- 10014 [354] G. Diana, *High-energy resummation in direct photon production*, Nucl. Phys. **B824** (2010) 154–167, arXiv:0906.4159 [hep-ph].
- 10015
- 10016 [355] G. Diana, J. Rojo, and R. D. Ball, *High energy resummation of direct photon production at hadronic colliders*, Phys.Lett. **B693** (2010) 430–437, arXiv:1006.4250 [hep-ph].
- 10017
- 10018 [356] S. Forte, G. Altarelli, and R. D. Ball, *Can we trust small x resummation?*, Nucl. Phys. Proc. Suppl. **191** (2009) 64–75, arXiv:0901.1294 [hep-ph].
- 10019
- 10020 [357] M. Dittmar et al., *Parton Distributions*, arXiv:0901.2504 [hep-ph].
- 10021 [358] J. Rojo, G. Altarelli, R. D. Ball, and S. Forte, *Towards small x resummed DIS phenomenology*, arXiv:0907.0443 [hep-ph].
- 10022
- 10023 [359] J. Rojo and F. Caola, *Parton distributions and small- x QCD at the Large Hadron Electron Collider*, arXiv:0906.2079 [hep-ph].
- 10024
- 10025 [360] C. Salgado, J. Alvarez-Muniz, F. Arleo, N. Armesto, M. Botje, et al., *Proton-Nucleus Collisions at the LHC: Scientific Opportunities and Requirements*, arXiv:1105.3919 [hep-ph]. * Temporary entry *.
- 10026
- 10027 [361] D. G. d’Enterria, *Quarkonia photoproduction at nucleus colliders*, Nucl.Phys.Proc.Suppl. **184** (2008) 158–162, arXiv:0711.1123 [nucl-ex].
- 10028
- 10029 [362] D. d’Enterria, *Forward jets physics in ATLAS, CMS and LHCb*, arXiv:0911.1273 [hep-ex].
- 10030 [363] R. Ichou and D. d’Enterria, *Sensitivity of isolated photon production at TeV hadron colliders to the gluon distribution in the proton*, Phys.Rev. **D82** (2010) 014015, arXiv:1005.4529 [hep-ph].
- 10031
- 10032 [364] LHCb Collaboration, F. de Lorenzi et al. Proceedings of DIS2010.
- 10033 [365] J. M. Jowett, *The LHC as a Nucleus-Nucleus Collider*, J.Phys.G **G35** (2008) 104028, arXiv:0807.1397 [nucl-ex]. * Temporary entry *.
- 10034
- 10035 [366] P. Quiroga-Arias, J. G. Milhano, and U. A. Wiedemann, *Testing nuclear parton distributions with pA collisions at the TeV scale*, Phys.Rev. **C82** (2010) 034903, arXiv:1002.2537 [hep-ph].
- 10036
- 10037 [367] K. Eskola, V. Kolhinen, and R. Vogt, *Obtaining the nuclear gluon distribution from heavy quark decays to lepton pairs in pA collisions*, Nucl.Phys. **A696** (2001) 729–746, arXiv:hep-ph/0104124 [hep-ph].
- 10038
- 10039 [368] F. Arleo and T. Gousset, *Measuring gluon shadowing with prompt photons at RHIC and LHC*, Phys.Lett. **B660** (2008) 181–187, arXiv:0707.2944 [hep-ph].
- 10040
- 10041 [369] H. Paukkunen and C. A. Salgado, *Constraints for the nuclear parton distributions from Z and W production at the LHC*, JHEP **1103** (2011) 071, arXiv:1010.5392 [hep-ph].
- 10042
- 10043 [370] A. Baltz, G. Baur, D. d’Enterria, L. Frankfurt, F. Gelis, et al., *The Physics of Ultrapерipheral Collisions at the LHC*, Phys.Rept. **458** (2008) 1–171, arXiv:0706.3356 [nucl-ex].
- 10044
- 10045 [371] BRAHMS Collaboration, I. Arsene et al., *On the evolution of the nuclear modification factors with rapidity and centrality in $d + Au$ collisions at $s(NN)^{1/2} = 200$ -GeV*, Phys.Rev.Lett. **93** (2004) 242303, arXiv:nucl-ex/0403005 [nucl-ex].
- 10046
- 10047
- 10048 [372] B. Kopeliovich, J. Nemchik, I. Potashnikova, M. Johnson, and I. Schmidt, *Breakdown of QCD factorization at large Feynman x* , Phys.Rev. **C72** (2005) 054606, arXiv:hep-ph/0501260 [hep-ph].
- 10049
- 10050 [373] STAR Collaboration, E. Braidot, *Suppression of Forward Pion Correlations in $d+Au$ Interactions at STAR*, arXiv:1005.2378 [hep-ph].
- 10051
- 10052 [374] L. Frankfurt and M. Strikman, *Energy losses in the black disc regime and correlation effects in the STAR forward pion production in $d Au$ collisions*, Phys.Lett. **B645** (2007) 412–421, arXiv:nucl-th/0603049 [nucl-th].
- 10053
- 10054 [375] J. L. Albacete and C. Marquet, *Azimuthal correlations of forward di-hadrons in $d+Au$ collisions at RHIC in the Color Glass Condensate*, Phys.Rev.Lett. **105** (2010) 162301, arXiv:1005.4065 [hep-ph].
- 10055
- 10056 [376] PHENIX Collaboration, A. Adare et al., *Suppression of back-to-back hadron pairs at forward rapidity in $d+Au$ Collisions at $\sqrt{s_{NN}} = 200$ GeV*, arXiv:1105.5112 [nucl-ex]. * Temporary entry *.
- 10057
- 10058 [377] F. Arleo et al., *Photon physics in heavy ion collisions at the LHC*, arXiv:hep-ph/0311131.
- 10059 [378] STAR Collaboration, B. Abelev et al., *Three-particle coincidence of the long range pseudorapidity correlation in high energy nucleus-nucleus collisions*, Phys.Rev.Lett. **105** (2010) 022301, arXiv:0912.3977 [hep-ex].
- 10060

- 10061 [379] CMS Collaboration, V. Khachatryan et al., *Observation of Long-Range Near-Side Angular Correlations in Proton-Proton Collisions at the LHC*, JHEP **1009** (2010) 091, [arXiv:1009.4122 \[hep-ex\]](#).
- 10062
- 10063 [380] CMS Collaboration, S. Chatrchyan et al., *Long-range and short-range dihadron angular correlations in central PbPb collisions at a nucleon-nucleon center of mass energy of 2.76 TeV*, [arXiv:1105.2438 \[nucl-ex\]](#). * Temporary entry *.
- 10064
- 10065 [381] A. Dumitru, K. Dusling, F. Gelis, J. Jalilian-Marian, T. Lappi, et al., *The Ridge in proton-proton collisions at the LHC*, Phys.Lett. **B697** (2011) 21–25, [arXiv:1009.5295 \[hep-ph\]](#).
- 10066
- 10067 [382] N. Armesto, *Predictions for the heavy-ion programme at the Large Hadron Collider*, [arXiv:0903.1330 \[hep-ph\]](#).
- 10068 [383] ALICE Collaboration, K. Aamodt et al., *Charged-particle multiplicity density at mid-rapidity in central Pb-Pb collisions at $\sqrt{s_{NN}} = 2.76$ TeV*, Phys.Rev.Lett. **105** (2010) 252301, [arXiv:1011.3916 \[nucl-ex\]](#). * Temporary entry *.
- 10069
- 10070 [384] ALICE Collaboration, J. Nystrand, *Photon-Induced Physics with Heavy-Ion Beams in ALICE*, Nucl.Phys.Proc.Suppl. **179-180** (2008) 156–161, [arXiv:0807.0366 \[nucl-ex\]](#).
- 10071
- 10072 [385] M. Arneodo, *Nuclear effects in structure functions*, Phys. Rept. **240** (1994) 301–393.
- 10073 [386] D. F. Geesaman, K. Saito, and A. W. Thomas, *The nuclear EMC effect*, Ann. Rev. Nucl. Part. Sci. **45** (1995) 337–390.
- 10074 [387] A. Accardi et al., *Hard probes in heavy ion collisions at the lhc: pdfs, shadowing and pa collisions*, [arXiv:hep-ph/0308248](#).
- 10075
- 10076 [388] D. de Florian and R. Sassot, *Nuclear parton distributions at next to leading order*, Phys. Rev. **D69** (2004) 074028, [arXiv:hep-ph/0311227](#).
- 10077
- 10078 [389] M. Hirai, S. Kumano, and T. H. Nagai, *Determination of nuclear parton distribution functions and their uncertainties at next-to-leading order*, Phys. Rev. **C76** (2007) 065207, [arXiv:0709.3038 \[hep-ph\]](#).
- 10079
- 10080 [390] V. Guzey and M. Strikman, *Color fluctuation approximation for multiple interactions in leading twist theory of nuclear shadowing*, Phys. Lett. **B687** (2010) 167–173, [arXiv:0908.1149 \[hep-ph\]](#).
- 10081
- 10082 [391] K. J. Eskola, V. J. Kolhinen, and C. A. Salgado, *The scale dependent nuclear effects in parton distributions for practical applications*, Eur. Phys. J. **C9** (1999) 61–68, [arXiv:hep-ph/9807297](#).
- 10083
- 10084 [392] K. Kovarik, I. Schienbein, F. Olness, J. Yu, C. Keppel, et al., *Nuclear corrections in neutrino-nucleus DIS and their compatibility with global NPDF analyses*, Phys.Rev.Lett. **106** (2011) 122301, [arXiv:1012.0286 \[hep-ph\]](#).
- 10085
- 10086 [393] H. Paukkunen and C. A. Salgado, *Compatibility of neutrino DIS data and global analyses of parton distribution functions*, JHEP **07** (2010) 032, [arXiv:1004.3140 \[hep-ph\]](#).
- 10087
- 10088 [394] A. Accardi et al., *Hard probes in heavy ion collisions at the LHC: Jet physics*, [arXiv:hep-ph/0310274](#).
- 10089 [395] M. Bedjidian et al., *Hard probes in heavy ion collisions at the LHC: Heavy flavor physics*, [arXiv:hep-ph/0311048](#).
- 10090 [396] M. Gyulassy and L. McLerran, *New forms of QCD matter discovered at RHIC*, Nucl. Phys. **A750** (2005) 30–63, [arXiv:nucl-th/0405013](#).
- 10091
- 10092 [397] D. G. d’Enterria, *Quark-gluon matter*, J. Phys. **G34** (2007) S53–S82, [arXiv:nucl-ex/0611012](#).
- 10093 [398] T. Lappi, *Initial conditions of heavy ion collisions and high energy factorization*, Acta Phys. Polon. **B40** (2009) 1997–2012, [arXiv:0904.1670 \[hep-ph\]](#).
- 10094
- 10095 [399] A. Accardi, F. Arleo, W. K. Brooks, D. D’Enterria, and V. Muccifora, *Parton Propagation and Fragmentation in QCD Matter*, Riv. Nuovo Cim. **032** (2010) 439–553, [arXiv:0907.3534 \[nucl-th\]](#).
- 10096
- 10097 [400] ALICE Collaboration, K. Aamodt et al., *Suppression of Charged Particle Production at Large Transverse Momentum in Central Pb–Pb Collisions at $\sqrt{s_{NN}} = 2.76$ TeV*, Phys.Lett. **B696** (2011) 30–39, [arXiv:1012.1004 \[nucl-ex\]](#). * Temporary entry *.
- 10098
- 10099
- 10100 [401] Atlas Collaboration, G. Aad et al., *Observation of a Centrality-Dependent Dijet Asymmetry in Lead-Lead Collisions at $\sqrt{s(NN)} = 2.76$ TeV with the ATLAS Detector at the LHC*, Phys.Rev.Lett. **105** (2010) 252303, [arXiv:1011.6182 \[hep-ex\]](#). * Temporary entry *.
- 10101
- 10102
- 10103 [402] CMS Collaboration, S. Chatrchyan et al., *Observation and studies of jet quenching in PbPb collisions at nucleon-nucleon center-of-mass energy = 2.76 TeV*, [arXiv:1102.1957 \[nucl-ex\]](#). * Temporary entry *.
- 10104
- 10105 [403] The NNPDF Collaboration, R. D. Ball et al., *Precision determination of electroweak parameters and the strange content of the proton from neutrino deep-inelastic scattering*, Nucl. Phys. **B823** (2009) 195–233, [arXiv:0906.1958 \[hep-ph\]](#).
- 10106
- 10107 [404] K. Golec-Biernat and A. M. Stasto, *F_L proton structure function from the unified DGLAP/BFKL approach*, Phys. Rev. **D80** (2009) 014006, [arXiv:0905.1321 \[hep-ph\]](#).
- 10108
- 10109 [405] J. L. Albacete, N. Armesto, J. G. Milhano, and C. A. Salgado, *Non-linear QCD meets data: A global analysis of lepton-proton scattering with running coupling BK evolution*, Phys. Rev. **D80** (2009) 034031, [arXiv:0902.1112 \[hep-ph\]](#).
- 10110
- 10111 [406] The NNPDF Collaboration, and others, *Reweighting NNPDFs: the W lepton asymmetry*, [arXiv:1012.0836 \[hep-ph\]](#).
- 10112 [407] NNPDF Collaboration, R. D. Ball et al., *A determination of parton distributions with faithful uncertainty estimation*, Nucl. Phys. **B809** (2009) 1–63, [arXiv:0808.1231 \[hep-ph\]](#).
- 10113
- 10114 [408] J. Jowett. Private communication.

- 10115 [409] N. Armesto, *A simple model for nuclear structure functions at small x in the dipole picture*, Eur. Phys. J. **C26** (2002)
10116 35–43, [arXiv:hep-ph/0206017](#).
- 10117 [410] PHENIX Collaboration, S. S. Adler et al., *Centrality dependence of π^0 and eta production at large transverse
10118 momentum in $s(NN)^{1/2} = 200\text{-GeV } d + Au$ collisions*, Phys. Rev. Lett. **98** (2007) 172302,
10119 [arXiv:nucl-ex/0610036](#).
- 10120 [411] S. J. Brodsky, I. Schmidt, and J.-J. Yang, *Nuclear antishadowing in neutrino deep inelastic scattering*, Phys.Rev. **D70**
10121 (2004) 116003, [arXiv:hep-ph/0409279](#) [hep-ph].
- 10122 [412] E. R. Cazaroto, F. Carvalho, V. P. Goncalves, and F. S. Navarra, *Constraining the nuclear gluon distribution in eA
10123 processes at RHIC*, Phys. Lett. **B669** (2008) 331–336, [arXiv:0804.2507](#) [hep-ph].
- 10124 [413] N. Armesto, H. Paukkunen, C. A. Salgado, and K. Tywoniuk, *Nuclear effects on the longitudinal structure function at
10125 small x* , Phys.Lett. **B694** (2010) 38–43, [arXiv:1005.2035](#) [hep-ph].
- 10126 [414] A. Bruni, X. Janssen, and P. Marage, *Exclusive Vector Meson Production and Deeply Virtual Compton Scattering at
10127 HERA*, Proceedings of the HERA-LHC Workshops, 2006-8, eds. Jung, de Roeck, DESY-PROC-2009-02 (2009) 427,
10128 2009.
- 10129 [415] A. D. Martin, C. Nockles, M. G. Ryskin, and T. Teubner, *Small x gluon from exclusive J/ψ production*, Phys. Lett.
10130 **B662** (2008) 252–258, [arXiv:0709.4406](#) [hep-ph].
- 10131 [416] A. Caldwell and H. Kowalski, *Investigating the gluonic structure of nuclei via J/ψ scattering*, Phys. Rev. **C81** (2010)
10132 025203.
- 10133 [417] S. Munier, A. M. Stasto, and A. H. Mueller, *Impact parameter dependent S -matrix for dipole proton scattering from
10134 diffractive meson electroproduction*, Nucl. Phys. **B603** (2001) 427–445, [arXiv:hep-ph/0102291](#).
- 10135 [418] K. Goeke, M. V. Polyakov, and M. Vanderhaeghen, *Hard Exclusive Reactions and the Structure of Hadrons*, Prog. Part.
10136 Nucl. Phys. **47** (2001) 401–515, [arXiv:hep-ph/0106012](#).
- 10137 [419] M. Diehl, *Generalized parton distributions*, Phys. Rept. **388** (2003) 41–277, [arXiv:hep-ph/0307382](#).
- 10138 [420] S. J. Brodsky, L. Frankfurt, J. F. Gunion, A. H. Mueller, and M. Strikman, *Diffractive leptonproduction of vector mesons
10139 in QCD*, Phys. Rev. **D50** (1994) 3134–3144, [arXiv:hep-ph/9402283](#).
- 10140 [421] J. C. Collins, L. Frankfurt, and M. Strikman, *Factorization for hard exclusive electroproduction of mesons in QCD*,
10141 Phys. Rev. **D56** (1997) 2982–3006, [arXiv:hep-ph/9611433](#).
- 10142 [422] M. Burkardt, *Impact parameter dependent parton distributions and off- forward parton distributions for zeta $\rightarrow 0$* ,
10143 Phys. Rev. **D62** (2000) 071503, [arXiv:hep-ph/0005108](#).
- 10144 [423] T. Rogers, V. Guzey, M. Strikman, and X. Zu, *Determining the proximity of gamma* N scattering to the black body
10145 limit using DIS and J/ψ production*, Phys. Rev. **D69** (2004) 074011, [arXiv:hep-ph/0309099](#).
- 10146 [424] H. Kowalski, T. Lappi, and R. Venugopalan, *Nuclear enhancement of universal dynamics of high parton densities*,
10147 Phys. Rev. Lett. **100** (2008) 022303, [arXiv:0705.3047](#) [hep-ph].
- 10148 [425] L. Frankfurt, M. Strikman, and C. Weiss, *Dijet production as a centrality trigger for pp collisions at CERN LHC*,
10149 Phys. Rev. **D69** (2004) 114010, [arXiv:hep-ph/0311231](#).
- 10150 [426] H1 Collaboration, F. D. Aaron et al., *Diffractive Dijet Photoproduction in ep Collisions at HERA*, Eur. Phys. J. **C70**
10151 (2010) 15–37, [arXiv:1006.0946](#) [hep-ex].
- 10152 [427] L. Frankfurt, C. E. Hyde, M. Strikman, and C. Weiss, *Generalized parton distributions and rapidity gap survival in
10153 exclusive diffractive pp scattering*, Phys. Rev. **D75** (2007) 054009, [arXiv:hep-ph/0608271](#).
- 10154 [428] M. Deile et al., *13th International Conference on Elastic and Diffractive Scattering (Blois Workshop) - Moving
10155 Forward into the LHC Era*, [arXiv:1002.3527](#) [hep-ph].
- 10156 [429] ZEUS Collaboration, S. Chekanov et al., *Exclusive electroproduction of J/ψ mesons at HERA*, Nucl. Phys. **B695**
10157 (2004) 3–37, [arXiv:hep-ex/0404008](#).
- 10158 [430] H1 Collaboration, A. Aktas et al., *Elastic J/ψ production at HERA*, Eur. Phys. J. **C46** (2006) 585–603,
10159 [arXiv:hep-ex/0510016](#).
- 10160 [431] H1 Collaboration, F. D. Aaron et al., *Measurement of Deeply Virtual Compton Scattering and its t -dependence at
10161 HERA*, Phys. Lett. **B659** (2008) 796–806, [arXiv:0709.4114](#) [hep-ex].
- 10162 [432] ZEUS Collaboration, S. Chekanov et al., *A measurement of the Q^2 , W and t dependences of deeply virtual Compton
10163 scattering at HERA*, JHEP **05** (2009) 108, [arXiv:0812.2517](#) [hep-ex].
- 10164 [433] C. Marquet and B. Wu, *Exclusive vs. diffractive vector meson production in DIS at small x or off nuclei*,
10165 [arXiv:0908.4180](#) [hep-ph].
- 10166 [434] T. Lappi and H. Mantysaari, *Incoherent diffractive J/ψ -production in high energy nuclear DIS*, (2010) ,
10167 [arXiv:1011.1988](#) [hep-ph].
- 10168 [435] W. Horowitz, *Measuring the Gluon Density in $e + A$ Collisions: KLN CGC, DGLAP Glauber, or Neither?*,
10169 [arXiv:1102.5058](#) [hep-ph]. * Temporary entry *.

- 10170 [436] L. Frankfurt, M. Strikman, D. Treleani, and C. Weiss, *Evidence for color fluctuations in the nucleon in high- energy*
10171 *scattering*, Phys. Rev. Lett. **101** (2008) 202003, arXiv:0808.0182 [hep-ph].
- 10172 [437] J. Bartels, K. J. Golec-Biernat, and K. Peters, *On the dipole picture in the nonforward direction*, Acta Phys. Polon.
10173 **B34** (2003) 3051–3068, arXiv:hep-ph/0301192.
- 10174 [438] C. Marquet, R. B. Peschanski, and G. Soyez, *Exclusive vector meson production at HERA from QCD with saturation*,
10175 Phys.Rev. **D76** (2007) 034011, arXiv:hep-ph/0702171 [HEP-PH].
- 10176 [439] M. G. Ryskin, *Diffraction J / psi electroproduction in LLA QCD*, Z. Phys. **C57** (1993) 89–92.
- 10177 [440] P. Newman, *Low x and Diffractive Physics at a Large Hadron electron Collider*, . In Proceedings of the 13th
10178 International (Blois) Conference on Elastic and Diffractive Scattering, EDS'09, CERN, 2009, p182.
- 10179 [441] B. List and A. Mastroberardino, *DIFVIM: A Monte Carlo generator for diffractive processes in ep scattering*,
10180 Proceedings of the Workshop on Monte Carlo Generators for HERA Physics, DESY-PROC-1992-02 (1999) 396, 1999.
- 10181 [442] J. R. Forshaw, R. Sandapen, and G. Shaw, *Colour dipoles and rho, Phi electroproduction*, Phys. Rev. **D69** (2004)
10182 094013, arXiv:hep-ph/0312172.
- 10183 [443] ZEUS Collaboration, S. Chekanov et al., *Exclusive photoproduction of J/psi mesons at HERA*, Eur. Phys. J. **C24**
10184 (2002) 345–360, arXiv:hep-ex/0201043.
- 10185 [444] ZEUS Collaboration, J. Breitweg et al., *Measurement of elastic Upsilon photoproduction at HERA*, Phys. Lett. **B437**
10186 (1998) 432–444, arXiv:hep-ex/9807020.
- 10187 [445] H1 Collaboration, C. Adloff et al., *Elastic photoproduction of J/psi and Upsilon mesons at HERA*, Phys. Lett. **B483**
10188 (2000) 23–35, arXiv:hep-ex/0003020.
- 10189 [446] ZEUS Collaboration, S. Chekanov et al., *Exclusive photoproduction of upsilon mesons at HERA*, Phys. Lett. **B680**
10190 (2009) 4–12, arXiv:0903.4205 [hep-ex].
- 10191 [447] B. E. Cox, J. R. Forshaw, and R. Sandapen, *Diffractive upsilon production at the LHC*, JHEP **06** (2009) 034,
10192 arXiv:0905.0102 [hep-ph].
- 10193 [448] E. Perez, L. Schoeffel, and L. Favart, *MILOU: A Monte-Carlo for deeply virtual Compton scattering*,
10194 arXiv:hep-ph/0411389 [hep-ph].
- 10195 [449] L. Frankfurt, A. Freund, and M. Strikman, *Diffractive exclusive photoproduction in DIS at HERA*, Phys.Rev. **D58**
10196 (1998) 114001, arXiv:hep-ph/9710356 [hep-ph].
- 10197 [450] H1 Collaboration, F. Aaron et al., *Deeply Virtual Compton Scattering and its Beam Charge Asymmetry in e+-*
10198 *Collisions at HERA*, Phys.Lett. **B681** (2009) 391–399, arXiv:arXiv:0907.5289 [hep-ex].
- 10199 [451] Fermilab Tagged Photon Spectrometer Collaboration, M. D. Sokoloff et al., *An Experimental Study of the a-Dependence*
10200 *of J/psi Photoproduction*, Phys. Rev. Lett. **57** (1986) 3003.
- 10201 [452] E665 Collaboration, M. R. Adams et al., *Measurement of nuclear transparencies from exclusive rho0 meson production*
10202 *in muon - nucleus scattering at 470-GeV*, Phys. Rev. Lett. **74** (1995) 1525–1529.
- 10203 [453] L. Frankfurt, V. Guzey, and M. Strikman, *Leading twist nuclear shadowing phenomena in hard processes with nuclei*,
10204 arXiv:1106.2091 [hep-ph].
- 10205 [454] B. Nicolescu, *Recent advances in odderon physics*, arXiv:hep-ph/9911334 [hep-ph].
- 10206 [455] C. Ewerz, *The Odderon in quantum chromodynamics*, arXiv:hep-ph/0306137 [hep-ph].
- 10207 [456] J. Bartels, *High-Energy Behavior in a Nonabelian Gauge Theory. 1. T(n,m) in the Leading Log Normal S*
10208 *Approximation*, Nucl.Phys. **B151** (1979) 293.
- 10209 [457] J. Bartels, *High-Energy Behavior in a Nonabelian Gauge Theory. 2. First Corrections to T(n,m) Beyond the Leading*
10210 *LNS Approximation*, Nucl.Phys. **B175** (1980) 365.
- 10211 [458] J. Kwiecinski and M. Praszalowicz, *Three Gluon Integral Equation and Odd c Singlet Regge Singularities in QCD*,
10212 Phys.Lett. **B94** (1980) 413.
- 10213 [459] R. Janik and J. Wosiek, *Solution of the odderon problem*, Phys.Rev.Lett. **82** (1999) 1092–1095, arXiv:hep-th/9802100
10214 [hep-th].
- 10215 [460] J. Bartels, L. Lipatov, and G. Vacca, *A New odderon solution in perturbative QCD*, Phys.Lett. **B477** (2000) 178–186,
10216 arXiv:hep-ph/9912423 [hep-ph].
- 10217 [461] H1 Collaboration, C. Adloff et al., *Search for odderon induced contributions to exclusive pi0 photoproduction at HERA*,
10218 Phys.Lett. **B544** (2002) 35–43, arXiv:hep-ex/0206073 [hep-ex].
- 10219 [462] J. Czyzewski, J. Kwiecinski, L. Motyka, and M. Sadzikowski, *Exclusive eta(c) photoproduction and electroproduction at*
10220 *HERA as a possible probe of the odderon singularity in QCD*, Phys.Lett. **B398** (1997) 400–406, arXiv:hep-ph/9611225
10221 [hep-ph].
- 10222 [463] S. J. Brodsky, J. Rathsman, and C. Merino, *Odderon-Pomeron interference*, Phys.Lett. **B461** (1999) 114–122,
10223 arXiv:hep-ph/9904280 [hep-ph].

- 10224 [464] A. Kaidalov, *Diffraction Production Mechanisms*, Phys.Rept. **50** (1979) 157–226.
- 10225 [465] K. A. Goulianos, *Diffraction Interactions of Hadrons at High-Energies*, Phys. Rept. **101** (1983) 169.
- 10226 [466] G. Ingelman and P. E. Schlein, *Jet Structure in High Mass Diffraction Scattering*, Phys. Lett. **B152** (1985) 256.
- 10227 [467] A. Donnachie and P. V. Landshoff, *Diffraction Deep Inelastic Lepton Scattering*, Phys. Lett. **B191** (1987) 309.
- 10228 [468] G. Wolf, *Review of High Energy Diffraction in Real and Virtual Photon Proton scattering at HERA*, Rept. Prog. Phys. **73** (2010) 116202, arXiv:0907.1217 [hep-ex].
- 10230 [469] H1 Collaboration, A. Aktas et al., *Diffraction deep-inelastic scattering with a leading proton at HERA*, Eur. Phys. J. **C48** (2006) 749–766, arXiv:hep-ex/0606003.
- 10232 [470] ZEUS Collaboration, S. Chekanov et al., *Deep inelastic scattering with leading protons or large rapidity gaps at HERA*, Nucl. Phys. **B816** (2009) 1–61, arXiv:0812.2003 [hep-ex].
- 10234 [471] F. Aaron et al., *Measurement of the Diffraction Deep-Inelastic Scattering Cross Section with a Leading Proton at HERA*, arXiv:1010.1476 [hep-ex].
- 10236 [472] H1 Collaboration, A. Aktas et al., *Measurement and QCD analysis of the diffraction deep- inelastic scattering cross-section at HERA*, Eur. Phys. J. **C48** (2006) 715–748, arXiv:hep-ex/0606004.
- 10238 [473] J. Blumlein and D. Robaschik, *On the scaling violations of diffraction structure functions: Operator approach*, Phys. Lett. **B517** (2001) 222–232, arXiv:hep-ph/0106037.
- 10240 [474] H1 Collaboration, A. Aktas et al., *Dijet Cross Sections and Parton Densities in Diffraction DIS at HERA*, JHEP **10** (2007) 042, arXiv:0708.3217 [hep-ex].
- 10242 [475] ZEUS Collaboration, S. Chekanov et al., *A QCD analysis of ZEUS diffraction data*, Nucl. Phys. **B831** (2010) 1–25, arXiv:0911.4119 [hep-ex].
- 10244 [476] A. D. Martin, M. G. Ryskin, and G. Watt, *Diffraction parton distributions from perturbative QCD*, Eur. Phys. J. **C44** (2005) 69–85, arXiv:hep-ph/0504132.
- 10246 [477] H1 Collaboration, A. Aktas et al., *Tests of QCD factorisation in the diffraction production of dijets in deep-inelastic scattering and photoproduction at HERA*, Eur. Phys. J. **C51** (2007) 549–568, arXiv:hep-ex/0703022.
- 10248 [478] H1 Collaboration, A. Aktas et al., *Diffraction open charm production in deep-inelastic scattering and photoproduction at HERA*, Eur. Phys. J. **C50** (2007) 1–20, arXiv:hep-ex/0610076.
- 10250 [479] P. Newman, *Deep Inelastic Scattering at the TeV Energy Scale and the LHeC Project*, Nucl. Phys. Proc. Suppl. **191** (2009) 307–319, arXiv:0902.2292 [hep-ex].
- 10252 [480] J. Bartels, J. R. Ellis, H. Kowalski, and M. Wusthoff, *An analysis of diffraction in deep-inelastic scattering*, Eur. Phys. J. **C7** (1999) 443–458, arXiv:hep-ph/9803497.
- 10254 [481] H. Collaboration, *Measurement of the Diffraction Longitudinal Structure Function at HERA*, . in litt.
- 10255 [482] H1 Collaboration, F. D. Aaron et al., *Measurement of Leading Neutron Production in Deep- Inelastic Scattering at HERA*, Eur. Phys. J. **C68** (2010) 381–399, arXiv:1001.0532 [hep-ex].
- 10257 [483] G. Watt and H. Kowalski, *Impact parameter dependent colour glass condensate dipole model*, Phys. Rev. **D78** (2008) 014016, arXiv:0712.2670 [hep-ph].
- 10259 [484] V. A. Abramovsky, V. N. Gribov, and O. V. Kancheli, *CHARACTER OF INCLUSIVE SPECTRA AND FLUCTUATIONS PRODUCED IN INELASTIC PROCESSES BY MULTI - POMERON EXCHANGE*, Yad. Fiz. **18** (1973) 595–616.
- 10262 [485] L. Frankfurt and M. Strikman, *Diffraction at HERA, color opacity and nuclear shadowing*, Eur. Phys. J. **A5** (1999) 293–306, arXiv:hep-ph/9812322.
- 10264 [486] L. Frankfurt, V. Guzey, and M. Strikman, *Leading twist nuclear shadowing: A user’s guide*, Phys. Rev. **D71** (2005) 054001, arXiv:hep-ph/0303022.
- 10266 [487] H. Abramowicz, L. Frankfurt, and M. Strikman, *Interplay of hard and soft physics in small x deep inelastic processes*, ECONF **C940808** (1994) 033, arXiv:hep-ph/9503437.
- 10268 [488] N. Armesto, A. Capella, A. Kaidalov, J. Lopez-Albacete, and C. Salgado, *Nuclear structure functions at small x from inelastic shadowing and diffraction*, Eur.Phys.J. **C29** (2003) 531–540, arXiv:hep-ph/0304119 [hep-ph].
- 10270 [489] K. Tywoniuk, I. Arsene, L. Bravina, A. Kaidalov, and E. Zabrodin, *Gluon shadowing in the Glauber-Gribov model at HERA*, Phys. Lett. **B657** (2007) 170–175, arXiv:0705.1596 [hep-ph].
- 10272 [490] L. Frankfurt, V. Guzey, and M. Strikman, *Leading twist coherent diffraction on nuclei in deep inelastic scattering at small x and nuclear shadowing*, Phys. Lett. **B586** (2004) 41–52, arXiv:hep-ph/0308189.
- 10274 [491] C. Marquet, *A Unified description of diffraction deep inelastic scattering with saturation*, Phys.Rev. **D76** (2007) 094017, arXiv:0706.2682 [hep-ph].
- 10276 [492] H. Kowalski, T. Lappi, C. Marquet, and R. Venugopalan, *Nuclear enhancement and suppression of diffraction structure functions at high energies*, Phys. Rev. **C78** (2008) 045201, arXiv:0805.4071 [hep-ph].

- 10278 [493] J. Collins and H. Jung, *Need for fully unintegrated parton densities*, arXiv:hep-ph/0508280.
- 10279 [494] J. C. Collins and D. E. Soper, *Back-To-Back Jets in QCD*, Nucl. Phys. **B193** (1981) 381.
- 10280 [495] J. C. Collins and D. E. Soper, *Parton Distribution and Decay Functions*, Nucl. Phys. **B194** (1982) 445.
- 10281 [496] J. C. Collins, *What exactly is a parton density?*, Acta Phys. Polon. **B34** (2003) 3103, arXiv:hep-ph/0304122.
- 10282 [497] J. Collins, *Rapidity divergences and valid definitions of parton densities*, PoS **LC2008** (2008) 028, arXiv:0808.2665 [hep-ph].
- 10284 [498] X.-d. Ji, J.-p. Ma, and F. Yuan, *QCD factorization for semi-inclusive deep-inelastic scattering at low transverse momentum*, Phys. Rev. **D71** (2005) 034005, arXiv:hep-ph/0404183.
- 10286 [499] M. Ciafaloni, *Coherence Effects in Initial Jets at Small q^2/s* , Nucl. Phys. **B296** (1988) 49.
- 10287 [500] S. Catani, F. Fiorani, and G. Marchesini, *QCD Coherence in Initial State Radiation*, Phys.Lett. **B234** (1990) 339.
- 10288 [501] S. Catani, F. Fiorani, and G. Marchesini, *Small x Behavior of Initial State Radiation in Perturbative QCD*, Nucl.Phys. **B336** (1990) 18.
- 10290 [502] G. Marchesini, *QCD coherence in the structure function and associated distributions at small x* , Nucl.Phys. **B445** (1995) 49–80, arXiv:hep-ph/9412327 [hep-ph].
- 10291
- 10292 [503] I. Balitsky, *High-energy QCD and Wilson lines*, arXiv:hep-ph/0101042.
- 10293 [504] J. C. Collins, *Foundations of Perturbative QCD*. Cambridge University Press, Cambridge, 2011. To be published.
- 10294 [505] S. Aybat and T. C. Rogers, *TMD Parton Distribution and Fragmentation Functions with QCD Evolution*, arXiv:1101.5057 [hep-ph]. * Temporary entry *.
- 10295
- 10296 [506] J. C. Collins and A. Metz, *Universality of soft and collinear factors in hard-scattering factorization*, Phys. Rev. Lett. **93** (2004) 252001, arXiv:hep-ph/0403249.
- 10297
- 10298 [507] F. Landry, R. Brock, P. M. Nadolsky, and C. P. Yuan, *Tevatron Run-1 Z boson data and Collins-Soper-Sterman resummation formalism*, Phys. Rev. **D67** (2003) 073016, arXiv:hep-ph/0212159.
- 10299
- 10300 [508] J. C. Collins, D. E. Soper, and G. F. Sterman, *Transverse Momentum Distribution in Drell-Yan Pair and W and Z Boson Production*, Nucl. Phys. **B250** (1985) 199.
- 10301
- 10302 [509] C. Marquet, B.-W. Xiao, and F. Yuan, *Semi-inclusive Deep Inelastic Scattering at small x* , Phys. Lett. **B682** (2009) 207–211, arXiv:0906.1454 [hep-ph].
- 10303
- 10304 [510] F. Dominguez, B.-W. Xiao, and F. Yuan, *kt-factorization for Hard Processes in Nuclei*, Phys. Rev. Lett. **106** (2011) 022301, arXiv:1009.2141 [hep-ph].
- 10305
- 10306 [511] H1 Collaboration, A. Aktas et al., *Inclusive dijet production at low Bjorken- x in deep inelastic scattering*, Eur. Phys. J. **C33** (2004) 477–493, arXiv:hep-ex/0310019.
- 10307
- 10308 [512] A. J. Askew, D. Graudenz, J. Kwiecinski, and A. D. Martin, *Dijet production at HERA as a probe of BFKL dynamics*, Phys. Lett. **B338** (1994) 92–97, arXiv:hep-ph/9407337.
- 10309
- 10310 [513] J. Kwiecinski, A. D. Martin, and A. M. Stasto, *Predictions for dijet production in DIS using small x dynamics*, Phys. Lett. **B459** (1999) 644–648, arXiv:hep-ph/9904402.
- 10311
- 10312 [514] A. Szczurek, N. N. Nikolaev, W. Schafer, and J. Speth, *Mapping the proton unintegrated gluon distribution in dijets correlations in real and virtual photoproduction at HERA*, Phys. Lett. **B500** (2001) 254–262, arXiv:hep-ph/0011281.
- 10313
- 10314 [515] M. Hansson and H. Jung, *Towards precision determination of uPDFs*, arXiv:0707.4276 [hep-ph].
- 10315 [516] F. Hautmann and H. Jung, *Angular correlations in multi-jet final states from kt-dependent parton showers*, JHEP **10** (2008) 113, arXiv:0805.1049 [hep-ph].
- 10316
- 10317 [517] J. Bartels, C. Ewerz, H. Lotter, and M. Wusthoff, *Azimuthal distribution of quark - anti-quark jets in DIS diffractive dissociation*, Phys.Lett. **B386** (1996) 389–396, arXiv:hep-ph/9605356 [hep-ph].
- 10318
- 10319 [518] J. Bartels, H. Jung, and M. Wusthoff, *Quark - anti-quark gluon jets in DIS diffractive dissociation*, Eur.Phys.J. **C11** (1999) 111–125, arXiv:hep-ph/9903265 [hep-ph].
- 10320
- 10321 [519] L. Lonnblad, *ARIADNE version 4: A Program for simulation of QCD cascades implementing the color dipole model*, Comput.Phys.Commun. **71** (1992) 15–31.
- 10322
- 10323 [520] H. Jung et al., *The CCFM Monte Carlo generator CASCADE 2.2.0*, Eur. Phys. J. **C70** (2010) 1237–1249, arXiv:1008.0152 [hep-ph].
- 10324
- 10325 [521] A. H. Mueller, *Parton distributions at very small x values*, Nucl. Phys. Proc. Suppl. **18C** (1991) 125–132.
- 10326 [522] A. H. Mueller, *Jets at LEP and HERA*, J. Phys. **G17** (1991) 1443–1454.
- 10327 [523] H1 Collaboration, S. Aid et al., *Transverse energy and forward jet production in the low x regime at HERA*, Phys. Lett. **B356** (1995) 118–128, arXiv:hep-ex/9506012.
- 10328
- 10329 [524] H1 Collaboration, C. Adloff et al., *Forward jet and particle production at HERA*, Nucl. Phys. **B538** (1999) 3–22, arXiv:hep-ex/9809028.
- 10330

- 10331 [525] H1 Collaboration, A. Aktas et al., *Forward jet production in deep inelastic scattering at HERA*, Eur. Phys. J. **C46**
10332 (2006) 27–42, [arXiv:hep-ex/0508055](#).
- 10333 [526] ZEUS Collaboration, J. Breitweg et al., *Forward jet production in deep inelastic scattering at HERA*, Eur. Phys. J. **C6**
10334 (1999) 239–252, [arXiv:hep-ex/9805016](#).
- 10335 [527] ZEUS Collaboration, J. Breitweg et al., *Measurement of the $E(T, \text{jet})^{**2}/Q^{**2}$ dependence of forward- jet production at*
10336 *HERA*, Phys. Lett. **B474** (2000) 223–233, [arXiv:hep-ex/9910043](#).
- 10337 [528] ZEUS Collaboration, S. Chekanov et al., *Forward jet production in deep inelastic $e p$ scattering and low- x parton*
10338 *dynamics at HERA*, Phys. Lett. **B632** (2006) 13–26, [arXiv:hep-ex/0502029](#).
- 10339 [529] J. Kwiecinski, S. C. Lang, and A. D. Martin, *Single particle spectra in deep inelastic scattering as a probe of small x*
10340 *dynamics*, Eur. Phys. J. **C6** (1999) 671–680, [arXiv:hep-ph/9707240](#).
- 10341 [530] J. Kwiecinski, A. D. Martin, and J. J. Outhwaite, *Small x QCD effects in DIS with a forward jet or a forward π^0* , Eur.
10342 Phys. J. **C9** (1999) 611–622, [arXiv:hep-ph/9903439](#).
- 10343 [531] G. Bottazzi, G. Marchesini, G. P. Salam, and M. Scorletti, *Small- x one-particle-inclusive quantities in the CCFM*
10344 *approach*, JHEP **12** (1998) 011, [arXiv:hep-ph/9810546](#).
- 10345 [532] H. Jung, *CCFM prediction on forward jets and F2: Parton level predictions and a new hadron level Monte Carlo*
10346 *generator CASCADE*, [arXiv:hep-ph/9908497](#).
- 10347 [533] H. Jung, *CCFM prediction for F2 and forward jets at HERA*, Nucl. Phys. Proc. Suppl. **79** (1999) 429–431,
10348 [arXiv:hep-ph/9905554](#).
- 10349 [534] H. Jung and G. P. Salam, *Hadronic final state predictions from CCFM: The hadron- level Monte Carlo generator*
10350 *CASCADE*, Eur. Phys. J. **C19** (2001) 351–360, [arXiv:hep-ph/0012143](#).
- 10351 [535] O. Kepka, C. Royon, C. Marquet, and R. B. Peschanski, *Next-leading BFKL effects in forward-jet production at HERA*,
10352 Phys. Lett. **B655** (2007) 236–240, [arXiv:hep-ph/0609299](#).
- 10353 [536] J. Bartels, V. Del Duca, and M. Wusthoff, *Azimuthal dependence of forward jet production in DIS in the high-energy*
10354 *limit*, Z.Phys. **C76** (1997) 75–79, [arXiv:hep-ph/9610450](#) [[hep-ph](#)].
- 10355 [537] A. Sabio Vera and F. Schwennsen, *Azimuthal decorrelation of forward jets in Deep Inelastic Scattering*, Phys. Rev.
10356 **D77** (2008) 014001, [arXiv:0708.0549](#) [[hep-ph](#)].
- 10357 [538] J. Kwiecinski, A. D. Martin, P. J. Sutton, and K. J. Golec-Biernat, *QCD predictions for the transverse energy flow in*
10358 *deep inelastic scattering in the HERA small x regime*, Phys. Rev. **D50** (1994) 217–225, [arXiv:hep-ph/9403292](#).
- 10359 [539] K. J. Golec-Biernat, J. Kwiecinski, A. D. Martin, and P. J. Sutton, *Transverse energy flow at HERA*, Phys. Lett. **B335**
10360 (1994) 220–225, [arXiv:hep-ph/9405400](#).
- 10361 [540] N. H. Brook et al., *A comparison of deep inelastic scattering Monte Carlo event generators to HERA data*,
10362 [arXiv:hep-ex/9912053](#).
- 10363 [541] G. P. Salam and G. Soyez, *A practical Seedless Infrared-Safe Cone jet algorithm*, JHEP **05** (2007) 086,
10364 [arXiv:0704.0292](#) [[hep-ph](#)].
- 10365 [542] Y. L. Dokshitzer, V. A. Khoze, A. H. Mueller, and S. I. Troyan, *Basics of perturbative QCD*, . Editions Frontieres 1991,
10366 274p.
- 10367 [543] D. de Florian, R. Sassot, and M. Stratmann, *Global analysis of fragmentation functions for pions and kaons and their*
10368 *uncertainties*, Phys.Rev. **D75** (2007) 114010, [arXiv:hep-ph/0703242](#) [[HEP-PH](#)].
- 10369 [544] D. de Florian, R. Sassot, and M. Stratmann, *Global analysis of fragmentation functions for protons and charged*
10370 *hadrons*, Phys.Rev. **D76** (2007) 074033, [arXiv:0707.1506](#) [[hep-ph](#)].
- 10371 [545] A. M. Stasto, *Physics of ultrahigh energy neutrinos*, Int. J. Mod. Phys. **A19** (2004) 317–340, [arXiv:astro-ph/0310636](#).
- 10372 [546] J. K. Becker, *High-energy neutrinos in the context of multimessenger physics*, Phys. Rept. **458** (2008) 173–246,
10373 [arXiv:0710.1557](#) [[astro-ph](#)].
- 10374 [547] E. Zas, *Neutrino Detection with Inclined Air Showers*, New J. Phys. **7** (2005) 130, [arXiv:astro-ph/0504610](#).
- 10375 [548] N. Armesto, C. Merino, G. Parente, and E. Zas, *Charged Current Neutrino Cross Section and Tau Energy Loss at*
10376 *Ultra-High Energies*, Phys. Rev. **D77** (2008) 013001, [arXiv:0709.4461](#) [[hep-ph](#)].
- 10377 [549] K. Hirata and E. Keil, *Barycentre motion of beams due to beam-beam interaction in asymmetric ring colliders*, Nuclear
10378 Instruments and Methods in Physics Research Section A: Accelerators, Spectrometers, Detectors and Associated
10379 Equipment **292** (1990) no. 1, 156 – 168.
10380 <http://www.sciencedirect.com/science/article/B6TJM-470F1H3-M/2/ff1b42fa7c847256a9e6c3245d3335d5>.
- 10381 [550] *Private Communication with Sylvain Weisz*, .
- 10382 [551] R. Appleby, *IRSYN*, (2010) .
- 10383 [552] S. Russenschuck, *Magnet Options for Q1 and Q2 (Ring-Ring and Linac-Ring, 3rd CERN-ECFA-NuPECC Workshop*
10384 *on the LHeC* (2010) .

- 10385 [553] N. Bernard, *Analytic Method to Calculate the Power Produced by Synchrotron Radiation in a Quadrupole Magnet*,
10386 CERN LHeC Note 2 (2010) .
- 10387 [554] H. Wiedemann, *Synchrotron Radiation*, Springer-Verlag Berlin Heidelberg (2003) .
- 10388 [555] I. B. *et al.*, *Study of beam-induced backgrounds in the ZEUS detector from 2002 HERA running*, (2002) .
- 10389 [556] S. Russenschuck, *Private Communication*, (2010) .
- 10390 [557] J. Jowett, *Heavy Ions in 2011 and Beyond*, . Chamonix 2011 Workshop on LHC Performance, Chamonix, France,
10391 CERN-ATS-2011-005.
- 10392 [558] O. S. Bruning, (Ed.) et al., *LHC design report. Vol. I: The LHC main ring*, . CERN-2004-003-V-1.
- 10393 [559] D. Barber and G. Ripken in *Handbook of Accelerator Physics and Engineering*, A. Chao and M. Tigner, eds. World
10394 Scientific, first ed., 2006. third printing.
- 10395 [560] D. Barber et al., *Several articles*, in *Proc. ICFE Workshop on Quantum Aspects of Beam Physics*. World Scientific,
10396 Monterey, CA, USA, 1999.
- 10397 [561] A. Sokolov and I. Ternov Sov. Phys. Dokl. **8** (1964) no. 12, 1203.
- 10398 [562] J. Jackson, *Classical Electrodynamics*. Wiley & Sons, third ed., 1998.
- 10399 [563] Y. Derbenev and A. Kondratenko Sov. Phys. JETP **37** (1973) 968.
- 10400 [564] S. Mane Phys. Rev. **A36** (1987) 105–130.
- 10401 [565] G. Hoffstätter, M. Vogt, and D. Barber Phys. Rev. ST Accel. Beams **11** (1999) no. 2, 114001.
- 10402 [566] D. Barber, G. Hoffstätter, and M. Vogt in *Proc. 14th Int. Spin Physics Symp.* AIP Conf. Proc. 570 (2001), 2000.
- 10403 [567] V. Baier and V. Katkov Sov. Phys. JETP **25** (1967) 944.
- 10404 [568] V. Baier, V. Katkov, and V. Strakhovenko Sov. Phys. JETP **31** (1970) 908.
- 10405 [569] R. Assmann et al. in *Proc. Part. Accel. Conf.*, p. 2999 and page 3002. New York, NY, USA, 1999.
- 10406 [570] D. Barber et al. Phys. Lett. **343B** (1995) 436.
- 10407 [571] S. Mane Nucl.Inst.Meth. **A292** (1990) 52.
- 10408 [572] S. Mane Nucl.Inst.Meth. **A321** (1992) 21.
- 10409 [573] D. Barber. SLICKTRACK is the extended version of SLICK [?] which includes Monte-Carlo spin-orbit tracking using
10410 the mathematical structures of SLICK.
- 10411 [574] D. Barber. SLICK is a thick lens version of SLIM [?] by D.P. Barber using the formalism of [?].
- 10412 [575] B. Montague Physics Reports **113** (1984) .
- 10413 [576] Y. Derbenev and H. Grote Tech. Rep. SL/Note 95-37, CERN, 1995.
- 10414 [577] V. Litvinenko, *LHeC with 100% Energy Recovery Linac*, 2nd CERN-ECFA-NuPECC Workshop on the LHeC,
10415 Divonne-les-Bains, 1–3 September 2009 (2009) .
- 10416 [578] P. Grosse-Wiesmann, *Colliding a Linear Electron Beam with a Storage Ring Beam*, NIM A **274** (1989) 21.
- 10417 [579] F. Ruggiero and F. Zimmermann, *Luminosity Optimization near the Beam-Beam Limit by Increasing Bunch Length or*
10418 *Crossing Angle*, PRST-AB **5** (2002) 061101.
- 10419 [580] F. Zimmermann et al., *Linac-LHC ep Collider Options*, Proc. EPAC’08 Genoa (2008) 2847–2849.
- 10420 [581] D. Schulte, *LHeC Ring-Linac Lattice and Beam Dynamics*, 3rd CERN-ECFA-NuPECC LHeC Workshop
10421 Chavannes-de-Bogis, December 2010 (2010) .
- 10422 [582] F. Zimmermann, K. Thompson, and R. Helm, *Electron-Electron Luminosity in the Next Linear Collider*,
10423 Int. J. Mod. Phys. A **13** (1998) 2443–2454.
- 10424 [583] H. Braun et al., *CLIC 2008 Parameters*, CLIC-Note-764 (2008) .
- 10425 [584] N. Phinney, N. Toge, and N. Walker, *LC Reference Design Report Volume 3 - Accelerator*, (2007) , [arXiv:0712.2361](#)
10426 [[physics.acc-ph](#)].
- 10427 [585] F. Gerigk et al., *Conceptual Design of the SPL II*, CRN-2006-006 (2006) .
- 10428 [586] C. Mayes and G. Hoffstaetter, *Cornell Energy Recovery Linac Lattice and Layout*, Proc. IPAC’10 Kyoto (2010) .
- 10429 [587] G. Neil, *Free Electron Lasers from THz to X-rays*, Invited Talk at UPHUK4, Bodrum, Turkey, 30 August 2010 (2010) .
- 10430 [588] Linnecar, T. and Tückmantel, J., , Private communication, 28 May 2008 (2008) .
- 10431 [589] O. Napoly, , Private communication, 6th EuCARD Steering Meeting, Malta, 12–13 October 2010. (2010) .
- 10432 [590] E. Ciapala, *RF for the LHeC*, 3rd CERN-ECFA-NuPECC LHeC Workshop Chavannes-de-Bogis, December 2010 (2010)
10433 .
- 10434 [591] J. Tuckmantel, , Comment at 2nd RFTech meeting, PSI, Villigen, 2–3 December 2010 (2010) .

- 10435 [592] V. Litvinenko and I. Ben-Zvi, , Private communications (2010) .
- 10436 [593] I. Ben-Zvi, , Private communications, 16 November 2010 (2010) .
- 10437 [594] D. Tommasini, *RR+RL Magnets*, 3rd CERN-ECFA-NuPECC LHeC Workshop Chavannes-de-Bogis, December 2010
10438 (2010) .
- 10439 [595] J. Skrabacz, *Optimizing Cost and Minimizing Energy Loss in the Recirculating Race-Track Design of the LHeC
10440 Electron Linac*, CERN-AB-Note-2008-043 (2008) .
- 10441 [596] A. Bogacz, *LHeC Recirculator with Energy Recovery – Beam Optics Choices*, JLAB-TN-10-040 (2010) .
- 10442 [597] D. Schulte and F. Zimmermann, , Private discussions (2010) .
- 10443 [598] D. Schulte, , Private communication (2010) .
- 10444 [599] D. Schulte and F. Zimmermann, *QCD Explorer Based on LHC and CLIC-1*, Proc. EPAC'04, Lucerne,
10445 CERN-AB-2004-079, and CLIC Note 608 (2004) .
- 10446 [600] K. Ohmi, R. Calaga, W. Hofle, R. Tomas, and F. Zimmermann, *Beam-Beam Effects with External Noise in LHC*,
10447 Proc. PAC07, Albuquerque (2007) 1496.
- 10448 [601] F. Zimmermann et al., *First Bunch Length Studies in the SLC South Final Focus*, Proc. EPAC 1998 Stockholm (1998)
10449 487.
- 10450 [602] C. Adolphsen et al., *Pulse-to-Pulse Stability Issues at the SLC*, Proc. IEEE PAC 1995 Dallas (1995) .
- 10451 [603] P. Chen and K. Yokoya, *Disruption Effects from the Interaction of Round $e+e-$ Beams*, Phys. Rev. D **38** (1988) 987.
- 10452 [604] M. Yamamoto, M. and Kuwahara, *Superlattice Photocathode Development for Low Emittance*, Photocathode Physics for
10453 Photoinjectors Workshop, BNL, October 2010 (2010) .
- 10454 [605] I. Bailey, *A Helical Undulator Based Positron Source for the International Linear Collider*, Proc. PoS HEP2005 (2006)
10455 368.
- 10456 [606] S. Araki et al., *Conceptual Design of a Polarised Positron Source Based on Laser Compton Scattering*,
10457 CARE/ELAN-Document-2005-013, CLIC Note 639, KEK Preprint 2005-60, LAL 05-94 (2005) , physics/0509016.
- 10458 [607] F. Zimmermann et al., *Stacking Simulations for Compton Positron Sources of Future Linear Colliders*, Proc. PAC'09
10459 Vancouver (2009) .
- 10460 [608] V. Litvinenko, *Recirculating Linac*, 2nd CERN-ECFA-NuPECC workshop on LHeC, Divonne-les-Bains (2009) .
- 10461 [609] I. Ginzburg, G. Kotkin, V. Serbo, and V. Telnov, *Colliding γe and $\gamma\gamma$ Beams Based on the Single Pass Accelerators (of
10462 VLEPP Type)*, Nucl. Instr. & Meth. **205** (1983) 47.
- 10463 [610] H. Burkhardt and V. Telnov, *CLIC 3-TeV Photon Collider Options*, CERN-SL-2002-013-AP, CLIC-Note-508 (2002) .
- 10464 [611] T. N. D. Group, *NLC Zeroth-Order Design Report for the Next Linear Collider, Appendix B*, LBNL-5424, SLAC-474,
10465 Appendix B (1996) .
- 10466 [612] Klemz, G. and Mönig, K. and Will, I. , *Design Study of an Optial Cavity for a Future Photon-Collider at ILC*, NIM A
10467 **564** (2006) 212.
- 10468 [613] H. Aksakal, Z. Nergiz, et al., *γp Option for LHeC*, Draft Note, October 2010 (2010) .
- 10469 [614] K. Yokoya, *CAIN: A Computer Simulation Code for the Interaction of Electron, Positron, Gamma Beams and Strong
10470 Lasers*, available at <http://lcdev.kek.jp/yokoya/CAIN> (2010) .
- 10471 [615] C. Johnstone, *Local chromaticity correction of the LHC*, PAC97 (1997) .
- 10472 [616] S. Fartoukh, *Optics Challenges and Solutions for the LHC Insertion Upgrade Phase I*, LHC Project Report 0038
10473 (2010) .
- 10474 [617] S. Fartoukh, *Towards the LHC Upgrade using the LHC well-characterized technology*, LHC Project Report 0049 (2010) .
- 10475 [618] P. Raimondi and A. Seryi, *Novel Final Focus Design for Future Linear Colliders*, Phys. Rev. Lett. **86** (2001) .
- 10476 [619] A. Gaddi, *Passive isolation*, Presented in IWLC 2010 (2010) .
- 10477 [620] A. Verdier, *Alignment optics for LHC*, LHC Project Note 325 (2003) .
- 10478 [621] D. Schulte, *Beam-Beam Simulations with GUINEA-PIG*, ICAP98 (1998) .
- 10479 [622] A. Bogacz, *LHeC Recirculator with Energy Recovery Beam Optics Choices*, CERN-LHeC-Note-2010-009 ACC,
10480 JLAB-TN-10-040 (2010) .
- 10481 [623] Y. Hao, K. D., V. Litvinenko, V. Ptitsyn, D. Trbojevic, and N. Tsoupas, *ERL Option for LHeC*,
10482 CERN-LHeC-Note-2010-010 ACC (2010) .
- 10483 [624] D. Schulte, *Multi-bunch calculations in the CLIC main linac*, PAC2009 Vancouver (2009) .
- 10484 [625] D. Schulte, *Simulation package beased on PLACET*, Proceedings PAC01, Chicago (2001) .
- 10485 [626] *International Linear Collider Reference Design Report*, ILC-Report-2007-001 (2007) .

- 10486 [627] I. Bazarov and G. Hoffstaetter, *Multi-pass Beam-breakup: Theory and Calculation*, EPAC2004 Lucerne (2004) .
- 10487 [628] D. Schulte, , to be published .
- 10488 [629] M. Schuh, , private communication .
- 10489 [630] F. Zimmermann, J. Byrd, A. Chao, S. Heifets, M. Minty, T. Raubenheimer, J. Seeman, S. G., and J. Thomson,
10490 *Experiments on the fast beam-ion instability at the ALS*, Report SLAC-PUB-7617 (1997) .
- 10491 [631] G. Hoffstaetter and M. Liepe, , NIM A **557** (2006) 205–212.
- 10492 [632] N. Hilleret, , Private communication .
- 10493 [633] B. Holzer, , Private communication .
- 10494 [634] V. Baglin, , Private communication .
- 10495 [635] F. Zimmermann et al., *CAIN: A Computer Simulation Code for the Interaction of Electron, Positron, Gamma Beams
10496 and Strong Lasers*, 3rd CERN-ECFA-NuPECC Workshop on the LHeC, <http://www.lhec.org.uk>, Nov. 12-13, 2010.
10497 (2010) .
- 10498 [636] L. Thomas, , Phil. Mag, **3** (1927) 1.
- 10499 [637] V. Ptitsin, *Symmetric Designs for Helical Spin Rotators at RHIC*, AGS/RHIC/SN No. 5 (1996) .
- 10500 [638] C. Yin Vallgren, A. Ashraf, S. Calatroni, P. Chiggiato, P. Costa Pinto, et al., *Low Secondary Electron Yield Carbon
10501 Coatings for Electron-cloud Mitigation in Modern Particle Accelerators*, .
- 10502 [639] C. Hauviller, *DEVELOPMENT OF COMPOSITE TUBES FOR EXPERIMENTAL VACUUM CHAMBERS OF
10503 COLLIDERS*, .
- 10504 [640] R. Appleby, L. Keller, T. W. Markiewicz, A. Seryi, D. Walz, et al., *The International linear collider beam dumps*,
10505 [arXiv:physics/0601103](https://arxiv.org/abs/physics/0601103) [physics].
- 10506 [641] J. Amann, R. Arnold, A. Seryi, D. Walz, K. Kulkarni, et al., *Design of an 18 MW Beam Dump for 500 GeV
10507 Electron/Positron Beams at an ILC*, .
- 10508 [642] M. Barnes, F. Caspers, L. Ducimetiere, N. Garrel, and T. Kroyer, *The beam screen for the LHC injection kicker
10509 magnets*, .
- 10510 [643] E. Carlier, U. Jansson, R. Jung, V. Mertens, S. Péraire, et al., *The LEP beam dumping system*, .
- 10511 [644] M. Klein, *The High Luminosity Design study for the LHC*, <https://espace.cern.ch/hl-lhc/default.aspx>.
- 10512 [645] E. Ciapala. Private communication, Edmund Ciapala, CERN, BE-RF group.
- 10513 [646] A. Yamamoto. <http://www.fnal.gov/directorate/ILCPAC/ILCPACNov2010/Yamamoto---cavityindustrialization.pdf>.
10514 Talk at ILC-PAC Eugene November 2010.
- 10515 [647] V. Mertens. Private communication, Volker Mertens, CERN, TE-ABT group.
- 10516 [648] J. Osborne. Private communication, John Osborne, CERN, GS-SE group.
- 10517 [649] *The XFEL construction calendar*. <http://www.xfel.eu/projekt/kalender/>.
- 10518 [650] M. Peininger. www.cockcroft.ac.uk/events/CSSA/presentations/Michael%20Peiniger.pdf. Talk at Cockcroft
10519 Institute seminar April 2011.
- 10520 [651] R. Ruber. www.isv.uu.se/~ziemann/teaching/ht10/ESS.pdf. Uppsala University.
- 10521 [652] *LINAC4 Project Page*. <http://linac4-project.web.cern.ch/linac4-project/>.
- 10522 [653] R. Ischebeck. www.cockcroft.ac.uk/events/eslsxvi/proceedings/psixfelischebeck.pdf. Talk given at the Sixteenth
10523 European Synchrotron Light Source workshop, England, Daresbury Laboratory, Crockcroft Institute, November 2008.
- 10524 [654] A. Mazzacane, *The 4th concept detector for the ILC*, Nucl.Instrum.Meth. **A617** (2010) 173–176.
- 10525 [655] M. Klein and R. Yoshida, *Collider Physics at HERA*, Prog.Part.Nucl.Phys. **61** (2008) 343–393, [arXiv:0805.3334](https://arxiv.org/abs/hep-ex/0805.3334)
10526 [hep-ex].
- 10527 [656] e. Pire, Bernard, e. Cirelli, Marco, e. Colas, Paul, e. Djouadi, Abdelhak, e. Lounis, Abdenour, et al., *High energy
10528 physics. Proceedings, 35th International Conference, ICHEP 2010, Paris, France, July 22-28, 2010*, .
- 10529 [657] e. Buchmuller, W. and e. Ingelman, G., *Physics at HERA. Proceedings, Workshop, Hamburg, Germany, October 29-30,
10530 1991. Vol. 1-3*, .
- 10531 [658] R. Gluckstern, *Uncertainties in track momentum and direction, due to multiple scattering and measurement errors*,
10532 Nucl.Instrum.Meth. **24** (1963) 381–389.
- 10533 [659] M. Regler, W. Mitaroff, M. Valentan, R. Fruhwirth, and R. Hofler, *The 'LiC Detector Toy' program*, J.Phys.Conf.Ser.
10534 **119** (2008) 032034.
- 10535 [660] P. Adragna, C. Alexa, K. Anderson, A. Antonaki, A. Arabidze, et al., *Measurement of pion and proton response and
10536 longitudinal shower profiles up to 20 nuclear interaction lengths with the ATLAS tile calorimeter*, Nucl.Instrum.Meth.
10537 **A615** (2010) 158–181.

- 10538 [661] ATLAS Collaboration, G. Aad et al., *The ATLAS Experiment at the CERN Large Hadron Collider*, JINST **3** (2008)
10539 S08003.
- 10540 [662] B. Holzer, , Private communication .
- 10541 [663] ATLAS Collaboration Collaboration, *ATLAS central solenoid: Technical design report*, . Hardcopy at DESY.
- 10542 [664] ATLAS Collaboration Collaboration, *ATLAS magnet system: Technical design report*, . Hardcopy at DESY.
- 10543 [665] *CMS, the Compact Muon Solenoid. Muon technical design report*, .
- 10544 [666] CMS Collaboration Collaboration, G. Acquistapace et al., *CMS, the magnet project: Technical design report*, .
- 10545 [667] E. Koffeman, *Gossip: Gaseous pixels*, Nucl.Instrum.Meth. **A582** (2007) 858–860.
- 10546 [668] H. van der Graaf, "Gossip and GridPix at LHeC", talk at 3rd CERN-ECFA-NuPECC Workshop on LHeC,
10547 Chavannes-de-Bogis, Switzerland, 12. November 2010.
10548 <http://indico.cern.ch/materialDisplay.py?contribId=51&sessionId=9&materialId=slides&confId=105142>.
- 10549 [669] H. van der Graaf, *Gaseous detectors*, Nucl.Instrum.Meth. **A628** (2011) 27–30.
- 10550 [670] R.Horrisberger, "Tracking at Phase II, Pixel, StriXel & Strips", CMS Tracker Week, La Biodola, Isola d'Elba 27. May
10551 2010.
- 10552 [671] R. Horrisberger, "Considerations for future Large Pixel Systems", talk CMS Pixel Detector Upgrade Workshop, FNAL
10553 10. October 2006.
- 10554 [672] P. Allport, "Conventional Silicon Pixel/Strip Tracker", talk at 3rd CERN-ECFA-NuPECC Workshop on LHeC,
10555 Chavannes-de-Bogis, Switzerland, 12. November 2010. <http://indico.cern.ch/getFile.py/access?contribId=50&sessionId=9&resId=0&materialId=slides&confId=105142>.
- 10556 [673] J. Brau, *The Science and Challenges for Future Detector Development in High Energy Physics*, .
- 10558 [674] N. Wermes, "Silicon Pixel Detectors for Tracking", talk at 1st CERN-ECFA Workshop on LHeC, Divonne-les-Bains,
10559 France, 1-3 September 2008.
10560 <http://indico.cern.ch/contributionDisplay.py?sessionId=19&contribId=63&confId=31463>.
- 10561 [675] ATLAS and CMS Collaboration, N. Hessey, *Overview and electronics needs of ATLAS and CMS high luminosity
10562 upgrades*, . <http://indico.cern.ch/getFile.py/access?contribId=140&sessionId=21&resId=0&materialId=paper&confId=21985>.
- 10563 [676] M. Nessi, "The Detector Upgrade and the Requirements on the Upgrade Scenarios".
10564 <http://cdsweb.cern.ch/record/1304568>.
- 10566 [677] C. Haber, "Lecture Silicon Detectors: Principles and Technology", talk at TIPP, Chicago, USA, June 2011. <https://indico.cern.ch/getFile.py/access?contribId=529&sessionId=25&resId=0&materialId=slides&confId=102998>.
- 10567 [678] D. Christian, "Semiconductor Detectors Overview", talk at TIPP, Chicago, USA, June 2011. <https://indico.cern.ch/getFile.py/access?contribId=527&sessionId=22&resId=1&materialId=slides&confId=102998>.
- 10568 [679] S. Cihanger, "Silicon sensor R&D for an upgraded CMS Tracker in HL-LHC", talk at TIPP, Chicago, USA, June
10571 2011. <https://indico.cern.ch/getFile.py/access?contribId=107&sessionId=22&resId=0&materialId=slides&confId=102998>.
- 10572 [680] A. Affolder, "Silicon Strip Detectors for the ATLAS sLHC Upgrade", talk at TIPP, Chicago, USA, June 2011.
10574 <https://indico.cern.ch/getFile.py/access?contribId=31&sessionId=22&resId=1&resmaterialId=slides&confId=102998>.
- 10575 [681] A. Macchiolo, "Performance of Silicon n-in-p Pixel Detectors irradiated up to 5^{15} n_{eq}/cm^2 for the future ATLAS
10576 Upgrades", talk at TIPP, Chicago, USA, June 2011. <https://indico.cern.ch/getFile.py/access?contribId=33&sessionId=22&resId=0&materialId=slides&confId=102998>.
- 10577 [682] U. Parzefall, "Silicon for High-Luminosity Tracking Detectors - Recent RD50 Results", talk at TIPP, Chicago, USA,
10580 June 2011. <https://indico.cern.ch/getFile.py/access?contribId=203&sessionId=22&resId=3&materialId=slides&confId=102998>.
- 10581 [683] I. Rubinskiy, "An EUDET/AIDA pixel beam telescope for detector development", talk at TIPP, Chicago, USA, June
10582 2011. <https://indico.cern.ch/getFile.py/access?contribId=25&sessionId=22&resId=0&materialId=slides&confId=102998>.
- 10583 [684] M. Bomben, "Recent progress of the ATLAS Planar Pixel Sensor R&D Project", talk at TIPP, Chicago, USA, June
10584 2011. <https://indico.cern.ch/getFile.py/access?contribId=436&sessionId=22&resId=0&materialId=slides&confId=102998>.
- 10585 [685] M. Mikuz, "Diamond for high energy radiation and particle detection", talk at TIPP, Chicago, USA, June 2011.
10588 <https://indico.cern.ch/getFile.py/access?contribId=463&sessionId=22&resId=1&materialId=slides&confId=102998>.
- 10589 [686] A. Mac Raighne, "3D pixel devices; design, production and characterisation in test beams", talk at TIPP, Chicago,
10591 USA, June 2011. <https://indico.cern.ch/getFile.py/access?contribId=249&sessionId=22&resId=1&materialId=slides&confId=102998>.
- 10592
10593

- 10594 [687] M. Garcia-Sciveres, "ATLAS pixels for 2017/18", talk at ACES 2011 Workshop, CERN 9. March 2011.
- 10595 [688] K.K.Gan, F.Vasey, T.Weidberg "Lessons Learned and to be Learned from LHC", talk at Joint ATLAS-CMS Working
10596 Group on Opto-Electronics for SLHC, Report from Sub-Group A, Joint ATLAS/CMS NOTE,
10597 ATL-COM-ELEC-2007-001. <https://edms.cern.ch/document/882775/3.8>.
- 10598 [689] A. Bell, E. Castro, R. Hall-Wilton, W. Lange, W. Lohmann, et al., *Fast Beam Conditions Monitor BCM1F for the
10599 CMS Experiment*, Nucl.Instrum.Meth. **A614** (2010) 433–438, [arXiv:0911.2480](https://arxiv.org/abs/0911.2480) [physics.ins-det].
- 10600 [690] L. Fernandez Hernando, D. Chong, R. Gray, C. Ilgner, A. Macpherson, et al., *Development of a CVD diamond beam
10601 condition monitor for CMS at the Large Hadron Collider*, Nucl.Instrum.Meth. **A552** (2005) 183–188.
- 10602 [691] A. Macpherson, *Beam Condition Monitoring and radiation damage concerns of the experiment, talk at ICHEP 2010,
10603 Paris, France, .*
- 10604 [692] D. Chong, L. Fernandez-Hernando, R. Gray, C. J. Ilgner, A. Oh, et al., *Validation of synthetic diamond for a beam
10605 condition monitor for the Compact Muon Solenoid experiment*, IEEE Trans.Nucl.Sci. **54** (2007) 182–185.
- 10606 [693] GEANT4 Collaboration, S. Agostinelli et al., *GEANT4: A Simulation toolkit*, Nucl.Instrum.Meth. **A506** (2003)
10607 250–303.
- 10608 [694] R. Brun and F. Rademakers, *ROOT - An Object Oriented Data Analysis Framework, Proceedings AIHENP'96
10609 Workshop, Lausanne, Sep. 1996*, Nucl. Inst. & Meth. in Phys. Res. A 389 (1997) 81–86.
- 10610 [695] R. Chytraccek, J. McCormick, W. Pokorski, and S. G., *Geometry Description Markup Language for Physics Simulation
10611 and Analysis Applications*, IEEE Trans. Nucl. Sci. **Vol. 53, Issue: 5, Part 2** 2892–2896.
- 10612 [696] V. V. Serbo, *Status of AIDA and JAS 3*, Nuclear Instruments and Methods in Physics Research Section A:
10613 Accelerators, Spectrometers, Detectors and Associated Equipment **502** (2003) no. 2-3, 663 – 665.
10614 <http://www.sciencedirect.com/science/article/pii/S0168900203005370>. Proceedings of the VIII International
10615 Workshop on Advanced Computing and Analysis Techniques in Physics Research.
- 10616 [697] A. Vasilescu and L. G., *Displacement damage in Silicon for neutrons, protons, pions, and electrons, .
10617 http://sesam.desy.de/members/gunnar/NIEL-allr.ps*.
- 10618 [698] F. Carminati and A. Morsch, *Simulation in ALICE*, [arXiv:physics/0306092](https://arxiv.org/abs/physics/0306092) [physics]. On behalf of the ALICE
10619 Offline Project.
- 10620 [699] ALICE Collaboration, I. Hrivnacova et al., *The Virtual Monte Carlo*, [arXiv:cs/0306005](https://arxiv.org/abs/cs/0306005) [cs-se].
- 10621 [700] ALICE Collaboration, I. Gonzalez Caballero, F. Carminati, A. Morsch, and I. Hrivnacova, *ALICE experience with
10622 GEANT4*, [arXiv:physics/0306025](https://arxiv.org/abs/physics/0306025) [physics].
- 10623 [701] J. Hauptman, *Particle Identification in 4th*, [arXiv:0812.3571](https://arxiv.org/abs/0812.3571) [hep-ex].
- 10624 [702] D. Green, *How physics defines the LHC environment and detectors*, Int.J.Mod.Phys. **A25** (2010) 1279–1313.
- 10625 [703] J. Freeman, *Innovations for the CMS HCAL*, Int.J.Mod.Phys. **A25** (2010) 2421–2436.
- 10626 [704] L. Mandelli, *The ATLAS electromagnetic calorimeters: Features and performance*, Int.J.Mod.Phys. **A25** (2010)
10627 1739–1760.
- 10628 [705] P. Bloch, *The CMS electromagnetic calorimeter: Crystals and APD productions*, Mod.Phys.Lett. **A25** (2010)
10629 1027–1045.
- 10630 [706] K. Anderson, T. Del Prete, E. Fullana, J. Huston, C. Roda, et al., *TileCal: The hadronic section of the central ATLAS
10631 calorimeter*, Int.J.Mod.Phys. **A25** (2010) 1981–2003.
- 10632 [707] H1 Collaboration, A. Babaev, *Performance of the H1 liquid argon calorimeter, .*
- 10633 [708] H1 Collaboration, I. Abt et al., *The H1 detector at HERA*, Nucl.Instrum.Meth. **A386** (1997) 310–347.
- 10634 [709] M. Fleischer, M. Keller, K. Meier, O. Nix, G. Schmidt, et al., *Performance and upgrade of H1 calorimeters: LAr
10635 calorimeter, SpaCal and VLQ, .*
- 10636 [710] C. Issever, *The calibration of the H1 liquid argon calorimeter, .*
- 10637 [711] H1 collaboration Collaboration, C. Schwanenberger, *The Jet calibration in the H1 liquid argon calorimeter,
10638 arXiv:physics/0209026 [physics].*
- 10639 [712] J. Seehafer, *Simulation of hadronic showers in the H1 liquid argon calorimeter with the simulation programs GHEISHA
10640 and CALOR, .*
- 10641 [713] C. Kiesling, A. Dubak, and B. Olivier, *The liquid argon jet trigger of the H1 experiment at HERA*, Nucl.Instrum.Meth.
10642 **A623** (2010) 513–515.
- 10643 [714] ATLAS Electromagnetic Barrel Liquid Argon Calorimeter Group Collaboration, B. Aubert et al., *Construction,
10644 assembly and tests of the ATLAS electromagnetic barrel calorimeter*, Nucl.Instrum.Meth. **A558** (2006) 388–418.
- 10645 [715] ATLAS Collaboration, A. Airapetian et al., *ATLAS calorimeter performance Technical Design Report, .*
- 10646 [716] O. Gildemeister, F. Nessi-Tedaldi, and M. Nessi, *An economic concept for a barrel hadron calorimeter with iron
10647 scintillator sampling and WLS-fiber readout, .*

- 10648 [717] I. Golutvin, B. Borgia, F. Carminati, M. Della Negra, S. Giani, et al., *A Silicon hadron calorimeter module operated in*
10649 *a strong magnetic field with VLSI readout for LHC*, .
- 10650 [718] OPAL Collaboration, B. Anderson et al., *The OPAL silicon - tungsten calorimeter front end electronics*, IEEE
10651 *Trans.Nucl.Sci.* **41** (1994) 845–852.
- 10652 [719] J. Adams, G. Bashindzhagian, V. Zatsepin, M. Merkin, M. Panasyuk, et al., *The silicon matrix as a charge detector for*
10653 *the ATIC experiment*, *Instrum.Exp.Tech.* **44** (2001) 455–461.
- 10654 [720] V. Zatsepin, J. Adams, H. Ahn, G. Bashindzhagian, K. Batkov, et al., *Experience of application of silicon matrix as a*
10655 *charge detector in the ATIC experiment*, .
- 10656 [721] V. Bonvicini, M. Boezio, E. Haslum, D. Matveev, M. Pearce, et al., *New concepts in silicon calorimetry for space*
10657 *experiments*, *Nucl.Instrum.Meth.* **A518** (2004) 186–187.
- 10658 [722] V. Bonvicini, A. Vacchi, V. Dzhorzhadze, R. Seto, E. Kistenev, et al., *Silicon-tungsten calorimeter for the forward*
10659 *direction in the PHENIX experiment at RHIC*, *IEEE Trans.Nucl.Sci.* **52** (2005) 874–878.
- 10660 [723] D. Strom "Silicon Tungsten Calorimetry", talk at SLAC Meeting, 8 January 2004.
- 10661 [724] D. M. Strom, R. Frey, M. Breidenbach, D. Freytag, N. Graf, et al., *Fine grained silicon-tungsten calorimetry for a*
10662 *linear collider detector*, *IEEE Trans.Nucl.Sci.* **52** (2005) 868–873.
- 10663 [725] A. Kaidalov and K. Ter-Martirosian, *Pomeron as Quark-Gluon Strings and Multiple Hadron Production at SPS*
10664 *Collider Energies*, *Phys.Lett.* **B117** (1982) 247–251.
- 10665 [726] M. Barbi "Calorimetry - 3rd course", talk at TRIUMF Summer Institute, July 2007.
- 10666 [727] C. Leroy and P. Rancoita, *Physics of cascading shower generation and propagation in matter: Principles of*
10667 *high-energy, ultrahigh-energy and compensating calorimetry*, *Rept.Prog.Phys.* **63** (2000) 505–606.
- 10668 [728] G. Barbiellini, G. Cecchet, J. Hemery, F. Lemeilleur, C. Leroy, et al., *ENERGY RESOLUTION AND*
10669 *LONGITUDINAL SHOWER DEVELOPMENT IN A Si/ W ELECTROMAGNETIC CALORIMETER*,
10670 *Nucl.Instrum.Meth.* **A235** (1985) 55.
- 10671 [729] J.-C. Brient and H. Videau, *The Calorimetry at the future e+ e- linear collider*, [arXiv:hep-ex/0202004](https://arxiv.org/abs/hep-ex/0202004) [hep-ex].
- 10672 [730] V. Morgunov, *Calorimetry design with energy-flow concept (imaging detector for high-energy physics)*, .
- 10673 [731] S. R. Magill, *Innovations in ILC detector design using a particle flow algorithm approach*, *New J.Phys.* **9** (2007) 409.
- 10674 [732] R. Wigmans, *Recent results from the DREAM project*, *J.Phys.Conf.Ser.* **160** (2009) 012018.
- 10675 [733] J. Hauptman, *Particle physics experiments at high energy colliders*, .
- 10676 [734] G. Gaudio and R. Wigmans, *Dual-Readout Calorimetry for High-Quality Energy Measurements*,
10677 *CERN-SPSC-2011-021/SPSC-SR-086/June 2011*.
- 10678 [735] G. Mikenberg, *The ATLAS muon spectrometer*, *Mod.Phys.Lett.* **A25** (2010) 649–667.
- 10679 [736] F. Gasparini, *The CMS muon detector: From the first thoughts to the final design*, *Int.J.Mod.Phys.* **A25** (2010)
10680 3121–3154.
- 10681 [737] J. Burnens, R. de Oliveira, G. Glonti, O. Pizzirusso, V. Polychronakos, et al., *A spark-resistant bulk-micromegas*
10682 *chamber for high-rate applications*, [arXiv:1011.5370](https://arxiv.org/abs/1011.5370) [physics.ins-det]. * Temporary entry *.
- 10683 [738] B. Bittner, J. Dubbert, S. Horvat, M. Kilgenstein, O. Kortner, et al., *Development of precision muon drift tube*
10684 *detectors for the high-luminosity upgrade of the LHC*, *Nucl.Phys.Proc.Suppl.* **215** (2011) 143–146.
- 10685 [739] H1 Collaboration, T. Ahmed et al., *Experimental Study of Hard Photon Radiation Processes at HERA*, *Z. Phys.* **C66**
10686 (1995) 529–542.
- 10687 [740] V. Andreev et al., *The new H1 luminosity system for HERA II*, *Nucl. Instrum. Meth.* **A494** (2002) 45–50.
- 10688 [741] ZEUS Luminosity Group Collaboration, J. Andruskow et al., *Luminosity measurement in the ZEUS experiment*, *Acta*
10689 *Phys. Polon.* **B32** (2001) 2025–2058.
- 10690 [742] ZEUS Collaboration, S. D. Paganis, *The upgraded luminosity system for the ZEUS experiment*, *Int. J. Mod. Phys.*
10691 **A16S1C** (2001) 1147–1149.
- 10692 [743] G. A. Schuler and H. Spiesberger, *DJANGO: The Interface for the event generators HERACLES and LEPTO*, . In
10693 *Hamburg 1991, Proceedings, Physics at HERA, vol. 3* 1419–1432. (see HIGH ENERGY PHYSICS INDEX 30 (1992)
10694 No. 12988).
- 10695 [744] A. Courau and P. Kessler, *QED Compton scattering in high-energy electron - proton collisions*, *Phys. Rev.* **D46** (1992)
10696 117–124.
- 10697 [745] S. Levonian, *H1LUMI - A Fast Simulation Package for the H1 Luminosity System*, . H1 internal note h1-0493-287
10698 (1993); <http://www.desy.de/~levonian/papers/H1lumi.pdf>.
- 10699 [746] R. Brun, M. Caillat, M. Maire, G. N. Patrick, and L. Urban, *THE GEANT3 ELECTROMAGNETIC SHOWER*
10700 *PROGRAM AND A COMPARISON WITH THE EGS3 CODE*, . CERN-DD/85/1.

- 10701 [747] ZEUS FNC Group Collaboration, S. Bhadra et al., *Design and test of a forward neutron calorimeter for the ZEUS*
10702 *experiment*, Nucl. Instrum. Meth. **A394** (1997) 121–135, [arXiv:hep-ex/9701015](#).
- 10703 [748] R. Arnaldi et al., *The Zero Degree Calorimeters for the ALICE Experiment*, Nucl. Instrum. Meth. **A581** (2007)
10704 397–401.
- 10705 [749] ALICE Collaboration, N. De Marco et al., *Commissioning and calibration of the zero degree calorimeters for the ALICE*
10706 *experiment*, J. Phys. Conf. Ser. **160** (2009) 012060.
- 10707 [750] A. Collaboration, *Zero degree calorimeters for ATLAS*, . CERN-LHCC-2007-01.
- 10708 [751] O. Grachov et al., *Commissioning of the CMS zero degree calorimeter using LHC beam*, [arXiv:1008.1157](#)
10709 [[physics.ins-det](#)].
- 10710 [752] LHCf Collaboration, O. Adriani et al., *The LHCf detector at the CERN Large Hadron Collider*, JINST **3** (2008) S08006.
- 10711 [753] A. Breskin et al., *The THGEM: A thick robust gaseous electron multiplier for radiation detectors*, Nucl. Instrum. Meth.
10712 **A623** (2010) 132–134.
- 10713 [754] V. Inshakov et al., *Development of detector active element based on thgem*, [arXiv:0906.4441](#) [[physics.ins-det](#)].
- 10714 [755] H. Mais and G. Ripken Tech. Rep. 83-62, DESY, 1983. Modern notation: replace \vec{n} by \vec{n}_0 .

10715 Appendix

10716 Scientific Advisory Committee

- 10717 Guido Altarelli (Roma)
- 10718 Sergio Bertolucci (CERN)
- 10719 Stan Brodsky (SLAC)
- 10720 Allen Caldwell (MPI Muenchen) - Chair
- 10721 Swapan Chattopadhyay (Cockcroft Institute)
- 10722 John Dainton (Liverpool)
- 10723 John Ellis (CERN)
- 10724 Jos Engelen (NWO)
- 10725 Joel Feltesse (Saclay)
- 10726 Roland Garoby (CERN)
- 10727 Rolf Heuer (CERN)
- 10728 Roland Horisberger (PSI)
- 10729 Young-Kee Kim (Fermilab)
- 10730 Aharon Levy (Tel Aviv)
- 10731 Lev Lipatov (St. Petersburg)
- 10732 Karlheinz Meier (Heidelberg)
- 10733 Richard Milner (MIT)
- 10734 Joachim Mnich (DESY)
- 10735 Steve Myers (CERN)
- 10736 Guenther Rosner (Glasgow)
- 10737 Alexander N. Skrinsky (INP Novosibirsk)
- 10738 Anthony Thomas (JLab)
- 10739 Steve Vigdor (Brookhaven)
- 10740 Ferdinand Willeke (Brookhaven)
- 10741 Frank Wilczek (MIT)
- 10742

10743

Steering Committee

- 10744 Oliver Bruening(CERN)
- 10745 John Dainton (Liverpool)
- 10746 Albert De Roeck (CERN)
- 10747 Stefano Forte (Milano)
- 10748 Max Klein (Liverpool) - Chair
- 10749 Paul Laycock (Liverpool)
- 10750 Paul Newman (Birmingham)
- 10751 Emmanuelle Perez (CERN)
- 10752 Wesley Smith (Wisconsin)
- 10753 Bernd Surrow (MIT)
- 10754 Katsuo Tokushuku (KEK)
- 10755 Urs Wiedemann (CERN)
- 10756 Frank Zimmermann (CERN)

10757 **Working Group Convenors**

10758 **Accelerator Design**

10759 Oliver Bruening (CERN)
10760 John Dainton (Liverpool)
10761

10762 **Interaction Region and Fwd/Bwd**

10763 Bernhard Holzer(CERN)
10764 Uwe Schneekloth (DESY)
10765 Pierre van Mechelen (Antwerpen)
10766

10767 **Detector Design**

10768 Peter Kostka (DESY)
10769 Alessandro Polini (Bologna)
10770 Rainer Wallny (Zurich)
10771

10772 **New Physics at Large Scales**

10773 Georges Azuelos (Montreal)
10774 Emmanuelle Perez (CERN)
10775 Georg Weiglein (Hamburg)
10776

10777 **Precision QCD and Electroweak**

10778 Olaf Behnke (DESY)
10779 Paolo Gambino (Torino)
10780 Thomas Gehrmann (Zurich)
10781 Claire Gwenlan (Oxford)
10782

10783 **Physics at High Parton Densities**

10784 Néstor Armesto (Santiago de Compostela)
10785 Brian A. Cole (Columbia)
10786 Paul R. Newman (Birmingham)
10787 Anna M. Stasto (PennState)

10788 **Referees of the Draft Report (Summer 2011)**

- 10789 **Ring Ring Design**
- 10790 Kurt Huebner (CERN)
- 10791 Alexander N. Skrinsky (INP Novosibirsk)
- 10792 Ferdinand Willeke (BNL)
- 10793 **Linac Ring Design**
- 10794 Reinhard Brinkmann (DESY)
- 10795 Andy Wolski (Cockcroft)
- 10796 Kaoru Yokoya (KEK)
- 10797 **Energy Recovery**
- 10798 Georg Hoffstaetter (Cornell)
- 10799 Ilan Ben Zvi (BNL)
- 10800 **Magnets**
- 10801 Neil Marks (Cockcroft)
- 10802 Martin Wilson (??)
- 10803 **Interaction Region**
- 10804 Daniel Pitzl (DESY)
- 10805 Mike Sullivan (SLAC)
- 10806 **Detector Design**
- 10807 Philippe Bloch (CERN)
- 10808 Roland Horisberger (PSI)
- 10809 **Installation and Infrastructure**
- 10810 Sylvain Weisz (CERN)
- 10811 **New Physics at Large Scales**
- 10812 Cristinel Diaconu (IN2P3 Marseille)
- 10813 Gian Giudice (CERN)
- 10814 Michelangelo Mangano (CERN)
- 10815 **Precision QCD and Electroweak**
- 10816 Guido Altarelli (Roma)
- 10817 Vladimir Chekelian (MPI Munich)
- 10818 Alan Martin (Durham)
- 10819 **Physics at High Parton Densities**
- 10820 Alfred Mueller (Columbia)
- 10821 Raju Venugopalan (BNL)
- 10822 Michele Arneodo (INFN Torino)